

UNCLASSIFIED

AD NUMBER	
AD384923	
CLASSIFICATION CHANGES	
TO:	UNCLASSIFIED
FROM:	CONFIDENTIAL
LIMITATION CHANGES	
TO: Approved for public release; distribution is unlimited.	
FROM: Distribution authorized to U.S. Gov't. agencies only; Administrative/Operational Use; AUG 1967. Other requests shall be referred to U.S. Army Aviation Materiel Laboratories, Fort Eustis, VA 237604.	
AUTHORITY	
USAAML ltr dtd 12 Feb 1971; USAAML ltr dtd 12 Feb 1971	

THIS PAGE IS UNCLASSIFIED

UNCLASSIFIED

AD

AD 384923

USAAVLABS TECHNICAL REPORT 67-30
ELEMENT DESIGN AND DEVELOPMENT
OF
SMALL CENTRIFUGAL COMPRESSOR (U)

VOLUME I

By
A. D. Welliver
J. Acurio

August 1967

U. S. ARMY AVIATION MATERIEL LABORATORIES
FORT EUSTIS, VIRGINIA

CONTRACT DA 44-177-AMC-173(T)

THE BOEING COMPANY
SEATTLE, WASHINGTON

This material contains information affecting
the national defense of the United States
within the meaning of the Espionage Laws
(18 U. S.
or reveal
unauthori

Downgraded from CONFIDENTIAL to Unclassified
- will appear in TAD 69-5 dated 1 March 1969
(cited in letter from DSC-NS dated
23 January 1969)

Fred J. Galante
Fred J. Galante FPS 24 January 1969

In addition to security requirements which
apply to this document and must be met, each
transmittal outside the agencies of the US
Government must have prior approval of US
Army Aviation Materiel Laboratories, Fort
Eustis, Virginia 23604.

UNCLASSIFIED

12 of 96 Copies

Disclaimers

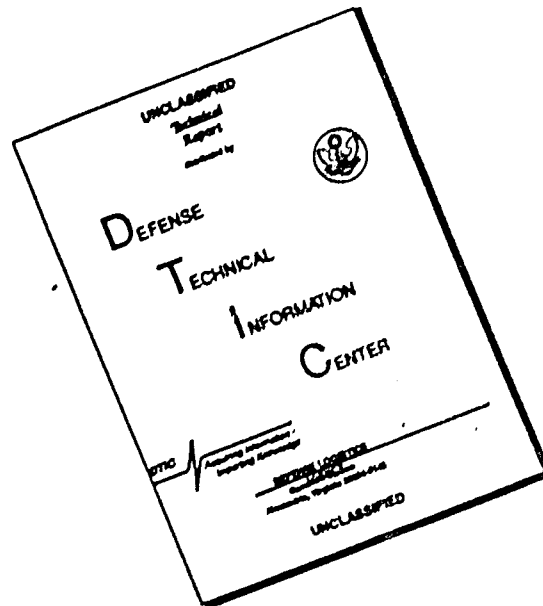
When Government drawings, specifications, or other data are used for any purpose other than in connection with a definitely related Government procurement operation, the United States Government thereby incurs no responsibility nor any obligation whatsoever; and the fact that the Government may have formulated, furnished, or in any way supplied the said drawings, specifications, or other data is not to be regarded by implication or otherwise as in any manner licensing the holder or any other person or corporation, or conveying any rights or permission, to manufacture, use, or sell any patented invention that may in any way be related thereto.

Trade names cited in this report do not constitute an official endorsement or approval of the use of such commercial hardware or software.

Disposition Instructions

When this report is no longer needed, Department of the Army organizations will destroy it in accordance with the procedures given in AR 380-5.

DISCLAIMER NOTICE



THIS DOCUMENT IS BEST QUALITY AVAILABLE. THE COPY FURNISHED TO DTIC CONTAINED A SIGNIFICANT NUMBER OF PAGES WHICH DO NOT REPRODUCE LEGIBLY.

UNCLASSIFIED



DEPARTMENT OF THE ARMY
U. S. ARMY AVIATION MATERIEL LABORATORIES
FORT EUSTIS, VIRGINIA 23604

(U) This Command has reviewed this report and concurs with the conclusions contained herein. The findings and recommendations as outlined in this report will be further considered and defined in a subsequent research report entitled "Design and Development of Small, Single-Stage Centrifugal Compressor."

MISSING PAGE NUMBERS ARE BLANK

UNCLASSIFIED

UNCLASSIFIED

Task 1M121401D14413
Contract DA 44-177-AMC-173(T)
USAAVLABS Technical Report 67-30
August 1967

ELEMENT DESIGN AND DEVELOPMENT
OF
SMALL CENTRIFUGAL COMPRESSOR (U)
VOLUME I

D4-3434

by

A. D. Welliver

J. Acurio

Prepared by

The Boeing Company
Seattle, Washington

This material contains information affecting
the national defense of the United States
within the meaning of the Espionage Laws
(18 U.S.C. 793 and 794), the transmission
or revelation of which in any manner to an
unauthorized person is prohibited by law.

for

U. S. ARMY AVIATION MATERIEL LABORATORIES
FORT EUSTIS, VIRGINIA

In addition to security requirements which
apply to this document and must be met, each
transmittal outside the agencies of the US
Government must have prior approval of US
Army Aviation Materiel Laboratories, Fort
Eustis, Virginia 23604.

Dissemination Control
Mark

UNCLASSIFIED

REF ID: A13113

Individual pages of Sections 2.0, 6.0, and 7.0 are unclassified; however, when compiled in complete sections, such material is classified as confidential.

13113

ii

REF ID: A13113

CONFIDENTIAL

(C) ABSTRACT (U)

The purpose of this research program was to define, by analysis and experimental evaluations, the design criteria and performance characteristics of a high-pressure-ratio, single-stage centrifugal compressor. The overall performance target was a pressure ratio of 10:1 at an efficiency of 80 percent and at an airflow rate of 2.0 pounds per second. The research was expected to lead to development of advanced technology, applicable to small gas-turbine engines.

The research plan was to design 4 impellers and 4 diffusers using the best available knowledge. The components were to be tested and the design methods evaluated. Further tests were to be conducted with modified components to evaluate improvements in the design methods and add to the basic understanding.

Each impeller was designed to provide a total-to-total pressure ratio of about 13:1 at a tip speed of 2000 fps, resulting in an absolute Mach number leaving the impeller of about 1.3. The inducers were designed with inlet-relative Mach numbers from 0.95 to 1.23, and the selected impeller diameters were from 6.0 to 8.0 inches.

The diffusers were designed to match the impeller discharge Mach number of 1.3. Water-table studies were conducted with diffuser models to develop preliminary evaluations of the flow characteristics. Four diffuser models were selected for test with the same impeller. The diffuser test rig was instrumented with schlieren photography to evaluate the shock system of the diffuser. Diffuser models were designed to vary vaneless-space-diameter ratio, throat Mach number and throat area for investigating flow behavior and variable-airflow-capacity as a means of improving part load fuel consumption.

From test results, best total-to-total pressure ratio was 10:1 for the research impellers and 11.6:1 for the diffuser research impeller, which was 1 to 2 atmospheres below the target. Based on these results, methods for predicting performance and evaluating the flow characteristics of the impellers were reviewed. A revised flow model was developed to account for differences in flow behavior for several impellers, including two from previous research programs.

Diffuser performance equal to the design requirements was demonstrated during compressor tests. A flow model created for the diffuser showed that the streamlines through the vaneless space did not follow a conventional free-vortex distribution. Instead, only modest diffusion took place in the vaneless and semivaneless spaces. Just before the vanes, a shock occurred which produced a subsonic Mach number in the channel throat. Single-channel diffuser tests were also conducted to obtain basic channel performance data. These tests showed, contrary to the available literature, that for two-dimensional-channel diffusers, performance was nearly constant to a throat Mach number of 1.0. This finding was a

UNCLASSIFIED

significant contribution to the fundamental understanding of subsonic two-dimensional diffusers and provided new information for channel design.

It was concluded from this compressor research program that there are no known fundamental reasons preventing the development of a high-pressure-ratio centrifugal stage. Overall compressor pressure ratios of 9.4:1 at efficiency levels of 72 percent were demonstrated. Principal performance deficiencies of the compressor were identified as impeller exit mixing and the diffuser channel loss. Although the diffuser met the original performance target, the research has shown that further improvement must be expected. Design methods were established which led to a new compressor to be presented in a follow-on report.

Although the targeted efficiency was not demonstrated in tests of the overall compressor, significant new technology was established, producing understanding of transonic flows in impellers and diffusers.

UNCLASSIFIED

(U) FOREWORD

The program reported in this document was conducted for the U. S. Army Aviation Materiel Laboratories (USAAVLABS) and was authorized by Task 1M121402D14413 under contract DA 44-177-AMC-173(T) in May, 1964. The work involved research aimed at advancing the technology of high-pressure-ratio centrifugal compressors; it was performed concurrently with similar programs related to high-temperature turbines and compact, lightweight regenerators for small gas-turbine engines.

This report covers basic studies, analyses, and experimental evaluations of impellers and diffusers designed to provide technologies for achieving a single-stage pressure ratio of 10:1 at an adiabatic efficiency of 80 percent. A follow-on report, USAAVLABS Technical Report 67-47 "Design and Development of Small, Single-Stage Centrifugal Compressor" (U) (Classified Confidential) covers the application and evaluation of these technologies for a complete compressor.

Portions of the report have been classified, inasmuch as they present new theories on flow phenomena throughout the compressor. Sections so designated are as follows:

Summary;

Section 2.0, Analytical Studies;

Section 6.0, Test Results;

Section 7.0, Evaluation of Test Results;

Appendix I, Impeller Radial-Equilibrium Design;

Appendix X, Schlieren Photographs.

Acknowledgment is given to Mr. LeRoy H. Hubert, Project Engineer for USAAVLABS, and to the following individuals from The Boeing Company who assisted in the preparation of material contained in this report: Messrs. D. F. Allred, Design Engineer; S. L. Bryant, Design Engineer; H. H. Burlingame, Instrumentation Engineer; T. D. Cohen, Instrumentation Engineer; C. R. Johnson, Test Engineer; C. M. Lewis, Stress Engineer; P. G. Schorr, Compressor Research Engineer; R. C. Walker, Instrumentation Engineer; and L. J. Winslow, Compressor Research Engineer.

For their assistance and efforts in specialized areas of research, credit is given to Dr. R. C. Dean and Dr. P. W. Runstadler, both of Creare, Incorporated, Hanover, New Hampshire.

(U) CONTENTS

	<u>Page</u>
ABSTRACT	iii
FOREWORD	v
LIST OF ILLUSTRATIONS	ix
LIST OF TABLES	xxiv
SYMBOLS	xxxvii
SUMMARY	1
1.0 INTRODUCTION	7
1.1 Objective	7
1.2 Previous Related Experience	10
1.3 Research Approach	12
2.0 ANALYTICAL STUDIES	17
2.1 Preliminary Design Requirements	17
2.2 Impeller Design	30
2.3 Diffuser Design	103
2.4 Mechanical Design	158
3.0 FABRICATION OF RESEARCH COMPONENTS	211
3.1 Impellers	211
3.2 Impeller Test Sections	218
3.3 Diffusers	225
3.4 Diffuser Test Sections	233

CONTENTS (Continued)

	<u>Page</u>
4.0 INSTRUMENTATION	241
4.1 Pressure-Measurement Instrumentation	241
4.2 Temperature-Measurement Probes	254
4.3 Impeller-Stress Measurement	254
4.4 Rotor-Thrust Measurement	262
4.5 Other Special Instrumentation	266
5.0 TEST EQUIPMENT AND PROCEDURES	273
5.1 Impeller Test Rig	273
5.2 Diffuser Test Rig	273
5.3 Support Equipment	278
5.4 Performance Data Acquisition	286
5.5 Test-Rig Operating Procedures	299
6.0 TEST RESULTS	319
6.1 Impellers	319
6.2 Diffusers	333
7.0 EVALUATION OF TEST RESULTS	541
7.1 Impeller Tests	541
7.2 Diffuser Tests	603
REFERENCES	675
APPENDIXES I through XII. Presented in Volume II.	
DISTRIBUTION	679

(U) ILLUSTRATIONS

<u>Figure</u>		<u>Page</u>
SECTION 1.0		
1	Effect of Compressor Performance on Simple-Cycle Engine	8
2	Effect of Compressor Performance on Regenerative Engine	9
3	Effect of Cycle Temperature and Pressure on Part-Load SFC	11
4	Single-Stage Centrifugal Compressor	13
5	Single-Stage Centrifugal Compressor With Redesigned Impeller	14
SECTION 2.0		
6	Typical Single-Stage Centrifugal Compressor	18
7	Comparison of Inducer Recovery With Transonic Axial Rotor Recovery	20
8	Comparison of Pressure Profile for Two Impellers	22
9	Impellers With Equal Blade Spacing at Inducer Hub	23
10	Mixed-Flow Impeller (Meridional View)	25
11	Diffuser Flow With Supersonic Inlet Velocity	27
12	Single-Stage Centrifugal Compressor (Variable-Flow-Capacity Demonstration; Reduced Diffuser Flow Areas With Inlet Guide Vane Adjustments)	29
13	Euler Work Relation	32
14	Inducer-Inlet Velocity Diagram.	34
15	Inducer Geometry.	34

ILLUSTRATIONS (Continued)

<u>Figure</u>		<u>Page</u>
16	Impeller Parameters (Overall P/P = 10:1, $\eta = 80$ Percent, $M_1 = 0.50$)	37
17	Comparison of Extrapolated Performance for Mixed- and Radial-Flow Impellers.	39
18	Comparison of Inducer Leading-Edge Blade Shapes	43
19	Inlet Velocity Diagrams for MF-1 Impeller Design	46
20	Diffusion Factor for MF-1 Impeller	47
21	Exit Velocity Diagrams for MF-1 Impeller	48
22	Meridional View of MF-1 Impeller	49
23	Impeller Design Parameters for MF-1; Design Speed, 57,000 rpm	50
24	Static-Pressure Distribution Across Passage, MF-1 Impeller; Design Speed, 57,000 rpm	51
25	Predicted Static-Pressure Rise Along MF-1 Impeller Shroud, Design Speed, 57,000 rpm	52
26	Blade-Surface Velocities of MF-1 Impeller; Design Speed, 57,000 rpm	53
27	Exit Flow Conditions for MF-1 Impeller; Design Speed, 57,000 rpm	54
28	Predicted Static-Pressure Rise Along MF-1 Impeller Shroud, Part Speed	55
29	Blade-Surface Velocities of MF-1 Impeller; 90-Percent Design Speed, 51,300 rpm	56
30	Blade-Surface Velocities of MF-1 Impeller; 80-Percent Design Speed, 45,600 rpm	57
31	Blade-Surface Velocities of MF-1 Impeller; 60-Percent Design Speed, 34,200 rpm	58

ILLUSTRATIONS (Continued)

<u>Figure</u>		<u>Page</u>
32	Inlet Velocity Diagrams for MF-2 Impeller Design . . .	59
33	Diffusion Factor for MF-2 Impeller	60
34	Exit Velocity Diagrams for MF-2 Impeller	61
35	Meridional View of MF-2 Impeller	62
36	Impeller Design Parameters for MF-2; Design Speed, 73,000 rpm	63
37	Static-Pressure Distribution Across Passage, MF-2 Impeller; Design Speed, 73,000 rpm	64
38	Predicted Static-Pressure Rise Along MF-2 Impeller Shroud; Design Speed, 73,000 rpm	65
39	Blade-Surface Velocities of MF-2 Impeller; Design Speed, 73,000 rpm	66
40	Exit Flow Conditions for MF-2 Impeller; Design Speed, 73,000 rpm	67
41	Predicted Static-Pressure Rise Along MF-2 Impeller Shroud, Part Speed	68
42	Blade-Surface Velocities of MF-2 Impeller; 90-Percent Design Speed, 65,700 rpm	69
43	Blade-Surface Velocities of MF-2 Impeller; 80-Percent Design Speed, 58,400 rpm	70
44	Blade-Surface Velocities of MF-2 Impeller; 60-Percent Design Speed, 43,800 rpm	71
45	Inlet Velocity Diagrams for MF-3 Impeller Design . . .	72
46	Diffusion Factor for MF-3 Impeller	73
47	Exit Velocity Diagrams for MF-3 Impeller	74

ILLUSTRATIONS (Continued)

<u>Figure</u>		<u>Page</u>
48	Meridional View of MF-3 Impeller	75
49	Impeller Design Parameters for MF-3; Design Speed, 65,000 rpm	76
50	Static-Pressure Distribution Across Passage, MF-3 Impeller; Design Speed, 65,000 rpm	77
51	Predicted Static-Pressure Rise Along MF-3 Impeller Shroud; Design Speed, 65,000 rpm	78
52	Blade-Surface Velocities of MF-3 Impeller; Design Speed, 65,000 rpm	79
53	Exit Flow Conditions for MF-3 Impeller; Design Speed, 65,000 rpm	80
54	Predicted Static-Pressure Rise Along MF-3 Impeller Shroud, Part Speed	81
55	Blade-Surface Velocities of MF-3 Impeller; 90-Percent Design Speed, 58,500 rpm	82
56	Blade-Surface Velocities of MF-3 Impeller; 80-Percent Design Speed, 52,000 rpm	83
57	Blade-Surface Velocities of MF-3 Impeller; 60-Percent Design Speed, 39,000 rpm	84
58	Inlet Vector Diagrams for RF-1 Impeller Design	85
59	Diffusion Factor for RF-1 Impeller	86
60	Exit Velocity Diagrams for RF-1 Impeller	87
61	Meridional View of RF-1 Impeller	88
62	Impeller Design Parameters for RF-1; Design Speed, 57,000 rpm	89
63	Static-Pressure Distribution Across Passage, RF-1 Impeller; Design Speed, 57,000 rpm	90

ILLUSTRATIONS (Continued)

<u>Figure</u>		<u>Page</u>
64	Predicted Static-Pressure Rise Along RF-1 Impeller Shroud; Design Speed, 57,000 rpm	91
65	Blade-Surface Velocities of RF-1 Impeller; Design Speed, 57,000 rpm	92
66	Exit Flow Conditions for RF-1 Impeller; Design Speed, 57,000 rpm	93
67	Predicted Static-Pressure Rise Along RF-1 Impeller Shroud, Part Speed	94
68	Blade-Surface Velocities of RF-1 Impeller; 90-Percent Design Speed, 51,300 rpm	95
69	Blade-Surface Velocities of RF-1 Impeller; 80-Percent Design Speed, 45,600 rpm	96
70	Blade-Surface Velocities of RF-1 Impeller; 60-Percent Design Speed, 34,200 rpm	97
71	MF-1 Impeller	98
72	MF-2 Impeller	99
73	MF-3 Impeller	100
74	RF-1 Impeller	101
75	Comparison of Research Impellers	102
76	Contractor's Other Channel Diffusers	103
77	Required Diffuser Recovery (Impeller Tip to Collector)	105
78	Diffuser Channel Total-Pressure Recovery Versus Area Ratio	107
79	Circular Water Table	108

ILLUSTRATIONS (Continued)

<u>Figure</u>		<u>Page</u>
80	Water-Table Facility	109
81	Dye-Injection Apparatus	110
82	Yaw Probe Traversing-Arm Installation	111
83	Water-Table Data on 1I8 Vane-Island Configuration	115
84	Water-Table Data on 2I8 Vane-Island Configuration	117
85	Water-Table Data on 2I16 Vane-Island Configuration	119
86	Water-Table Data on 2I24 Vane-Island Configuration	121
87	Water-Table Data on 5C24 Cascade Configuration	129
88	90-Vane Cascade	131
89	Water-Table Shadowgraph, Single-Stage Cascade.	133
90	Water-Table Ink Trace, Two-Stage Cascade.	134
91	Water-Table Ink Trace, Three-Stage Cascade	135
92	Water-Table Shadowgraph, Three-Stage Cascade.	136
93	Cascade Diffuser	137
94	Vectors at Entrance to Vaneless Space	139
95	Variation in Total-Pressure Recovery, Inlet Flow Angle, and Diameter Ratio for Vaneless Space	140
96	Estimated Pressure Recovery Through a Two-Stage Cascade Diffuser	143
97	Breakdown of the Pressure Recovery Through a Two- Stage Vane-Island-Type Diffuser'	144
98	Alignment of Vane Leading Edge	145

ILLUSTRATIONS (Continued)

<u>Figure</u>		<u>Page</u>
99	Vane-Island Diffuser Layout	147
100	DI-1 Diffuser Vane (1.06 Radius Ratio, Design Throat Area)	150
101	DI-2 Diffuser Vane (1.06 Radius Ratio, Design Throat Area)	151
102	DI-3 Diffuser Vane (1.06 Radius Ratio, Design Throat Area)	153
103	DC-1 Diffuser (1.10 Radius Ratio, Design Throat Area)	154
104	Workhorse Impeller Vector Diagrams	157
105	Meridional View of Workhorse Impeller	158
106	Diffuser Test Rig	159
107	Aerodynamic Design Information	161
108	Aerodynamic Design Information	162
109	Aerodynamic Design Information	163
110	Aerodynamic Design Information	164
111	Strength-to-Weight Ratio Versus Temperature	166
112	Modulus of Elasticity and Coefficient of Thermal Expansion Versus Temperature	167
113	Estimated Temperature Distribution	169
114	Physical Properties of 6A1-4V Titanium Versus Temperature	170
115	Stress Versus Temperature for 6A1-4V Titanium	171
116	Stress Versus Temperature for 6A1-4V Titanium	172

ILLUSTRATIONS (Continued)

<u>Figure</u>		<u>Page</u>
117	Stress Versus Temperature for 6A1-4V Titanium . . .	173
118	Goodman Diagrams	174
119	Sample Campbell Diagram (MF-1)	175
120	Disk Sections for Stress Analysis	177
121	Hub Extension	178
122	MF-1 Test Section	179
123	Impeller Test Rig.	181
124	Impeller Shaft Arrangements	182
125	Critical Speed Versus Bearing Stiffness	183
126	Critical Speed Versus Bearing Stiffness	184
127	Rotor Stations Used in Predicting Critical Speeds . . .	186
128	MF-2 Critical Speed Versus Bearing Stiffness	188
129	Effects of Viscous Damping	190
130	Frictionless Coupling	191
131	MF-1 Labyrinth Seal	192
132	Thrust Balance Disk	193
133	Impeller Rotor System	195
134	Aerodynamic Design Information	196
135	Diffuser Vane-Islands	197
136	Cascade Diffuser Vane	197

ILLUSTRATIONS (Continued)

<u>Figure</u>		<u>Page</u>
137	Impeller Vibratory Stress Test.	199
138	Diffuser Rig	201
139	Diffuser-Rig Test Section	202
140	Inlet Guide Vane Assembly.	203
141	Schlieren Window Installation	204
142	Bearing Stiffness Versus Rotor Speed	206
143	Shaft Mode Shapes.	207
144	Diffuser-Rig Rotor System	209

SECTION 3.0

145	Impellers	212
146	Workhorse Impeller	213
147	Example of Impeller Cavity Model	214
148	Tape-Controlled Drafting Machine	216
149	Impeller Optical Template (MF-1)	217
150	RF-1 Front Coverplate	219
151	MF-1 Front Coverplate	220
152	MF-2 Front Coverplate	221
153	MF-3 Front Coverplate	222
154	RF-1 Backplate	224
155	Backplate Cone	225

ILLUSTRATIONS (Continued)

<u>Figure</u>		<u>Page</u>
156	MF-1 Backplate	226
157	MF-2 Backplate	227
158	MF-3 Backplate	228
159	Collector, Section View	229
160	MF-1 Inlet Assembly	230
161	Vane-Islands	231
162	Vane-Island Inspection Chart	232
163	Diffuser-Rig Front Coverplate	234
164	Coverplate and Inlet	235
165	Backplate With Vane-Islands and Collector	236
166	Inlet Guide Vane Construction	238
167	Inlet Guide Vane Components	239

SECTION 4.0

168	Pressure and Temperature Probes	242
169	Total-Pressure Rake	243
170	Yaw Pressure Probe	244
171	Pressure-Probe Sensitivity Calibration Facility	245
172	Three-Probe Rake Calibration	246
173	Diffuser-Rig Backplate	247
174	Traversing Probe Path	248

ILLUSTRATIONS (Continued)

<u>Figure</u>		<u>Page</u>
175	Traversing Total-Pressure Probe Detail	249
176	Working Model of Traversing Total-Pressure Probe	250
177	Close-up of Traversing Total-Pressure Probe (Working Model)	251
178	Water-Cooled Transducer	252
179	Digital Data System	253
180	Slotted-Shield Total-Temperature Probe	254
181	Strain-Gage Installation (Test Specimen)	256
182	Slip-Ring Connector (Side View)	258
183	Slip-Ring Connector (Front View)	259
184	Slip-Ring Installation, Impeller-Stress Test	260
185	Impeller-Stress Data-Recording Setup	261
186	Rotor-Thrust-Measurement Instrumentation	263
187	Thrust-Bearing-Cage Instrumentation	264
188	Radial-Bearing-Cage Accelerometer and Thermo-couple	265
189	Shaft Displacement Measurement (Block Diagram)	267
190	Bearing-Cage Accelerometer Installation	269
191	Rub-Sensor Fabrication	270
192	Rub-Sensor Assembly	271

ILLUSTRATIONS (Continued)

<u>Figure</u>		<u>Page</u>
SECTION 5.0		
193	Diffuser-Rig and Impeller-Rig Cell Installation . . .	274
194	Plan View of Test-Cell Area	275
195	Impeller Test Rig.	276
196	Diffuser Test Rig.	277
197	Workhorse Impeller	279
198	Diffuser-Rig Turbodriven Unit	280
199	Positive-Displacement Air Compressor	281
200	Centrifugal Air Compressor	282
201	Centrifugal Air Compressor Performance Curve. . .	283
202	Dynamic Balancing Machine	284
203	Dynamic Balancing Machine	285
204	Test-Cell Control Console	287
205	Pressure-Hookup Identification Sheet	289
206	Dummy Impellers.	292
207	Yaw Probe Zero-Angle Calibration	293
208	Sample Data Sheet for Temperatures	295
209	Compressor Inlet Plenum Chamber.	297
210	Compressor Airflow Manometer	298
211	Test Cell Pressure Manifold	300
212	Sample Data Sheet for Pressures	301

ILLUSTRATIONS (Continued)

<u>Figure</u>		<u>Page</u>
213	Sample Data Sheet for Pressures	303
214	Multichannel Pressure Gages and Manometer Banks	305
215	Impeller-Rig Lubrication Cart	308
216	Impeller-Rig Turbodriven Unit Thrust-Disk Pressure . .	309
217	Modal Balance Plot	310
218	Impeller-Shroud and Diffuser-Passage Width Reductions (RF-1).	311
219	Impeller-Shroud and Diffuser-Passage Width Reductions (MF-1)	312
220	Diffuser-Rig Inlet Oil Pressure Versus Rotor Speed . .	315
221	Impeller Stress-Test Setup	316

SECTION 6.0

222	Pressure Transducer Trace	327
223	Transducer Pressure Readings.	350
224	Pressure-Fluctuation Frequencies	351
225	Pressure Ratio Versus Airflow, MF-1, Vaneless Diffuser .	352
226	Collector Temperature Versus Airflow, MF-1, Vaneless Diffuser.	353
227	Impeller-Exit Temperature, MF-1, Vaneless Diffuser	354
228	Impeller-Exit Total Pressure, MF-1, Vaneless Diffuser	355

ILLUSTRATIONS (Continued)

<u>Figure</u>		<u>Page</u>
229	Impeller-Exit Total Pressure, MF-1, Vaneless Diffuser	357
230	Impeller-Exit Total Pressure, MF-1, Vaneless Diffuser	359
231	Inlet Duct Static Pressure, MF-1, Vaneless Diffuser	361
232	Shroud Static-Pressure Rise, MF-1, Vaneless Diffuser	363
233	Circumferential Variation of Impeller-Exit Static Pressure, MF-1, Vaneless Diffuser	365
234	Circumferential Variation of Impeller-Exit Static Pressure, MF-1, Vaneless Diffuser	367
235	Impeller-Tip Absolute Mach Number Survey, MF-1, Vaneless Diffuser	369
236	Impeller-Exit Absolute Flow Angle, MF-1, Vaneless Diffuser	371
237	RMS Inlet Vector Diagrams, MF-1, Vaneless Diffuser	373
238	RMS Inlet Vector Diagrams, MF-1, Vaneless Diffuser	375
239	Mean Vector Diagrams at 1.02 Diameter Ratio, MF-1, Vaneless Diffuser	377
240	Mean Vector Diagrams at 1.02 Diameter Ratio, MF-1, Vaneless Diffuser	379
241	Radial Variation of Inducer Incidence, MF-1, Vaneless Diffuser.	381
242	Radial Variation of Inducer incidence, MF-1, Vaneless Diffuser	383

<u>Figure</u>		<u>Page</u>
243	Slip Factor Versus Passage Width, MF-1, Vaneless Diffuser	385
244	Slip Factor Versus Passage Width, MF-1, Vaneless Diffuser	386
245	Slip Factor Versus Airflow, MF-1, Vaneless Diffuser	387
246	Temperature-Rise Factor Versus Passage Width, MF-1, Vaneless Diffuser	389
247	Temperature-Rise Factor Versus Airflow, MF-1, Vaneless Diffuser.	391
248	Inlet Blockage Factor Versus Airflow, MF-1, Vaneless Diffuser	392
249	Pressure Ratio Versus Airflow, RF-1	393
250	Pressure Ratio Versus Airflow, RF-1	394
251	Compressor Temperature Rise Versus Airflow, RF-1	395
252	Impeller-Exit Total-Temperature Survey, RF-1	397
253	Impeller-Exit Total-Temperature Survey, RF-1	399
254	Inlet Duct Static Pressures, RF-1	401
255	Inlet Duct Static Pressures, RF-1	403
256	Static-Pressure Rise Along Shroud, RF-1	405
257	Impeller-Exit Static Pressure Versus Circumferential Distance, RF-1	407
258	Impeller-Exit Static Pressure Versus Circumferential Distance, RF-1	409

ILLUSTRATIONS (Continued)

<u>Figure</u>		<u>Page</u>
259	Impeller-Exit Static Pressure Versus Circumferential Spacing, RF-1	411
260	Impeller-Exit Total Pressure, RF-1	413
261	Impeller-Exit Mach Number Versus Passage Width, RF-1	415
262	Impeller-Exit Flow-Angle Survey, RF-1	417
263	Impeller-Exit Flow-Angle Survey, RF-1	419
264	RMS Inlet Vector Diagrams, RF-1	421
265	RMS Inlet Vector Diagrams, RF-1	423
266	RMS Inlet Vector Diagrams, RF-1	425
267	Mean Vector Diagrams at 1.02 Diameter Ratio, RF-1	427
268	Mean Vector Diagrams at 1.02 Diameter Ratio, RF-1	429
269	Radial Variation of Inducer Incidence, RF-1	431
270	Radial Variation of Inducer Incidence, RF-1	433
271	Variation of Slip Factor Across Impeller Tip, RF-1	435
272	Temperature-Rise Factor Across Impeller Tip, RF-1	437
273	Inlet Blockage Factor, RF-1	439
274	Pressure Ratio Versus Airflow, Workhorse	440
275	Temperature Rise Versus Airflow, Workhorse	441
276	Impeller-Exit Total Temperature, Workhorse	442
277	Impeller-Exit Total Temperature, Workhorse	443

ILLUSTRATIONS (Continued)

<u>Figure</u>		<u>Page</u>
278	Impeller-Exit Total Pressure, Workhorse	445
279	Impeller-Exit Total Pressure, Workhorse	447
280	Exit Mach Number Survey, Workhorse	449
281	Static-Pressure Rise Along Shroud, Workhorse	451
282	Static-Pressure Rise Along Shroud, Workhorse	452
283	Static-Pressure Rise Along Shroud, Workhorse	453
284	Static-Pressure Rise Along Shroud, Workhorse	454
285	Static-Pressure Rise Along Shroud, Workhorse	455
286	Static-Pressure Rise Along Shroud, Workhorse	456
287	Static-Pressure Rise Along Shroud, Workhorse	457
288	Static-Pressure Rise Along Shroud, Workhorse	458
289	Static-Pressure Rise Along Shroud, Workhorse	459
290	Static-Pressure Rise Along Shroud, Workhorse	460
291	Inlet Blockage Factor, Workhorse	461
292	Impeller-Exit Flow Angles, Workhorse	462
293	Impeller-Exit Flow Angles, Workhorse	463
294	Impeller-Exit Flow Angles, Workhorse	464
295	Impeller-Exit Flow Angles, Workhorse	465
296	Impeller-Exit Flow Angles, Workhorse	466
297	RMS Inlet Vector Diagrams, Workhorse	467
298	RMS Inlet Vector Diagrams, Workhorse	469

ILLUSTRATIONS (Continued)

<u>Figure</u>		<u>Page</u>
299	Mean Vector Diagrams at 1.02 Diameter Ratio, Workhorse	471
300	Mean Vector Diagrams at 1.02 Diameter Ratio, Workhorse	473
301	Inducer Incidence, Workhorse	475
302	Average Temperature-Rise Factor, Workhorse	477
303	Temperature-Rise Factor Across Impeller Tip, Workhorse	479
304	Average Slip Factor, Workhorse	481
305	Variation of Slip Factor Across Impeller Tip, Workhorse	483
306	Diffuser-Rig Traversing Total-Pressure Probe	485
307	Diffuser-Vane Modifications	486
308	Cascade Configuration	487
309	Modified Cascade Vane	487
310	Pressure Ratio Versus Airflow, DI-1	489
311	Pressure Ratio Versus Airflow, DI-1	490
312	Pressure Ratio Versus Airflow, DI-1	493
313	Pressure Ratio Versus Airflow, DI-1	494
314	Pressure Ratio Versus Airflow, DI-1	495
315	Pressure Ratio Versus Airflow, DI-1	496
316	Pressure Ratio Versus Airflow, DI-1	497
317	Pressure Ratio Versus Airflow, DI-1	498

ILLUSTRATIONS (Continued)

<u>Figure</u>		<u>Page</u>
318	Pressure Ratio Versus Airflow, DI-1	499
319	Pressure Ratio Versus Airflow, DI-1	500
320	Pressure Ratio Versus Airflow, DI-1 (Comparison at 1.06 and 1.10 Radius Ratio)	501
321	Pressure Ratio Versus Airflow, DI-1	502
322	Pressure Ratio Versus Airflow, DI-1-2	503
323	Pressure Ratio Versus Airflow, DI-1-2	504
324	Pressure Ratio Versus Airflow, DI-1-2 (With and Without Schlieren Windows)	505
325	Pressure Ratio Versus Airflow, DI-2	506
326	Pressure Ratio Versus Airflow, DI-2	507
327	Pressure Ratio Versus Airflow, DI-2	508
328	Pressure Ratio Versus Airflow, DI-2	509
329	Pressure Ratio Versus Airflow, DI-2 (Comparison at 1.06 and 1.10 Radius Ratio)	510
330	Pressure Ratio Versus Airflow, DI-2 (Comparison at 125-, 100-, and 75-Percent Throat Areas)	511
331	Pressure Ratio Versus Airflow, DI-2	512
332	Pressure Ratio Versus Airflow, DI-2-2	513
333	Pressure Ratio Versus Airflow, DI-2 (Comparison of Reruns)	514
334	Pressure Ratio Versus Airflow, DI-3	515
335	Pressure Ratio Versus Airflow, DI-3	516
336	Pressure Ratio Versus Airflow, DI-1-3	517

ILLUSTRATIONS (Continued)

<u>Figure</u>		<u>Page</u>
337	Pressure Ratio Versus Airflow, DI-3	518
338	Pressure Ratio Versus Airflow, DI-3	519
339	Pressure Ratio Versus Airflow, DI-X1	520
340	Pressure Ratio Versus Airflow, DI-X1-2	521
341	Pressure Ratio Versus Airflow, DI-X1-2	522
342	Midchannel Total Pressure Versus Flow-Path Length, DI-1	523
343	Midchannel Total Pressure Versus Flow-Path Length, DI-1	524
344	Midchannel Total Pressure Versus Flow-Path Length, DI-1	525
345	Midchannel Total Pressure Versus Flow-Path Length, DI-1	526
346	Midchannel Total Pressure Versus Flow-Path Length, DI-1	527
347	Midchannel Total Pressure Versus Flow-Path Length, DI-1	528
348	Midchannel Total Pressure Versus Flow-Path Length, DI-1	529
349	Midchannel Total Pressure Versus Flow-Path Length, DI-1	530
350	Midchannel Total Pressure Versus Flow-Path Length, DI-1	531
351	Midchannel Total Pressure Versus Flow-Path Length, DI-1	532

ILLUSTRATIONS (Continued)

<u>Figure</u>		<u>Page</u>
352	Midchannel Total Pressure Versus Flow-Path Length, DI-1	533
353	Midchannel Total Pressure Versus Flow-Path Length, DI-1	534
354	Midchannel Total Pressure Versus Flow-Path Length, DI-1	535
355	Pressure Ratio Versus Airflow, DC-1 Cascade	536
356	Pressure Ratio Versus Airflow, DI-1	537
357	Impeller-Exit Total Pressure, DI-1 and DC-1	538
358	Impeller-Exit Total Pressure, DI-1 and DC-1	539
359	Impeller-Exit Total Pressure, DI-1 and DC-1	540

SECTION 7.0

360	Temperature-Rise Factor and Slip Factor, Workhorse .	545
361	Temperature-Rise Factor and Slip Factor, Workhorse .	547
362	Static-Pressure Amplitude, RF-1	552
363	Design Diffusion Factors, Workhorse and RF-1 Inducers	559
364	Blade-Surface Velocities, Workhorse	560
365	Blade-Surface Velocities, RF-1	561
366	Blockage-Flow and Area Calculation, Constant Blade Thickness	563
367	Blockage-Flow and Area Calculation, Circular-Arc Blade	564

ILLUSTRATIONS (Continued)

<u>Figure</u>		<u>Page</u>
368	Schematic of Impeller Flow	566
369	Impeller-Exit Mixing Loss	571
370	Impeller-Exit Mixing Loss	572
371	Impeller-Exit Mixing Loss	573
372	Impeller-Exit Mixing Loss	574
373	Jet-Wake Relative-Velocity Profile	577
374	Overvelocity Coefficients	579
375	Trailing-Edge Pressure Divergence	584
376	Critical Mach Number Versus Nose Geometry	585
377	Airfoil Separation Regimes	587
378	Flow-Attachment Boundary	587
379	Boundaries for Onset of Separation	589
380	Boundaries of Separation Effects	590
381	Suction-Surface Slope Distribution	591
382	Suction-Surface Slope Distribution	591
383	Suction-Surface Slope Distribution	592
384	Pearcey Parameter, κ	592
385	Incidence Versus Mach Number, RF-1 and Workhorse	594
386	Incidence Versus Approach Mach Number	594
387	Separation Effects	595

ILLUSTRATIONS (Continued)

<u>Figure</u>		<u>Page</u>
388	Inducer Leading-Edge Blade Sections, RF-1	596
389	Inducer Leading-Edge Blade Sections, Workhorse	598
390	Suction-Surface Slope Distribution, RF-1 and Workhorse	599
391	Relative-Velocity Distributions.	602
392	Equilibrium — Boundary-Layer Notation	603
393	Pressure-Ratio Comparison, DI-1	605
394	Characteristic Shape of Pressure Ratio Versus Airflow for Impeller and Diffuser	606
395	Compressor Characteristic Showing Impeller and Diffuser Airflow Limit	606
396	Two-Dimensional Diffuser Channel Performance	607
397	Compressor Characteristic Curve	608
398	Vane-Island Diffuser	609
399	Length of Impeller Mixing in Vaneless Space	611
400	Total Pressure Measured Along Streamline With Channel Movable Probe	612
401	Carbon-Black Traces (Shows Bleeding of Suction Surface)	613
402	Static-Pressure Field, DI-1	615
403	Streamlines Through Vaneless and Semivaneless Space	617
404	Static-Pressure Field, DI-2	619
405	Flow Patterns Through a Vane-Island Diffuser	625
406	Conical Diffuser Performance	628

ILLUSTRATIONS (Continued)

<u>Figure</u>		<u>Page</u>
407	Static-Pressure Field, DI-2	629
408	Incidence on Diffuser Vane	631
409	Static-Pressure Field, DI-2	632
410	Comparison of Pressure Recovery for Compressor Channel With Two-Dimensional Diffuser Data	636
411	Difference in Vane Geometry Between DI-1 and DI-2	637
412	W/W* on Characteristic Speed Line	639
413	Length of Shock Versus Mach Number Preceding Shock (1.000-in.-Diameter Tube)	639
414	Characteristic C_p Versus M for Fixed-Geometry Diffusers	643
415	Flow-Regime Map	644
416	Diffuser Geometric Parameters	646
417	Pressure-Ratio Comparison, DI-2 and DI-X1-3	650
418	Static-Pressure Field, DI-X1-3	653
419	Comparison of Three Diffusers Showing Match to Impeller	655
420	Modification of DI-1 to DI-1-2	656
421	Pressure-Ratio Comparison, DI-1 and DI-2	657
422	Static-Pressure Field, DI-1-2	659
423	Pressure Recovery of Two-Dimensional Diffusers With Turbulent Inlet Boundary Layers	662
424	Pressure-Ratio Comparisons, DI-2, DI-X1, and DI-X1-2	663

ILLUSTRATIONS (Continued)

<u>Figure</u>		<u>Page</u>
425	Increase in DI-2 Vane Angle	664
426	Pressure-Ratio Comparison, DI-1 and DI-2-2	665
427	Throat Blockage Factor Versus Mach Number Ahead of Shock	665

(U) TABLES

<u>Table</u>		<u>Page</u>
SECTION 1.0		
I	Performance Comparisons	8
SECTION 2.0		
II	Impeller Radial-Equilibrium Computer Program	41
III	Impeller Designs	44
IV	Water-Table Diffuser Models	112
V	Design Parameters for Vane-Island Diffusers	152
VI	Diffuser Variable Geometry	155
VII	Design Parameters for Cascade Diffuser DC-1	156
VIII	Workhorse Impeller Design Parameters	156
IX	Minimum Factors of Safety	168
X	Impeller Stress Analysis Results	178
XI	Critical Speeds	187
SECTION 5.0		
XII	Impeller-Rig Mechanical Limitations	307
XIII	Diffuser-Rig Mechanical Limitations	313
SECTION 6.0		
XIV	MF-1 Impeller Tests With Vaneless Diffuser	320
XV	Vaneless Diffuser Pressure Transducer Locations	326
XVI	RF-1 Impeller Tests	328

TABLES (Continued)

<u>Table</u>	<u>Page</u>
XVII Workhorse Impeller Tests	332
XVIII DI-1 Diffuser and Modifications	335
XX DI-2 Diffuser and Modifications	340
XX DI-3 Diffuser and Modifications	347
XXI DI-1 Cascade Diffuser	348

SECTION 7.0

XXII RF-1 Clearance Tests.	549
XXIII RF-1 Diffuser Geometry	554
XXIV Performance Comparison of RF-1 and Workhorse Impellers .	557
XXV Inlet Mach Number and Incidence, Workhorse and RF-1 . .	560
XXVI Inducer κ Calculations	593
XXVII Static-Pressure Rise Through Diffuser	622
XXVIII Variable for 2-Dimensional Diffuser Tests	647

(U) SYMBOLS

A	area (in. ²)
A*	area at station where the Mach number is unity (in. ²)
A/A*	isentropic area ratio
A _{nf}	area normal to flow direction (in. ²)
A _{nm}	area in plane normal to meridional plane (in. ²)
a	acoustic velocity (fps), $a = \sqrt{k g R T_s}$
B	blockage, $B = 1 - \frac{A_{\text{flow}}}{A_{\text{geometric}}}$
b	impeller - tip blade width (in.) or diffuser passage depth (in.)
C	total bearing clearance (in.)
C _L	lift coefficient
c	chord length (in.)
c _f	friction coefficient
c _p	static pressure recovery
D	diameter (in.)
d	diameter (in.)
d _H	hydraulic diameter (in.)
DC	diffuser cascade
DF	diffusion factor
DI	diffuser island
D/D	diameter ratio

(U) SYMBOLS (Continued)

E	compressor work $\left(\frac{\text{Btu}}{\text{lb}}\right)$, $E = \frac{U_4^2 - U_1^2 + V_4^2 - V_1^2 + V_2^2 - V_3^2}{2 gJ}$
e	base of Napierian system of logarithms (2.7182)
F	Froude number
F_f	failure force (lb)
F_{td}	force component of the disk (lb)
F_{tt}	force component due to blade loading (lb)
F_{tw}	total centrifugal force, including blades (lb), $F_{tw} = F_{td} + F_{tt}$
f	friction factor
g	gravitational constant (32.17 ft/sec ²)
H	total passage width at survey station (in.)
H_∞	total pressure of approach flow (psia)
h	passage width (in.) or specific enthalpy (Btu/lb)
I_m	mass moment of inertia (lb-in.-sec ²)
IGV	inlet guide vane
J	mechanical equivalent of heat $\frac{778 \text{ ft-lb}}{\text{Btu}}$
K	spring rate (lb/in.), gage-factor nominal value or a constant
K_n	spring rate (lb/in.)
K'	gage-factor sensitivity compensation

(U) SYMBOLS (Continued)

k ratio of specific heats,

$$k = \frac{C_p}{C_v}$$

L flow path length (ft or in.) or loss coefficient,

$$L = \frac{\Delta P_t}{q}$$

l bearing length (in.)

M Mach number

M_x Mach number ahead of normal shock

M_y Mach number behind normal shock

M_L local Mach number

MF mixed flow

m meridional distance (in.)

N rotational speed (rpm)

N_v number of diffuser vanes

n clearance (in.) or normal distance (in.)

P_o total pressure before mixing (psia)

P_o^{*} total pressure after mixing (psia)

P_s static pressure (psia or in. Hg)

P_{se} static pressure at throat exit (psia or in. Hg)

P_{sf} static pressure in collector (psia or in. Hg)

P_t total pressure (psia or in. Hg)

(U) SYMBOLS (Continued)

P_{tc}	core total pressure (psia or in. Hg)
P/P	pressure ratio
\bar{P}	mass-averaged pressure (psia or in. Hg)
q	dynamic pressure (psia or in. Hg), $q = 1/2 \rho V^2$
R	radius (in.) or gas constant for air $\left(53.3 \frac{\text{ft-lb}}{\text{lb-}^\circ\text{F}} \right)$
Re	Reynolds number
R_g	resistance of strain gage (ohms)
R_L	resistance of lead wire to strain gage (ohms)
R_s	calibration shunt resistor (ohms)
RF	radial flow
RMS	root mean square
R/R	radius ratio
r	radius (in.)
S	stress (psi) or entropy (Btu/ $^\circ R$)
S_m	mean stress (psi)
S_n	endurance limit (psi)
S_r	yield stress for Rene' 41 (psi)
S_t	yield stress for titanium (psi)
S_v	vibratory stress (psi)
S_y	yield strength (psi)

(U) SYMBOLS (Continued)

$S_{f,v}$ failure stress corresponding to the temperature
in the center of segment v (psi)

SF slip factor,

$$SF = \frac{V_T^4}{U_4^4}$$

SF_s safety factor based on rupture stress

SF_u safety factor based on ultimate stress

SF_y safety factor based on yield stress

SFC specific fuel consumption $\left(\frac{\text{lb of fuel}}{\text{HP-hr}} \right)$

T_n bearing stiffness $\left(\frac{\text{lb-sec}}{\text{in.}} \right)$

T_s absolute static temperature ($^{\circ}\text{R}$)

T_t absolute total temperature ($^{\circ}\text{R}$)

TIT turbine-inlet temperature ($^{\circ}\text{F}$)

TRF temperature-rise factor,

$$TRF = \Delta h_t / (U_4^2 / gJ)$$

\bar{T} mass-averaged absolute temperature ($^{\circ}\text{R}$)

t blade thickness (in.)

U impeller peripheral velocity (fps)

V velocity (fps)

V_L local velocity (fps)

V_T tangential component of velocity (fps)

W_a airflow (lb/sec)

(U) SYMBOLS (Continued)

W	airflow (lb/sec) or diffuser height (in.)
W*	minimum airflow for which diffuser throat core Mach number is unity (lb/sec)
\bar{W}	integrated airflow (lb/sec)
x	distance (in.)
y	distance (in.)
Z	number of impeller blades or axial distance
α	angle (degrees)
α_1	angle between impeller-inlet absolute vector and meridional plane (degrees)
α_2	angle between impeller-inlet relative vector and meridional plane (degrees)
α_3	angle between impeller-exit relative vector and meridional plane (degrees)
α_4	angle between impeller-exit absolute vector and meridional plane (degrees)
α_s	angular spacing of diffuser vanes (degrees), $\alpha_s = \frac{360^\circ}{N_v}$
α_v	cascade-vane stagger angle measured from radial (degrees)
β	angle between impeller vane and meridional plane (degrees) or diffuser-vane wedge angle (degrees)

(U) SYMBOLS (Continued)

γ	ratio of specific heats, $\gamma = \frac{C_p}{C_v}$ or material density (lb/in. ³)
γ_r	density of Rene' 41 (lb/in. ³)
γ_t	density of titanium (lb/in. ³)
δ	boundary layer thickness (in.) or $\frac{\text{measured ambient pressure (in. Hg)}}{29.92 \text{ in. Hg}}$
δ^*	boundary layer displacement thickness (in.)
ϵ	ratio of wake width to blade pitch at impeller exit
η	adiabatic efficiency (percent)
θ	channel-diffuser angle (degrees) or $\frac{\text{measured ambient temperature (°R)}}{519.7 \text{ °R}}$
κ	airfoil nose-shape parameter
λ	tangent of the angle between the bulk-mean absolute flow vector and the meridional plane at the impeller exit
μ	dynamic viscosity $\left(\frac{\text{lb}_m}{\text{sec-ft}} \right)$
ν	kinematic viscosity $\left(\frac{\text{ft}^2}{\text{sec}} \right)$
ξ	angular coordinate of logarithmic spiral (degrees)
ρ	density of air $\left(\text{lb}_m/\text{ft}^3 \right)$
ρ_s	static density of air $\left(\text{lb}_m/\text{ft}^3 \right)$

(U) SYMBOLS (Continued)

ρ_t	total density of air (lb _m /ft ³)
σ	blade solidity $\sigma = \frac{\text{chord}}{\text{pitch}}$
τ	shear stress (psi)
ϕ	blockage factor $\phi = 1 - B$
χ	airfoil suction-surface parameter
ω	impeller angular velocity (rad/sec)

Subscripts:

e	impeller exit
h	hub
i	impeller inlet
t	throat, total or tip
1	impeller-inlet absolute vector
2	impeller-inlet relative vector
3	impeller-exit relative vector
4	impeller-exit absolute vector
∞	undisturbed approach flow

CONFIDENTIAL

(C) SUMMARY (U)

(U) The research program discussed in this report was conducted for the U. S. Army Aviation Materiel Laboratories. The purpose of the work was to define, by analyses and experimental evaluations, the design criteria and performance characteristics of a high-pressure-ratio, single-stage centrifugal compressor. The overall-performance target was a pressure ratio of 10:1 at an adiabatic efficiency of 80 percent and at an airflow rate of 2 pounds per second. The research was expected to lead to development of advanced technology, applicable to small gas-turbine engines. The potential advances identified were:

- 1) Doubling of current power-to-weight ratios;
- 2) Reducing full- and part-load fuel consumption;
- 3) Minimizing cost per horsepower.

To illustrate the advances possible, two types of thermodynamic cycles (simple and regenerative) were studied. It was shown that a compressor meeting the above targets would provide an opportunity for reducing specific fuel consumption to 0.49 pound per horsepower per hour, simple cycle, and to 0.38 pound per horsepower per hour, regenerated.

(C) RESEARCH COMPONENTS (U)

Previous experience related to centrifugal compressors was used to identify the research objectives. Studies of Boeing designs in the pressure-ratio range of 3.5:1 to 7:1 formed the background for this work. Specifically, refinements were necessary in blade shape and aerodynamic loading; therefore the program was directed toward the following:

- 1) Minimizing the effect of transonic-flow conditions at the inducer and diffuser entrance;
- 2) Determining the influence of inducer hub-to-tip-diameter ratio and its effect on impeller performance;
- 3) Establishing methods to provide operating range at high pressure ratios;
- 4) Establishing a flow model for the impeller and diffuser for the purpose of identifying losses throughout the compressor.

(C) Preliminary design studies of impellers and diffusers led to the selection of the research components. Computer programs, developed through prior research, were used to assess the geometric variables, and 4 impellers and 4

CONFIDENTIAL

CONFIDENTIAL

diffusers were chosen to cover the field of interest. The impellers were designated as MF-1, MF-2, MF-3, and RF-1 (MF and RF refer to mixed-flow and radial-flow types, respectively). Mixed-flow impellers warranted study, because it was believed that the reduced amount of radial turning (compared to a radial type) had a potential advantage of 1 to 2 percent in efficiency. Each impeller was designed to provide a total-to-total pressure ratio of about 13:1 at a tip speed of 2000 fps. Absolute Mach number leaving the impeller was about 1.3. The ranges in size, speed, and aerodynamic parameters were as follows:

- 1) MF-1 was designed for an inducer hub-to-tip-diameter ratio of 0.4 with an inducer-tip relative Mach number of 0.95 at 57,000 rpm. The tip diameter was about 8.0 inches, and 18 blades were used.
- 2) MF-2 had an inlet hub-to-tip-diameter ratio of 0.5 and an inducer-tip relative Mach number of 1.23. The design speed was 73,000 rpm, and the impeller had a tip diameter of about 6.3 inches with 20 blades.
- 3) MF-3 was designed for an inlet hub-to-tip-diameter ratio of 0.5, with an inducer-tip relative Mach number of 1.13. The design speed was 65,000 rpm (midway between MF-1 and MF-2) and the impeller-tip diameter was about 7.1 inches with 20 blades.
- 4) RF-1 was designed close to MF-1 to obtain performance comparisons for the two types of impellers. The inlet hub-to-tip-diameter ratio, however, was 0.6, and the inducer-tip relative Mach number of 1.09. Speed and overall diameter were 57,000 rpm and about 8.0 inches, respectively (same as MF-1). The impeller was designed with 22 blades.

(C) For the diffuser investigations, the configurations were designated as DI-1, DI-2, DI-3, and DC-1. The first 3 were vane-island types (channels), and the fourth was a single-stage cascade. The vane-island types were designed to match the impeller discharge Mach number of 1.3, but they were designed with a capability of varying vaneless-space-diameter ratio and throat Mach number. Water-table studies were conducted with diffuser models to develop an analogy for preliminary evaluations of performance. In addition, prior shadowgraph studies at diffuser-entrance Mach numbers of over 1.2 were used to provide background for identifying shocks and for estimating their effect on pressure recovery. From these studies, it was believed that the primary research effort should be directed toward establishing the influence of design-throat Mach number and vaneless- and semivaneless-space flow patterns on shock strength and location. Each vane-island diffuser was designed to the same channel-divergence angle, 10 degrees. It was assumed that the boundary-layer-blockage factor in the throat would be 0.88. Other factors included number of vanes, vaneless-space-diameter ratio, vane-wedge angle, channel-area ratio, and throat length. Axial

CONFIDENTIAL

CONFIDENTIAL

width of the passage was the same for all configurations (0.25 inch) and was governed by the geometry of the impeller (workhorse) used in the diffuser-test rig. The significant parameters selected were as follows:

- 1) DI-1 was designed with 8 vanes at a vaneless-space-diameter ratio of 1.06 and a throat Mach number of 0.90. The leading-edge wedge angle was 7 degrees and the area ratio of the channel was 2.76.
- 2) DI-2 was also an 8-vaned diffuser designed to a vaneless-space-diameter ratio of 1.06; however, the throat area was sized for a Mach number of 0.75. The wedge angle was 9 degrees, and the channel-area ratio was 2.63.
- 3) DI-3 was designed with 16 vanes at a diameter ratio of 1.06 and with the same throat Mach number and wedge angle as those of DI-2 (0.75 and 9 degrees, respectively). The area ratio was 4.70.

(C) The channel designs also included a variable-area capability for investigating a variable-airflow-capacity concept. Areas of DI-1 and DI-2 were varied by pivoting the vanes at their leading edges to change their angular orientation and to match the flow direction. In addition, the vanes were adjustable to other radial positions to evaluate the effect of vaneless-space-diameter ratio.

(C) For the cascade, the vane design was based on water-table studies and previously established techniques used for axial-compressor stators. It was believed that thin, flat plates would avoid high aerodynamic loadings and would result in subsonic flow behind the blade row. In addition, the single-stage investigation was expected to provide information essential to the design of following blade rows. The cascade (DC-1) had 31 vanes with a chord length of 1.20 and a solidity of 1.17. Vane thickness was 0.06 inch, and the passage width was consistent with the 3 vane-islands (0.25 inch) to match the workhorse impeller.

(C) The impeller used in the diffuser investigations was a modification of a previous high-pressure-ratio design. It was a radial-flow type, modified to pass 2.43 pounds per second airflow at a tip speed of 2000 fps. The tip diameter was 9.2 inches, and 23 blades were used. The inlet hub-to-tip-diameter ratio was 0.63 with an inducer-tip relative Mach number of 1.15. Basic impeller test data from this configuration were also used in the impeller investigation.

(C) Two test rigs were provided for this research — 1 for the impellers and the other for the diffusers. Each impeller test section and diffuser test section was adaptable to the respective rigs.

(C) Early testing with these rigs was delayed by mechanical difficulties encountered at the high rotor speeds and dynamic loads. Solutions to these problems led to a

CONFIDENTIAL

CONFIDENTIAL

reevaluation of the test plan; 2 impellers, the MF-2 and MF-3, were deleted from the program in favor of enlarging the effort essential to the MF-1, RF-1, and workhorse impellers.

(C) IMPELLER TESTS (U)

Each research impeller was targeted for a total-to-total pressure ratio near 13:1 to allow for downstream losses; however, both MF-1 and RF-1 were deficient by over 4.0 atmospheres during initial tests. It was determined that because these impellers were used with a vaneless diffuser, a rotating-stall phenomenon occurred, and the impeller discharge was forced into a condition of nonuniform backpressure. This stall caused the static pressure at the impeller tip to fluctuate at a frequency of $1/5$ to $1/7$ of rotor speed. Rotating stall was corrected by installing a set of 12 vane-island diffusers in the RF-1 test section. The resulting total-to-total pressure ratio of RF-1 was 10:1. Because performance still was below design predictions, studies of internal fluid-flow mechanics were initiated. From static pressure measurements along the impeller shroud, it was determined that early flow separation had occurred in MF-1 and RF-1. A similar condition was found in the workhorse impeller. The studies showed that the inducers operated at high incidence and blockage, which resulted in flow acceleration around the leading-edge suction surface of the blade. In combination with the already high-transonic relative Mach numbers at the inlet, these factors led to losses from which the remainder of the impeller could not recover. In addition, they contributed to large wakes at the impeller discharge and led to high exit mixing losses.

(C) Methods for predicting performance of the impellers were reviewed and a flow model was contrived to match test results with flow theories. A revised theory was developed to account for differences in flow behavior for several impellers, including two from previous research programs. Application of empirical data and airfoil theories showed that inducer leading-edge shapes had a strong influence on determining the acceleration around the suction surface and that over-velocities ($V_{\text{local}}/V_{\text{inlet}}$) in excess of 1.5 would intensify the early separation in the inducer. This condition caused the flow to continue through the impeller in high Mach number jets (without diffusion) and large wakes, which resulted in the suspected high exit mixing loss. Other losses (friction and clearance), by comparison, were low and within available prediction techniques.

(C) Reassessment of the designs with this information showed agreement with test data to the degree that a new impeller could be designed that would minimize the losses caused by early separation and would reduce exit mixing losses. The new design, a 2-piece inducer and radial section incorporating the revised design technology, is presented in USAAVLABS Technical Report 67-47 "Design and Development of Small, Single-Stage Centrifugal Compressor" (U) (Classified Confidential).

CONFIDENTIAL

CONFIDENTIAL

(C) DIFFUSER TESTS (U)

Each diffuser element was tested under the same impeller (workhorse) discharge conditions. DI-1 showed good performance potential and good range. DI-2, although showing poor airflow range, had the best performance potential. DI-3 performance and range were shown to be between those of DI-1 and DI-2. Static-pressure surveys in the vaneless and semivaneless spaces and through the channels were used in conjunction with schlieren photographs of the flow process to describe the flow behavior within each diffuser. As theories were developed for a flow model of the diffusers, modifications and redesigns were tested to confirm expected trends. Total-pressure recovery of the channels was close to the predicted performance; however, the vaneless and semivaneless spaces did not produce the expected static-pressure rise.

(C) It was determined that flow through the vaneless space did not follow a conventional free-vortex distribution with a large radial increase in static pressure. Instead, the flow continued into the semivaneless space with only modest diffusion and accelerated ahead of the vane tips. Just before the vanes, a shock occurred, which produced a subsonic Mach number in the channel throats. If the diffuser was designed for a high-subsonic Mach number, as with DI-1 (0.90), wall friction within the parallel-sided throat caused a buildup of boundary layer (increased blockage) and an acceleration to over Mach 1.0 in the early portion of the channel-diverging section. These conditions produced shocks in the channels which thickened the boundary layer and further reduced channel performance. Even with the shock system, the DI-1 channel met its design prediction; however, it was evident that further improvement was possible if the shocks could be eliminated.

(C) For a comparison, a design throat Mach number of 0.75 (as with DI-2) produced the same flow behavior through the vaneless space. However, the adjustment and acceleration ahead of the throat in the semivaneless space were more pronounced and produced a stronger shock to reach the lower throat Mach number. At the reduced Mach number in the throat, the boundary-layer (blockage) buildup and friction were not sufficient to cause the attendant acceleration to reach Mach 1.0 at the diverging-channel entrance. With subsonic flow after the throat, more conventional diffusion occurred downstream. To minimize the effects of flow acceleration in the parallel-walled throat, its length was shortened so as to reduce the boundary-layer buildup and friction; the shock at the diverging-channel entrance was eliminated by this technique.

(C) Each diffuser appeared to surge at the same Mach number ahead of the throat-entry shock. At an entry shock of about Mach 1.3, streamlines changed direction through the shock, which resulted in high incidence at the vane leading edges. It was shown that the behavior was the same for the 16-vane-island diffuser (DI-3).

CONFIDENTIAL

CONFIDENTIAL

(C) Prior to this contract, other tests showed that best performance was achieved at vaneless-space-diameter ratios of about 1.06. In addition, variable-capacity tests showed that the concept was feasible if inlet guide vanes were used to compensate for incidence changes at the inducer inlet.

(C) The initial diffuser tests demonstrated that good diffuser recovery could be attained even at throat Mach numbers near 1.0. This was in contrast to diffuser data presented in the literature where a sharp decline in performance is predicted at channel-entrance Mach numbers above 0.80. Therefore, single-channel diffuser tests were conducted to obtain basic data. The tests demonstrated that nearly constant channel performance could be attained at throat Mach numbers up to 1.0. The tests further demonstrated that the channel performance was critically dependent on the entrance boundary-layer-blockage conditions.

(C) Relative to the cascade tests, it was determined that aerodynamic loading of the vanes was sufficiently high to cause considerable separation. Several adjustments were made to the vanes (angular orientation and camber) to alleviate the apparent deficiencies, but it was evident that considerable effort, well beyond the intended scope of this program, would be required to develop a suitably performing, high-Mach-number cascade row. Therefore, these preliminary tests on the first row led to the conclusion that although the cascade-type diffuser had potential, the development of second, third, and fourth stages in combination with the first, would dilute the effort on the vane-island types. On this basis, further cascade-diffuser research was deleted.

(C) Development of the channel-diffuser flow model was accomplished with concurrent tests on the compressor test rig and on the separate Boeing-owned single-channel-diffuser flow rig. From these test results, a new vane-island diffuser was designed to match the previously mentioned new impeller. A description of the design and test results of this diffuser, in which the new knowledge has been incorporated, is presented in a follow-on report entitled "Design and Development of Small, Single-Stage Centrifugal Compressor" (U) (Classified Confidential) (USAAVLABS Technical Report 67-47).

CONFIDENTIAL

(U) 1.0 INTRODUCTION

To meet future Army aviation and ground-equipment powerplant requirements, the following advances in small-gas-turbine-engine component technology were identified: (1) doubling of current power-to-weight ratios, (2) reducing full- and part-load specific fuel consumption, and (3) minimizing cost per horsepower. To achieve these goals, Boeing conducted preliminary design studies in 1963 and, under contract to USAAVLABS since 1964, has continued these research activities with detail design studies. These studies have shown that the best approach for accomplishing these objectives is to develop a high-temperature turbine and a high-pressure-ratio, single-stage compressor.

1.1 OBJECTIVE

The objective of this compressor research program was to advance single-stage centrifugal-compressor technology to a pressure ratio of 10:1 at 80-percent efficiency. This advancement and expected gains in high-temperature turbine technology will reduce specific fuel consumption to 0.49 pound per horsepower per hour for current simple-cycle engines and to 0.38 pound per horsepower per hour for regenerative engines, with a corresponding 34- to 50-percent reduction in part-load specific fuel consumption. Because airflow requirements at a given horsepower decrease with advanced component technology and engine performance, lower airflow requirements have been projected for small gas-turbine engines to be used by the Army in the future. Consistent with these projections, Boeing conducted a compressor research program to achieve the 2-pound-per-second airflow lower limit of the 2- to 5-pound-per-second airflow range specified by USAAVLABS.

Table I compares a future gas-turbine engine, incorporating an advanced technology single-stage centrifugal compressor and a high-temperature turbine, with a current production engine.

The proposed high-pressure-ratio, high-efficiency compressor is required to achieve the above specific-fuel-consumption goals. Figures 1 and 2 show the effects of compressor pressure ratio and efficiency on the overall performance of future high-temperature regenerative and nonregenerative engines. For a simple-cycle engine, an increase in pressure ratio at a given efficiency decreases specific fuel consumption and increases specific power. For example, Figure 1 shows that specific fuel consumption decreases approximately 19 percent and that specific power increases about 9 percent for a simple-cycle engine when the compressor pressure ratio increases from 6:1 to 10:1. For a regenerative engine, an optimum pressure ratio exists for minimum specific fuel consumption. Figure 2 indicates that specific fuel consumption decreases approximately 3 percent and specific power increases about 8 percent when the compressor pressure ratio is increased from 6:1 to 10:1 at 80-percent compressor efficiency.

TABLE I			
PERFORMANCE COMPARISONS			
	Current Engine	Future Engine (Nonregenerative)	Future Engine (Regenerative)
Specific Power (hp/lb-airflow/sec)	93	190	182
Specific Fuel Consumption (lb/hp/hr)	0.68	0.49	0.5
Turbine-Inlet Temp. (° F)	1650	2300	2300
Compressor Pressure Ratio	6:1	10:1	10:1

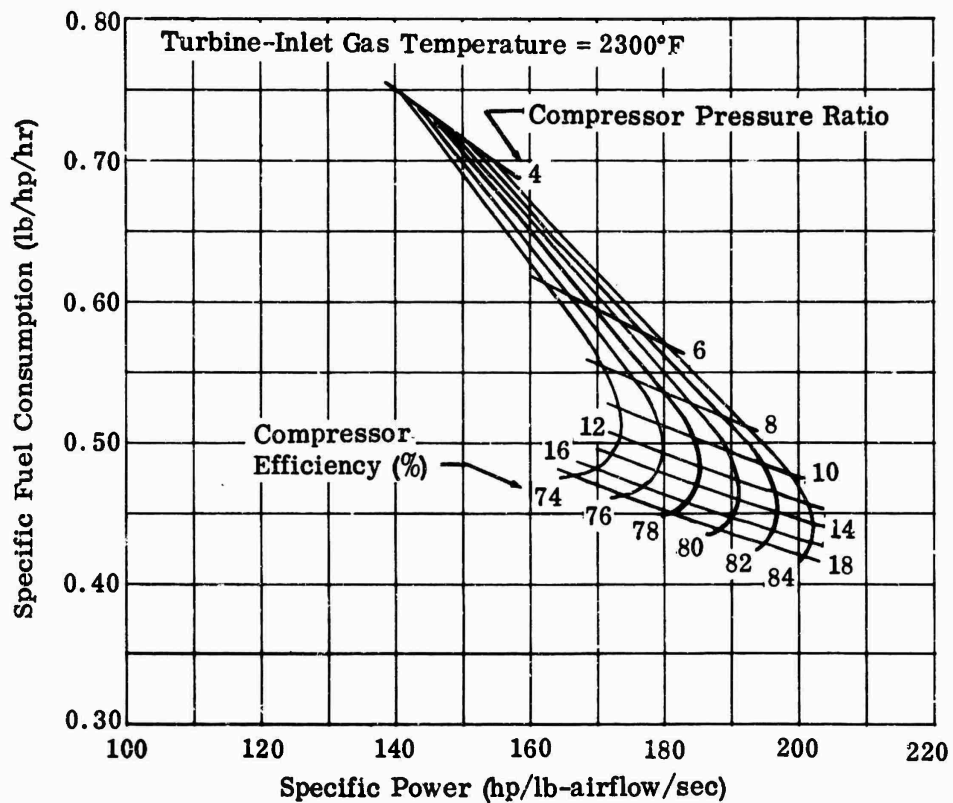


Figure 1. Effect of Compressor Performance on Simple-Cycle Engine.

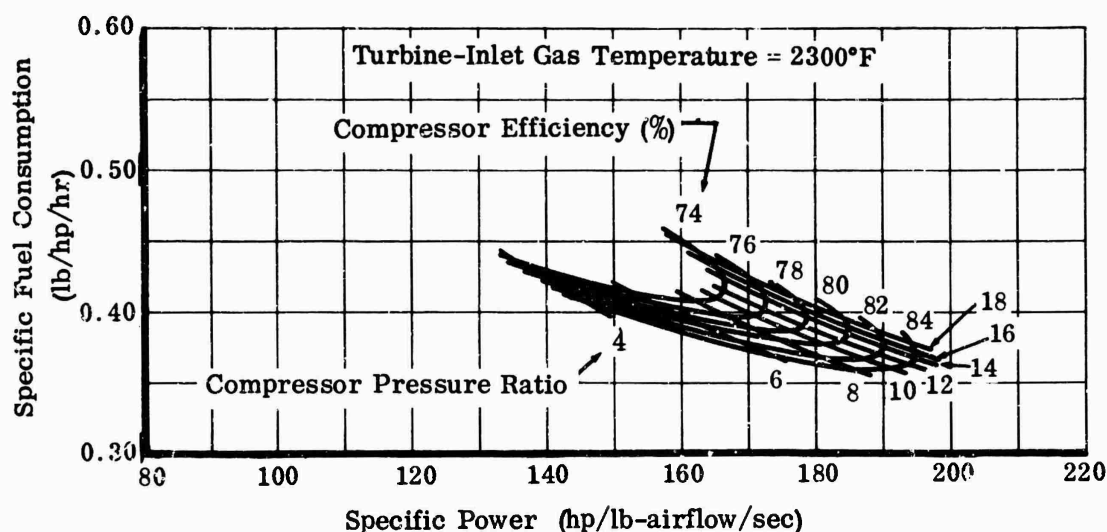


Figure 2. Effect of Compressor Performance on Regenerative Engine.

An itemized breakdown of design-point cycle parameters used to prepare Figures 1 and 2 is given below:

Gas-Producer-Turbine Total-to-Total Efficiency (Percent)	86
Power-Turbine Total-to-Static Efficiency (Percent)	83
Burner Pressure Drop (Percent)	4
Burner Efficiency (Percent)	98
Gas-Producer-Rotor Mechanical Loss (Percent)	2
Turbine-Output-Section Mechanical Loss (Percent)	3
Lower Heating Value of Fuel (Btu/lb)	18,400

The gas-producer-turbine and power-turbine efficiencies selected for the cycle studies are compatible with current Boeing technology; moreover, this performance does not require improvement in turbine aerodynamics. Boeing research programs completed in 1965 have indicated the feasibility of reducing the combustion-system pressure drop in high-temperature combustors below 4 percent and of increasing combustion intensity, while maintaining a 100° to 150° F peak-to-mean exit temperature spread. Gas-producer-section, turbine output-section, and accessory-drive mechanical losses are based on current test experience.

The relationship of part- to full-load specific fuel consumption is significant in most powerplant applications. The effect of high-cycle pressure ratio and high-cycle temperature on this relationship has been investigated. Figure 3 compares part-load performance of both the regenerative and nonregenerative future engines with the performance of a current engine. As shown, the fuel consumption advantage of the future high-pressure, high-temperature engine increases as power decreases. At 40-percent load, the simple-cycle engine shows a 34-percent reduction in part-load specific fuel consumption relative to current engines, and the regenerative engine shows a 50-percent reduction. In each instance, the performance of the advanced technology engine meets the requirements of future Army gas turbines.

1.2 PREVIOUS RELATED EXPERIENCE

Development of centrifugal compressors for small-gas-turbine applications was initiated by The Boeing Company in the mid 1940's. Early efforts were based on supercharger design principles and led to the development of a centrifugal compressor with a pressure ratio of about 3:1 at an efficiency of 74 percent. This compressor was the basis for the first production engines; however, research programs were initiated to advance compressor technology. These early studies resulted in the development of 4.3:1 pressure ratio at an efficiency of 76.5 percent. This performance was attained by improving the design of the inducer section of the impeller and by advancing the impeller-tip wheel speed to 1530 feet per second.

At this point, Boeing elected to advance its single-stage compressor technology, and a new design based on experience gained from earlier compressor development resulted in a 6:1 pressure ratio at 76-percent efficiency. This 6:1 pressure-ratio compressor advanced Boeing technology into the region of transonic Mach numbers at the impeller tip. It was discovered that impeller-tip Mach numbers of about 1.2 could be accepted without performance loss. This successful operation in the transonic region also indicated that still higher impeller-tip Mach numbers were attainable without large efficiency losses (approximately 3 to 5 percent). Thus, the potential existed for achieving pressure ratios with a single-stage compressor previously reached only in multistage designs.

Research to develop analytical methods for studying transonic impeller characteristics was begun. To advance the centrifugal-compressor research effort, Boeing developed computer programs for studying aerodynamic conditions throughout the impeller and the diffuser and for analyzing impeller blade shape and diffuser passage design. These computer analyses and newly developed water-table techniques for diffuser analyses permitted preliminary evaluations of many configurations in a short time. Test and analysis of transonic diffuser-element performance showed that better diffuser-vane (passage) configuration designs were necessary to advance compressor pressure ratio further.

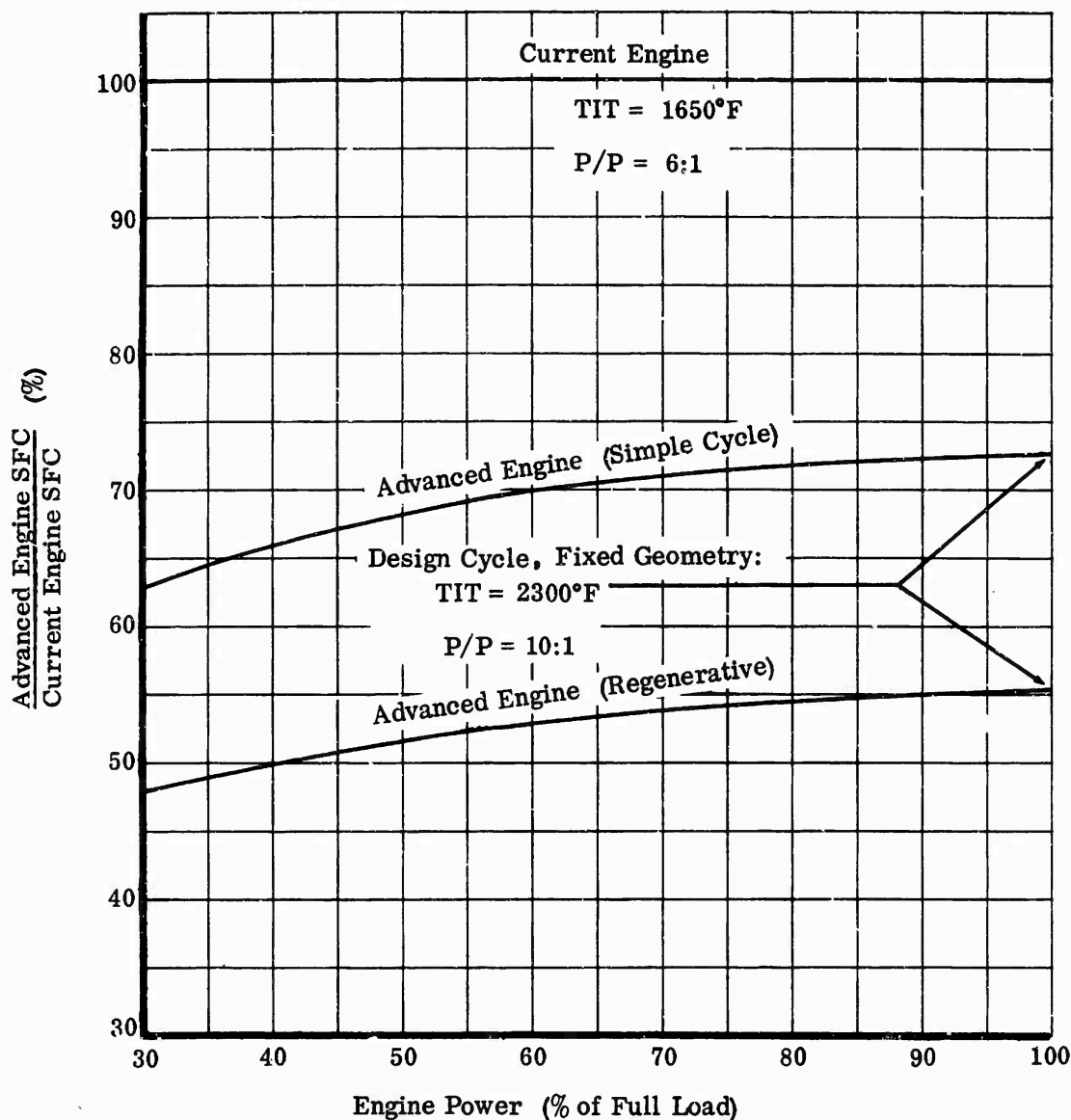


Figure 3. Effect of Cycle Temperature and Pressure on Part-Load SFC.

The centrifugal impeller for the 6:1-pressure-ratio compressor was developed by treating the inducer and impeller as a single unit. A later investigation, in which the inducer was analyzed separately, showed a tip diffusion factor of 0.66, much higher than normally is accepted for axial-compressor designs. This factor was reduced to an acceptable 0.45 by decreasing the rate of diffusion through the inducer, which was accomplished by reducing the exit area of the inducer while maintaining the original inlet conditions. The tip diameter along the inducer

length was kept constant. Compressor performance was improved by designing a new impeller to match the modified inducer and by incorporating these components into a complete compressor. Test results from this new configuration were compared with results from previous tests. Figure 4 shows the original 6:1 compressor map, and Figure 5 shows the compressor map for the modified configuration. Performance of the modified configuration increased by 4 percent, to 80-percent efficiency. The 6:1 pressure-ratio, single-stage, centrifugal-compressor program indicated that an axial-compressor design criterion, the diffusion factor, was directly applicable to inducer analysis. This type of analysis and other analytical design methods developed for centrifugal compressors showed that even higher performance levels could be reached.

Further studies indicated that pressure ratios of 10:1 at high efficiency were possible. Research areas were identified, and it was determined that available design information would require further refinement if high centrifugal-stage pressure ratios were to be achieved. Analyses of the internal fluid mechanics of impellers were inadequate and not suitable for use in reaching the 10:1 pressure ratio. Consequently, research was conducted to establish new criteria for internal-flow diffusion, turning, and separation. Another critical factor in achieving a high pressure ratio was an improved understanding of the complex flow fields from the impeller tip to the diffuser inlet. The changing character of transonic flow in this vaneless region required more thorough assessment. The diffuser-channel flow behavior was carefully studied.

1.3 RESEARCH APPROACH

From previous analytical studies to achieve a single-stage pressure ratio of 10:1, it was established that significant technical advances would be necessary in both impeller and diffuser designs. Specific areas of investigation for the USAAVLABS centrifugal-compressor research program were: (1) minimizing the effects of transonic flow conditions at the inducer and the diffuser entrance, (2) determining the influence of inducer hub-to-tip diameter and its effect on inducer and impeller performance, and (3) establishing methods to provide adequate operating range at high pressure ratios.

The high pressure ratio and efficiency at low design airflows had to be achieved; thus, the program was planned for a compressor in the 2-pound-per-second range. Other compressor research at low design airflows (where Reynolds number, scale effects, and manufacturing tolerances are particularly important) had indicated that scaling compressor sizes upward in flow capacity was easier than scaling them downward. Therefore, the greatest technological advantage will most probably be realized with the smallest component size.

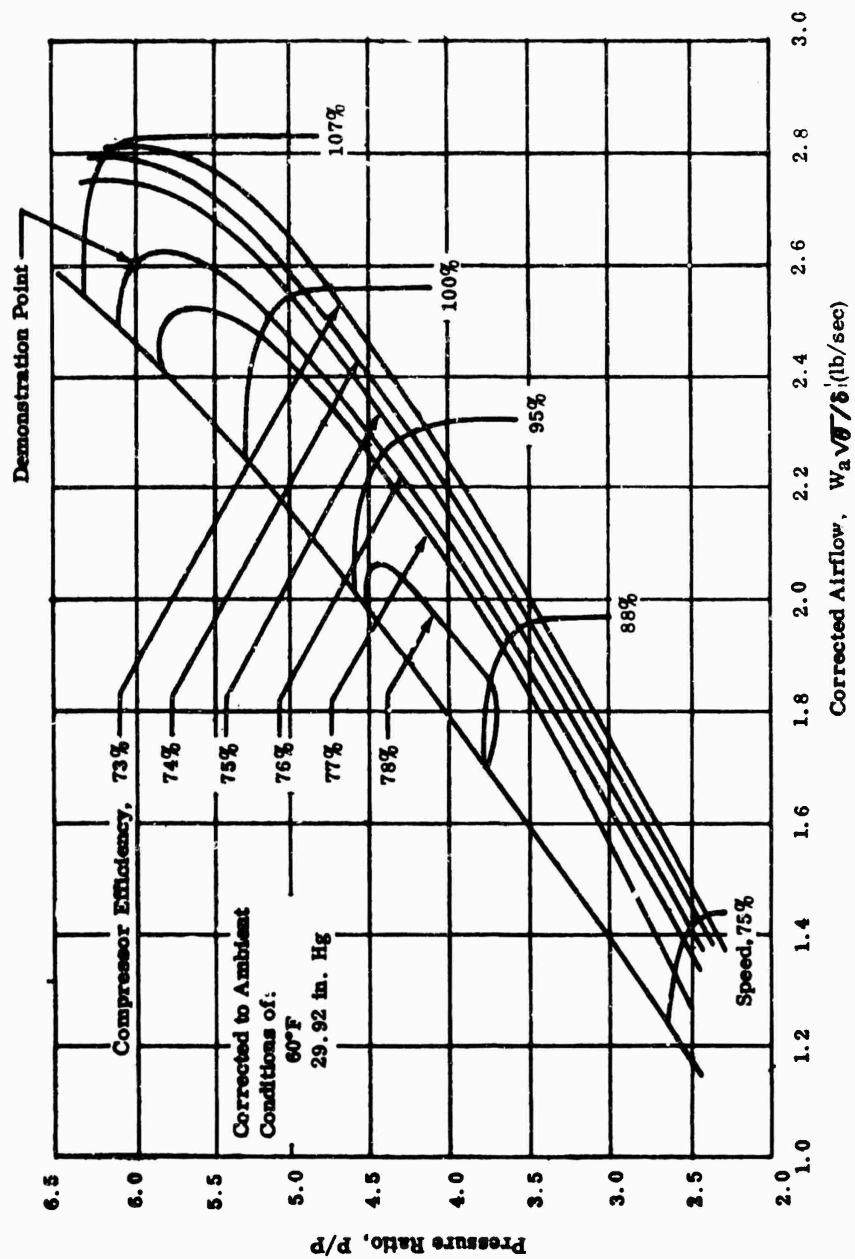


Figure 4. Single-Stage Centrifugal Compressor.

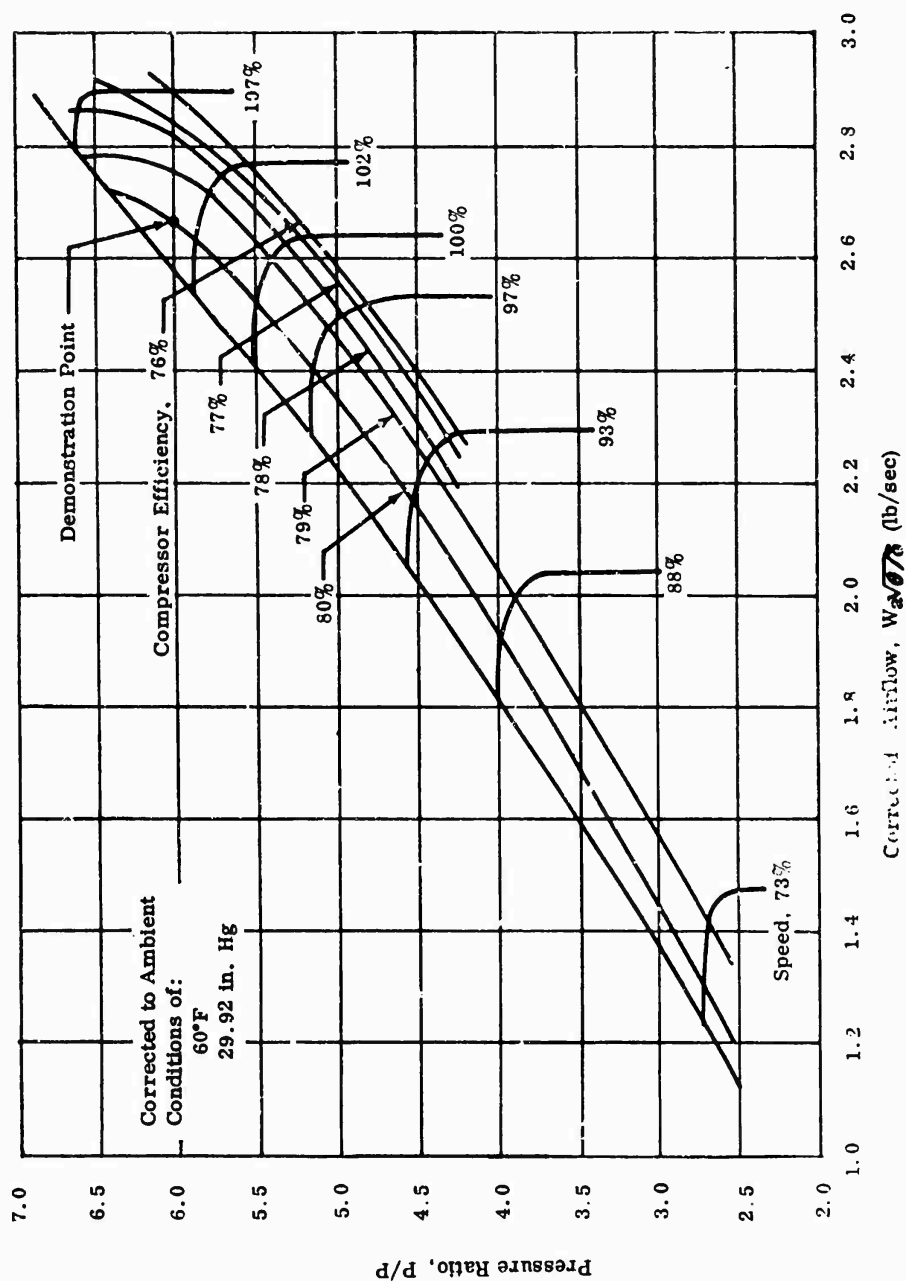


Figure 5. Single-Stage Centrifugal Compressor With Redesigned Impeller.

Early in 1964, impeller and diffuser elements were designed to provide the technology required to reach a 10:1 pressure ratio at 80-percent efficiency. These first elements were tested and evaluated concurrently to define the physical dimensions and flow dynamics of components. From this performance evaluation, a new, complete compressor was designed to reach the specified performance levels.

CONFIDENTIAL

(C) 2.0 ANALYTICAL STUDIES (U)

The purpose of this research program was to establish the technology for a future high-pressure-ratio, high-efficiency, single-stage centrifugal compressor that would provide a pressure ratio of 10:1 at 80-percent efficiency with an airflow of 2 pounds per second. The general approach in the analytical studies was to determine the relationships of the various parameters that affect centrifugal-compressor performance. The following sections present the details of the studies made to define the aerodynamic components.

2.1 PRELIMINARY DESIGN REQUIREMENTS

The feasibility of reaching this performance was based on a review (early in 1964) of available compressor technology discussed in Section 1.0, Introduction, of this report. The compressor map shown in Figure 5 of Section 1.0 is the result of tests conducted before the start of this program. In part, these data formed the basis of the studies discussed in this section. Pressure ratios of 6:1 to 6.7:1 were achieved at efficiencies of 78 to 80 percent, respectively, and airflows between 2 and 3 pounds per second. By expanding this earlier research with technology from the Army-contracted program, higher pressure ratio will be possible at equally good efficiency.

To reach the performance levels shown in Figure 5, design principles were re-evaluated. For analysis, the impeller was divided into 2 sections: the inducer section and the radial section. Figure 6 is a sketch of a typical centrifugal compressor. The greater part of the work performed by the impeller is done in the radial section, where the air is brought to the tip at absolute velocities approaching wheel speeds. However, the achievement of high pressure ratio depends not only on high tip velocities, but also on the passage design. It was believed that inducers operate similarly to axial-flow compressors; thus, for evaluation, Boeing adopted the method of analyzing this section by using axial-compressor criteria. The work to demonstrate the effectiveness of this experimental approach was begun in 1963.

For performance demonstration, an existing Boeing compressor with a 6:1 pressure ratio at 76-percent efficiency was analyzed. The inducer section was found to be aerodynamically overloaded when compared to an axial compressor and had a tip diffusion factor of 0.66. Therefore, this section of the compressor was redesigned for an acceptable tip diffusion factor of 0.45, and the overall compressor efficiency was increased by 4 percent. This experiment showed that flow separation losses had been minimized by improving the flow-area schedule through the inducer-impeller combination. Diffusion factors and turbulent-boundary-layer shape criteria were used to select the correct flow-area schedule. This new design indicated that further efficiency gains could be achieved as refinements were developed through additional research.

CONFIDENTIAL

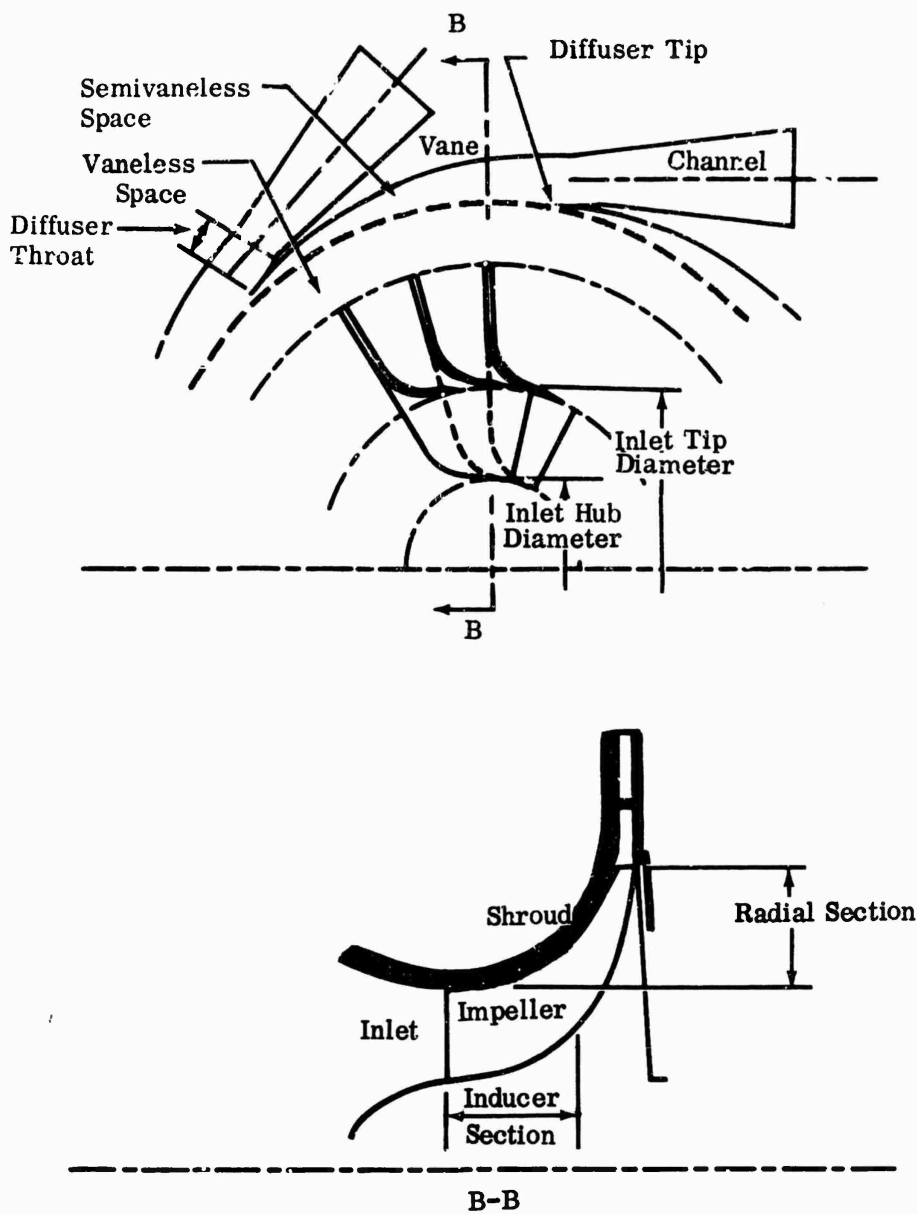


Figure 6. Typical Single-Stage Centrifugal Compressor.

CONFIDENTIAL

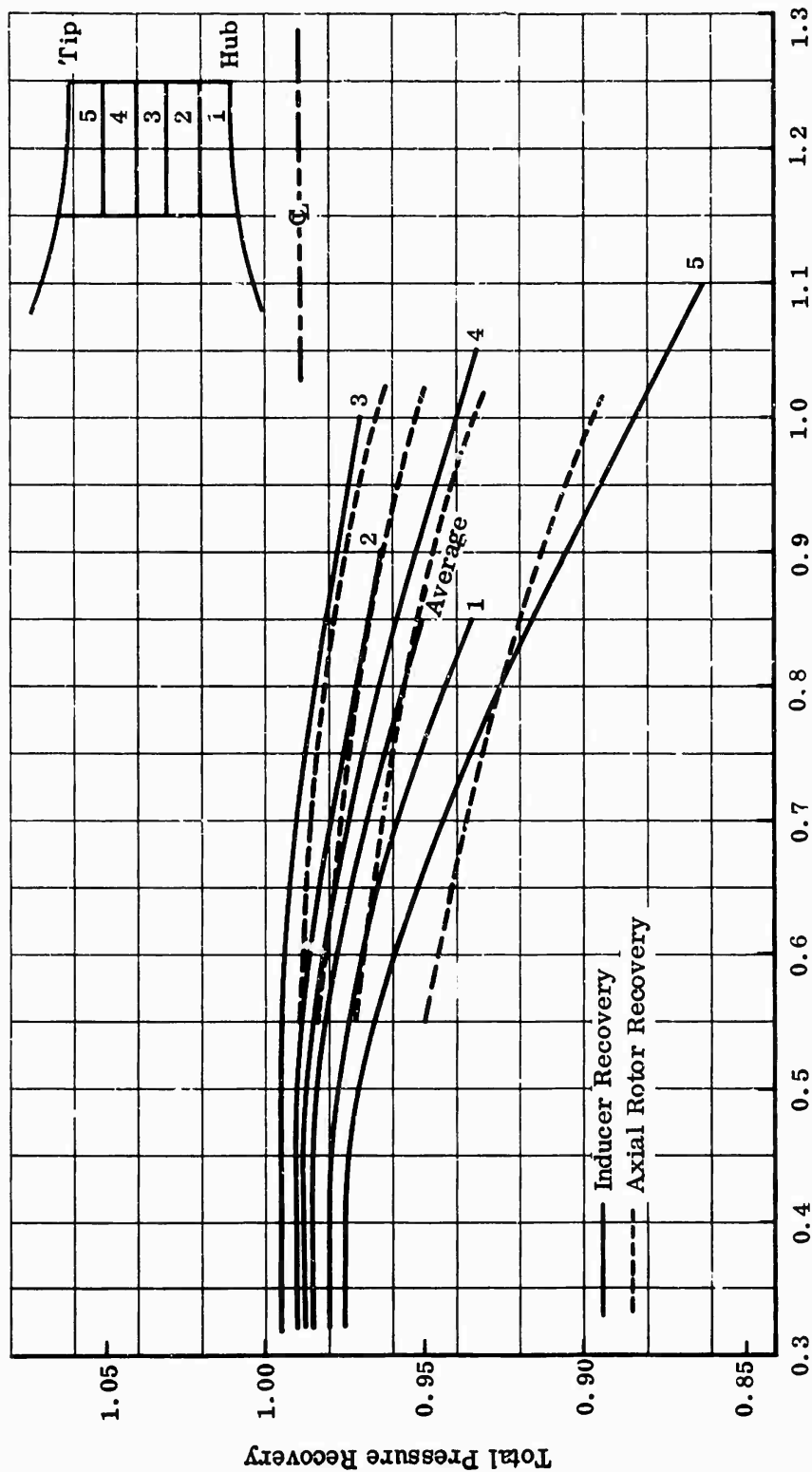
In conjunction with the above program, isolated inducers were experimentally evaluated at tip Mach numbers up to 1.1. The results of this work showed that efficient rotors could be designed for operation in the transonic region. It was shown that the tip geometry of the inducer section could be made more consistent with axial-compressor designs without incurring large efficiency losses. In general, earlier conventional inducers were designed with leading-edge thicknesses of 0.05 to 0.06 inch. However, transonic axial stages were constructed with leading-edge thicknesses of 0.01 to 0.015 inch. A comparison of the two showed that, at subsonic inlet relative Mach numbers, the inducer pressure losses were similar to those of axial compressors. For higher Mach numbers (Mach numbers up to 1.1), pressure losses were greater for the inducer than for the transonic axial compressors. Figure 7 shows total pressure recovery at various relative inlet Mach numbers for the inducer sections and current transonic axial rotors. The indicated performance gains led to isolated inducer testing where the leading edges were trimmed to 0.025 inch. The tests showed that losses could be correlated with inlet relative Mach number and compared to transonic axial-compressor experimental data. Based on conclusions from these tests, the inducers for the Army centrifugal-compressor research program were designed with leading edges similar to those of the transonic axial rotors. With these data available for the inducer portion of the impeller, the remaining radial section could be analyzed to determine the range of geometries and rotor speeds required to attain a 10:1 pressure ratio.

2.1.1 IMPELLERS

This preliminary evaluation and the Euler work relation (page 30) showed that the required impeller-tip speed for the 10:1 pressure ratio was 2000 fps. This tip speed results in a large-diameter impeller unless a high rotor speed (rpm) was used. For a given inlet hub-to-tip-diameter ratio, the limits applied to the inlet relative Mach number directly influence rotor rpm, and, therefore, overall impeller diameter. To obtain this technology for a small, lightweight engine, the ability to achieve Mach numbers as high as those for a transonic compressor must be investigated. Therefore, inducer analysis required further refinement of geometric data on the inlet area selected for the 2-pound-per-second airflow.

As an example of the factors considered, design at conventional inlet Mach numbers (below 0.85) would require a small inducer hub-to-tip-diameter ratio (i.e., a small hub diameter) and would result in a large-diameter impeller at low rpm. In addition, the small inducer hub diameter would limit the number of blades that could be used; usually the number of blades would be so few as to cause wide blade spacing at the impeller tip. Consequently, control of the flow near the impeller tip would not be possible, and large regions of flow separation would occur. To avoid this difficulty, blade spacing in some designs has been reduced by adding half blades in the radial portion of the impeller. However, this method has met with only limited success because the half blades have been

CONFIDENTIAL



Inducer Inlet Relative Mach Number (M_2)

Figure 7. Comparison of Inducer Recovery With Transonic Axial Rotor Recovery.

CONFIDENTIAL

located midway between the full blades, placing them in a region where high incidence at their leading edges has offset the predicted efficiency gains. This incidence results from nonuniform velocity distributions through the blade passages.

The basic impeller design problem is to achieve the best balance of the various parameters that affect performance, which are:

- 1) Inducer hub-to-tip-diameter ratio;
- 2) Inducer-tip relative Mach number;
- 3) Rotor speed (rpm) and its effect on impeller-tip diameter;
- 4) Number of blades at the inducer and their effect on spacing near the impeller tip;
- 5) Area schedule through the blade passages.

In each design studied, the objective was to control aerodynamic loading through the passages to avoid early separation. The investigations included studying inducer-tip Mach number at various hub-to-tip ratios for the various rpm selected. Throughout the study, blade spacing at the impeller tip was used as a parameter in determining whether overall proportions were suitable for further study. Figure 8 shows a schematic comparison of flow separation at the tip for 2 impellers having different numbers of blades. A flow separation is shown on the suction surface of the blades and accounts for the relative air outlet angles being less than 90 degrees. This angle varied with the aerodynamic loading of each impeller. Figure 8 also shows that separation occurs earlier in the passage and that exit wake is greater (total pressure loss and aerodynamic slip are higher) for the impeller with fewer blades, so that the flow leaves the impeller in a direction farther from radial. For an increased number of blades, the relative velocity vector is more nearly radial, which results in a larger energy input to the air at a given rotor speed.

Figure 9 shows three impellers with equal blade spacing at the hub but with different hub and tip diameters. The inducer with the lowest hub-to-tip ratio has the largest impeller blade tip spacing — this type of design would be subject to early flow separation. However, the highest hub-to-tip ratio shows the smallest blade spacing at the tip but operates at the highest inducer-tip Mach number. In each case, a higher rpm would reduce the impeller-tip diameter and improve the spacing relationships in that area but would require a higher Mach number at the inducer inlet. These analyses were conducted on impellers having only radial blade elements, although some compressors explored by other researchers have had backward-curved impeller blades to minimize flow separation near the tip

CONFIDENTIAL

CONFIDENTIAL

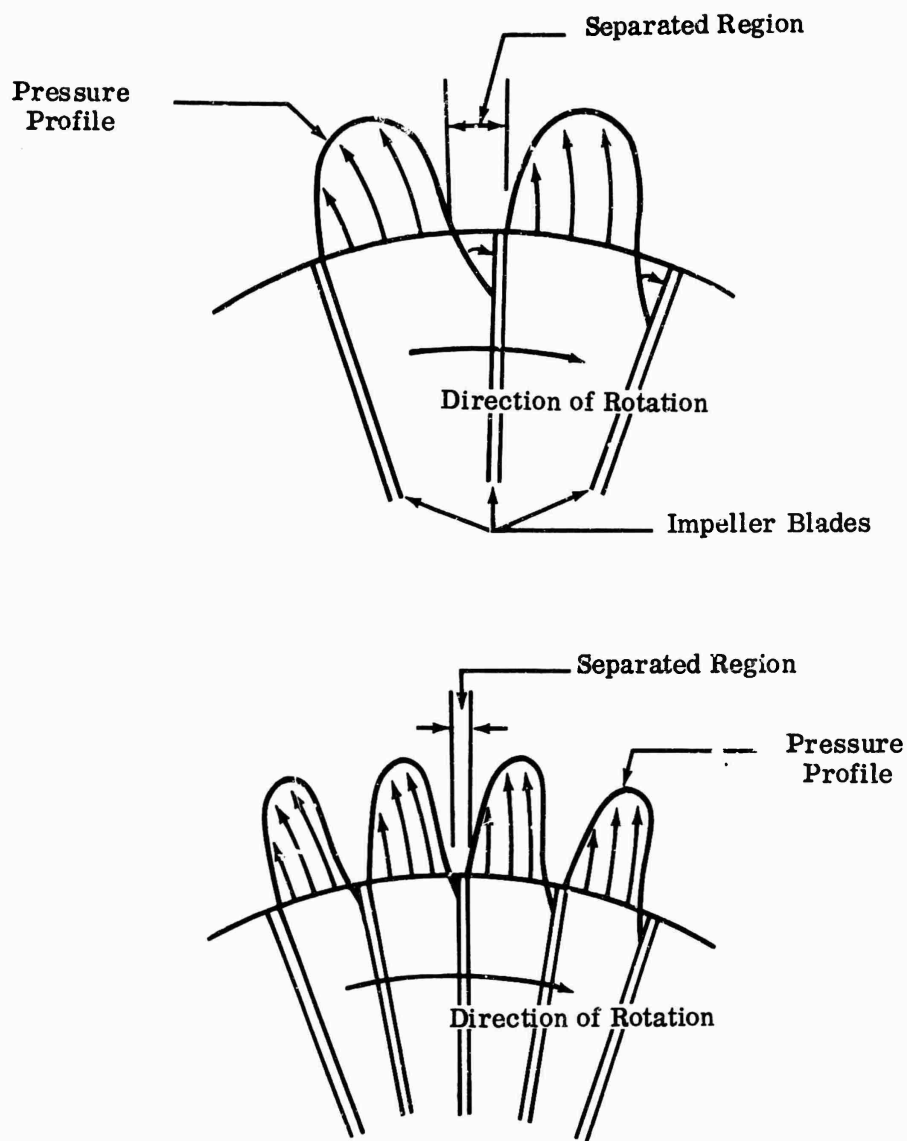


Figure 8. Comparison of Pressure Profile for Two Impellers.

CONFIDENTIAL

CONFIDENTIAL

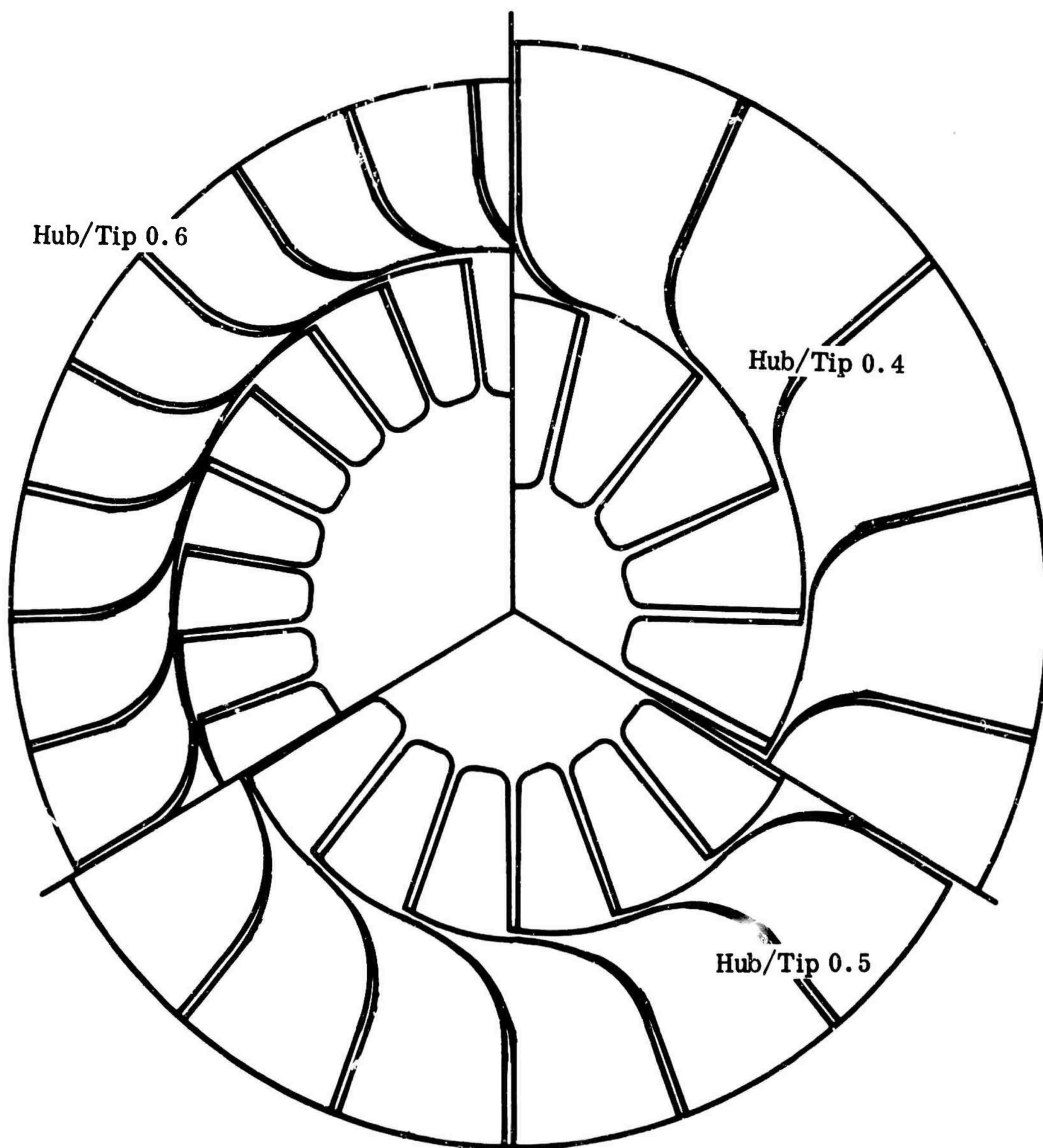


Figure 9. Impellers With Equal Blade Spacing at Inducer Hub.

CONFIDENTIAL

CONFIDENTIAL

region. This approach was considered but was dismissed early in the program because of structural difficulties from high stresses caused by the nonradial blade elements. In addition, backward curving would be accompanied by a further increase in stress because the required tip speed would be increased beyond 2000 fps to compensate for the reduced change in momentum at the tip. At lower pressure ratios and tip speeds, this design can reduce aerodynamic loading at the impeller tip; thus, it should be considered for use where centrifugal stresses are low enough to warrant a more complete investigation.

A review of other designs indicated that mixed-flow impellers should also be considered. It was believed that 1 to 2 efficiency points can be gained over the conventional radial-type impellers because of the reduced amount of radial turning from inlet to exit in the mixed-flow impeller. This design is characterized by a rearward lean of the blade passage in a meridional view. Figure 10 illustrates a mixed-flow impeller, typical of those considered for further research work. Such designs should be evaluated not only because of predicted efficiency gains but also because of possible improvements in blade root stresses from reductions in radial blade height. The disadvantages of this impeller design are that the diffuser must be positioned between conical walls, which makes fabrication difficult, and that there is a greater axial impeller length, which results in higher rotor weight than in the radial-type impeller.

At the outset, the research plan was to evaluate both the radial- and mixed-flow impellers to determine the advantages of each at the higher pressure ratios. Because major Boeing research already had been concentrated on the radial-flow impellers, early efforts in this program were to understand the mixed-flow impeller better. Therefore, the program plan included 3 mixed-flow impellers and 1 radial-flow impeller. All 4 were intended for high-pressure-ratio research on a special impeller test rig. A fifth impeller (radial type) was designed to evaluate different diffuser designs on another test rig. This impeller was designed for the same test condition and also yielded valuable design information.

2.1.2 DIFFUSERS

In establishing the research effort for diffusers, the preliminary design objectives were to define the complex flow fields from the impeller tip through the diffuser and to determine the highest possible pressure recovery. Achieving the necessary high efficiency in this area is complicated by flow-field changes in the vaneless space. For example, upon leaving the impeller, the flow must mix and assume a vortex distribution so that static pressure will rise in the radial direction. At some point in the vaneless space, an adjustment or transition in flow direction has to occur before the air reaches the diffuser tip, at which point the pressure rise becomes nonradial and normal to the flow direction through the diffuser passages. In addition, it was not clear whether efficient diffusion would occur before reaching the diffuser tip, because the area in the

CONFIDENTIAL

CONFIDENTIAL

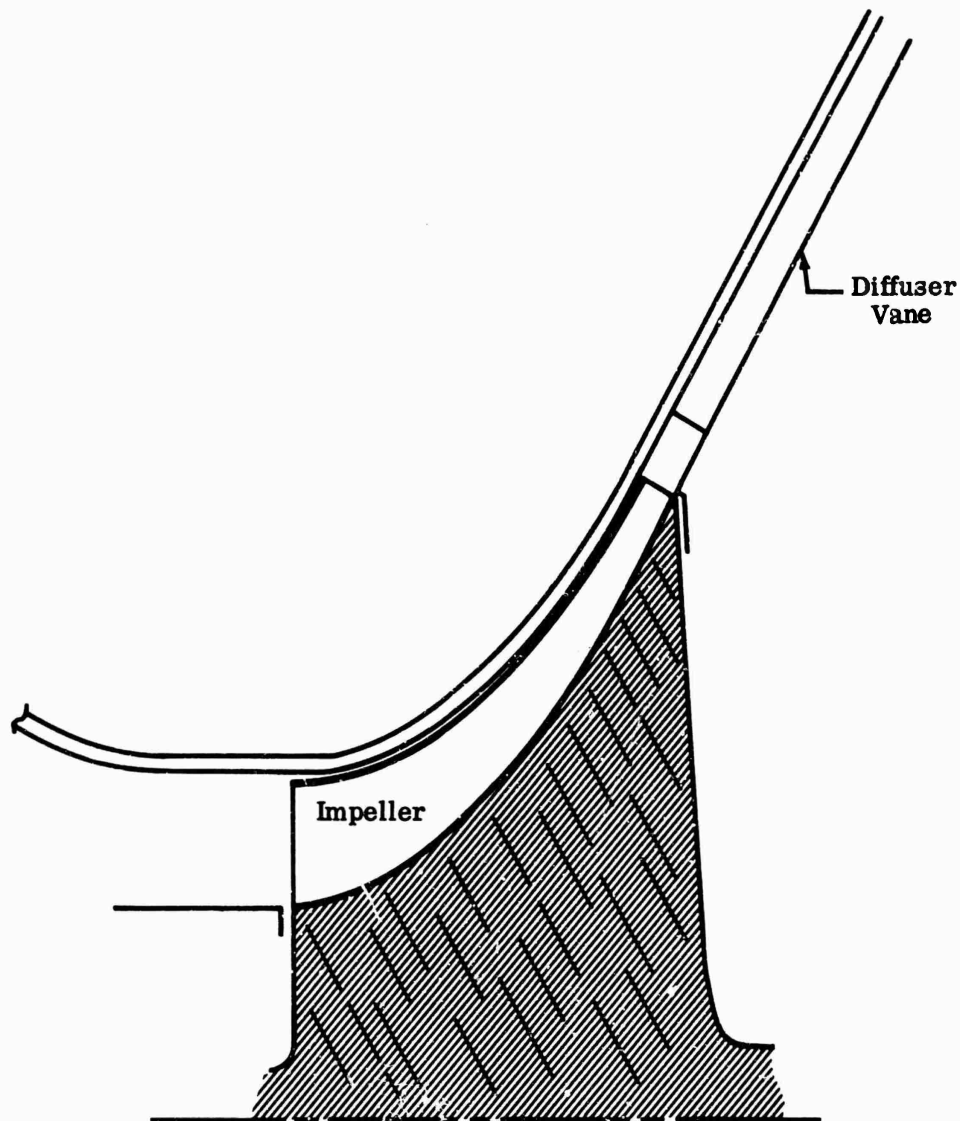


Figure 10. Mixed-Flow Impeller (Meridional View).

vaneless space increases in the radial direction during initial supersonic flow. Shocks were expected to occur ahead of the diffuser throat. A study of these effects was essential to the goals of this program; thus, tests of several configurations were planned.

CONFIDENTIAL

CONFIDENTIAL

To ensure an efficient diffusion process, specific problem areas were thoroughly investigated. For example, a 10:1 pressure-ratio compressor will operate with diffuser-tip Mach numbers of about 1.3 at a tip-blade height of about 0.20 inch. Some background information was available from earlier research in which Boeing used a shadowgraph technique to study a compressor at a pressure ratio of 7:1. For this case, Mach numbers at the vane leading edges were about 1.2. The effort produced the first clear evidence of shocks at the throat inlet. Figure 11 shows 1 of the pictures taken during the investigations. The effects of the shocks ahead of and at the channel entrance were known to influence boundary-layer development; consequently, performance of the downstream subsonic diffuser section will depend on the conditions existing at the beginning of the diverging section. If the shock were located in a region where the boundary layer was thinnest, separation effects and the influence of the boundary-layer conditions could be minimized.

Two basic types of diffusers were considered. The first was a cascade-type diffuser with airfoil vanes grouped in stages, and the second was the channel-type diffuser used in nearly all previous Boeing compressors. In studying each type, several factors were considered:

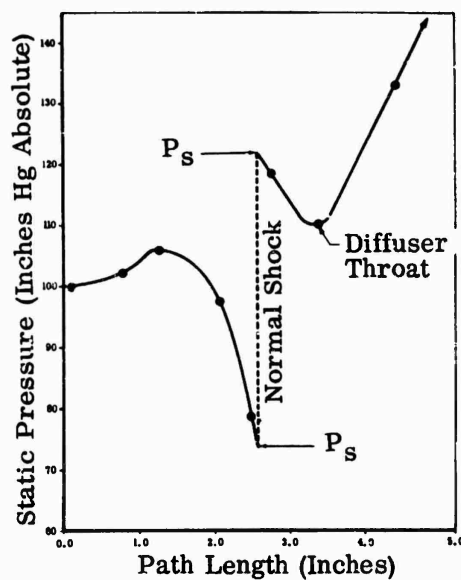
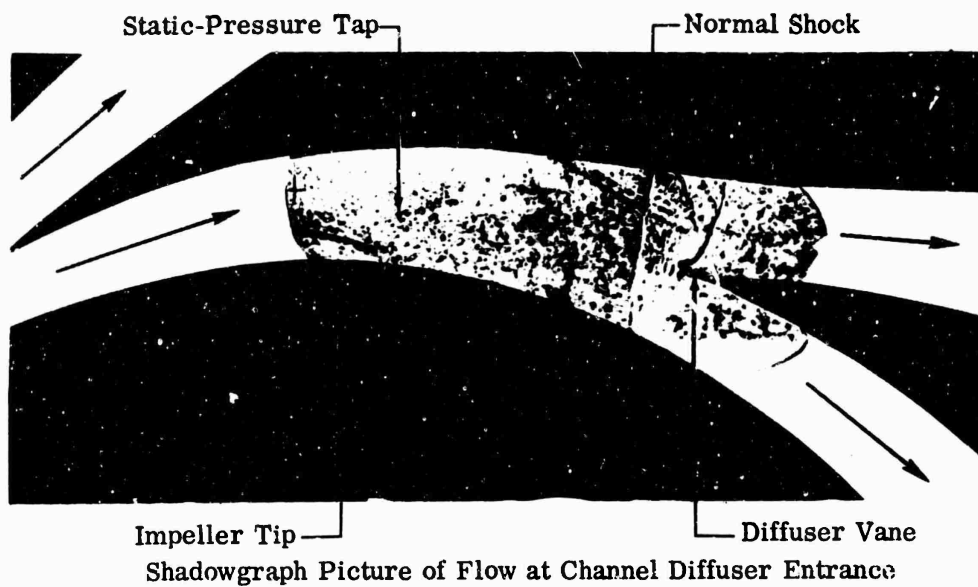
- 1) Friction loss depends on the air velocities and the wetted surface area. To minimize the effects in the vaneless and semivaneless space, a study of the number of vanes and diffuser-tip-to-impeller-tip-diameter ratio (diffuser-diameter ratio) was conducted.
- 2) Separation loss depends on Mach number, flow irregularities, and diffusion rate. The number of vanes and diffuser-diameter ratio also influence this loss.

For the cascade-type diffuser, 30 to 40 vanes would be required in the first row to minimize the path length from the impeller tip to the throat. In addition, a small diffuser-to-impeller-tip-diameter ratio, with the vanes located close to the impeller tip, would locate the shock early in the flow path, leaving the remaining portions of the path for subsonic diffusion. By reaching subsonic conditions as soon as possible, these friction losses in the vaneless and semi-vaneless space would be reduced. Further, the shock could be used to produce an efficient large static pressure rise in a short distance. Before establishing a configuration, a trade study of these parameters was made to assess performance. Losses from the shock were only 1 to 2 percent of total pressure. A more complete study was conducted of component design and cascade vanes to determine if this type of diffuser warranted further investigation.

The contractor has extensive research and development experience with the principal configuration, a channel-type diffuser (often referred to as a vane-island diffuser). Again, as with the cascade diffuser, trade studies were

CONFIDENTIAL

CONFIDENTIAL



Static-Pressure Distribution Along Flow Path

Figure 11. Diffuser Flow With Supersonic Inlet Velocity.

CONFIDENTIAL

CONFIDENTIAL

conducted for a range of designs, considering the various factors that affect diffuser performance. Three basic configurations were selected that would provide the test data necessary to validate the analytical studies. The components were designed to evaluate differences in diameter ratio, throat Mach number, and number of channels.

In these diffuser studies, variable airflow of the compressor at constant rotor speed was investigated. By holding compressor pressure ratio constant while reducing airflow for part-load engine operation, low specific fuel consumption throughout most of the operating range can be achieved if a turbine that meets the variable airflow conditions can be developed. To demonstrate these potentials, a rig test, for which available research components were used, was conducted during 1963. A set of variable guide vanes was used at the inducer inlet of a single-stage centrifugal compressor, which included an 8-channel diffuser. The diffuser channels were modified in a series of steps, and axial depth of the passages was reduced to agree with areas required for the expected flow changes. The guide vanes were used to adjust flow angles at the inlet to match the inducer angles. The objective was to determine performance characteristics at 3 settings: 100-, 75-, and 50-percent design airflow. The results of this preliminary test are shown in Figure 12. The results from this test warranted additional research on the concept, which was included in the Army centrifugal-compressor research program. A set of adjustable inlet guide vanes and adjustable diffuser channels was considered early in the design effort. However, the primary objective was to establish criteria for determining the best diffuser performance at design airflows; the secondary objective was to study variable flow capacity.

To gain the required technology, new information on flow phenomena ahead of the diffuser vane was necessary. Therefore, new techniques for gathering these data were studied.

- 1) **Recording of Pressure Data** — A thorough definition of static-pressure profiles in vaneless, semivaneless, and throat regions was essential. To study this flow field, static-pressure taps were located close together throughout the path to record small pressure changes. Approximately 100 taps in each of the 2 side walls were required, but manual recording of this many pressures was not feasible. Therefore, to achieve the desired result, a new system for instantaneously and automatically recording the pressures was purchased by Boeing for this research program.
- 2) **Water-Table Analogies** — A water table was available from previous research programs for preliminary evaluation of diffuser elements. The table was used for visually determining shock locations and flow separation regions; it provided an opportunity to study many configurations qualitatively in a short time.

CONFIDENTIAL

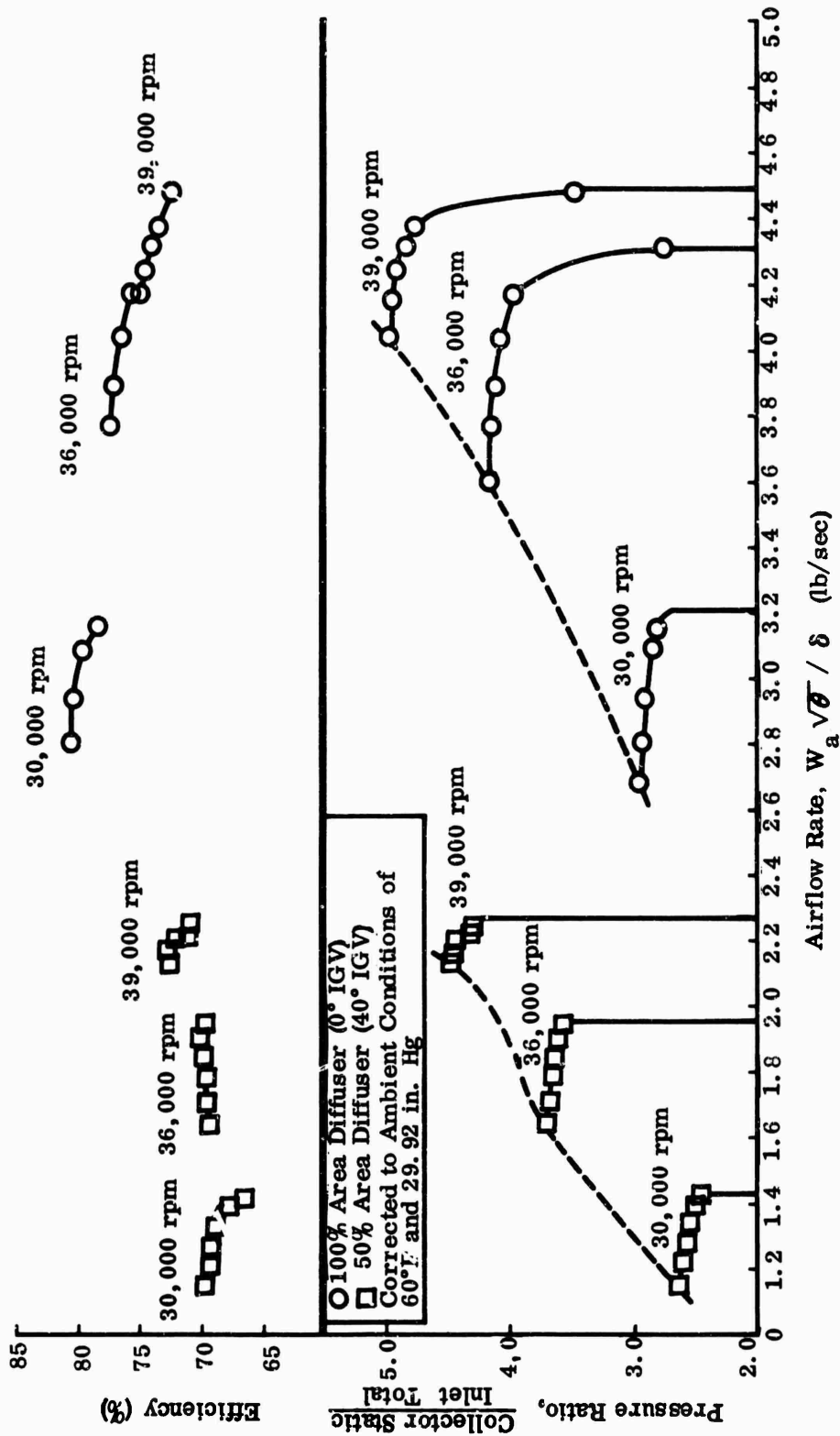


Figure 12. Single-Stage Centrifugal Compressor (Variable-Flow-Capacity Demonstration; Reduced Diffuser Flow Areas With Inlet Guide Vane Adjustments).

CONFIDENTIAL

- 3) Schlieren Studies — The best technique for correlating the above pressure surveys and water-table analogies was a schlieren system. The objective was to obtain visual evidence of density changes and to locate shocks along the early part of the diffuser path in the environment of the compressor test rig. Previous attempts to measure only pressure data were often misleading. Consequently, the contractor developed a special schlieren unit for use with the diffuser tests planned for the Army centrifugal-compressor research program.

The following sections present details of the above analytical studies used to select specific impeller and diffuser designs.

2.2 IMPELLER DESIGN

The detail design analyses reported in this section include parametric studies of impellers and impeller aerodynamics. In these analyses, inducer-diameter ratio, relative inlet Mach number, rotor speed, number of blades, impeller-tip geometry, and passage-area schedule were thoroughly studied. The relationship among the various parameters was determined, and areas requiring additional research and analytical development were identified.

Each impeller design was carefully evaluated through a logical sequence of analysis, beginning with the parametric study of design requirements, followed by the establishment of design methods, and ending with the definition of aerodynamic design criteria. This process led to the mechanical design of impeller test components.

2.2.1 PARAMETRIC ANALYSIS

The parametric analysis work included investigations in which performance trends were compared to geometric parameters. For this purpose, certain fundamental principles were used in evaluating the size, speed, and work relations. For a 10:1 pressure ratio at 80-percent efficiency, the value of work done, E , was calculated as 144.8 Btu/lb of airflow.

Using the Euler energy-transfer relation between a rotor and fluid, the impeller tip speed was determined as follows:

$$E = \frac{U_4^2 - U_1^2 + V_4^2 - V_1^2 + V_2^2 - V_3^2}{2 gJ} \quad (1)$$

CONFIDENTIAL

This equation can be simplified by using the geometric relationships from the vector diagrams shown in Figure 13.

$$E = \frac{V_T U_4}{gJ} \quad (\text{Zero Prewhirl Case}) \quad (2)$$

Introducing the definition of slip factor,

$$SF = \frac{V_T}{U_4} \quad (3)$$

Equation (2) becomes

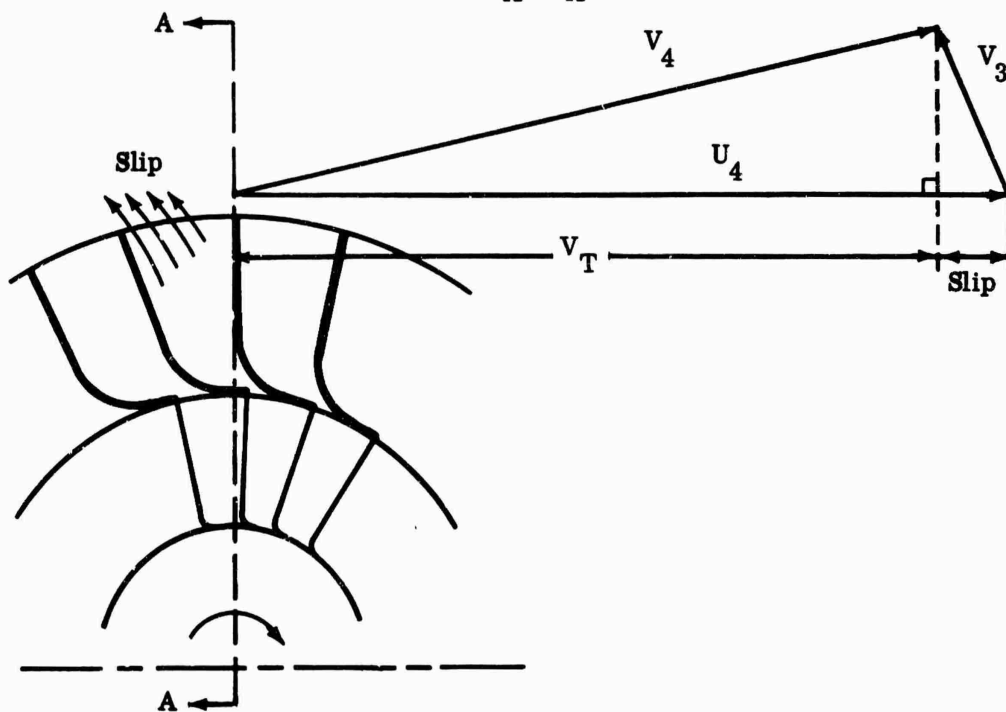
$$E = \frac{SF U_4^2}{gJ} \quad (4)$$

The symbols used in the above equations are:

- U_1 = inducer blade speed, fps
- U_4 = impeller blade-tip speed, fps
- V_1 = absolute air velocity at inducer inlet, fps
- V_4 = absolute air velocity at impeller blade tip, fps
- V_2 = relative air velocity at inducer inlet, fps
- V_3 = relative air velocity at impeller tip, fps

Assuming that the inducer inlet absolute velocity is axial, the amount of slip had to be estimated to determine impeller-blade-tip speed. Primarily, slip varies with the number of blades (i. e., wide spacing of blade tips produces more slip than when the blades are close together). The effect is also illustrated in Figure 13. To reach the required work input, impeller-blade-tip speed would have to be about 2000 fps.

CONFIDENTIAL



32

CONFIDENTIAL

CONFIDENTIAL

The following expression of overall size and speed relationships applies to each point along the blade:

$$U = \frac{\pi DN}{720} \quad (5)$$

where:

U = blade speed at any selected point, fps

D = diameter at selected point on blade, in.

N = rotor speed, rpm

NOTE: The constant value of 720 is used to convert blade speed from in./min to fps. If impeller-blade-tip speed is known, rotor speed (N) and tip diameter (D) are related — either parameter will define the other.

To determine rotor speed, inlet conditions at the inducer must be established, as shown in the inlet velocity diagram (Figure 14).

The initial analytical calculations involve the vectors shown in this diagram. In practice, limits imposed on the inlet relative velocity and Mach number (M) at the inducer tip indirectly establish the required rotor speed. In this study, maximum Mach numbers ranged from 0.80 to 1.40. A second influence on rotor speed is inducer-inlet hub-to-tip-diameter ratio. Industry experience indicated that this ratio should range from 0.40 to 0.70 to maintain good performance, stress, and vibration characteristics. For each design, blade diameters were selected for flow continuity and axial inlet velocity. By using the rotor-speed relations of Figure 14, the inducer-geometry shown in Figure 15, the rotor size and speed can be determined from

$$W_a = \rho_s A_s V_s \phi \quad (6)$$

where

$$\rho_s = \frac{\rho_t}{\left[1 + \left(\frac{k-1}{2} \right) M_1^2 \right]^{\frac{1}{k-1}}} \quad (7)$$

CONFIDENTIAL

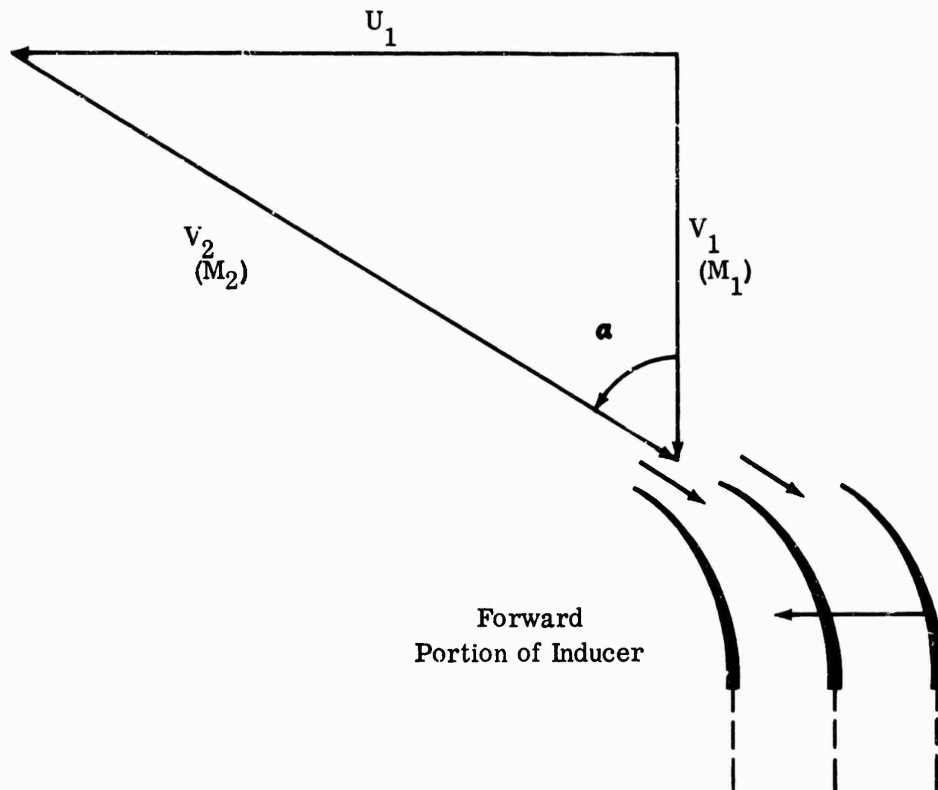


Figure 14. Inducer-Inlet Velocity Diagram.

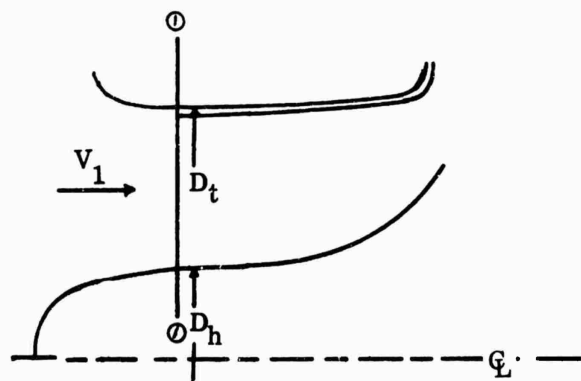


Figure 15. Inducer Geometry.

CONFIDENTIAL

CONFIDENTIAL

By definition:

$$M_1 = \frac{V_1}{a} \quad \text{and} \quad M_2 = \frac{V_2}{a} \quad (8)$$

$$A_1 = \frac{\pi}{4} \left(D_t^2 - D_h^2 \right) = \frac{\pi}{4} \left(D_t^2 \right) \left[1 - \left(\frac{D_h}{D_t} \right)^2 \right] \quad (9)$$

Symbols used in Figure 15 and the above equations are:

- W_a = airflow rate, lb/sec
- ρ_s = air density based on static conditions, lb/ft³
- ρ_t = air density based on total conditions, lb/ft³
- A_1 = inducer-inlet free area, in.²
- V_1 = absolute air velocity at inducer inlet, fps
- V_2 = relative air velocity at inducer inlet, fps
- ϕ = inlet blockage factor (dimensionless ratio: area blocked by blades and flow irregularities to free area just ahead of inducer)
- k = dimensionless ratio: specific heat at constant pressure to specific heat at constant volume
- M_1 = absolute inlet Mach number
- M_2 = relative inlet Mach number
- D_t = inducer-tip diameter, in.
- D_h = inducer-hub diameter, in.
- a = acoustic velocity, fps

Combining the relations given in Equations 6 through 9 yields:

CONFIDENTIAL

$$W_a = \frac{\rho_t \frac{\pi}{4} D_t^2 \left[1 - \left(\frac{D_h}{D_t} \right)^2 \right] V_1 \phi}{\left[1 + \left(\frac{k-1}{2} \right) \frac{V_1}{V_2} M_2 \right] \frac{1}{k-1}} \quad (10)$$

If the total inlet conditions are known, ρ_t is a constant, and k is assumed to be 1.40. By eliminating these terms, the related parameters become inducer-tip diameter, blockage, hub-to-tip-diameter ratio, absolute velocity, relative Mach number, and relative velocity. The relationship between V_1 and V_2 defines inducer-tip speed (Figure 14) and, hence, rotor speed.

Before geometric and performance trends could be plotted in this parametric analysis, inlet blockage and impeller slip (the number of blades) had to be known. For consistency, the number of blades was determined by setting a 0.20-inch spacing at the inducer hub. Also for consistency, the blade height (passage-area height) at the impeller tip was 0.20 inch. All other rotor parameters are determined by selecting hub-to-tip-diameter ratios and relative Mach numbers. The results of this parametric analysis are given in Figure 16. The plot of impeller efficiency is based on the pressure recovery study discussed in Section 2.1 of this report.

While these analyses represent the parametric trends for radial-flow impellers, additional comparisons were necessary for mixed-flow impellers. Prior studies indicated a consistent 1 to 2 efficiency-point advantage for the mixed-flow impeller over the radial-flow impeller, and this information was extrapolated for overall compressor efficiency (see Figure 17).

In reviewing the study results, the range of geometries best suited for research had to be determined. For example, to achieve small size and light weight, inducer-inlet relative Mach numbers should range from 0.95 to 1.2. In this range, impeller-blade-tip diameter would be between 6 and 8 inches for inducer hub-to-tip-diameter ratios ranging from 0.40 to 0.65. The resulting rotor speeds were between 57,000 rpm for the larger impellers and 74,000 rpm for the smaller impellers. The parameters in Figure 16 indicate only impeller performance. To achieve the overall target value of 10:1 compressor pressure ratio at 80-percent efficiency, the impeller total-to-total pressure ratio should range from 12.5:1 to 13.5:1.

CONFIDENTIAL

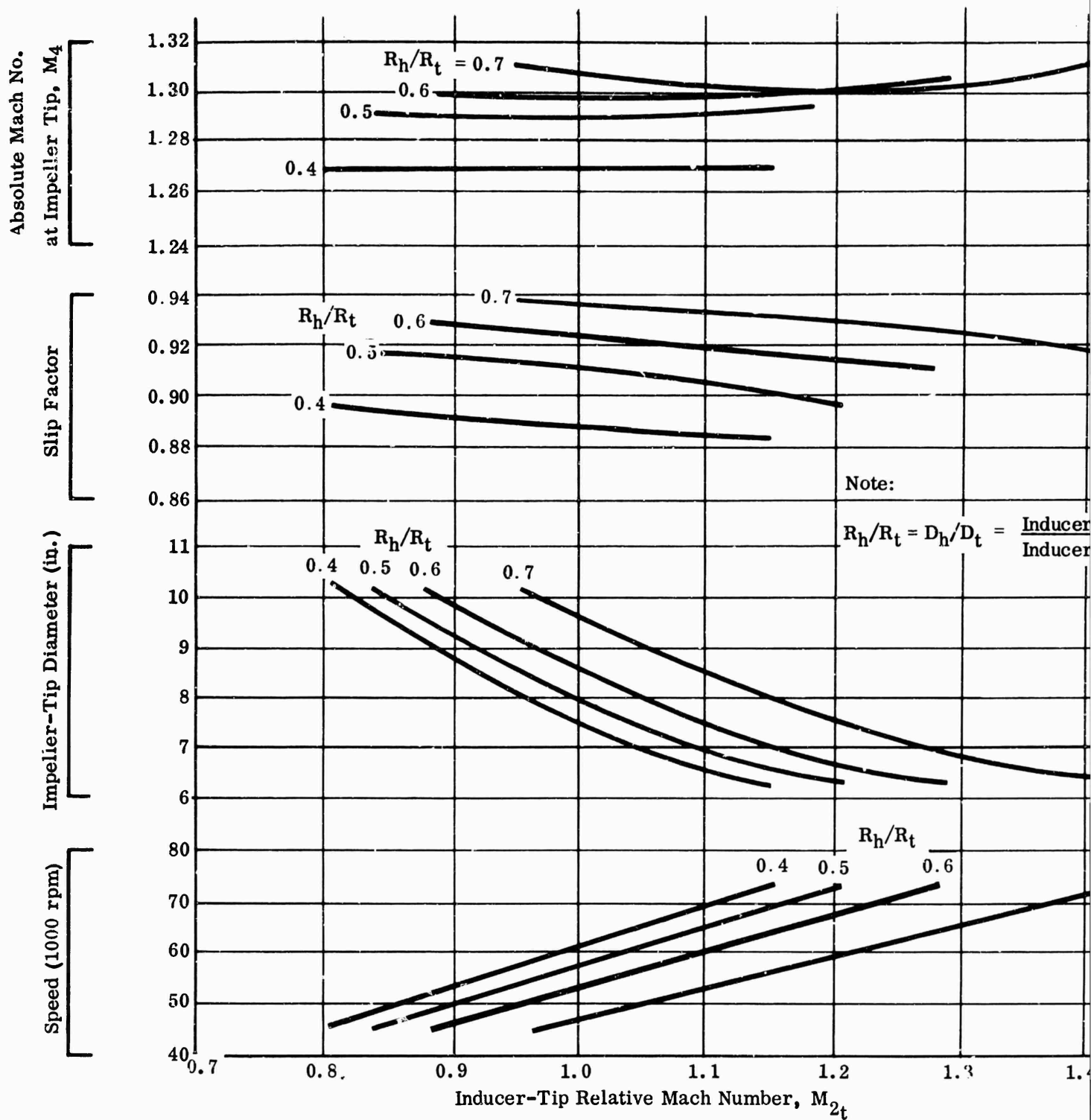
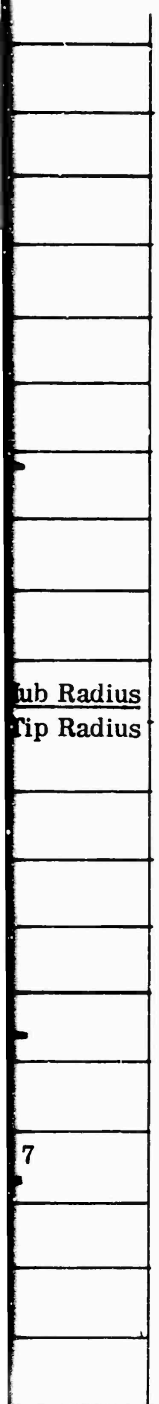


Figure 16. Impeller Parameters (Overall P/P = 10:1, $\eta = 80$ Percent, $M_1 = 0.50$).

CONFIDENTIAL



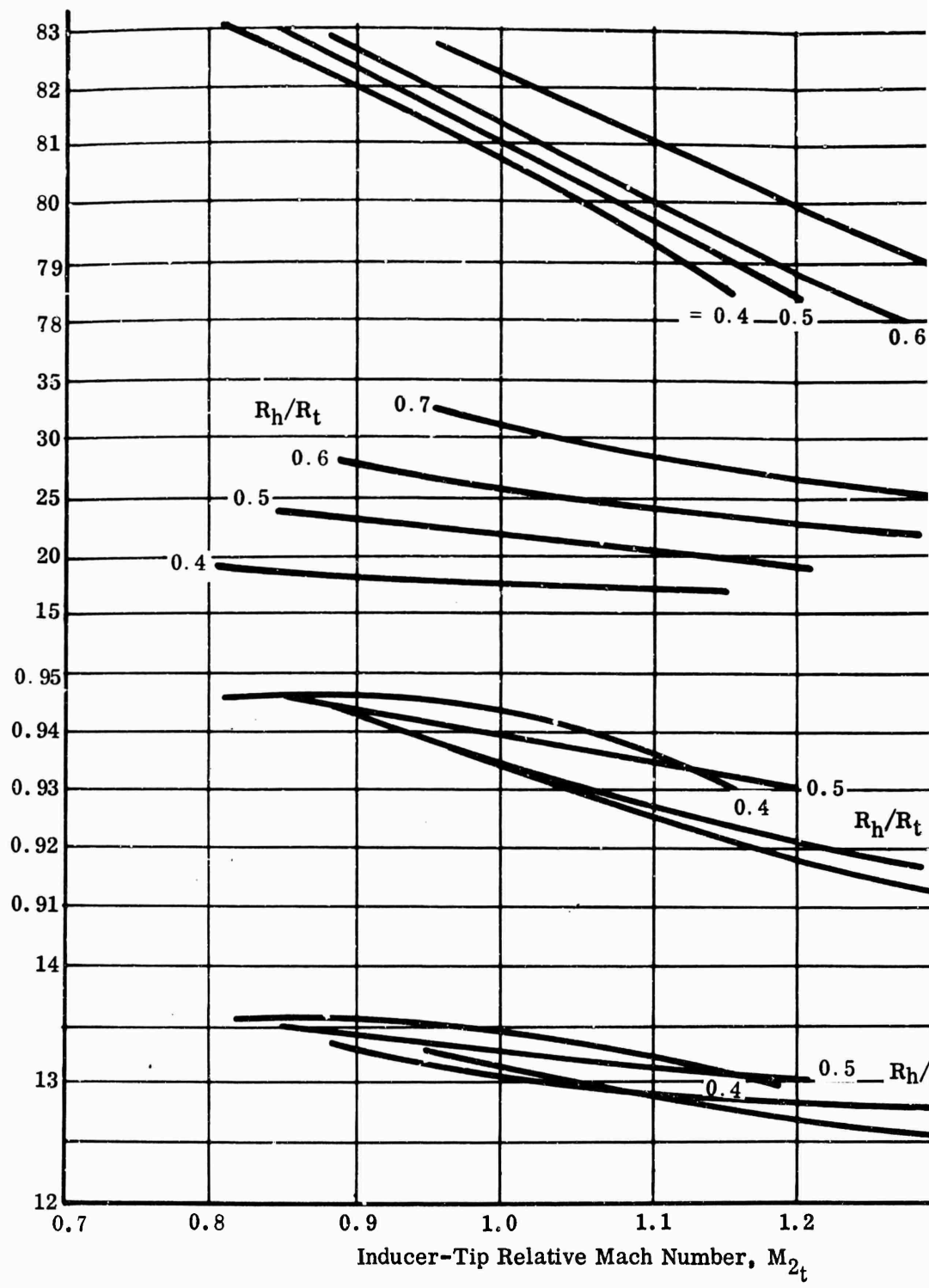
1.5

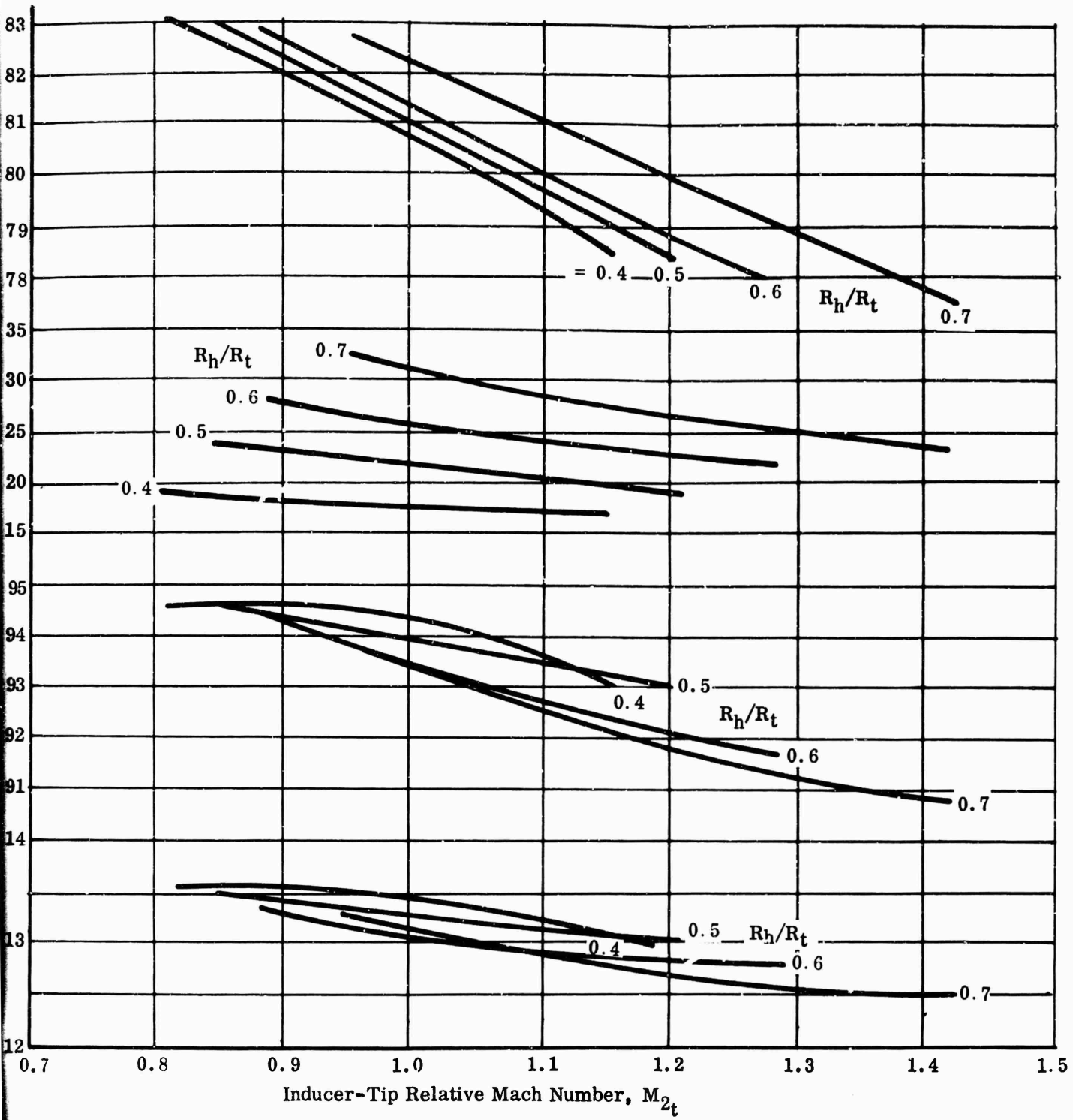
Absolute Angle
(from Radial Direction) at
Impeller Tip, α_4 (Degrees)

Number of Blades

Impeller Pressure Ratio

Impeller Efficiency (%)





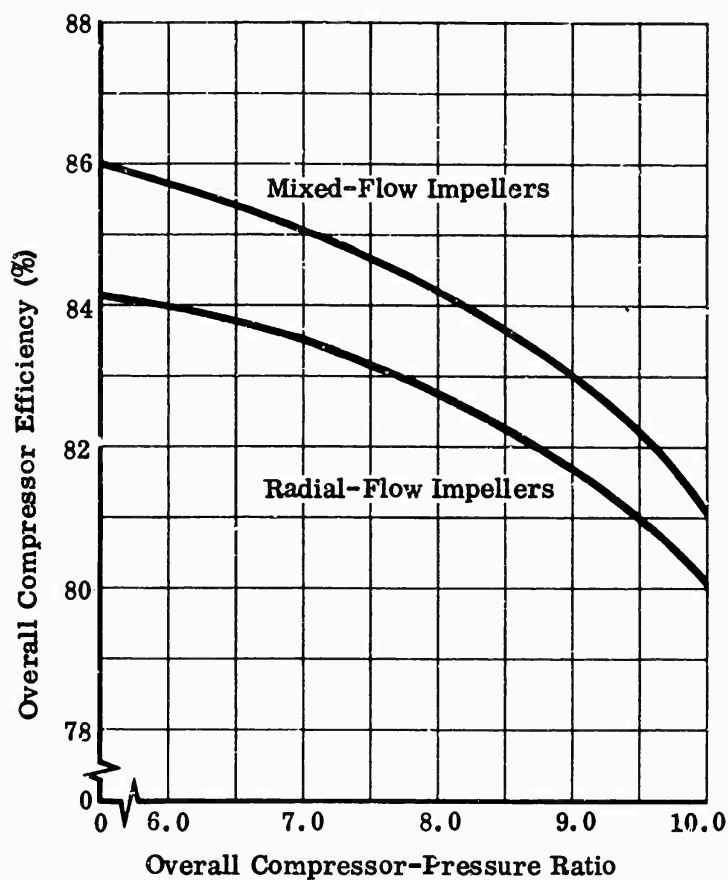


Figure 17. Comparison of Extrapolated Performance for Mixed- and Radial-Flow Impellers.

2.2.2 DESIGN METHOD

Four basic impeller designs were selected from the data generated in the parametric studies. For each design, a detailed internal-flow analysis was conducted. First, the inlet and exit velocities (vector diagrams) were constructed from the parametric study data. The inducer-inlet absolute Mach number (M_1) was assumed constant from hub to tip, because each configuration was designed without prewhirl. In addition, the blades were designed with only radial elements. The final designs were influenced by the following considerations.

Inlet Blockage — The inlet blockage factor (ϕ) is:

CONFIDENTIAL

$$\phi = \frac{\text{total annulus area} - (\text{blade area} + \text{boundary-layer area})}{\text{total annulus area}} \quad (11)$$

Blockage was determined by the number of blades and their thickness distribution from hub to tip. For the designs being evaluated, blockage from boundary-layer thickness was assumed to be 0.02. Overall blockage factors calculated from the above equation ranged from 0.90 to 0.96, depending on inducer geometry. In addition, blockage at the station of minimum area, just inside the blade row, determined the passage area and blade height for a given diameter ratio. Vector diagrams similar to those of Section 2.2.1 were then constructed and used to set the incidence angle at this station for the mean camber line. This incidence angle ranged from 0 to 1 degree.

One-Dimensional Analysis — With the vector diagrams established, a 1-dimensional analysis was conducted to determine airflow continuity through the impeller passage and to solve for blade-thickness blockage along the airflow path from the impeller inlet to exit. Blade turning, airflow-area schedule, and diffusion rates were determined through an iterative procedure in which the diffusion factor (see Reference 1) was used as the diffusion limit, which was set at 0.45 (refer to criteria discussed in Section 1.0, Introduction, of this report). The equation was:

$$DF = 1 - \frac{V_3}{V_2} + \frac{\Delta V_T}{2\sigma V_2} \quad (12)$$

This equation was used to calculate the diffusion factor at successive stations along the blade. The solidity (σ) and change in the tangential component of the relative velocity (ΔV_T) were determined from changes in airflow conditions at each succeeding blade station, with the inlet station being used as the fixed reference point. Having approximated the impeller shape in the 1-dimensional analysis, flow equilibrium now had to be established.

Flow Equilibrium Analysis — Radial equilibrium was established for airflow conditions through the impeller. In addition, at each station along the impeller airflow path, velocities on the blade and at midpassage were determined. Points at which rapid acceleration or deceleration occurred were identified, and passage-area geometry was adjusted. Because this work required numerous, time-consuming velocity calculations, a 5-streamtube computer program was developed.

CONFIDENTIAL

CONFIDENTIAL

The method of analyzing radial equilibrium was derived from Reference 2, and the complete computer program is presented in Appendix I. A brief description of its use is given below and in Table II.

TABLE II	
IMPELLER RADIAL-EQUILIBRIUM COMPUTER PROGRAM	
Knowns (Required for Analysis)	Assumptions (Required for Analysis)
Hub and Tip Radius Schedule	Nonviscous, Compressible Fluid Flow*
Blade Blockage Schedule	Uniform Velocity, Blade to Blade
Number of Blades	Relative Flow Angle Same as Blade Angle
Thickness of Blades	Steady-Flow Process
Blade Turning Schedule	Equal Mass Flow per Streamtube
Rotor Speed	Total-Pressure Recovery
Station Locations	
Overall Pressure and Temperature	
Rise, Using Inlet Station as Fixed	
Reference Point	
*Thermodynamic properties of air were derived from the gas tables of Reference 3.	

From these knowns and assumptions required for analysis of impeller radial equilibrium (see Table II), the 5-streamtube computer program can be used to calculate the forces acting on air particles in the streamline. These forces — Force 1 is a tangential component of blade-surface force normal to the meridional streamline; Force 2 is the centrifugal force from the curvilinear path; Force 3 is the centrifugal force from rotation around the impeller axis — form an analytical equation that is used to set the forces equal to pressure changes in the impeller

CONFIDENTIAL

CONFIDENTIAL

hub-to-shroud direction. After combining this force equation with the general energy equation, the known airflow continuity is then used in determining the streamline velocity distribution, which also depends on impeller geometry.

First-assumption inputs to the computer program are the estimated streamlines and impeller-hub velocity. Impeller hub-to-tip velocity distribution is now calculated by integrating the known parameters. However, if the above assumptions do not satisfy radial equilibrium, the streamlines have to be adjusted and re-plotted, and the above calculations have to be repeated, with new velocity and density values being used. These values and plots are used: (1) to estimate the new streamlines, (2) to determine the average blade-to-blade velocities (relative velocity), and (3) to determine the mean static-pressure rise.

Finally, having approximated the desired results through recalculation and analysis, these new data are plotted to show radial-equilibrium conditions at each station along the impeller airflow path. These recalculated computer output data include the desired streamlines, velocity distributions, pressure profiles, and other data required for geometric analysis of impeller radial equilibrium.

Blade-to-Blade Velocity Analysis — In all impellers, pressure losses are associated with flow separation along the blade surfaces. Boundary-layer growth in the presence of decelerating velocities will cause separation and large mixing losses. Also, acceleration to supersonic velocities causes local shock losses. To predict either condition, velocity distribution on the impeller blades had to be determined. A rapid approximation method was developed by Stanitz and Prian (see Reference 4) for both compressible and incompressible 2-dimensional flow between blades. The method is adaptable to radial or mixed-flow impellers with arbitrary passage and blade shapes; the method was subsequently incorporated in the 5-streamtube computer program described in Appendix I of this report. By solving the continuity equations, this method can be used to determine average relative velocities and flow angles between blades along the streamlines. The average relative velocity between blades was then equated to one-half the sum of the suction and pressure surface velocities. The suction (or trailing) surface velocity depends on the rate of change in vector quantities at each station on the streamlines with respect to the meridional distance from the inlet station. In using this method, it was assumed that the air particles were guided until slip occurred. The location and value of slip were checked by the method shown in Reference 5; for each impeller, slip began at the point where tangential blade turning was completed.

Average slip was determined from Reference 5. The procedure for determining average relative velocities is iterative because rapid decelerations and accelerations are corrected by adjusting blade profiles and passage contours and by repeating the analyses of References 2 and 3 until the desired velocity distributions are obtained.

CONFIDENTIAL

CONFIDENTIAL

The design analysis methods described in Appendix I of this report were used to establish the 4 impeller configurations for mechanical design analysis.

2.2.3 SELECTED DESIGNS

To define the aerodynamic configurations of the 4 impellers, parametric studies were conducted to establish rotor sizes and speeds and to estimate performance requirements. In addition, a design method, which included analyses of the 1-dimensional flow path, radial equilibrium, and blade-surface velocities, was established. The techniques used in these analyses are described in Sections 2.2.1 and 2.2.2 of this report. From these studies, the designs were selected for investigating inlet hub-to-tip-diameter ratio, inducer-tip relative Mach number, solidity, blade shape, and impeller type to establish criteria for high-pressure-ratio impellers. The principal objective was to define a design method that was supported by improved performance predictions.

The 4 research impellers are listed in Table III, which also shows their significant design parameters. Each impeller was given a design designation for reference: the first mixed-flow impeller was designated MF-1; the second, MF-2; and the third, MF-3. The radial-flow impeller was called RF-1. These designations will be used throughout this report to identify the specific impeller being discussed.

The impellers were designed with leading edges that approximated the double circular arc blade profiles commonly used in axial compressors. This selection was made because axial compressors with similar profiles have operated successfully in the range of relative inlet Mach numbers chosen for the 4 impellers. The more conventional inducer blade profiles used in previous inducer designs are compared with the double circular arc profiles in Figure 18.

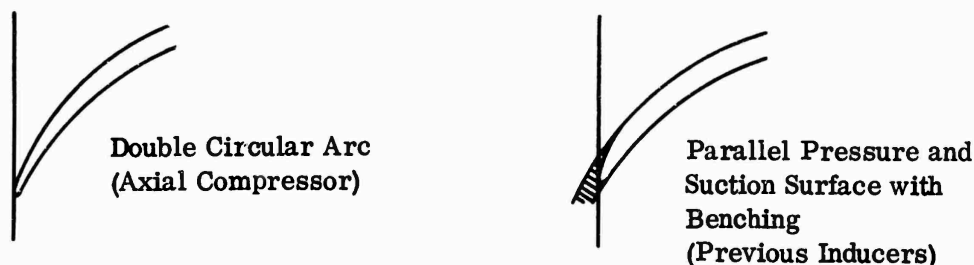


Figure 18. Comparison of Inducer Leading-Edge Blade Shapes.

TABLE II IMPELLER DESIGNS				
Configuration	MF-1 (Mixed flow)	MF-2 (Mixed flow)	MF-3 (Mixed flow)	RF-1 (Radial flow)
Impeller Total-to-Total Pressure Ratio	13.0	12.92	12.8	13.0
Efficiency (%)	93.0	92.5	92.0	93.0
Speed (rpm)	57,000	73,000	65,000	57,000
Inlet Relative Mach Number (tip)	0.95	1.23	1.13	1.09
Mean Tip Diameter (in.)	8.01	6.32	7.07	8.08
Number of Blades	18	20	20	22
Inducer Hub-to-Tip Ratio	0.4	0.5	0.5	0.6
Exit Absolute Mach Number (tip)	1.288	1.279	1.295	1.298
Inducer-Tip Relative Flow Angle (degrees from axial)	58.2	60.8	57.89	61.6
Average Impeller-Tip Flow Angle (degrees from radial)	79.45	79.96	79.4	80.8
Design parameters: $W_a = 2.00$ lb/sec; overall compressor pressure ratio = 10:1.				

CONFIDENTIAL

MF-1 Impeller Design

This impeller was designed to have the lowest relative inlet Mach number (0.95) of the 4 configurations. It was also sized at the lower inlet hub-to-tip-diameter ratio (0.40) to be investigated, and the inlet axial Mach number was 0.50. The velocity diagrams for these conditions are shown in Figure 19; they represent design conditions at mean points for the tip, RMS, and hub streamtubes. The relation between airflow continuity and the vector diagram (see Equations 6 through 9 and Figure 15 of Section 2.2.1) was used to determine inducer-tip diameter (3.50 inches) and rotor speed (57,000 rpm). Inducer aerodynamic loading was determined from diffusion factor criteria — the values used for MF-1 are compared to a previous impeller design in Figure 20. The lower aerodynamic loading of MF-1 was chosen to avoid early flow separation. Impeller-exit velocity diagrams are given in Figure 21, and the meridional shape of the blade passage area is shown in Figure 22. Both illustrations were derived by using the procedures outlined in Appendix I, which includes the computer program for establishing radial equilibrium and for determining blade-surface velocities. The rearward lean of the mixed-flow passage was set at 30 degrees (Figure 22). Flow-passage area, blockage, blade height, and turning schedules developed in the computer calculations are shown in Figure 23. Static-pressure gradients through the blade passage area were determined from the radial-equilibrium analysis. These gradients, plotted in Figure 24, were used to estimate static-pressure rise along the shroud (see Figure 25). During the evaluation portions of this program, data will be recorded for comparing these predictions with test results. These comparisons will provide a check against the mathematical models used to prepare the computer program. Regions in which test values fall below the predicted line will indicate where flow separation has occurred. This information will be used in correcting design techniques and in modifying the test impellers. The predicted average and blade-surface velocities are shown in Figure 26 for the hub, RMS, and tip streamtubes. Calculated variations in absolute and relative flow angles, static and total pressures, and total temperature across the tip section of the impeller are presented in Figure 27. These values will also be checked by measurement in the impeller test rig.

Having established the impeller design-point geometry, the computer program was used to determine static-pressure rise along the shroud and blade-to-blade velocities at part-speed conditions. The points chosen were at 90-, 80-, and 60-percent design speed; the calculated data are plotted in Figures 28 through 31.

MF-2 Impeller Design

This impeller was designed for a higher relative inlet Mach number at the tip (1.23) and for a larger inlet hub-to-tip-diameter ratio (0.50) than MF-1. Because the design was intended for use in investigating high speed and small size (discussed in Section 2.2.1), the absolute inlet Mach number was increased to 0.60.

CONFIDENTIAL

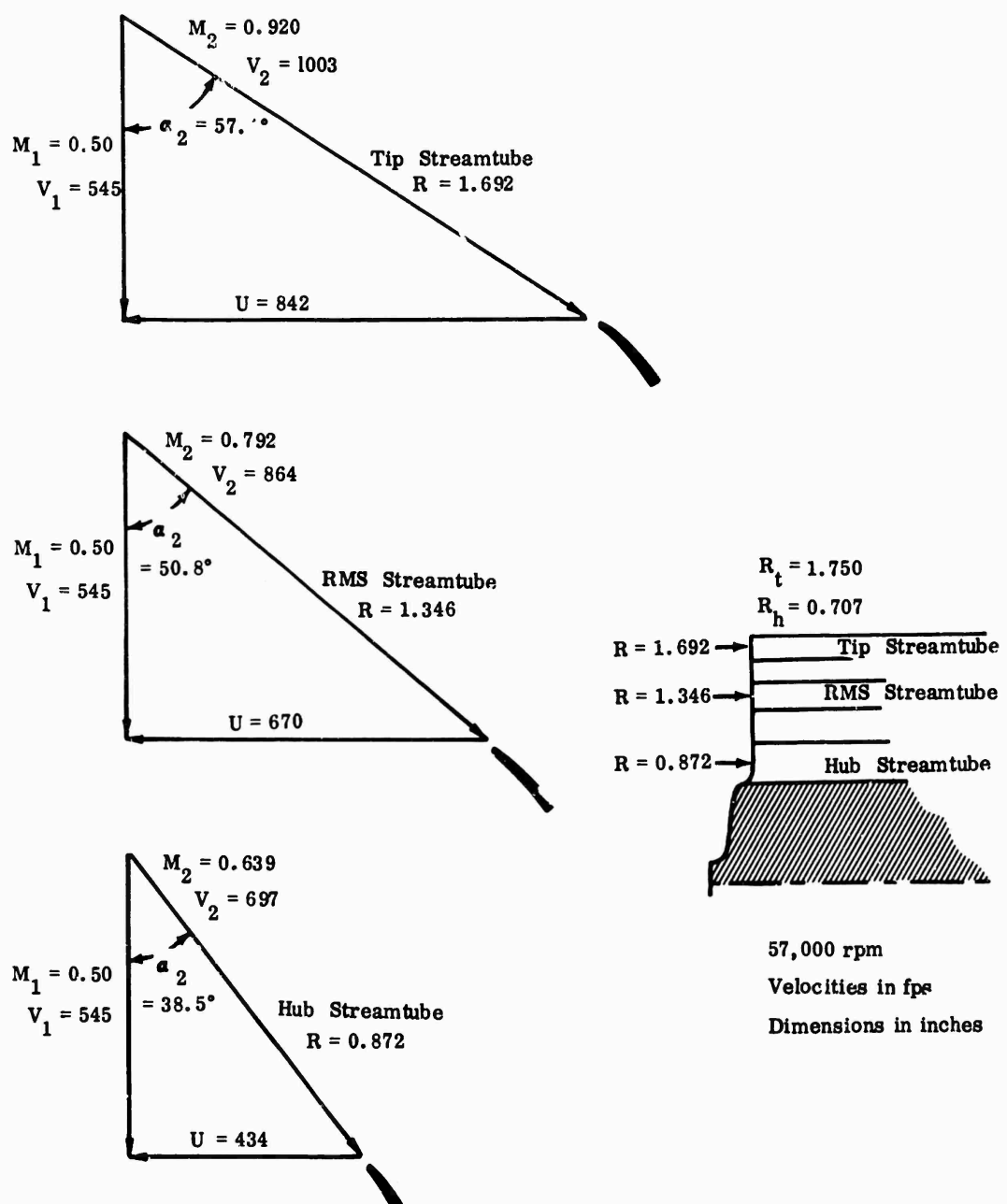


Figure 19. Inlet Velocity Diagrams for MF-1 Impeller Design.

CONFIDENTIAL

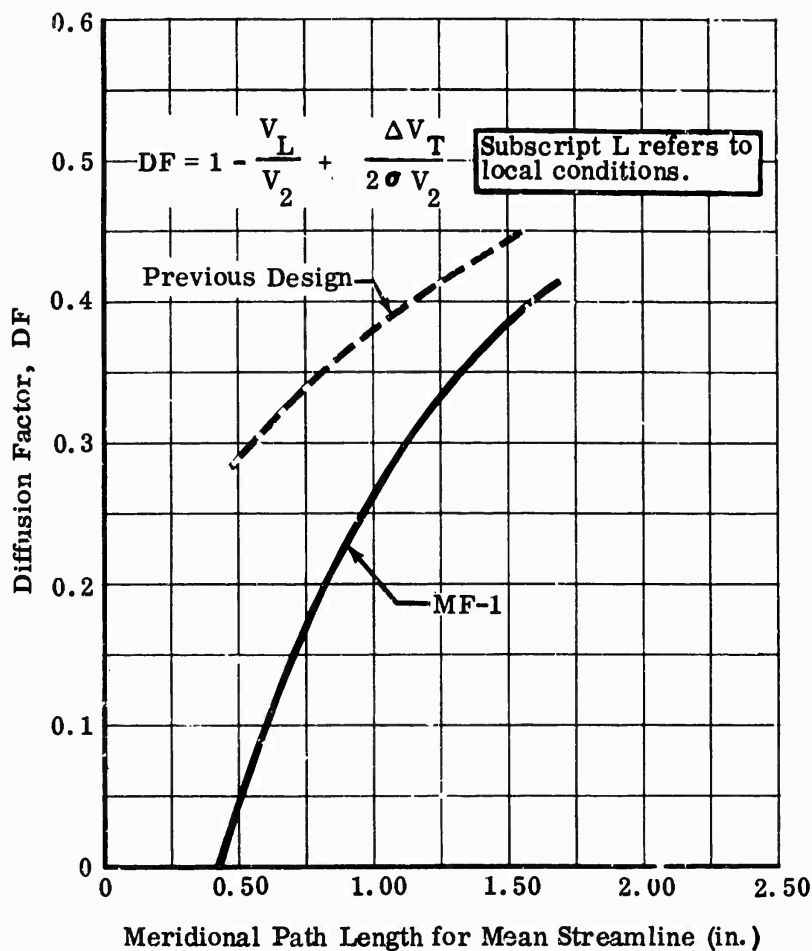


Figure 20. Diffusion Factor for MF-1 Impeller.

With these values, an inlet blockage factor of 0.90, and the continuity equations, the inducer-tip diameter was established as 3.60 inches and the rotor speed was determined as 73,000 rpm. The resultant inlet velocity diagrams are shown in Figure 32. As with the MF-1 impeller, the MF-2 was analyzed by using the computer techniques of Appendix I. Diffusion factors used in the RMS calculations are compared to an earlier high-performance compressor tested by the contractor (80-percent efficiency at a pressure ratio of 5.5:1) in Figure 33. Diffusion rates at the RMS diameter are about the same.

The impeller-tip velocity diagrams are presented in Figure 34. Using the speed-size relationship, the tip diameter of this mixed-flow design was calculated to be about 6.3 inches. Because this diameter was smaller than that of MF-1 (8.0

CONFIDENTIAL

CONFIDENTIAL

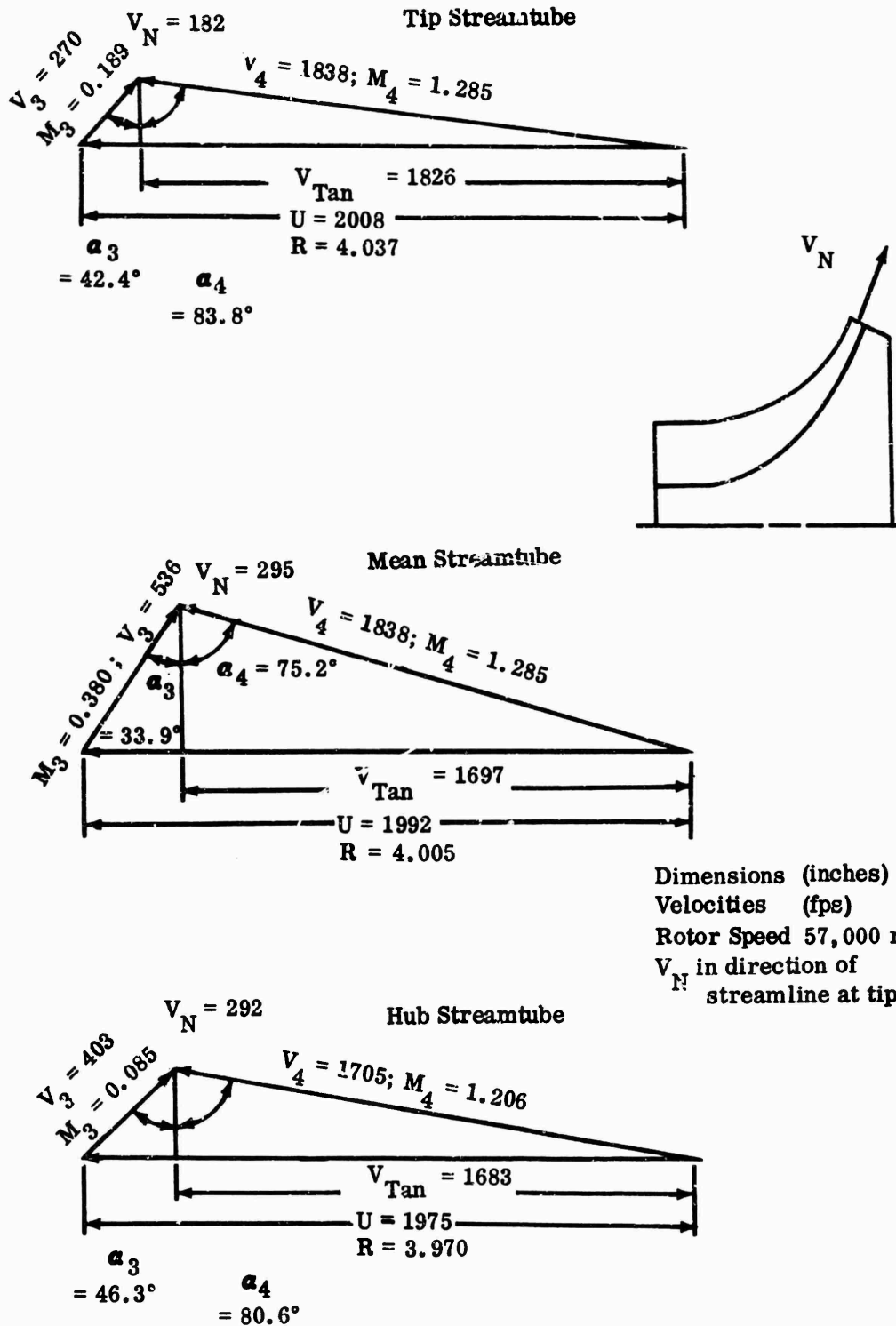


Figure 21. Exit Velocity Diagrams for MF-1 Impeller.

CONFIDENTIAL

CONFIDENTIAL

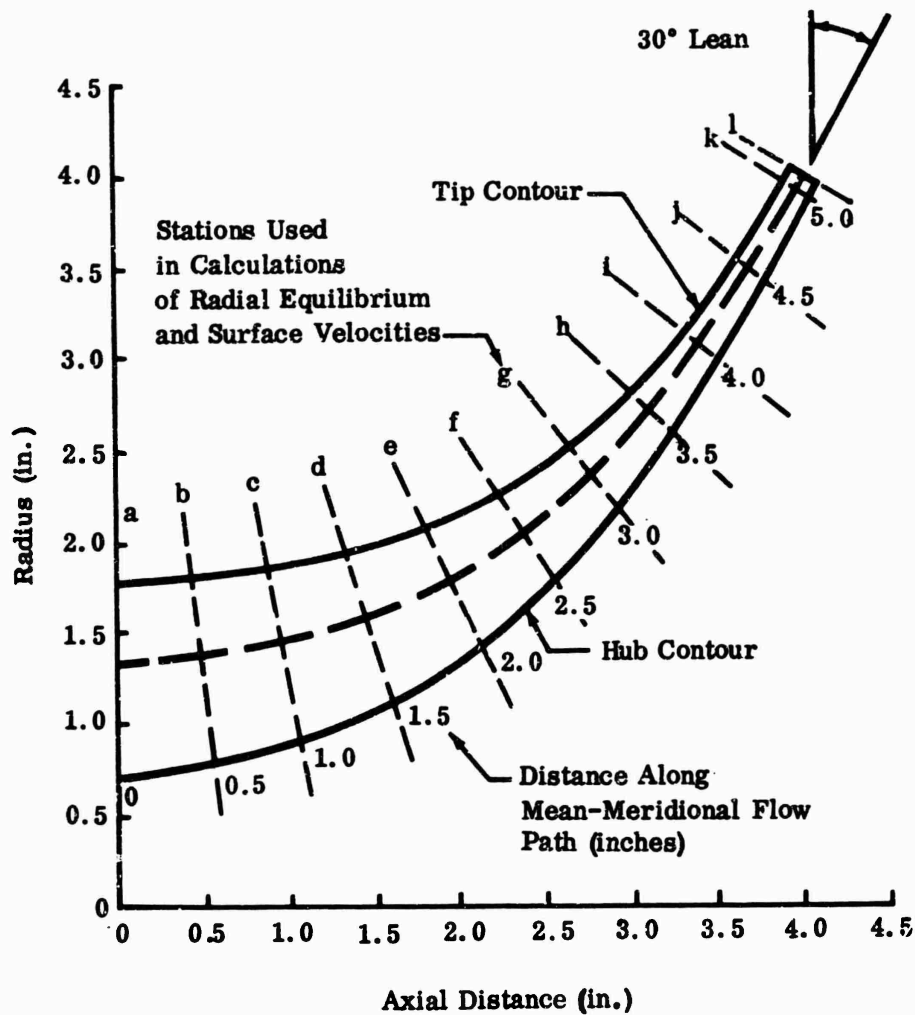


Figure 22. Meridional View of MF-1 Impeller.

inches), blade-tip height was enlarged to 0.25 inch to maintain airflow continuity. The overall meridional view of the blade passage area is shown in Figure 35; rearward lean of the mixed-flow passage at the tip was the same as in MF-1 (30 degrees). Flow area, blockage, blade height, and turning schedules are illustrated in Figure 36. The results of the radial-equilibrium analysis (see Appendix I) are shown in Figures 37 through 44 for the same parameters used in evaluating MF-1.

CONFIDENTIAL

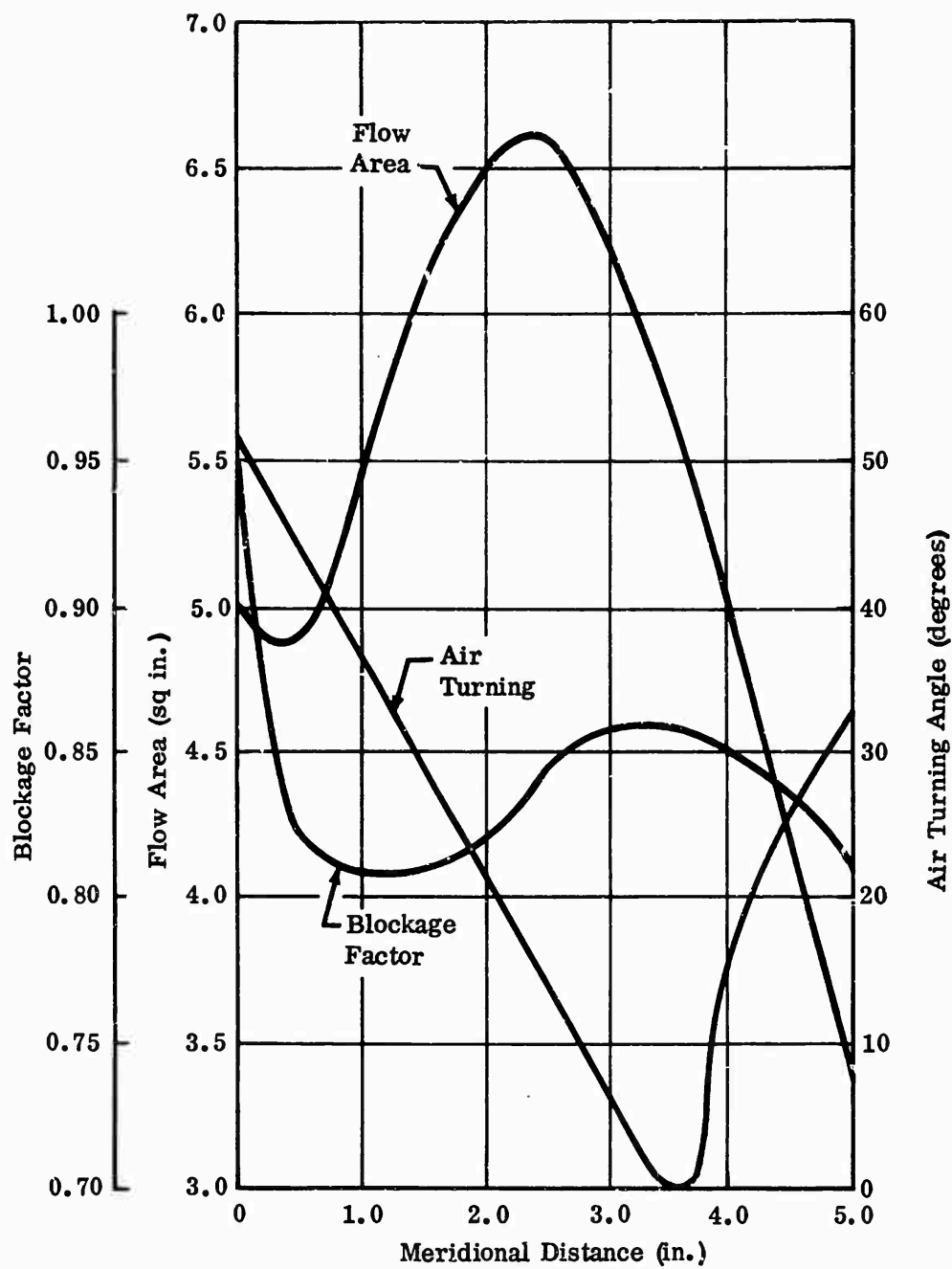


Figure 23. Impeller Design Parameters for MF-1; Design Speed, 57,000 rpm.

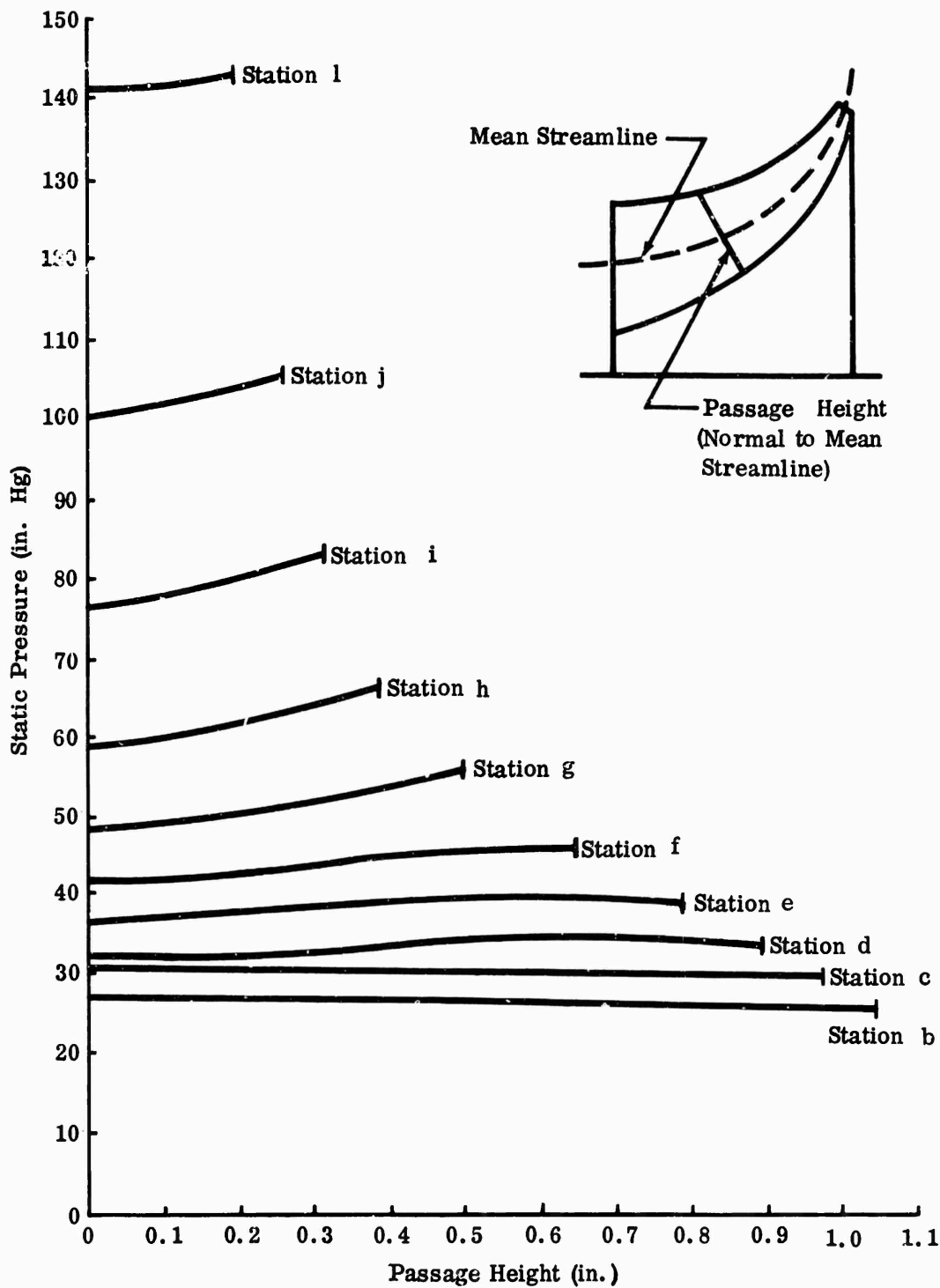


Figure 24. Static-Pressure Distribution Across Passage, MF-1 Impeller; Design Speed, 57,000 rpm.

CONFIDENTIAL

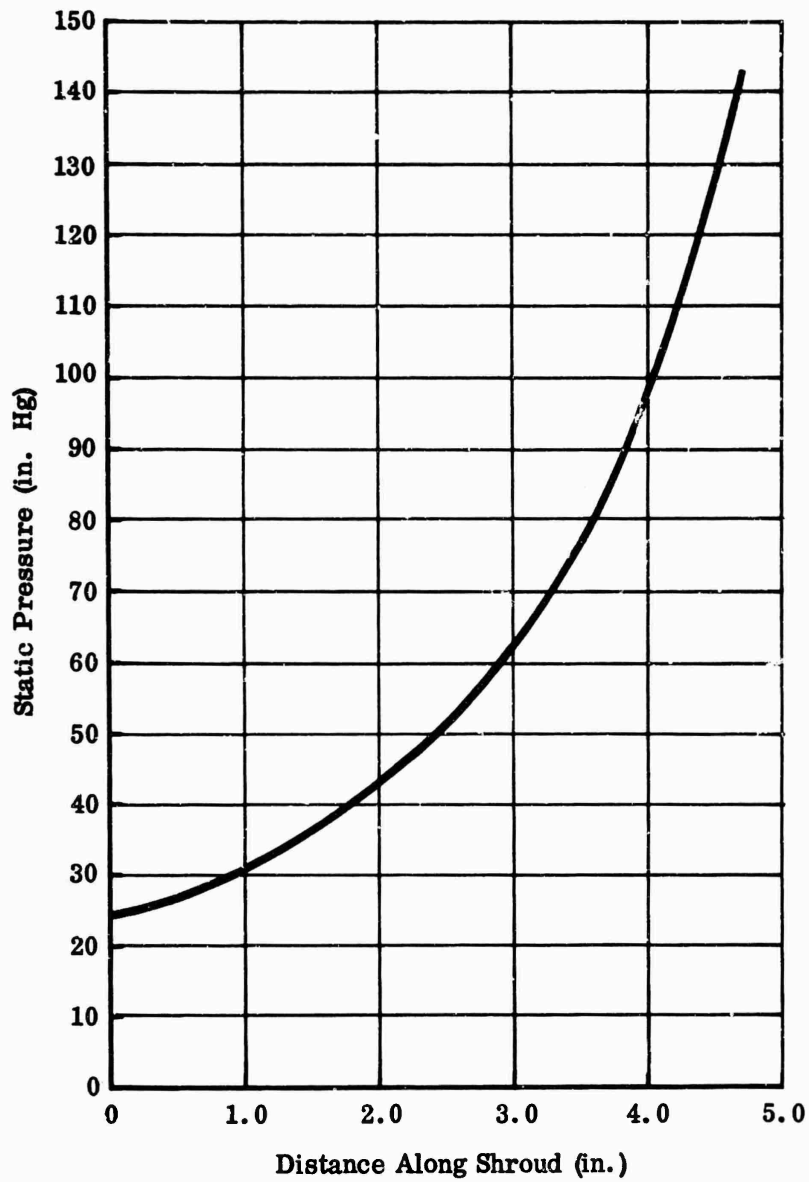


Figure 25. Predicted Static-Pressure Rise Along MF-1 Impeller Shroud; Design Speed, 57,000 rpm.

MF-3 Impeller Design

This impeller was sized between MF-1 and MF-2 for an assessment of geometric parameters. Accordingly, an inducer-tip relative Mach number of 1.13 was selected; the inlet hub-to-tip-diameter ratio was 0.50, and the absolute axial

CONFIDENTIAL

CONFIDENTIAL

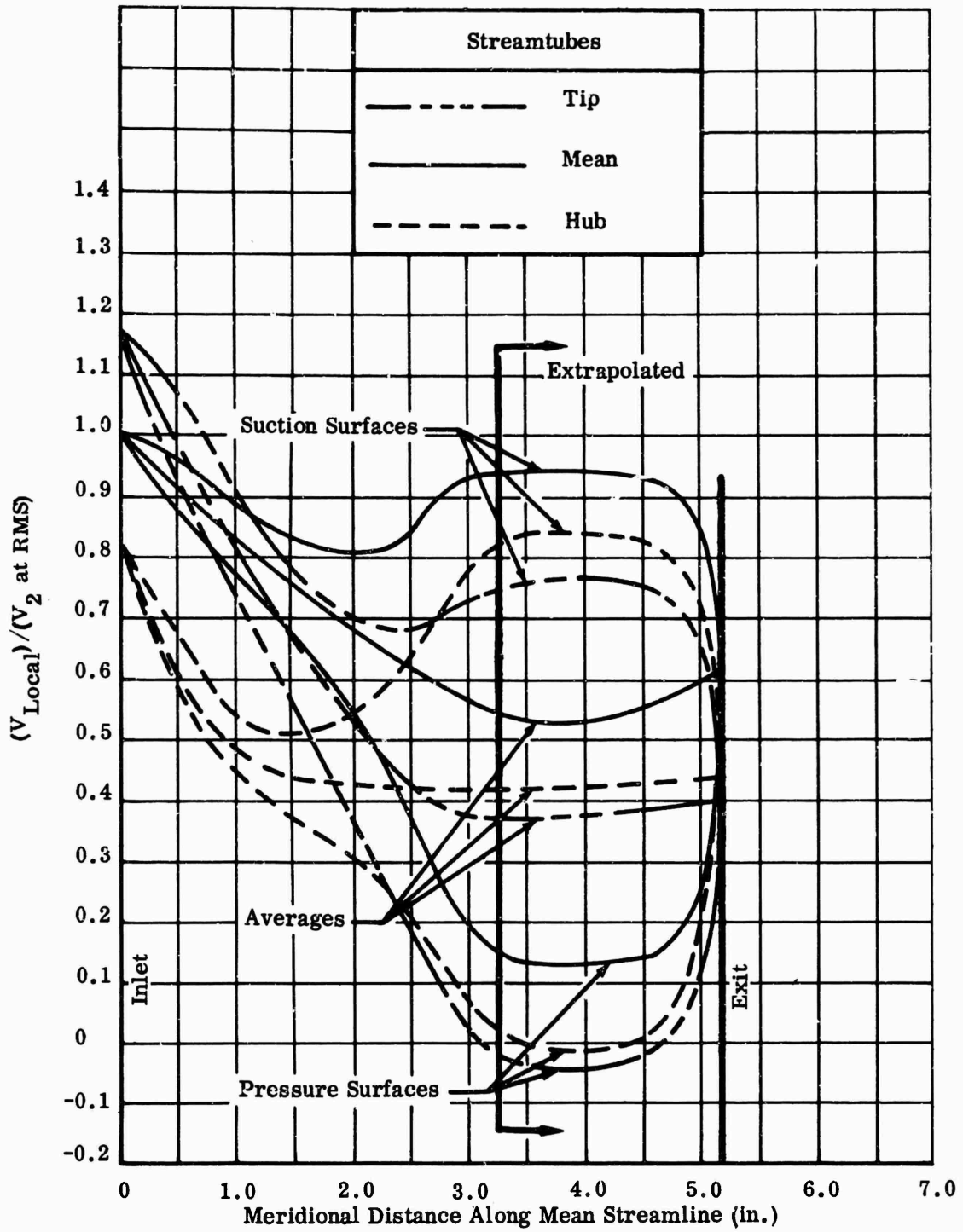


Figure 26. Blade-Surface Velocities of MF-1 Impeller; Design Speed, 57,000 rpm.

CONFIDENTIAL

CONFIDENTIAL

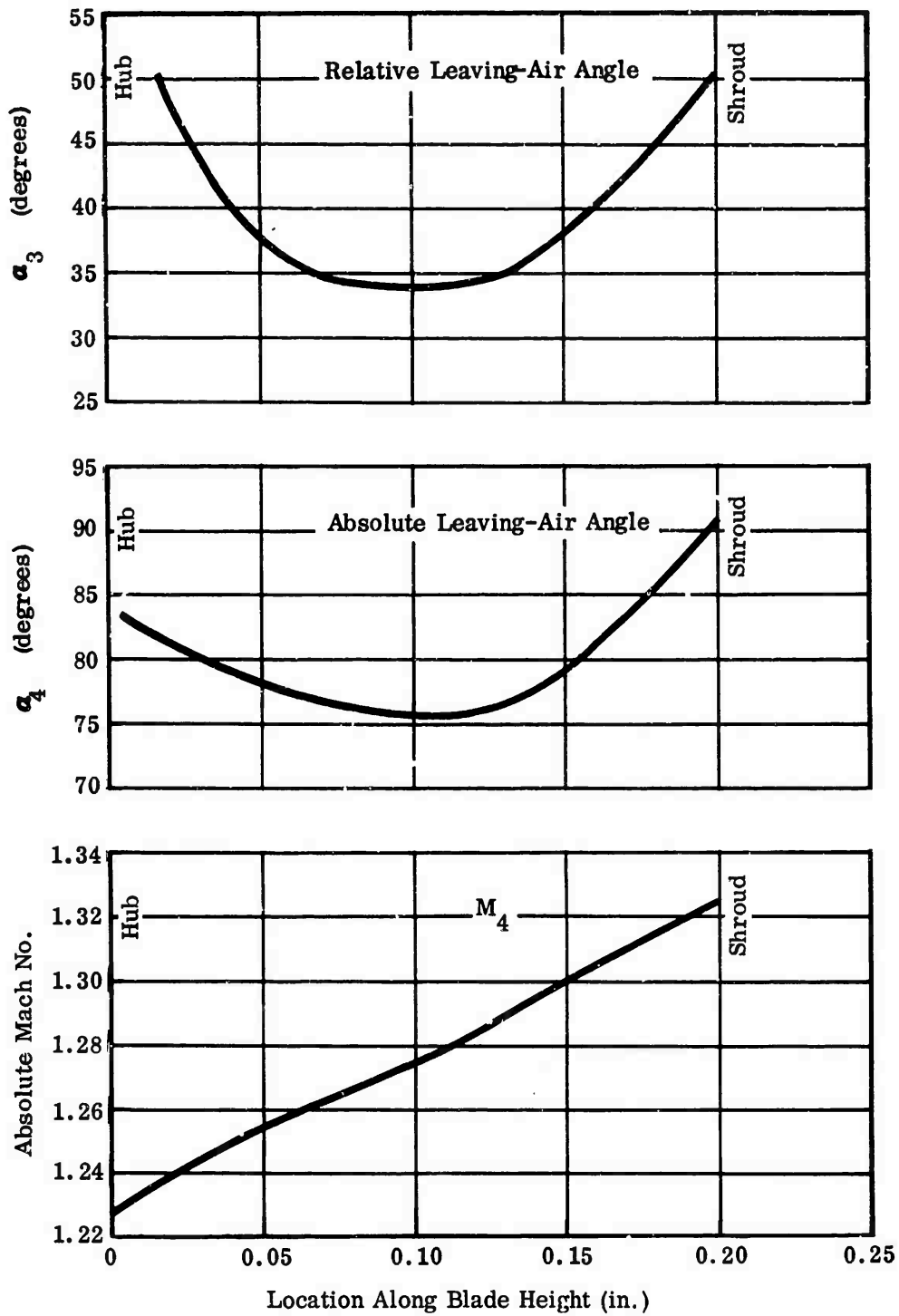


Figure 27. Exit Flow Conditions for MF-1 Impeller; Design Speed, 57,000 rpm.

CONFIDENTIAL

CONFIDENTIAL

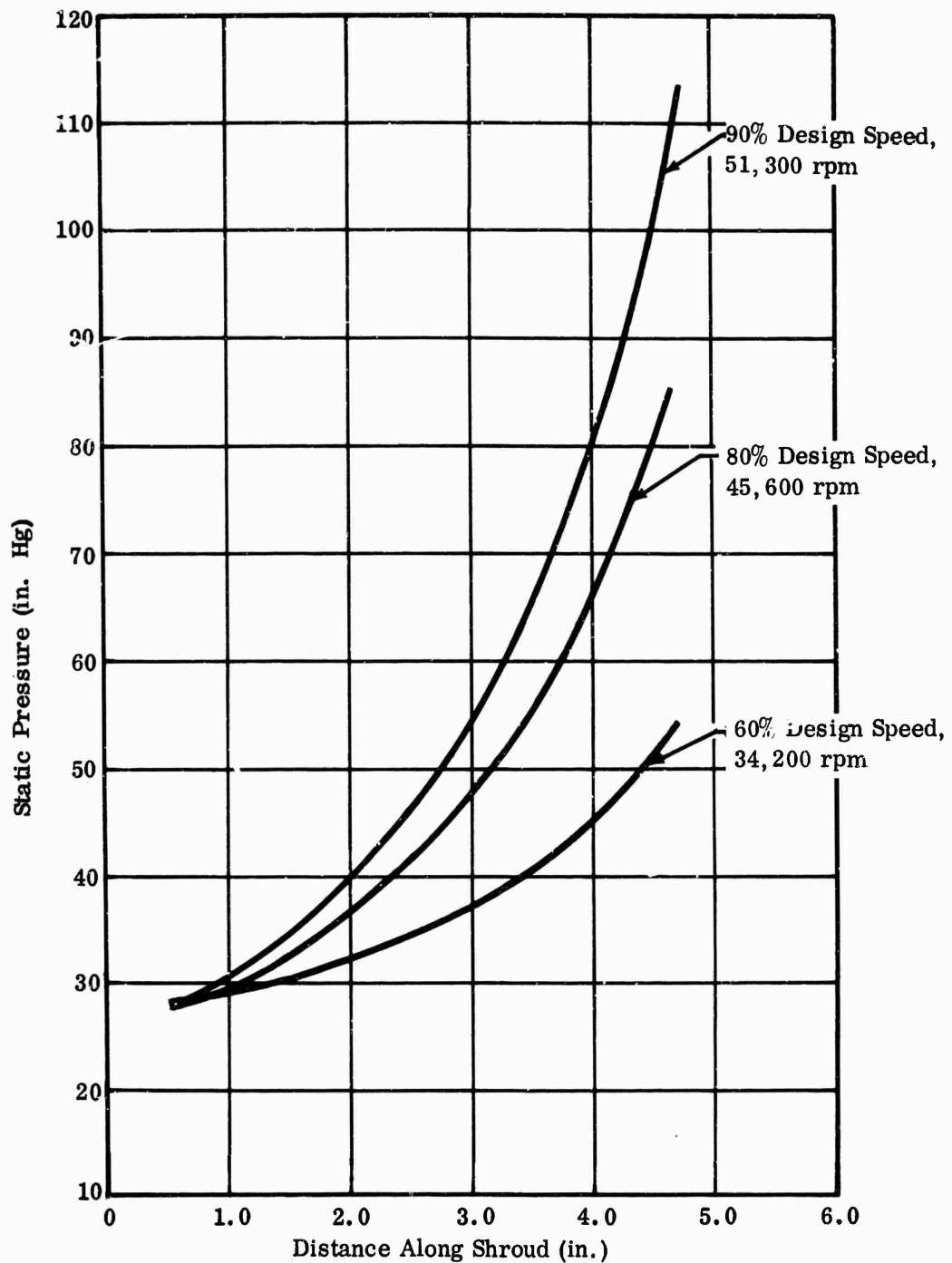


Figure 28. Predicted Static-Pressure Rise Along MF-1 Impeller Shroud, Part Speed.

CONFIDENTIAL

CONFIDENTIAL

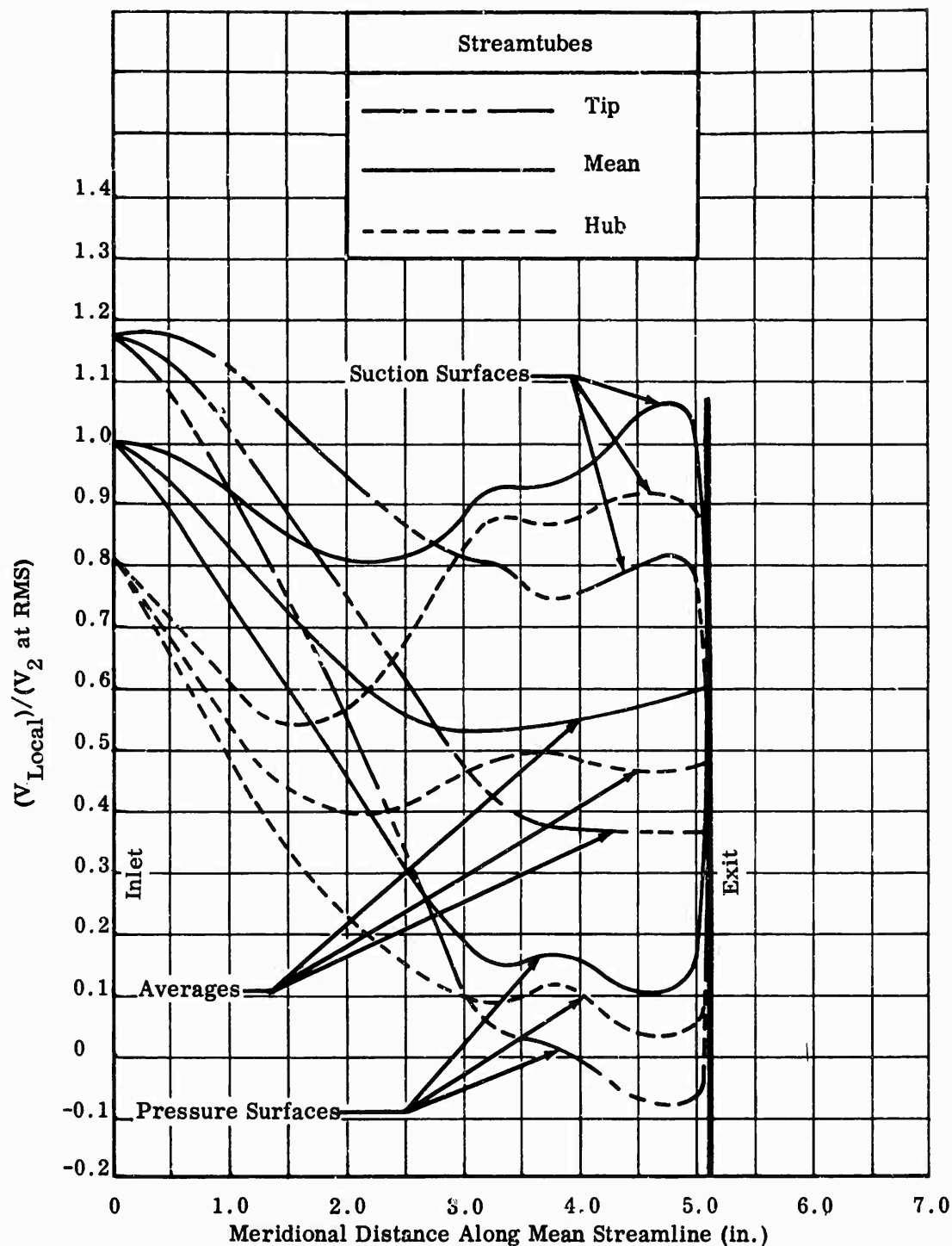


Figure 29. Blade-Surface Velocities of MF-1 Impeller; 90-Percent Design Speed, 51,300 rpm.

CONFIDENTIAL

CONFIDENTIAL

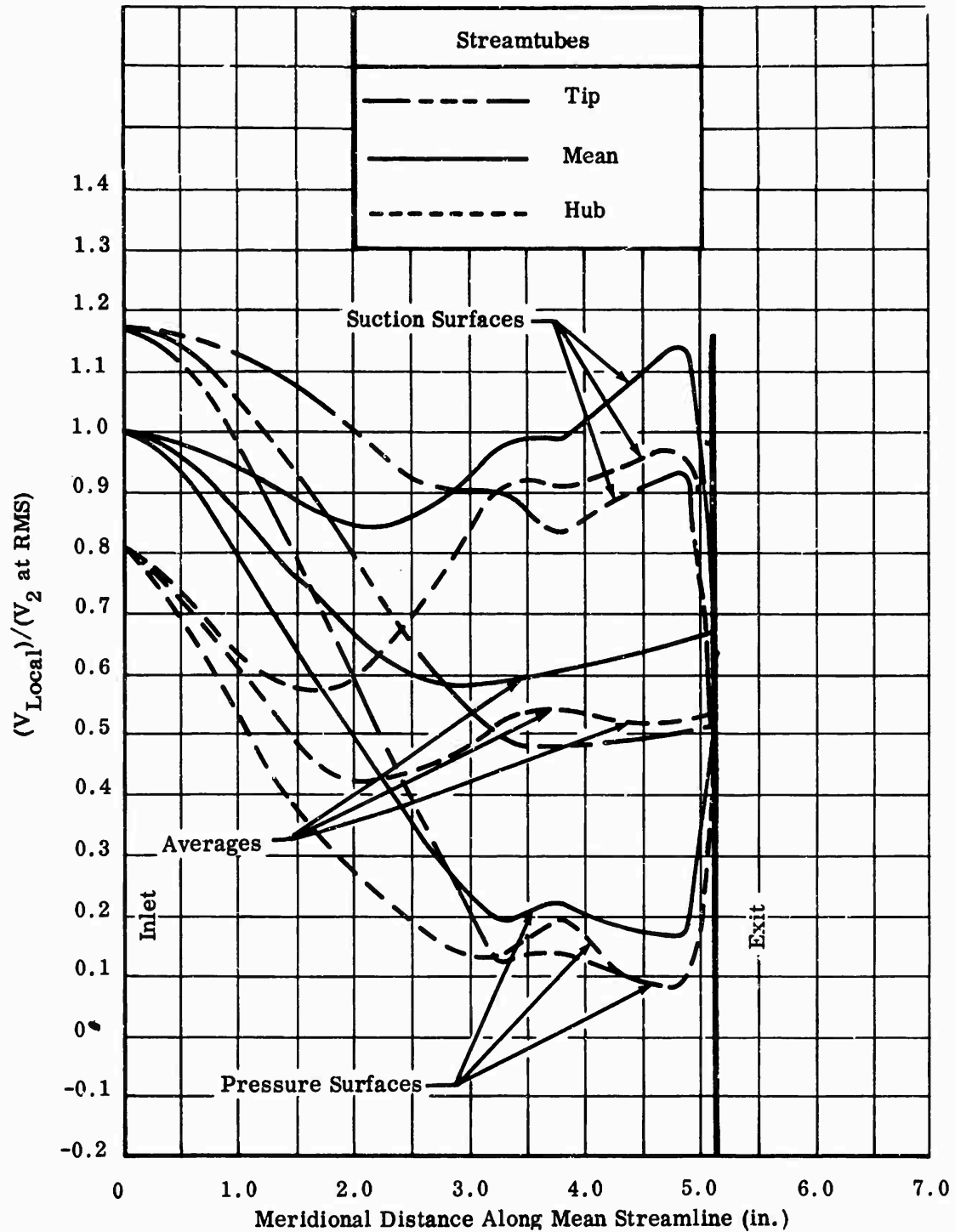


Figure 30. Blade-Surface Velocities of MF-1 Impeller; 80-Percent Design Speed, 45,600 rpm.

CONFIDENTIAL

CONFIDENTIAL

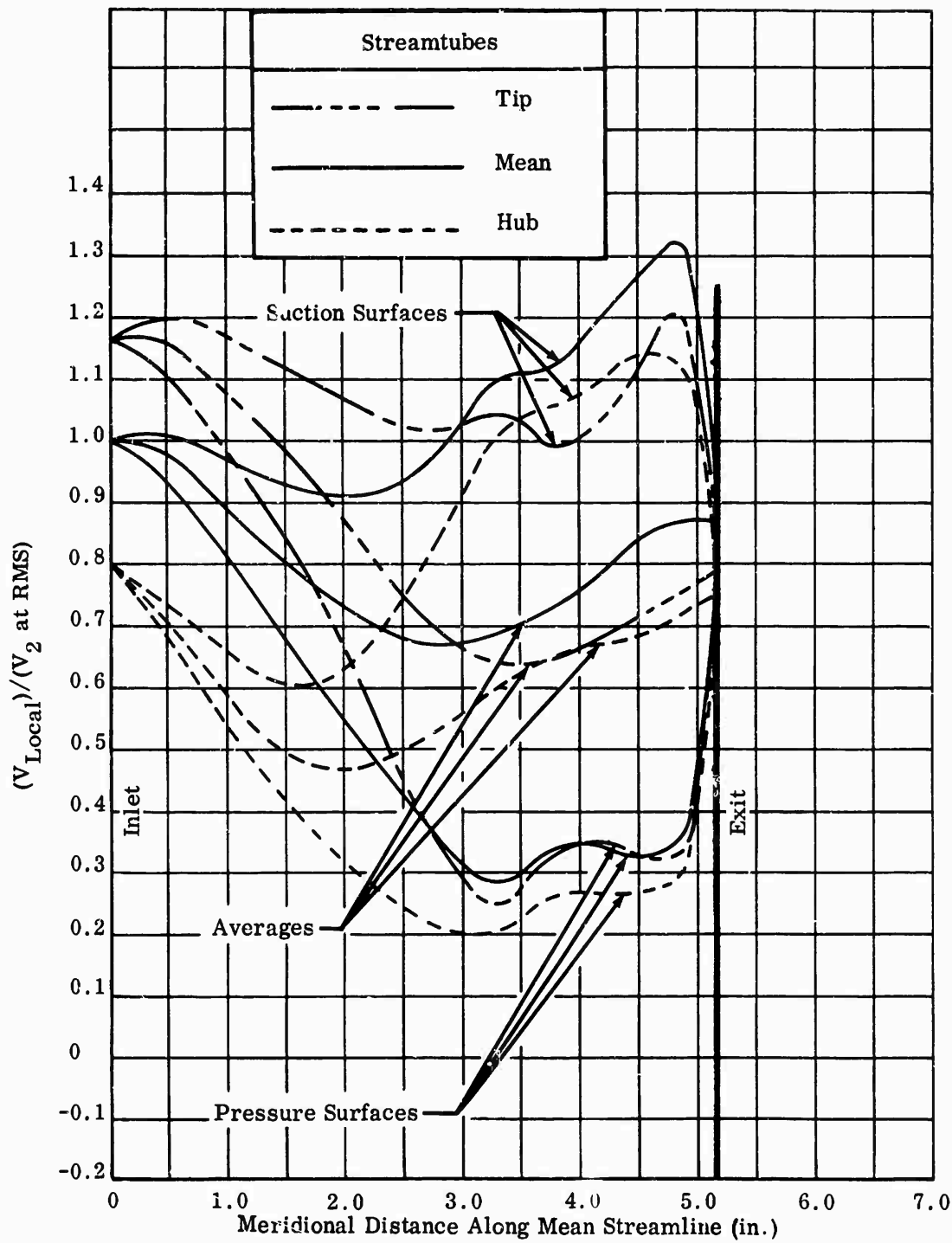


Figure 31. Blade-Surface Velocities of MF-1 Impeller; 60-Percent Design Speed, 34,200 rpm.

CONFIDENTIAL

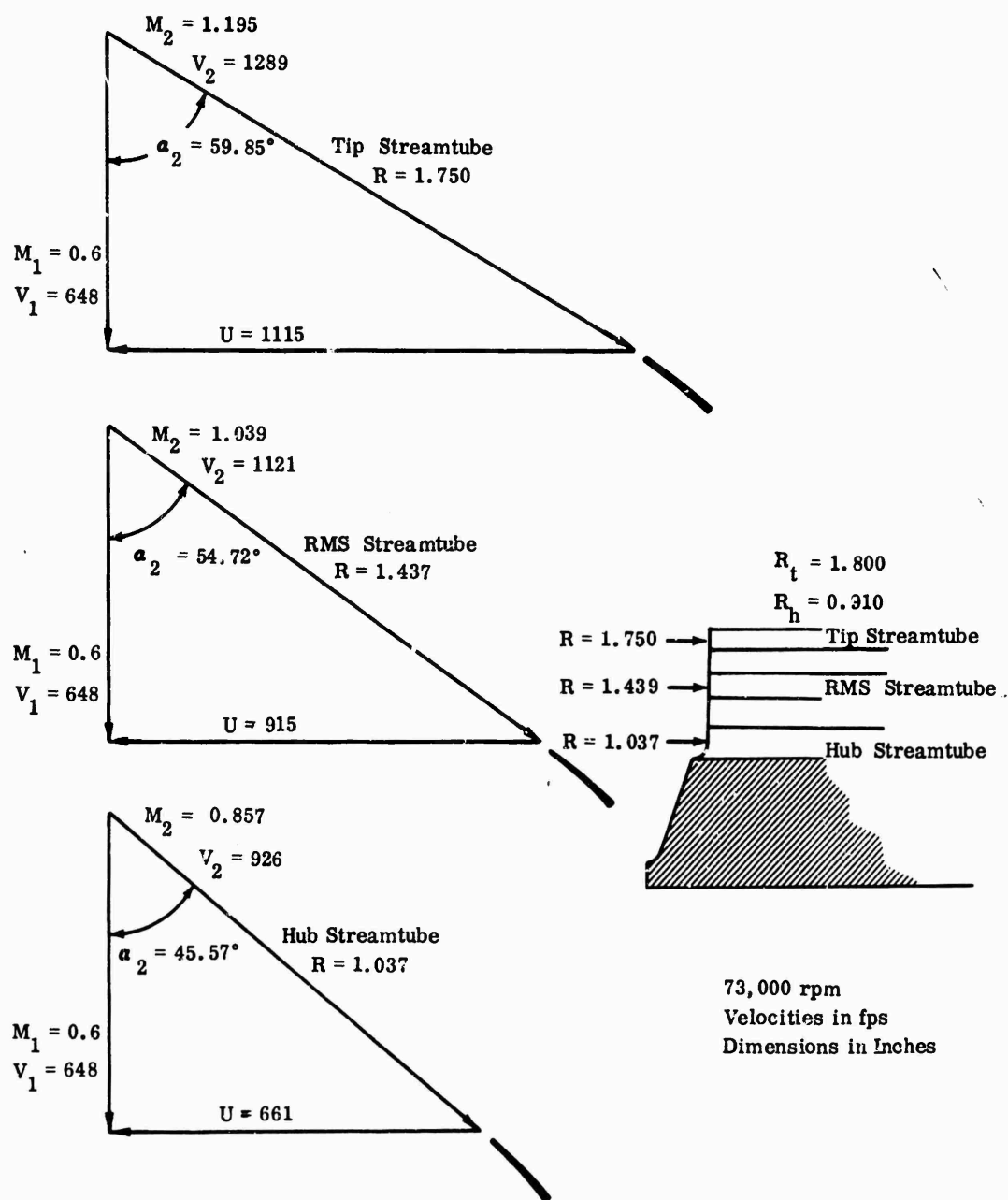


Figure 32. Inlet Velocity Diagrams for MF-2 Impeller Design.

CONFIDENTIAL

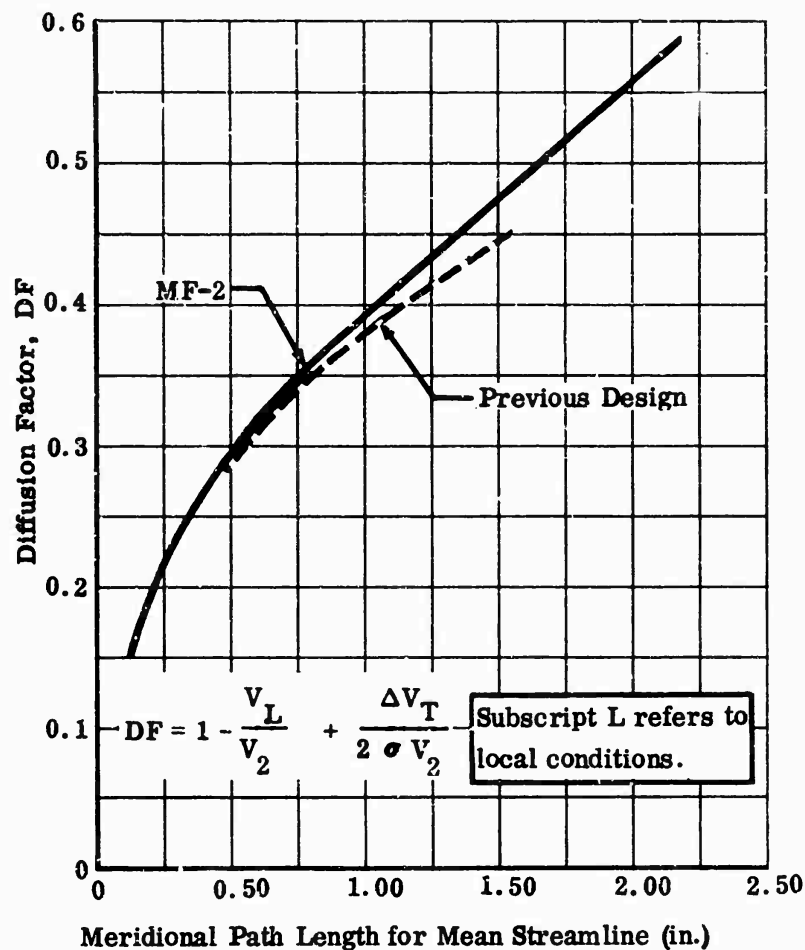


Figure 33. Diffusion Factor for MF-2 Impeller.

Mach number was 0.60. The resultant inlet velocity diagrams are depicted in Figure 45. Using the radial-equilibrium techniques presented in Appendix I, this impeller was analyzed in accordance with procedures consistent with those used to evaluate the MF-1 and MF-2. Diffusion rates at the RMS diameter are given in Figure 46. From these parameters, inducer diameter (3.60 inches) and rotor speed (65,000 rpm) were determined.

The impeller-tip velocity diagrams are given in Figure 47. From the speed-size relationship, the average tip diameter of the MF-3 was determined to be 7.09 inches, which is about halfway between the MF-1 and MF-2 diameters. At the tip, blade height was 0.20 inch; the overall meridional view is shown in Figure 48. As in the MF-1 and MF-2 impellers, the rearward lean of the blade passage area

CONFIDENTIAL

CONFIDENTIAL

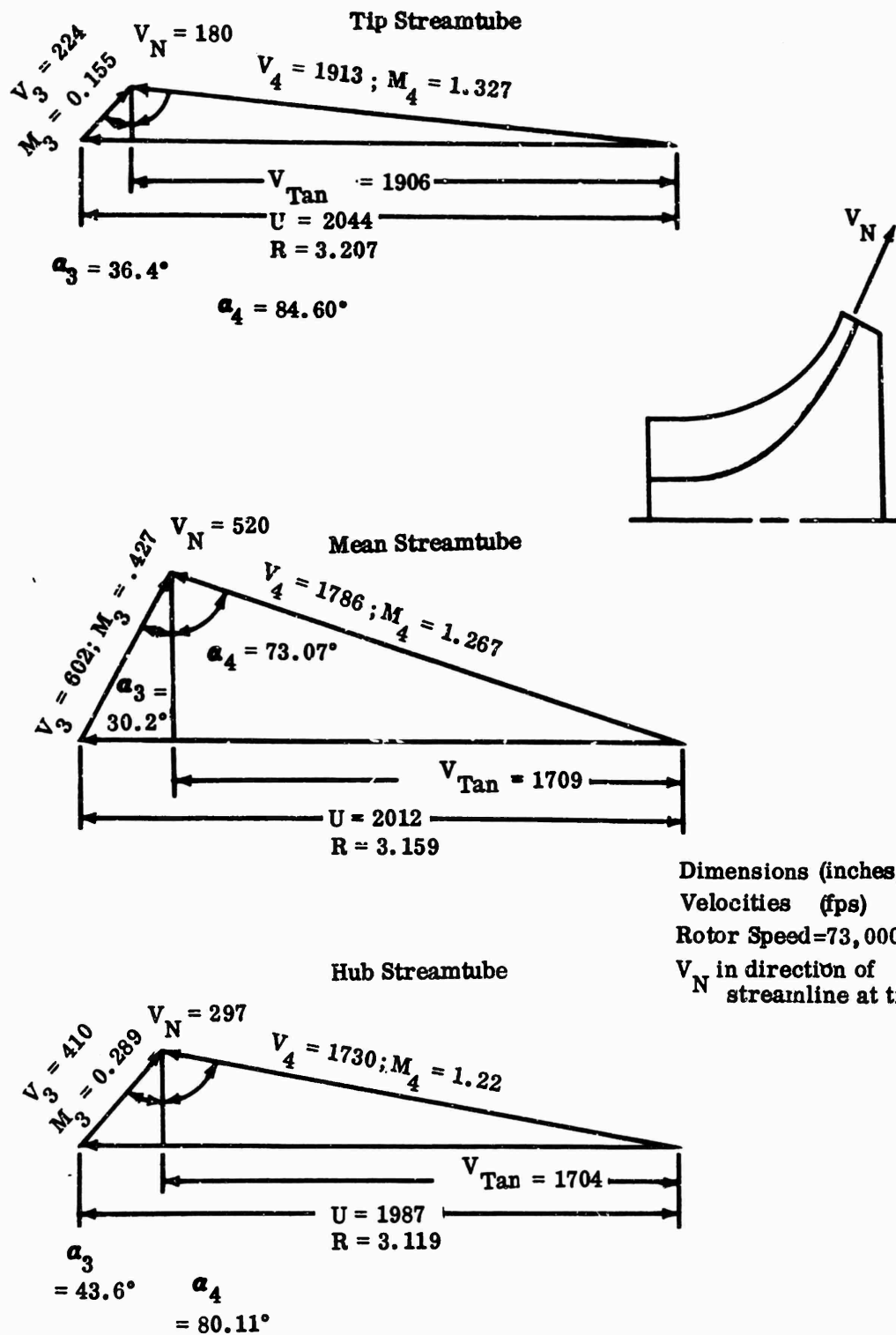


Figure 34. Exit Velocity Diagrams for MF-2 Impeller.

CONFIDENTIAL

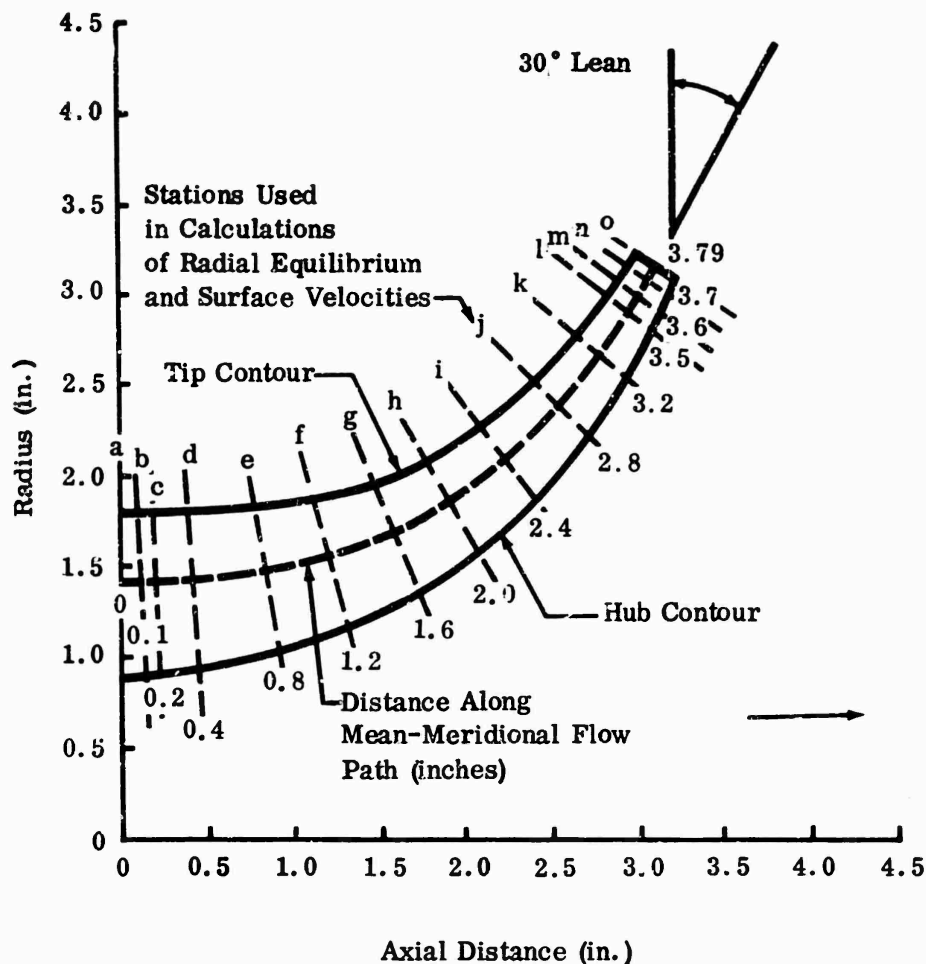


Figure 35. Meridional View of MF-2 Impeller.

was set at 30 degrees from radial. Flow area, blockage, blade height, and turning schedules are presented in Figure 49. Plotted results of the radial-equilibrium and surface-velocity analyses are given in Figures 50 through 57.

RF-1 Impeller Design

In comparing mixed- and radial-flow configurations, the RF-1 impeller was designed to the same overall size and speed conditions as MF-1. However, the inlet hub-to-tip-diameter ratio was increased to 0.60, and the inducer-tip relative Mach number was 1.09. These parameters are compared to those of the other 3 impellers in Table III. The increased diameter ratio and Mach number were chosen to investigate their influence on inducer performance. The RF-1

CONFIDENTIAL

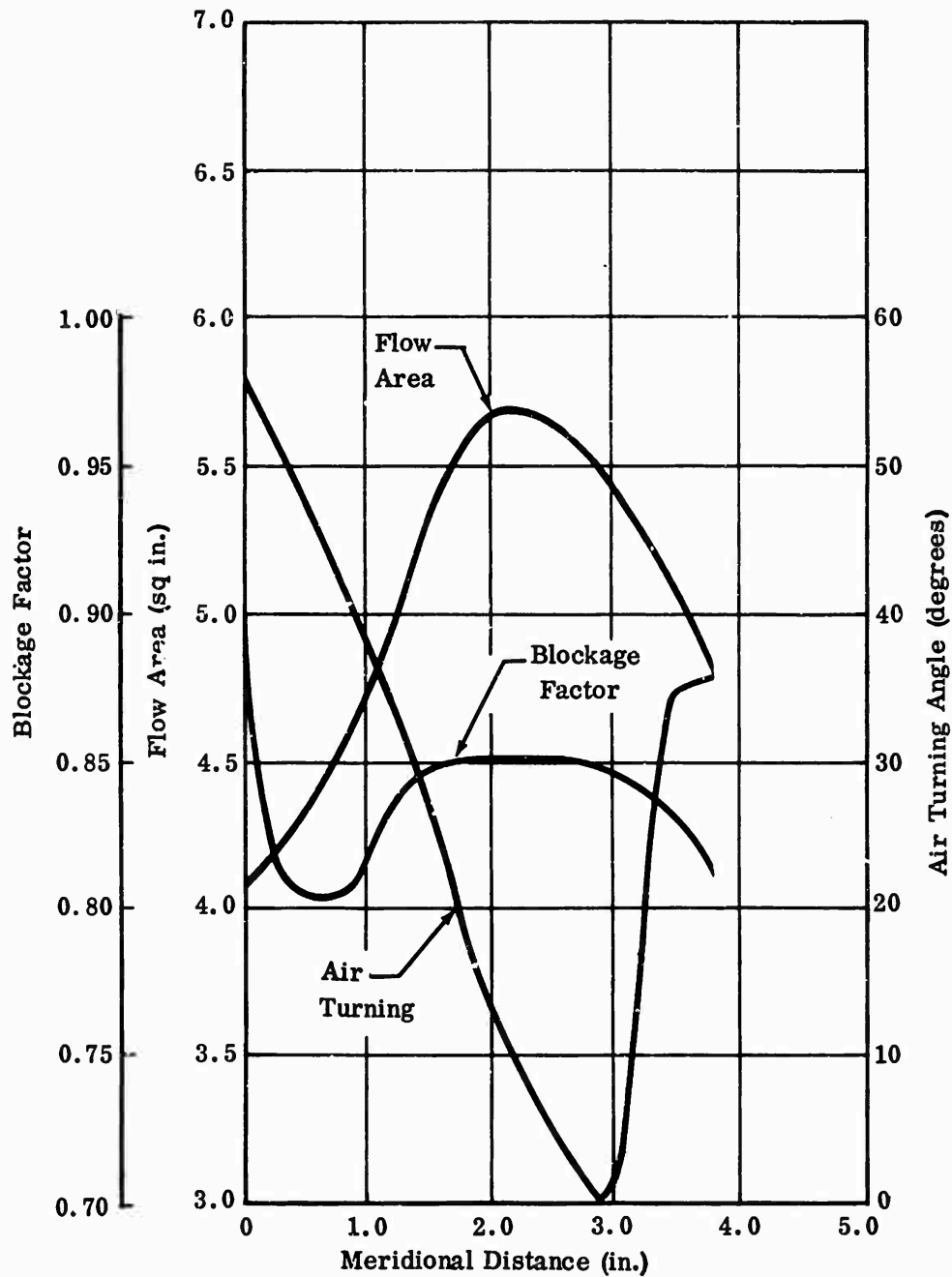


Figure 36. Impeller Design Parameters for MF-2;
Design Speed, 73,000 rpm.

CONFIDENTIAL

CONFIDENTIAL

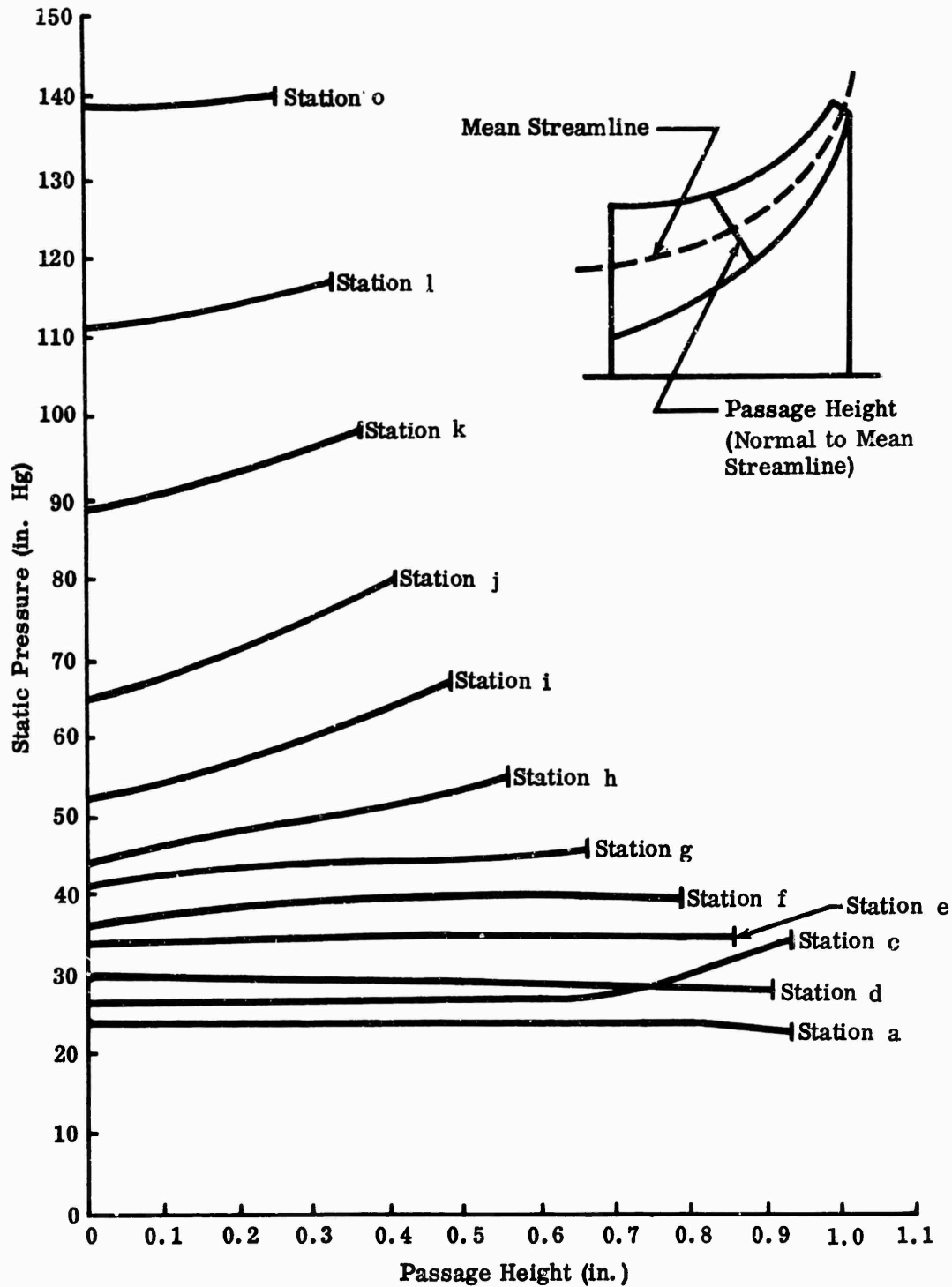


Figure 37. Static-Pressure Distribution Across Passage, MF-2 Impeller; Design Speed, 73,000 rpm.

CONFIDENTIAL

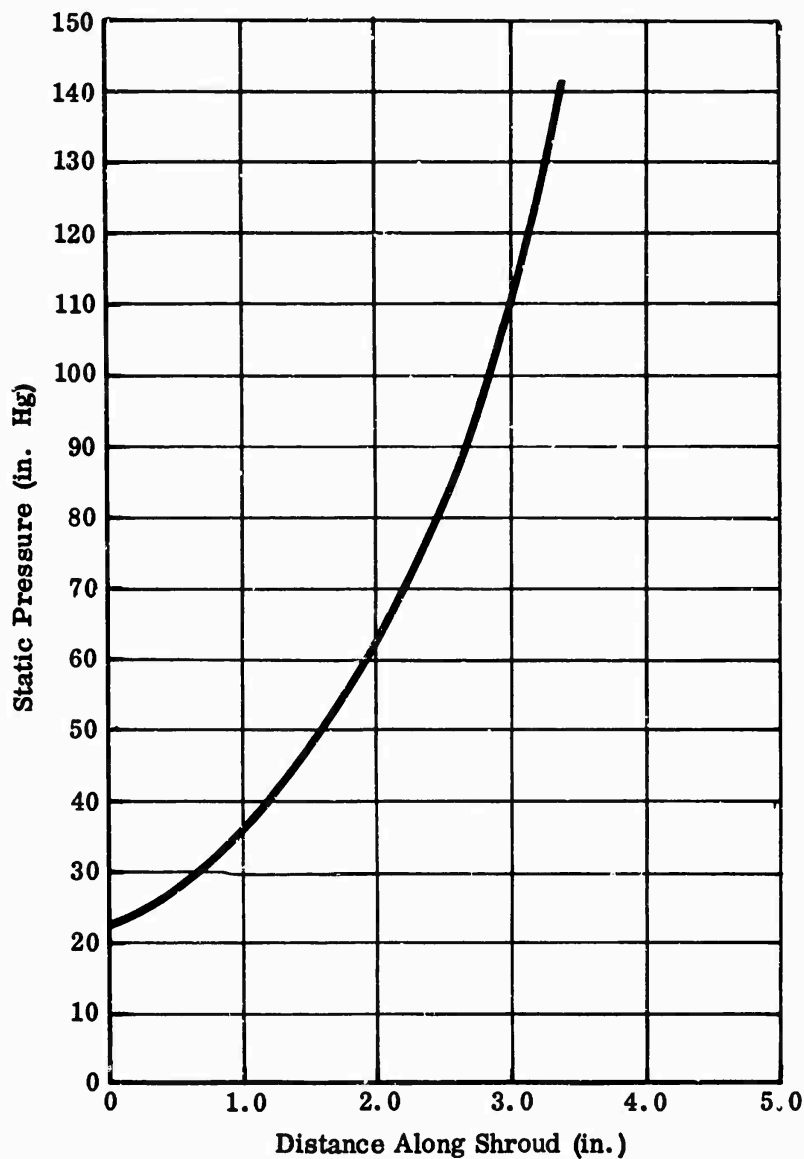


Figure 38. Predicted Static-Pressure Rise Along MF-2 Impeller Shroud; Design Speed, 73,000 rpm.

CONFIDENTIAL

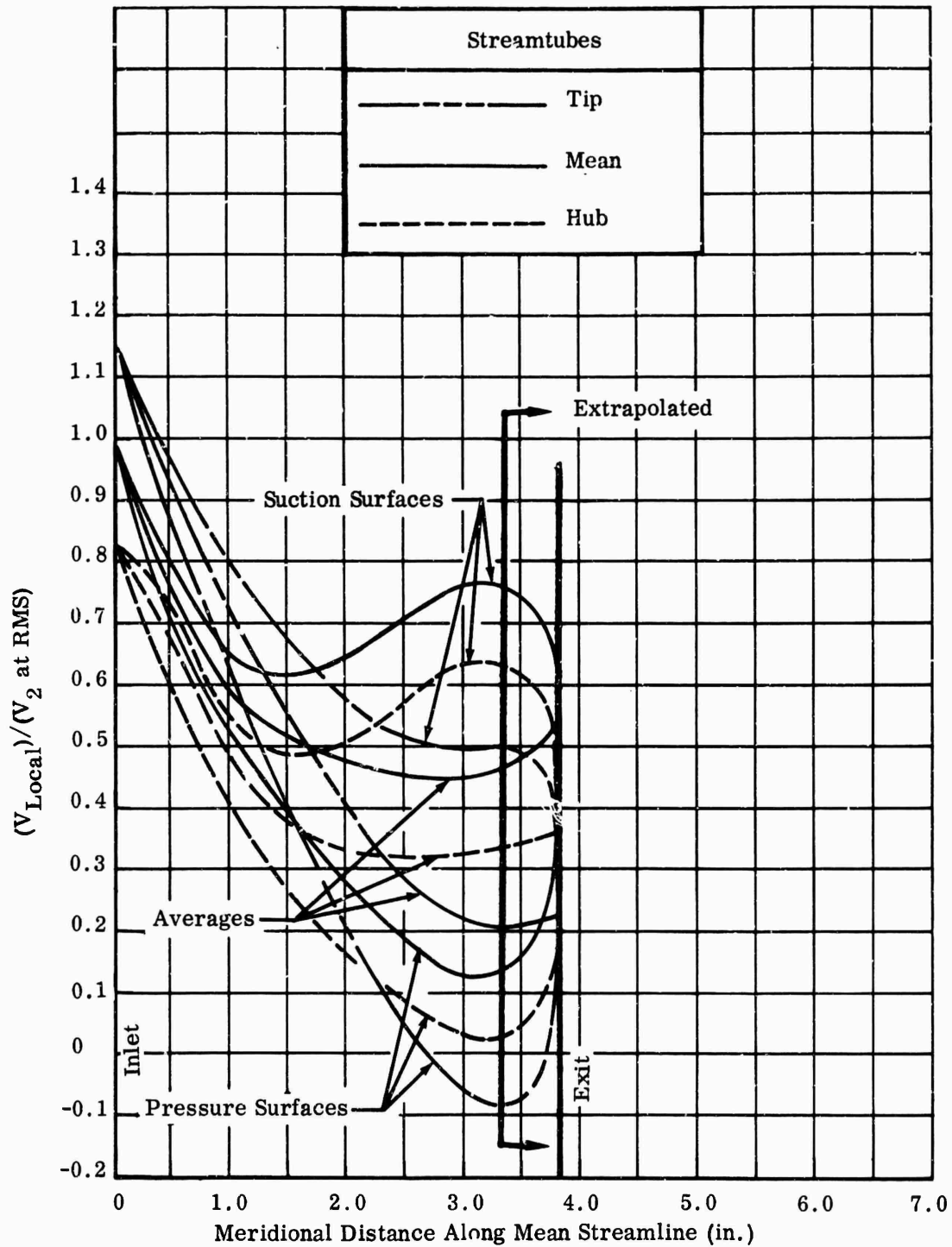


Figure 39. Blade-Surface Velocities of MF-2 Impeller;
Design Speed, 73,000 rpm.

CONFIDENTIAL

CONFIDENTIAL

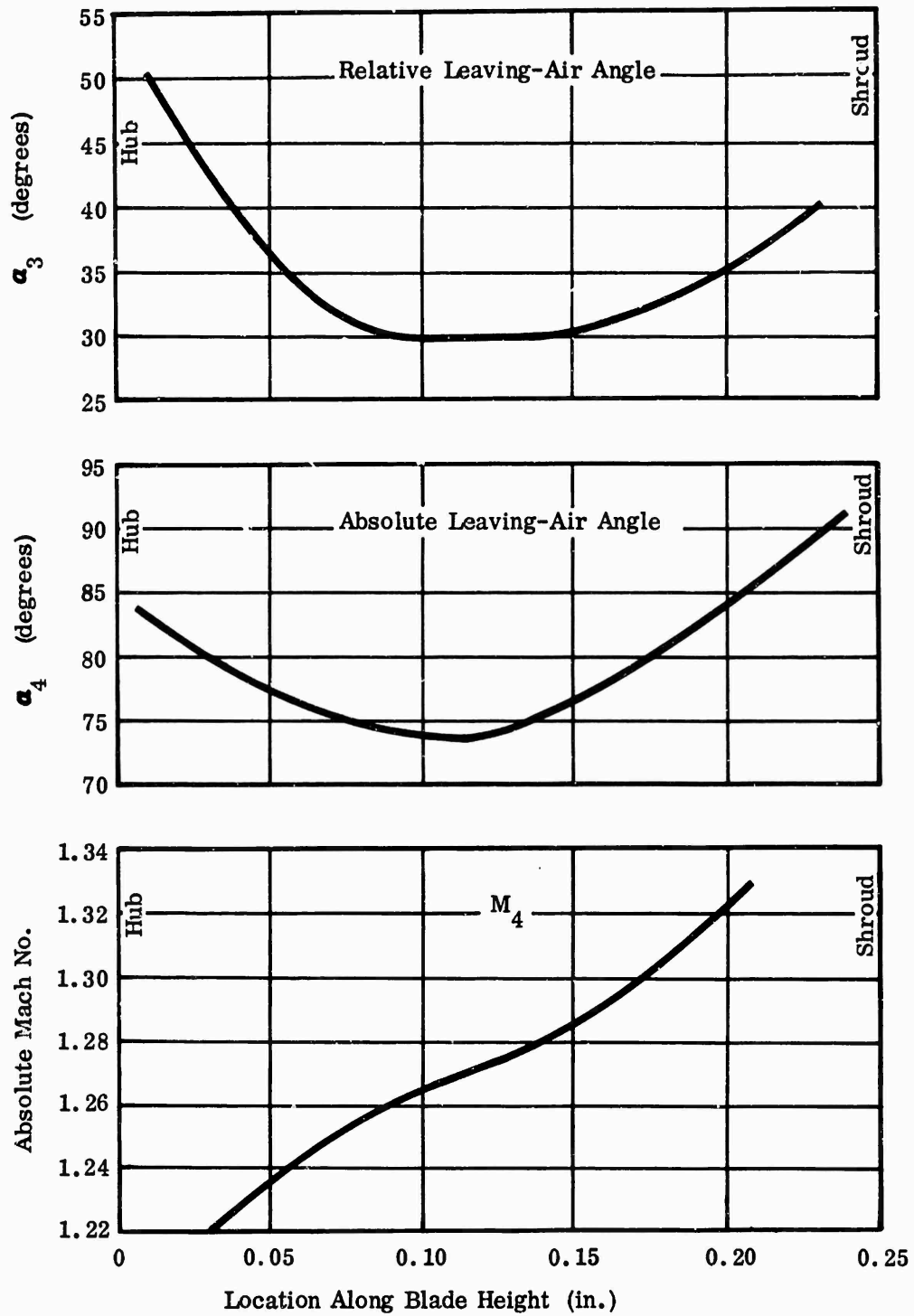


Figure 40. Exit Flow Conditions for MF-2 Impeller;
Design Speed, 73,000 rpm.

CONFIDENTIAL

CONFIDENTIAL

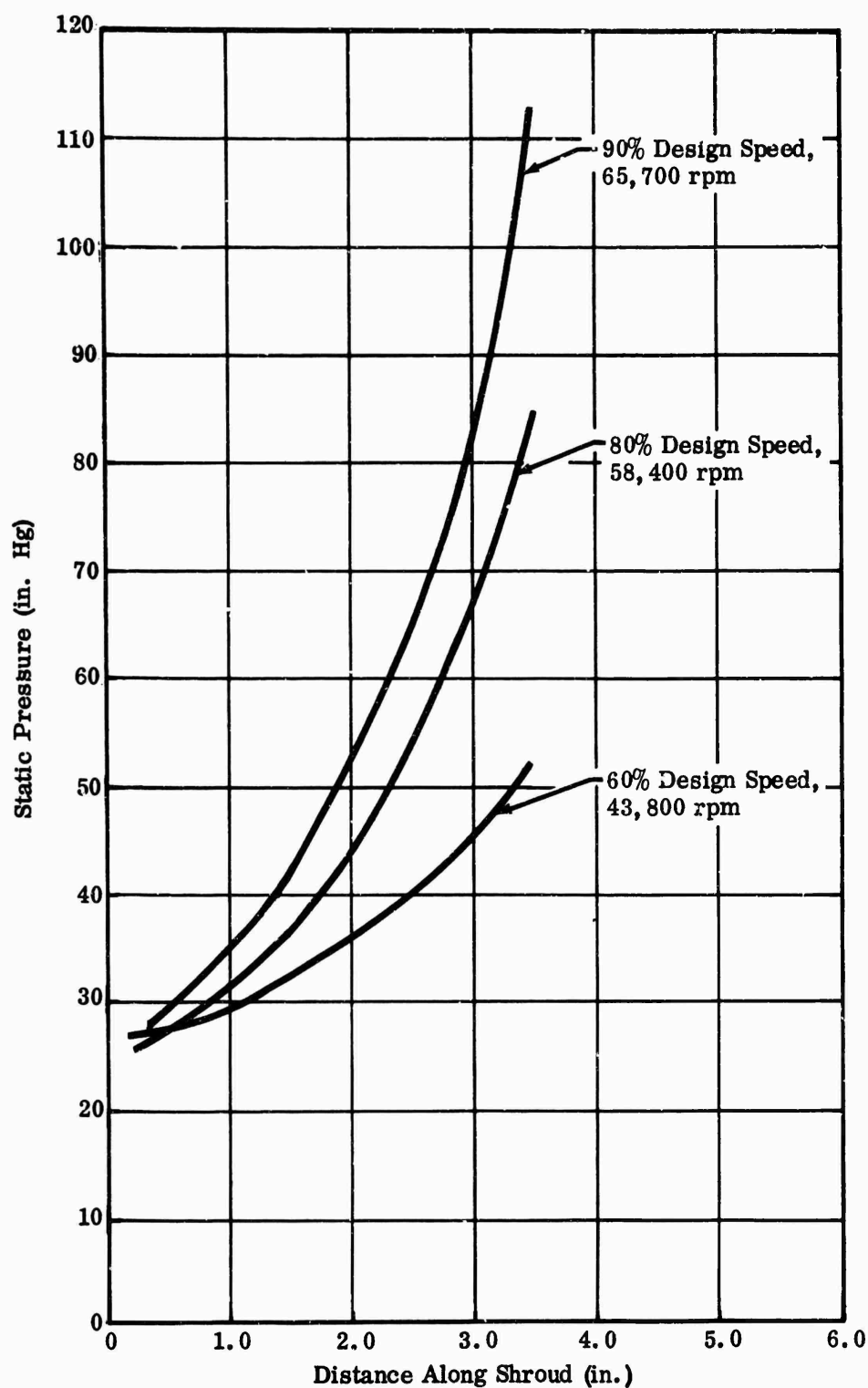


Figure 41. Predicted Static-Pressure Rise Along MF-2 Impeller Shroud, Part Speed.

CONFIDENTIAL

CONFIDENTIAL

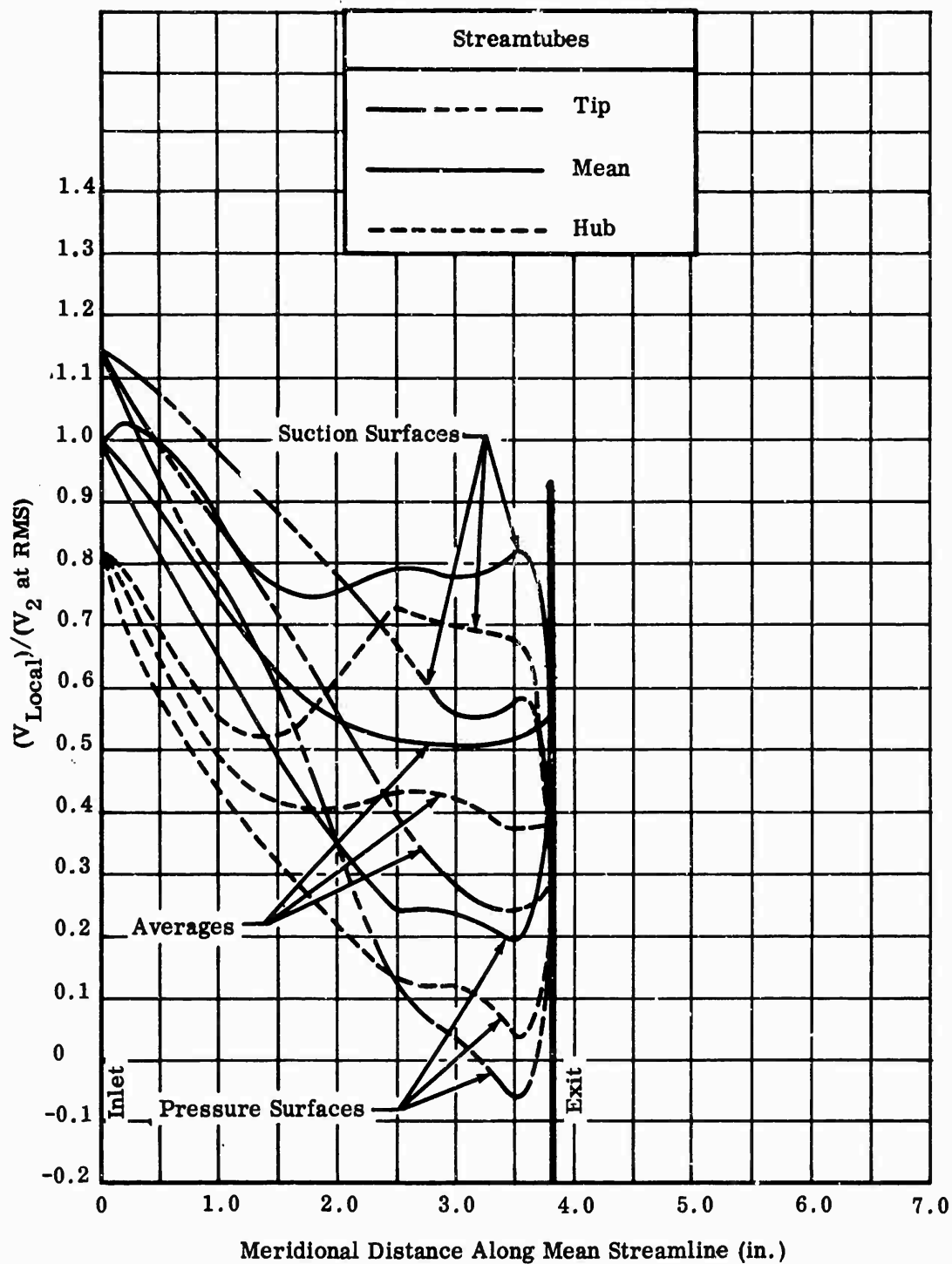


Figure 42. Blade-Surface Velocities of MF-2 Impeller;
90-Percent Design Speed, 65,700 rpm.

CONFIDENTIAL

CONFIDENTIAL

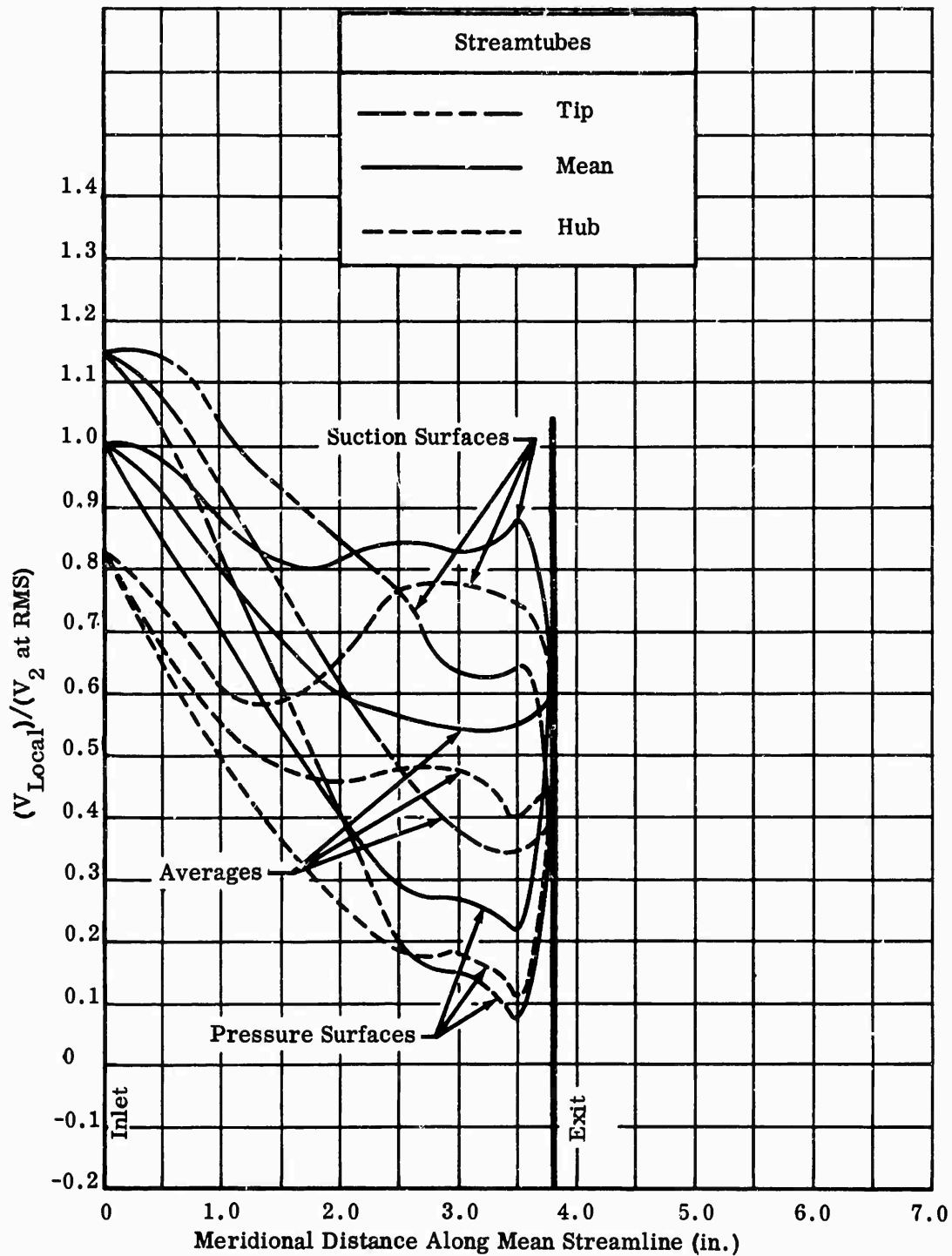


Figure 43. Blade-Surface Velocities of MF-2 Impeller;
80-Percent Design Speed, 58,400 rpm.

CONFIDENTIAL

CONFIDENTIAL

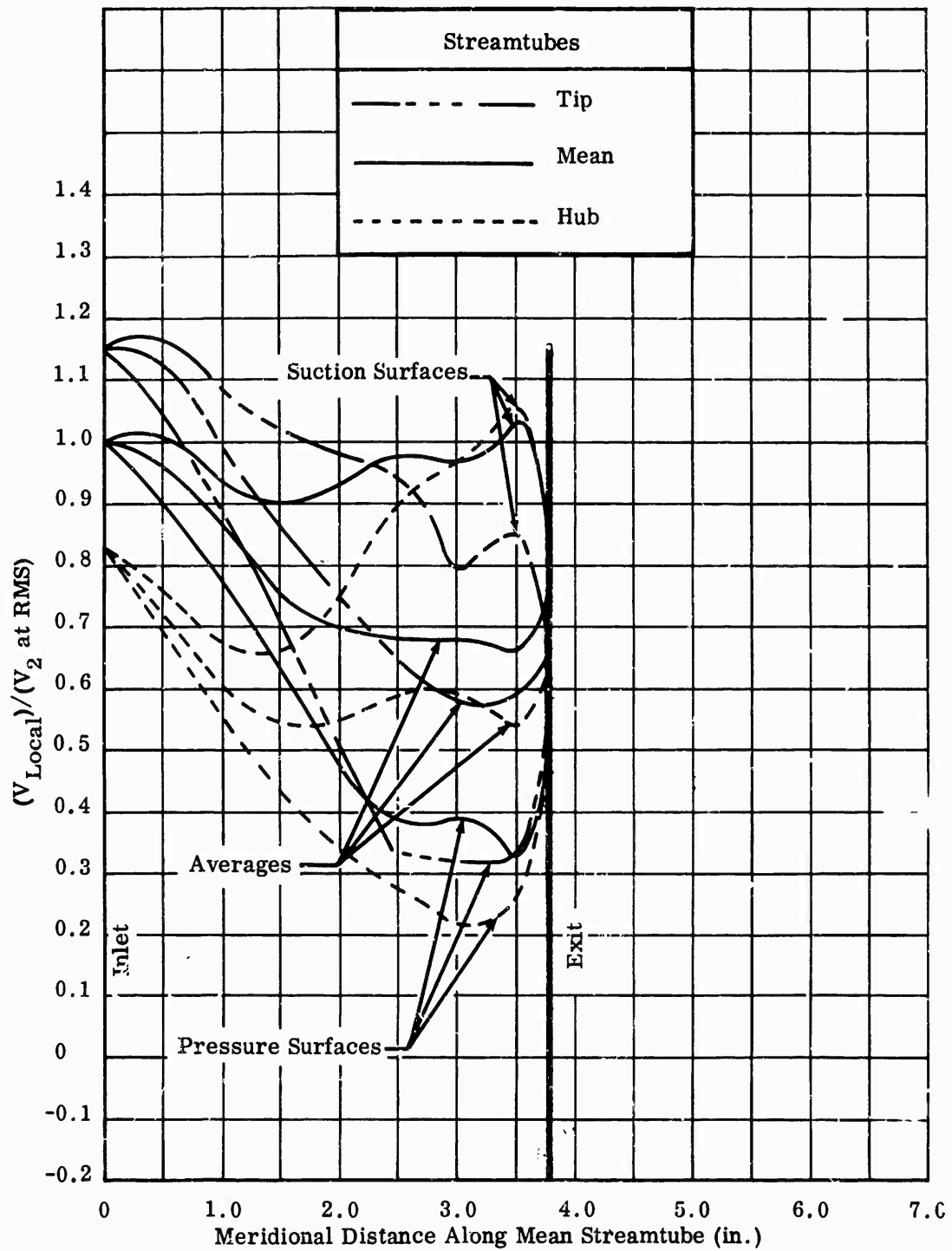


Figure 44. Blade-Surface Velocities of MF-2 Impeller;
60-Percent Design Speed, 43,800 rpm.

CONFIDENTIAL

CONFIDENTIAL

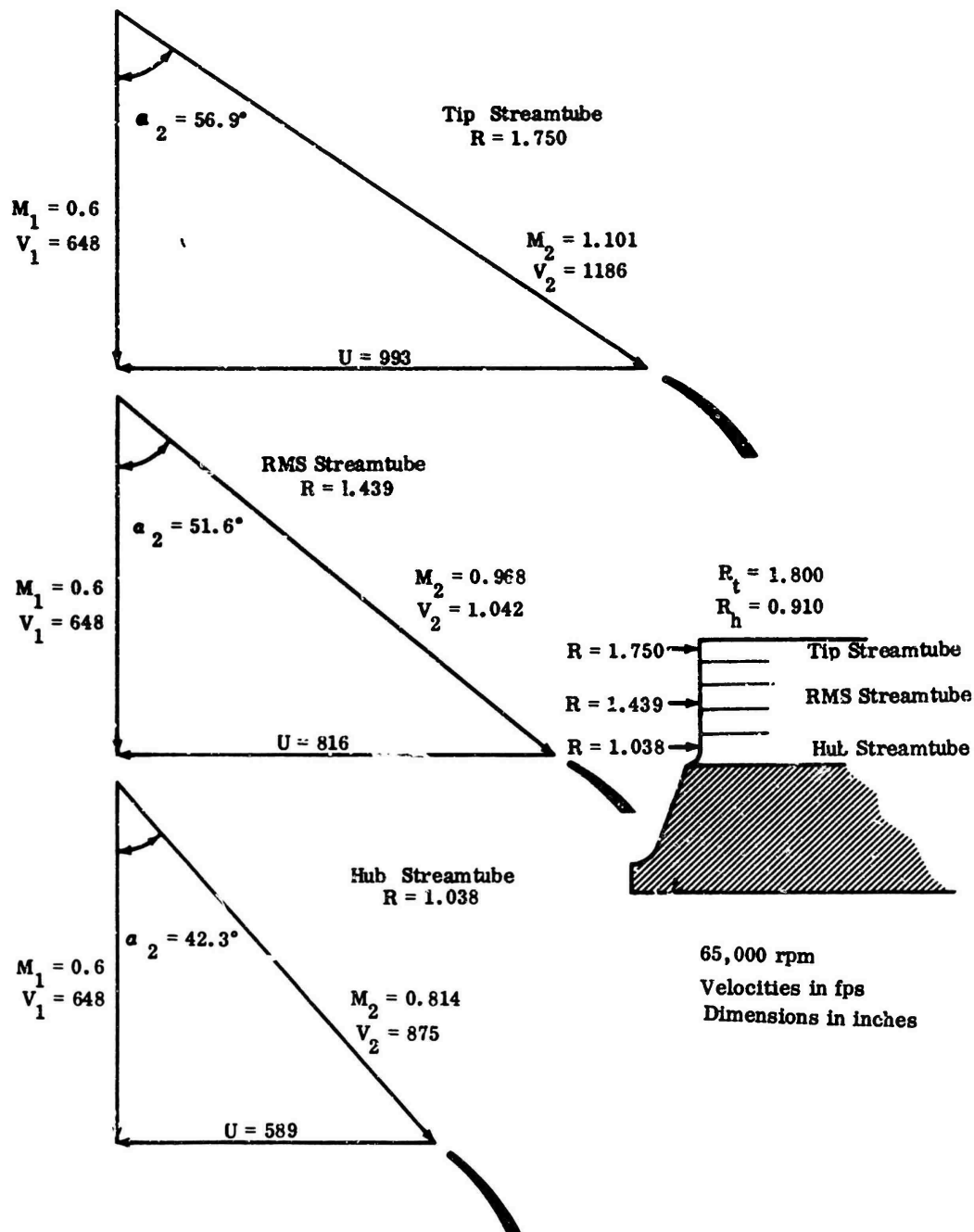


Figure 45. Inlet Velocity Diagrams for MF-3 Impeller Design.

CONFIDENTIAL

CONFIDENTIAL

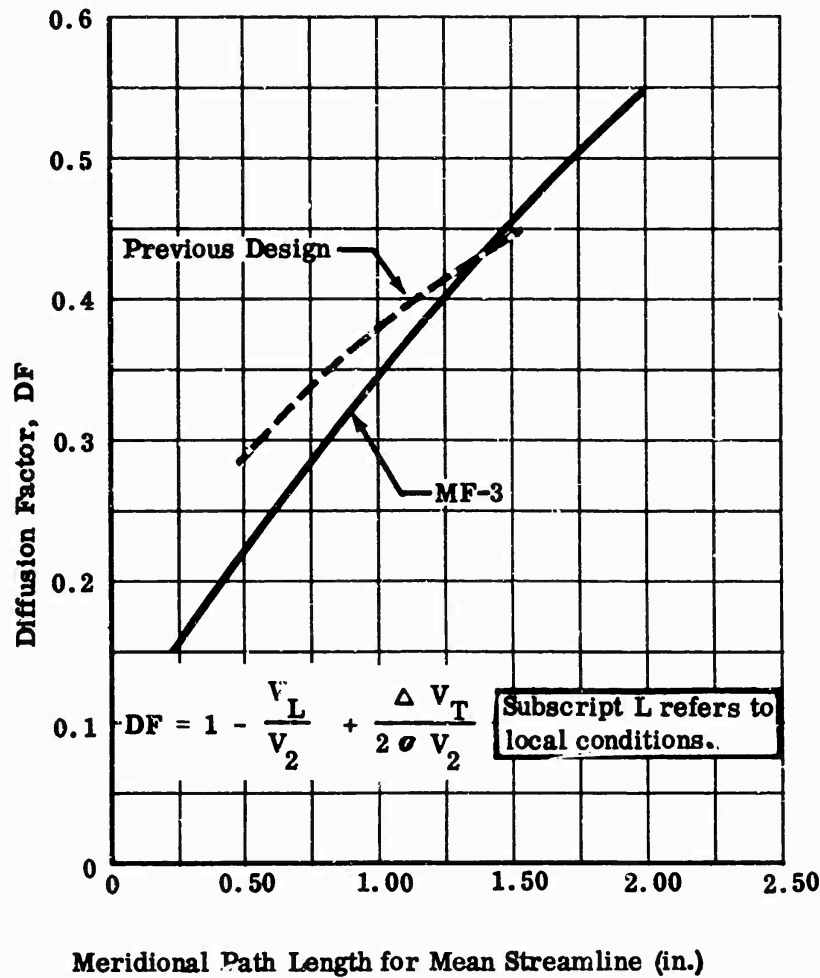


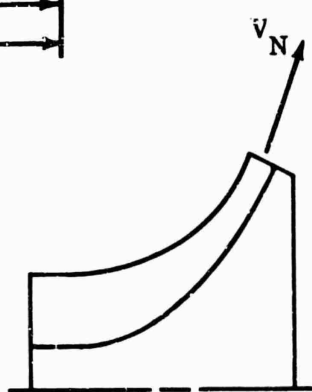
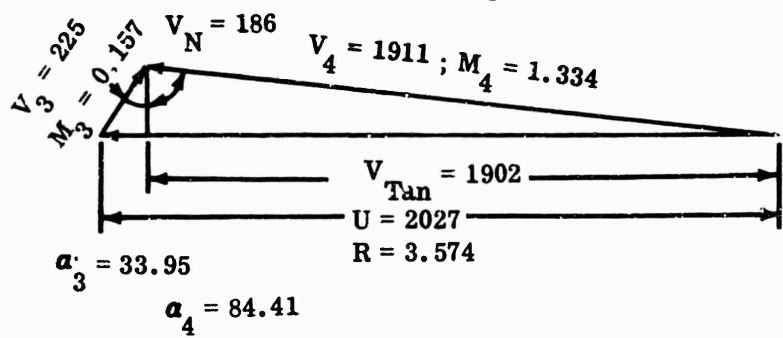
Figure 46. Diffusion Factor for MF-3 Impeller.

absolute axial Mach number was 0.60, compared to 0.50 used in the MF-1 design. The resultant inlet velocity diagrams are shown in Figure 58. To be consistent with the parameters used in designing the MF-1, MF-2, and MF-3, the RF-1 diffusion factor was compared with the values from a previous design done by the contractor (see Figure 59). The methods described in Appendix I of this report were used to analyze the radial-flow design. Inducer-tip diameter was calculated as 3.9 inches, and rotor speed was 57,000 rpm, the same as that of MF-1.

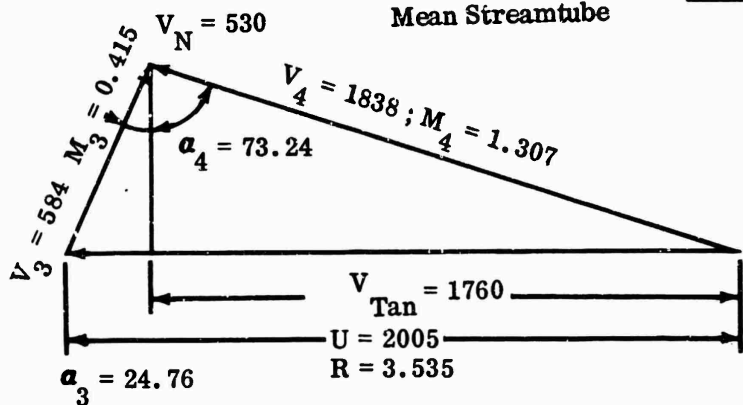
Impeller-tip velocity diagrams are shown in Figure 60. From previously established size and speed parameters, the RF-1 tip diameter was determined to be 8.08 inches, about the same as that of MF-1. At the tip, blade height was

CONFIDENTIAL

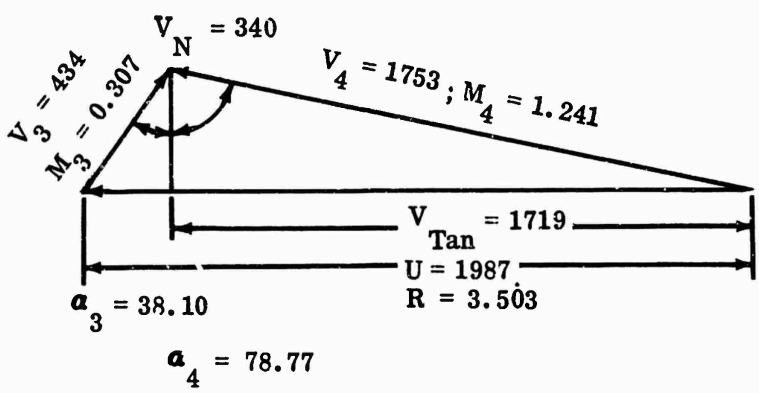
Tip Streamtube



Mean Streamtube



Hub Streamtube



Dimensions (inches)
Velocities (fps)
Rotor Speed 65,000 rpm
 V_N in direction of
streamline at tip.

Figure 47. Exit Velocity Diagrams for MF-3 Impeller.

CONFIDENTIAL

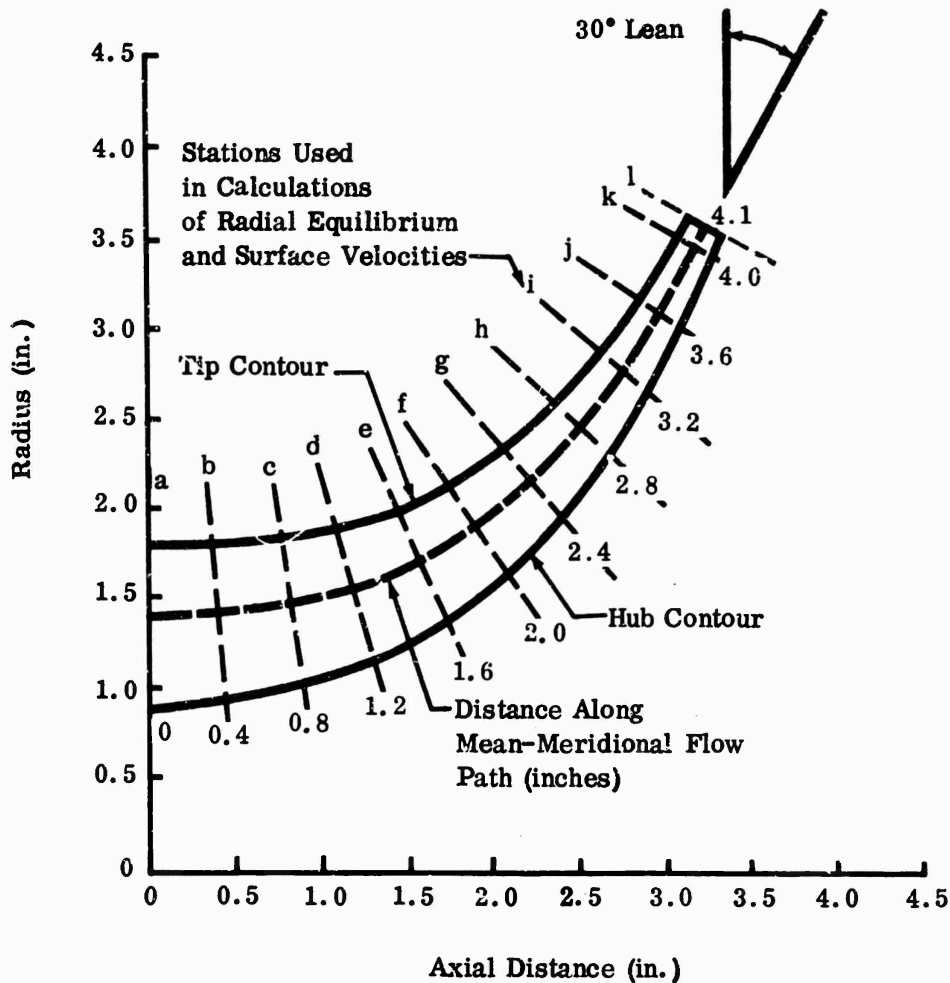


Figure 48. Meridional View of MF-3 Impeller.

maintained at 0.20 inch, the same as MF-1. The overall meridional view of the impeller is shown in Figure 61. Because of strength requirements, it was essential that some rearward lean be incorporated in the disk shape. This lean is common to all high-tip-speed impellers and must be incorporated to alleviate centrifugal blade load and disk tangential stress. For the RF-1 impeller design, this rearward lean was 17.5 degrees from radial. Flow area, blockage, blade height, and turning schedules are depicted in Figure 62. Figures 63 through 70 show the results of the radial-equilibrium and blade-surface velocity calculations made by using the methods of Appendix I.

CONFIDENTIAL

CONFIDENTIAL

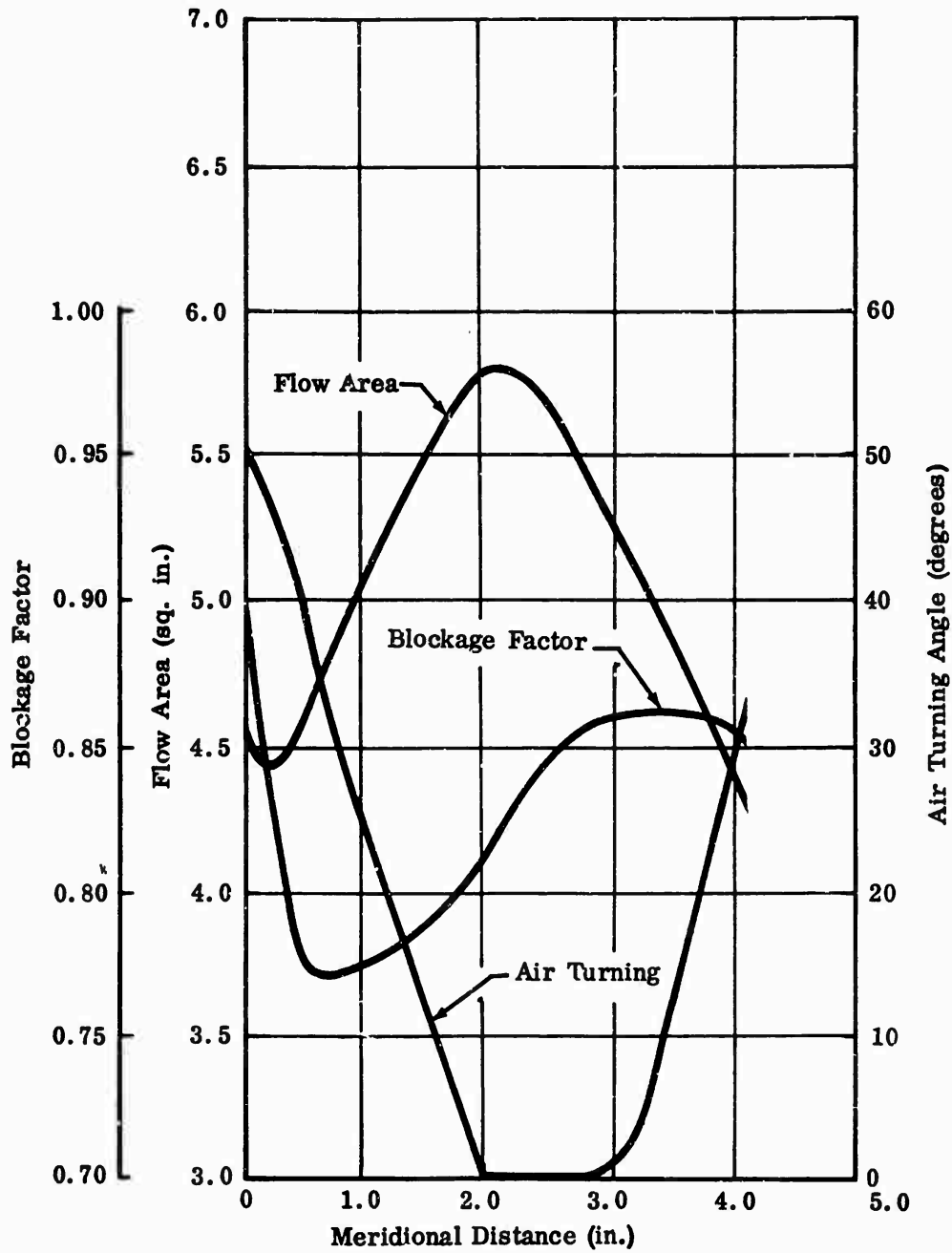


Figure 49. Impeller Design Parameters for MF-3;
Design Speed, 65,000 rpm.

CONFIDENTIAL

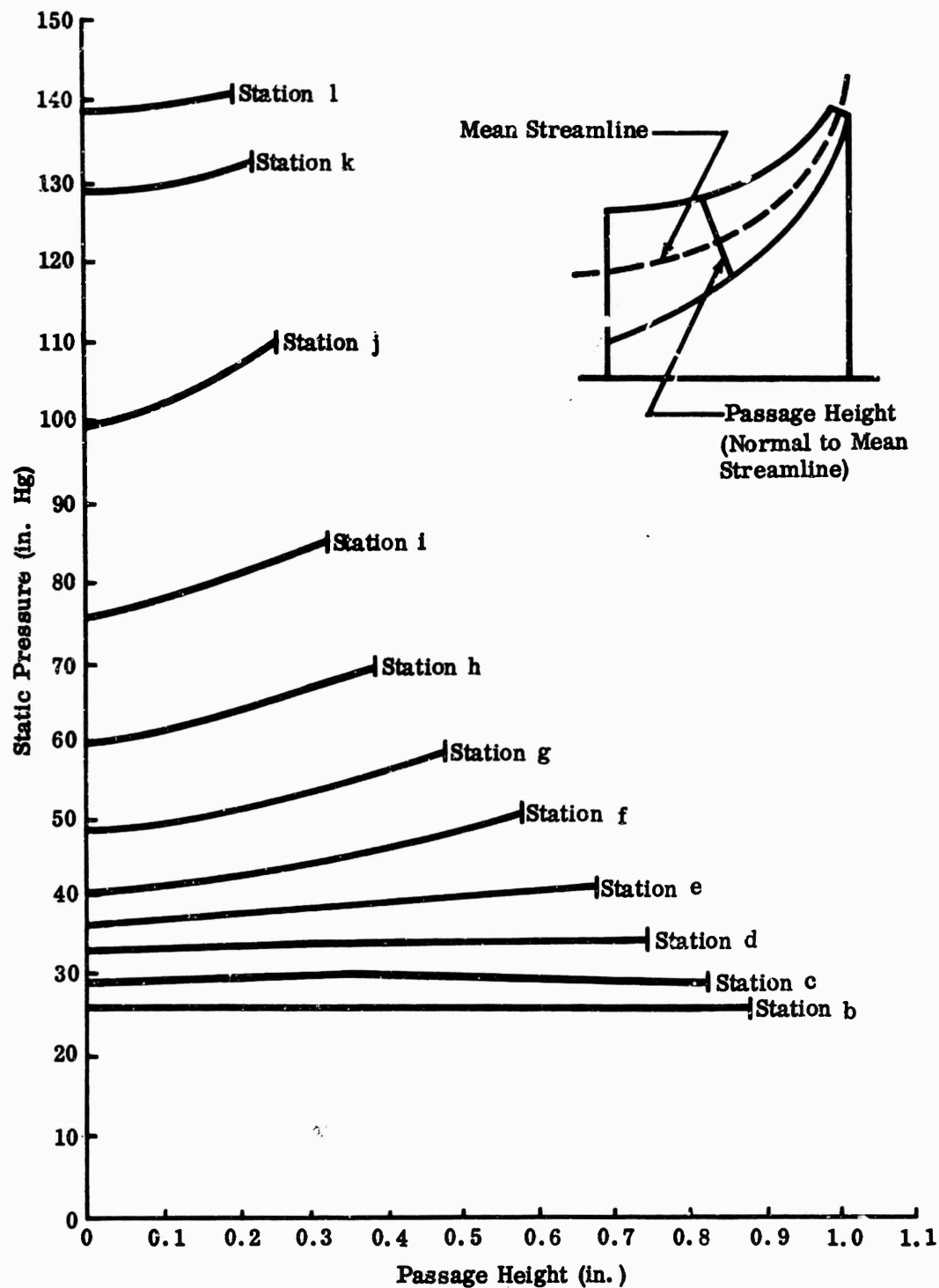


Figure 50. Static-Pressure Distribution Across Passage, MF-3 Impeller; Design Speed, 65,000 rpm.

CONFIDENTIAL

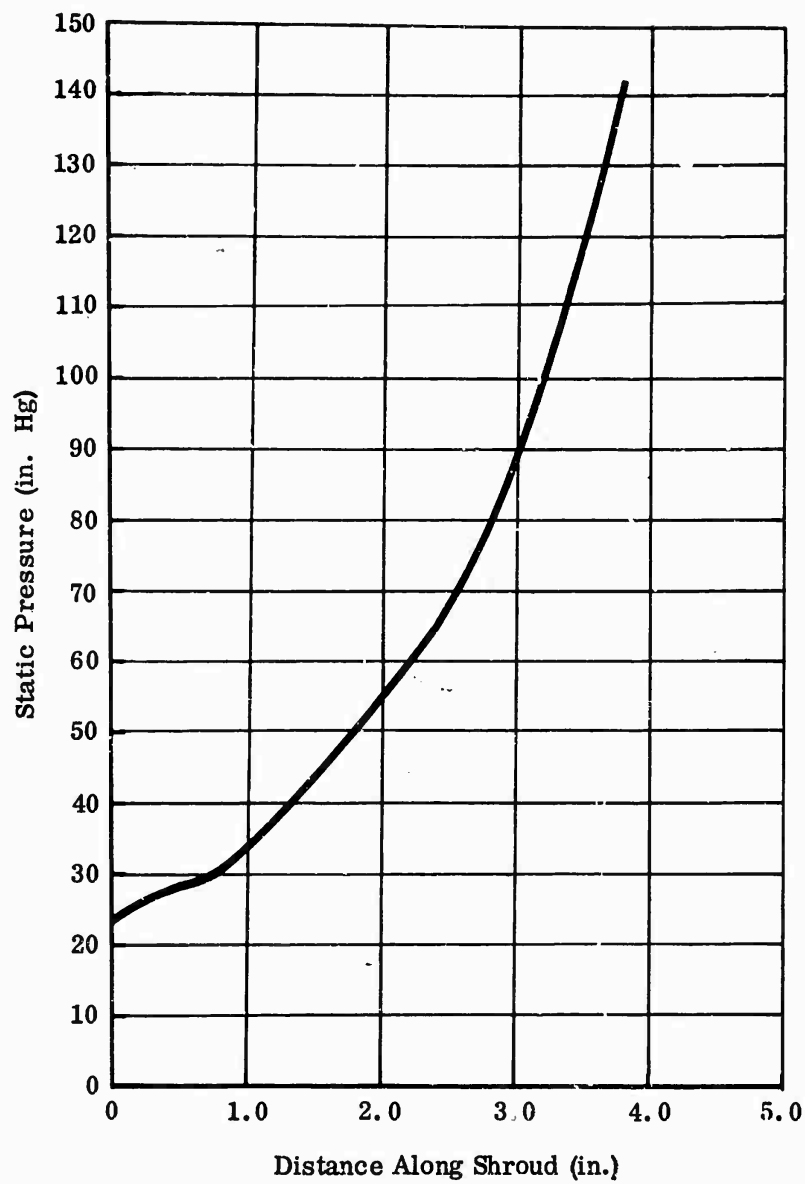


Figure 51. Predicted Static-Pressure Rise Along MF-3 Impeller Shroud; Design Speed, 65,000 rpm.

CONFIDENTIAL

CONFIDENTIAL

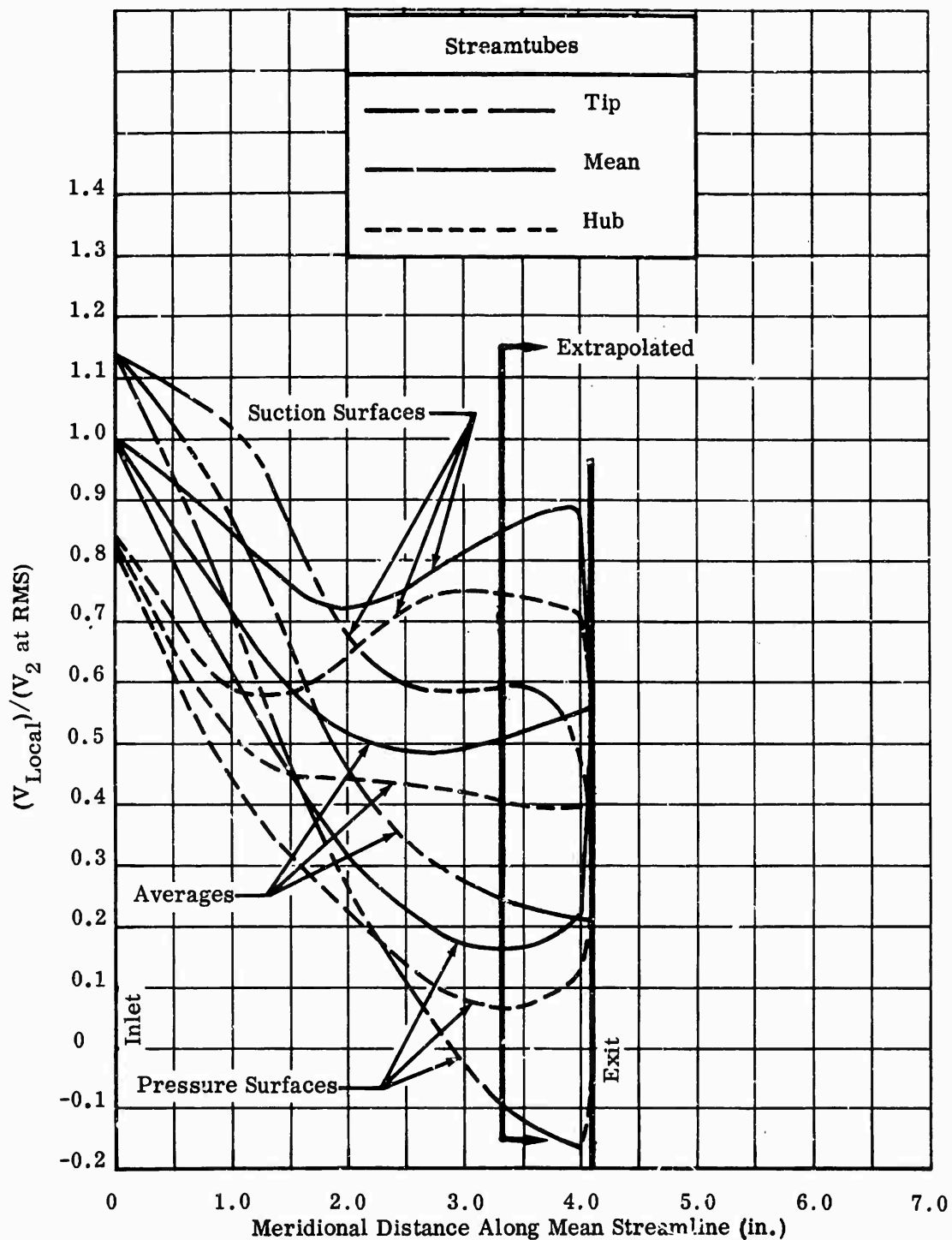


Figure 52. Blade-Surface Velocities of MF-3 Impeller;
Design Speed, 65,000 rpm.

CONFIDENTIAL

CONFIDENTIAL

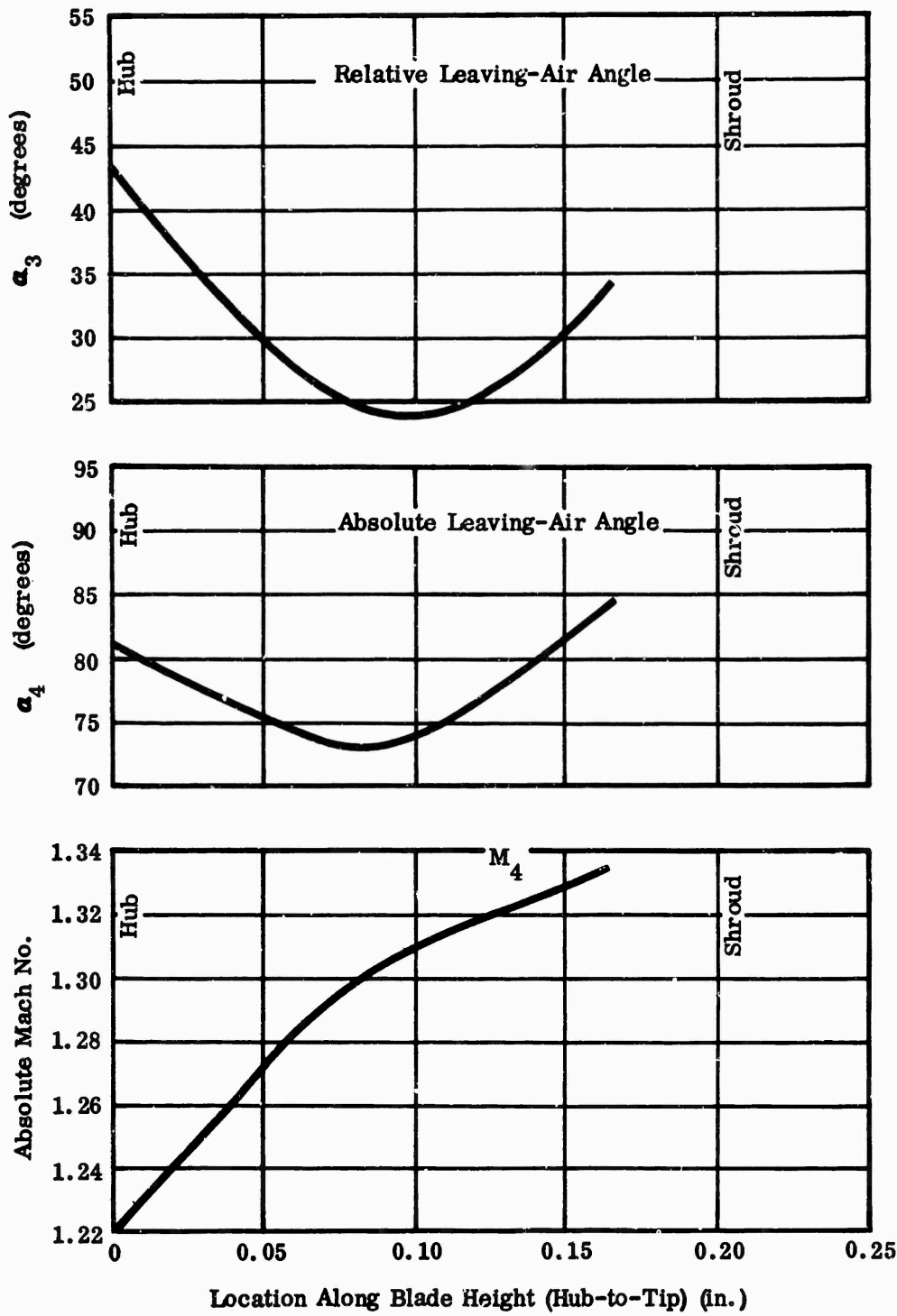


Figure 53. Exit Flow Conditions for MF-3 Impeller;
Design Speed, 65,000 rpm.

CONFIDENTIAL

CONFIDENTIAL

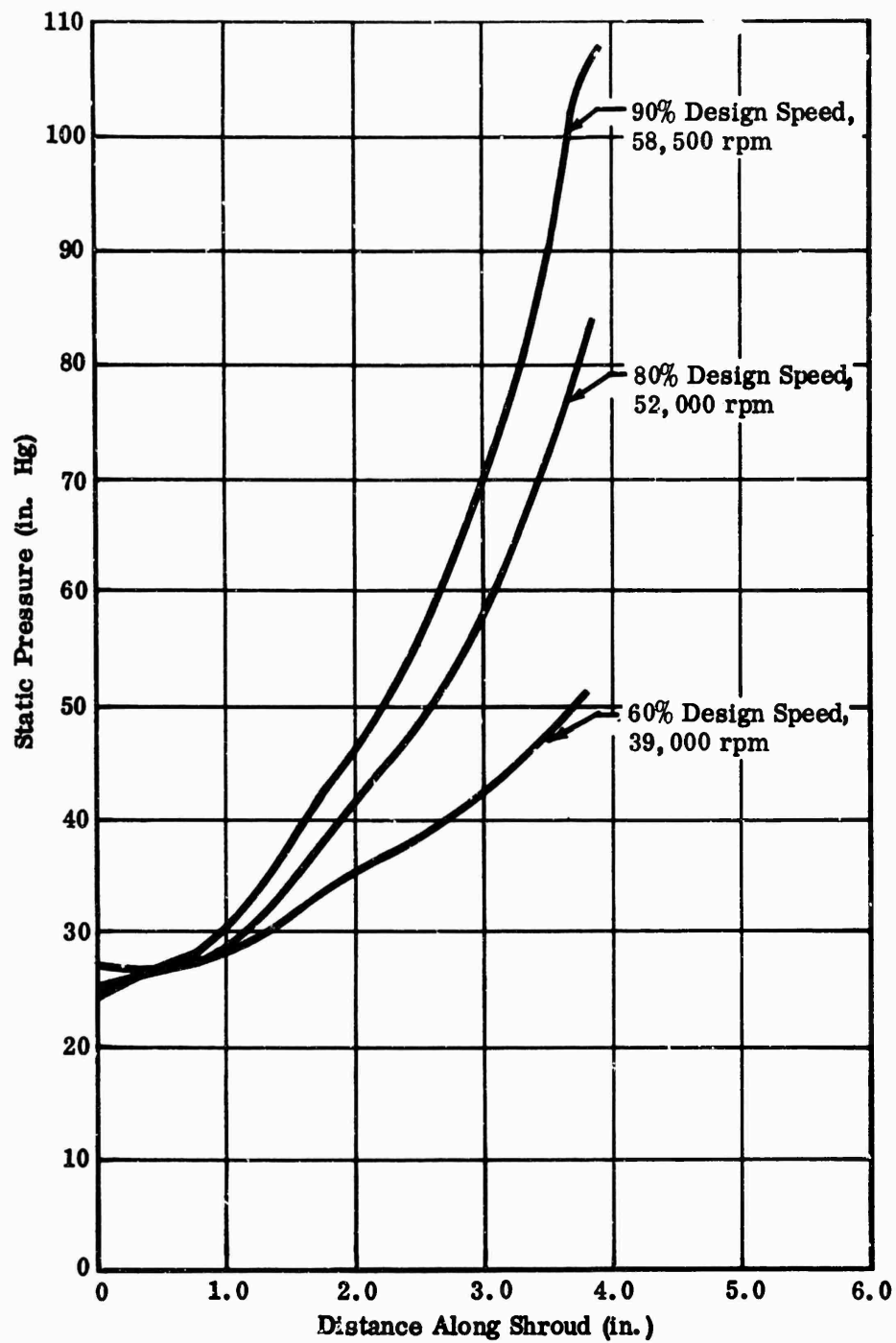


Figure 54. Predicted Static-Pressure Rise Along MF-3 Impeller Shroud, Part Speed.

CONFIDENTIAL

CONFIDENTIAL

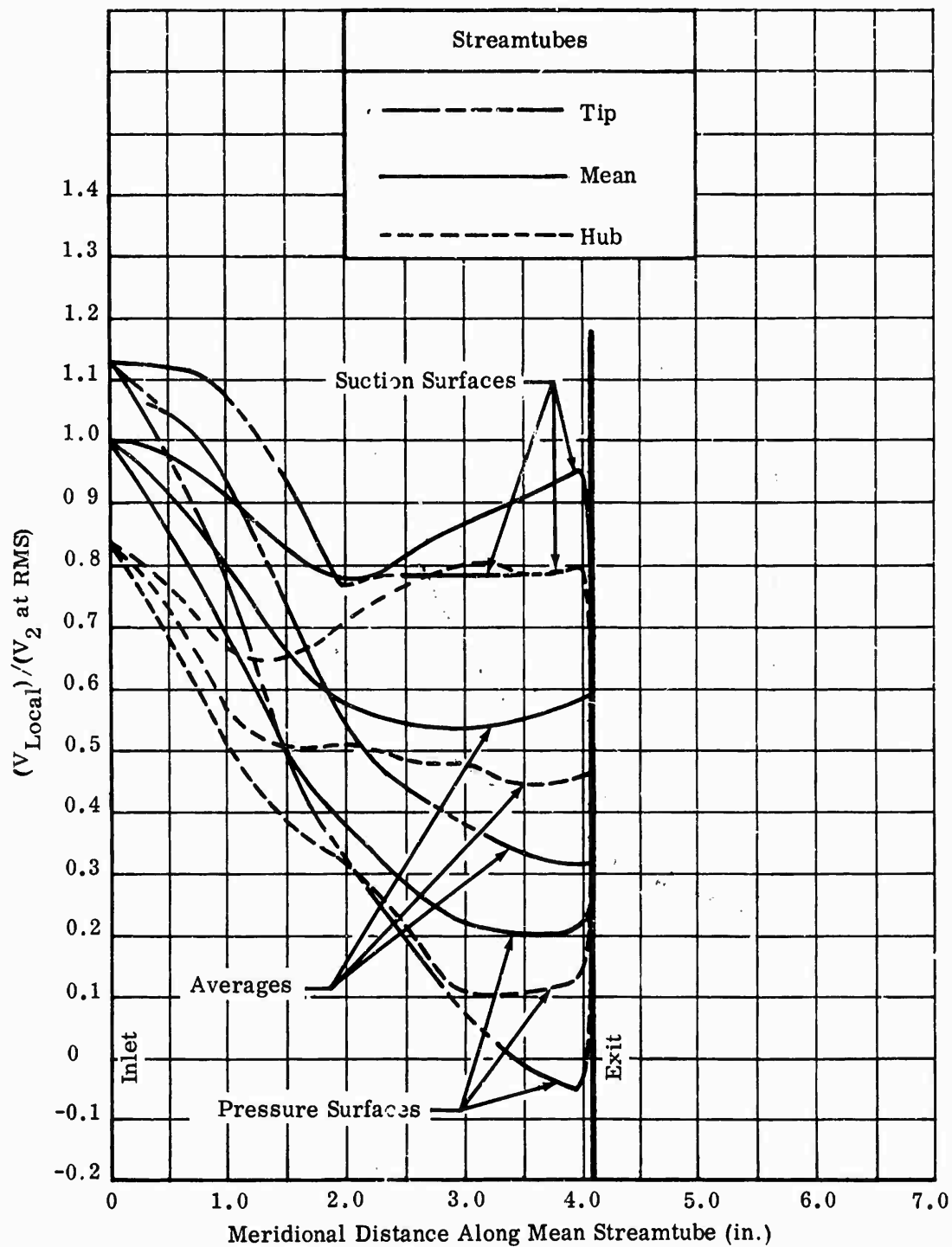


Figure 55. Blade-Surface Velocities of MF-3 Impeller; 90-Percent Design Speed, 58,500 rpm.

CONFIDENTIAL

CONFIDENTIAL

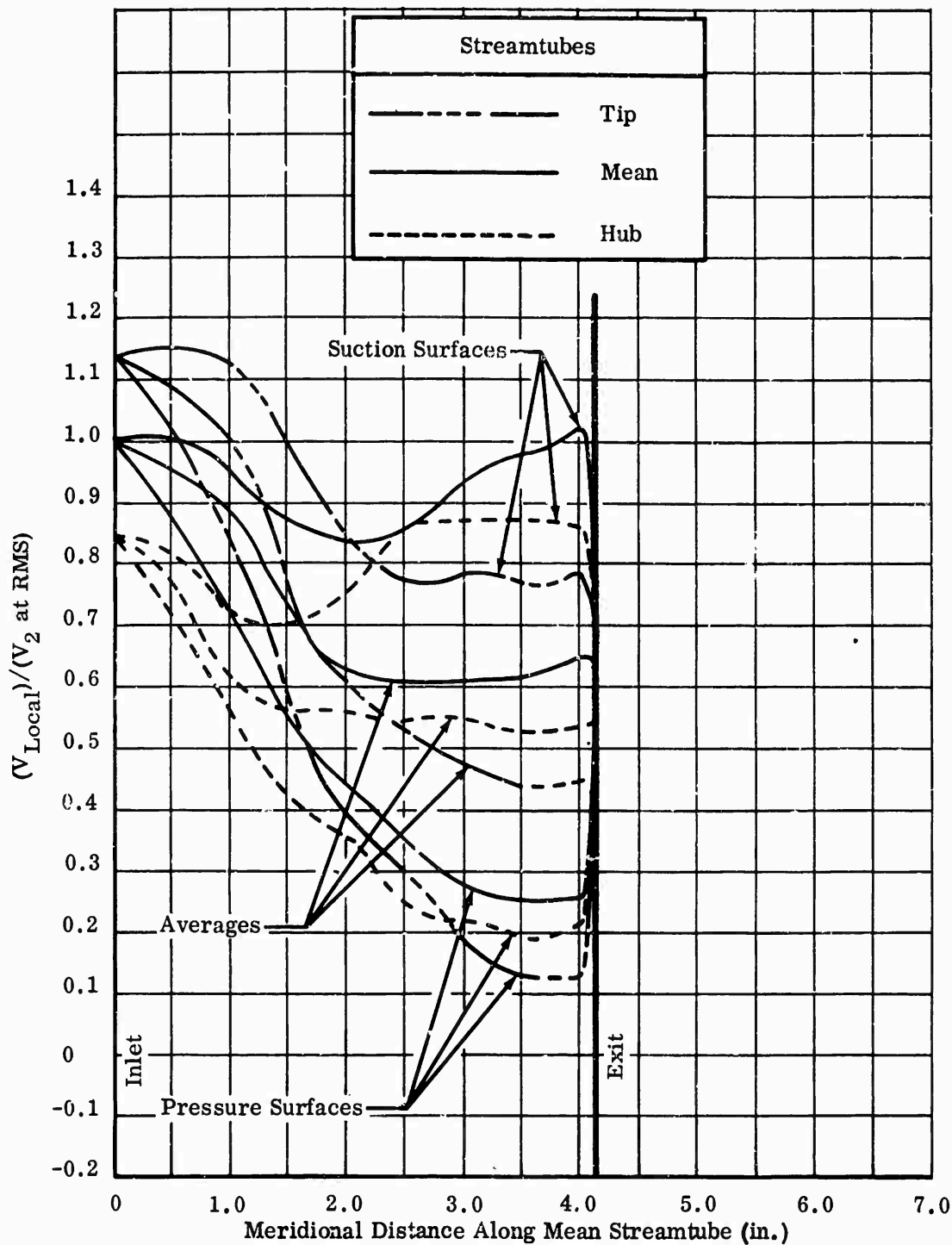


Figure 56. Blade-Surface Velocities of MF-3 Impeller; 80-Percent Design Speed, 52,000 rpm.

CONFIDENTIAL

CONFIDENTIAL

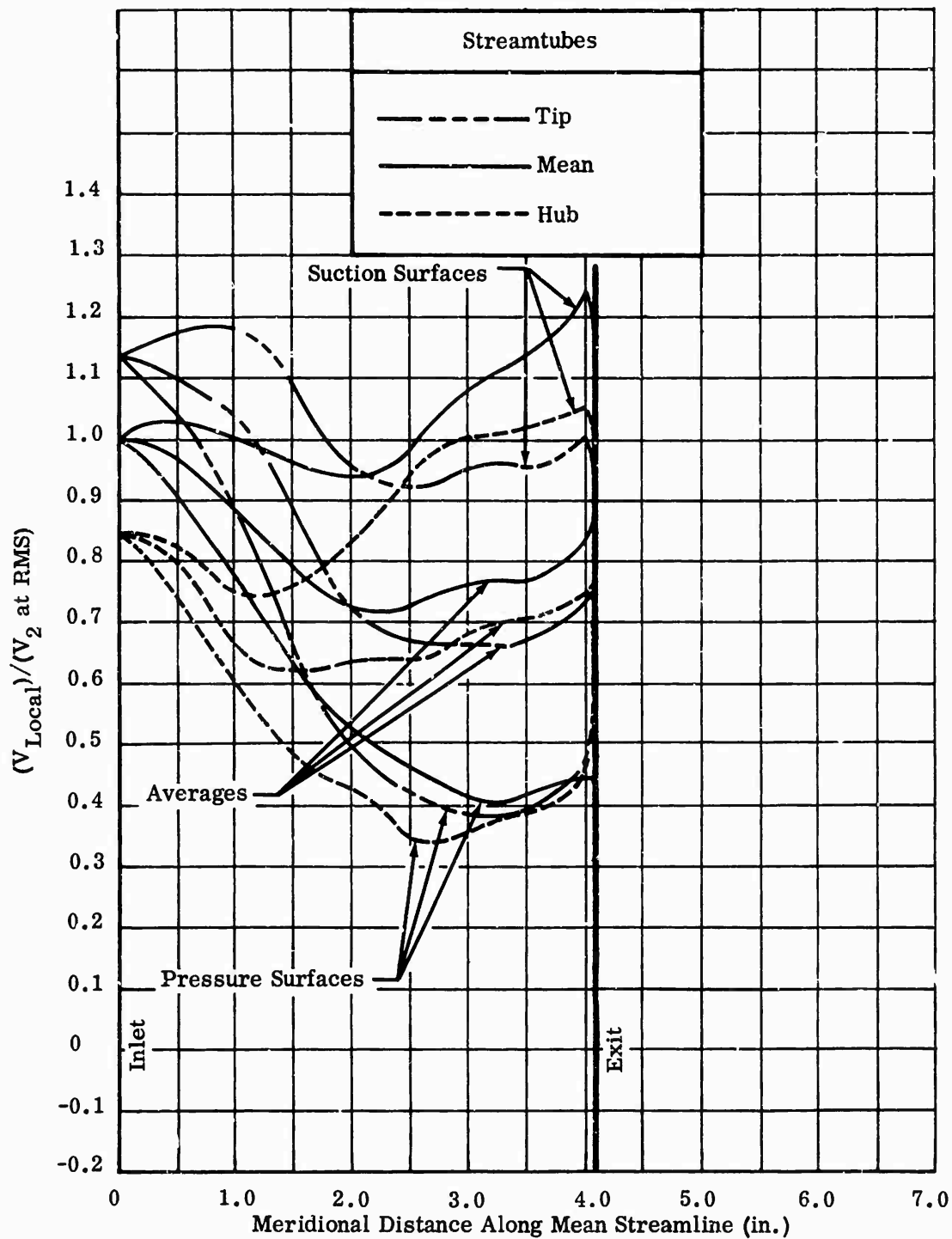


Figure 57. Blade-Surface Velocities of MF-3 Impeller;
60-Percent Design Speed, 39,000 rpm.

CONFIDENTIAL

CONFIDENTIAL

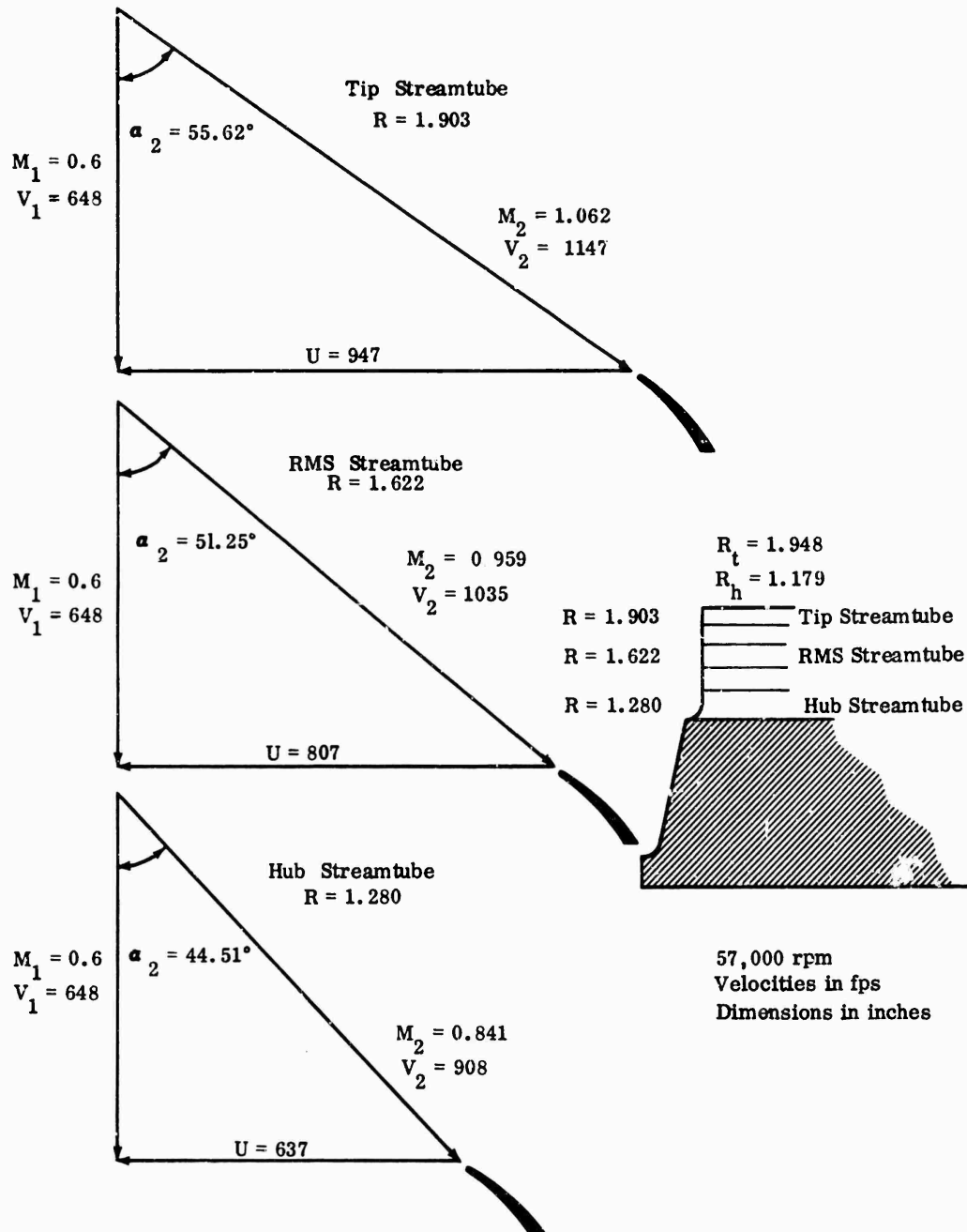


Figure 58. Inlet Vector Diagrams for RF-1 Impeller Design.

CONFIDENTIAL

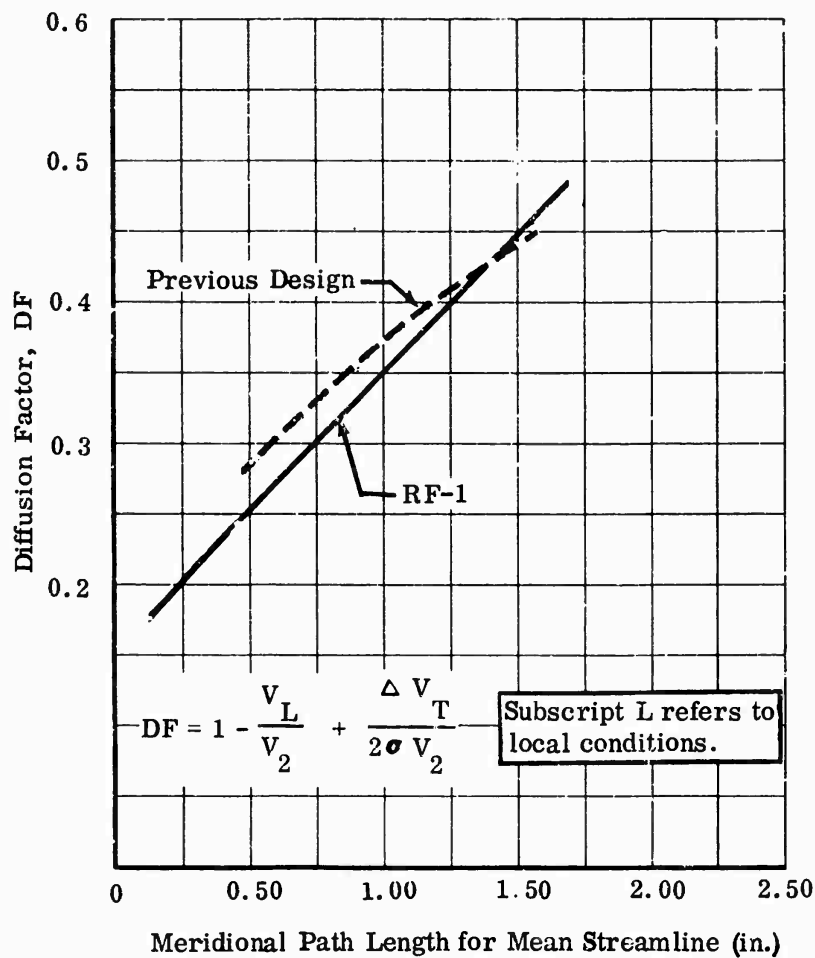


Figure 59. Diffusion Factor for RF-1 Impeller.

Impeller Similarities

The stress analyses of the 4 impellers are presented in Appendix II of this report. In addition, mechanical-design considerations and design solutions for the required test rigs are discussed in Section 2.4.1. To present a general comparison of impeller design parameters, Figures 71 through 75 are photographs of the 4 impellers discussed in this section and throughout the remainder of this report.

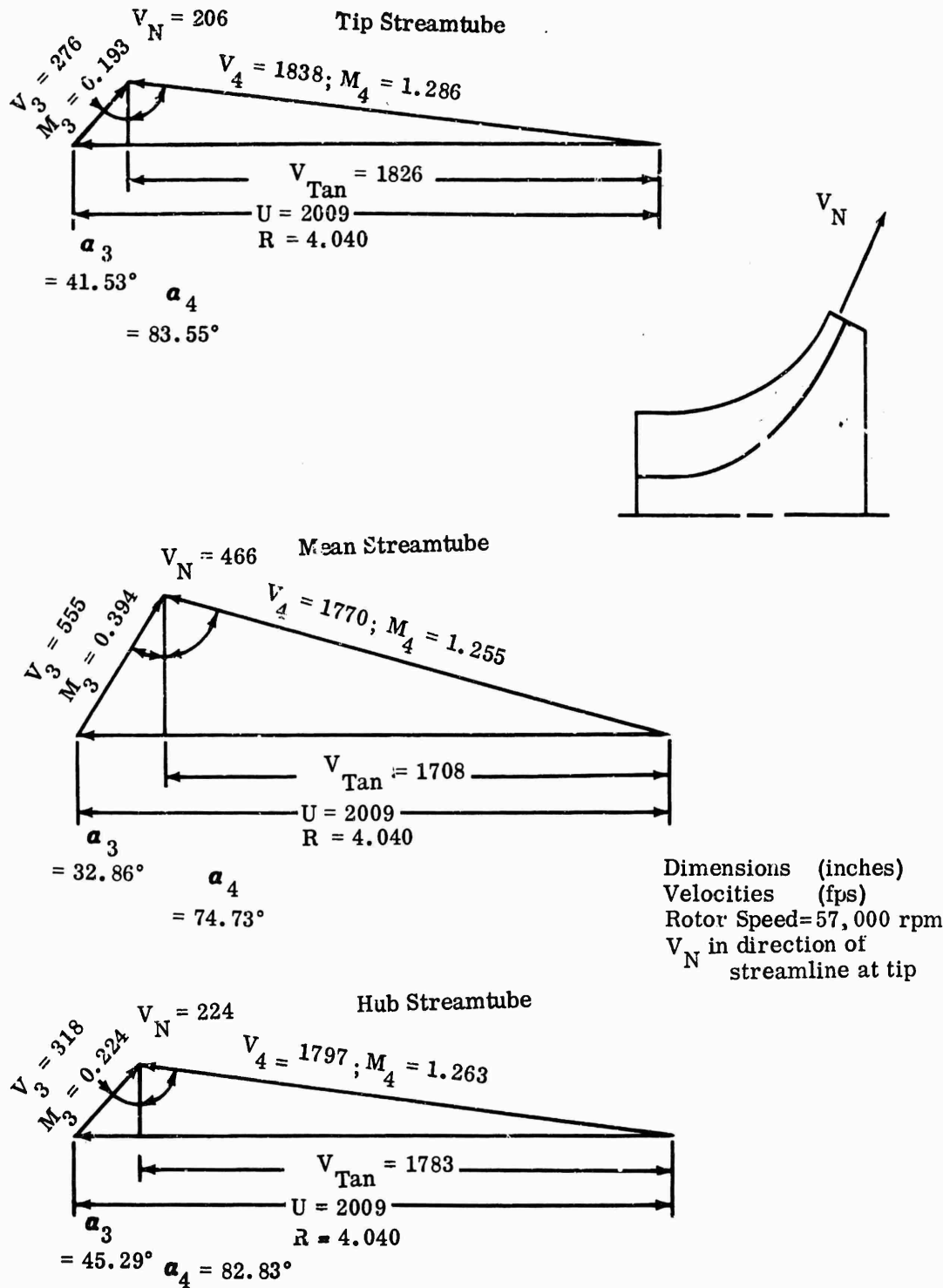


Figure 60. Exit Velocity Diagrams for RF-1 Impeller.

CONFIDENTIAL

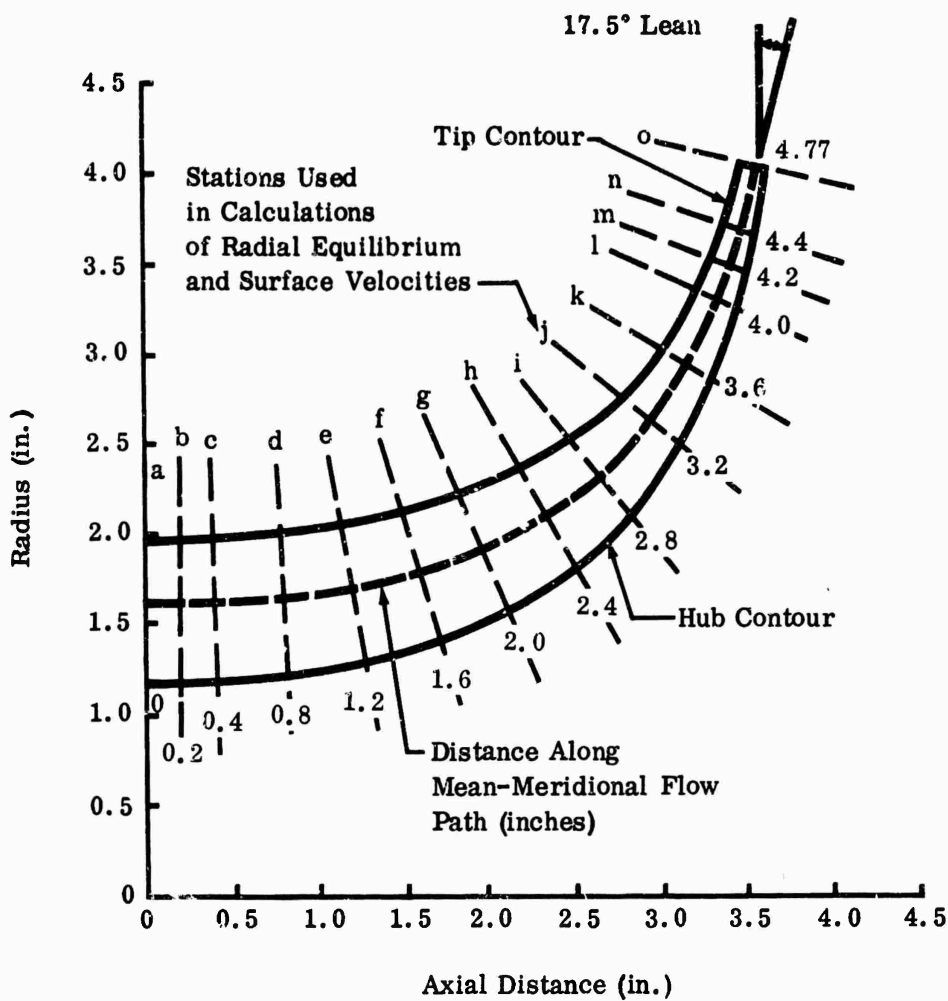


Figure 61. Meridional View of RF-1 Impeller.

CONFIDENTIAL

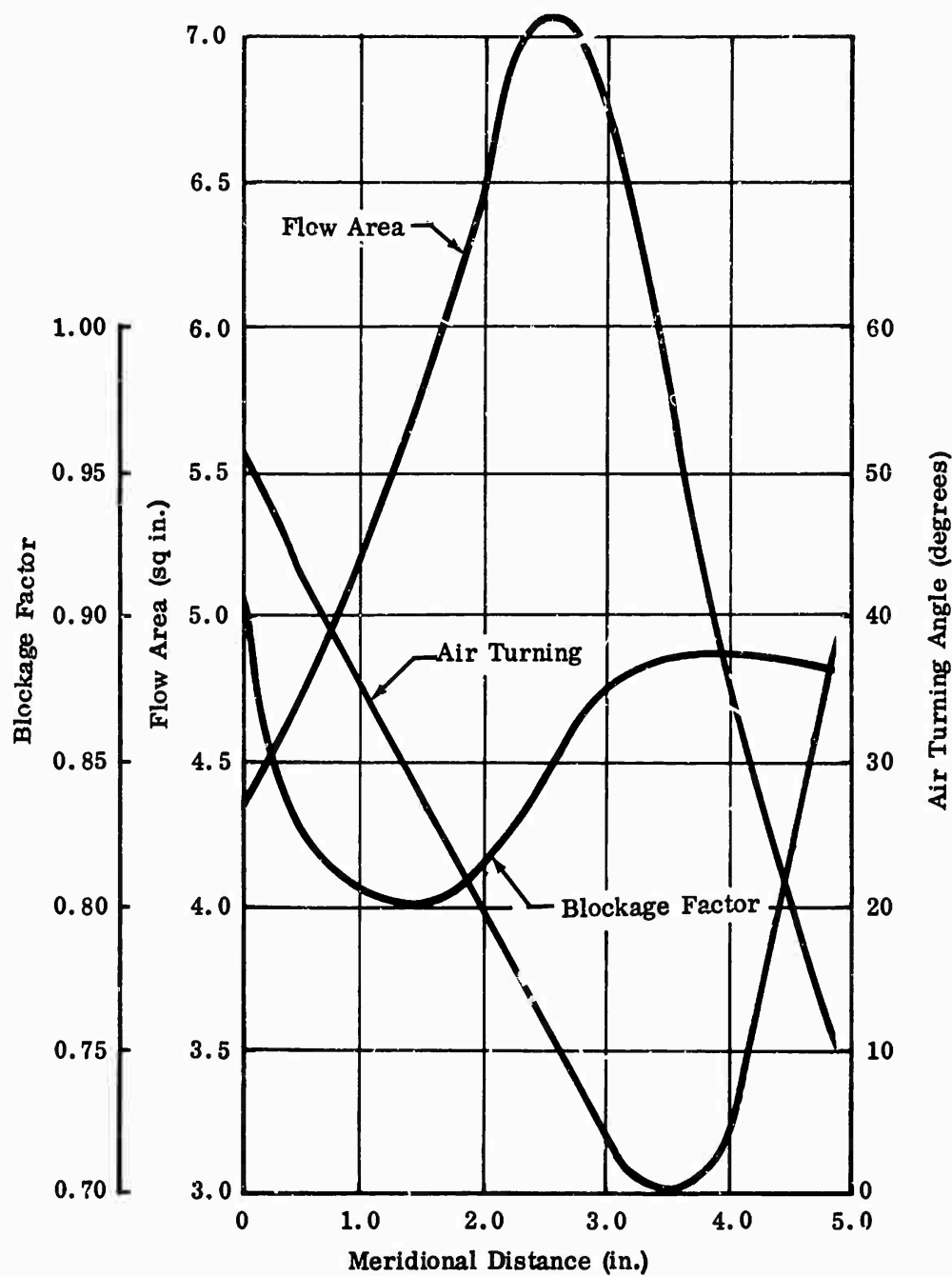


Figure 62. Impeller Design Parameters for RF-1; Design Speed, 57,000 rpm.

CONFIDENTIAL

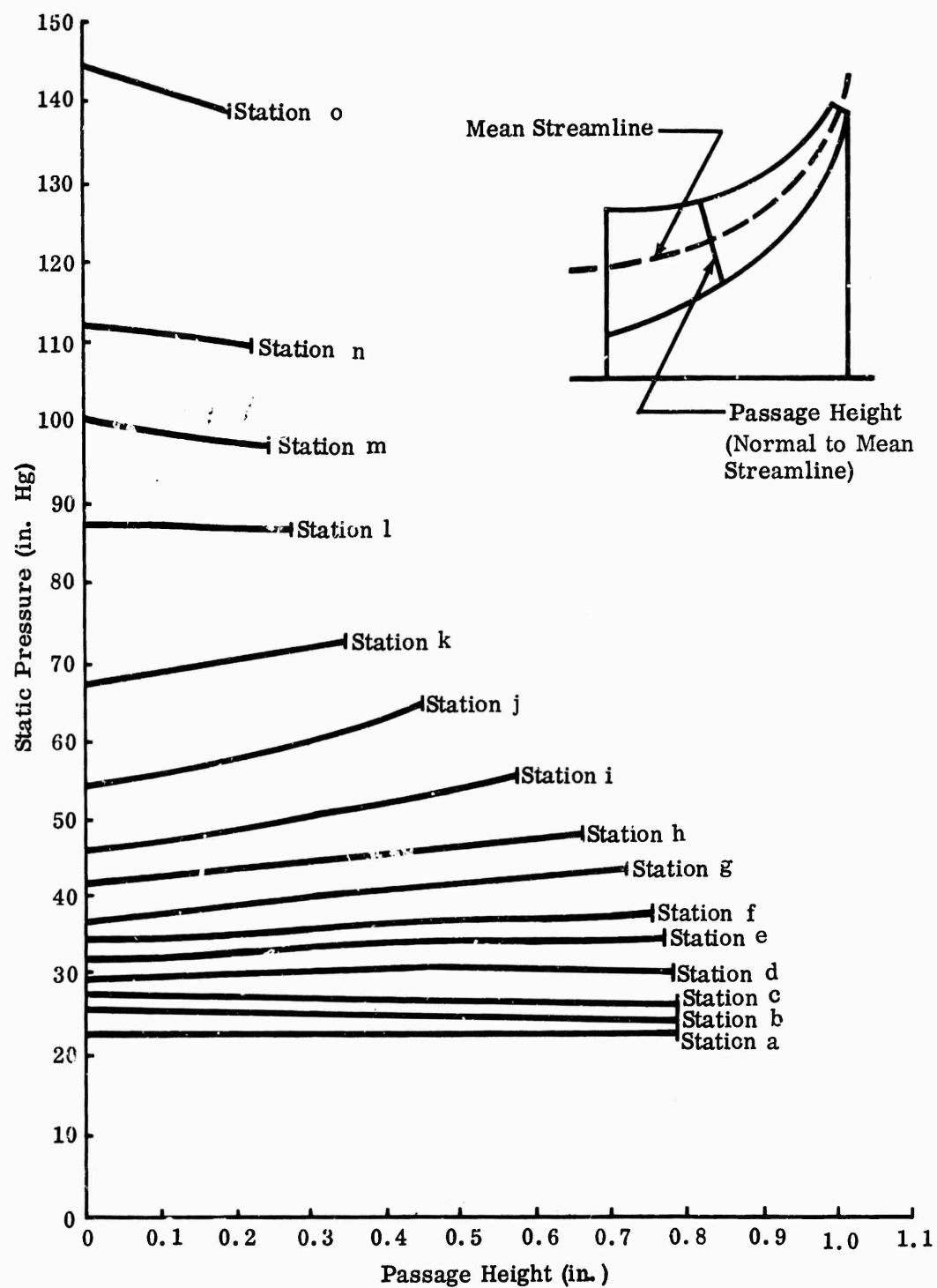


Figure 63. Static-Pressure Distribution Across Passage, RF-1 Impeller; Design Speed, 57,000 rpm.

CONFIDENTIAL

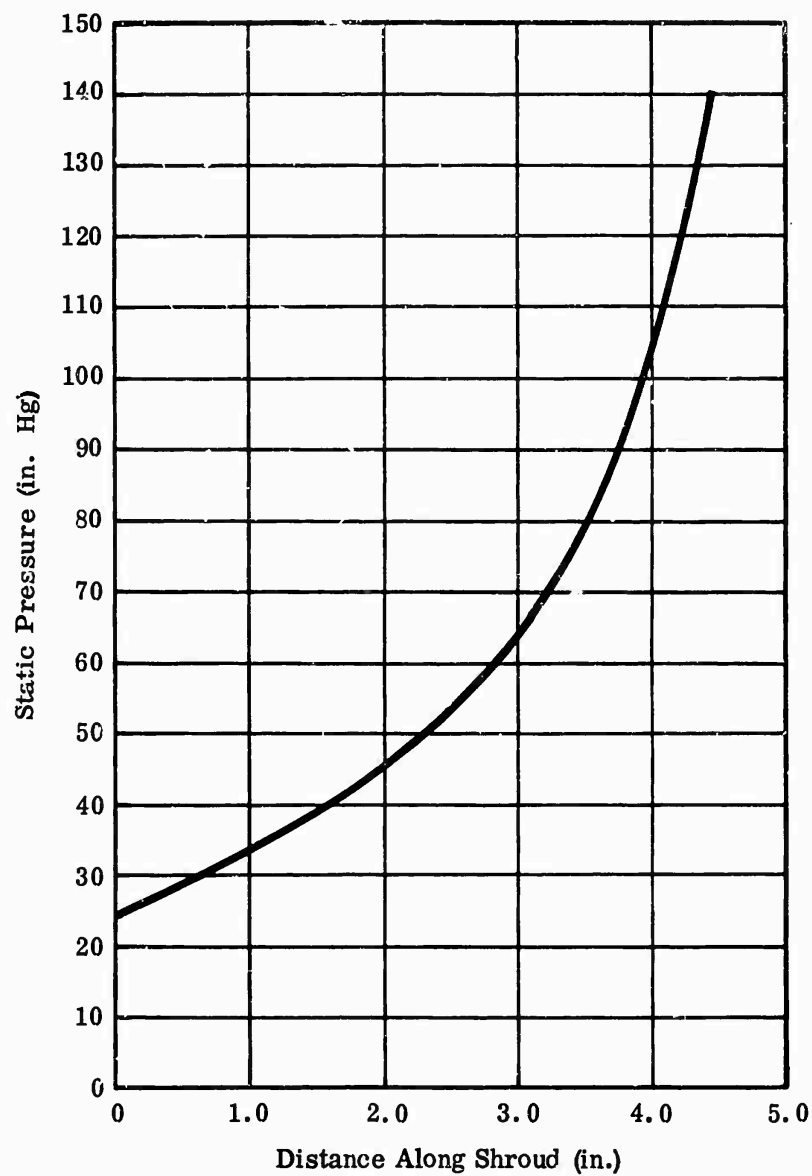


Figure 64. Predicted Static-Pressure Rise Along RF-1 Impeller Shroud; Design Speed, 57,000 rpm.

CONFIDENTIAL

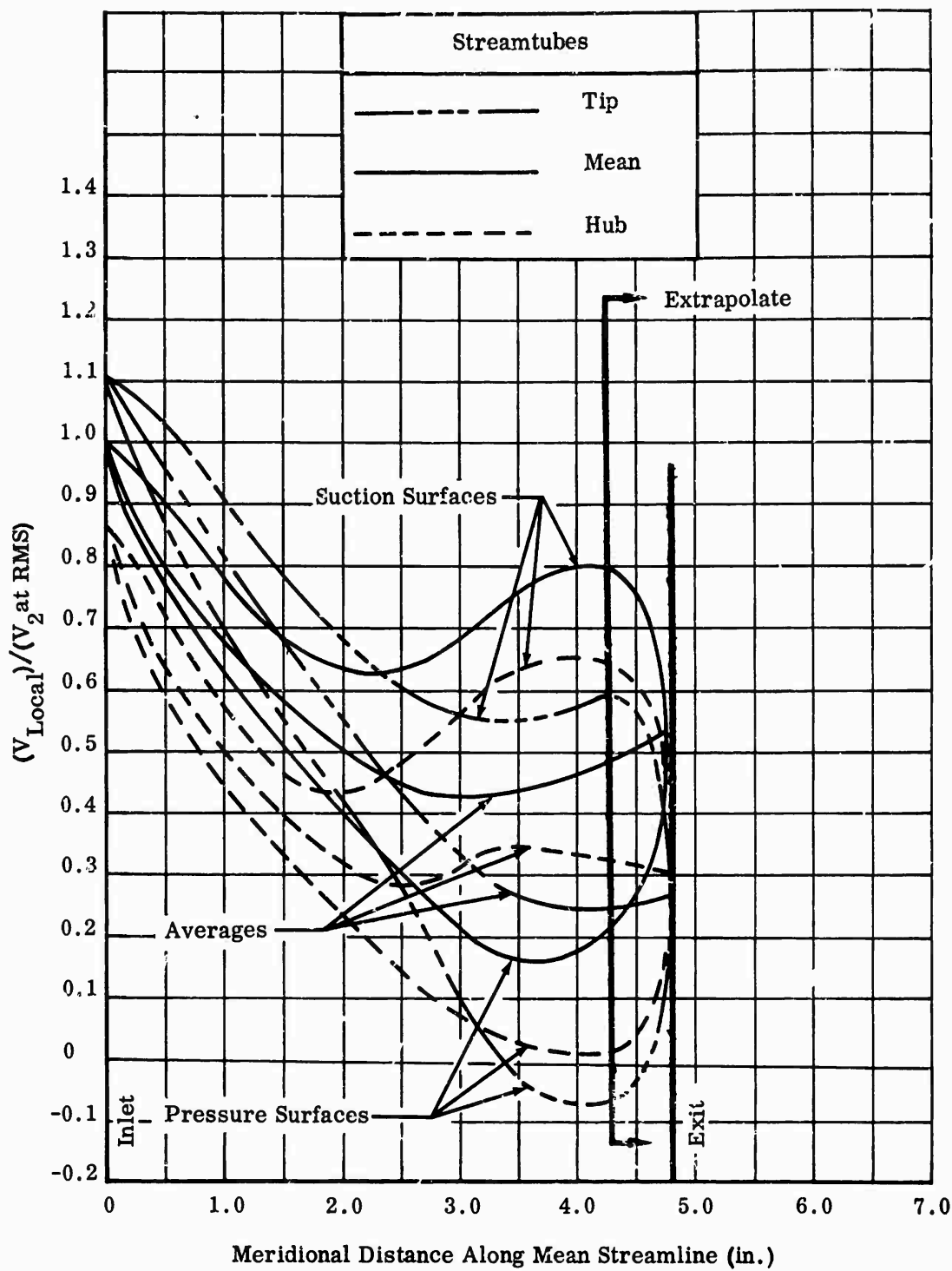


Figure 65. Blade-Surface Velocities of RF-1 Impeller; Design Speed, 57,000 rpm.

CONFIDENTIAL

CONFIDENTIAL

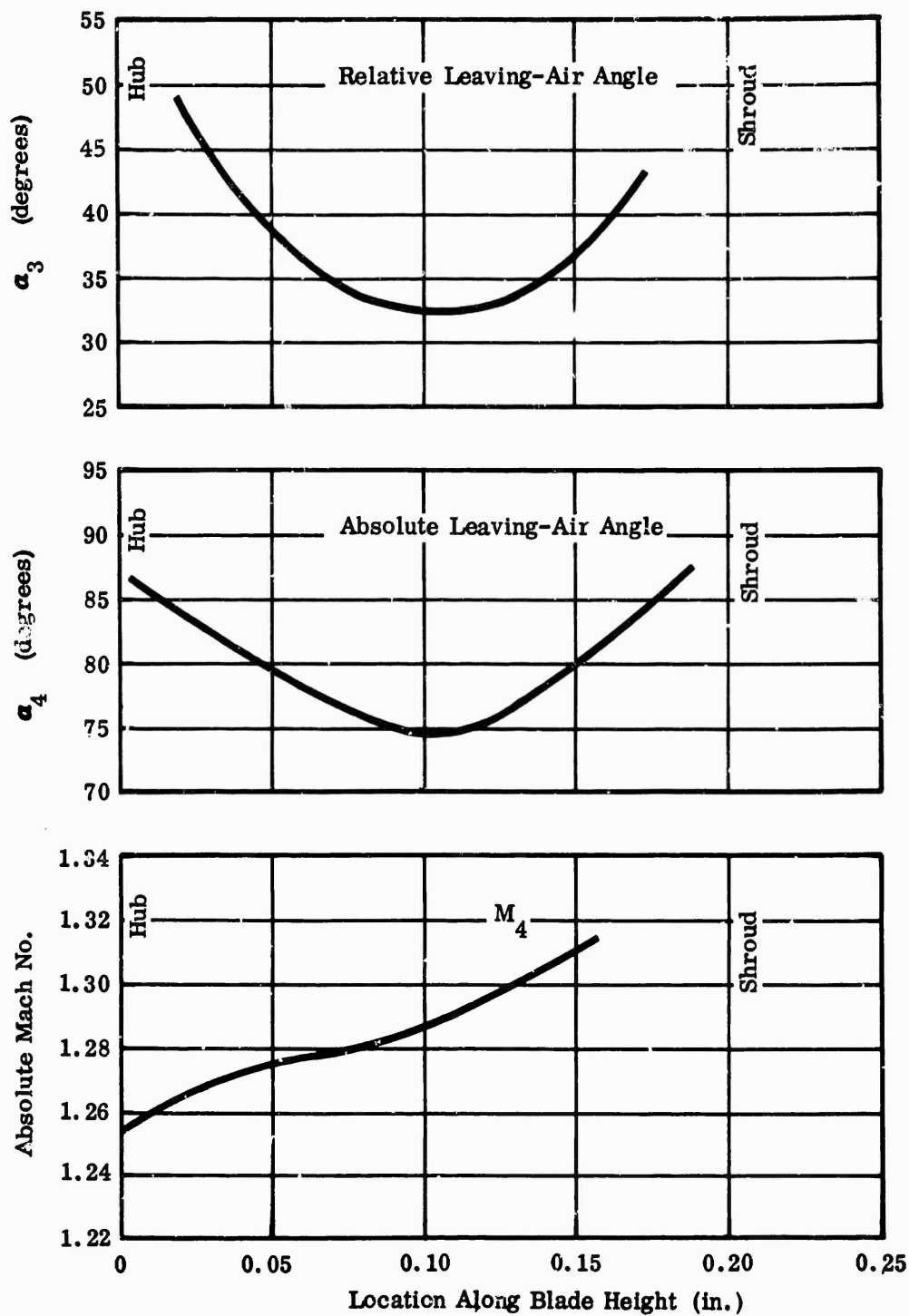


Figure 66. Exit Flow Conditions for RF-1 Impeller;
Design Speed, 57,000 rpm.

CONFIDENTIAL

CONFIDENTIAL

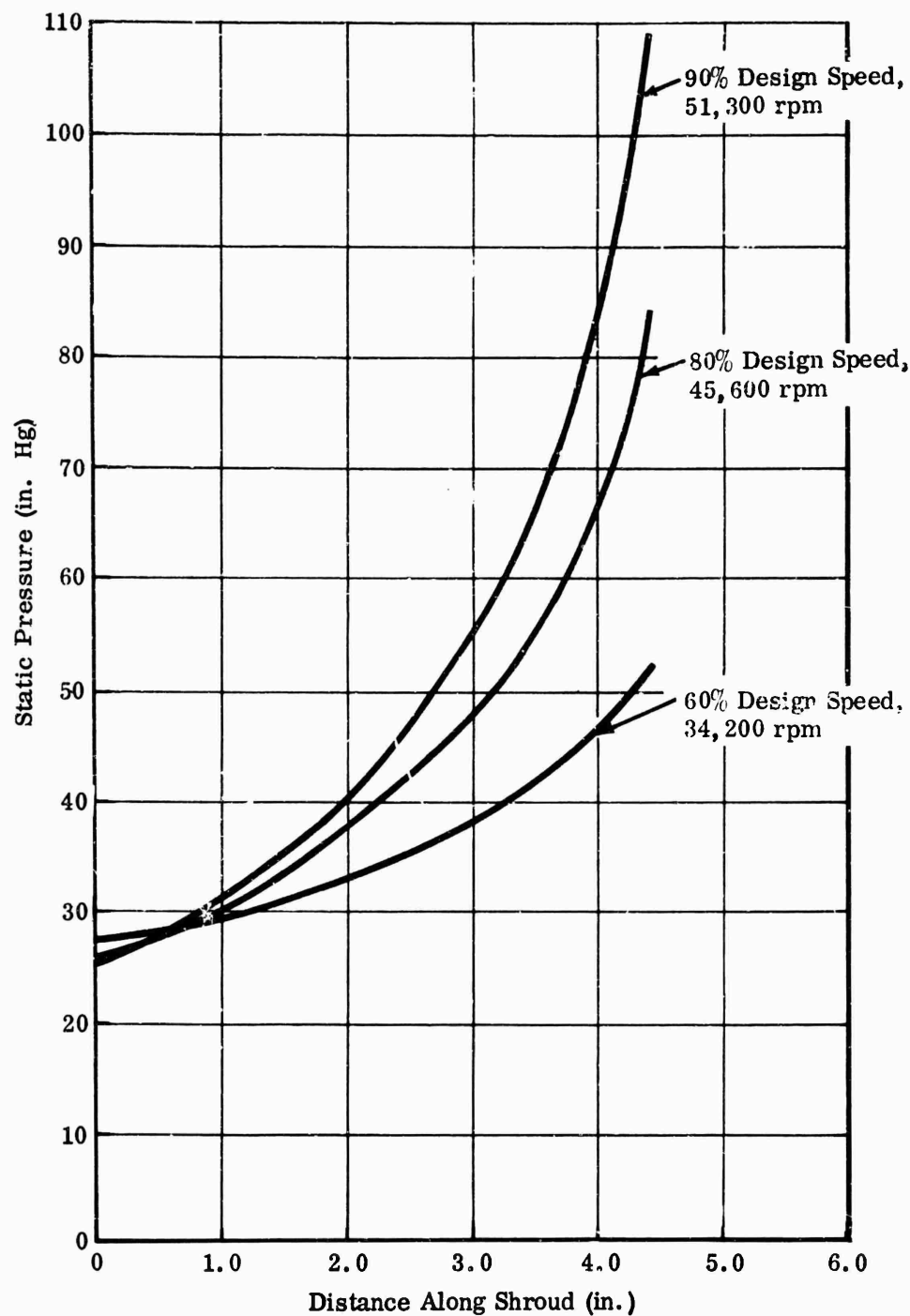


Figure 67. Predicted Static-Pressure Rise Along RF-1 Impeller Shroud, Part Speed.

CONFIDENTIAL

CONFIDENTIAL

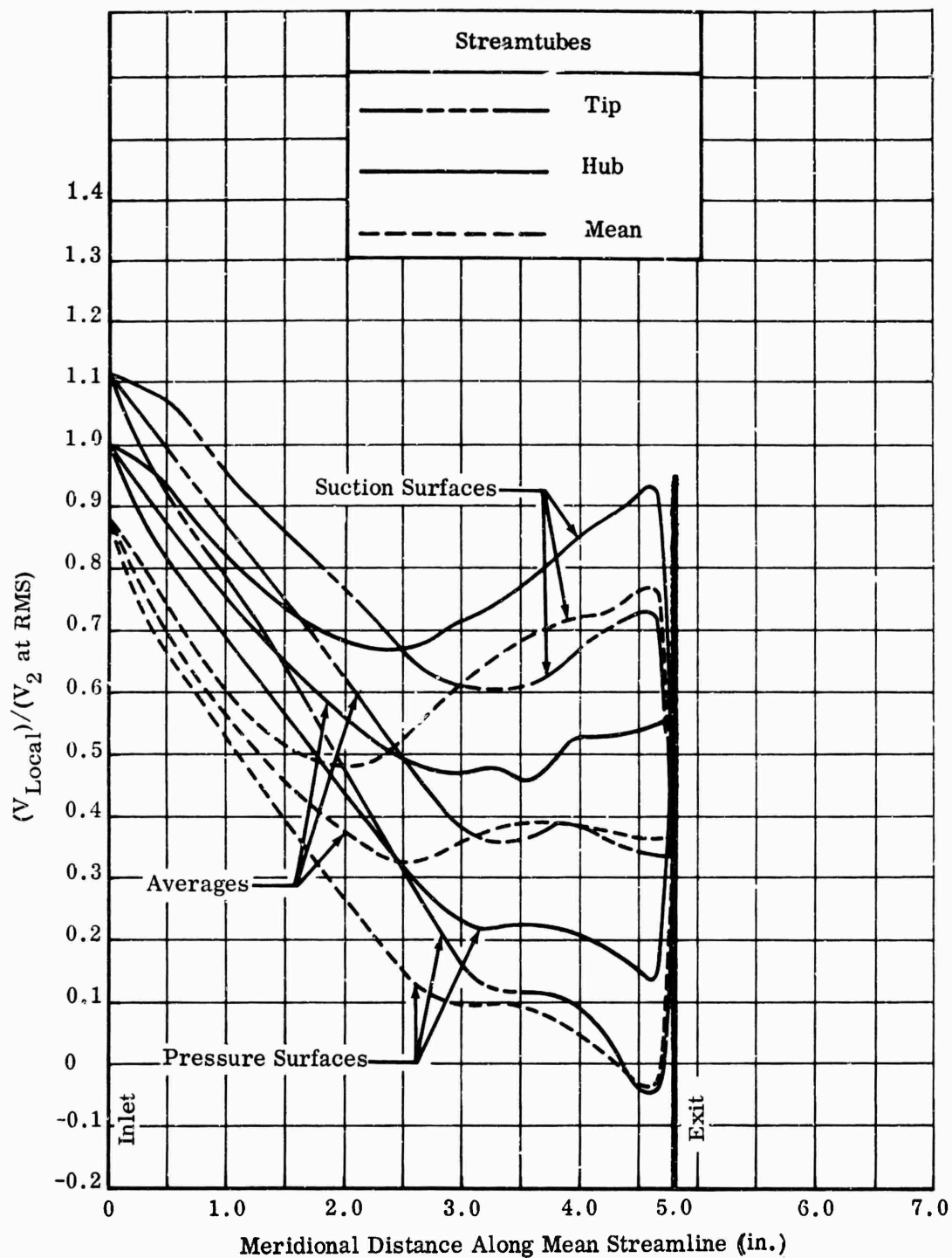


Figure 68. Blade-Surface Velocities of RF-1 Impeller;
90-Percent Design Speed, 51,300 rpm.

CONFIDENTIAL

CONFIDENTIAL

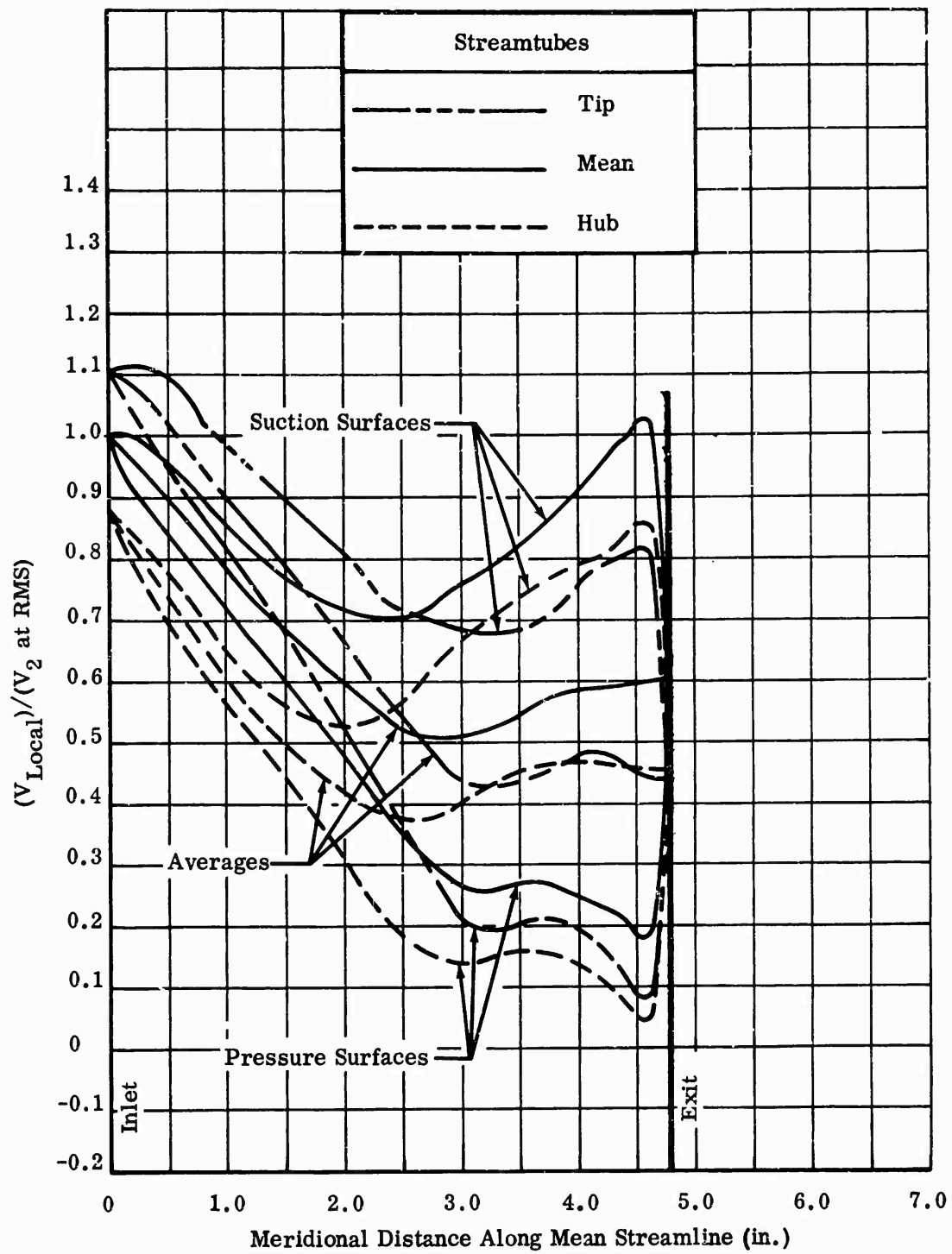


Figure 69. Blade-Surface Velocities of RF-1 Impeller;
80-Percent Design Speed, 45,600 rpm.

CONFIDENTIAL

CONFIDENTIAL

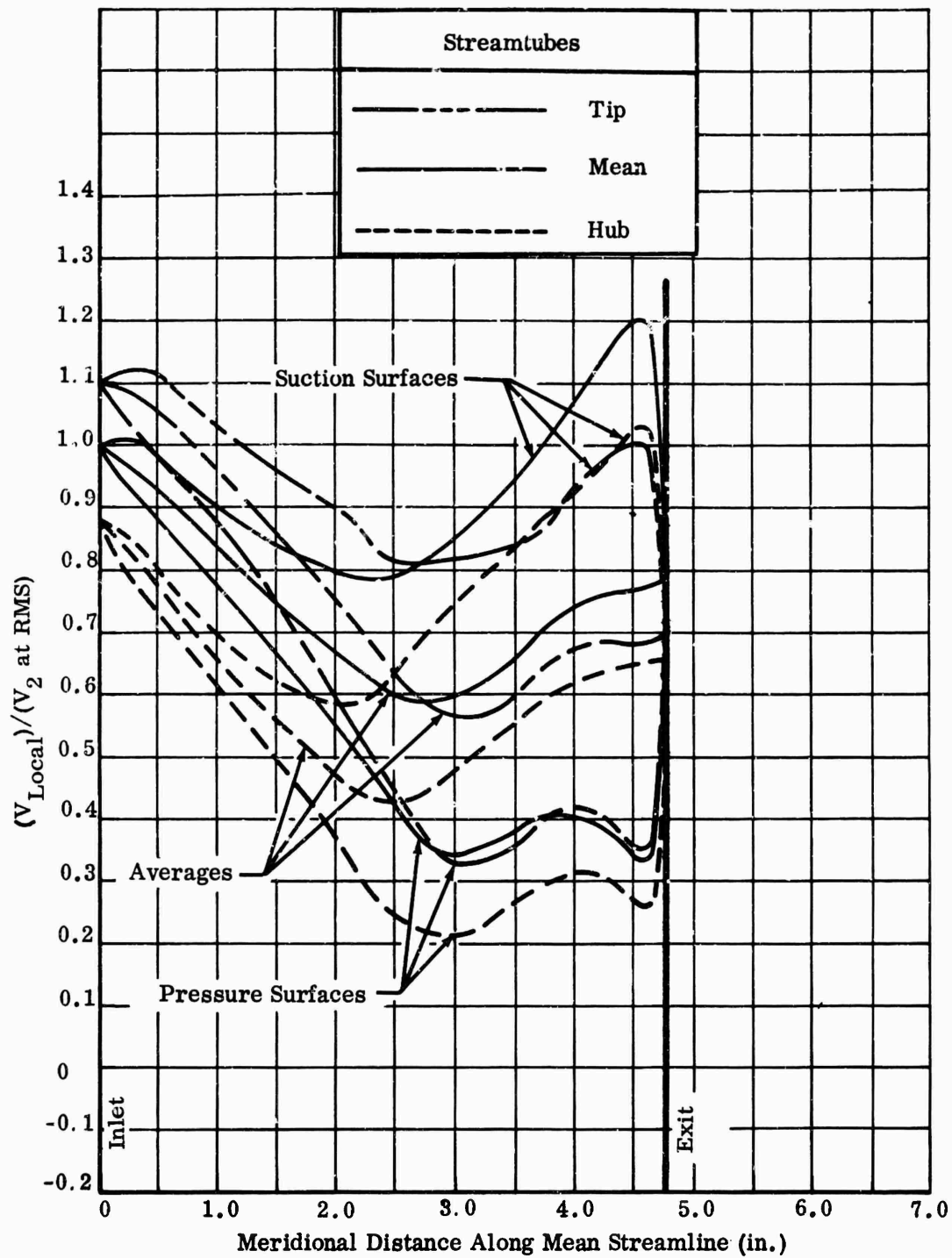


Figure 70. Blade-Surface Velocities of RF-1 Impeller;
60-Percent Design Speed, 34,200 rpm.

CONFIDENTIAL



Figure 71. MF-1 Impeller.



Figure 72. MF-2 Impeller.

CONFIDENTIAL



Figure 73. MF-3 Impeller.

CONFIDENTIAL

CONFIDENTIAL



Figure 74. RF-1 Impeller.

CONFIDENTIAL



Figure 75. Comparison of Research Impellers.

CONFIDENTIAL

2.3 DIFFUSER DESIGN

During studies conducted before the Army centrifugal-compressor research program, impeller-exit (diffuser-entrance) Mach numbers up to 1.3 were investigated, with vane-island channels being used. These vanes were characterized by a wedge-shaped leading edge followed by a concave suction surface that guides the air into a subsonic channel diffuser. Figure 75 is a photograph of several earlier channel diffusers. Occasionally, a second diffuser stage was attached to each channel to recover additional static pressure.

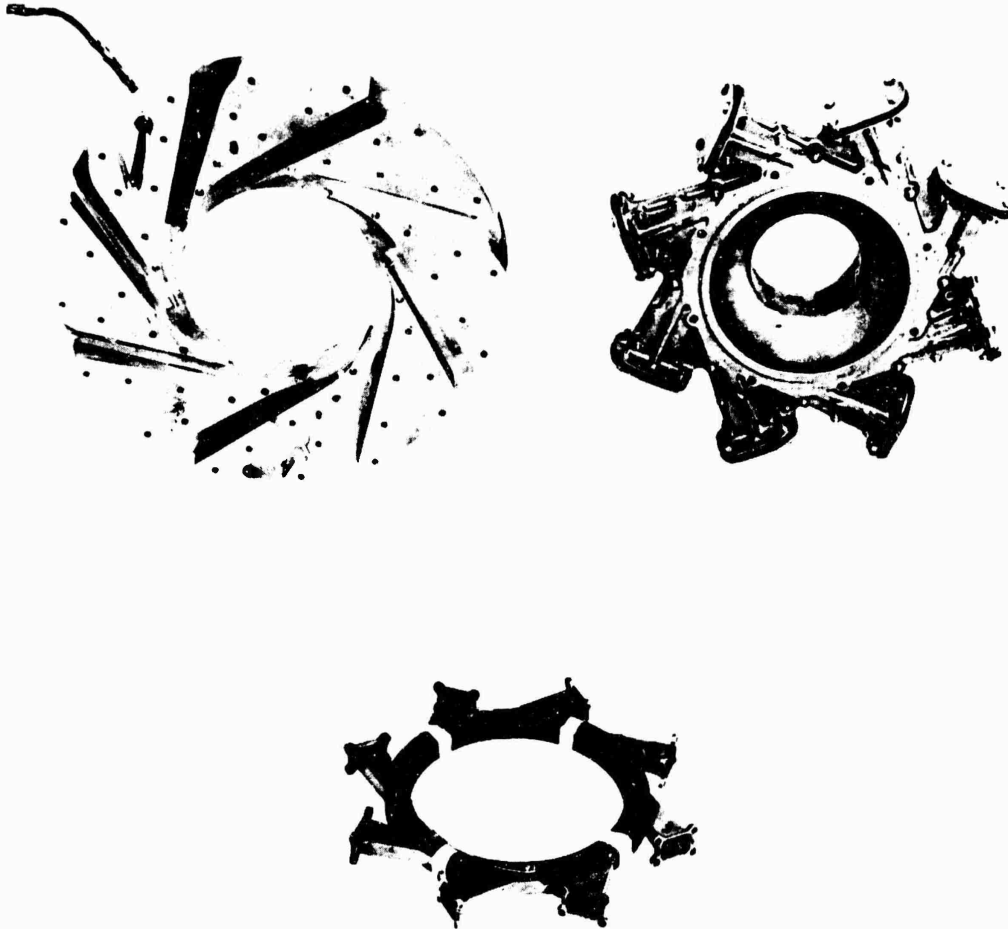


Figure 76. Contractor's Other Channel Diffusers.

CONFIDENTIAL

Because the Mach 1.3 entrance-flow condition might degrade diffuser performance, shock-system development was studied. Revisions to previous design techniques were expected to be required. To initiate these studies, shadowgraphs were taken during a research program for investigating the flow path from the impeller tip through the throat of a vane-island diffuser. This work is discussed by Stahler in Reference 6. Figure 11 (shown in Section 2.1.2 of this report) is a typical shadowgraph from that research program. Both a bow shock and a lambda shock on the vane leading edge are visible. Although this program showed that a shock system existed, the mechanics of flow through the diffuser had not been well defined. It was believed that diffuser performance would be improved by a better understanding of the flow process.

To achieve these higher pressure ratios, the plan for the Army diffuser design development was to study vane-island types, first, and to use current design techniques. In addition, the suitability of cascade vanes for this application was investigated. Several vane-island diffusers were designed and tested to provide comparative data and information for selecting the diameter ratio and throat Mach number for best overall performance. Other objectives were to establish criteria for selecting the number of vanes and to evaluate a variable-airflow concept in which the channel throat areas were adjusted by moving the vanes in a radial plane. At the completion of the basic tests and analyses, it was planned that a final set of diffusers be designed to reach the program performance target by applying knowledge from the first test series.

2.3.1 PARAMETRIC ANALYSIS AND WATER-TABLE STUDIES

The parametric study of the diffusers was made in conjunction with the impeller parametric study (i.e., impeller performance predictions were used to determine recovery requirements for the diffusers). As described in Section 2.2 of this report, an impeller pressure ratio of about 13:1 was required to achieve an overall compressor pressure ratio of 10:1. The required diffuser performance was calculated as total-pressure recovery for each impeller point studied. The required recovery was based on a diffuser discharge Mach number of about 0.10, so that:

$$\text{Total-pressure recovery} = \frac{\text{Total pressure in collector (at } M \approx 0.10)}{\text{Total pressure at impeller tip}} \quad (13)$$

Figure 77 shows the required diffuser total-pressure recovery for the impellers under consideration. This figure shows that the highest recovery is necessary with the smallest impeller. The previously demonstrated performance level of the contractor's diffusers is also given in Figure 77, which shows the improvement necessary to meet the overall compressor performance goals. To provide new information, it was planned that the research include a complete mapping of

CONFIDENTIAL

CONFIDENTIAL

the critical flow field between the impeller tip and the diverging section of the channel by pressure surveys, schlieren studies, and water-table analogies.

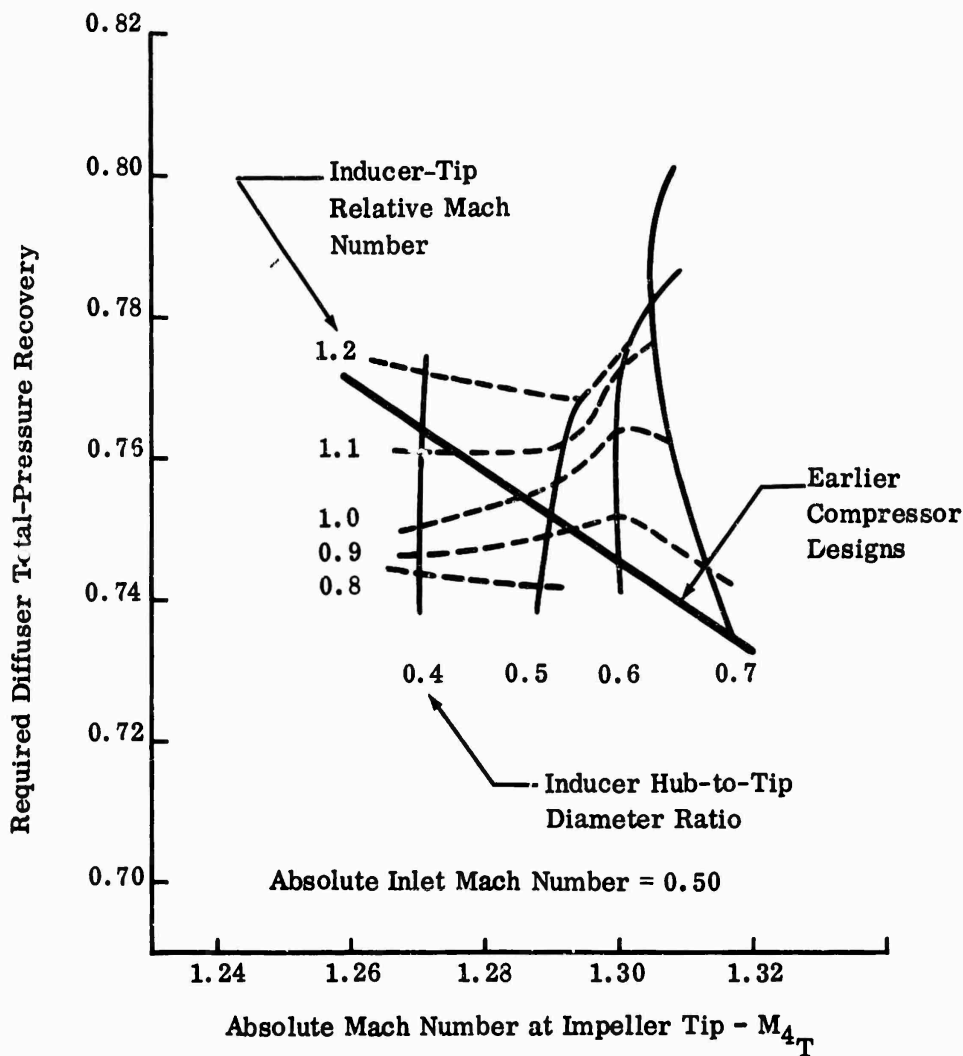


Figure 77. Required Diffuser Recovery (Impeller Tip to Collector).

Preliminary Studies

To predict pressure losses in diffuser channels, 1-dimensional parametric studies were based on the work reported by Patterson (Reference 7) and Henry (Reference 8). The Patterson report discusses the losses attributed to various diffusion rates, and the report by Henry describes duct pressure-loss characteristics. Studies of channel inlet Mach numbers of from 0.50 to 0.90 were

CONFIDENTIAL

conducted. The results for an entrance Mach number of 0.80 are presented in Figure 78. Mach 0.80 was selected for study because it represented the highest value for which consistent data was available. This figure shows the relationship between area ratio and total-pressure recovery for several channel divergence angles. It was assumed in the analysis that no separation occurred in the channel and that flow distribution across the channel was uniform. The total-pressure recovery shown in Figure 78 includes a sudden dump loss at the diffuser exit, obtained by assuming that one-half of the remaining dynamic pressure head is lost. This assumption has been used in previous diffuser designs and is considered to be common practice for low Mach numbers.

Water-Table Studies of Vane-Island Configurations

Detailed investigation of flow phenomena in diffusers was essential in achieving the high-pressure, high-efficiency, centrifugal-compressor research objectives. The preliminary investigation of flow in both vane-island and cascade-diffuser configurations was accomplished through water-table visualization. The water-table analogies provided an inexpensive and rapid method of conducting preliminary design surveys of diffusers; the analogies were expected to show the configurations that warranted further evaluation in the compressor test rigs. However, because this method of evaluating diffusers for high-pressure-ratio centrifugal compressors was new and was attempted before the compressor rig tests, specific conclusions about diffuser flow characteristics could not be established. Therefore, some of the following discussion presents only observations.

The water table is an apparatus designed to simulate two-dimensional diffuser flow conditions. Water-table analysis is based on hydraulic analogy of Mach number to Froude number and on gas density to water depth. Mach number (M) is the ratio of gas velocity to the local speed of sound, and Froude number (F) is the ratio of water-flow rate to the speed of wave propagation. Water-flow conditions analogous to subsonic gas and supersonic gas flow are termed subcritical and supercritical flow. A flow discontinuity occurs in water at $F = 1.0$ which is analogous to a shock wave in a gas and is termed a hydraulic jump. For compressible gases, density can vary along a streamline as a function of velocity; for an incompressible liquid, the analogous condition is a variation in depth as a function of flow rate.

As discussed by Shapiro in Reference 9, the hydraulic analogy is theoretically correct for a gas with a specific heat ratio of 2. However, a good approximation between water flow and gas flow can be obtained for a gas specific heat ratio of 1.4, if the hydraulic analogy is restricted to Mach number and density. Laitone (Reference 10) indicated that the hydraulic analogy was valid for simulating subsonic and supersonic gas flow to approximately Mach 1.5. Above Mach 1.5 the energy loss across the shock (or hydraulic jump) degrades the validity of the analogy.

CONFIDENTIAL

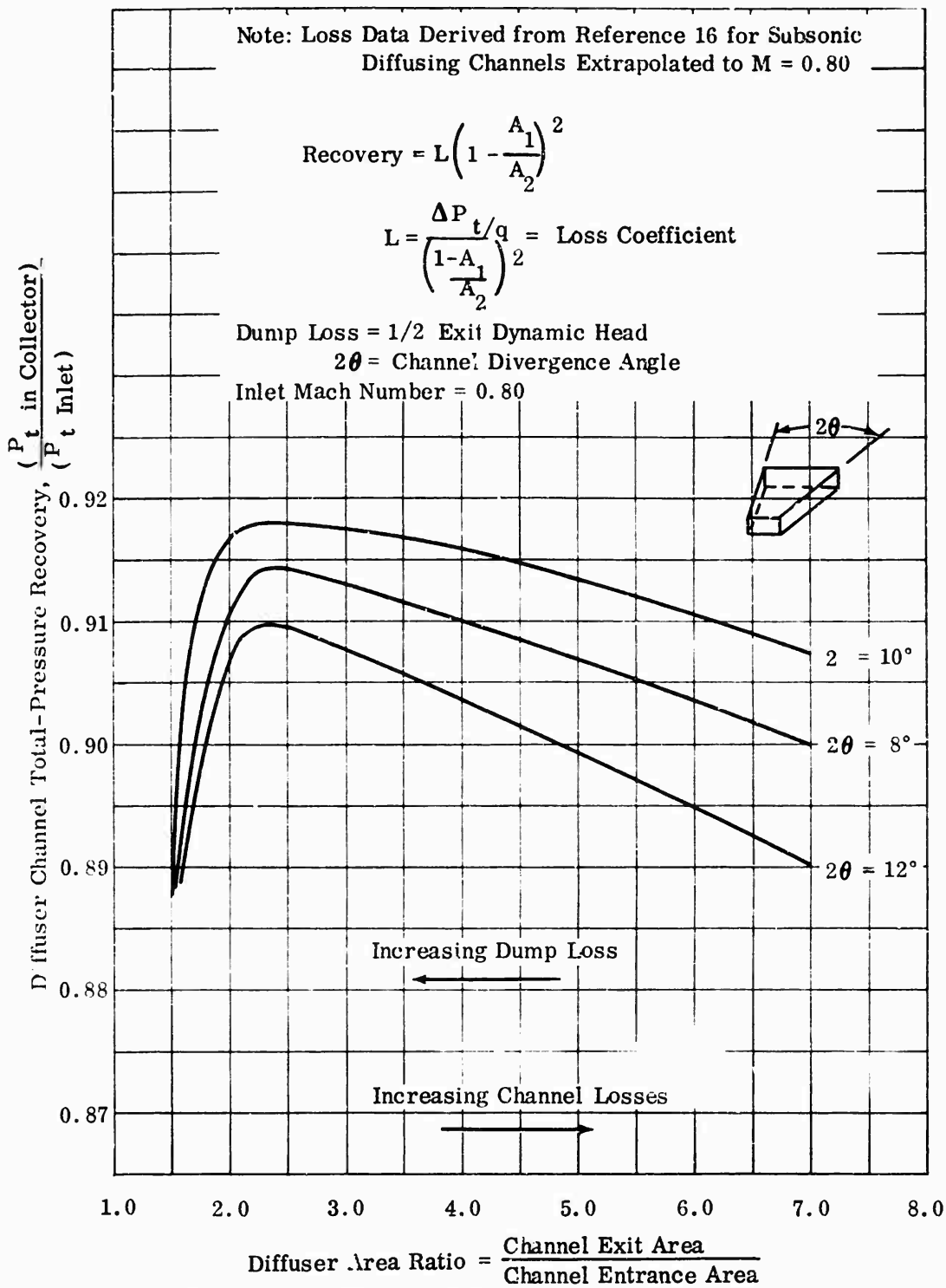


Figure 78. Diffuser Channel Total-Pressure Recovery Versus Area Ratio.

CONFIDENTIAL

Figure 79 is a sketch of the water table, and Figure 80 is a photograph of the table with a set of diffuser vanes installed. Water is pumped from the reservoir through a set of straightening tubes and flows radially outward from the center of the table across the glass tabletop. The plate shown in Figure 79 directs water flow in the radial direction and acts as a valve to regulate water height and water velocity entering the table. The flow rate can also be varied with a bypass valve, which controls pump pressure. The outside diameter of the glass tabletop has an adjustable weir to simulate back pressure on the table. Rotating screens are used to transmit a uniform tangential component to the radial flow over the full depth. The screen drive is equipped with a variable-speed motor for adjusting the tangential velocity, as desired to simulate impeller speed. The tangential flow screen is shown in Figure 80. A camera was used to record shadowgraphs and streamline traces from dye injection.

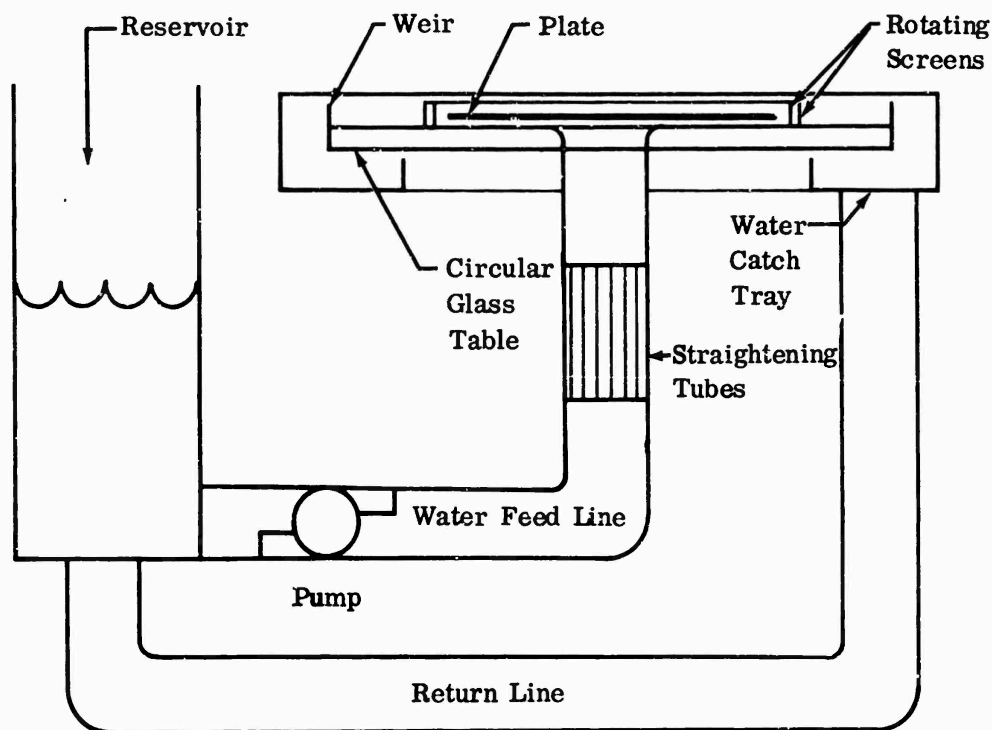


Figure 79. Circular Water Table.

CONFIDENTIAL

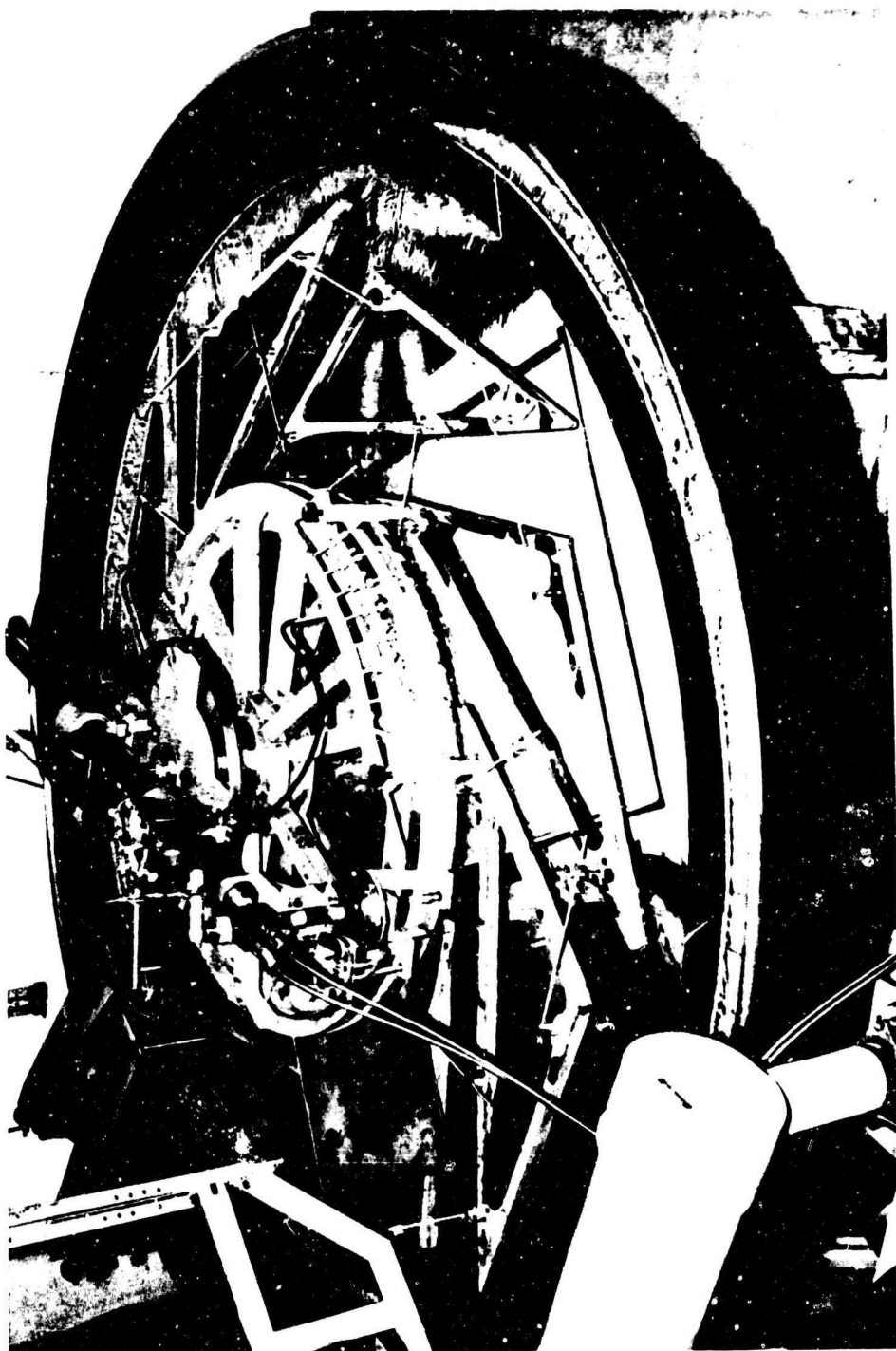


Figure 80. Water-Table Facility.

CONFIDENTIAL

CONFIDENTIAL

The water table was equipped with a light source and frosted glass to produce the shadowgraph. Dye for streamline visualization and for detecting separation was injected with hypodermic syringes. Figure 81 shows the apparatus used to inject dye circumferentially at 7 points near the rotating screen. The rake was adjustable along its radius. Changes in surface height and flow angle were measured with micrometers and yaw probes mounted on a traversing arm (see Figure 82). By adding particles to the water surface (aluminum powder demonstrated the best results), stream-direction and water-surface-height changes could be observed and photographed simultaneously.

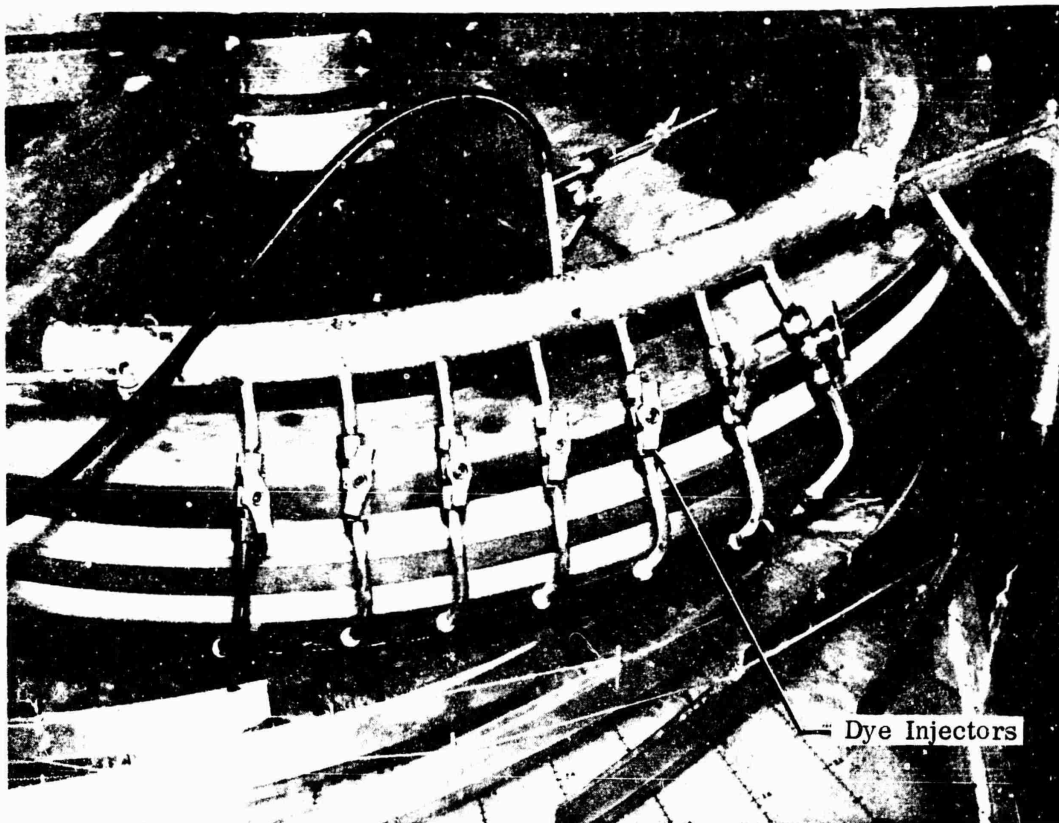


Figure 81. Dye-Injection Apparatus.

CONFIDENTIAL

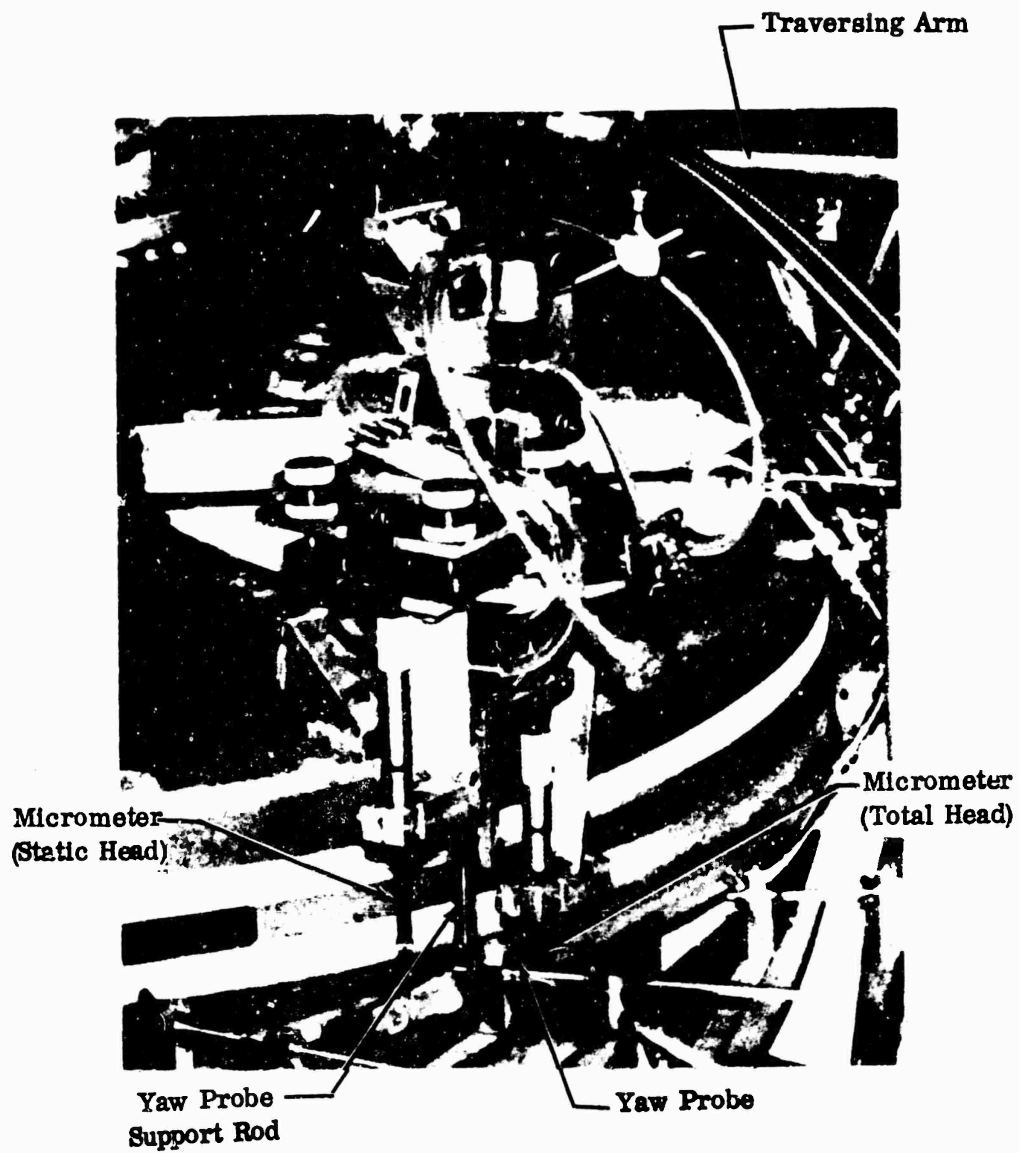


Figure 82. Yaw Probe Traversing-Arm Installation.

CONFIDENTIAL

CONFIDENTIAL

Specific objectives of the studies were to determine:

- 1) Effect of vane-island wedge angle;
- 2) Effect of number of vane-island channels;
- 3) Comparison between vane-island and cascade diffusers.

For these investigations, 6 different tests were planned. The model designations, configurations, and test conditions are summarized in Table IV.

TABLE IV				
WATER-TABLE DIFFUSER MODELS				
Diffuser	Type	Number of Passages	Design Mach Number at Vane Leading Edge	Vane-Tip Wedge Angle (degrees)
1I8	island	8	1.12	12
2I8	island	8	1.12	5
2I16	island	16	1.12	5
2I24	island	24	1.12	5
4C64	cascade	Short flat plates to be used with any of the above		
5C24	cascade	24	1.12	-
Double circular arc blades of mean solidity = 2.26				
Design parameters common to all models:				
1) Scale: 6.31 times full size;				
2) Vane-tip radius ratio = 1.08;				
3) Angle to vane tip underside = 75 degrees;				
4) Equivalent included angle = 7 degrees.				

Water-table conditions were the same for all 6 tests, and nominal water depth of 0.5 inch was used. This depth was shallow enough for vertical accelerations to be considered negligible. For all vane-island configurations tested, a suction-surface tip angle of 75 degrees was used. Water-flow rate and speed of the rotating screen were adjusted to match this flow direction. The models were scaled about 6.31 times larger than the compressor test rig.

CONFIDENTIAL

Data on the 4 vane-island configurations is plotted in Figures 83 through 86. Each figure shows separate plots of (1) Froude number, (2) water height, and (3) flow angle.

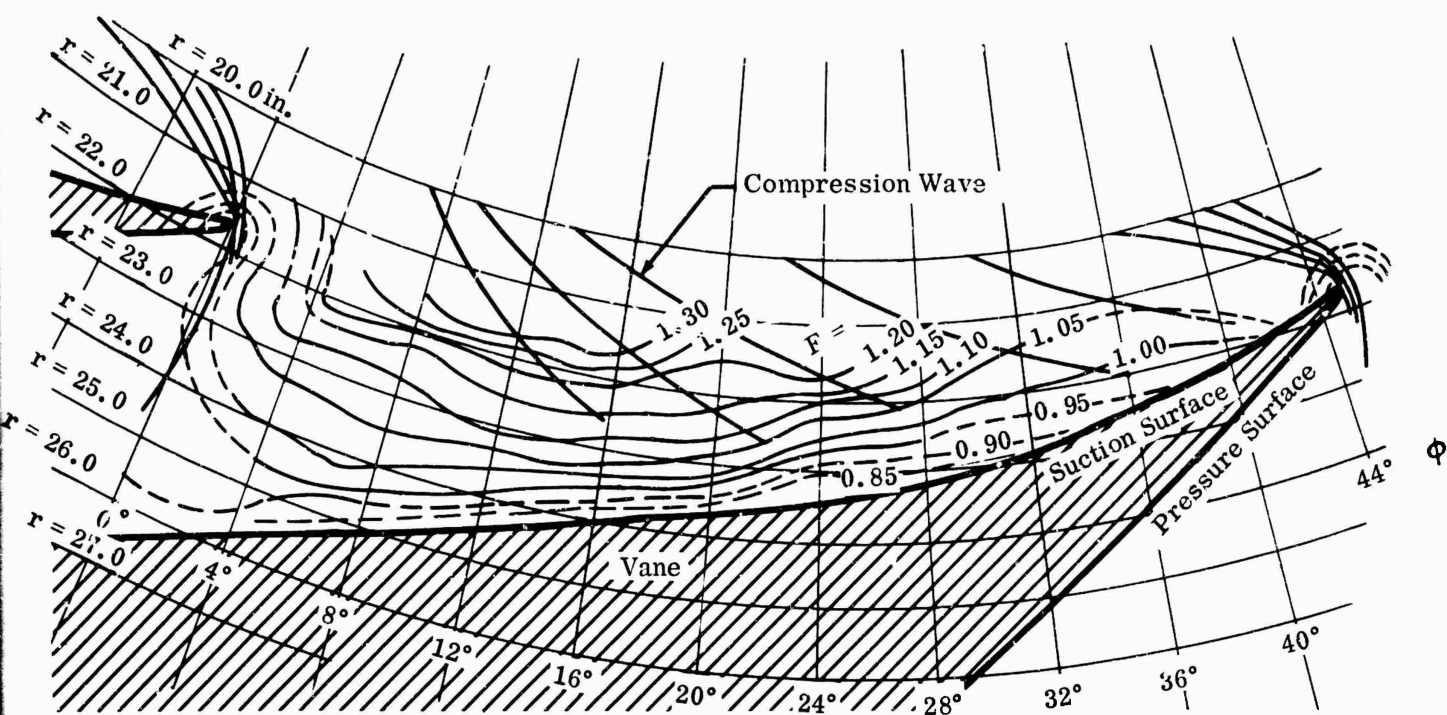
Configuration 118 — To establish a basis for comparing the 4 vane-island configurations and test results, a detailed analysis of the flow characteristics of the first test configuration, 118, is presented. This configuration was designed with a 12-degree vane-island-tip wedge angle. The throat walls were parallel for 1 inch of the diffuser passage; the walls then diverged at an included passage angle of 7 degrees. This configuration consisted of eight vane islands. The impeller-tip Mach number for the first test was 1.3, and the flow angle was expected to equal the suction-surface angle of 75 degrees. However, the observed Mach number and flow angle revealed hydraulic choking of the diffuser throat. With choked-flow conditions (i.e., flow limited), the resultant of the radial and tangential velocity vectors yielded a flow angle greater than the expected 75 degrees. In addition, a nonuniform, circumferential flow-angle distribution was observed which resulted from the Mach wave system at the vane tip and vane suction surface. This wave system was caused by the curve-wall (suction-surface) constraint on the supersonic flow path in the vaneless and semivaneless space.

This initial test of Configuration 118 illustrated the complexity of the continuity-wave system and the interaction of flow conditions in the vaneless and semivaneless spaces. This interaction was studied further in the diffuser test rig.

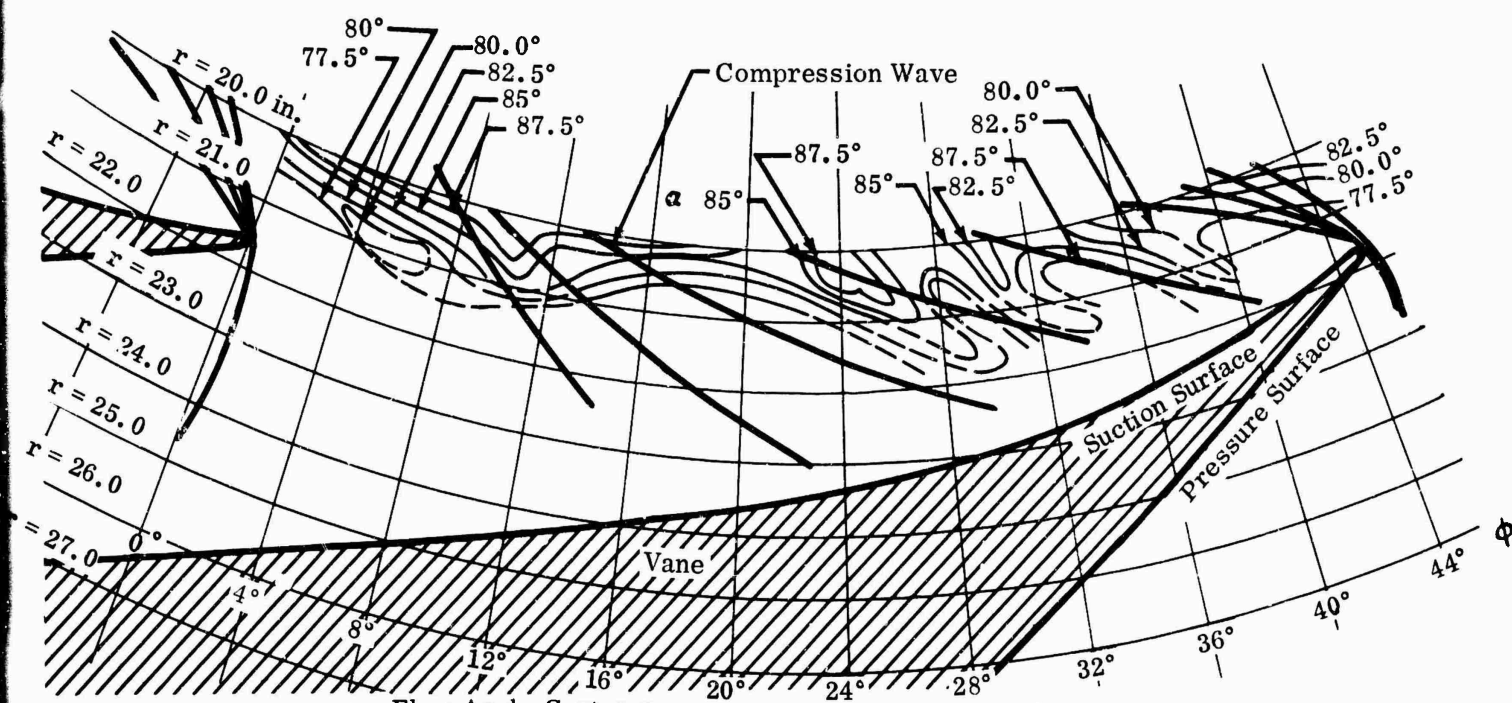
Figure 83 shows Froude number contours, height (density) contours, and flow-angle contours for Configuration 118. These curves were made using the water-table measurements and shadowgraph data. The tip-wave system is characterized by a series of expansion waves around the suction side of the vane leading edge that extends to the impeller tip. These waves are related to the adjustment and alignment of flow with the suction-surface angle of 75 degrees. An oblique shock wave was observed about 1.5 inches from the leading edge of the vanes. This shock results from supersonic flow along the concave suction surface; the influence of the vanes causes deceleration at the tip region to near sonic velocity. A second shock occurs 1.5 to 2 inches further along the flow path. This shock turns the flow into the channel along the concave suction surface and produces deceleration. This oblique shock pattern, followed by moderate expansion, is repeated to the throat; however, the waves become progressively weaker. The water-table visualization does not indicate whether the tip-expansion-wave system is preceded by a weak bow-shock wave. Water-depth measurements in the vaneless space were required to determine if a bow shock existed, but instrumentation was not available for such measurements.

A definite shock exists off the pressure side of the throat entrance. This shock (called passage shock) does not extend completely across the passage, because,

CONFIDENTIAL

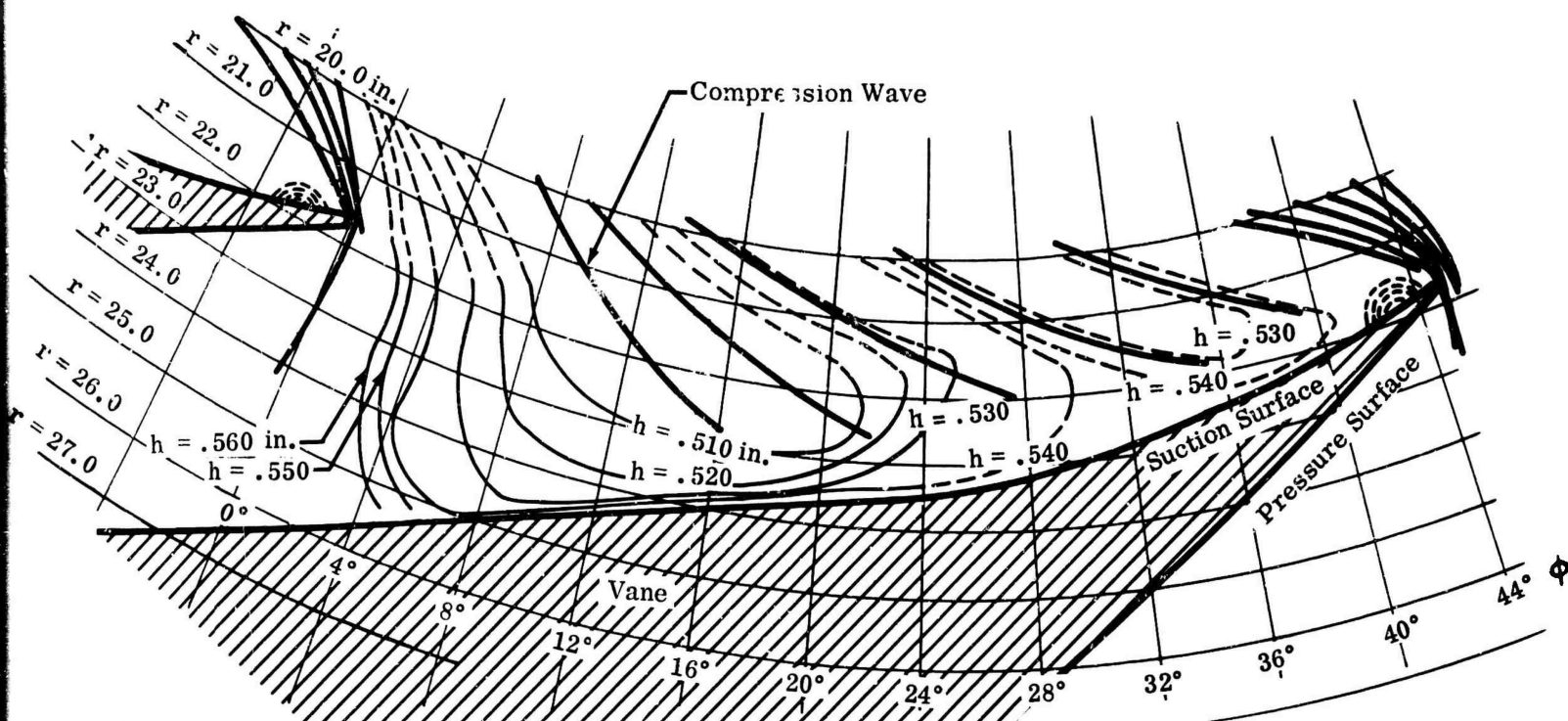


a. Froude-Number Contours.



c. Flow-Angle Contours.

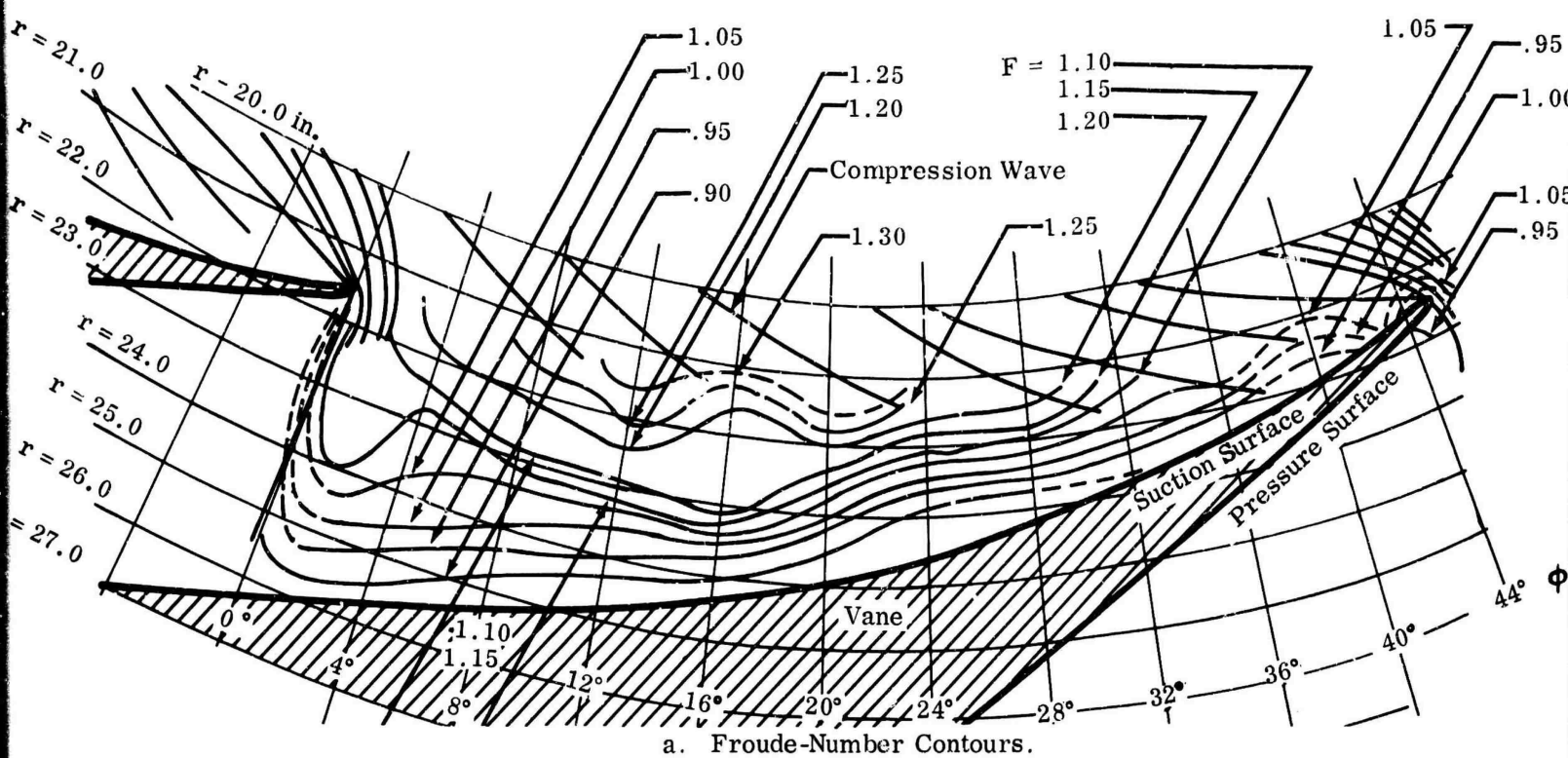
Figure 83. Water-Table Data on 118 Vane-Island Configuration.



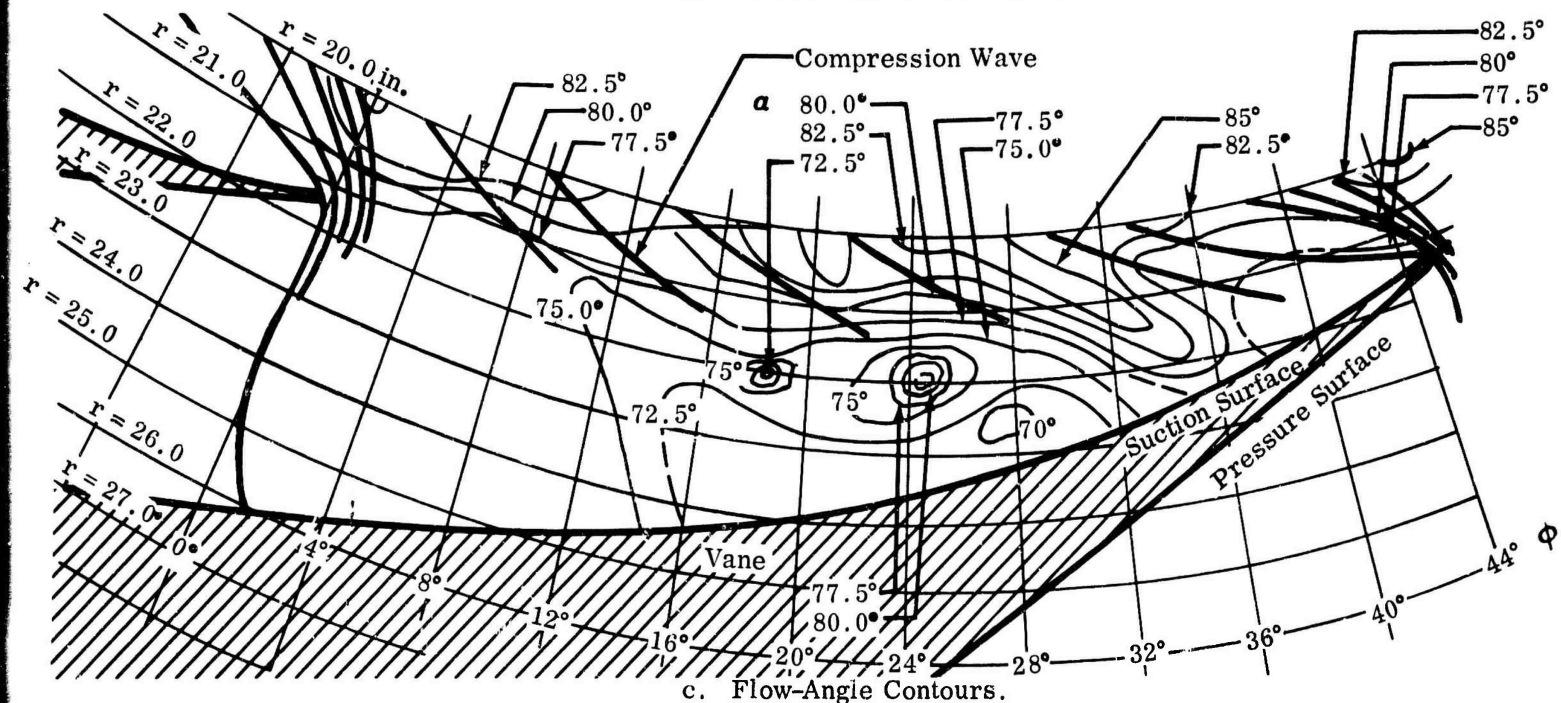
b. Water-Height Contours.

- Notes:
1. r radii (inches)
 2. α flow angle referenced to radial line (degrees)
 3. Froude contours (dimensionless)
 4. Water-height contours (inches)
 5. Flow-angle contours (degrees)

CONFIDENTIAL



a. Froude-Number Contours.



c. Flow-Angle Contours.

Figure 84. Water-Table Data on 2I8 Vane-Island Configuration.

CONFIDENTIAL

CONFIDENTIAL

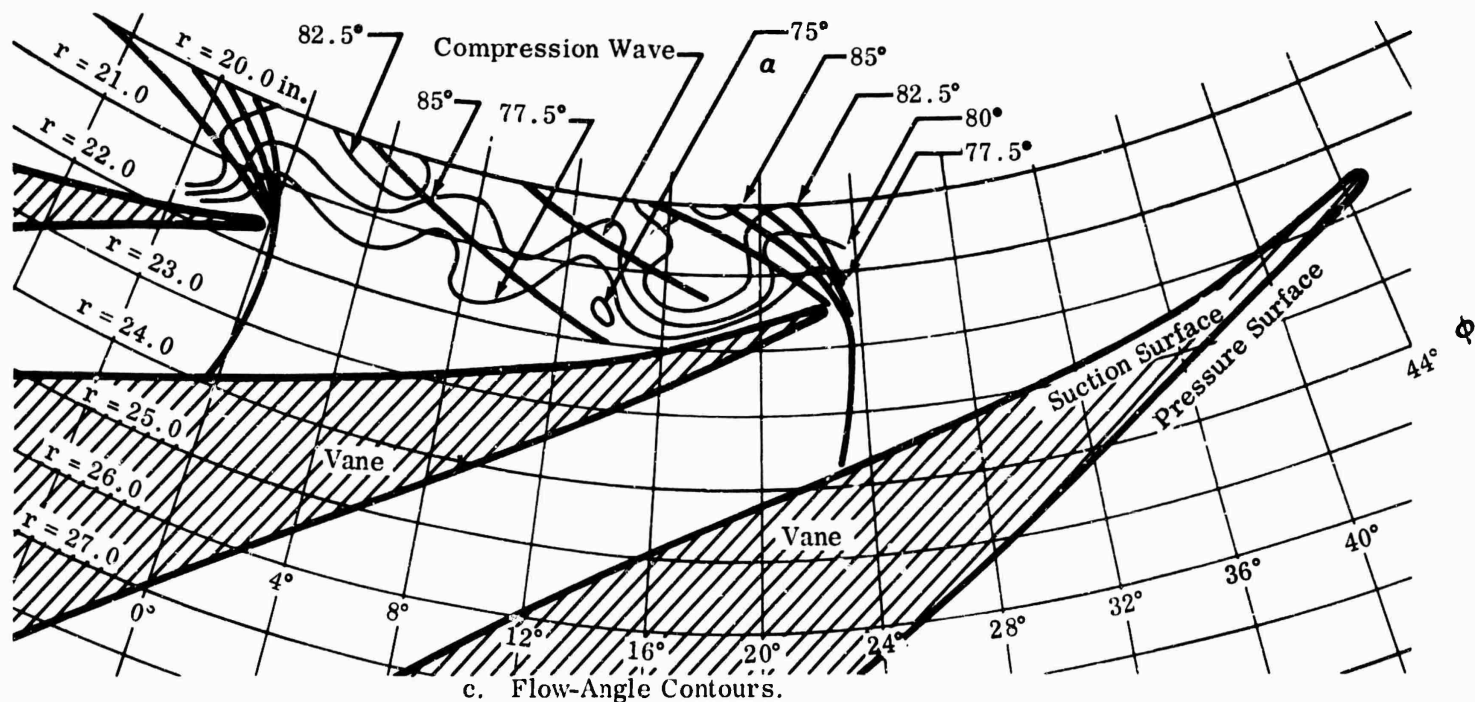
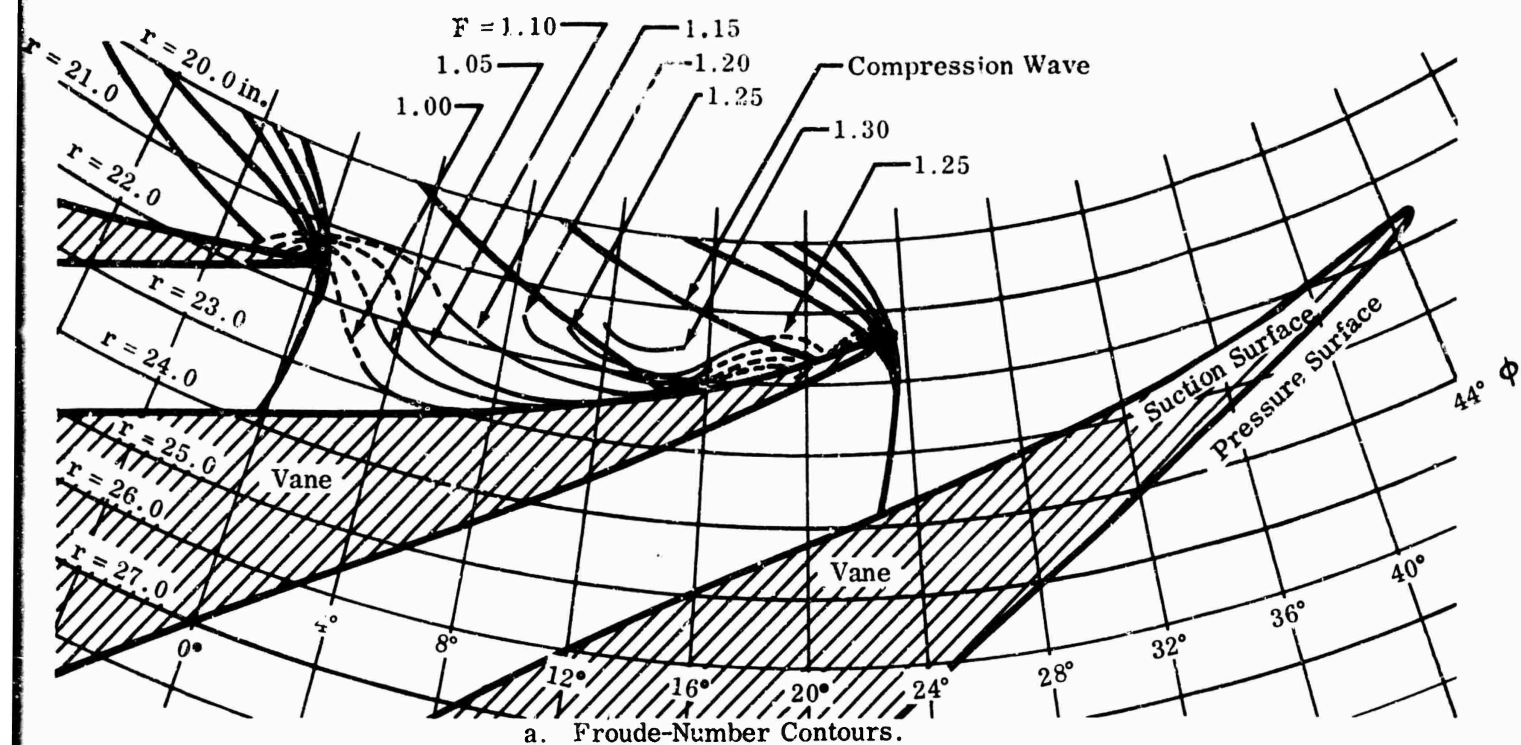
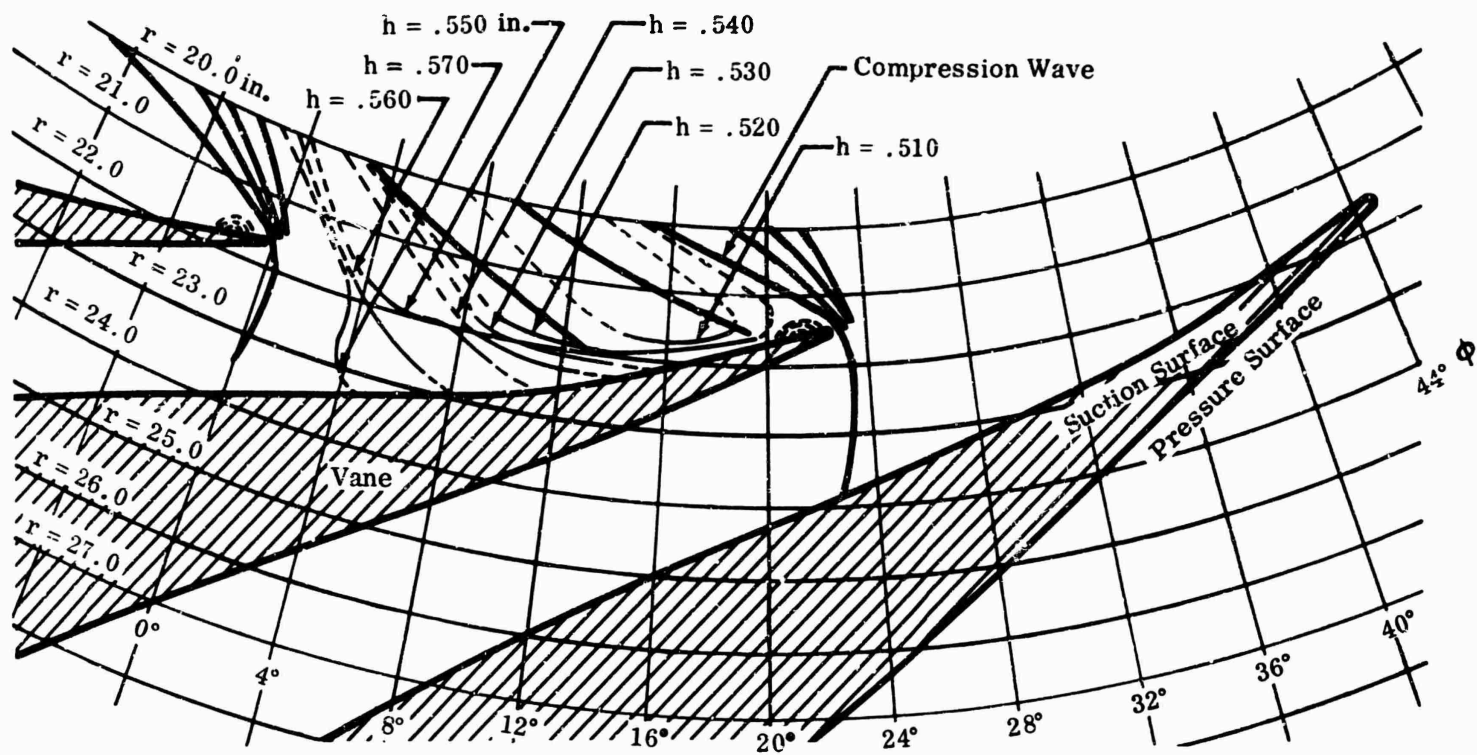


Figure 85. Water-Table Data on 2I16 Vane-Island Configuration.

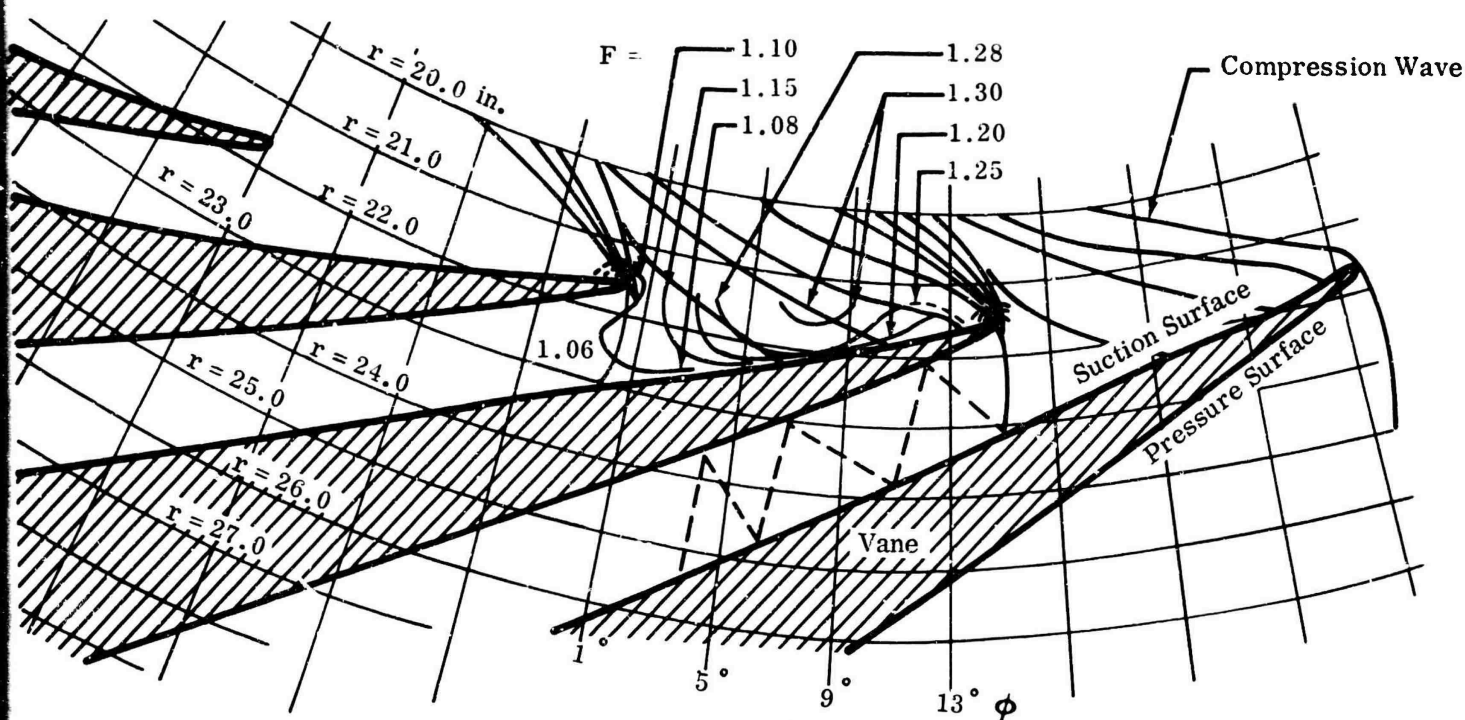
CONFIDENTIAL



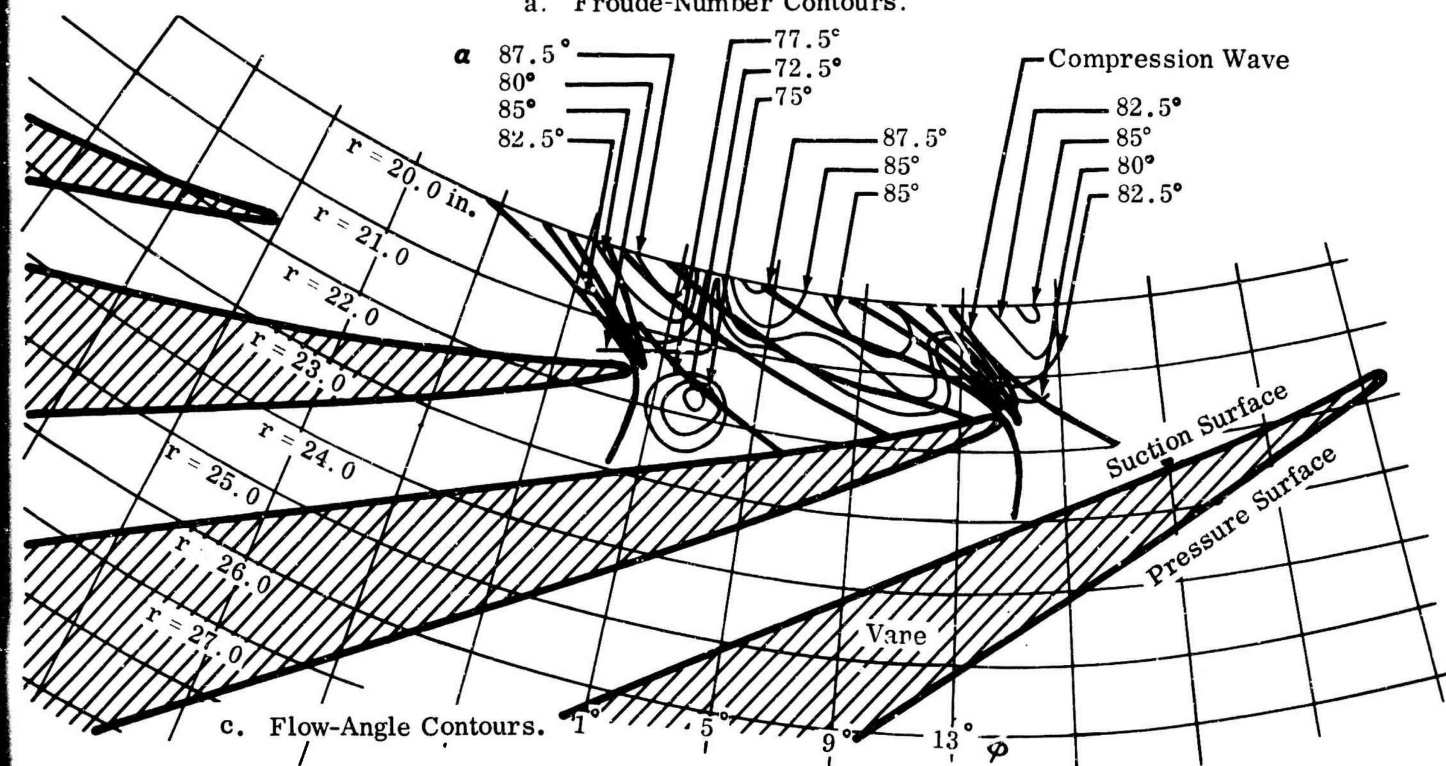
b. Water-Height Contours.

- Notes:
1. r radii (inches)
 2. α flow angle referenced to radial line (degrees)
 3. Froude contours (dimensionless)
 4. Water-height contours (inches)
 5. Flow-angle contours (degrees)

CONFIDENTIAL



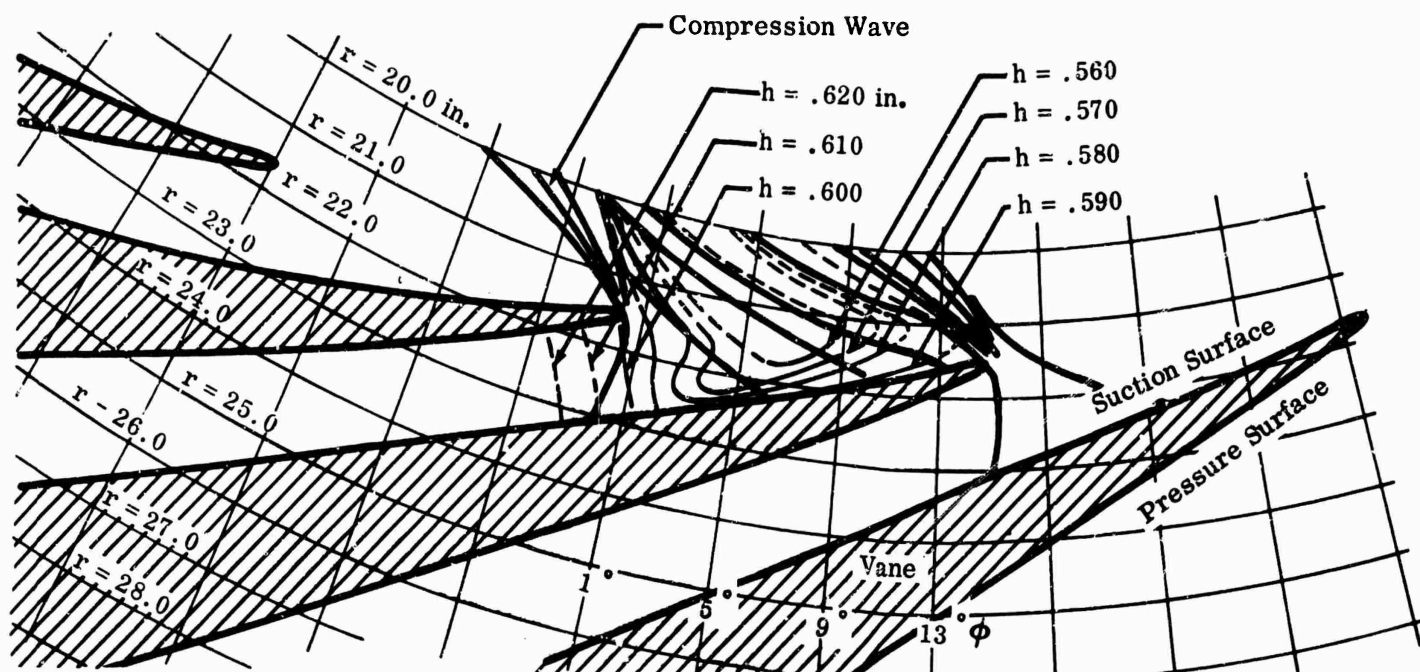
a. Froude-Number Contours.



c. Flow-Angle Contours.

Figure 86. Water-Table Data on 2I24 Vane-Island Configuration.

CONFIDENTIAL



b. Water-Height Contours.

- Notes:
1. r radii (inches)
 2. α flow angle referenced to radial line (degrees)
 3. Froude contours (dimensionless)
 4. Water-height contours (inches)
 5. Flow-angle contours (degrees)

CONFIDENTIAL

as shown in Figure 83, the flow is subsonic near the suction contour. Figure 83a shows the Froude number contours, which indicate a high Mach number area located about one-third of the way across the passage downstream from the vane leading edge.

Further evidence of nonuniform flow distribution was shown by the flow-angle contours. At $\phi = 15$ degrees, the contours showed a nearly linear gradient in Mach number across the semivaneless space — that part of the semivaneless space was subsonic. At $\phi = 0$ degree, flow was subsonic for about one-third of the path length in the semivaneless space. At 15 degrees, the subsonic region was reduced to about one-fifth of the path length; at 40 degrees, the flow was subsonic. Circumferential Mach number gradients existed both upstream and downstream from the $F = 1.30$ area; the upstream gradient was less pronounced than the downstream gradient. Near the throat, the flow-angle contours tended to turn in the radial direction, with the high Mach number contours turning first. Therefore, the flow at the throat entered at Mach 0.92 to 1.05.

The contours around the pressure side of the vane leading edge are shown as dashed lines to indicate that the flow accelerates around the tip and must then decelerate to subsonic values along the suction-surface contour.

Figure 83b shows water-height (density) contours in the semivaneless space. A low-gas-density area was noted at $\phi = 15$ degrees and $r = 22$ inches. This area extended about the same distance from the downstream vane leading edge as the high Mach number area, but was farther toward the throat in the radial direction. The contours became more radial as the flow approached the throat, indicating compression. Just before the passage shock, the height was almost radially uniform at 0.56 inch. Estimated contours at the suction surface of the vane leading edge indicate local expansion in this region.

Figure 83c shows the flow-angle contours measured in the vaneless space during this first test. The flow over the first third of the vaneless-space inlet arc was nearly flat; the 87.5-degree contour extends from $\phi = 1$ degree to 19 degrees. For this test, readings were not taken closer to the screen than $r = 21$ inches; therefore, the flow-angle contours in the rest of the vaneless space and early semivaneless space were estimated. The flow angles along a streamline near the island tip become steeper (angle decreases), which indicates an expansion across the tip-wave system; this is followed by a flattening (angle increases) near the first shock. The flow angles decreased and, subsequently, increased across a second expansion region to the second oblique shock. Because they are nearly uniform from $\phi = 1$ degree to 19 degrees, the Mach waves shown are weak.

Configuration 2I8 — The second test, during which Configuration 2I8 was used, was run to evaluate the effect of wedge angle. This diffuser was identical to the previously tested Configuration 1I8, except that the vane-island-tip wedge angle

CONFIDENTIAL

CONFIDENTIAL

was decreased from 12 to 5 degrees. The throat area was the same as in the previous configuration, but because of the different wedge angle, the suction-surface contour of Configuration 2I8 was more concave than that of Configuration 1I8.

Figure 84 shows the observed Mach wave pattern and the related Froude number, water height, and flow-angle contours (from water-table instrumentation and an average of 3 photographs). The wave pattern shows an expansion around the tip, followed by a series of oblique shocks, which indicates additional expansion regions.

Figure 84a indicates Mach number variations across the semivaneless space. As with Configuration 1I8, part of the semivaneless space adjacent to the suction surface was subsonic. At the diffuser throat, the central passage streamlines showed a slight acceleration ahead of the passage shock, and all other streamlines showed a deceleration to the throat.

Figure 84b shows the water-height variations, and the water-flow angles are shown in Figure 84c. From $\phi = -2$ degrees to $+11$ degrees, the water-flow angles are approximately 82.5 degrees. Small areas where flow angles increased to 85 degrees were observed along the impeller tip at $\phi = 0, 21,$ and 26 degrees. Flow angles within the arc corresponding to the semivaneless space ($\phi = 0$ to 28 degrees) are about 77.5 degrees. The angles then flatten because of the tip shocks, and from $\phi = 37$ to 45 degrees, the angles are again about 77.5 degrees. Again, as with 1I8, the circumferential flow distribution was not uniform.

For a Froude number of 1.30 at the impeller (screen), water flow approached the diffuser tip at 77.5 degrees (or at an angle of 2.5 degrees to the suction surface); it had to generate a series of waves analogous to Prandtl-Meyer waves to expand around the pressure side of blade tip. Similarly, the flow was at 7.5 degrees to the pressure surface, producing an oblique shock on the pressure surface. The flow angle and shadowgraph waves shown in Figure 84c were similar to those observed for 1I8.

Figure 84c shows that the flow angle within the semivaneless space between $\phi = 18$ and 28 degrees becomes steeper as r increases from 22 to 22.5 inches. Secondary flows, as mentioned in Reference 10, could have caused the flow angle to steepen near the wall. Flow angles in the vaneless space fluctuated during the test, which could be caused by the measurements not being true time-averaged values.

By comparison, the subsonic region of Configuration 2I8 was slightly smaller than that of 1I8. Also, the fluid in the center of the passage just upstream of the throat accelerated slightly upon reaching the diffuser throat of Configuration 2I8; this did not occur with Configuration 1I8. Further, some regions in 1I8 were lower in

CONFIDENTIAL

density than some regions in 2I8. This indicated that the fluid accelerated to minimum density for 1I8, and then decelerated. However, differences between the two configurations were minor. Water-height changes in the low-density regions ($\phi = 12$ and 41 degrees) were about the same for 1I8 and 2I8.

Two primary wedge-angle effects were observed. First, the 12-degree wedge angle produced a wave that simulated a normal shock more than the one produced by the 5-degree wedge angle. Second, the tip expansion wave was stronger for the sharper, 5-degree wedge angle. For the smaller wedge, the influence of geometry on streamline acceleration at the diffuser was greater than for the larger, 12-degree wedge angle. However, the larger wedge angle had a more pronounced effect on streamline shape.

At the conclusion of this second test, it was believed that the previous observations would be verified by tests in the diffuser test rig. After test-rig substantiation from schlieren pictures and pressure measurements, design criteria could be established. It was believed that the larger wedge angle, with a more normal shock, would produce a uniform velocity profile and would minimize downstream Mach-wave reflections.

Because both the 5- and 12-degree wedge-angle configurations showed certain advantages, the best configuration could not be determined from water-table visualization. Later diffuser rig tests were expected to provide additional data for correlating rig data with the water-table results.

Configuration 2I16 — The third vane-island configuration was tested to evaluate increases in the number of diffuser channels. This set, Configuration 2I16, was a 16-channel diffuser with a tip wedge angle of 5 degrees, as was Configuration 2I8. Because the number of channels was doubled, throat width was one-half the size of the throats in Configurations 1I8 and 2I8 to maintain consistent flow conditions; impeller Froude number (F) for the test was the same as in the 2 previous tests ($F = 1.30$).

Figure 85 shows Configuration 2I16 information from water-table data. Figure 85a shows that the highest Mach-number region was about halfway between vane tips and was again 1.30. The subsonic region was estimated as confined to a thin layer adjacent the suction-surface contour. For the last one-fifth of the suction-surface contour, a sizable subsonic region existed near the wall; in this region, the flow in the center of the passage was nearly Mach 1.0. The diffusion rate along the streamlines appeared to be uniform throughout the passage, except at the suction-surface contour. The contours of Figure 85b revealed a low-density region that was closer to the upstream vane tip than the high-Mach-number region in Figure 85a. Moreover, the density increased gradually (almost uniformly) from the 0.510 region to 0.570 near the throat. The flow-angle contours shown in Figure 85a indicated that for about one-half the vaneless diffuser inlet arc, the

CONFIDENTIAL

flow angles were steeper than for 2I8 and ranged from 80 to 82.5 degrees. Flow angles at the inlet to the semivaneless space ranged from 75 to 77.5 degrees, with flatter angles near the first oblique shock, as expected from the previous water-table tests.

Configuration 2I24 — The fourth vane-island configuration tested was a continuation of the investigation on the influence of the number of channels. This configuration, designated 2I24, had the same wedge angle as that with Configurations 2I8 and 2I16, but the number of diffuser channels was increased to 24.

Figure 86 shows the water-table data, as was shown for the previous three diffuser water-table tests. The wave pattern in Figure 86a shows the previously observed expansion around the vane tip, followed by 2 oblique shocks. Shadow-graph pictures showed that the expansion zone between the 2 shocks could have been caused by waves reflecting off the impeller, and then off the suction surface. The Mach contour map (Figure 86a) again showed that the highest velocity region was at $M = 1.30$, centered about midway between the vane tips. The flow in the semivaneless space was supersonic (except the boundary-layer flow). Flow decelerated uniformly to the throat but accelerated again through the tip-expansion region.

As expected, the lowest density region was at the vane-tip radius midway between vanes. Conditions at the throat were uniform. Streamlines near the tip decelerated from a height of 0.560 to 0.600 inch; those near the wall, where density was higher, did not decelerate as much. However, all streamlines showed the previously observed acceleration and then deceleration at the diffuser throat. However, the second shock in Figure 86c influenced flow angles at the impeller tip and caused them to flatten (e.g., the 87.5-degree flow-angle contour). The flow then expanded around the tip, as in previous water-table tests. The contour near the semivaneless inlet arc showed a flow angle of 80 degrees and was nearly uniform across this arc.

Comparison of Vane-Island Configurations — Of the 4 vane-island diffusers tested, Configuration 1I8 had the flattest overall flow angle. The flat flow angle would result in the longest flow path, and, hence, in the highest friction loss. The steepest angle occurred with Configuration 2I16, and this vane set should show the lowest vaneless and semivaneless space losses. Along the inlet arc to the semivaneless space, the flow angles for Configuration 2I16 were the most uniform — between 75.0 and 77.5 degrees. The flow angles along the arc of $r = 21.6$ inches were nearly uniform for Configuration 2I24 but were flatter than for Configuration 2I16 (between 77.5 and 80.0 degrees).

Froude number (F) near the vane tip was highest for Configuration 2I16 ($F = 1.25$). By comparison, Froude numbers in the same region were about 0.96 for 1I8, 0.96 for 2I8, and 1.19 for 2I24. The Froude number of 1.25 occurred in the region of

CONFIDENTIAL

CONFIDENTIAL

greatest acceleration, and the 0.96 value of 1I8 and 2I8 indicated the effect of the first shock. It was believed that the 1.19 Froude number of 2I24 was in a region where deceleration had already begun.

In general, increasing the number of diffuser channels improved diffuser flow characteristics. However, the Froude numbers (F) recorded for the 24-channel diffuser (Configuration 2I24) indicated supersonic flow downstream of the throat shock. Further study of these phenomena was planned for the diffuser test rig.

The principal vane-island elements investigated were wedge angle and the number of diffuser channels. Increasing the wedge angle from 5 to 12 degrees caused the passage-shock shape to become nearly normal. Also, the smaller 5-degree wedge angle intensified the tip-expansion shock wave. However, no conclusion was reached from the water-table visualization on whether large or small wedge angles should be used.

Wave patterns for all four diffuser water-table tests were similar. In each test, the tip-expansion waves were followed by 2 oblique, slightly curved, shock waves. The shock waves extended to near the impeller tip, within about 0.25 inch of each other. Closer to the vane, the waves diverged slightly, but never by more than 1.0 inch. The cause of this divergence is believed to be the different flow conditions along the vane surface — even the cascade sets in the discussions that follow this vane-island evaluation revealed the same pattern. However, the expansion was more pronounced for the cascade vanes, and the 2 shocks were closer to the vane tip than for Configurations 1I8 and 2I8.

All diffusers tested had identical suction-surface contours from the vane tip for 4 to 5 inches. This similarity in shock-wave pattern suggested that this part of the suction surface has the greatest influence on the wave system.

The test results showed that the density contours of 2I16 and 2I24 had the most uniformity in the semivaneless space. The 8-channel diffusers, Configurations 1I8 and 2I8, showed greater variations in Mach number across the semivaneless space; subsonic and supersonic flows occurred simultaneously.

Measurements of both Froude number (F) and water height were not obtained in the vaneless space; however, estimates of Froude number were made for this region. Theoretically, the density contours should be aligned with the Mach-wave pattern, thus providing a guide for estimating the Mach contours.

Reflection of expansion waves off the impeller tip toward the suction-surface contour caused streamlines to bend from the wave to a flatter angle. Some of the regions in which this effect occurred also experienced increased density.

CONFIDENTIAL

CONFIDENTIAL

In general, water-table visualization of the vane-island tests provided a basis for correlating the vanes with the diffuser test rig. Diffuser-test-rig data were required for passage and semivaneless-space densities, reflected expansion-wave effects, throat-shock behavior, and wedge-angle effects to confirm water-table observations.

Water-Table Studies of Cascade Configurations

The objective of this comparative testing was to establish flow characteristics of the first stage of a cascade diffuser. Several rows (4 or 5) were required to achieve the same diffusion as in a channel, and first-stage exit Mach numbers would be about 0.8. Therefore, visual evidence of flow through a single row was attempted, and the studies were then to be expanded to multiple stages.

Two basic cascade-vane configurations were tested. The first configuration was a long-chord, single-row cascade, designated 5C24. The second was a short-chord cascade, designated 4C64. This cascade was originally designed for 64 values. However, the number of vanes was increased to 90 before testing for better throat definition.

The long-chord cascade, Configuration 5C24, was constructed of double circular arc vanes with a mean solidity of 2.26. The 90-vane, short-chord cascade had flat plates spaced at 4-degree intervals. Solidity of this configuration was 1.14.

The cascade-vane testing included investigating:

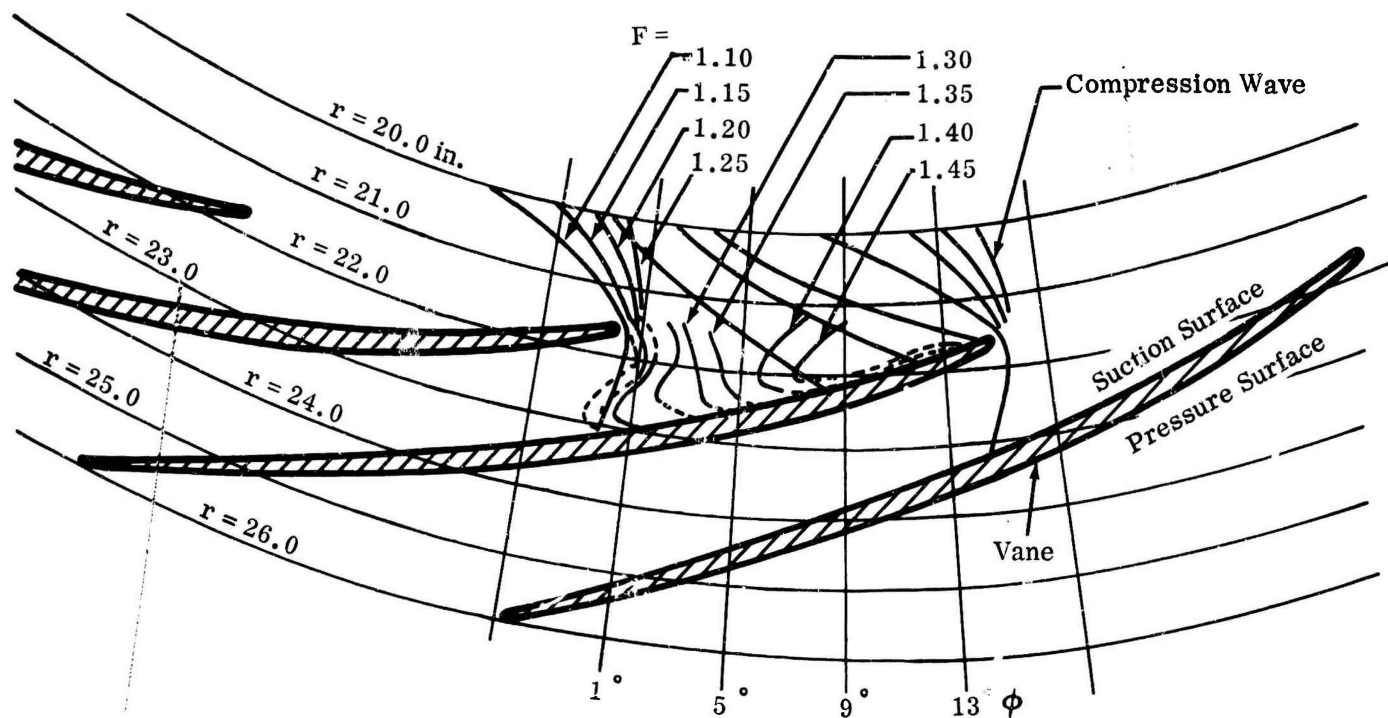
- 1) Flow characteristics of long- versus short-chord cascades related to first-stage diffusion of transonic flow;
- 2) Diffusion rates of short-chord cascades and long-chord cascades.

Cascade Configurations — The 5C24 cascade test data are plotted in Figure 87. This figure indicates separation over one-half of the blade suction surface, as observed from dye traces injected near the separation point.

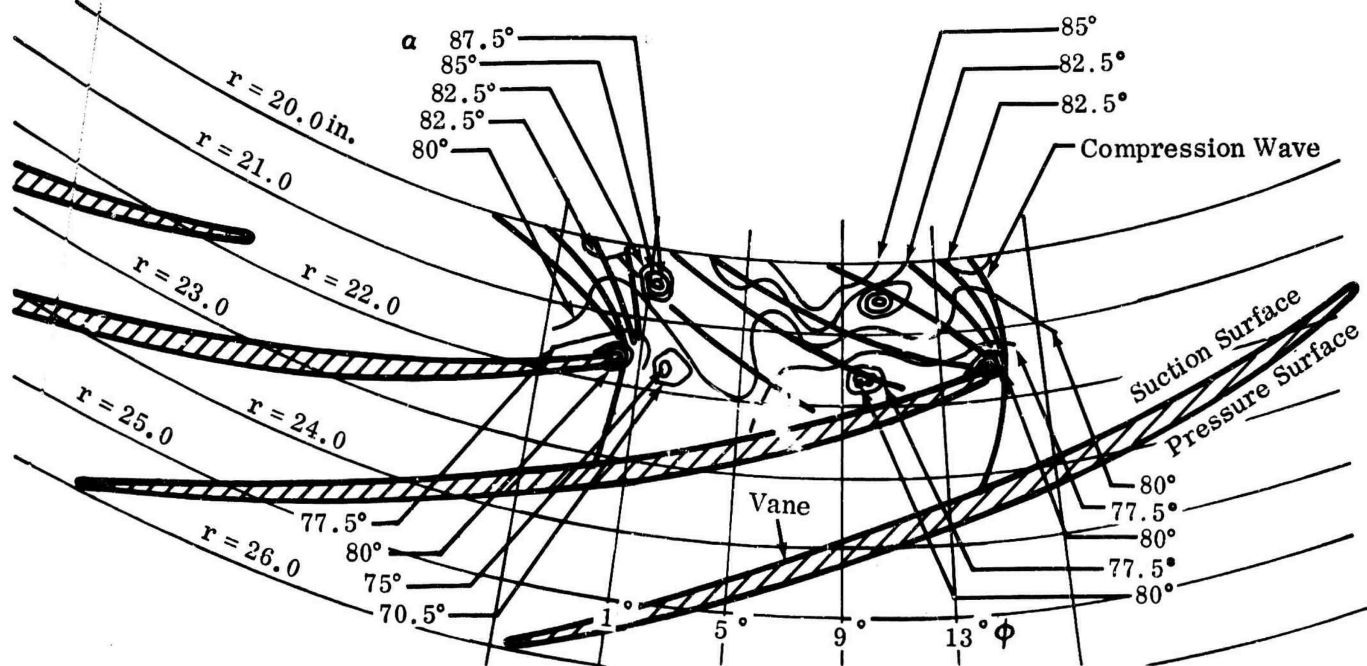
The Mach number was 1.30, as in previous water-table testing. A peak Mach number of 1.48 was observed near the vane tip, which indicates a strong expansion about the tip. The water-height contours analogous to density varied from 0.470 to 0.600. The flow realignment from this separation can also be seen in the illustration. Flow angles at the impeller tip are evenly spaced — from $\phi = 5$ to 11 degrees, they are about 85 degrees. Elsewhere, the flow enters at an angle of approximately 82.5 degrees. The wave pattern and flow-angle contour maps show the influence of the first shock at the diffuser tip (Figure 87a).

CONFIDENTIAL

CONFIDENTIAL



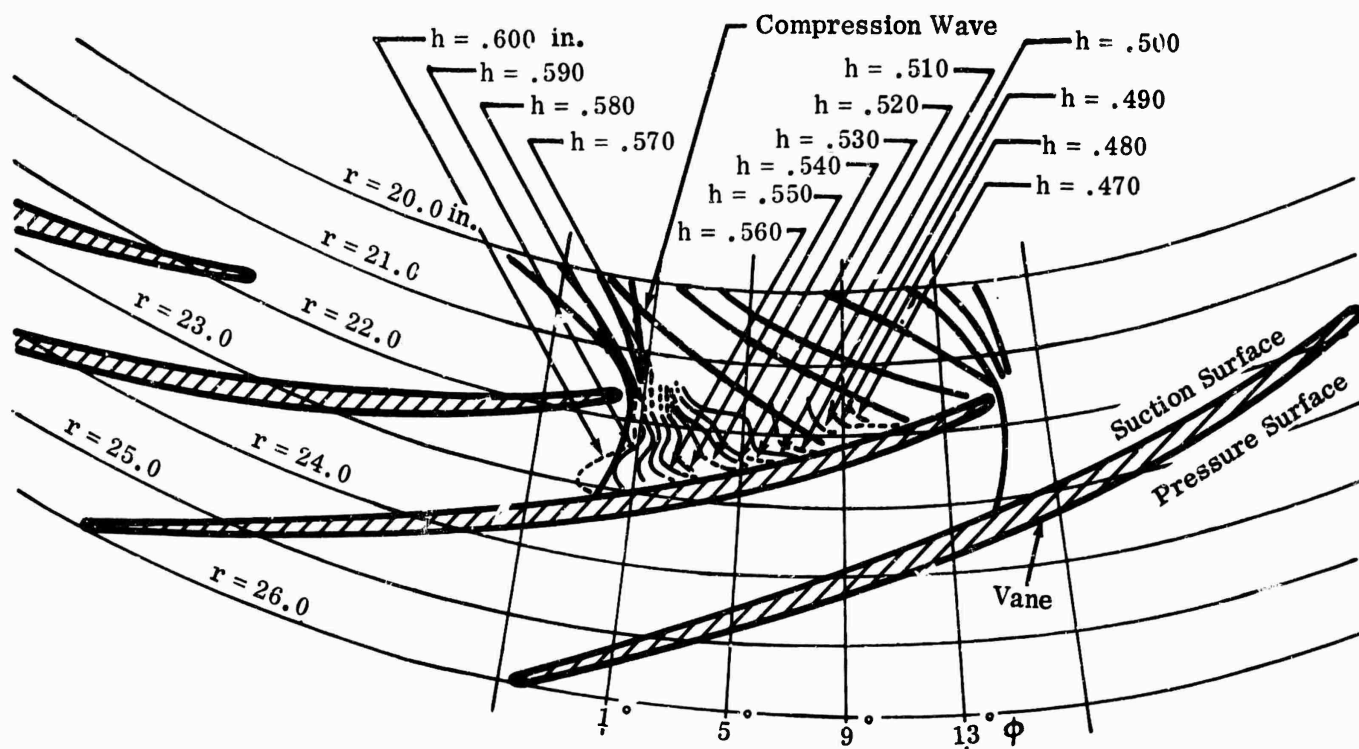
a. Froude-Number Contours.



c. Flow-Angle Contours.

Figure 87. Water-Table Data on 5C24 Cascade Configuration.

CONFIDENTIAL



b. Water-Height Contours.

- Notes:
1. r radii (inches)
 2. α flow angle referenced to radial line (degrees)
 3. Froude contours (dimensionless)
 4. Water-height contours (inches)
 5. Flow-angle contours (degrees)

CONFIDENTIAL

At the inlet arc to the semivaneless space, the flow angle varies from 75 to 80 degrees. Just off the vane tip, the angle is 75 degrees, which indicates the influence of the vanes in turning the flow to the required direction at the throat.

Tests of the 5C24 cascade configuration showed that flow separated from the vanes and that they were overloaded. It was believed that the long chord of 5C24 caused boundary-layer buildup and that the long flow path through the vanes required a lighter loading. Therefore, the second test was a short-chord cascade (4C64). The cascade had 90 vanes composed of short, flat plates. Figure 88 shows a sketch of this cascade arrangement and a cross-sectional sketch of a vane. Solidity was 1.16 based on the pitch at the vane leading edge. The water-table-data curves similar to Figure 83 were not prepared for Configuration 4C64. The close spacing of the vanes made this type of data presentation impractical. Instead, shadowgraphs are included throughout the 4C64 test-series discussion to show the water-table flow characteristics.

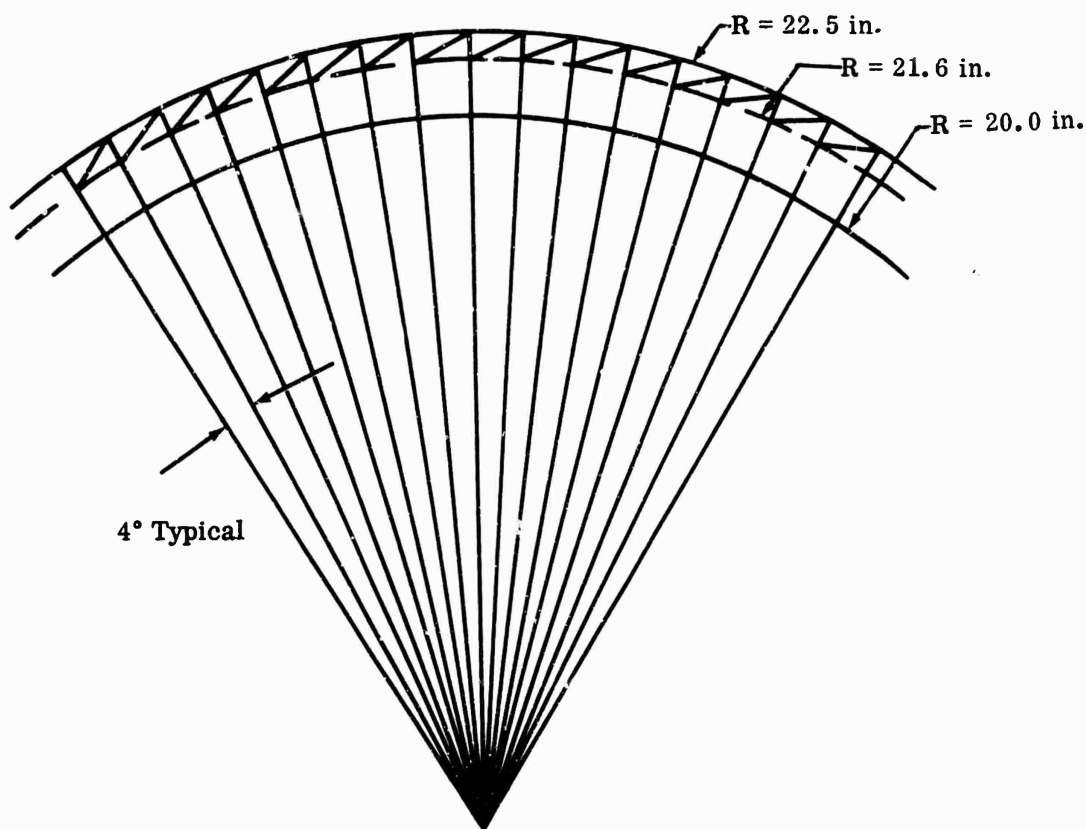


Figure 88. 90-Vane Cascade.

CONFIDENTIAL

Figure 89 shows a water-table shadowgraph of flow through the cascade. A distinct normal shock was seen at the vane throat, and no separation from the vane surfaces was detected. The average entrance Mach number was approximately 1.3 and the exit Mach number was about 0.8. This test demonstrated that a short-vane cascade would restrict the shock to the leading edge and that subsonic flow could be established downstream. It was then necessary to study ways of diffusing the flow from the Mach 0.8 of the first stage.

To diffuse the Mach 0.8 flow, a second-stage cascade, the original 5C24, was added to 4C64. The combination of Configurations 4C64 and 5C24 as first and second stages showed promising results. Figure 90 shows an ink trace of the model; separation could be detected in either stage. The simulated Mach number was approximately 1.3 at the first-stage entrance and 0.8 at the exit. The simulated Mach number at the second-stage throat was about 0.5.

A comparison of the polar lines and the vane positions in Figure 91 shows that the airflow approaches radial in the 2 cascade stages. To obtain a more radial flow at the diffuser outlet, and thus more diffusion, the 5C24 vanes were cut at mid-chord and the trailing halves were installed with the camber reversed to form a third-stage cascade. The pitch of the second and third stages was reduced to maintain the solidity of these stages with the reduced chord length. With this 3-stage cascade, the flow was turned to within 32 degrees of radial in the vane passages. Figure 91 shows no separation, and Figure 92 is a shadowgraph of the cascade showing that, following a shock upstream of the first stage, the flow within the cascade is subsonic.

Comparison of Cascade Configurations — From these tests, it was concluded that a single row of cascade vanes could effectively diffuse the supersonic flow ($M \approx 1.3$) through a single shock. In addition, multiple, short-chord cascades minimized the tendency of flow to separate, as occurred in the long-chord cascades.

From the results of the water-table tests, a short-chord cascade was designed for the diffuser rig tests, instead of the long-chord cascade as originally planned. The vanes had zero camber, with a solidity of 1.17 on the leading-edge pitch. Figure 93 is a photograph of the diffuser-test-rig cascade. It was planned that only the first blade row be tested to confirm water-table data; the results are presented in Sections 6.0 and 7.0 of this centrifugal-compressor report.

2.3.2 DESIGN METHOD

The diffuser designs were based on methods used in previous centrifugal-compressor research programs. From the parametric analyses and water-table studies, conditions were predicted at the impeller outlet and the region of the diffuser vanes. In addition, basic information on subsonic diffusers was available.

CONFIDENTIAL

CONFIDENTIAL

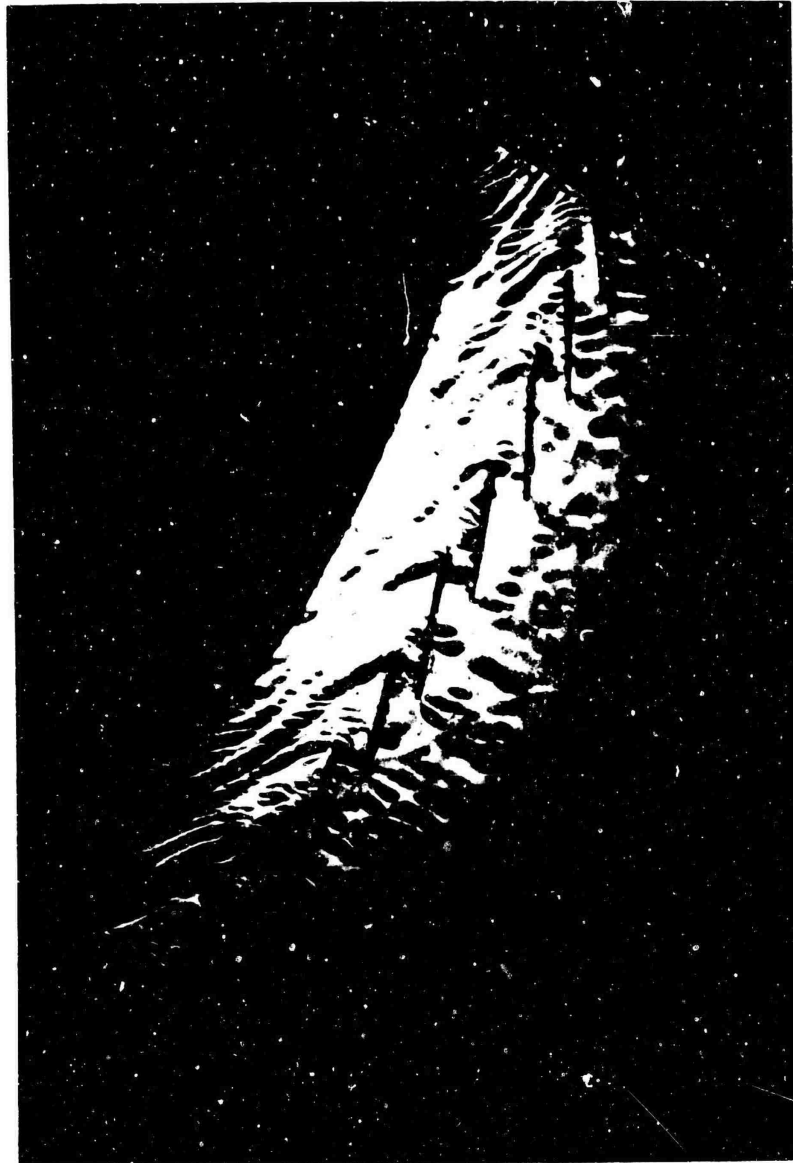


Figure 89. Water-Table Shadowgraph, Single-Stage Cascade.

CONFIDENTIAL

CONFIDENTIAL



Figure 90. Water-Table Ink Trace, Two-Stage Cascade.

CONFIDENTIAL

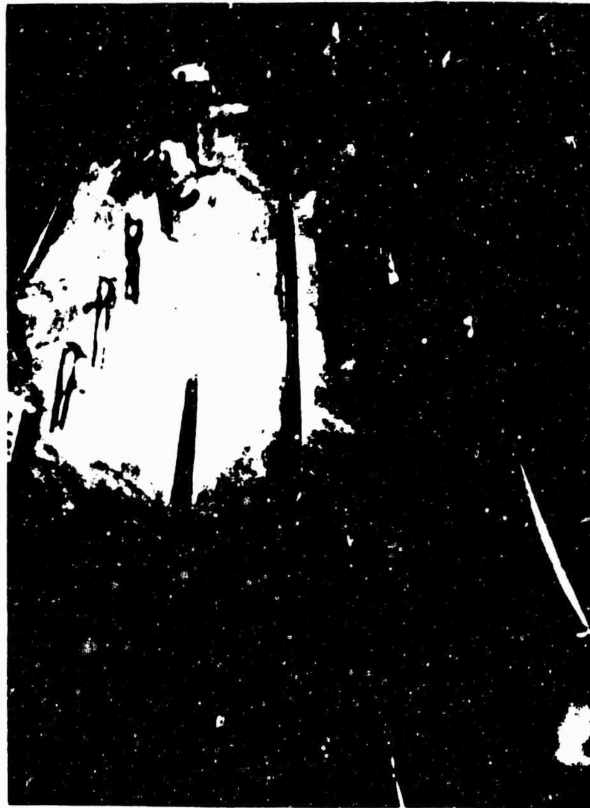


Figure 91. Water-Table Ink Trace, Three-Stage Cascade.

Geometric relations and their influence on pressure recovery were reviewed, and parameters requiring further research were identified for diffuser design and test. The factors considered and the layout methods used are given in the discussion that follows.

Design Considerations for Vane-Island Configurations

For detailed analysis, the diffuser was divided into 2 parts:

- 1) The vaneless space, which included the region from the impeller tip to the channel throat;
- 2) The channel, which included the path from the throat to the collector.

CONFIDENTIAL



Figure 92. Water-Table Shadowgraph, Three-Stage Cascade.

136

CONFIDENTIAL

CONFIDENTIAL

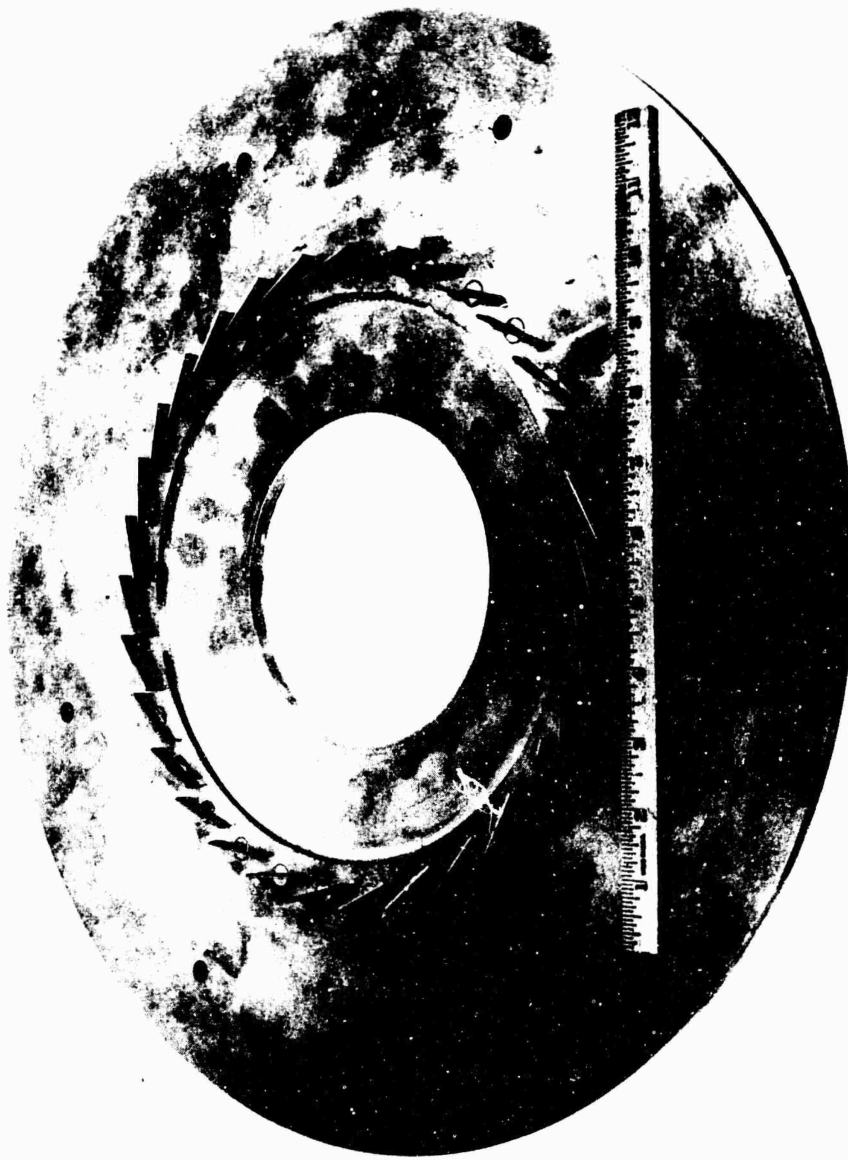


Figure 93. Cascade Diffuser.

CONFIDENTIAL

CONFIDENTIAL

Vaneless Space — Methods described in Reference 1 for the vaneless space of a radial-inflow turbine were used. It was assumed that conditions at the impeller tip were symmetrical and that instantaneous mixing occurred at the vaneless diffuser inlet. With this simplification of the wake-mixing process, the fluid was considered to be controlled only by the diffusion rate and the wall boundary layer. Therefore, the flow was assumed to be 1-dimensional, and the pressure loss was accounted for by introducing side-wall friction. Hence, for the cases studied, the average compressible flow conditions at the vaneless diffuser inlet were used.

The equations of motion (energy, continuity, and momentum equations) for a control volume bounded by the diffuser side walls were combined with the equation of state and the semi-empirical relation for friction coefficient (given in equation 14) to provide a solution of the flow field.

$$\frac{c_f}{2} = 0.0296 (R_e)^{-0.20} \left(1 + \frac{k-1}{2} M^2\right)^{-0.45} \quad (14)$$

This solution gave the desired information on velocity, friction loss, and direction of flow at any point in the vaneless space. So that the method would have wide applicability, the numerical solutions were programmed in FORTRAN II language for data processing systems. The complete description of its use for a turbine vaneless space is presented in Reference 11, under the title Program VLS, Vaneless Space.

The analysis of vaneless-space losses showed that, under the influence of friction, the absolute flow angle continuously required adjustment toward the tangential direction to satisfy the above vortex and the continuity relations. Inlet vectors used in the analysis are defined in Figure 94.

Dynamic-head loss caused by side-wall friction is dependent on the path length to the throat (primarily wetted surface area) and the local velocity. The effect of the loss can be expressed in terms of total-pressure recovery by the following relation:

$$\text{Vaneless-space recovery} = \frac{\text{Total pressure (local)}}{\text{Total pressure at impeller tip}} \quad (15)$$

CONFIDENTIAL

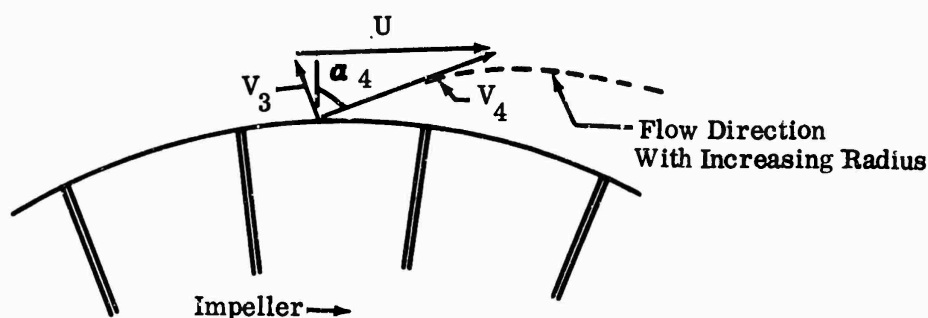


Figure 94. Vectors at Entrance to Vaneless Space.

The shortest flow path results when the absolute velocity is more nearly radial. A short flow path also results if the diffuser vane tips are located close to the impeller at a small vaneless-space-diameter ratio (diameter at vane leading edge to diameter at impeller tip). However, as shown by Stanitz (Reference 12), Brown (Reference 13), and Faulders (Reference 14), consideration must be given to other aerodynamic parameters.

As a first step in analyzing the vaneless space, the VLS program was used to plot Figure 95, showing the relation of total-pressure recovery to vaneless-space-diameter ratio, Mach number, and flow angle. The illustration indicates that loss can be minimized (highest recovery achieved) by designing for a steep-impeller-discharge angle and a small-diameter ratio. But, for these parameters, Mach number at the vane leading edge will be highest. Likewise, the resulting shock system would be strongest at the small-diameter ratio; its influence on boundary-layer growth can be expected to cause other losses that are unaccounted for in Figure 95. For example, because the flow mixes as it leaves the impeller, a small-diameter ratio should be avoided. The work of Johnston and Dean (Reference 15) suggests the diameter ratio at which the mixing would be completed, and normal practice at pressure ratios lower than 6:1 has been to maintain the ratio greater than 1.05 to avoid the unsteady-flow region. In addition, flow in the vaneless space is influenced by the number and location of the vanes. This effect was noted visually during the water-table tests described earlier. Because it was not possible to define the flow in detail in this region, the assumption was made that circumferential distribution at the vane leading

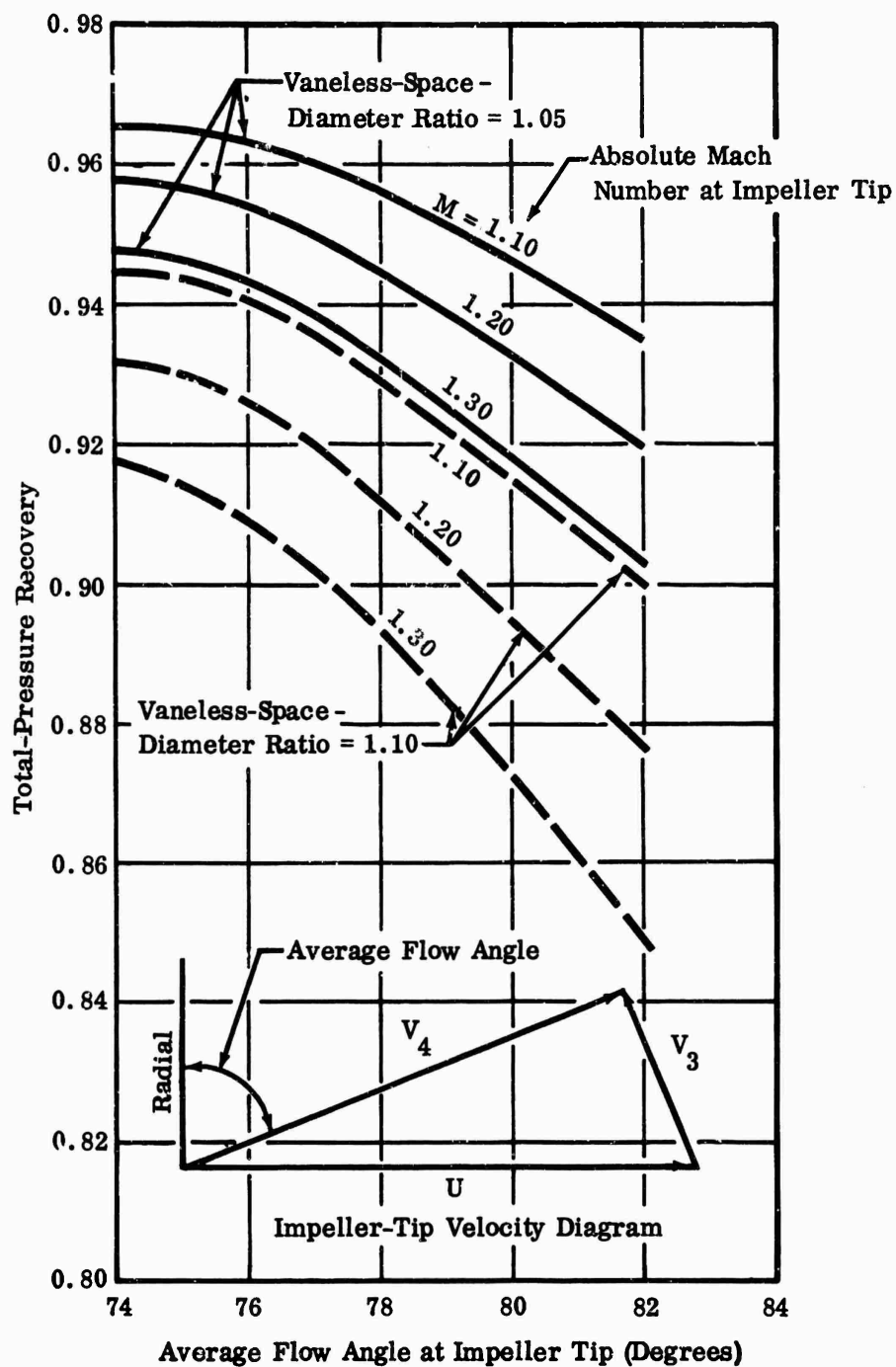


Figure 95. Variation in Total-Pressure Recovery, Inlet Flow Angle, and Diameter Ratio for Vaneless Space.

edge was uniform. While this assumption formed the basis for the design of the vanes, it was planned that later pressure surveys and schlieren studies from test rigs would be used to formulate theories on the flow patterns.

Channel

A 1-dimensional parametric study was conducted for the channel portion of the diffuser. The channel inlet Mach numbers used in the analysis were in the range of 0.50 to 0.90. Data on losses were derived from the work reported by Patterson (Reference 7), Henry (Reference 8), and Henry and Wood (Reference 16). These references provided basic information relative to area ratio and rate of diffusion. For analysis, dump loss at the channel exit was estimated as half of the remaining discharge dynamic head, as discussed in the previous section of this report. The results of the study at a channel inlet Mach number of 0.80 were given in Figure 78. These data represent conditions that do not account for local flow effects around the vane leading edges. The shock system and its influence on pressure distribution also were not considered in this initial assessment of performance.

It was evident that initial predictions would have to be modified on the basis of new test data to be generated in this research program. Therefore, to determine the trade in parameters, it was planned that the test components include diffusers designed for 2 different diameter ratios. To evaluate a short flow path and strong shock, a diameter ratio of 1.06 was selected. Possible flow unsteadiness in this region was also of interest. For study of a longer flow path with a weaker shock, a diameter ratio of 1.10 was chosen.

In addition, diffuser recovery at throat Mach numbers in the region of 0.80 required further study. Work reported by Friedlich (Reference 17) indicated that for maximum recovery, a throat Mach number above 0.80 should be avoided. Channel performance above this critical-throat Mach number was believed to fall off rapidly. However, additional tests conducted by the contractor prior to awarding of the Army contract showed that Mach numbers as high as 0.90 could be used at the throat. To investigate the critical conditions, Mach numbers of 0.75 and 0.90 were selected for the diffuser throats.

For further study of friction losses, both 8- and 16-vane channels were planned for test at the 1.06 tip-diameter ratio. It was also expected that the influence of the number of vanes on flow distribution in the vaneless space would be determined. Equally important was the effect of number of channels on flow range and surge. It was believed that the expansion regions observed at the vane tips on the water table (and earlier shadowgraphs) were related to flow range and the surge phenomena.

Design Considerations for Cascade Configurations

The vaneless-space analysis for the cascade diffusers was the same as that used for the vane-island diffusers. With wetted surface area being used as a criterion for comparison with the vane-island configurations, it was evident that because of the larger number of vanes in the first row (several times the vane-islands), the cascade had potential for minimizing the flow path to the throat. Therefore, lower friction losses in the vaneless and semivaneless spaces were expected for the cascade. In addition, the larger number of vanes was expected to produce a more uniform flow distribution ahead of the vanes.

For a multistage cascade, it was expected that flow downstream of the first-stage throat would behave like that over a wing with slotted flaps (i.e., at the wing-to-flap hinge line, flow through the slot energizes the cambered-surface boundary layer and thus delays separation). Relating this effect to the cascades showed that boundary-layer growth could be expected to be significantly less than with a vane-island. Further, it was expected that a higher diffusion rate through cascades could be used. It was recognized that trailing-edge wakes would occur and that for best performance, they had to be minimized. However, some compensation for these unavoidable wakes was expected from their effects on side-wall boundary layer. Acting as vortex generators to energize the side-wall boundary layer, these wakes had potential for inhibiting separation.

Estimated pressure losses through a 2-stage, cascade-type diffuser are given in Figure 96. The losses for the blade rows were estimated from axial compressor stator information reported by NASA in Reference 1. A similar plot for a 2-stage channel diffuser is presented in Figure 97. Based on the results from the water-table tests, a single-row cascade was planned for compressor rig tests for basic comparison with the vane-islands. The selected diameter ratio was 1.10.

Layout Method for Vane-Island Diffusers

Geometric parameters necessary for the layout of vane islands were:

- 1) Number of vanes, N_v ;
- 2) Vaneless-space-diameter ratio, D/D_i ;
- 3) Vane wedge angle, β ;
- 4) Area ratio, A_2/A_1 ;
- 5) Divergence angle, 2θ ;

CONFIDENTIAL

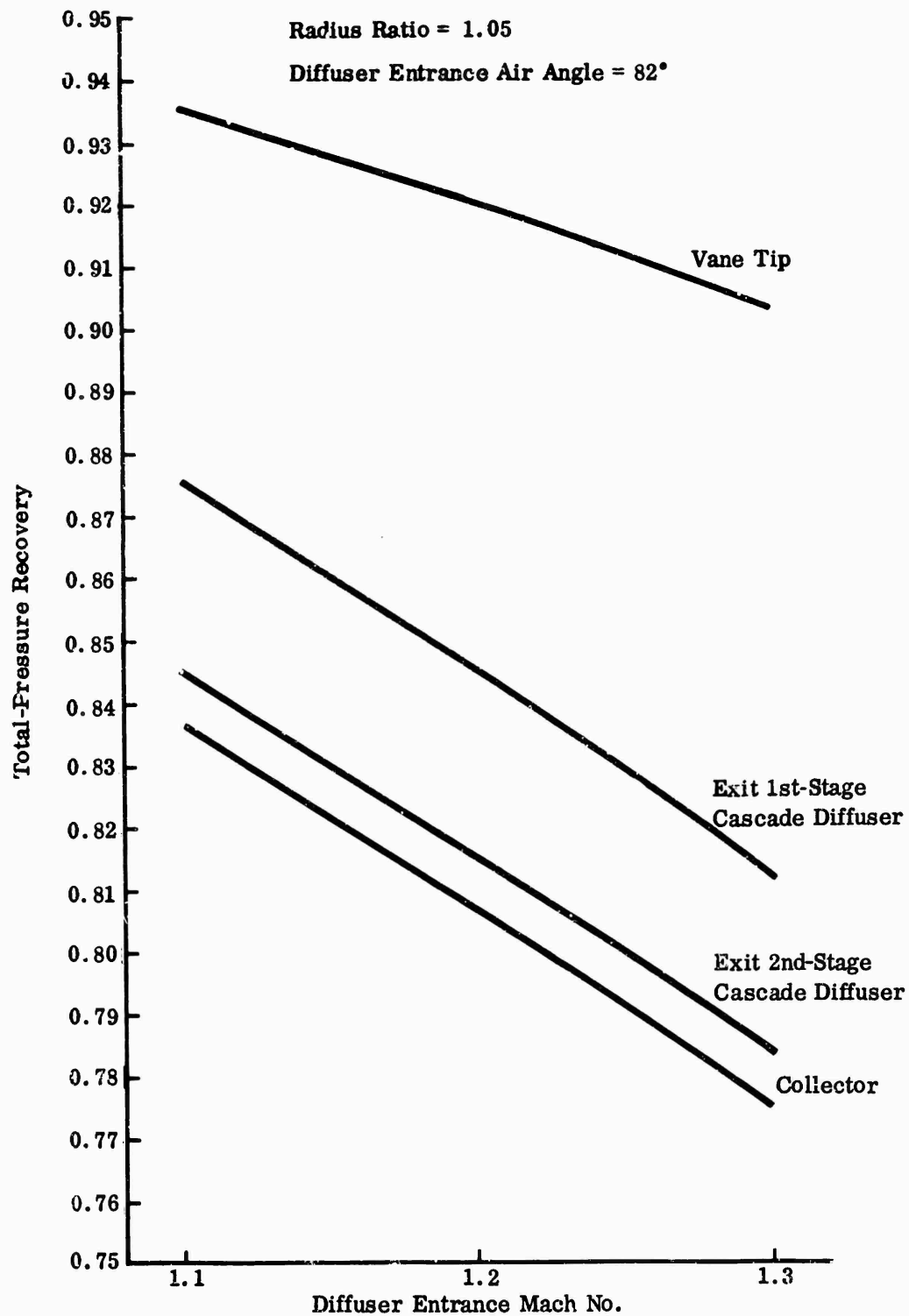


Figure 96. Estimated Pressure Recovery Through a Two-Stage Cascade Diffuser.

CONFIDENTIAL

CONFIDENTIAL

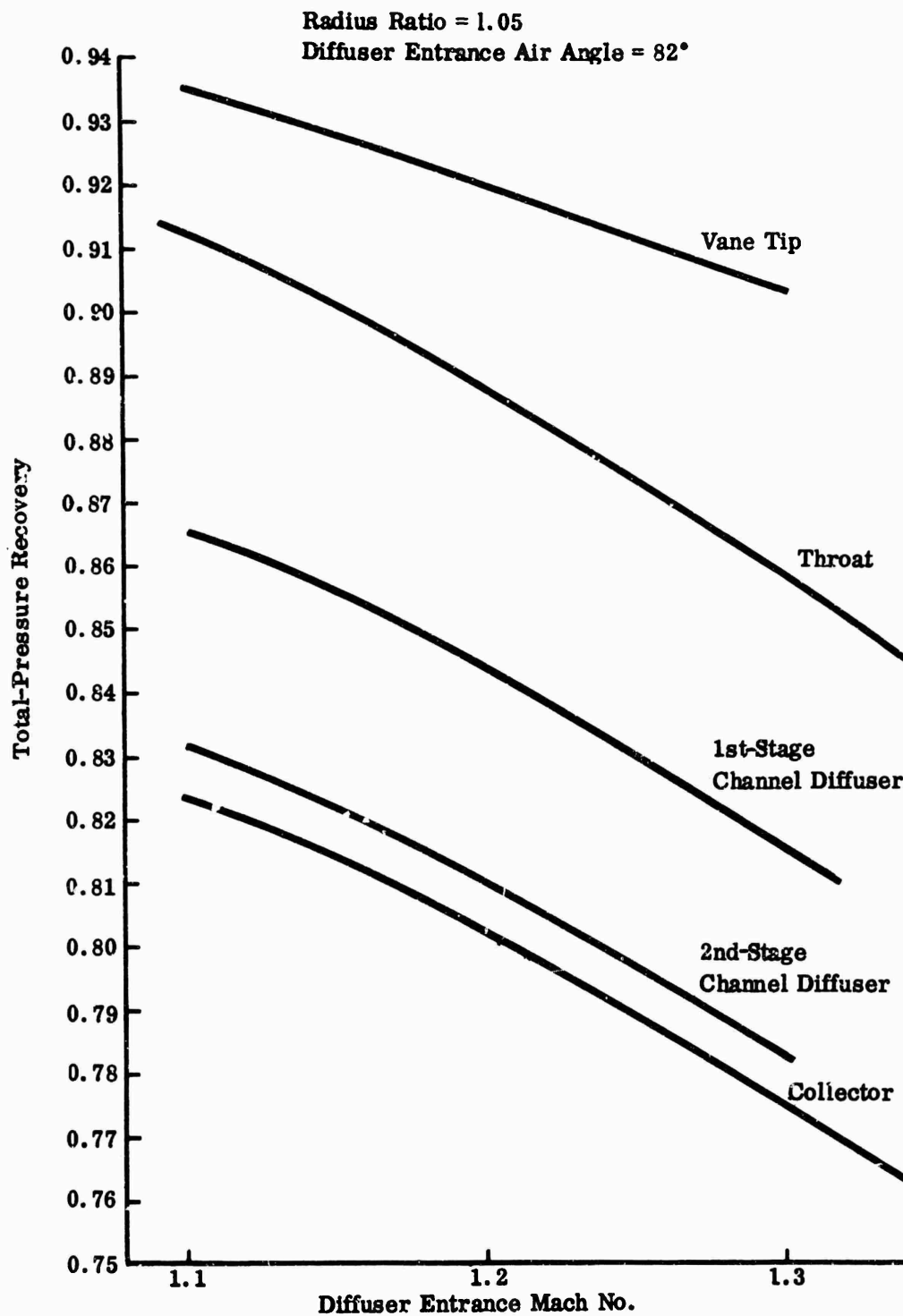


Figure 97. Breakdown of the Pressure Recovery Through a Two-Stage Vane-Island-Type Diffuser.

CONFIDENTIAL

CONFIDENTIAL

- 6) Throat length, l ;
- 7) Passage depth, b .

Flow conditions at the vane leading edges were predicted from the vaneless space (VLS) computer program. The essential aerodynamic parameters were Mach number, flow angle, and total and static pressure and temperature. From this information, the suction surface at the vane leading edge was set at zero incidence for the design airflow rate, as illustrated in Figure 98.

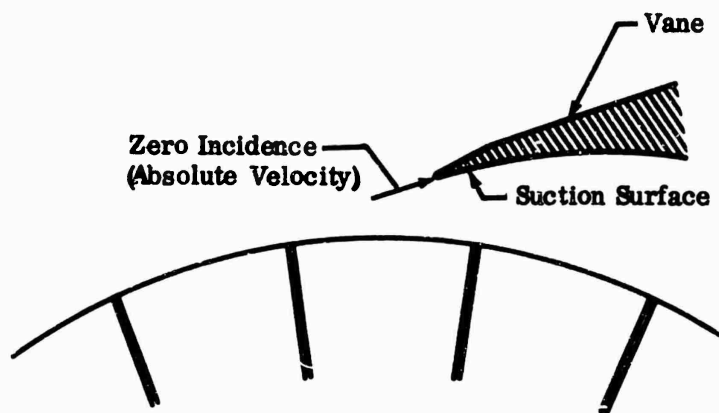


Figure 98. Alignment of Vane Leading Edge.

The throat height was determined from continuity using the predicted-state conditions as follows:

$$h_t = \frac{W_a \sqrt{T_T} A/A^*}{N_v K P_T b_t \phi_t} \quad (16)$$

where:

- T_T = total temperature of air at the throat
- P_T = total pressure of air at the throat
- A/A^* = ratio of area required for the design Mach number to area required for Mach 1.0

CONFIDENTIAL

- b_t = passage depth
 ϕ_t = aerodynamic blockage factor at the throat
 K = constant
 N_v = number of diffuser vanes

Blockage at the throat was estimated from boundary-layer displacement-thickness calculations over a flat plate, based on the following relation:

$$\delta^* = \left(\frac{0.37x}{8} \right) \left(\frac{V_4}{\nu} x \right)^{-1/5} \quad (17)$$

where:

- V_4 = absolute velocity at the impeller tip
 ν = kinematic viscosity in the vaneless space
 x = path length from the impeller tip to the throat midpoint
 $\frac{0.37x}{8}$ = factor derived from Schlichting (Reference 18).

The same conditions at the impeller tip were used for each diffuser. To establish a basis for later evaluation of the designs, it was planned that a single impeller be used in all diffuser tests. Accordingly, a fifth impeller (different from MF-1, MF-2, MF-3, and RF-1) was designed for the diffuser test rig. A description of this design is presented under Workhorse Impeller in Section 2.3.3.

The geometric construction of the vanes is illustrated in Figure 99.

The geometric construction of the vane-island diffuser layout is as follows:

- 1) Determine the angle of a vane-island sector from the equation

$$\alpha_s = \frac{360^\circ}{\text{number of channels}}; \quad (18)$$

CONFIDENTIAL

CONFIDENTIAL

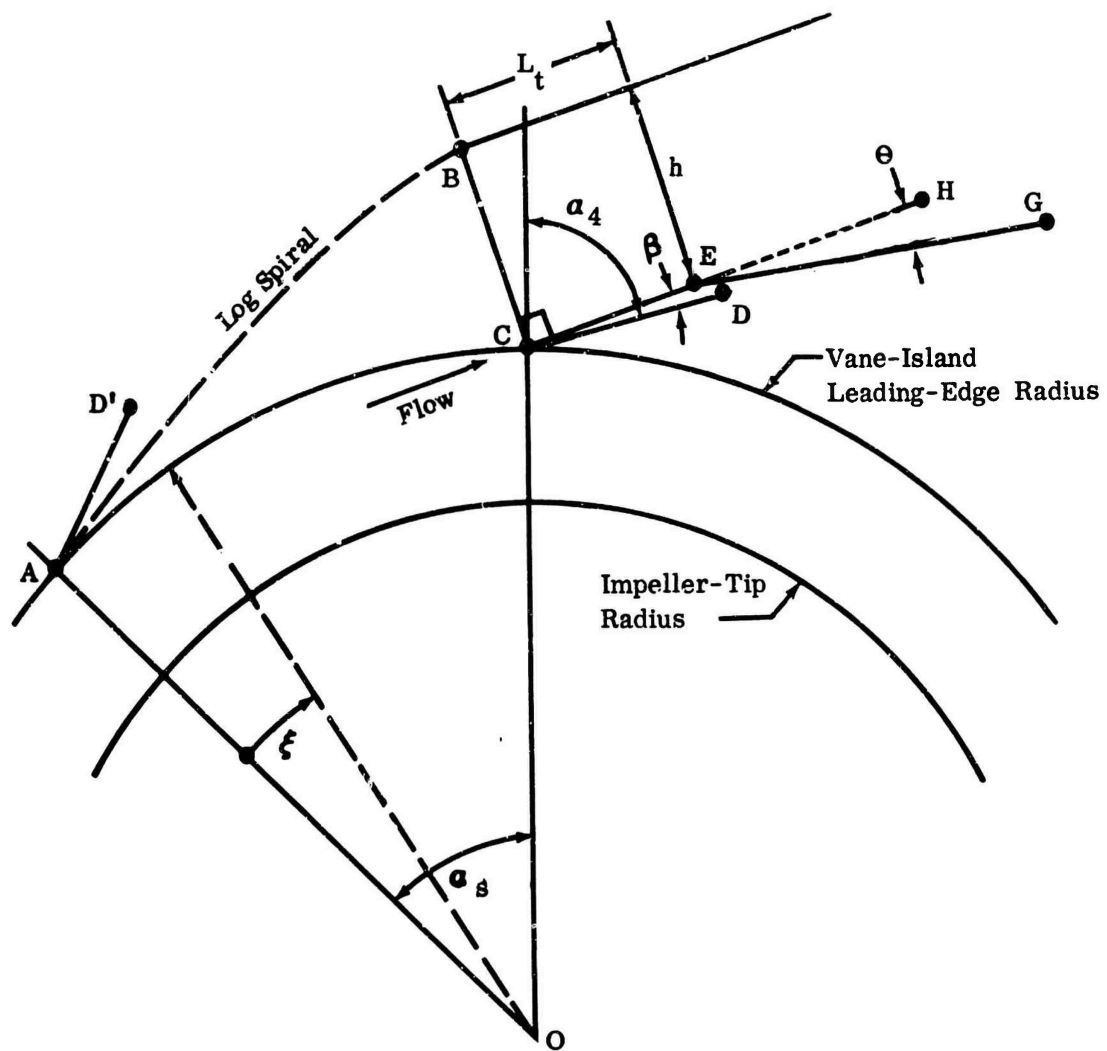


Figure 99. Vane-Island Diffuser Layout.

CONFIDENTIAL

CONFIDENTIAL

- 2) Draw 2 circular arcs about point O with an included angle α_8 corresponding to the impeller-tip radius and the vane-island leading-edge radius;
- 3) Draw the flow incidence line CD and AD' at the angle of incidence, α_4 , from lines OC and OA;
- 4) Draw the line CE with length L_t (throat length) such that angle DCE corresponds to the wedge angle, β ;
- 5) From point E, draw the line EG such that angle HEG corresponds to the diffuser divergence angle, θ ;
[The construction of the pressure surface CEH has now been completed.]
- 6) Construct a line BC perpendicular to CE at C with length h (h corresponding to throat height);
- 7) Calculate the equation of a log spiral curve through the angle AOC from the equation

$$r = ae^{m\xi} \quad (19)$$

where:

a = the vane-island radius

m = $\cot \alpha_4$

ξ = variable angle through AOC;

- 8) Adjust the log spiral curve to pass through points A and B and to be tangent to line AD';

[This line AB transferred to point C defines the suction surface of the vane.]

Layout Method for Cascade Diffusers

Geometric parameters necessary for layout of cascades were:

- 1) Number of vanes, N_v ;
- 2) Vaneless-space-diameter ratio, D/D ;

CONFIDENTIAL

CONFIDENTIAL

- 3) Leading-edge thickness;
- 4) Chord length, c ;
- 5) Passage depth, b ;
- 6) Vane airfoil configuration.

Flow conditions at the cascade vane leading edges were predicted from the vaneless-space (VLS) computer program by the same method as for the vane-island case previously discussed.

The geometric layout for the cascade was relatively simple. Once the geometric parameters were fixed, the cascade airfoils were drawn with their suction surface at zero incidence to the flow at the vane leading edge.

2.3.3 SELECTED DESIGNS

Three different vane-island diffuser configurations and one cascade configuration were designed for the program. These 4 diffusers were designated as follows: the vane-island, DI-1 (Diffuser-Island Set No. 1), DI-2, DI-3, and the cascade DC-1.

DI-1

The design parameters selected for the DI-1 diffuser elements are listed in Table V. This design, which was similar to previous Boeing designs, is shown in Figure 100. The figure shows that the channel was designed with all the 10-degree divergence on the pressure surface. This type design was selected because it was believed that the boundary layer on the suction surface would be quite large because of the long wall length from the vane leading edge.

The vanes were designed to be rotated, varying the throat area from 125 percent to 25 percent of the design value. The provision to install the vane at a 1.10 radius ratio at approximately the design throat area was also included in this design. The various settings for these diffuser elements are listed in Table VI along with the vane angle at each setting.

DI-2

The DI-2 geometry was similar to the DI-1 except for the throat Mach number. This design was tested to investigate the effect of throat Mach number on performance. The design parameters for the DI-2 diffuser elements are listed in Table V, and the configuration is shown in Figure 101. This design, like DI-1, had the capability of a variable throat area and two radius ratios.

CONFIDENTIAL

CONFIDENTIAL

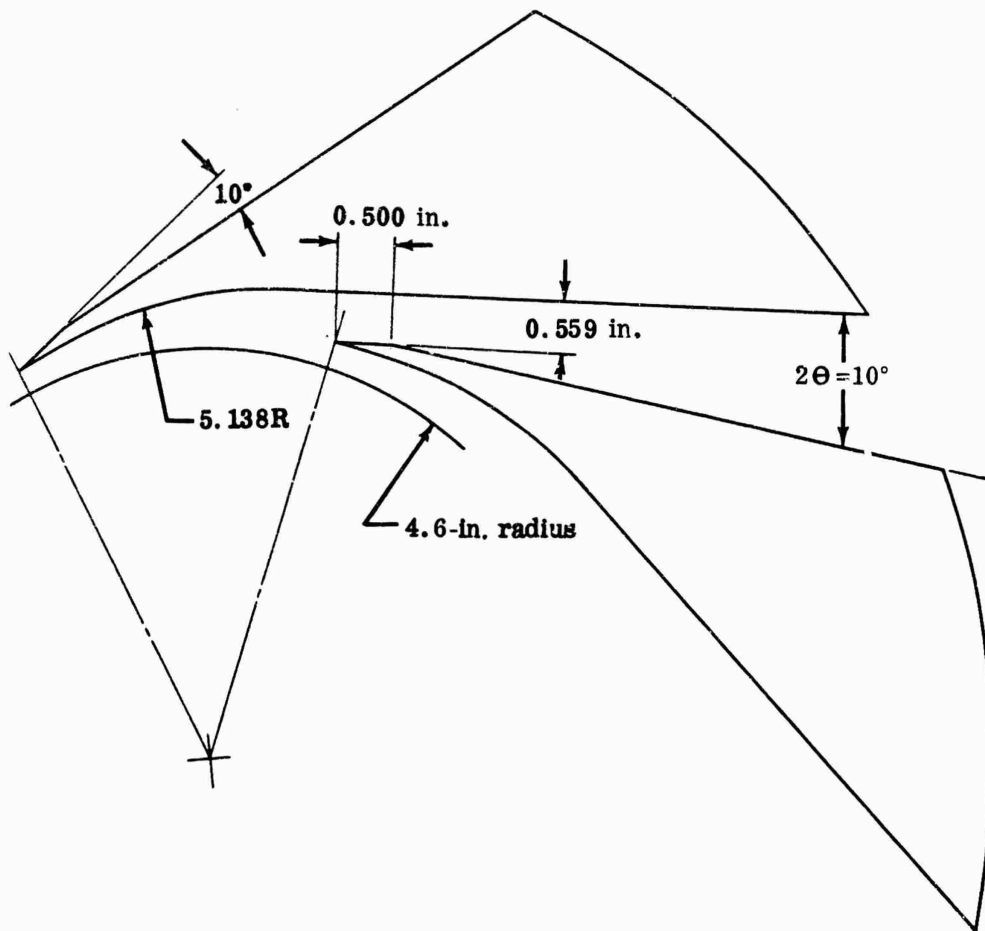


Figure 100. DI-1 Diffuser Vane (1.06 Radius Ratio, Design Throat Area).

CONFIDENTIAL

CONFIDENTIAL

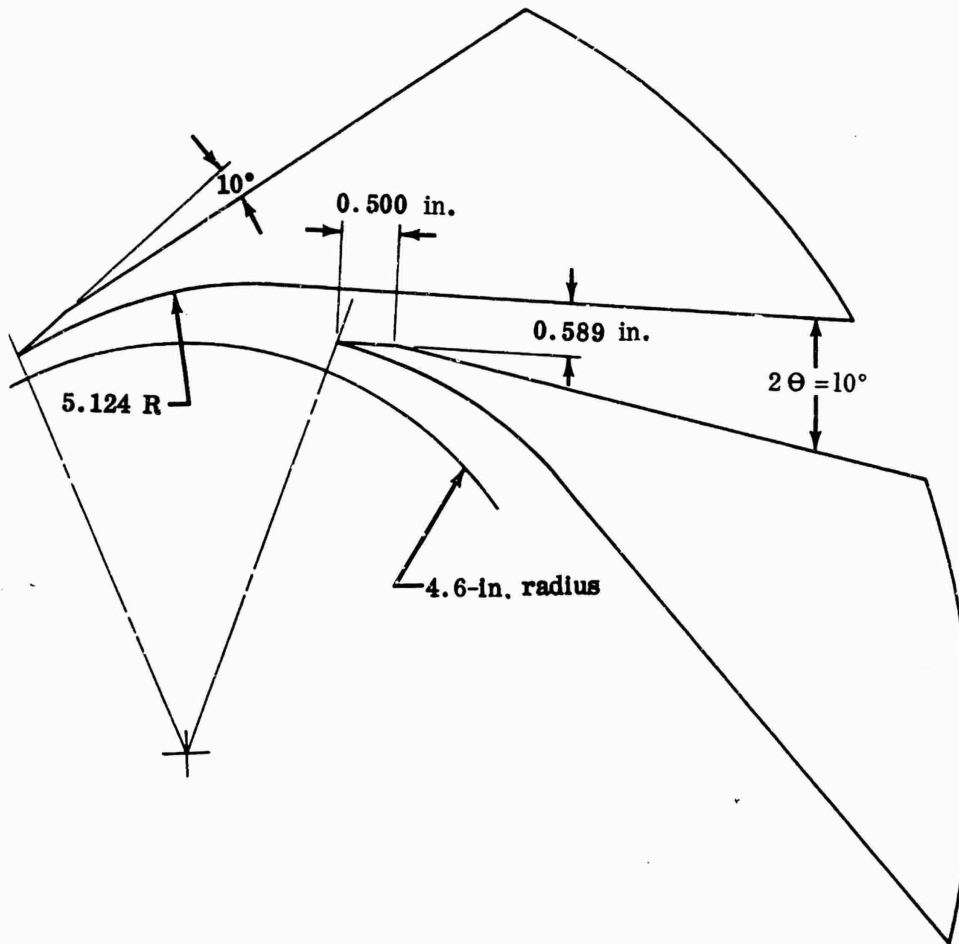


Figure 101. DI-2 Diffuser Vane (1.06 Radius Ratio, Design Throat Area).

CONFIDENTIAL

CONFIDENTIAL

TABLE V			
DESIGN PARAMETERS FOR VANE-ISLAND DIFFUSERS			
	DI-1	DI-2	DI-3
Number of Vanes	8	8	16
Throat Mach Number	0.90	0.75	0.75
Throat Height (in.)	0.559	0.589	0.295
Wedge Angle	7°	9°	9°
Channel Divergence Angle	10°	10°	10°
Area Ratio	2.76	2.63	4.70
Throat Length (in.)	0.500	0.500	0.250
Passage Depth (in.)	0.250	0.250	0.250
Blockage	0.88	0.88	0.88
Tip Radius (in.)	0.01	0.01	0.01

DI-3

The third set of diffuser vane elements (DI-3) was designed with 16 vanes and a throat Mach number of 0.75. This configuration was provided as a means of investigating a diffuser with better flow control and a shorter flow path length. The design parameters selected for this configuration are listed in Table V. This design is shown in Figure 102.

DC-1

The cascade diffuser set, DC-1, was based on the results of water-table testing. Design parameters for the DC-1 configuration are given in Table VII. This diffuser design is shown in Figure 103. Only the first-stage cascade was tested to evaluate the cascade concept.

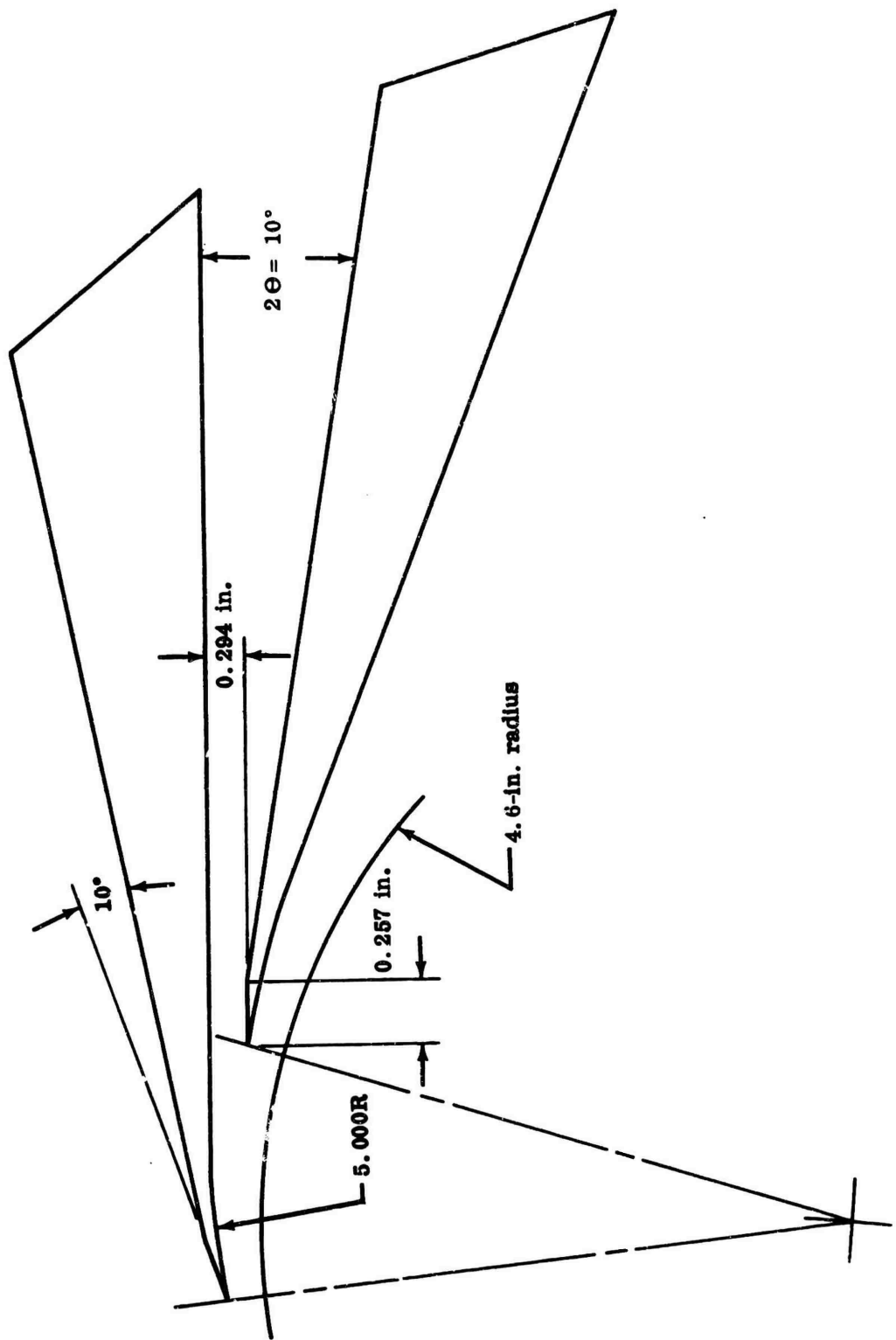


Figure 102. DI-3 Diffuser Vane (1.06 Radius Ratio, Design Throat Area).

CONFIDENTIAL

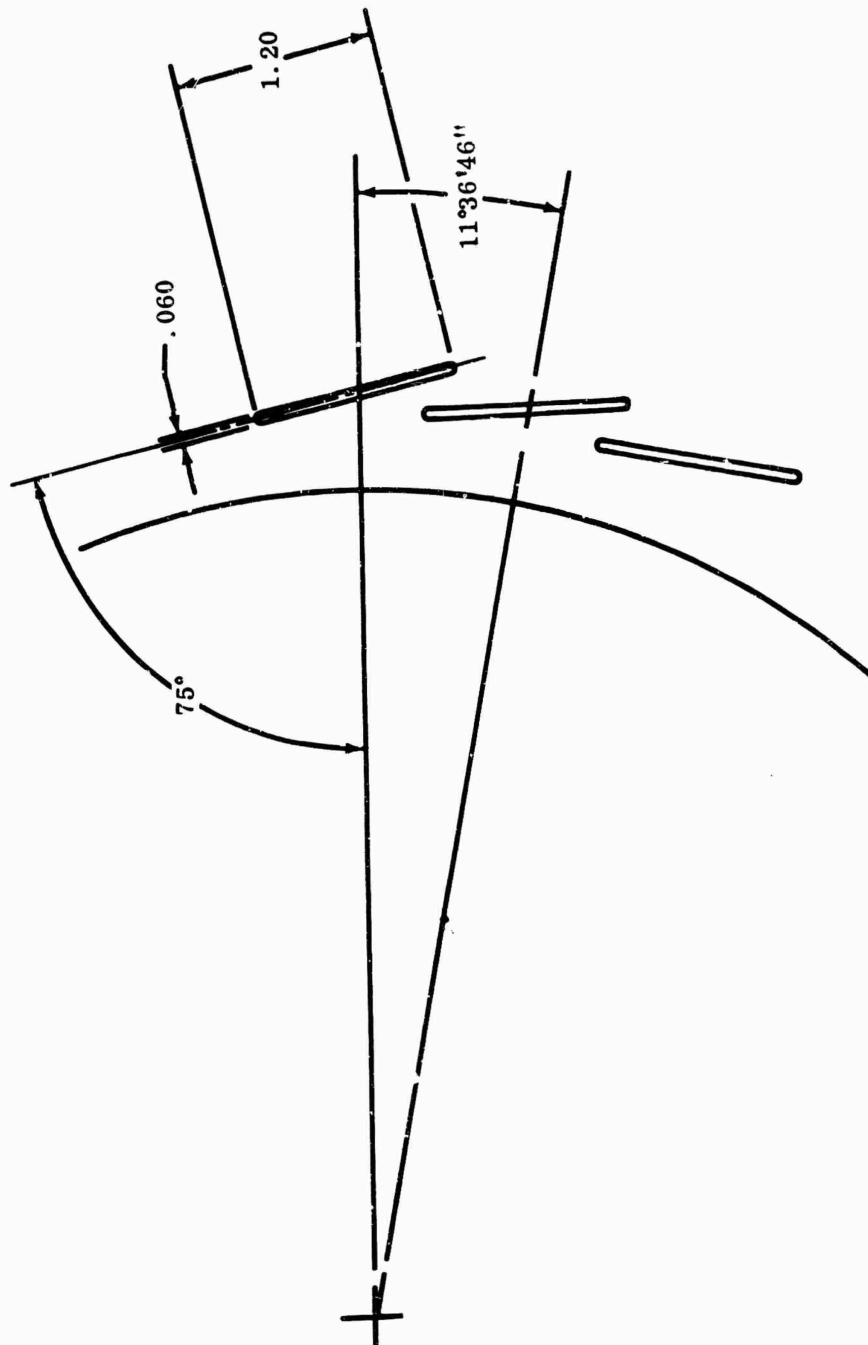


Figure 103. DC-1 Diffuser (1.10 Radius Ratio, Design Throat Area).

CONFIDENTIAL

CONFIDENTIAL

TABLE VI				
DIFFUSER VARIABLE GEOMETRY				
	Radius Ratio	Throat Height (inch)	Throat Area (% of Design Value)	Vane Angle (α_4 degrees)
DI-1				
	1.06	0.559	100	82.25
	1.10	0.581	104	84.60
	1.06	0.698	125	80.10
	1.06	0.418	75	84.40
	1.06	0.279	50	86.60
DI-2				
	1.06	0.589	100	82.25
	1.10	0.613	104	84.50
	1.06	0.736	125	80.10
	1.06	0.442	75	84.40
	1.06	0.295	50	86.60

Workhorse Impeller

To expedite design, fabrication, and test of the diffuser test section, an existing Boeing impeller was modified for use in the test rig. It was made from titanium to permit operation at tip speeds and flow conditions consistent with the previously discussed MF-1, MF-2, MF-3, and RF-1 impellers. Design tip speed was 2000 fps at an airflow of about 2.4 pounds per second. The inlet axial Mach number was about 0.76 with an inducer hub-to-tip-diameter ratio of 0.63. The blockage used was 0.847, based on previous testing of the same size inducers. Relative inlet Mach number was about 1.15 and the design rotor speed was 50,000 rpm. Significant design parameters are given in Table VIII.

The inlet and exit vector diagrams are shown in Figure 104, and a meridional view of the impeller is given in Figure 105. A sketch of the contemplated test rig arrangement is presented in Figure 106.

CONFIDENTIAL

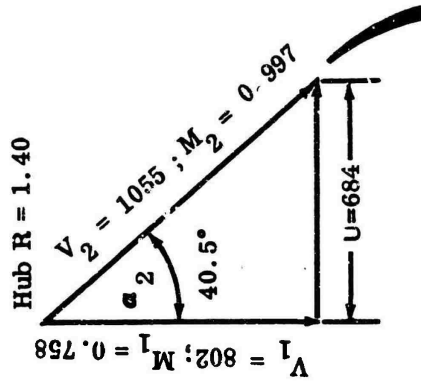
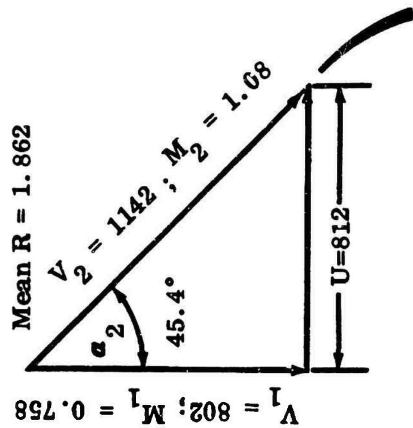
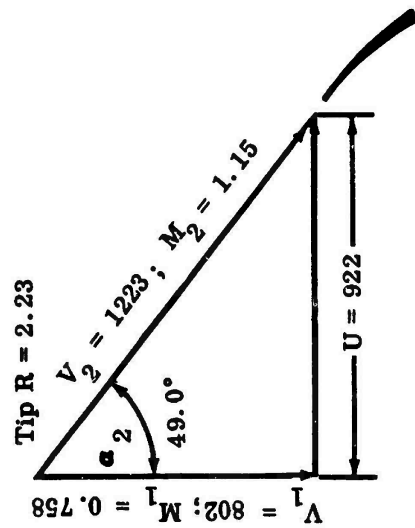
CONFIDENTIAL

TABLE VII		
DESIGN PARAMETERS FOR CASCADE DIFFUSER DC-1		
Number of Vanes	-	31
Chord Length	-	1.20
Passage Depth	-	0.250
Leading Edge Thickness	-	0.040
Airfoil Configuration	-	Flat Plate
Solidity	-	1.17

TABLE VIII	
WORKHORSE IMPELLER DESIGN PARAMETERS	
Type	Radial
Pressure Ratio	12.3
Adiabatic Efficiency (total-total)	87.8 percent
Speed	50.000 rpm
Inlet Relative Mach Number (tip)	1.15
Tip Diameter	9.2 in.
Number of Blades	23
Inducer Hub-to-Tip Diameter Ratio	0.63
Exit Absolute Mach Number	1.27
Inducer-Tip Relative Flow Angle (degrees from axial)	49°
Average Impeller-Tip Flow Angle (degrees from radial)	82.8°
Airflow	2.43 lb/sec

CONFIDENTIAL

Inducer Inlet



157

50,000 rpm
Velocities in fps
Dimensions in inches

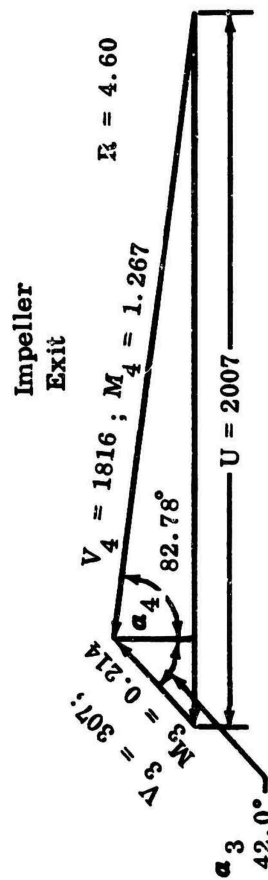


Figure 104. Workhorse Impeller Vector Diagrams.

CONFIDENTIAL

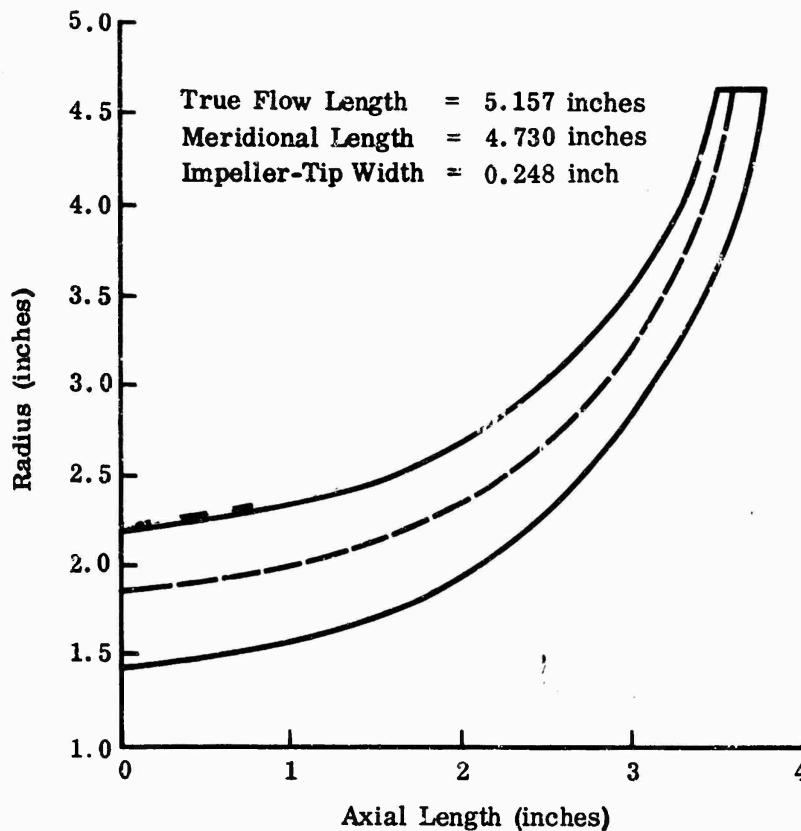


Figure 105. Meridional View of Workhorse Impeller.

2.4 MECHANICAL DESIGN

This section discusses the mechanical design and requirements of the impellers, diffusers, and test rigs required for aerodynamic evaluation of those components. Four impeller configurations were identified for testing: 3 mixed-flow impellers (MF-1, MF-2, and MF-3), and 1 radial-flow impeller (RF-1). It was planned that 1 test rig be designed to accommodate the 4 impellers. Diffuser configurations selected were three vane-island types and one cascade type. Two of the vane-island configurations were 8-channel (DI-1 and DI-2); the other, 16 channel (DI-3). The cascade (DC-1) was a short-chord, single-row design. It was planned that tests of these diffusers would be conducted on a separate rig, with the use of another high-pressure-ratio impeller and interchangeable diffuser sections.

CONFIDENTIAL

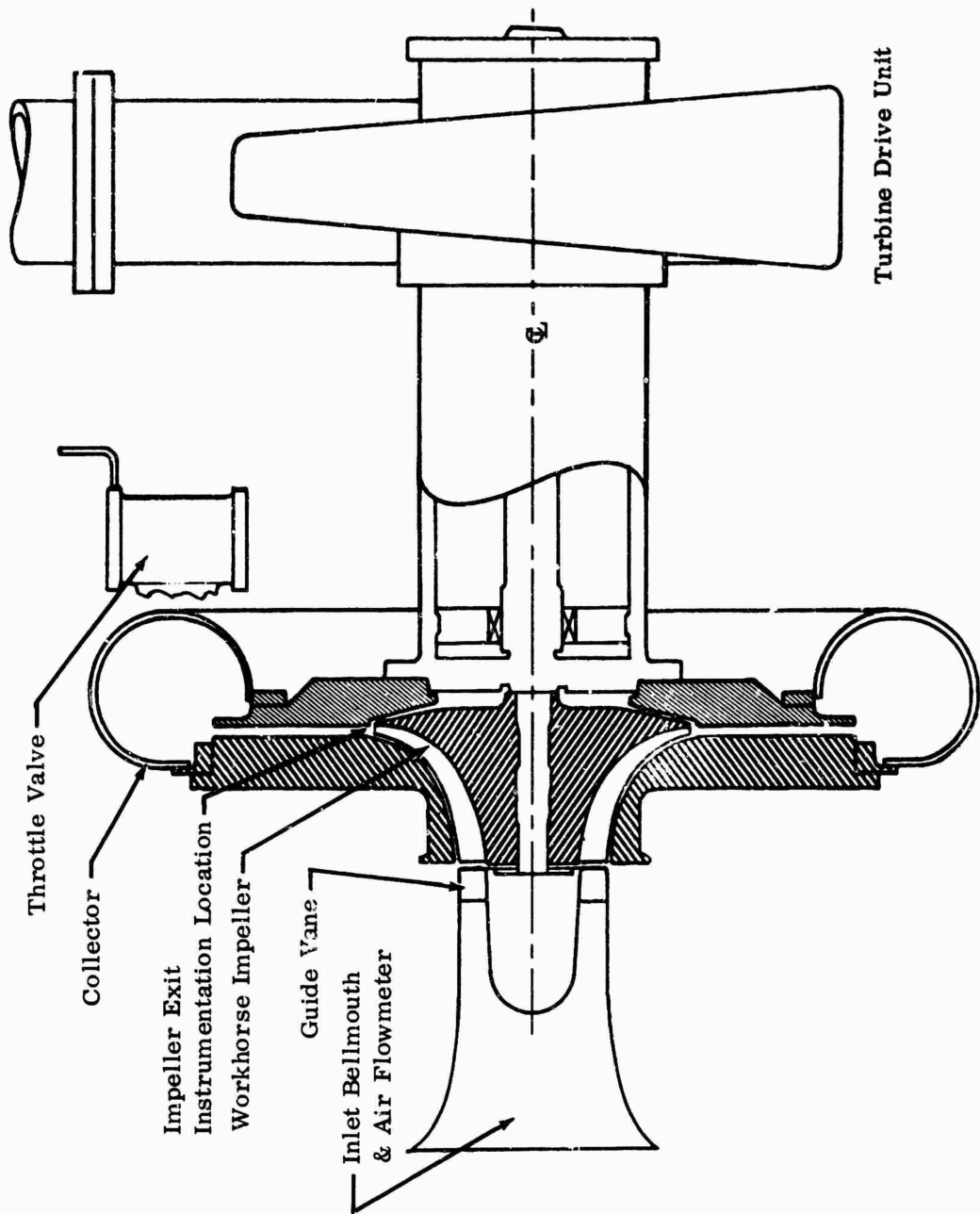


Figure 106. Diffuser Test Rig.

CONFIDENTIAL

2.4.1 IMPELLERS

Figures 107 through 110 show design information relative to overall impeller sizes, blade configurations, impeller hub and tip radii, blade profile, turning schedule, and axial length. The mechanical design objectives and studies are presented in this section of the report, since they are related to the above parameters. The design rpm was dictated by the required blade-tip velocity of 2000 feet per second. However, the impellers were designed to a 10-percent overspeed, which was the basic objective for all components related to the rotor system. Consistent with these objectives, the impeller blades had to be checked in terms of thickness and hub-to-tip thickness ratio to maintain low blockage and allowable stress levels. In addition, the natural frequency spectrum of the blades had to be investigated throughout the operating range. The blade-to-shroud clearance goal was 0.02 inch to avoid mechanical rubs and to minimize flow leakage between the blade tips and shroud. The disk was required to withstand the stresses resulting from the centrifugal and aerodynamic loading of the blades as well as the centrifugal forces of the disk itself.

Allowable stress levels were based on minimum material properties, which accounted for temperatures and vibration levels. A life objective of 10,000 hours was established, and the design impeller-tip speed required a material with a high strength-to-weight ratio. In addition, it was desirable that the selected material have a low coefficient of thermal expansion and that it be machinable by conventional methods.

The principal objective for the test rig was to design test sections for four impellers that were adaptable to one rig. In addition, these test sections had to be instrumented to acquire the aerodynamic data, including:

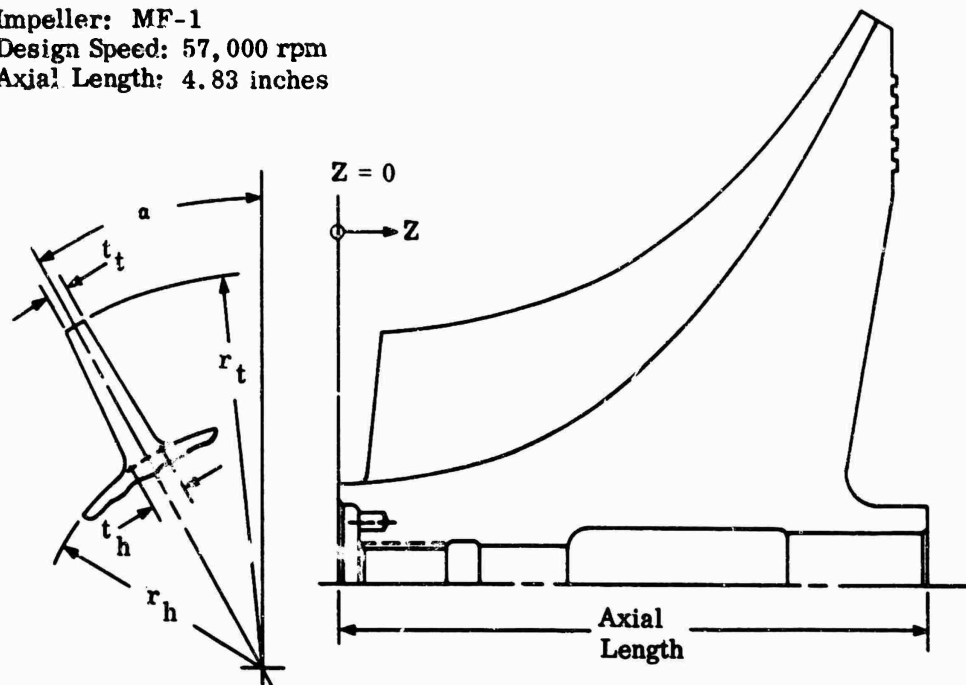
- 1) Static and total pressures and temperatures at the impeller inlet and exit, in the diffuser passage, and in the collector;
- 2) Static pressures along the impeller shroud;
- 3) Impeller-exit flow-angle measurements; and
- 4) Blade-to-shroud clearance and diffuser passage width measurements.

Material Selection

Since all four impellers were designed for approximately the same conditions, the work done and the temperature rise were considered to be the same for mechanical design purposes. It was calculated that maximum material temperatures

CONFIDENTIAL

Impeller: MF-1
Design Speed: 57,000 rpm
Axial Length: 4.83 inches



Blade Geometry

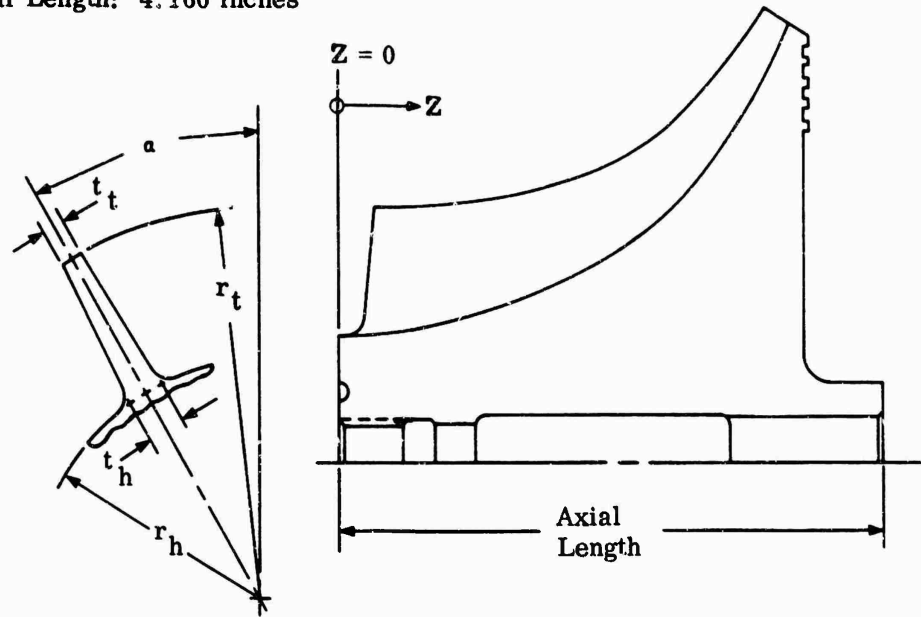
Axial Distance Z	Blade Turning Angle α	Hub Radius r_h	Tip Radius r_t	Hub Thickness t_h	Tip Thickness t_t
0.300	0	0.710	--	0.027	--
0.400	5.0	0.715	1.748	0.052	0.050
0.500	9.8	0.724	1.755	0.073	0.050
0.600	14.4	0.733	1.763	0.090	0.050
0.700	18.7	0.745	1.771	0.104	0.051
0.790	22.6	0.759	1.780	0.113	0.051
1.040	31.8	0.802	1.808	0.126	0.052
1.288	39.7	0.861	1.847	0.135	0.052
1.535	46.4	0.938	1.899	0.139	0.052
1.776	52.4	1.029	1.963	0.142	0.054
1.996	57.1	1.135	2.040	0.143	0.054
2.444	63.9	1.416	2.238	0.138	0.051
2.850	67.5	1.762	2.476	0.122	0.044
3.224	69.0	2.162	2.772	0.104	0.040
3.410	69.3	2.389	2.945	0.096	0.039
4.012	69.3	3.268	3.690	0.066	0.029
4.246	69.3	3.668	4.036	0.053	0.025
4.400	69.3	3.950	--	0.045	--

Figure 107. Aerodynamic Design Information.

CONFIDENTIAL

CONFIDENTIAL

Impeller: MF-2
Design Speed: 73,000 rpm
Axial Length: 4.160 inches



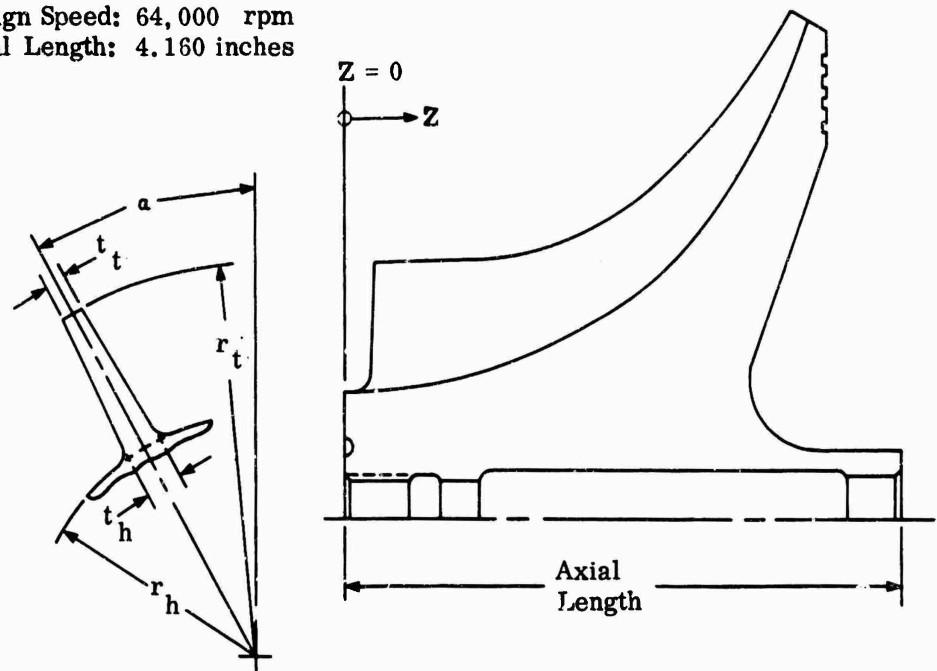
Blade Geometry

Axial Distance Z	Blade Turning Angle α	Hub Radius r_h	Tip Radius r_t	Hub Thickness t_h	Tip Thickness t_t
0.200	0	0.910	--	0.031	--
0.300	5.4	0.913	1.806	0.063	0.050
0.400	10.5	0.919	1.815	0.093	0.050
0.500	15.2	0.926	1.823	0.115	0.051
0.592	19.4	0.935	1.831	0.133	0.051
0.700	24.0	0.951	1.840	0.144	0.052
0.800	27.9	0.969	1.848	0.152	0.053
0.994	34.5	1.015	1.865	0.163	0.054
1.200	40.8	1.079	1.887	0.168	0.057
1.480	47.9	1.179	1.931	0.172	0.058
1.759	52.9	1.294	1.994	0.169	0.053
2.105	56.7	1.487	2.127	0.153	0.045
2.435	58.2	1.738	2.338	0.129	0.040
2.724	58.5	2.030	2.601	0.107	0.034
2.973	58.5	2.344	2.900	0.090	0.030
3.191	58.5	2.694	3.219	0.073	0.025
3.391	58.5	3.105	--	0.054	--

Figure 108. Aerodynamic Design Information

CONFIDENTIAL

Impeller: MF-3
Design Speed: 64,000 rpm
Axial Length: 4.160 inches



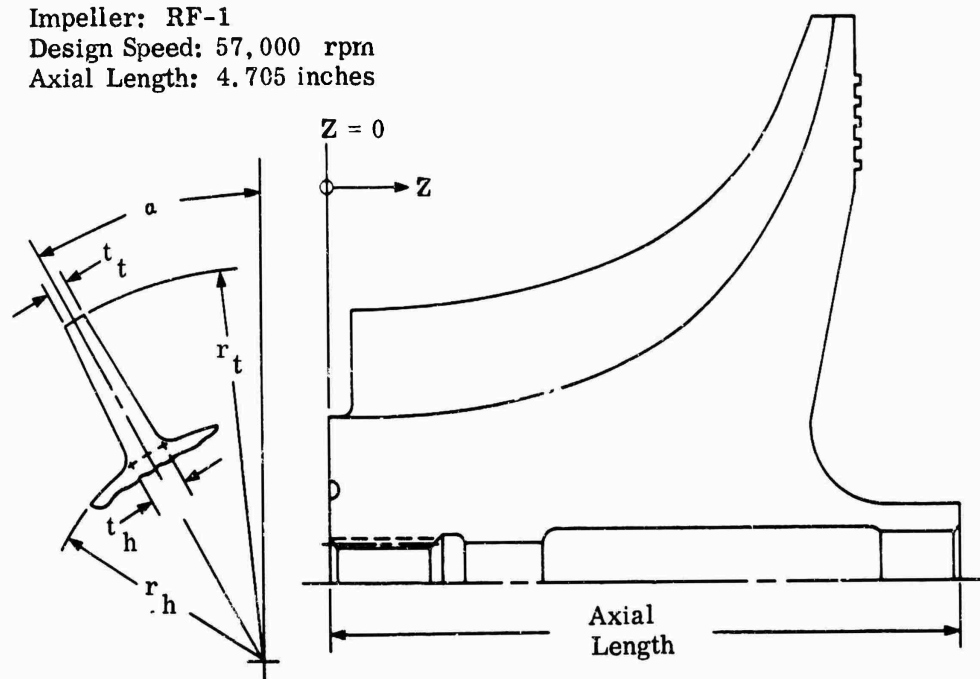
Blade Geometry

Axial Distance Z	Blade Turning Angle α	Hub Radius r_h	Tip Radius r_t	Hub Thickness t_h	Tip Thickness t_t
0.190	0	0.910	1.800	0.043	0.044
0.390	8.9	0.932	1.800	0.098	0.051
0.590	16.3	0.955	1.800	0.133	0.054
0.789	22.4	0.983	1.804	0.150	0.054
0.987	27.5	1.020	1.819	0.150	0.054
1.167	31.1	1.064	1.845	0.157	0.055
1.372	34.6	1.131	1.888	0.158	0.055
1.618	37.5	1.232	1.966	0.164	0.053
1.914	39.4	1.391	2.095	0.164	0.052
2.102	39.7	1.515	2.194	0.156	0.052
2.422	39.7	1.788	2.424	0.139	0.048
2.701	39.7	2.103	2.690	0.121	0.042
2.944	39.7	2.456	3.000	0.103	0.036
3.147	39.7	2.813	3.306	0.086	0.031
3.325	39.7	3.178	3.584	0.067	0.027
3.480	39.7	3.493	--	0.054	--

Figure 109. Aerodynamic Design Information.

CONFIDENTIAL

Impeller: RF-1
Design Speed: 57,000 rpm
Axial Length: 4.705 inches



Distance Z	Turning Angle α	Radius r_h	Radius r_t	Thickness t_h	Thickness t_t
0.200	0	1.179	1.948	0.054	0.045
0.300	4.2	1.180	1.949	0.065	0.044
0.400	8.2	1.181	1.951	0.077	0.043
0.600	15.6	1.187	1.957	0.110	0.039
1.000	27.7	1.215	1.981	0.145	0.035
1.300	37.3	1.272	2.034	0.157	0.031
1.783	44.4	1.364	2.120	0.165	0.029
2.160	49.6	1.500	2.244	0.165	0.027
2.515	52.9	1.676	2.414	0.155	0.026
2.838	54.9	1.909	2.623	0.136	0.026
3.113	55.6	2.191	2.868	0.118	0.025
3.348	55.7	2.526	3.195	0.113	0.025
3.520	55.7	2.882	3.592	0.104	0.025
3.676	55.7	3.354	4.040	0.090	0.025
3.862	55.7	4.040	4.040	0.045	0.045

Figure 110. Aerodynamic Design Information.

CONFIDENTIAL

CONFIDENTIAL

would be about 460°F near the tip and about 130° to 300°F at the bore. Figures 111 and 112 show strength-to-weight ratio, modulus of elasticity, and coefficient of thermal expansion for Rene' 41, Waspaloy, 2014T-6 aluminum, and 6A1-4V titanium. A comparison of these material properties showed a marked decrease in the strength of aluminum at the design temperature. Titanium showed the best strength-to-weight ratio and the lowest coefficient of thermal expansion. Availability and machinability of titanium were approximately equal to the high-temperature super alloys. Although the modulus of elasticity for titanium was about half that of Rene' 41 and Waspaloy, the better strength-to-weight ratio of titanium compensated for this difference. Therefore, titanium was chosen for the impellers to be used on this program. The importance of the strength-to-weight ratio can be demonstrated by the basic centrifugal stress relationship. For a given blade geometry and rotor speed, centrifugal stress is directly proportional to the material density, so that

$$S = \gamma r \omega^2 \quad (20)$$

Comparing titanium and Rene' 41,

$$\frac{S_t}{S_r} = \frac{\gamma_t}{\gamma_r} = \frac{0.160}{0.398} = 0.536 \quad (21)$$

where, for a given geometry,

S_t = yield stress for titanium (psi)

S_r = yield stress for Rene' 41 (psi)

γ_t = density of titanium (lb/in.³)

γ_r = density of Rene' 41 (lb/in.³)

Therefore, the stress in titanium would be approximately half of that in Rene' 41 or similar steels.

Impeller Stress

Each impeller was analyzed to achieve the best balance between allowable stress levels and the desired aerodynamic configuration. The same stress analysis

CONFIDENTIAL

CONFIDENTIAL

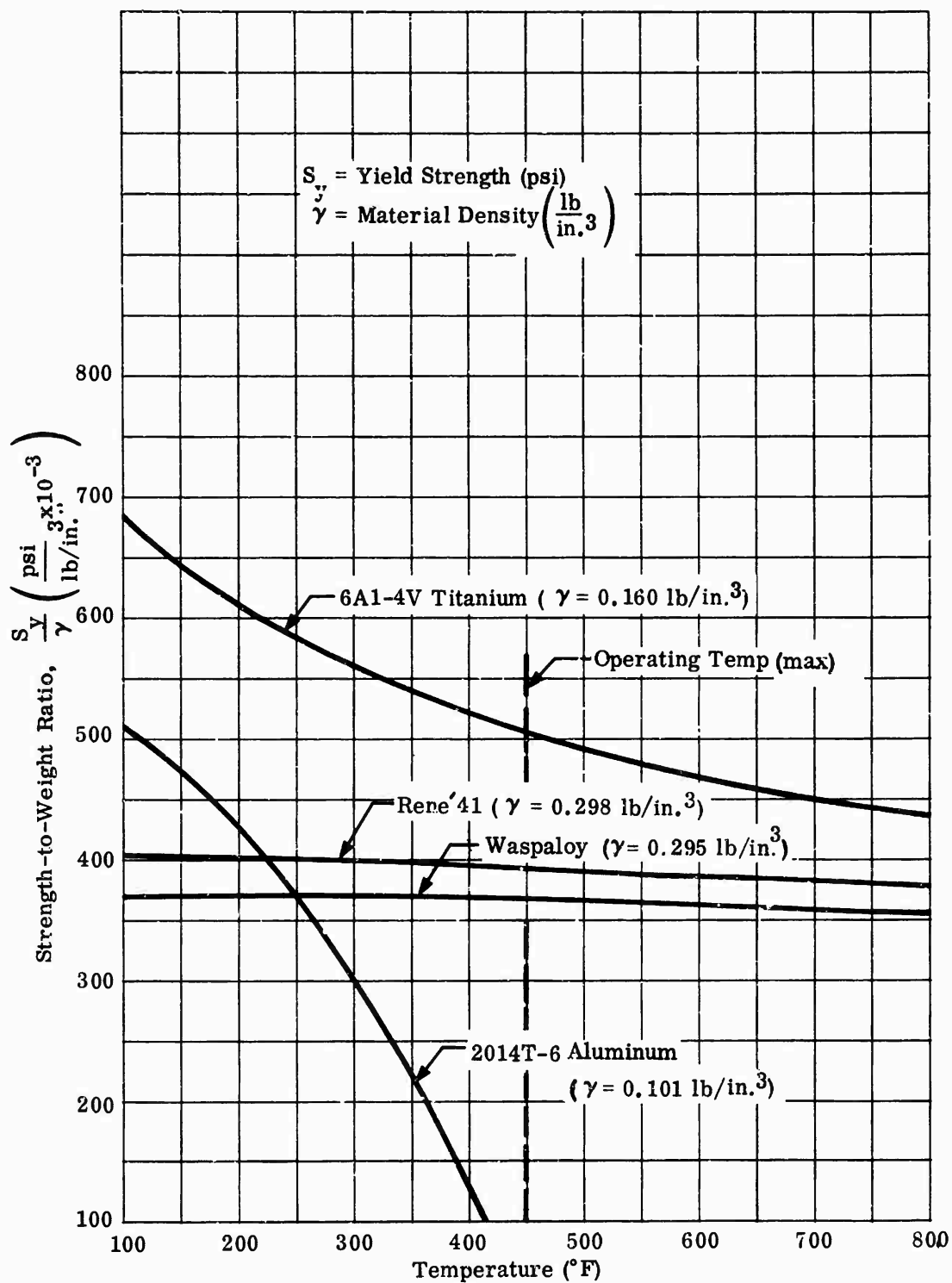


Figure 111. Strength-to-Weight Ratio Versus Temperature.

CONFIDENTIAL

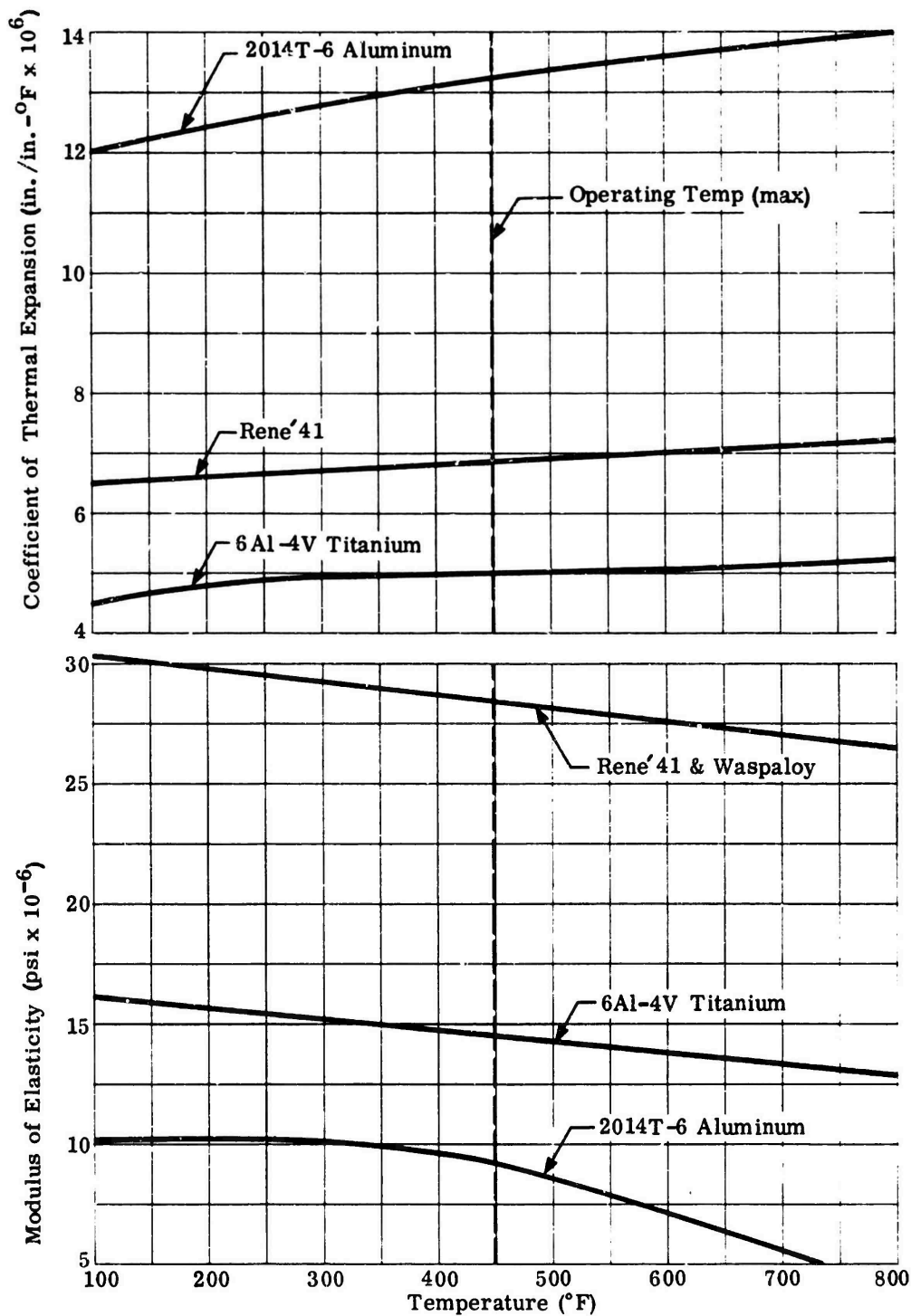


Figure 112. Modulus of Elasticity and Coefficient of Thermal Expansion Versus Temperature.

CONFIDENTIAL

procedure was applied to each impeller and consisted of 2 principal parts: the blade analysis and the disk analysis. The blade analysis was performed first because disk stresses were dependent on the blade configuration. Blade sections were stress-checked, and the disk shape was estimated to serve as an analysis starting point. Temperature profiles throughout the impeller were obtained by calculating the relative temperature rise along the flow path and the temperature at the inlet hub. A temperature of 300°F was assumed at the aft hub. An example of the temperature profiles is shown in Figure 113. Impeller stress levels and factors of safety were determined using minimum physical properties and material data given in Figures 114 through 117. Minimum allowable factors of safety for the blades and the disks were established for 2 conditions: steady-state at design speed, and momentary 10-percent overspeed, as shown in Table IX.

TABLE IX			
MINIMUM FACTORS OF SAFETY			
Element	Steady-State Condition	Momentary Overspeed Condition	
	SF_s	SF_y	SF_u
Blade	1.25	1.15	1.25
Disk	1.25	1.10	1.25
SF_s = Factor of safety based on rupture stress or 0.2% yield, whichever is smaller.			
SF_y = Factor of safety based on 0.2% yield stress.			
SF_u = Factor of safety based on ultimate stress.			

Impeller blade factors of safety included allowable vibratory stresses of 20,000 psi for the inducer section (25 percent of the hub meridional length) and 12,000 psi for the radial section. Because of limited experience with titanium for high-speed rotors, these values were based on the allowable vibratory stresses used for steel; they are considered to be conservative. A lower vibratory stress was allowed for the radial section because of the higher mean stress and temperature, as illustrated by the Goodman diagrams in Figure 118.

CONFIDENTIAL

CONFIDENTIAL



CONFIDENTIAL

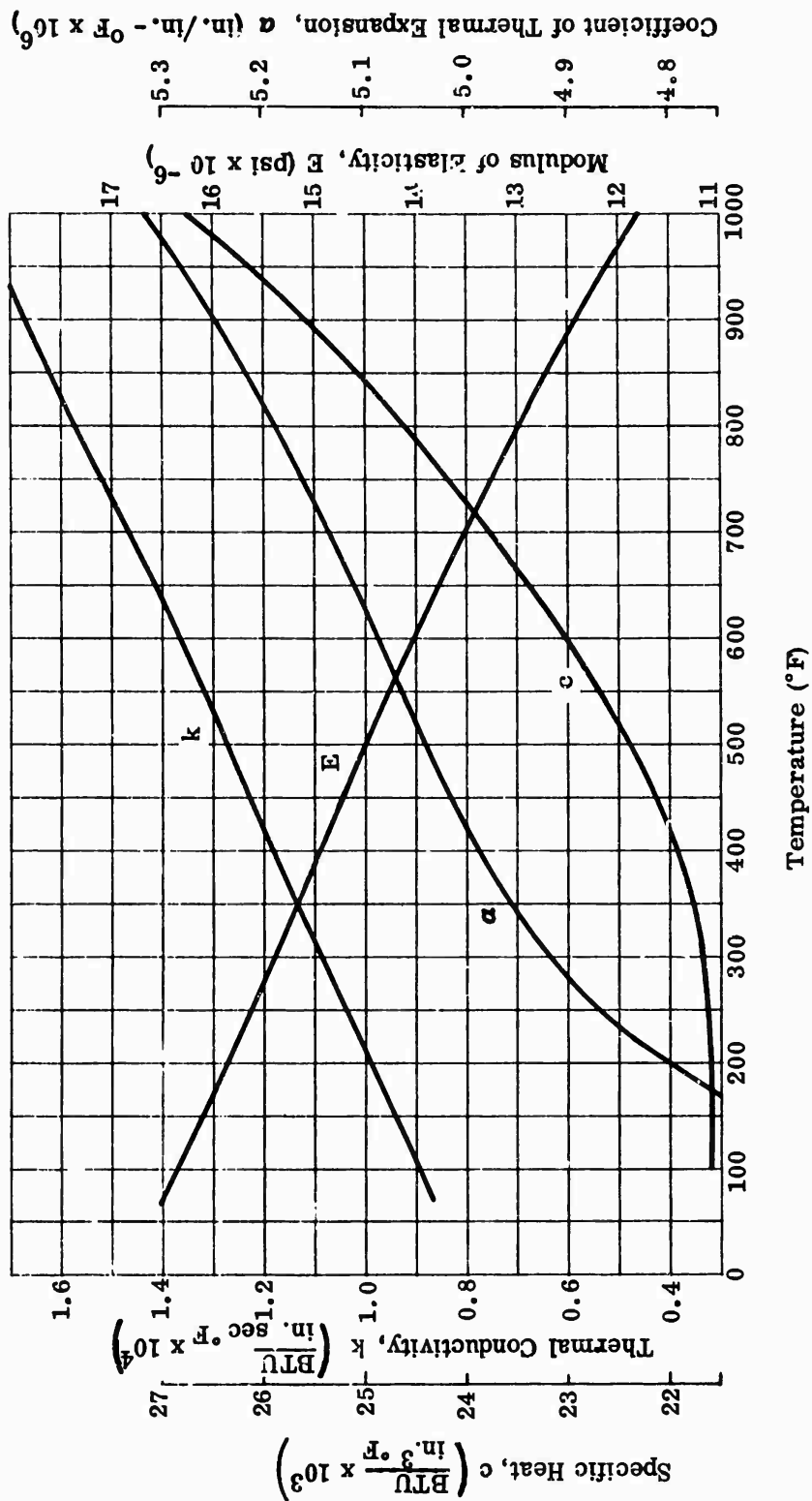


Figure 114. Physical Properties of 6Al-4V Titanium Versus Temperature.

CONFIDENTIAL

CONFIDENTIAL

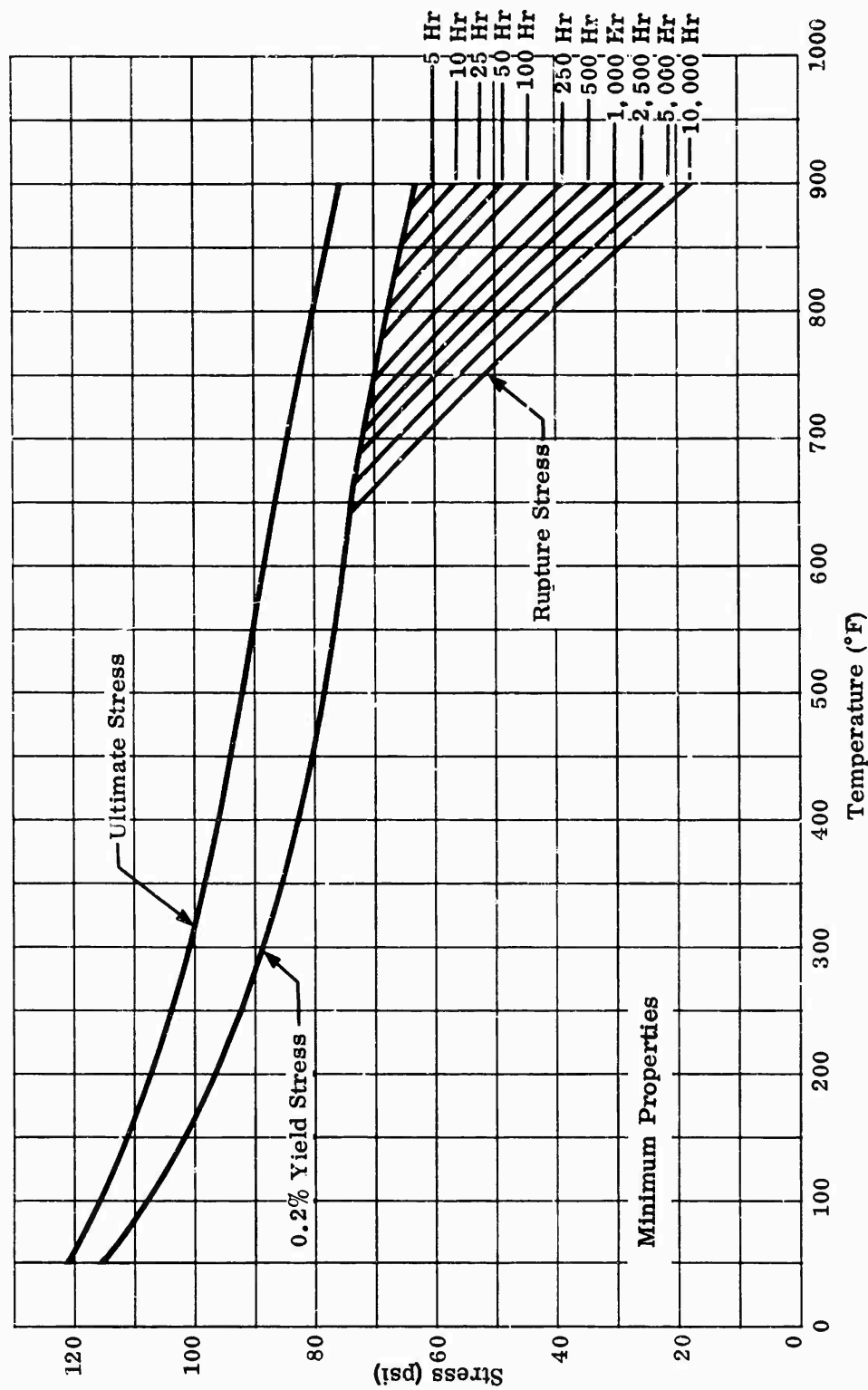


Figure 115. Stress Versus Temperature for 6Al-4V Titanium.

CONFIDENTIAL

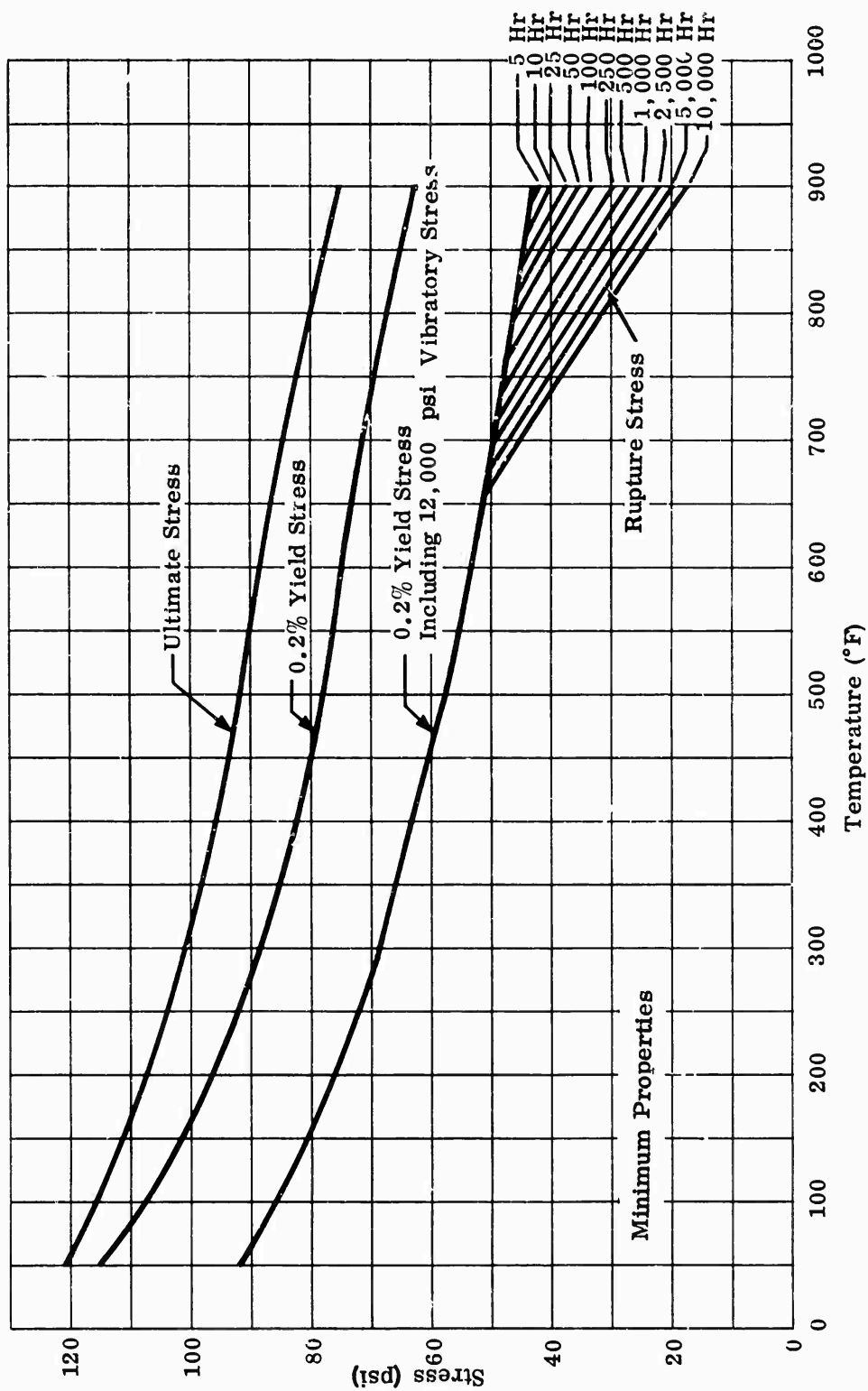


Figure 116. Stress Versus Temperature for 6Al-4V Titanium.

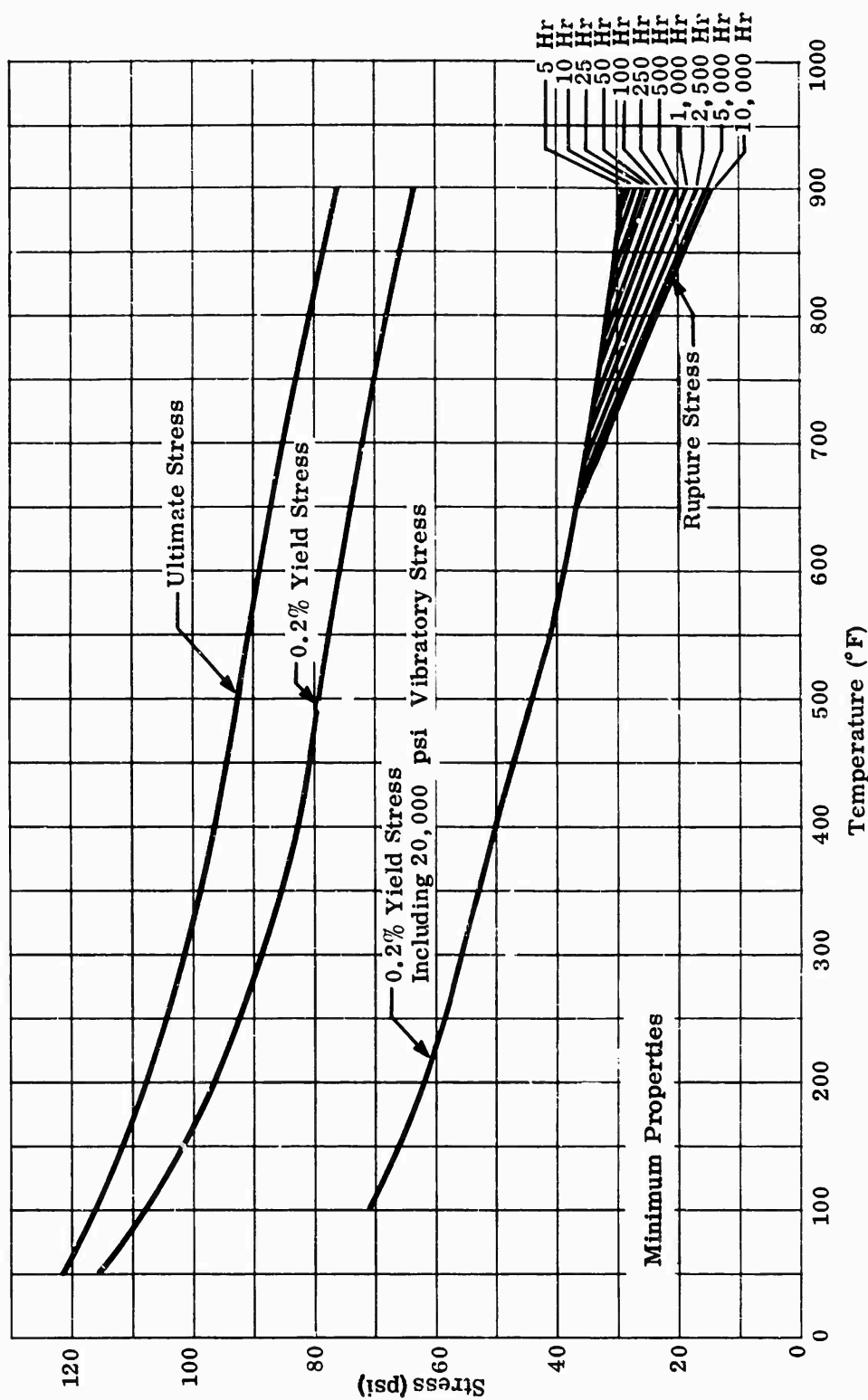


Figure 117. Stress Versus Temperature for 6Al-4V Titanium.

CONFIDENTIAL

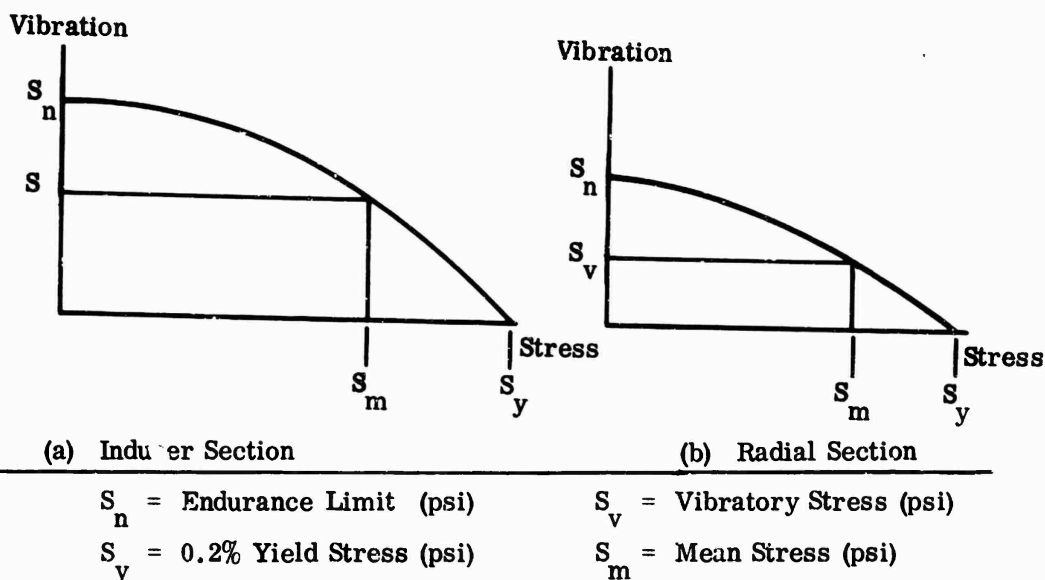


Figure 118. Goodman Diagrams.

The rupture-stress region of titanium was in a temperature range well above the maximum impeller metal temperature, which ensured an unlimited design life in this respect.

Blade Stress

The blade sections were analyzed for centrifugal loading and for the natural frequency spectrum. Bending stress at the blade root, imposed by aerodynamic loading, was about 2000 psi at the overspeed condition and was ignored. The centrifugal stress was determined by dividing the blade into segments in a plane normal to the impeller axis and by applying conventional centrifugal force and stress calculation methods. Blade natural frequency and rotor-excitation speed were calculated; the predicted natural frequency spectrum was plotted versus rotational speed on a Campbell diagram. Rotor order for the frequency spectrum and mode of blade vibration are identified at the various rotor speeds within the operating range. The Campbell diagram for MF-1 is shown in Figure 119. Blade section adjustments were made to change the natural frequency if an excitation speed coincided with a prime test operation speed. The natural frequency analysis and the corresponding relative displacements were determined by representing the actual blade as a system of point masses connected by weightless flat triangular plates of constant thicknesses. All node points were allowed to vibrate in three translatory degrees of freedom, except those on the fixed boundary formed by the disk, which were allowed no freedom. The node-point coordinates, node masses, plate thicknesses, and the normal vectors to the blade in a node

CONFIDENTIAL

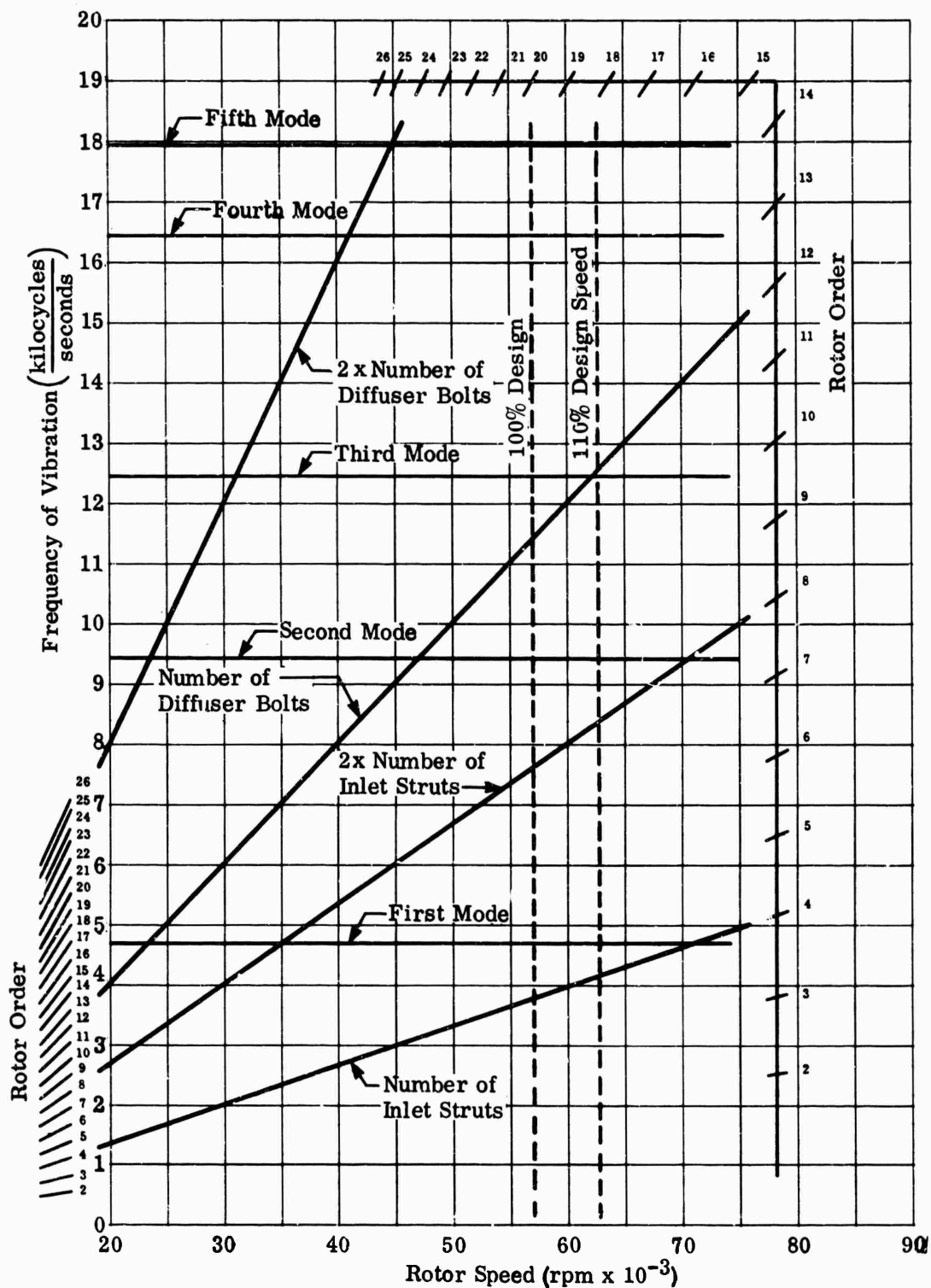


Figure 119. Sample Campbell Diagram (MF-1).

CONFIDENTIAL

CONFIDENTIAL

point were determined by a computer program developed by the contractor. These data, together with the material modulus of elasticity, were used as the input for a second program that computed the natural frequencies and relative displacements. Both programs can be run simultaneously on a computer. Adjustments for either mechanical or aerodynamic reasons required iterative solution.

Disk Stress

The structural integrity of the impeller disk was verified by comparing the applied average force to the allowable average force in cylindrical sections within the disk. From this comparison, factor of safety, SF_s , for each section was determined as follows (see Figure 120 for disk section):

$$SF_s = \frac{F_{tw}}{F_f} = \frac{F_{td} + F_{tt}}{F_f} \quad (22)$$

where:

F_{tw} = total centrifugal force including blades and disk

F_{td} = force component of the disk itself

F_{tt} = force component due to blade loading

F_f = failure force

The following equations give F_{td} and F_f :

$$F_{td} = \frac{2 \gamma \omega^2}{g} \int_{r_b}^{r_s} r^2 t \, dr = \frac{2 \gamma \omega^2}{g} \sum_{v=1}^n r_v^2 t_v \Delta r_v \quad (23)$$

CONFIDENTIAL

$$F_f = (0.81) (2) \int_{r_b}^{r_s} S_f t dr = 1.62 \sum_{v=1}^n S_{f,v} t_v \Delta r_v \quad (24)$$

where:

$$\gamma = \text{density} \left(\frac{\text{lb}}{\text{in.}^3} \right)$$

$$\omega = \text{rotational speed} \left(\frac{\text{radians}}{\text{sec}} \right)$$

$$g = \text{gravitational constant} \left(\frac{\text{ft}}{\text{sec}^2} \right)$$

$S_{f,v}$ = failure stress corresponding to the temperature in the center of segment v (psi).

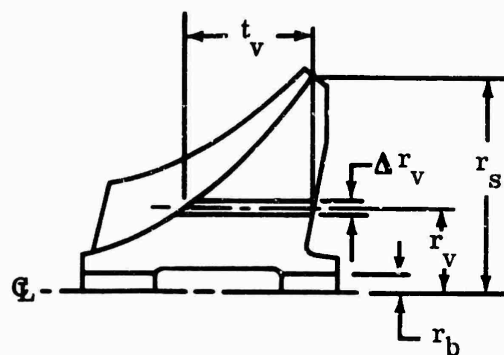


Figure 120. Disk Sections for Stress Analysis.

The 0.81 factor in equation (24) is based on an average of previous spin-pit tests.

To avoid elastic deformation of the impeller bore with an increase of speed, which would cause the bore to loosen on the shaft, the impeller was proof-spun at a speed that would produce plastic deformation and a permanent compressive stress at the impeller bore. Further, the aft hub was extended beyond the main disk body to provide a pinching action, as shown in Figure 121.

Weight[†], mass moment of inertia, and minimum factors of safety for the four impellers are shown in Table X.

CONFIDENTIAL

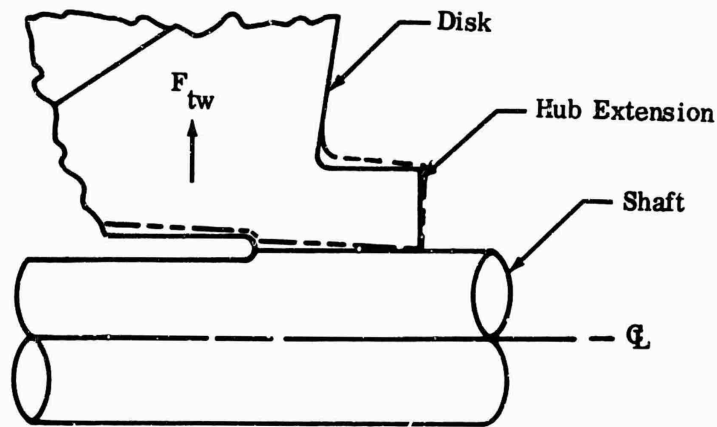


Figure 121. Hub Extension.

TABLE X					
IMPELLER STRESS ANALYSIS RESULTS					
Impeller	Weight (lb)	I_m (lb-in. sec ²)	$(SF_y)^*$ blade	(SF_y) disk	(SF_u) disk
MF-1	8.40	0.0961	3.42	1.44	1.62
MF-2	5.24	0.0347	1.95	1.34	1.53
MF-3	5.30	0.0450	3.07	1.80	2.02
RF-1	7.20	0.0699	2.20	1.74	1.99
<p>*(SF_y) blade includes vibratory stresses.</p> <p>SF_y and SF_u are the minimum safety factors.</p> <p>I_m is the mass moment of inertia.</p>					

Test Sections

Four separate test sections were required because of differences in size and shape of the impellers. In addition to the impellers, the test sections included those parts related to the aerodynamics; i.e., the inlet, the front cover (with liner), the backplate, and the collector (Figure 122). The front cover extended from the impeller inlet to the collector, forming the front shroud and 1

CONFIDENTIAL

CONFIDENTIAL

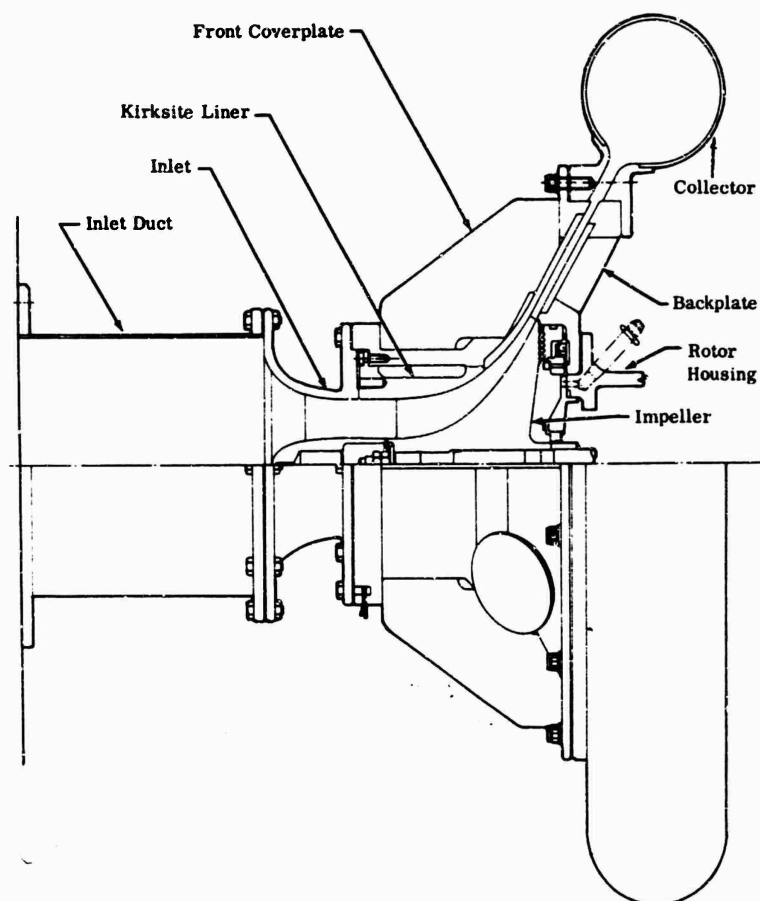


Figure 122. MF-1 Test Section.

vaneless-diffuser wall. The backplate formed the other wall and attached to the rotor housing, providing the structural base for the test section. The compressor collector formed the structural link between the backplate and front cover. The inlet extended from the front cover to the air-intake plenum chamber. Airfoil struts supported the impeller-hub fairing. All 4 front covers were designed with a Kirksite liner-insert to provide an abradable surface. Its purpose was to allow close blade-to-shroud clearances without risking damage to the impeller. The RF-1 front cover was designed as a 1-piece plate with 3 stiffening webs on the exterior. The mixed-flow impeller front covers were designed as welded or brazed assemblies. The RF-1 backplate was a 1-piece design; whereas, the mixed-flow backplates were 3-piece weldments or brazements. Eight stiffening webs were added to each plate for rigidity. A minimum section thickness of 0.25 inch was maintained for front covers and backplates to facilitate installation of the instrumentation and other equipment. The material selected for the front cover and backplate was AISI 321 stainless steel for the first design (MF-1) because of its corrosion resistant

CONFIDENTIAL

CONFIDENTIAL

properties at the high (750°F) design temperature. Fabrication difficulties with this material negated this advantage, however, and AISI 4130/4340 was designated for subsequent designs.

One collector was designed to function both as a pressure vessel and as the structural tie between the front cover and backplate for all test sections. It was a formed torus with an annular opening adaptable to each diffuser-section discharge. Rigidity of the unit was provided by pins across the opening, brazed in the opposing collector flanges. Two ducts, leading from the rear side of the collector, were joined in a common exhaust duct ahead of an airflow control valve.

Details of test section component construction and assembly are given in Section 3.0 of this report.

Rotor System

The rotor design objective was to provide a system common to all four impellers. Because of the wide range in design speeds (55,000 to 74,000 rpm), 2 rotors were required. One was common to the RF-1 and MF-1 impellers, and the second was for MF-2 and MF-3. However, all were adaptable to the same housing and bearing mounts. In addition, smaller shaft and bearing sizes were required for the higher rotational speeds of the MF-2 and MF-3. Both rotors were supported by 2 high-speed ball bearings, with the impeller cantilevered on the forward end of the shaft. Power was supplied from the opposite end by a turbodriven unit through a flexible coupling, as shown in Figure 123. The bearing mounts were flexible to minimize the effects of increased radial loads that would be encountered at the rotor critical speeds.

Before selecting a test-section design, three rotor configurations were studied (Figure 124). The first 2 systems, Configurations A and B, were straddle-mounted with the impeller between 2 bearings. For Configuration A, a one-piece shaft passed through the impeller; for B, a stub shaft was attached to each end of the impeller. Configuration C was the cantilevered system selected for the rig. Rotor Configurations A and C were analyzed for the first 4 critical speeds as a function of bearing support stiffness rates, and the results are shown in Figures 125 and 126. Configuration B was not analyzed because of its similarity to A. The critical-speed analysis was performed with the aid of a digital computer program developed by the contractor for analysis of all rotor types; it also determined the mode shapes of the shaft deflections. In this program, bearing stiffness could be assumed (1) as constant with speed for any given spring rate (such as in this case), (2) to vary linearly with speed, or (3) to be a combination of the 2. The method of calculation assumed no damping or deflections due to shear, and bearing supports were taken as ideal linear springs. Only synchronous whirl modes were considered by this program. The inputs required were

CONFIDENTIAL

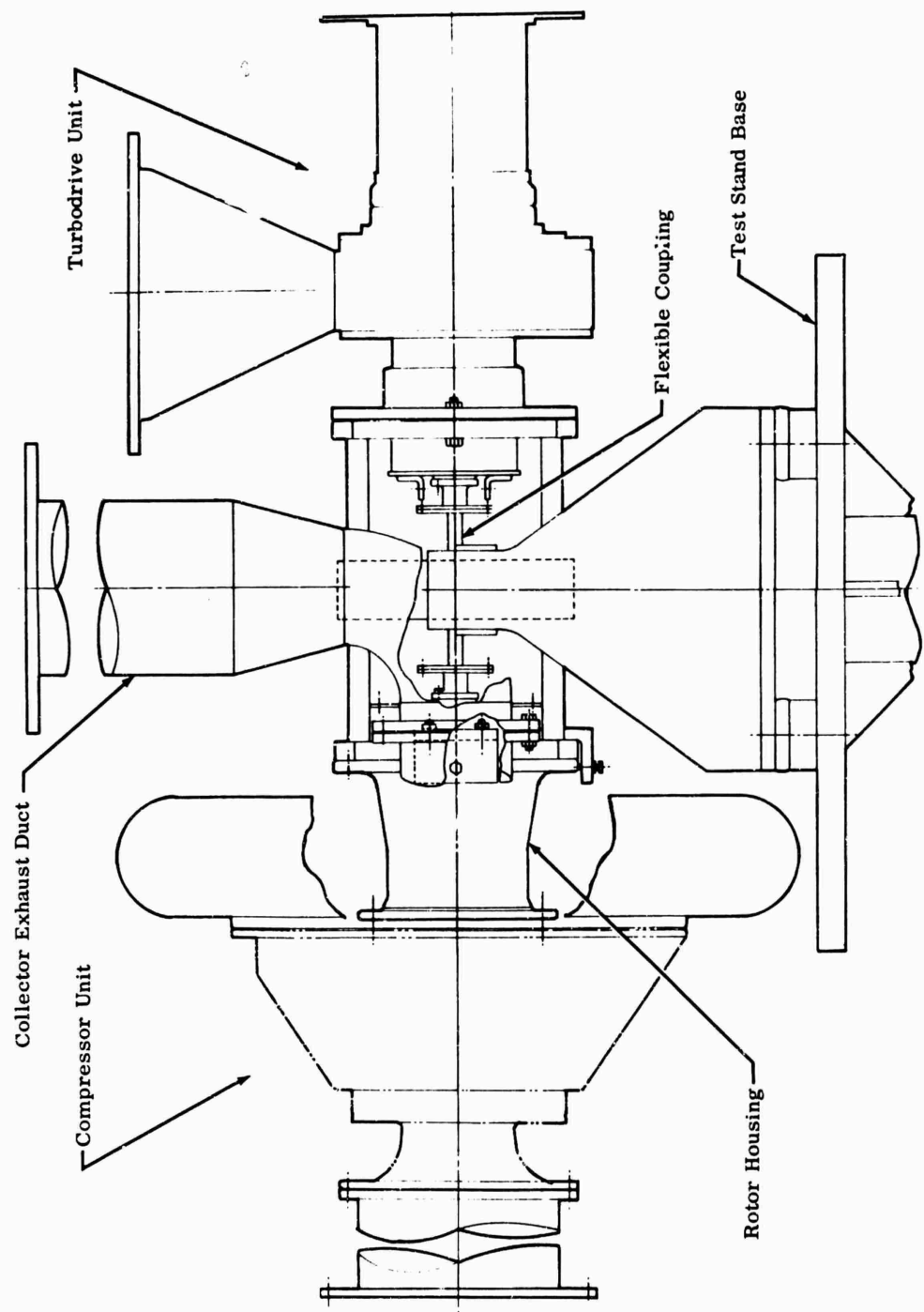


Figure 123. Impeller Test Rig.

CONFIDENTIAL

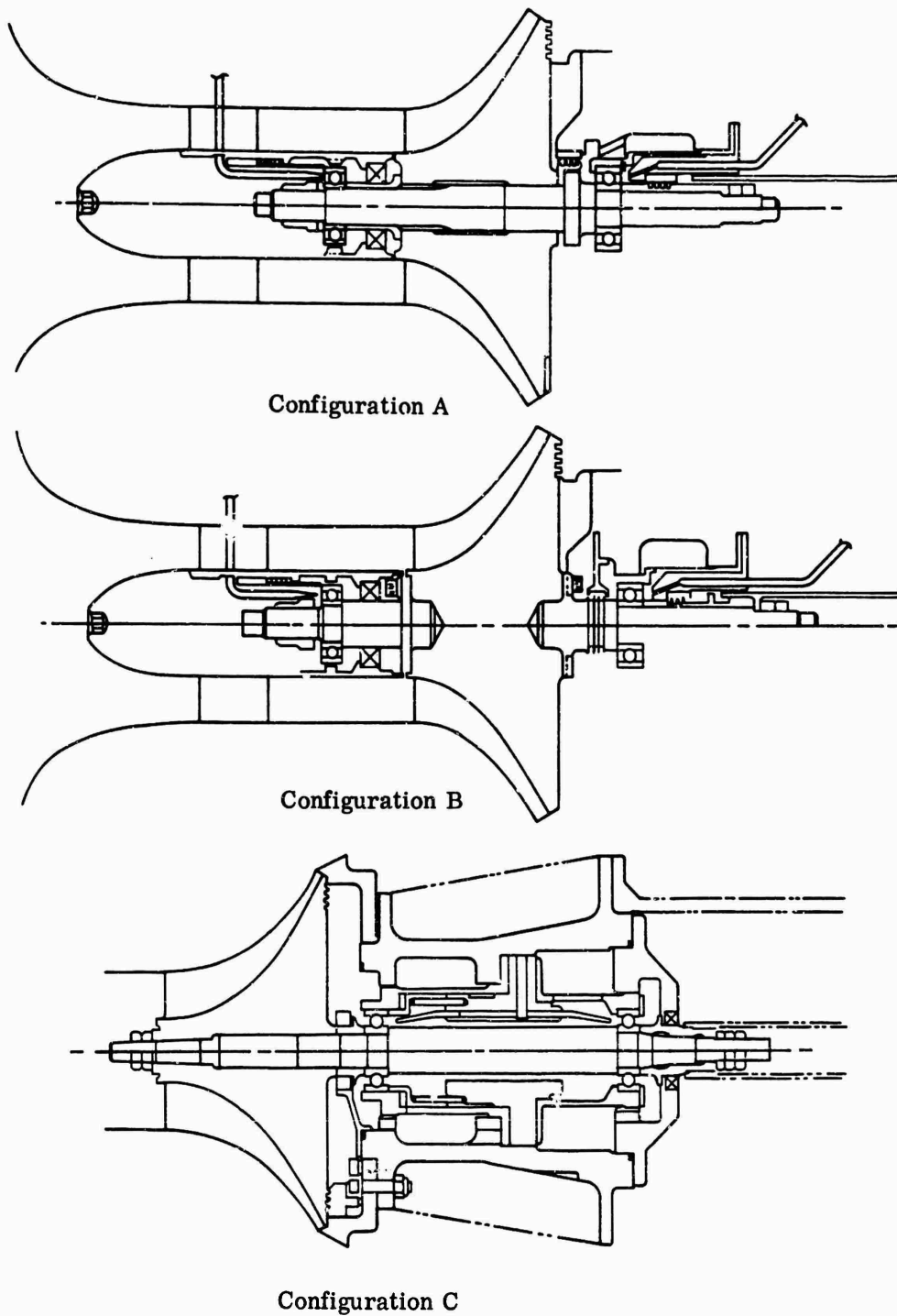


Figure 124. Impeller Shaft Arrangements.

CONFIDENTIAL

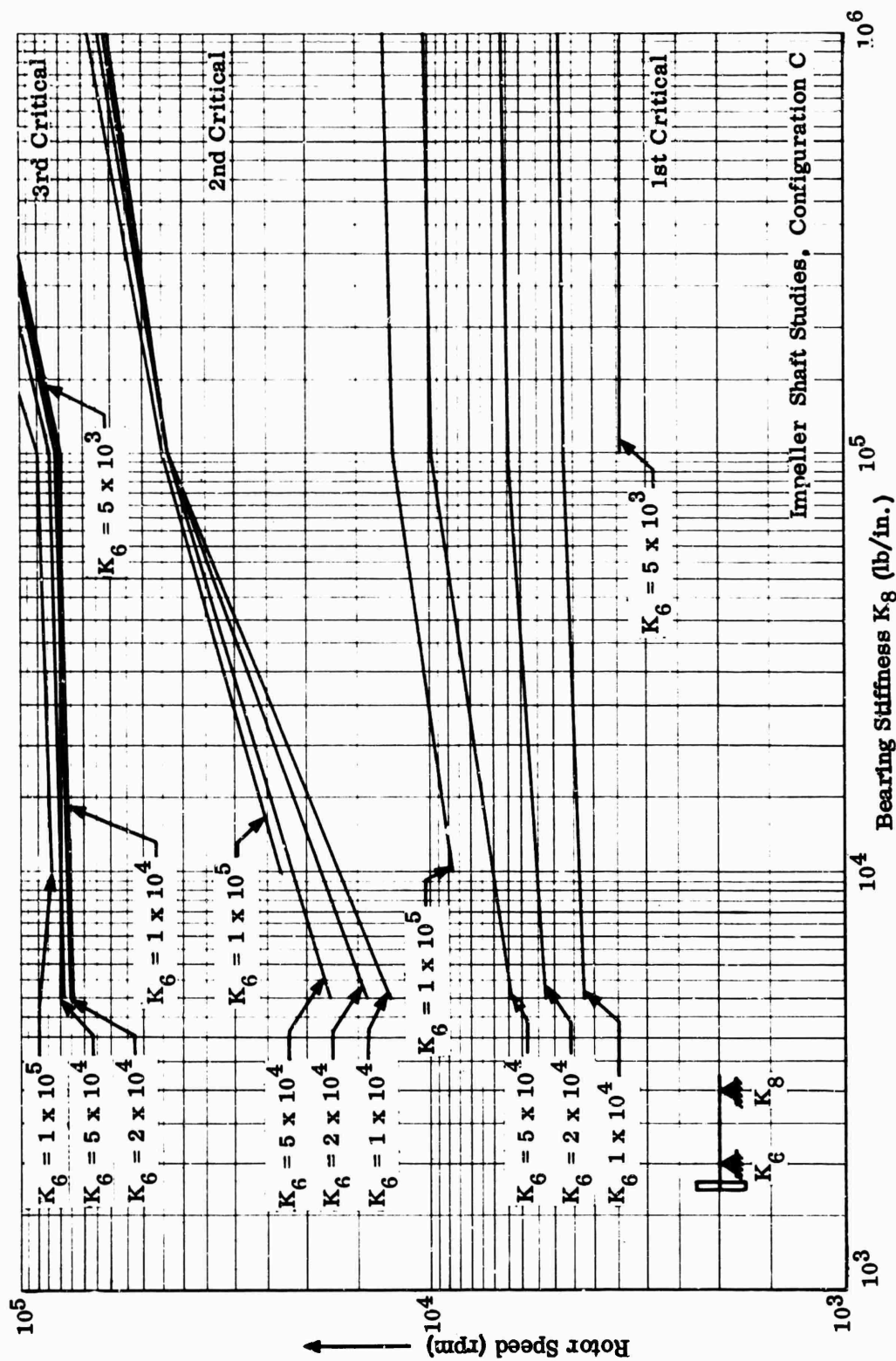


Figure 125. Critical Speed Versus Bearing Stiffness.

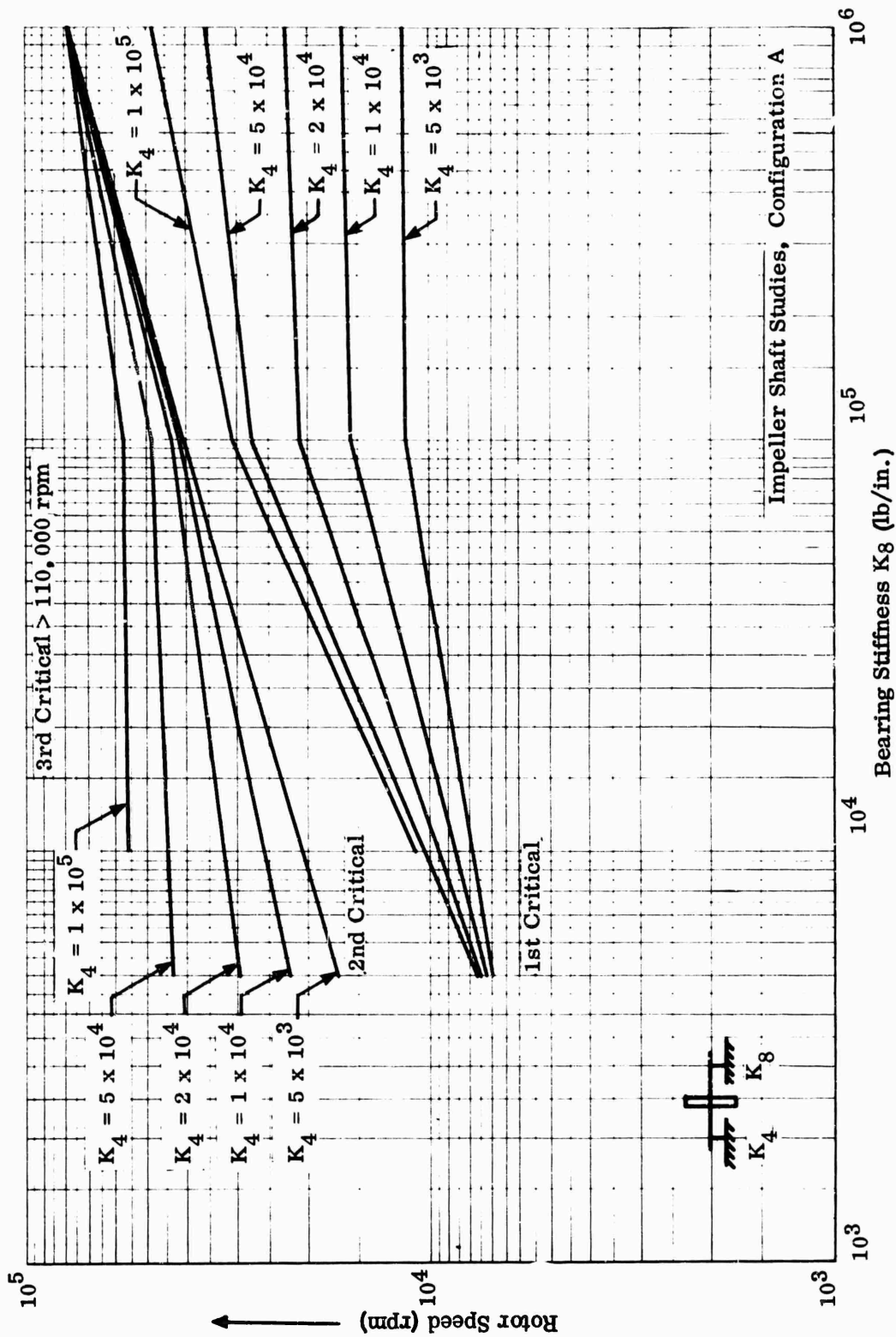


Figure 126. Critical Speed Versus Bearing Stiffness.

CONFIDENTIAL

area and polar moments of inertia, modulus of elasticity, support stiffness coefficients, and mass at 10 stations along the rotor. These stations were located at the centers of large masses (such as at the impeller) and at bearing locations, with the remaining stations being distributed as evenly as possible (Figure 127). To obtain a mathematical formulation for the critical speeds of the rotor, it was assumed that a balanced, undamped rotor was deformed in a single plane in a natural mode shape, which rotated about the axis at rotor speed. This condition was expressed in terms of rotor deflections and corresponding critical speeds. A study of the results indicated that Configuration C (Figure 124) with front- and rear-bearing mount spring rates of 10,000 pounds per inch would be the best design from the rotor dynamics standpoint. This design would allow operation between the second and third criticals, which were 17,000 and 80,000 rpm, respectively. Configuration A was a more rigid system with a third critical of 110,000 rpm. The second critical, however, was broad and projected into the operating range. A spring rate of 10,000 pounds per inch gave first, second, and third critical speeds of 8,600, 25,500, and 115,000 rpm. For Configuration C, the cantilevered design, the impeller could be removed from the shaft without disassembly of the rotor system; and the impeller inlet was not limited in size nor obstructed by bearing mounts forward of the inlet. The predicted critical speeds for MF-1 and RF-1 are shown in Table XI.

The specific analysis of the MF-2 and MF-3 rotors was directed toward resolving a shaft that would adapt to the configuration selected for the other 2 impellers by adjusting the shaft size. Results of this analysis are shown in Figure 128. With a bearing spring rate of 10,000 pounds per inch, the critical speeds for MF-2 were 13,000, 36,000, and 102,000 rpm for the 0.70-inch-diameter shaft, which was selected as being most suitable for this application.

The actual critical speeds were found to be approximately 30 percent lower than the calculated values for RF-1 and MF-1 during test-rig operation. The third (bending) critical for MF-1 was 56,000 rpm and for RF-1 was 48,000 rpm, both of which were in the operating range. A study made to determine the reason for the discrepancies (Appendix III) showed that the calculations required a more discrete distribution of the mass sections used as computer inputs. The large mass sections were lumped as 1 section, allowing more sections to define the more flexible portions of the shaft. New calculations made with refined inputs provided the results shown in Table XI.

These calculations agreed well with the RF-1 and MF-1 critical-speed values determined during rig operation. Critical speeds for MF-2 and MF-3 could not be verified because they were not tested owing to fabrication and proof-spinning problems encountered (Appendix IV).

CONFIDENTIAL

CONFIDENTIAL

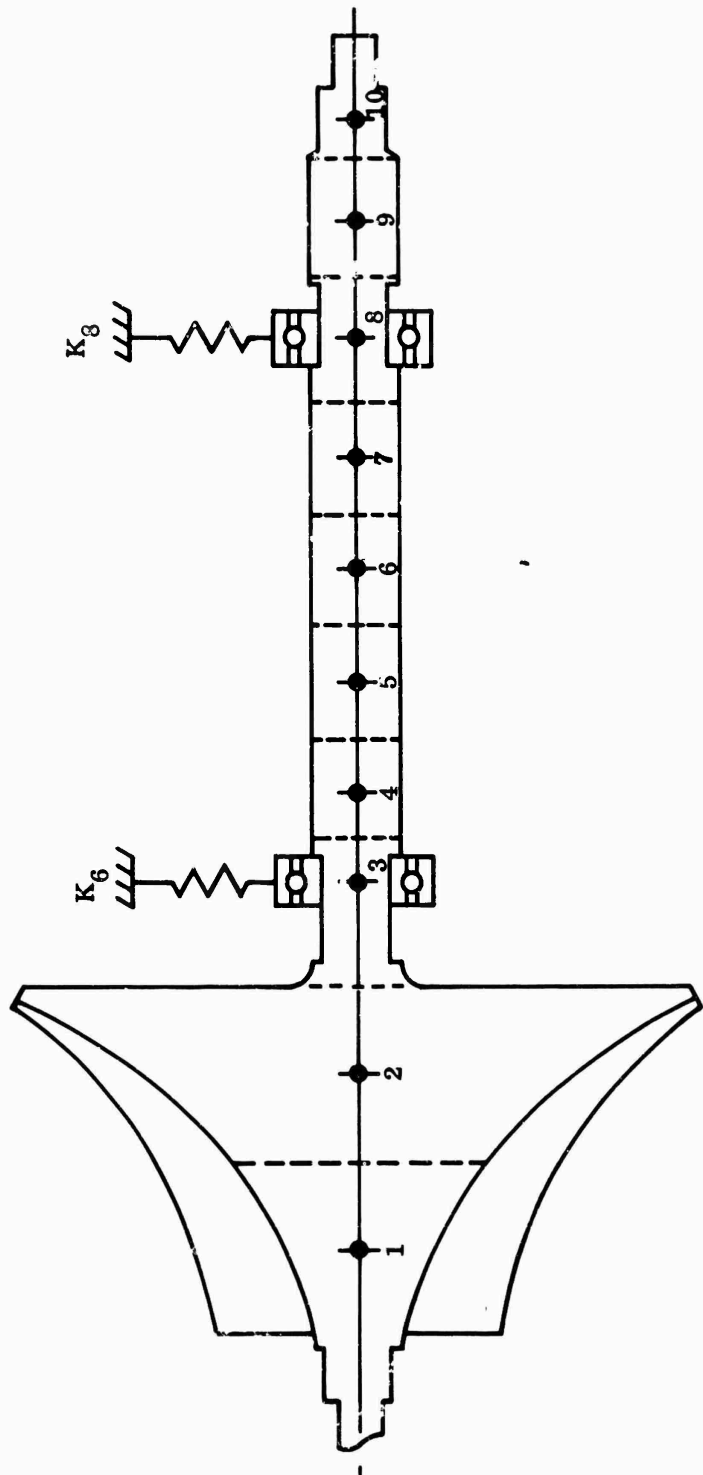


Figure 127. Rotor Stations Used in Predicting Critical Speeds.

CONFIDENTIAL

CONFIDENTIAL

TABLE XI					
CRITICAL SPEEDS					
		First	Second	Third	Fourth
Original Predictions:					
	MF-1	4,200	16,500	83,800	218,200
	MF-2	13,000	36,000	102,000	-
	MF-3	3,900	7,700	31,800	99,400
	RF-1	4,500	17,000	66,000	-
Experimentally Determined:					
	MF-1	-	-	56,000	-
	RF-1	-	-	48,000	-
Revised Analysis:					
	MF-1	3,200	8,500	56,100	-
	MF-2	3,900	7,700	28,800	87,100
	MF-3	3,900	7,700	31,800	99,400
	RF-1	3,300	8,800	48,300	155,400

CONFIDENTIAL

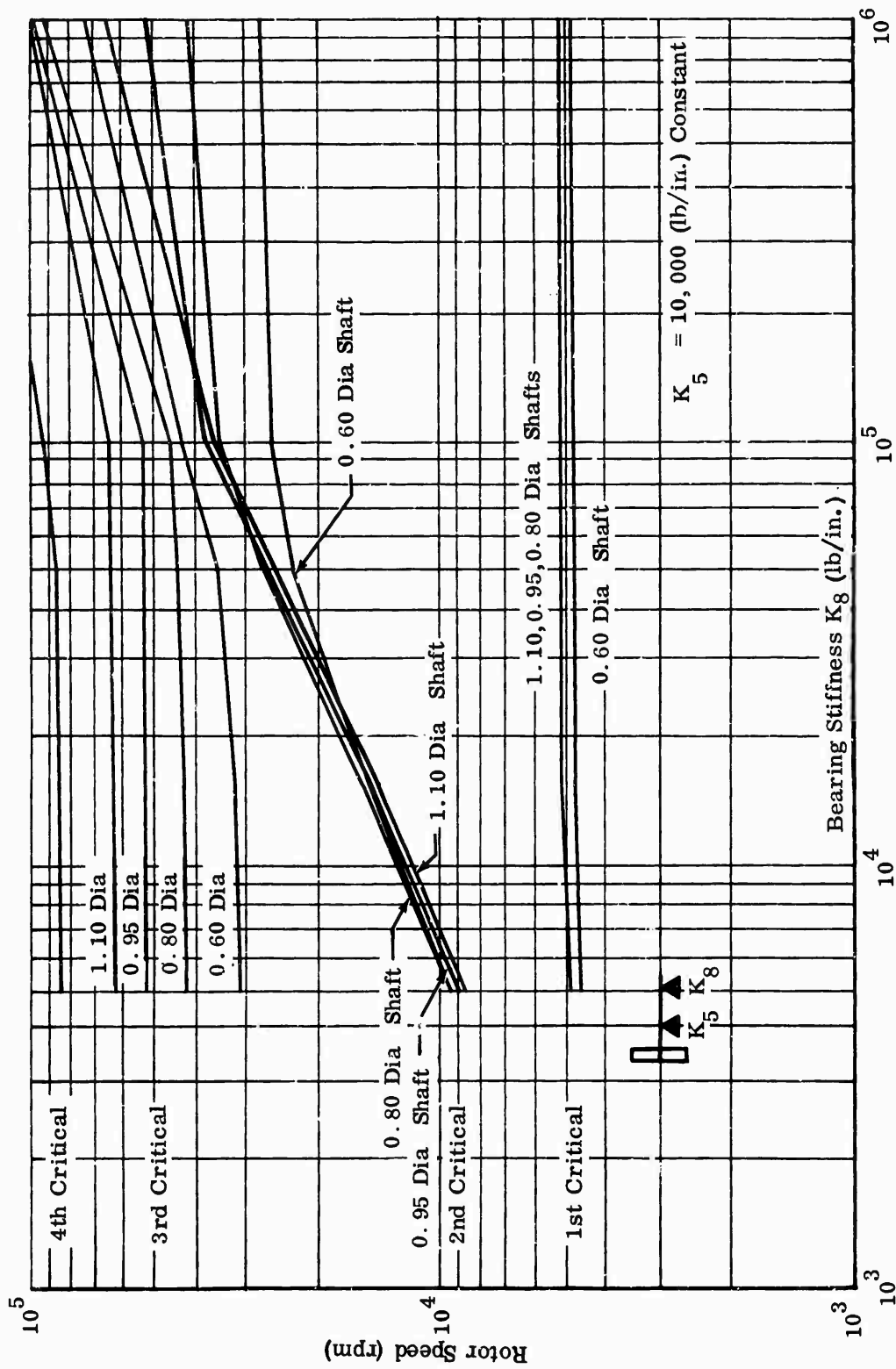


Figure 128. MF-2 Critical Speed Versus Bearing Stiffness.

CONFIDENTIAL

Operation of the MF-1 rig in the critical speed range resulted in vibration above an acceptable level of 100 g's, as shown in Figure 129. This figure also shows the effect of viscous damping of the flexible bearing mounts, provided by pressurized oil between the mounts and rotor housing, which reduced the vibration level. Critical-speed vibration was reduced to safe levels by a modal balance method (Appendix V), which applied a moment to the shaft that opposed the imbalance created by the critical-speed mode shape, in this case the third, or bending, mode.

The splined coupling between the turbodrives and compressor unit was a source of forced excitation to the rotor system as a result of the friction generated in the loose splines at high speed. This effect was verified by independent observations of a similar coupling on a turbine-dynamometer test rig. The splined coupling was therefore replaced by a frictionless coupling, as shown in Figure 130.

Selection of preloaded precision ball bearings was made to minimize axial and radial displacement and to accommodate the high rotational speeds. The flexible bearing mounts were limited to 0.002-inch displacement in any direction by snubbers to prevent excessive motion and to protect the mounts from overstress. Preliminary studies of the bearing application revealed that the pressure buildup on the back face of the impeller would result in excessive thrust loads, calculated to be a net maximum of approximately 1500 pounds for MF-1 (Appendix III). A labyrinth seal between the impeller tip on the back face and the rotor housing (Figure 131) with a controlled vent was planned to limit the thrust to 60 pounds. However, forward deflection of the impeller tip during actual rig operation caused an excessive seal gap, which resulted in an insufficient pressure drop to reduce the thrust load. The labyrinth seal method of reducing thrust loads was replaced by a pressure balancing disk located on the aft end of the shaft, with the cavity in front of it pressurized from an external air source (Figure 132). The balance pressure in the cavity was regulated manually, as determined by loads read directly by strain gages mounted on the thrust-bearing mount. A maximum rotor imbalance of 0.005 ounce-inch was specified to limit the dynamic radial bearing force to 43 pounds for the larger rotor at 60,000 rpm and to 55 pounds for the smaller rotor at 80,000 rpm (Appendix III). A bearing life of 500 hours was established to meet anticipated operating requirements. This is equivalent to an average life of 2500 hours. Bearing investigations, based on manufacturer's data and recommendations, resulted in selection of 20 mm single-row, deep-groove precision bearings with SAE 52100 chrome steel balls held by aluminum-phenolic retainers for the rotor common to RF-1 and MF-1. The bearings for the MF-2 and MF-3 rotors were 17 mm of the same type. The smaller size was selected for the MF-2 and MF-3 rotors because the high centrifugal loading of the balls on the outer race made the 20 mm bearings marginal at 80,000 rpm. Bearing life for the 20 mm bearings was the required 500 hours (Appendix III); however, MF-2 and MF-3 bearing life was reduced to 280 hours, which was acceptable because of the lower (100 hours) life

CONFIDENTIAL

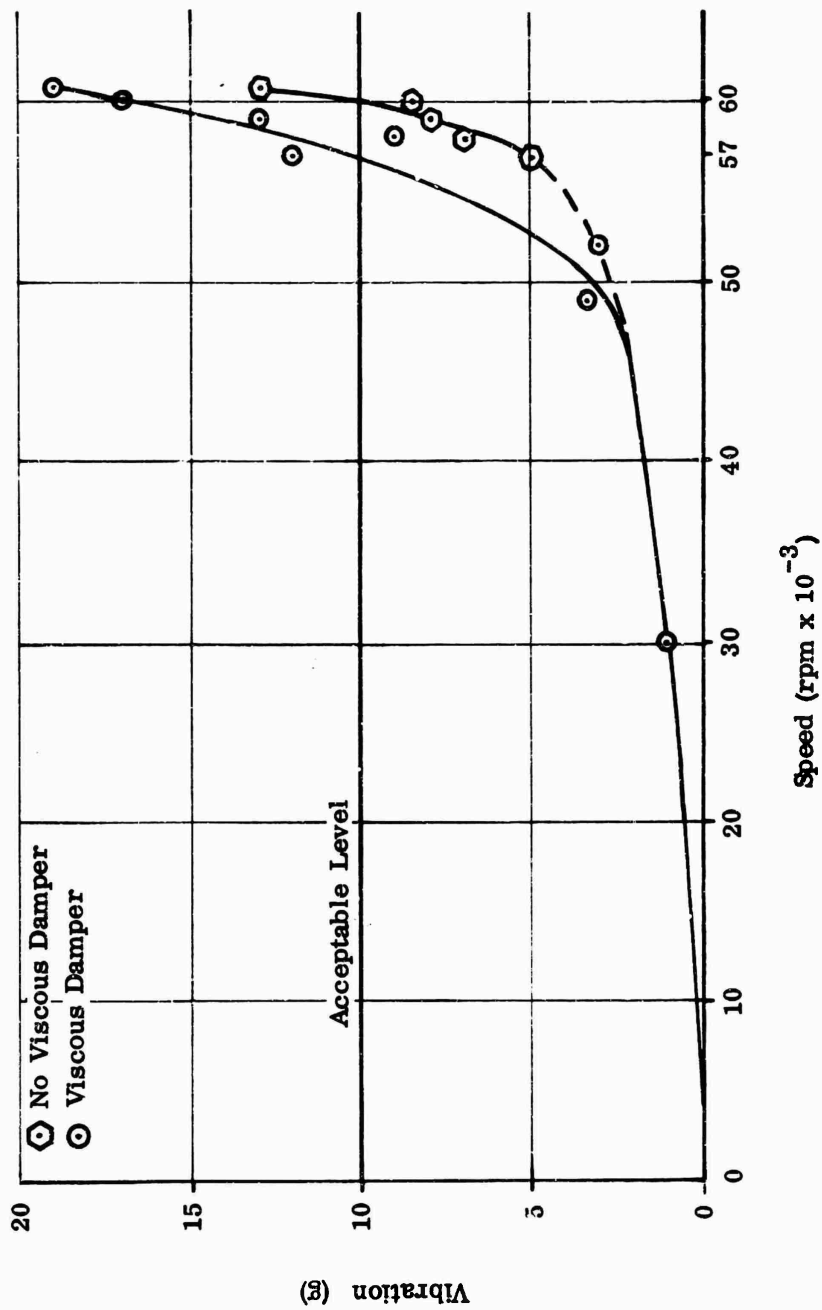


Figure 129. Effects of Viscous Damping.

CONFIDENTIAL

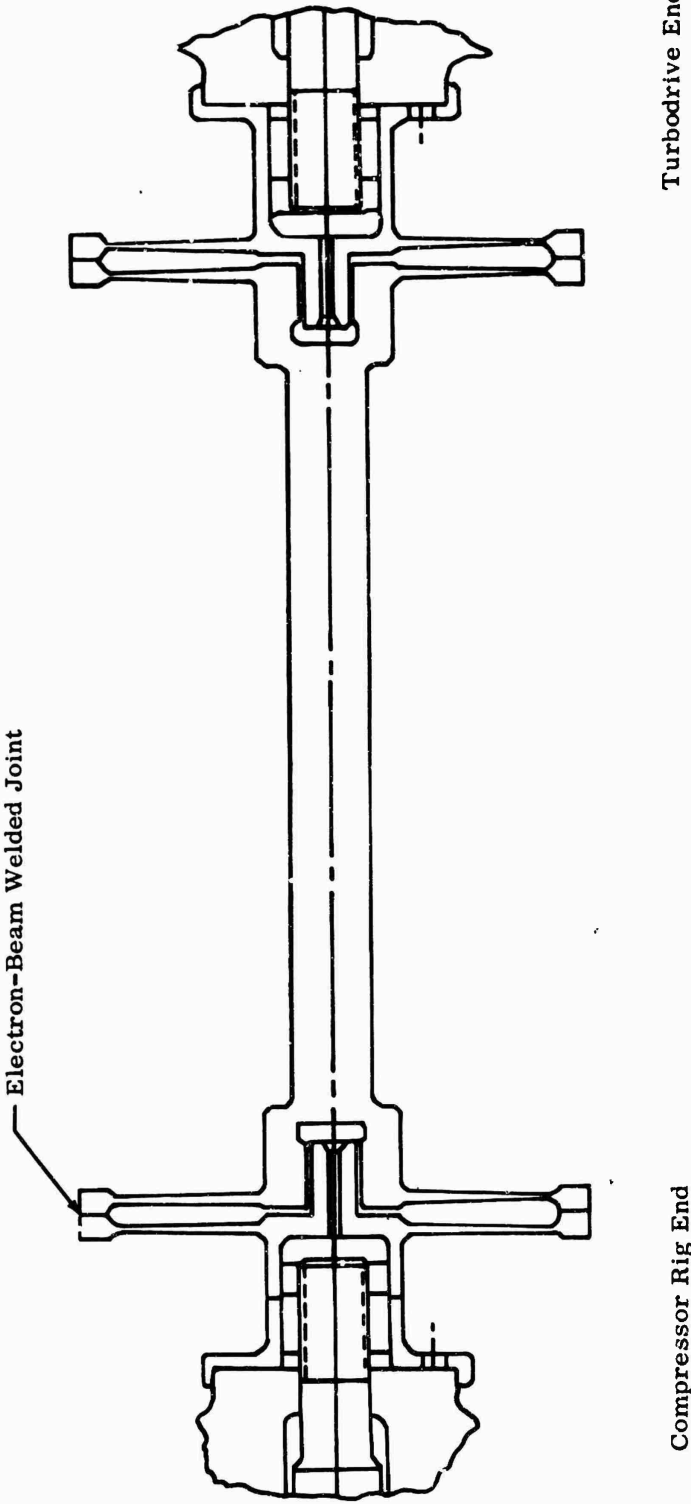


Figure 130. Frictionless Coupling.

CONFIDENTIAL

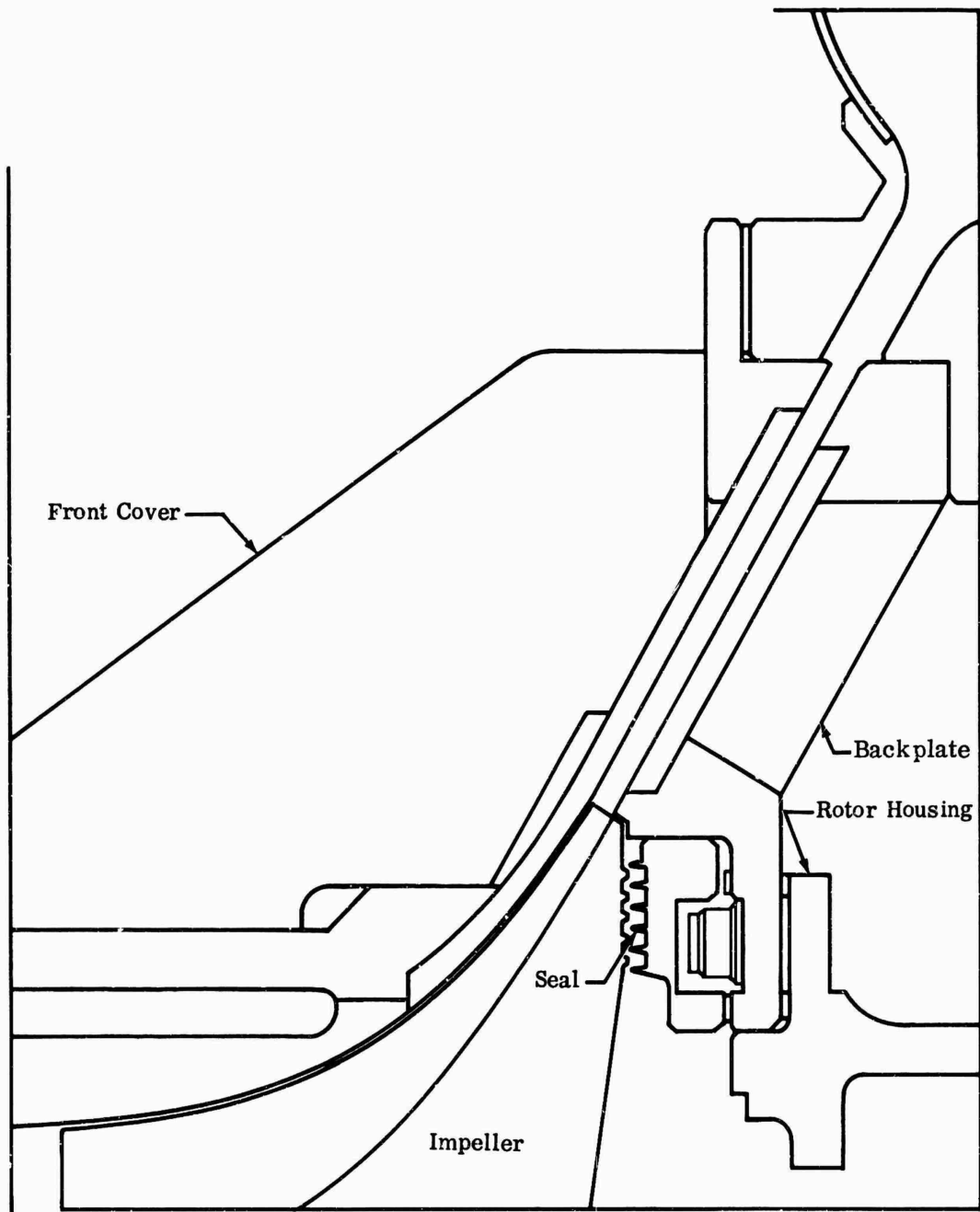


Figure 131. MF-1 Labyrinth Seal.

CONFIDENTIAL

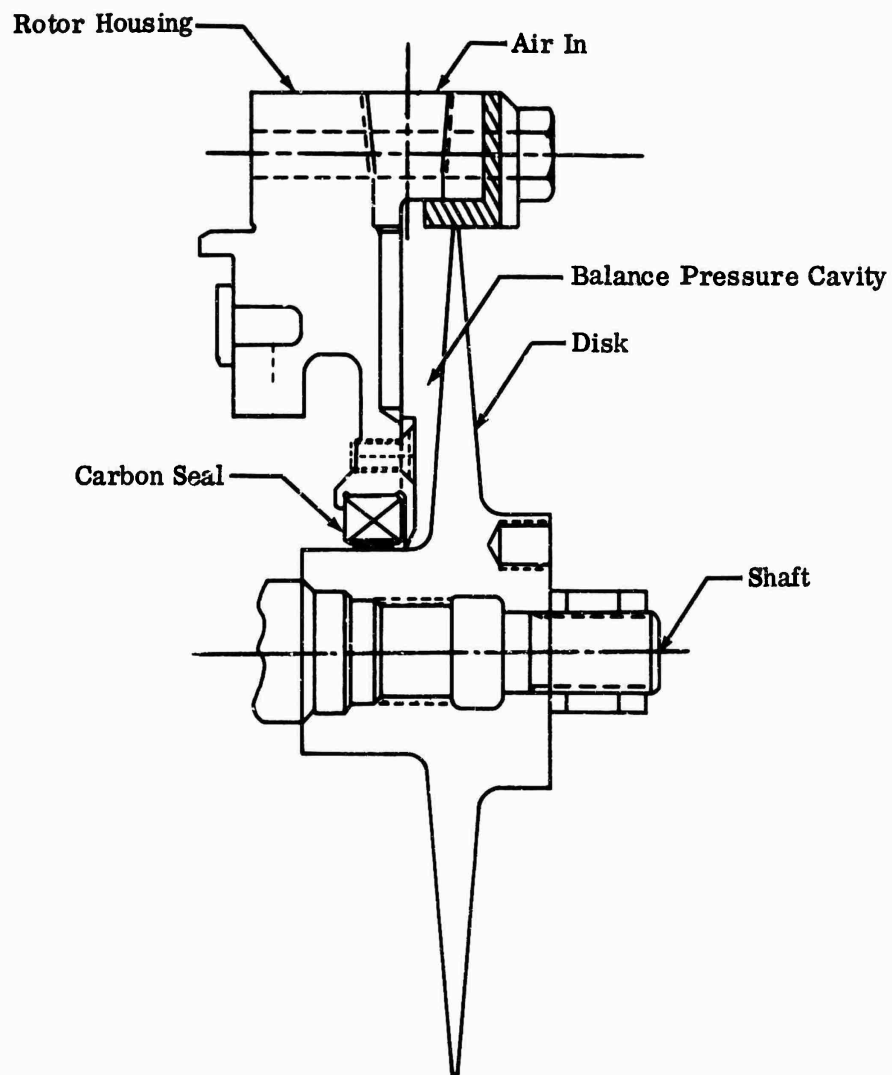


Figure 132. Thrust Balance Disk.

CONFIDENTIAL

CONFIDENTIAL

requirement. The predicted operating temperature for both bearings was 300°F. A preload of 40 pounds was specified for each bearing. Positive contact carbon seals were located next to each bearing. Lubrication of the bearings of both rotors was specified to be air-oil mist, with MIL 7808 synthetic oil being used, which was also considered to be adequate to remove the heat generated by the bearing friction. This method was changed to a jet-spray system after initial testing to provide more lubricant to the seals and better bearing cooling. This change reduced the bearing temperature from 300°F at 30,000 rpm to 160°F at 60,000 rpm. Figure 133 shows the final design for the 20 mm bearing rotor system.

2.4.2 DIFFUSERS

The aerodynamic design of the diffusers called for three vane-island types and one cascade type. The vane-islands were designed to provide diameter-ratio settings of 1.02, 1.06, and 1.10, and throat areas of 25, 50, 75, 100, and 125 percent of the design area at a radius ratio of 1.06. The cascade vanes were to be adjustable about their center of rotation. The impeller used to test the diffusers (workhorse impeller) was required to operate at a tip speed of 2,000 feet per second, with an allowance for 10-percent overspeed, consistent with the other impellers. Figure 134 shows the impeller design information. The mechanical design objectives for this impeller were the same as for the other 4 impellers discussed in Section 2.4.1. It was essential that the test section accommodate each vane set by simple replacement. In addition, adjustable impeller inlet guide vanes and windows for schlieren photography of flow phenomena at the channel inlet were to be included in the design. Test-section instrumentation for the diffuser tests was to be similar to that on the impeller test rigs, except additional static taps were required in the diffuser section, and a movable total-pressure probe was required to traverse from the impeller tip to the diffuser exit along the channel centerline.

Vane-Islands

The vane-islands were clamped between the test-section diffuser walls and were positioned with 2 pins in each vane. Combinations of pin holes in the vanes and rear diffuser walls provided the required diameter ratio and throat-area settings. The angle of attack was the same for each diameter-ratio setting. Throat-area changes were made by pivoting the vanes about the tip. A sample vane is shown in Figure 135.

CONFIDENTIAL

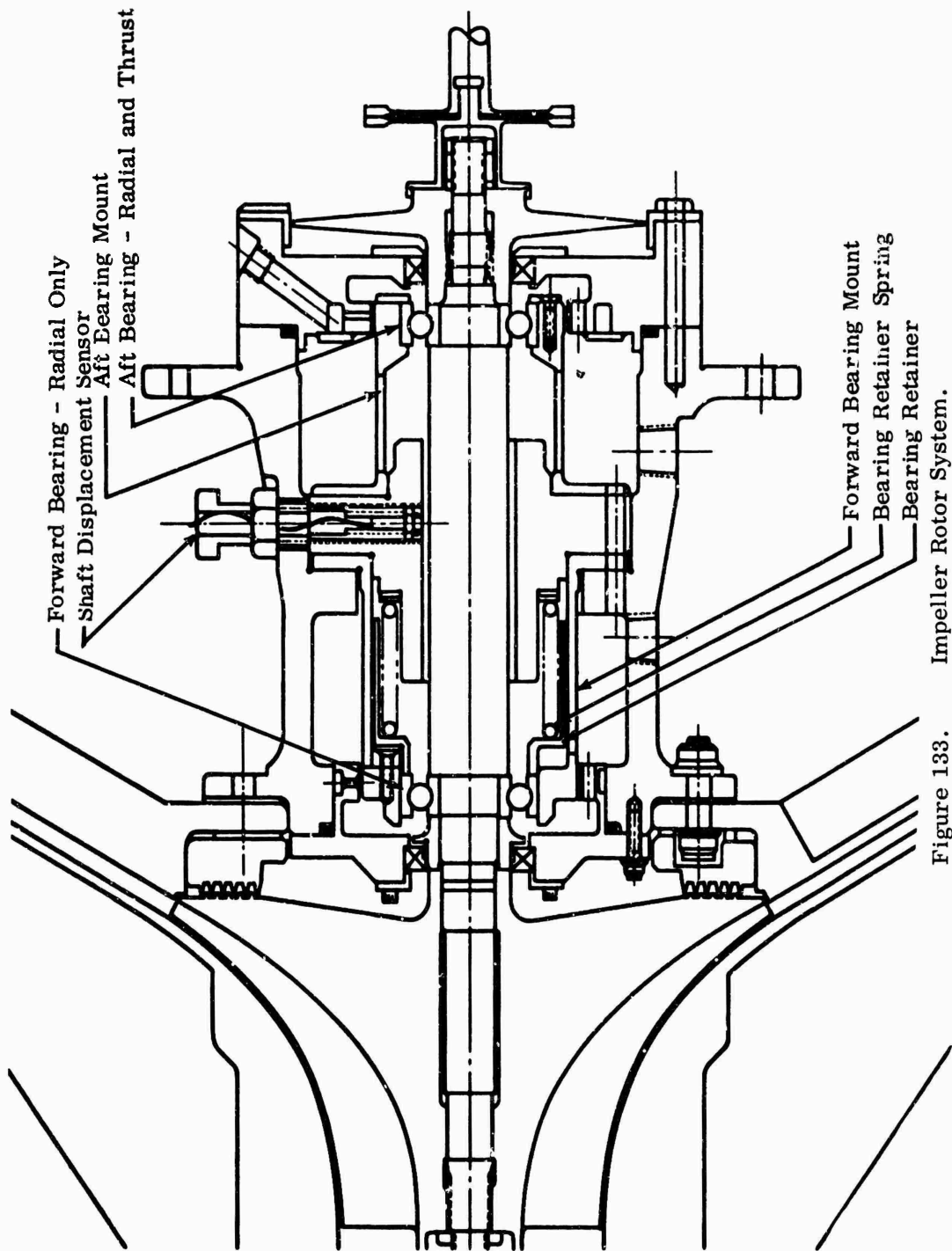
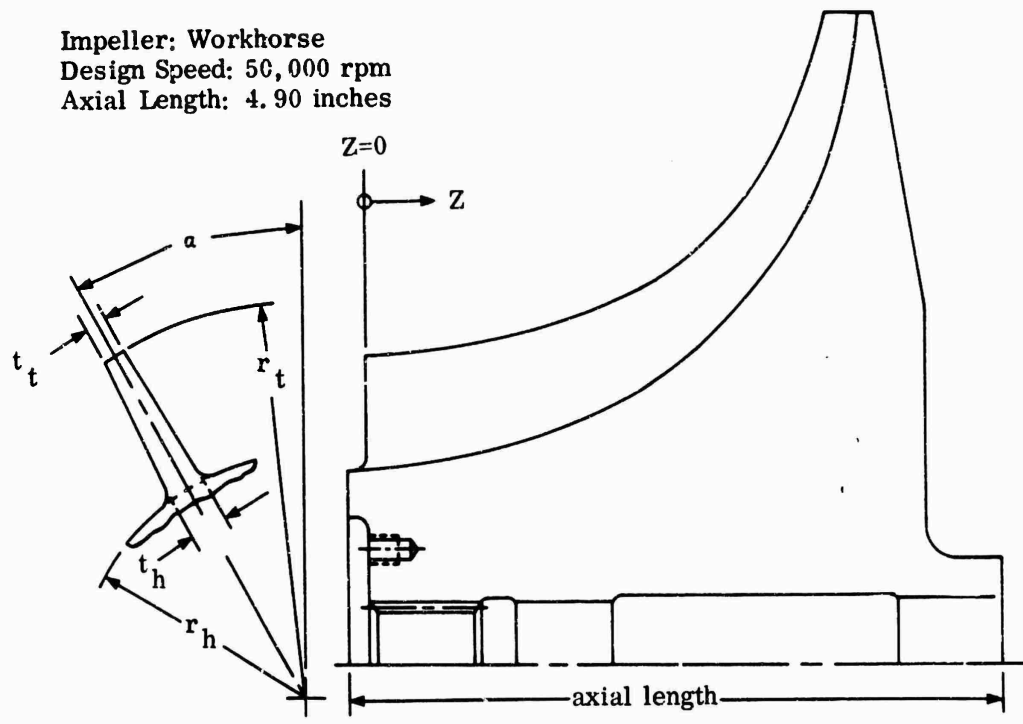


Figure 133. Impeller Rotor System.

CONFIDENTIAL



Axial Distance Z	Blade Turning Angle α	Hub Radius r_h	Tip Radius r_t	Hub Thickness t_h	Tip Thickness t_t
0	0	1.400	2.210	0.080	0.075
0.341	10.05	1.440	2.240	0.100	0.080
0.682	18.90	1.490	2.280	0.112	0.081
1.023	26.30	1.565	2.340	0.103	0.072
1.360	32.05	1.660	2.415	0.095	0.065
1.690	36.20	1.775	2.520	0.090	0.060
2.010	38.95	1.930	2.660	0.086	0.057
2.300	40.60	2.110	2.825	0.085	0.057
2.560	41.40	2.320	3.025	0.084	0.056
2.780	41.70	2.530	3.240	0.086	0.058
2.970	41.80	2.735	3.470	0.089	0.061
3.110	41.80	2.930	3.675	0.094	0.064
3.200	41.80	3.070	3.860	0.101	0.069
3.350	41.80	3.340	4.220	0.090	0.055
3.500	41.80	3.680	4.600	0.077	0.040
3.600	41.80	4.020	4.600	0.068	0.045
3.700	41.81	-	4.600	-	0.050

Figure 134. Aerodynamic Design Information.

CONFIDENTIAL

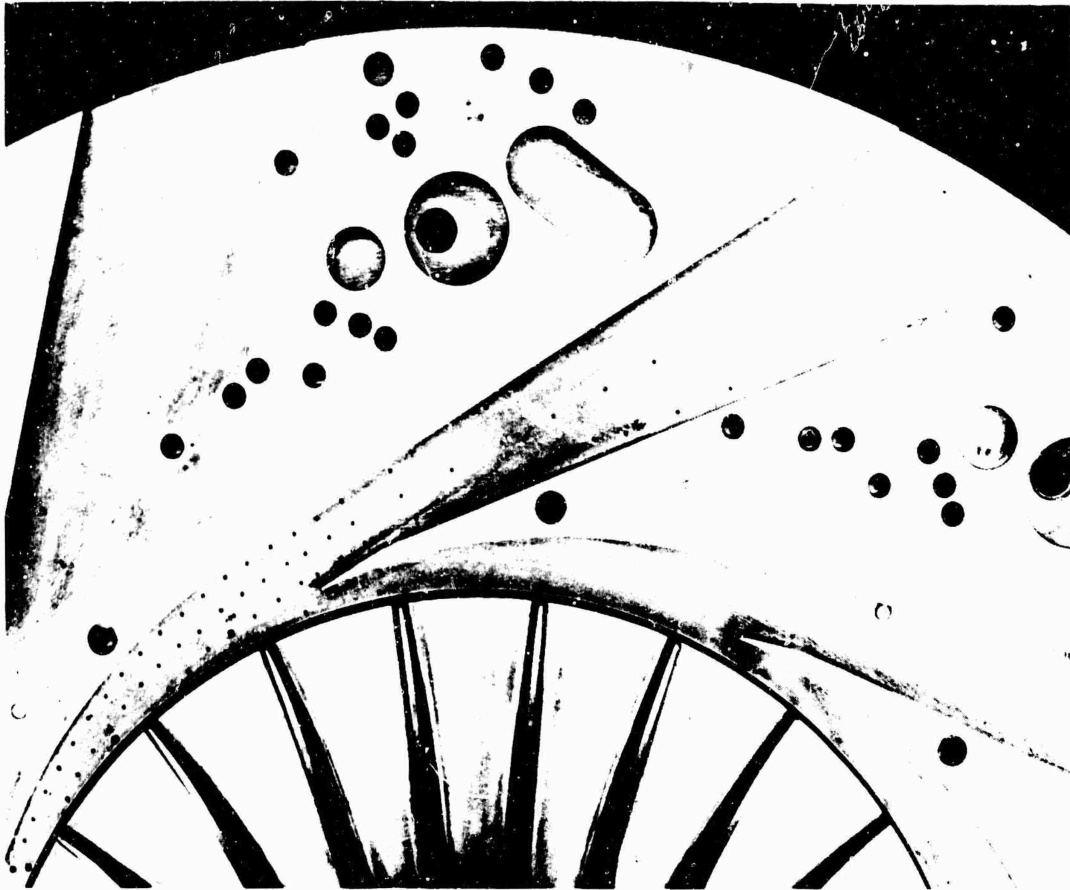


Figure 135. Diffuser Vane-Islands.

Cascade Vanes

The cascade vanes were designed as 1-piece vane-stud airfoils that attached through the rear diffuser wall as shown in Figure 136.

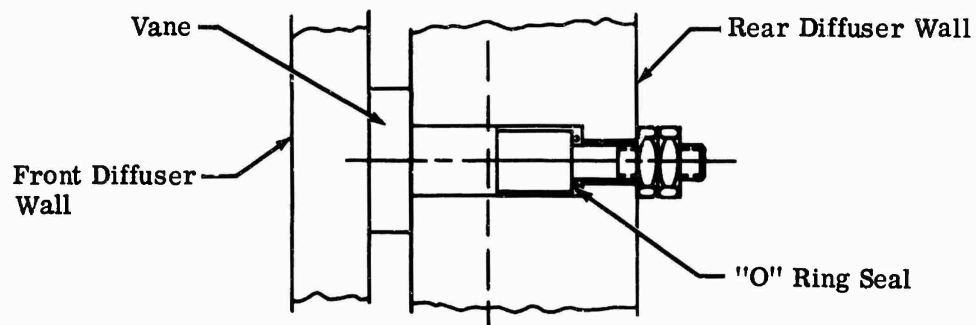


Figure 136. Cascade Diffuser Vane.

CONFIDENTIAL

CONFIDENTIAL

The maximum stress resulting from the 12-pound aerodynamic side load and 25-inch-pound nut torque was calculated to be approximately 32,000 psi.

Impeller

The performance characteristics for this impeller were similar to those of the four impellers of Section 2.4.1; therefore, the material selection and stress analysis methods were the same. Minimum factors of safety were 1.67 for the disk, and 1.91 for the blades, both based on 0.2-percent yield. Details of the analysis are given in Appendix II.

Impeller-Stress Test — A diffuser-test-rig impeller was tested to determine the blade vibration stresses, frequencies, and modes throughout the compressor map. The vibration stresses were found to be below the 20,000 psi allowable except in 3 rpm ranges near surge, as shown in Figure 137. The complete test procedure and results are presented in Appendix VI.

Test Sections

One basic test section was designed to accommodate the different vane configurations. Three backplates were required: 1 for the cascade vanes, 1 for the DI-1 and DI-2 vanes, and 1 for the DI-3 vanes. Figures 138 and 139 show typical test section installations. The backplate, which attached to the rotor housing, was a 1-piece design, machined from 321 stainless plate. The front cover was a 2-piece brazement, 1 piece forming the impeller shroud and the other forming the front diffuser wall. One collector was common to all test sections. The inlet guide vanes (Figure 140) were 2-piece blades with a fixed leading edge and a moveable trailing edge that was remotely controlled through ± 50 degrees of travel. Windows for schlieren photography were planned for all diffuser configurations (Figure 141). The spaces between the inner and outer windows were pressurized with diffuser air through bleed holes to minimize the pressure differential across the inner window, which also carried a high thermal gradient. The vane-island window configuration was later changed to a single lens mounted in an Invar frame to reduce stresses in the lens caused by thermal distortion of the window seat. This was also done to eliminate the collection of contaminants between the double windows. The window sealant was silicone rubber. The original window material was quartz, but was later changed to a 96-percent silica glass because of its better resistance to mechanical shock.

Rotor System

The rotor design objective was to provide a system to operate in a speed range of from 33,000 rpm to 55,000 rpm. The impeller was cantilevered on the rotor shaft, which was supported by 2 full-floating hydrodynamic bearings. Thrust in both directions was carried by hydrodynamic slipper bearings. Power was

CONFIDENTIAL

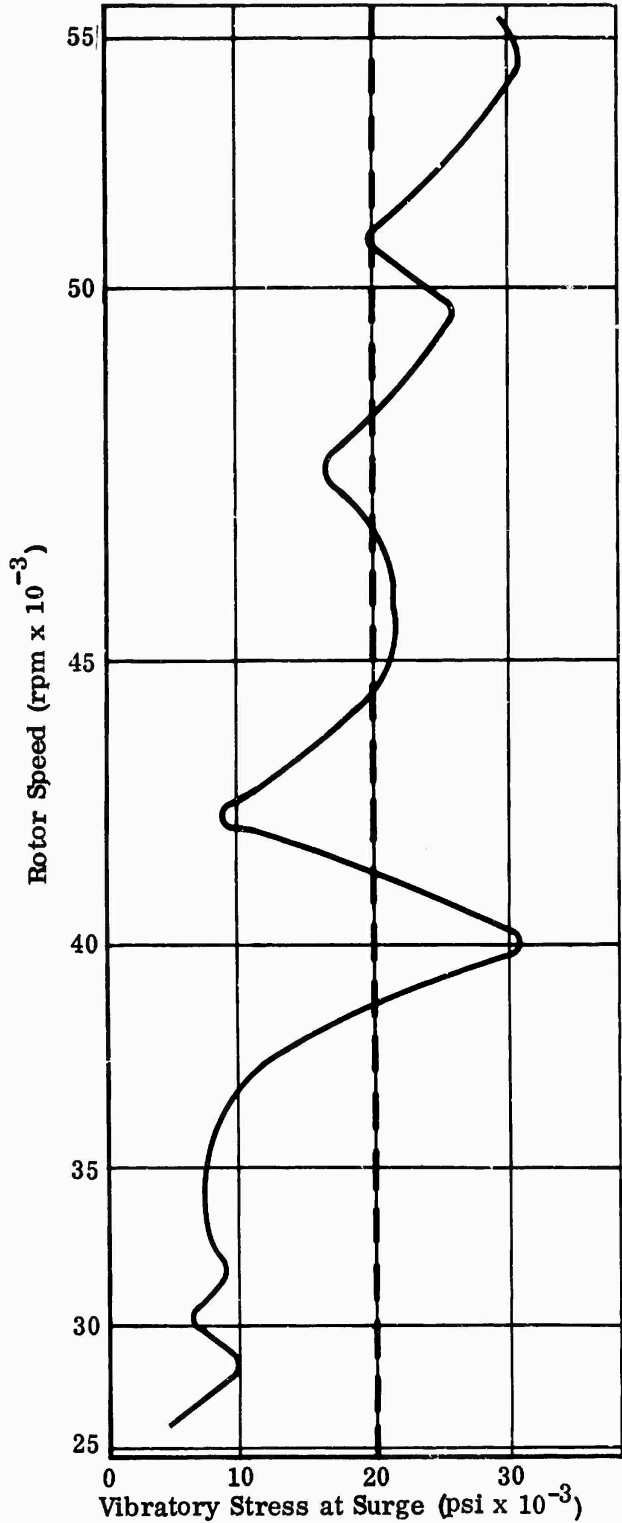
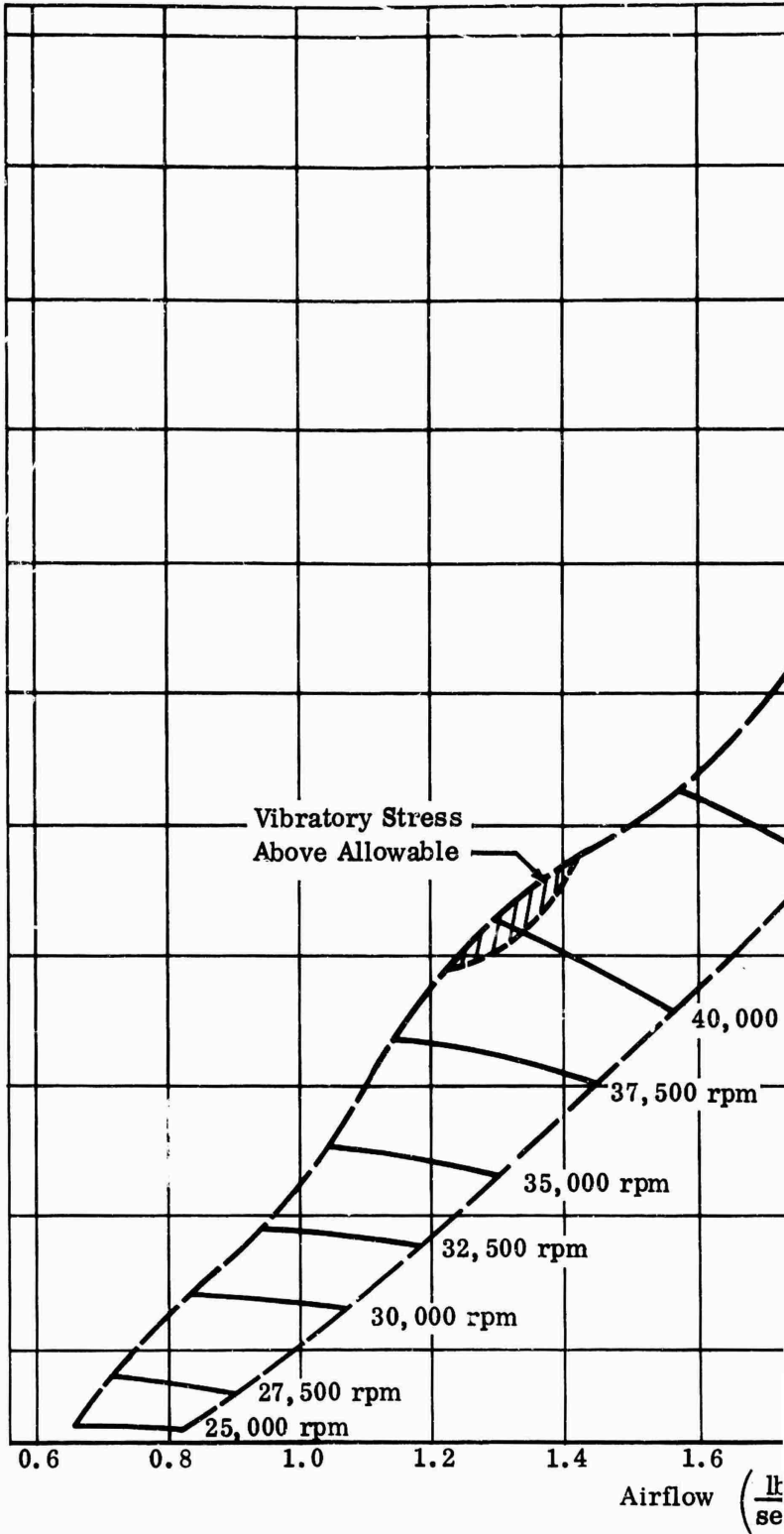
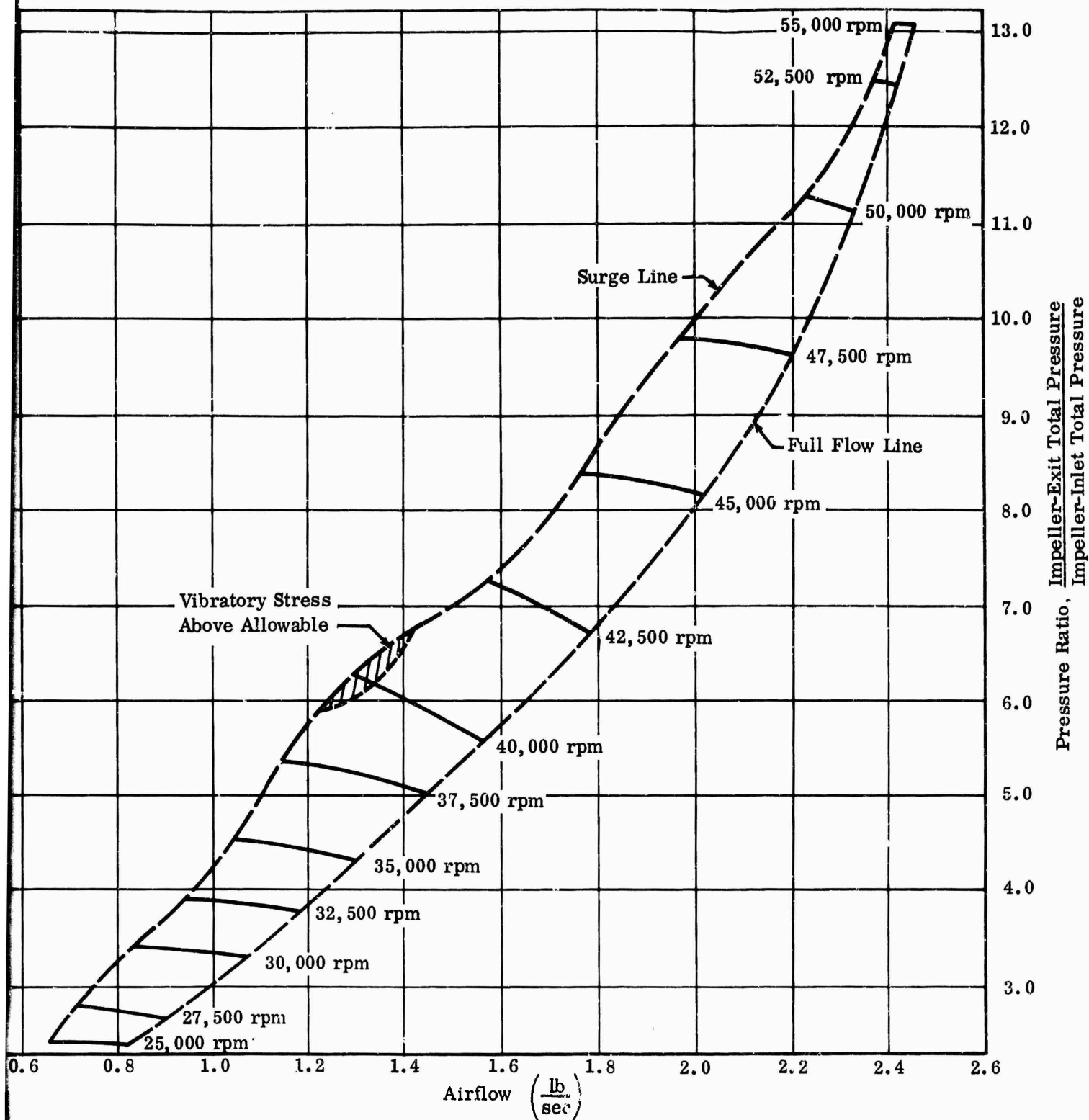


Figure 137. Impeller Vibratory Stress Test.





CONFIDENTIAL

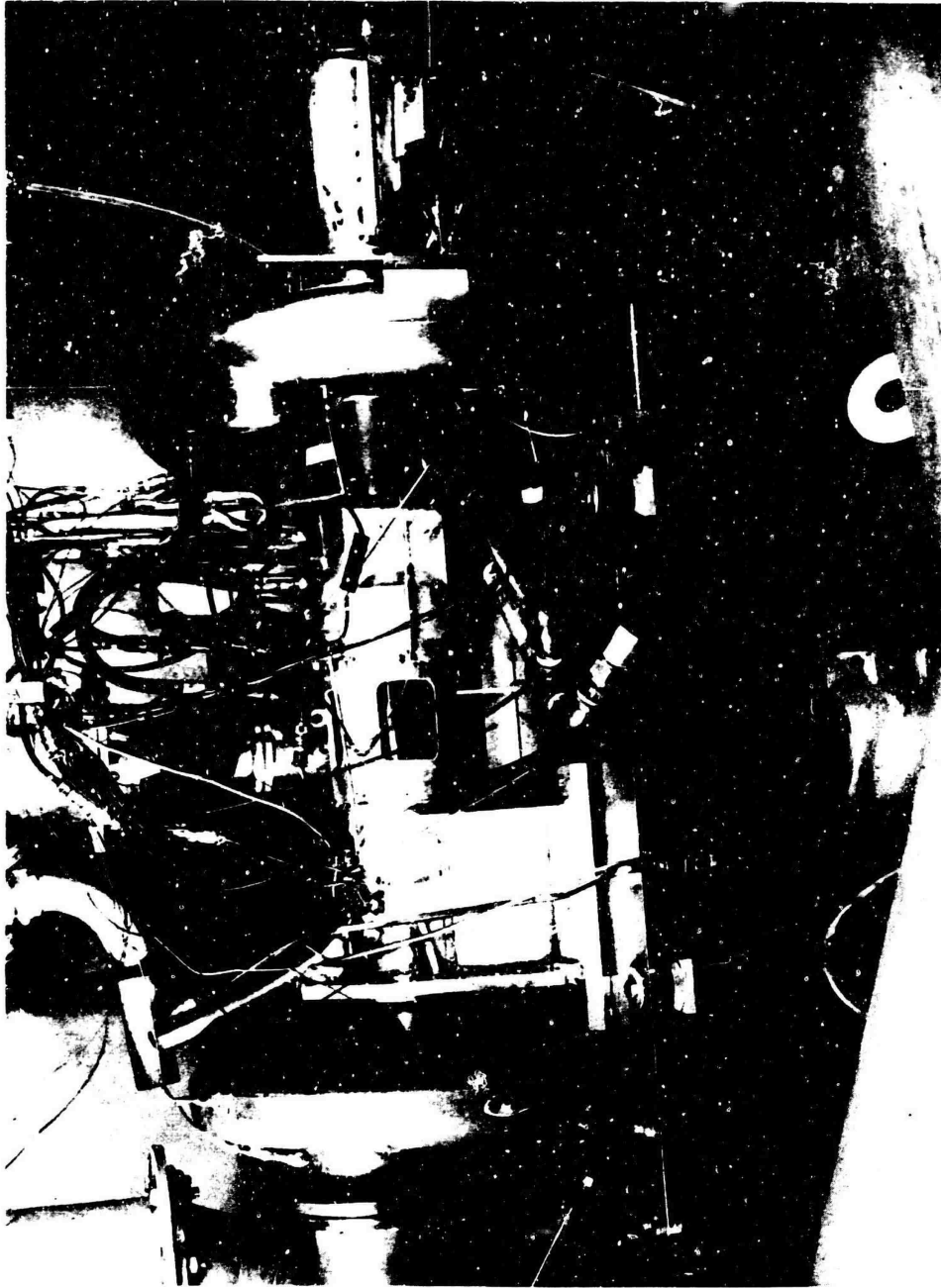


Figure 138. Diffuser Rig.

CONFIDENTIAL

CONFIDENTIAL



Figure 139. Diffuser-Rig Test Section.

CONFIDENTIAL

CONFIDENTIAL

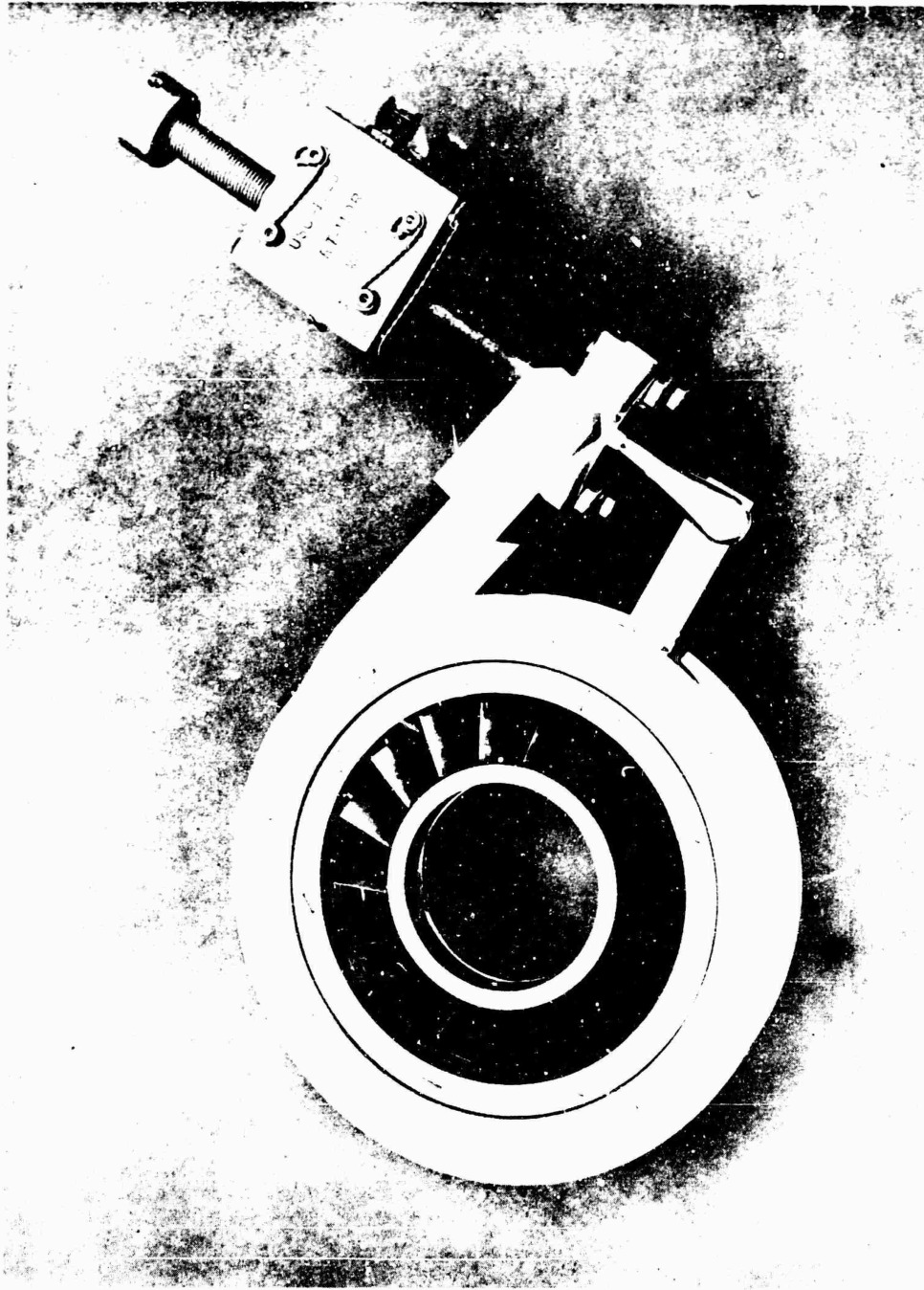


Figure 140. Inlet Guide Vane Assembly.

CONFIDENTIAL

CONFIDENTIAL

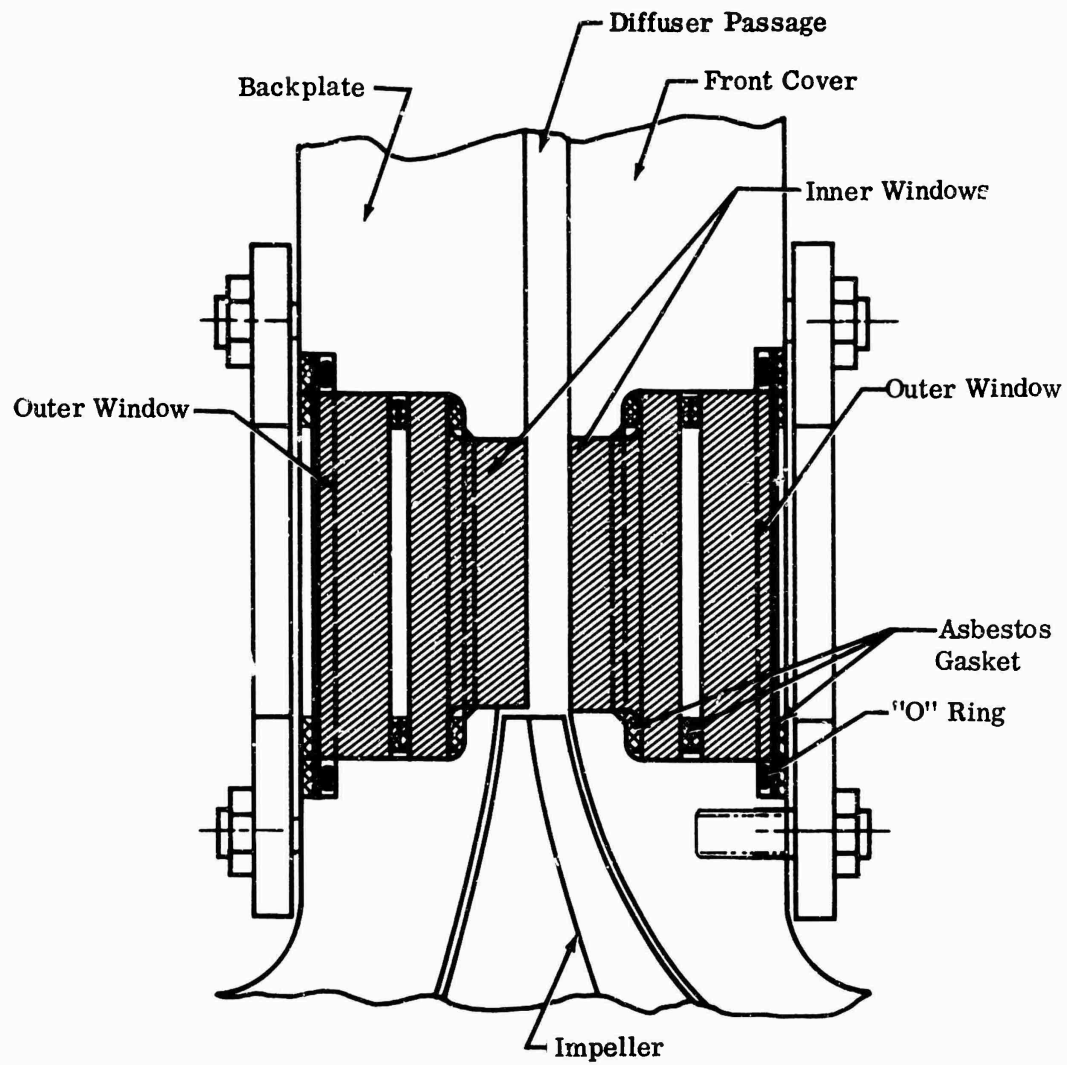


Figure 141. Schlieren Window Installation.

CONFIDENTIAL

CONFIDENTIAL

provided by a radial-in-flow turbodrives unit through a flexible coupling between the turbodrives shaft and compressor shaft. Design details for the bearings and shaft are in Appendix III. Full-floating sleeve bearings were used to provide maximum radial load capacity. By comparison, it was expected that conventional journal bearings of the same size would overheat at design speeds and would require more oil flow with an increase in clearance, which in turn would reduce the load-carrying capacity below that for the full-floating sleeve bearings.

Rotor dynamics characteristics were predicted by the same method used for the impeller rig rotors (Section 2.4.1) with the radial oil film stiffness

$K_n \left(\frac{\text{lb}}{\text{sec}} \right)$ defined by the empirical relation —

$$K_n = \frac{\mu \ell^3 DN}{6.08 C^3} \quad (25)$$

where:

- μ = absolute viscosity (lb-sec/in.²)
- ℓ = bearing length (in.)
- D = bearing diameter (in.)
- N = rotor speed (rpm)
- C = total bearing clearance (in.)

Figures 142 and 143 show the bearing stiffness, T_n , which equals K_n divided by the rotor speed at the point in question. Also shown are the shaft mode shapes at a constant T_n value of $25 \frac{\text{lb-sec}}{\text{in.}}$. These curves show the first 2 natural

frequencies to be below 20,000 rpm for T_n values of less than 50 lb-sec/in. and they show the third, or bending, critical to be within the operating range for T_n values below 50 lb-sec/in. However, previous calculations of similar rotor systems indicated that the probable critical speed would be 67,000 rpm, 22 percent higher than the maximum design speed. During rig development, the actual critical speed was found to be at 46,000 rpm. Refined calculations yielded essentially the same results as the original, but comparison of the calculated and experimentally determined free-free criticals indicated that the predicted values for critical speeds were 11 percent high. With this correction, critical speed calculations showed correlation with the actual results.

CONFIDENTIAL

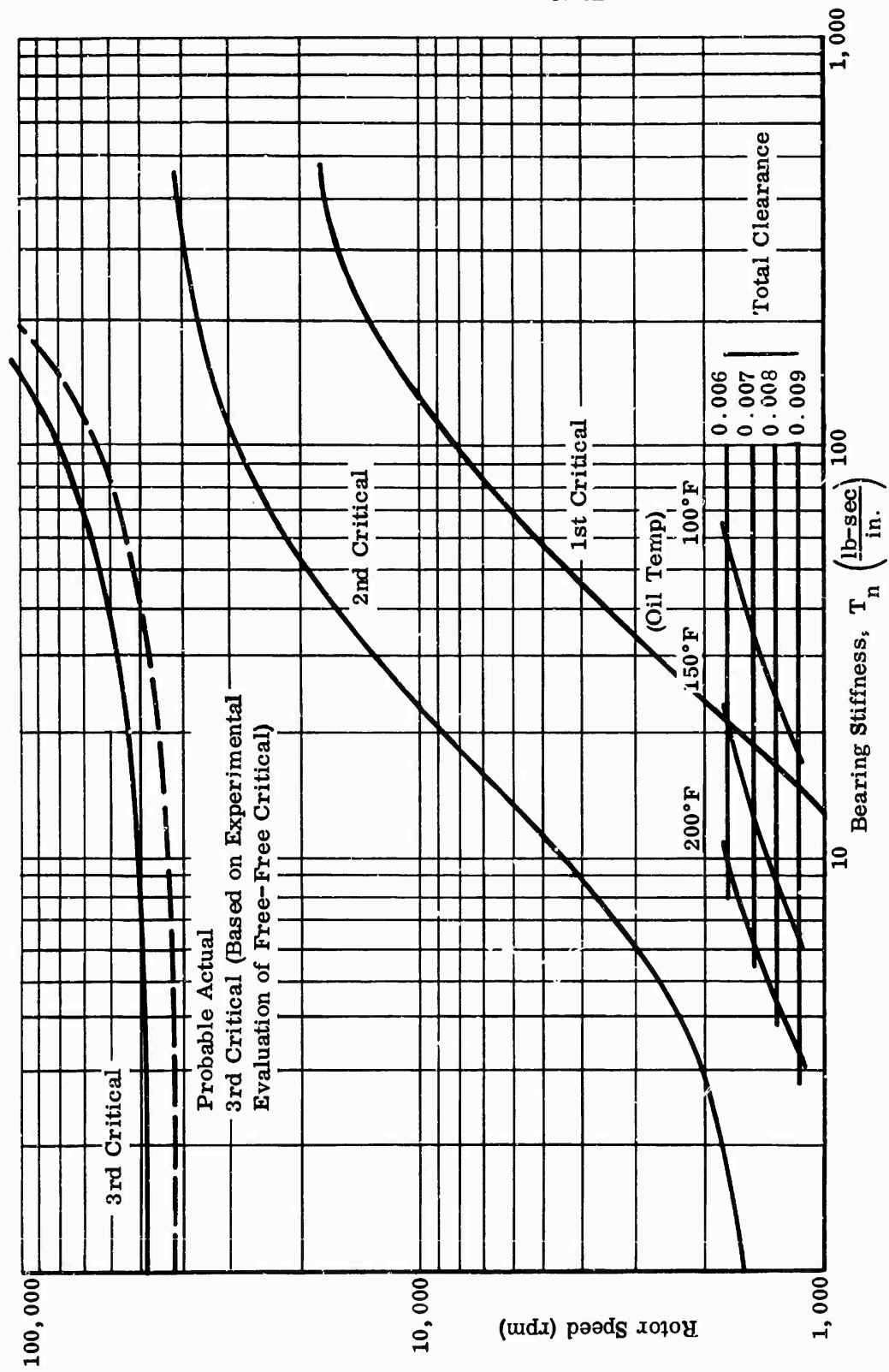
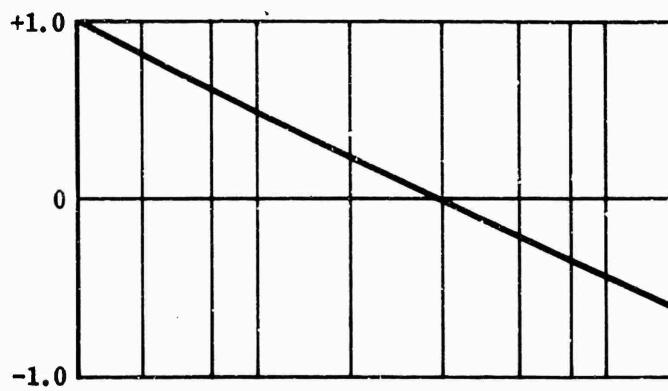
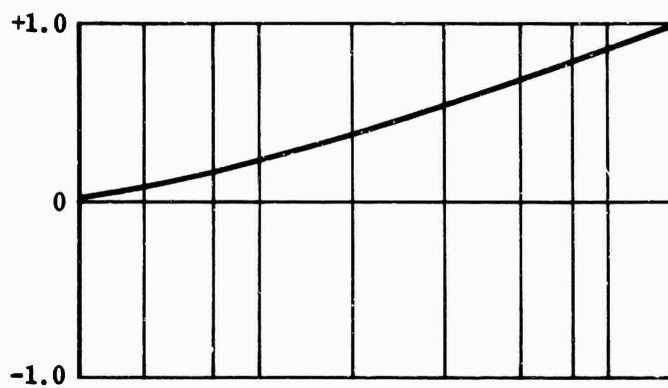


Figure 142. Bearing Stiffness Versus Rotor Speed.

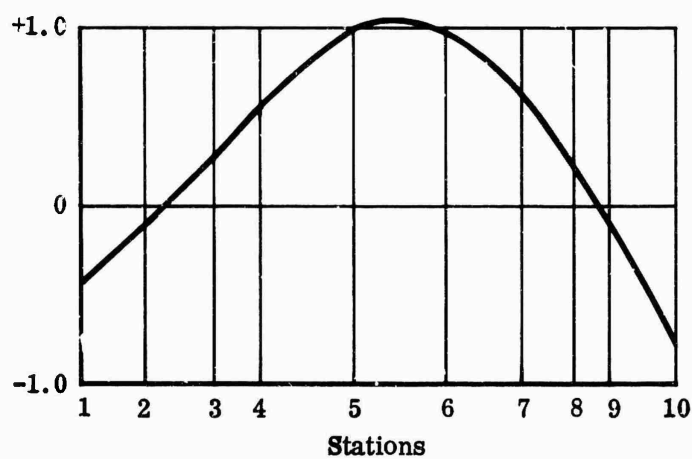
CONFIDENTIAL



Mode Shape
1st Critical



Mode Shape
2nd Critical



Mode Shape
3rd Critical

$$T_n = 25 \frac{\text{lb-sec}}{\text{in.}}$$

Figure 143. Shaft Mode Shapes.

CONFIDENTIAL

CONFIDENTIAL

During the operational checkout, radial loads were found to be higher than anticipated; therefore, the forward bearing mount was replaced with a flexible, damped mount. In addition, oil flow was increased by increasing pressure from 50 to 70 psi with a 90-percent increase in the bearing oil orifice area. Also, the reverse thrust bearing was modified to carry radial loads as well as thrust, which provided an additional bearing near the middle of the shaft. These modifications reduced the critical speed to 43,000 rpm, and the lower radial loads were easily transcended during operation.

The splined coupling between the turbodriven unit and the compressor rotor was considered as a possible source of excitation and was replaced with a frictionless coupling similar to the one used on the impeller rig, Section 2.4.1 of this report. Figure 144 shows the final rotor configuration.

CONFIDENTIAL

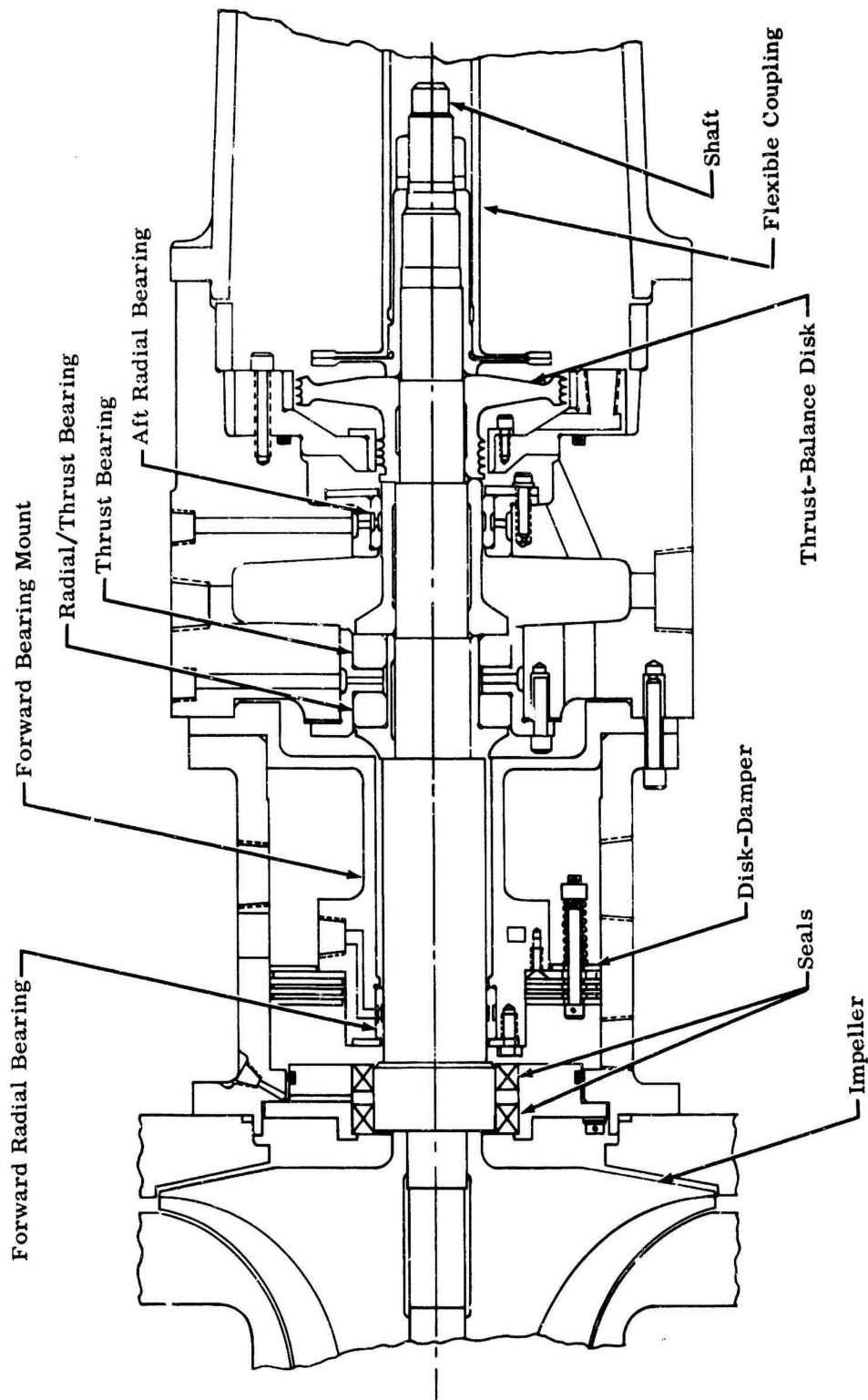


Figure 144. Diffuser-Rig Rotor System.

(U) 3.0 FABRICATION OF RESEARCH COMPONENTS

Components necessary for conducting the various impeller and diffuser investigations were fabricated in 2 primary efforts corresponding to the work on the 2 test rigs. For the impeller test rig, a new impeller and test section were required for each of the 4 impeller configurations; however, for the diffuser test rig, 1 test-section design and 1 impeller accommodated all diffuser configurations, although variations in the vane attachments and instrumentation were required for the diffuser designs.

3.1 IMPELLERS

Eleven impellers were fabricated: 2 each for MF-1, MF-2, MF-3, and RF-1 (Figure 145), and 3 workhorse impellers (Figure 146). All were fabricated from 6Al-4V titanium forgings. On-site inspection was conducted by the contractor's quality control personnel; proof-spinning, splining, finish boring, and balancing were performed in the contractors' facilities.

The impellers were fabricated by using a cavity milling process which involved positioning a rotary cutter on the workpiece by tracing a 10-times-size model of the surface to be generated. The model of the spacing between 2 blades, or the cavity, was built with 10-times-size blade sections spaced at proper intervals and filled with epoxy; then it was hand-worked to the required dimensions (see Figure 147). The blades were machined by milling out successive cavities; an indexing fixture was used to position the part for each blade. Other surfaces were generated by standard machining practices.

Machining tolerances were specified to produce impellers that provided the aerodynamic characteristics and ensured economic fabrication. Specific tolerances for each impeller varied slightly; but in general, blade thickness was to be within ± 0.005 inch and blade contour was to be within ± 0.003 inch. The finished bore dimensions were to be within 0.0004 inch. Blade position was required to be radial within 0.002 inch and to be located within 0.2 degree of true position.

As part of the fabrication process, the blades were machined towards the low or high tolerance on blade thickness, as required to balance the impeller within 0.020 ounce-inch about the axis of rotation.

3.1.1 INSPECTION

Each impeller was inspected for dimensional, surface finish, and structural compliance. The dimensional and surface finish inspections were performed at the vendor's plant by the contractor's quality control personnel, who used optical templates with an optical comparator. Structural inspection was performed at

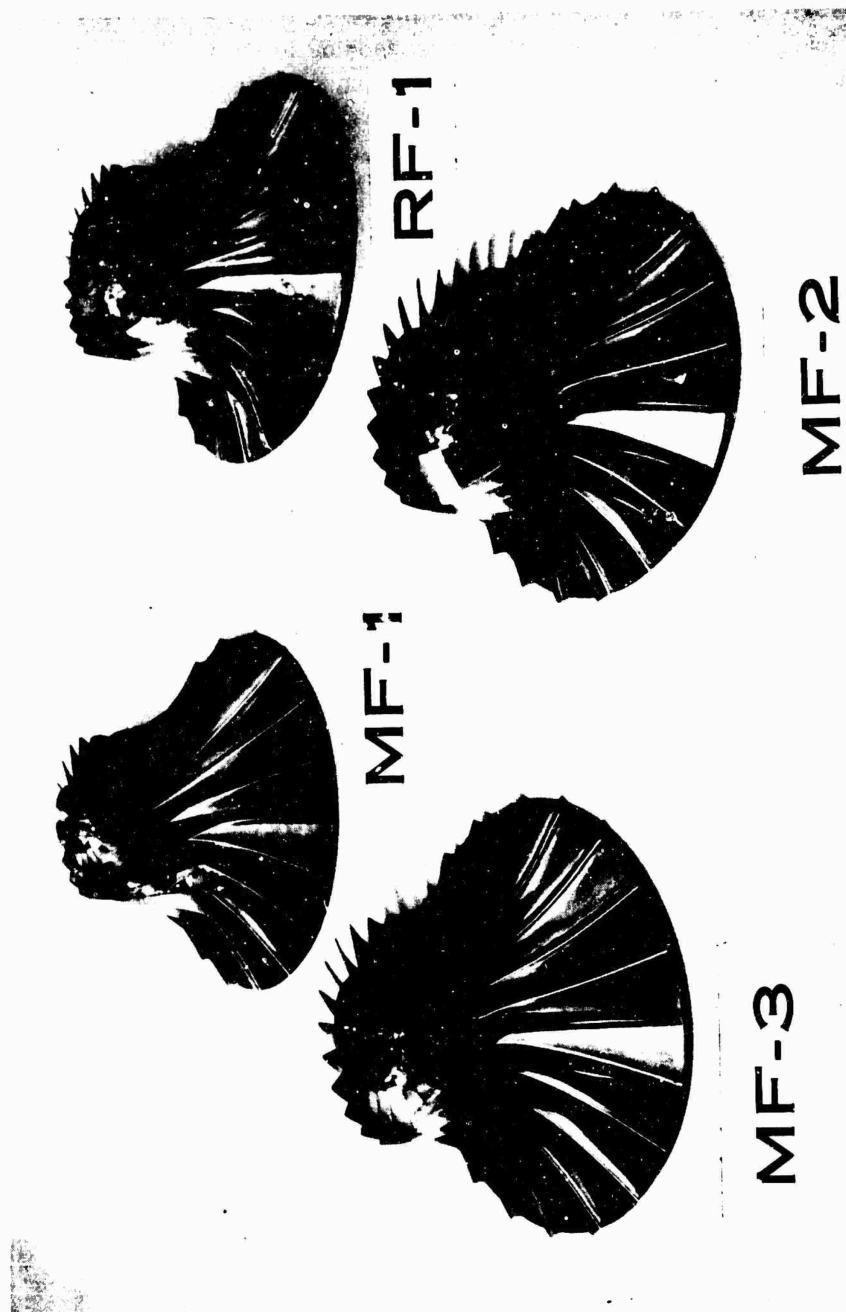


Figure 145. Impellers.



Figure 146. Workhorse Impeller.



Figure 147. Example of Impeller Cavity Model.

the contractor's facilities, both visually and with penetrant and magnetic-particle inspection techniques, for flaws and surface cracks after proof-spin and machining operations.

Optical template masters (see Figure 149) were produced by a tape-controlled drafting machine on scribe-coat Mylar (Figure 148). The templates were 10 times actual size, drawn to an accuracy of ± 0.001 inch. Blade profiles, showing the tolerance band, were prepared in planes normal to the impeller axis and at various stations along the axis, as illustrated in Figure 149.

3.1.2 PROOF-SPINNING

Each impeller was proof-spun to ensure the structural integrity of the original forging. In addition, proof-spinning introduced a permanent compressive stress at the inner bore, which would reduce growth of the bore at operating speeds. Proof-spin speed was selected to produce an average tangential stress of 90 percent of the material yield stress. The bore diameter was left 0.010 inch under the finish bore size to allow for growth during spinning.

Impellers were mounted on a spin arbor and were dynamically balanced to within 0.005 ounce-inch of imbalance before installation in the spin pit facility. The arbor was attached to the drive quill shaft with a shear pin as a precaution against impeller damage. The spin pit was evacuated to 0.5 inch Hg to reduce impeller-pumping and drive-power requirements. Impeller pumping was further reduced by rotating the impeller opposite the normal direction.

The MF-2 impeller did not complete proof-spin testing successfully. The difficulty was traceable to the spin pit rather than to the impeller. The report of this difficulty is also contained in Appendix IV, along with detailed spin pit information.

3.1.3 BORING AND SPLINING

An impeller and shaft were assembled as an integral unit; this necessitated that close tolerances be used in machining and aligning the bore and spline. The bores were precision ground to provide an interference fit of approximately 0.0003 inch with the shaft and a concentricity between front and aft bores of 0.0002 to 0.0004 inch to avoid misalignment, which would cause bending of the shaft and adverse rotor-dynamics effects. The internal impeller splines were shaped and referenced to the shaft spline, which was hobbled.

The impeller-shaft assembly was checked for runout before balancing to minimize material removal in achieving an acceptable balance. The impeller was rotated on the shaft until optimum runout was reached and then was indexed, disassembled, and reassembled several times and rechecked to ensure reliable results.



Figure 148. Tape-Controlled Drafting Machine.

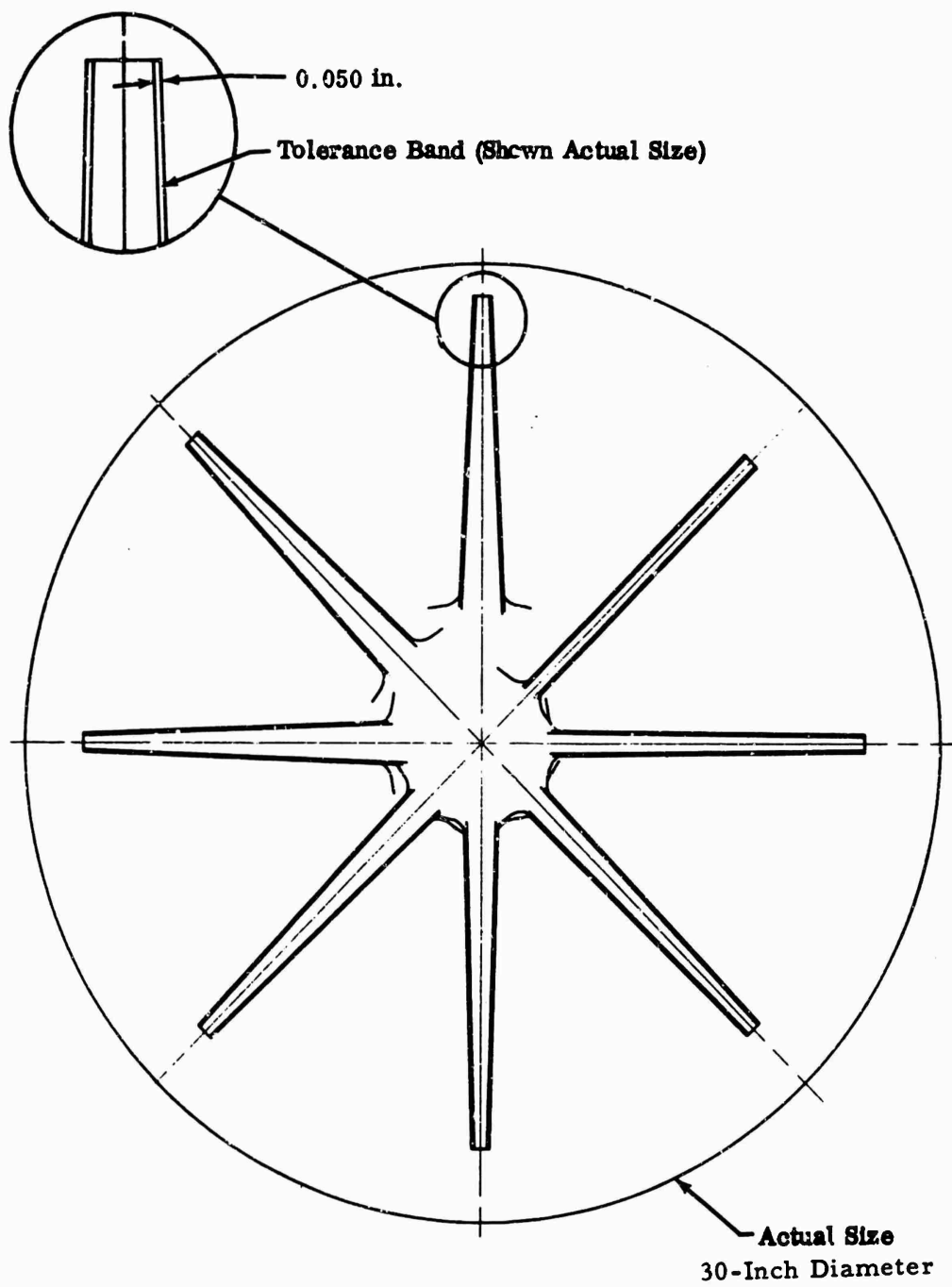


Figure 149. Impeller Optical Template (MF-1).

Because some variations existed between impeller bores and the mating shaft, a process of plating and grinding the shaft to fit was used rather than risking a regrind of the bore.

3.2 IMPELLER TEST SECTIONS

Test sections for the 4 impellers were adaptable to a common housing. In addition to the impellers, each test section consisted of a frontplate and a backplate, a collector, an impeller shroud, and an inlet. The methods used in the fabrication of these components are discussed in the following paragraphs.

3.2.1 FRONT COVERPLATES

Separate coverplates were required for each of the 4 impellers; each had a Kirksite liner that bolted into the plate to form the shroud contour, which was machined to the shape of the impeller profile with a 0.020-inch allowance for running clearance. The RF-1 coverplate was machined in 1 piece (excluding the liner) from an AISI 4130 annealed steel plate as shown in Figure 150. The first step was a roughing-out operation, with excess left on the controlled surfaces. Three AISI 4130 webs (0.25-inch thick) were then furnace-brazed to the outer surface for rigidity, after which the finish dimensions were machined, except for the shroud contour. The final stage of machining was to cut the shroud contour on a tracer lathe with the Kirksite liner installed. The holes for alignment, attachment pins, and bolts were machined in the finished plate with a precision jig-bore machine. The Kirksite liners for all 4 covers were machined from a cast block.

Coverplates for the 3 mixed-flow impellers were welded or brazed assemblies, because they were longer, axially, than the RF-1 plate. This coverplate design was dictated by limitations in sizes of materials available. The MF-1 front cover, which was the first plate to be fabricated, was made initially by spinning a 0.25-inch-thick plate of 321 stainless steel to a 120-degree cone, with the inside portion flared to approximately the impeller profile. This plate was brazed with flanges and stiffening webs. During machining of the profile, the wall thickness of the spun plate was reduced to less than 0.10 inch and the part was used only for the mechanical shakedown of the rig. A design change was made, and the second part was fabricated in 4 pieces (plus webs) and brazed into an assembly (Figure 151). The second part was used for aerodynamic testing. Covers for MF-2 and MF-3 were fabricated from 3 parts (excluding the 4 stiffener webs on each cover) rather than 4, and were similar in construction (Figures 152 and 153). The fabrication process was similar to those previously discussed.

Shroud contours were held within 0.002 inch of the basic contour dimensions, and concentricities were held to within 0.001 inch on RF-1 and MF-1 and to within 0.0005 inch on MF-2 and MF-3. Flanges (or other mating surfaces) were held

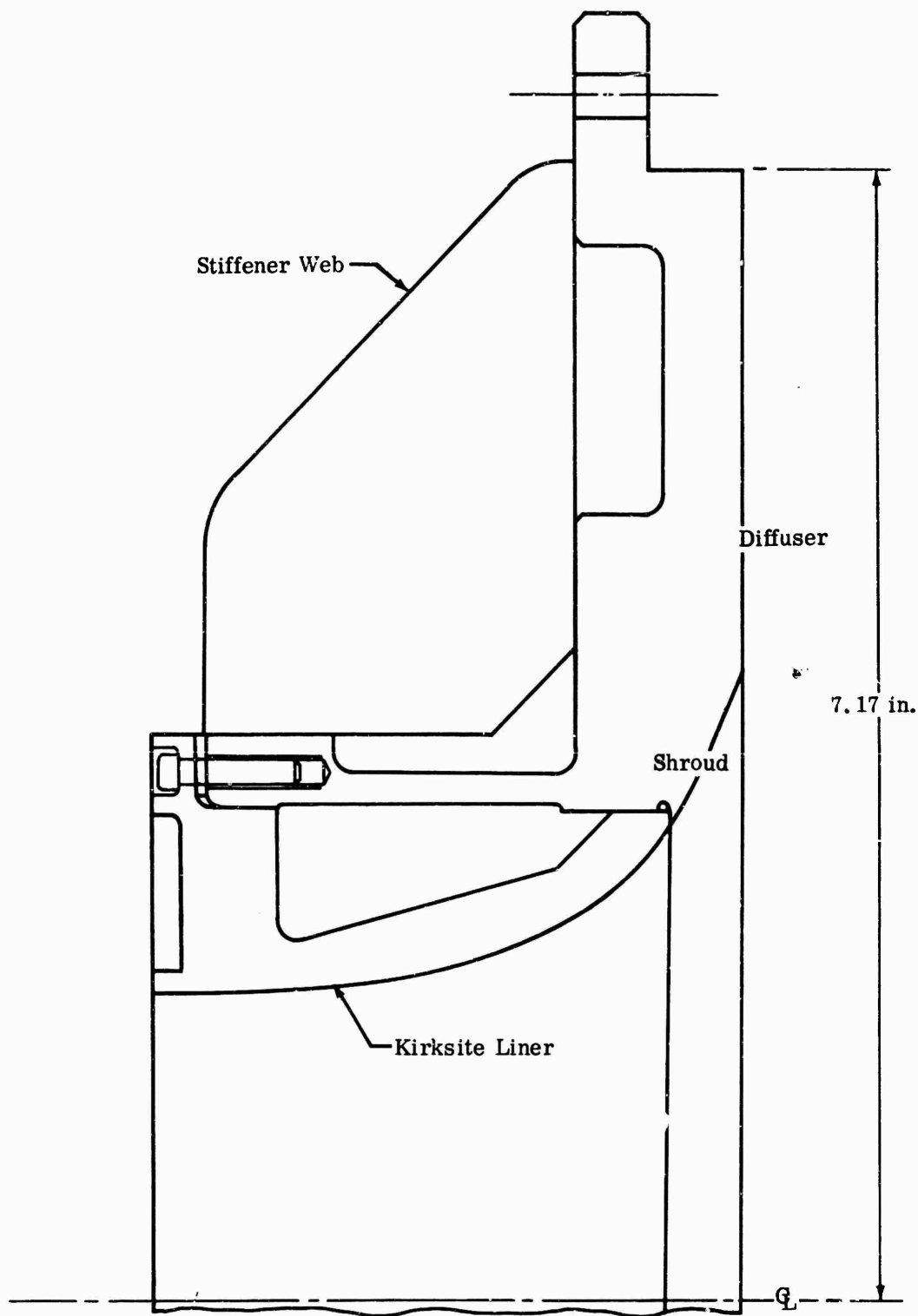


Figure 150. RF-1 Front Coverplate.

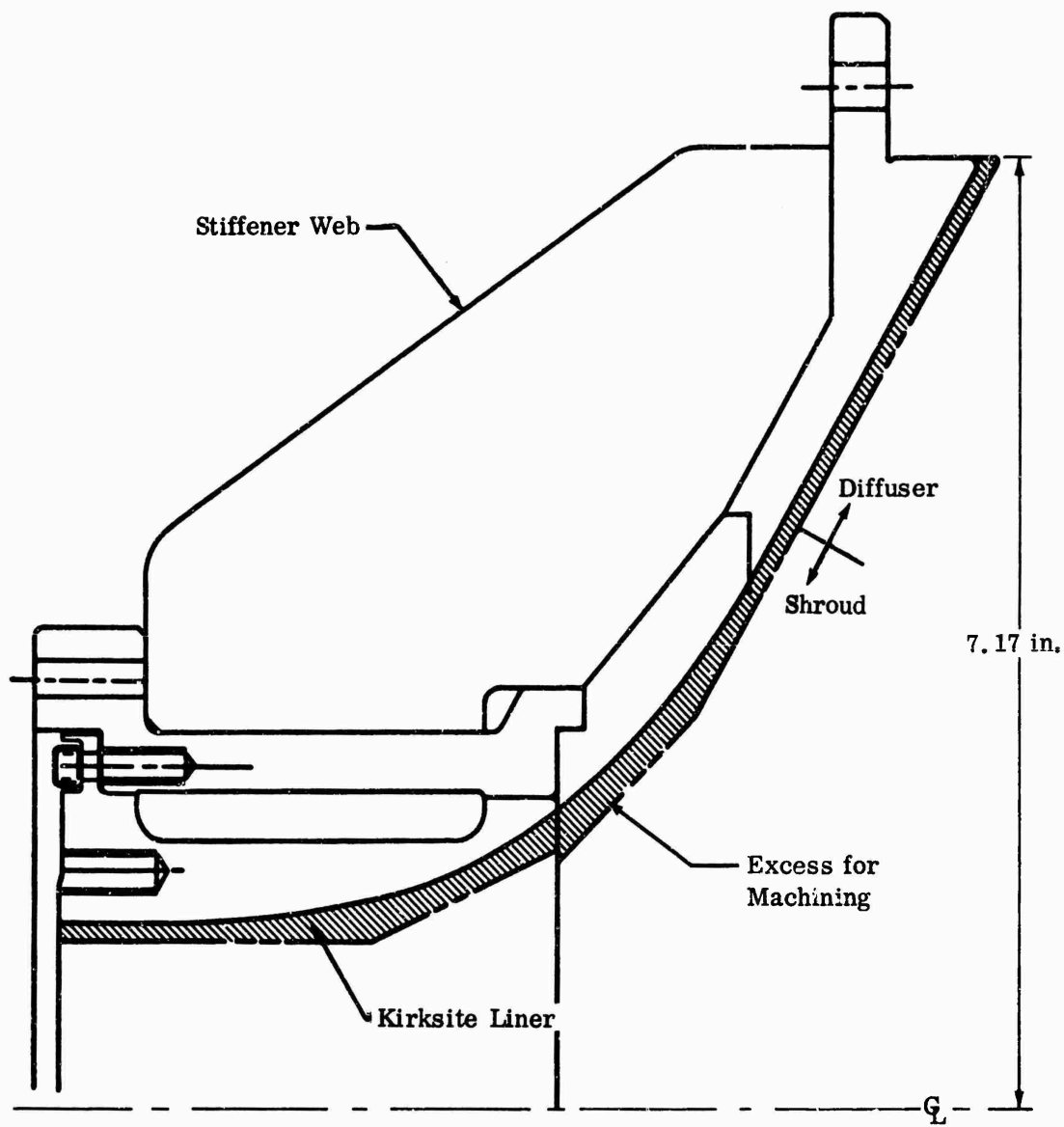


Figure 151. MF-1 Front Coverplate.

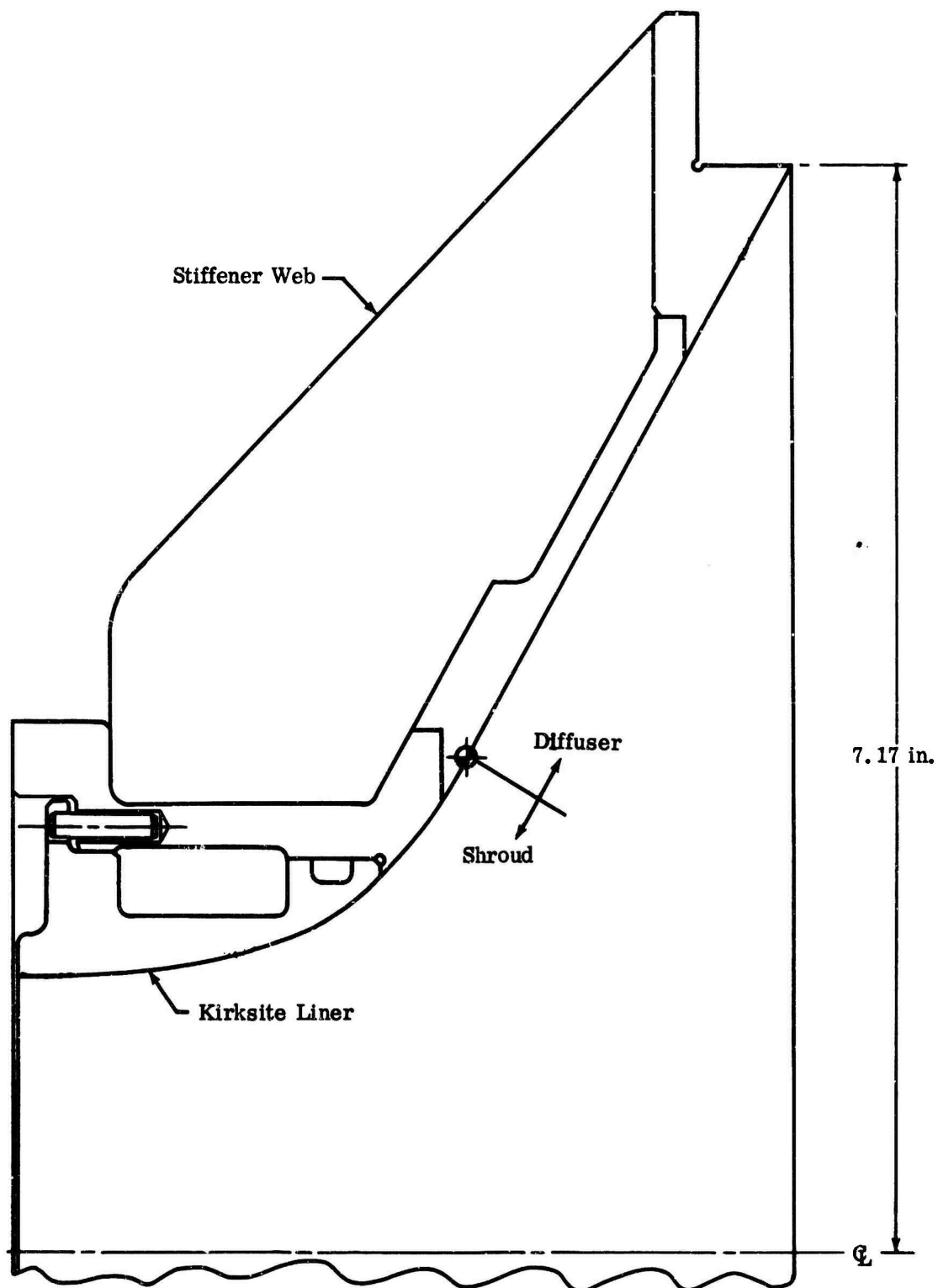


Figure 152. MF-2 Front Coverplate.

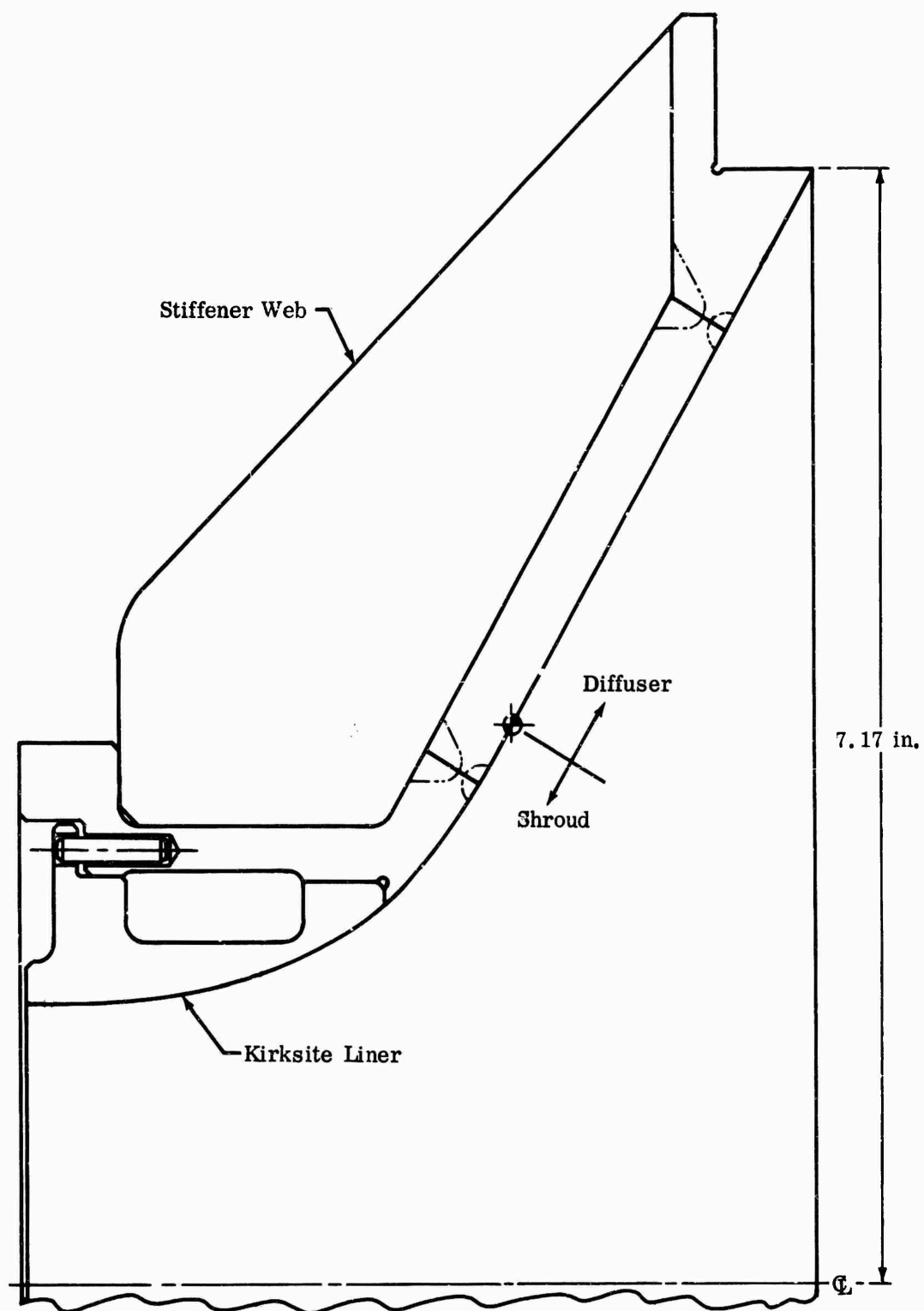


Figure 153. MF-3 Front Coverplate.

parallel within 0.002 on MF-1, 0.001 on RF-1, and 0.005 on MF-2 and MF-3. Noncritical surfaces were fabricated to a ± 0.010 tolerance.

3.2.2 BACKPLATES

Although the 3 mixed-flow backplates were similar, a separate backplate was required for each impeller. The RF-1 backplate (Figure 154) was machined from AISI 4340 plate, with eight 0.25-inch stiffening webs brazed in the back side. The roughed out plate and webs were heat treated to 140,000 psi (prior to brazing at 2150° to 2175° F in a hydrogen atmosphere for 30 minutes). All finish dimensions were machined after brazing.

The mixed-flow backplates formed a cone angle of 120 degrees, and all were 3-piece assemblies, excluding the webs. A center cone plate with an inner flange that mated with the rotor housing and with an outer flange that mated with the collector was typical of all 3 mixed-flow backplates. The MF-1 backplate was fabricated from 321 stainless, whereas MF-2 and MF-3 backplates were fabricated from AISI 4340 and AISI 4130, respectively. The cone plates for MF-1 and MF-2 were formed from 0.25- and 0.50-inch plate, respectively, with a radial seam weld at the joint as shown in Figure 155. The MF-3 backplate cone, however, was machined from a solid plate. The MF-1 and MF-2 backplates were brazed assemblies similar to that of the RF-1, but the MF-3 backplate was a welded assembly with stress relief prior to final machining. Figures 156, 157, and 158 show cross-sectional views of the MF-1, MF-2, and MF-3. The dimensional tolerance requirements were consistent with the respective front-cover assemblies.

3.2.3 COLLECTOR

One collector (Figure 159) was fabricated and used for all test sections and was attached to the front cover and backplate. The collector was made by spinning 2 half tori out of 0.06-inch-thick 321 stainless steel, which were seam-welded into a complete donut. This torus was reworked to include adapter flanges and 2 exhaust port holes. The flange surfaces were machined to the proper dimensions to complete the collector. The mean torus diameter was 20.35 inches, and the inside diameter of the cross section was 4.0 inches. To maintain dimensions under load, 8 pins were brazed in both flanges, as shown in Figure 159.

3.2.4 INLETS

The inlets (Figure 160) were similar for each rig. They consisted of 2 fairings (inner and outer), matched to the impeller inlet dimensions. The fairings were welded in place with airfoil struts. The front of the inlet was flared to provide a smooth transition between the large inlet plenum and the straight section of the inlet. All wetted surfaces were blended to eliminate surface discontinuities.

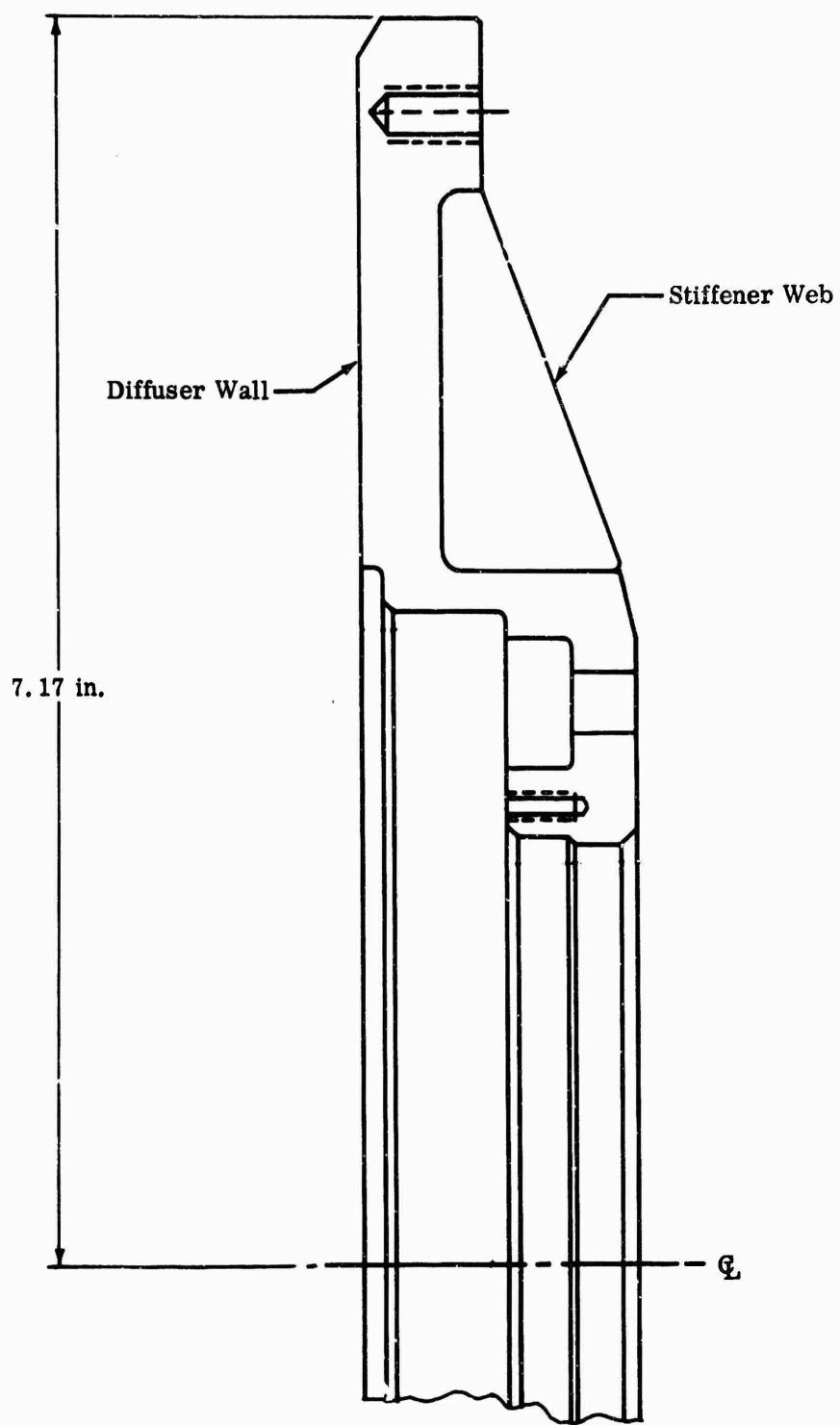


Figure 154. RF-1 Backplate.

OD = 12.8 inches
ID = 8.2 inches
Thickness = 0.25 inch

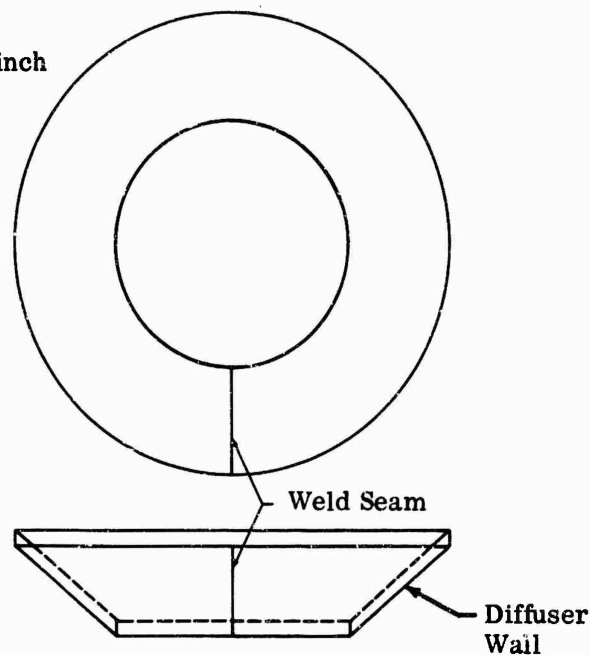


Figure 155. Backplate Cone.

The hub fairing was machined internally to accept the portion of the shaft that protruded beyond the impeller, and final machining was done after assembly to ensure proper alignment with the impeller hub.

3.3 DIFFUSERS

Four sets of diffuser vanes were fabricated initially: DI-1, DI-2, DI-3, and DC-1. Three additional sets of vane-islands were made later in the program as variations of the originals. The DC-1 cascade vanes were machined in 1 piece from AISI 4130 steel. The first 3 vane-island sets were made by tracing a vane model on a hydraulic-head milling machine and by drilling the pin holes on a precision jig bore; all surfaces and holes were referenced to tooling holes in each vane blank. DI-1 was 321 stainless, but all others were AISI 4130 or tool steel for easier machining. The later vane-island sets were set up in tooling fixtures and were ground on a surface grinder, which allowed finishing all vanes in a set together and eliminated the need for a model. Figure 161 shows 2 examples of the vane-islands.

3.3.1 INSPECTION

The first 3 vane-island sets were inspected on an optical comparator by using optical templates (Figure 162) similar to the impeller inspection templates

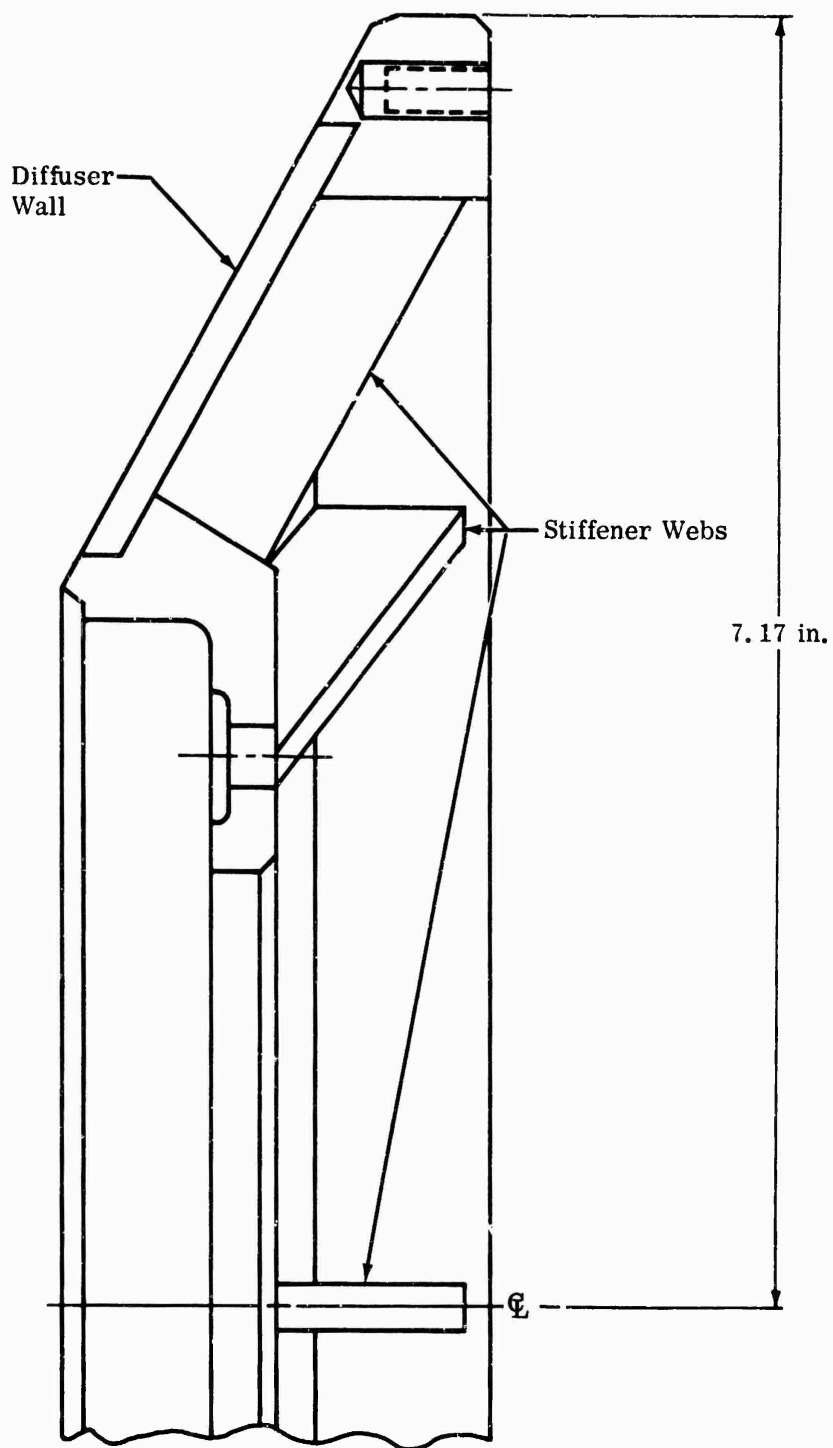


Figure 156. MF-1 Backplate.

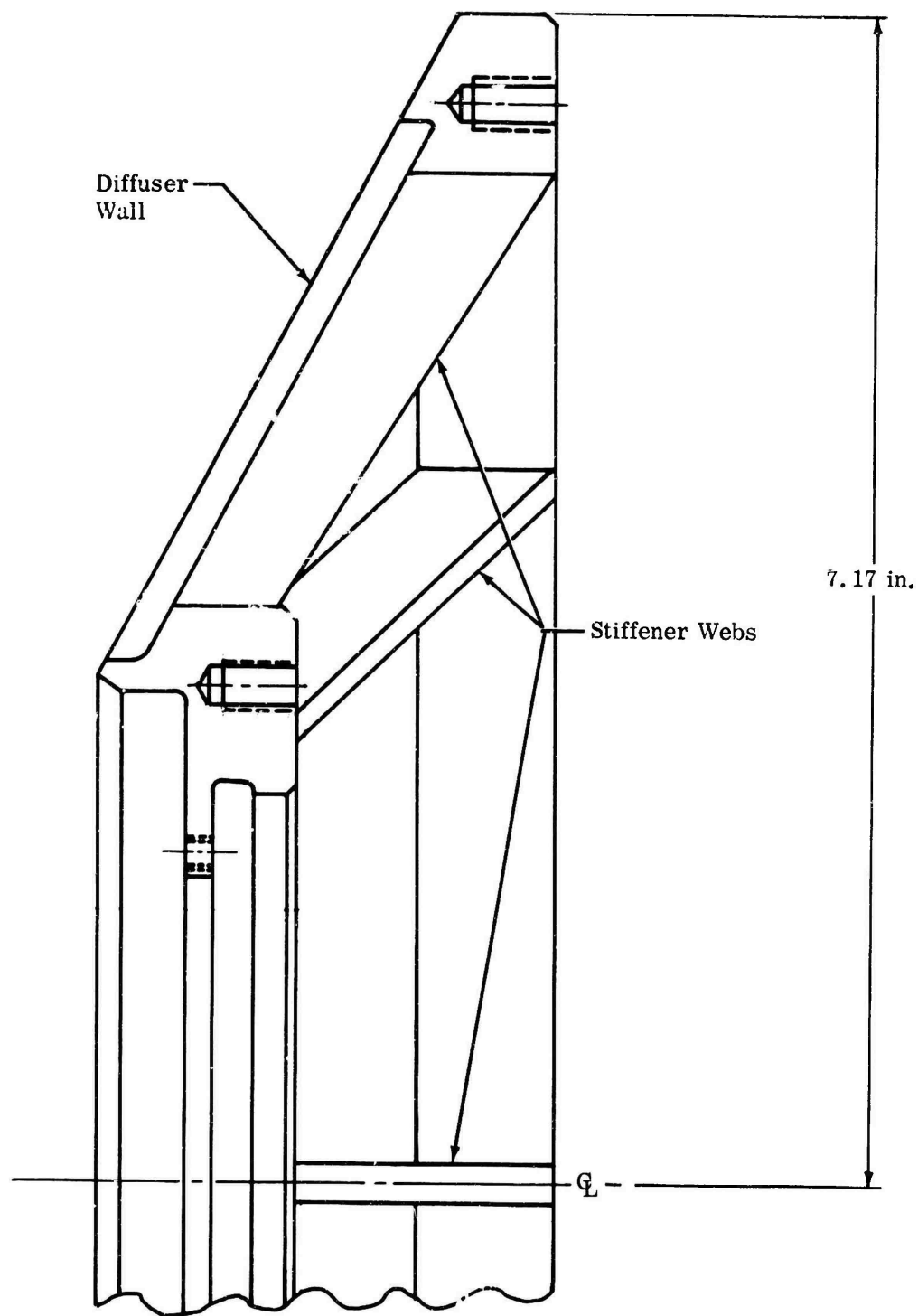


Figure 157. MF-2 Backplate.

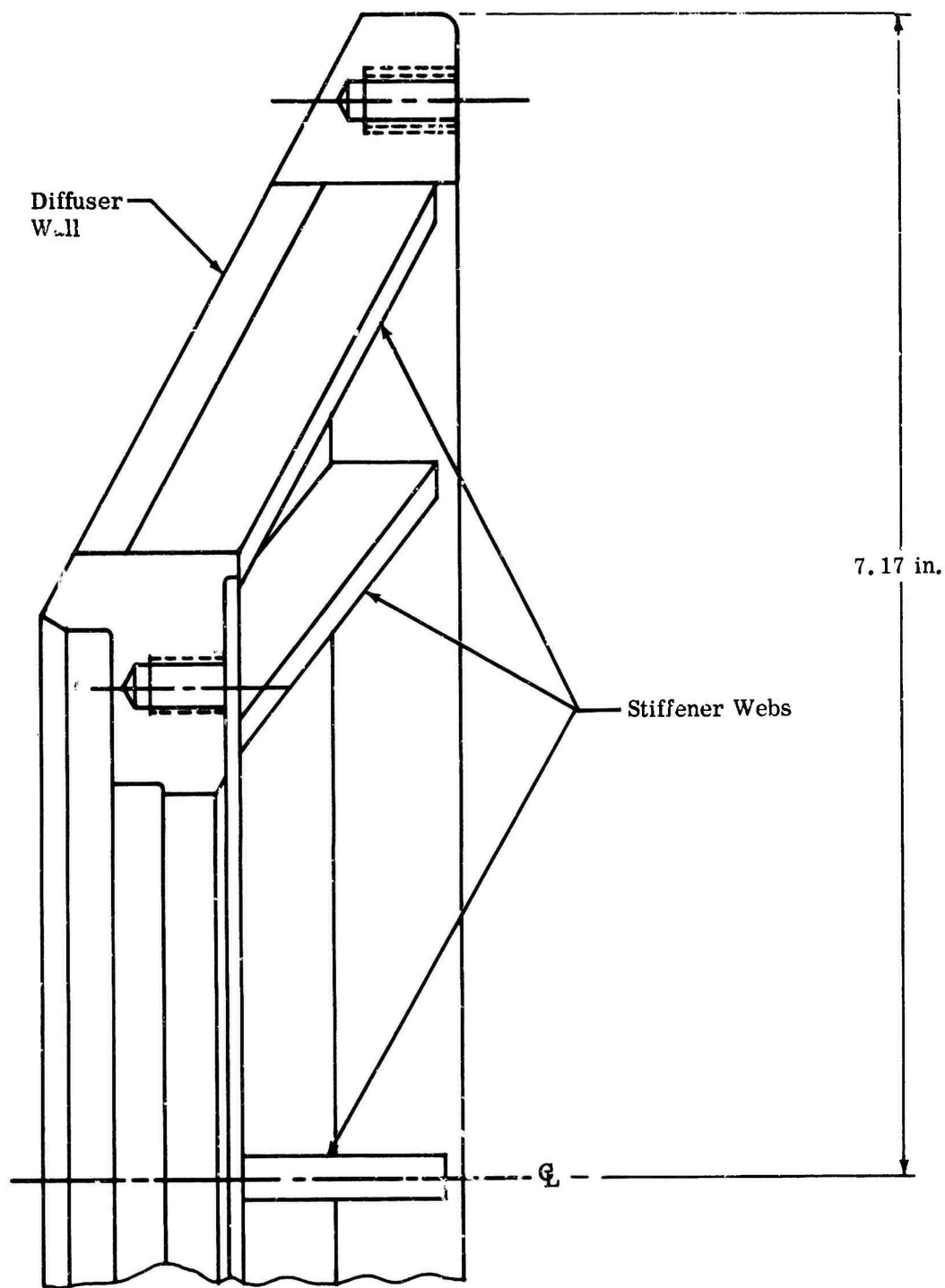


Figure 158. MF-3 Backplate.

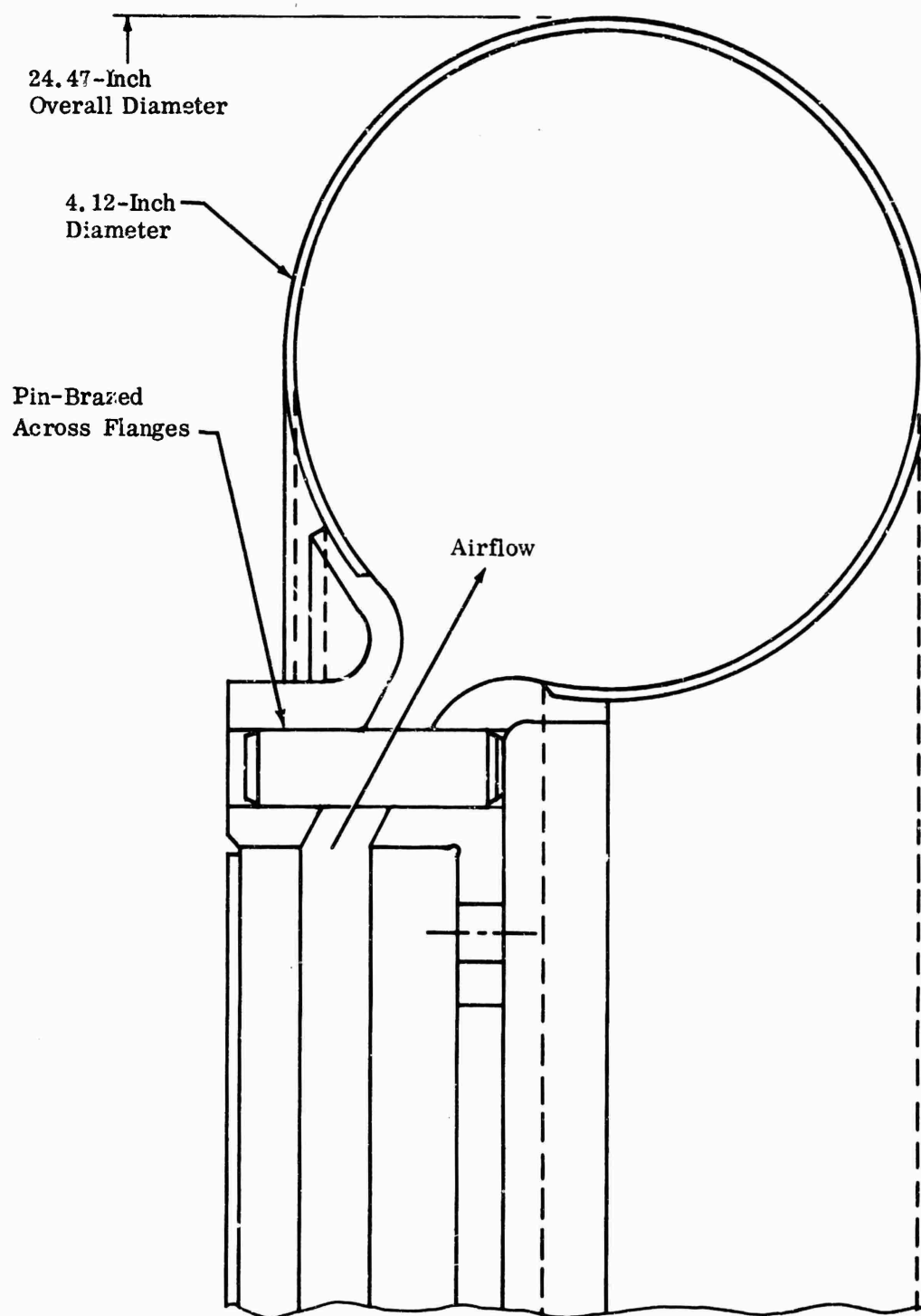


Figure 159. Collector, Section View.

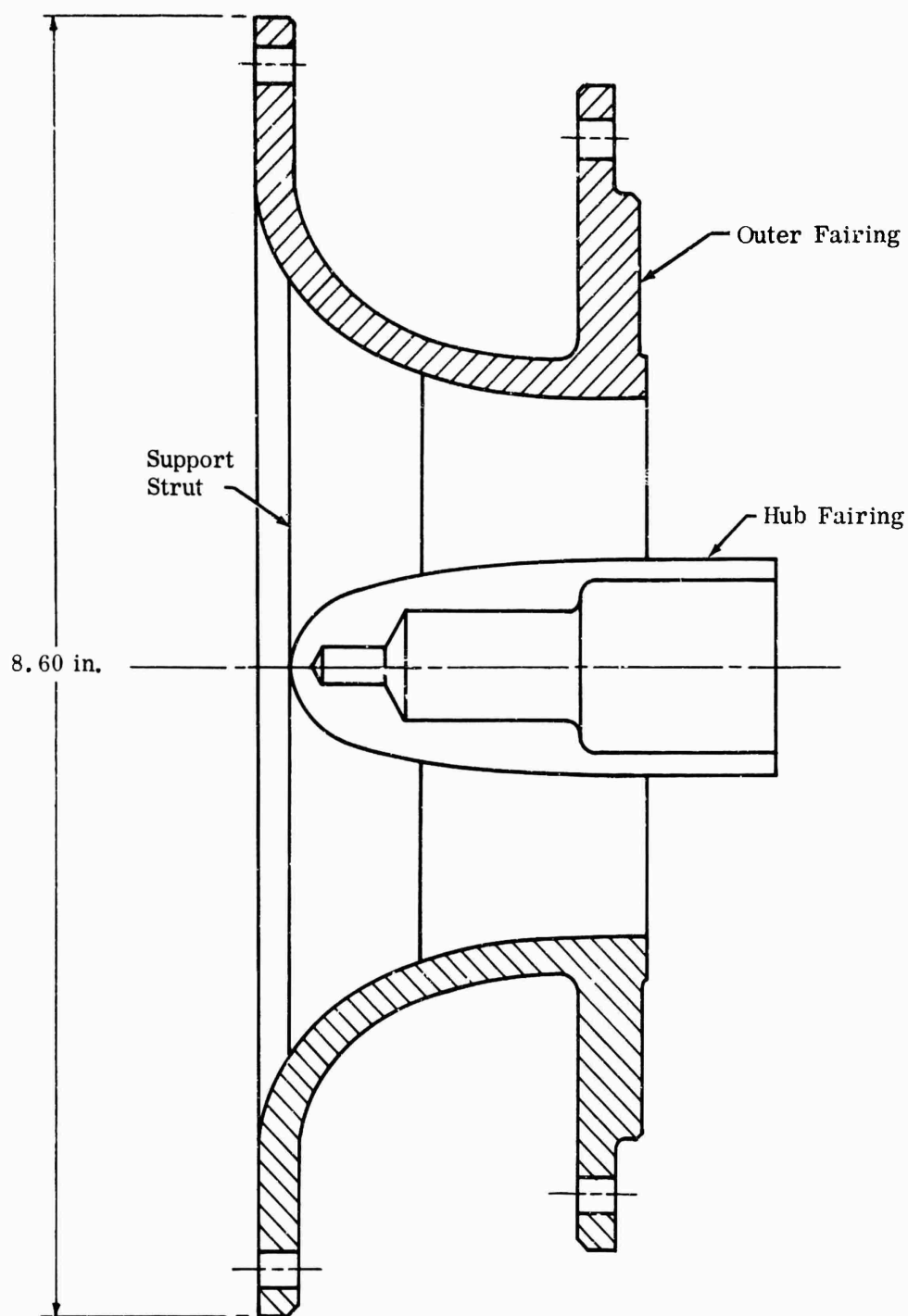


Figure 160. MF-1 Inlet Assembly.

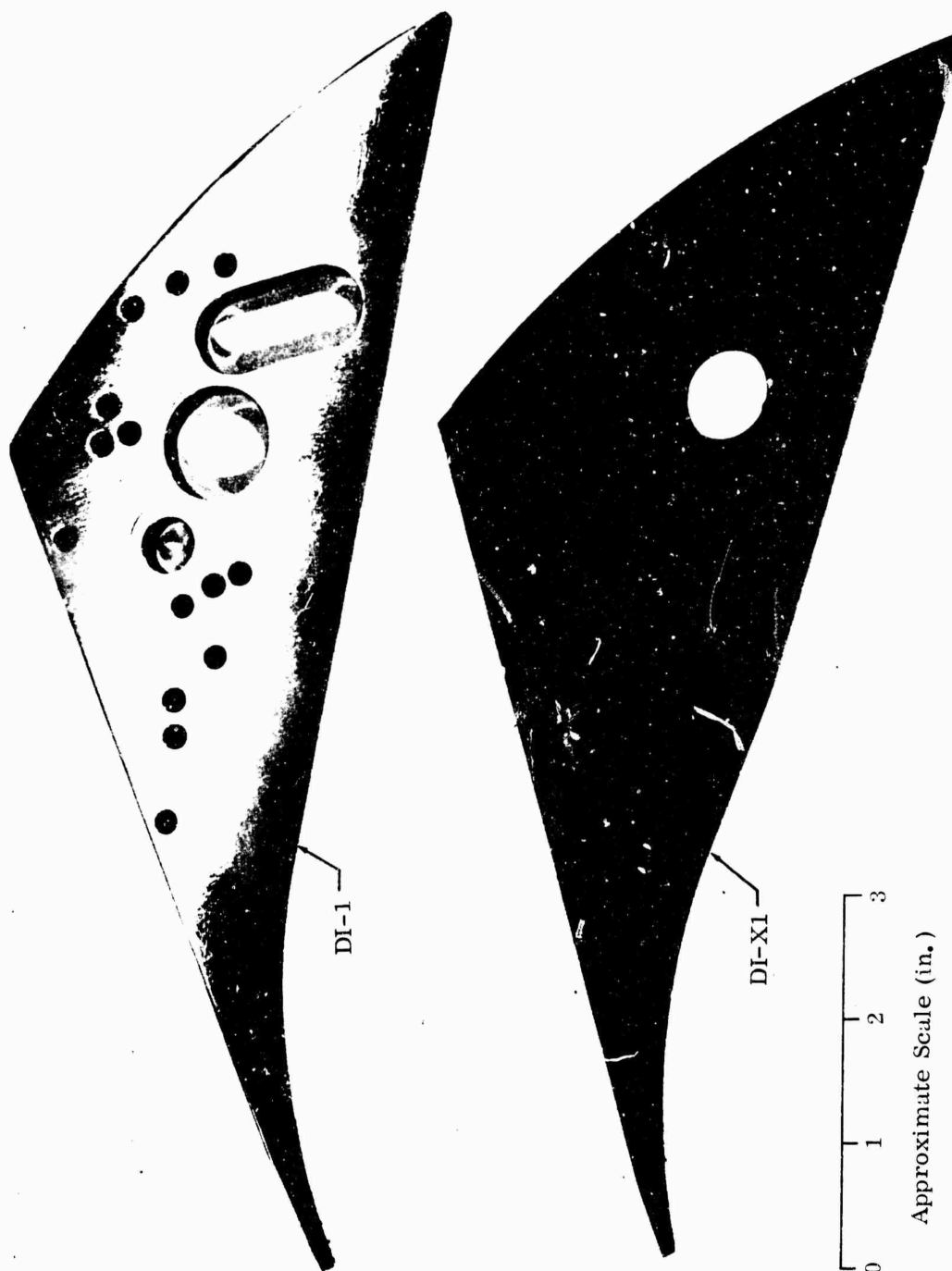


Figure 161. Vane-Islands.

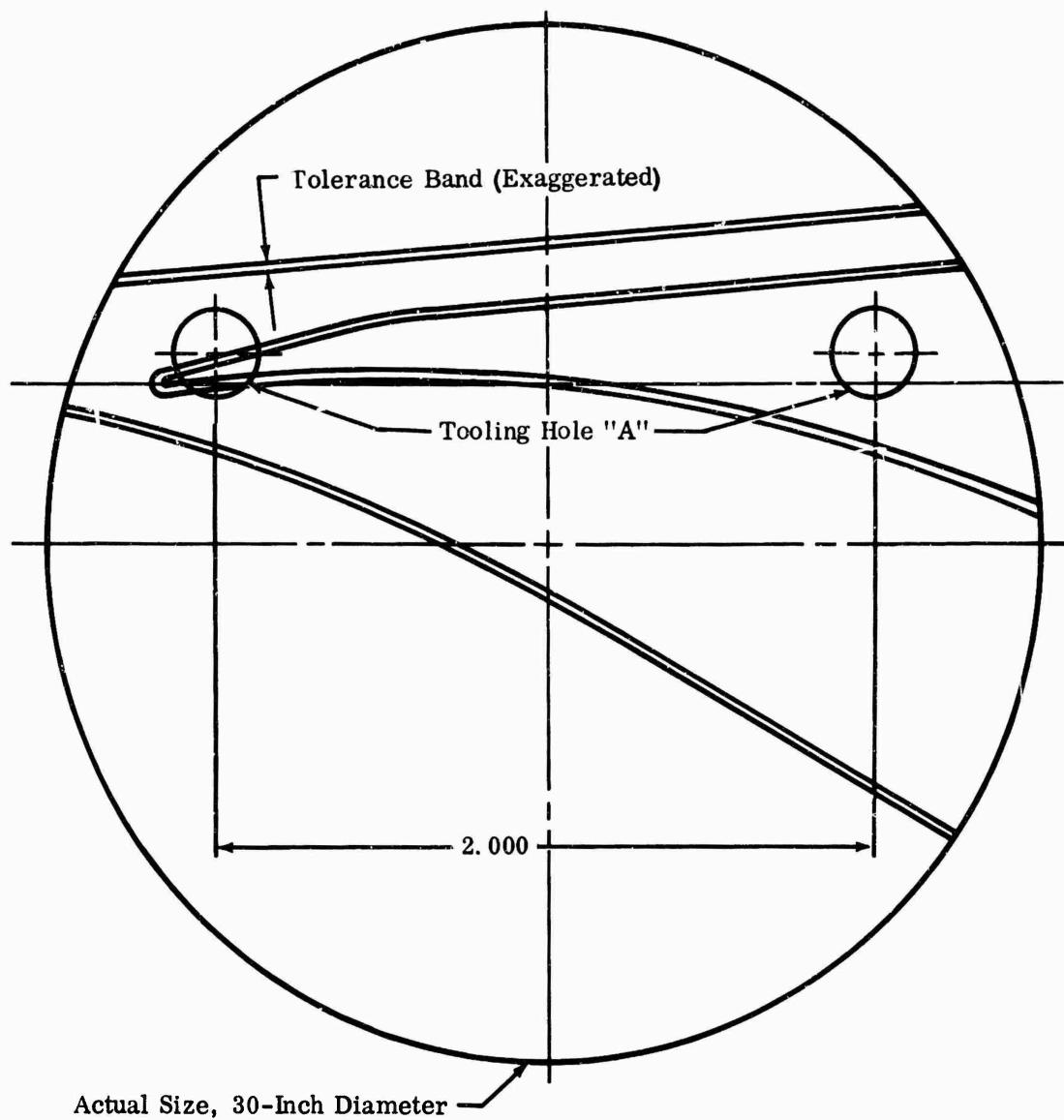


Figure 162. Vane-Island Inspection Chart.

(Section 3.1.1). The other vane-islands were inspected with standard instruments, and the tooling fixtures were used as reference. Profiles were to be within 0.002 inch of the basic contour for all vanes, and holes were to be located within 0.001 inch of true position.

3.4 DIFFUSER TEST SECTIONS

Test sections for the 4 diffusers were fabricated from 1 basic design, consisting of an inlet, inlet guide vanes, front coverplate, backplate, and collector. Three coverplate-backplate pairs were fabricated because of the different installation and instrumentation requirements for the various vane sets. DI-1 and DI-2 used a common pair. The other test section components were used for all diffuser configurations.

3.4.1 COVERPLATES

The coverplates were 2-piece brazed assemblies, machined from 321 stainless steel with integral stiffener webs (Figure 163). Exterior surfaces were finish-machined before brazing. The static-pressure-tap tubing was brazed in place during the assembly-brazing operation, as shown in Figure 163. The shroud contours and diffuser walls were machined in 1 operation on a tracer lathe after brazing. Shroud contours were held to within 0.003 inch of the basic contour, and concentricities were held to within 0.001 inch. Holes for fasteners and instrumentation (except for static taps) were machined in the finished part on a precision jig-bore machine to within 0.001 inch of true position. Other tolerances were ± 0.010 inch for noncritical surfaces. A front cover, with the inlet extension and inlet guide vane assembly attached, is shown in Figure 164.

Stainless steel was selected for the coverplates (and backplates described in the following section) because of its corrosion-resistant properties at the high operating temperatures predicted for this rig. However, this advantage was negated by the thermal gradients in the coverplate, combined with the rate of thermal expansion (50 percent higher than steel) which caused warpage, and the flat surface of the diffuser wall became dished after several operating cycles.

3.4.2 BACKPLATES

Backplates were machined in 1 piece from 321 stainless steel plate, with integral stiffener webs similar to those for the coverplates. Static-tap tubing was swaged in place before final machining, as described in Section 5.0. Other holes for fasteners, vane-locating pins, and instrumentation were machined on a precision jig-bore machine. Figure 165 shows a backplate with the collector attached and a vane set installed. Dimensional tolerances for the backplates were consistent with those for the coverplates.

3.4.3 COLLECTOR

The collector was fabricated in the same manner as the collector for the impeller test sections, except that there were no structural ties between the 2 flanges.

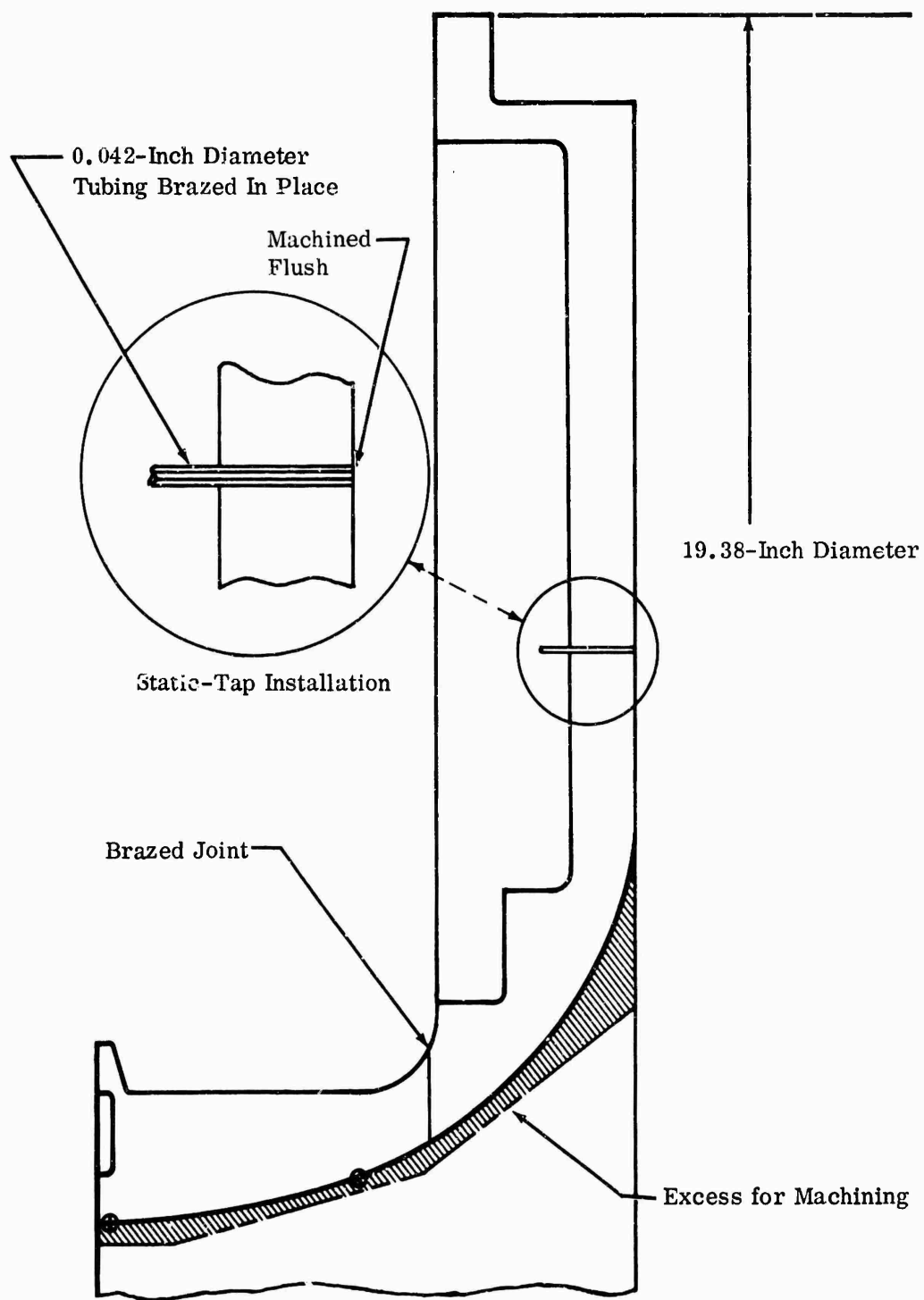


Figure 163. Diffuser-Rig Front Coverplate.

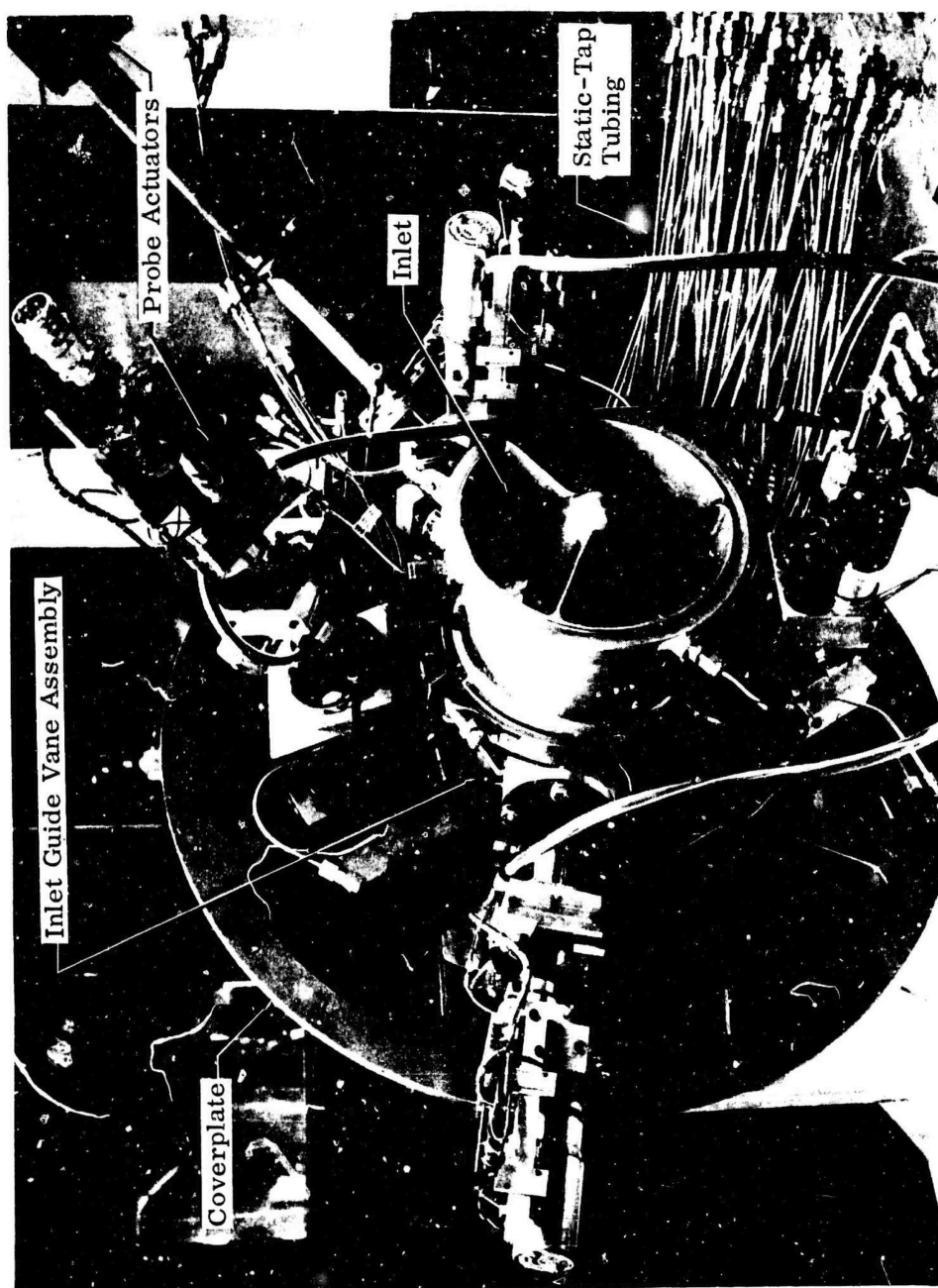


Figure 164. Coverplate and Inlet.



Figure 165. Backplate With Vane-Islands and Collector.

3.4.4 INLET

The inlet (refer to Figure 164) was fabricated from aluminum and was similar to the ones for the impeller test sections of Section 3.2.4.

3.4.5 INLET GUIDE VANES

The leading edges of the guide vanes were stationary with adjustable trailing edges. The leading edges and mounting rings were brazed into an assembly that installed into the outer housing. The trailing sections pivoted on pins located about midchord of the vane assembly; they were rotated by a slave ring and pin arrangement, as shown in Figure 166. Figure 167 shows the inlet guide vane components. The vane angle was remotely adjustable by using a motorized drive to actuate the slave-ring lever.

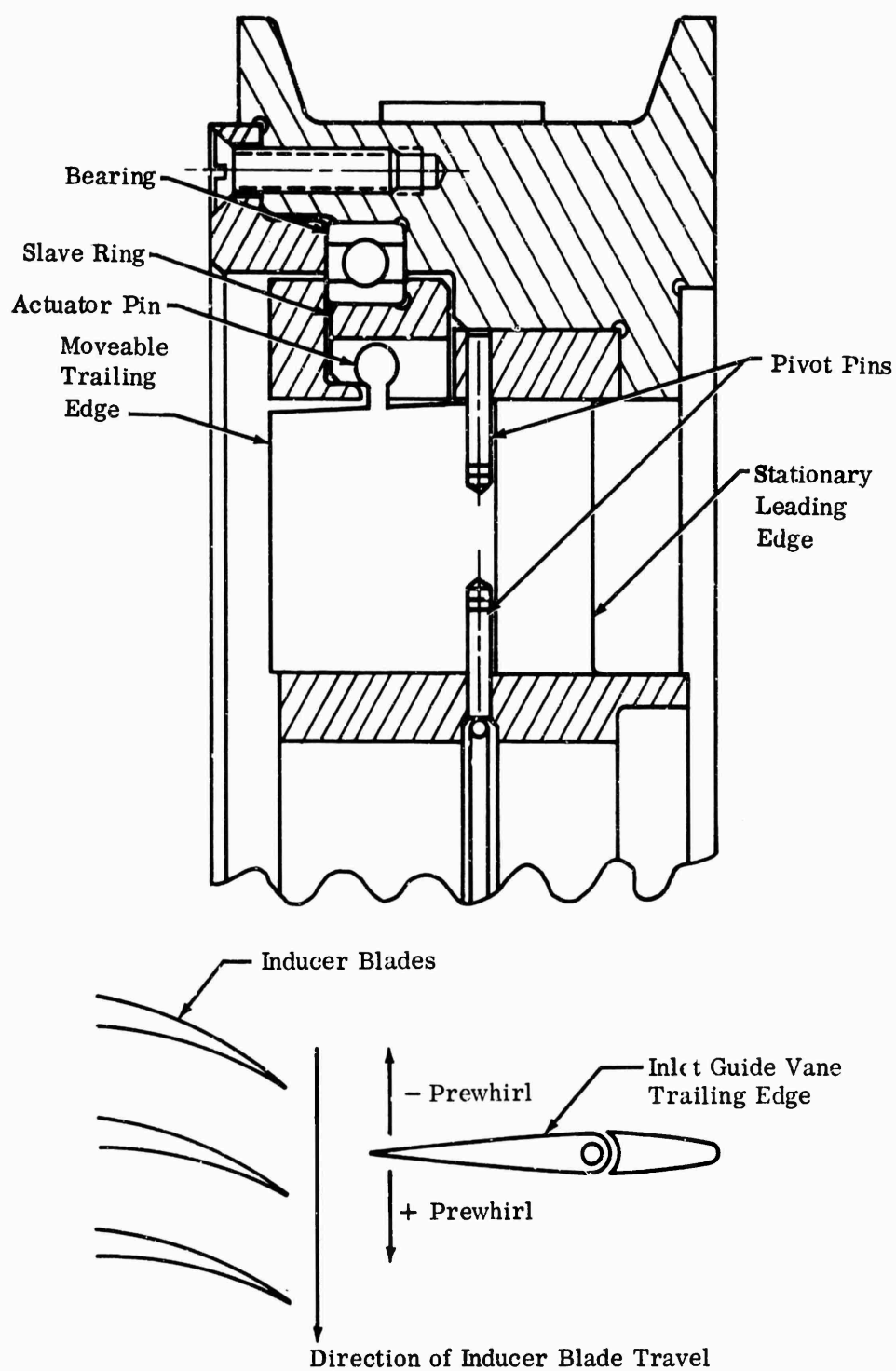


Figure 166. Inlet Guide Vane Construction.

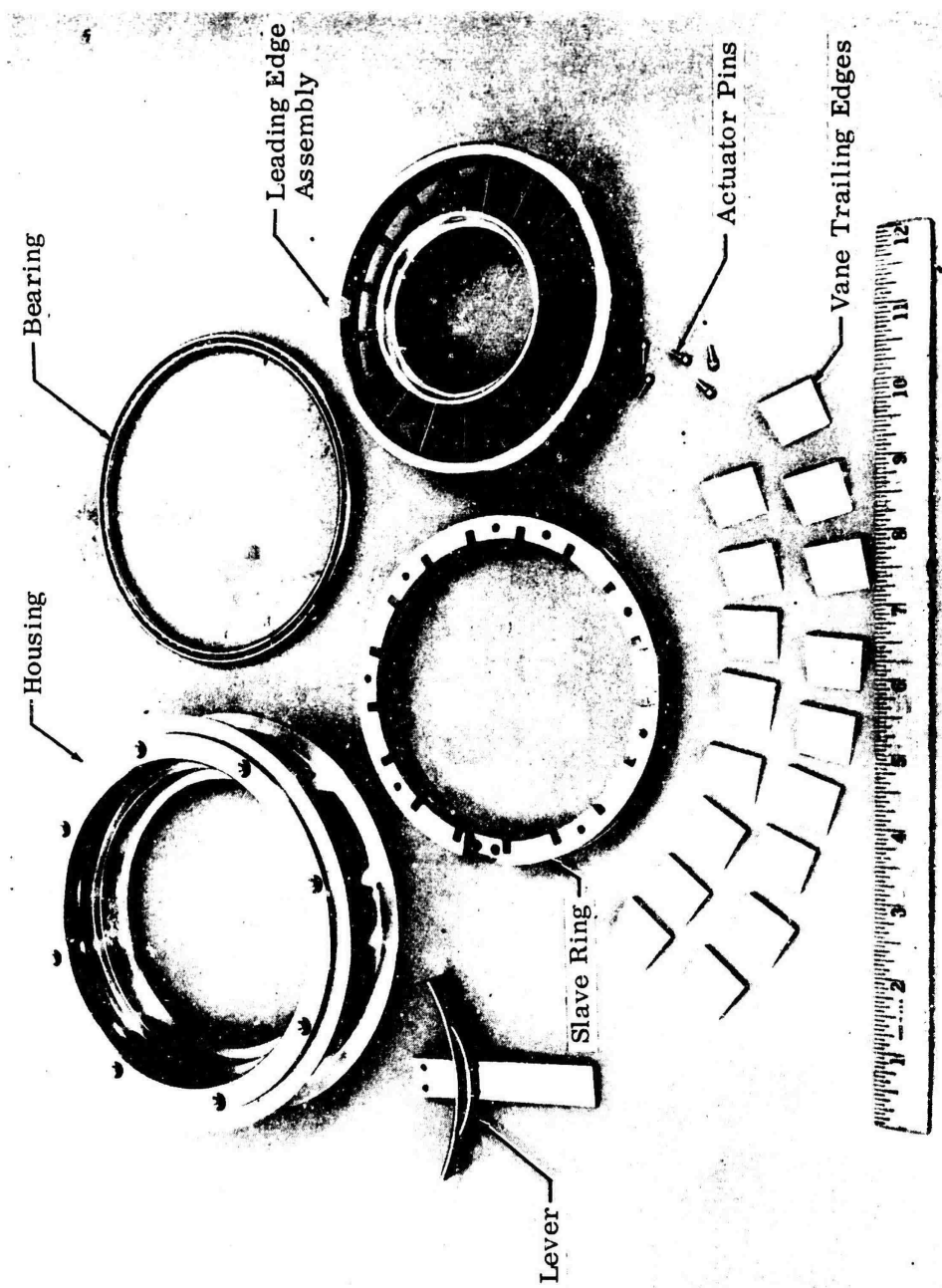


Figure 167. Inlet Guide Vane Components.

(U) 4.0 INSTRUMENTATION

Items of instrumentation used in measuring the various impeller-shroud pressures, diffuser pressures, impeller discharge temperature, impeller stress, and rotor thrust are described in the following sections. Figure 168 shows the various types of probes used. Other special instrumentation is also discussed in this section.

4.1 PRESSURE-MEASUREMENT INSTRUMENTATION

Total-pressure rakes (3 probes each) were designed to measure discharge profiles across the impeller tip. Several rakes were designed with different probe spacings (Figure 169). Two rakes were located at different circumferential positions; the center probe of each rake was at the same depth from the wall so that data could be compared. By this means, a pressure profile of 5 data points was measured from the 2 rakes, with a check at the center point. Details of probe size and design are also shown in Figure 169.

A yaw-pressure probe was also installed at the impeller tip to measure flow angle and total pressure. The yaw probe is shown in Figure 170. The probe tip was cantilevered from a stem that extended across the passage. The stem was anchored in both walls to minimize probe flutter.

The rakes and yaw probes were calibrated for angle sensitivity in a small wind-tunnel section with a Mach capability of 1.3 (Figure 171). Typical results are shown in Figure 172.

Static-pressure taps were installed in accordance with Reference 19. The taps had 0.020-inch-diameter holes with sharp corners. Figure 173 shows the static-pressure taps in a backplate of the diffuser rig with an 8-vane-island diffuser. Kiel probes were installed in the diffuser passages to measure total pressure. These probes were designed with a 0.10-inch-diameter venturi-type throat.

A traversing total-pressure probe was installed in the side wall of the diffuser rig to measure pressure along a streamline from the impeller tip through the diffuser passage. Figure 174 shows the path of this traversing probe. The probe-tube was designed to slide in a slotted track embedded in the diffuser wall, with a total-pressure probe mounted on the end of the sliding tube. Figure 175 is a sketch of the probe design, and Figures 176 and 177 are photographs of a working model of the probe. The model was fabricated before its installation in the rig to prove the concept. In the diffuser test rig, the probe was traversed by a remote-control actuator. The pressure probe was fabricated from 0.018-inch-diameter tubing. This size was the smallest-practical to maintain reasonable strength and to minimize blockage, flow disturbance, and plugging.

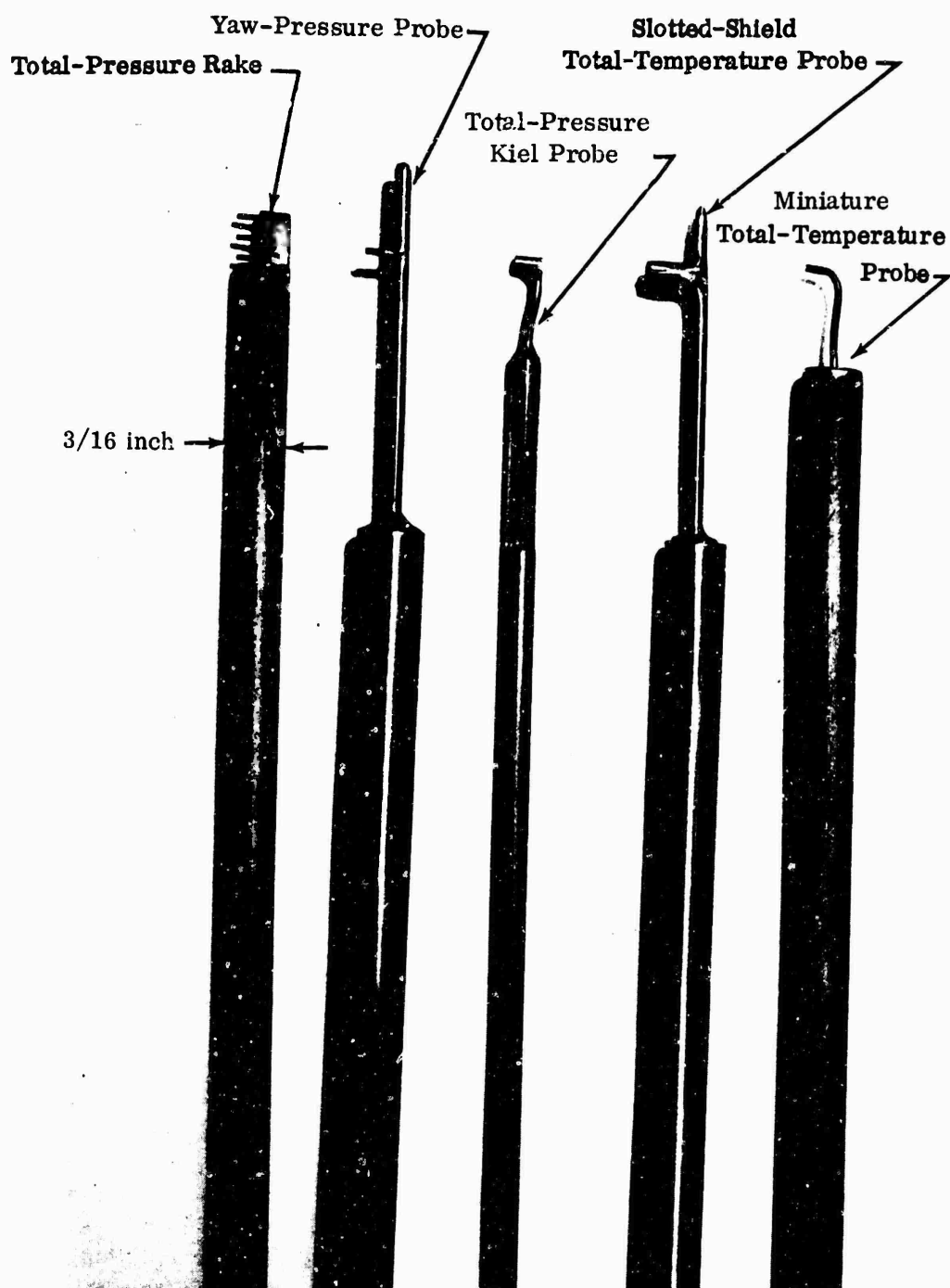


Figure 168. Pressure and Temperature Probes.

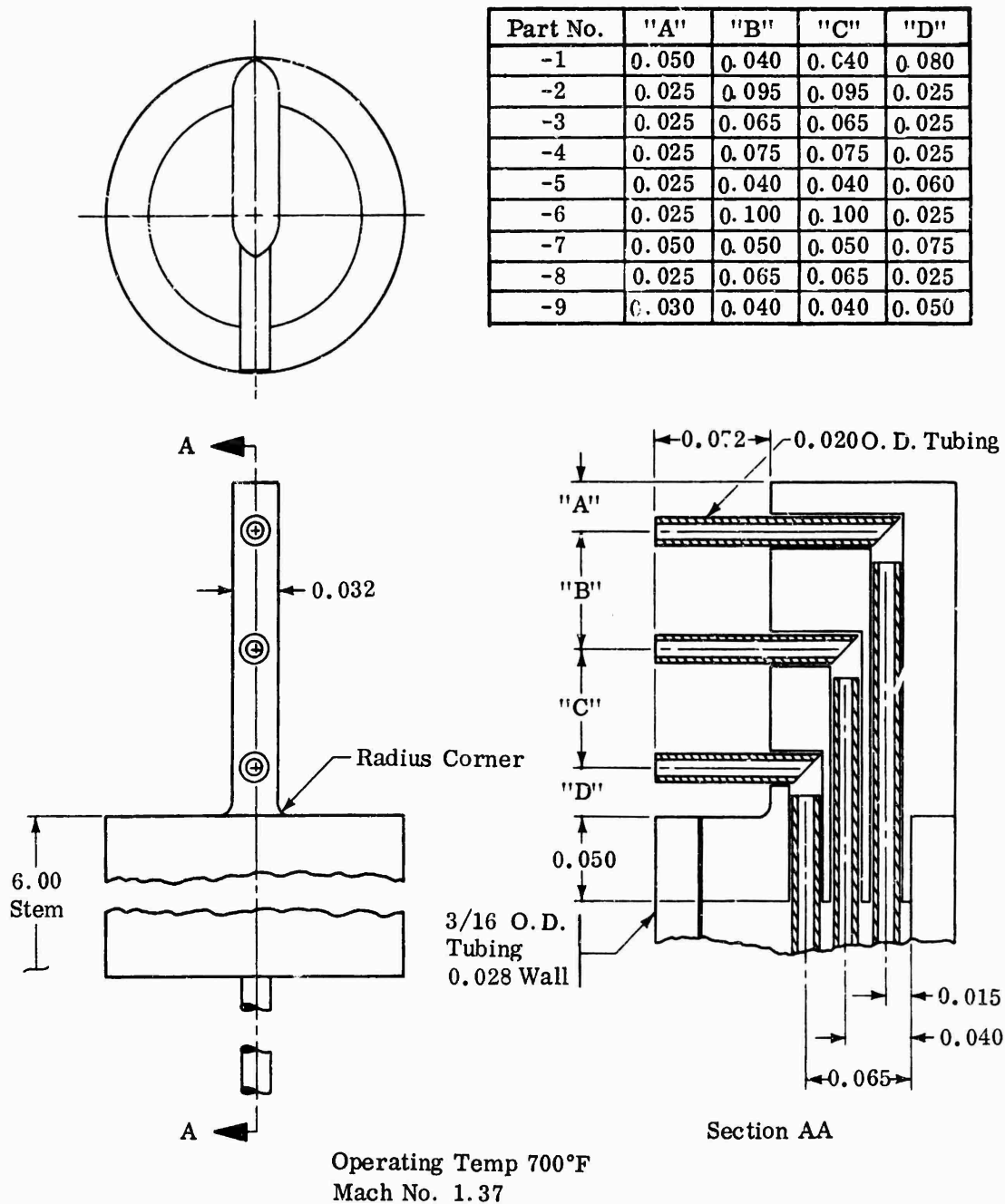


Figure 169. Total-Pressure Rake.

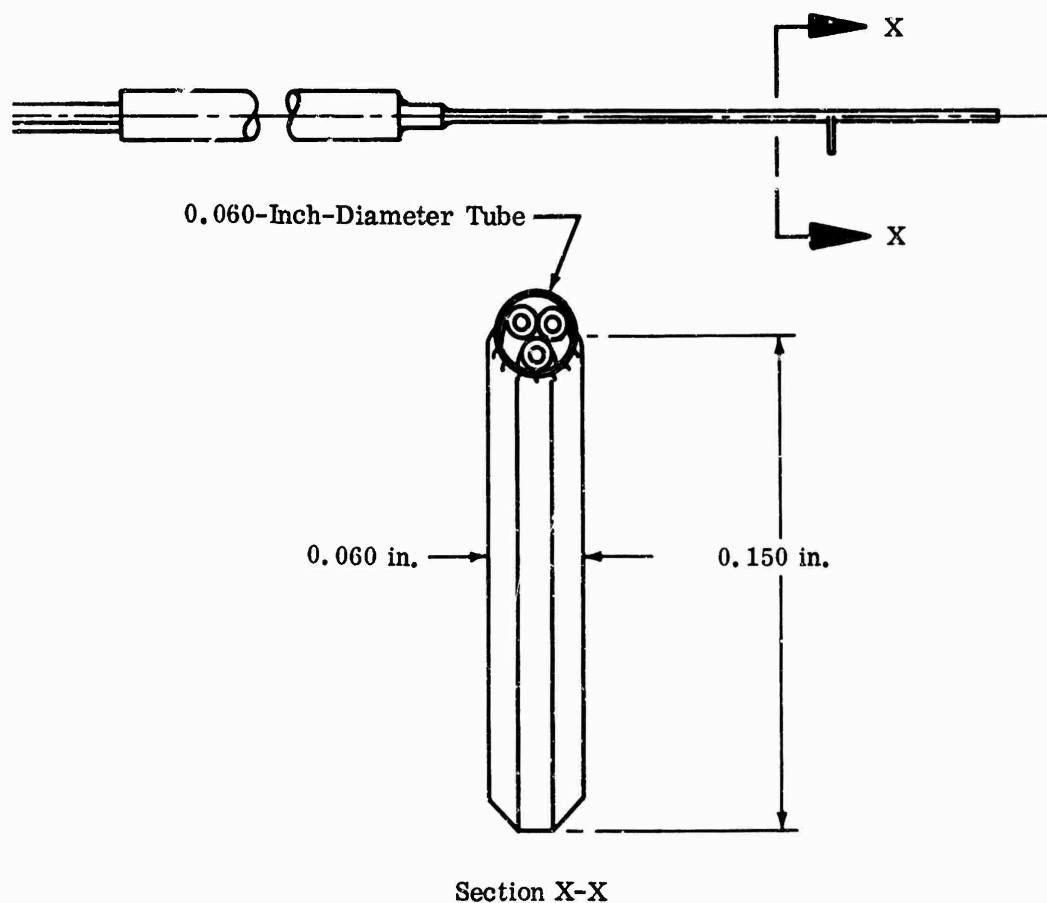


Figure 170. Yaw Pressure Probe.

Static-pressure transducers were used in the vaneless space to determine static-pressure fluctuations from the impeller tip. A transducer with a water-cooled jacket was used for these measurements (Figure 178). This transducer was selected for its small size and high-frequency response; with water cooling, it could be used at the temperature level of the impeller tip.

The digital data system was designed to measure pressures at 184 stations. This system (Figure 179) consisted of eight 24-channel cutoff valves; a storage volume for each pressure; 4 Scanivalves, which were used to port the stored pressures to 4 pressure transducers; and the 2010G system, which included a digital voltmeter and a paper tape punch.

When each data point was recorded, the pressures were trapped in the storage volumes and then were measured in groups of 46 with 2 reference pressures. The

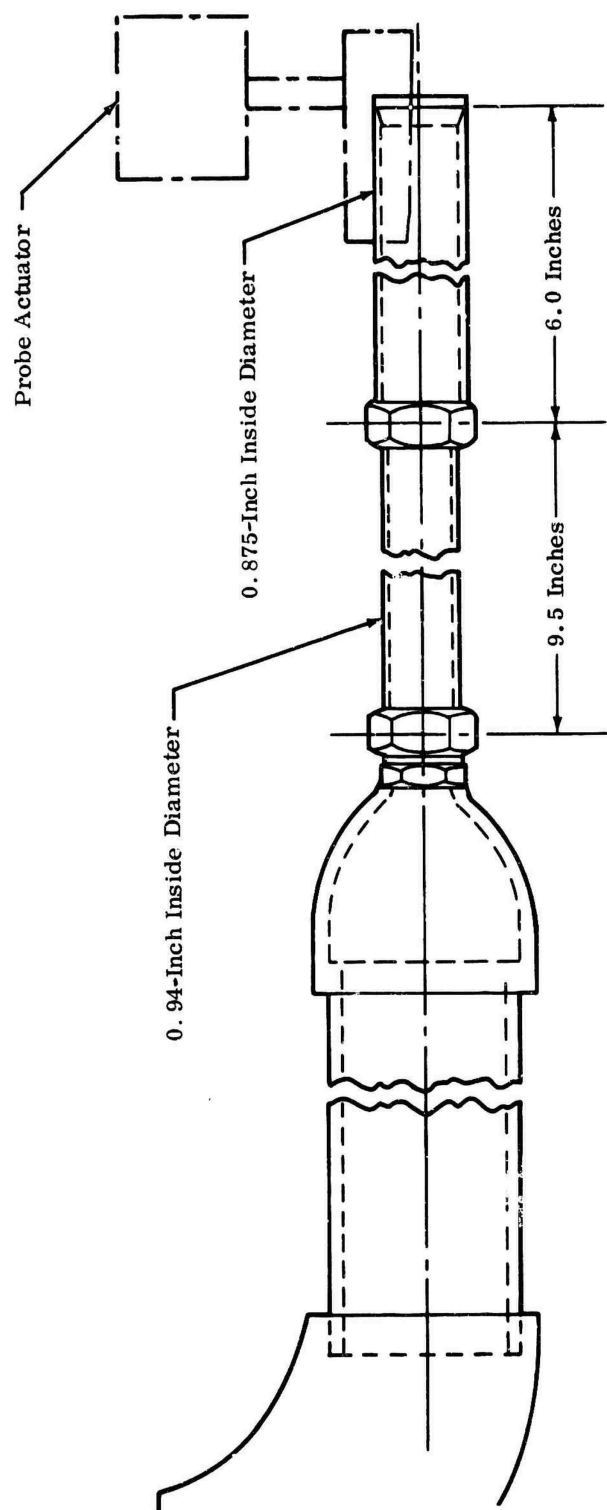


Figure 171. Pressure-Probe Sensitivity Calibration Facility.

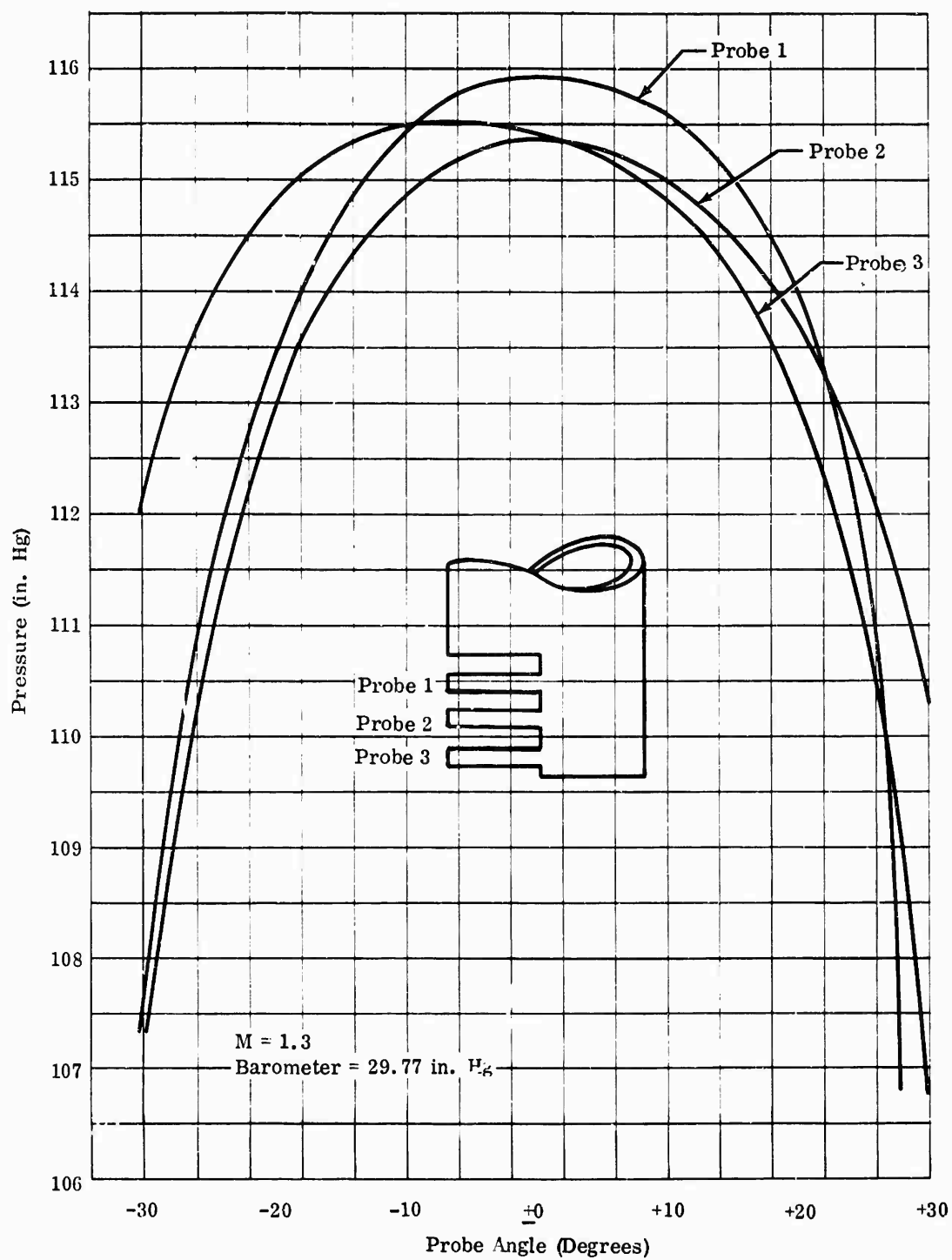


Figure 172. Three-Probe Rake Calibration.

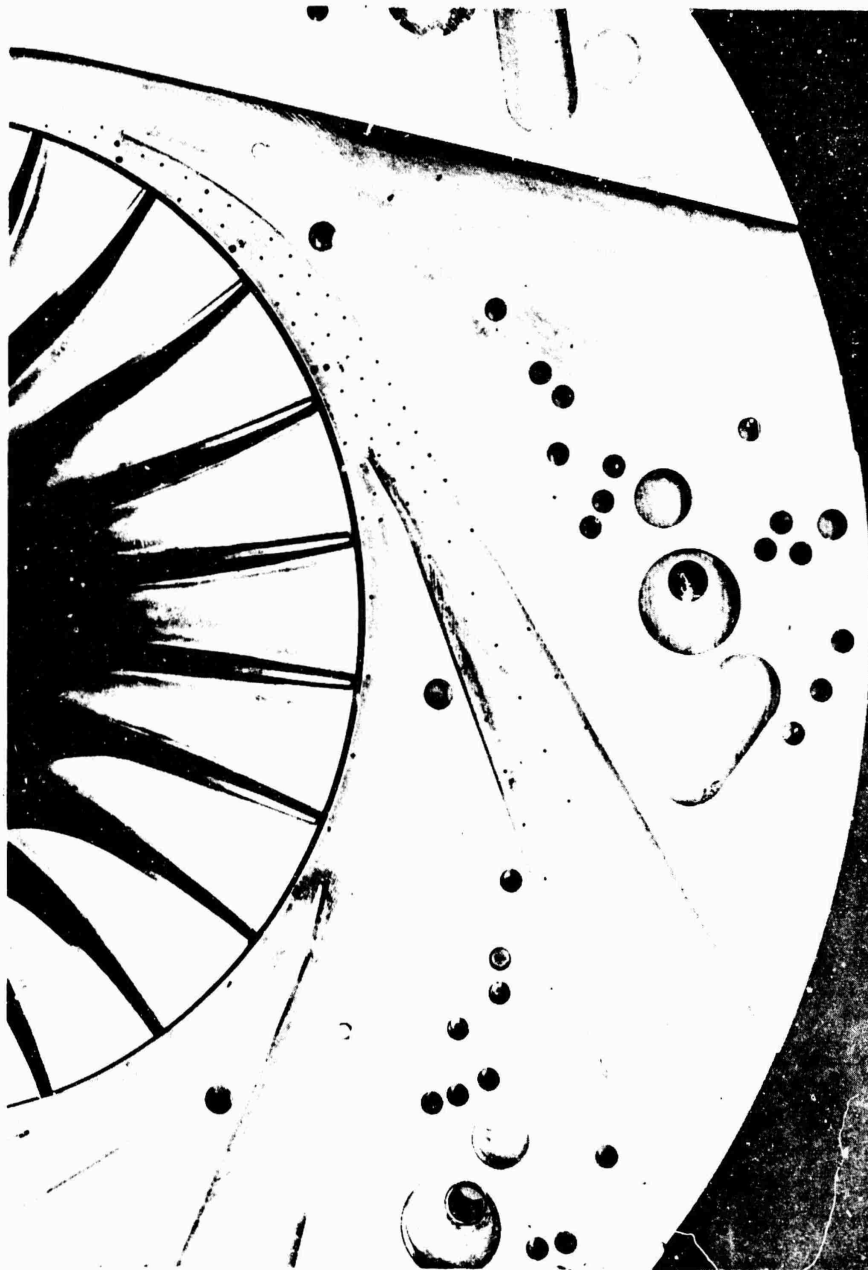


Figure 173. Diffuser-Rig Backplate.

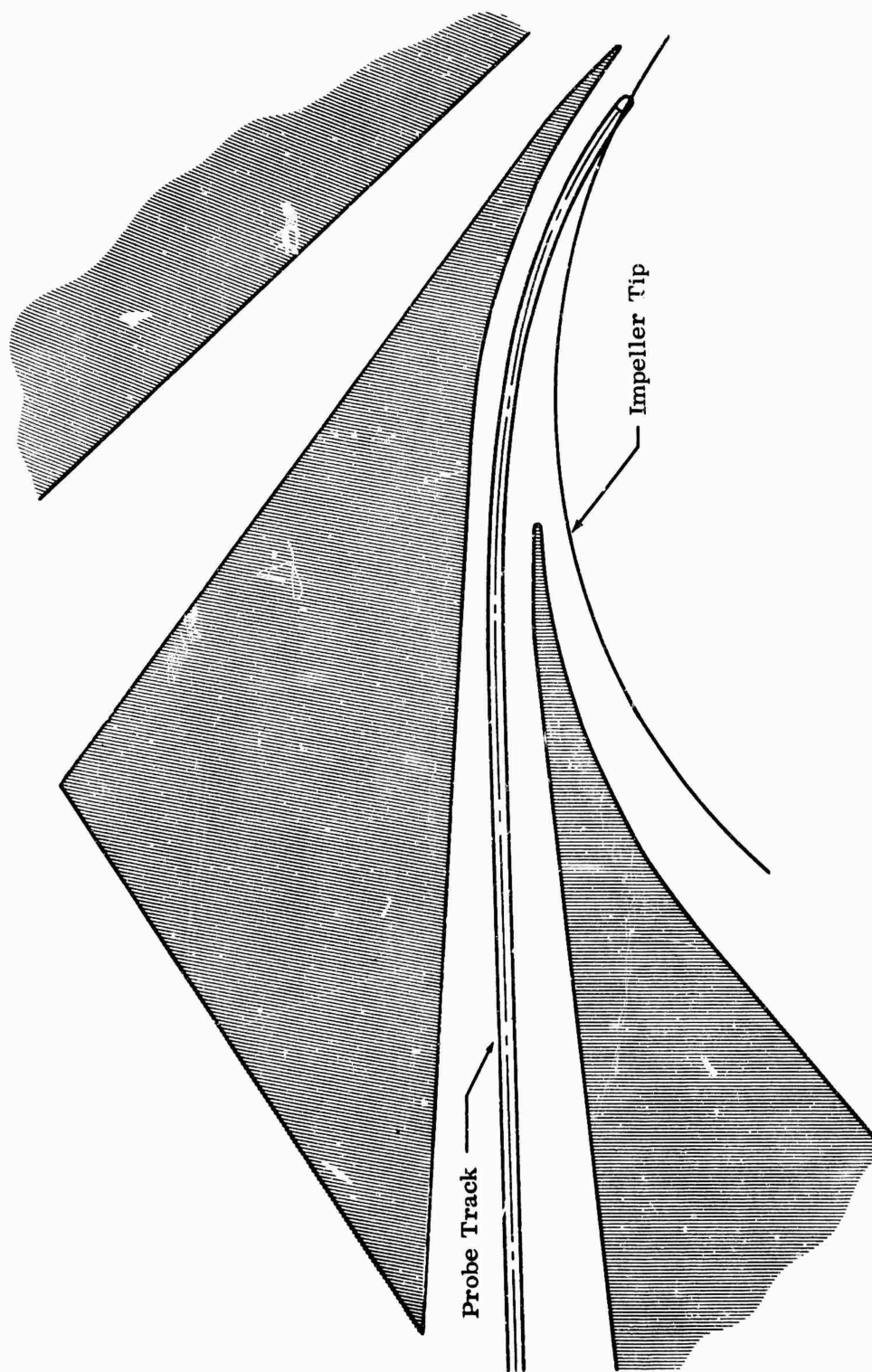


Figure 174. Traversing Probe Path.

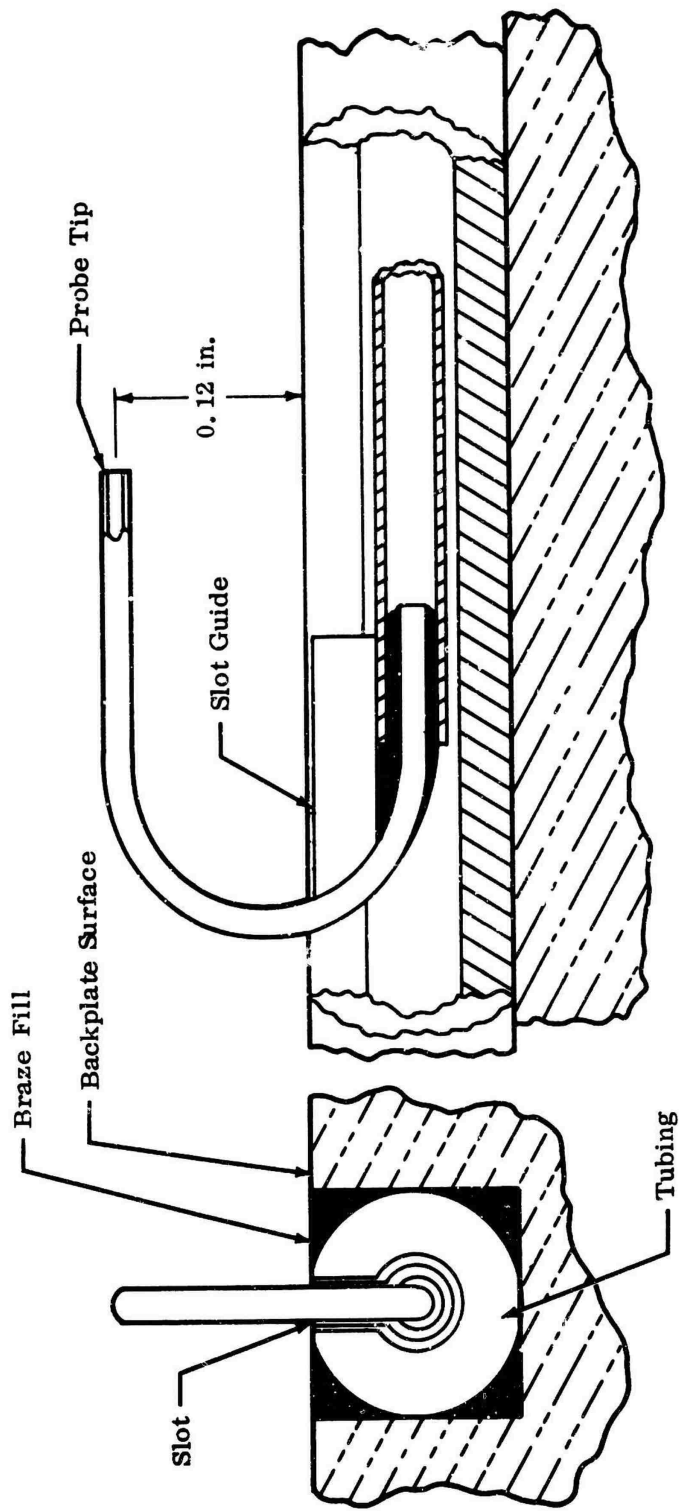


Figure 175. Traversing Total-Pressure Probe Detail.



Figure 176. Working Model of Traversing Total-Pressure Probe.



Figure 177. Close-up of Traversing Total-Pressure Probe (Working Model).

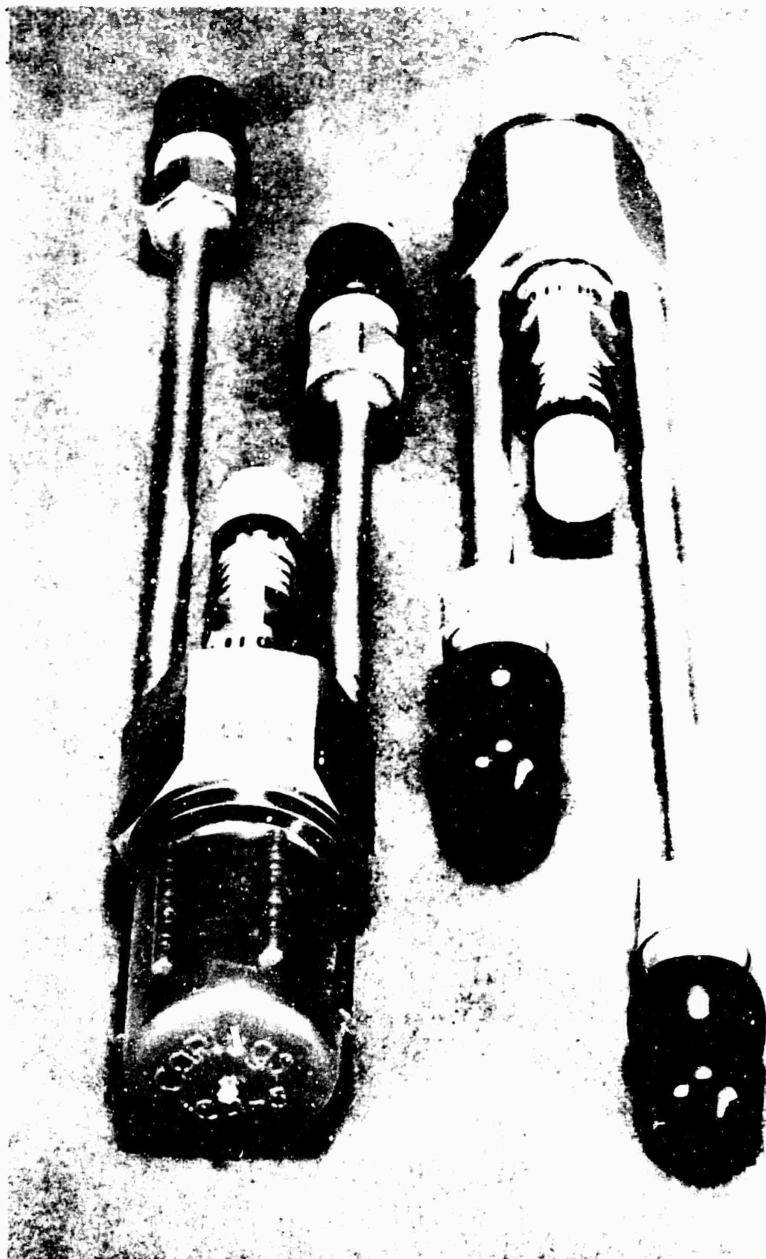


Figure 178. Water-Cooled Transducer.

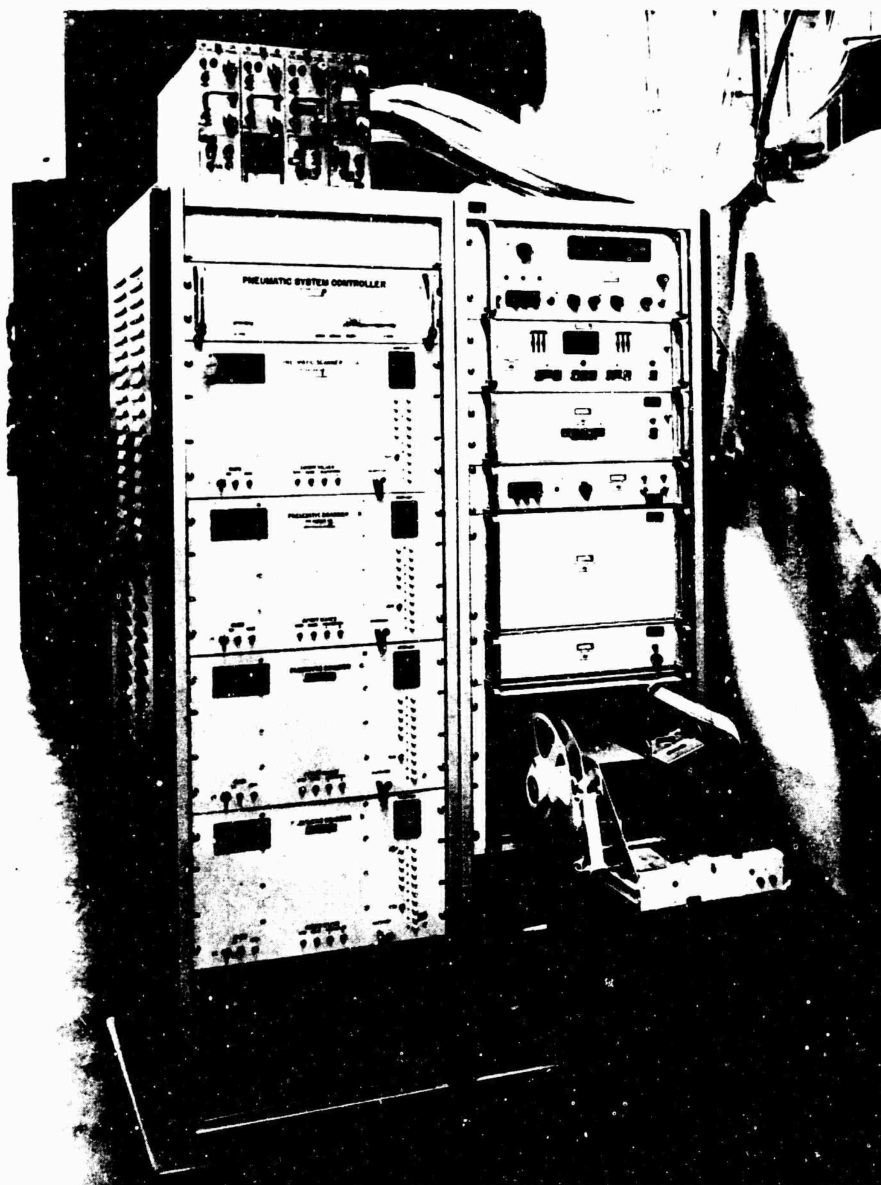


Figure 179. Digital Data System.

pressures in each group were sequentially sampled by a pressure transducer, and the signal from the transducer was transferred to the digital voltmeter and fed to the paper-tape punch. The pressures were read at a rate of 7 per second. After the pressures were recorded on punched paper tape, the cutoff valves were opened and the system was ready for the next data point.

4.2 TEMPERATURE-MEASUREMENT PROBES

Probes to measure air temperature just outside of the impeller tip were selected for minimum size and high accuracy. Each was made as small as possible to minimize airflow disturbance. The temperature probe (Figure 180) was calibrated in a small wind tunnel to check the predicted recovery correction for Mach number. The effect of the pulsating-flow stream on probe accuracy was thoroughly evaluated. An analysis was conducted, including a critique of the temperature-probe design, to determine this effect, and the results are presented in Appendix VII.

4.3 IMPELLER-STRESS MEASUREMENT

In measuring impeller stress, strain gages and a slip-ring assembly developed by the contractor were used. After the strain was measured, it was recorded and then reproduced. The system is described in the following paragraphs.

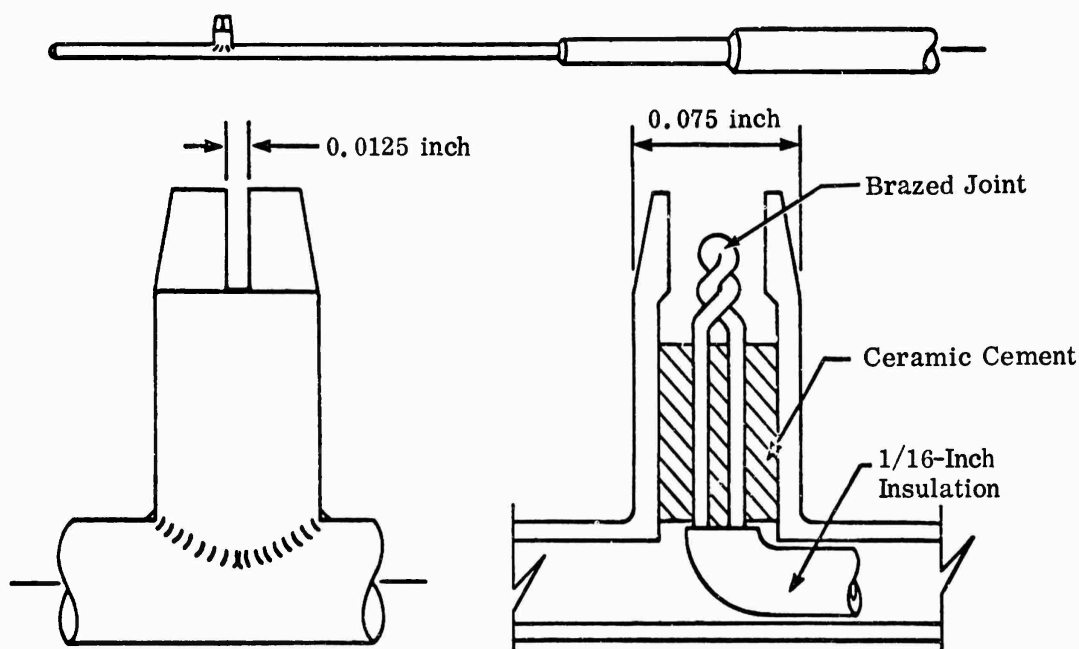


Figure 180. Slotted-Shield Total-Temperature Probe.

4.3.1 STRAIN GAGES

Baldwin-Lima-Hamilton, Type ABF-19S6-WL, 1/8-inch constantan-wire-grid, bakelite-base strain gages were used to instrument the impeller. All strain gages on the impeller were from the manufacturer's Lot Number B-29-BO; they had a gage factor of 1.99 ± 3 percent.

Extension lead wires were attached to the strain gages before they were cemented on the impeller. The leads were No. 32 AWG solid conductors with baked-on enamel insulation. Leads were attached to the strain gages by first removing about 0.25 inch of insulation from the lead ends. The ends were twisted together with the strain-gage leads, and the lead ends were then fused using a heli-arc-welding process.

Preparation of titanium for strain-gage installation required careful evaluation of the chemicals used. The common degreaser, trichloroethylene, could not be used because of halogenation. However, the standard metal conditioners and neutralizer solutions supplied by most strain-gage manufacturers could be used where the temperature of the titanium parts was less than 700° F. Beyond 700° F, titanium is subject to hydrogen embrittlement.

For the impeller-stress test, the impeller surface was degreased by soaking the areas to be instrumented in Dow Chemical Company 19AC-E-Z Strip, and by following this with repeated washings in household ammonia. The surface was then sanded lightly and washed with metal-conditioner and neutralizer solutions. A base coat of cement about 0.001-inch thick was immediately applied to areas on which the strain gages and lead wires were to be placed to ensure adequate bonding of the strain gage installation. This base coat was required because titanium rapidly forms a very thin, dense, self-protective oxide coating upon exposure of the surface to normal atmosphere. This oxide coating is an inherent corrosion-protection reaction similar to that produced by aluminum alloys; however, such coatings restrict the strength of critical bond fastenings. The cement used was a 2-part epoxy. Curing of the cement took 5 hours at 350° F.

A preliminary test specimen of titanium was prepared to verify the strain-gage installation procedure before instrumenting the impeller. Strain gages were mounted on the specimen to test the cement in shear and tension under actual centrifugal loads and temperatures (Figure 181).

An 8-ring, water-flooded, slip-ring system was used for the impeller-stress test. The 55,000-rpm test requirement was about one-half the slip-ring capability. A special connector assembly was fabricated, and the receptacle was designed to shrink-fit within the impeller-hub face.



Figure 181. Strain-Gage Installation (Test Specimen).

Figures 182 and 183 show the receptacle mounted in the hub face. The connector-assembly plug was mounted directly on the slip-ring flexible drive shaft. Two threaded studs held the plug-receptacle assembly together — 16 female pins were installed on the impeller receptacle and 8 male pins on the slip-ring plug. The pin-pattern design enabled repositioning of the slip-ring connector (180 degrees with respect to the impeller) so that a different set of pins could be mated if desired. This design permitted installing twice the number of strain gages that could be handled by an 8-ring system and increased its utility. The added capability was used to compare strain data from 2 separate impeller blades.

The slip-ring assembly was cradled in an enclosed support duct at the diffuser-rig inlet. The duct was tapered to prevent airflow restrictions, and the core of the duct, which supports the slip ring, was held in place by 4 thin vanes. Two of the vanes carried cooling water and instrumentation leads to the slip-ring assembly. Figure 184 shows the duct installed on the rig and opened for slip-ring access.

4.3.2 STRAIN-GAGE DATA-RECORDING METHODS

Because only dynamic strain-gage data were required, potentiometric circuitry was used. A 1200-ohm ballast resistor was used in series with each 120-ohm strain gage, and the outputs were capacitively coupled to the amplifiers. Rings 1 through 6 were used for strain-gage data, and Rings 7 and 8 were paralleled for power return.

Resistance of the strain gages after installation (R_g') and strain-gage and lead-wire resistance ($R_g' + R_L$) were measured to the nearest 0.1 ohm. Gage-factor sensitivity compensations (K') were computed by:

$$K' = \frac{R_g'}{R_g' + R_L} (K) \quad (26)$$

where:

K is the gage-factor nominal value specified by the fabricator.

Strain gages were calibrated with shunt resistors using:

$$\text{Strain (microinches/inch)} = \frac{R_g' + R_L}{(R_g' + R_L + R_s)} (K') \quad (27)$$

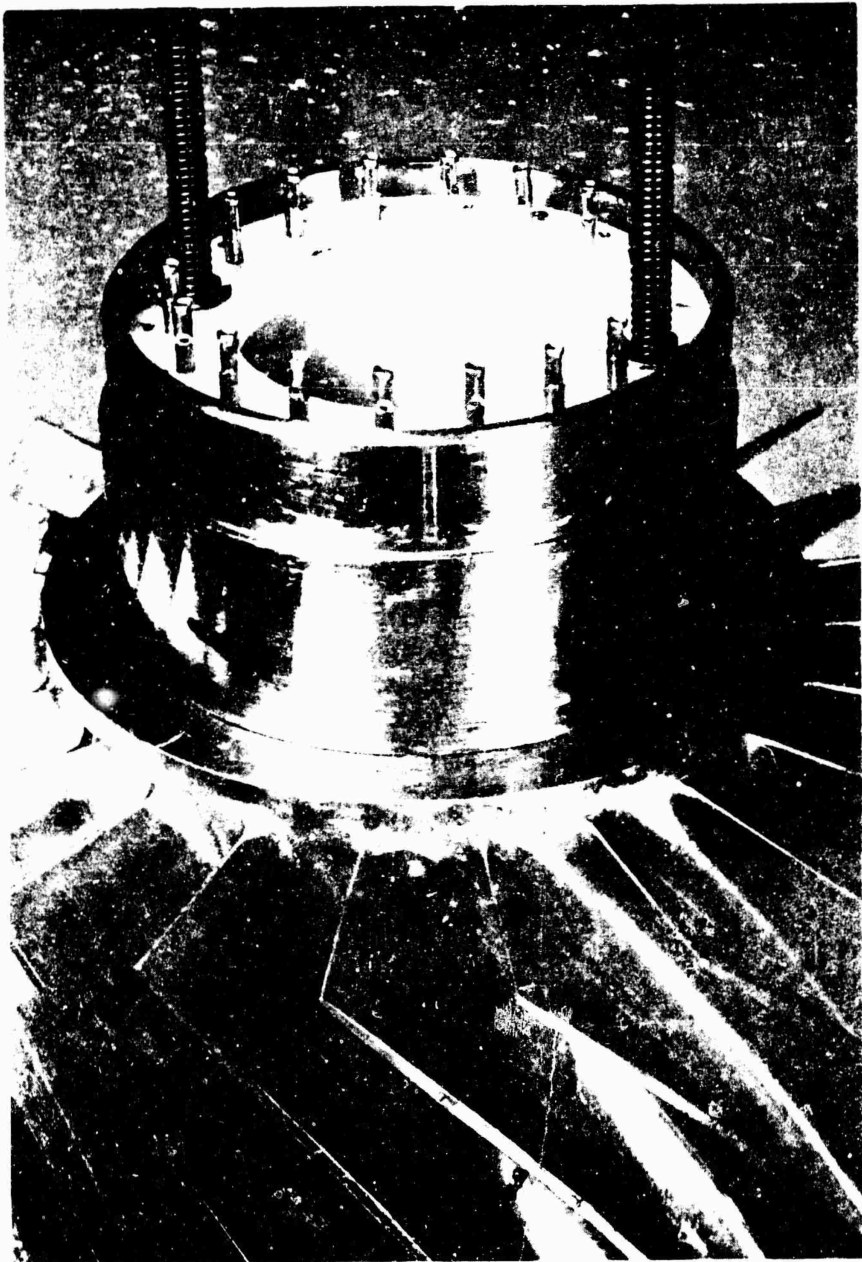


Figure 182. Slip-Ring Connector (Side View).

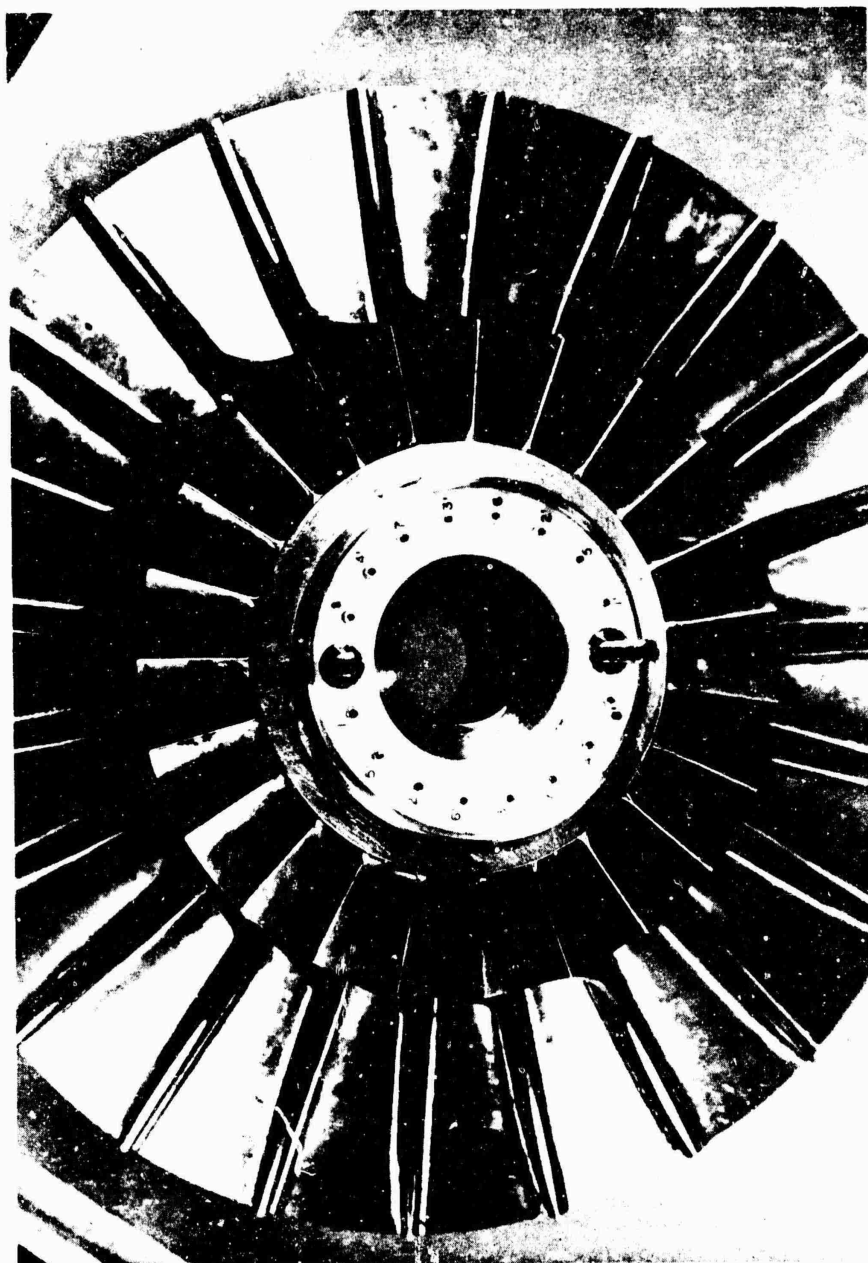


Figure 183. Slip-Ring Connector (Front View).

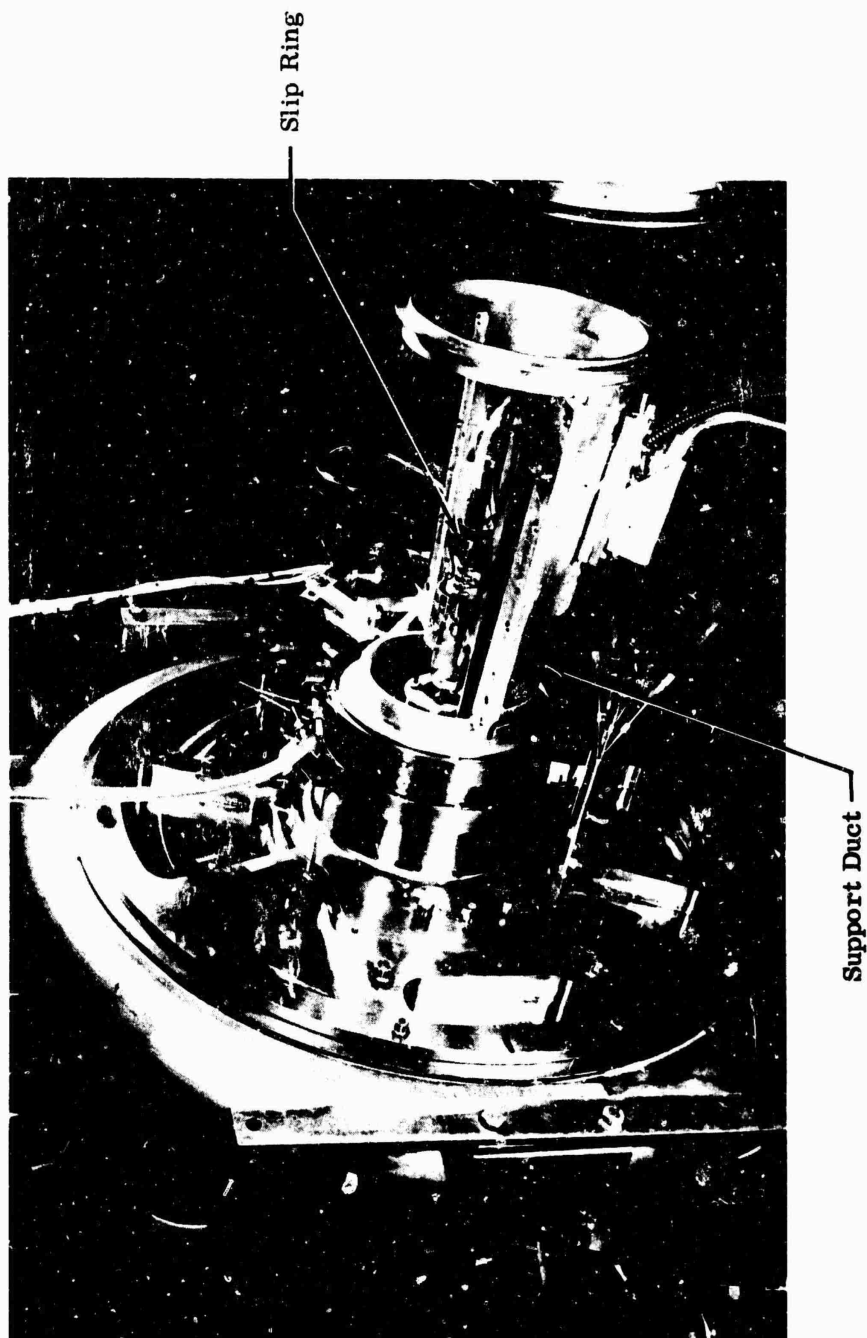


Figure 184. Slip-Ring Installation, Impeller-Stress Test.

where:

R_s is the calibration shunt resistor.

Gage-factor sensitivity compensation for temperature was not necessary because the metal temperature was below 300° F in the areas where strain gages were installed; strain gages were not necessary in the higher temperature regions near the impeller tip because of the shorter, stiffer blade sections in this region. During the test, strain-gage data were recorded on a light-beam oscillograph and an FM magnetic-tape recorder. Figure 185 shows the data-recording system setup. The oscillograph was operated at low speed to produce a condensed picture of the strain profile with no frequency resolution. A binary code, prerecorded on the magnetic tape, was reproduced on the oscillograph for precise time reference for the reproduction of strain data from the FM tape. The magnetic-tape recorder was operated at 60 inches per second to permit time-base expansion during data reproduction for increased frequency resolution of the strain-gage data. Strain

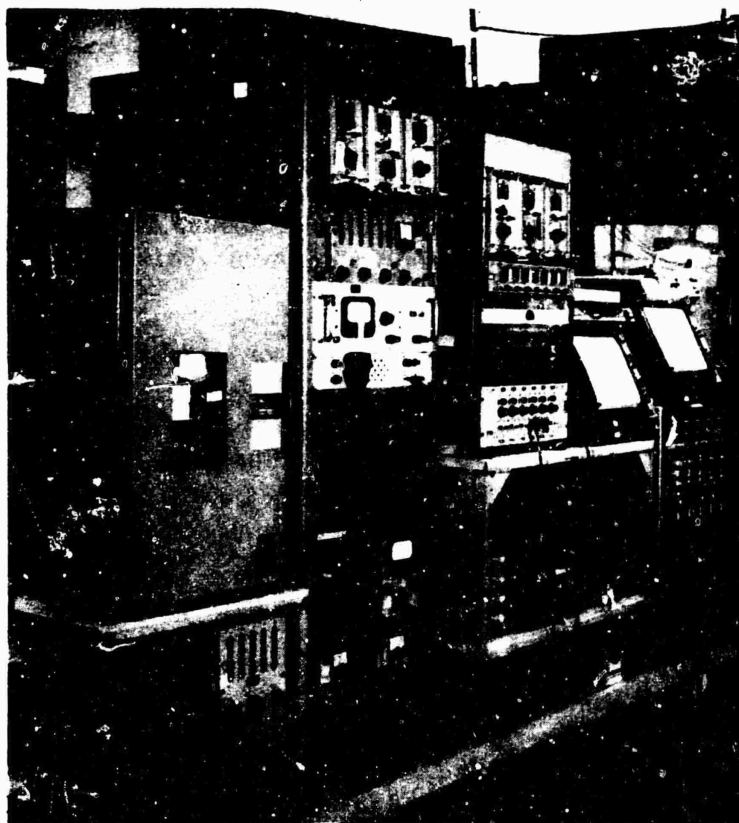


Figure 185. Impeller-Stress Data-Recording Setup.

signals were monitored visually on an oscilloscope during the impeller-stress test. In addition to the strain data, shaft speed, rig temperatures and pressures, and guide vane positions were also recorded on the oscillograph. Data desired for reproduction were selected from the condensed oscillograph recordings and were located by using the binary code. These data points were then reproduced from the magnetic tape onto the oscillograph at reduced tape speed and increased oscillograph speed for better resolution of both strain-gage amplitude and frequency.

4.4 ROTOR-THRUST MEASUREMENT

Rotor thrust was measured and adjusted during impeller-rig testing to maintain an acceptable, positive axial load on the thrust bearing. Thrust was measured by placing strain gages on 3 of the 4 flexural members of the thrust-bearing cage. Each flexural member had a rectangular cross section of 0.105 by 0.110 inch. Four foil gages with a nominal gage length of 1/32 inch were used on each of the 3 members; 2 active gages and 2 poisson (temperature-compensating) gages connected to form a half-bridge. The strain-gage instrumentation is shown in Figure 186. Two gages were necessary in each bridge leg to increase gage sensitivity, because stress levels of the bearing cage were low. See Figures 187 and 188 for gage installation.

Gages were attached with a two-part epoxy cement and cured for 4 hours at 350° F. Bearing-cage load was calibrated with a universal testing machine, and temperature was calibrated in a controlled-temperature oven. Calibration ranges were 0 to 300 pounds of load at 70° to 300° F.

Bridge-completion resistors were located at the recording equipment and were thermally insulated to avoid temperature errors. Each of the 3 bridges was connected to a bridge-balance and power-supply unit, to a dc amplifier, and to indicating meters of 1-milliampere sensitivity. The panel-mounted meters were located in the test control area so that the bearing thrust-load could be monitored constantly. Adjustments in balance pressure were made during rig operation to keep the load within the specified bearing limits.

Shunt resistors provided meter calibration before the rig runs. Because low strain was measured, hysteresis and gage-temperature sensitivity affected the signal output. In addition, the copper lead wires connecting the half-bridge to the outside bridge-completion resistors and power supply were subject to temperature variations. The resistance change in these lead wires from the temperature changes further contributed to degradation of signal-output accuracy. Typical strain-gage levels were 300 microinches per inch for 300 pounds of load. Later calibrations were made by attaching weights to the shaft-bearing assembly through a system of pulleys, and these calibrations were set for a full-scale load of 200 pounds. Hysteresis and nonrepeatability were typically as high as 50

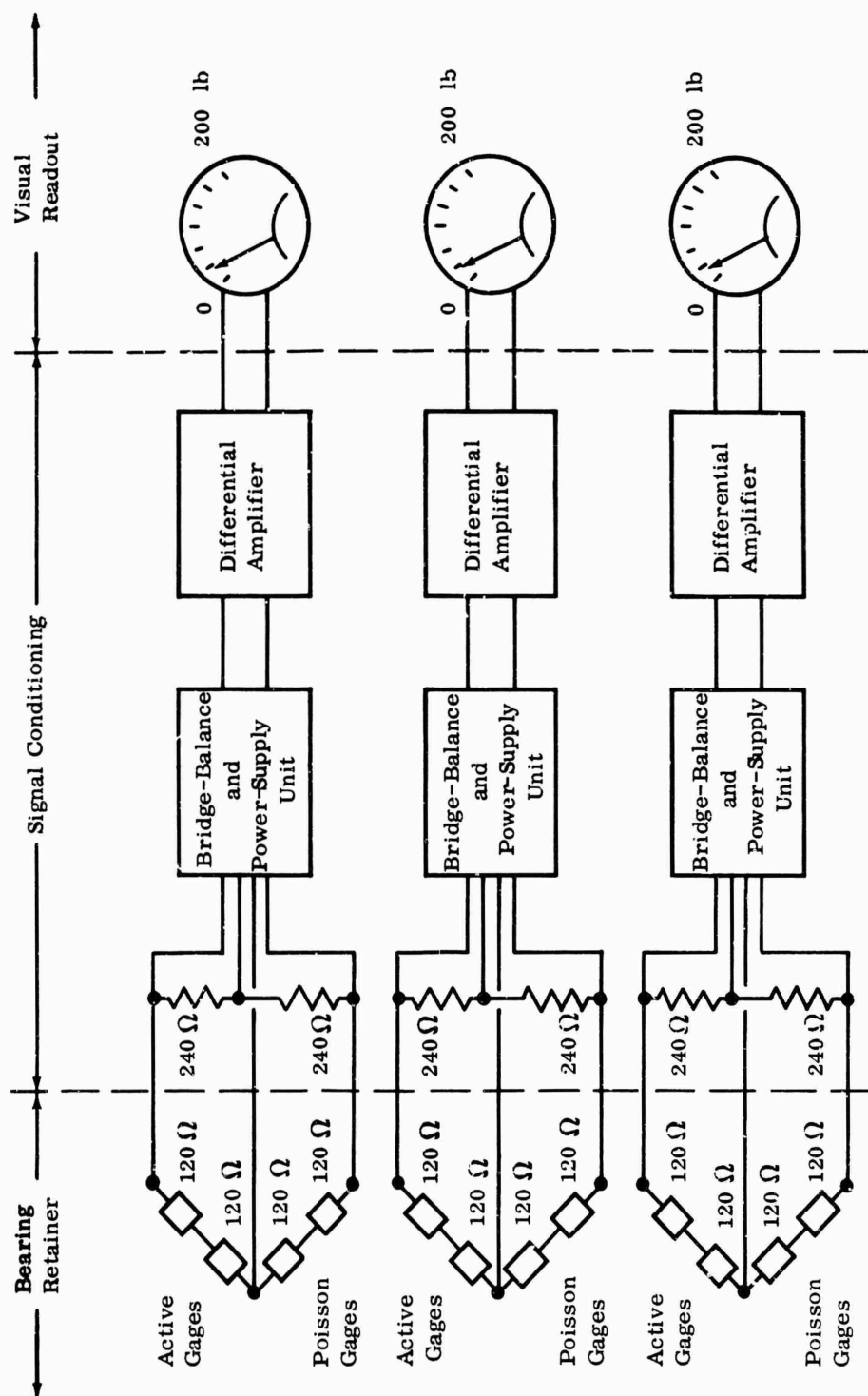


Figure 186. Rotor-Thrust-Measurement Instrumentation.

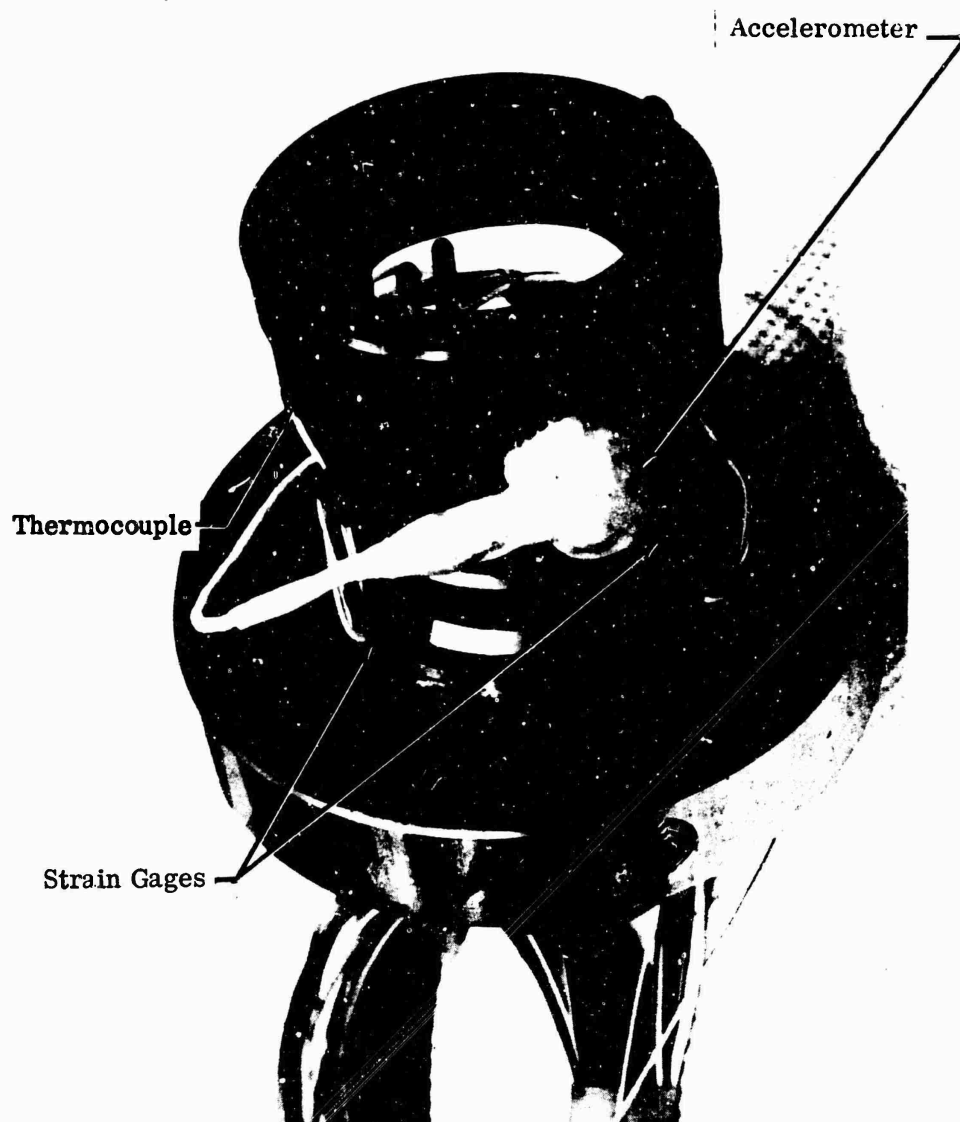


Figure 187. Thrust-Bearing-Cage Instrumentation.

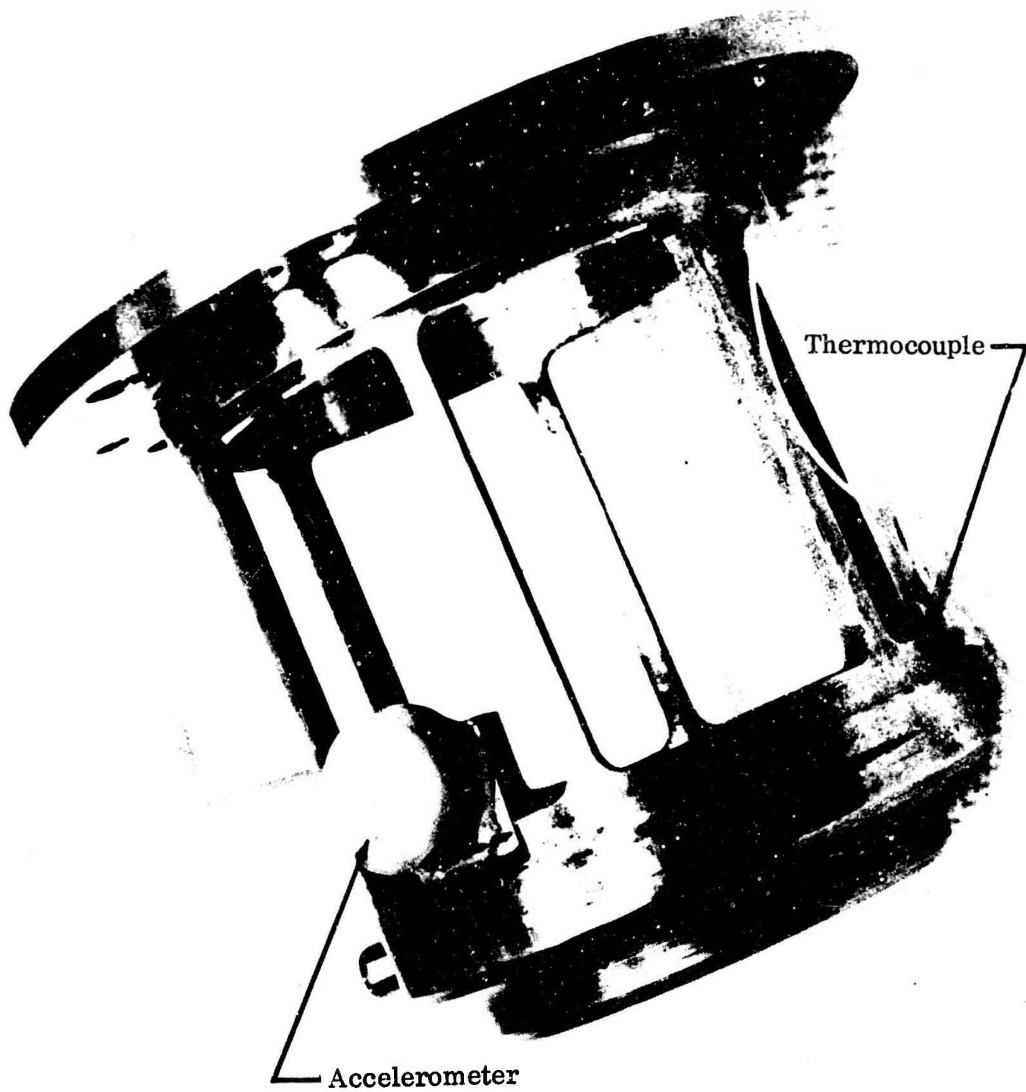


Figure 188. Radial-Bearing-Cage Accelerometer and Thermocouple.

pounds. In addition, temperature drift during rig-test runs varied from 150 to 200 pounds in a negative direction. By maintaining the meter at midscale through balance-pressure adjustment, the bearing thrust-load was never more than 300 pounds and was always positive.

4.5 OTHER SPECIAL INSTRUMENTATION

Examples of other special instrumentation used to evaluate impeller- and diffuser-rig testing included: (1) a proximity-probe system consisting of a detector and detector-driver, (2) bearing-cage accelerometers, and (3) a rub-sensor probe developed by the contractor for measuring impeller-tip-to-shroud clearance.

4.5.1 PROXIMITY PROBE

A proximity-probe system was used during modal balance and testing to monitor rotor-shaft displacement. This system consisted of a sensor (or detector) and an oscillator-demodulator or detector-driver. A 12- to 18-volt dc power supply was required to power the detector-driver. Output signals varied from zero to power-supply voltage, and output impedance was 250 ohms. System frequency response was adequate to handle the 1000-Hz maximum signal frequency from shaft rotation.

The sensor was an eddy-current sensitive device that consists of a coil of fine wire mounted on the probe tip. A high-frequency current, supplied by the detector-driver is passed through the coil; the resultant magnetic field induces eddy currents in the nearby shaft. Loading of the coil (or ac coupling) caused the coil impedance to vary, depending on the proximity of the coil to the shaft surface. The impedance change was detected by the detector-driver as a phase change, and a dc signal proportional to proximity resulted.

The detector, mounted in the test-rig housing, operated satisfactorily in a MIL-L-23699 lubrication-oil environment at temperatures to 200° F. Calibration was accomplished by moving the probe away from the shaft surface and by measuring the distance moved by the probe with a dial indicator. Calibration range from the shaft surface was 0.010 to 0.030 inch.

The detector-driver output was attenuated and fed into a dc amplifier. The output of the dc amplifier provided sufficient output current to drive a high-frequency, light-beam galvanometer in a direct-writing oscillograph recorder, as shown in Figure 189. System accuracy was limited by the dial indicator and calibration method but was within ± 0.0005 inch.

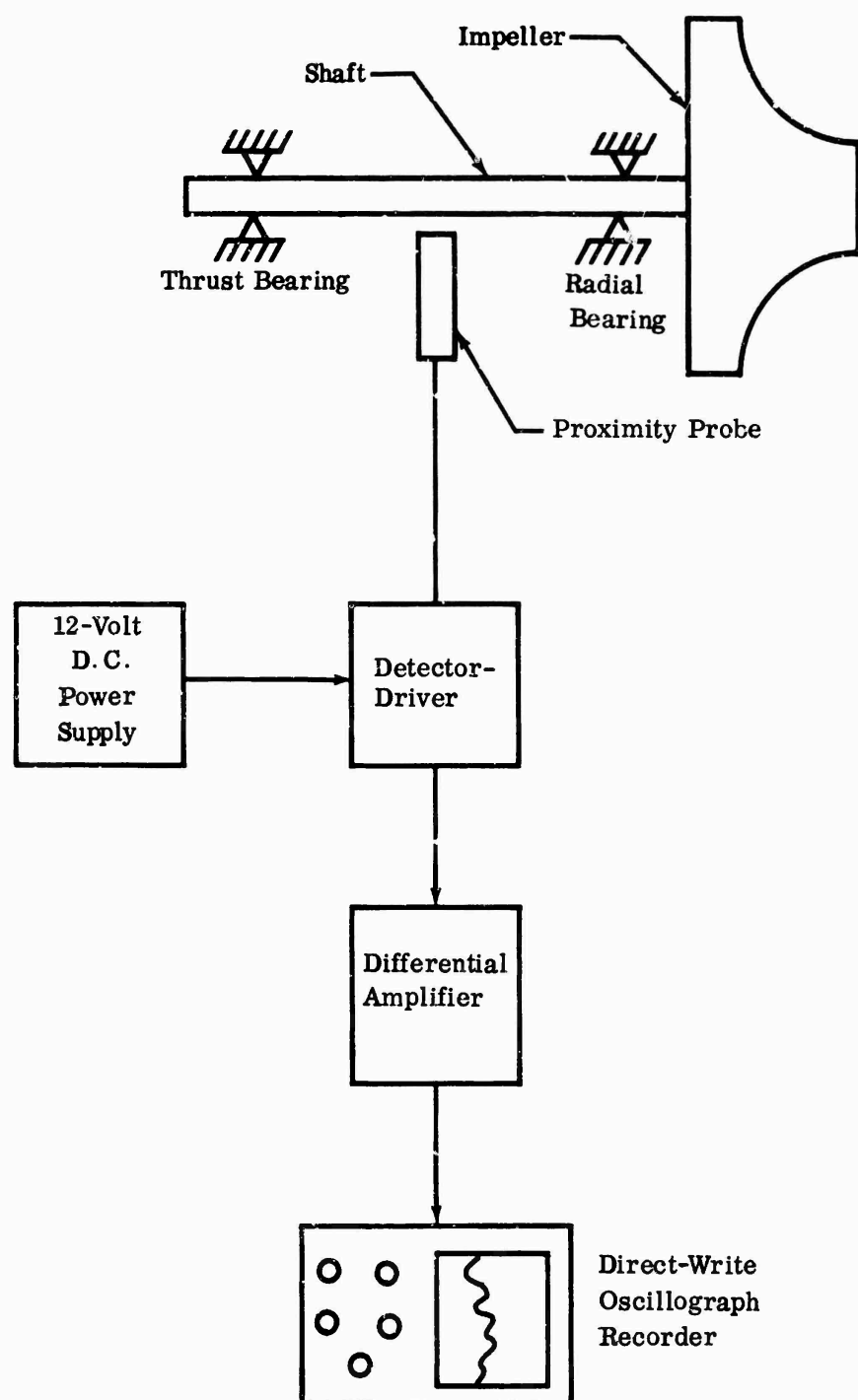


Figure 189. Shaft Displacement Measurement (Block Diagram).

4.5.2 BEARING-CAGE ACCELEROMETERS

Accelerometers were mounted on the thrust- and radial-bearing cages to measure vibrational loads on the bearings. Accelerometer installations are shown in Figures 187 and 188. The accelerometers were O-ring-shaped piezoelectric types. They weighed 11 grams and were about 0.25 inch high. They were attached to the bearing cage with a 6-32 bolt through the accelerometer center. The accelerometers, cable connector, and about 0.5 inch of cable were potted with an epoxy cement to protect them from the MIL-L-23699 lubrication-oil environment. Each of the accelerometers was connected to an electrostatic-charge amplifier, a dc amplifier, and a high-frequency light-beam galvanometer on a direct-writing oscillograph recorder. This setup is shown in Figure 190.

The accelerometers and associated charge amplifiers were calibrated on a vibration exciter before installation on the bearing cages. The resultant calibration was in volts per g of acceleration at a given frequency. System calibration was recorded by input of a voltage equivalent to the desired acceleration at the calibration frequency. Normal calibration range was 100 g peak-to-peak, full scale; dynamic system accuracy was estimated as ± 10 g.

4.5.3 ACTUATED RUB SENSORS

Impeller-tip-to-shroud clearance was measured at various speeds with a foil-tipped rub-sensor probe. The probe consisted of a loop of constantan foil, 1/64-inch wide and 0.001-inch thick, stretched around the wedge-shaped end of a two-hole cylindrical alumina insulator. Heavier copper wires were resistance-welded to the foil. The foil insulator assembly was inserted into a metal-tube sheath, and its wedge-shaped end was potted with ceramic cement so that only the foil at the tip of the wedge was exposed. The copper wires were terminated at an electrical connector on the opposite end of the probe. Figures 191 and 192 illustrate the steps in the construction of a rub sensor. An electric current was passed through the probe, and the electrical continuity of the probe was sensed with a silicon-controlled rectifier circuit. When the foil tip was rubbed by the impeller, the foil broke and a signal, both audible and visible, was received by the test operator. The probe was traversed by a subminiature probe actuator. The actuator was mounted on the impeller shroud, and control and indication of probe travel were provided by a remote control and switch box. Calibration was accomplished by comparing the probe travel, as measured by a height gage, with the control-box travel indication. Each time a probe was rubbed, a new probe had to be installed. Overall system repeatability, run-to-run at the same speed, was ± 0.005 inch.

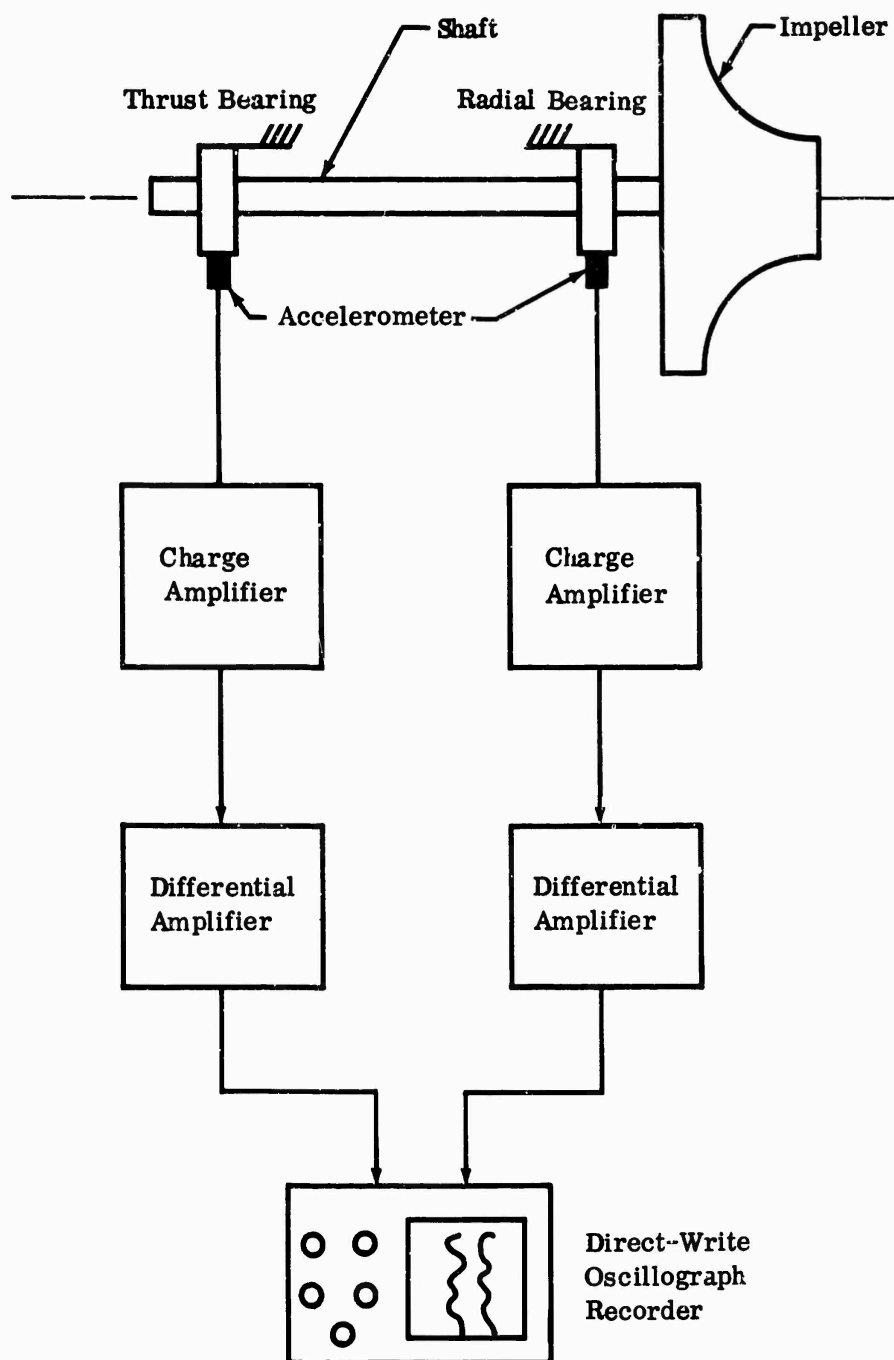


Figure 190. Bearing-Cage Accelerometer Installation.

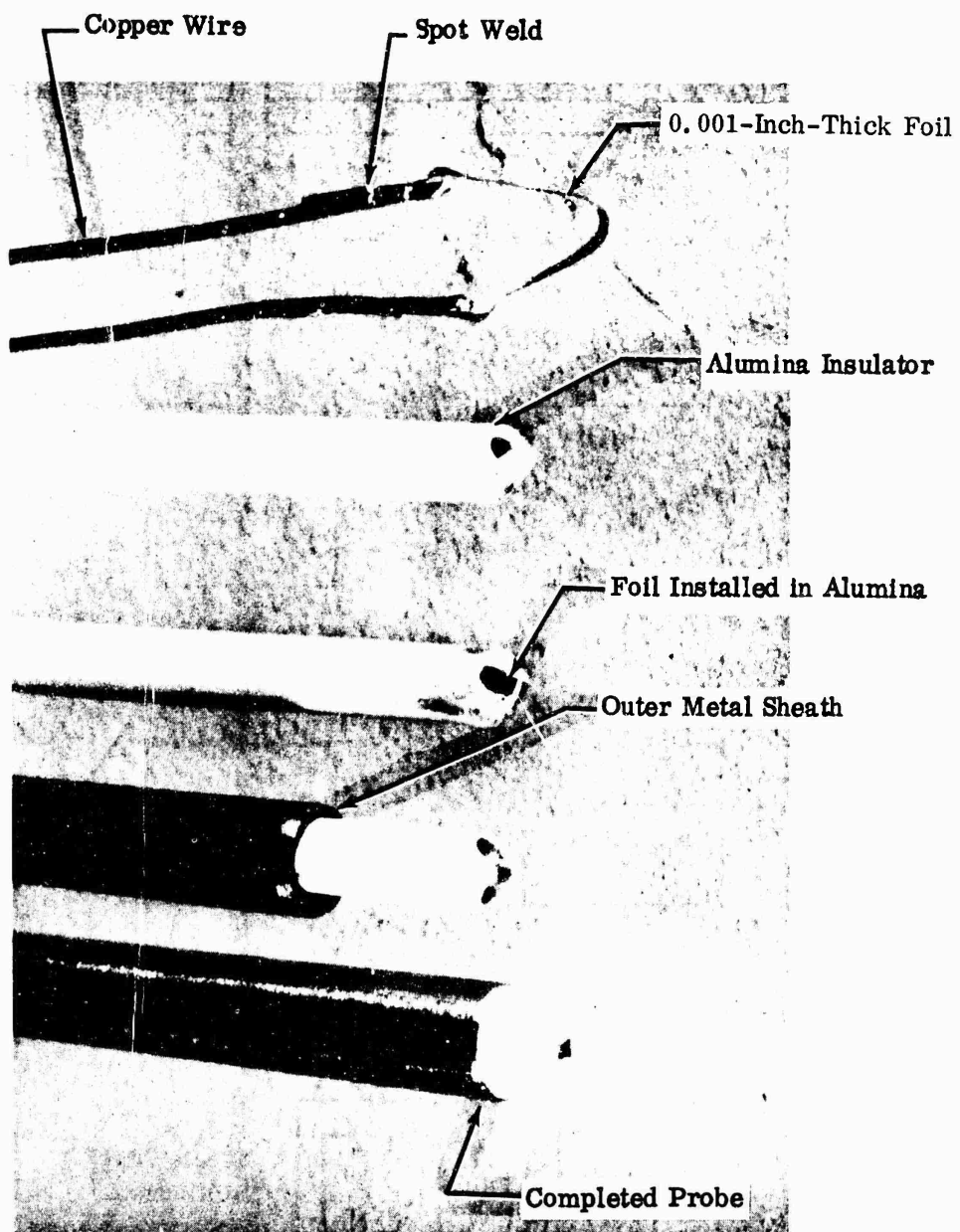


Figure 191. Rub-Sensor Fabrication.

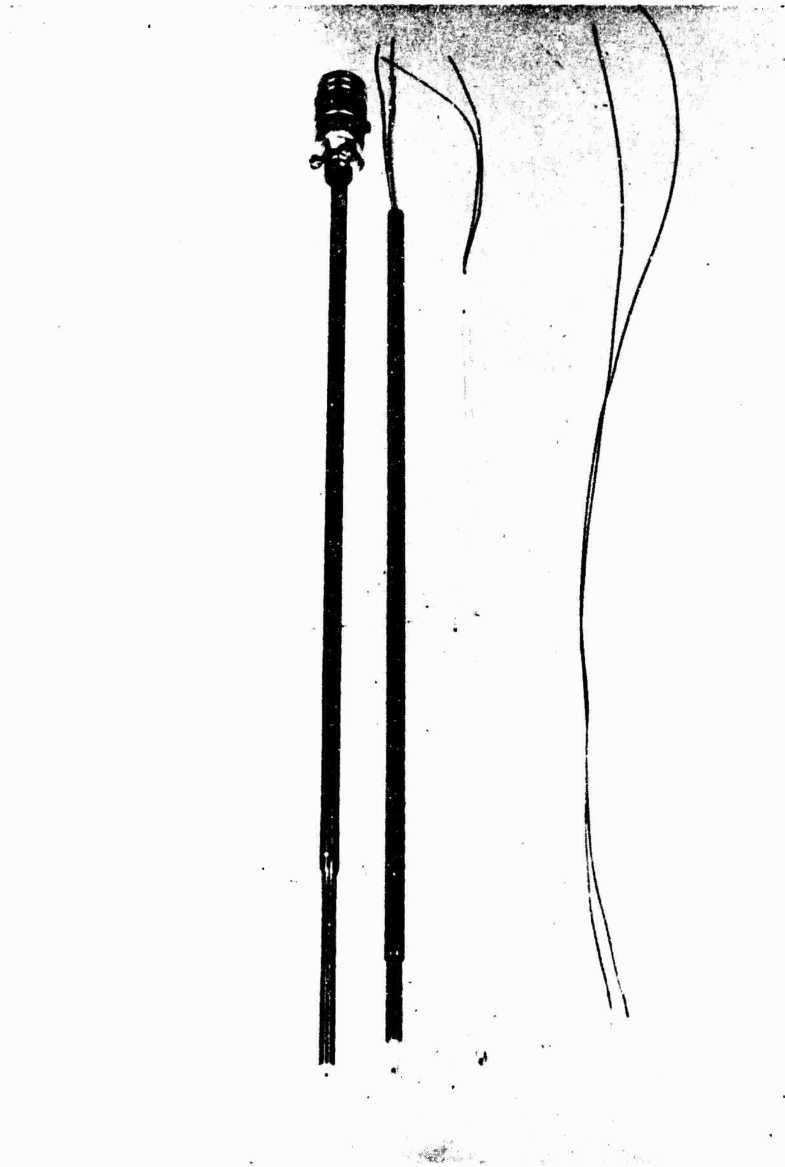


Figure 192. Rub-Sensor Assembly.

(U) 5.0 TEST EQUIPMENT AND PROCEDURES

Procedures discussed in this section are for mechanical checkout and aerodynamic tests of the impellers and diffusers and their Boeing-built turbodrives. Two rigs were used, each consisting of a compressor unit and a turbodriven unit connected by a flexible coupling. The rigs were identified as an impeller test rig for impeller studies and as a diffuser test rig for diffuser studies.

The compressor performance tests were conducted at the contractor's development laboratories. Figure 193 is a photograph of the impeller and diffuser test setups in the Development Laboratories Test Cell 8. This facility was equipped for installation and operation of the two test rigs with minimum downtime for changeover. Figure 194 is a sketch of the test-cell area and shows the location of compressor-inlet air and exhaust stacks and cell dimensions.

5.1 IMPELLER TEST RIG

The impeller test rig is shown in Figure 195. The basic design concept of this unit provided a common rotor system that accommodated the interchangeable MF-1 and RF-1 impeller test sections, which were the 2 units tested.

Five MF-1 impeller performance tests were conducted from December 1964 through March 1966. Six RF-1 performance tests were made during December 1965 through August 1966. Data obtained and the configuration used for each test are reported in Section 6.0 of this report. Mechanical checkout tests and results are discussed in this section and in Appendix III.

The impeller was powered by a high-speed (80,000 rpm maximum) turbodriven unit with an axial-flow turbine designed to produce 252 horsepower at 68,500 rpm with 3.2 pounds per second of airflow. The turbodriven unit was connected to the compressor through a frictionless flexible coupling. This coupling was a change in the original concept to eliminate forced vibration excitation, which occurred with the splined quill shaft used in the initial design.

5.2 DIFFUSER TEST RIG

The diffuser test rig (Figure 196) was designed to accommodate 4 basic configurations: DI-1, DI-2, DI-3, and DC-1. The first 3 were vane-island diffusers (see Figure 165) and DC-1 was a single-stage cascade diffuser (see Figure 93). The rig was also used in a vaneless configuration. The DI-1 and DI-2 diffusers were 8-channel configurations; and DI-3, 16-channel.

Three radial-flow workhorse impellers were used in the program. One impeller used in the checkout tests suffered blade damage because thermal distortion of the impeller shroud and elastic deformation of the impeller caused mechanical

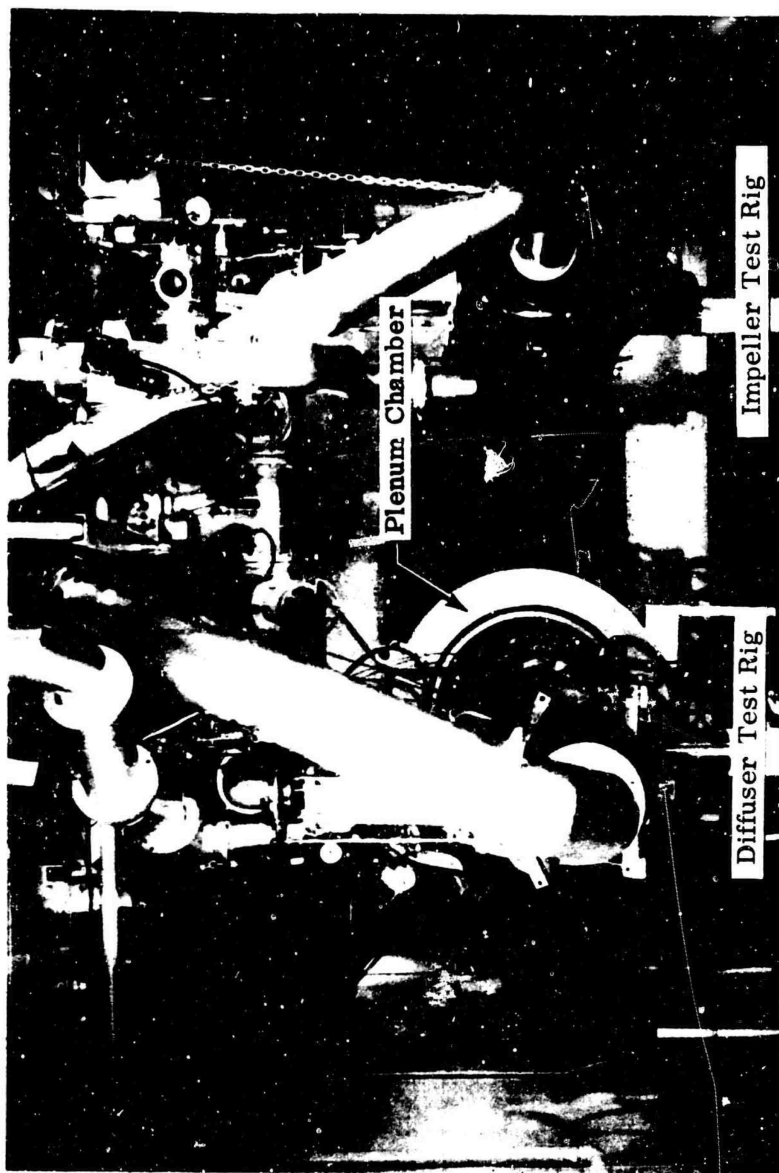


Figure 193. Diffuser-Rig and Impeller-Rig Cell Installation.

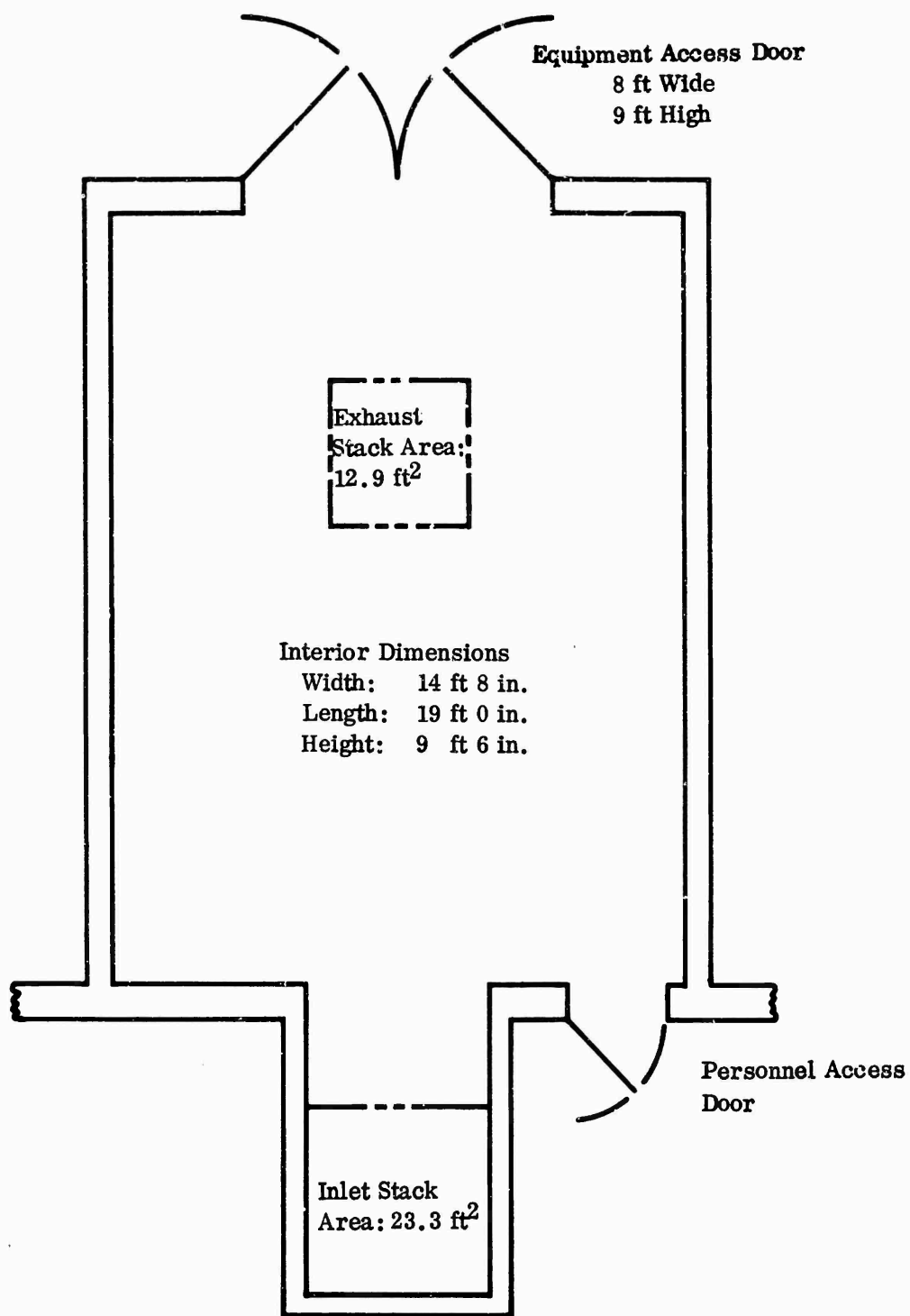


Figure 194. Plan View of Test-Cell Area.

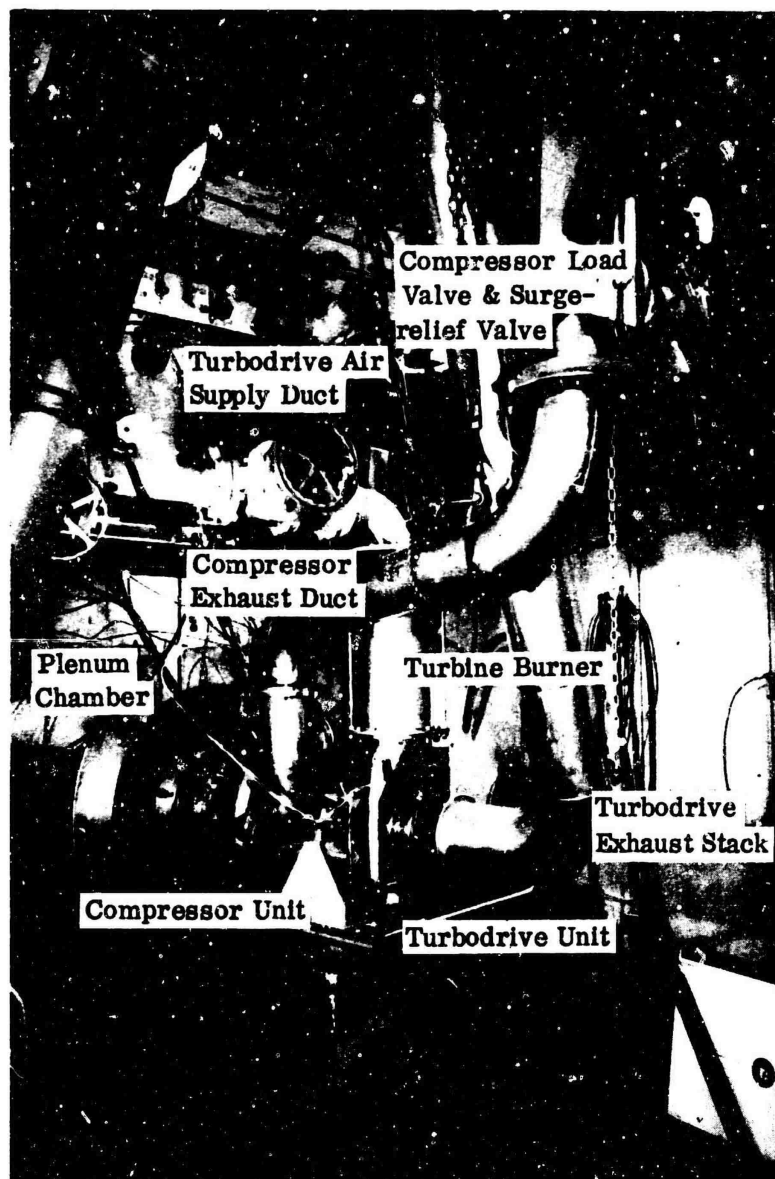


Figure 195. Impeller Test Rig.

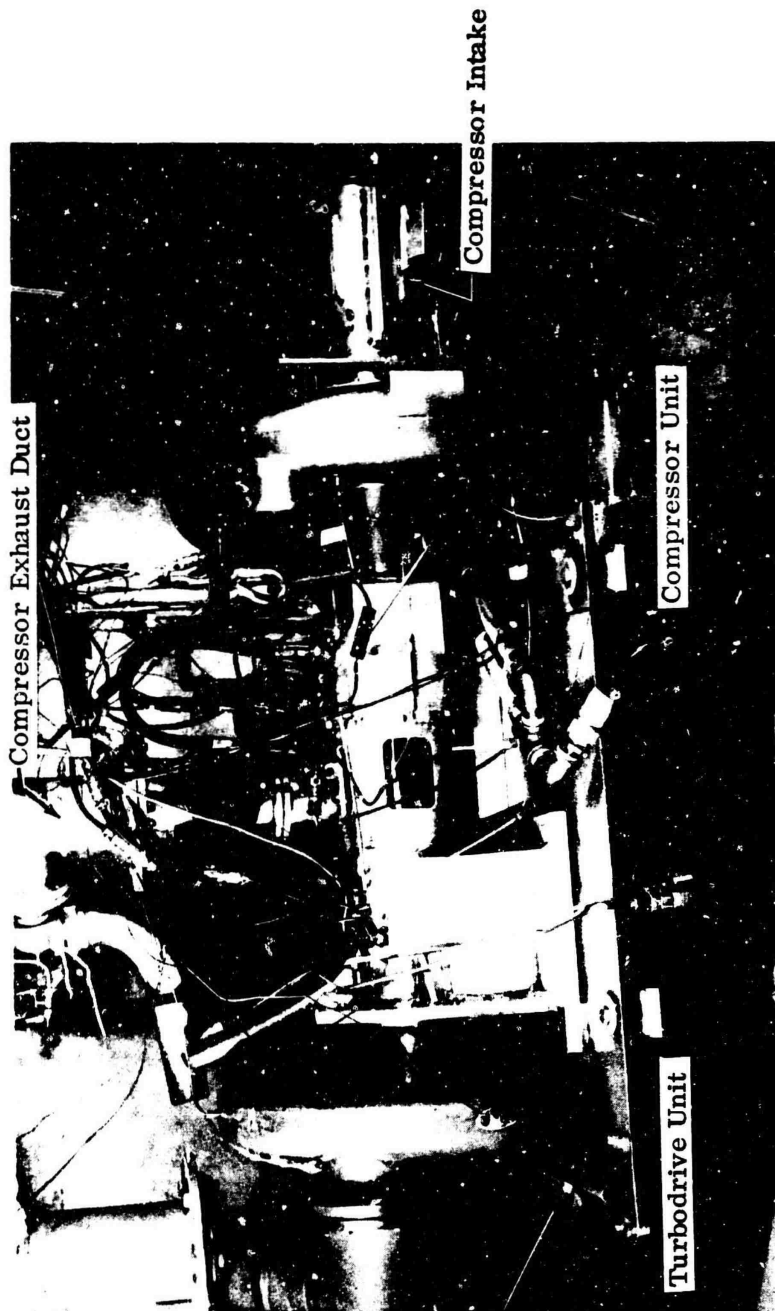


Figure 196. Diffuser Test Rig.

rub between the blades and the shroud. Diffuser-rig mechanical checkout and results are discussed in this section and in Appendix III. A second impeller was used for the impeller-blade stress investigation. The third impeller was used for the aerodynamic performance tests (Figure 197).

The diffuser test rig was driven by a radial-inflow turbine unit, capable of producing 1280 horsepower at 55,000 rpm, with 1200° F turbine-inlet temperature and about 7.9 pounds per second of airflow. As in the impeller studies, this turbodriven unit was also connected to the compressor through a frictionless, flexible coupling. The turbodriven unit is shown in Figure 198.

5.3 SUPPORT EQUIPMENT

Support equipment for the test rigs included a high-pressure air supply, facilities for dynamic balancing, and test cells with associated control equipment.

5.3.1 AIR SUPPLY

Air supply for turbodriven operation was obtained from either of two high-flow-capacity, motor-driven air compressors located near the test cell. A 1500-horsepower positive-displacement compressor (Figure 199) delivered a maximum airflow of 9 pounds per second at a discharge pressure of 145 psig. A 2500-horsepower centrifugal compressor (Figure 200) provided oil-free air at a maximum rate of 9 pounds per second with a 100- to 300-psig discharge pressure. Each of the 2 compressors met the impeller and diffuser turbodriven air requirements and both were used. Figure 201 gives the performance details of the centrifugal compressor.

5.3.2 COMPONENT DYNAMIC BALANCING

Precision dynamic balancing of rotor components and assemblies was accomplished before each rig buildup. Two dynamic-balancing machines were available. Figure 202 shows one with a sensitivity of 0.003 ounce-inch at speeds of from 1000 to 2000 rpm. Figure 203 shows another with a sensitivity better than 0.001 ounce-inch at speeds of from 1000 to 3000 rpm. The balancing procedure was an iterative process; small amounts of material were ground off the components to offset the imbalance (indicated by the machine) in as many steps as were required to obtain an acceptable balance.

Individual components were balanced separately before a final assembly balance. Impellers were balanced on special arbors machined to fit each individual impeller. The shaft for the impeller rig was balanced with the bearing installed on the shaft, but the shaft for the diffuser rig, which used hydrodynamic bearings, was not.



Figure 197. Workhorse Impeller.



Figure 198. Diffuser-Rig Turbodriven Unit.

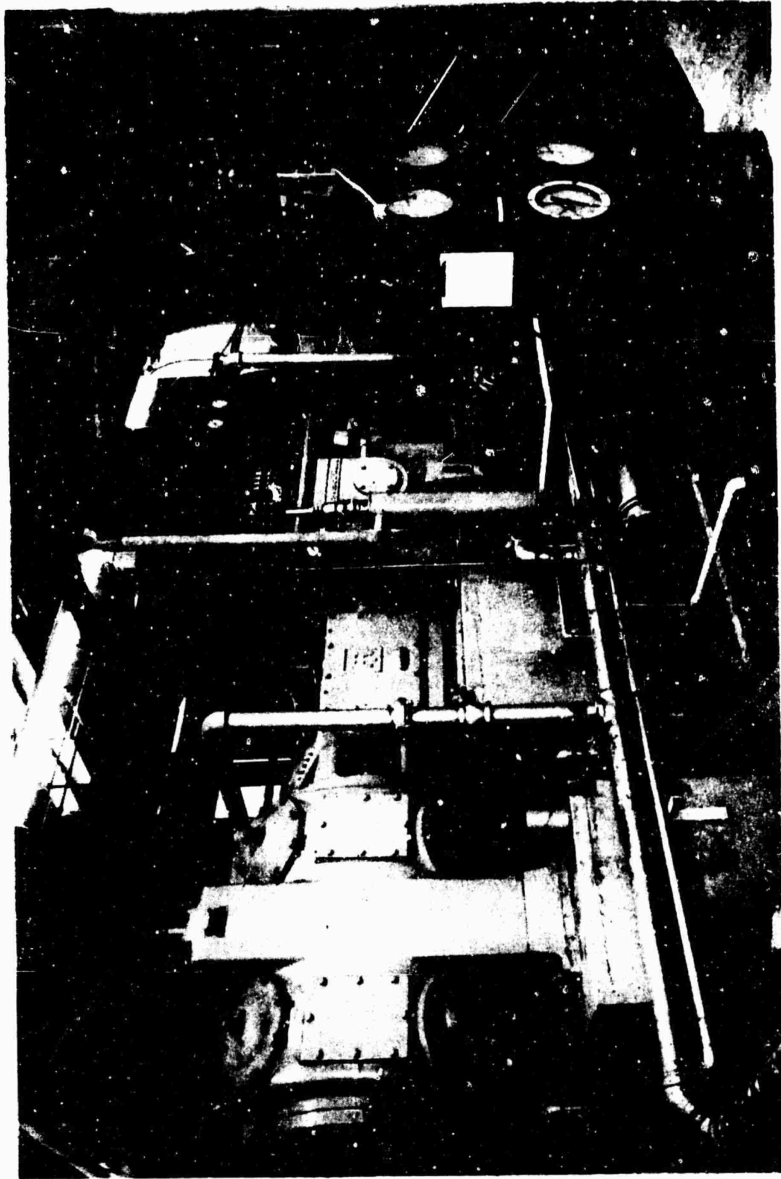


Figure 199. Positive-Displacement Air Compressor.

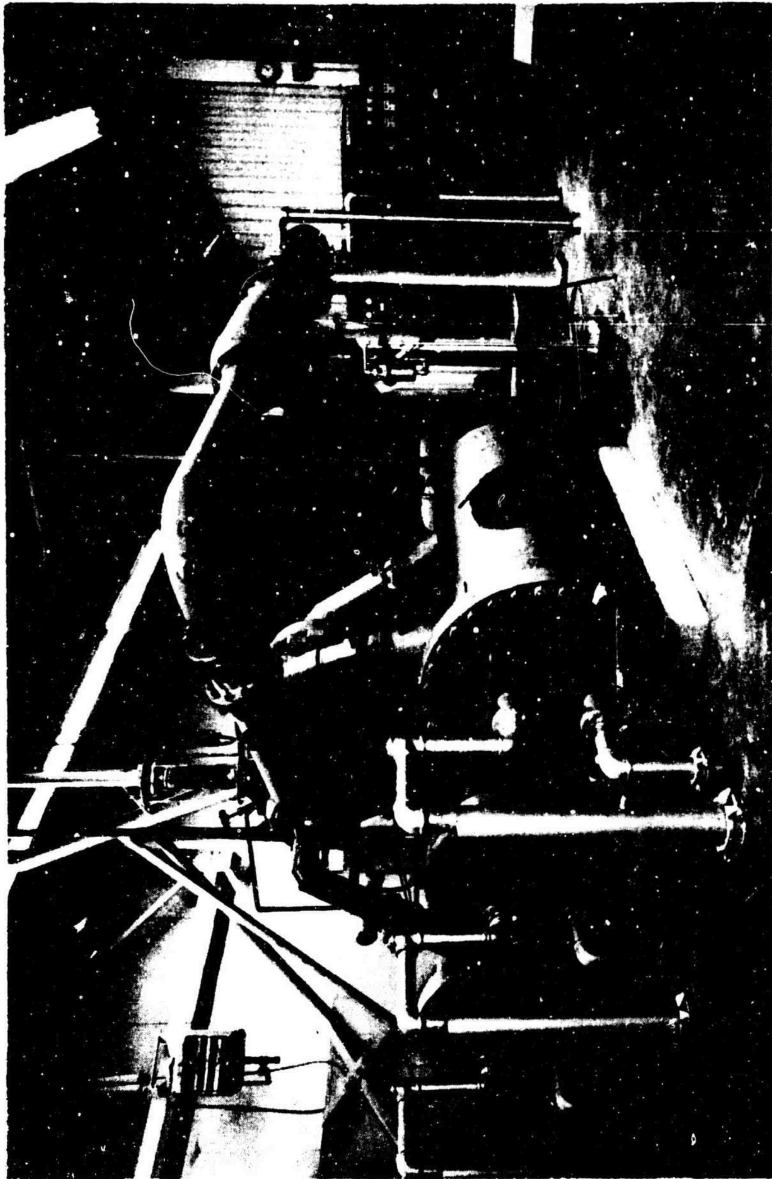


Figure 200. Centrifugal Air Compressor.

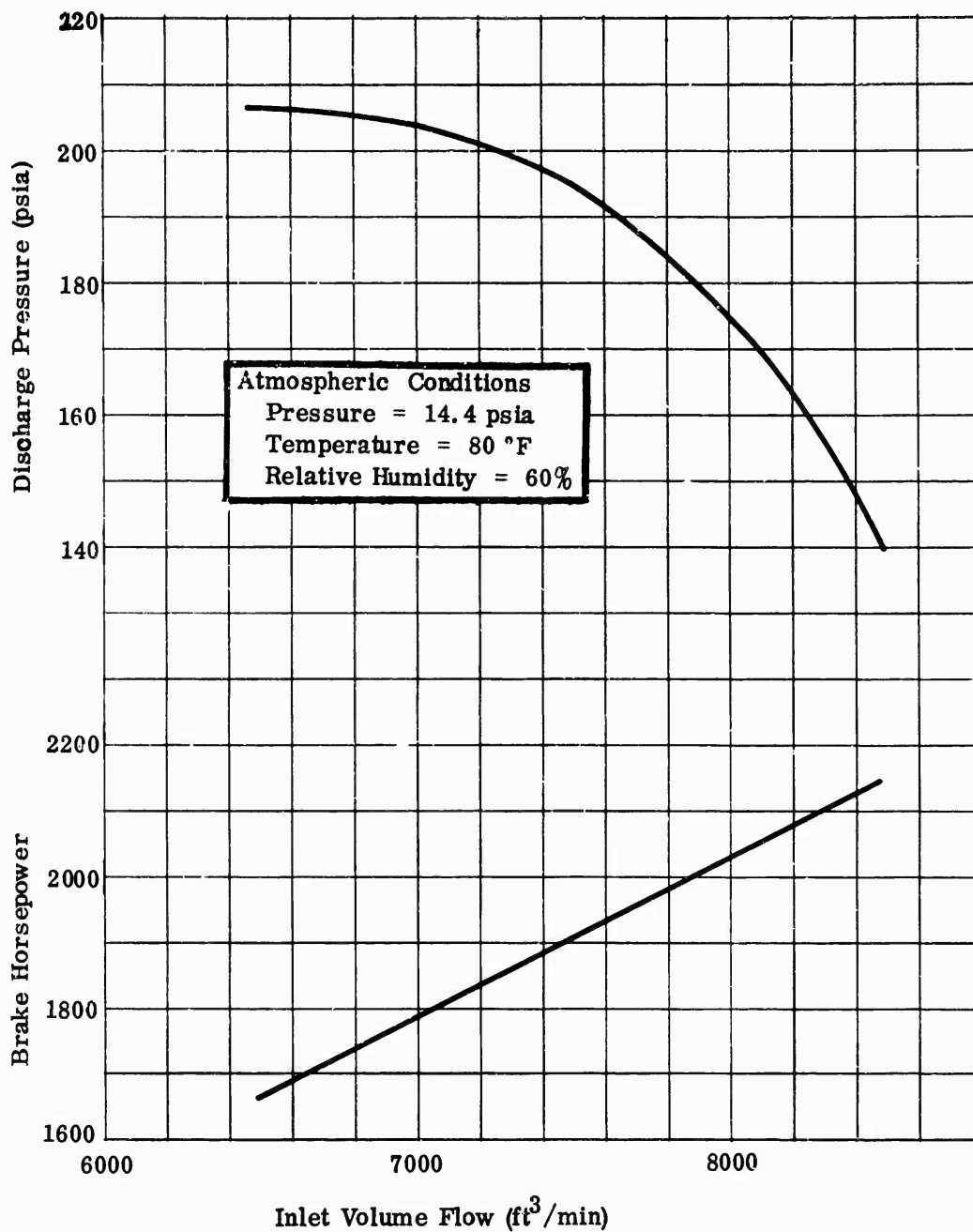


Figure 201. Centrifugal Air Compressor Performance Curve.

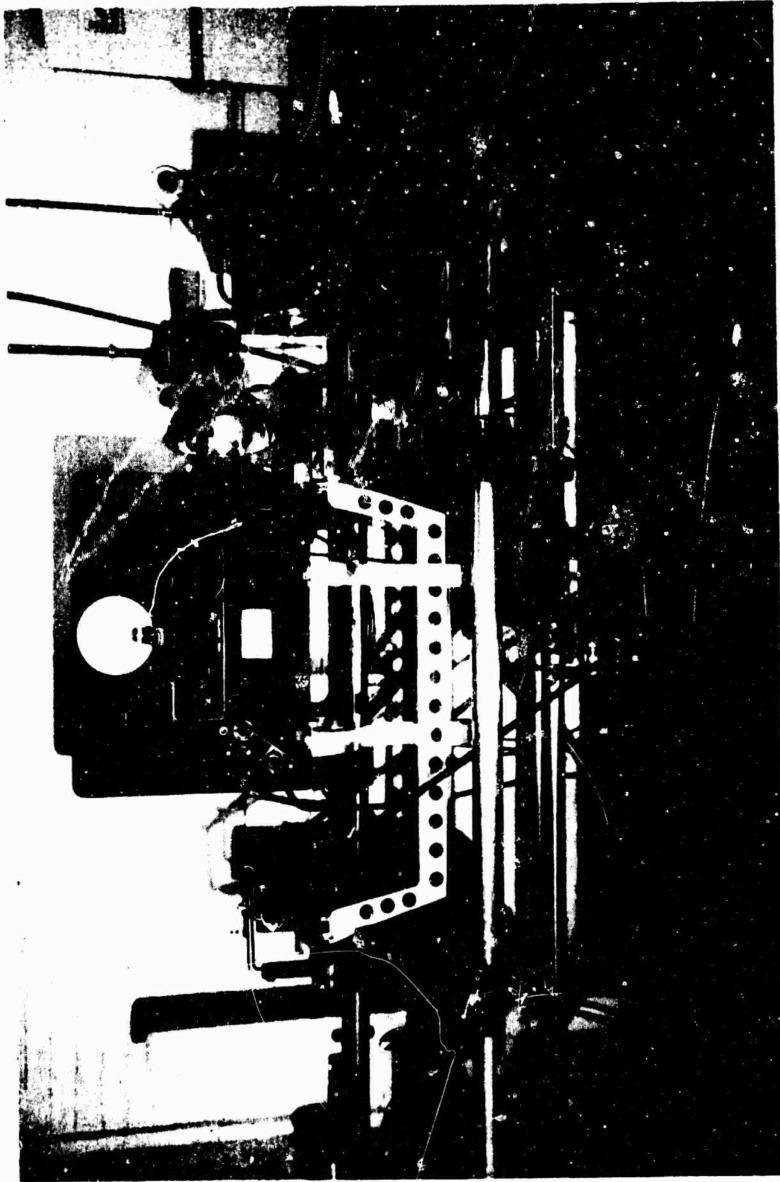


Figure 202. Dynamic Balancing Machine.



Figure 203. Dynamic Balancing Machine.

5.3.3 TEST-CELL CONTROL CONSOLE

The test control console and operating instruments are shown in Figure 204. The control panel was equipped with instruments for monitoring bearing temperatures, compressor and turbine air temperatures, seal and thrust-balance air pressures, lubrication pressures, and compressor speed. Temperature measurements of compressor and turbine bearings and of turbine inlet air were monitored to protect against overheating. Automatic safety-trip circuits were used, and allowable limits were preset in each of these temperature indicators.

Two magnetic speed pickups were used on each of the 2 turbodrives — one pickup provided the overspeed trip signal and the other an accurate compressor-speed readout. An electronic counter with an accuracy of 0.025 percent (company quoted) was connected to the compressor-speed pickup. Compressor speed was adjusted manually at the console by controlling the turbodrive fuel and airflow rates. Compressor and turbodrive vibration was monitored with vibration meters.

5.4 PERFORMANCE DATA ACQUISITION

Performance data were recorded manually and with electronic recording equipment. Temperatures, some pressures, speed, and impeller clearance were recorded manually; however, most of the pressure data were recorded on the digital data system. The instrumentation equipment used for these tests is discussed in detail in Section 4.0.

5.4.1 IMPELLER AERODYNAMIC INSTRUMENTATION

Instrumentation for the MF-1 and RF-1 test sections included static-pressure taps in the inlet, shroud, vaneless diffuser, and collector; total-pressure probes at the impeller inlet and exit; total-temperature probes at the impeller inlet and exit, and in the collector; and a static-pressure dynamic transducer at the impeller exit. The probes at the impeller exit were removeable to permit performance evaluation without the influence of flow disturbances created by these probes. Figure 205 is an example of the hookup identification sheets.

The static-pressure taps in the front and rear impeller shrouds were sharp-edged, 0.020-inch-diameter holes. The pressure connections to the static taps were stainless-steel tubes, 0.042 inch in diameter, which were silver brazed in 0.125-inch-diameter, drilled copper slugs about 0.3 inch long. These slugs were staked into 0.128-inch-diameter holes, concentric with the static taps, in the back of the plates. The 0.042-inch tubes extended about 15 inches from the plates and were connected to the cell pressure manifold with 0.125-inch-diameter nylon tubing and compression fittings.

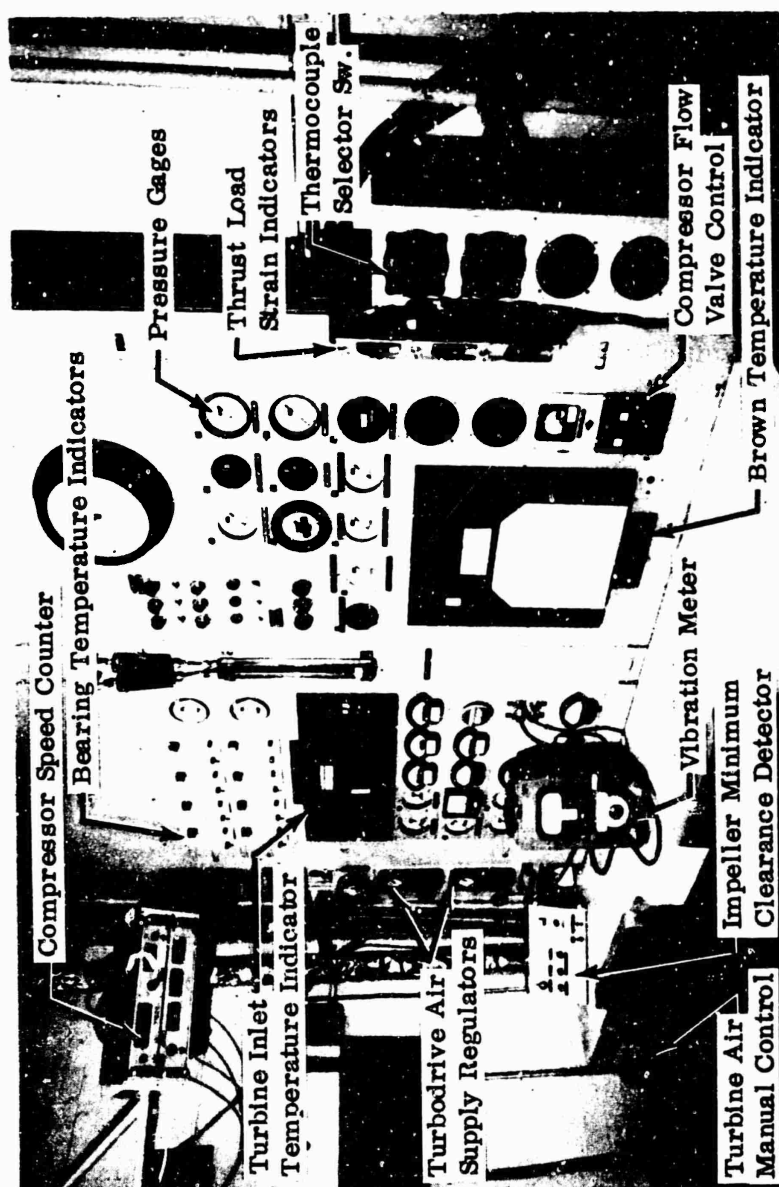


Figure 204. Test-Cell Control Console.

Compressor-inlet total pressure was measured with three Kiel probes, individually connected to a water manometer board and recorded manually. Total pressure at the impeller tip was obtained with total-pressure rakes and yaw probes. Angle setting of the fixed total-pressure rake was determined from the yaw-angle measurement for each test speed and flow condition. Impeller-tip total pressure was recorded both manually and on the digital data system.

Compressor-discharge static pressure in the collector was measured at six tap locations around the outer circumference of the collector. Collector pressures were recorded manually and on the digital data system. A 0 to 200 psig gage was used for manual readout. Six thermocouples installed adjacent to the collector static-pressure taps measured the compressor-discharge air temperature, and one thermocouple at the impeller exit measured the impeller-discharge temperature. Compressor-inlet air temperature was measured with 3 thermocouples located in the inlet duct at three different depths. The compressor inlet and discharge thermocouples were AWG-20 bare-wire iron-constantan junction type.

MF-1 and RF-1 impeller data obtained from initial tests indicated the need for faster-response pressure measurements in the vaneless passage. A microsecond-rise-time dynamic pressure transducer was installed in the front shroud near the impeller tip to measure static-pressure fluctuation in the vaneless passage. Results from these measurements are given in Section 6.0.

5.4.2 DIFFUSER AERODYNAMIC INSTRUMENTATION

Instrumentation used in the diffuser analyses included static-pressure taps in the inlet, shroud, diffuser channels, and collector; total-pressure and total-temperature probes in the inlet, at the impeller exit, and in the diffuser channels; and total-temperature probes in the collector.

Static-pressure wall taps (0.020-inch-diameter) were machined in the front and rear diffuser plates. Three rows in 1 channel were used. The 78 static-pressure taps machined in the front diffuser plate were matched with an equal number at the same locations in the backplate. Diffuser-channel static-pressure tap hookup to the digital data system used the same forms as those for the impeller tests (Figure 205).

Static pressures along the impeller shroud were measured at 4 radial stations, with 2 pressure taps 180 degrees apart at each station. Three impeller-inlet static-pressure taps, 120 degrees apart, were installed in both the inner hub and outer shroud of the variable inlet guide vane. Static pressure upstream of the inlet guide vane along the inner and outer shrouds was measured with 3 pressure taps on each surface, positioned in line with the downstream static-pressure taps. Flush-machined, 0.020-inch-diameter hypodermic tubing was used for the inlet

Tap No.	Description Of Tap	Tap No.	Description Of Tap	Tap No.	Description Of Tap
1		49		97	
2		50		98	
3		51		99	
4		52		100	
5		53		101	
6		54		102	
7		55		103	
8		56		104	
9		57		105	
10		58		106	
11		59		107	
12		60		108	
13		61		109	
14		62		110	
15		63		111	
16		64		112	
17		65		113	
18		66		114	
19		67		115	
20		68		116	
21		69		117	
22		70		118	
23		71		119	
24		72		120	
25		73		121	
26		74		122	
27		75		123	
28		76		124	
29		77		125	
30		78		126	
31		79		127	
32		80		128	
33		81		129	
34		82		130	
35		83		131	
36		84		132	
37		85		133	
38		86		134	
39		87		135	
40		88		136	
41		89		137	
42		90		138	
43		91		139	
44		92		140	
45		93		141	
46		94		142	
47		95		143	
48		96		144	

1-2

3-4

5-6

7-8

Sp. Gr.

Sp. Gr.

Sp. Gr.

Sp. Gr.

U-Tubes

ref. 47-62

ref. 63-7

Sp. Gr.

2.95

Board

Sp. Gr.

2.95

Board

109 - 132

W & T

Hg

145

146

147

148

149

150

151

152

153

154

Date

Lessard 1-6-64

Pr

T

S

Figure 205. Pressure-Hookup Identification Sheet.

Tap No.	Description Of Tap	1-2	3-4	5-6	7-8	ref. 11-20	ref. 21-30	ref. 31-46
97		Sp. Gr. — Sp. Gr. — Sp. Gr. — Sp. Gr.	Sp. Gr. — Sp. Gr. — Sp. Gr. — Sp. Gr.	Sp. Gr. — Sp. Gr. — Sp. Gr. — Sp. Gr.	Sp. Gr. — Sp. Gr. — Sp. Gr. — Sp. Gr.	Sp. Gr. 1.00 Board	Sp. Gr. 1.00 Board	Sp. Gr. 1.00 Board
98								
99								
100								
101								
102								
103								
104		U-Tubes						
105		ref. 47-62 Sp. Gr. 2.95 Board	ref. 63-78 Sp. Gr. 2.95 Board	ref. 79-88 Sp. Gr. — Board	Oper. Instrn. 90-105	Spares 9, 10, 89, 106-108		
106								
107								
108								
109								
110								
111								
112								
113								
114								
115								
116								
117								
118								
119								
120								
121								
122								
123								
124								
125								
126								
127								
128								
129								
130								
131								
132								
133								
134								
135								
136								
137								
138								
139								
140								
141								
142								
143								
144								

109 - 132
W & T
Hg

133 - 156
W & T
Hg

157 - 180
W & T
Hg

145		155	
146		156	
147		157	
148		158	
149		159	
150		160	
151		161	
152		162	
153		163	
154		164	

Date	Test No
Lessard 1-6-64	

Pressure Instrumentation
Installation Summary

THE BOEING COMPANY
Seattle 24, Washington

Page

Sheet.

static-pressure taps. Compressor-inlet static pressure was connected to 2.95 specific-gravity fluid-manometer banks and was recorded manually.

Compressor-inlet total pressure was measured with three Kiel total-pressure probes, spaced at 120-degree intervals in the bellmouth inlet duct. The probes were positioned at the center of 3 equal-area radial sections of the inlet to obtain the average total inlet pressure. Three compressor-inlet bare-wire thermocouples were installed immediately upstream of the Kiel total-pressure probes at different circumferential locations.

Impeller-exit total pressure was measured with total-pressure yaw probes, 3-probe rakes, and a diffuser-channel total-pressure traversing probe. Impeller-exit total pressure at various depths from the wall was obtained by traversing the yaw probes and aligning them with the direction of flow. To define the angle of flow at the impeller exit, the probe was set visually on the radial centerline, a position defined at the mechanical-zero angle. However, visual angle setting of the probe was not within the required accuracy of 1 degree needed for data analysis because the short (6.2 inch) probe length was not sufficient for true alignment with the radial centerline. Therefore, the compressor section was partially assembled with 1 of the bladeless dummy rotors (Figure 206), and an aerodynamic zero-angle calibration was made. Impeller-inlet airflow was directed by the dummy impeller to a true radial-flow field at the yaw-probe station, as shown in Figure 207.

Aerodynamic zero, or reference angle, was then determined by balancing the probe outside pressure ports. Total pressure at 3 fixed depths across the passage was obtained with the 3-probe rake aligned in the flow direction.

Diffuser midchannel total-pressure measurements were made with a 0.020-inch-diameter traversing probe (refer to Figures 174 and 175, Section 4.0). Pressures were measured at 9 stations extending 0.060 inch from the impeller tip to within 1 inch of the diffuser exit. The different channel stations at which total pressures were measured are described in Section 6.0.

Compressor-discharge pressure was obtained from four wall static-pressure taps installed at different circumferential positions around the collector. Collector pressure was recorded manually to make preliminary map plots, and it was recorded on the digital data system for each test speed.

Temperatures used in analyzing compressor performance were measured on a circular potentiometer with a range of 0° to 800° F. Temperatures were recorded manually on the data sheet shown in Figure 208. Thermocouples used in the tests were calibrated periodically.

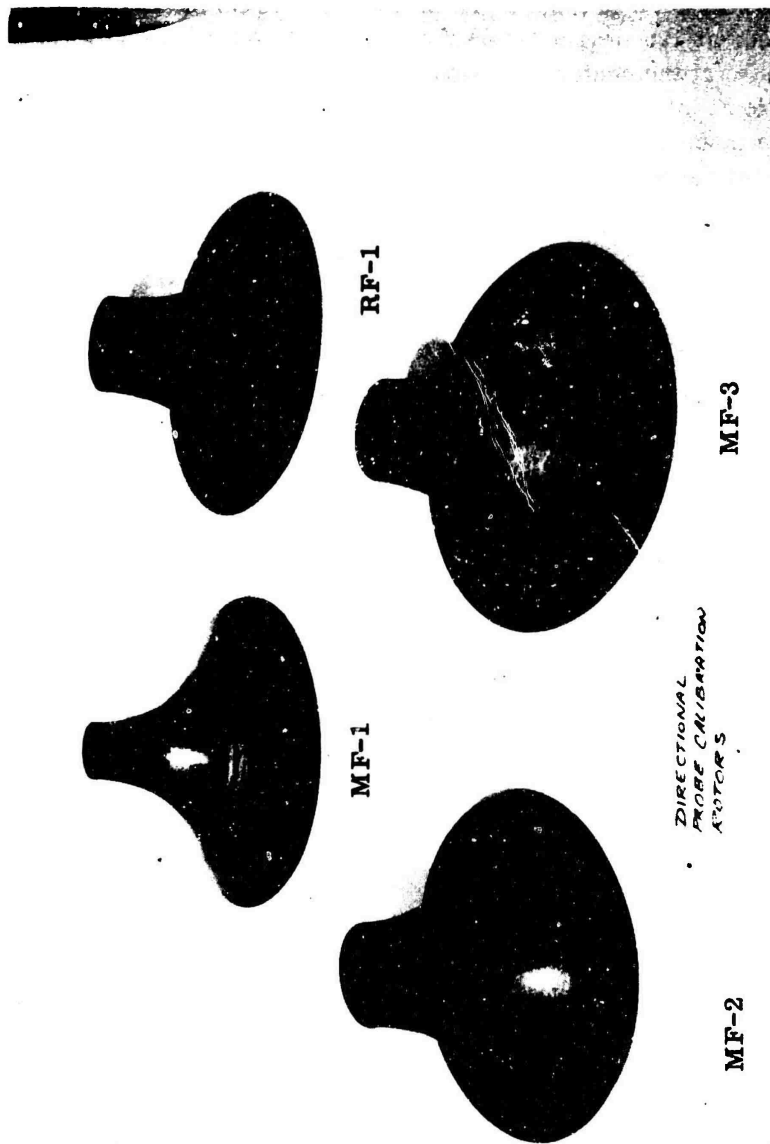


Figure 206. Dummy Impellers.

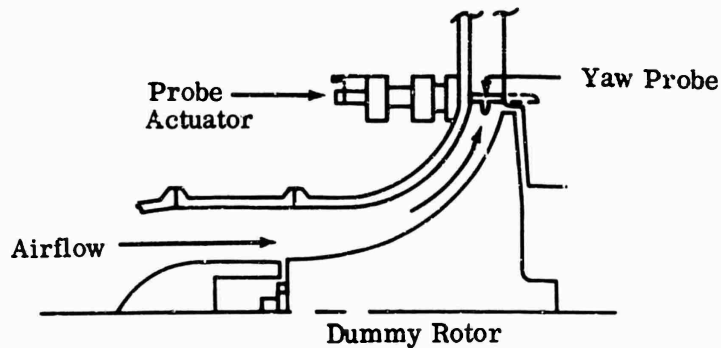


Figure 207. Yaw Probe Zero-Angle Calibration.

Bare-wire iron-constantan thermocouples were used to measure compressor-inlet and collector air temperatures. Three were used to measure compressor-inlet air temperature, and 6 to 12 thermocouples installed at various depths in the collector were used to obtain an average collector-discharge temperature for the analytical computations.

Impeller-exit total temperature was measured with a split-shield thermocouple probe positioned at the same flow angle as the total-pressure yaw probe. Impeller-exit total temperatures were measured in the vaneless passage at three depths to determine a temperature profile. When the exit profile was not well defined by measurements at three stations, additional probes were used.

The total-temperature-probe reference angle was established by visual alignment with the rig radial centerline in a manner similar to that used with the total-pressure yaw probes. The probe was rotated to the approximate operating flow angle to prevent contact with the impeller; later it was adjusted to coincide with the flow angle measured by the yaw probe. This was the procedure used for each depth traversed and each flow condition. An electrical actuator and a mechanical actuator were used to rotate and traverse this probe.

5.4.3 COMPRESSOR AIRFLOW MEASUREMENT

Compressor airflow was measured with a 7-inch-throat-diameter nozzle, and a 5.46-inch-diameter A.S.M.E. nozzle. The flow nozzle was mounted at the entrance of the 60-cubic-foot plenum chamber shown in Figure 209. A 2-foot-diameter by 2-foot-long extension duct preceded the flow nozzle and acted as a flow straightener. An air-baffle wall between the test cell and the plenum intake prevented air circulation within the cell that could cause a variation in compressor-inlet temperature.

Flow-nozzle pressure measurements were made with a 6- to 16-inch water (ΔP) inclined manometer (Figure 210). Resolution accuracy of this instrument was

TEMPER A

[illegible]

Figure 208. Sample Data Sheet for Temperatures.

ATURES

28	29	30	31	32	33	34	35	36	37	38	39	40	41	42	43	44	45	46	47	48	49	50	51	52	53	54	55	56	57	58	59	60	61	62	63	64	65	66	67	68	69	70	71	72	73	74	75	76	77	78	79	80	81	82	83	84	85	86	87	88	89	90	91	92	93	94	95	96	97	98	99	100
----	----	----	----	----	----	----	----	----	----	----	----	----	----	----	----	----	----	----	----	----	----	----	----	----	----	----	----	----	----	----	----	----	----	----	----	----	----	----	----	----	----	----	----	----	----	----	----	----	----	----	----	----	----	----	----	----	----	----	----	----	----	----	----	----	----	----	----	----	----	----	----	-----



॥

This image shows a full page of blank graph paper. The grid consists of small squares formed by thin black lines. A vertical line runs down the center of the page, dividing it into two equal halves. There are also horizontal lines spaced evenly across the entire page. The paper is otherwise completely blank, with no text or markings other than the grid itself.

START _____ TEST ENGINEER _____
FINISH _____ RECORDED BY _____

TEST NO. _____
SPEED : _____

NOTES:

 Do not keyp
 Keypunch tl

PREWHIRL VANE SETTING _____

50 ☐ 51 ☐ 52 ☐ 53 ☐ 54 ☐ 55 ☐ 56 ☐ 57 ☐ 58 ☐ 59 ☐ 60 ☐ 61 ☐ 62 ☐ 63 ☐ 64 ☐ 65 ☐ 66 ☐ 67 ☐ 68 ☐ 69 ☐ 70 ☐ 71 ☐ 72 ☐ 73 ☐ 74 ☐ 75 ☐ 76 ☐ 77 ☐ 78 ☐ 79 ☐ 80 ☐ 81 ☐ 82 ☐ 83 ☐ 84 ☐ 85 ☐ 86 ☐ 87 ☐ 88 ☐ 89 ☐ 90 ☐ 91 ☐ 92 ☐ 93 ☐ 94 ☐ 95 ☐ 96 ☐ 97 ☐ 98 ☐ 99 ☐ 100 ☐ 101 ☐ 102 ☐ 103 ☐ 104 ☐ 105 ☐ 106 ☐ 107 ☐ 108 ☐ 109 ☐ 110 ☐ 111 ☐ 112 ☐ 113 ☐ 114 ☐ 115 ☐ 116 ☐ 117 ☐ 118 ☐ 119 ☐ 120 ☐ 121 ☐ 122 ☐ 123 ☐ 124 ☐ 125 ☐ 126 ☐ 127 ☐ 128 ☐ 129 ☐ 130 ☐ 131 ☐ 132 ☐ 133 ☐ 134 ☐ 135 ☐ 136 ☐ 137 ☐ 138 ☐ 139 ☐ 140 ☐ 141 ☐ 142 ☐ 143 ☐ 144 ☐ 145 ☐ 146 ☐ 147 ☐ 148 ☐ 149 ☐ 150 ☐ 151 ☐ 152 ☐ 153 ☐ 154 ☐ 155 ☐ 156 ☐ 157 ☐ 158 ☐ 159 ☐ 160 ☐ 161 ☐ 162 ☐ 163 ☐ 164 ☐ 165 ☐ 166 ☐ 167 ☐ 168 ☐ 169 ☐ 170 ☐ 171 ☐ 172 ☐ 173 ☐ 174 ☐ 175 ☐ 176 ☐ 177 ☐ 178 ☐ 179 ☐ 180 ☐ 181 ☐ 182 ☐ 183 ☐ 184 ☐ 185 ☐ 186 ☐ 187 ☐ 188 ☐ 189 ☐ 190 ☐ 191 ☐ 192 ☐ 193 ☐ 194 ☐ 195 ☐ 196 ☐ 197 ☐ 198 ☐ 199 ☐ 200 ☐ 201 ☐ 202 ☐ 203 ☐ 204 ☐ 205 ☐ 206 ☐ 207 ☐ 208 ☐ 209 ☐ 210 ☐ 211 ☐ 212 ☐ 213 ☐ 214 ☐ 215 ☐ 216 ☐ 217 ☐ 218 ☐ 219 ☐ 220 ☐ 221 ☐ 222 ☐ 223 ☐ 224 ☐ 225 ☐ 226 ☐ 227 ☐ 228 ☐ 229 ☐ 230 ☐ 231 ☐ 232 ☐ 233 ☐ 234 ☐ 235 ☐ 236 ☐ 237 ☐ 238 ☐ 239 ☐ 240 ☐ 241 ☐ 242 ☐ 243 ☐ 244 ☐ 245 ☐ 246 ☐ 247 ☐ 248 ☐ 249 ☐ 250 ☐ 251 ☐ 252 ☐ 253 ☐ 254 ☐ 255 ☐ 256 ☐ 257 ☐ 258 ☐ 259 ☐ 260 ☐ 261 ☐ 262 ☐ 263 ☐ 264 ☐ 265 ☐ 266 ☐ 267 ☐ 268 ☐ 269 ☐ 270 ☐ 271 ☐ 272 ☐ 273 ☐ 274 ☐ 275 ☐ 276 ☐ 277 ☐ 278 ☐ 279 ☐ 280 ☐ 281 ☐ 282 ☐ 283 ☐ 284 ☐ 285 ☐ 286 ☐ 287 ☐ 288 ☐ 289 ☐ 290 ☐ 291 ☐ 292 ☐ 293 ☐ 294 ☐ 295 ☐ 296 ☐ 297 ☐ 298 ☐ 299 ☐ 300 ☐ 301 ☐ 302 ☐ 303 ☐ 304 ☐ 305 ☐ 306 ☐ 307 ☐ 308 ☐ 309 ☐ 310 ☐ 311 ☐ 312 ☐ 313 ☐ 314 ☐ 315 ☐ 316 ☐ 317 ☐ 318 ☐ 319 ☐ 320 ☐ 321 ☐ 322 ☐ 323 ☐ 324 ☐ 325 ☐ 326 ☐ 327 ☐ 328 ☐ 329 ☐ 330 ☐ 331 ☐ 332 ☐ 333 ☐ 334 ☐ 335 ☐ 336 ☐ 337 ☐ 338 ☐ 339 ☐ 340 ☐ 341 ☐ 342 ☐ 343 ☐ 344 ☐ 345 ☐ 346 ☐ 347 ☐ 348 ☐ 349 ☐ 350 ☐ 351 ☐ 352 ☐ 353 ☐ 354 ☐ 355 ☐ 356 ☐ 357 ☐ 358 ☐ 359 ☐ 360 ☐ 361 ☐ 362 ☐ 363 ☐ 364 ☐ 365 ☐ 366 ☐ 367 ☐ 368 ☐ 369 ☐ 370 ☐ 371 ☐ 372 ☐ 373 ☐ 374 ☐ 375 ☐ 376 ☐ 377 ☐ 378 ☐ 379 ☐ 380 ☐ 381 ☐ 382 ☐ 383 ☐ 384 ☐ 385 ☐ 386 ☐ 387 ☐ 388 ☐ 389 ☐ 390 ☐ 391 ☐ 392 ☐ 393 ☐ 394 ☐ 395 ☐ 396 ☐ 397 ☐ 398 ☐ 399 ☐ 400 ☐ 401 ☐ 402 ☐ 403 ☐ 404 ☐ 405 ☐ 406 ☐ 407 ☐ 408 ☐ 409 ☐ 410 ☐ 411 ☐ 412 ☐ 413 ☐ 414 ☐ 415 ☐ 416 ☐ 417 ☐ 418 ☐ 419 ☐ 420 ☐ 421 ☐ 422 ☐ 423 ☐ 424 ☐ 425 ☐ 426 ☐ 427 ☐ 428 ☐ 429 ☐ 430 ☐ 431 ☐ 432 ☐ 433 ☐ 434 ☐ 435 ☐ 436 ☐ 437 ☐ 438 ☐ 439 ☐ 440 ☐ 441 ☐ 442 ☐ 443 ☐ 444 ☐ 445 ☐ 446 ☐ 447 ☐ 448 ☐ 449 ☐ 450 ☐ 451 ☐ 452 ☐ 453 ☐ 454 ☐ 455 ☐ 456 ☐ 457 ☐ 458 ☐ 459 ☐ 460 ☐ 461 ☐ 462 ☐ 463 ☐ 464 ☐ 465 ☐ 466 ☐ 467 ☐ 468 ☐ 469 ☐ 470 ☐ 471 ☐ 472 ☐ 473 ☐ 474 ☐ 475 ☐ 476 ☐ 477 ☐ 478 ☐ 479 ☐ 480 ☐ 481 ☐ 482 ☐ 483 ☐ 484 ☐ 485 ☐ 486 ☐ 487 ☐ 488 ☐ 489 ☐ 490 ☐ 491 ☐ 492 ☐ 493 ☐ 494 ☐ 495 ☐ 496 ☐ 497 ☐ 498 ☐ 499 ☐ 500 ☐ 501 ☐ 502 ☐ 503 ☐ 504 ☐ 505 ☐ 506 ☐ 507 ☐ 508 ☐ 509 ☐ 510 ☐ 511 ☐ 512 ☐ 513 ☐ 514 ☐ 515 ☐ 516 ☐ 517 ☐ 518 ☐ 519 ☐ 520 ☐ 521 ☐ 522 ☐ 523 ☐ 524 ☐ 525 ☐ 526 ☐ 527 ☐ 528 ☐ 529 ☐ 530 ☐ 531 ☐ 532 ☐ 533 ☐ 534 ☐ 535 ☐ 536 ☐ 537 ☐ 538 ☐ 539 ☐ 540 ☐ 541 ☐ 542 ☐ 543 ☐ 544 ☐ 545 ☐ 546 ☐ 547 ☐ 548 ☐ 549 ☐ 550 ☐ 551 ☐ 552 ☐ 553 ☐ 554 ☐ 555 ☐ 556 ☐ 557 ☐ 558 ☐ 559 ☐ 560 ☐ 561 ☐ 562 ☐ 563 ☐ 564 ☐ 565 ☐ 566 ☐ 567 ☐ 568 ☐ 569 ☐ 570 ☐ 571 ☐ 572 ☐ 573 ☐ 574 ☐ 575 ☐ 576 ☐ 577 ☐ 578 ☐ 579 ☐ 580 ☐ 581 ☐ 582 ☐ 583 ☐ 584 ☐ 585 ☐ 586 ☐ 587 ☐ 588 ☐ 589 ☐ 590 ☐ 591 ☐ 592 ☐ 593 ☐ 594 ☐ 595 ☐ 596 ☐ 597 ☐ 598 ☐ 599 ☐ 600 ☐ 601 ☐ 602 ☐ 603 ☐ 604 ☐ 605 ☐ 606 ☐ 607 ☐ 608 ☐ 609 ☐ 610 ☐ 611 ☐ 612 ☐ 613 ☐ 614 ☐ 615 ☐ 616 ☐ 617 ☐ 618 ☐ 619 ☐ 620 ☐ 621 ☐ 622 ☐ 623 ☐ 624 ☐ 625 ☐ 626 ☐ 627 ☐ 628 ☐ 629 ☐ 630 ☐ 631 ☐ 632 ☐ 633 ☐ 634 ☐ 635 ☐ 636 ☐ 637 ☐ 638 ☐ 639 ☐ 640 ☐ 641 ☐ 642 ☐ 643 ☐ 644 ☐ 645 ☐ 646 ☐ 647 ☐ 648 ☐ 649 ☐ 650 ☐ 651 ☐ 652 ☐ 653 ☐ 654 ☐ 655 ☐ 656 ☐ 657 ☐ 658 ☐ 659 ☐ 660 ☐ 661 ☐ 662 ☐ 663 ☐ 664 ☐ 665 ☐ 666 ☐ 667 ☐ 668 ☐ 669 ☐ 670 ☐ 671 ☐ 672 ☐ 673 ☐ 674 ☐ 675 ☐ 676 ☐ 677 ☐ 678 ☐ 679 ☐ 680 ☐ 681 ☐ 682 ☐ 683 ☐ 684 ☐ 685 ☐ 686 ☐ 687 ☐ 688 ☐ 689 ☐ 690 ☐ 691 ☐ 692 ☐ 693 ☐ 694 ☐ 695 ☐ 696 ☐ 697 ☐ 698 ☐ 699 ☐ 700 ☐ 701 ☐ 702 ☐ 703 ☐ 704 ☐ 705 ☐ 706 ☐ 707 ☐ 708 ☐ 709 ☐ 710 ☐ 711 ☐ 712 ☐ 713 ☐ 714 ☐ 715 ☐ 716 ☐ 717 ☐ 718 ☐ 719 ☐ 720 ☐ 721 ☐ 722 ☐ 723 ☐ 724 ☐ 725 ☐ 726 ☐ 727 ☐ 728 ☐ 729 ☐ 730 ☐ 731 ☐ 732 ☐ 733 ☐ 734 ☐ 735 ☐ 736 ☐ 737 ☐ 738 ☐ 739 ☐ 740 ☐ 741 ☐ 742 ☐ 743 ☐ 744 ☐ 745 ☐ 746 ☐ 747 ☐ 748 ☐ 749 ☐ 750 ☐ 751 ☐ 752 ☐ 753 ☐ 754 ☐ 755 ☐ 756 ☐ 757 ☐ 758 ☐ 759 ☐ 760 ☐ 761 ☐ 762 ☐ 763 ☐ 764 ☐ 765 ☐ 766 ☐ 767 ☐ 768 ☐ 769 ☐ 770 ☐ 771 ☐ 772 ☐ 773 ☐ 774 ☐ 775 ☐ 776 ☐ 777 ☐ 778 ☐ 779 ☐ 780 ☐ 781 ☐ 782 ☐ 783 ☐ 784 ☐ 785 ☐ 786 ☐ 787 ☐ 788 ☐ 789 ☐ 790 ☐ 791 ☐ 792 ☐ 793 ☐ 794 ☐ 795 ☐ 796 ☐ 797 ☐ 798 ☐ 799 ☐ 800 ☐ 801 ☐ 802 ☐ 803 ☐ 804 ☐ 805 ☐ 806 ☐ 807 ☐ 808 ☐ 809 ☐ 810 ☐ 811 ☐ 812 ☐ 813 ☐ 814 ☐ 815 ☐ 816 ☐ 817 ☐ 818 ☐ 819 ☐ 820 ☐ 821 ☐ 822 ☐ 823 ☐ 824 ☐ 825 ☐ 826 ☐ 827 ☐ 828 ☐ 829 ☐ 830 ☐ 831 ☐ 832 ☐ 833 ☐ 834 ☐ 835 ☐ 836 ☐ 837 ☐ 838 ☐ 839 ☐ 840 ☐ 841 ☐ 842 ☐ 843 ☐ 844 ☐ 845 ☐ 846 ☐ 847 ☐ 848 ☐ 849 ☐ 850 ☐ 851 ☐ 852 ☐ 853 ☐ 854 ☐ 855 ☐ 856 ☐ 857 ☐ 858 ☐ 859 ☐ 860 ☐ 861 ☐ 862 ☐ 863 ☐ 864 ☐ 865 ☐ 866 ☐ 867 ☐ 868 ☐ 869 ☐ 870 ☐ 871 ☐ 872 ☐ 873 ☐ 874 ☐ 875 ☐ 876 ☐ 877 ☐ 878 ☐ 879 ☐ 880 ☐ 881 ☐ 882 ☐ 883 ☐ 884 ☐ 885 ☐ 886 ☐ 887 ☐ 888 ☐ 889 ☐ 890 ☐ 891 ☐ 892 ☐ 893 ☐ 894 ☐ 895 ☐ 896 ☐ 897 ☐ 898 ☐ 899 ☐ 900 ☐ 901 ☐ 902 ☐ 903 ☐ 904 ☐ 905 ☐ 906 ☐ 907 ☐ 908 ☐ 909 ☐ 910 ☐ 911 ☐ 912 ☐ 913 ☐ 914 ☐ 915 ☐ 916 ☐ 917 ☐ 918 ☐ 919 ☐ 920 ☐ 921 ☐ 922 ☐ 923 ☐ 924 ☐ 925 ☐ 926 ☐ 927 ☐ 928 ☐ 929 ☐ 930 ☐ 931 ☐ 932 ☐ 933 ☐ 934 ☐ 935 ☐ 936 ☐ 937 ☐ 938 ☐ 939 ☐ 940 ☐ 941 ☐ 942 ☐ 943 ☐ 944 ☐ 945 ☐ 946 ☐ 947 ☐ 948 ☐ 949 ☐ 950 ☐ 951 ☐ 952 ☐ 953 ☐ 954 ☐ 955 ☐ 956 ☐ 957 ☐ 958 ☐ 959 ☐ 960 ☐ 961 ☐ 962 ☐ 963 ☐ 964 ☐ 965 ☐ 966 ☐ 967 ☐ 968 ☐ 969 ☐ 970 ☐ 971 ☐ 972 ☐ 973 ☐ 974 ☐ 975 ☐ 976 ☐ 977 ☐ 978 ☐ 979 ☐ 980 ☐ 981 ☐ 982 ☐ 983 ☐ 984 ☐ 985 ☐ 986 ☐ 987 ☐ 988 ☐ 989 ☐ 990 ☐ 991 ☐ 992 ☐ 993 ☐ 994 ☐ 995 ☐ 996 ☐ 997 ☐ 998 ☐ 999 ☐ 1000 ☐ 1001 ☐ 1002 ☐ 1003 ☐ 1004 ☐ 1005 ☐ 1006 ☐ 1007 ☐ 1008 ☐ 1009 ☐ 1010 ☐ 1011 ☐ 1012 ☐ 1013 ☐ 1014 ☐ 1015 ☐ 1016 ☐ 1017 ☐ 1018 ☐ 1019 ☐ 1020 ☐ 1021 ☐ 1022 ☐ 1023 ☐ 1024 ☐ 1025 ☐ 1026 ☐ 1027 ☐ 1028 ☐ 1029 ☐ 1030 ☐ 1031 ☐ 1032 ☐ 1033 ☐ 1034 ☐ 1035 ☐ 1036 ☐ 1037 ☐ 1038 ☐ 1039 ☐ 1040 ☐ 1041 ☐ 1042 ☐ 1043 ☐ 1044 ☐ 1045 ☐ 1046 ☐ 1047 ☐ 1048 ☐ 1049 ☐ 1050 ☐ 1051 ☐ 1052 ☐ 1053 ☐ 1054 ☐ 1055 ☐ 1056 ☐ 1057 ☐ 1058 ☐ 1059 ☐ 1060 ☐ 1061 ☐ 1062 ☐ 1063 ☐ 1064 ☐ 1065 ☐ 1066 ☐ 1067 ☐ 1068 ☐ 1069 ☐ 1070 ☐ 1071 ☐ 1072 ☐ 1073 ☐ 1074 ☐ 1075 ☐ 1076 ☐ 1077 ☐ 1078 ☐ 1079 ☐ 1080 ☐ 1081 ☐ 1082 ☐ 1083 ☐ 1084 ☐ 1085 ☐ 1086 ☐ 1087 ☐ 1088 ☐ 1089 ☐ 1090 ☐ 1091 ☐ 1092 ☐ 1093 ☐ 1094 ☐ 1095 ☐ 1096 ☐ 1097 ☐ 1098 ☐ 1099 ☐ 1100 ☐ 1101 ☐ 1102 ☐ 1103 ☐ 1104 ☐ 1105 ☐ 1106 ☐ 1107 ☐ 1108 ☐ 1109 ☐ 1110 ☐ 1111 ☐ 1112 ☐ 1113 ☐ 1114 ☐ 1115 ☐ 1116 ☐ 1117 ☐ 1118 ☐ 1119 ☐ 1120 ☐ 1121 ☐ 1122 ☐ 1123 ☐ 1124 ☐ 1125 ☐ 1126 ☐ 1127 ☐ 1128 ☐ 1129 ☐ 1130 ☐ 1131 ☐ 1132 ☐ 1133 ☐ 1134 ☐ 1135 ☐ 1136 ☐ 1137 ☐ 1138 ☐ 1139 ☐ 1140 ☐ 1141 ☐ 1142 ☐ 1143 ☐ 1144 ☐ 1145 ☐ 1146 ☐ 1147 ☐ 1148 ☐ 1149 ☐ 1150 ☐ 1151 ☐ 1152 ☐ 1153 ☐ 1154 ☐ 1155 ☐ 1156 ☐ 1157 ☐ 1158 ☐ 1159 ☐ 1160 ☐ 1161 ☐ 1162 ☐ 1163 ☐ 1164 ☐ 1165 ☐ 1166 ☐ 1167 ☐ 1168 ☐ 1169 ☐ 1170 ☐ 1171 ☐ 1172 ☐ 1173 ☐ 1174 ☐ 1175 ☐ 1176 ☐ 1177 ☐ 1178 ☐ 1179 ☐ 1180 ☐ 1181 ☐ 1182 ☐ 1183 ☐ 1184 ☐ 1185 ☐ 1186 ☐ 1187 ☐ 1188 ☐ 1189 ☐ 1190 ☐ 1191 ☐ 1192 ☐ 1193 ☐ 1194 ☐ 1195 ☐ 1196 ☐ 1197 ☐ 1198 ☐ 1199 ☐ 1200 ☐ 1201 ☐ 1202 ☐ 1203 ☐ 1204 ☐ 1205 ☐ 1206 ☐ 1207 ☐ 1208 ☐ 1209 ☐ 1210 ☐ 1211 ☐ 1212 ☐ 1213 ☐ 1214 ☐ 1215 ☐ 1216 ☐ 1217 ☐ 1218 ☐ 1219 ☐ 1220 ☐ 1221 ☐ 1222 ☐ 1223 ☐ 1224 ☐ 1225 ☐ 1226 ☐ 1227 ☐ 1228 ☐ 1229 ☐ 1230 ☐ 1231 ☐ 1232 ☐ 1233 ☐ 1234 ☐ 1235 ☐ 1236 ☐ 1237 ☐ 1238 ☐ 1239 ☐ 1240 ☐ 1241 ☐ 1242 ☐ 1243 ☐ 1244 ☐ 1245 ☐ 1246 ☐ 1247 ☐ 1248 ☐ 1249 ☐ 1250 ☐ 1251 ☐ 1252 ☐ 1253 ☐ 1254 ☐ 1255 ☐ 1256 ☐ 1257 ☐ 1258 ☐ 1259 ☐ 1260 ☐ 1261 ☐ 1262 ☐ 1263 ☐ 126

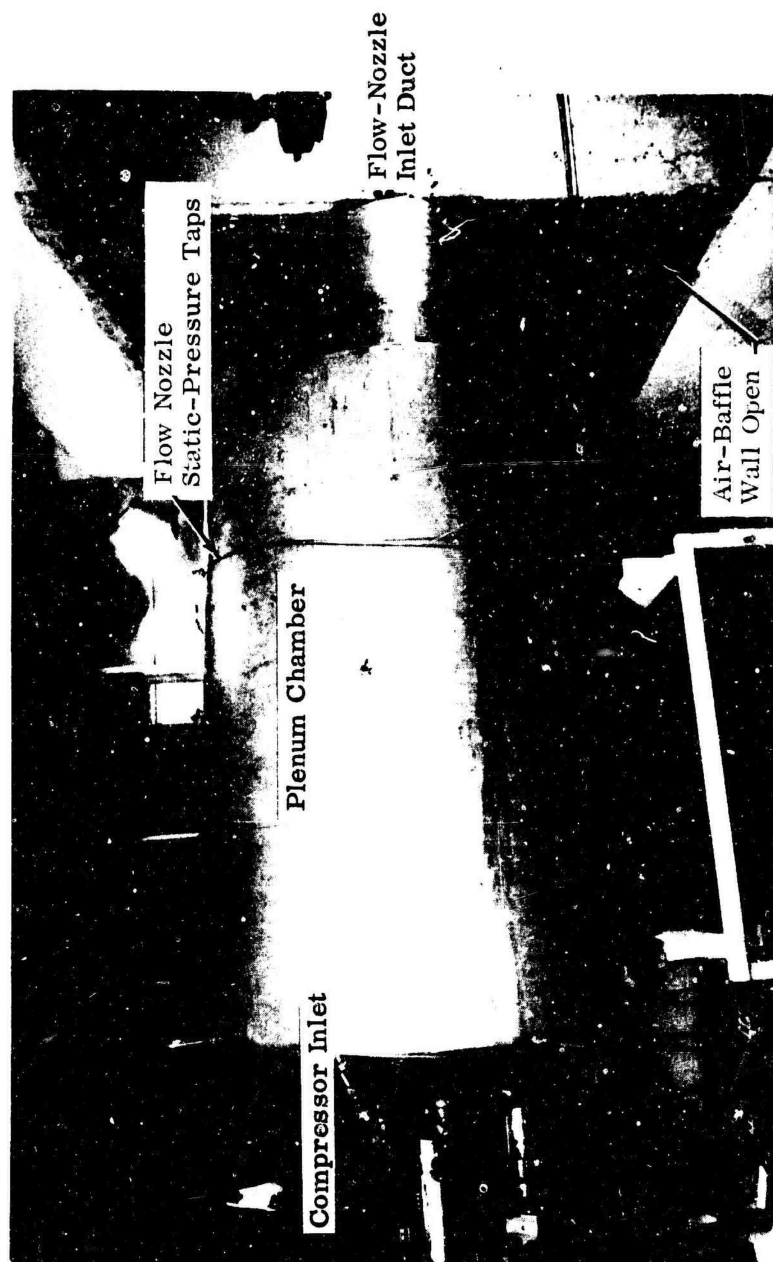
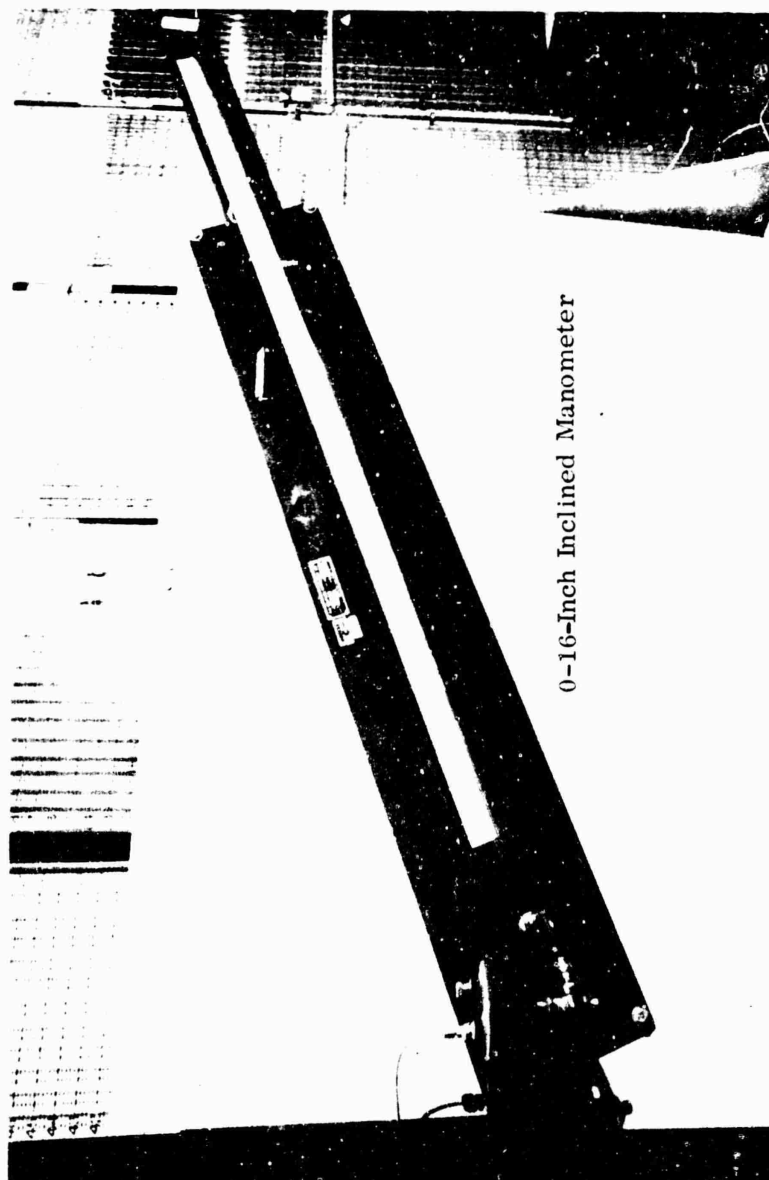


Figure 209. Compressor Inlet Plenum Chamber.



0-16-Inch Inclined Manometer

Figure 210. Compressor Airflow Manometer.

0.01-inch water. Three static-pressure taps in the plenum-chamber wall at the flow-nozzle-exit plane were connected in parallel to the low-pressure side of the manometer. The high-pressure side of the manometer was referenced to the flow-nozzle-inlet ambient total pressure. This instrument was calibrated periodically and was checked for pressure leaks before each test.

5.4.4 DIGITAL DATA SYSTEM

Most compressor-performance pressure data were recorded by the digital data system; Figure 211 shows 1 of the 2 test-cell pressure manifolds, with provision for 300 pressure connections. Nylon tubing (1/8 inch in diameter) was used to transmit impeller and diffuser pressures from the manifolds to the digital data system. After a minimum pressure-stabilization period of 5 minutes at the required performance condition, the digital data system read-command circuit was energized; the pressures were trapped and retained in storage volumes within the system. The pressure in each storage volume was then ported sequentially to a transducer, and the output from this transducer was digitally recorded on punched paper tape. A known, accurate reference pressure was recorded on the tape with the performance data for each cycle. The reference pressure was used to verify that no appreciable calibration drift of the electronic measuring system had occurred during the test.

All pressure lines were tested for leaks before each test, and the data system was pressure-calibrated before and after each test run. Digital data system pressure-calibration data were used in the computer program to reduce the measured pressure data to tabulated engineering units. Pressure data not compatible with the pressure range of the data system were recorded manually. Typical data sheets used for manual pressure recording are shown in Figures 212 and 213. Manual readout of compressor-map data permitted preliminary performance analysis. The pressure gages equipped with suitable multiple inputs, as shown in Figure 214, were used for manual readout of pressures from 0 to 300 inches Hg and from 0 to 200 psig. The manometer banks (also shown in Figure 214) were used to measure compressor-inlet and shroud pressures below atmospheric pressure. Manometer readings were recorded manually. Meriam 2.95-specific-gravity fluid and water were the manometer fluids.

5.5 TEST-RIG OPERATING PROCEDURES

Operating procedures for both rigs were established to ensure operation within mechanical limits. These procedures consisted of 4 basic steps: (1) prestart checklist; (2) start and low-speed operation (to 25,000 rpm); (3) high-speed operation; and (4) shutdown.



Figure 211. Test Cell Pressure Manifold.

PRESSURES

STATION	P (REF)	FLOW NOZZ. L.	FLOW NOZZ. R.	INLET DUCT																							
INSTR'M'T		MANOMETER	MANOMETER	MANOMETER																							
1	27	8	14	15	21	22	28	29	35	36	42	43	49	50	56	57	63	64	70	1	7	8	14	15	21	22	28
UN/REF		H ₂ O	2.95	H ₂ O	2.95	H ₂ O 2.95 P(REF)												HG									
TAP NO																											
1	7	8	14	15	21	22	28	29	35	36	42	43	49	50	56	57	63	64	70	1	7	8	14	15	21	22	28
1																											
2																											
3																											
4																											
5																											
6																											
7																											
8																											

Calc.			REVISED	DATE	COMPRESSOR TEST
Trac					
Chk					
Appr.					
Appr.					THE BOEING COMPANY SEATTLE 24 WASHINGTON

DATA SHEET #

Figure 212. Sample Data Sheet for Pressures.



COLLECTOR														BAROM.																																																																																																																																																																																																																																																																																																																																																																																																																																																																																																																																																																																																																																																																																																																																																																																																																																									
W & T GAGE																																																																																																																																																																																																																																																																																																																																																																																																																																																																																																																																																																																																																																																																																																																																																																																																																																																							
<input type="checkbox"/> 28	<input type="checkbox"/> 29	<input type="checkbox"/> 30	<input type="checkbox"/> 31	<input type="checkbox"/> 32	<input type="checkbox"/> 33	<input type="checkbox"/> 34	<input type="checkbox"/> 35	<input type="checkbox"/> 36	<input type="checkbox"/> 37	<input type="checkbox"/> 38	<input type="checkbox"/> 39	<input type="checkbox"/> 40	<input type="checkbox"/> 41	<input type="checkbox"/> 42	<input type="checkbox"/> 43	<input type="checkbox"/> 44	<input type="checkbox"/> 45	<input type="checkbox"/> 46	<input type="checkbox"/> 47	<input type="checkbox"/> 48	<input type="checkbox"/> 49	<input type="checkbox"/> 50	<input type="checkbox"/> 51	<input type="checkbox"/> 52	<input type="checkbox"/> 53	<input type="checkbox"/> 54	<input type="checkbox"/> 55	<input type="checkbox"/> 56	<input type="checkbox"/> 57	<input type="checkbox"/> 58	<input type="checkbox"/> 59	<input type="checkbox"/> 60	<input type="checkbox"/> 61	<input type="checkbox"/> 62	<input type="checkbox"/> 63	<input type="checkbox"/> 64	<input type="checkbox"/> 65	<input type="checkbox"/> 66	<input type="checkbox"/> 67	<input type="checkbox"/> 68	<input type="checkbox"/> 69	<input type="checkbox"/> 70	<input type="checkbox"/> 71	<input type="checkbox"/> 72	<input type="checkbox"/> 73	<input type="checkbox"/> 74	<input type="checkbox"/> 75	<input type="checkbox"/> 76	<input type="checkbox"/> 77	<input type="checkbox"/> 78	<input type="checkbox"/> 79	<input type="checkbox"/> 80	<input type="checkbox"/> 81	<input type="checkbox"/> 82	<input type="checkbox"/> 83	<input type="checkbox"/> 84	<input type="checkbox"/> 85	<input type="checkbox"/> 86	<input type="checkbox"/> 87	<input type="checkbox"/> 88	<input type="checkbox"/> 89	<input type="checkbox"/> 90	<input type="checkbox"/> 91	<input type="checkbox"/> 92	<input type="checkbox"/> 93	<input type="checkbox"/> 94	<input type="checkbox"/> 95	<input type="checkbox"/> 96	<input type="checkbox"/> 97	<input type="checkbox"/> 98	<input type="checkbox"/> 99	<input type="checkbox"/> 100	<input type="checkbox"/> 101	<input type="checkbox"/> 102	<input type="checkbox"/> 103	<input type="checkbox"/> 104	<input type="checkbox"/> 105	<input type="checkbox"/> 106	<input type="checkbox"/> 107	<input type="checkbox"/> 108	<input type="checkbox"/> 109	<input type="checkbox"/> 110	<input type="checkbox"/> 111	<input type="checkbox"/> 112	<input type="checkbox"/> 113	<input type="checkbox"/> 114	<input type="checkbox"/> 115	<input type="checkbox"/> 116	<input type="checkbox"/> 117	<input type="checkbox"/> 118	<input type="checkbox"/> 119	<input type="checkbox"/> 120	<input type="checkbox"/> 121	<input type="checkbox"/> 122	<input type="checkbox"/> 123	<input type="checkbox"/> 124	<input type="checkbox"/> 125	<input type="checkbox"/> 126	<input type="checkbox"/> 127	<input type="checkbox"/> 128	<input type="checkbox"/> 129	<input type="checkbox"/> 130	<input type="checkbox"/> 131	<input type="checkbox"/> 132	<input type="checkbox"/> 133	<input type="checkbox"/> 134	<input type="checkbox"/> 135	<input type="checkbox"/> 136	<input type="checkbox"/> 137	<input type="checkbox"/> 138	<input type="checkbox"/> 139	<input type="checkbox"/> 140	<input type="checkbox"/> 141	<input type="checkbox"/> 142	<input type="checkbox"/> 143	<input type="checkbox"/> 144	<input type="checkbox"/> 145	<input type="checkbox"/> 146	<input type="checkbox"/> 147	<input type="checkbox"/> 148	<input type="checkbox"/> 149	<input type="checkbox"/> 150	<input type="checkbox"/> 151	<input type="checkbox"/> 152	<input type="checkbox"/> 153	<input type="checkbox"/> 154	<input type="checkbox"/> 155	<input type="checkbox"/> 156	<input type="checkbox"/> 157	<input type="checkbox"/> 158	<input type="checkbox"/> 159	<input type="checkbox"/> 160	<input type="checkbox"/> 161	<input type="checkbox"/> 162	<input type="checkbox"/> 163	<input type="checkbox"/> 164	<input type="checkbox"/> 165	<input type="checkbox"/> 166	<input type="checkbox"/> 167	<input type="checkbox"/> 168	<input type="checkbox"/> 169	<input type="checkbox"/> 170	<input type="checkbox"/> 171	<input type="checkbox"/> 172	<input type="checkbox"/> 173	<input type="checkbox"/> 174	<input type="checkbox"/> 175	<input type="checkbox"/> 176	<input type="checkbox"/> 177	<input type="checkbox"/> 178	<input type="checkbox"/> 179	<input type="checkbox"/> 180	<input type="checkbox"/> 181	<input type="checkbox"/> 182	<input type="checkbox"/> 183	<input type="checkbox"/> 184	<input type="checkbox"/> 185	<input type="checkbox"/> 186	<input type="checkbox"/> 187	<input type="checkbox"/> 188	<input type="checkbox"/> 189	<input type="checkbox"/> 190	<input type="checkbox"/> 191	<input type="checkbox"/> 192	<input type="checkbox"/> 193	<input type="checkbox"/> 194	<input type="checkbox"/> 195	<input type="checkbox"/> 196	<input type="checkbox"/> 197	<input type="checkbox"/> 198	<input type="checkbox"/> 199	<input type="checkbox"/> 200	<input type="checkbox"/> 201	<input type="checkbox"/> 202	<input type="checkbox"/> 203	<input type="checkbox"/> 204	<input type="checkbox"/> 205	<input type="checkbox"/> 206	<input type="checkbox"/> 207	<input type="checkbox"/> 208	<input type="checkbox"/> 209	<input type="checkbox"/> 210	<input type="checkbox"/> 211	<input type="checkbox"/> 212	<input type="checkbox"/> 213	<input type="checkbox"/> 214	<input type="checkbox"/> 215	<input type="checkbox"/> 216	<input type="checkbox"/> 217	<input type="checkbox"/> 218	<input type="checkbox"/> 219	<input type="checkbox"/> 220	<input type="checkbox"/> 221	<input type="checkbox"/> 222	<input type="checkbox"/> 223	<input type="checkbox"/> 224	<input type="checkbox"/> 225	<input type="checkbox"/> 226	<input type="checkbox"/> 227	<input type="checkbox"/> 228	<input type="checkbox"/> 229	<input type="checkbox"/> 230	<input type="checkbox"/> 231	<input type="checkbox"/> 232	<input type="checkbox"/> 233	<input type="checkbox"/> 234	<input type="checkbox"/> 235	<input type="checkbox"/> 236	<input type="checkbox"/> 237	<input type="checkbox"/> 238	<input type="checkbox"/> 239	<input type="checkbox"/> 240	<input type="checkbox"/> 241	<input type="checkbox"/> 242	<input type="checkbox"/> 243	<input type="checkbox"/> 244	<input type="checkbox"/> 245	<input type="checkbox"/> 246	<input type="checkbox"/> 247	<input type="checkbox"/> 248	<input type="checkbox"/> 249	<input type="checkbox"/> 250	<input type="checkbox"/> 251	<input type="checkbox"/> 252	<input type="checkbox"/> 253	<input type="checkbox"/> 254	<input type="checkbox"/> 255	<input type="checkbox"/> 256	<input type="checkbox"/> 257	<input type="checkbox"/> 258	<input type="checkbox"/> 259	<input type="checkbox"/> 260	<input type="checkbox"/> 261	<input type="checkbox"/> 262	<input type="checkbox"/> 263	<input type="checkbox"/> 264	<input type="checkbox"/> 265	<input type="checkbox"/> 266	<input type="checkbox"/> 267	<input type="checkbox"/> 268	<input type="checkbox"/> 269	<input type="checkbox"/> 270	<input type="checkbox"/> 271	<input type="checkbox"/> 272	<input type="checkbox"/> 273	<input type="checkbox"/> 274	<input type="checkbox"/> 275	<input type="checkbox"/> 276	<input type="checkbox"/> 277	<input type="checkbox"/> 278	<input type="checkbox"/> 279	<input type="checkbox"/> 280	<input type="checkbox"/> 281	<input type="checkbox"/> 282	<input type="checkbox"/> 283	<input type="checkbox"/> 284	<input type="checkbox"/> 285	<input type="checkbox"/> 286	<input type="checkbox"/> 287	<input type="checkbox"/> 288	<input type="checkbox"/> 289	<input type="checkbox"/> 290	<input type="checkbox"/> 291	<input type="checkbox"/> 292	<input type="checkbox"/> 293	<input type="checkbox"/> 294	<input type="checkbox"/> 295	<input type="checkbox"/> 296	<input type="checkbox"/> 297	<input type="checkbox"/> 298	<input type="checkbox"/> 299	<input type="checkbox"/> 300	<input type="checkbox"/> 301	<input type="checkbox"/> 302	<input type="checkbox"/> 303	<input type="checkbox"/> 304	<input type="checkbox"/> 305	<input type="checkbox"/> 306	<input type="checkbox"/> 307	<input type="checkbox"/> 308	<input type="checkbox"/> 309	<input type="checkbox"/> 310	<input type="checkbox"/> 311	<input type="checkbox"/> 312	<input type="checkbox"/> 313	<input type="checkbox"/> 314	<input type="checkbox"/> 315	<input type="checkbox"/> 316	<input type="checkbox"/> 317	<input type="checkbox"/> 318	<input type="checkbox"/> 319	<input type="checkbox"/> 320	<input type="checkbox"/> 321	<input type="checkbox"/> 322	<input type="checkbox"/> 323	<input type="checkbox"/> 324	<input type="checkbox"/> 325	<input type="checkbox"/> 326	<input type="checkbox"/> 327	<input type="checkbox"/> 328	<input type="checkbox"/> 329	<input type="checkbox"/> 330	<input type="checkbox"/> 331	<input type="checkbox"/> 332	<input type="checkbox"/> 333	<input type="checkbox"/> 334	<input type="checkbox"/> 335	<input type="checkbox"/> 336	<input type="checkbox"/> 337	<input type="checkbox"/> 338	<input type="checkbox"/> 339	<input type="checkbox"/> 340	<input type="checkbox"/> 341	<input type="checkbox"/> 342	<input type="checkbox"/> 343	<input type="checkbox"/> 344	<input type="checkbox"/> 345	<input type="checkbox"/> 346	<input type="checkbox"/> 347	<input type="checkbox"/> 348	<input type="checkbox"/> 349	<input type="checkbox"/> 350	<input type="checkbox"/> 351	<input type="checkbox"/> 352	<input type="checkbox"/> 353	<input type="checkbox"/> 354	<input type="checkbox"/> 355	<input type="checkbox"/> 356	<input type="checkbox"/> 357	<input type="checkbox"/> 358	<input type="checkbox"/> 359	<input type="checkbox"/> 360	<input type="checkbox"/> 361	<input type="checkbox"/> 362	<input type="checkbox"/> 363	<input type="checkbox"/> 364	<input type="checkbox"/> 365	<input type="checkbox"/> 366	<input type="checkbox"/> 367	<input type="checkbox"/> 368	<input type="checkbox"/> 369	<input type="checkbox"/> 370	<input type="checkbox"/> 371	<input type="checkbox"/> 372	<input type="checkbox"/> 373	<input type="checkbox"/> 374	<input type="checkbox"/> 375	<input type="checkbox"/> 376	<input type="checkbox"/> 377	<input type="checkbox"/> 378	<input type="checkbox"/> 379	<input type="checkbox"/> 380	<input type="checkbox"/> 381	<input type="checkbox"/> 382	<input type="checkbox"/> 383	<input type="checkbox"/> 384	<input type="checkbox"/> 385	<input type="checkbox"/> 386	<input type="checkbox"/> 387	<input type="checkbox"/> 388	<input type="checkbox"/> 389	<input type="checkbox"/> 390	<input type="checkbox"/> 391	<input type="checkbox"/> 392	<input type="checkbox"/> 393	<input type="checkbox"/> 394	<input type="checkbox"/> 395	<input type="checkbox"/> 396	<input type="checkbox"/> 397	<input type="checkbox"/> 398	<input type="checkbox"/> 399	<input type="checkbox"/> 400	<input type="checkbox"/> 401	<input type="checkbox"/> 402	<input type="checkbox"/> 403	<input type="checkbox"/> 404	<input type="checkbox"/> 405	<input type="checkbox"/> 406	<input type="checkbox"/> 407	<input type="checkbox"/> 408	<input type="checkbox"/> 409	<input type="checkbox"/> 410	<input type="checkbox"/> 411	<input type="checkbox"/> 412	<input type="checkbox"/> 413	<input type="checkbox"/> 414	<input type="checkbox"/> 415	<input type="checkbox"/> 416	<input type="checkbox"/> 417	<input type="checkbox"/> 418	<input type="checkbox"/> 419	<input type="checkbox"/> 420	<input type="checkbox"/> 421	<input type="checkbox"/> 422	<input type="checkbox"/> 423	<input type="checkbox"/> 424	<input type="checkbox"/> 425	<input type="checkbox"/> 426	<input type="checkbox"/> 427	<input type="checkbox"/> 428	<input type="checkbox"/> 429	<input type="checkbox"/> 430	<input type="checkbox"/> 431	<input type="checkbox"/> 432	<input type="checkbox"/> 433	<input type="checkbox"/> 434	<input type="checkbox"/> 435	<input type="checkbox"/> 436	<input type="checkbox"/> 437	<input type="checkbox"/> 438	<input type="checkbox"/> 439	<input type="checkbox"/> 440	<input type="checkbox"/> 441	<input type="checkbox"/> 442	<input type="checkbox"/> 443	<input type="checkbox"/> 444	<input type="checkbox"/> 445	<input type="checkbox"/> 446	<input type="checkbox"/> 447	<input type="checkbox"/> 448	<input type="checkbox"/> 449	<input type="checkbox"/> 450	<input type="checkbox"/> 451	<input type="checkbox"/> 452	<input type="checkbox"/> 453	<input type="checkbox"/> 454	<input type="checkbox"/> 455	<input type="checkbox"/> 456	<input type="checkbox"/> 457	<input type="checkbox"/> 458	<input type="checkbox"/> 459	<input type="checkbox"/> 460	<input type="checkbox"/> 461	<input type="checkbox"/> 462	<input type="checkbox"/> 463	<input type="checkbox"/> 464	<input type="checkbox"/> 465	<input type="checkbox"/> 466	<input type="checkbox"/> 467	<input type="checkbox"/> 468	<input type="checkbox"/> 469	<input type="checkbox"/> 470	<input type="checkbox"/> 471	<input type="checkbox"/> 472	<input type="checkbox"/> 473	<input type="checkbox"/> 474	<input type="checkbox"/> 475	<input type="checkbox"/> 476	<input type="checkbox"/> 477	<input type="checkbox"/> 478	<input type="checkbox"/> 479	<input type="checkbox"/> 480	<input type="checkbox"/> 481	<input type="checkbox"/> 482	<input type="checkbox"/> 483	<input type="checkbox"/> 484	<input type="checkbox"/> 485	<input type="checkbox"/> 486	<input type="checkbox"/> 487	<input type="checkbox"/> 488	<input type="checkbox"/> 489	<input type="checkbox"/> 490	<input type="checkbox"/> 491	<input type="checkbox"/> 492	<input type="checkbox"/> 493	<input type="checkbox"/> 494	<input type="checkbox"/> 495	<input type="checkbox"/> 496	<input type="checkbox"/> 497	<input type="checkbox"/> 498	<input type="checkbox"/> 499	<input type="checkbox"/> 500	<input type="checkbox"/> 501	<input type="checkbox"/> 502	<input type="checkbox"/> 503	<input type="checkbox"/> 504	<input type="checkbox"/> 505	<input type="checkbox"/> 506	<input type="checkbox"/> 507	<input type="checkbox"/> 508	<input type="checkbox"/> 509	<input type="checkbox"/> 510	<input type="checkbox"/> 511	<input type="checkbox"/> 512	<input type="checkbox"/> 513	<input type="checkbox"/> 514	<input type="checkbox"/> 515	<input type="checkbox"/> 516	<input type="checkbox"/> 517	<input type="checkbox"/> 518	<input type="checkbox"/> 519	<input type="checkbox"/> 520	<input type="checkbox"/> 521	<input type="checkbox"/> 522	<input type="checkbox"/> 523	<input type="checkbox"/> 524	<input type="checkbox"/> 525	<input type="checkbox"/> 526	<input type="checkbox"/> 527	<input type="checkbox"/> 528	<input type="checkbox"/> 529	<input type="checkbox"/> 530	<input type="checkbox"/> 531	<input type="checkbox"/> 532	<input type="checkbox"/> 533	<input type="checkbox"/> 534	<input type="checkbox"/> 535	<input type="checkbox"/> 536	<input type="checkbox"/> 537	<input type="checkbox"/> 538	<input type="checkbox"/> 539	<input type="checkbox"/> 540	<input type="checkbox"/> 541	<input type="checkbox"/> 542	<input type="checkbox"/> 543	<input type="checkbox"/> 544	<input type="checkbox"/> 545	<input type="checkbox"/> 546	<input type="checkbox"/> 547	<input type="checkbox"/> 548	<input type="checkbox"/> 549	<input type="checkbox"/> 550	<input type="checkbox"/> 551	<input type="checkbox"/> 552	<input type="checkbox"/> 553	<input type="checkbox"/> 554	<input type="checkbox"/> 555	<input type="checkbox"/> 556	<input type="checkbox"/> 557	<input type="checkbox"/> 558	<input type="checkbox"/> 559	<input type="checkbox"/> 560	<input type="checkbox"/> 561	<input type="checkbox"/> 562	<input type="checkbox"/> 563	<input type="checkbox"/> 564	<input type="checkbox"/> 565	<input type="checkbox"/> 566	<input type="checkbox"/> 567	<input type="checkbox"/> 568	<input type="checkbox"/> 569	<input type="checkbox"/> 570	<input type="checkbox"/> 571	<input type="checkbox"/> 572	<input type="checkbox"/> 573	<input type="checkbox"/> 574	<input type="checkbox"/> 575	<input type="checkbox"/> 576	<input type="checkbox"/> 577	<input type="checkbox"/> 578	<input type="checkbox"/> 579	<input type="checkbox"/> 580	<input type="checkbox"/> 581	<input type="checkbox"/> 582	<input type="checkbox"/> 583	<input type="checkbox"/> 584	<input type="checkbox"/> 585	<input type="checkbox"/> 586	<input type="checkbox"/> 587	<input type="checkbox"/> 588	<input type="checkbox"/> 589	<input type="checkbox"/> 590	<input type="checkbox"/> 591	<input type="checkbox"/> 592	<input type="checkbox"/> 593	<input type="checkbox"/> 594	<input type="checkbox"/> 595	<input type="checkbox"/> 596	<input type="checkbox"/> 597	<input type="checkbox"/> 598	<input type="checkbox"/> 599	<input type="checkbox"/> 600	<input type="checkbox"/> 601	<input type="checkbox"/> 602	<input type="checkbox"/> 603	<input type="checkbox"/> 604	<input type="checkbox"/> 605	<input type="checkbox"/> 606	<input type="checkbox"/> 607	<input type="checkbox"/> 608	<input type="checkbox"/> 609	<input type="checkbox"/> 610	<input type="checkbox"/> 611	<input type="checkbox"/> 612	<input type="checkbox"/> 613	<input type="checkbox"/> 614	<input type="checkbox"/> 615	<input type="checkbox"/> 616	<input type="checkbox"/> 617	<input type="checkbox"/> 618	<input type="checkbox"/> 619	<input type="checkbox"/> 620	<input type="checkbox"/> 621	<input type="checkbox"/> 622	<input type="checkbox"/> 623	<input type="checkbox"/> 624	<input type="checkbox"/> 625	<input type="checkbox"/> 626	<input type="checkbox"/> 627	<input type="checkbox"/> 628	<input type="checkbox"/> 629	<input type="checkbox"/> 630	<input type="checkbox"/> 631	<input type="checkbox"/> 632	<input type="checkbox"/> 633	<input type="checkbox"/> 634	<input type="checkbox"/> 635	<input type="checkbox"/> 636	<input type="checkbox"/> 637	<input type="checkbox"/> 638	<input type="checkbox"/> 639	<input type="checkbox"/> 640	<input type="checkbox"/> 641	<input type="checkbox"/> 642	<input type="checkbox"/> 643	<input type="checkbox"/> 644	<input type="checkbox"/> 645	<input type="checkbox"/> 646	<input type="checkbox"/> 647	<input type="checkbox"/> 648	<input type="checkbox"/> 649	<input type="checkbox"/> 650	<input type="checkbox"/> 651	<input type="checkbox"/> 652	<input type="checkbox"/> 653	<input type="checkbox"/> 654	<input type="checkbox"/> 655	<input type="checkbox"/> 656	<input type="checkbox"/> 657	<input type="checkbox"/> 658	<input type="checkbox"/> 659	<input type="checkbox"/> 660	<input type="checkbox"/> 661	<input type="checkbox"/> 662	<input type="checkbox"/> 663	<input type="checkbox"/> 664	<input type="checkbox"/> 665	<input type="checkbox"/> 666	<input type="checkbox"/> 667	<input type="checkbox"/> 668	<input type="checkbox"/> 669	<input type="checkbox"/> 670	<input type="checkbox"/> 671	<input type="checkbox"/> 672	<input type="checkbox"/> 673	<input type="checkbox"/> 674	<input type="checkbox"/> 675	<input type="checkbox"/> 676	<input type="checkbox"/> 677	<input type="checkbox"/> 678	<input type="checkbox"/> 679	<input type="checkbox"/> 680	<input type="checkbox"/> 681	<input type="checkbox"/> 682	<input type="checkbox"/> 683	<input type="checkbox"/> 684	<input type="checkbox"/> 685	<input type="checkbox"/> 686	<input type="checkbox"/> 687	<input type="checkbox"/> 688	<input type="checkbox"/> 689	<input type="checkbox"/> 690	<input type="checkbox"/> 691	<input type="checkbox"/> 692	<input type="checkbox"/> 693	<input type="checkbox"/> 694	<input type="checkbox"/> 695	<input type="checkbox"/> 696	<input type="checkbox"/> 697	<input type="checkbox"/> 698	<input type="checkbox"/> 699	<input type="checkbox"/> 700	<input type="checkbox"/> 701	<input type="checkbox"/> 702	<input type="checkbox"/> 703	<input type="checkbox"/> 704	<input type="checkbox"/> 705	<input type="checkbox"/> 706	<input type="checkbox"/> 707	<input type="checkbox"/> 708	<input type="checkbox"/> 709	<input type="checkbox"/> 710	<input type="checkbox"/> 711	<input type="checkbox"/> 712	<input type="checkbox"/> 713	<input type="checkbox"/> 714	<input type="checkbox"/> 715	<input type="checkbox"/> 716	<input type="checkbox"/> 717	<input type="checkbox"/> 718	<input type="checkbox"/> 719	<input type="checkbox"/> 720	<input type="checkbox"/> 721	<input type="checkbox"/> 722	<input type="checkbox"/> 723	<input type="checkbox"/> 724	<input type="checkbox"/> 725	<input type="checkbox"/> 726	<input type="checkbox"/> 727	<input type="checkbox"/> 728	<input type="checkbox"/> 729	<input type="checkbox"/> 730	<input type="checkbox"/> 731	<input type="checkbox"/> 732	<input type="checkbox"/> 733	<input type="checkbox"/> 734	<input type="checkbox"/> 735	<input type="checkbox"/> 736	<input type="checkbox"/> 737	<input type="checkbox"/> 738	<input type="checkbox"/> 739	<input type="checkbox"/> 740	<input type="checkbox"/> 741	<input type="checkbox"/> 742	<input type="checkbox"/> 743	<input type="checkbox"/> 744	<input type="checkbox"/> 745	<input type="checkbox"/> 746	<input type="checkbox"/> 747	<input type="checkbox"/> 748	<input type="checkbox"/> 749	<input type="checkbox"/> 750	<input type="checkbox"/> 751	<input type="checkbox"/> 752	<input type="checkbox"/> 753	<input type="checkbox"/> 754	<input type="checkbox"/> 755	<input type="checkbox"/> 756	<input type="checkbox"/> 757	<input type="checkbox"/> 758	<input type="checkbox"/> 759	<input type="checkbox"/> 760	<input type="checkbox"/> 761	<input type="checkbox"/> 762	<input type="checkbox"/> 763	<input type="checkbox"/> 764	<input type="checkbox"/> 765	<input type="checkbox"/> 766	<input type="checkbox"/> 767	<input type="checkbox"/> 768	<input type="checkbox"/> 769	<input type="checkbox"/> 770	<input type="checkbox"/> 771	<input type="checkbox"/> 772	<input type="checkbox"/> 773	<input type="checkbox"/> 774	<input type="checkbox"/> 775	<input type="checkbox"/> 776	<input type="checkbox"/> 777	<input type="checkbox"/> 778	<input type="checkbox"/> 779	<input type="checkbox"/> 780	<input type="checkbox"/> 781	<input type="checkbox"/> 782	<input type="checkbox"/> 783	<input type="checkbox"/> 784	<input type="checkbox"/> 785	<input type="checkbox"/> 786	<input type="checkbox"/> 787	<input type="checkbox"/> 788	<input type="checkbox"/> 789	<input type="checkbox"/> 790	<input type="checkbox"/> 791	<input type="checkbox"/> 792	<input type="checkbox"/> 793	<input type="checkbox"/> 794	<input type="checkbox"/> 795	<input type="checkbox"/> 796	<input type="checkbox"/> 797	<input type="checkbox"/> 798	<input type="checkbox"/> 799	<input type="checkbox"/> 800	<input type="checkbox"/> 801	<input type="checkbox"/> 802	<input type="checkbox"/> 803	<input type="checkbox"/> 804	<input type="checkbox"/> 805	<input type="checkbox"/> 806	<input type="checkbox"/> 807	<input type="checkbox"/> 808	<input type="checkbox"/> 809	<input type="checkbox"/> 810	<input type="checkbox"/> 811	<input type="checkbox"/> 812	<input type="checkbox"/> 813	<input type="checkbox"/> 814	<input type="checkbox"/> 815	<input type="checkbox"/> 816	<input type="checkbox"/> 817	<input type="checkbox"/> 818	<input type="checkbox"/> 819	<input type="checkbox"/> 820	<input type="checkbox"/> 821	<input type="checkbox"/> 822	<input type="checkbox"/> 823	<input type="checkbox"/> 824	<input type="checkbox"/> 825	<input type="checkbox"/> 826	<input type="checkbox"/> 827	<input type="checkbox"/> 828	<input type="checkbox"/> 829	<input type="checkbox"/> 830	<input type="checkbox"/> 831	<input type="checkbox"/> 832	<input type="checkbox"/> 833	<input type="checkbox"/> 834	<input type="checkbox"/> 835	<input type="checkbox"/> 836	<input type="checkbox"/> 837	<input type="checkbox"/> 838	<input type="checkbox"/> 839	<input type="checkbox"/> 840	<input type="checkbox"/> 841	<input type="checkbox"/> 842	<input type="checkbox"/> 843	<input type="checkbox"/> 844	<input type="checkbox"/> 845	<input type="checkbox"/> 846	<input type="checkbox"/> 847	<input type="checkbox"/> 848	<input type="checkbox"/> 849	<input type="checkbox"/> 850	<input type="checkbox"/> 85

PRESSURES

[illegible]

Figure 213. Sample Data Sheet for Pressures.

1. Only two manometers or W · T gages (with different reference pressures, may be recorded on this page.
2. Both pressure recorders must have same fluids in gage.
3. Separate readings from each gage by solid line.
4. Any number of readings from each gage can be recorded up to combined total of 20 for both gages.

		Keypunch this column in noted card
		and position.

2



Figure 214. Multichannel Pressure Gages and Manometer Banks.

5.5.1 IMPELLER RIG OPERATION

Mechanical limitations for the impeller rig compressor and turbodrive units (presented in Table XII) were determined by design analysis and experimental evaluation.

A prestart inspection was made of the bearing- and oil-temperature thermocouples, the oil supply, and the rig assembly. The compressor-load valve was opened to prevent low-speed surge, oil-supply pumps were started and regulated, and turbodrive seal air and oil-mist valves were turned on and set. The compressor-unit thrust-bearing strain-gage system was reset and checked for readout, and the turbodrive thrust-balance pressure indicator was pressure-tested. A separate lubrication cart was used (Figure 215).

The rig was started by applying air to the turbodrive rotor and by rotating at 5000 rpm for 5 minutes. With the turbine cooling air set at 45 psig, the rotor speed was increased to 13,000 rpm, at which speed the turbine burner was ignited. Compressor and turbodrive thrust loads and thrust-balance pressures were monitored continually and were adjusted to maintain thrust within the prescribed limits. All other indicators were observed during operation for normal running condition. If an abnormal condition were noted, an emergency switch was actuated to shut down the rig. Operation in a compressor surge condition was prevented by a surge-relief valve parallel to the compressor-discharge back-pressure valve, which was actuated by pressure fluctuations accompanying the start of surge; the compressor was then returned to full flow. The back pressure was maintained slightly below the knee of the compressor map during speed transition.

The procedure for shutdown was to decelerate slowly to 20,000 rpm, while maintaining proper back pressure and safe bearing-thrust loads. After a 5-minute stabilization period at this speed, the turbine fuel was shut off, and the speed was reduced further to 10,000 rpm for another 5-minute period to allow cooling of the rig components. The turbine air was shut off, which stopped the rig; this was followed by a complete shutdown of all systems.

Modal Balance

Included in the preparations for rig testing of the impeller was the modal balance of the compressor rotor to allow operation through the third critical speed (Appendix V). This procedure required repeated runs at slightly below the critical speed to establish amount and angular location of a compensating imbalance weight placed at the front end of the impeller shaft. An example of the reduction in displacement amplitude by this method is given in Figure 217.

TABLE XII	
IMPELLER-RIG MECHANICAL LIMITATIONS	
Impeller-Test Rig Operational Limits	
Maximum Rotor Speed	59,000 rpm
Maximum Bearing-Outer-Race Temperature	300° F
Continuous Maximum* Positive Thrust Load	80 pounds
Maximum Positive Thrust Load for Less Than 1 Minute	300 pounds
Maximum Thrust-Balance-Disk Pressure	55 psig
Maximum Center-Shaft Displacement	2 mils (peak-to-peak)
Maximum Bearing-Support Vibration	
Forward Bearing-Support Acceleration	120 g (peak-to-peak)
Rear Bearing-Support Acceleration	100 g (peak-to-peak)
Maximum Housing Vibration (0 to 2000 cps)	
Housing Acceleration	10 g
Housing Displacement	0.5 mil (peak-to-peak)
Bearing Inlet Oil (MIL-L-7808) Pressure	20 to 25 psig
Maximum Bearing-Support Oil (MIL-L-7808) Damper Pressure	50 to 60 psig
Impeller Turbodrives Operational Limits	
Maximum Rotor Speed	77,000 rpm
Maximum Bearing-Outer-Race Temperatures	300° F
Thrust-Balance-Disk Pressure Schedule	(Figure 216)
Maximum Housing Vibration (0 to 2000 cps)	
Housing Acceleration	10 g
Housing Displacement	0.5 mil (peak-to-peak)
Maximum Design Pressure Ratio	5:1
*In direction of impeller inlet.	

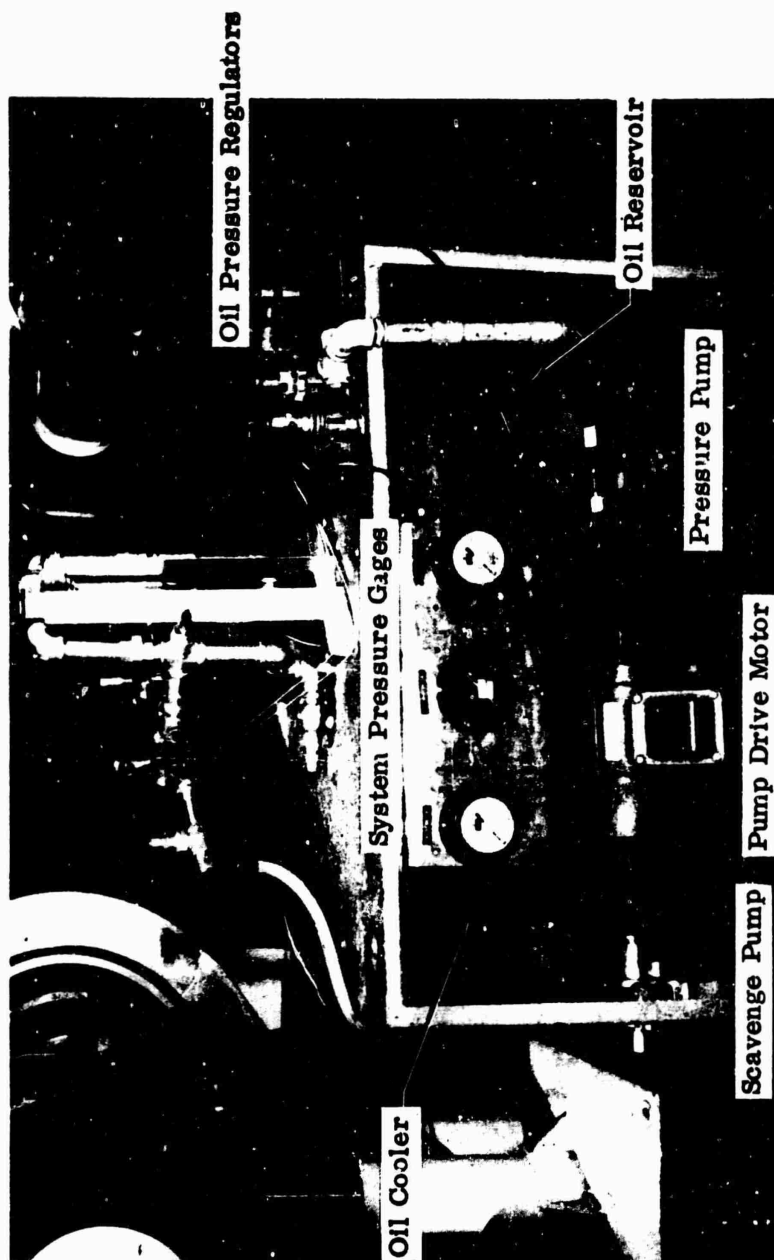


Figure 215. Impeller-Rig Lubrication Cart.

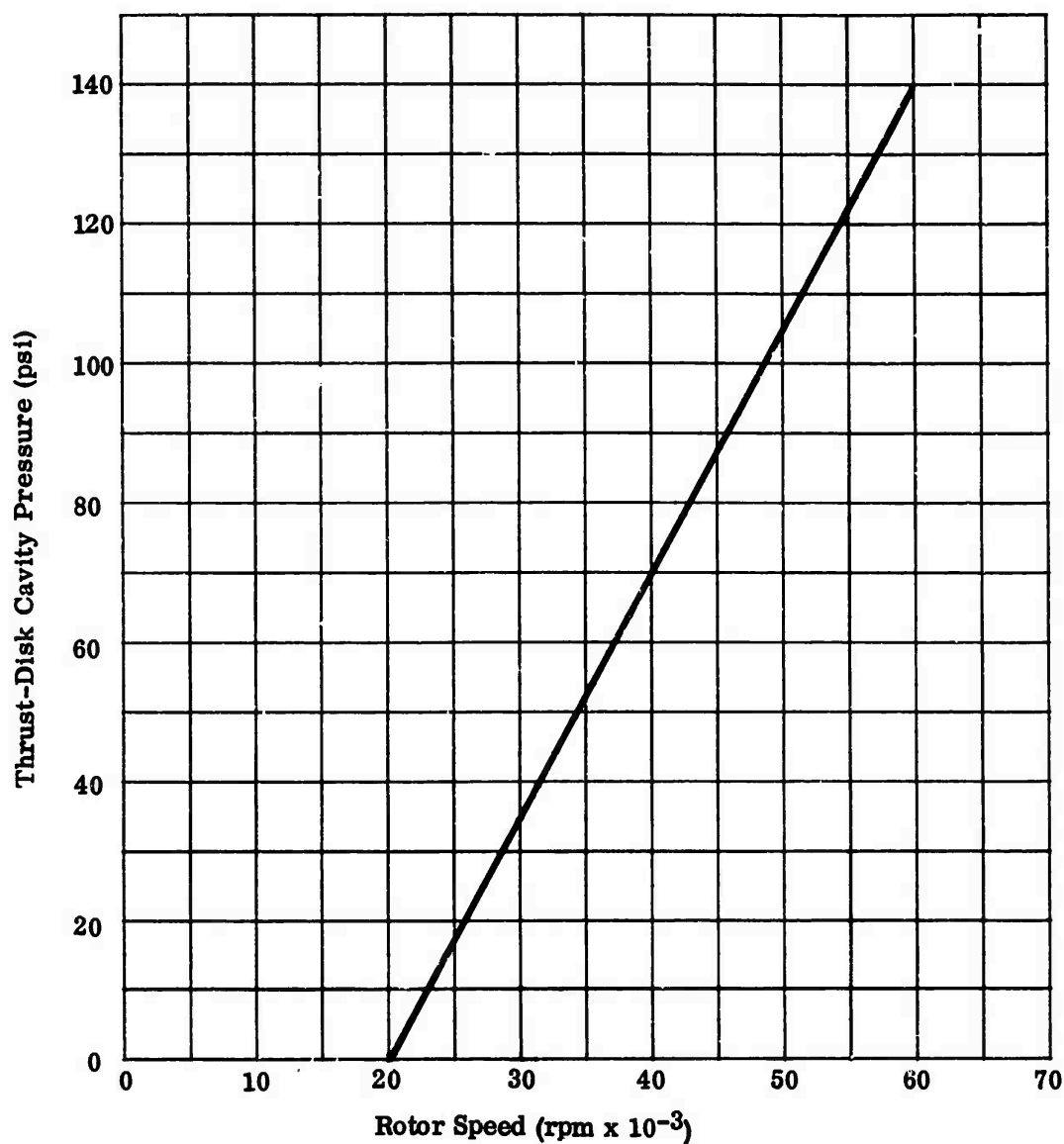


Figure 216. Impeller-Rig Turbodriven Unit Thrust-Disk Pressure.

Running Clearance

Relative movement between the impeller and shroud, caused by thermal distortion of the shroud and forward bending of the impeller, was determined with tip-clearance sensors (rub sensors) for various speeds to establish buildup clearances that would give the desired 0.020-inch running clearance. Initially, fixed rub sensors were installed in the shroud at various depths (0.010, 0.020, 0.030, and

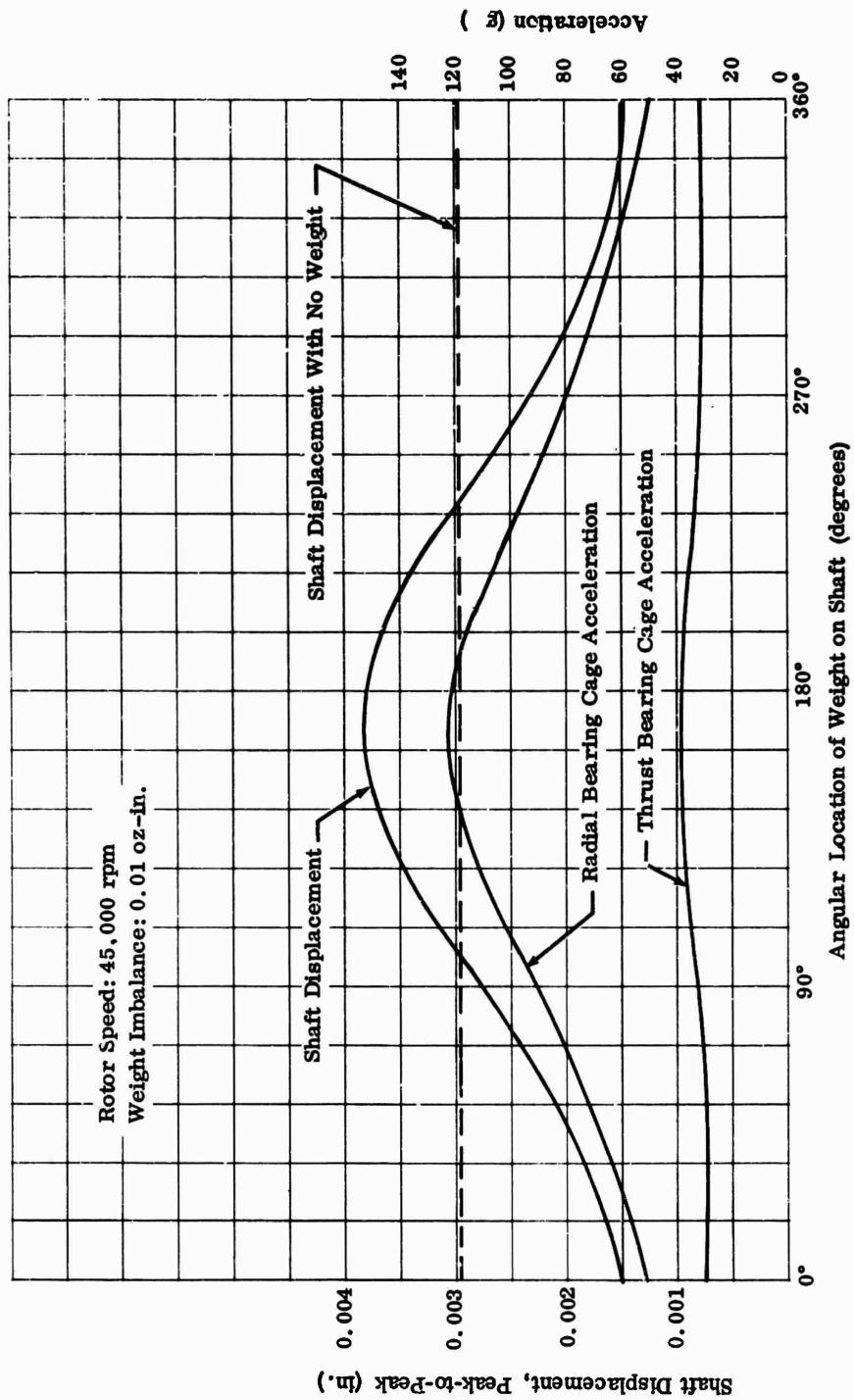


Figure 217. Modal Balance Plot.

0.050 inch) to provide the relationship between clearance and speed, shown in Figures 218 and 219. Mechanically actuated sensors later were used for this purpose, and the fixed rub sensors were used to warn the operator of impending impeller rub. The diffuser passage-width measurements, shown in Figures 218 and 219, were made with actuated electrical-contact probes.

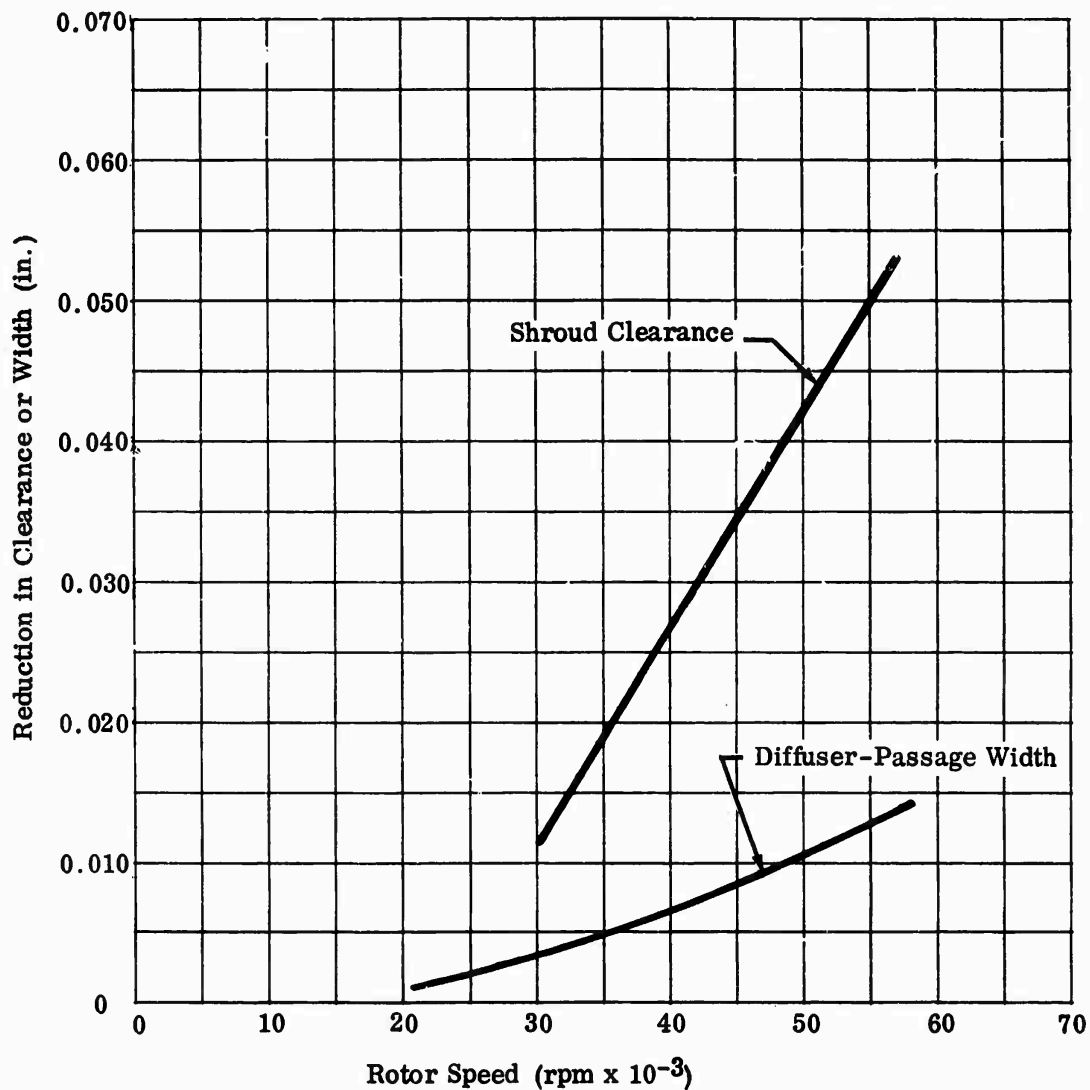


Figure 218. Impeller-Shroud and Diffuser-Passage Width Reductions (RF-1).

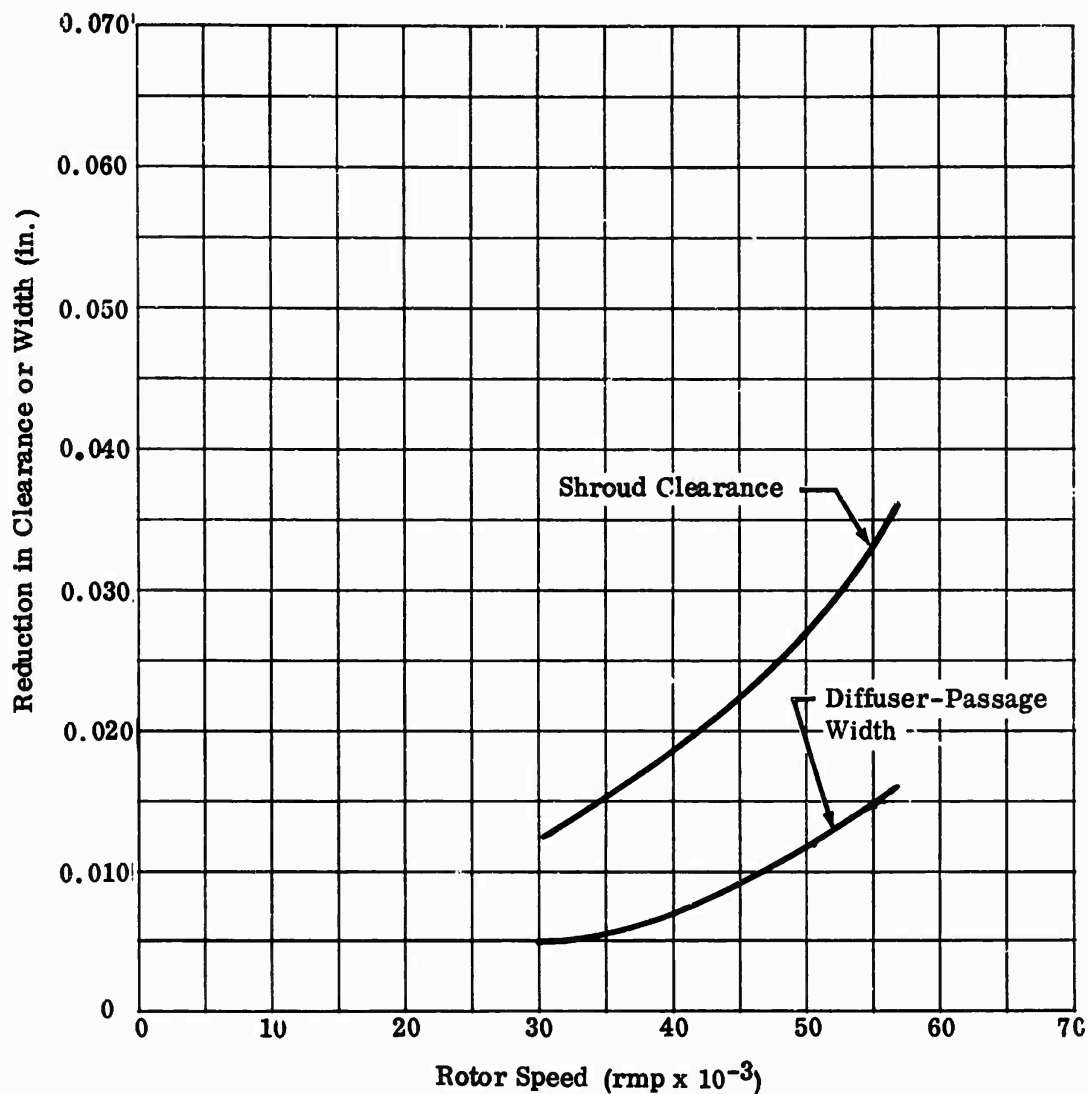


Figure 219. Impeller-Shroud and Diffuser-Passage Width Reductions (MF-1).

5.5.2 DIFFUSER-RIG OPERATION

Mechanical limitations for the diffuser rig compressor and turbodrives units are presented in Table XIII.

A prestart inspection was made of the bearing, lubrication oil, and nozzle-box thermocouples along with the oil supply and the rig assembly. The oil pumps were turned on and the pressure was regulated; air pressures were set for cooling

TABLE XIII	
DIFFUSER-RIG MECHANICAL LIMITATIONS	
Compressor Unit Operational Limits	
Maximum Rotor Speed	50,000 rpm
Maximum Oil Inlet Temperature	110° F
Maximum Bearing Temperature	200° F
Bearing Manifold Oil Inlet Pressure	(Figure 220)
Compressor Forward Carbon Seal Air	30 psig
Maximum Thrust Disk Pressure	5 psig
Maximum Sustained Housing Vibration (0 to 2000 cps)	10 g
Turbodrive Unit Operational Limits	
Maximum Rotor Speed	50,000 rpm
Maximum Oil Inlet Temperature	110° F
Maximum Bearing Retainer Temperature	200° F
Bearing Oil Inlet Pressure	(Figure 220)
Turbodrive Forward Air Labyrinth Seal	5 psig
Turbodrive Aft Turbine Cooling Air	10 psig
Turbine Nozzle Box Temperature	800 to 100° F
Maximum Housing Vibration (0 to 2000 cps)	10 g

of the turbine rotor and for the seals and thrust-balance disks on both units. The rig was started by delivering high-pressure air to the turbine and by accelerating slowly to 13,000 rpm. This speed was held for 3 to 5 minutes. If the ring-bearing temperature rise exceeded 50° F during this period, it was an indication that the bearing was not floating properly because of excess oil pressure and that a restart with reduced oil pressure was necessary. Bearing oil inlet pressure was regulated as shown in Figure 220.

With the ring-bearing temperature rise below 50° F, the turbine burner was ignited, and the speed was increased in 5,000-rpm increments until the desired operating speed was reached. Operation in the compressor-shaft critical-speed range (42,000 to 45,000 rpm) was avoided by rapidly accelerating through it. As with the impeller rig, the compressor-discharge backpressure was maintained just below the knee of the compressor map during speed transition and an automatic surge-relief valve was in parallel with the backpressure valve. Also, an emergency shutdown switch was available, and rub sensors were used to warn of an impending impeller rub.

The procedure for rig shutdown was to decelerate slowly (except in the critical-speed range) to 20,000 rpm. After 5 minutes at this speed, to allow rig cooling, the turbine burner was turned off, and the speed was reduced to 10,000 rpm for another 5-minute cooling-off period. The rig was then stopped and the oil-pressure pump was turned off. Operation of the oil-scavenge pump was continued 10 to 15 seconds to allow complete draining of the system. Seal air and turbine cooling air were left on until the oil inlet pressure reached zero.

Impeller-Stress Test Procedure

A workhorse impeller was tested with strain gages attached to 4 impeller blades to determine the vibratory blade stresses, frequencies, and modes over the entire compressor map. Section 4.0 discusses the instrumentation required, and Appendix VI gives a detailed account of the test. Figure 221 shows the rig with test equipment installed.

Stress- and map-performance data were recorded simultaneously at constant speed intervals of 500 rpm from 24,000 to 55,000 rpm. Data were recorded from 50,000 rpm down to 24,000 rpm, and then from 50,500 rpm to 55,000 rpm. The compressor flow valve was varied from full flow to surge during each speed run. At surge, the automatic relief valve was used to return the compressor to full flow. The inlet guide vane angle was set at zero degrees for all speed-line data except 35,000 and 50,000 rpm, the points of maximum vibratory stress. For these 2 speeds, the inlet guide vane angle was varied between +40 and -20 degrees.

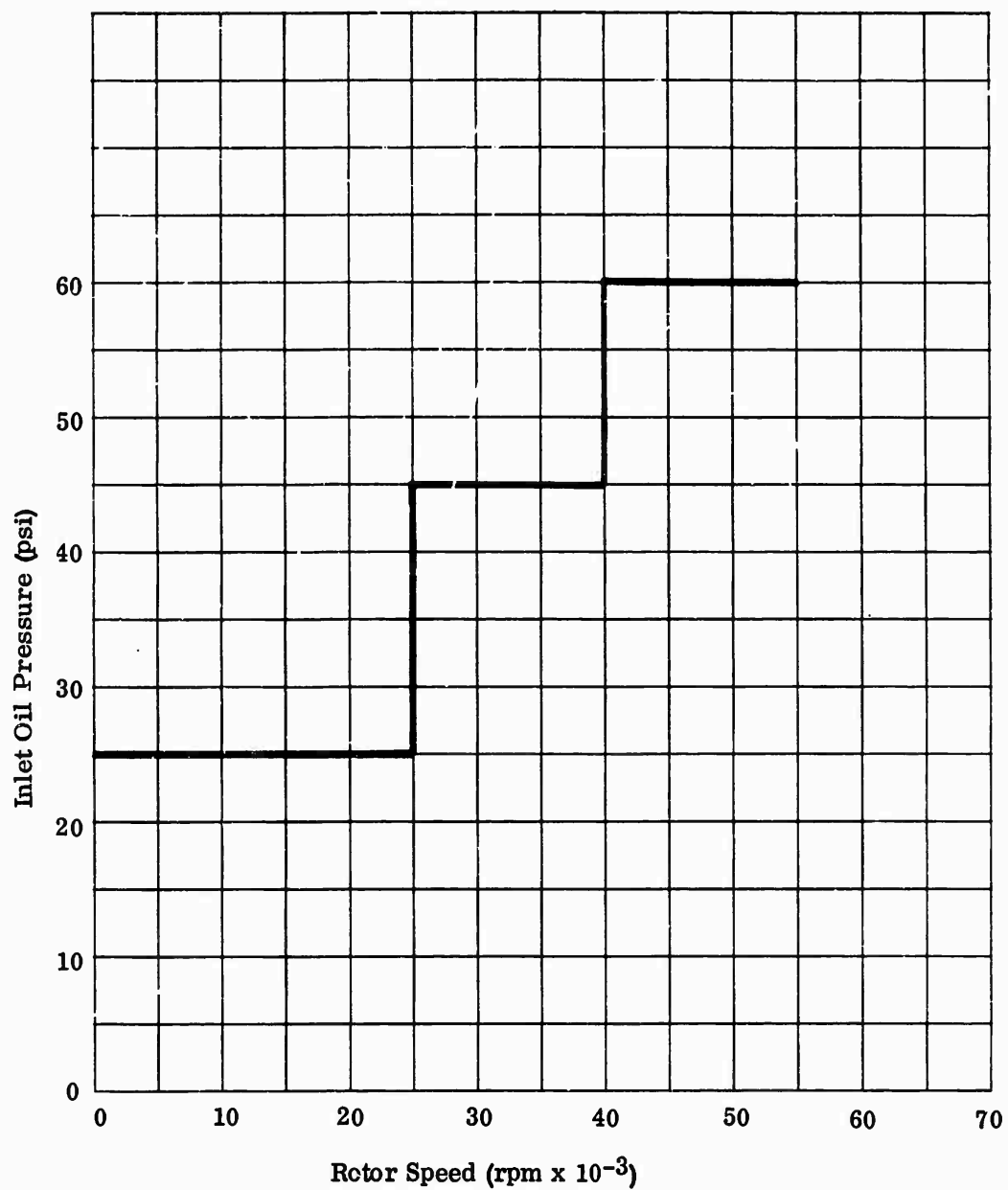


Figure 220. Diffuser-Rig Inlet Oil Pressure Versus Rotor Speed.

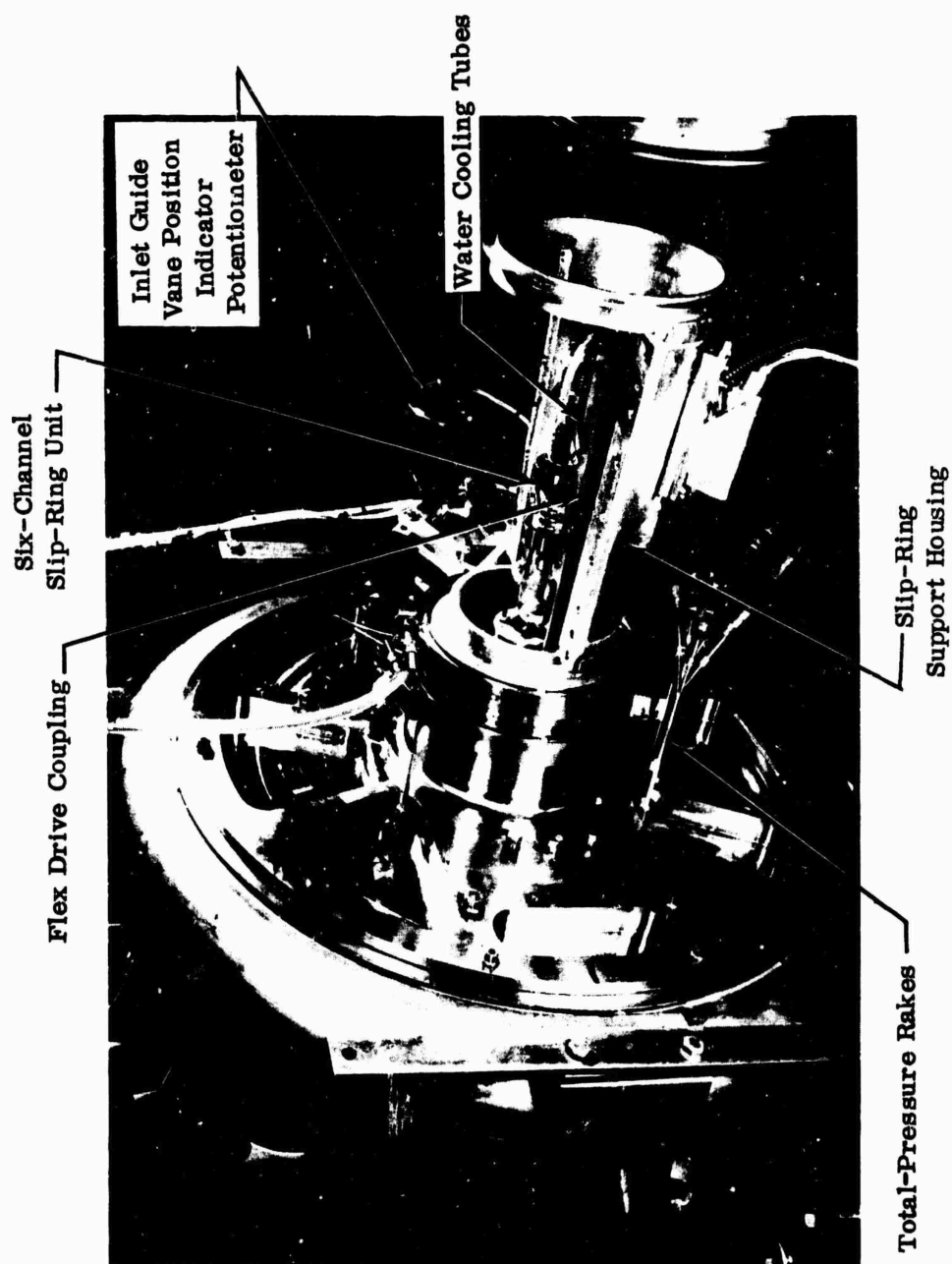


Figure 221. Impeller Stress-Test Setup.

Data were recorded continuously on oscillographs and on a magnetic-tape recorder. Also, compressor-map data were recorded manually at 4 speed lines and compared with the oscillograph traces. Run time at each speed line, except for the manual-data-recording speeds, was held to less than 2 minutes to preserve strain-gage life.

CONFIDENTIAL

(C) 6.0 TEST RESULTS (U)

This section of the report presents the results of the impeller and diffuser testing. During the Army centrifugal-compressor research program, 3 impeller configurations and 4 diffuser configurations were tested. In addition, modifications to the basic impeller and diffuser configurations were made, and these modifications were also tested. Performance data from impeller and diffuser tests are presented in Sections 6.1.4 and 6.2, respectively.

6.1 IMPELLERS

This section presents the test plan, performance measurements, calculated inlet and exit vector diagrams, modifications, and test results. A single test rig for the impeller configurations was planned. This test rig was designed to achieve the best balance in the instrumentation required for adapting 1 rig to several different impellers.

6.1.1 MF-1 IMPELLER

The MF-1 impeller test results and data were derived by using a systematic test plan to establish impeller performance and to determine the necessary test modifications.

Test Plan

Table XIV gives the test plan for the MF-1 impeller. Data are presented for the tabulated tests, and each data set is identified by test number. Data taken during the tests included:

- 1) Inlet total temperature;
- 2) Inlet total pressure;
- 3) Inlet airflow;
- 4) Static pressures along the impeller shroud;
- 5) Static pressures along the inlet duct shroud;
- 6) Static pressures along the inlet duct hub;
- 7) Impeller-exit total pressure (rake);

CONFIDENTIAL

TABLE XIV		
MF-1 IMPELLER TESTS WITH VANELESS DIFFUSER		
Test Number	Impeller Speed (rpm)	Remarks
3401	34,000	Mechanical checkout test.
	51,300	
	55,000	
3401A	20,000	Mechanical checkout test.
	30,000	
	34,000	
	40,000	
	45,000	
	50,000	
	51,300	
3402	34,000	Aerodynamic test (0.056-inch tip clearance at static condition).
	45,500	
	51,500	
	57,000	
3402A	34,000	Aerodynamic test (0.030-inch tip clearance at static condition).
	39,000	
3405	35,000	Investigation of vaneless diffuser rotating stall.
	40,000	
	45,000	
	50,000	
	52,000	
	54,000	
	55,000	
	56,000	
	57,000	

CONFIDENTIAL

- 8) Impeller-exit yaw-probe flow angles;
- 9) Impeller-exit total temperature;
- 10) Static pressure at the impeller exit;
- 11) Static pressure along the vaneless-diffuser wall;
- 12) Collector temperature;
- 13) Collector static pressure;
- 14) Vaneless-diffuser total pressure.

Performance Measurements

To define the impeller performance, the following information was required:

- 1) Temperature rise;
- 2) Pressure rise;
- 3) Vector diagrams;
- 4) Slip factor;
- 5) Blockage factor.

In addition, a rotating-stall condition, which significantly affected performance, was encountered during testing; investigation of this stall required additional measurements.

Compressor Temperature Rise — To determine adiabatic efficiency, compressor temperature was measured at 2 places — the impeller exit and the collector. It had been expected that these 2 measurements would provide agreement consistent with heat-transfer losses (8° to 10° F) between the impeller exit and collector. However, the test data showed a temperature differential much greater than expected, the difference being approximately 60° F.

For the MF-1 impeller, the requirement for flow-angle measurements in close proximity to the rotating impeller restricted the rotation of inner-radius yaw probes. For this reason, complete tip-flow angle data were not obtained.

CONFIDENTIAL

CONFIDENTIAL

Two phenomena were observed in the MF-1 tests that were believed to have resulted in the larger-than-expected impeller-tip-to-collector temperature differential. These were early flow separation in the impeller and rotating stall in the vaneless diffuser, both of which affected the mass average from the total-temperature rake at the impeller exit. It was believed that separation upstream from the rake caused turbulent, separated flow in the region of 1 or more of the thermocouples. The remaining thermocouples were believed to be located in a region of high temperature gradient. With separated flow across part of the impeller tip, and a high temperature gradient across the remaining exit area, meaningful mass-averaged total-temperature data were difficult to obtain. The rotating stall in the vaneless diffuser, with associated backflow and turbulence at the impeller exit, also made it difficult to accurately determine the total temperature.

Another cause that might have contributed to the large temperature differential was shroud clearance. Backflow through the clearance gap could have introduced a reheat effect, thus locally raising the impeller-exit temperature with respect to the collector temperature. To investigate the adequacy of the instrumentation at the impeller exit, a research program sponsored by the contractor was begun. This program is discussed in detail in Appendix VIII.

To provide a basis for comparing the performance of the impellers tested, collector temperature was used in all 3 configurations (MF-1, RF-1, and workhorse) for calculation of adiabatic efficiency. In analyzing MF-1 temperature data, a temperature-rise factor was calculated. This factor, which is defined by Equation 28, is the ratio of the actual enthalpy change of the air to the theoretical enthalpy change.

$$\text{TRF} = \frac{(\Delta h_{\text{impeller}}) (g) (J)}{U_t^2} \quad (28)$$

where:

TRF = temperature-rise factor

$\Delta h_{\text{impeller}}$ = total enthalpy change of air passing through the impeller (Btu/lb)

g = gravitational constant (32.17 ft/sec²)

CONFIDENTIAL

CONFIDENTIAL

J	= mechanical equivalent of heat (778.3 ft-lb/Btu)
U_t	= peripheral speed at impeller tip (fps)

Pressure Rise — As discussed previously, the yaw-probe data were not obtained in all tests. Therefore, in some cases, the impeller-exit total pressures could not be mass-averaged. In Tests 3402 and 3402A, an indirect mass average was obtained by using measured outer-radius yaw-probe data and a typical flow-angle profile obtained during concurrent testing with the workhorse impeller. The measured exit total pressures for Tests 3402 and 3402A (MF-1) are shown in Section 6.4.1. The same factors that contributed to the uncertainty of accuracy in the impeller-exit temperature measurements also affected impeller-exit total-pressure measurements. One of the additional instrumentation research studies discussed in Appendix VIII was total-pressure measurement in pulsating fields.

An impeller-performance map, based on the indirect mass-averaged total pressure and temperature measured at the collector, was plotted (Figure 225). The circumferential variations of impeller-exit static pressure in Tests 3402 and 3402A were also prepared.

Inlet Vector Diagrams — Data required for the inlet vector diagrams included (1) inlet static pressures in the duct, (2) inlet total temperature, and (3) inlet total pressure. The inlet vector diagrams and plots of incidence variations along the blade for Tests 3402 and 3402A are presented in Figures 237 and 238 and Figures 241 and 242 respectively.

Exit Vector Diagrams — The calculation of the exit vector diagrams is dependent on determination of the mass-averaged values of total pressure, total temperature, and flow angle. The integrated airflow, \bar{W} , is given by the equation

$$\bar{W} = 4.881\sqrt{\gamma} \int_0^H \frac{\left[r_4(h) \right] \left[M_4(h) \right] \left\{ 1 + \frac{\gamma-1}{2} \left[M_4(h) \right]^2 \right\}^{0.5} \left[\cos \alpha_4(h) \right] \left[P_{s_4}(h) \right]}{\sqrt{T_{t_4}(h)}} dh \quad (29)$$

CONFIDENTIAL

where:

4.881	=	dimensional constant
γ	=	the ratio of specific heats (C_p/C_v)
H	=	total passage width at survey station (inches)
h	=	distance across passage at survey station (inches)
M_4	=	absolute Mach number at survey station $f \left[\frac{P_s(h)}{P_t(h)} \right]$
α_4	=	absolute flow angle at survey station (degrees)
T_{t4}	=	absolute total temperature at survey station ($^{\circ}R$)
P_{s4}	=	static pressure at survey station (psia)

The mass average, \overline{X} , of any flow property, X (total pressure, total temperature, and flow angle), is given by the equation

$$\overline{X} = \frac{4.881}{\overline{W}} \int_0^H \frac{[X(h)] [r_4(h)] \left\{ 1 + \frac{\gamma-1}{2} [M_4(h)]^2 \right\}^{0.5} [\cos \alpha_4(h)]}{\sqrt{T_{t4}(h)}} dh \quad (30)$$

From these 2 equations, the mass-averaged quantities of total temperature $\overline{T_{t4}}$, total pressure $\overline{P_{t4}}$, and flow angle $\overline{\alpha_4}$ were determined.

The parameters required for construction of the exit vector diagrams are as follows:

$$1) \quad (M_4)_{avg} = f \left[\frac{(P_{s4})_{avg}}{P_{t4}} \right]$$

$$2) \quad (T_{s4})_{avg} = f \left[\bar{T}_{t4}, (M_4)_{avg} \right]$$

$$3) \quad \text{Sonic velocity} = \sqrt{\gamma g_o R (T_{s4})_{avg}}$$

$$4) \quad V_4 = (M_4)_{avg} [\text{sonic velocity}]$$

$$5) \quad (V_4)_{radial} = V_4 \cos \bar{\alpha}_4$$

$$6) \quad (V_4)_{tangential} = V_4 \sin \bar{\alpha}_4$$

The method for constructing the exit vector diagram was as follows:

- 1) From the impeller-exit total-pressure, static-pressure, and total-temperature data, the absolute velocity, V_4 , was calculated.
- 2) Using the mass-averaged flow angle $\bar{\alpha}_4$, the absolute velocity vector was established.
- 3) The exit diagram was then completed by using the impeller-tip speed calculated from measured rpm and the tip diameter.

Slip Factor — Slip factor, which is defined as the ratio of the tangential component of the absolute velocity at the impeller exit to the impeller-tip velocity, is determined from the exit velocity diagrams. The calculated slip factors were based on exit velocity diagrams determined by the previously described method. In addition, variation of average slip factor with airflow for different impeller speeds was calculated.

CONFIDENTIAL

Shroud Static Pressure — The rise in static pressure from inducer inlet to impeller exit was plotted for Tests 3402 and 3402A. These static-pressure data indicate the early separation in the impeller.

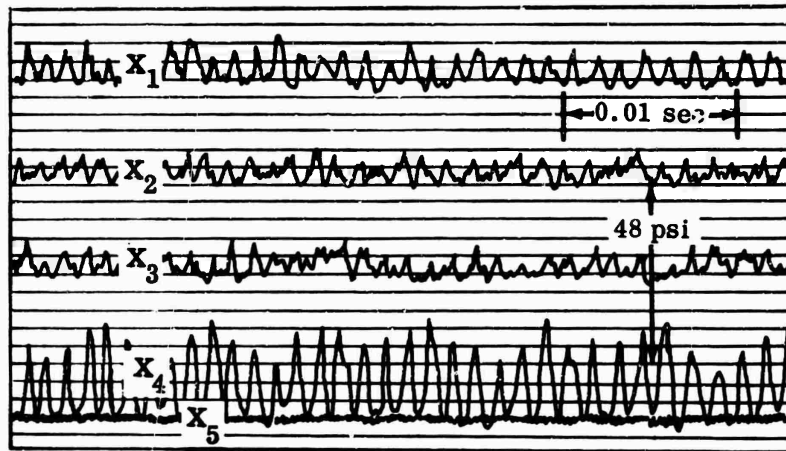
Test Modification

The large temperature difference between the impeller exit and the collector indicated that rotating stall in the vaneless diffuser may have occurred. The possibility of this stall occurrence was investigated analytically with the assistance of Dr. R.C. Dean, Jr. (a Boeing consultant from Creare, Inc.). To determine experimentally if this rotating stall was present in the vaneless diffuser, pressure transducers (described in Section 4.0) were installed in the walls of the vaneless diffuser at the stations tabulated below:

TABLE XV	
VANELESS DIFFUSER PRESSURE TRANSDUCER LOCATIONS	
Radius Ratio	Number of Transducers
1.10	1
1.20	1
1.44	2

A sample visicorder trace of the transducer data is shown in Figure 222 (page 327). The change in static-pressure variation with impeller-rotational speed and transducer radial location is shown in Figure 223 (page 350). The frequency of static-pressure fluctuation is shown in Figure 224 (page 351).

CONFIDENTIAL



- X₁ = Transducer at 1.20 Diameter Ratio
- X₂ = Transducer at 1.44 Diameter Ratio
- X₃ = Transducer at 1.44 Diameter Ratio
- X₄ = Transducer at 1.10 Diameter Ratio
- X₅ = Transducer Externally Mounted

Figure 222. Pressure Transducer Trace.

6.1.2 RF-1 IMPELLER

The RF-1 impeller test results and data were derived by using test procedures and approach similar to those of the MF-1 tests.

Test Plan

Table XVI gives the test plan for the RF-1 impeller. Data are presented for the tabulated sets, except for the mechanical checkout Test 3404, and each data set is identified by test number. Data taken during tests were the same as for the previously discussed MF-1 tests. The table shows that several modifications to the vaneless diffuser were made during Test 3404. These test modifications will be discussed in a following paragraph, Test Modifications.

CONFIDENTIAL

CONFIDENTIAL

TABLE XVI			
RF-1 IMPELLER TESTS			
Test Number	Test Speeds (rpm)	Diffuser	Comments
3403	30,000	Vaneless	Mechanical checkout test.
	43,000		
	53,000		
	54,400		
	57,000		
3404	34,000	Vaneless	Aerodynamic test with impeller shimmed for zero step and approximately 0.020-inch clearance at 57,000 rpm.
	34,000		Aerodynamic test with impeller shimmed for zero step and approximately 0.020-inch clearance at 42,000 rpm.
	42,000		
	42,000*		Aerodynamic test with impeller shimmed for zero step and approximately 0.020-inch clearance rpm. Rerun with re-calibrated pressure probes and wall thermocouples installed.
	34,000*		Aerodynamic test with impeller shimmed for zero step and approximately 0.020-inch clearance at 34,000 rpm.
	42,000*		Aerodynamic test with impeller shimmed for zero step and approximately 0.020-inch clearance at 57,000 rpm.
3406	34,000*	Vaned	Aerodynamic test with impeller shimmed for zero step and approximately 0.020-inch clearance at 57,000 rpm with diffuser rear-wall rework.
	42,000*		
	42,000		
	51,300		
	57,000		

CONFIDENTIAL

TABLE XVI (Continued)
RF-1 IMPELLER TESTS

Test Number	Test Speeds (rpm)	Diffuser	Comments
	57,000		Rerun of design speed with all impeller-exit instrumentation removed except one 3-probe total-pressure rake.
3407	57,000	Vaned	Rerun of design speed with full aerodynamic instrumentation and chamfer removed from diffuser rear wall.
3408	57,000	Vaned	Aerodynamic test with fixed (+18°) IGV installed and all impeller-exit instrumentation removed except one 3-probe total-pressure rake.
*Variations in pressure and temperature measurements occurred during testing and led to a recalibration of the total-pressure rakes and yaw probes and to the installation of thermocouples in the test-rig walls at several locations.			

Performance Measurements

RF-1 impeller performance was defined, as for MF-1, by the following information:

- 1) Temperature rise;
- 2) Pressure rise;
- 3) Vector diagrams;
- 4) Slip factor;
- 5) Blockage factor.

During the RF-1 tests conducted with the vaneless diffuser, the same type of rotating stall condition was observed as in MF-1. A vane-island diffuser was installed to eliminate the phenomenon, and additional diffuser instrumentation was used.

CONFIDENTIAL

Compressor Temperature Rise — The measurement of compressor temperature rise with the vaneless diffuser showed the same characteristic as that for the MF-1 impeller (i.e., a large temperature differential between impeller exit and collector). However, when the vane-island diffuser was installed, the impeller-exit-to-collector temperature difference dropped to about 25° F. Consistent with MF-1 testing, the collector temperature was used as the standard for calculation and comparison of impeller performance.

Pressure Rise — For this test series, the yaw-probe flow-angle data were recorded, including the inner radius measurements. During Test 3404, the pressure instrumentation was recalibrated. The vaneless-diffuser rotating stall and the impeller separation caused the same difficulty in achieving accurate measurement as in the MF-1 tests. For calculation of compressor performance, the mass-averaged total pressure at the impeller exit and the collector temperature were used. Impeller performance maps were prepared (Figures 249 and 250).

Inlet Vector Diagrams — The inlet vector diagrams were calculated by the same method as that for the MF-1 impeller. These diagrams are shown in Figures 264 through 266. The variation of inducer incidence with radius is shown in Figures 269 and 270.

Exit Vector Diagrams — The exit vector diagrams were constructed by the same method as that for the MF-1 impeller. The variation in exit Mach number with impeller-tip blade height was also calculated.

Slip Factor and Temperature-Rise Factor — The slip factor and temperature-rise factor variations across the impeller tip were calculated. The variation of the average value of these factors with airflow and impeller speed was also derived.

Inlet-Blockage Factor — The variation of the inlet-blockage factor with airflow as a function of impeller speed is presented in Section 6.1.4.

Static-Pressure Rise — The measured static-pressure data along the shroud for Tests 3404 and 3406 are shown in Section 6.1.4.

Test Modification — Two major modifications were accomplished during RF-1 testing. These were (1) installation of an inlet guide vane to reduce operating incidence on the inducer, and (2) installation of a vane-island diffuser to eliminate rotating stall. In addition, modifications were made during testing on both the vaneless and vane-island diffusers to improve performance. These modifications and their sequence in the RF-1 test series are given in Table XVI.

CONFIDENTIAL

The first major modification, that of adding prewhirl to the inlet air using a set of fixed guide vanes, was accomplished in Test 3408. Prior testing had indicated that the inducer section of the impeller was choked at the design speed of 57,000 rpm and operated at a positive incidence of 6 degrees. To reduce the operating incidence, the vanes were set at +18 degrees.

The second major modification was the installation of a 12-channel vane-island diffuser. To ensure the elimination of the rotating stall, it was desirable to have as many diffuser channels as possible. However, blade natural frequency considerations and installation in the existing test rig without major modification limited the number of channels to 12. A pressure transducer was installed at a radius ratio of 1.1 to detect rotating stall.

6.1.3 WORKHORSE IMPELLER

The workhorse impeller, a modification of a previously designed Boeing impeller, was used as an air supply in the diffuser rig. Concurrent testing indicated a higher level of performance was achieved than for either the MF-1 or RF-1 impellers (pressure ratio at design speed for the workhorse was higher by 1 to 1.5 atmospheres). Therefore, further testing of this impeller was conducted to provide additional comparative data.

Test Plan

Table XVII gives the test plan for the workhorse impeller. Although more testing than is tabulated was accomplished, the listed tests were to define impeller performance. The others were run in connection with the diffuser evaluations. For the 2 tests listed in the table, run with complete instrumentation, the same parameters were measured as for the tests on MF-1 and RF-1.

Performance Measurements

The performance measurements taken during workhorse impeller testing were essentially the same as those for MF-1 and RF-1 tests. The impeller inlet guide vanes were not calibrated for this test series, and total pressure measured upstream of the guide vanes was used to calculate impeller pressure ratio. Therefore, the performance maps shown for the workhorse impeller include the guide vane losses. Because the inlet guide vanes were not calibrated, it was also necessary to estimate the flow deviation by using Carter's rule for the construction of the inlet vector diagrams.

CONFIDENTIAL

CONFIDENTIAL

TABLE XVII		
WORKHORSE IMPELLER TESTS		
Test Number	Impeller Speed (rpm)	Remarks
3306A (IGV = +17 degrees)	30,000	Aerodynamic test with DI-1 diffuser installed and inlet guide vanes set at +17 degrees.
	35,000	
	40,000	
	46,000	
	50,000	
3306B (IGV = 0 degrees)	30,000	Aerodynamic test with DI-1 diffuser vanes installed and inlet guide vanes set at 0 degrees.
	35,000	
	40,000	
	46,000	
	50,000	

The performance maps for the workhorse impeller, the inlet and exit vector diagrams, the slip-factor data, and inlet-blockage data are shown in Section 6.1.4, Test Results.

6.1.4 TEST RESULTS

Data for all 3 impellers are presented in this section. Evaluation of the results is presented in Section 7.0.

MF-1

Test data for the MF-1 impeller (Tests 3402 and 3402A) are presented in this section, Figures 225 through 248. The arrangement of the data is as follows: (1) performance map, (2) measured data (such as impeller exit total pressure), and (3) calculated data (such as the vector diagrams). Section 7 evaluates the test results presented here.

During the program, some tests were run to obtain specific information. For these tests, only data significant to the purpose of the test were recorded.

CONFIDENTIAL

RF-1

The test data for the RF-1 impeller (Tests 3404 and 3406) are presented in Figures 249 through 273. The data are organized in the same manner as MF-1, and include the results of testing with both the vaneless and vane-island diffusers.

Test 3407 was run to evaluate the effects of the diffuser chamfer on performance. Performance was the same with or without the chamfer.

Test 3408 was run with most of the impeller-exit instrumentation removed. Thus, only partial data are presented for this test.

Workhorse

Figures 274 through 305 show the data for the workhorse impeller, also organized similar to MF-1. Data are presented for Test 3306 (IGV = +17 and 0 degrees). Positive and negative prewhirl are defined in Figure 166. The static-pressure-rise data for the workhorse impeller are important because they indicate that this impeller did not exhibit early separation, thus accounting for the better performance.

6.2 DIFFUSERS

Different diffuser configurations, both vane-island and cascade, were tested and their performance was evaluated. This section of the report presents the results of the diffuser testing. All data obtained during the program were reviewed and curves were selected to provide a complete performance description for each diffuser configuration. Data not presented in this section are contained in Appendix IX. Schlieren data are presented in Appendix X.

6.2.1 DI-1 DIFFUSER

DI-1 was the first vane-island diffuser to be tested. In addition, modifications of the basic configuration were evaluated and are discussed in Test Modifications.

Test Plan

Table XVIII presents the test plan for the DI-1 diffuser and its modifications. The data evaluations were based on the following.

- 1) Static pressures in channels and vaneless and semivaneless spaces;

CONFIDENTIAL

CONFIDENTIAL

- 2) Schlieren photographs;
- 3) Total pressure at the impeller exit;
- 4) Total temperature at the impeller exit;
- 5) Flow angle at the impeller exit;
- 6) Traversing total pressure ahead of and in the channel;
- 7) Total pressure at Station I;
- 8) Collector pressure.

Table XVIII shows the instrumentation used during each test of the original and modified DI-1 configurations.

Map Data

The pressure ratio and efficiency versus airflow for representative tests of the original and modified DI-1 diffusers are given in the Test Results section. These curves show pressure ratio based on measurements in the collector and at Station I, which was defined as the point in the channel where the area ratio (channel area/throat area) was equal to 2:1. It also represents the point in the diffuser channel where the Mach number was expected to be approximately 0.3.

It was anticipated early in the program that a 2-stage vane-island diffuser configuration, using the first-stage elements from this research, would lead to the best channel design for an engine. Station I, with a Mach number of 0.3, was the point at which it was expected that the second diffuser stage would be added, based on previous tests conducted by the contractor. It should be noted that the design-point pressure ratio at Station I was higher than 10:1. The pressure ratio difference between Station I and the collector represented an allowance for loss in total pressure through the originally proposed second stage.

In preparing the diffuser performance maps, pressure ratio at Station I was computed on the basis of a mass-averaged total pressure (3 Kiel probes) except in cases where the probes were not required in obtaining specific test information. For these cases, collector pressure was used to prepare the performance maps. The adiabatic efficiency shown on the map was based on numerical average of the collector temperatures.

CONFIDENTIAL

TABLE XVIII

DI-1 DIFFUSER AND MODIFICATIONS (See Figure 307 for Modifications)

Test No.	Diffuser No.	Radius Ratio	Throat Area (percent)	I.G.V. Setting (degrees)	Speed (rpm)	Measurements*	Remarks
3306A	DI-1	1.06	100	+17	30,000; 35,000; 40,000; 46,000; 50,000	$P_{R_{1-2}} ; P_{T_{1-2}} ; P_c ; P_{T_R}$	
3306B	DI-1	1.06	100	0	Same as 3306A	Same as 3306A	
3306C	DI-1	1.06	100	0	39,000; 50,000	Same as 3306A	
3306D	DI-1	1.06	100	+10	Same as 3306C	$P_{R_1} ; P_{T_1} ; T_1 ; P_c ; P_{T_R}$	
3306E	DI-1	1.06	100	-16	Same as 3306C	Same as 3306D	
3306F	DI-1	1.06	100	0	Same as 3306C	$P_c ; P_{T_R}$	Repeat of 3306B w/o impeller-exit probes.
3307	DI-1	1.06	100	0	39,000; 46,000; 50,000	$P_{R_{1-2}} ; P_{T_1} ; T_1 ; P_c$	Schlieren run; windows fractured; no pictures obtained.
3309A	DI-1	1.06	100	0	39,000; 50,000	$P_{T_1} ; T_1 ; P_{T_R}$	
3309B	DI-1	1.06	75	0	Same as 3309A	Same as 3309A	Test run with and without insulation on collector.
3309C	DI-1	1.06	75	No Vanes	Same as 3309A	$T_{T_1} ; P_{T_R}$ (1 point only)	

TABLE XVIII (Continued)							
DI-1 DIFFUSER AND MODIFICATIONS (See Figure 307 for Modifications)							
Test No.	Diffuser No.	Radius Ratio	Throat Area (percent)	I. G. V. Setting (degrees)	Speed (rpm)	Measurements*	Remarks
3309D	DI-1	1.06	75	0	Same as 3309A	P_{T_R}	
3309E	DI-1	1.06	50	0	Same as 3309A	P_{T_R} (1 point only)	
3309F	DI-1	1.10	104	0	Same as 3309A	P_{T_R} (1 point only)	
3309G	DI-1	1.06	125	0	Same as 3309A	P_{T_R}	
3311	DI-1	1.06	100	0	15, 000; 20, 000; 30, 000; 35, 000; 40, 000	P_C	Schlieren run.
3311A	DI-1	1.06	100	0	30, 000; 39, 000	Same as 3311	Schlieren run.
3317	DI-1	1.06	100	0	50, 000	$P_C; P_{T_R}$ (1 point only)	I. G. V. set at +10, -10, and -15 degrees at line 7.
3339	DI-1	1.06	100	No Vanes	50, 000		Second set of hardware.
3340	DI-1-3	1.06	100	No Vanes	50, 000		
3347A	DI-1	1.06	100	0	50, 000	P_{R_1}	Second set of hardware S/N-1 Front Plate.

TABLE XVIII (Continued)							
DI-1 DIFFUSER AND MODIFICATIONS (See Figure 307 for Modifications)							
Test No.	Diffuser No.	Radius Ratio	Throat Area (percent)	I. G. V. Setting (degrees)	Speed (rpm)	Measurements*	Remarks
3347B	DI-1	1.06	100	+10	50, 000	P_{R_1}	Second set of hardware.
3347C	DI-1	1.06	100	+20	50, 000	P_{R_1}	Same as 3347B.
3347D	DI-1	1.06	100	+25	50, 000	P_{R_1}	Same as 3347B.
3348	DI-1	1.06	100	0	50, 000	P_{R_1}	Lamp black flow pattern.
3350	DI-1	1.06	100	0	50, 000		
*Note:							
$P_{R_{1-2}}$		= Impeller-exit total-pressure rakes 1 and 2.			P_C	= Kiel probe at Station 1.	
$P_{T_{1-2}}$		= Impeller-exit yaw probes 1 and 2.			P_{T_R}	= Traversing total-pressure probe.	
T_{T_1}		= Impeller-exit total-temperature probe.			Collector pressure measured on all tests.		

CONFIDENTIAL

Diffuser testing was begun with tip instrumentation at the workhorse impeller exit. Although this instrumentation was believed helpful in defining diffuser performance separate from impeller, the impeller-tip instrumentation interfered with the flow into the diffuser and had an adverse effect on diffuser performance. For this reason the majority of tests were conducted without impeller-tip instrumentation.

Static Pressure Measurements

The front and backplates of the diffusers were instrumented with approximately 160 static-pressure taps. The locations of these taps are shown in Appendix IX along with the recorded data. The static pressures measured for representative tests are given in the Test Results section.

Schlieren Photographs

The schlieren photographs show the locations of shocks in the diffuser. They were used in conjunction with the previously discussed static-pressure measurements to establish the nature and strength of the shocks. Significant schlieren photographs are contained in Appendix X.

Total-Pressure Traverse

The diffuser test rig was equipped with a traversing total-pressure probe which was used to measure pressure along the predicted flow path from the impeller tip to Station I. This probe is described in detail in Section 4.0. The path of travel for the traversing probe is shown in Figure 306. Plots of total pressure versus distance through the diffuser for representative tests are shown in the Test Results section. These curves show the change in total pressure through the diffuser. Impeller-exit peak total pressure and traversing-probe total pressure measured at the impeller exit also are presented.

Impeller-Exit Surveys

Measurements of total temperature, total pressure, and flow angle were taken at the workhorse impeller exit for several of the DI-1 tests and modifications. A discussion of the workhorse impeller data is given in Section 6.1.

Inlet Guide Vanes

During the DI-1 test series, an investigation was conducted to determine the pre-whirl necessary for best compressor performance. Runs were made by setting the inlet guide vanes at angles of 0, +17, +10, and -16 degrees during Tests 3306A,

CONFIDENTIAL

3306C, 3306D, and 3306E. The map data for these tests are given in the Test Results section. The effect of prewhirl on impeller performance is discussed in Section 6.1.

Variable Capacity

A series of tests to investigate the feasibility of varying compressor-flow capacity through variable-diffuser geometry were accomplished. For these tests, throat areas were set at 50, 75, and 125 percent of the original DI-1 throat area. The results of these tests are included in the Test Results section.

Radius Ratio

A test was conducted to determine the effect of radius ratio on compressor performance. For this test, the DI-1 vanes were set at a 1.10 radius ratio. The resulting throat area was 104 percent of the original DI-1 design. The results of this test, compared to the 1.06 radius ratio of DI-1, are shown in Figure 329.

Test Modifications

During the DI-1 testing, analysis of the data provided information which indicated the need for further investigation, and modifications to the original vane configuration were identified. These modifications are described in the following discussion.

DI-1-2 — The DI-1-2 configuration had the same throat area, vane contour, and channel geometry as DI-1. However, the throat length was reduced from 0.50 to 0.125 inch. A comparison of DI-1 and DI-1-2 vane configurations is shown in Figure 307.

DI-1-3 — This modification reduced the DI-1-2 throat length from 0.125 inch to 0.10 inch, as shown in Figure 307.

6.2.2 DI-2 DIFFUSER

DI-2 was also a vane-island-type diffuser. As in the DI-1 testing, modifications of the DI-2 configuration were tested and are discussed in Test Modifications.

Test Plan

Table XIX shows the plan of test for the DI-2 diffuser and its modifications. Data taken included the same parameters as for the DI-1 tests. During DI-2 testing,

CONFIDENTIAL

TABLE XIX

DI-2 DIFFUSER AND MODIFICATIONS (See Figure 307 for Modifications)

Test No.	Diffuser No.	Radius Ratio	Throat Area (percent)	I.G. V. Setting (degrees)	Speed (rpm)	Measurements*	Remarks
3310A	DI-2	1.06	100	0	39,000; 50,000	P_{T_R}	Schlieren run, minimum map data. Motion picture schlieren. Schlieren run, minimum map data. Schlieren run with knife edge rotated 90 degrees. I.G. V. were rotated.
3310B	DI-2	1.06	75	0	39,000; 50,000	P_{T_R} (1 point only)	
3310C	DI-2	1.06	125	0	39,000; 50,000	$P_c; P_{T_R}$	
3310D	DI-2	1.10	100	0	39,000; 50,000	$P_c; P_{T_R}$	
3312	DI-2	1.06	100	0	30,000; 39,000; 46,000		
3313	DI-2	1.06	100	0			
3313A	DI-2	1.06	100	0	30,000; 35,000; 39,000; 46,000		
3313B	DI-2	1.06	100	0	30,000		
3315	DI-X1	1.06	100	0	50,000	P_c	
3316	DI-2	1.06	100	0	50,000	$P_c; P_{T_R}$ (1 point only)	

TABLE XIX (Continued)

DI-2 DIFFUSER AND MODIFICATIONS (See Figure 307 for Modifications)

Test No.	Diffuser No.	Radius Ratio	Throat Area (percent)	I. G. V. Setting (degrees)	Speed (rpm)	Measurements*	Remarks
3318	DI-X1-2	1.06	100	0	50,000	Same as 3316	Remachined front cover. Rerun of 3332 to obtain static-pressure data.
3320	DI-2	1.06	100	0	46,000; 50,000		
3321	DI-2	1.06	100	0	50,000	Minimum map data	Remachined front cover. Rerun of 3332 to obtain static-pressure data.
3322	DI-2	1.06	100	0	50,000		
3323	DI-2	1.06	100	0	50,000	Minimum map data	Remachined front cover. Rerun of 3332 to obtain static-pressure data.
3324	DI-2	1.06	100	No Vanes	50,000		
3325	DI-2	1.06	100	No Vanes	50,000	Minimum map data	Replaced bent vane.
3326	DI-X1-3	1.06	100	No Vanes	50,000		
3327	DI-2-2	1.06	100	No Vanes	50,000	Minimum map data	Replaced bent vane.
3328	DI-2	1.06	100	No Vanes	50,000		
3329	DI-2	1.06	100	No Vanes	50,000	Minimum map data	Replaced bent vane.

CONFIDENTIAL

TABLE XIX (Continued)							
DI-2 DIFFUSER AND MODIFICATIONS (See Figure 307 for Modifications)							
Test No.	Diffuser No.	Radius Ratio	Throat Area (percent)	I. G. V. Setting (degrees)	Speed (rpm)	Measurements*	Remarks
3330	DI-2	1.06	100	No Vanes	50,000		Replaced front cover — vane installed incorrectly.
3331	DI-2	1.06	100	No Vanes	50,000		Rerun of 3330 with vane installed correctly.
3332	DI-2-2	1.06	100	No Vanes	50,000		
3333	DI-X1-3	1.06	100	No Vanes	50,000		
3334	DI-1-2	1.06	100	No Vanes	50,000		
3335	DI-1-2	1.06	100	0	50,000		Schlieren windows installed in new front plate and schlieren pictures taken.
3336	DI-1-2	1.06	100	No Vanes	50,000		Window plugs installed.
3337	DI-1-2	1.06	100	No Vanes	50,000		Window plugs potted.
3341	DI-X1-2	1.06	100	No Vanes	50,000		

CONFIDENTIAL

TABLE XIX (Continued)							
DI-2 DIFFUSER AND MODIFICATIONS (See Figure 307 for Modifications)							
Test No.	Diffuser No.	Radius Ratio	Throat Area (percent)	I. G. V. Setting (degrees)	Speed (rpm)	Measurements*	Remarks
3348	DI-X1-2	1.06	100	0	50,000	P_{R_1}	
3349	DI-X1-2	1.06	100	0	50,000	P_{R_1}	
*Note:							
$P_{R_{1-2}}$		= Impeller-exit total-pressure rakes 1 and 2.			P_c	= Kiel probe at Station No. 1.	
$P_{T_{1-2}}$		= Impeller-exit yaw probes 1 and 2.			P_{T_R}	= Traversing total-pressure probe.	
T_{T_1}		= Impeller-exit total-temperature probe.			Collector pressure measured on all tests.		

CONFIDENTIAL

Station I was maintained at the same location relative to DI-1 to avoid changing the diffuser instrumentation. Therefore, for DI-2, the area ratio at Station I was 2 percent below the previous 2:1. Also, for commonality reasons, the static-pressure taps in the diffuser walls, which had been located relative to the DI-1 vanes, were not changed when the DI-2 vanes were installed. As a result, a few of these static taps were covered by the DI-2 vanes.

Map Data

Maps similar to those of DI-1 were prepared, and representative curves are contained in the Test Results section.

Schlieren Photographs

The schlieren photographs taken during tests of the original DI-2 configuration and its subsequent modifications are contained in Appendix X. During the DI-2-2 testing, schlieren windows were installed in a spare frontplate to check out differences in the window installation. This rig modification had an adverse effect on performance as shown on the map for Test 3335. To recover the original performance, the windows were replaced with plugs and sealed with potting material. Performance was improved but did not attain its former level.

Total-Pressure Traverse and Impeller-Exit Surveys

As with the DI-1 diffuser, the traversing probe was used to establish changes in total pressure through the diffuser. Additionally, the workhorse impeller instrumentation was used to establish the impeller-exit conditions when required for diffuser performance evaluation. These data are given for representative tests in the Test Results section.

Inlet Guide Vanes

During the DI-2 tests, the effects of inlet guide vanes were not evaluated. When the guide vanes were removed, maximum airflow increased by approximately 3 percent, giving some indication of their influence on flow. To compare the map performance between tests with and without inlet guide vanes, the following corrections were applied to the data without guide vanes:

$$(W_a)_{\text{corr}} = (W_a)_{\text{obs}} \left(\frac{(W_{a \text{ max}})_{\text{no IG}}}{(W_{a \text{ max}})_{\text{IG}}} \right) \quad (31)$$

$$(P/P)_{\text{corr}} = (P/P)_{\text{obs}} \left(\frac{(W_{a \text{ max}})_{\text{no IGV}}}{(W_{a \text{ max}})_{\text{IGV}}} \right) \quad (32)$$

Radius Ratio

Tests 3310 and 3310D were run with radius ratios of 1.06 and 1.10, respectively. The test objectives were the same as for similar tests conducted with the DI-1 diffuser. Data are shown in the Test Results section.

Test Modifications

As with DI-1, several modifications were made to the original DI-2 configuration. These modifications and tests are described in the following discussion.

DI-X1 — The DI-X1 configuration was the same as DI-2 except that the asymmetrical divergence angle of 10 degrees was revised to a symmetrical divergence angle of 8 degrees.

DI-X1-2 — This configuration was the same as DI-X1 except that the symmetrical divergence angle was changed from 8 to 10 degrees.

DI-X1-3 — This configuration (shown in Figure 307) was a modification of the DI-X1-2 vanes. The throat area was enlarged approximately 3.4 percent, thus decreasing design throat Mach number from 0.75 to 0.70. To maintain a parallel-walled throat with this configuration, the vane contour ahead of the throat was also modified.

DI-2-2 — This configuration (shown in Figure 307) had the same throat area and geometry as the original DI-2. However, the vane angle was set 2 degrees flatter. This change required a modification to the vane contour to maintain the throat and the 1.06 radius ratio, as in previous tests.

Rig Frontplate Warpage — During testing of DI-X1, low overall performance was observed in Test 3315. Test 3316, with the original DI-2 configuration, was conducted to determine if rig anomalies were responsible for the drop in performance. Test 3316 revealed that the static-pressure field was greatly different than it had been for the first DI-2 test, 3310. Investigation of the rig showed that the frontplate had warped, and it was concluded that air leaking under the leading edge of the vanes had resulted in the observed performance deterioration. Corrective action was taken by replacing the frontplate with the reworked frontplate, and performance was restored.

6.2.3 DI-3 DIFFUSER

Nine tests were accomplished on a DI-3 diffuser configuration. Included in this testing were two modifications of the original DI-3. The test plan of the DI-3 testing is given in Table XX.

Testing of DI-3 and Modifications

The original DI-3 configuration was designed for a 0.75 throat Mach number with 16 channels. Testing of DI-3 and its two modifications was accomplished similar to DI-1 and DI-2. Tests were run to define performance and to investigate the effects of varying the inlet guide vane setting. The first modification, DI-3-2, was accomplished by notching the channel to provide a boundary-layer trip, thus delaying separation. The original DI-3 configuration and the notched DI-3-2 modifications had the same throat. The second modification, DI-3-3, was the same as DI-3 except that the original asymmetrical 10-degree channel divergence was revised to a 6-degree symmetrical divergence.

6.2.4 DC-1 CASCADE

Testing of the cascade diffuser (DC-1) consisted of a series of 6 tests which are summarized in Table XXI. The first 3 tests in the series (3308, 3308.1, and 3308.2) were run with the stagger angle of the vanes (α_v) set at 82.4 degrees. A sketch of this configuration is shown in Figure 308. The diffuser was instrumented with four 3-probe total-pressure rakes and 5 static-pressure taps at the exit of the stage.

The total pressure at the exit of the stage was mass-flow averaged and the results are presented in Section 6.2.5.

TABLE XX						
DI-3 DIFFUSER AND MODIFICATIONS						
Test No.	Diffuser No.	Radius Ratio	Throat Area (percent)	I. G. V. Setting (degrees)	Speed (rpm)	Measurements*
3314A	DI-3	1.06	100	0	46,000	P_{R_1}
3314B	DI-3-2	1.06	100	0	46,000	
3314C	DI-3-2	1.06	100	+ 5 +10 +15 +20	46,000	
3314D	DI-3-2	1.06	100	+ 5	50,000	
3342	DI-3-2	1.06	100	No Vanes	50,000	
3343	DI-3-3	1.06	100	No Vanes	50,000	
3344	DI-3-3	1.06	100	No Vanes	50,000	
3345	DI-3-3	1.06	100	No Vanes	50,000	
3346	DI-3-3	1.06	100	0 -20 -10 + 7 +15 +20	50,000	
*Note: P_{R_1} = Impeller-exit total-pressure rake no. 1. Collector pressure measured on all tests.						

TABLE XXI
DC-1 CASCADE DIFFUSER

Test No.	Vane No.	Radius Ratio	Throat Area (percent)	I. G. V. Setting (degrees)	Speed (rpm)	Measurements*	Remarks
3308	DC-1	1.10	---	None	30, 000; 39, 000; 46, 000; 50, 000	P_{R_1} , P_{R_E}	Schlieren
3308.1	DC-1	1.10	---	0°			
3308.2	DC-1	1.10	---	None	30, 000; 39, 000; 46, 000; 50, 000	P_{T_2} , P_{R_E}	
3308A	DC-1	1.10	---	None	30, 000; 35, 000; 50, 000	P_{R_1}	
3308B	DC-1	1.10	---	None	30, 000; 50, 000		
3308B.1	DC-1	1.10	---	None	Same as 3308B	P_{T_2}	
<p>*Note: P_{R_1} = Impeller-exit total-pressure rake 1. P_{T_2} = Impeller-exit yaw probe 2. P_{R_E} = Cascade-exit total-pressure rake. Collector pressure measured on all tests.</p>							

CONFIDENTIAL

Test 3308.1 was run to obtain schlieren photographs; however, the attempt was not successful due to system difficulties. Because of the recurrent performance deficiencies with the cascade, further schlieren runs were not made.

The third test in this series (3308.2) was run to obtain total-pressure measurements at the tip of the impeller. These data are given for 50,000 rpm in Section 6.2.5 for comparison with the impeller-tip total-pressure measurements obtained in Test 3306.

Because of indicated incidence and wake losses, the vanes were modified as shown in Figure 309. This configuration was tested (3308A) with the vane stagger angle (α_v) set at 84.4 degrees (see Figure 309). Results of this test again showed separation. Because the previously observed difficulty persisted, the cascade vanes were restaggered to 86.65 degrees and rerun (Test 3308B). The map for this test was prepared, and a repeat run was conducted (Test 3308B.1) to obtain total-pressure data at the impeller tip. A comparison of the results is presented in Section 6.2.5.

6.2.5 TEST RESULTS

Representative data for all diffusers are presented in groups, corresponding to each configuration tested. Evaluation of the results is presented in Section 7.0. Additional data are contained in Appendix IX, and schlieren photographs are given in Appendix X.

CONFIDENTIAL

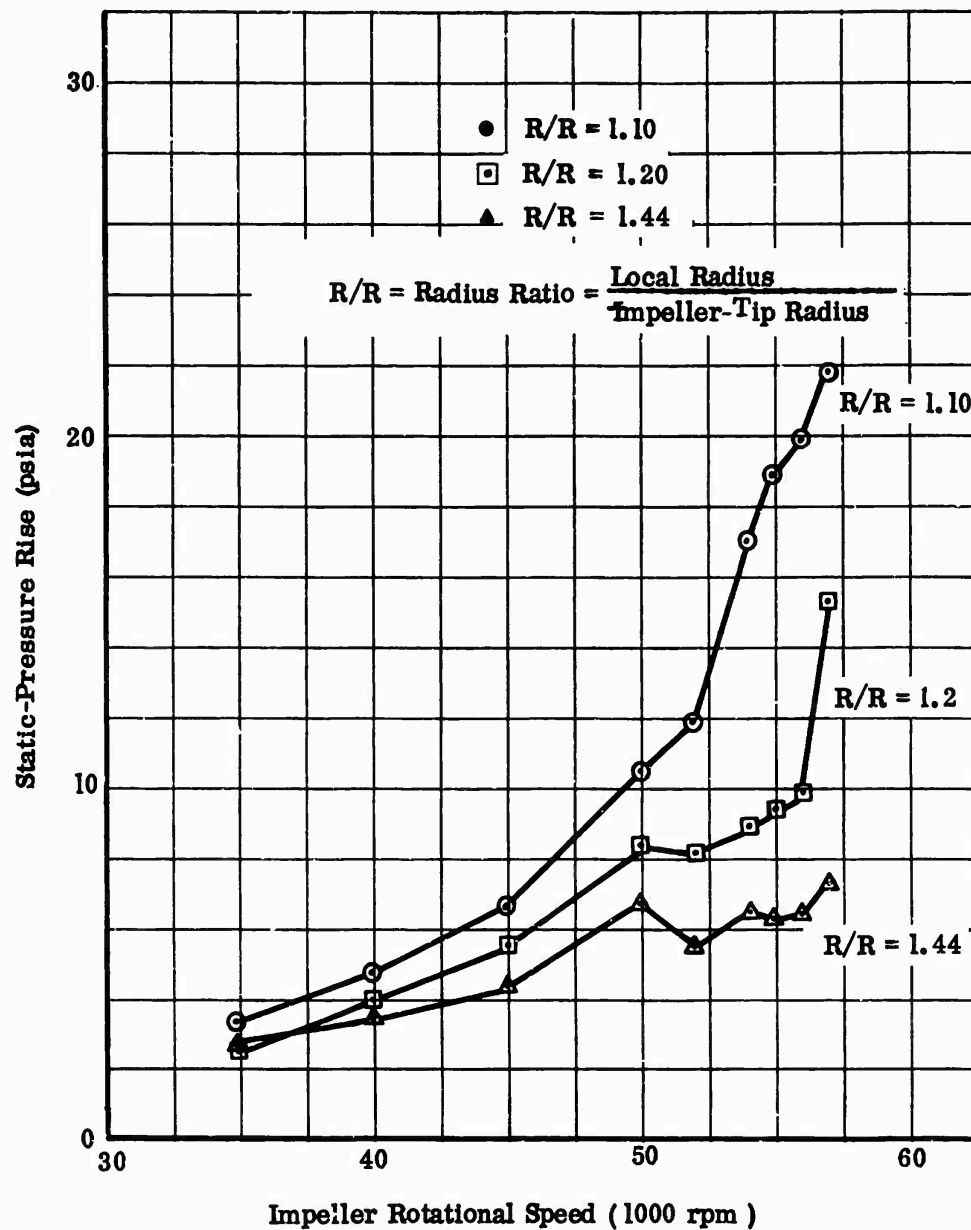


Figure 223. Transducer Pressure Readings.

CONFIDENTIAL

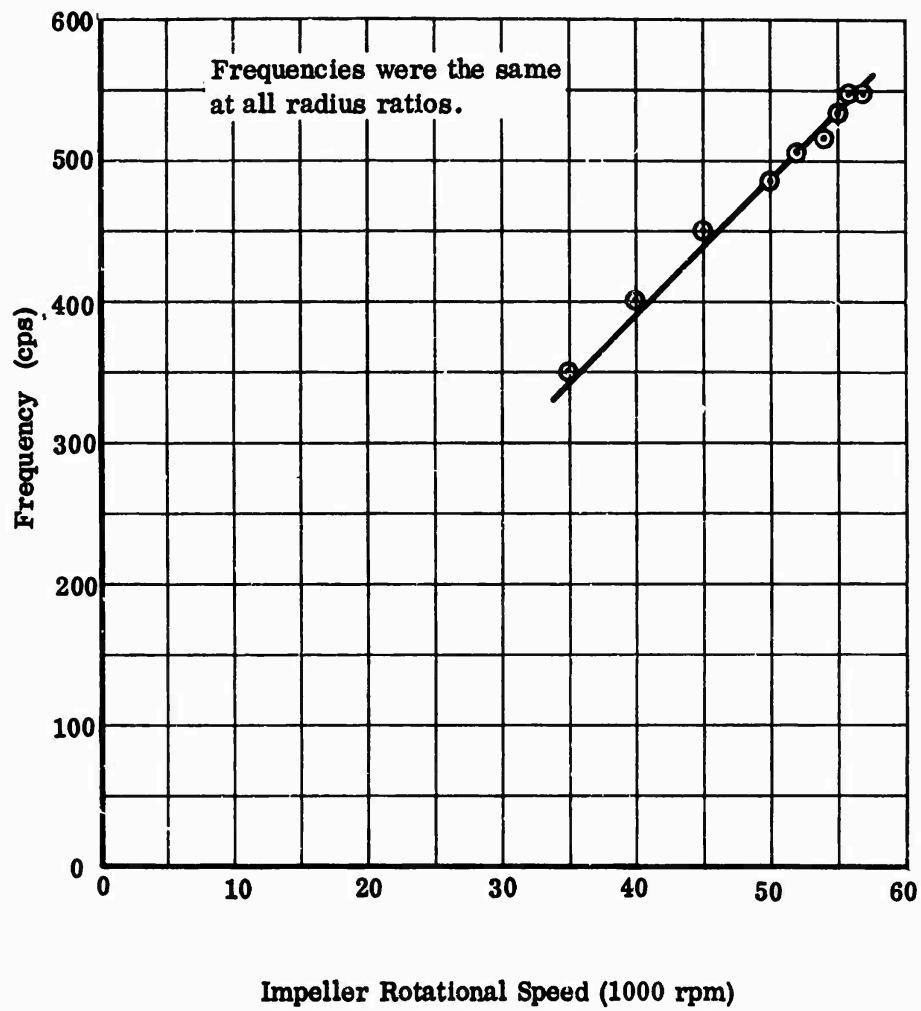


Figure 224. Pressure-Fluctuation Frequencies.

CONFIDENTIAL

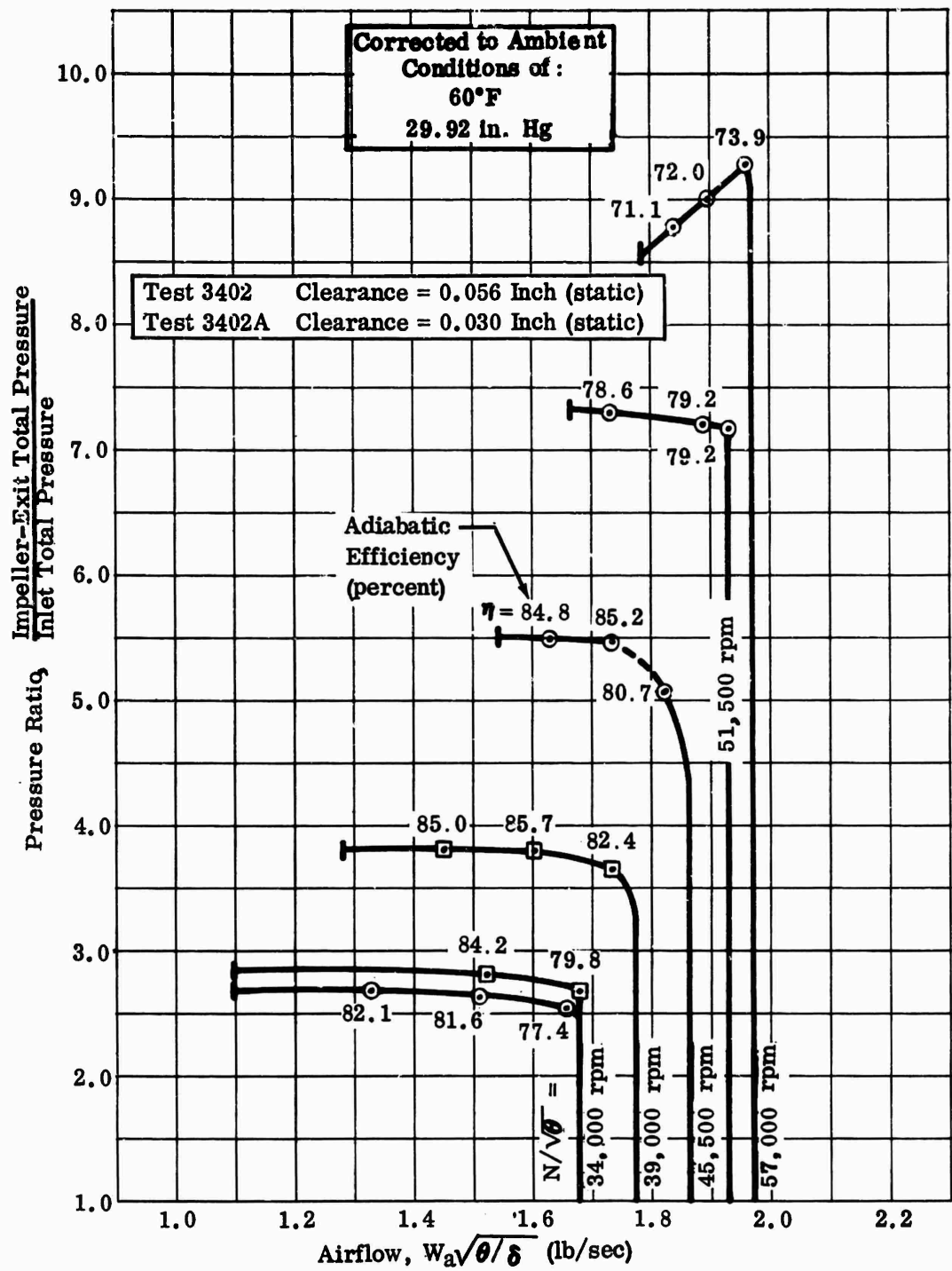


Figure 225. Pressure Ratio Versus Airflow, MF-1, Vaneless Diffuser.

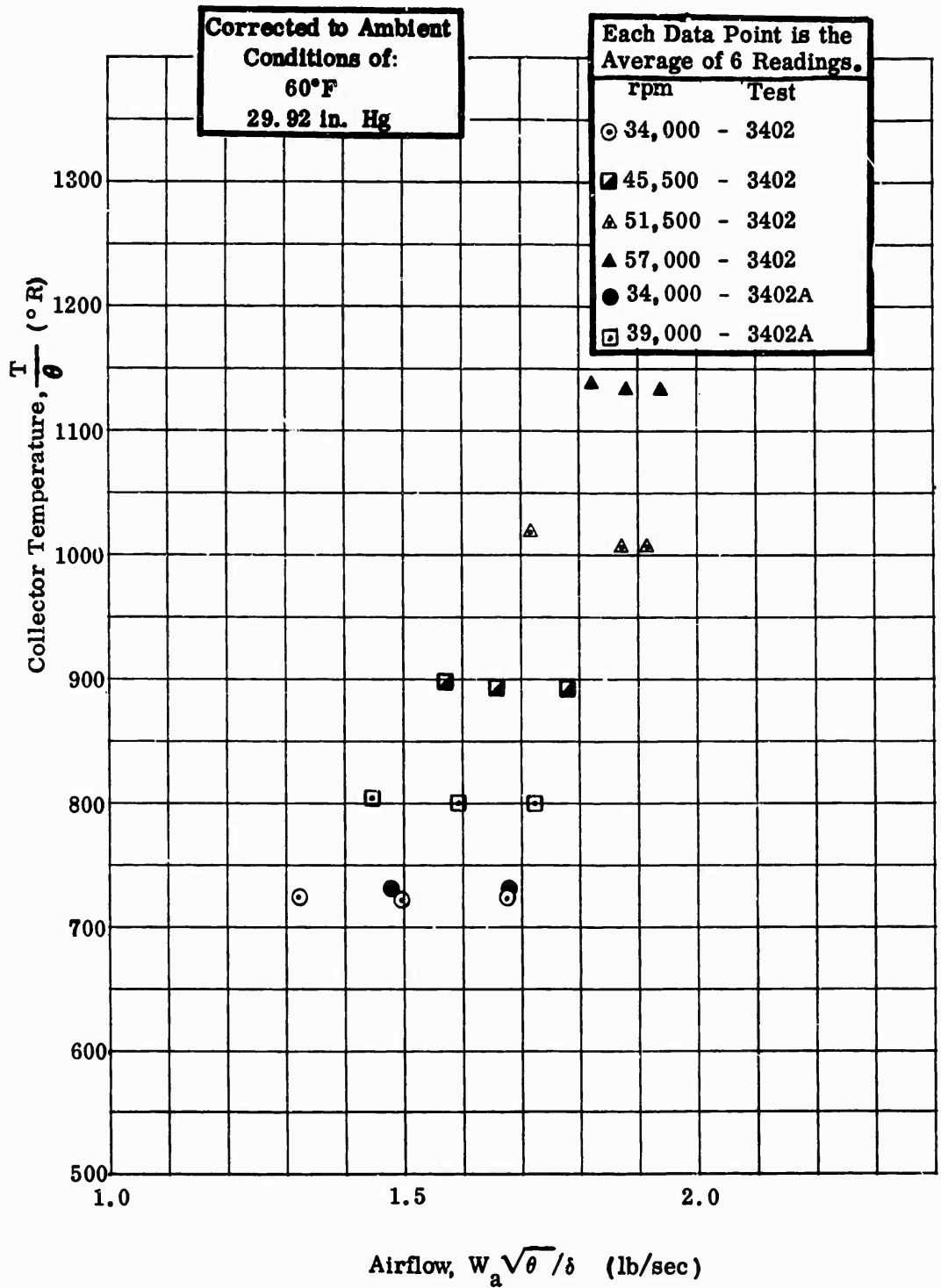


Figure 226. Collector Temperature Versus Airflow, MF-1, Vaneless Diffuser.

CONFIDENTIAL

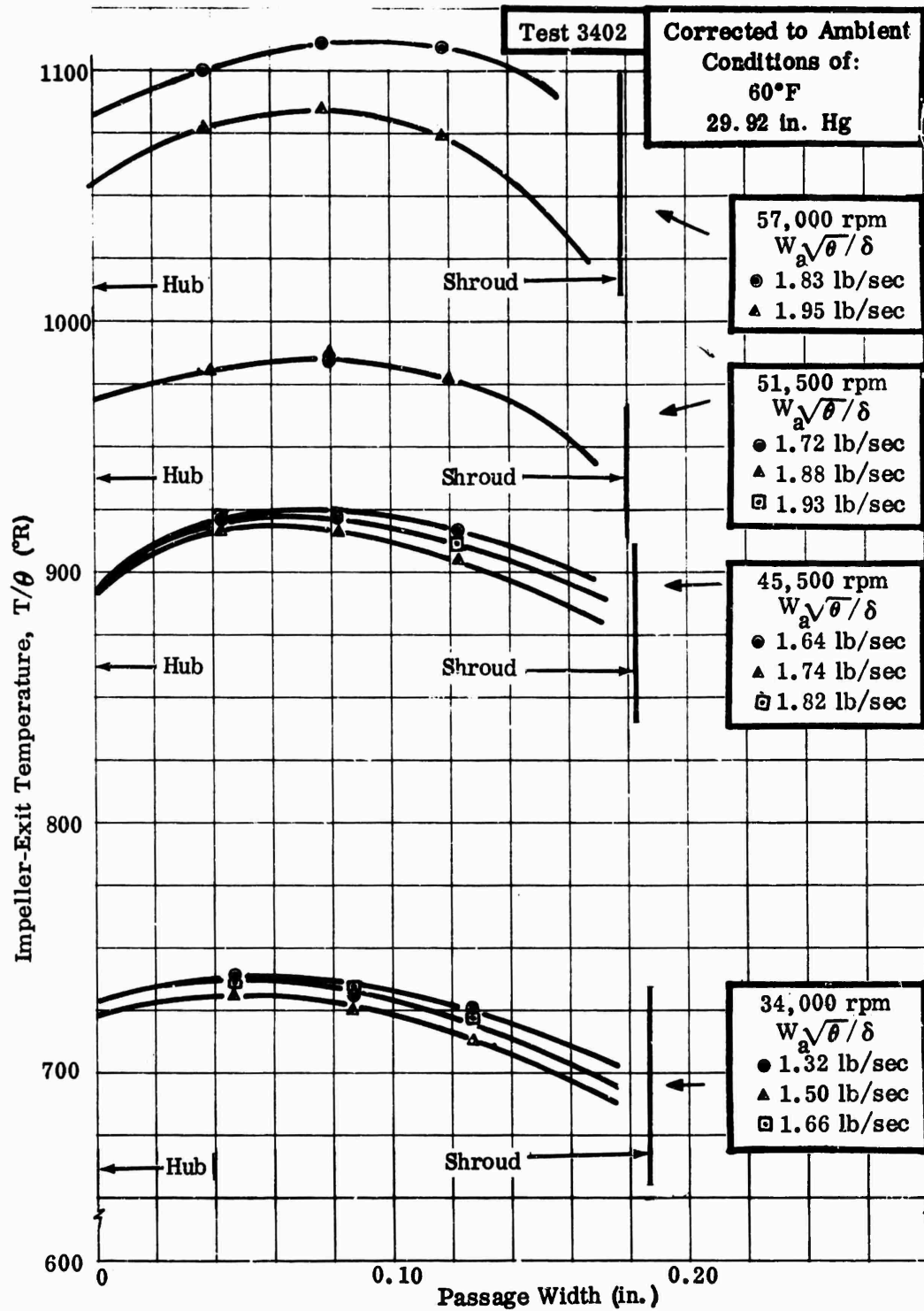


Figure 227. Impeller-Exit Temperature, MF-1, Vaneless Diffuser.

CONFIDENTIAL

CONFIDENTIAL

Test 3402

- ⊙ 3-Probe Rake
- Keil Probe
- ▲ Yaw Probe

Corrected to Ambient
Conditions of:
60°F
29.92 in. Hg

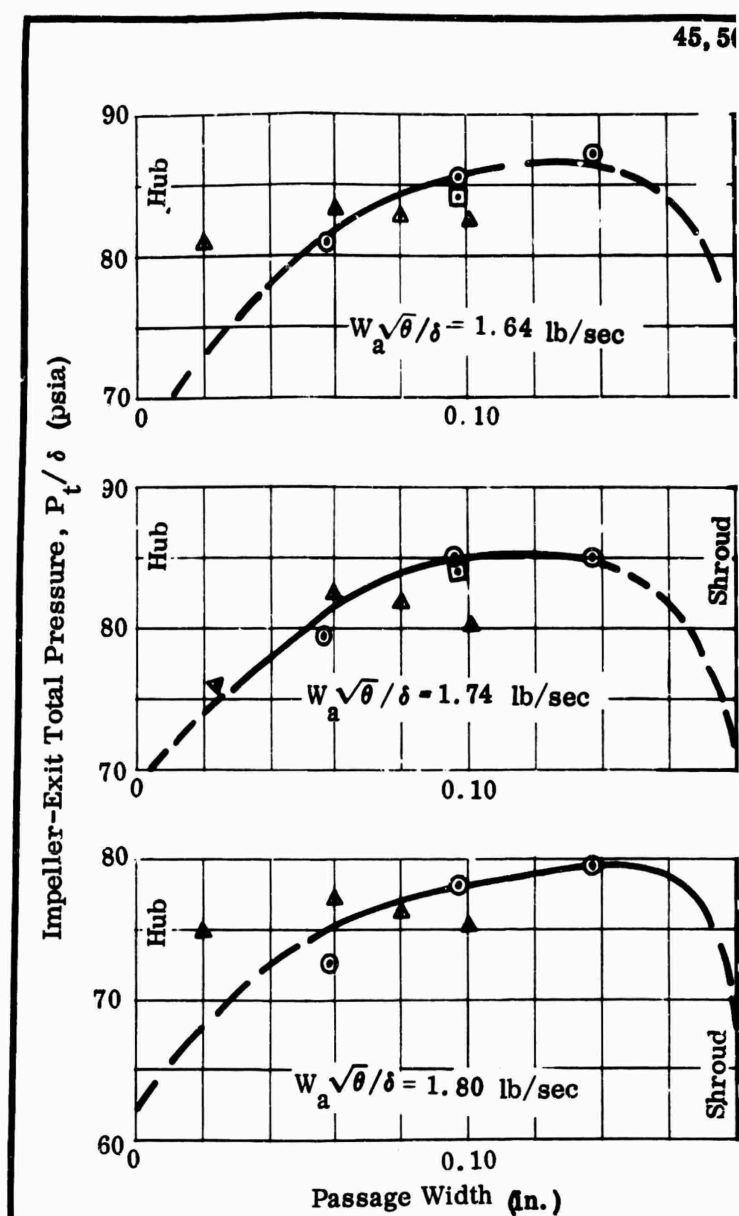
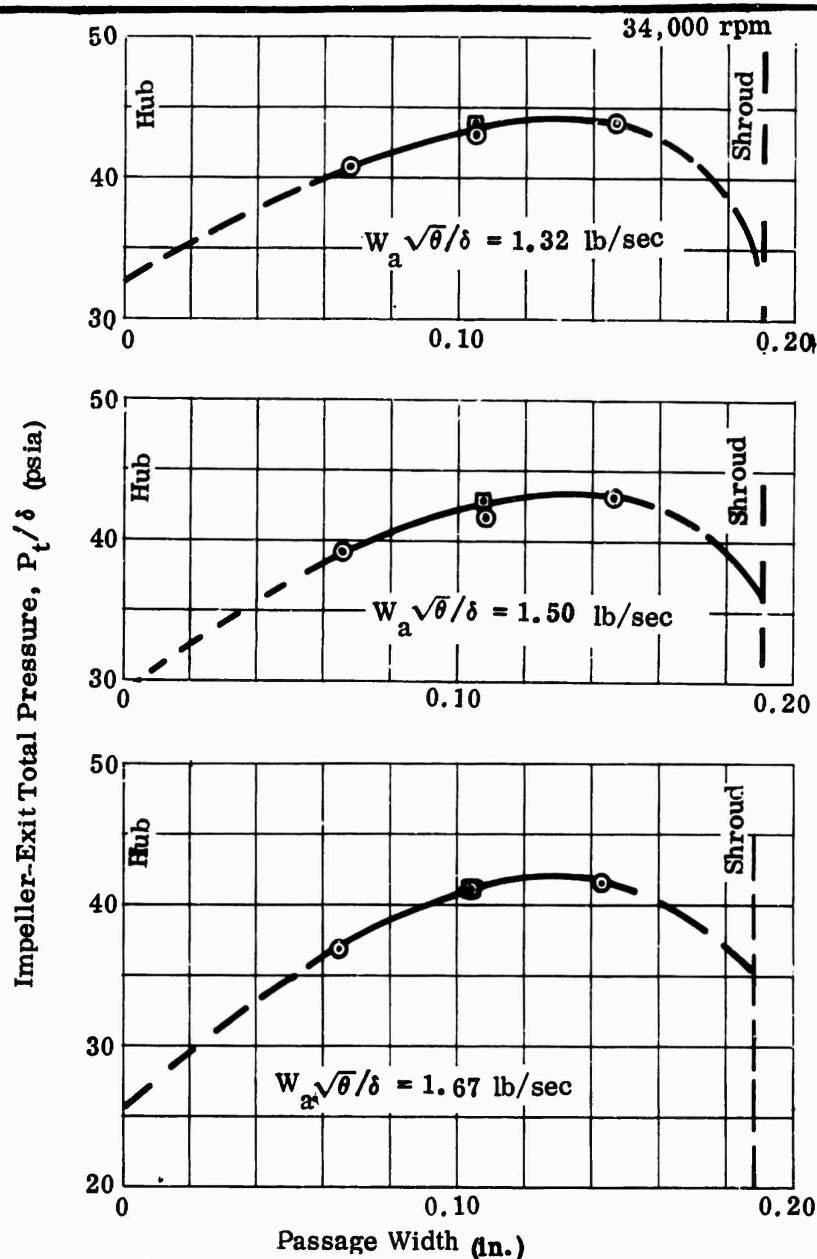


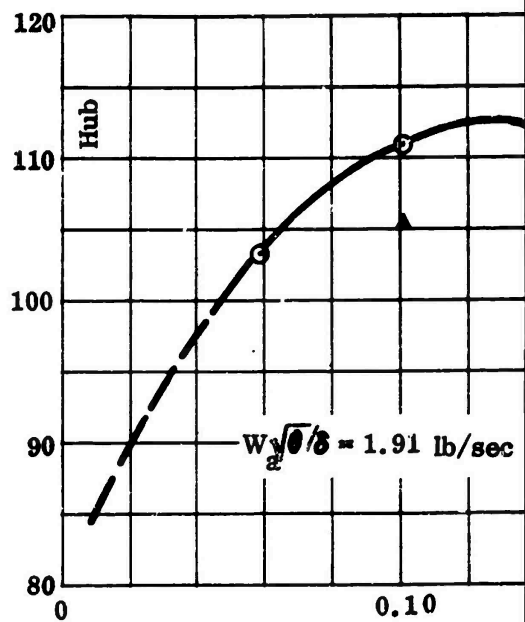
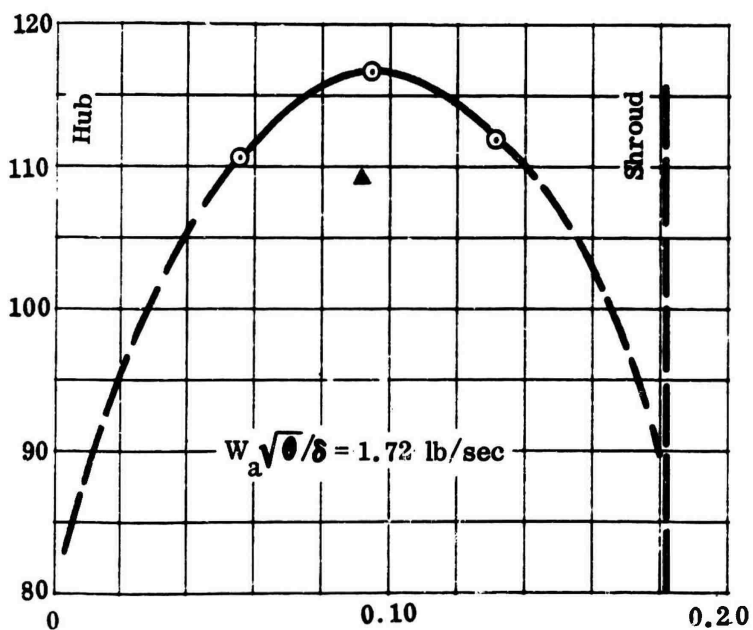
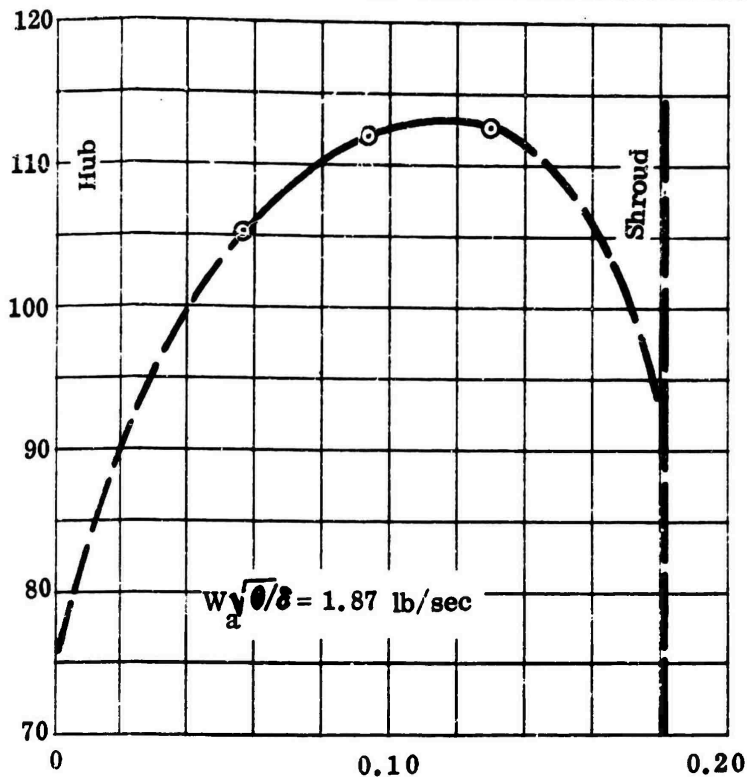
Figure 228. Impeller-Exit Total Pressure, MF-1, Vaneless Diffuser.

355

CONFIDENTIAL

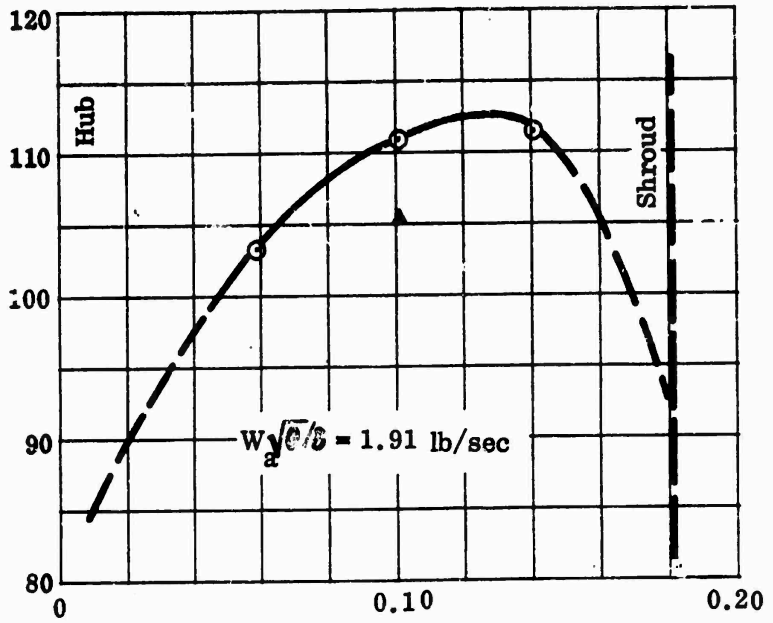
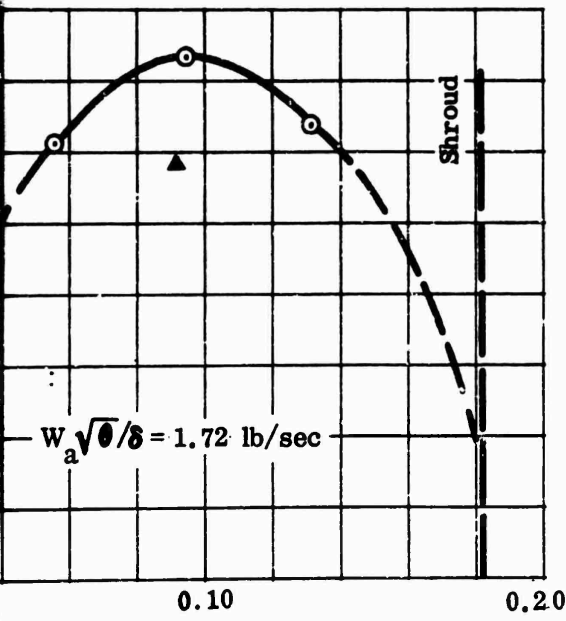
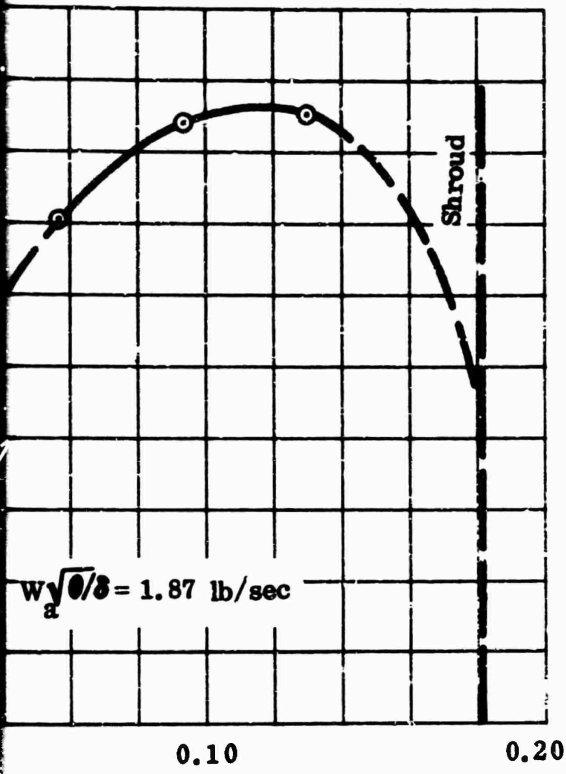
1

Impeller-Exit Total Pressure, P_t / δ (psia)



Passage Width (in.)

51,500 rpm



Passage Width (in.)

CONFIDENTIAL

Test 3402
 $\sqrt{\theta} = 57,000$ rpm
 ○ 3-Probe Rake
 □ Keil Probe
 △ Yaw Probe

Corrected to Ambient
 Conditions of:
 60°F
 29.92 in. Hg

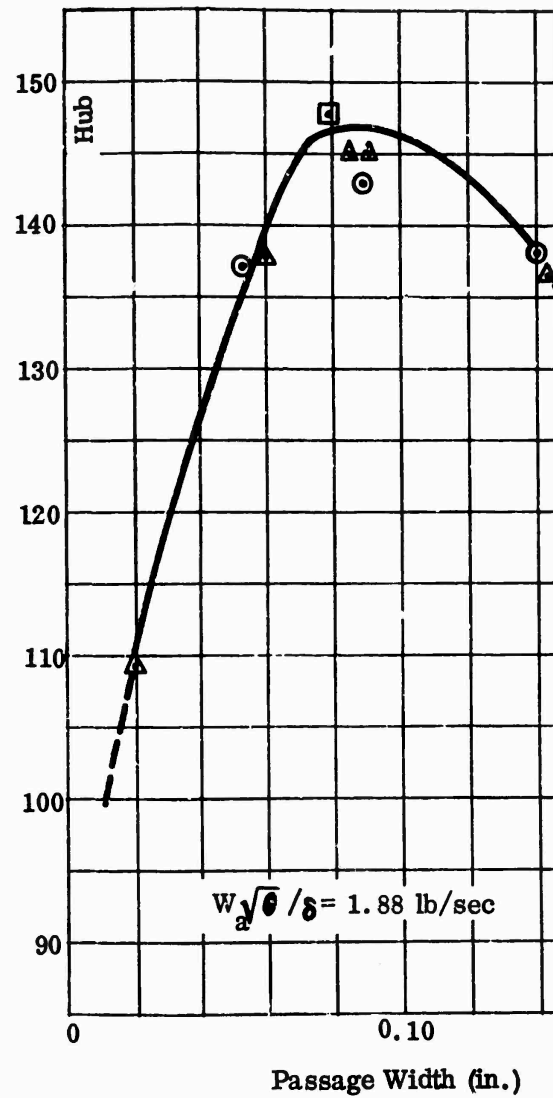
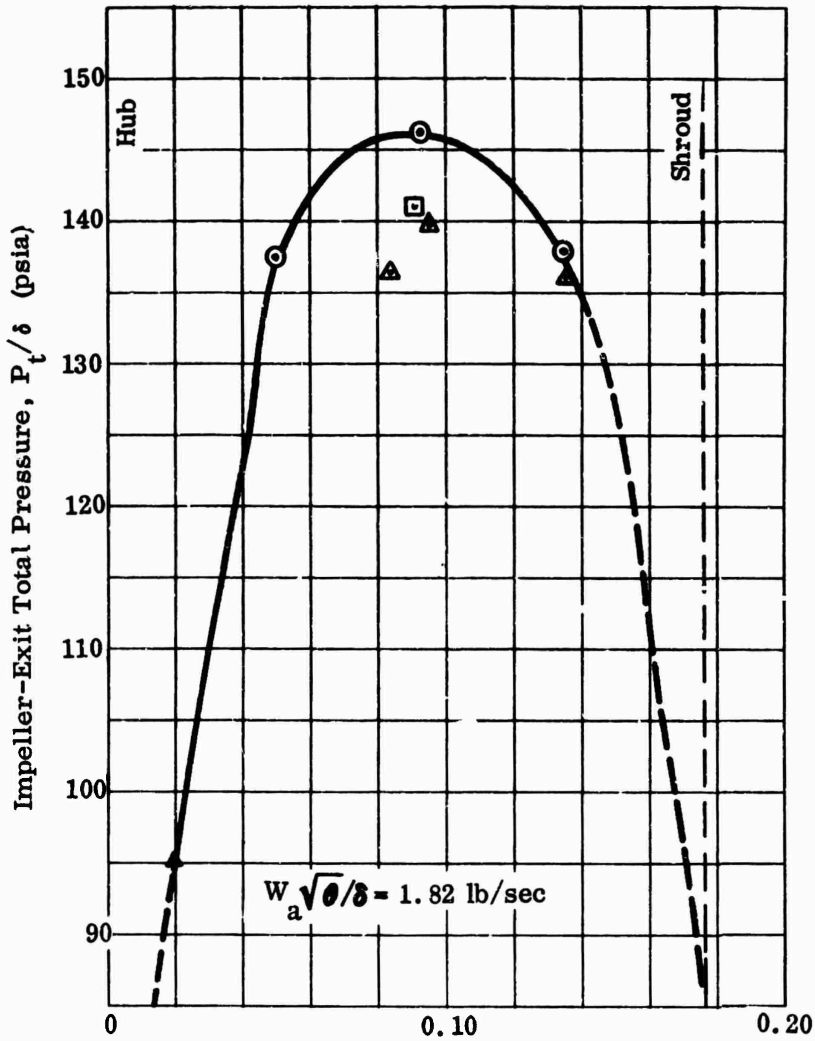
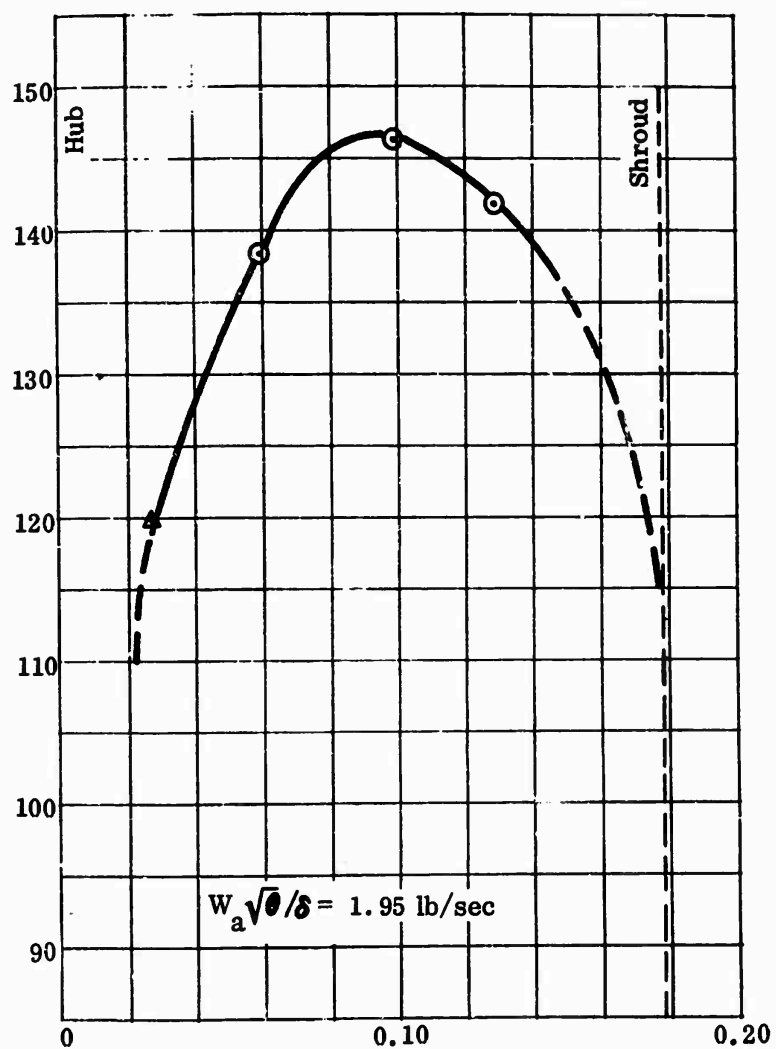
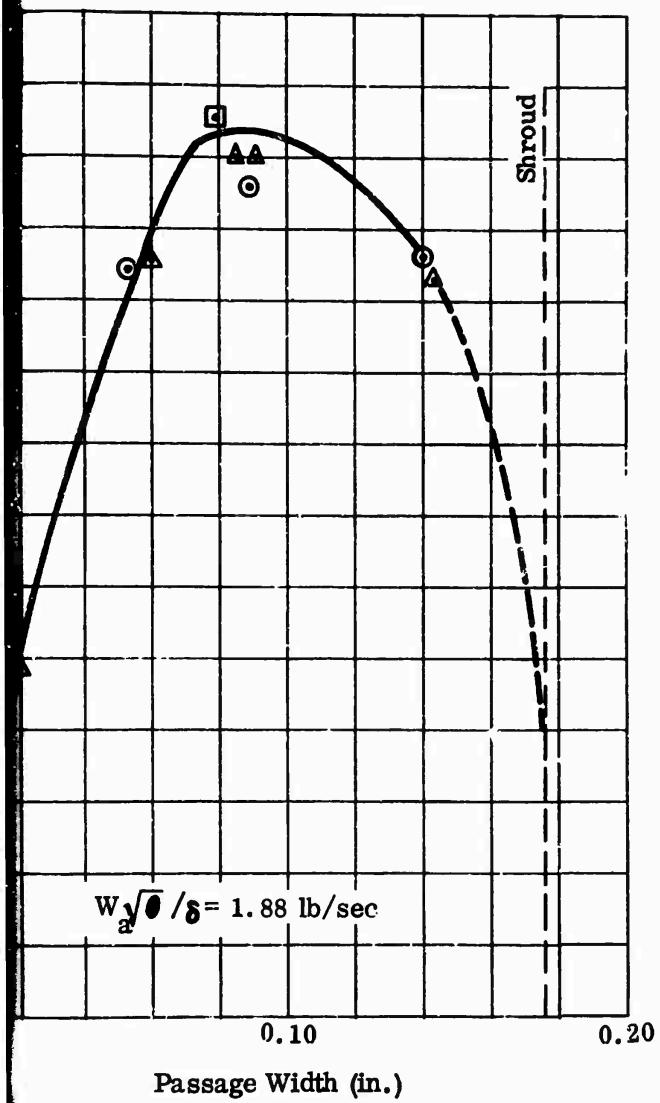


Figure 229. Impeller-Exit Total Pressure, MF-1, Vaneless Diffuser.

CONFIDENTIAL



CONFIDENTIAL

Test 3402A

⊙ 3-Probe Rake
⊠ Keil Probe
▲ Yaw Probe

Corrected to Ambient
Conditions of:
60°F
29.92 in. Hg

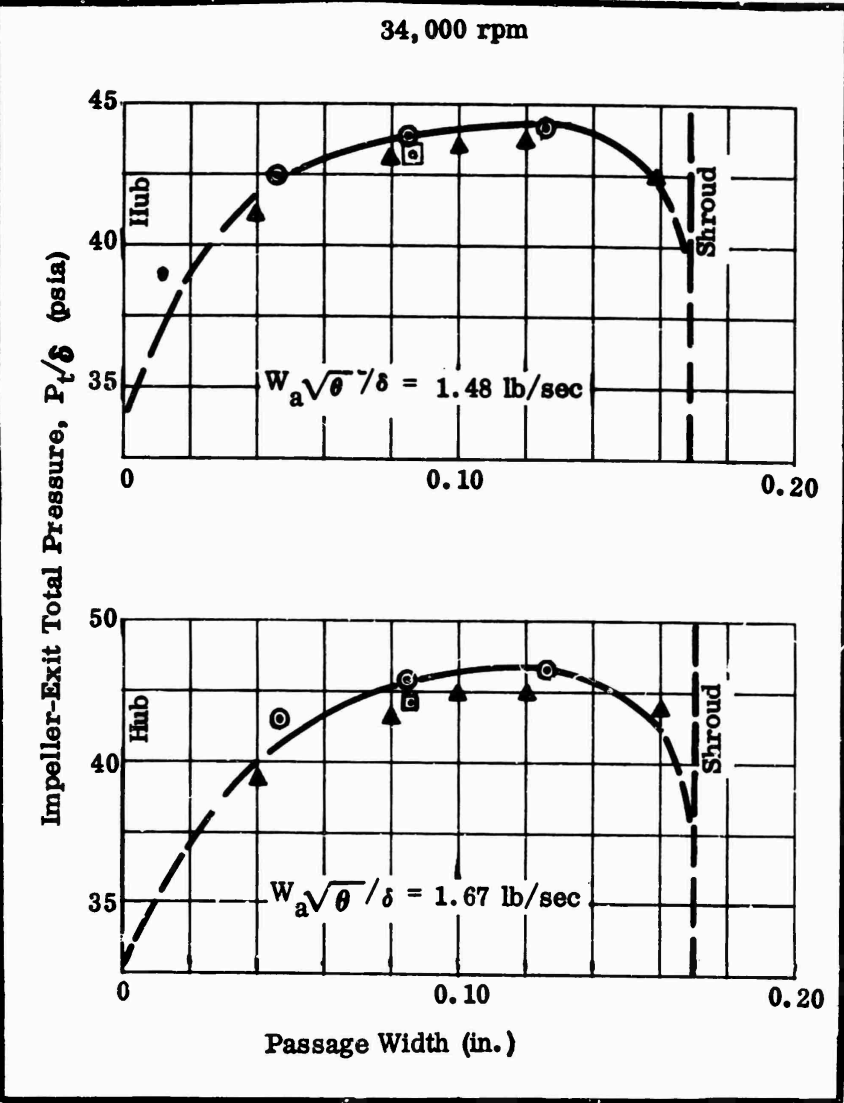
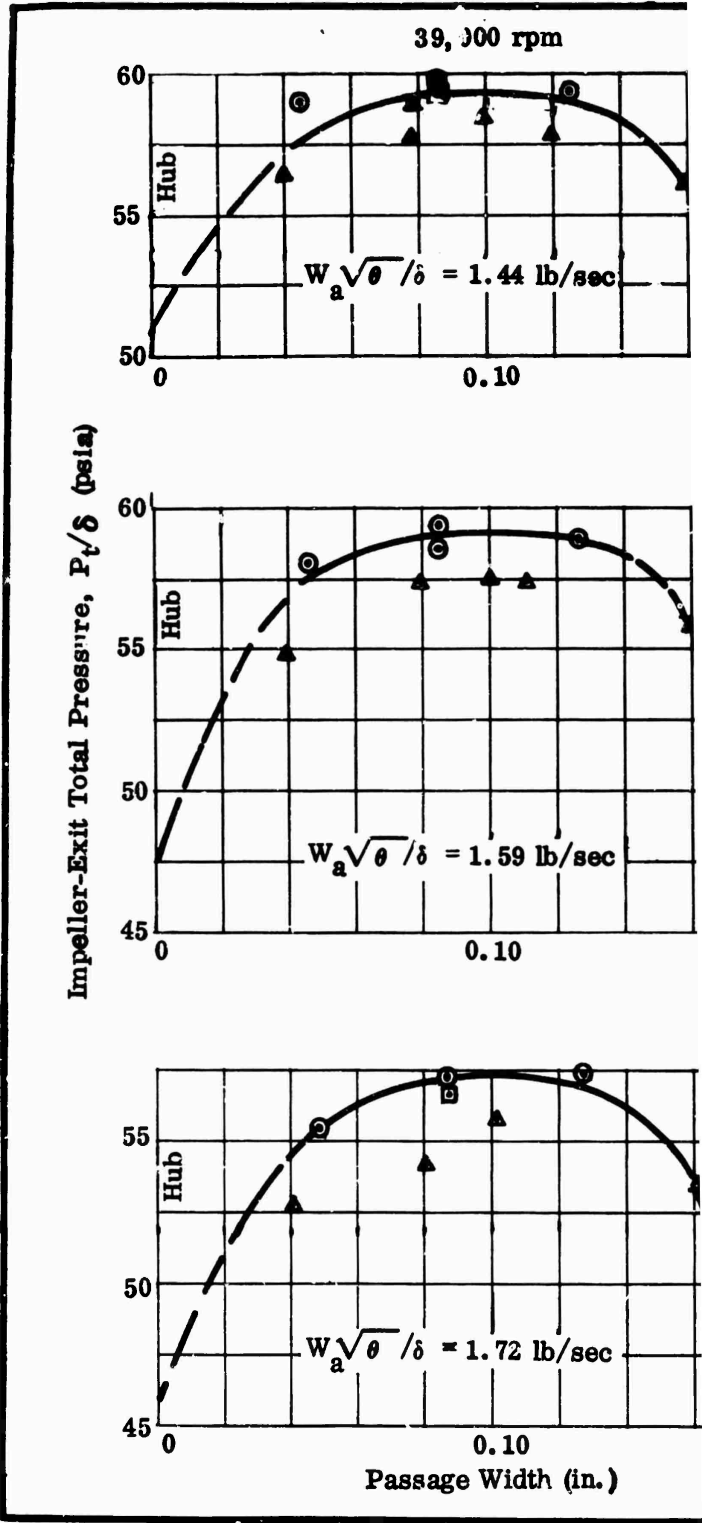


Figure 230. Impeller-Exit Total pressure, MF-1, Vaneless Diffuser.

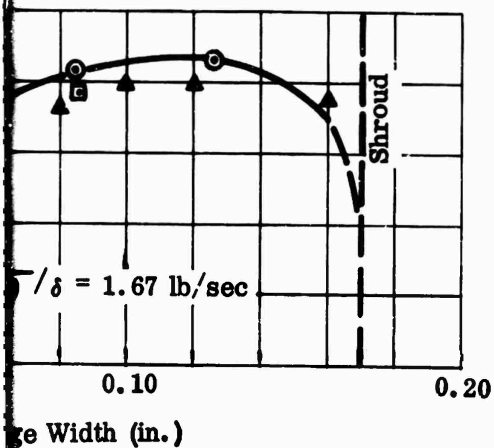
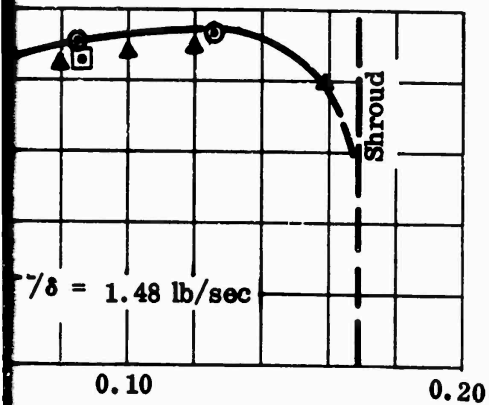
CONFIDENTIAL



CONFIDENTIAL

Corrected to Ambient
Conditions of:
60°F
29.92 in. Hg

34,000 rpm

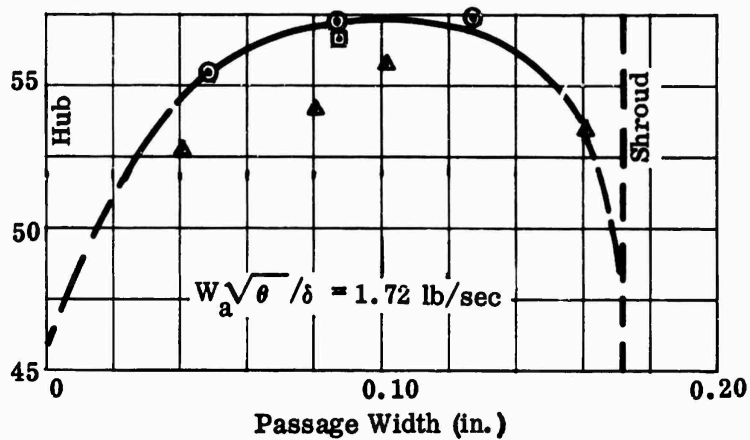
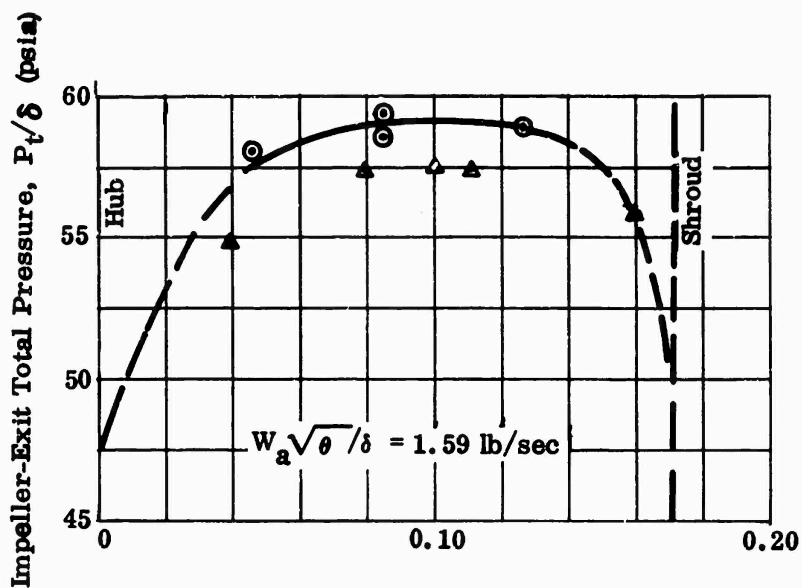
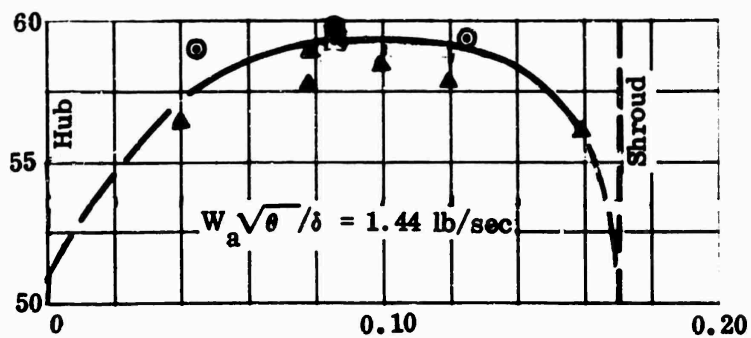


Impeller-Exit Total pressure, MF-1,
Needless Diffuser.

359

CONFIDENTIAL

39,000 rpm



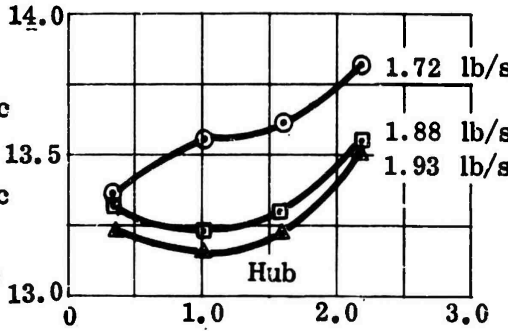
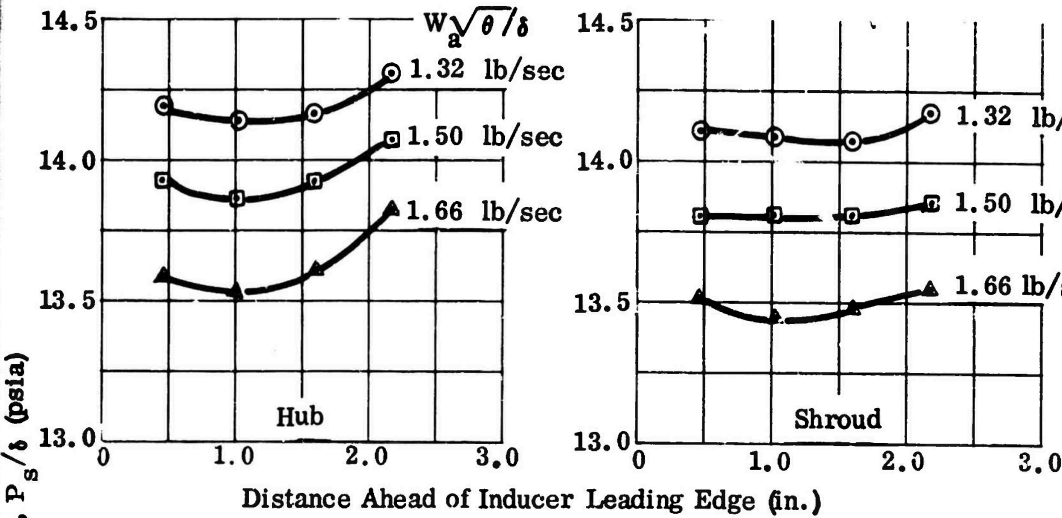
Test 3402
Test 3402A

Corrected to Ambient
Conditions of:
60°F
29.92 in. Hg

Test 3402

34,000 rpm

51,5



57,0

45,500 rpm

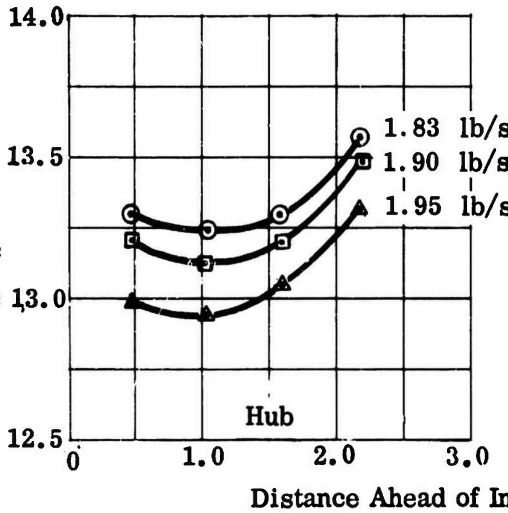
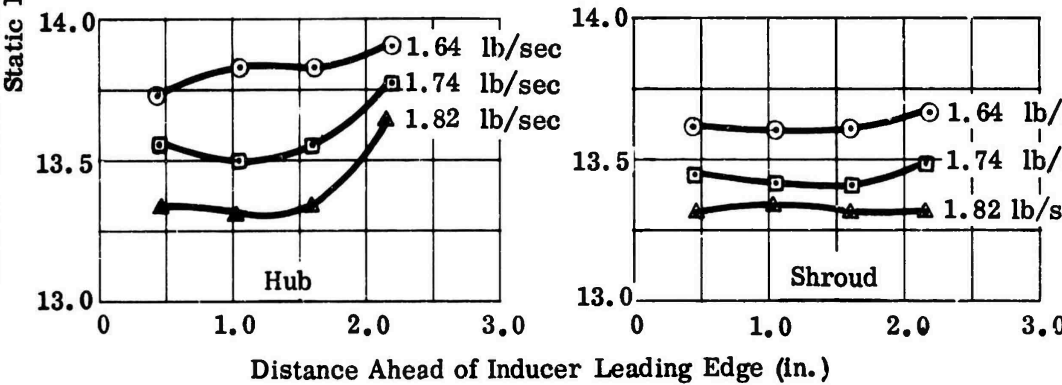
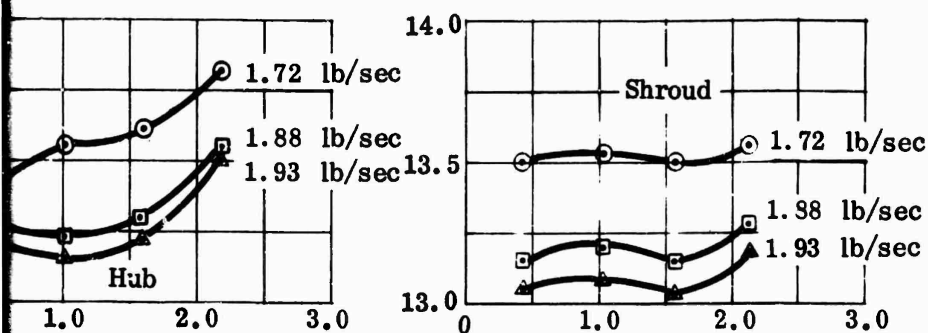
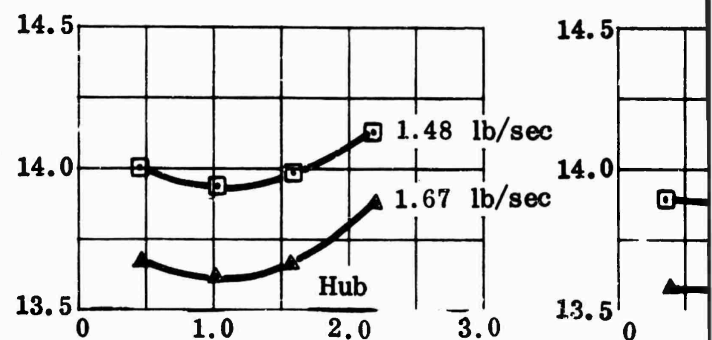


Figure 231. Inlet Duct Static Pressure, MF-1, Vaneless Diffuser.

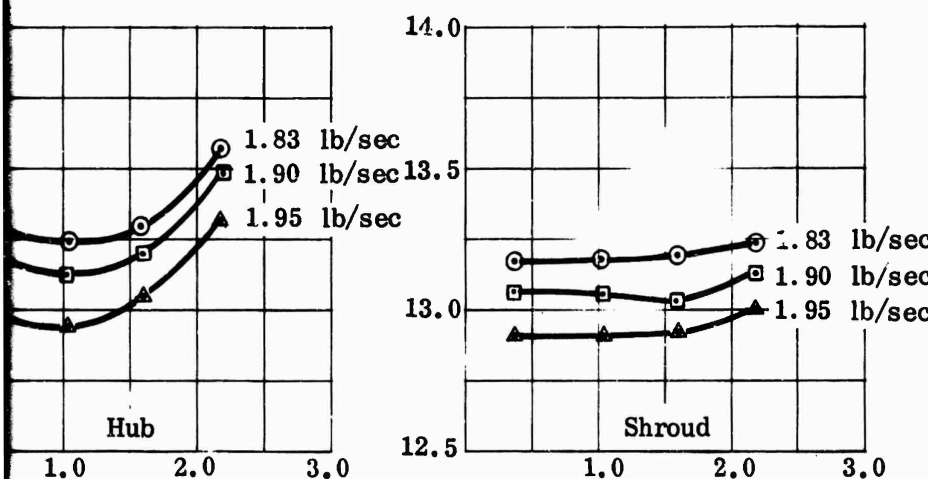
51,500 rpm



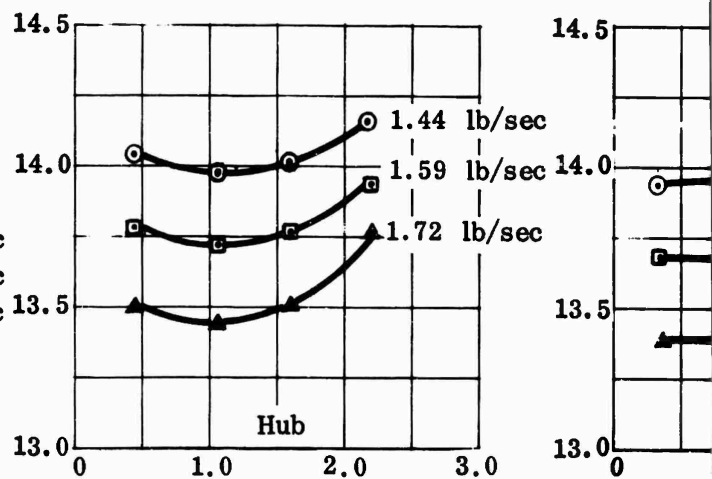
34,000 rpm



57,000 rpm



39,000 rpm

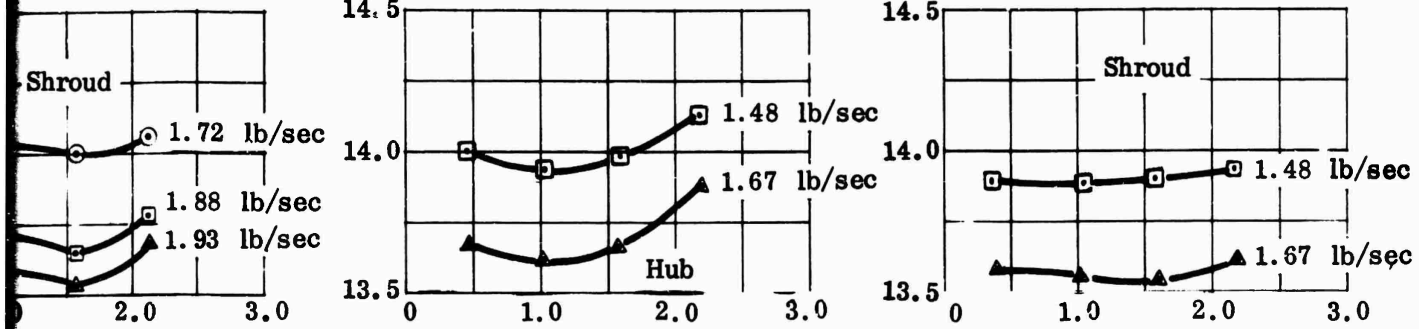


Distance Ahead of Inducer Leading Edge (in.)

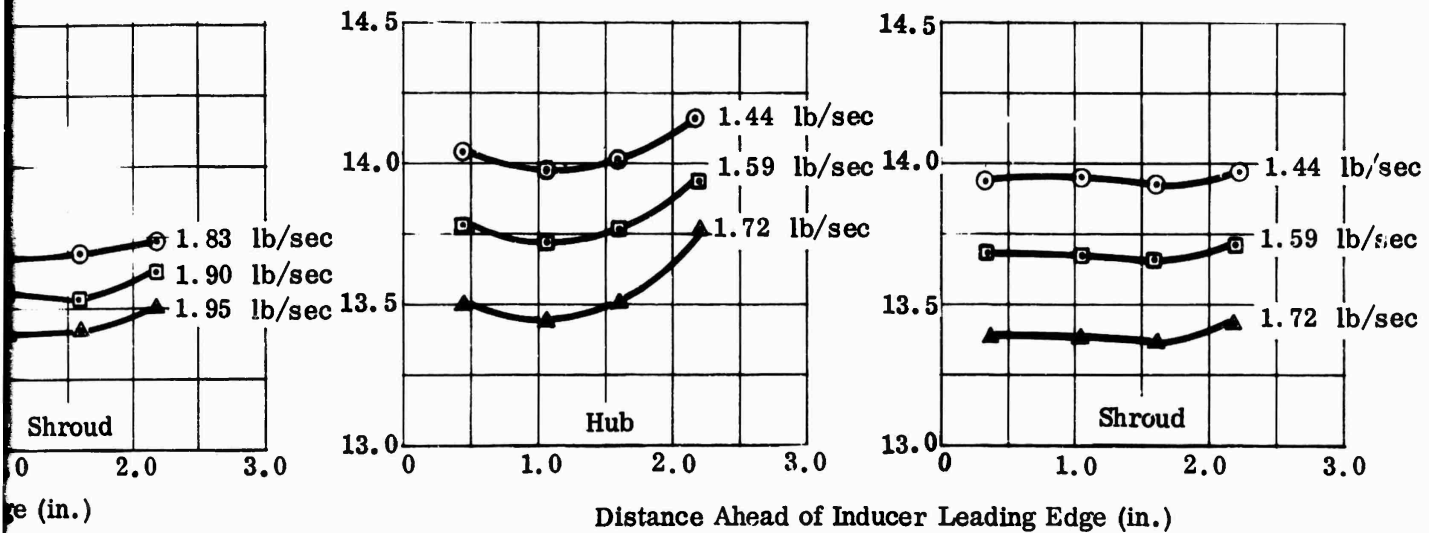
Distance Ahead of Inducer Leading

Test 3402A

34,000 rpm



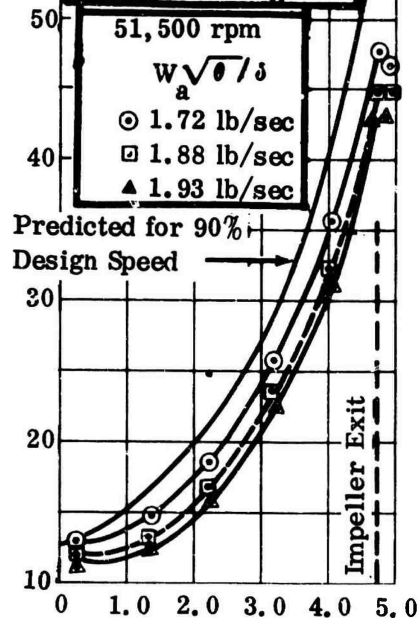
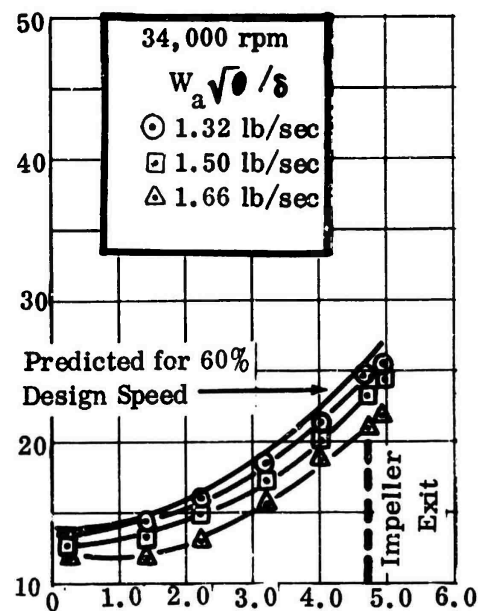
39,000 rpm



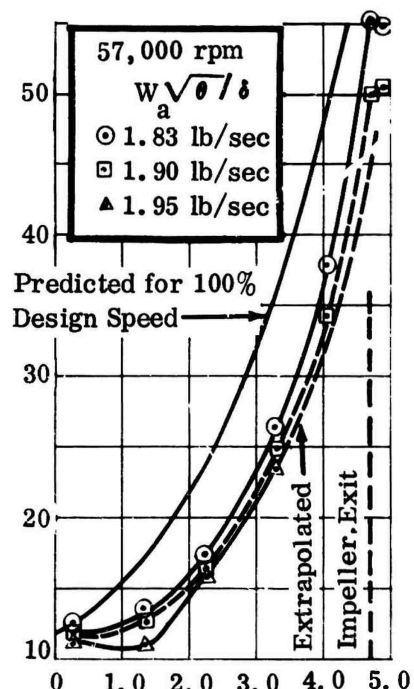
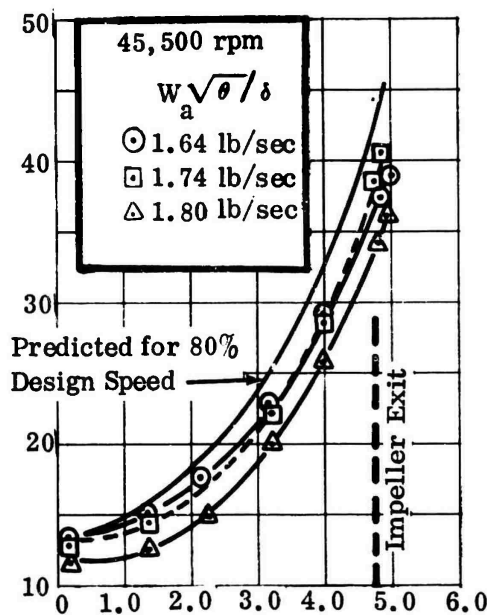
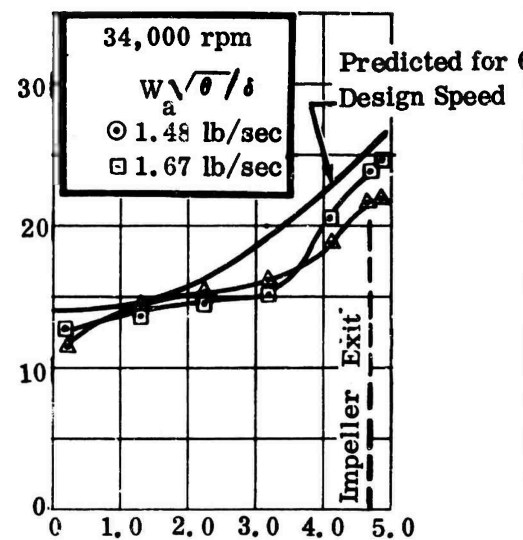
CONFIDENTIAL

Test 3402

Corrected to Ambient
Conditions of:
60°F
29.92 in. Hg



Test 3402A



Static Pressure, P_s / δ (psia)

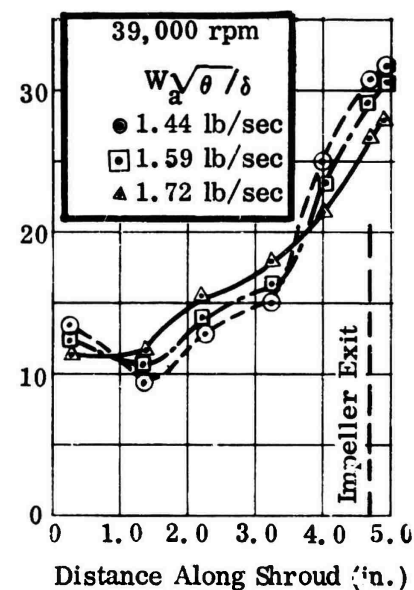
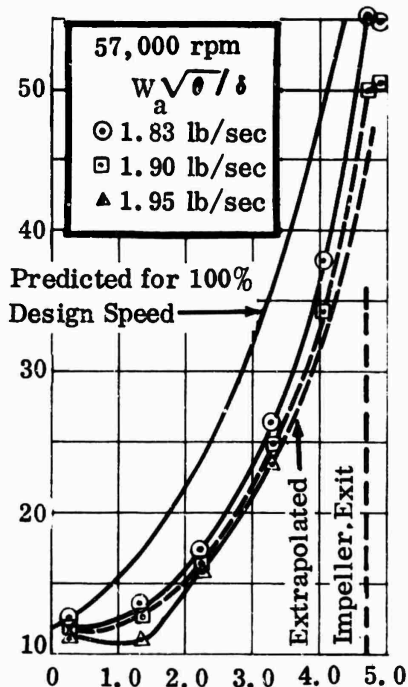
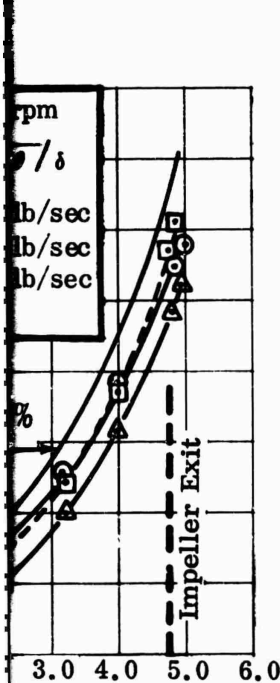
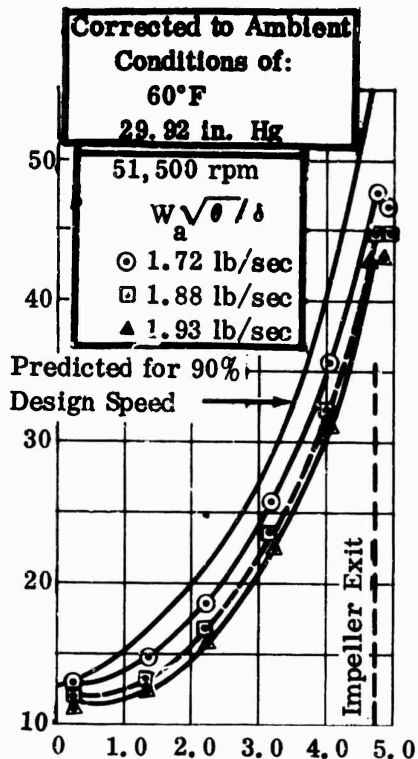
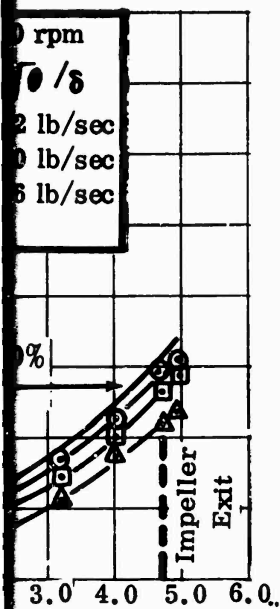


Figure 232. Shroud Static-Pressure Rise, MF-1, Vaneless Diffuser.

CONFIDENTIAL

CONFIDENTIAL

Test 3402

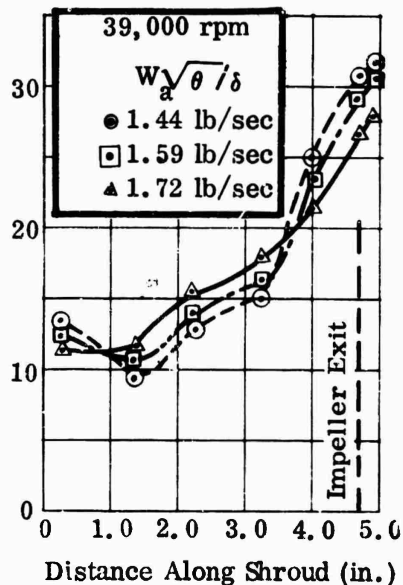
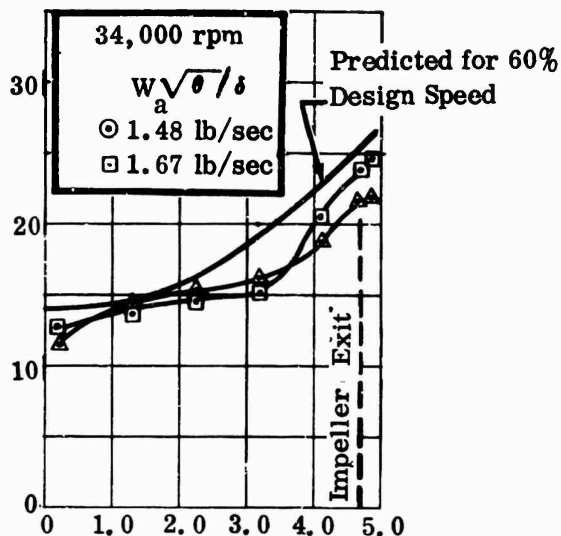


Distance Along Shroud (in.)
Shroud Static-Pressure Rise, MF-1, Vaneless Diffuser.

363

CONFIDENTIAL

Test 3402A



Static Pressure, P_s/δ (psia)

Test 3402	$S_o = 6.43$ Inches	Corrected to Ambient
--- Shroud	(covers one quadrant at $R/R = 1.02$)	Conditions of :
— Hub		60°F
		29.92 in. Hg

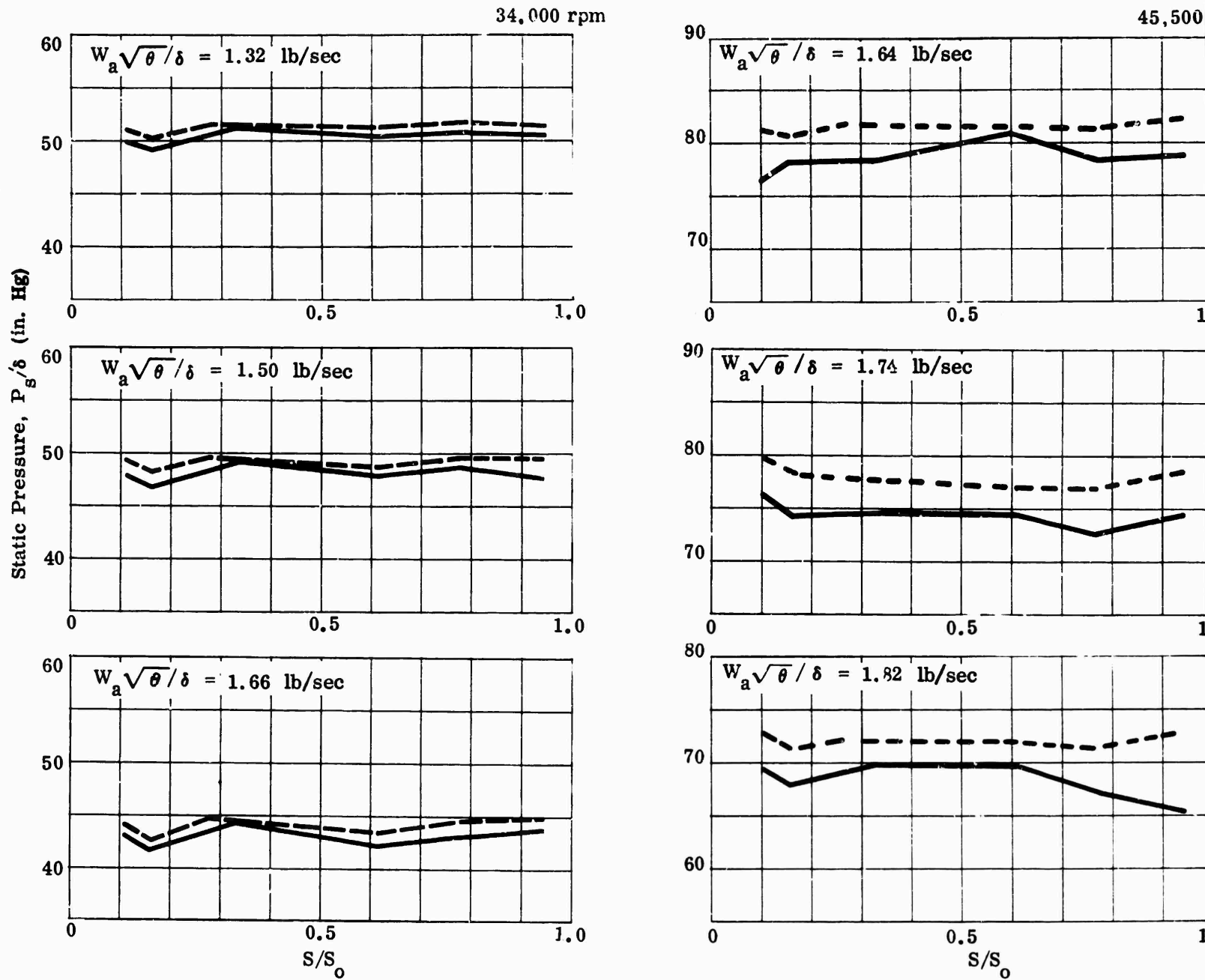
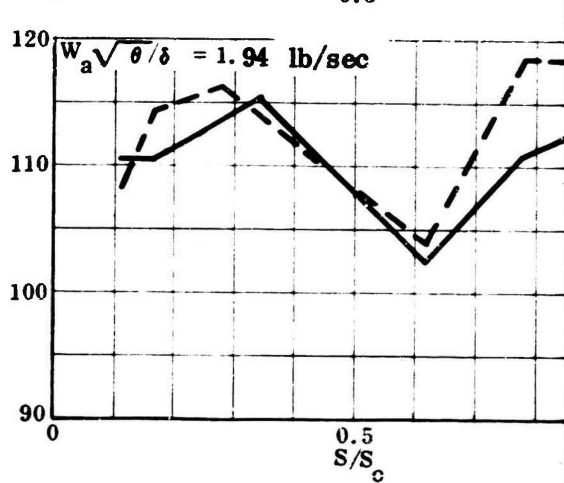
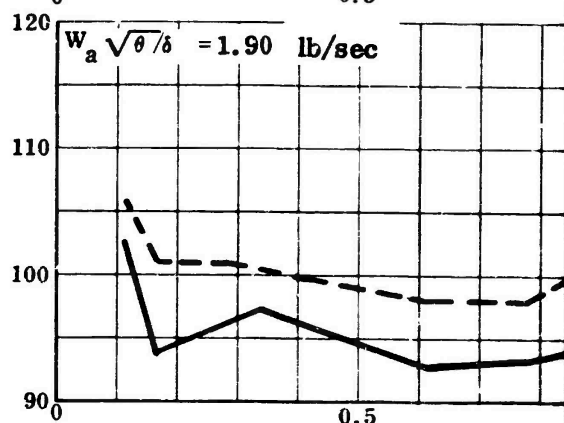
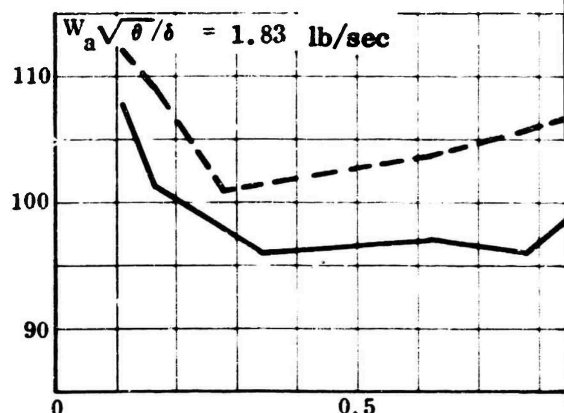
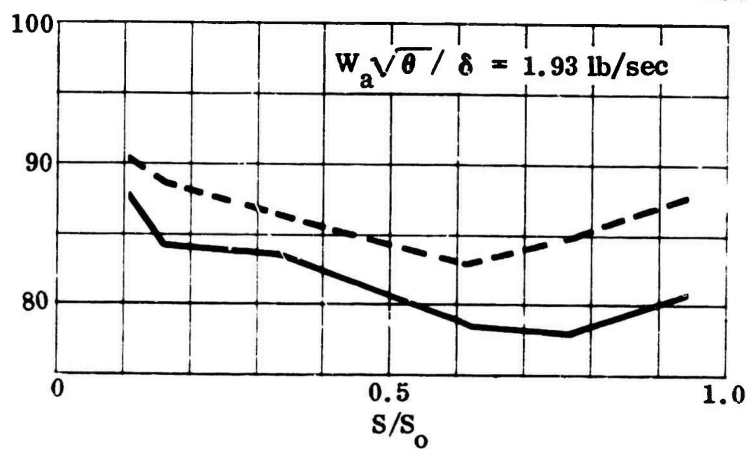
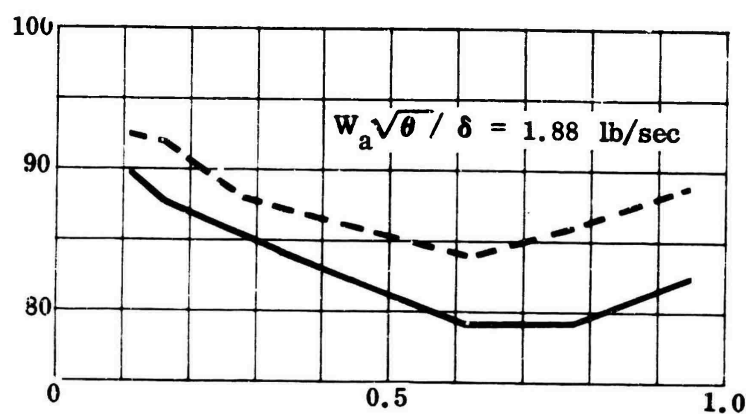
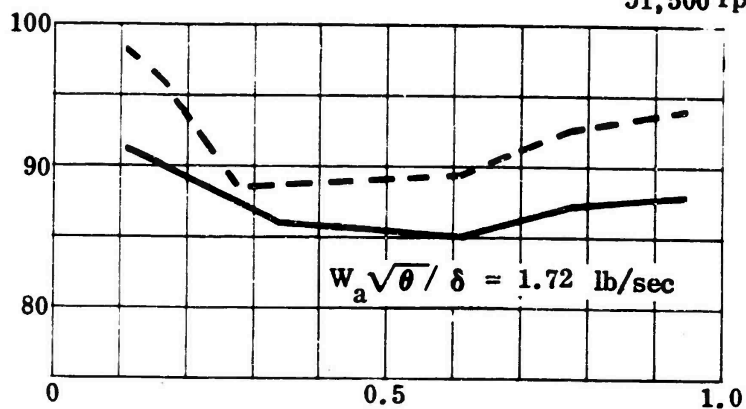


Figure 233. Circumferential Variation of Impeller-Exit Static Pressure, MF-1, Vaneless Diffuser.

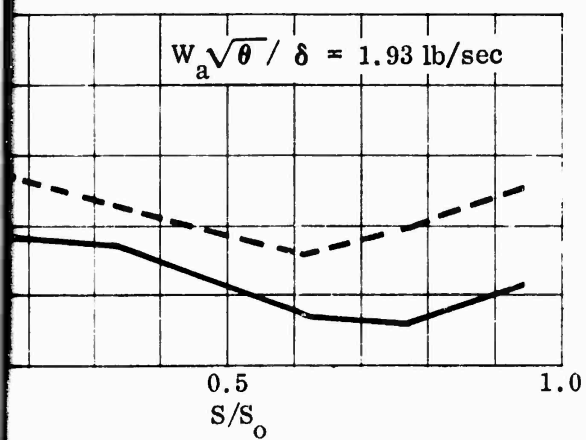
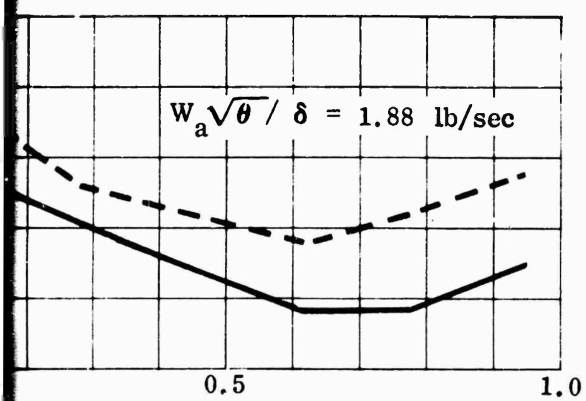
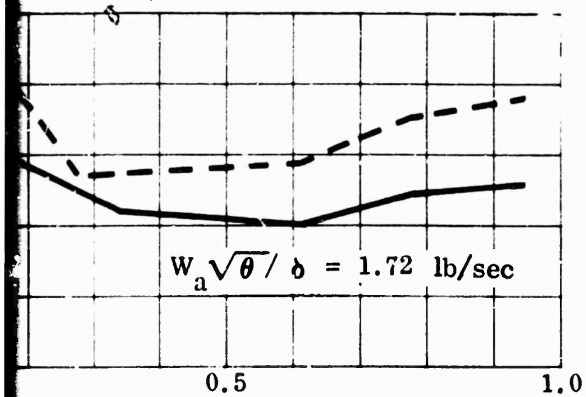
5,500 rpm



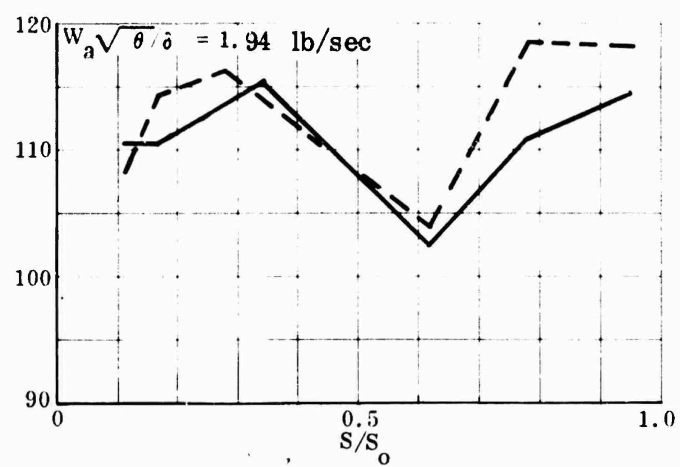
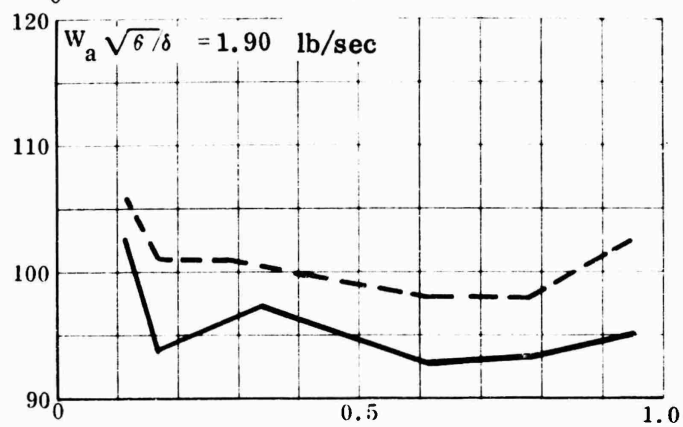
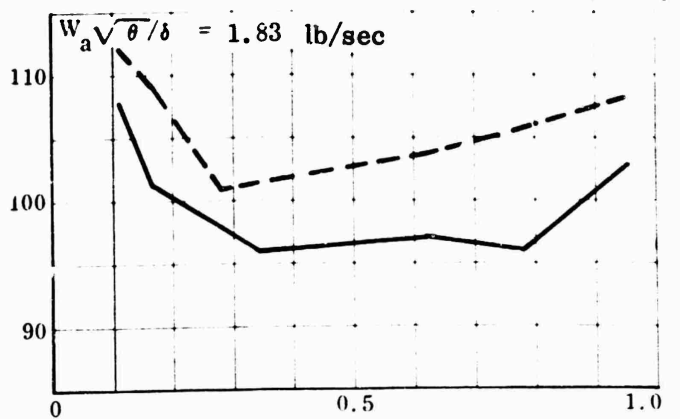
51,500 rpm



51,500 rpm



57,000 rpm



CONFIDENTIAL

Test 3402A	$S_o = 6.43$ Inches	Corrected to Ambient Conditions of : 60°F 29.92 in. Hg
----- Shroud	(covers one quadrant at R/R = 1.02)	
----- Hub		

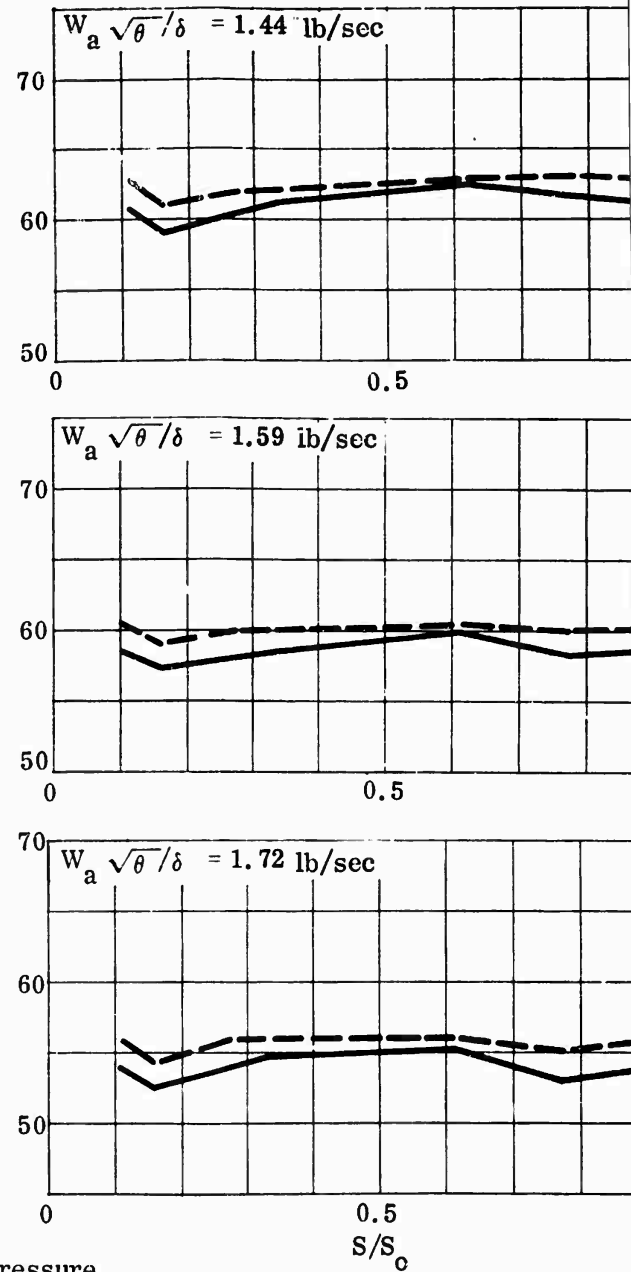
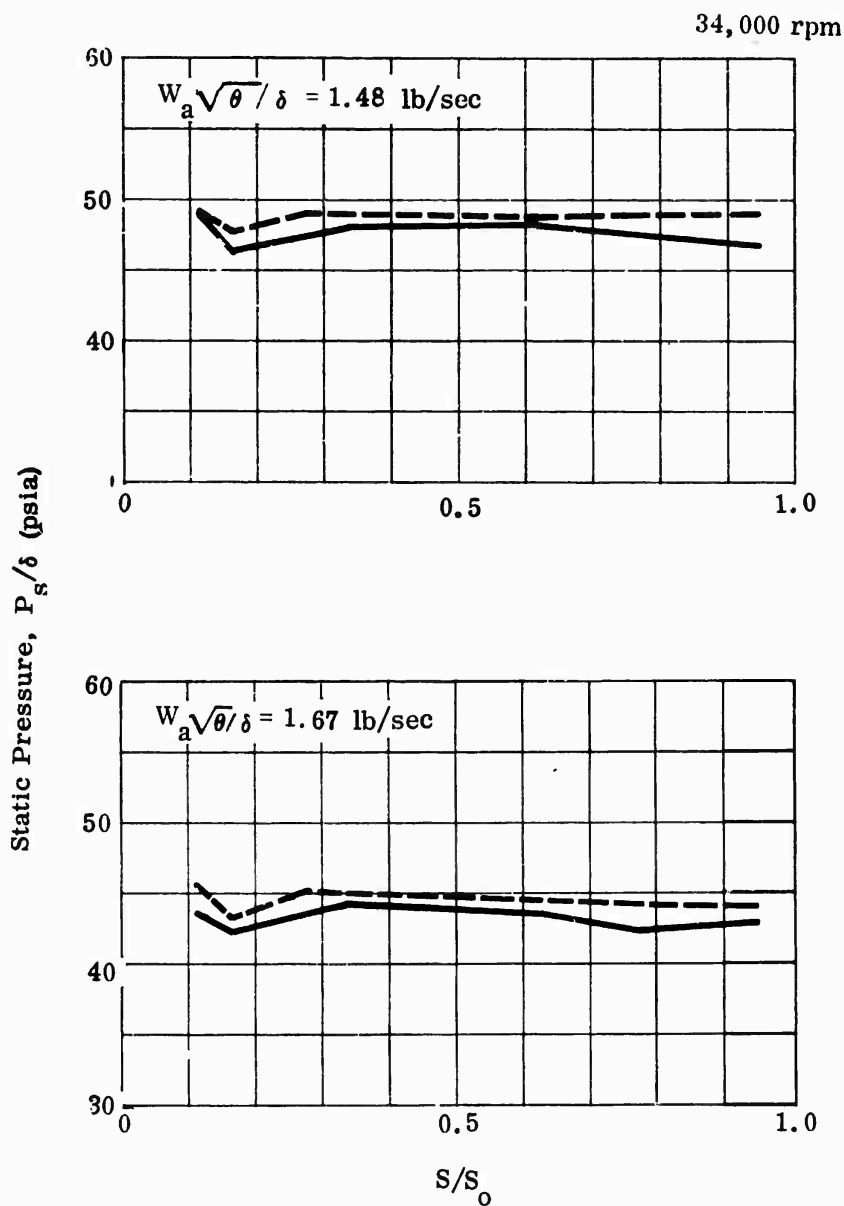


Figure 234. Circumferential Variation of Impeller-Exit Static Pressure, MF-1, Vaneless Diffuser.

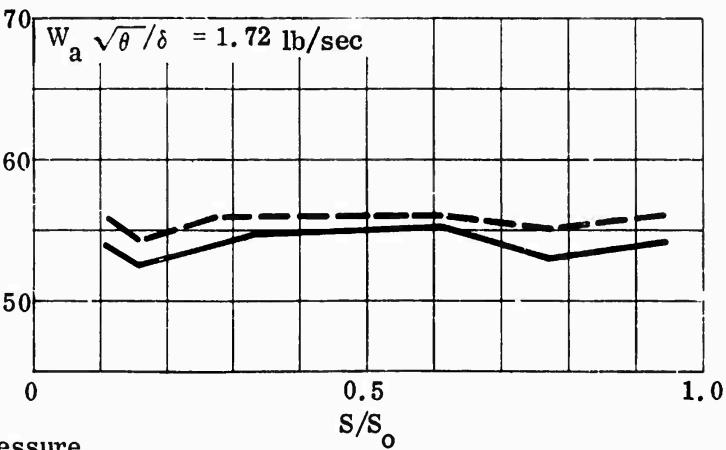
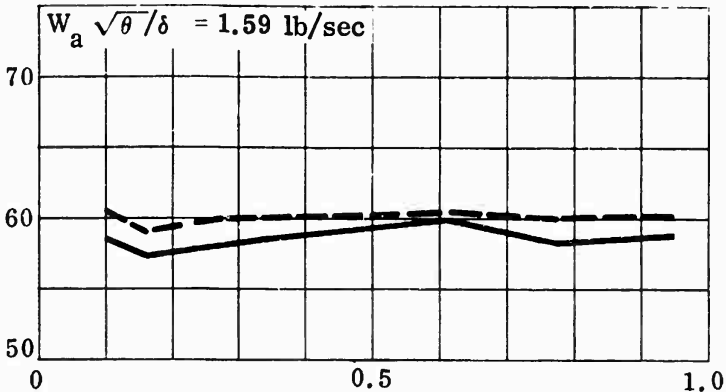
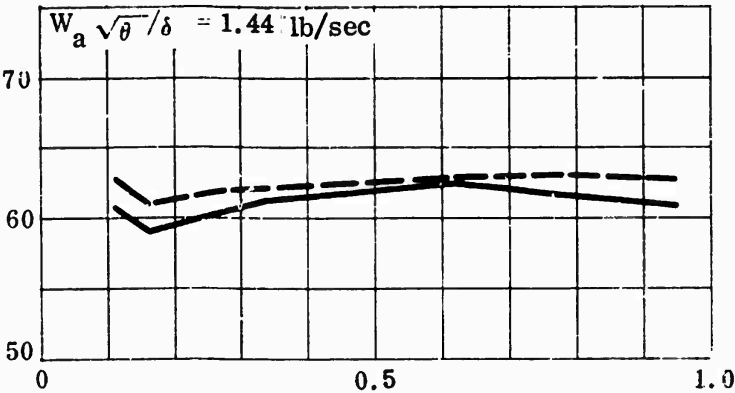
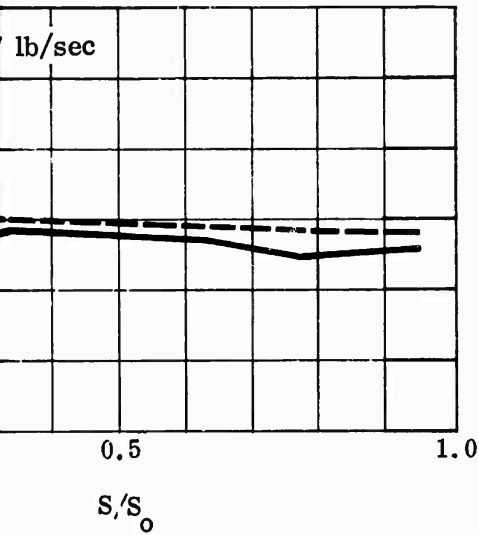
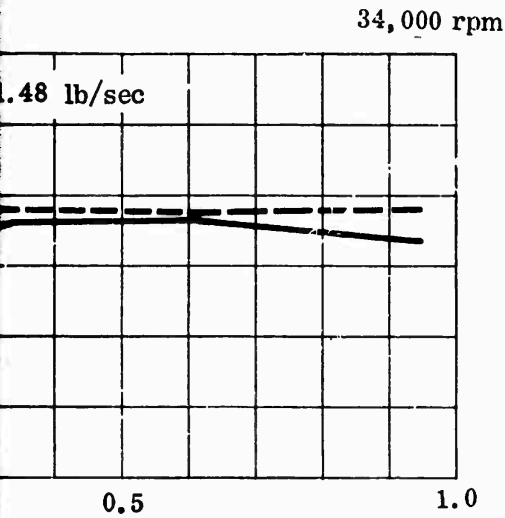
367

CONFIDENTIAL

$S_o = 6.43$ Inches
(covers one quadrant
at $R/R = 1.02$)

Corrected to Ambient
Conditions of :
60°F
29.92 in. Hg

39,000 rpm



Differential Variation of Impeller-Exit Static Pressure,
1, Vaneless Diffuser.

Test 3402
Test 3402A

Corrected to Ambient
Conditions of:
60°F
29.92 in. Hg

Test 34

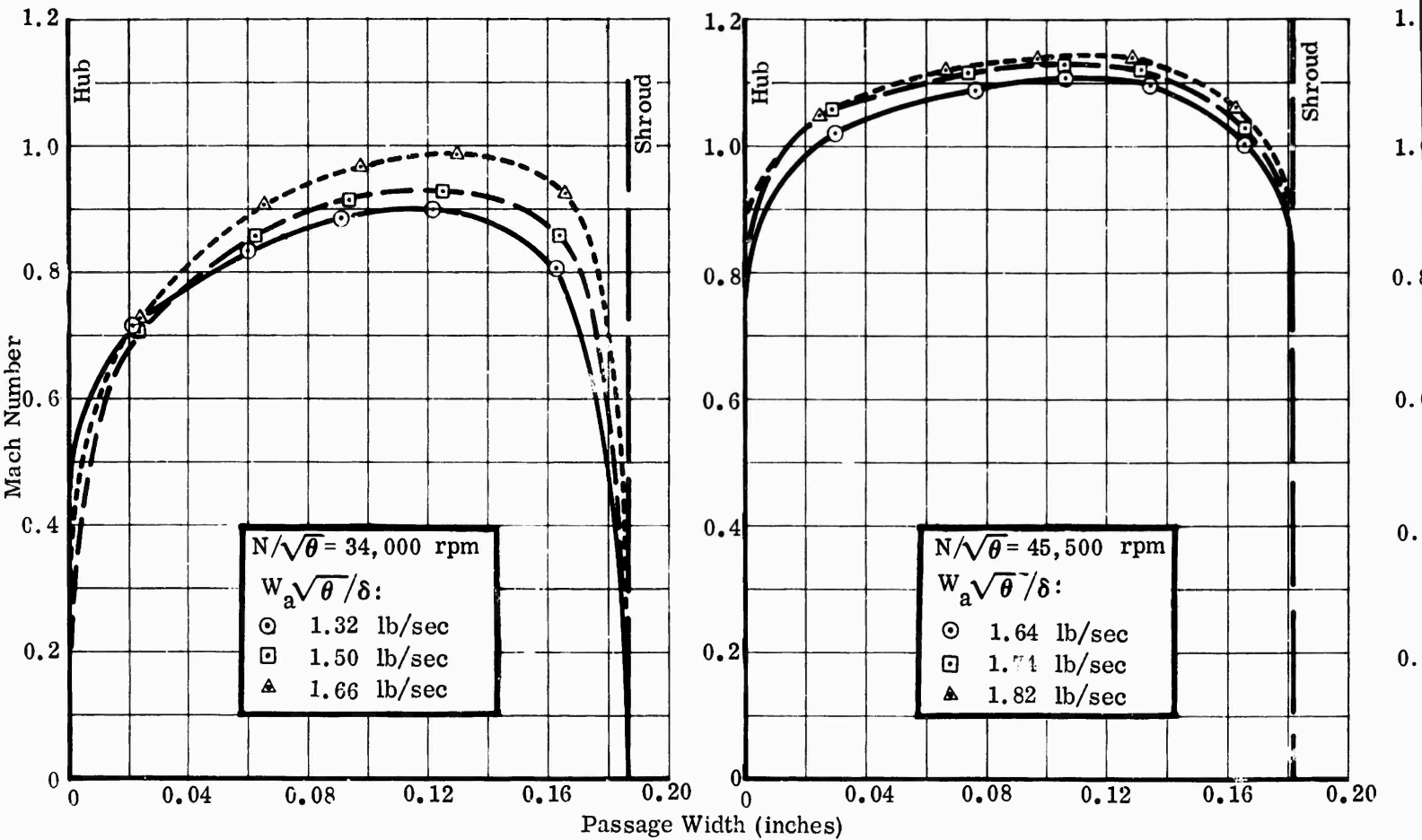
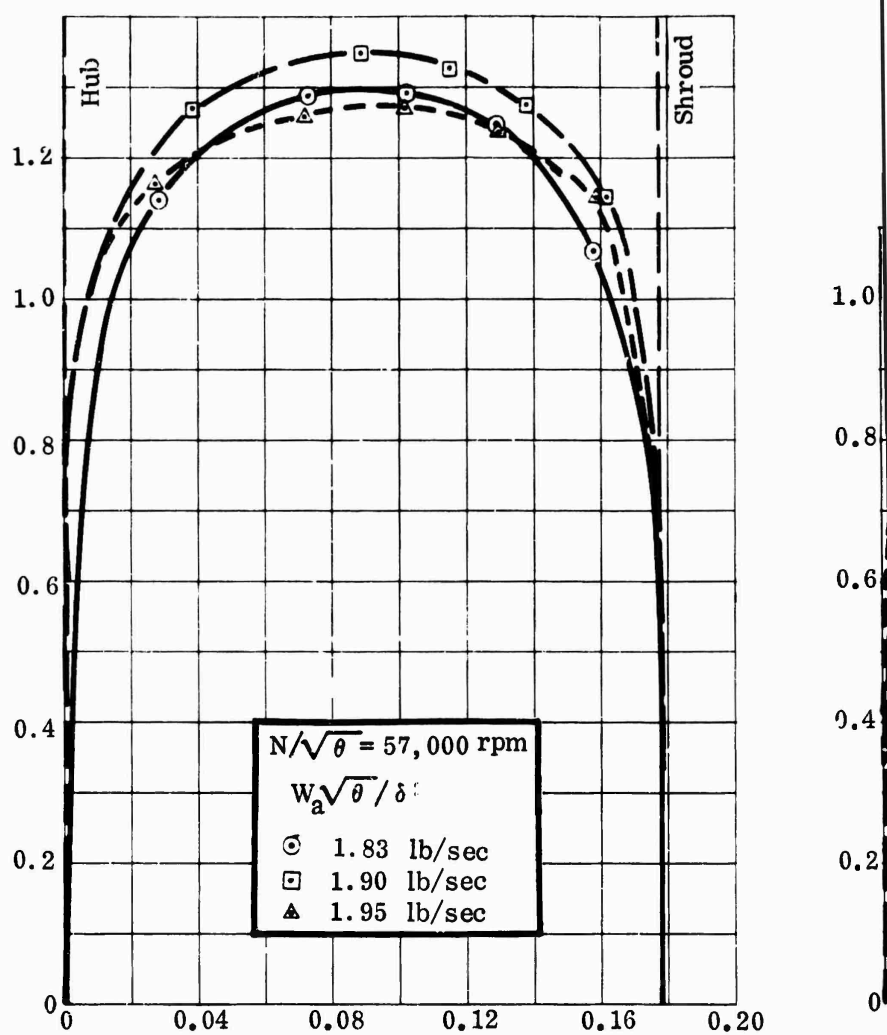
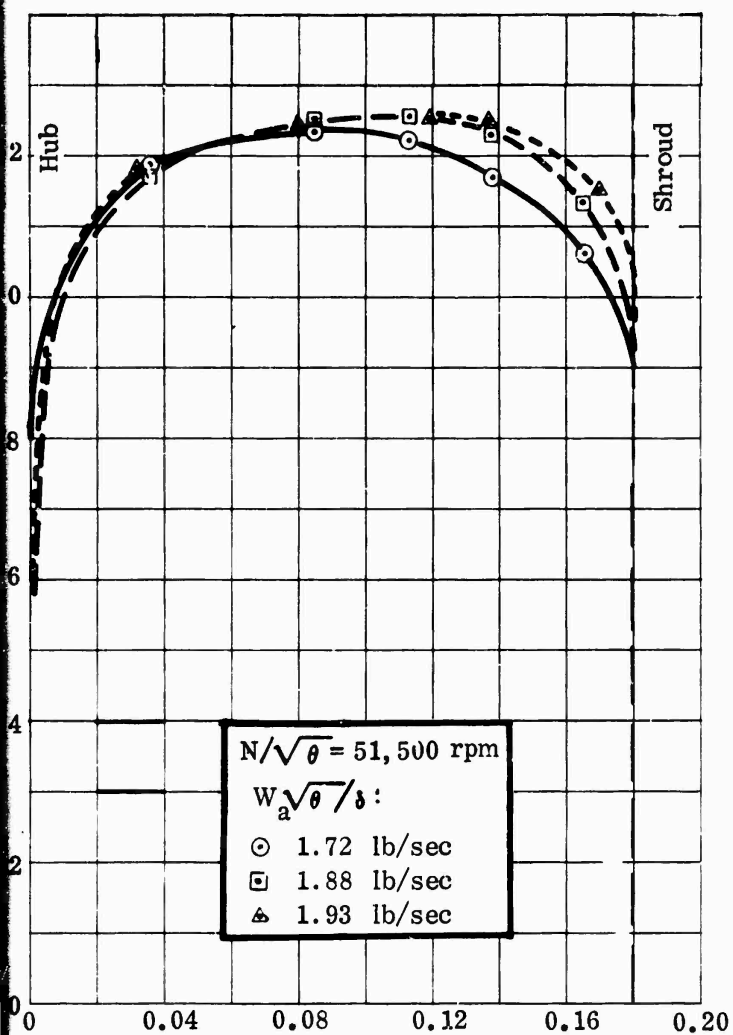
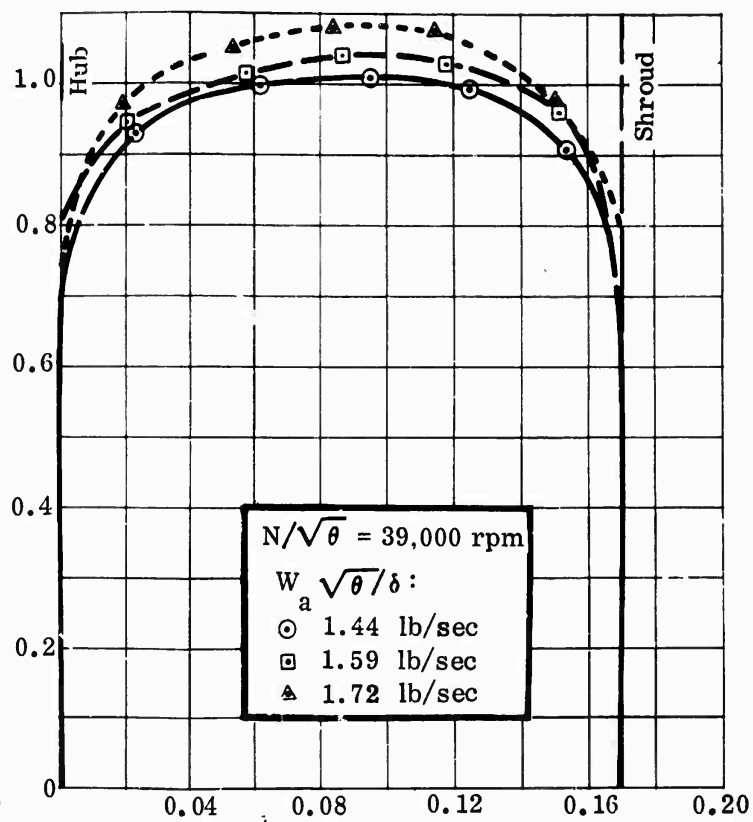
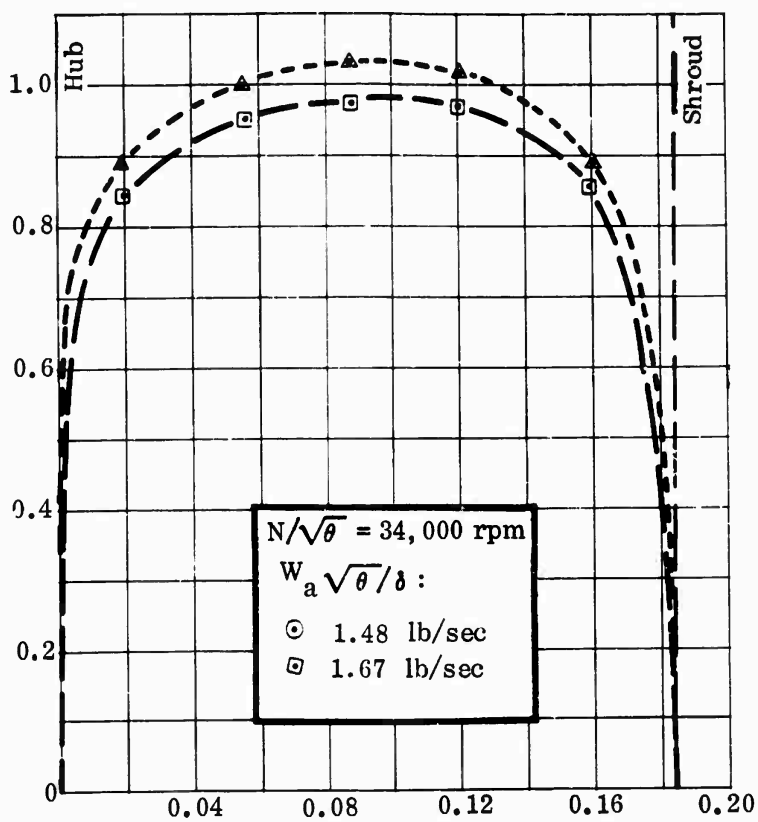


Figure 235. Impeller-Tip Absolute Mach Number Survey, MF-1, Vaneless Diffuser.



Test 3402A



CONFIDENTIAL

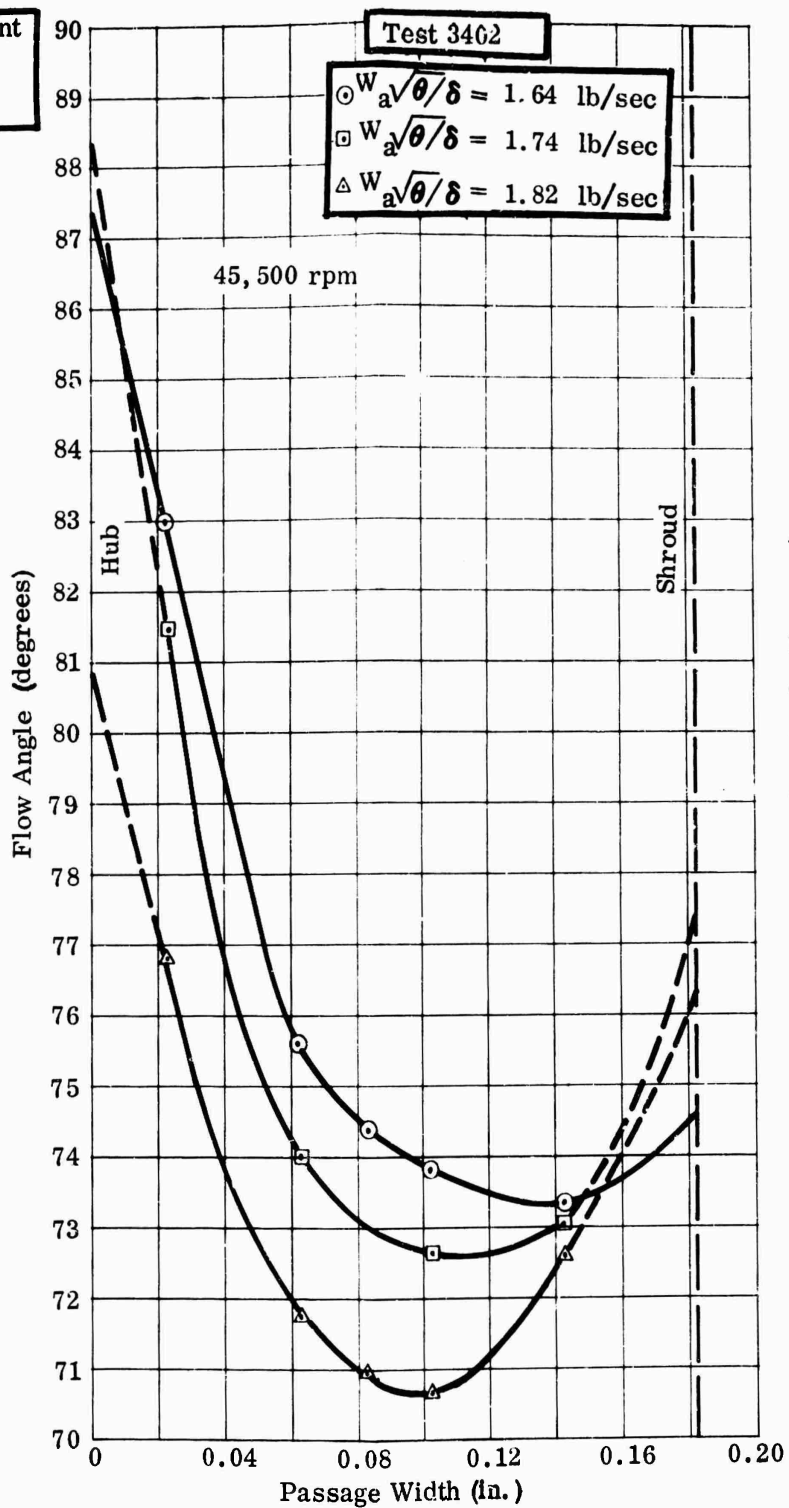
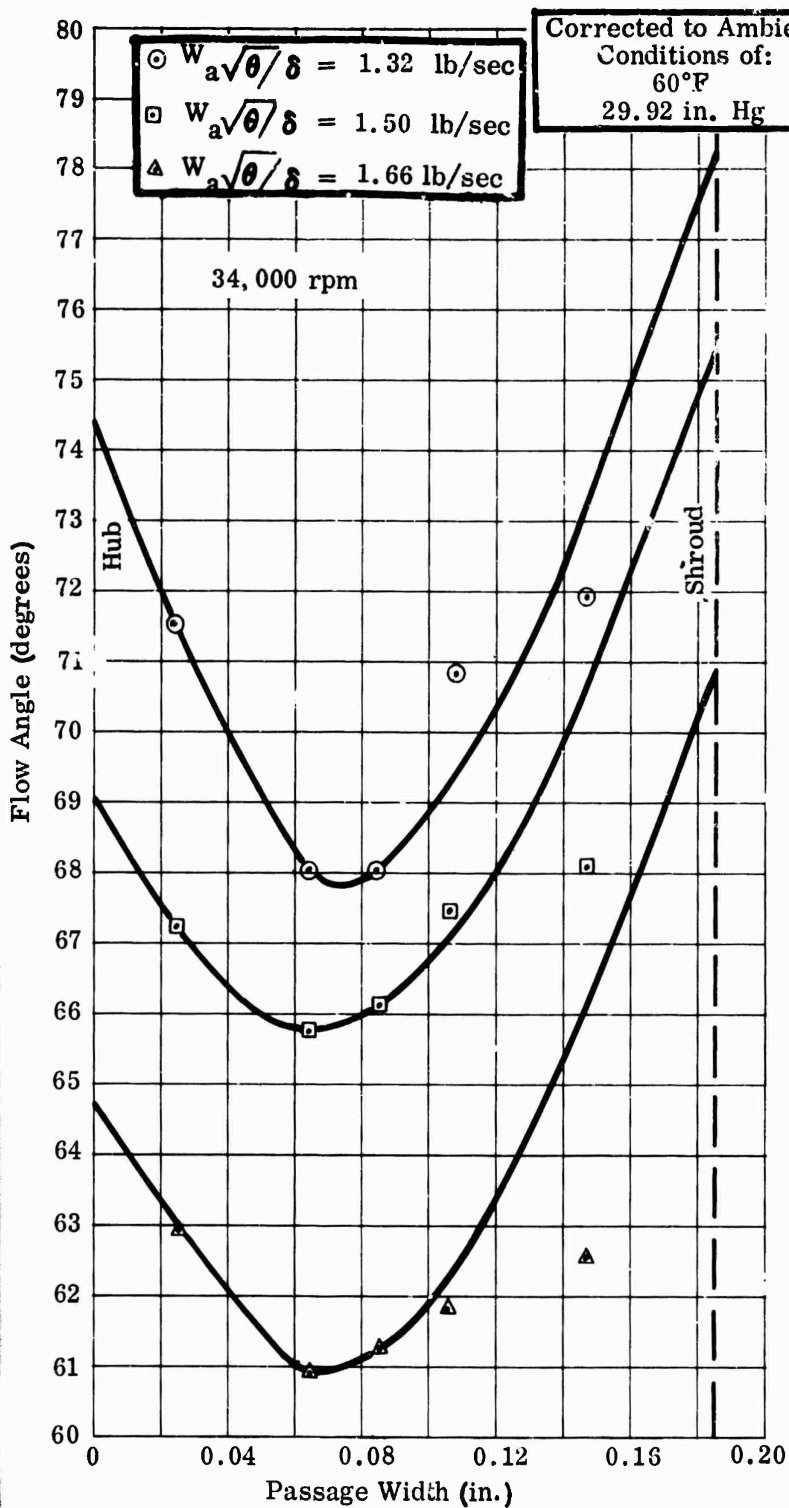
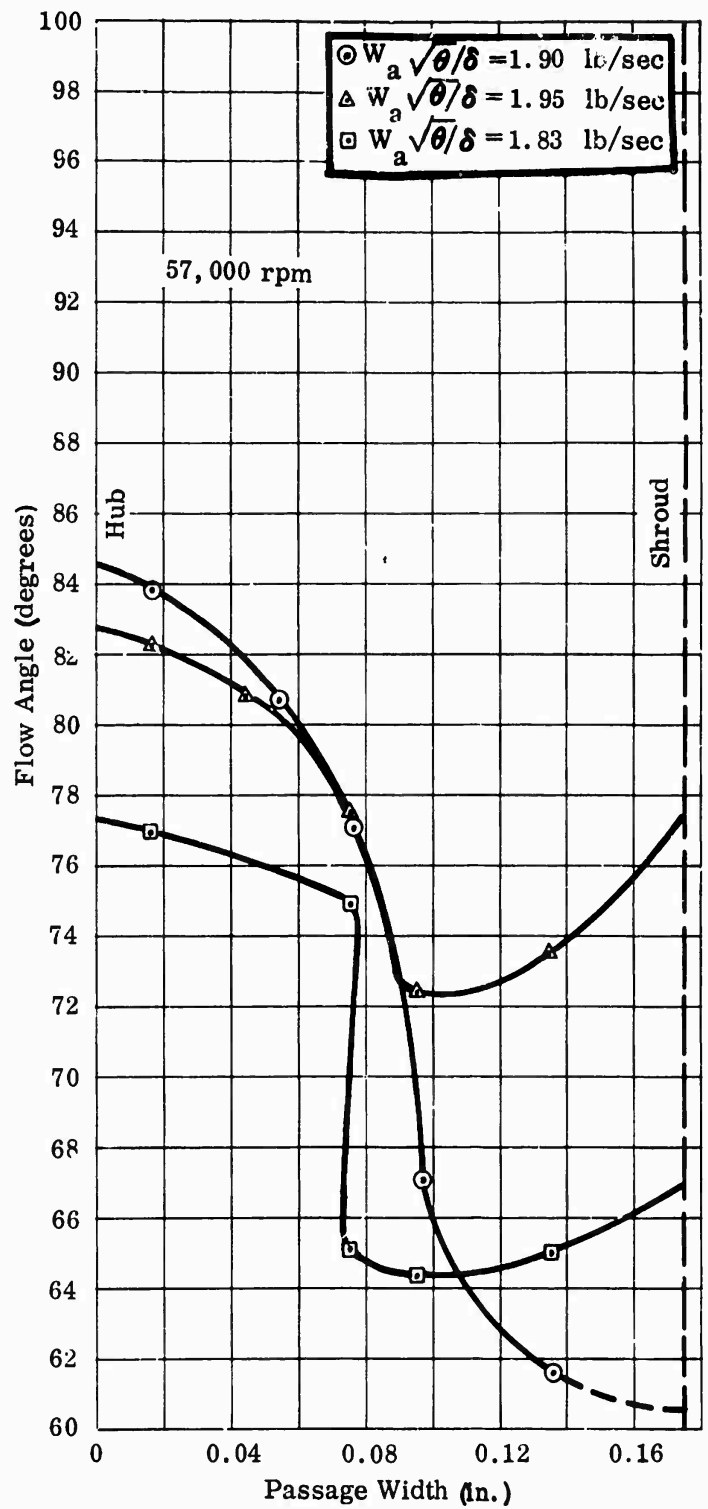
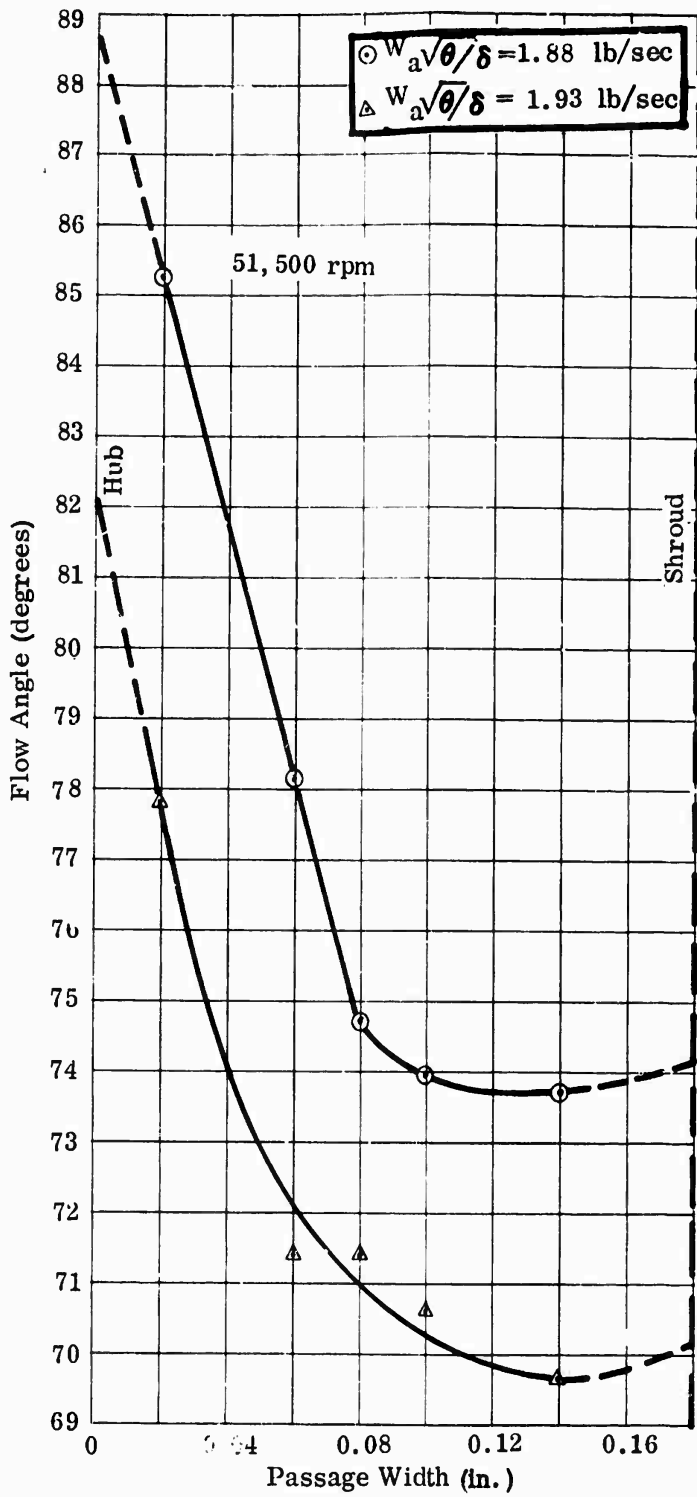


Figure 236. Impeller-Exit Absolute Flow Angle, MF-1, Vaneless Diffuser.

371

CONFIDENTIAL



CONFIDENTIAL

Corrected to Ambient
Conditions of:
60°F
29.92 in. Hg
All Velocities in fps

Test 3402

$$N/\sqrt{r} = 34,000 \text{ rpm}$$

$$N/\sqrt{r} = 45,500$$

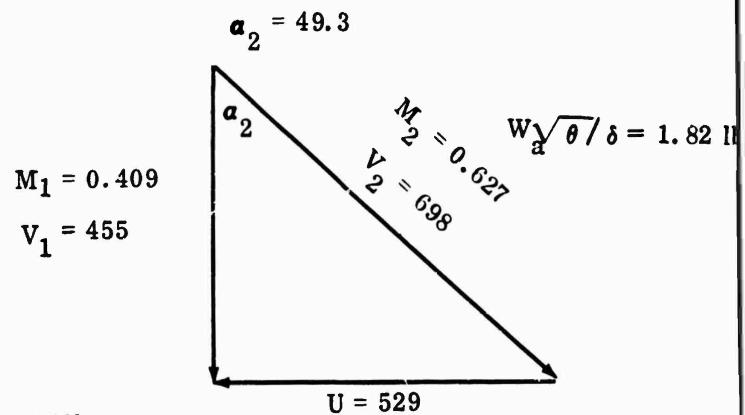
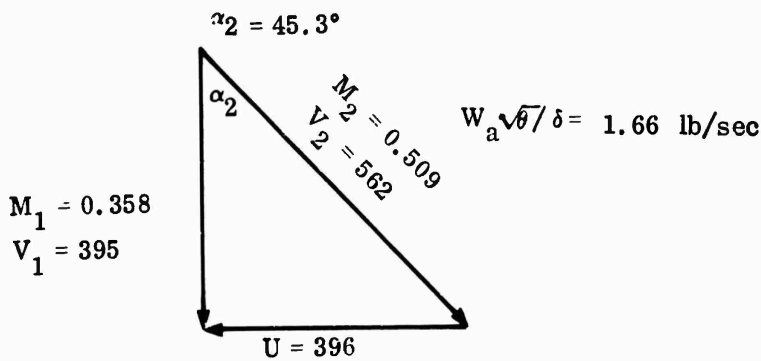
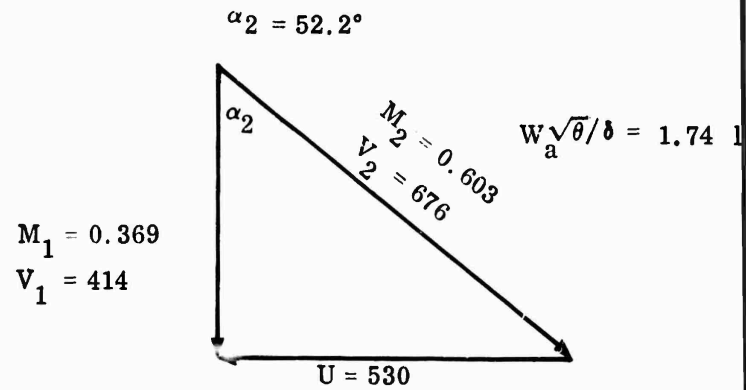
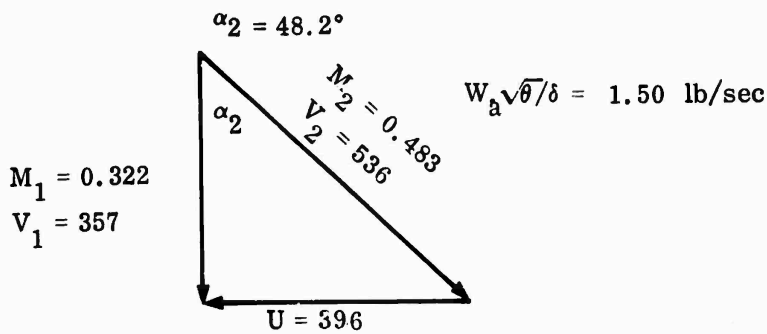
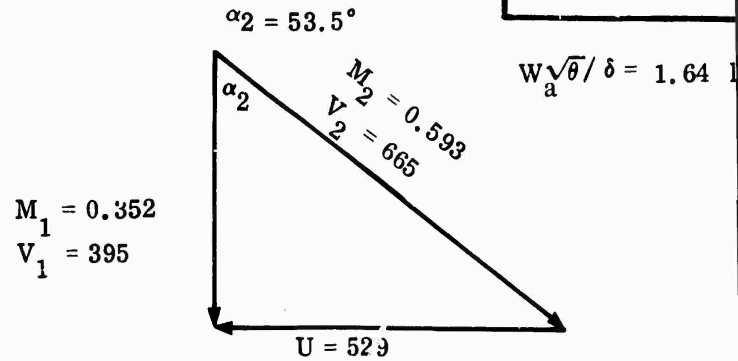
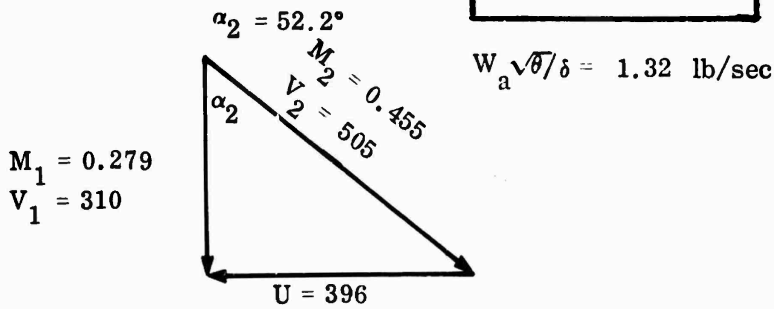


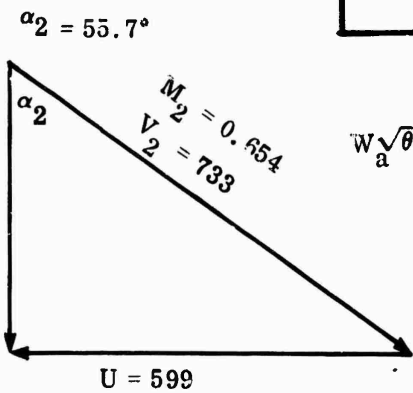
Figure 237. RMS Inlet Vector Diagrams, MF-1, Vaneless Diffuser.

CONFIDENTIAL

5,500 rpm

1.64 lb/sec

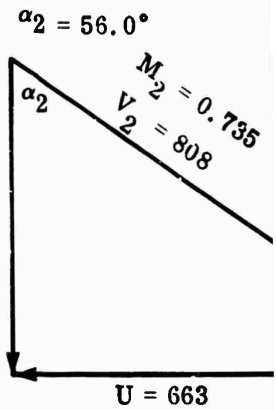
$M_1 = 0.369$
 $V_1 = 413$



$N \sqrt{\theta} = 51,500 \text{ rpm}$

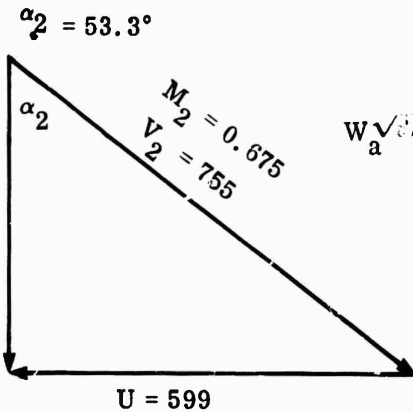
$W_a \sqrt{\theta} / \delta = 1.72 \text{ lb/sec}$

$M_1 = 0.411$
 $V_1 = 451$



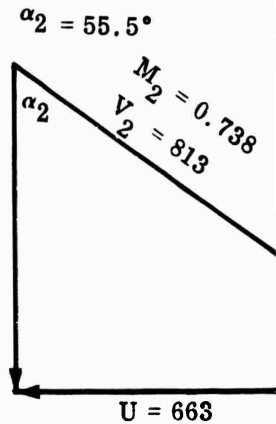
1.74 lb/sec

$M_1 = 0.404$
 $V_1 = 452$



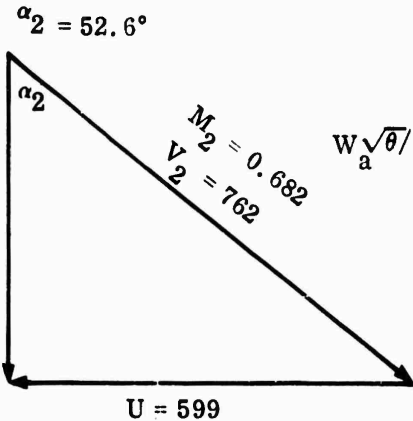
$W_a \sqrt{\theta} / \delta = 1.88 \text{ lb/sec}$

$M_1 = 0.418$
 $V_1 = 460$



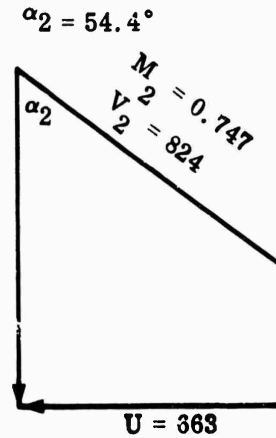
1.82 lb/sec

$M_1 = 0.414$
 $V_1 = 463$



$W_a \sqrt{\theta} / \delta = 1.93 \text{ lb/sec}$

$M_1 = 0.435$
 $V_1 = 479$



$$N \sqrt{A} = 51,500 \text{ rpm}$$

$$\alpha_2 = 5.7^\circ$$

$$M_2 = 0.654$$

$$V_2 = 733$$

$$W_a \sqrt{\theta} / \delta = 1.72 \text{ lb/sec}$$

$$U = 599$$

$$\alpha_2 = 3.3^\circ$$

$$M_2 = 0.675$$

$$V_2 = 755$$

$$W_a \sqrt{\theta} / \delta = 1.88 \text{ lb/sec}$$

$$U = 599$$

$$\alpha_2 = 2.6^\circ$$

$$M_2 = 0.682$$

$$V_2 = 762$$

$$W_a \sqrt{\theta} / \delta = 1.93 \text{ lb/sec}$$

$$U = 599$$

$$\alpha_2 = 56.0^\circ$$

$$N / \sqrt{\theta} = 57,000 \text{ rpm}$$

$$M_2 = 0.735$$

$$V_2 = 808$$

$$W_a \sqrt{\theta} / \delta = 1.83 \text{ lb/sec}$$

$$U = 663$$

$$\alpha_2 = 55.5^\circ$$

$$M_2 = 0.738$$

$$V_2 = 813$$

$$W_a \sqrt{\theta} / \delta = 1.90 \text{ lb/sec}$$

$$U = 663$$

$$\alpha_2 = 54.4^\circ$$

$$M_2 = 0.747$$

$$V_2 = 824$$

$$W_a \sqrt{\theta} / \delta = 1.95 \text{ lb/sec}$$

$$U = 663$$

$$M_1 = 0.411$$

$$V_1 = 451$$

$$M_1 = 0.418$$

$$V_1 = 460$$

$$M_1 = 0.435$$

$$V_1 = 479$$

CONFIDENTIAL

Test 3402A

**Corrected to Ambient
Conditions of:
60°F
29.92 in. Hg
All Velocities in fps**

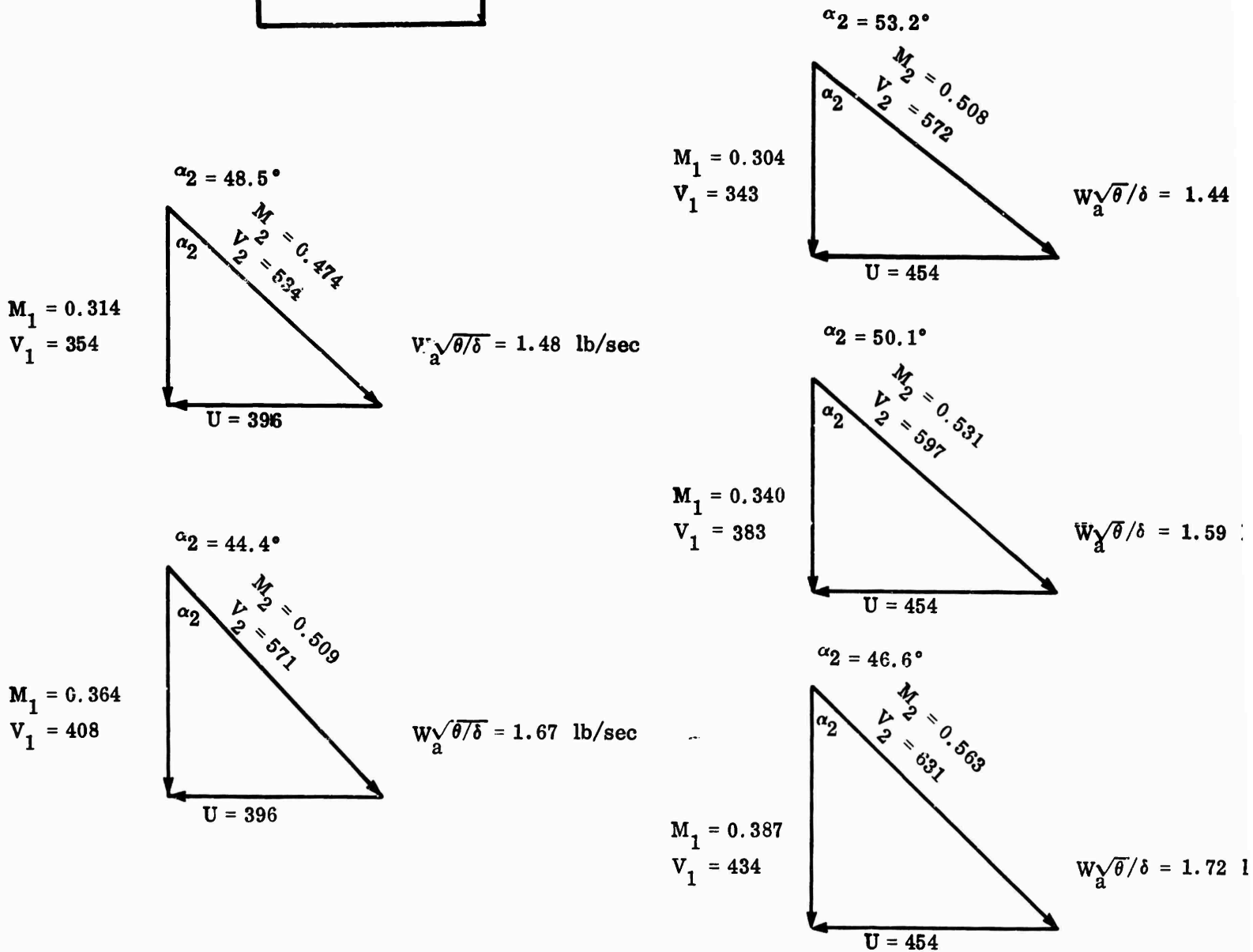
$$N/\sqrt{\theta} = 39,000 \text{ rpm}$$
$$N/\sqrt{\theta} = 34,000 \text{ rpm}$$


Figure 238. RMS Inlet Vector Diagrams, MF-1, Vaneless Diffuser.

CONFIDENTIAL

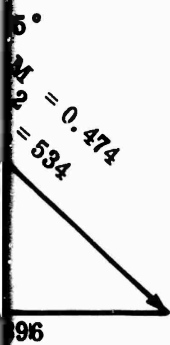
CONFIDENTIAL

Test 3402A

Corrected to Ambient
Conditions of:
60°F
29.92 in. Hg
All Velocities in fps

$N/\sqrt{\theta} = 39,000 \text{ rpm}$

$N/\sqrt{\theta} = 34,000 \text{ rpm}$

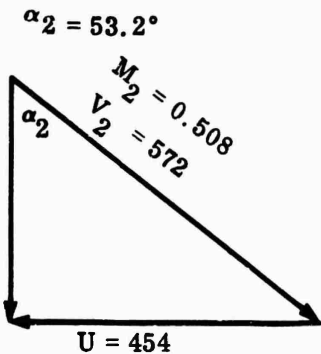


$W_a \sqrt{\theta/\delta} = 1.48 \text{ lb/sec}$



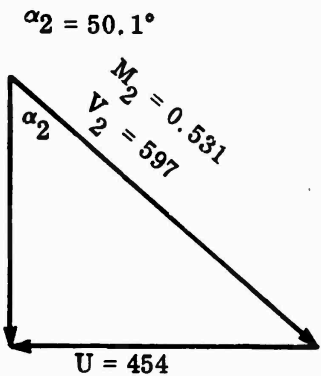
$W_a \sqrt{\theta/\delta} = 1.67 \text{ lb/sec}$

$M_1 = 0.304$
 $V_1 = 343$



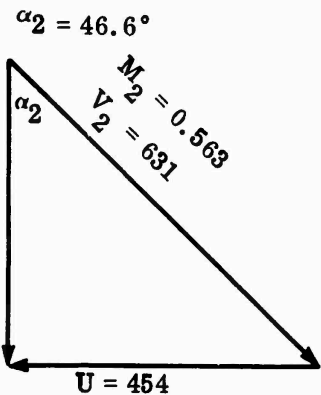
$W_a \sqrt{\theta/\delta} = 1.44 \text{ lb/sec}$

$M_1 = 0.340$
 $V_1 = 383$



$W_a \sqrt{\theta/\delta} = 1.59 \text{ lb/sec}$

$M_1 = 0.387$
 $V_1 = 434$



$W_a \sqrt{\theta/\delta} = 1.72 \text{ lb/sec}$

3 Inlet Vector Diagrams, MF-1, Vaneless Diffuser.

375

CONFIDENTIAL

CONFIDENTIAL

$N/\sqrt{\theta} = 34,000 \text{ rpm}$

Test 3402

Corrected to Ambient
Conditions of:
60°F
29.92 in. Hg
All Velocities in fps

$N/\sqrt{\theta} = 45,500 \text{ rpm}$

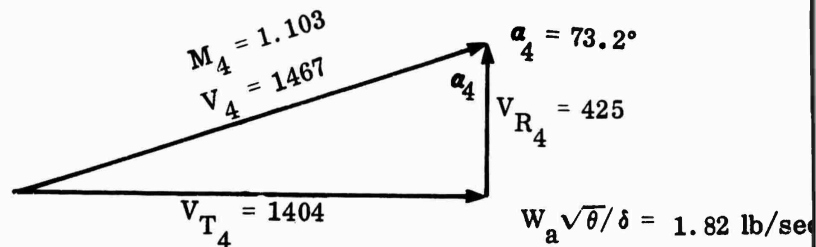
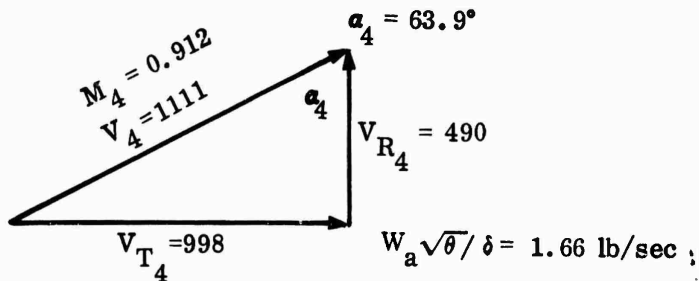
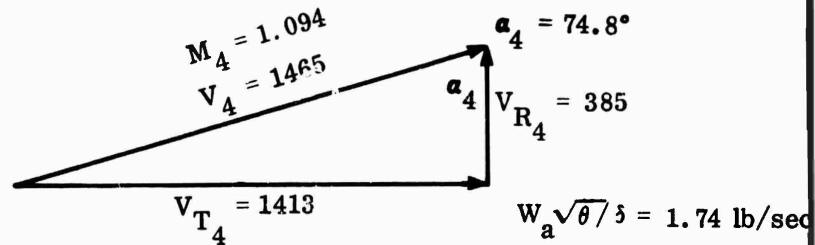
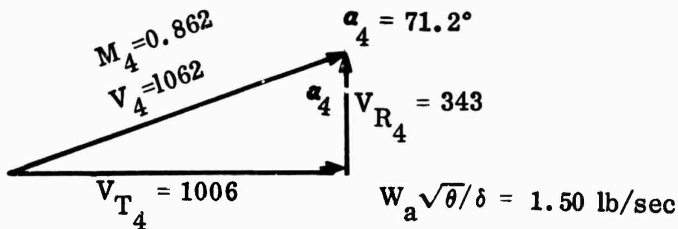
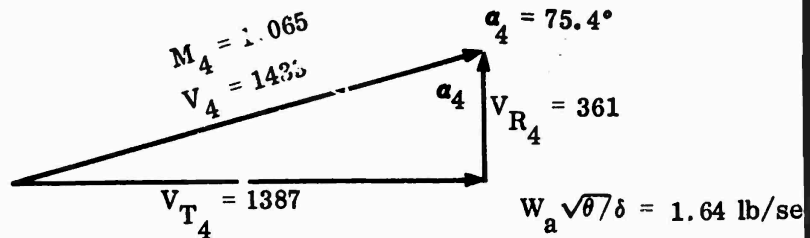
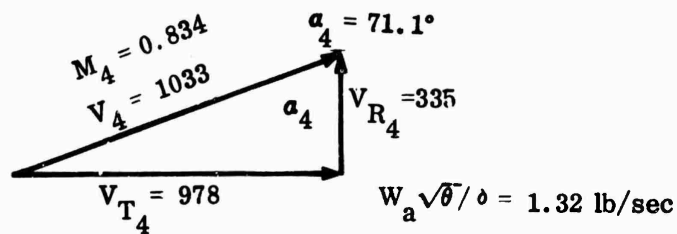
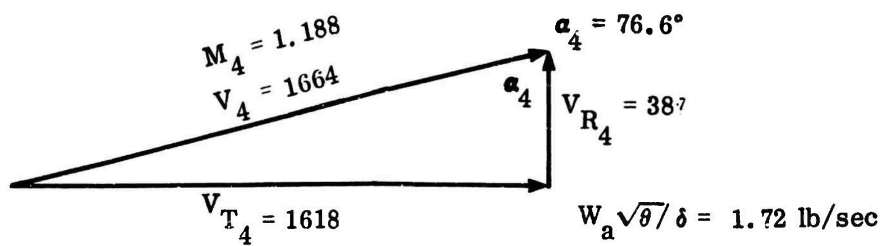


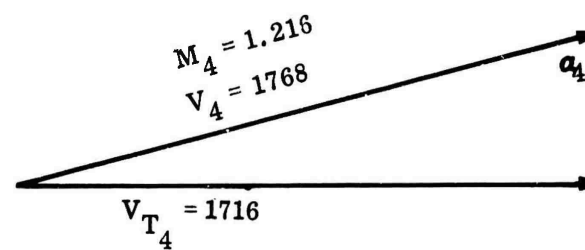
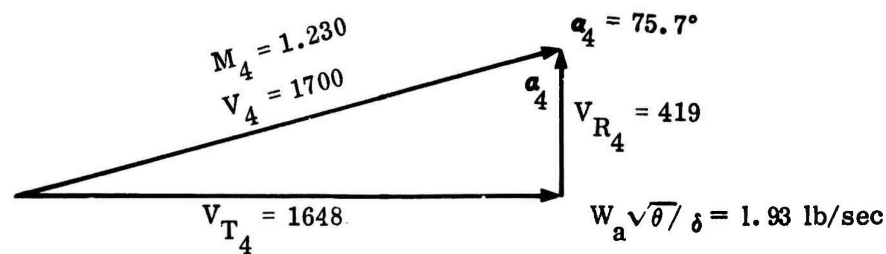
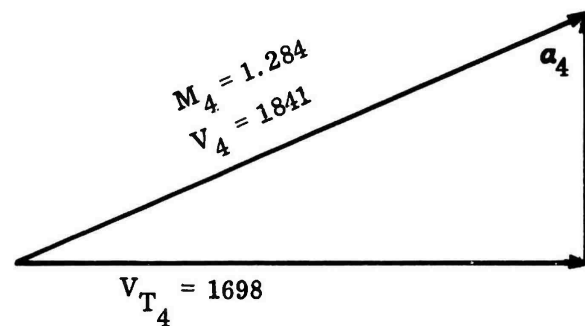
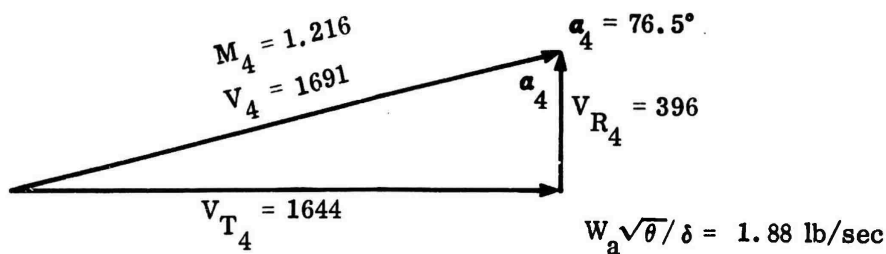
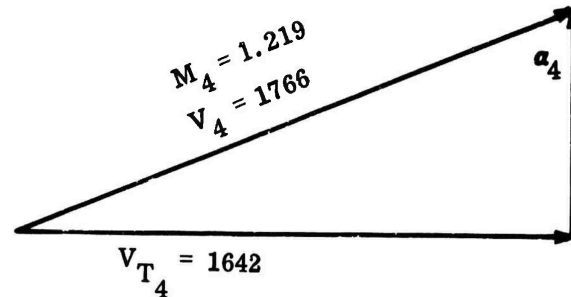
Figure 239. Mean Vector Diagrams at 1.02 Diameter Ratio, MF-1, Vaneless Diffuser.
377

CONFIDENTIAL

$$N/\sqrt{\theta} = 51,500 \text{ rpm}$$

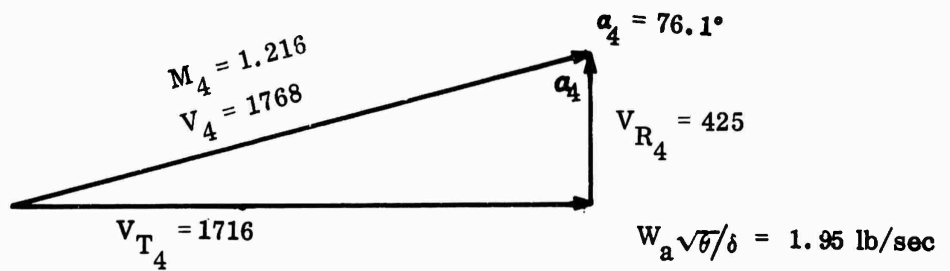
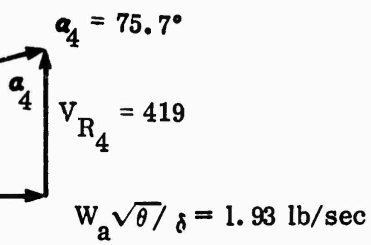
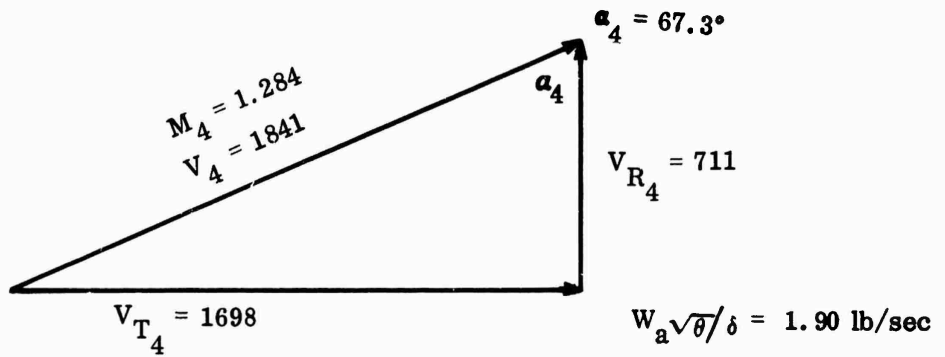
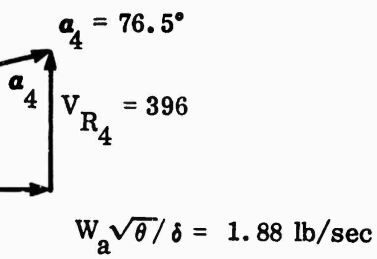
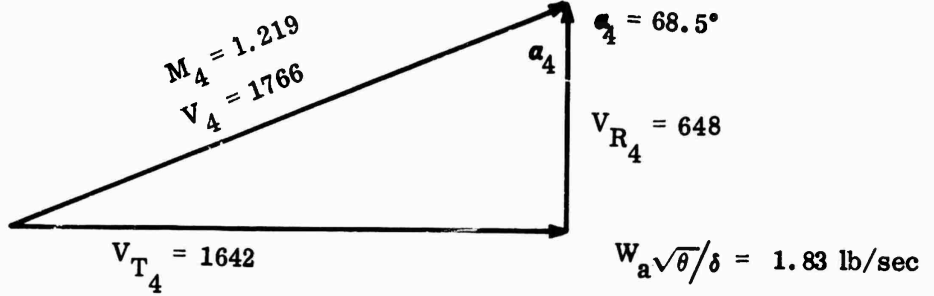
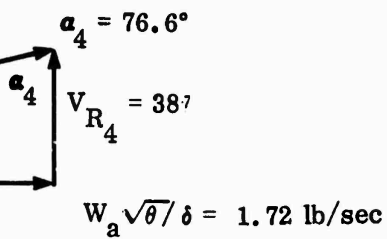


$$N/\sqrt{\theta} = 57,000 \text{ rpm}$$



$$N/\sqrt{\theta} = 51,500 \text{ rpm}$$

$$N/\sqrt{\theta} = 57,000 \text{ rpm}$$



CONFIDENTIAL

$N/\sqrt{\theta} = 34,000 \text{ rpm}$

Test 3204A

Corrected to Ambient
Conditions of:
60°F
29.92 in. Hg
All Velocities in fps

$N/\sqrt{\theta} = 39,000 \text{ rpm}$

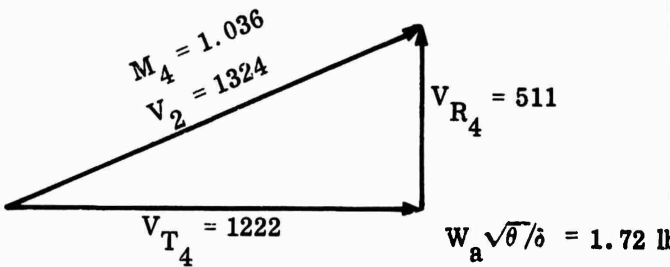
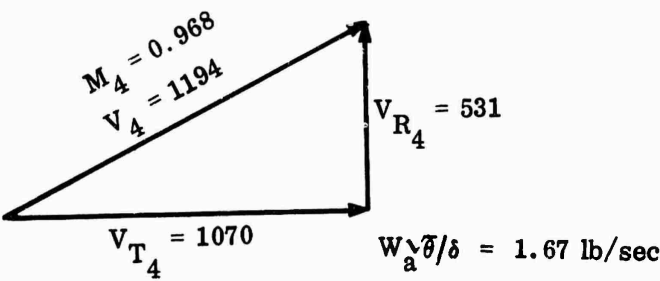
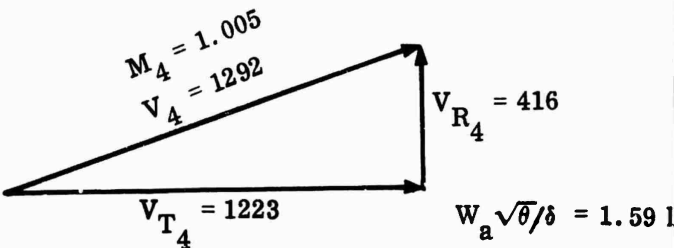
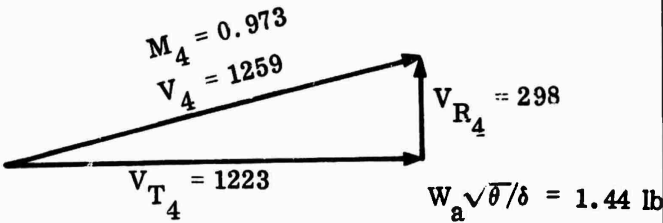
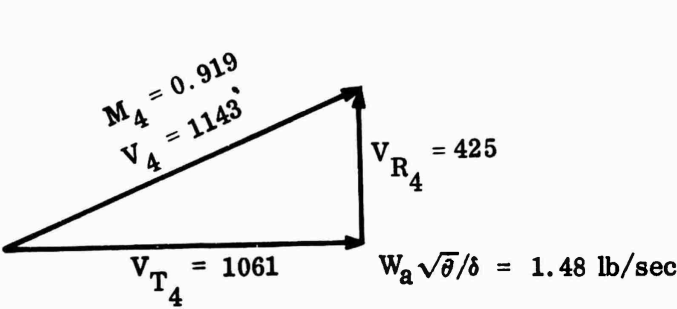


Figure 240. Mean Vector Diagrams at 1.02 Diameter Ratio, MF-1, Vaneless Diffuser.

CONFIDENTIAL

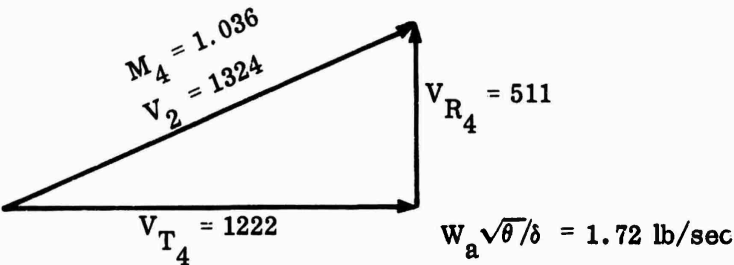
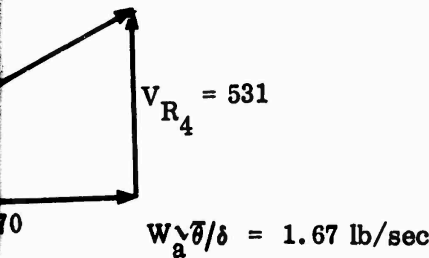
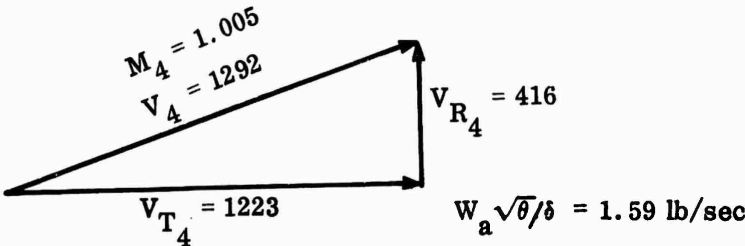
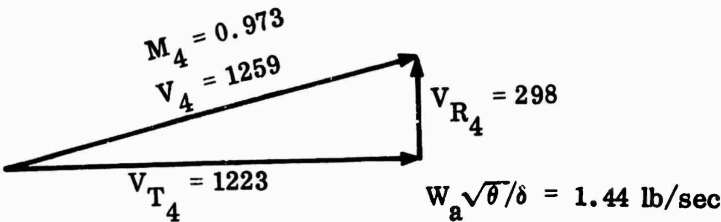
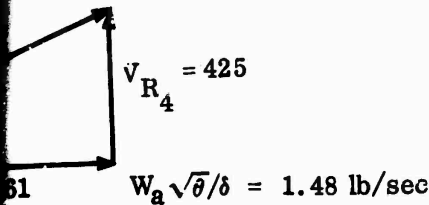
1

CONFIDENTIAL

Test 3204A

Corrected to Ambient
Conditions of:
60°F
29.92 in. Hg
All Velocities in fps

$N/\sqrt{\theta} = 39,000 \text{ rpm}$



Mean Vector Diagrams at 1.02 Diameter Ratio,
MF-1, Vaneless Diffuser.

379

CONFIDENTIAL

CONFIDENTIAL

Test 3402

Corrected to Ambient
Conditions of:
60°F
29.92 in. Hg

$N/\sqrt{\theta} = 34,000$ rpm

$N/\sqrt{\theta} = 45,500$ rpm

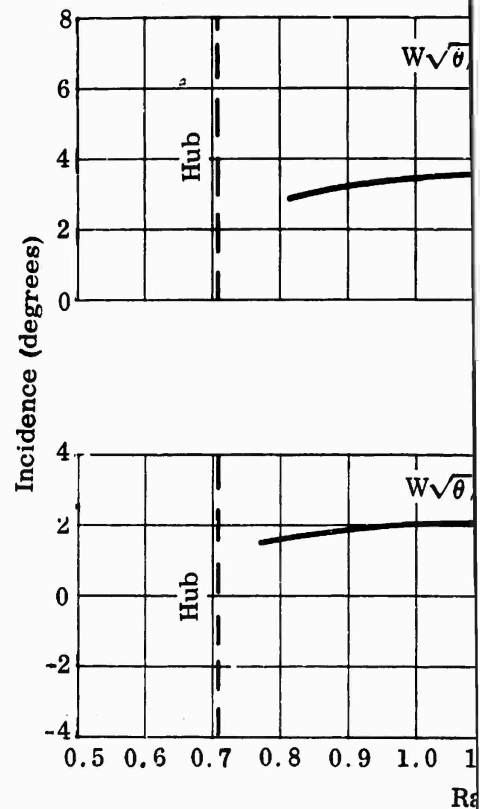
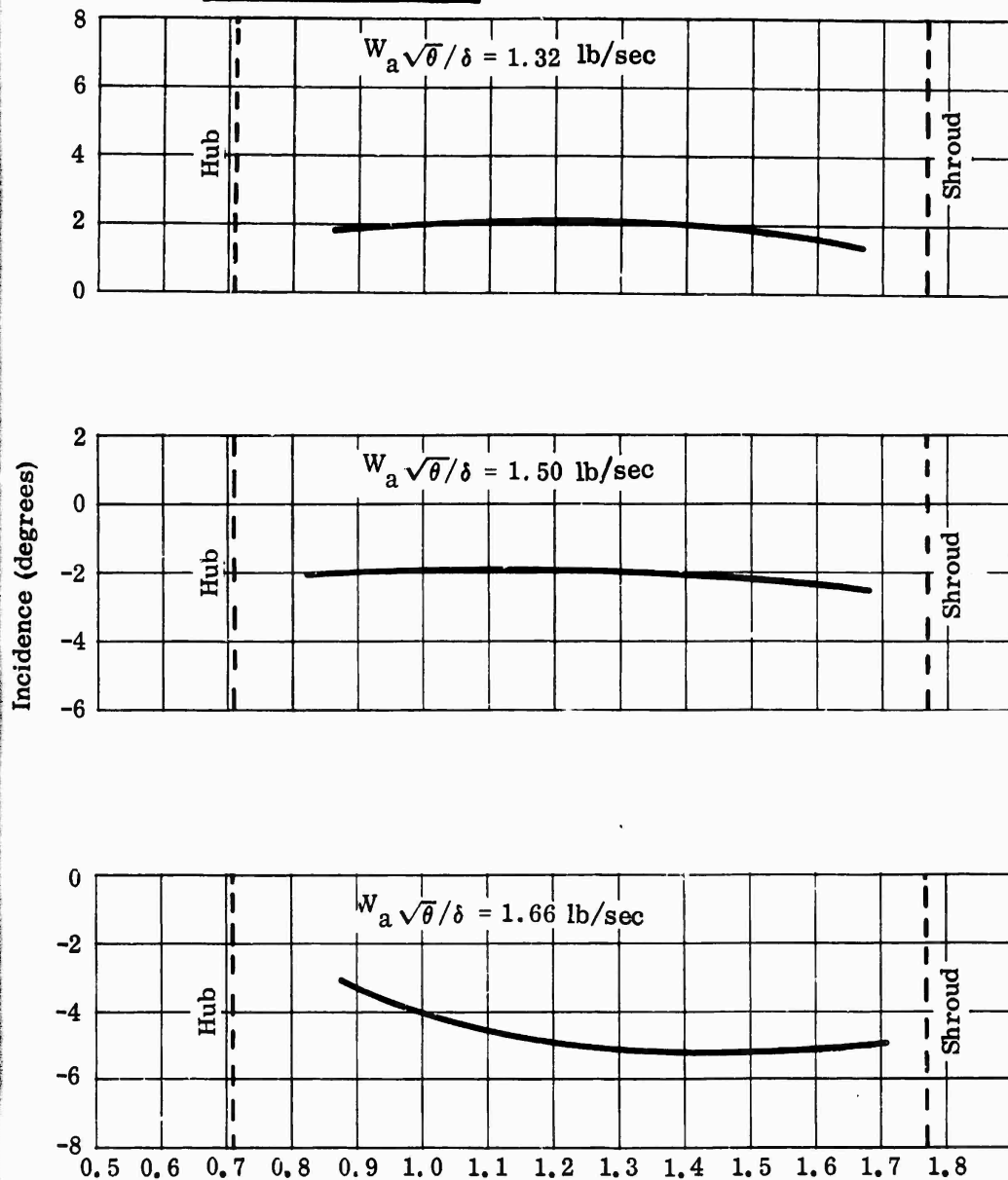
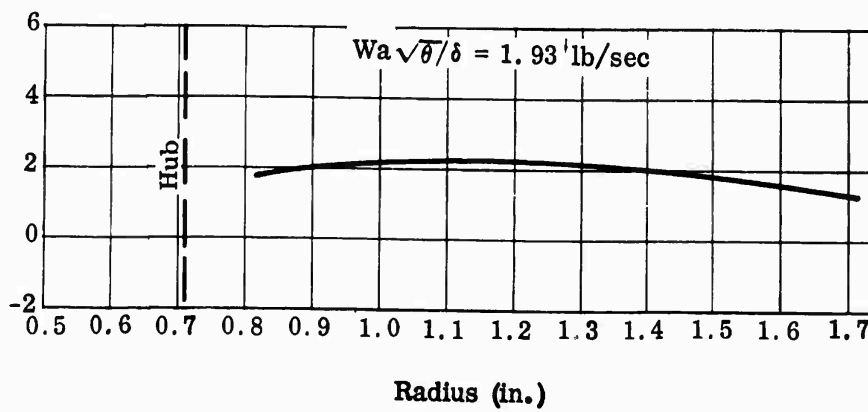
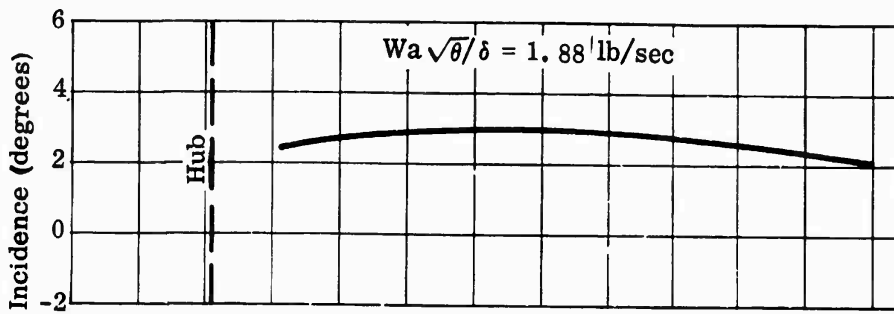
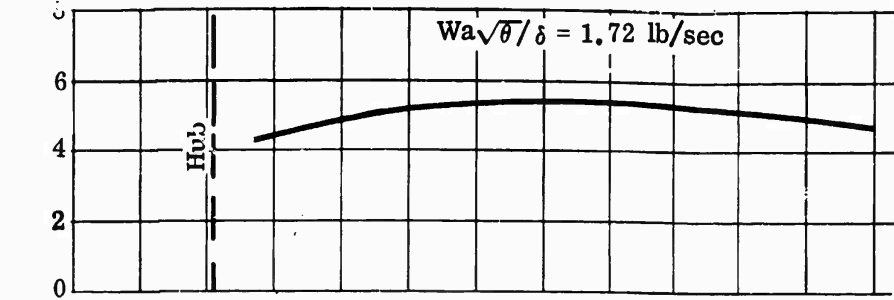
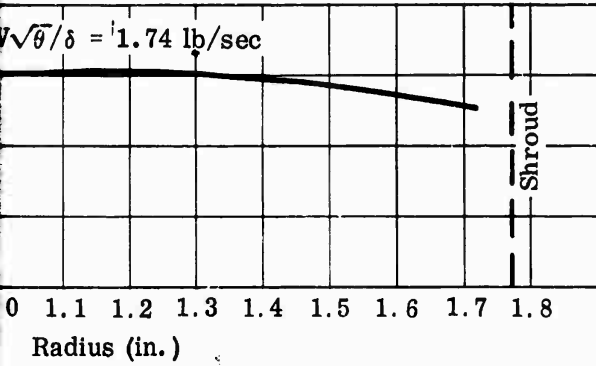
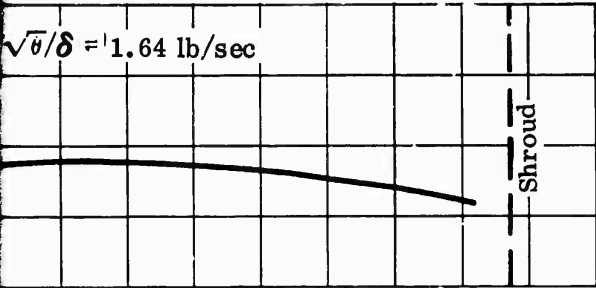


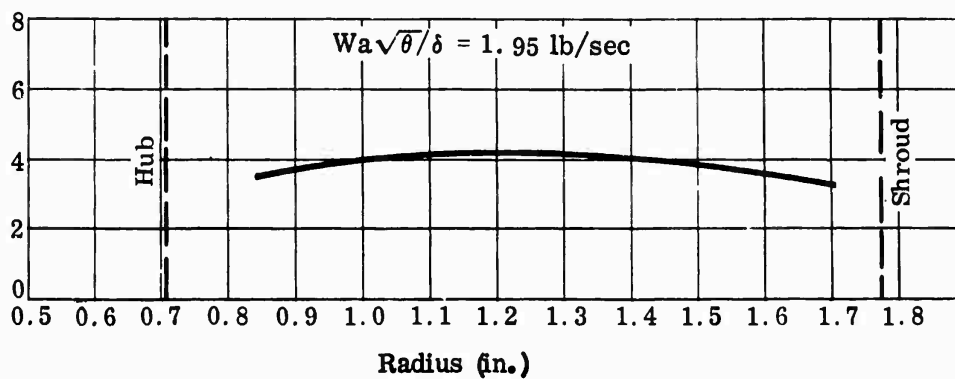
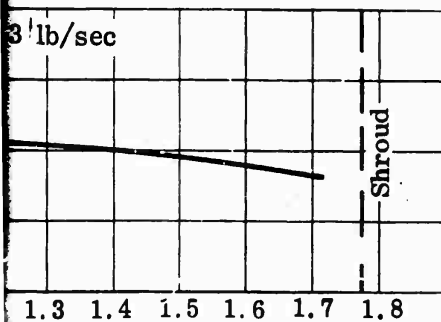
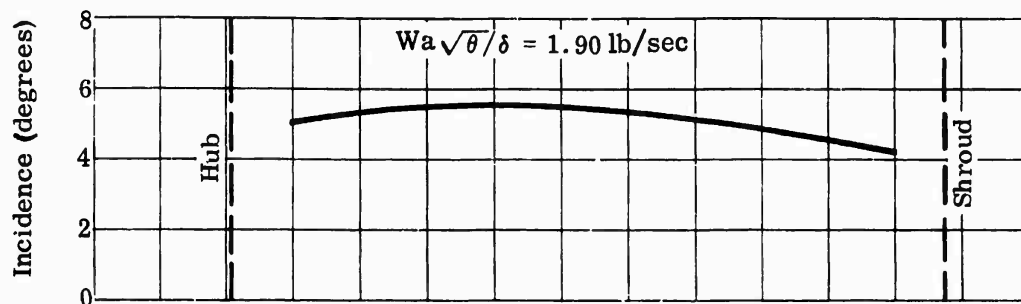
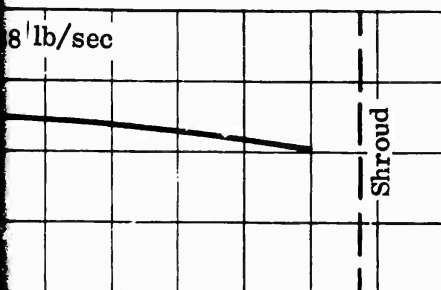
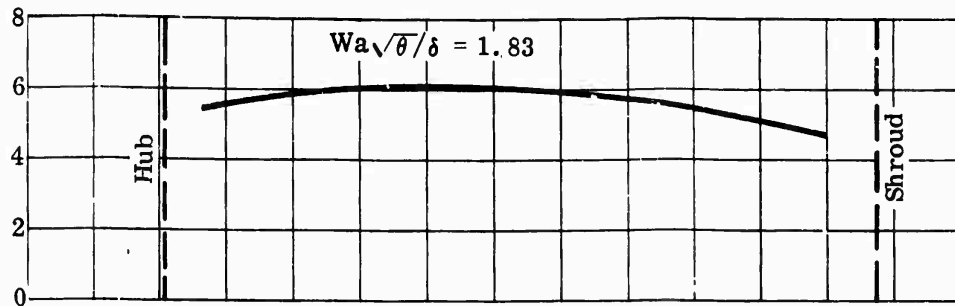
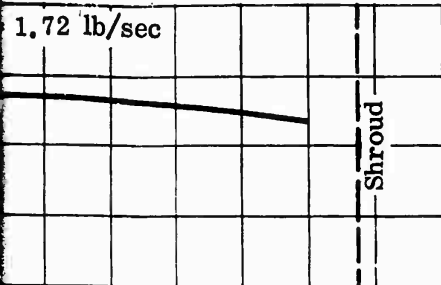
Figure 241. Radial Variation of Inducer Incidence, MF-1, Vaneless Diffuser.

CONFIDENTIAL

$N\sqrt{\theta} = 51,500 \text{ rpm}$



$$N\sqrt{\theta} = 57,000 \text{ rpm}$$



CONFIDENTIAL

Test 3402 A
 $N/\sqrt{\theta} = 34,000 \text{ rpm}$

Corrected to Ambient
Conditions of:
60°F
29.92 in. Hg

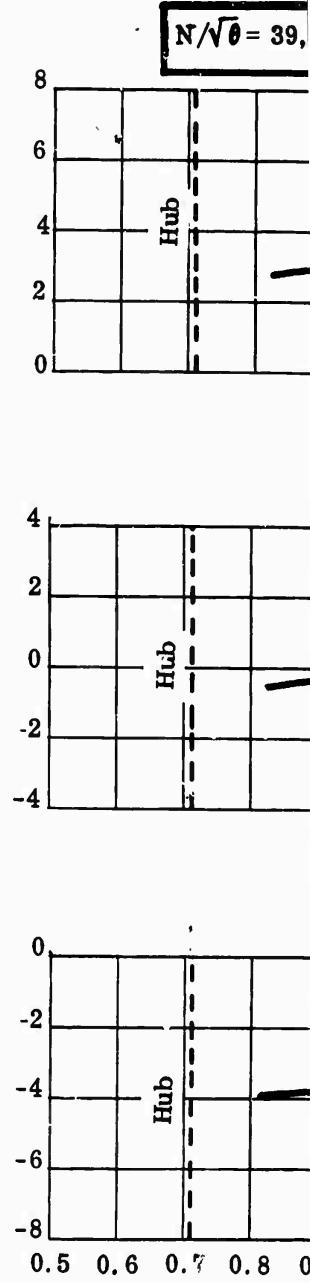
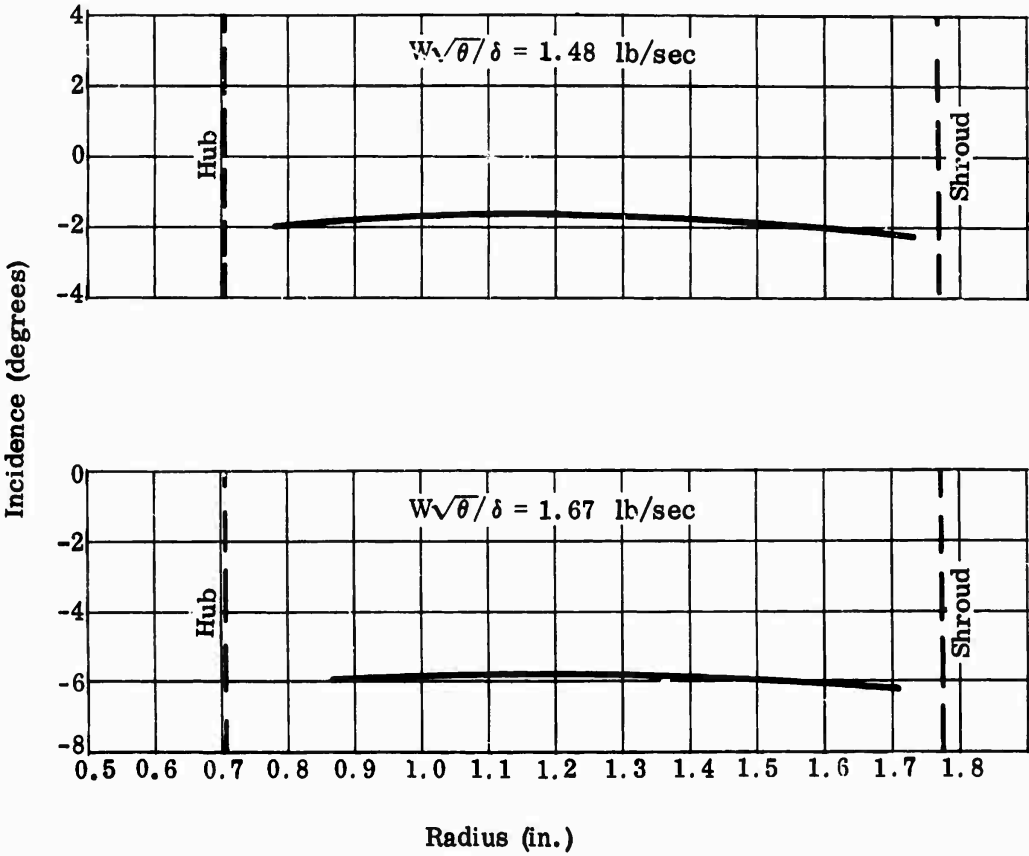
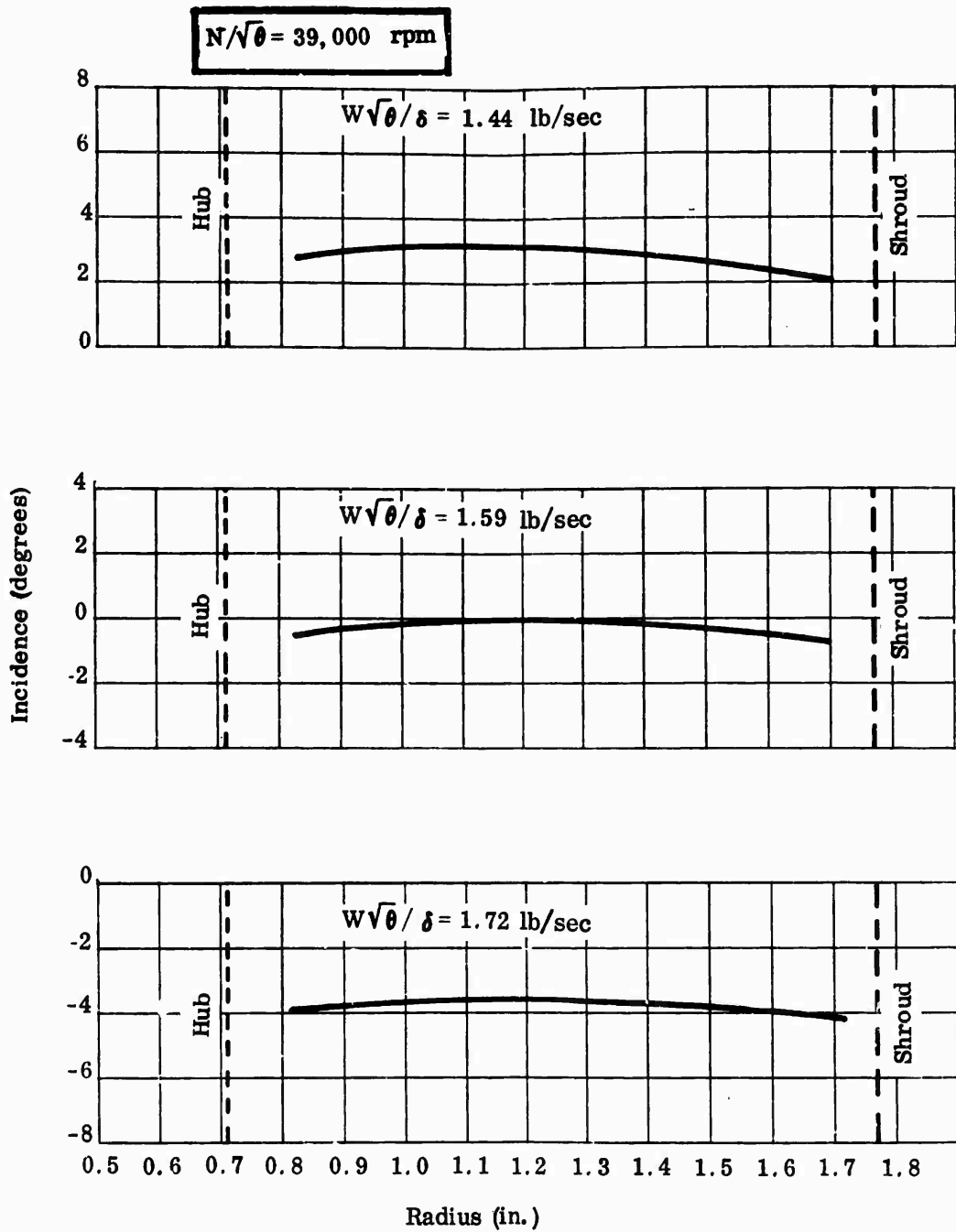
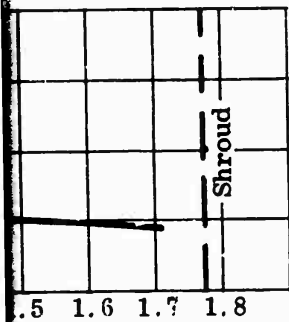
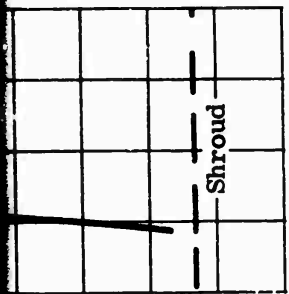


Figure 242. Radial Variation of Inducer Incidence, MF-1, Vaneless Diffuser.

CONFIDENTIAL

1

Ambient
n. Hg



, Vaneless Diffuser.

CONFIDENTIAL

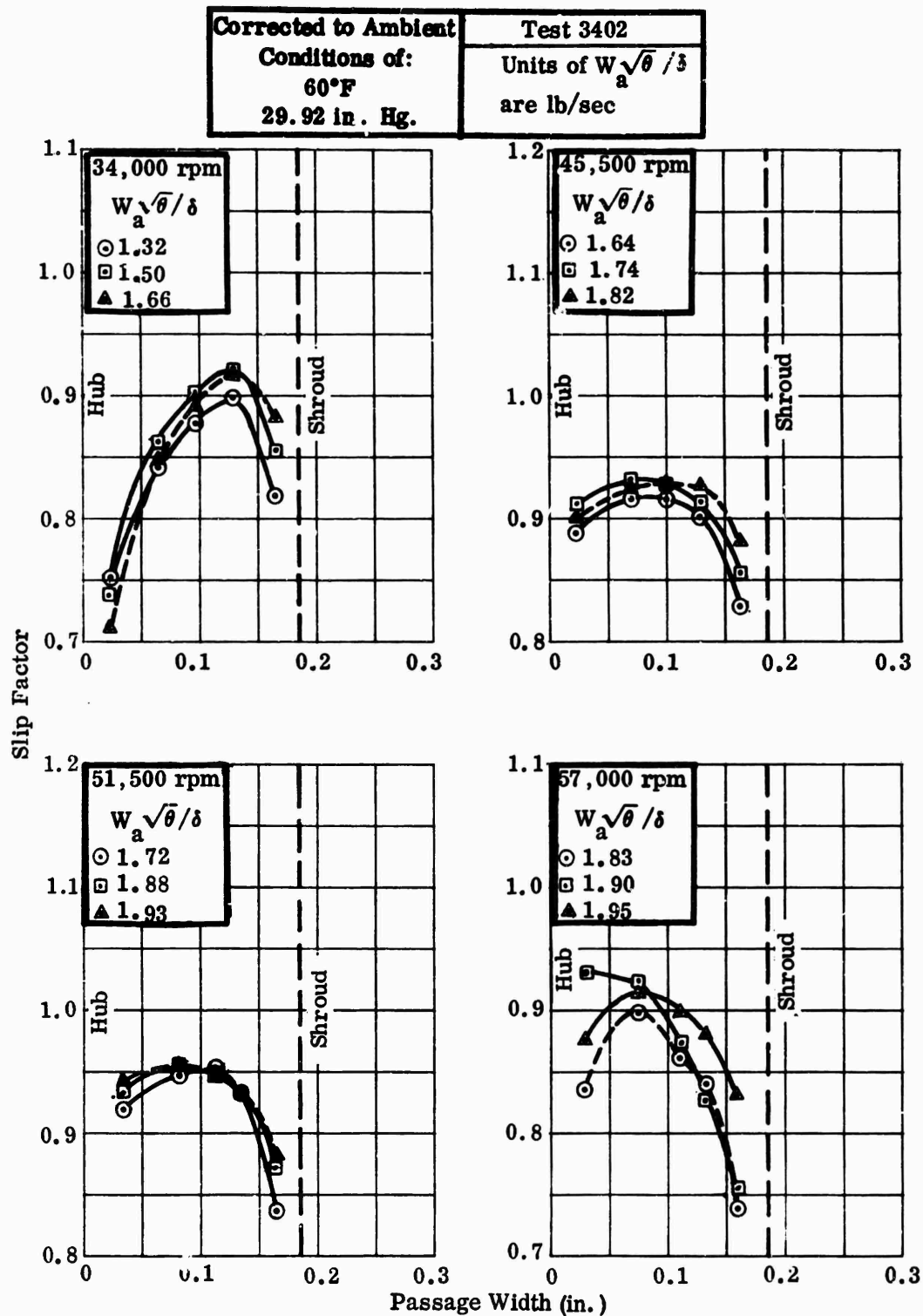


Figure 243. Slip Factor Versus Passage Width, MF-1, Vaneless Diffuser.

CONFIDENTIAL

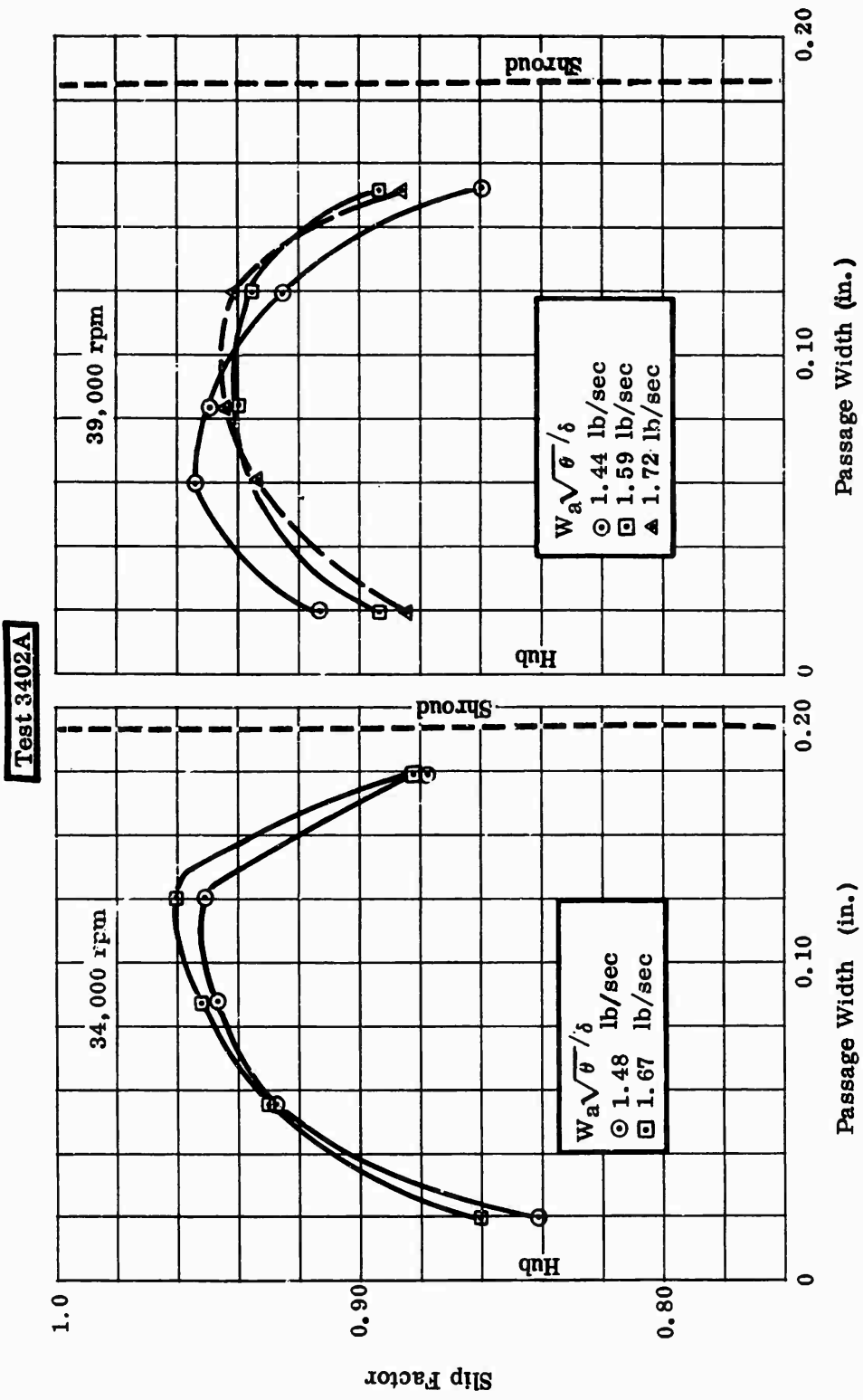


Figure 244. Slip Factor Versus Passage Width, MF-1, Vaneless Diffuser.

CONFIDENTIAL

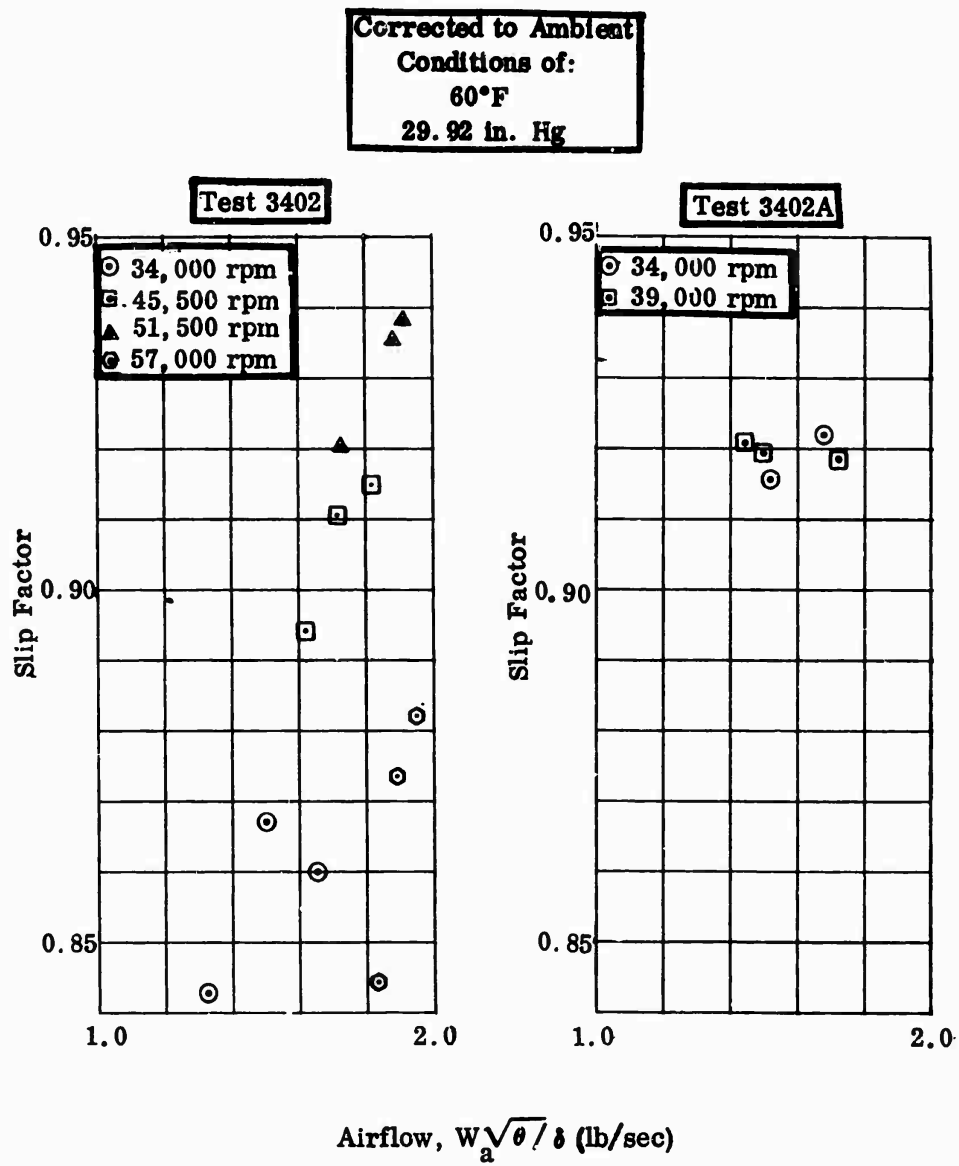


Figure 245. Slip Factor Versus Airflow, MF-1, Vaneless Diffuser.

CONFIDENTIAL

CONFIDENTIAL

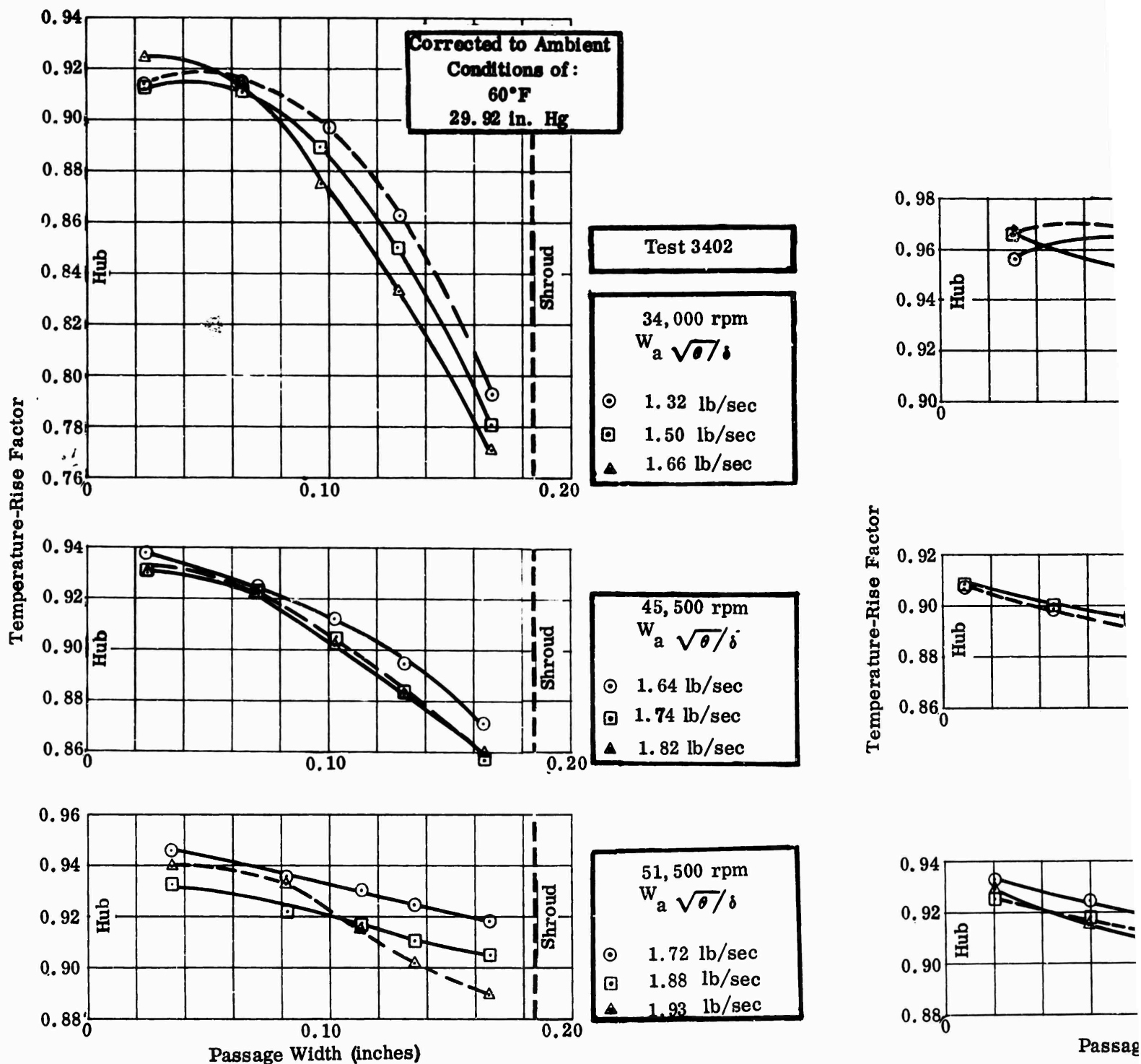


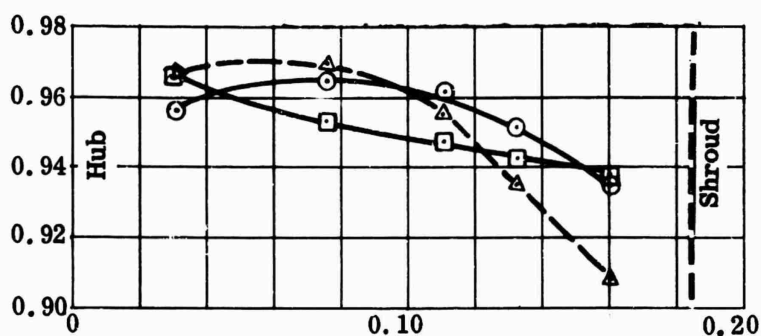
Figure 246. Temperature-Rise Factor Versus Passage Width, MF-1, Vaneless Diffuser.

CONFIDENTIAL

Test 3402

34,000 rpm
 $W_a \sqrt{\theta/\delta}$

- 1.32 lb/sec
- 1.50 lb/sec
- ▲ 1.66 lb/sec



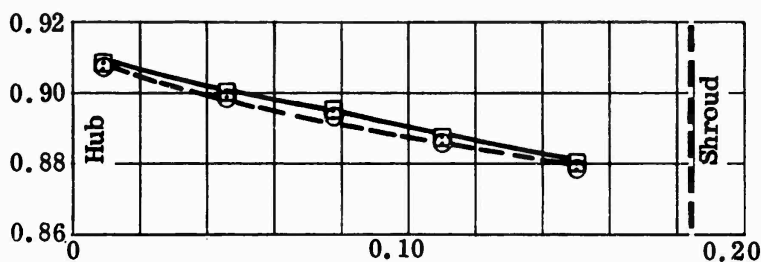
Test 3402

57,000 rpm

$W_a \sqrt{\theta/\delta}$

- 1.83 lb/sec
- 1.90 lb/sec
- ▲ 1.95 lb/sec

Temperature-Rise Factor



Test 3402A

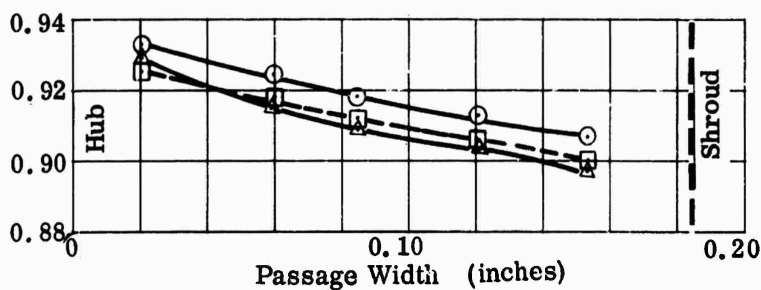
34,000 rpm

$W_a \sqrt{\theta/\delta}$

- 1.48 lb/sec
- 1.67 lb/sec

51,500 rpm
 $W_a \sqrt{\theta/\delta}$

- 1.72 lb/sec
- 1.88 lb/sec
- ▲ 1.93 lb/sec



Test 3402A

39,000 rpm

$W_a \sqrt{\theta/\delta}$

- 1.44 lb/sec
- 1.59 lb/sec
- ▲ 1.72 lb/sec

Passage Width (inches)

Width, MF-1,

CONFIDENTIAL

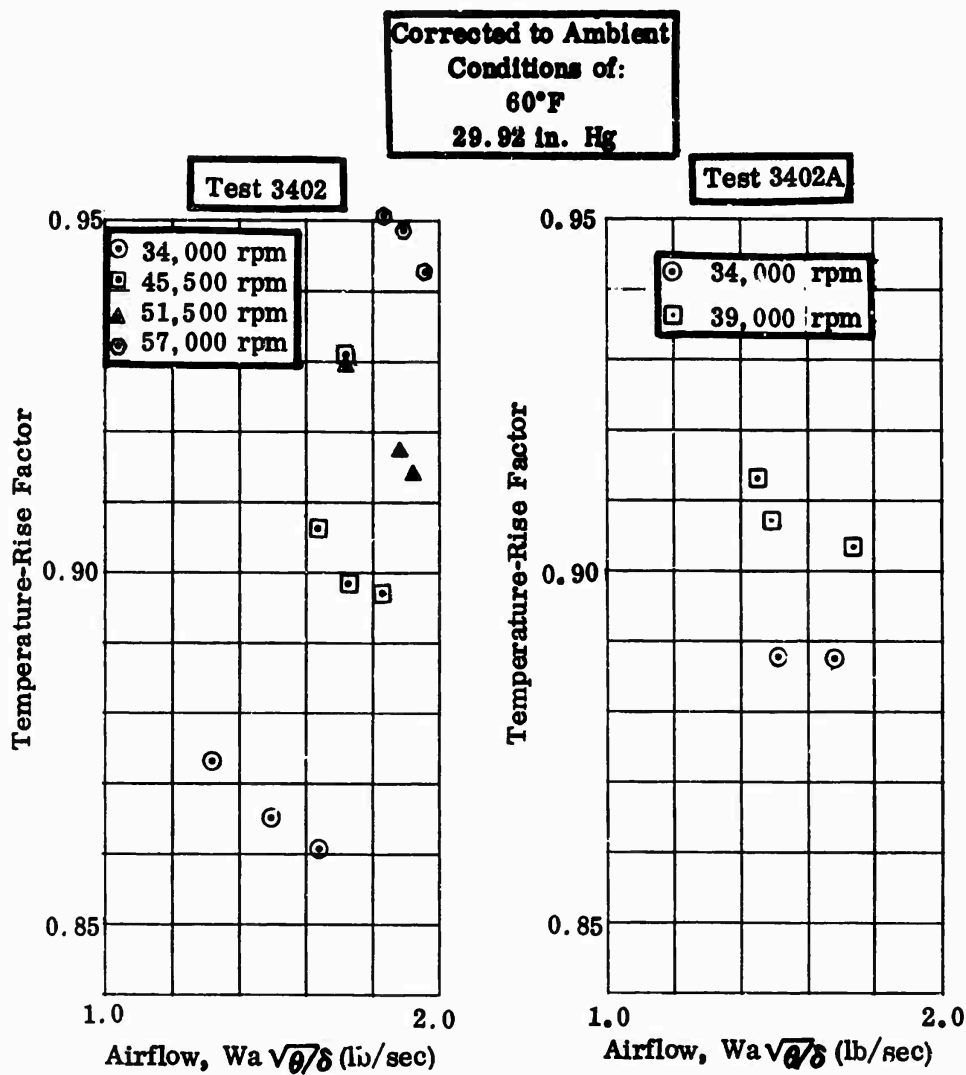


Figure 247. Temperature-Rise Factor Versus Airflow, MF-1, Vaneless Diffuser.

CONFIDENTIAL

CONFIDENTIAL

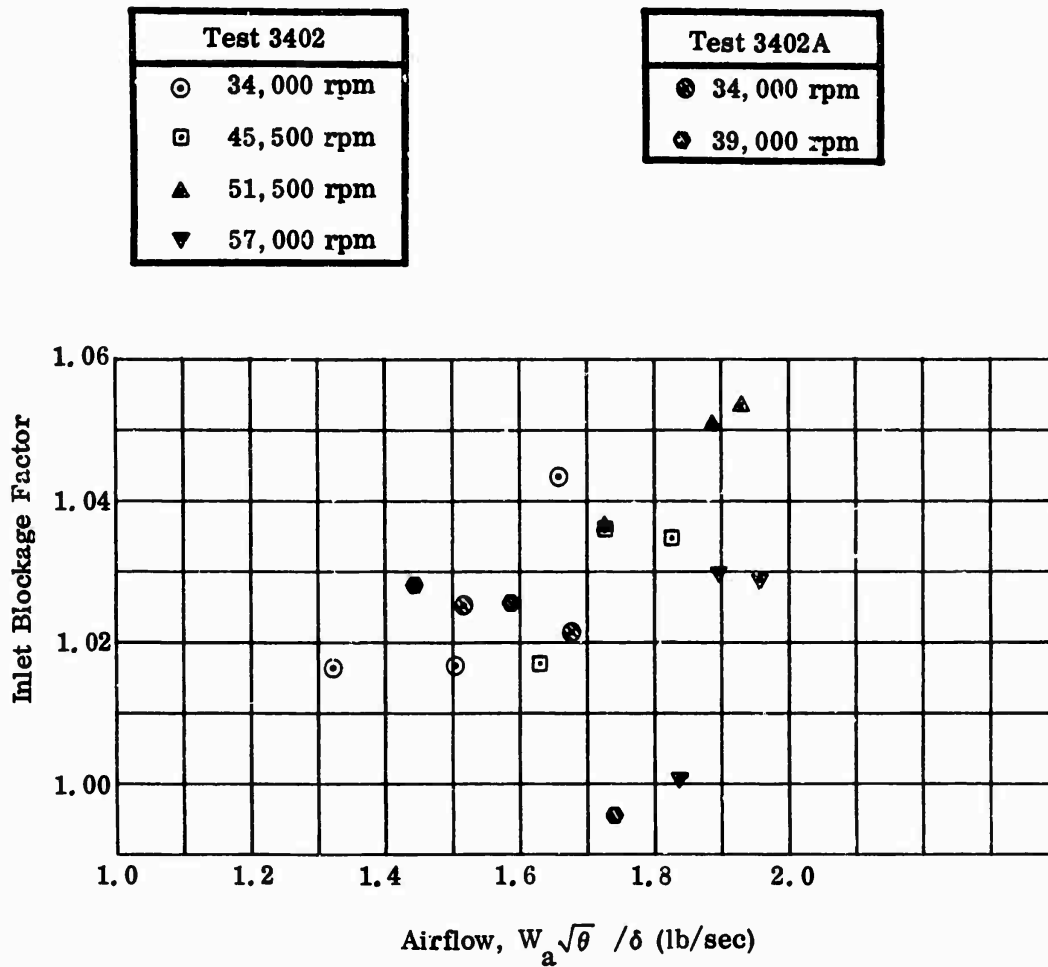


Figure 248. Inlet Blockage Factor Versus Airflow,
MF-1, Vaneless Diffuser.

CONFIDENTIAL

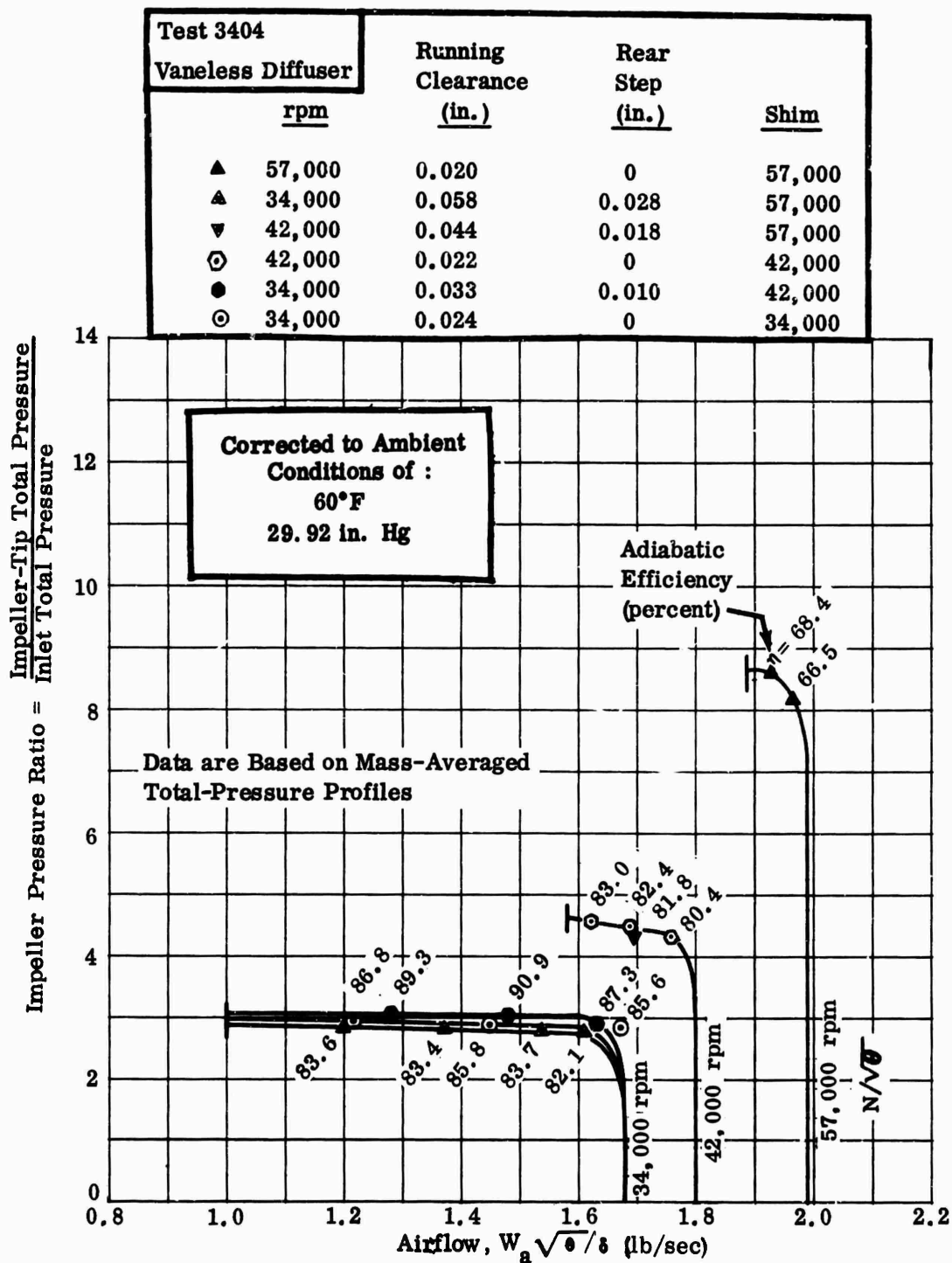


Figure 249. Pressure Ratio Versus Airflow, RF-1.

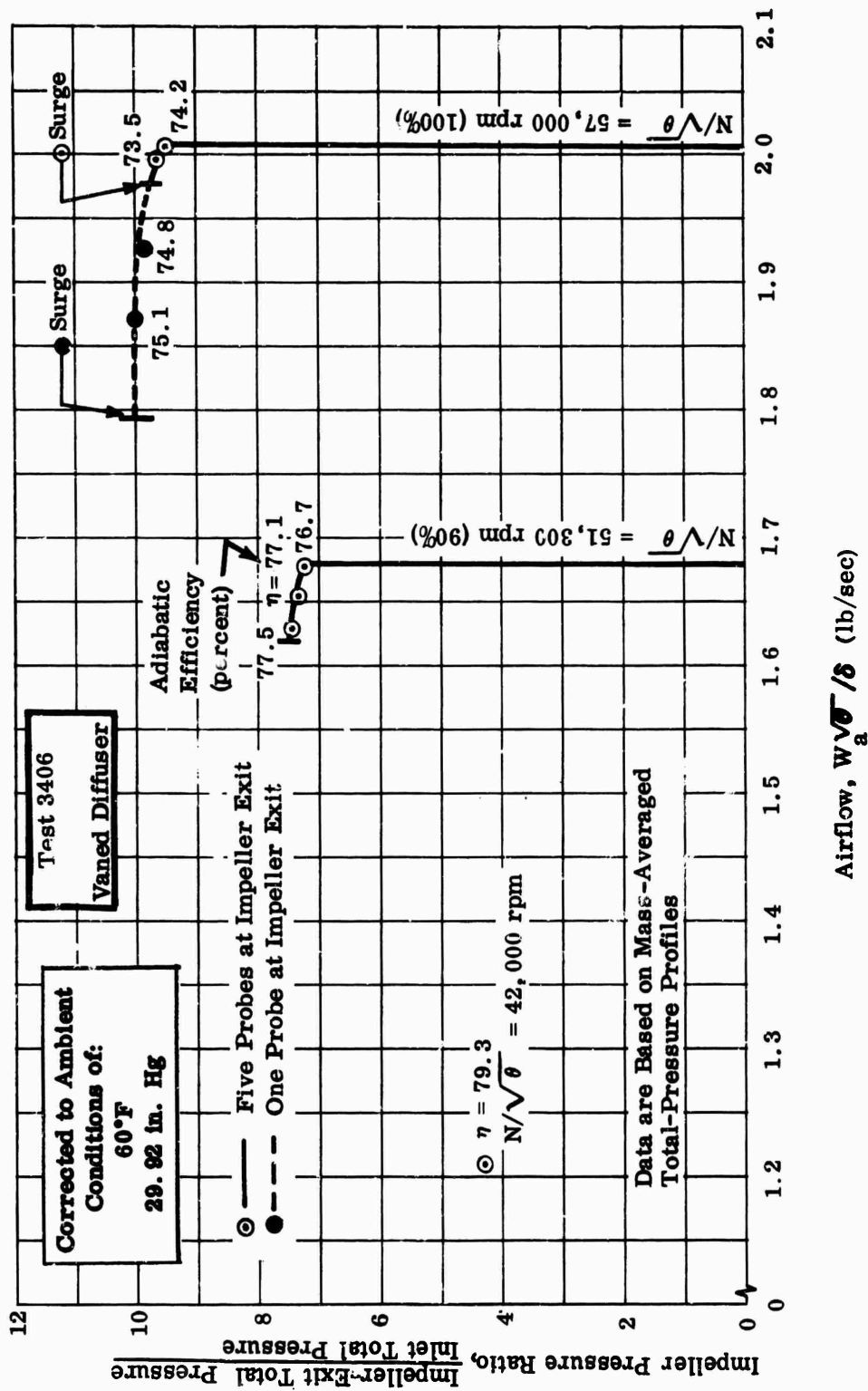


Figure 250. Pressure Ratio Versus Airflow, RF-1.

CONFIDENTIAL

	Test	rpm	Running Clearance (in.)	Rear Step (in.)	Shimmed for (rpm)	Diffuser
▲	3404	57,000	0.020	0	57,000	Vaneless
▲	3404	34,000	0.058	0.028	57,000	Vaneless
▼	3404	42,000	0.044	0.018	57,000	Vaneless
□	3404	42,000	0.022	0	42,000	Vaneless
■	3404	34,000	0.033	0.010	42,000	Vaneless
○	3404	34,000	0.024	0	34,000	Vaneless
●	3406	42,000	0.032	0.007	57,000	Vaned
◆	3406	51,300	0.028	0.003	57,000	Vaned
◆	3406	57,000	0.025	0	57,000	Vaned

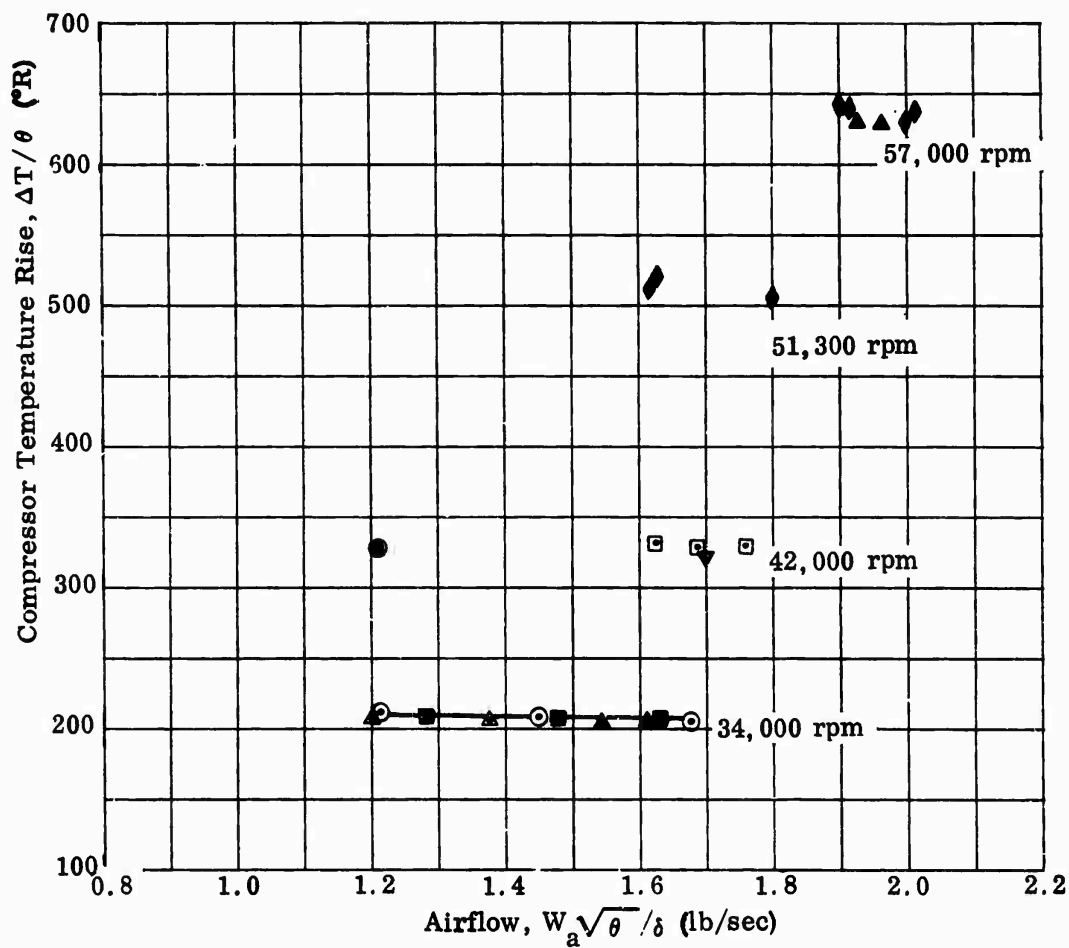


Figure 251. Compressor Temperature Rise Versus Airflow, RF-1.

CONFIDENTIAL

CONFIDENTIAL

Corrected to Ambient
Conditions of:
60°F
29.82 in. Hg

Test 3404
Vaneless Diffuser

$N/\sqrt{\theta} = 34,000 \text{ rpm}$

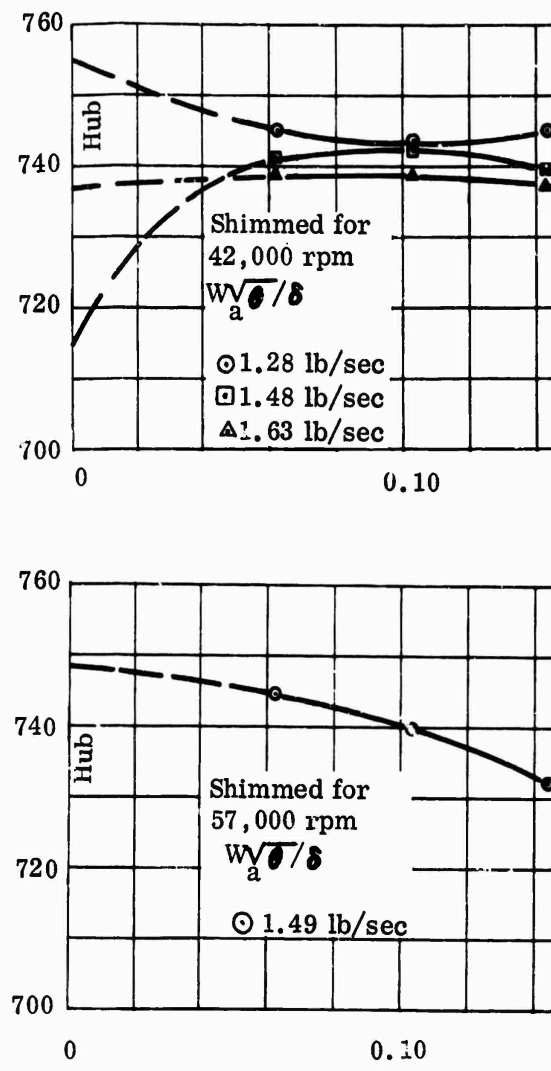
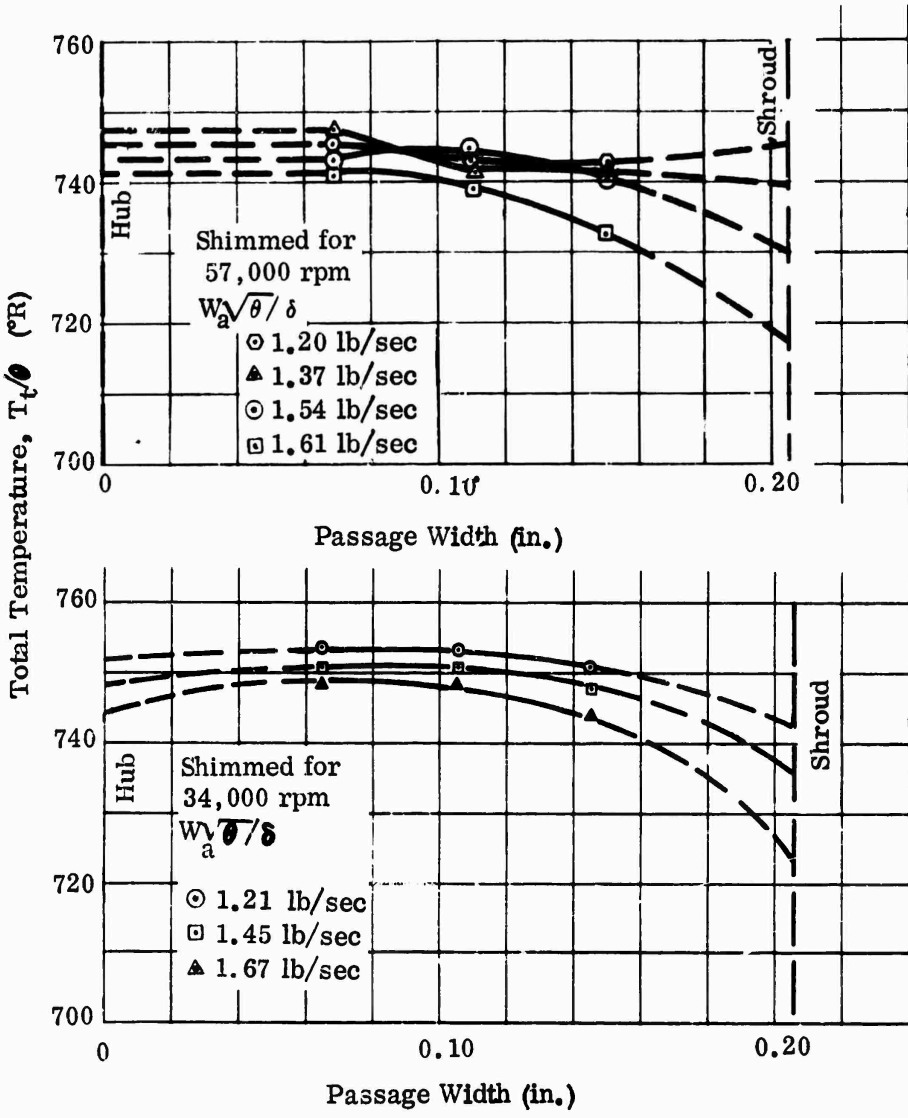
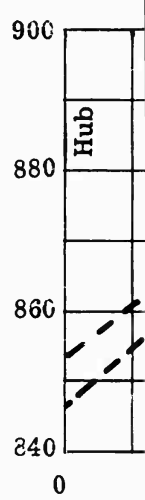
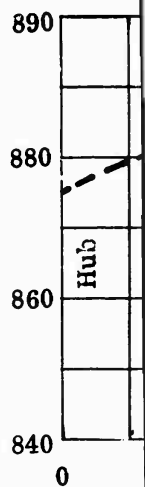
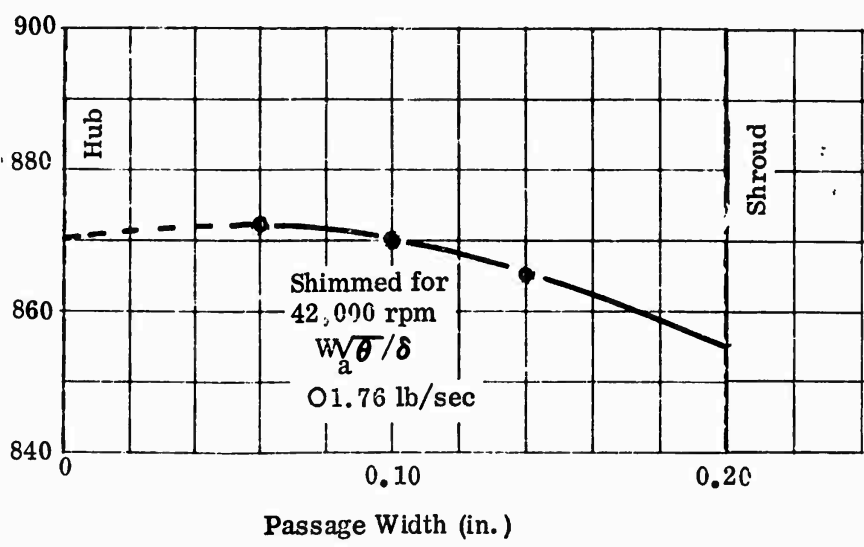
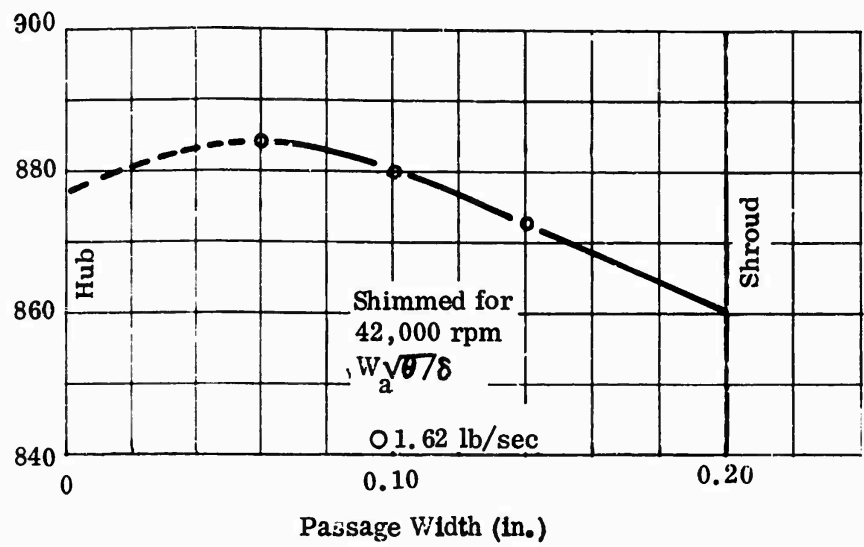


Figure 252. Impeller-Exit Total-Temperature Survey, RF-1.

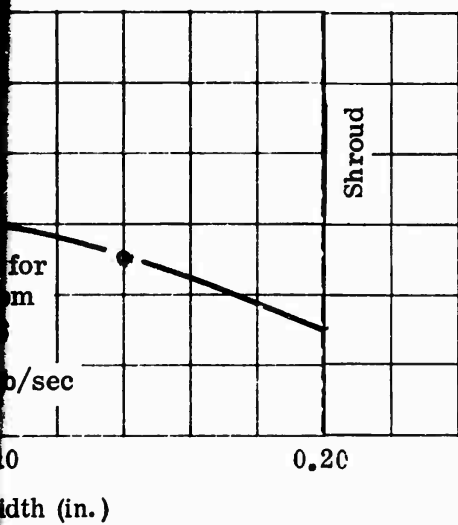
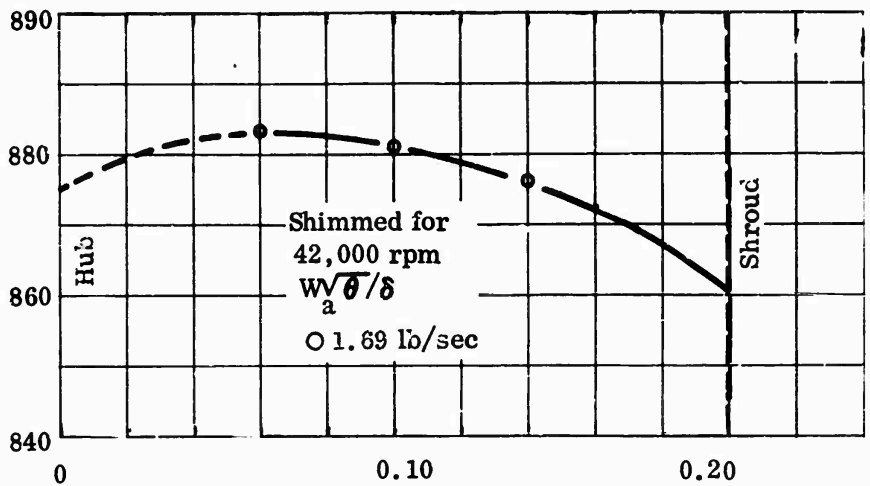
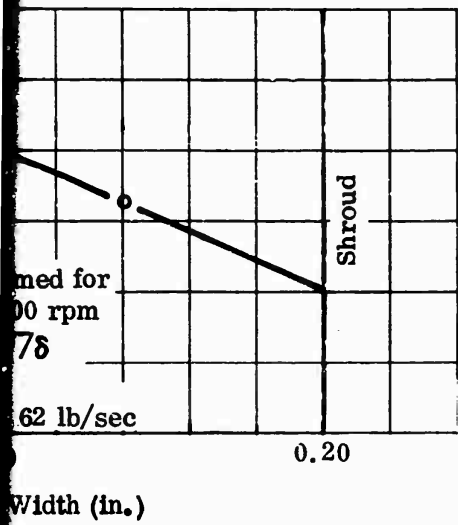
CONFIDENTIAL

1

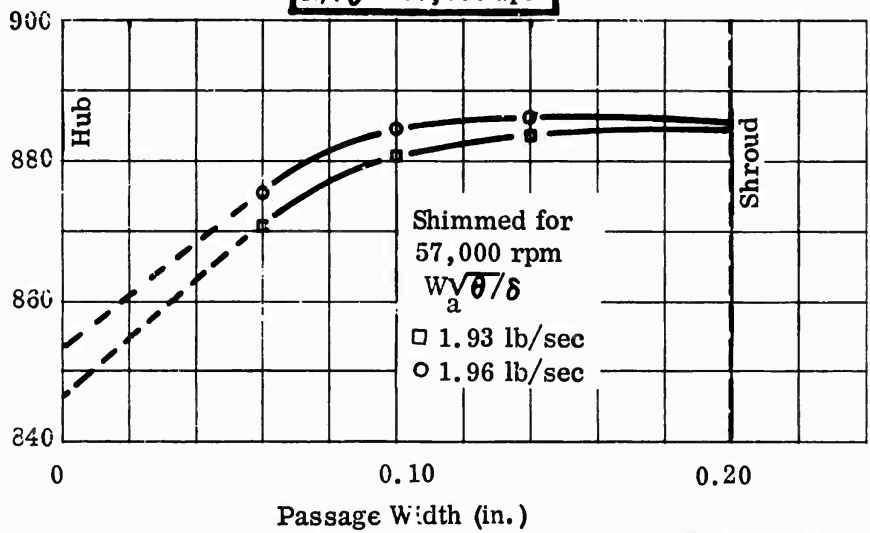
$$N/\sqrt{\theta} = 42,000 \text{ rpm}$$



$N/\sqrt{\theta} = 42,000 \text{ rpm}$



$N/\sqrt{\theta} = 57,000 \text{ rpm}$



CONFIDENTIAL

Corrected to Ambient
Conditions of :
60°F
29.92 in. Hg

□ T_{t1} at 1.034 Diameter Ratio
○ T_{t2} at 1.123 Diameter Ratio

Test 3406
Vaned Diffuser

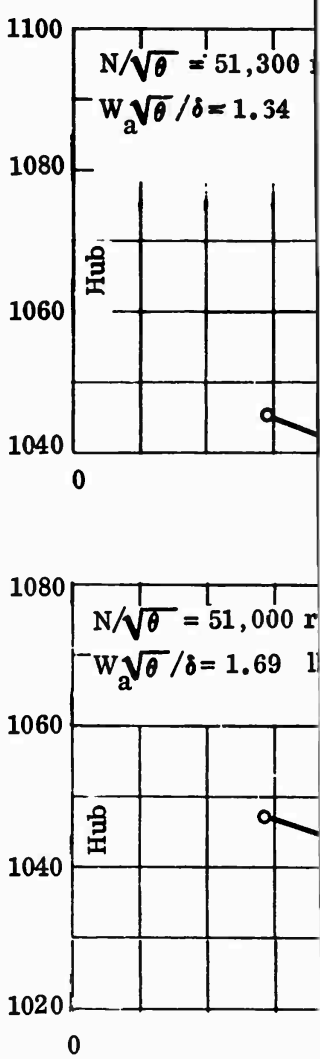
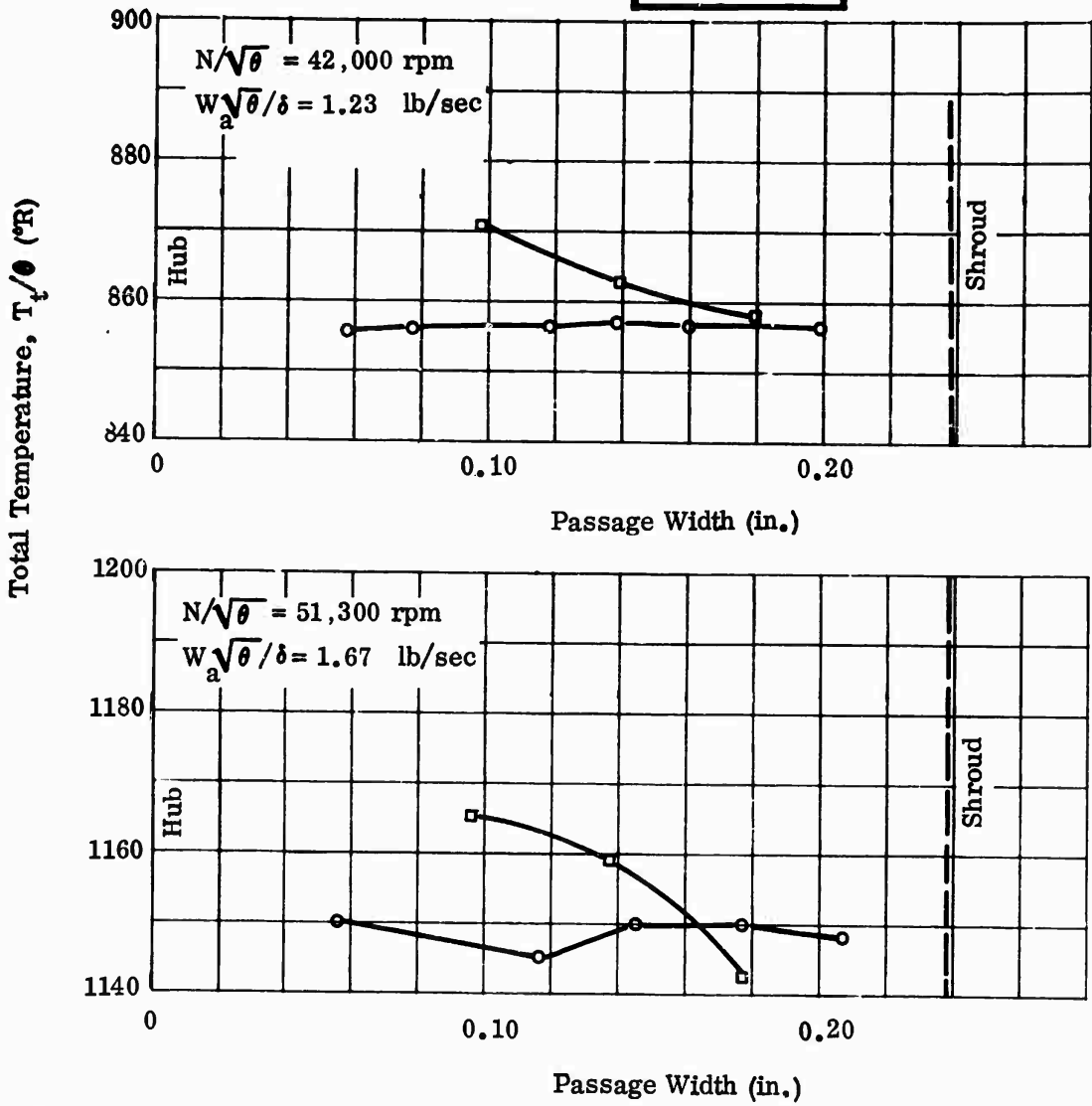
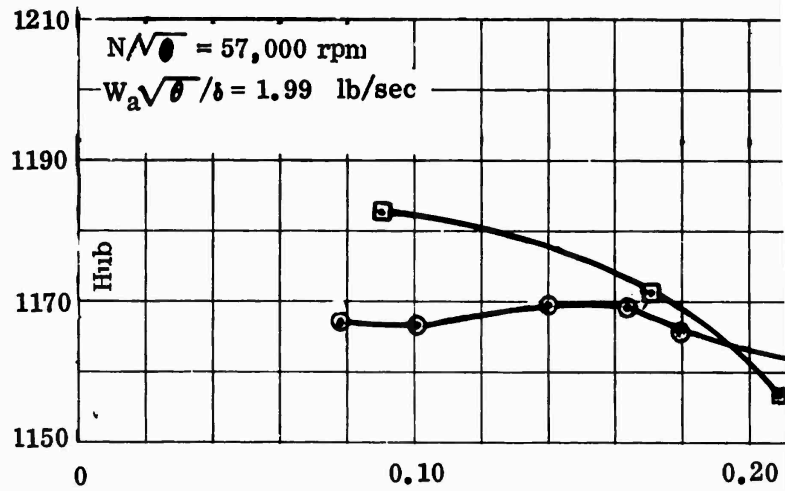
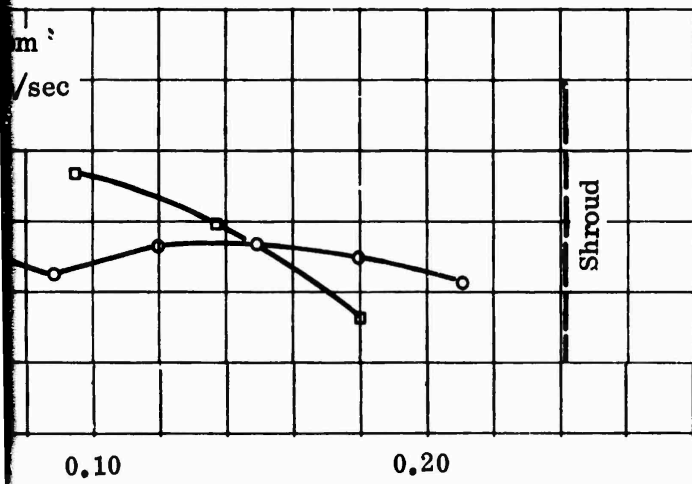
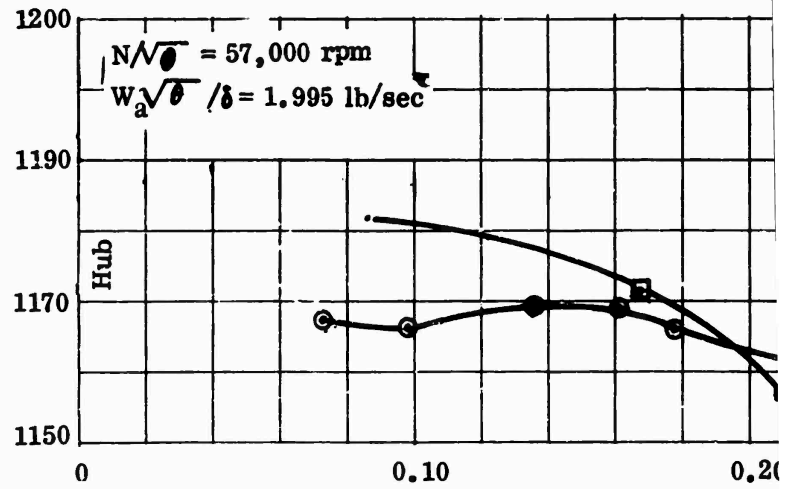
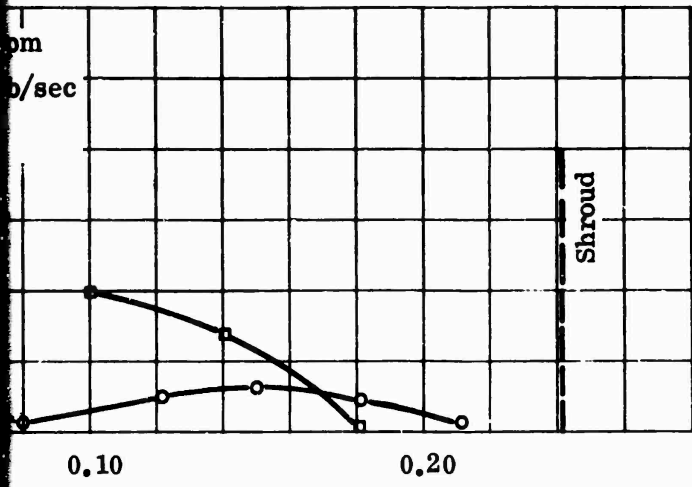
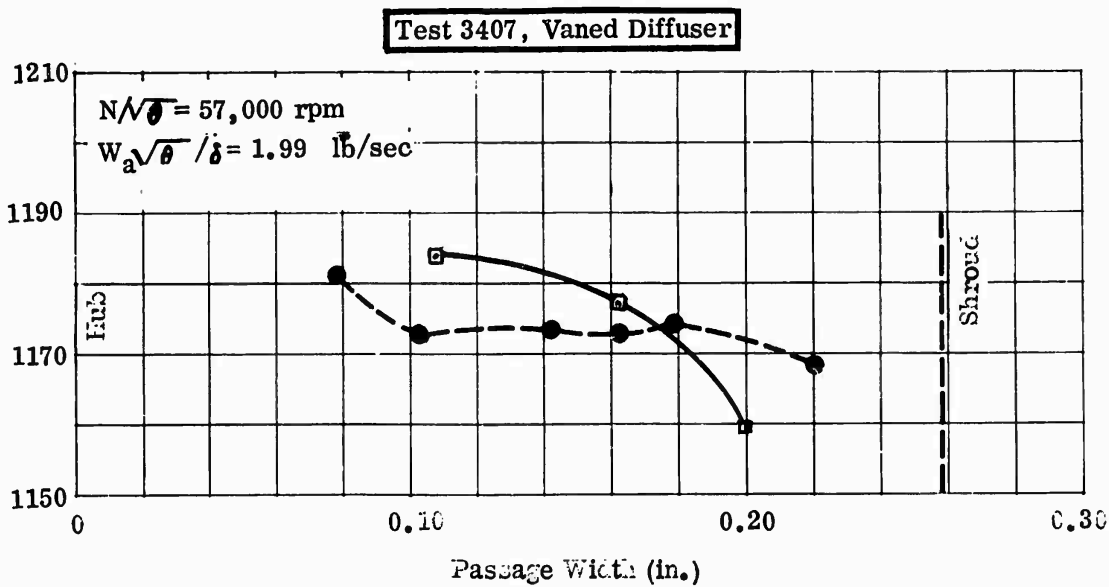
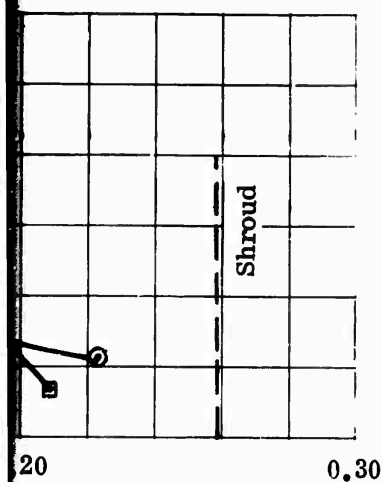
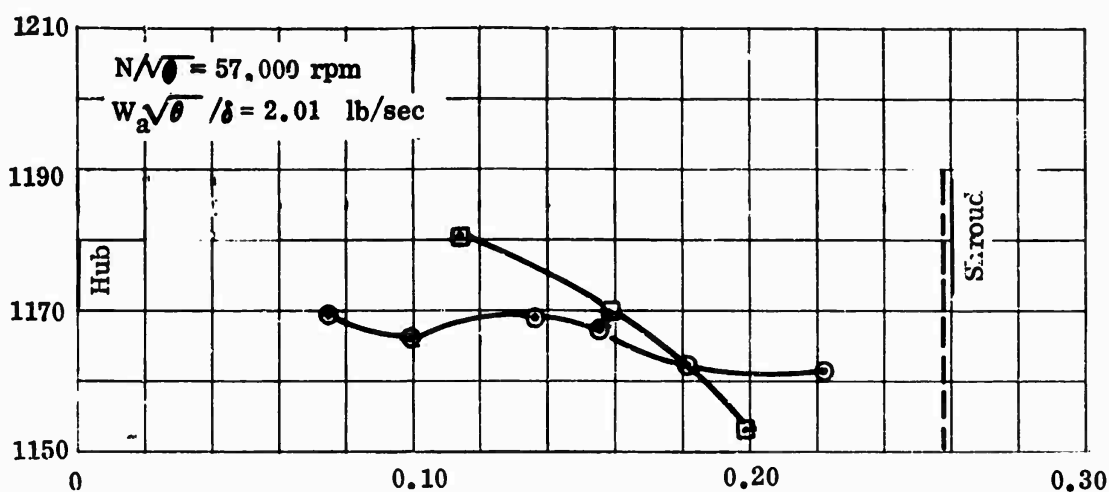
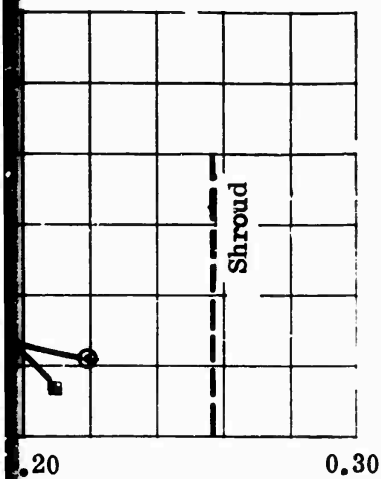


Figure 253. Impeller-Exit Total-Temperature Survey, RF-1.

CONFIDENTIAL

1



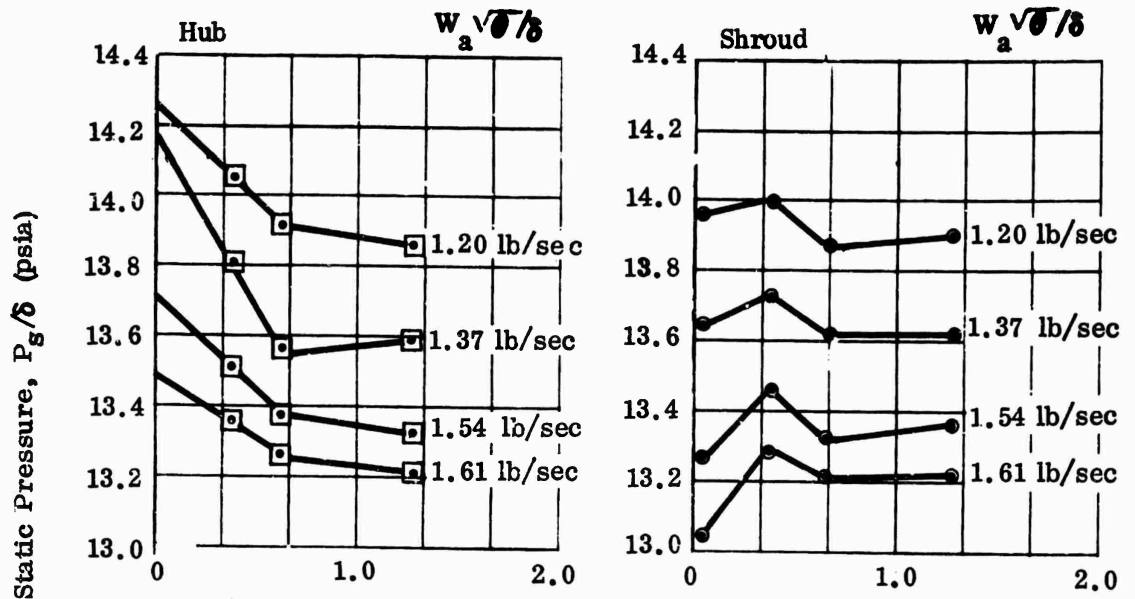


CONFIDENTIAL

Corrected to Ambient
Conditions of:
60°F
29.92 in. Hg

Test 3404
Vaneless Diffuser

$N/\sqrt{\theta} = 34,000$ rpm
Shimmed for 57,000 rpm



$N/\sqrt{\theta} = 34,000$ rpm
Shimmed for 57,000 rpm

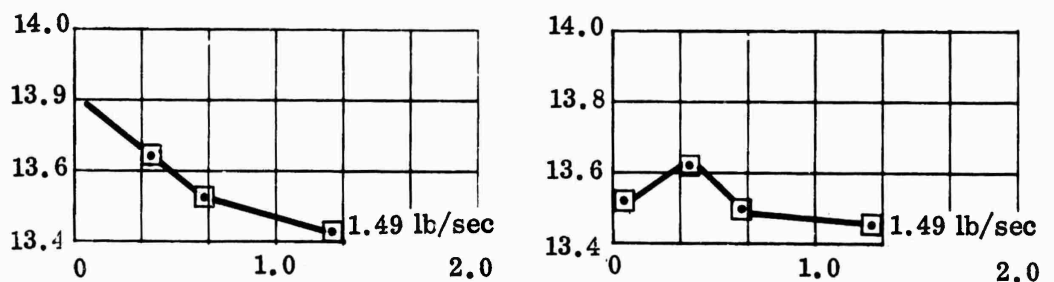
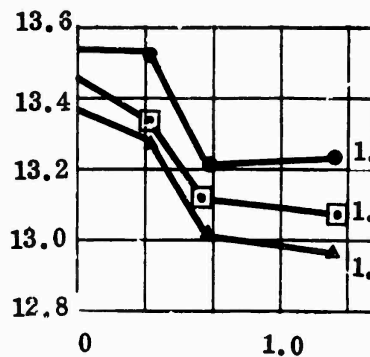
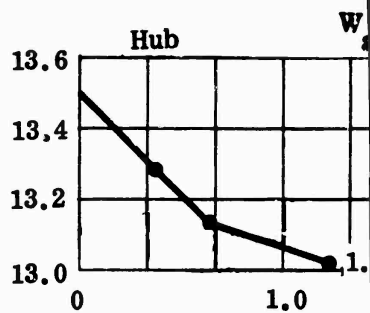
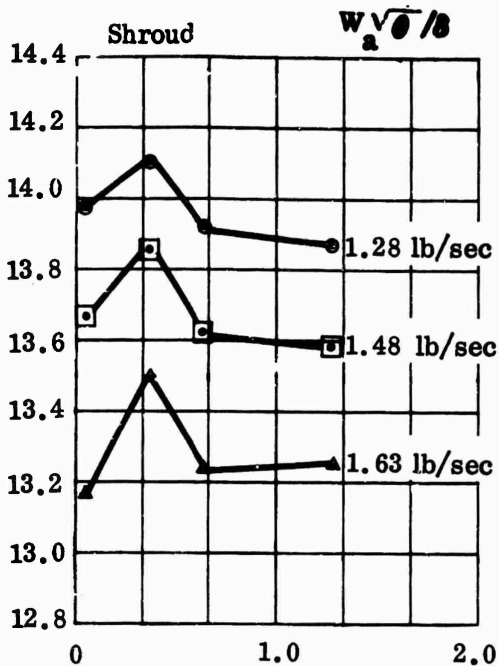
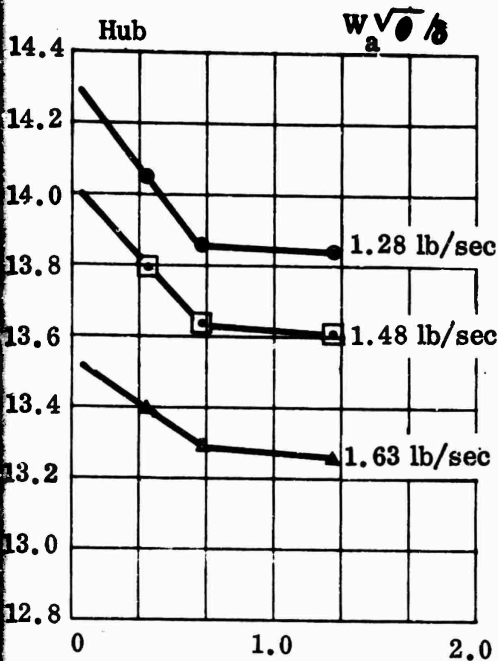


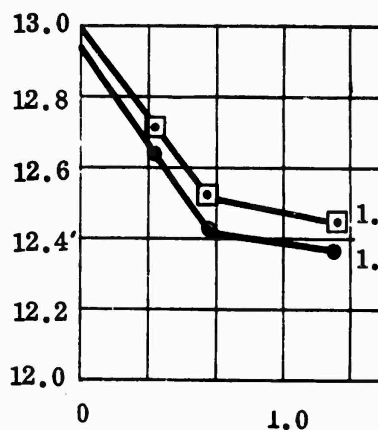
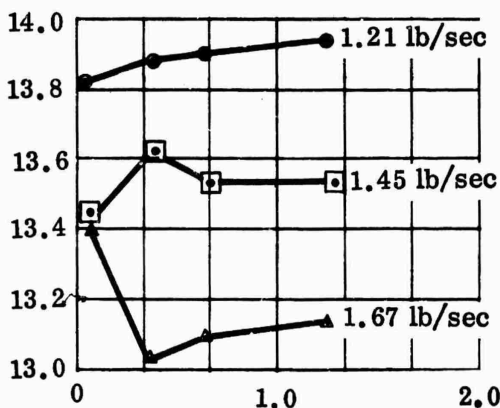
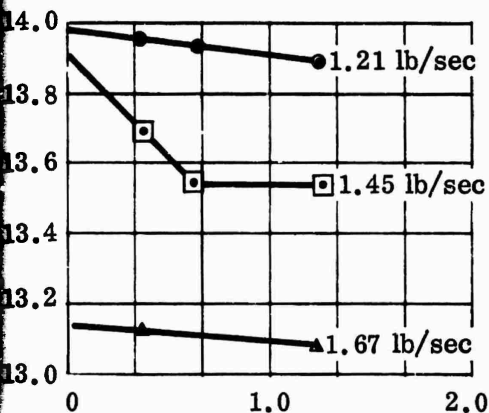
Figure 254. Inlet Duct Static Pressures, RF-1.

CONFIDENTIAL

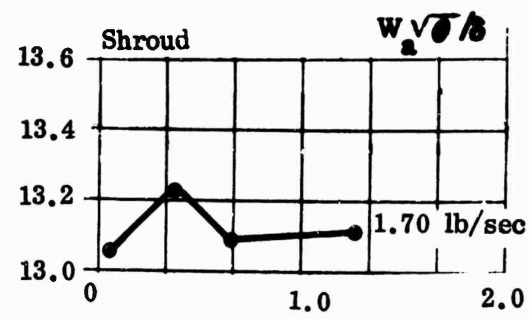
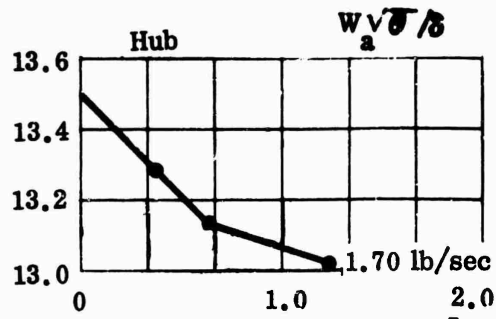
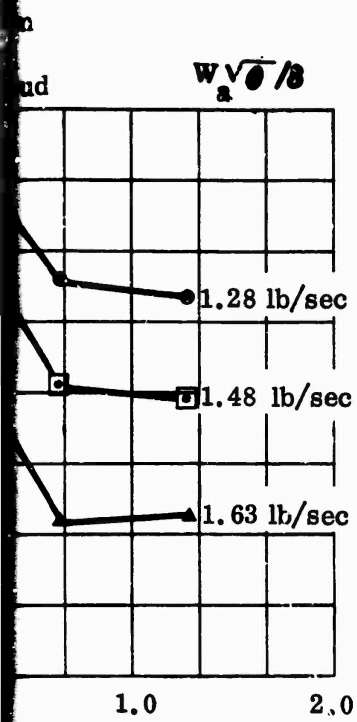
$N/\sqrt{\theta} = 34,000 \text{ rpm}$
 Shimmed for 42,000 rpm



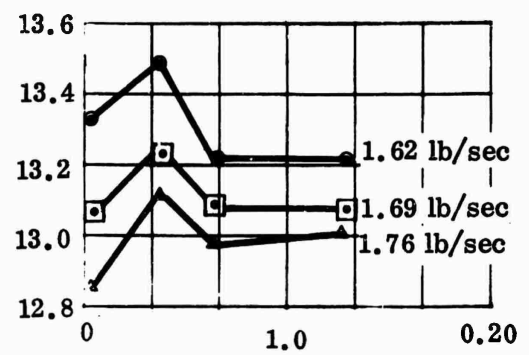
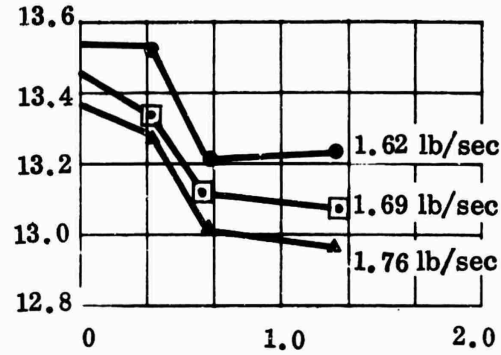
$N/\sqrt{\theta} = 34,000$
 Shimmed for 34,000 rpm



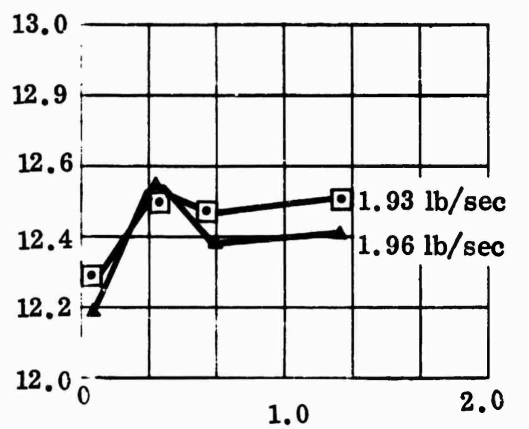
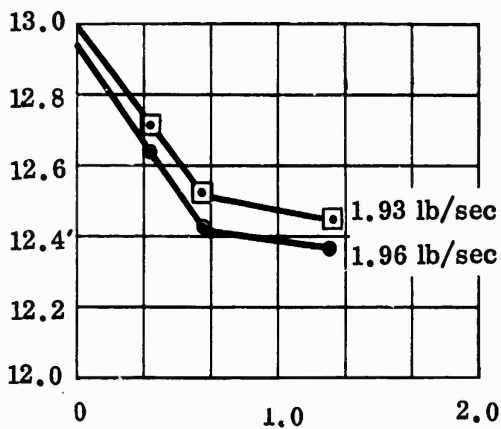
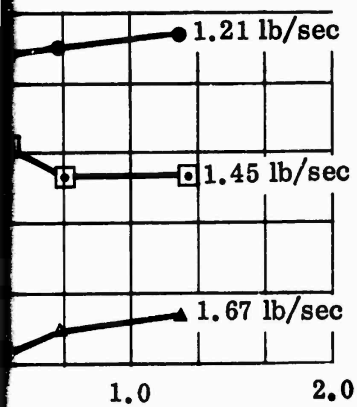
$N/\sqrt{\theta} = 42,000$ rpm
Shimmed for 57,000 rpm



$N/\sqrt{\theta} = 42,000$ rpm
Shimmed for 57,000 rpm



$N/\sqrt{\theta} = 57,000$ rpm
Shimmed for 57,000 rpm



Corrected to Ambient
Conditions of:
60°F
29.92 in. Hg

Test 3406
Vaned Diffuser

Static Pressure, P_g/δ (psia)

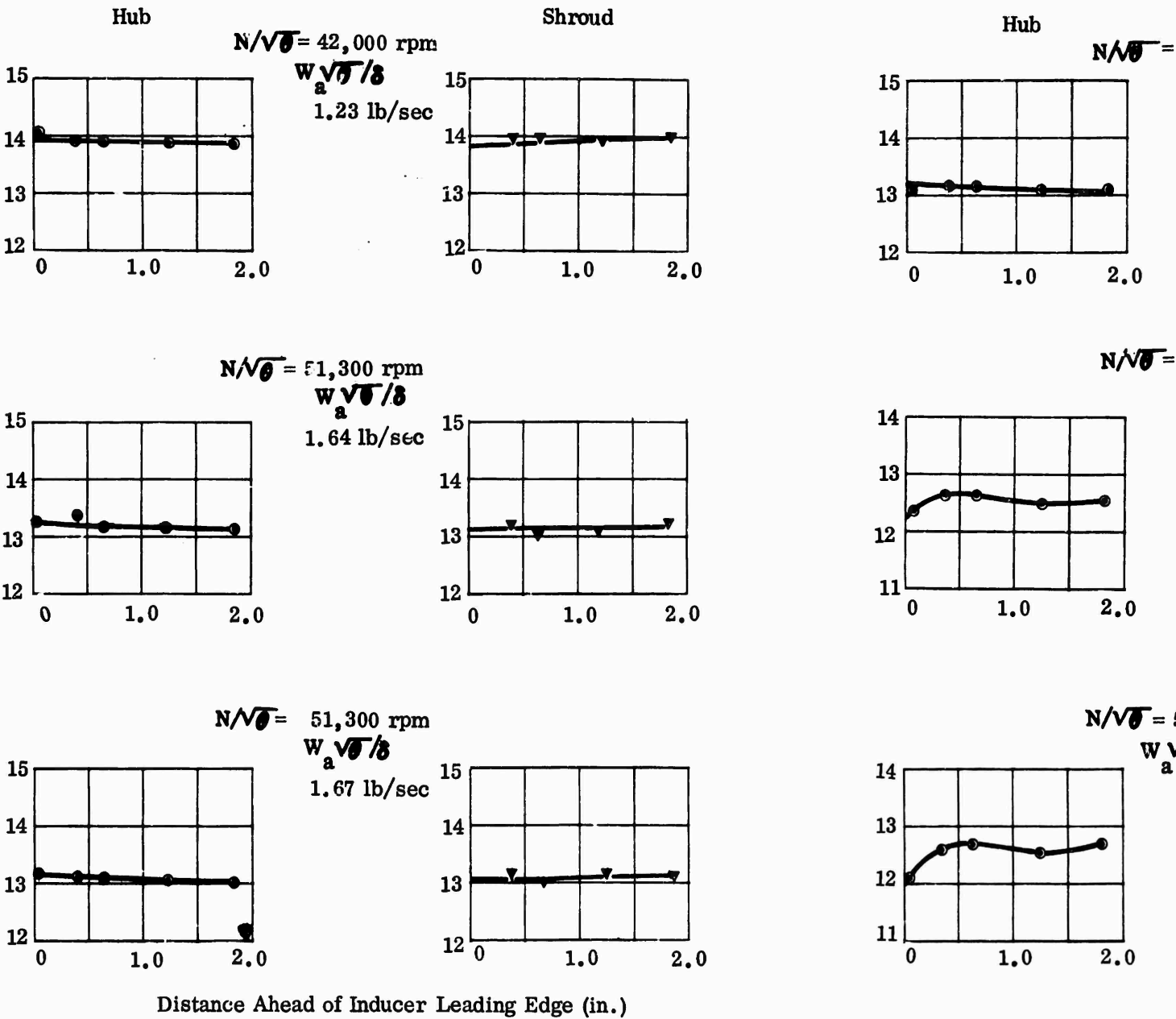


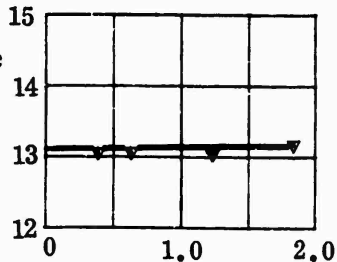
Figure 255. Inlet Duct Static Pressures, RF-1.

Shroud

51,300 rpm

$W_a \sqrt{\theta} / \delta$

1.69 lb/sec

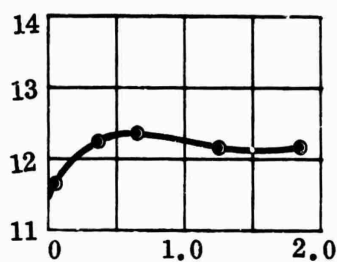


Hub

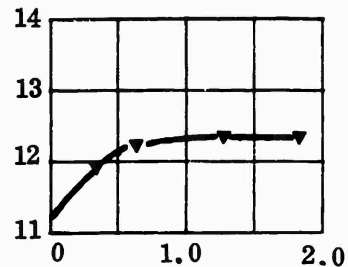
$N/\sqrt{\theta} = 57,000$ rpm

$W_a \sqrt{\theta} / \delta$

2.01 lb/sec



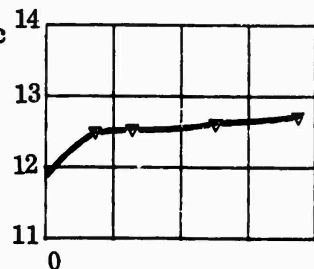
Shroud



57,000 rpm

$W_a \sqrt{\theta} / \delta$

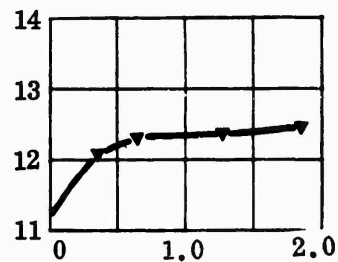
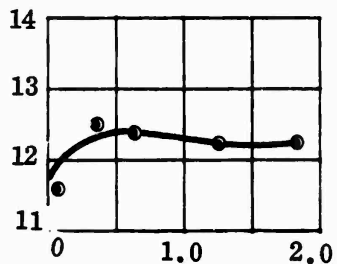
1.88 lb/sec



$N/\sqrt{\theta} = 57,000$ rpm

$W_a \sqrt{\theta} / \delta$

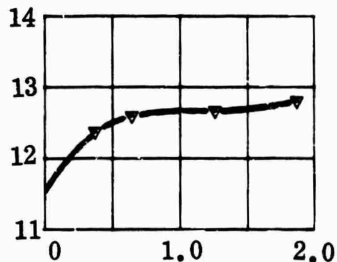
1.99 lb/sec



7,000 rpm

$W_a \sqrt{\theta} / \delta$

0.93 lb/sec



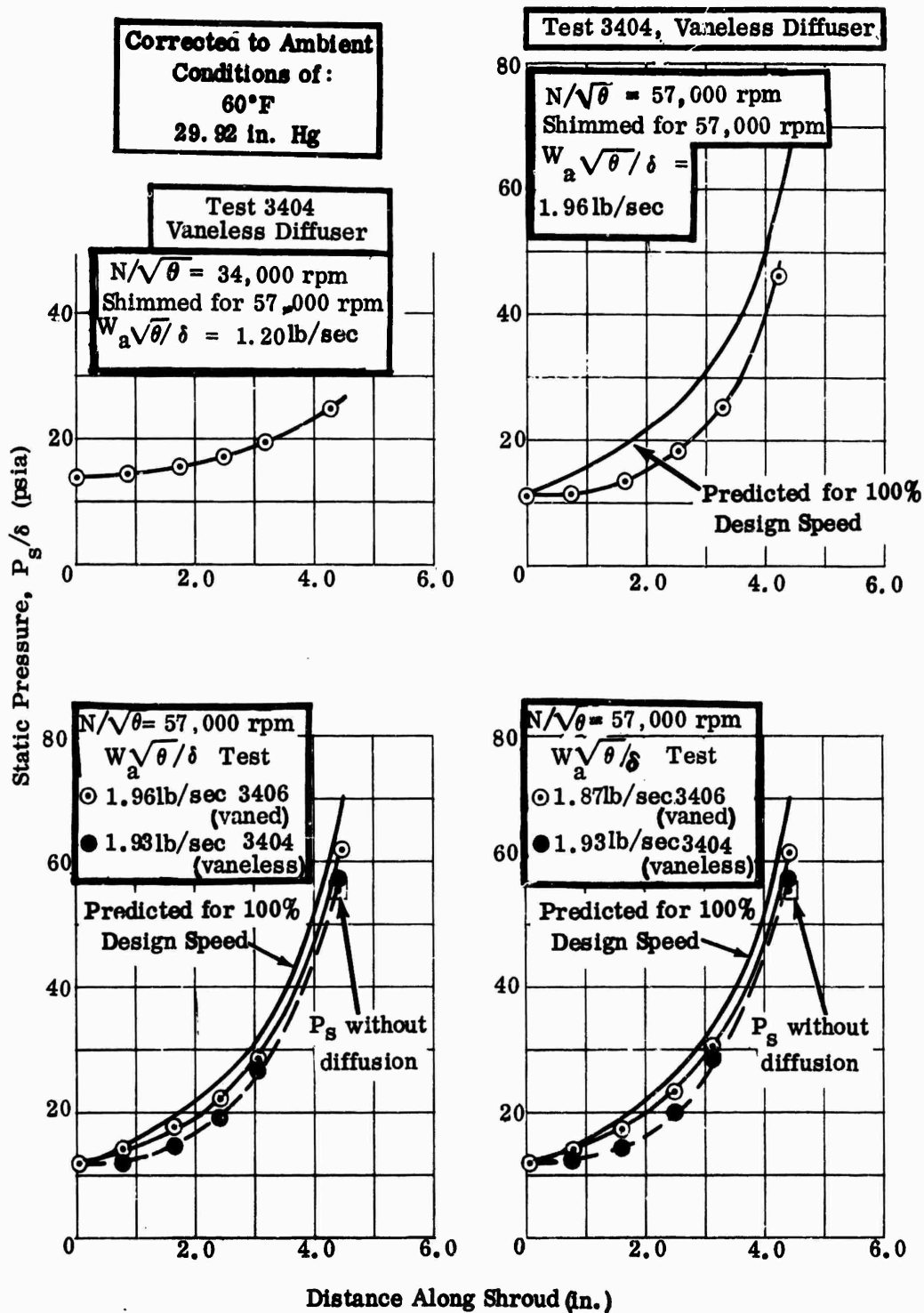


Figure 256. Static-Pressure Rise Along Shroud, RF-1.

CONFIDENTIAL

Corrected to Ambient
Conditions of:
60°F
29.92 in. Hg

Test 3404
Vaneless Diffuser

--- Shroud
— Hub

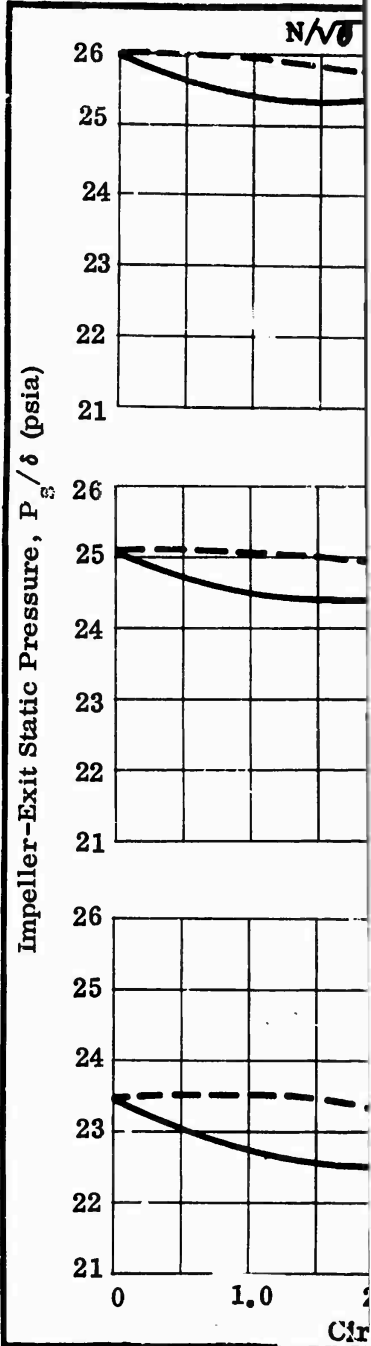
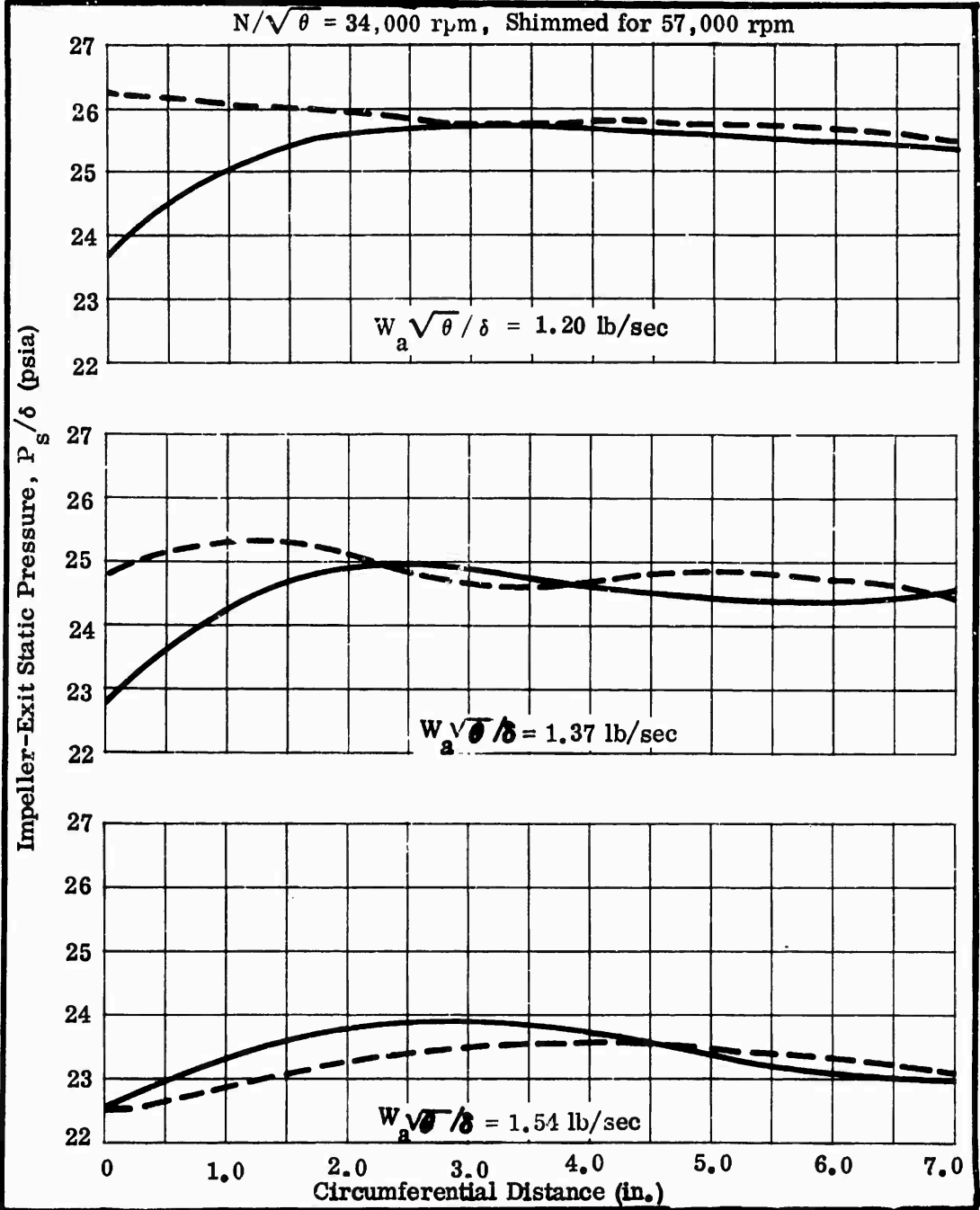


Figure 257. Impeller-Exit Static Pressure Versus Circumferential Distance, RF-1.

CONFIDENTIAL

1

$N/\sqrt{\theta}$ 34,000 rpm, Shimmed for 42,000 rpm

$$W_a \sqrt{\theta} / \delta = 1.28 \text{ lb/sec}$$

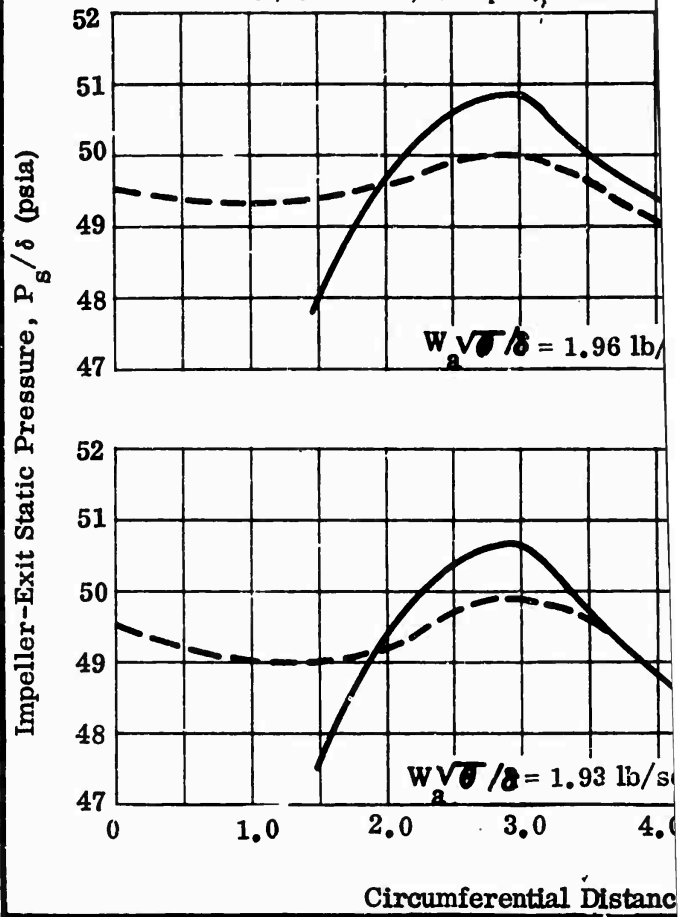
$$W_a \sqrt{\theta} / \delta = 1.48 \text{ lb/sec}$$

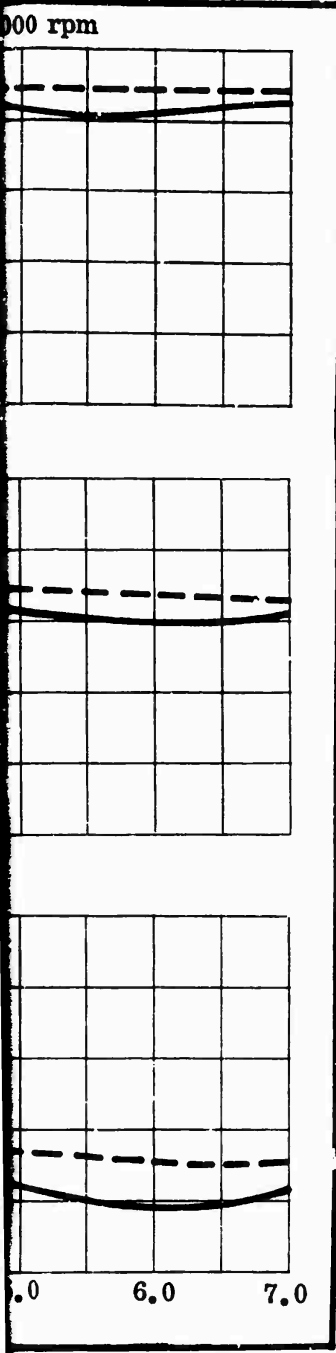
$$W_a \sqrt{\theta} / \delta = 1.63 \text{ lb/sec}$$

Circumferential Distance (in.)

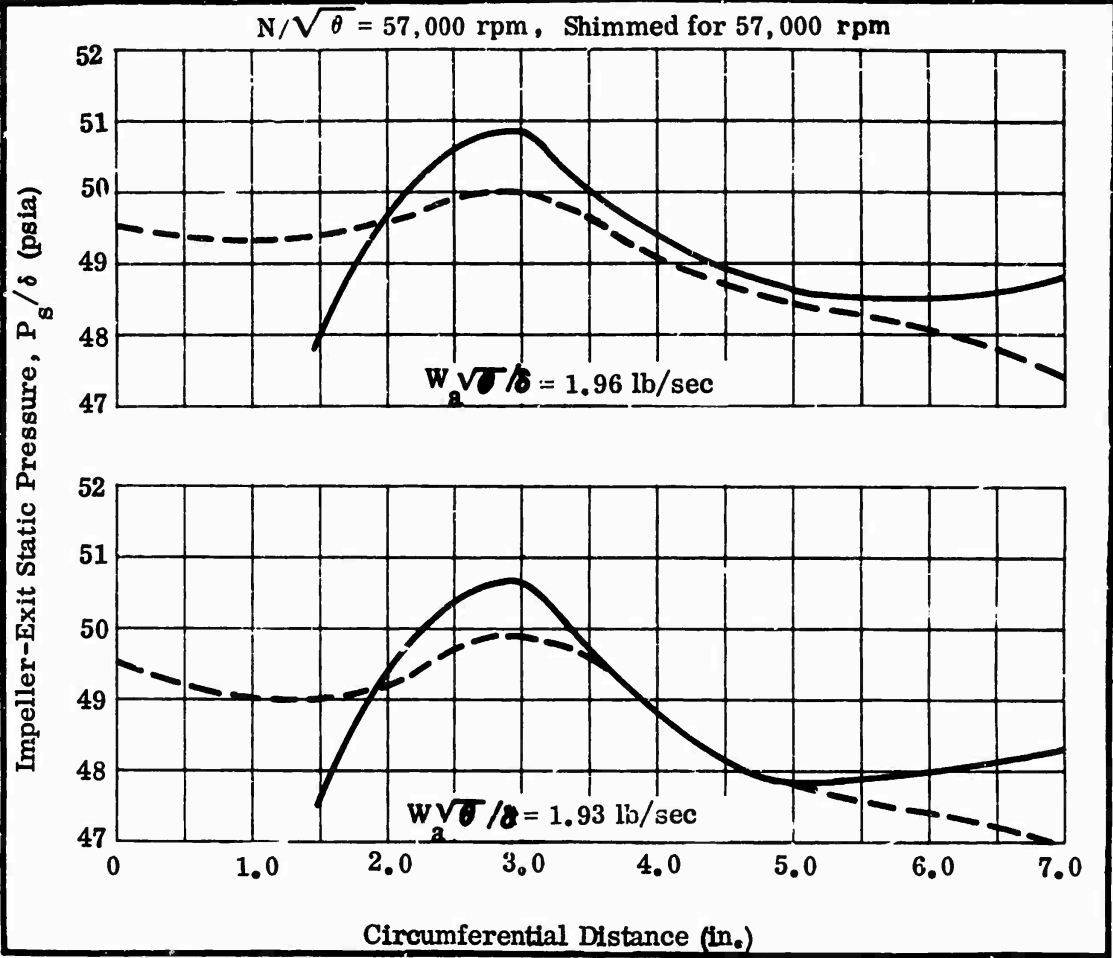
E

$N/\sqrt{\theta} = 57,000 \text{ rpm, Shimmed}$





E



CONFIDENTIAL

Corrected to Ambient
Conditions of:
60°F
29.92 in. Hg

Test 3404
Vaneless Diffuser

----- Shroud
————— Hub

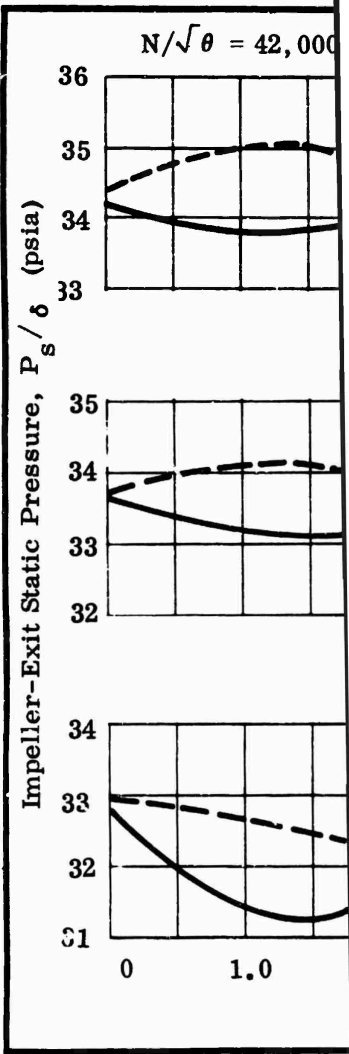
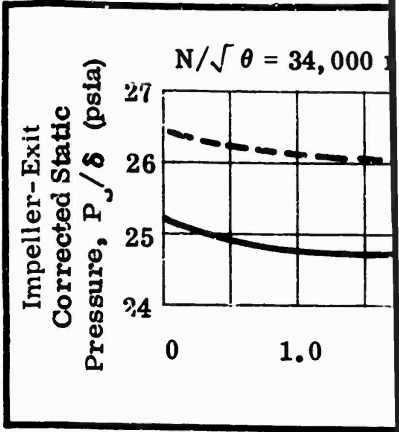
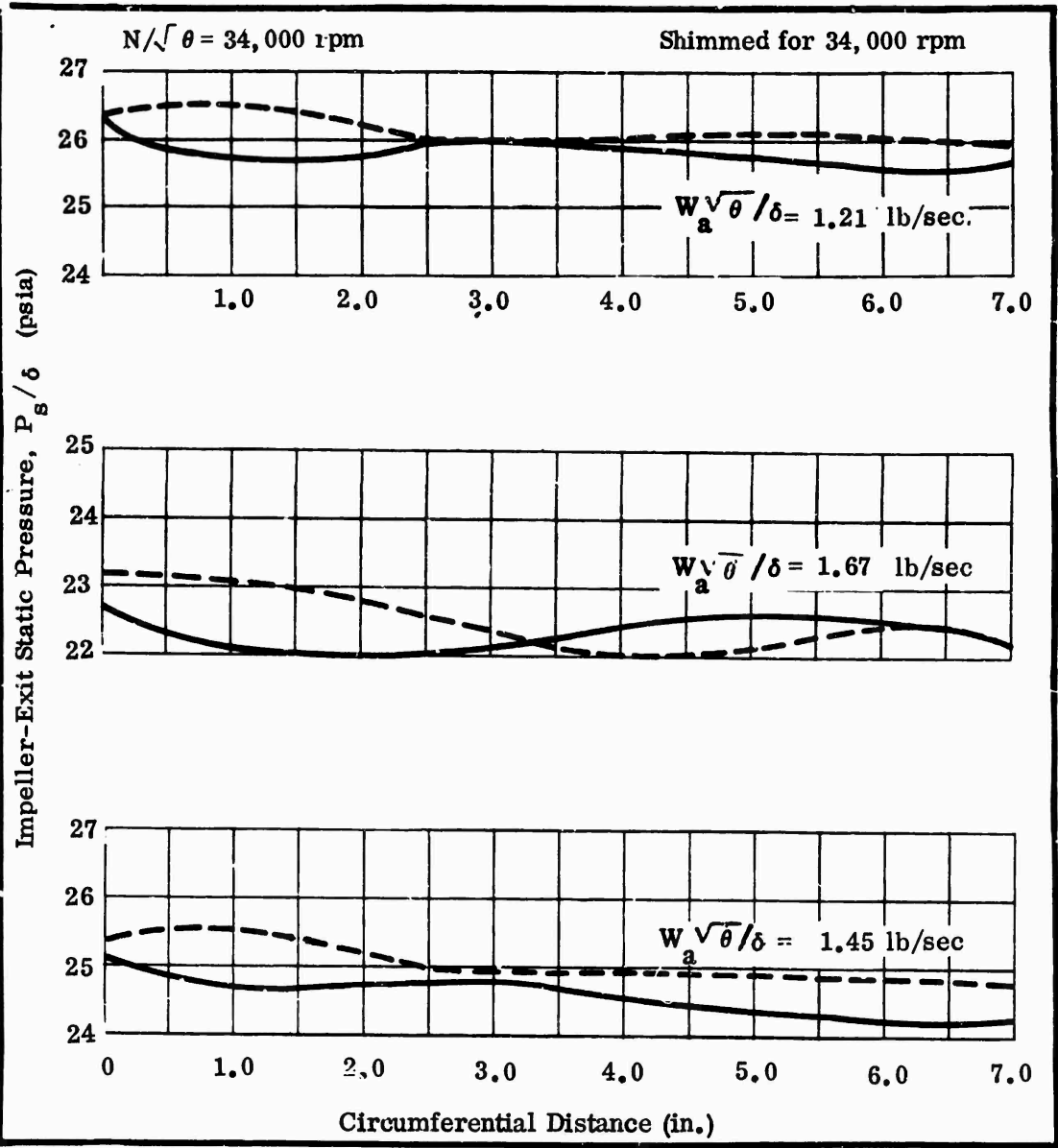
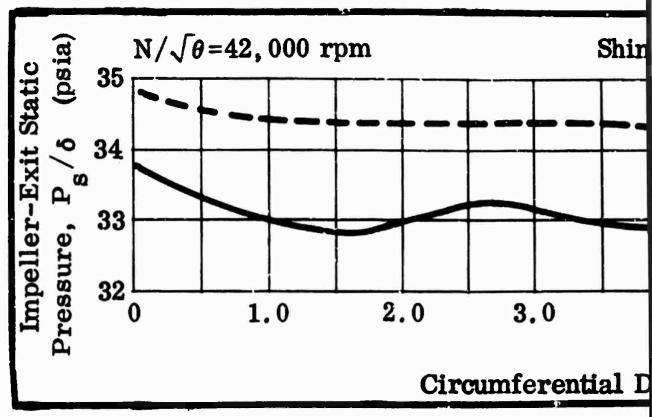
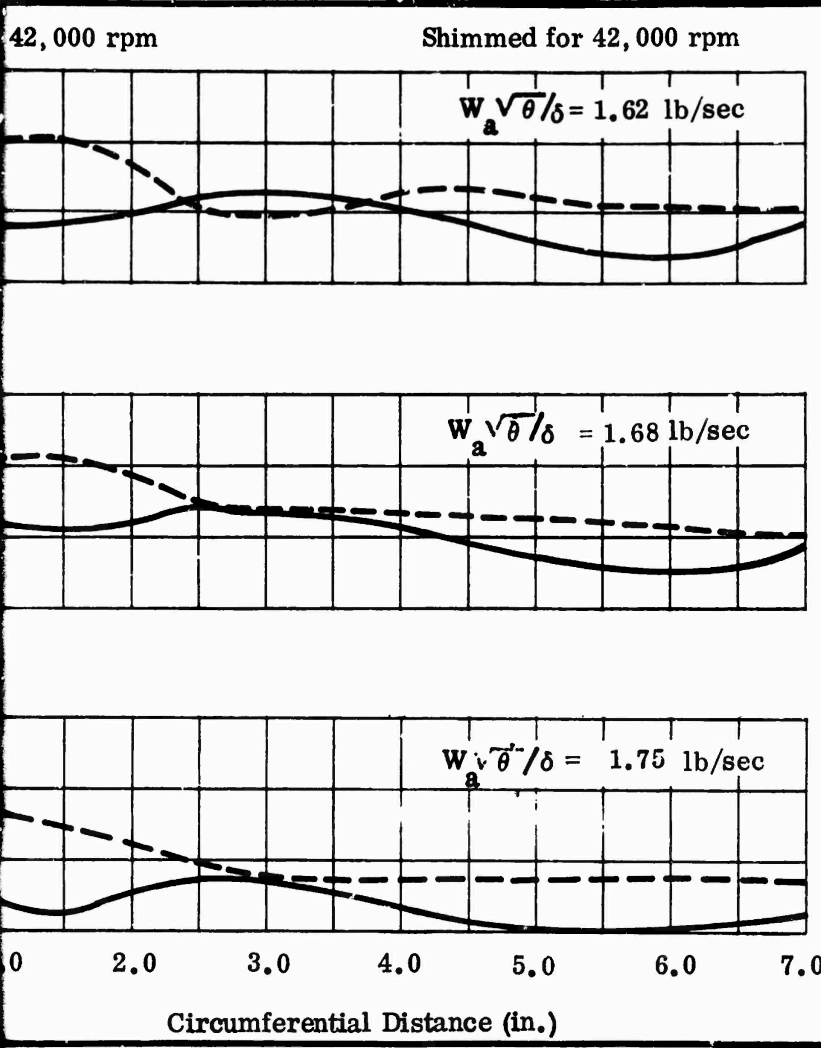
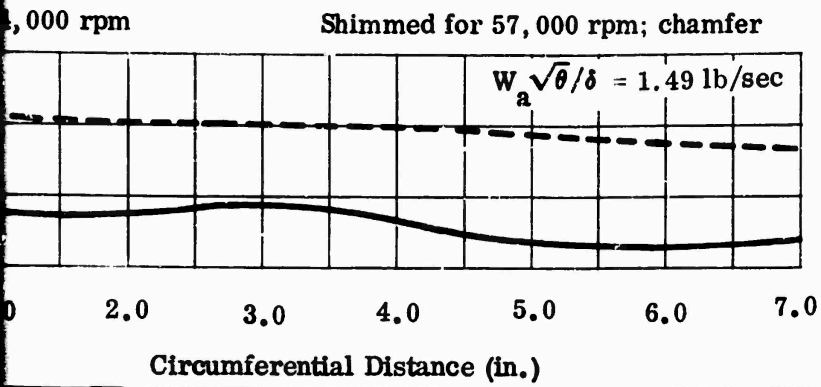


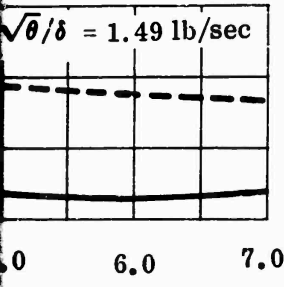
Figure 258. Impeller-Exit Static Pressure Versus Circumferential Distance, RF-1.

CONFIDENTIAL

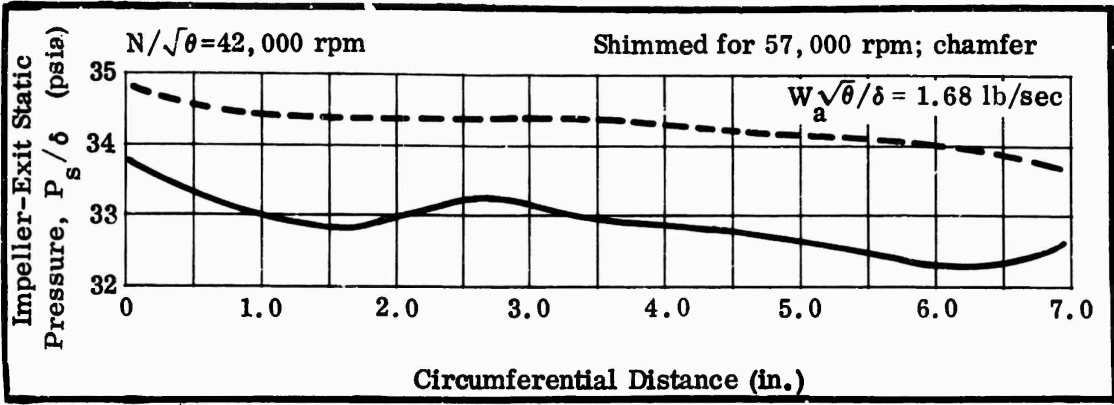
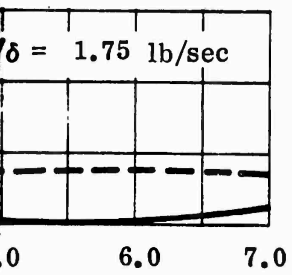
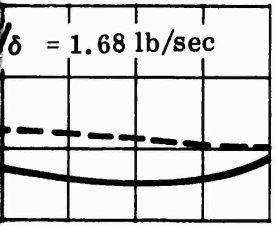
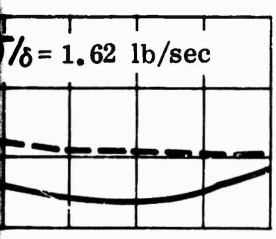
1



000 rpm; chamfer



for 42,000 rpm



CONFIDENTIAL

Test 3407
Vaned Diffuser

S_0 is the circumferential spacing between adjacent vane tips (2.17 in.).

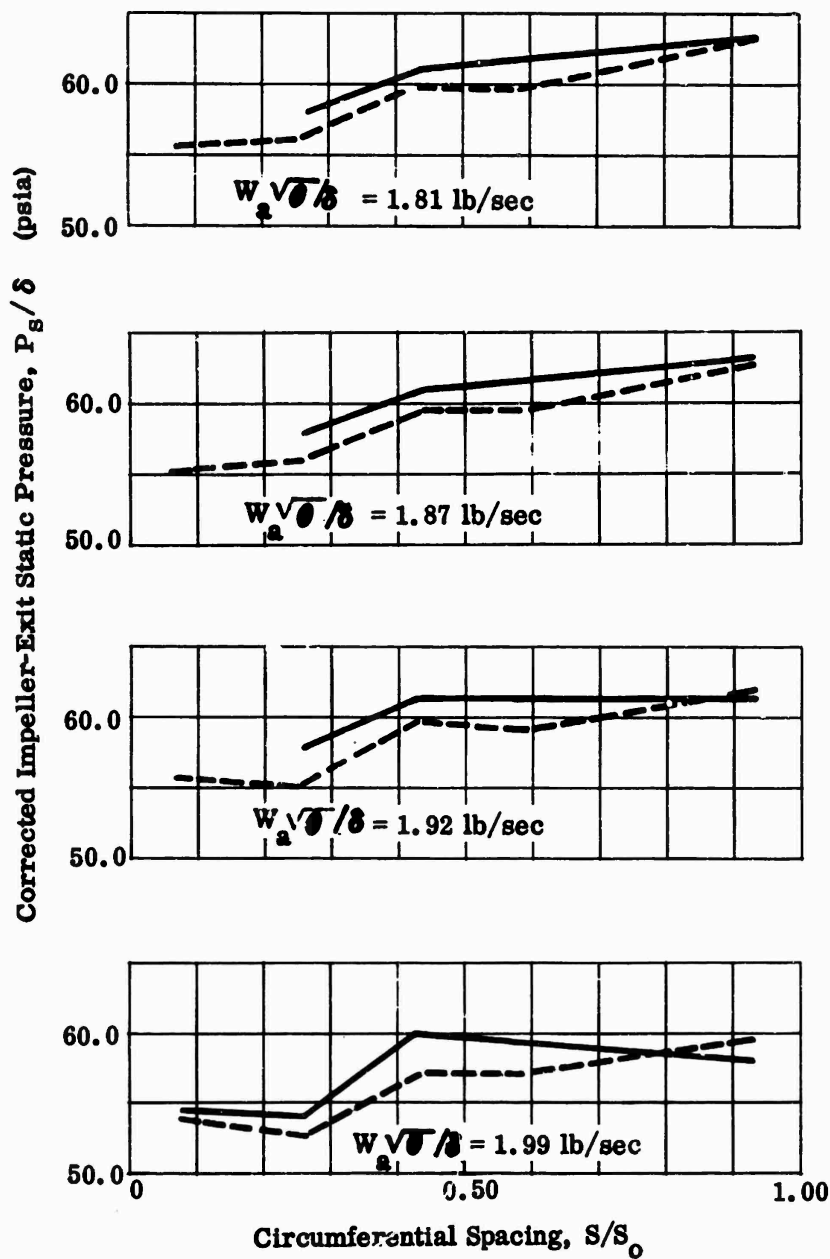


Figure 259. Impeller-Exit Static Pressure Versus Circumferential Spacing, RF-1.

CONFIDENTIAL

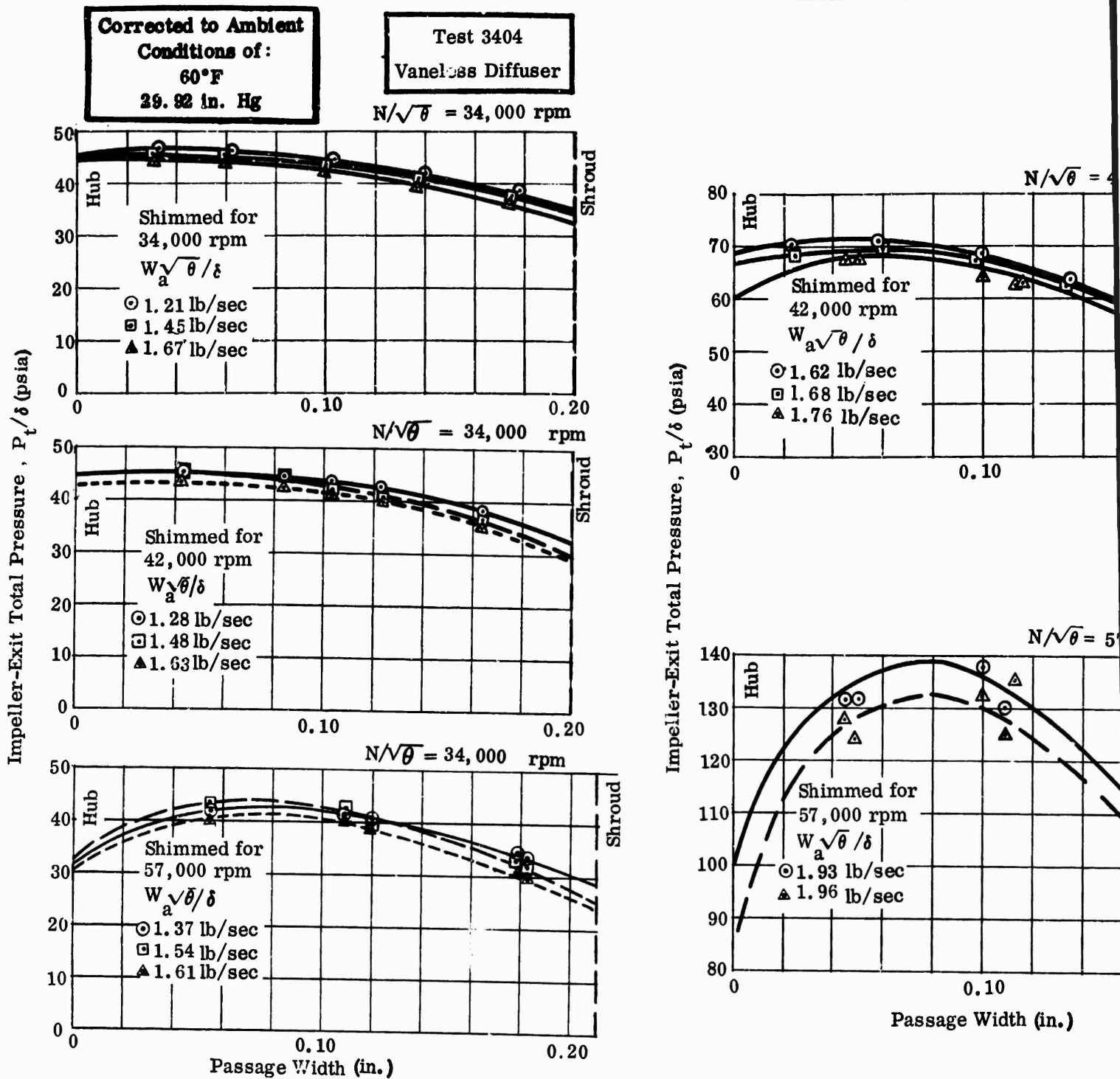
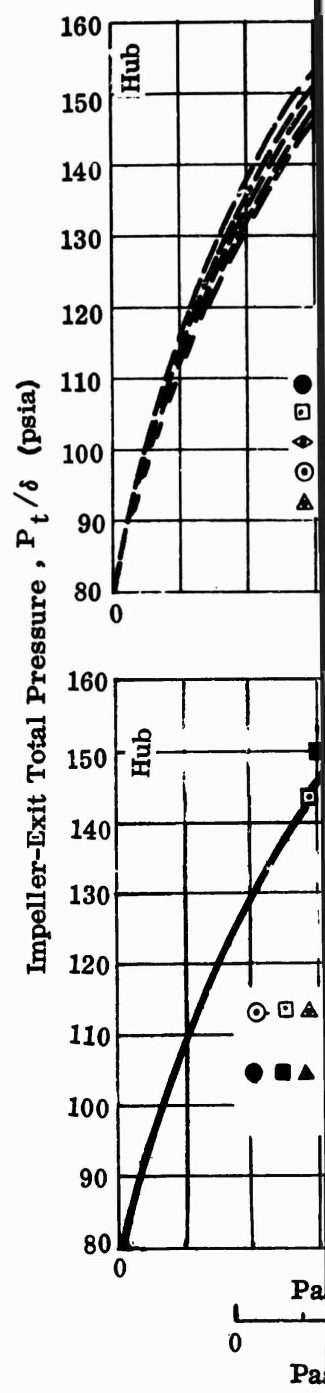
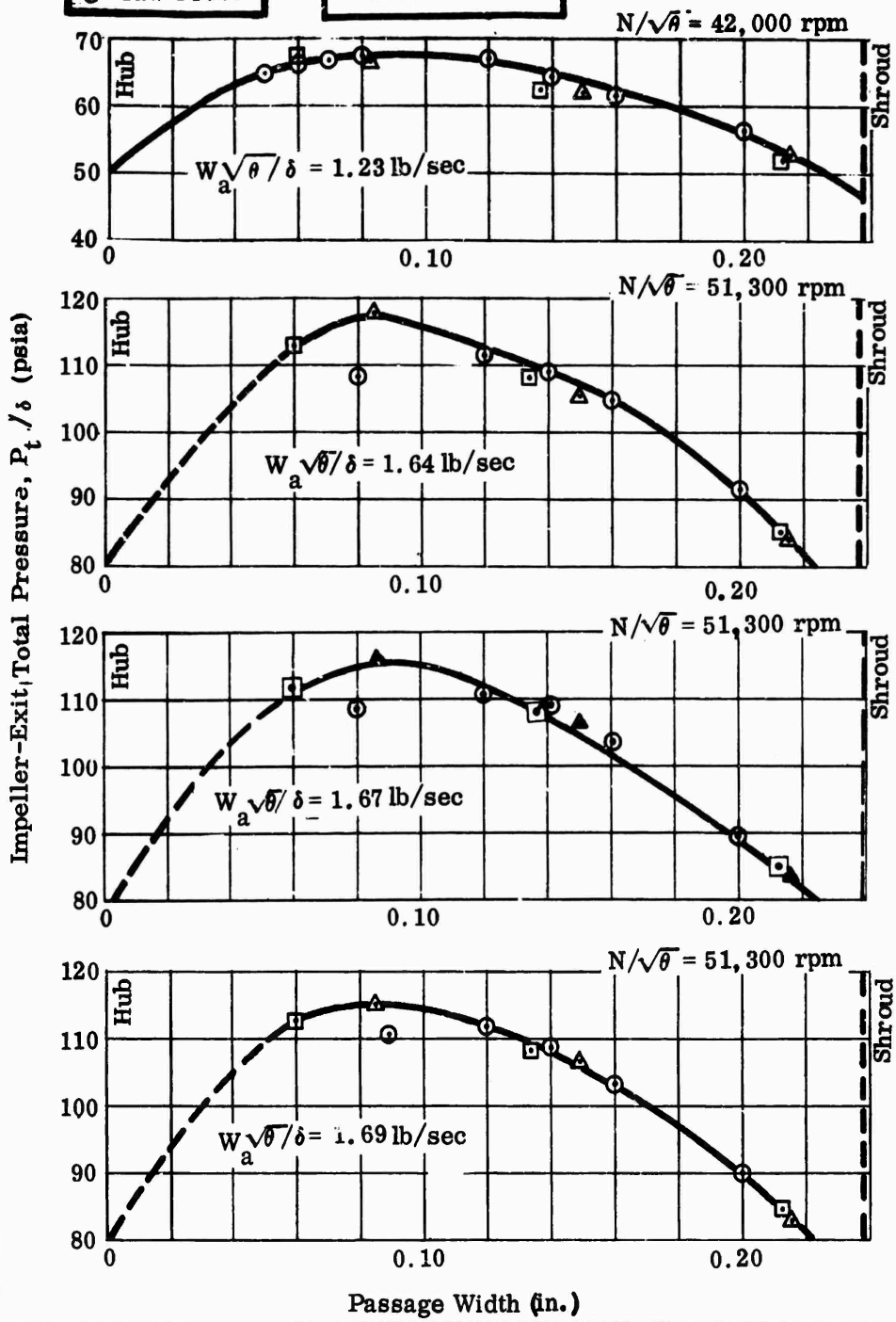
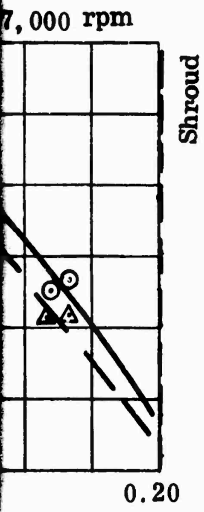
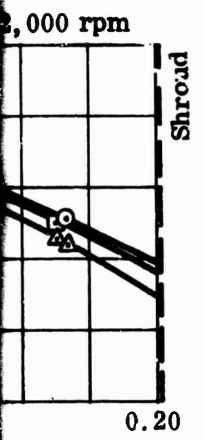
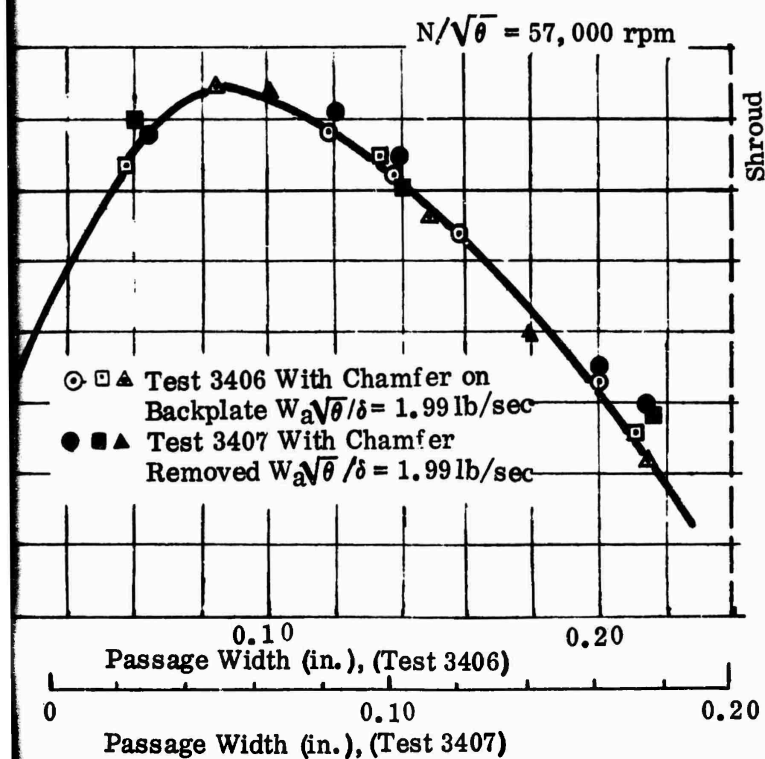
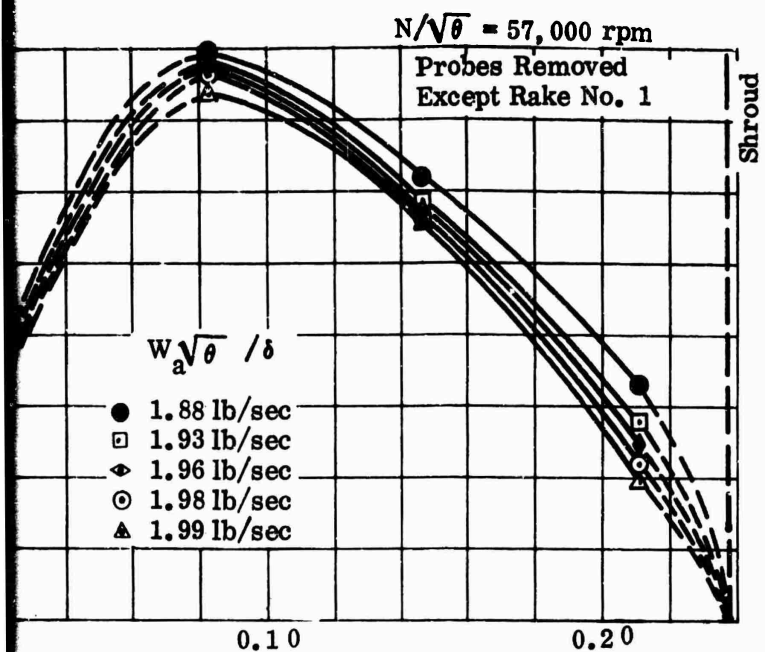


Figure 260. Impeller-Exit Total Pressure, RF-1.

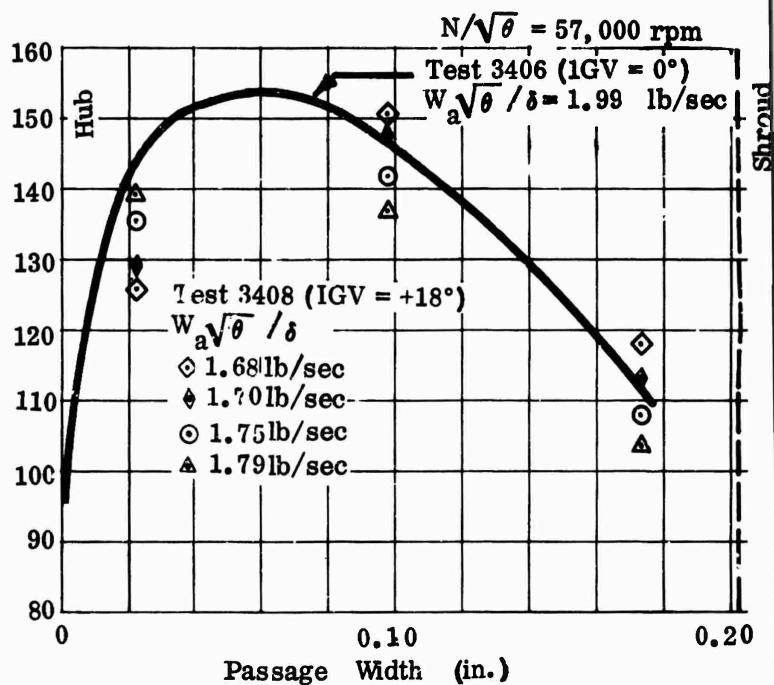
- ▲ Rake No. 1
- Rake No. 2
- Yaw Probe

Test 3406
Vaned Diffuser





Corrected to Ambient
Conditions of:
60°F
29.92 in. Hg.



CONFIDENTIAL

Corrected to Ambient
Conditions of:
60°F
29.92 in. Hg.

Test 3404
Vaneless Diffuser

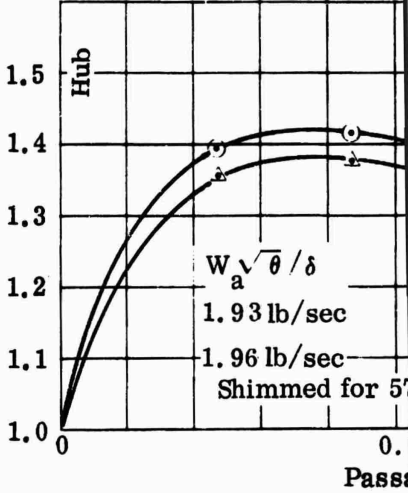
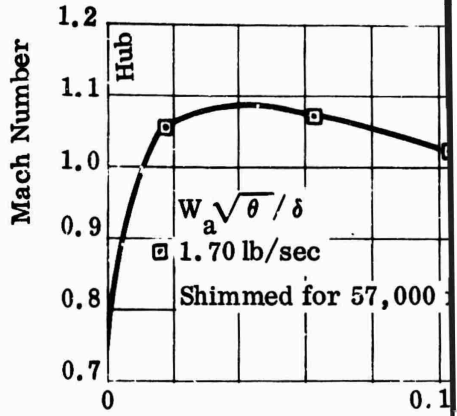
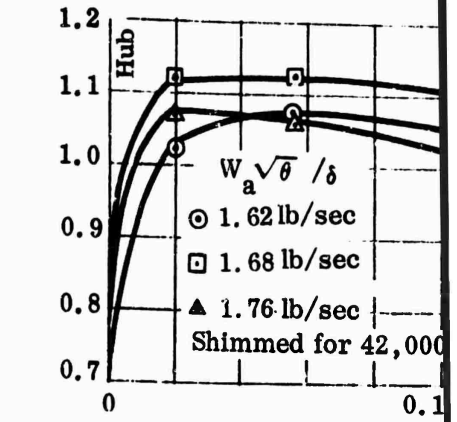
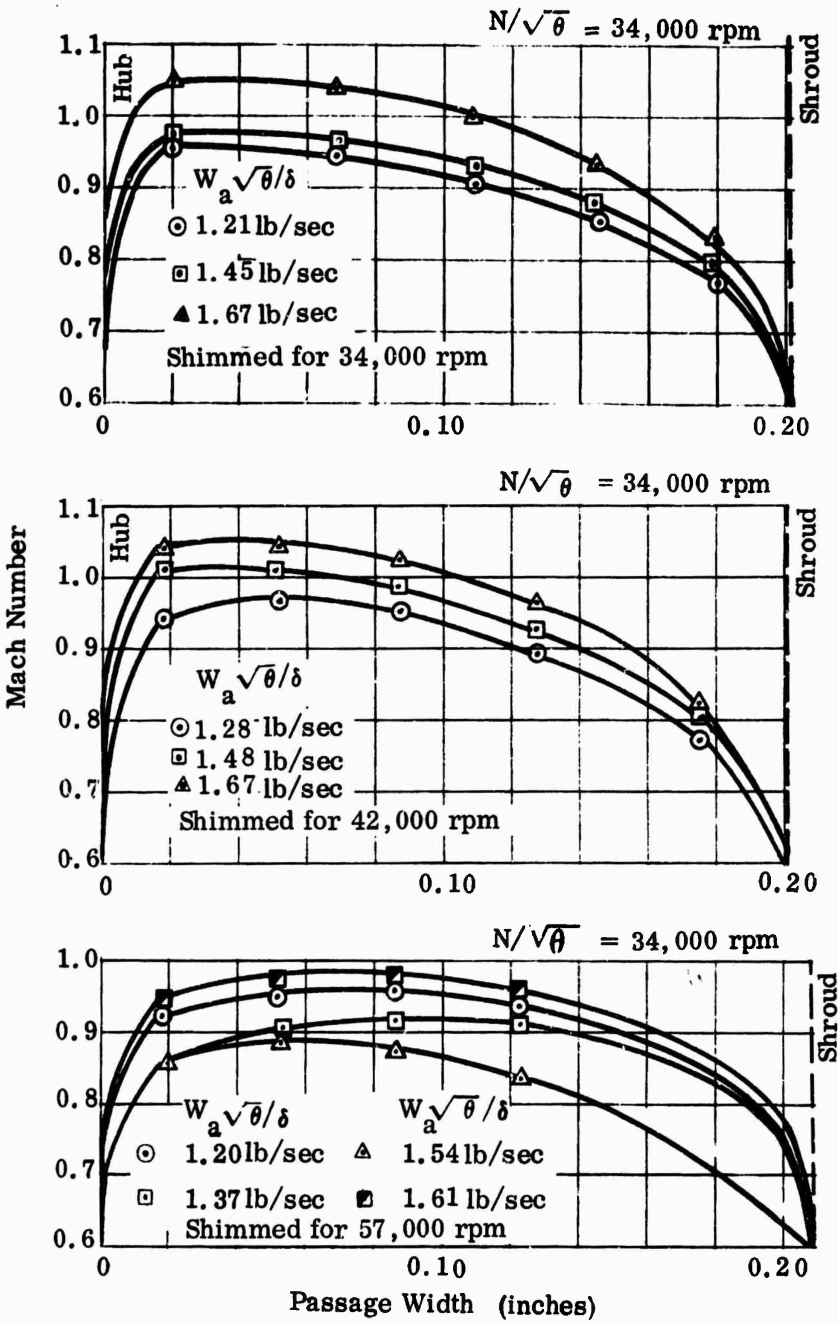
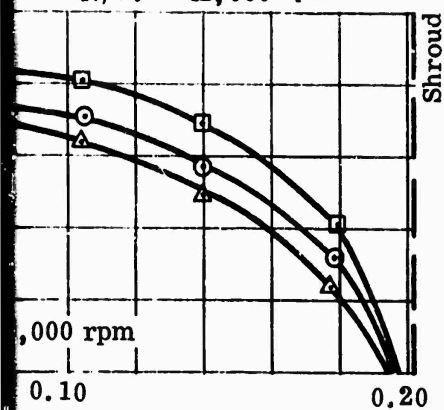


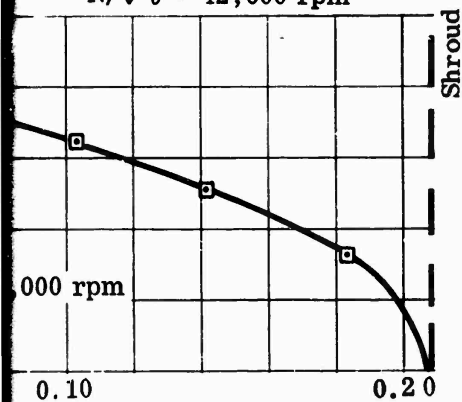
Figure 261. Impeller-Exit Mach Number Versus Passage Width, RF-1.

CONFIDENTIAL

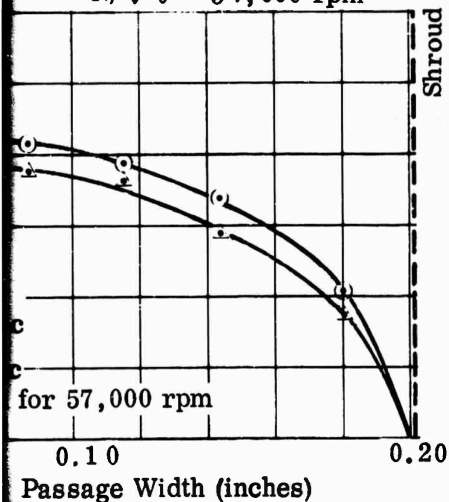
$N/\sqrt{\theta} = 42,000 \text{ rpm}$



$N/\sqrt{\theta} = 42,000 \text{ rpm}$



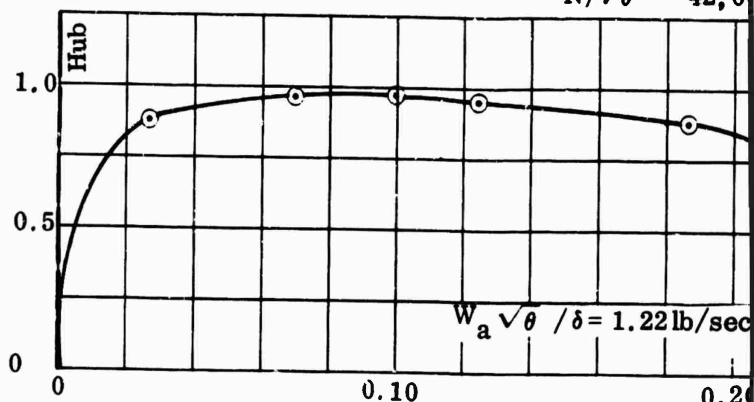
$N/\sqrt{\theta} = 57,000 \text{ rpm}$



Test 3406

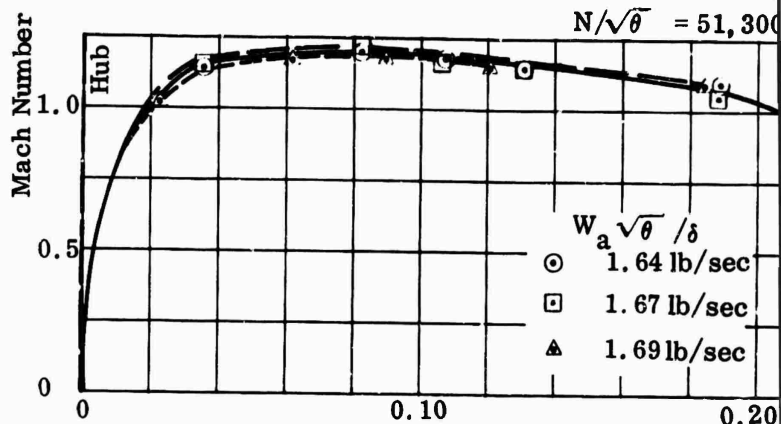
Vaned Diffuser

$N/\sqrt{\theta} = 42,000$



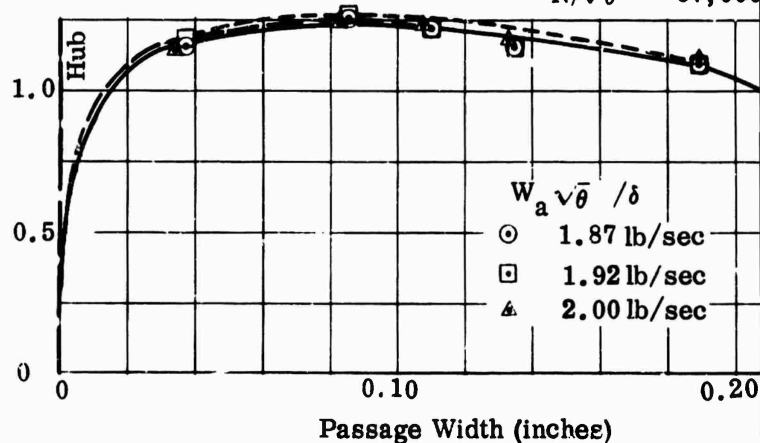
$W_a \sqrt{\theta} / \delta = 1.22 \text{ lb/sec}$

$N/\sqrt{\theta} = 51,300$



$W_a \sqrt{\theta} / \delta$
 \odot 1.64 lb/sec
 \square 1.67 lb/sec
 \triangle 1.69 lb/sec

$N/\sqrt{\theta} = 57,000$

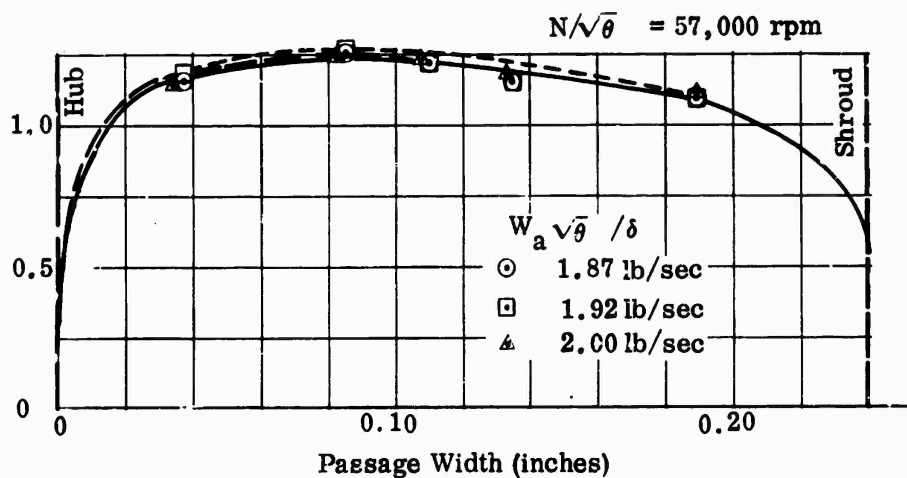
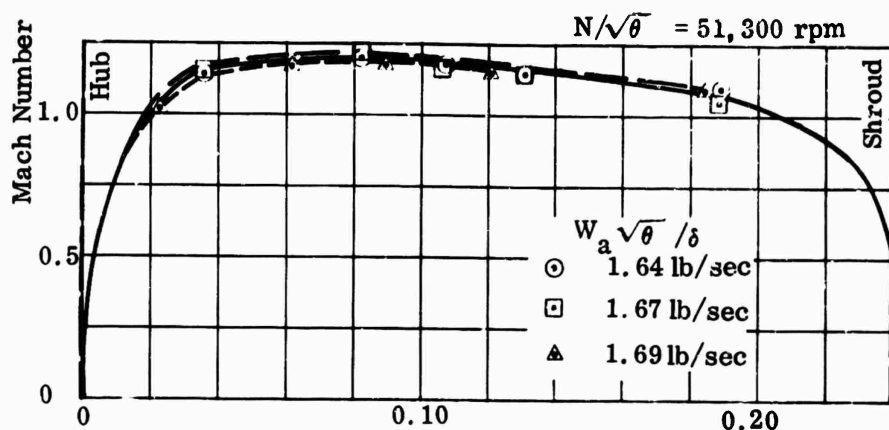
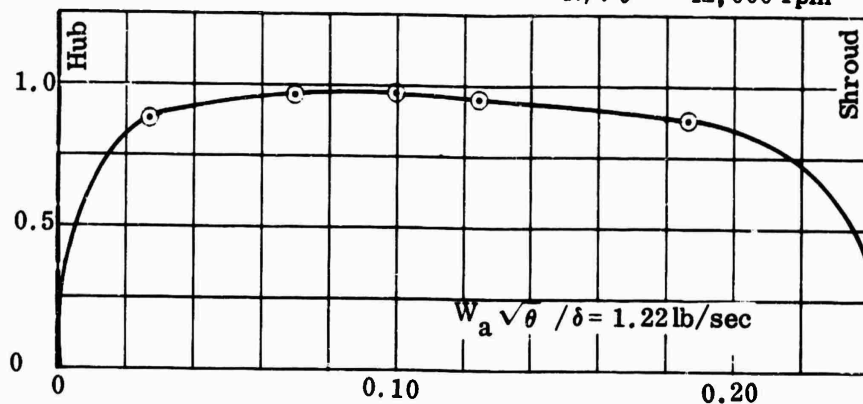


$W_a \sqrt{\theta} / \delta$
 \odot 1.87 lb/sec
 \square 1.92 lb/sec
 \triangle 2.00 lb/sec

Test 3406

Vaned Diffuser

$N/\sqrt{\theta} = 42,000 \text{ rpm}$



CONFIDENTIAL

Corrected to Ambient
Conditions of:
60°F
29.92 in. Hg

Test 3404
Vaneless Diffuser

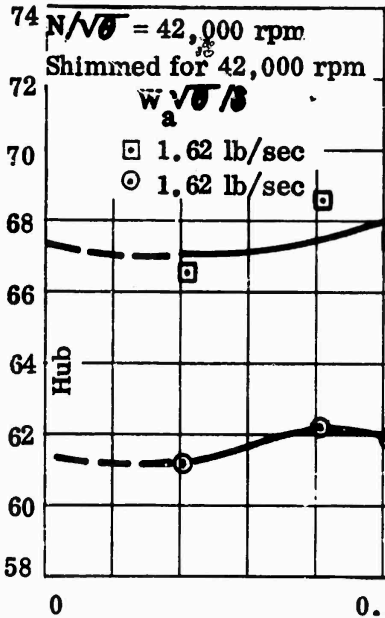
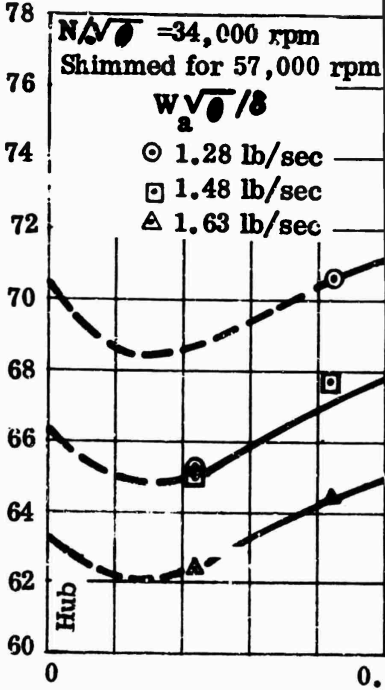
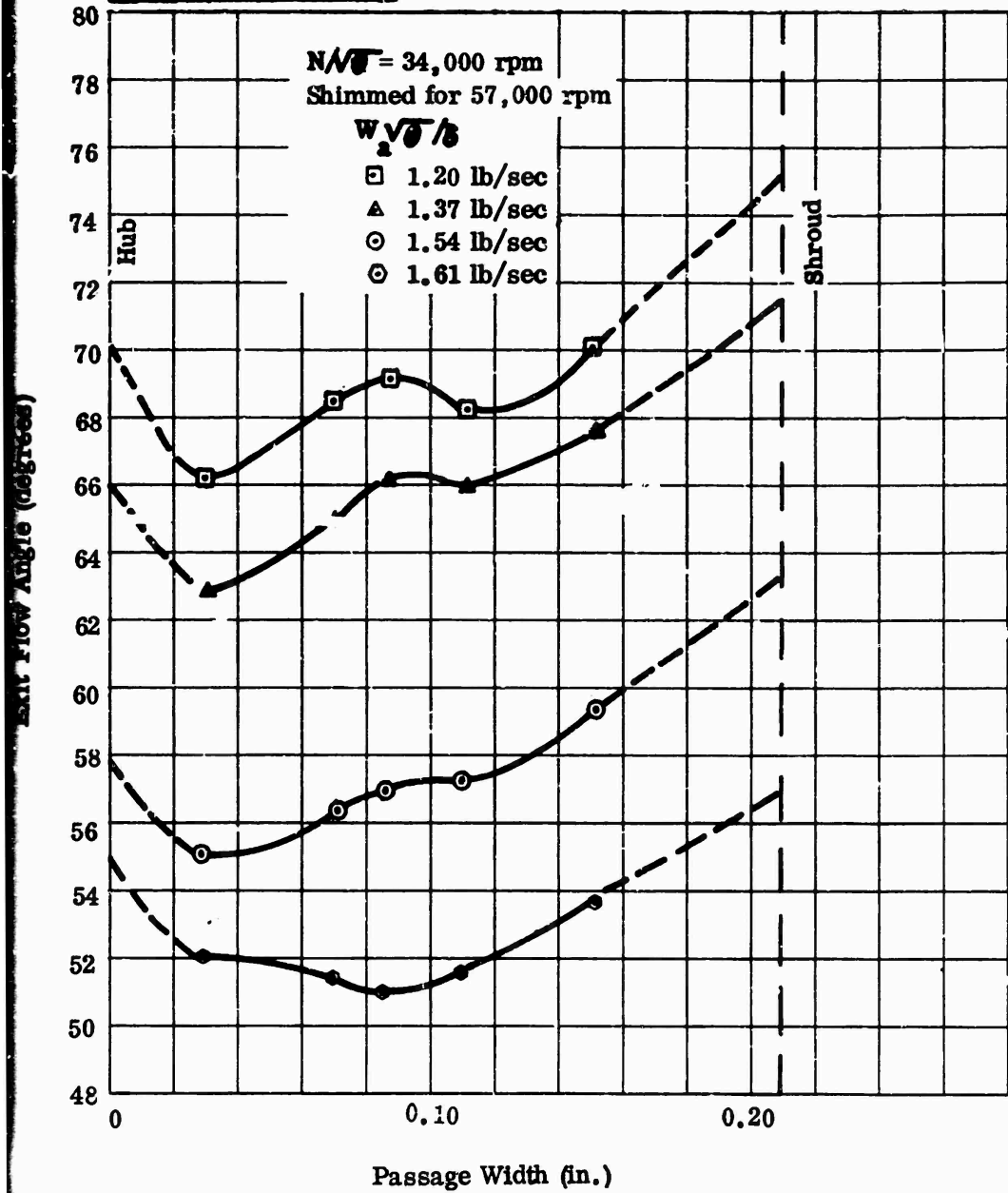
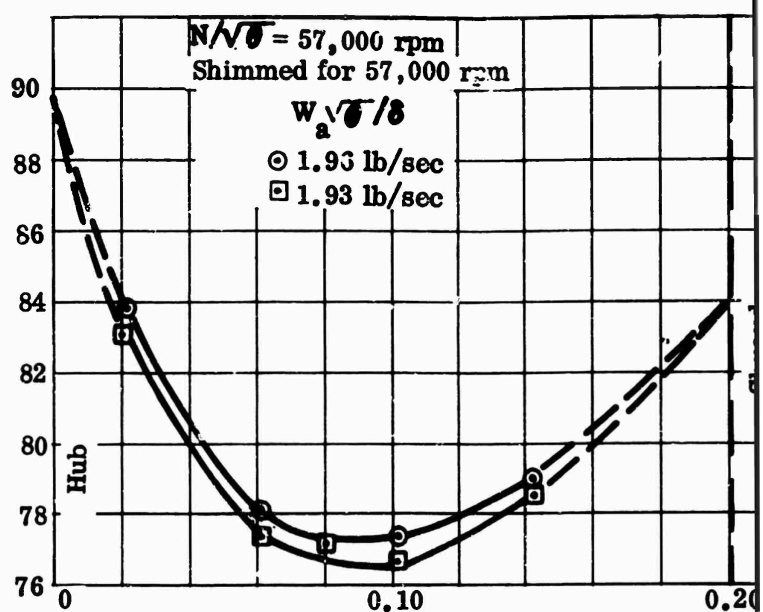
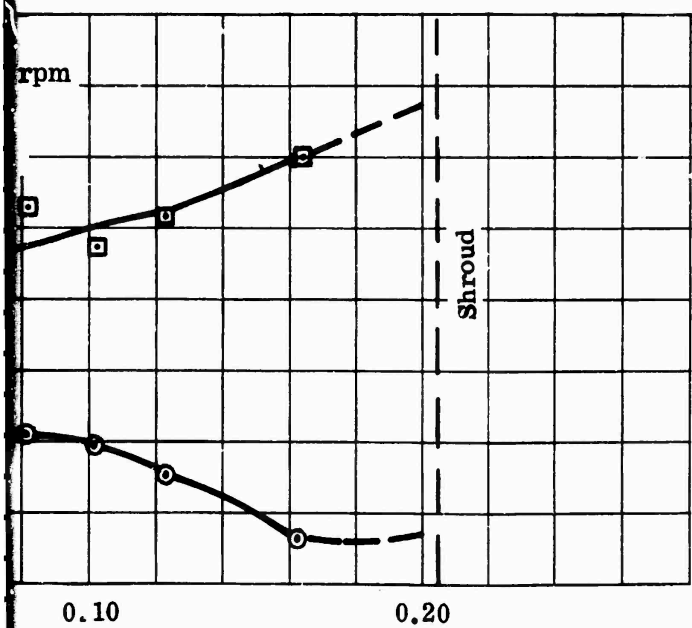
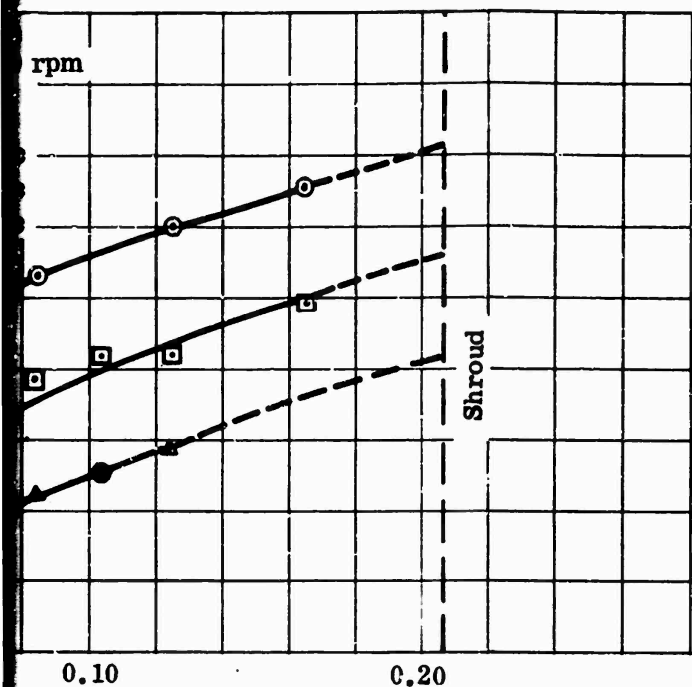
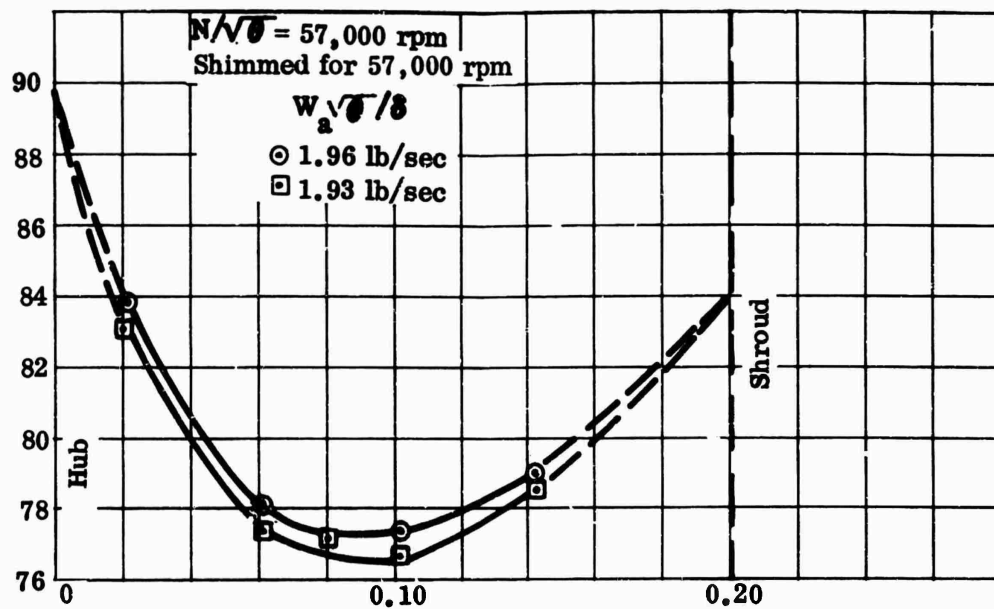


Figure 262. Impeller-Exit Flow-Angle Survey, RF-1.

CONFIDENTIAL





CONFIDENTIAL

Exit Flow Angle (degrees)

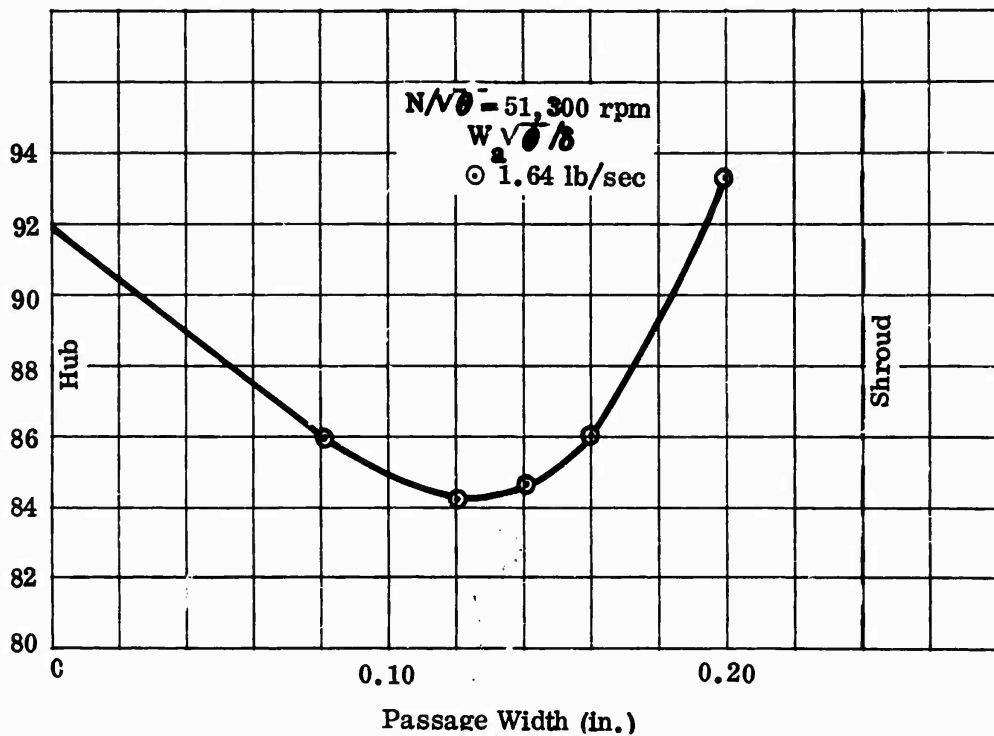
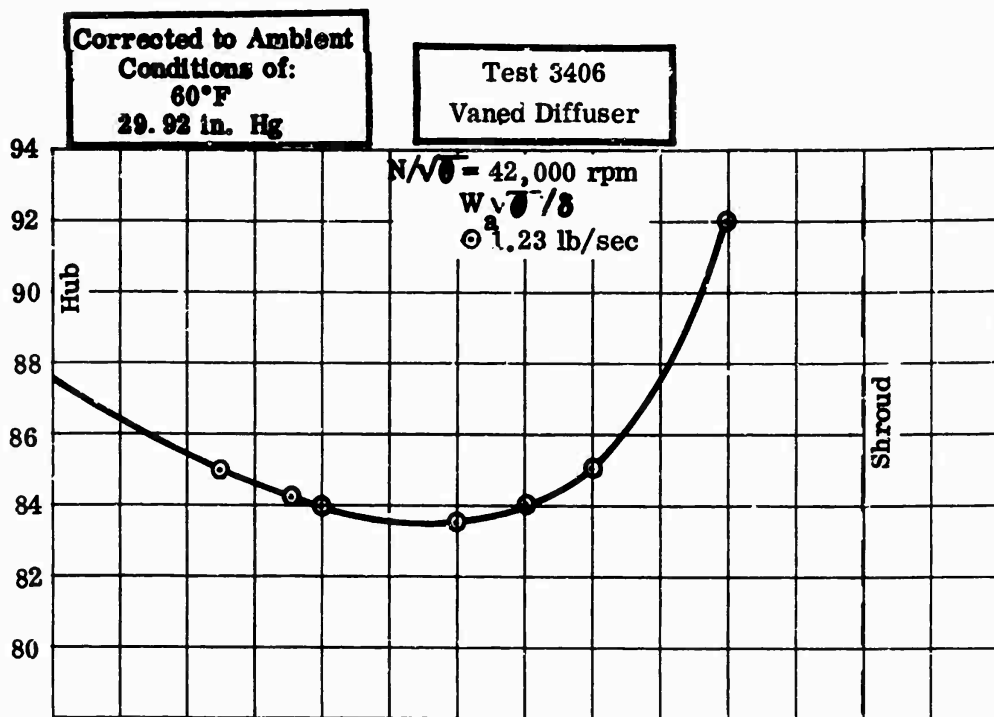
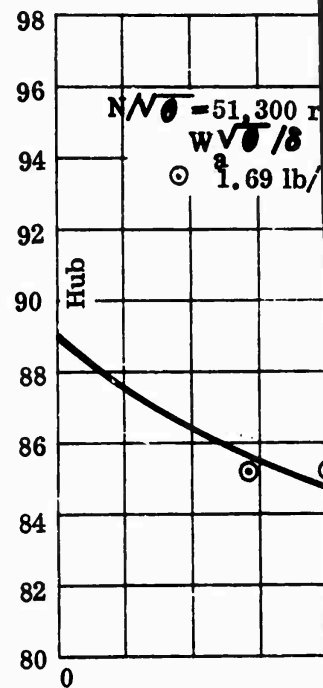
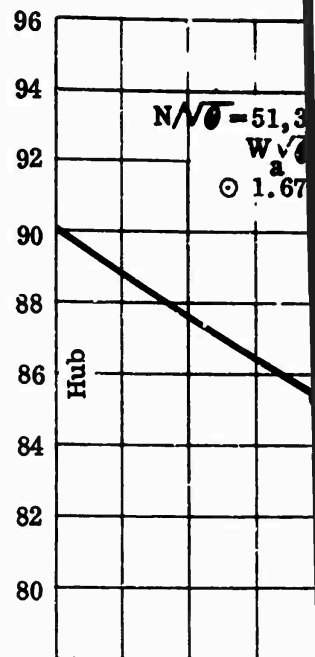
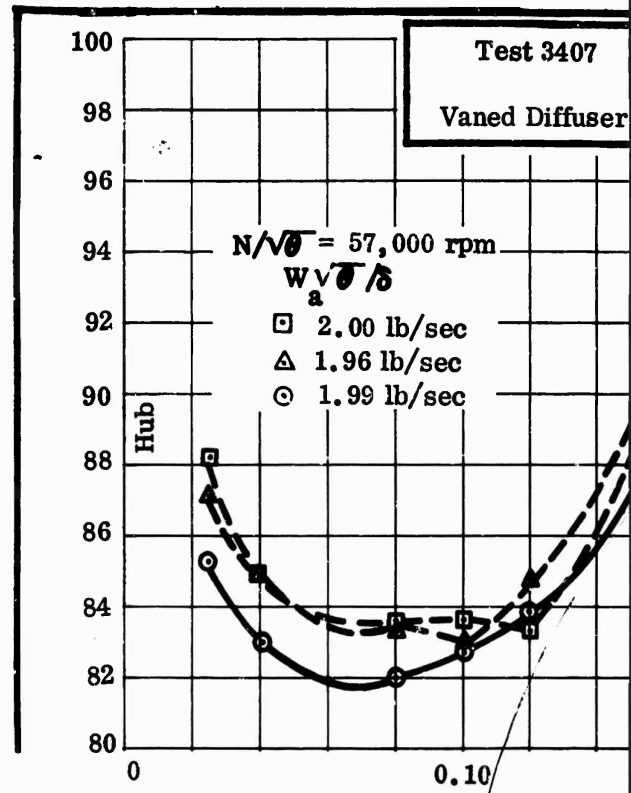
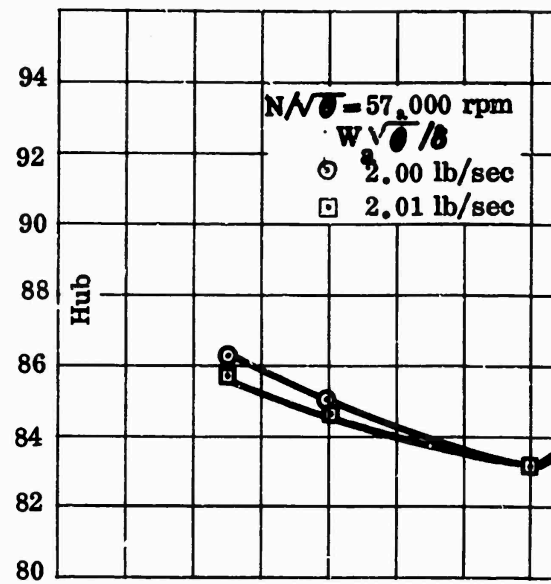
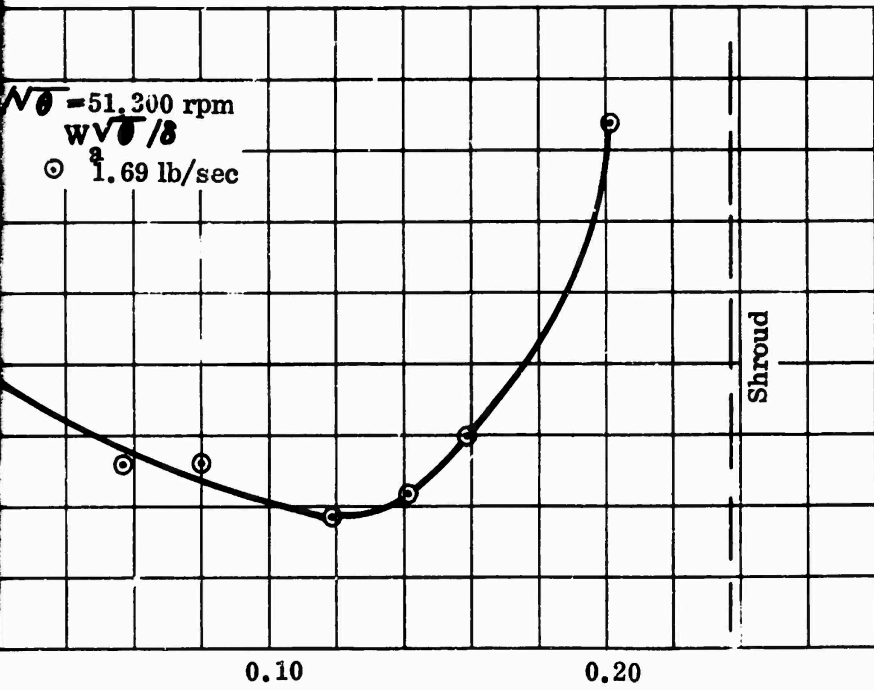
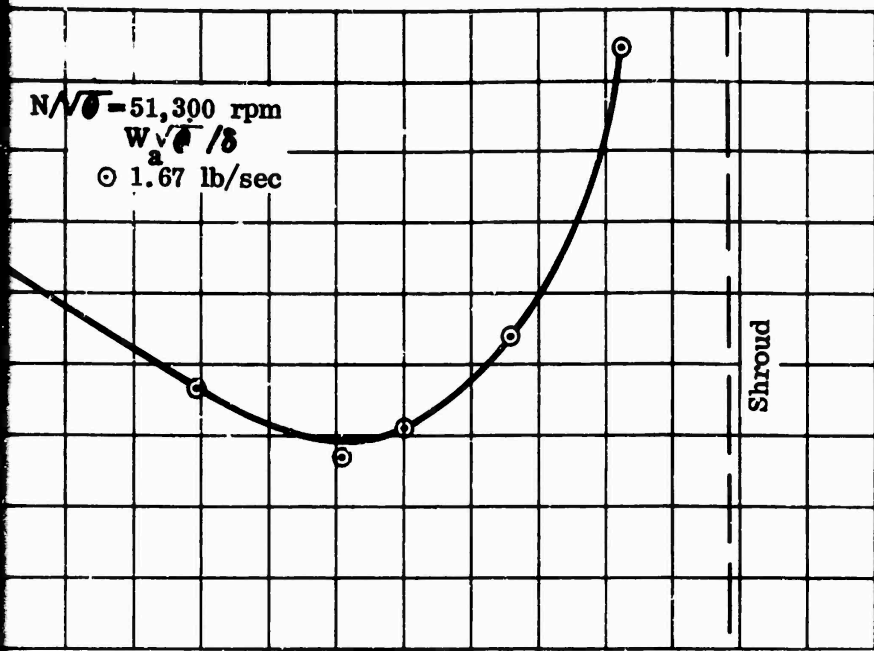
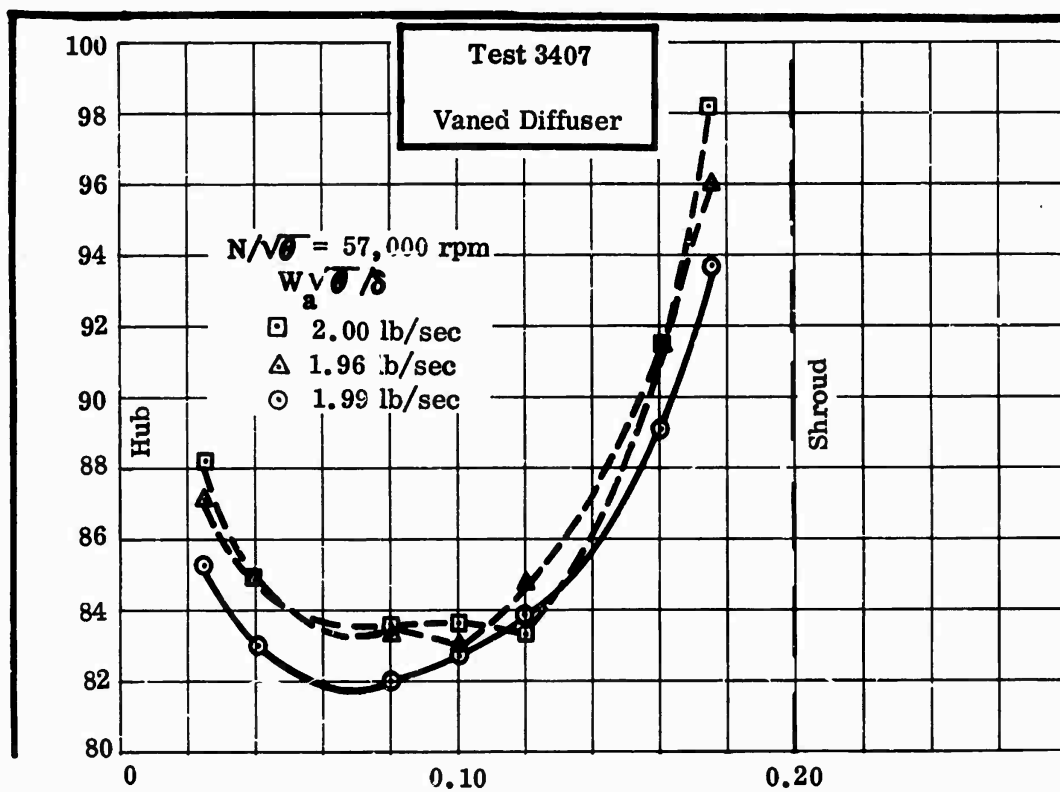
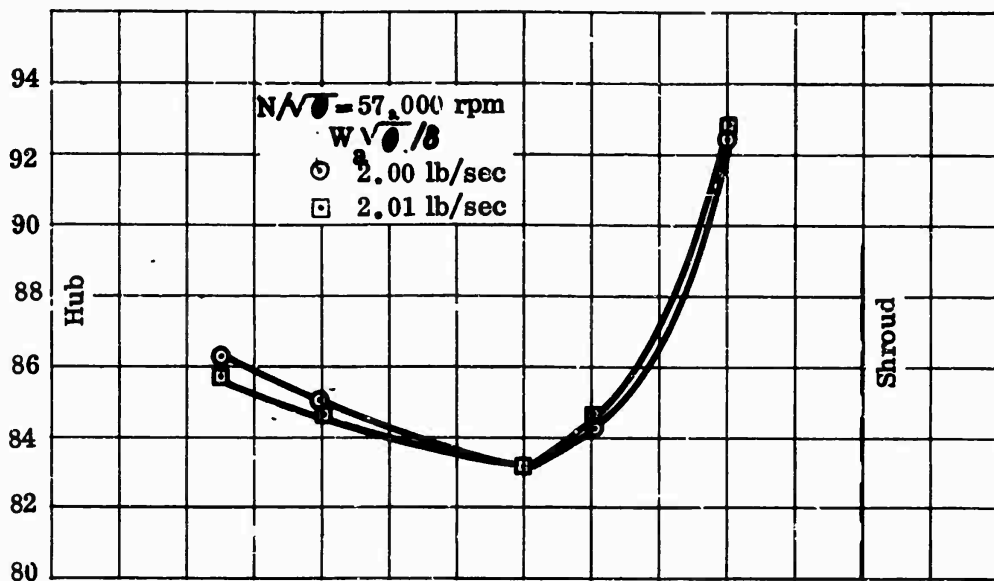


Figure 263. Impeller-Exit Flow-Angle Survey, RF-1.

CONFIDENTIAL







CONFIDENTIAL

Test 3404
Vaneless Diffuser

Corrected to Ambient
Conditions of:
60°F
29.92 in. Hg
All Velocities in fps

$N/\sqrt{\theta} = 34,000$ rpm
Shimmed for 42,000 rpm

$N/\sqrt{\theta} = 34,000$ rpm
Shimmed for 34,000 rpm

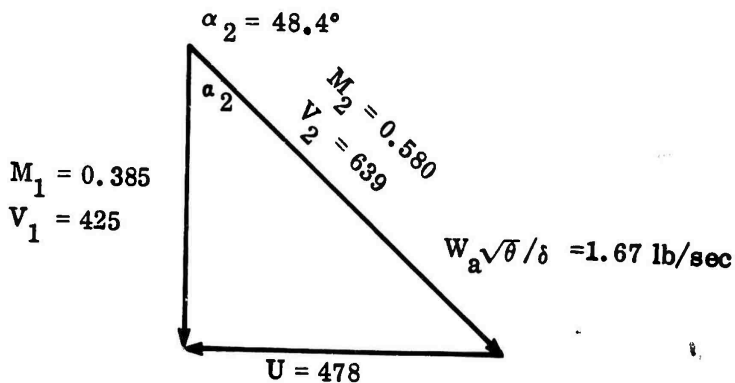
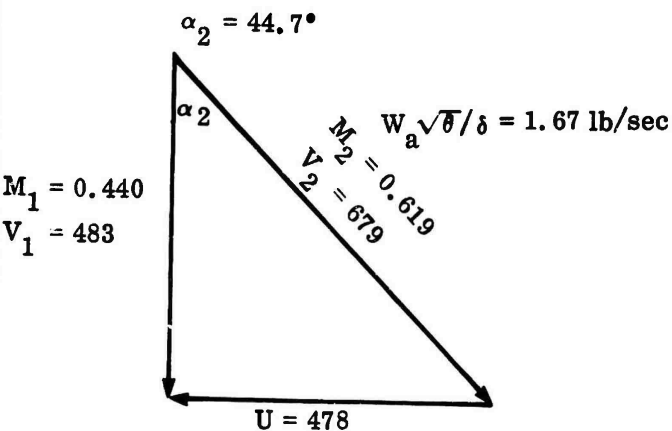
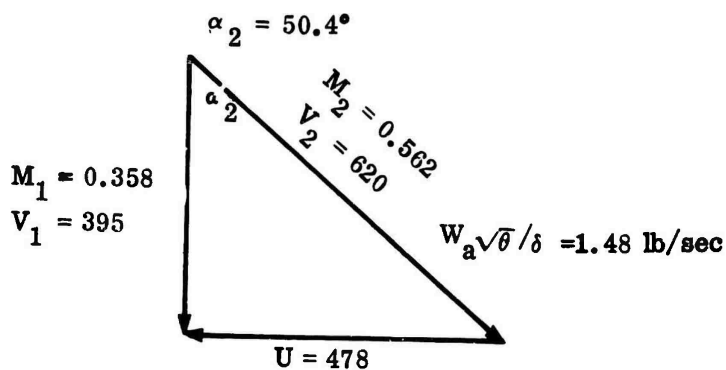
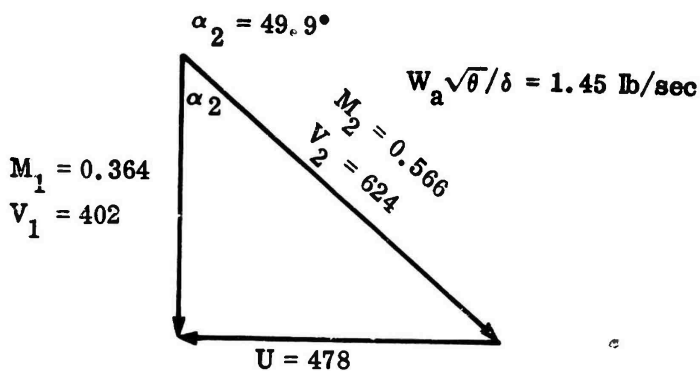
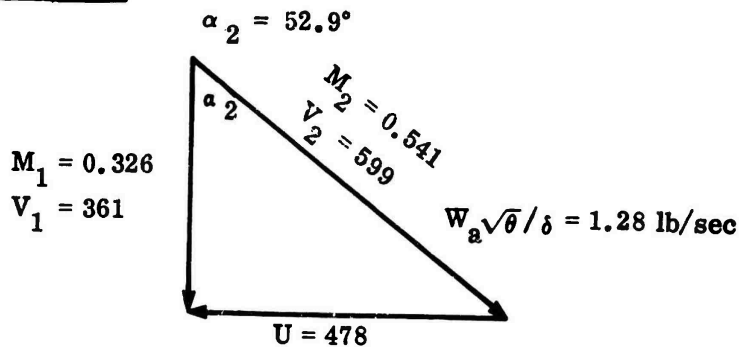
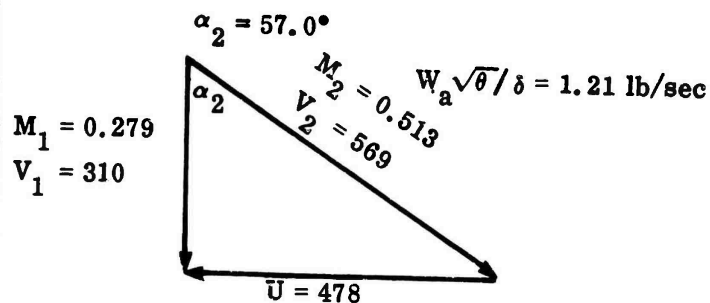
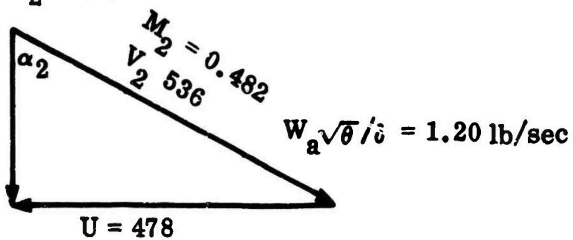


Figure 264. RMS Inlet Vector Diagrams, RF-1.

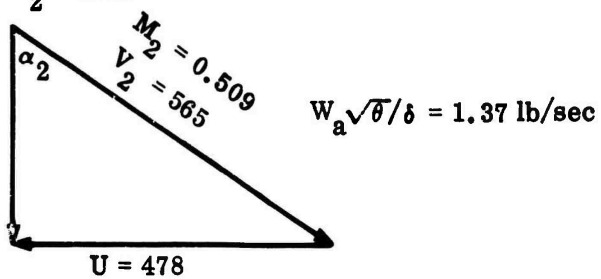
CONFIDENTIAL

$N/\sqrt{\theta} = 34,000 \text{ rpm}$
Shimmed for 57,000 rpm

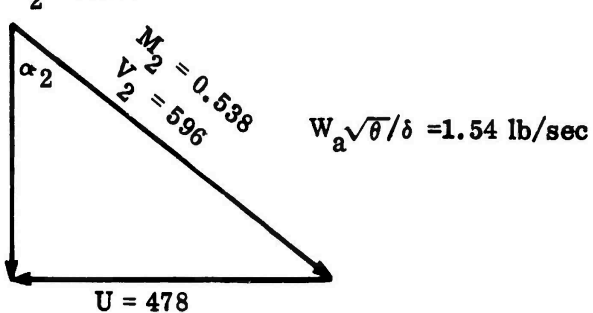
$$\alpha_2 = 63.0^\circ$$



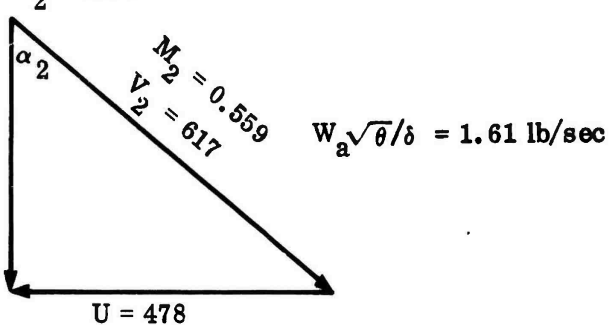
$$\alpha_2 = 57.8^\circ$$



$$\alpha_2 = 53.3^\circ$$



$$\alpha_2 = 50.7^\circ$$

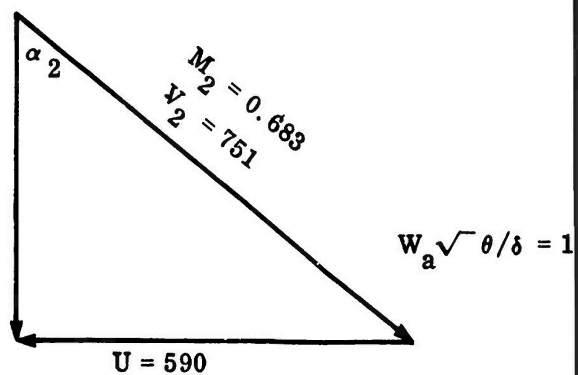


$N/\sqrt{\theta} = 42,000 \text{ rpm}$
Shimmed for 42,000 rpm

$$\alpha_2 = 51.8^\circ$$

$$M_1 = 0.422$$

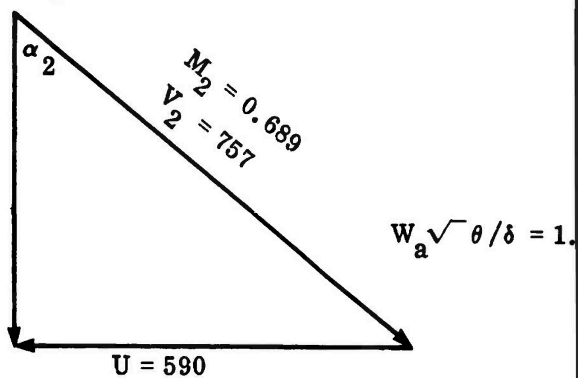
$$V_1 = 464$$



$$\alpha_2 = 51.2^\circ$$

$$M_1 = 0.432$$

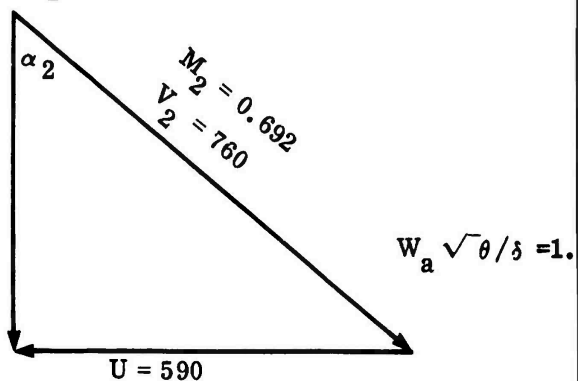
$$V_1 = 474$$



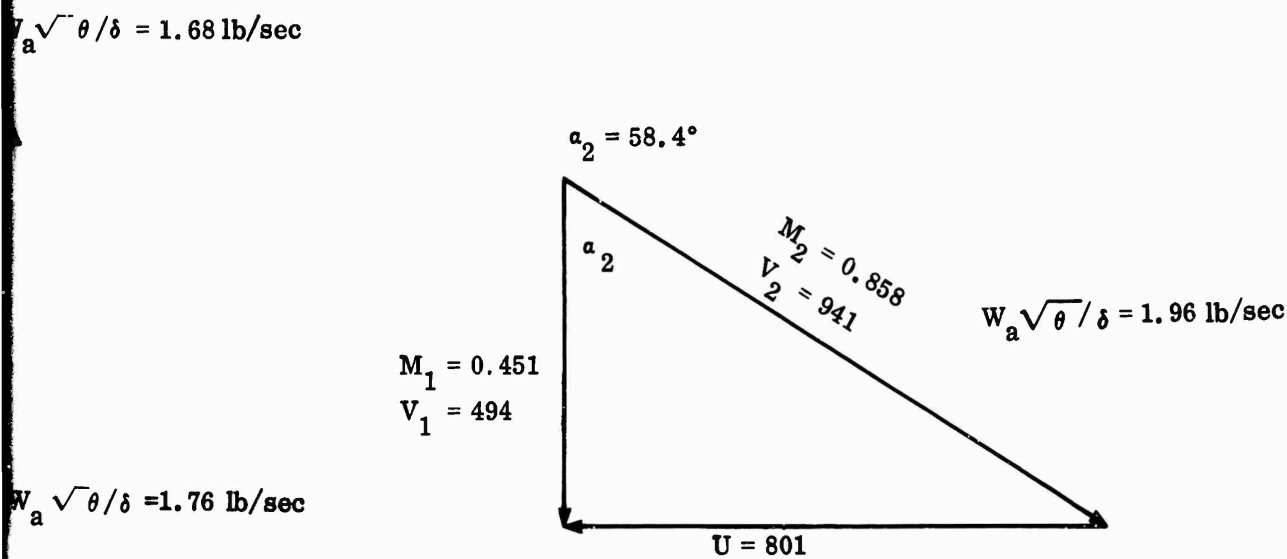
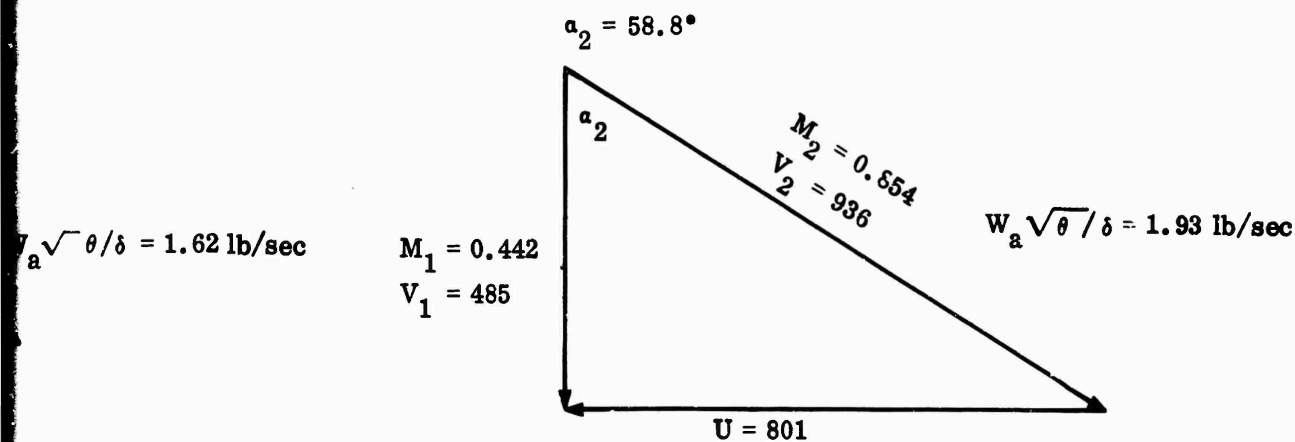
$$\alpha_2 = 51.0^\circ$$

$$M_1 = 0.436$$

$$V_1 = 478$$



$N/\sqrt{\theta} = 57,000 \text{ rpm}$
 Shimmed for 57,000 rpm



CONFIDENTIAL

Corrected to Ambient
Conditions of:
60°F
29.92 in. Hg
All Velocities in fpe

Test 3406
Vaned Diffuser

$N/\sqrt{\theta} = 42,000$ rpm

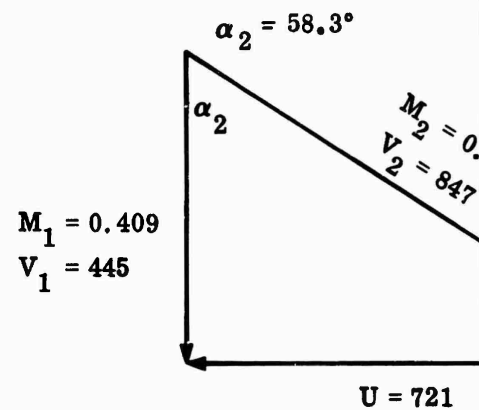
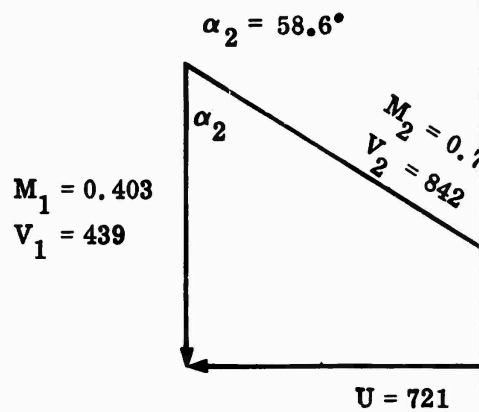
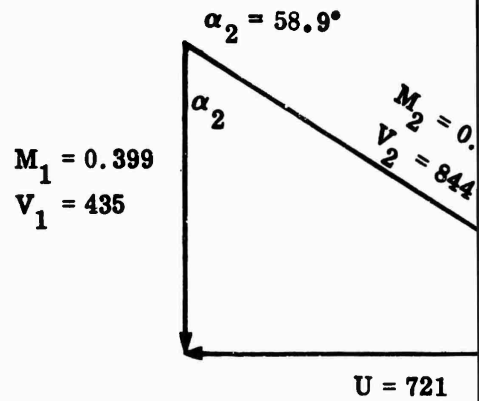
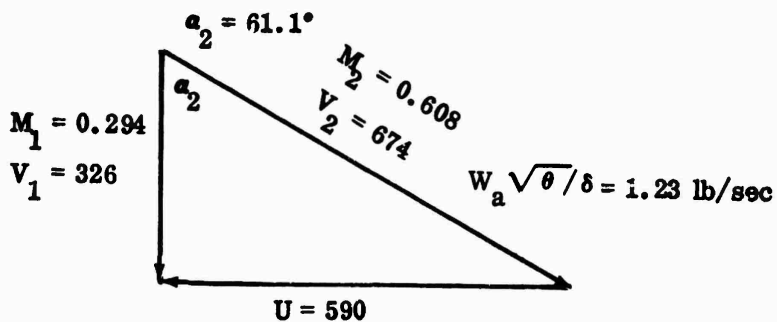


Figure 265. RMS Inlet Vector Diagrams, RF-1.

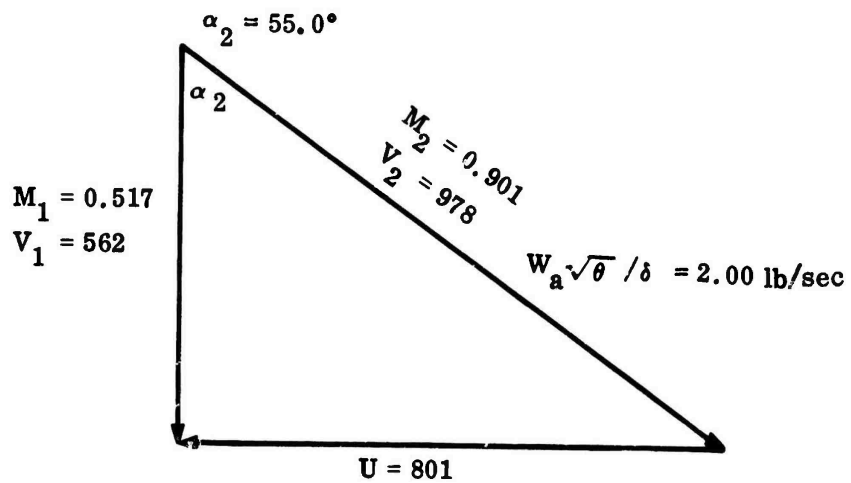
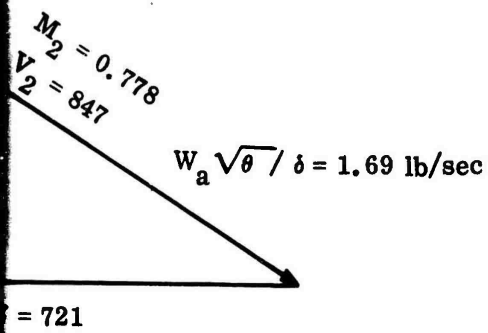
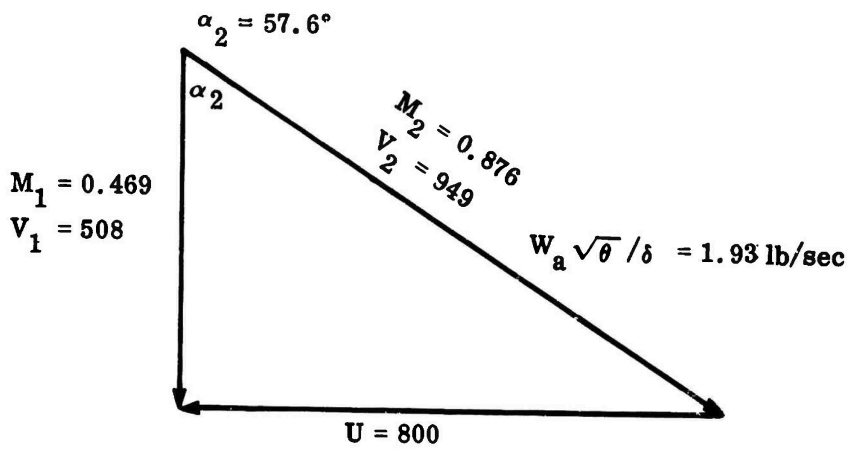
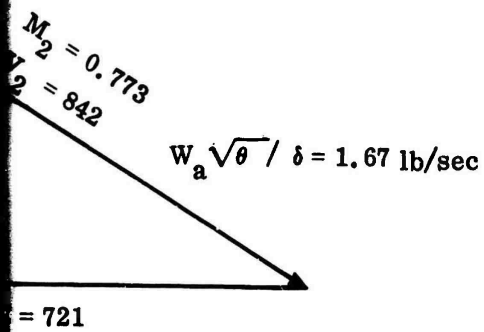
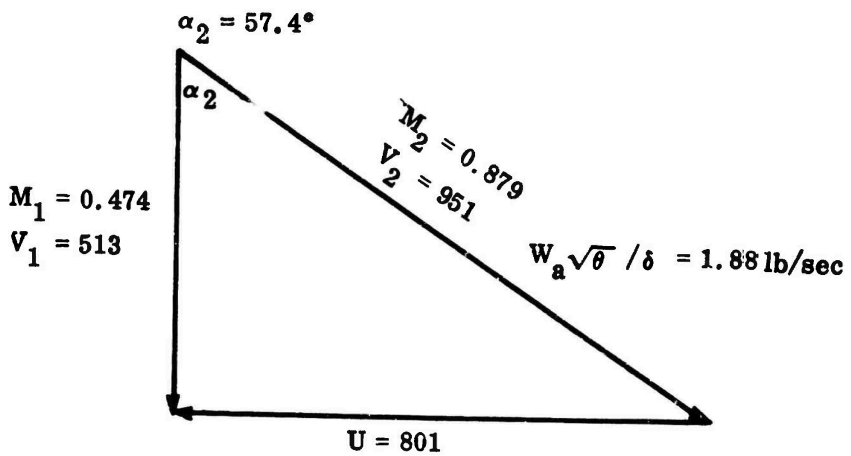
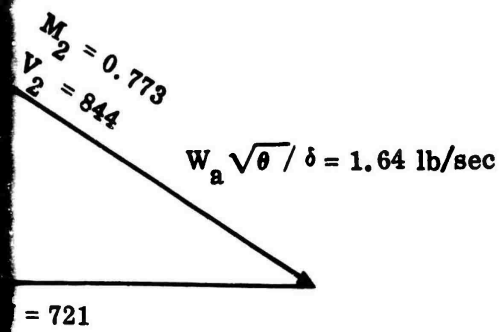
423

CONFIDENTIAL

1

$$N/\sqrt{\theta} = 51,300 \text{ rpm}$$

$$N/\sqrt{\theta} = 57,000 \text{ rpm}$$



CONFIDENTIAL

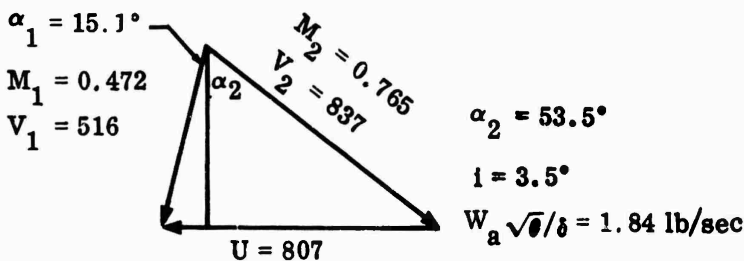
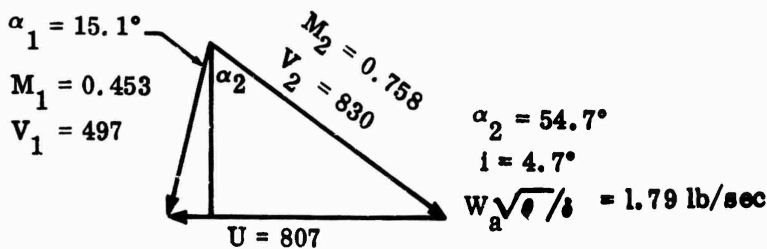
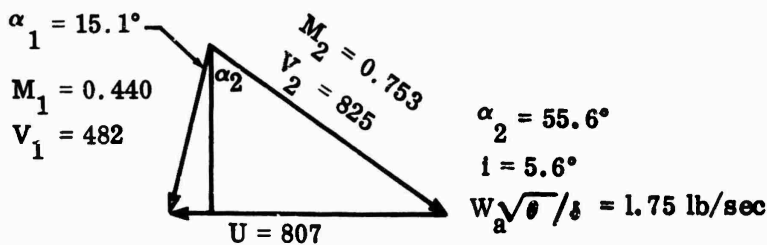
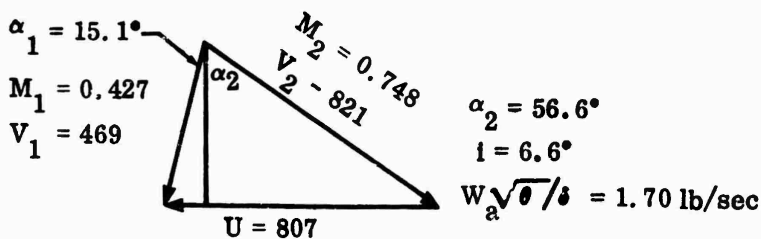
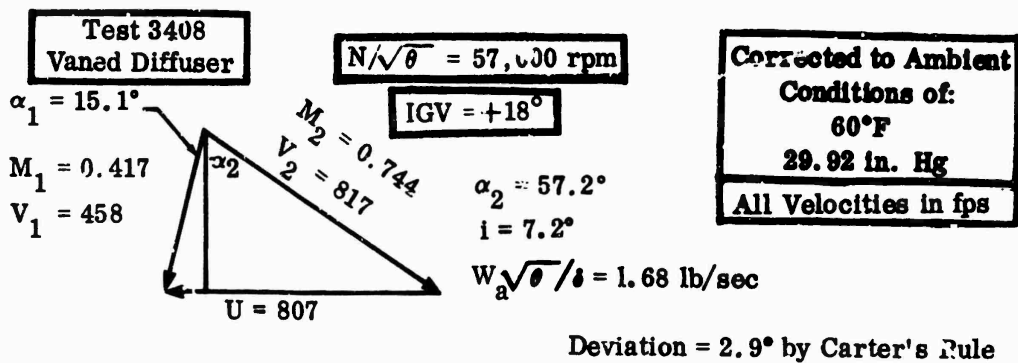


Figure 266. RMS Inlet Vector Diagrams, RF-1.

CONFIDENTIAL

Test 3404
Vaneless Diffuser

$N/\sqrt{\theta} = 34,000$ rpm
Shimmed for 34,000 rpm

Corrected to Ambient
Conditions of:
60°F
29.92 in. Hg

All Velocities in fps

$N/\sqrt{\theta} = 34,000$ rpm
Shimmed for 42,000 rpm

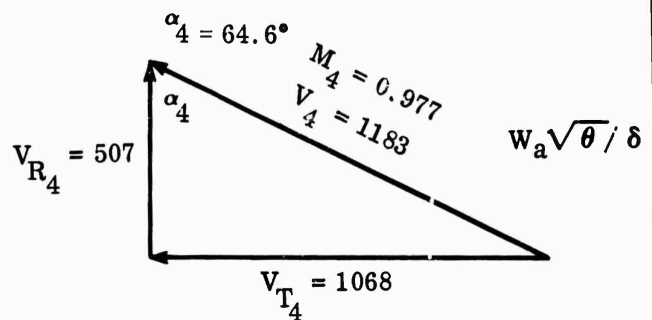
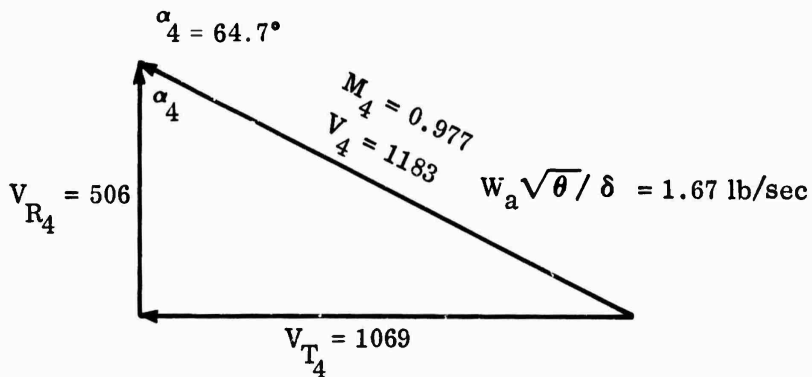
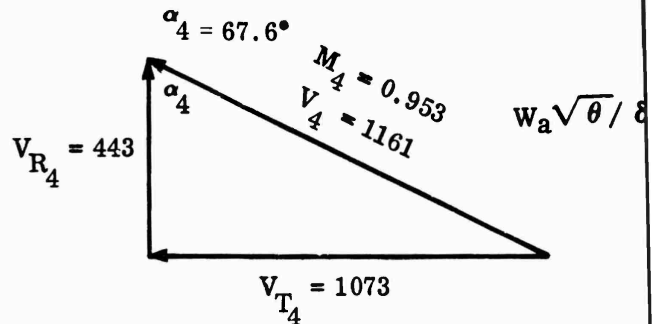
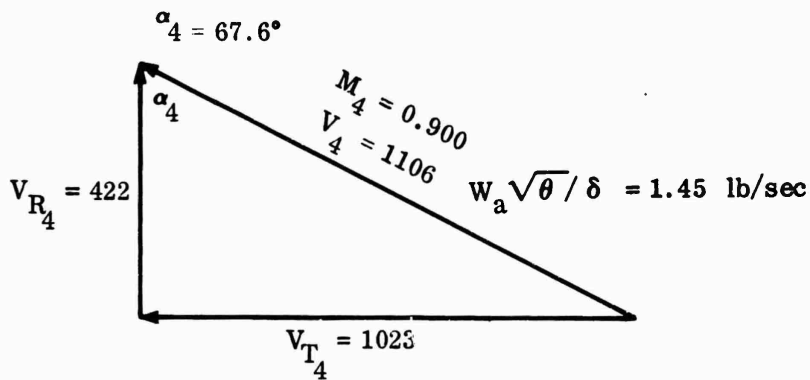
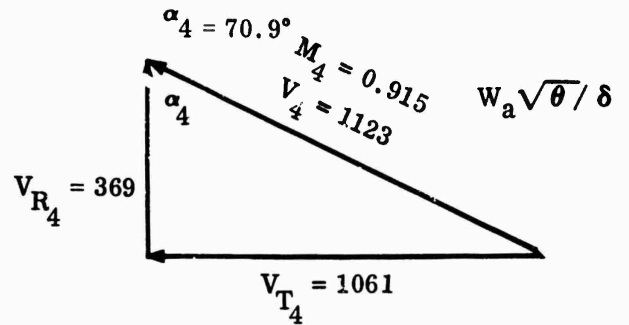
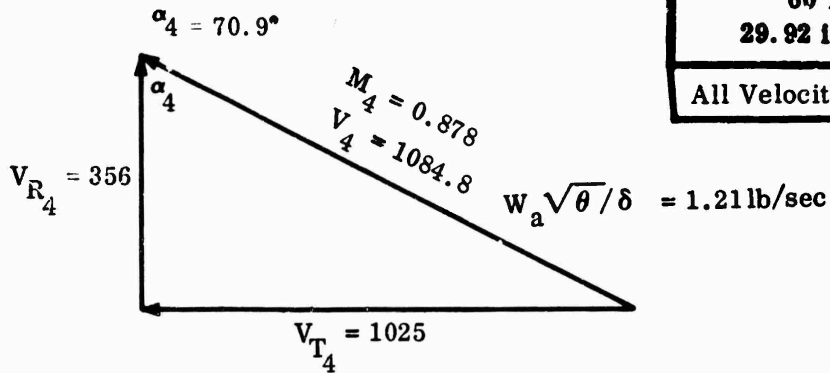


Figure 267. Mean Vector Diagrams at 1.02 Diameter Ratio, RF-1.

427

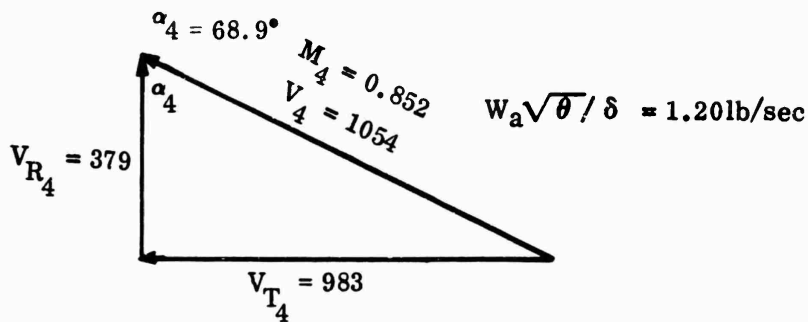
CONFIDENTIAL

T
1

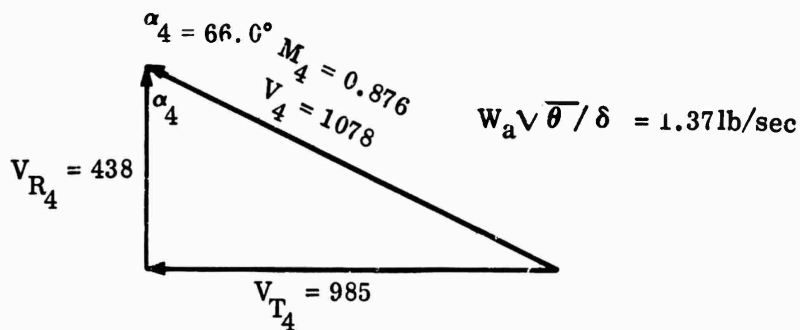
$N/\sqrt{\theta} = 34,000 \text{ rpm}$
 Shimmed for 57,000 rpm

$N/\sqrt{\theta} = 42,000$
 Shimmed for 42,000 rpm

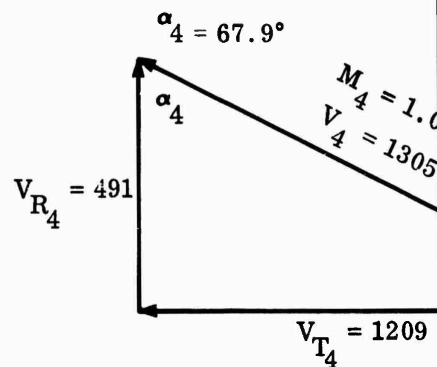
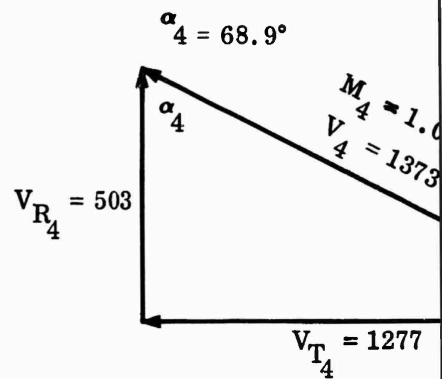
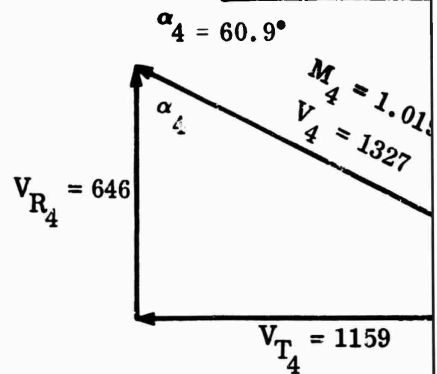
28 lb/sec



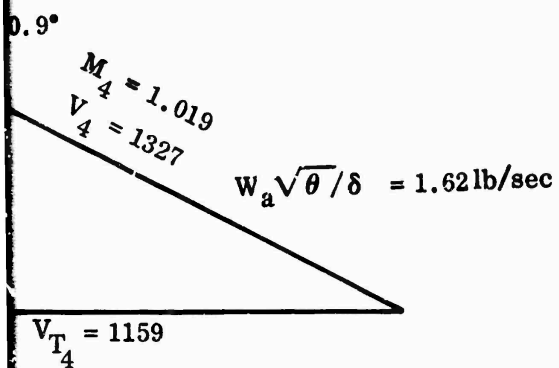
1.48 lb/sec



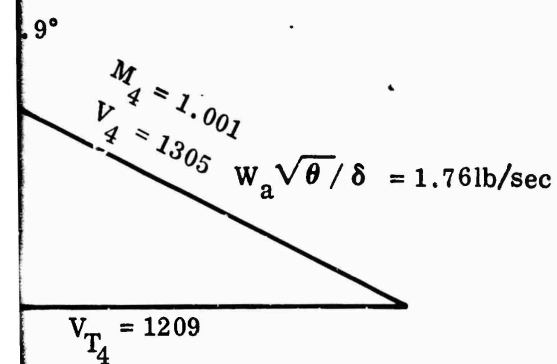
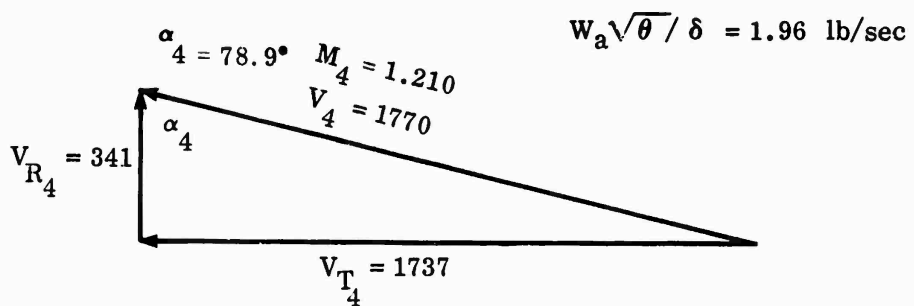
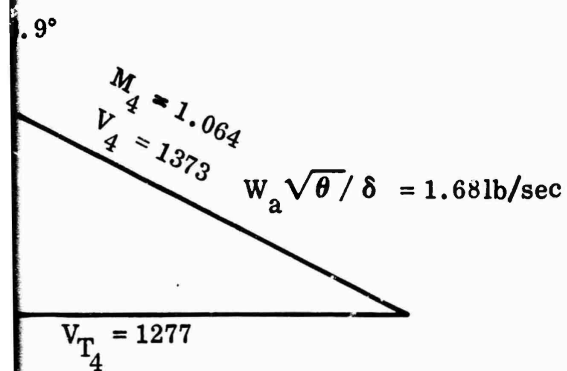
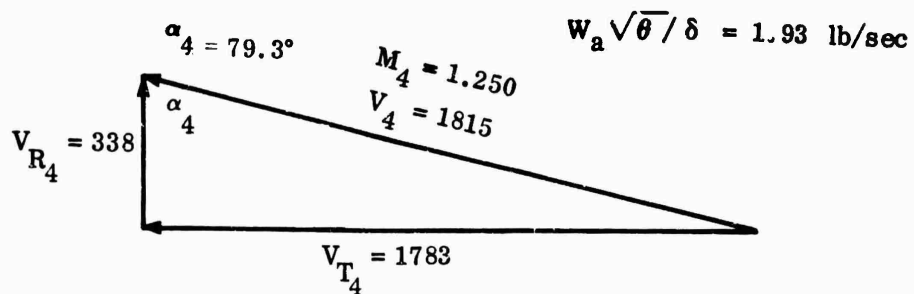
1.67 lb/sec



$N/\sqrt{\theta} = 42,000 \text{ rpm}$
 Shimmed for 42,000 rpm



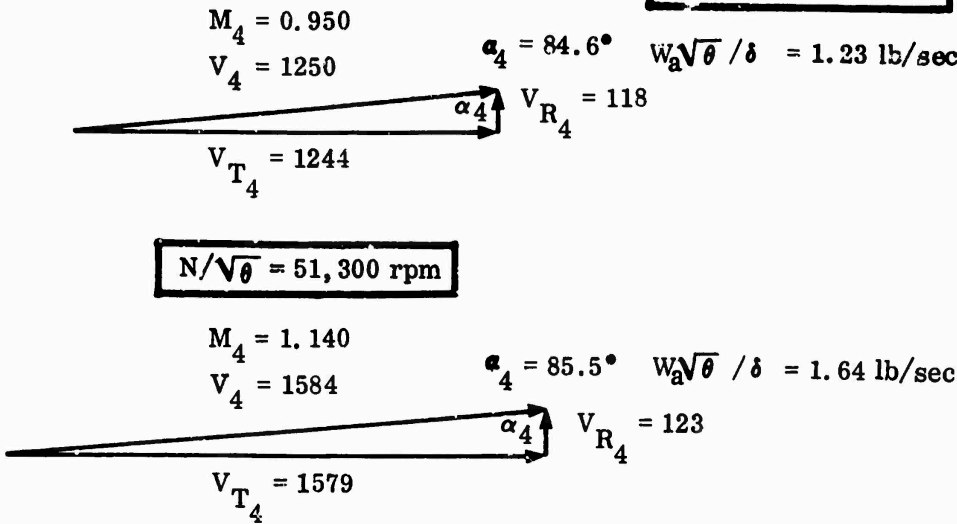
$N/\sqrt{\theta} = 57,000 \text{ rpm}$
 Shimmed for 57,000 rpm



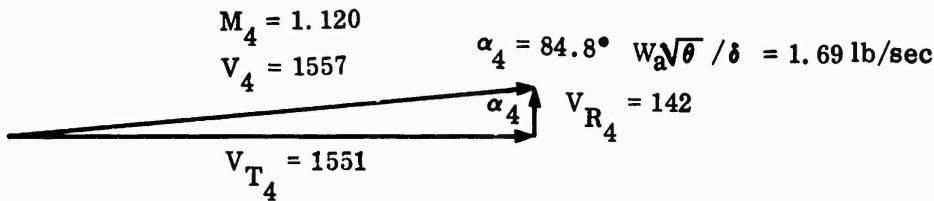
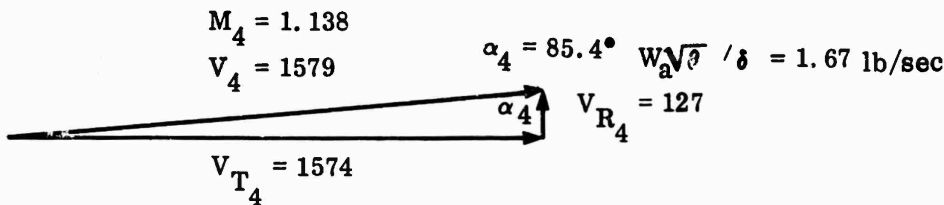
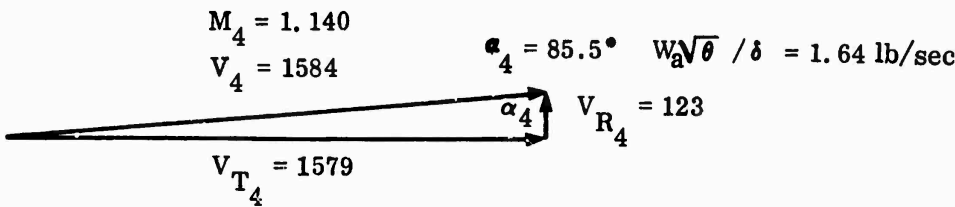
CONFIDENTIAL

Test 3406
Vaned Diffuser
 $N/\sqrt{\theta} = 42,000 \text{ rpm}$

Corrected to Ambient
Conditions of:
60°F
29.92 in. Hg
All Velocities in fps



$N/\sqrt{\theta} = 51,300 \text{ rpm}$



$N/\sqrt{\theta} = 57,000$

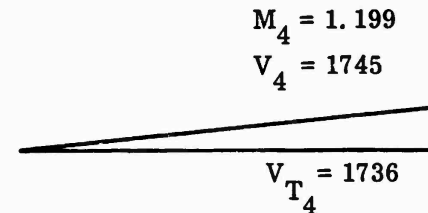
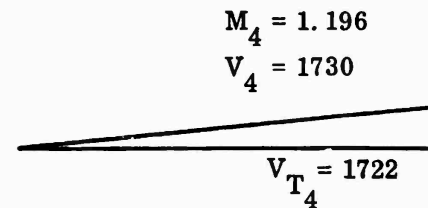
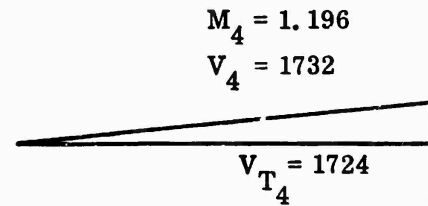


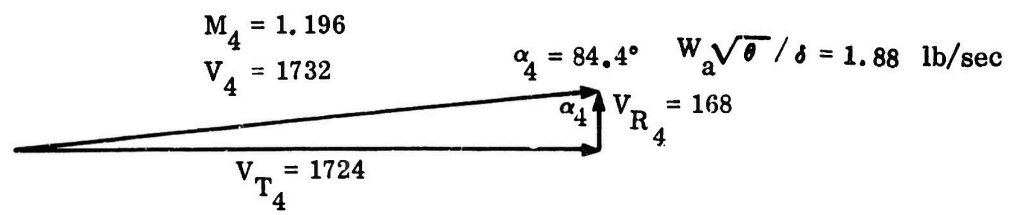
Figure 268. Mean Vector Diagrams at 1.02 Diameter Ratio, RF-1.

CONFIDENTIAL

Corrected to Ambient
Conditions of:
60°F
29.92 in. Hg
All Velocities in fps

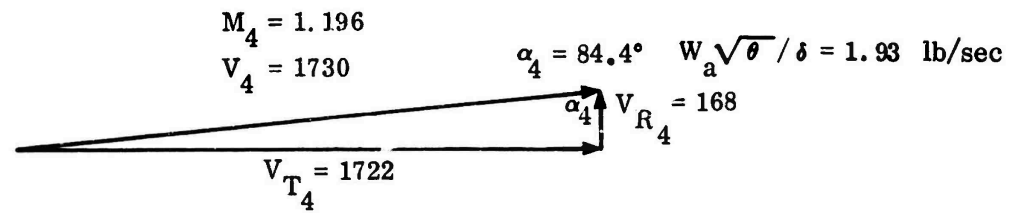
$\sqrt{\theta} / \delta = 1.23 \text{ lb/sec}$

$N/\sqrt{\theta} = 57,000 \text{ rpm}$



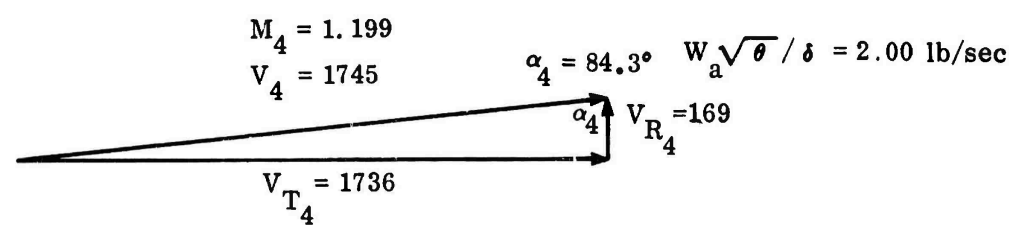
$\sqrt{\theta} / \delta = 1.64 \text{ lb/sec}$

23



$\sqrt{\theta} / \delta = 1.67 \text{ lb/sec}$

27



$\sqrt{\theta} / \delta = 1.69 \text{ lb/sec}$

2

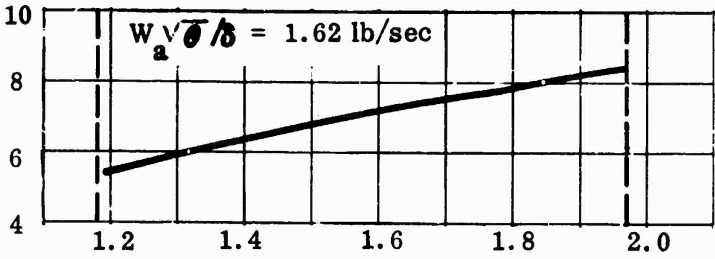
Parameter Ratio, RF-1.

Corrected to Ambient
Conditions of:
60°F
29.92 in. Hg

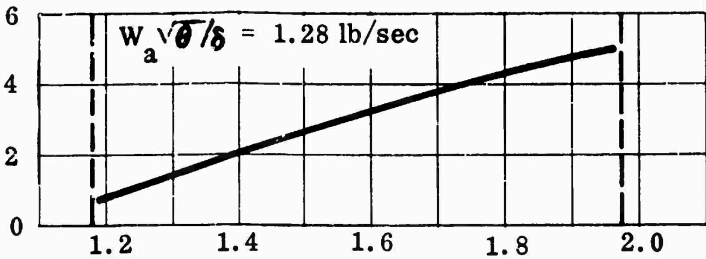
Test 3404
Vaneless Diffuser

$N/\sqrt{r} = 34,000$ rpm

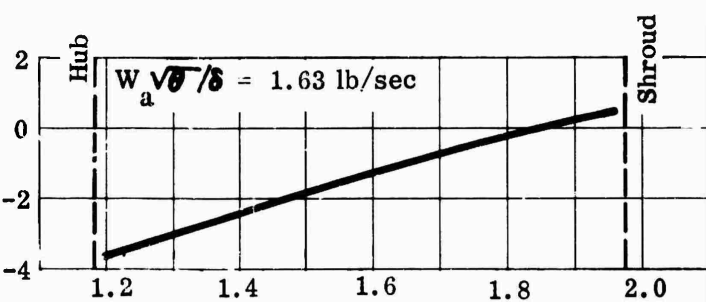
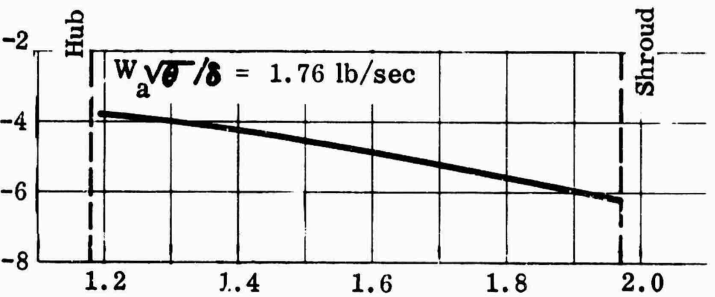
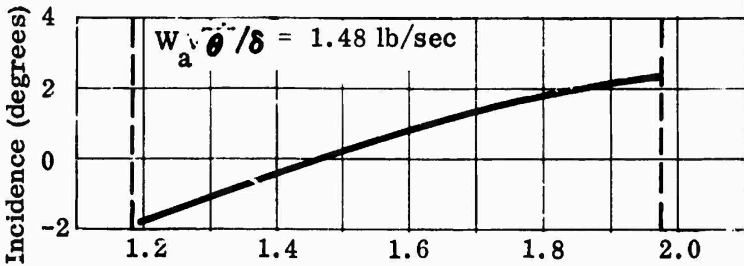
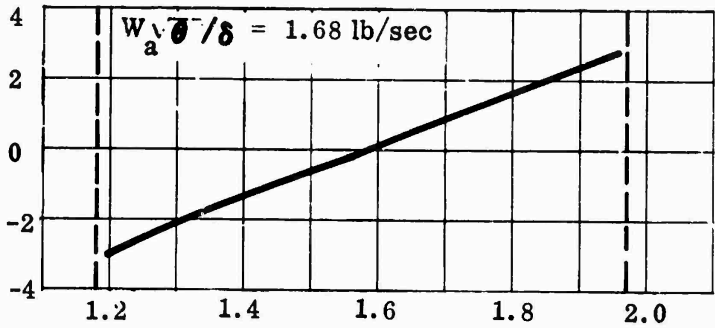
Shimmed for 34,000 rpm



Shimmed for 42,000 rpm



Incidence (degrees)



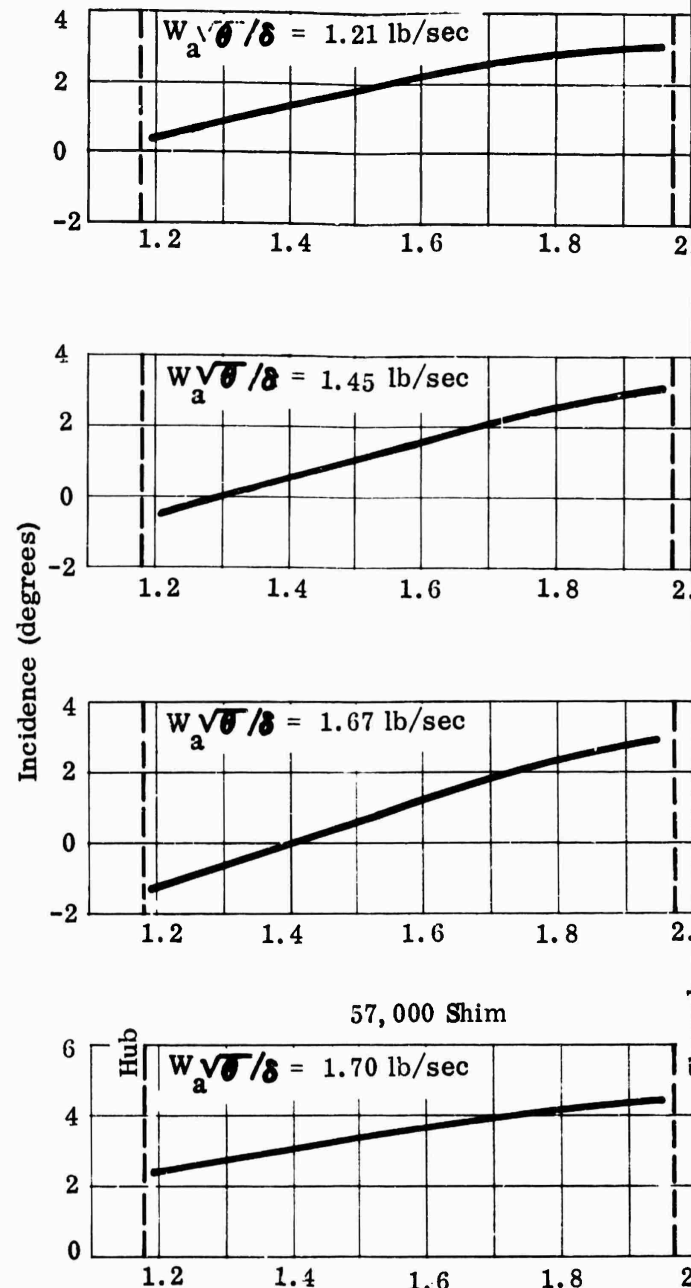
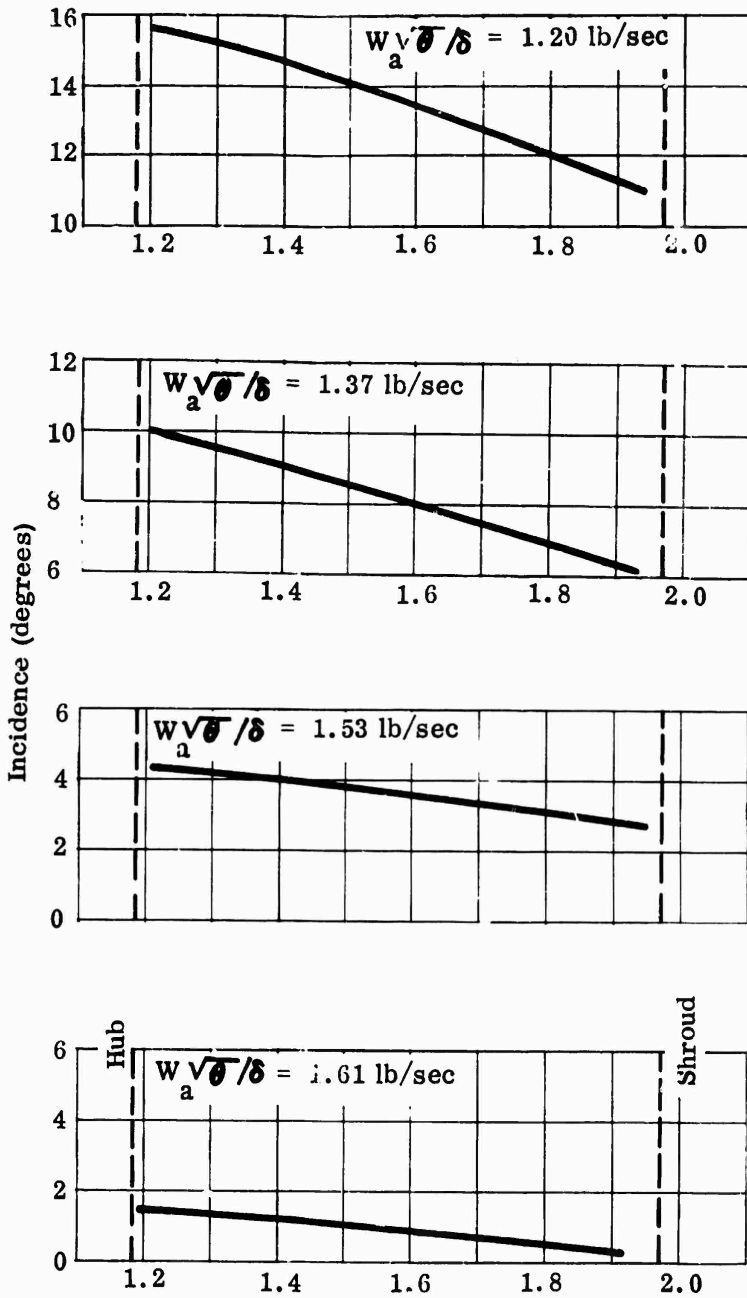
Radius (in.)

Figure 269. Radial Variation of Inducer Incidence, RF-1.

$$N/\sqrt{\theta} = 42,000 \text{ rpm}$$

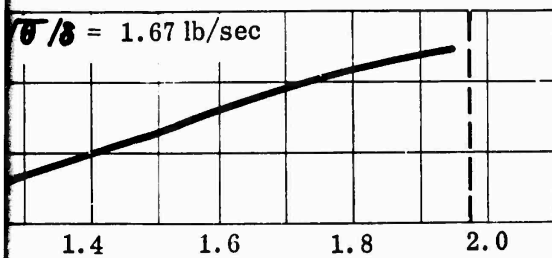
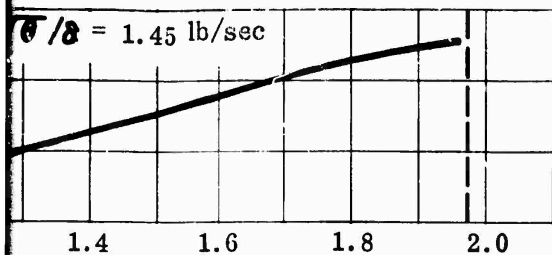
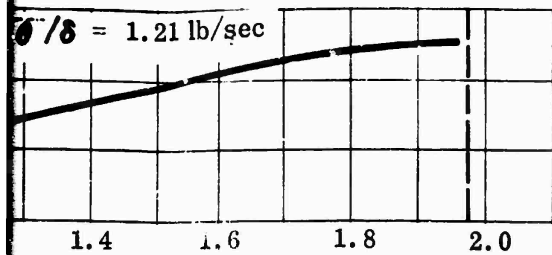
Shimmed for 57,000 rpm

Shimmed for 42,000 rpm

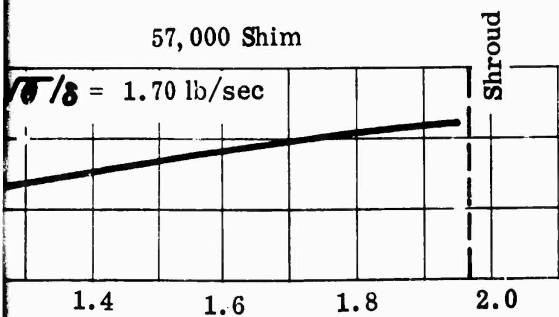


$N/\sqrt{\theta} = 42,000 \text{ rpm}$

Shimmed for 42,000 rpm

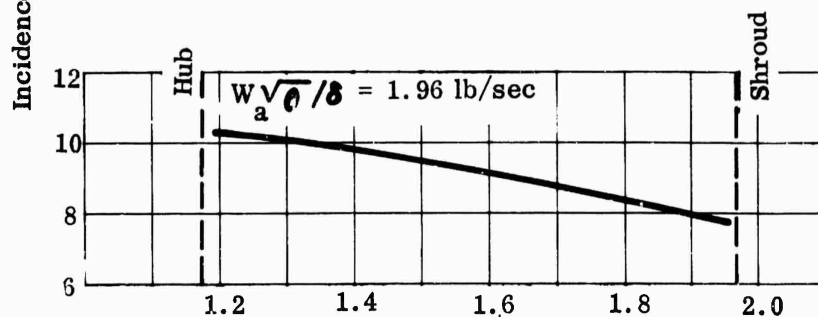
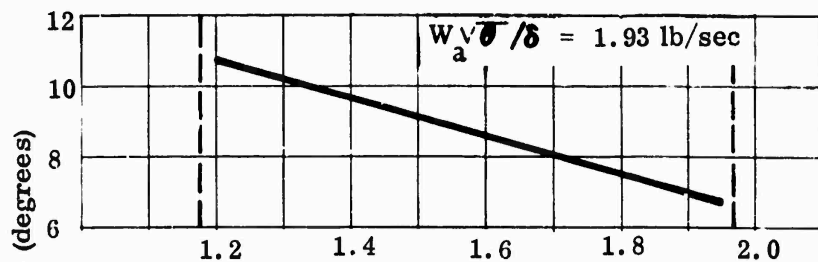


57,000 Shim



$N/\sqrt{\theta} = 57,000 \text{ rpm}$

Shimmed for 57,000 rpm



Corrected to Ambient
Conditions of:
60°F
29.92 in. Hg

Test 3406
Vaned Diffuser

$N/\sqrt{\theta} = 51,300 \text{ rpm}$

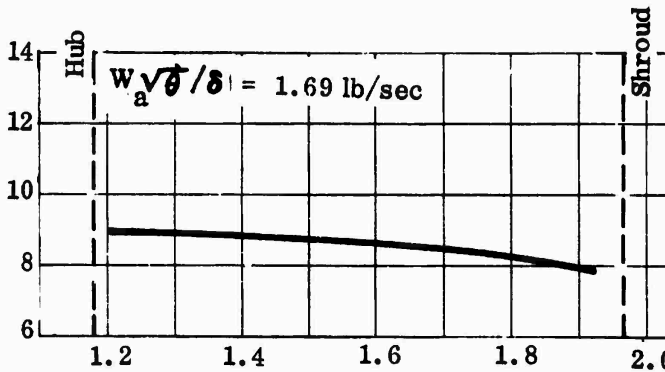
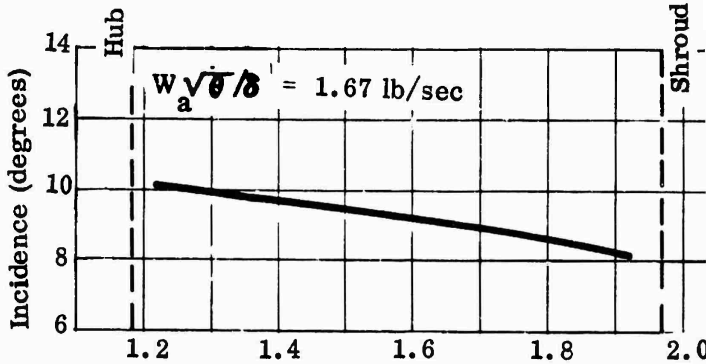
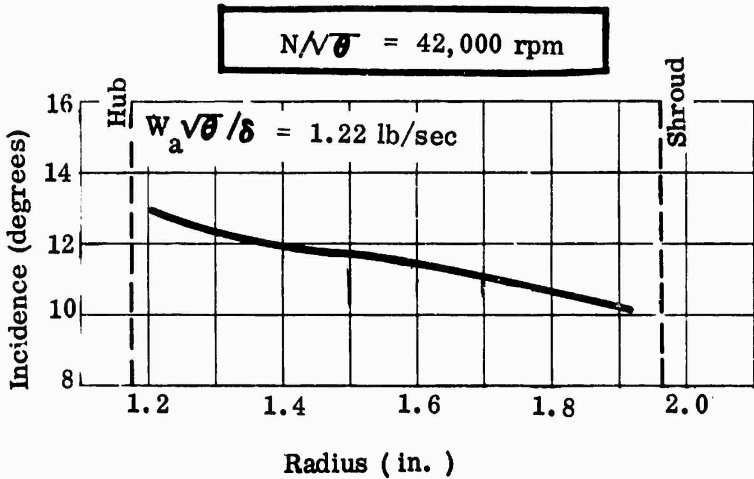
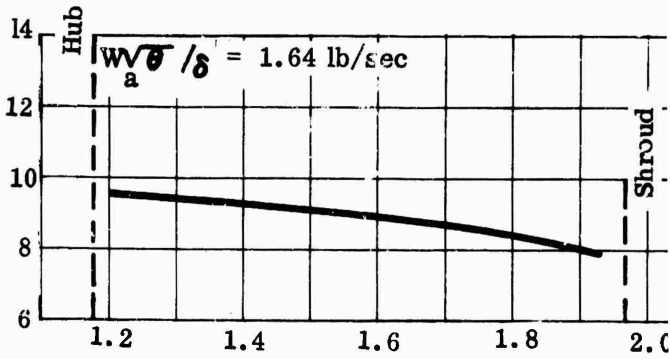
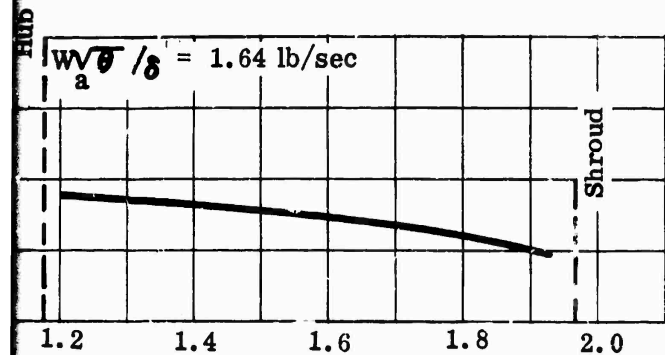


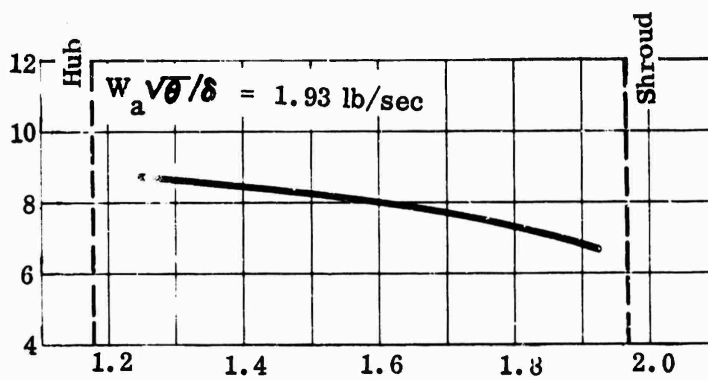
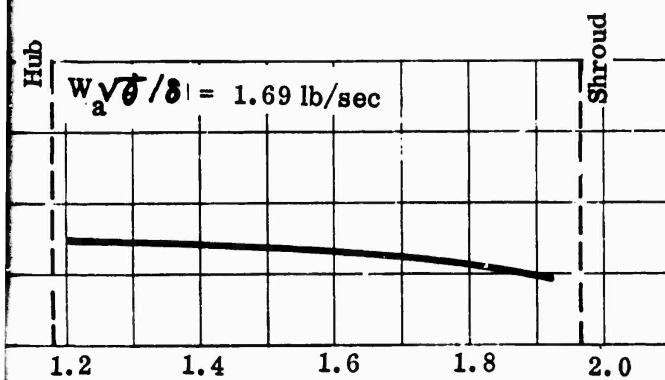
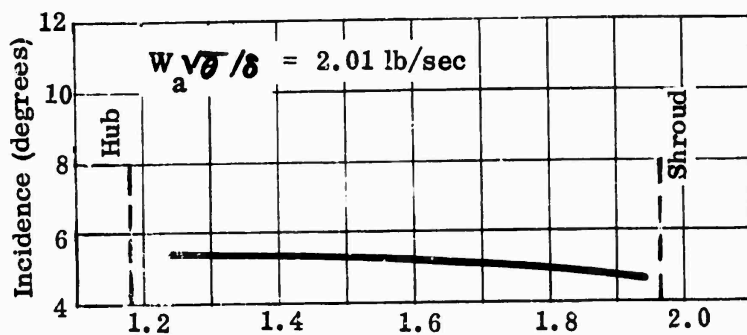
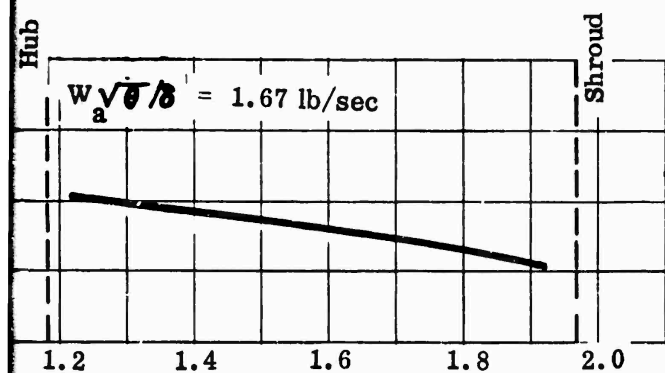
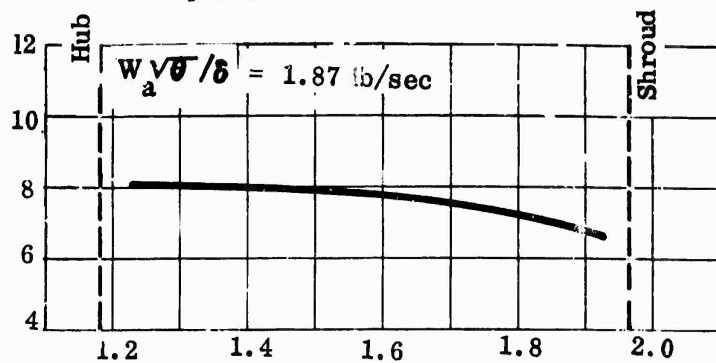
Figure 270. Radial Variation of Inducer Incidence, RF-1.

1

$N/\sqrt{\theta} = 51,300 \text{ rpm}$



$N/\sqrt{\theta} = 57,000 \text{ rpm}$



Corrected to Ambient
Conditions of:
60°F
29.92 in. Hg

Test 3404
Vaneless Diffuser

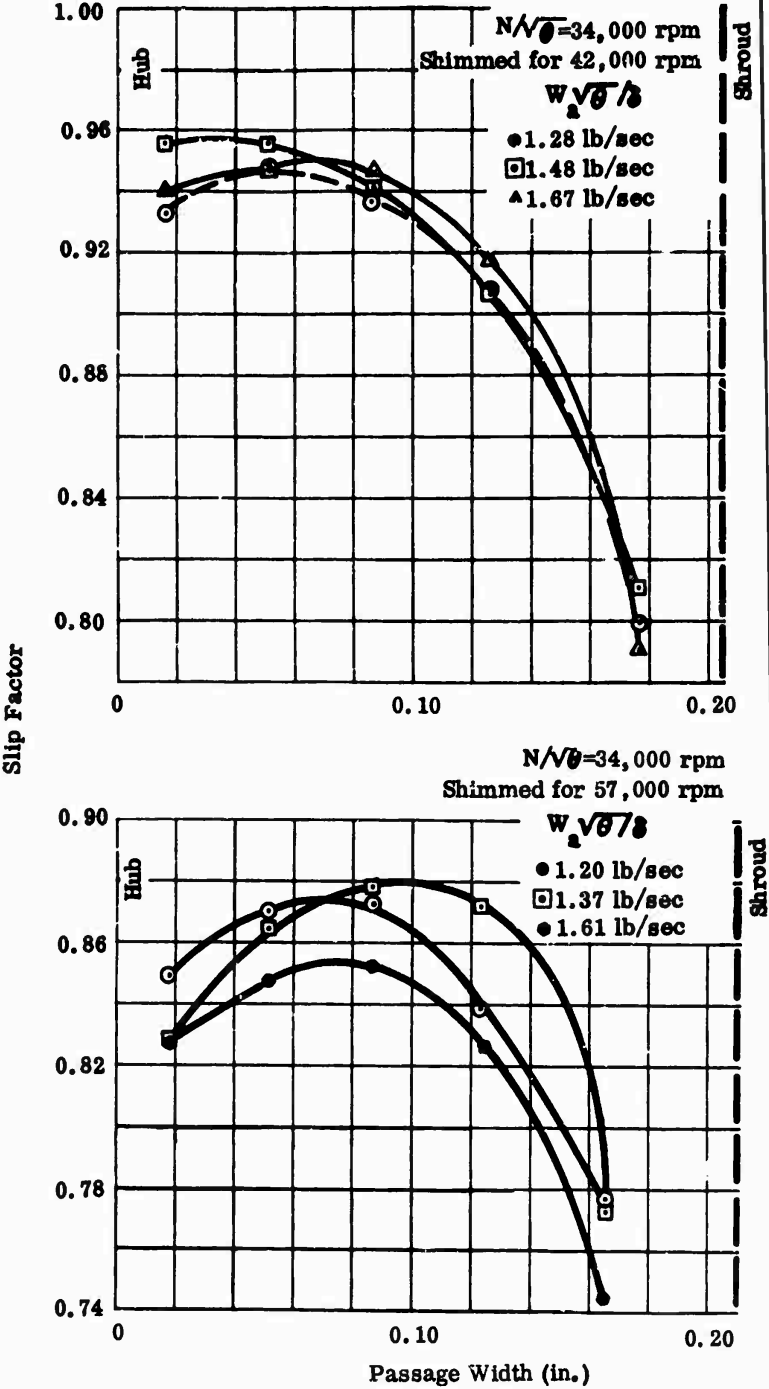
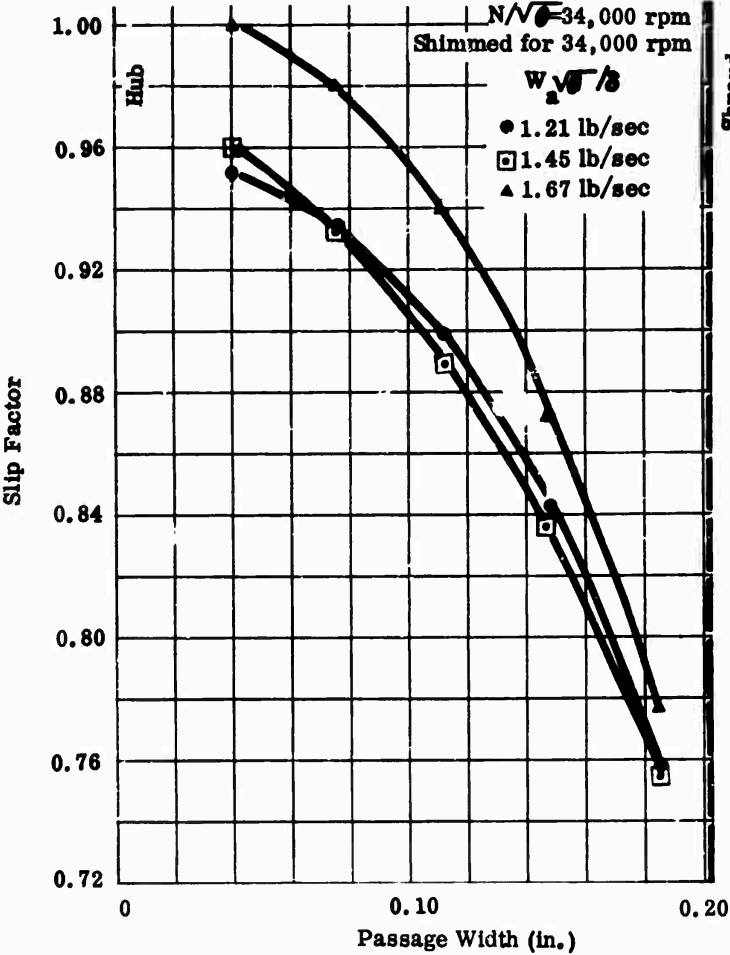
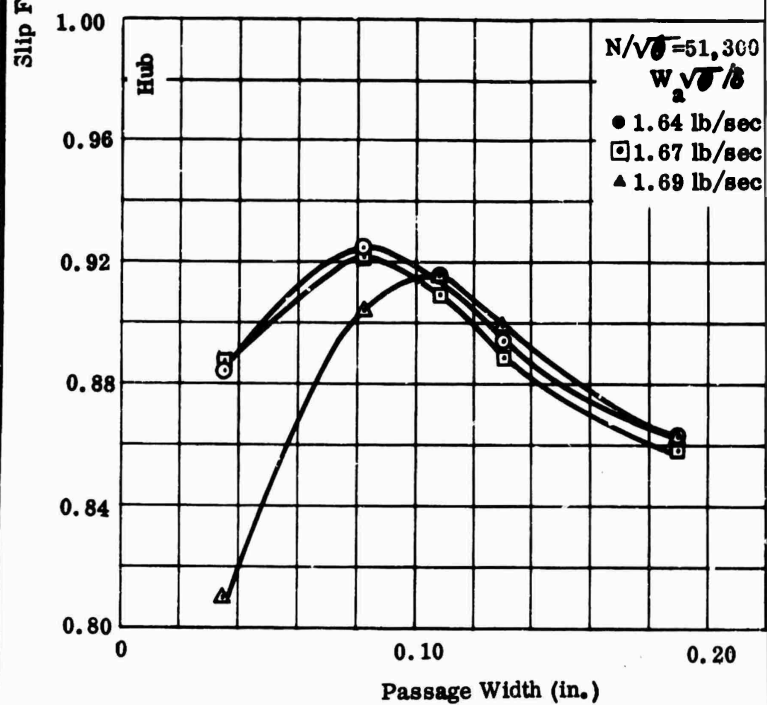
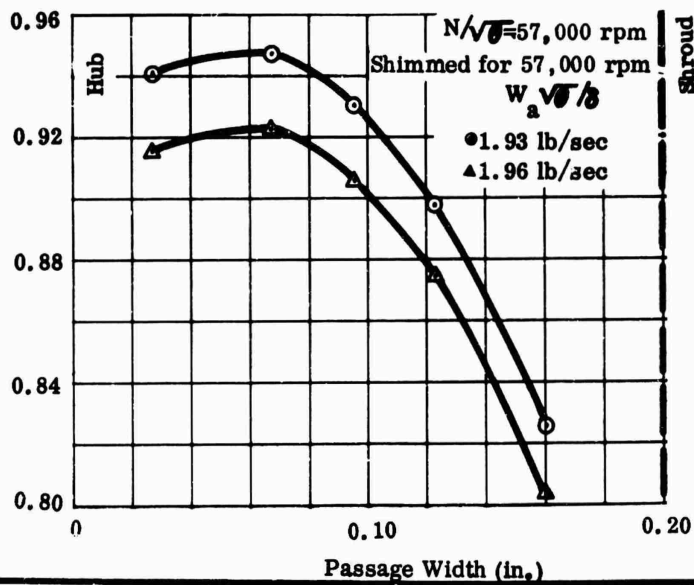
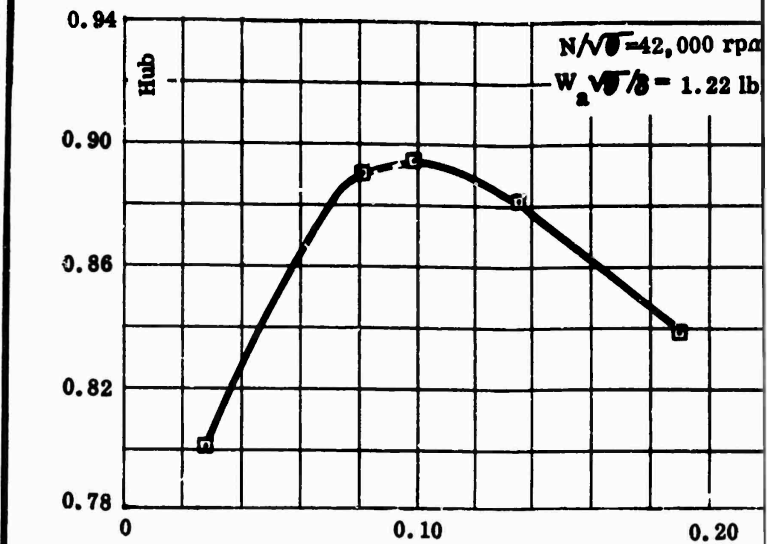
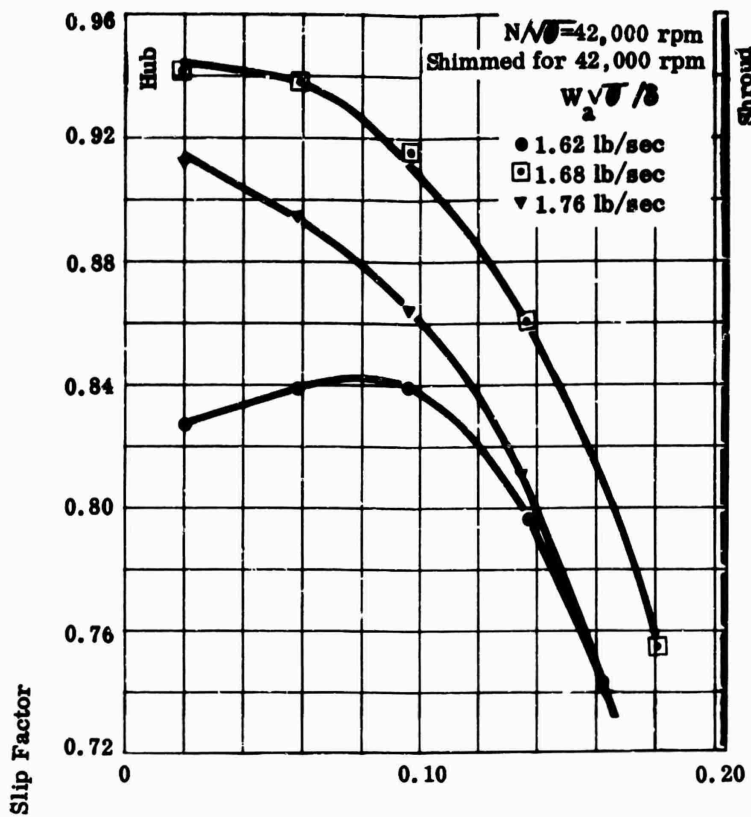
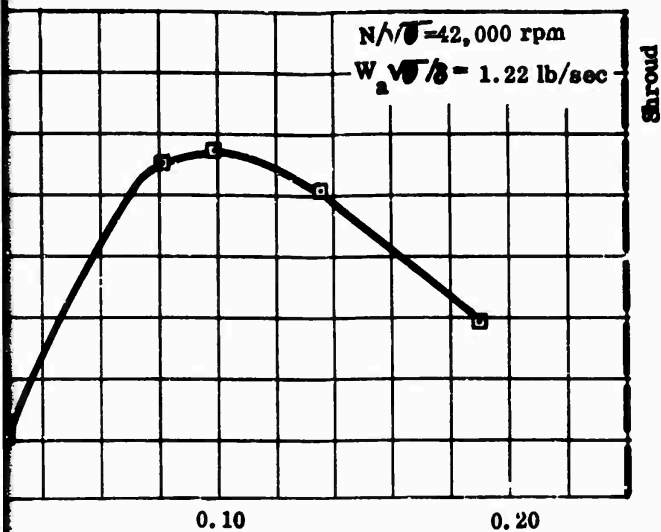
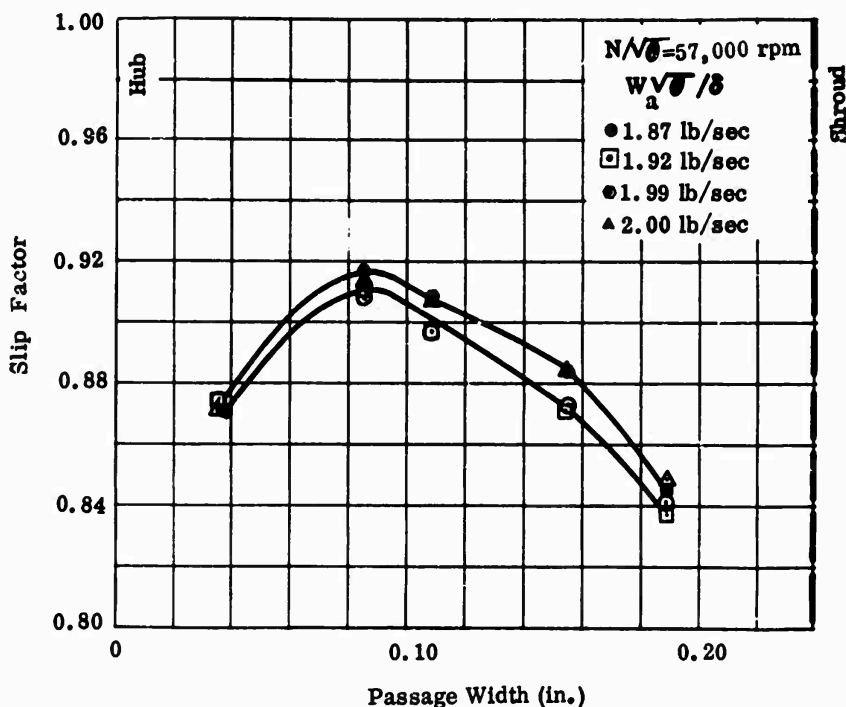
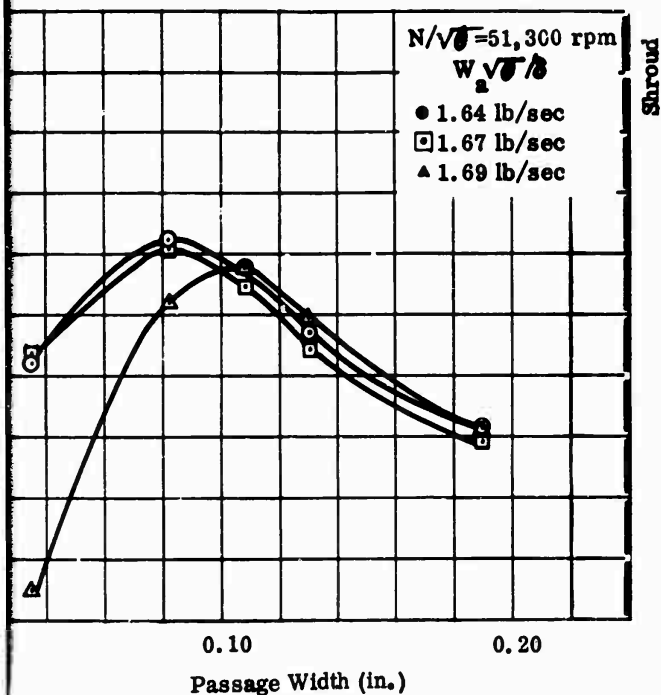


Figure 271. Variation of Slip Factor Across Impeller Tip, RF-1.

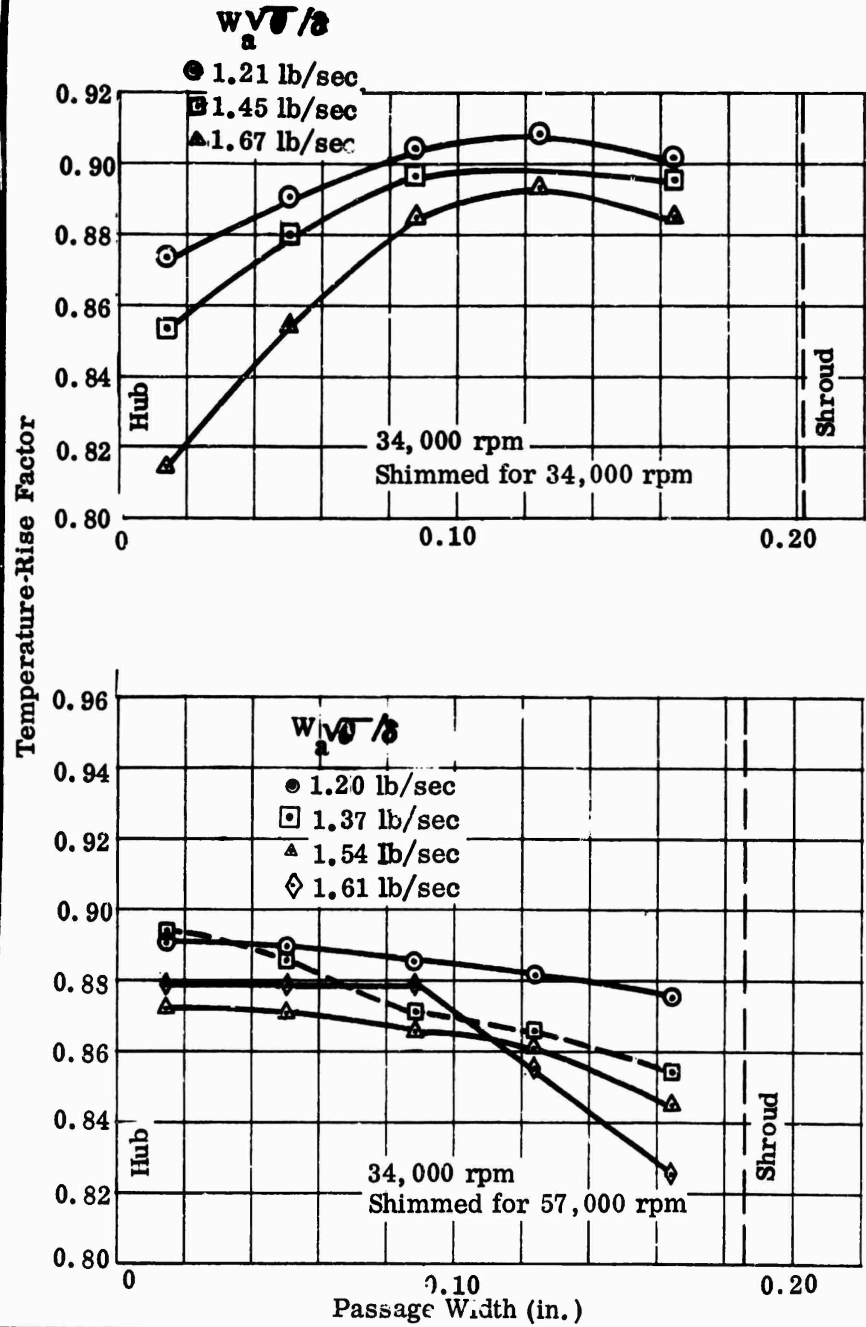




Test 3406
Vaned Diffuser



Corrected to Ambient
Conditions of:
60°F
29.92 in. Hg



Test 3404
Vaneless Diffuser

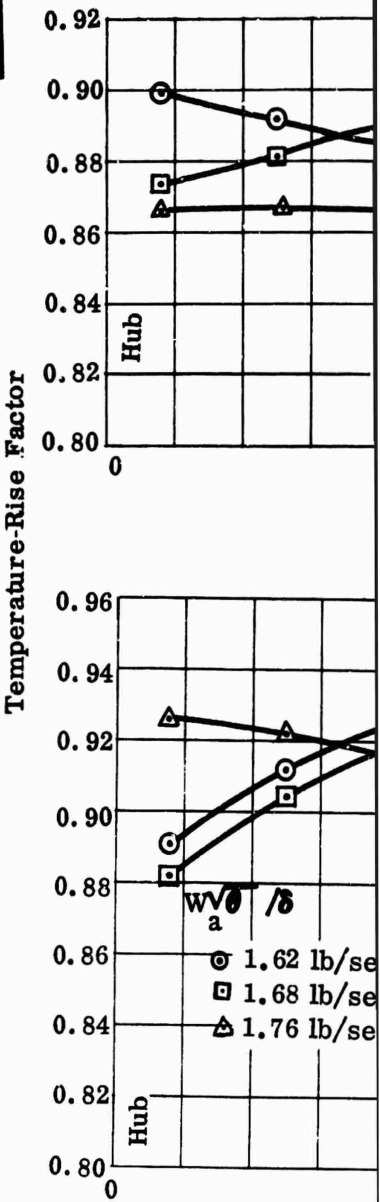
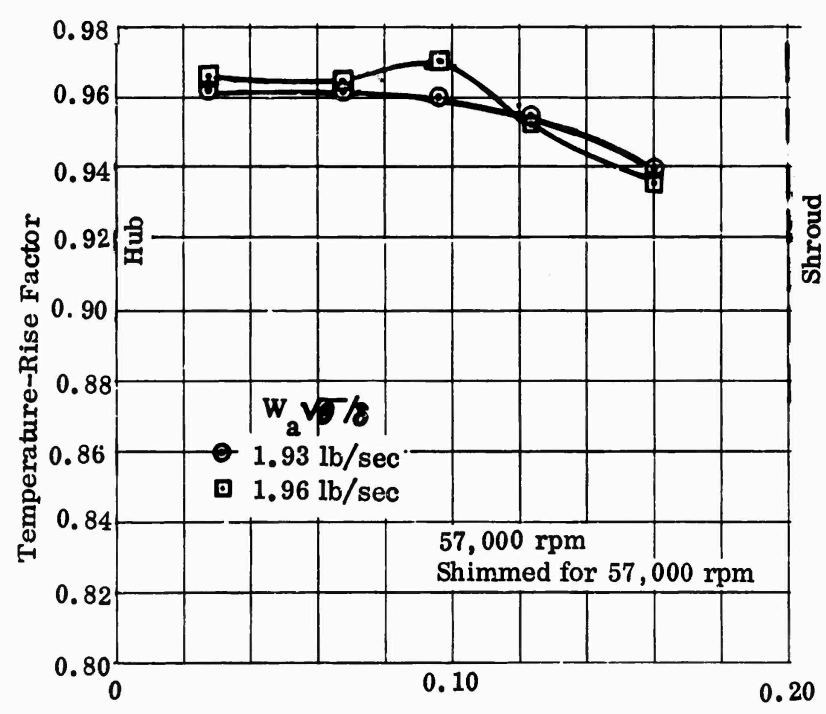
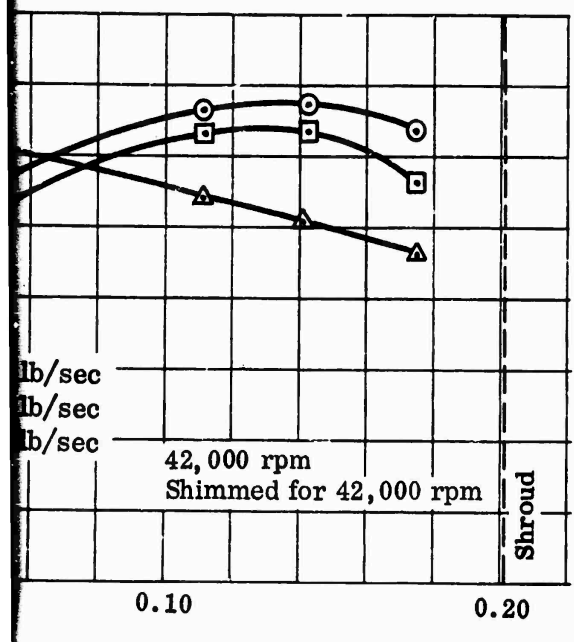
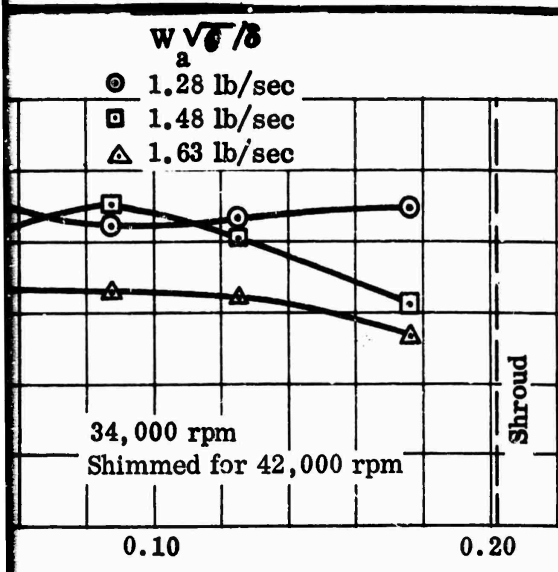
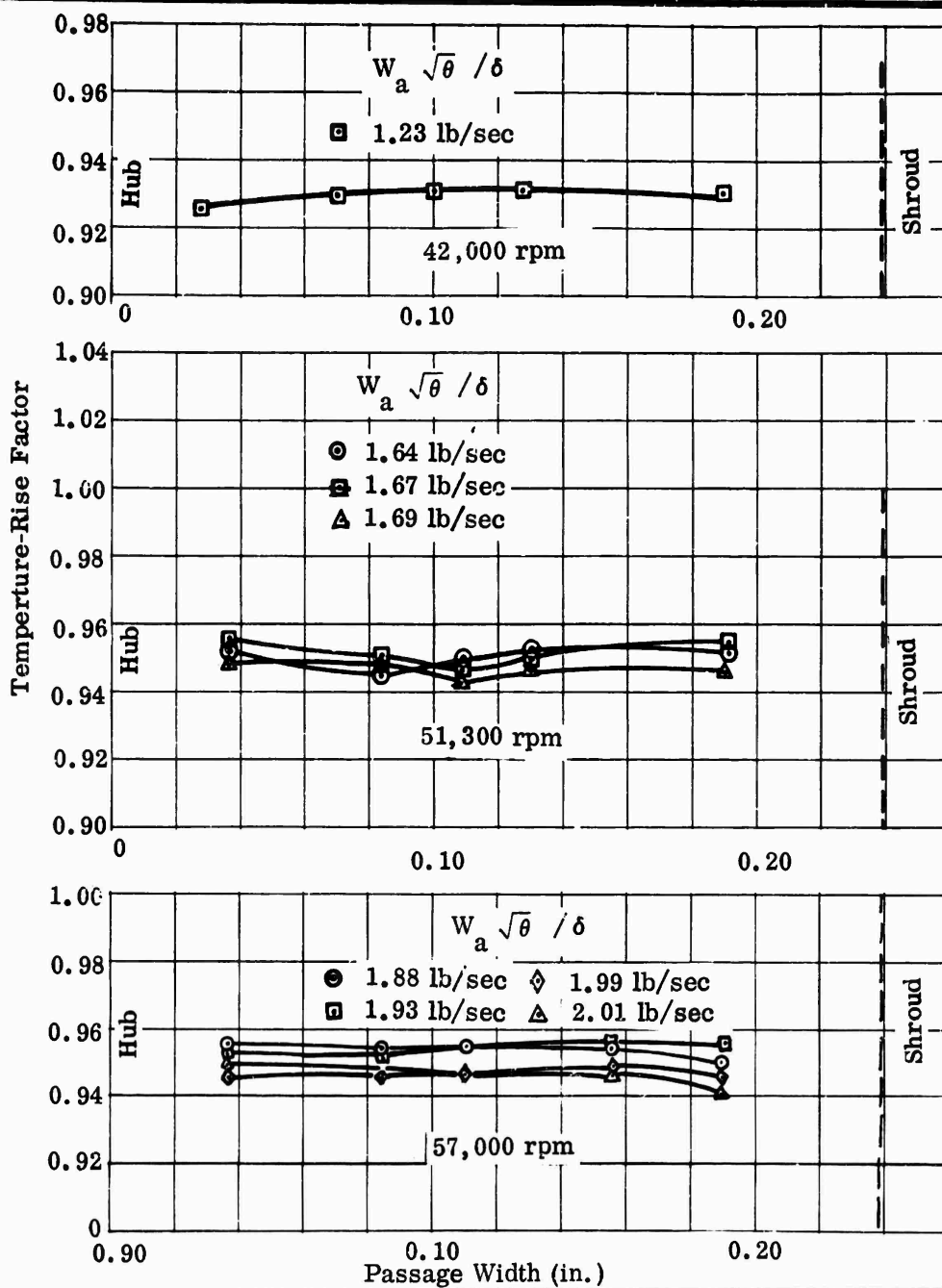


Figure 272. Temperature-Rise Factor Across Impeller Tip, RF-1.



Test 3406
Vaned Diffuser



CONFIDENTIAL

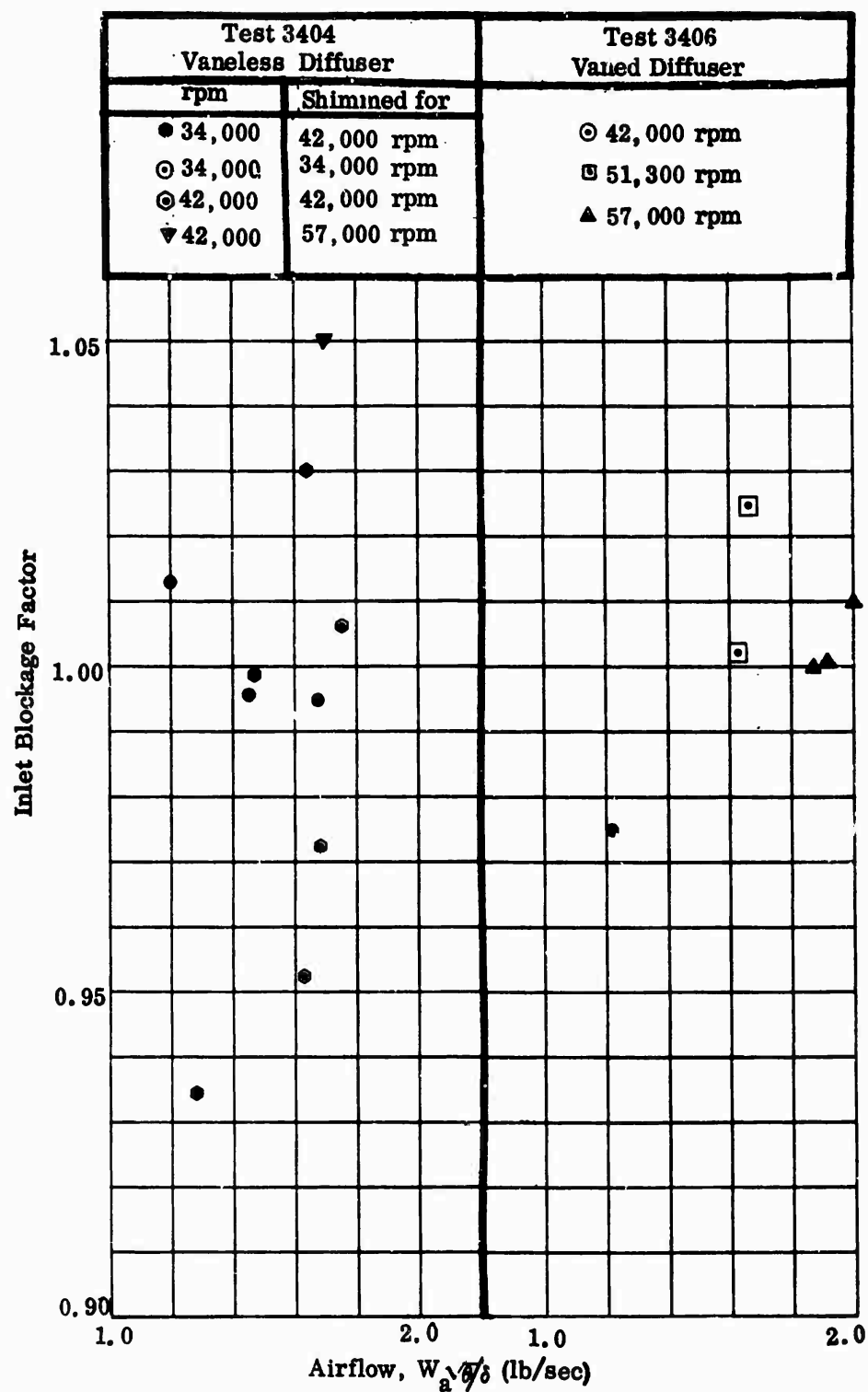


Figure 273. Inlet Blockage Factor, RF-1.

CONFIDENTIAL

CONFIDENTIAL

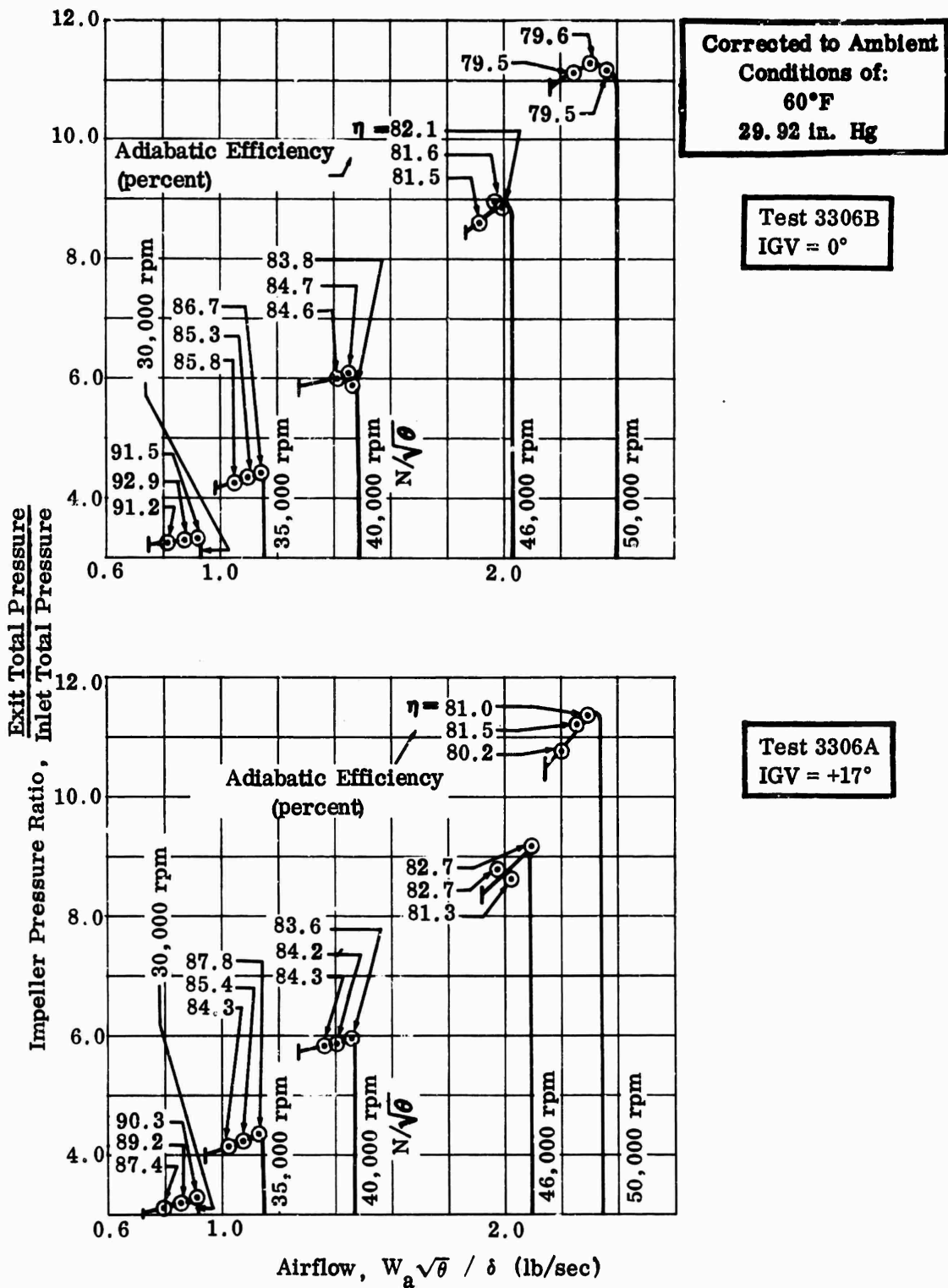


Figure 274. Pressure Ratio Versus Airflow, Workhorse.

CONFIDENTIAL

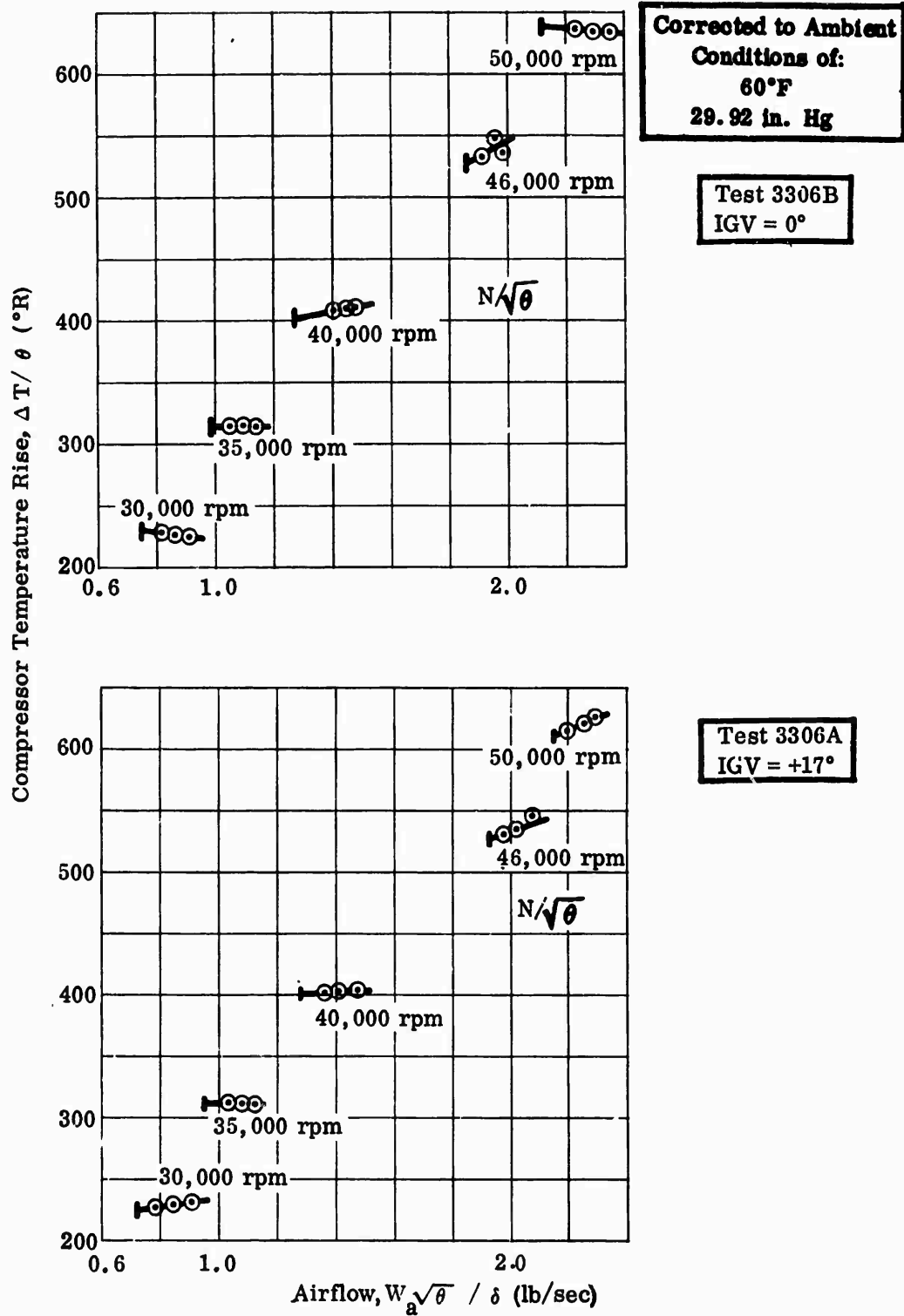


Figure 275. Temperature Rise Versus Airflow, Workhorse.

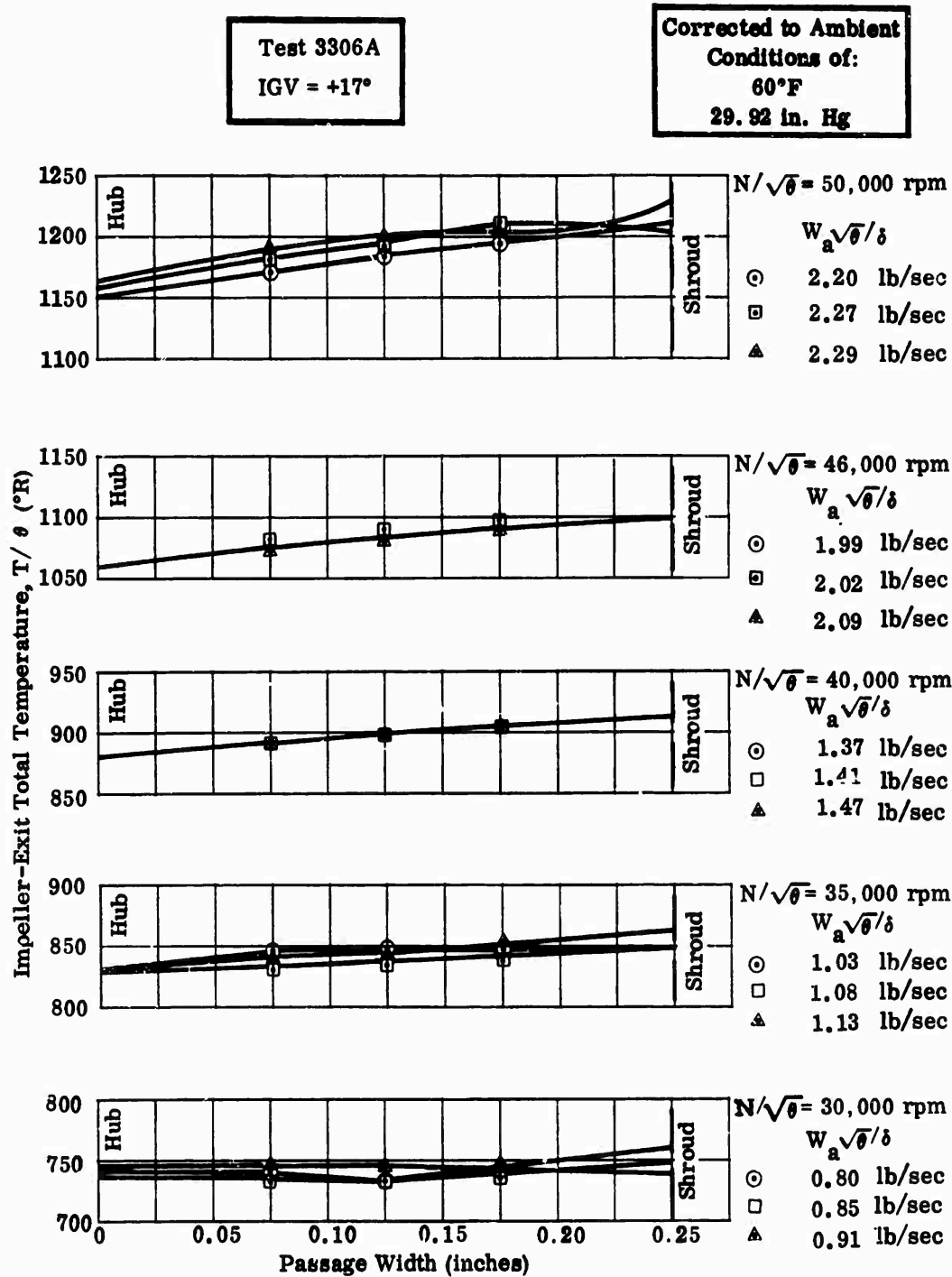


Figure 276. Impeller-Exit Total Temperature, Workhorse.

CONFIDENTIAL

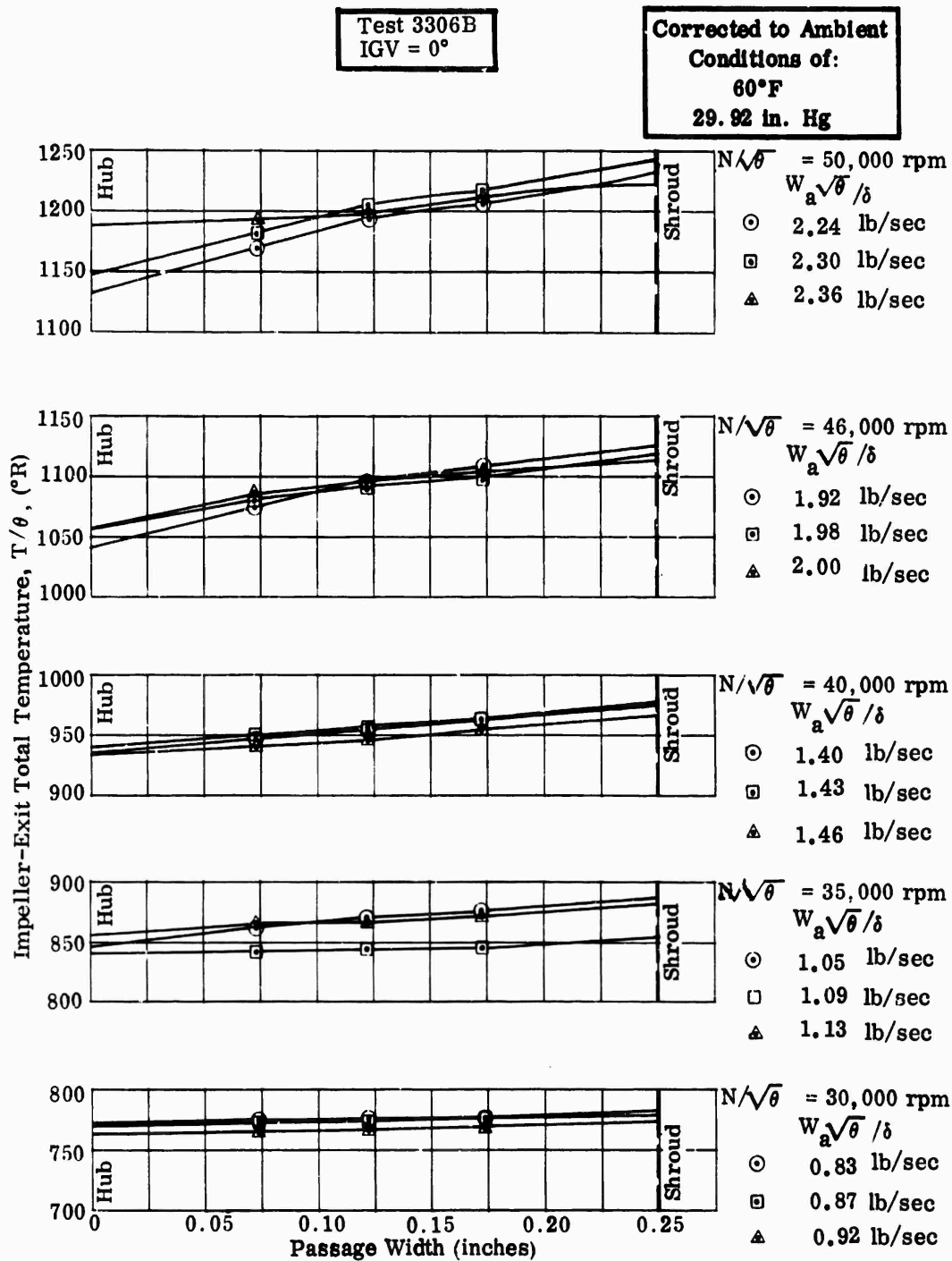


Figure 277. Impeller-Exit Total Temperature, Workhorse.

CONFIDENTIAL

Corrected to Ambient
Conditions of:
60°F
29.92 in. Hg.

Test 3306A
IGV = +17°
⊙ Yaw Probe
□ Rake I
▲ Rake II

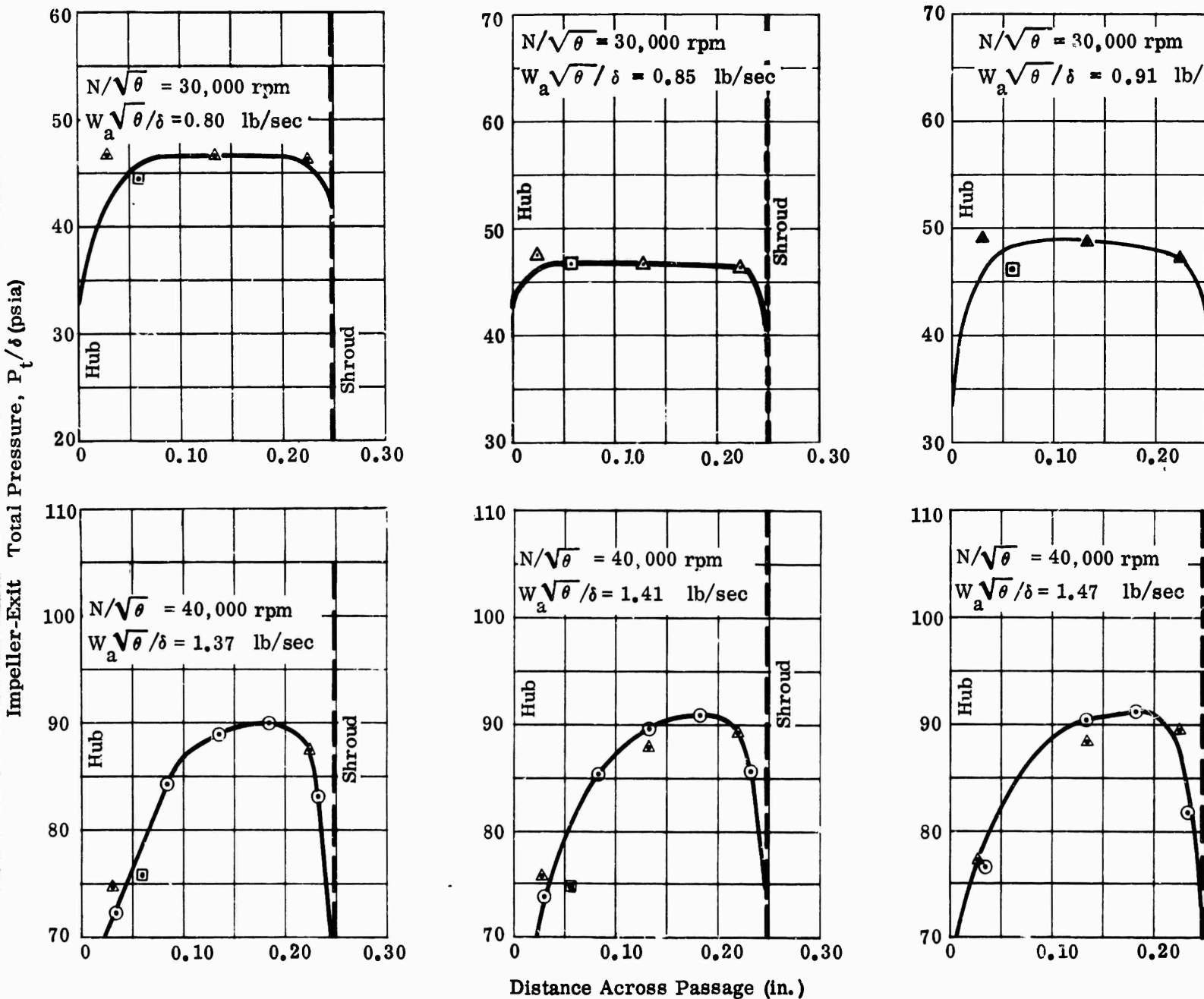
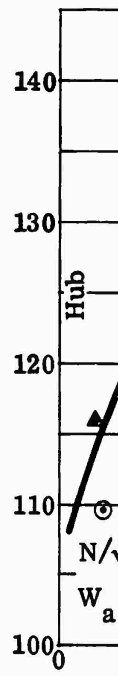
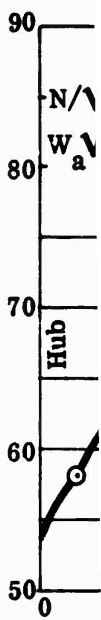
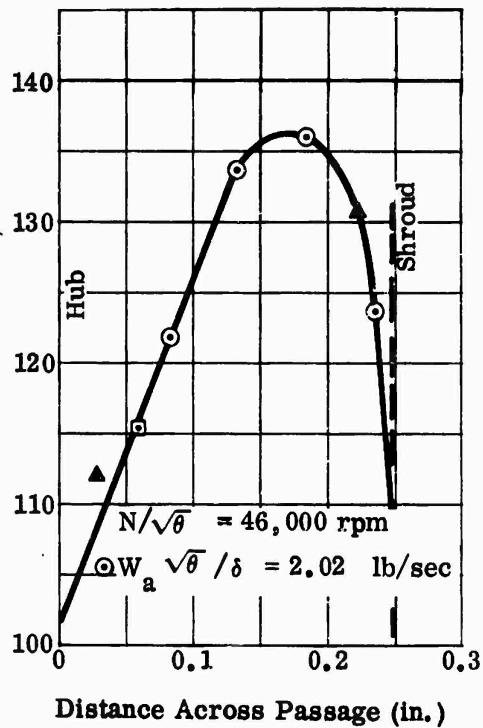
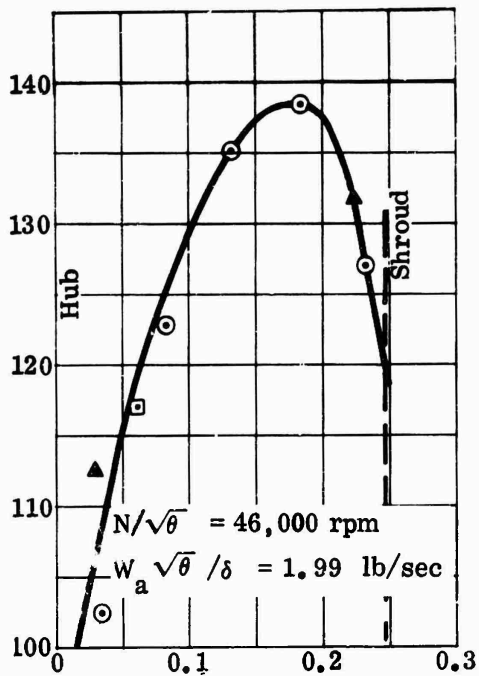
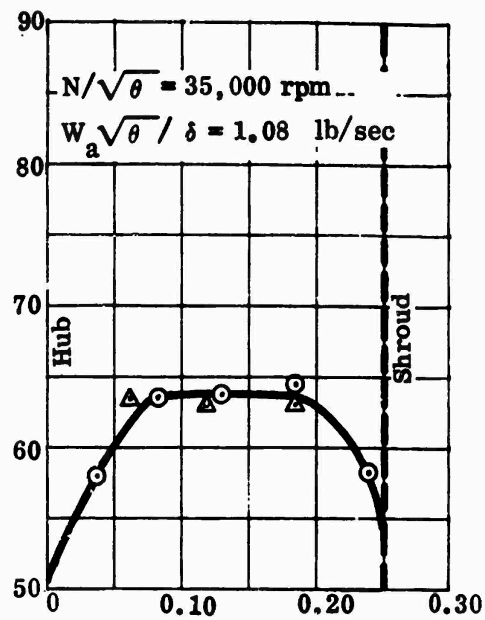
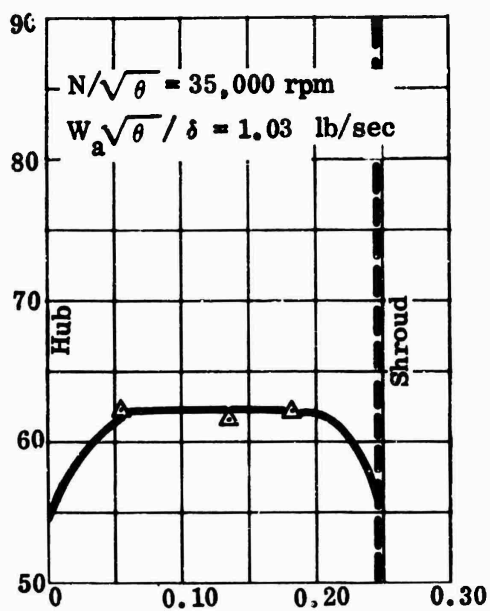
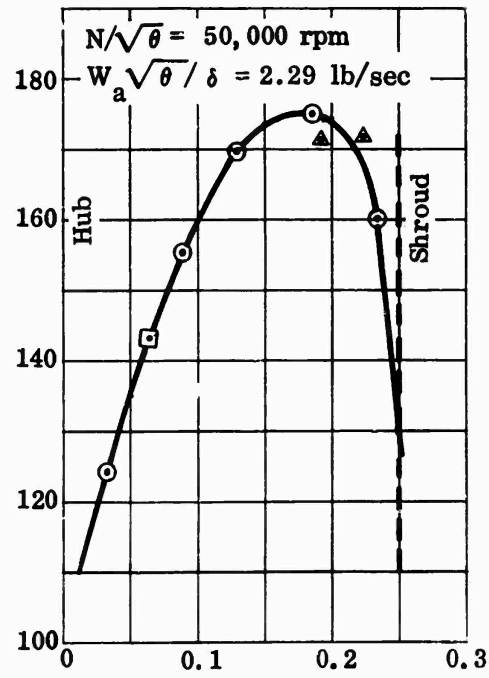
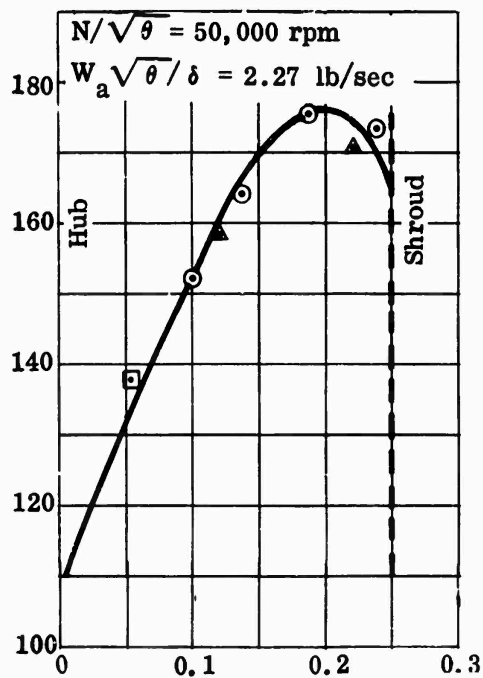
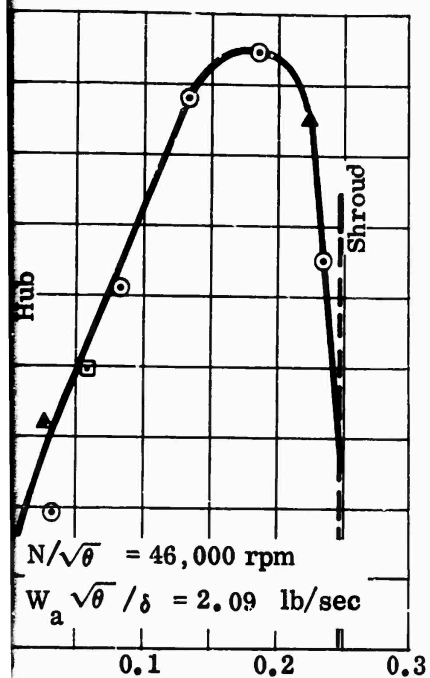
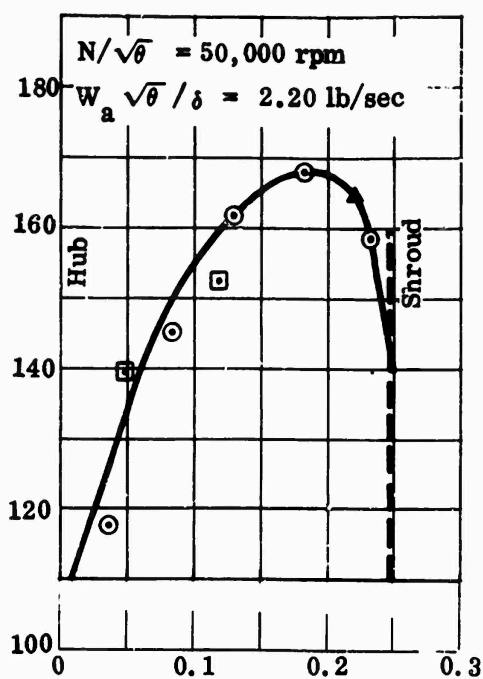
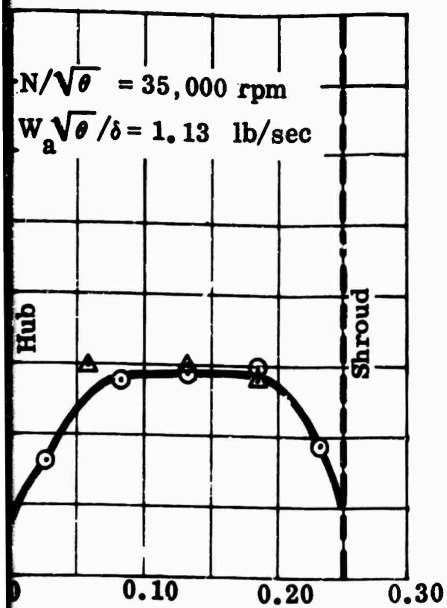


Figure 278. Impeller-Exit Total Pressure, Workhorse.





Distance Across Passage (in.)

Corrected to Ambient Conditions of: 60°F 29.92 in. Hg	Test 3306B	○ Yaw Probe
	IGV = 0°	□ Rake I
		▲ Rake II

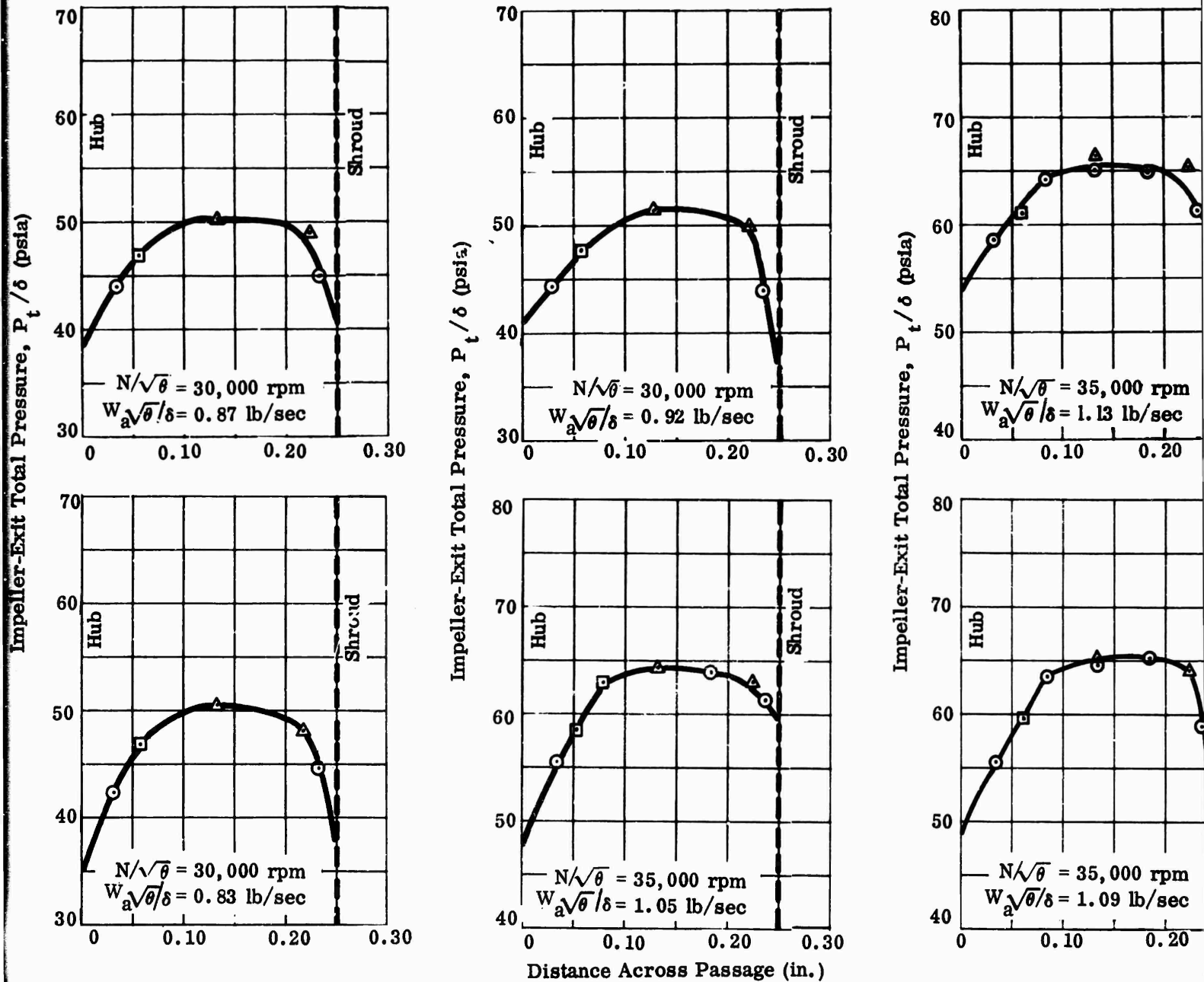
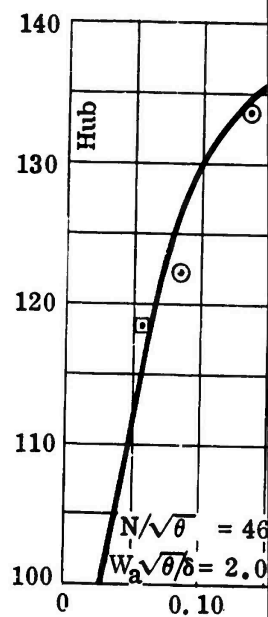
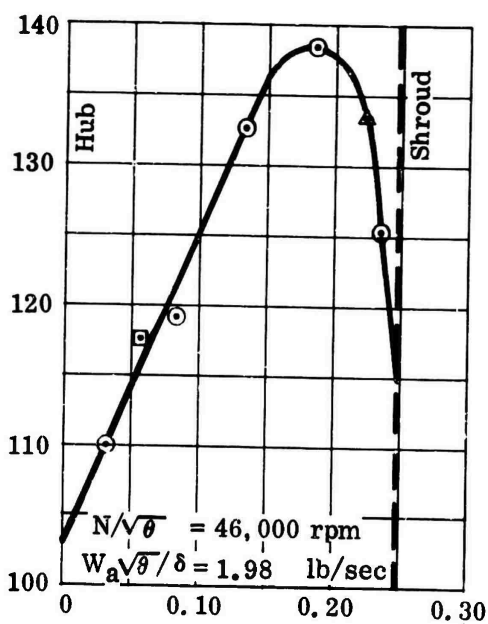
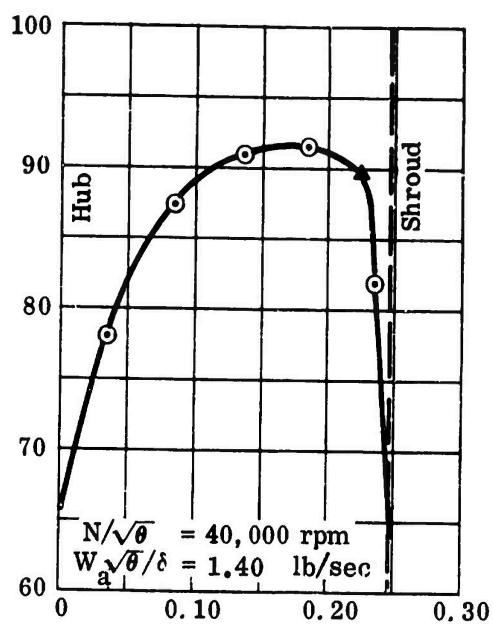
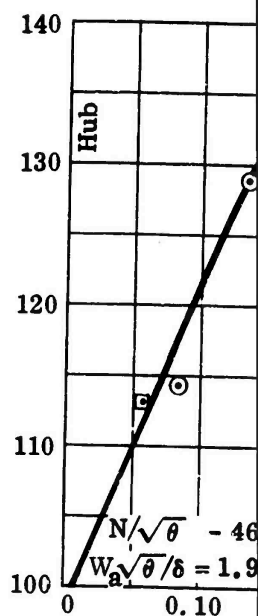
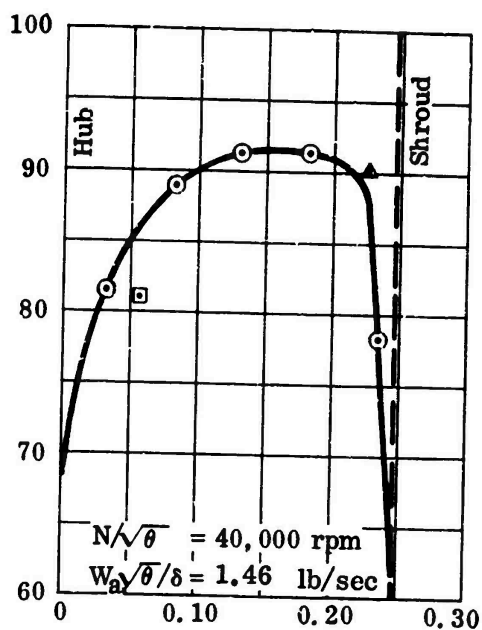
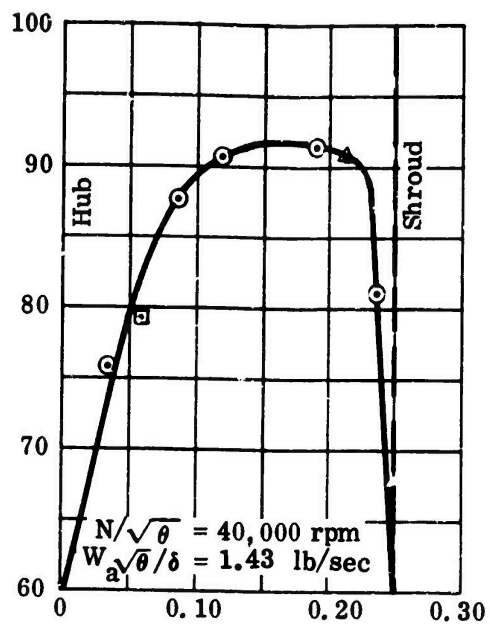
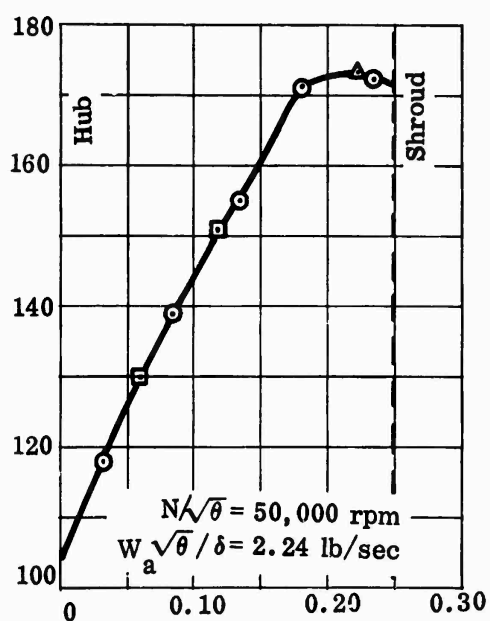
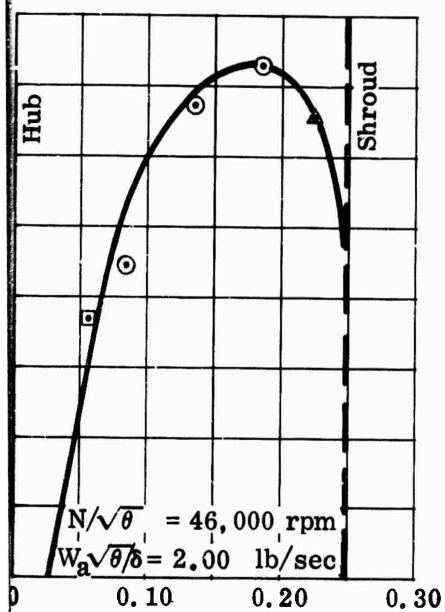
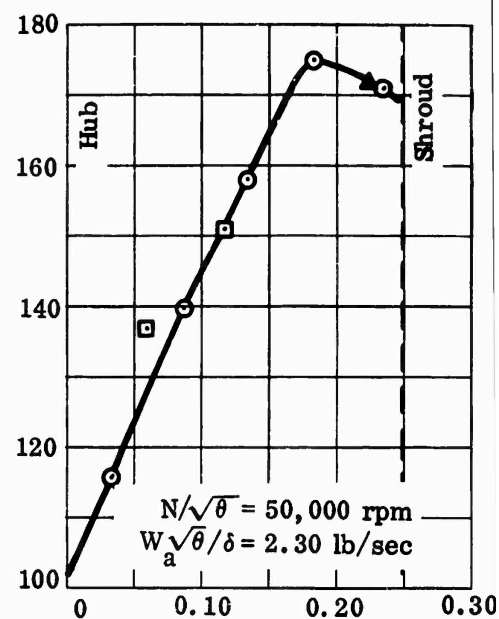
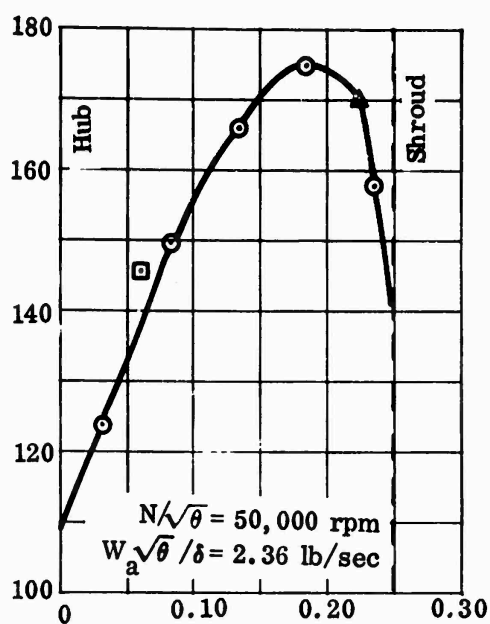
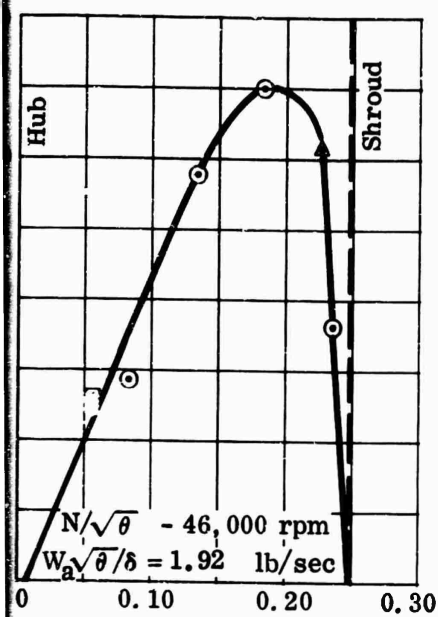


Figure 279. Impeller-Exit Total Pressure, Workhorse.





Distance Across Passage (in.)

Corrected to Ambient
Conditions of:
60°F
29.92 in. Hg

Test 3306A
IGV = 17°

Hub at 0.0 in.
Shroud at 0.248 in.

Absolute Mach Number

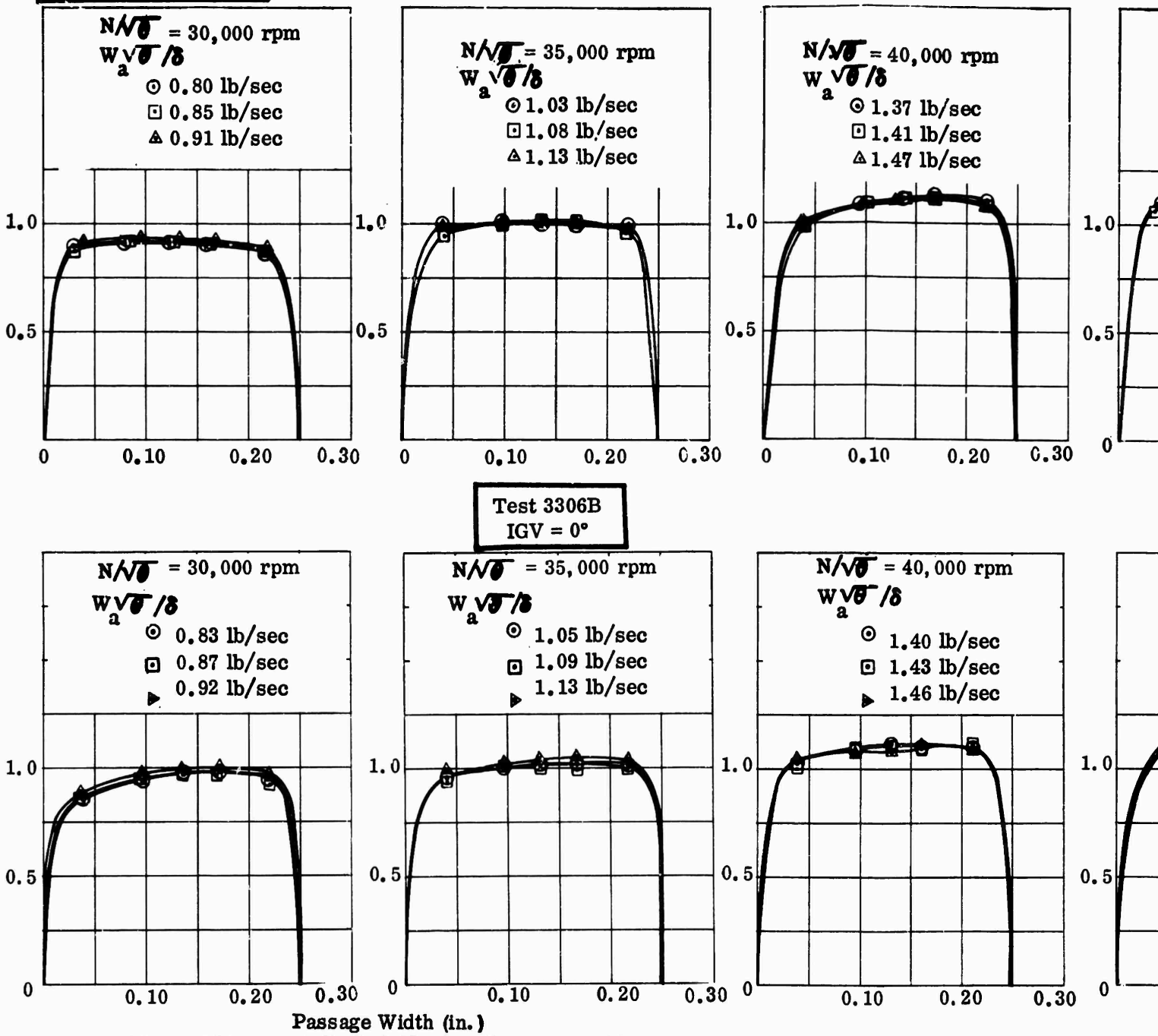
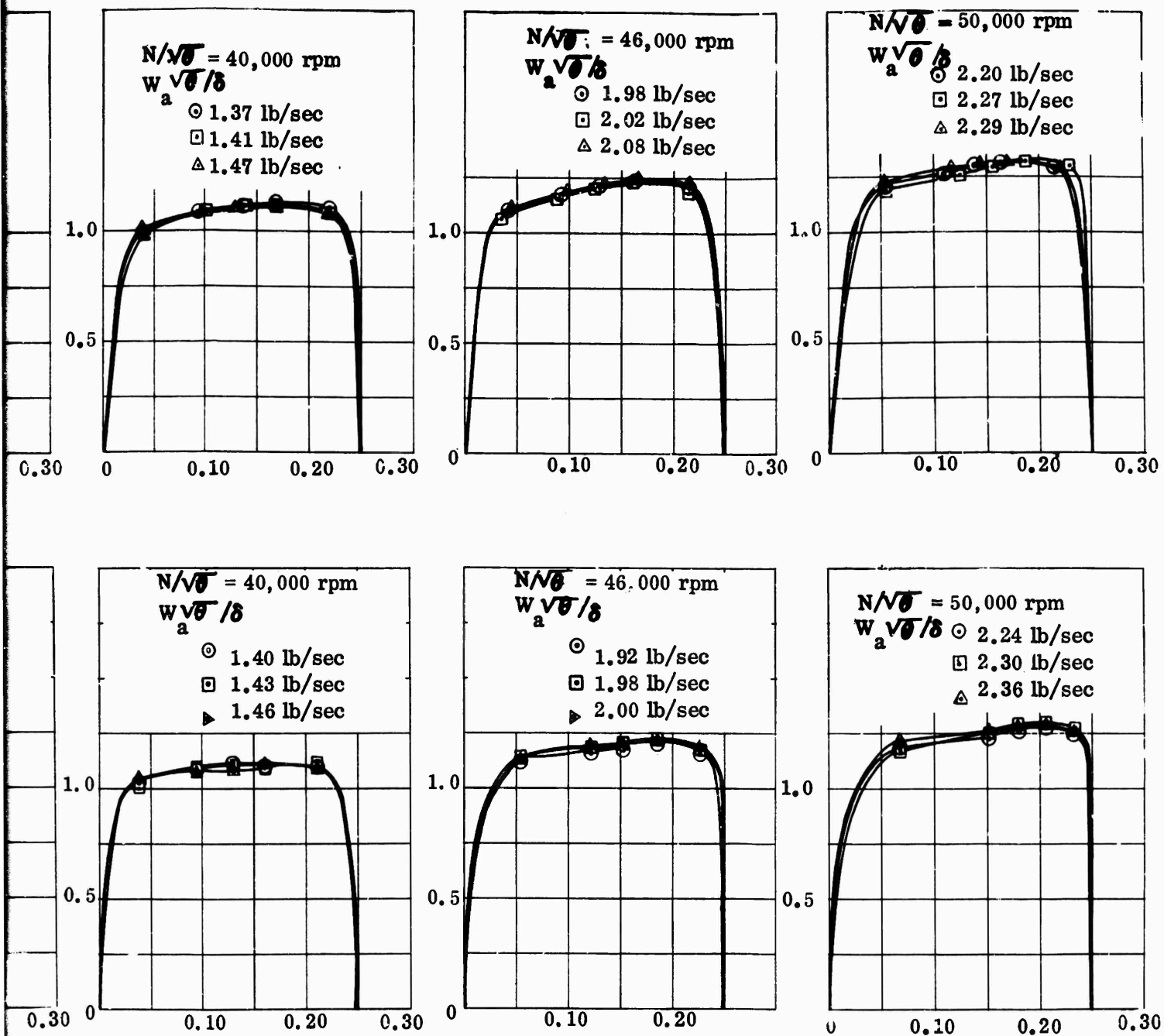


Figure 280. Exit Mach Number Survey, Workhorse.

0 in.
0.248 in.



CONFIDENTIAL

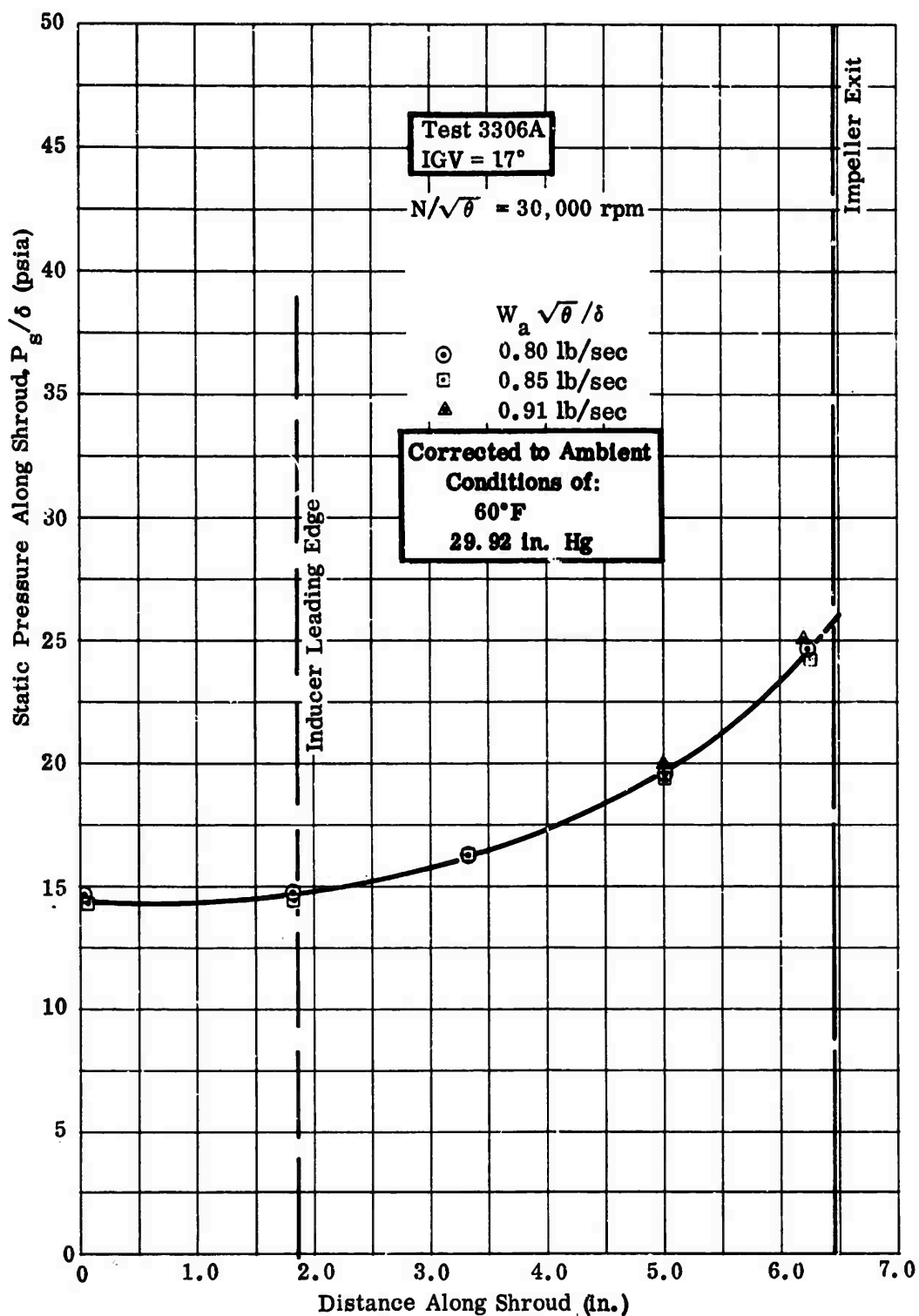


Figure 281. Static-Pressure Rise Along Shroud, Workhorse.

CONFIDENTIAL

CONFIDENTIAL

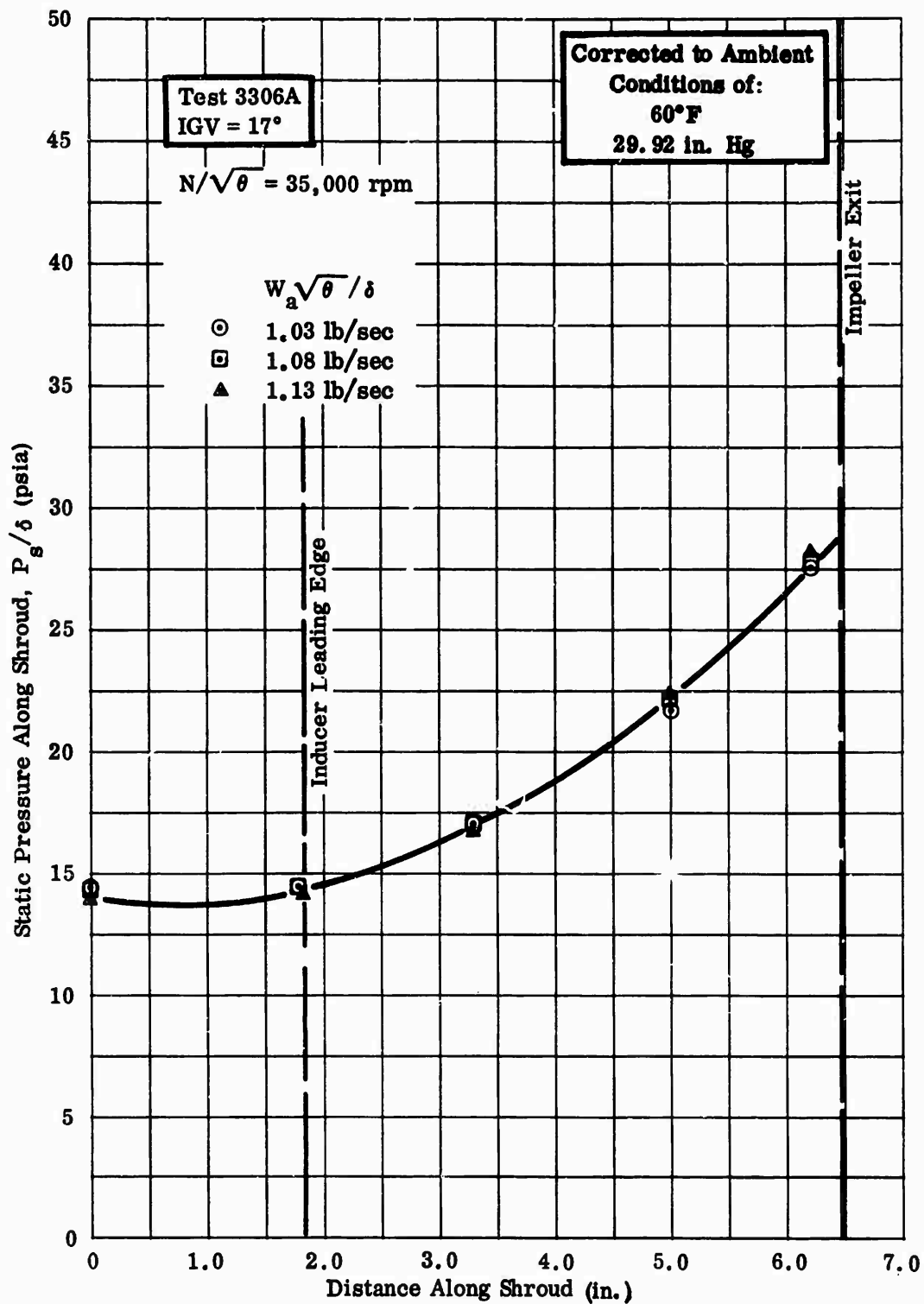


Figure 282. Static-Pressure Rise Along Shroud, Workhorse.

CONFIDENTIAL

CONFIDENTIAL

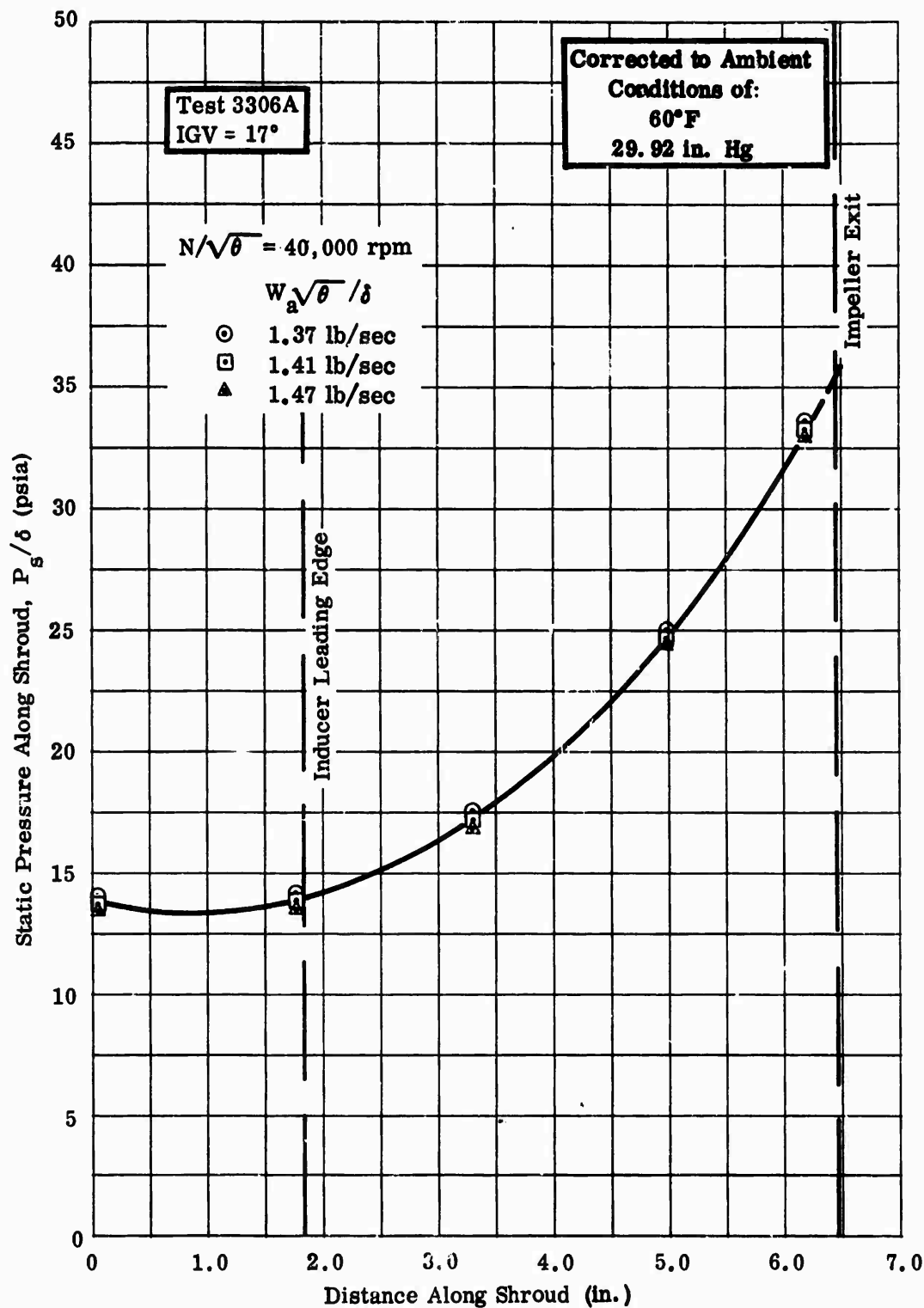


Figure 283. Static-Pressure Rise Along Shroud, Workhorse.

CONFIDENTIAL

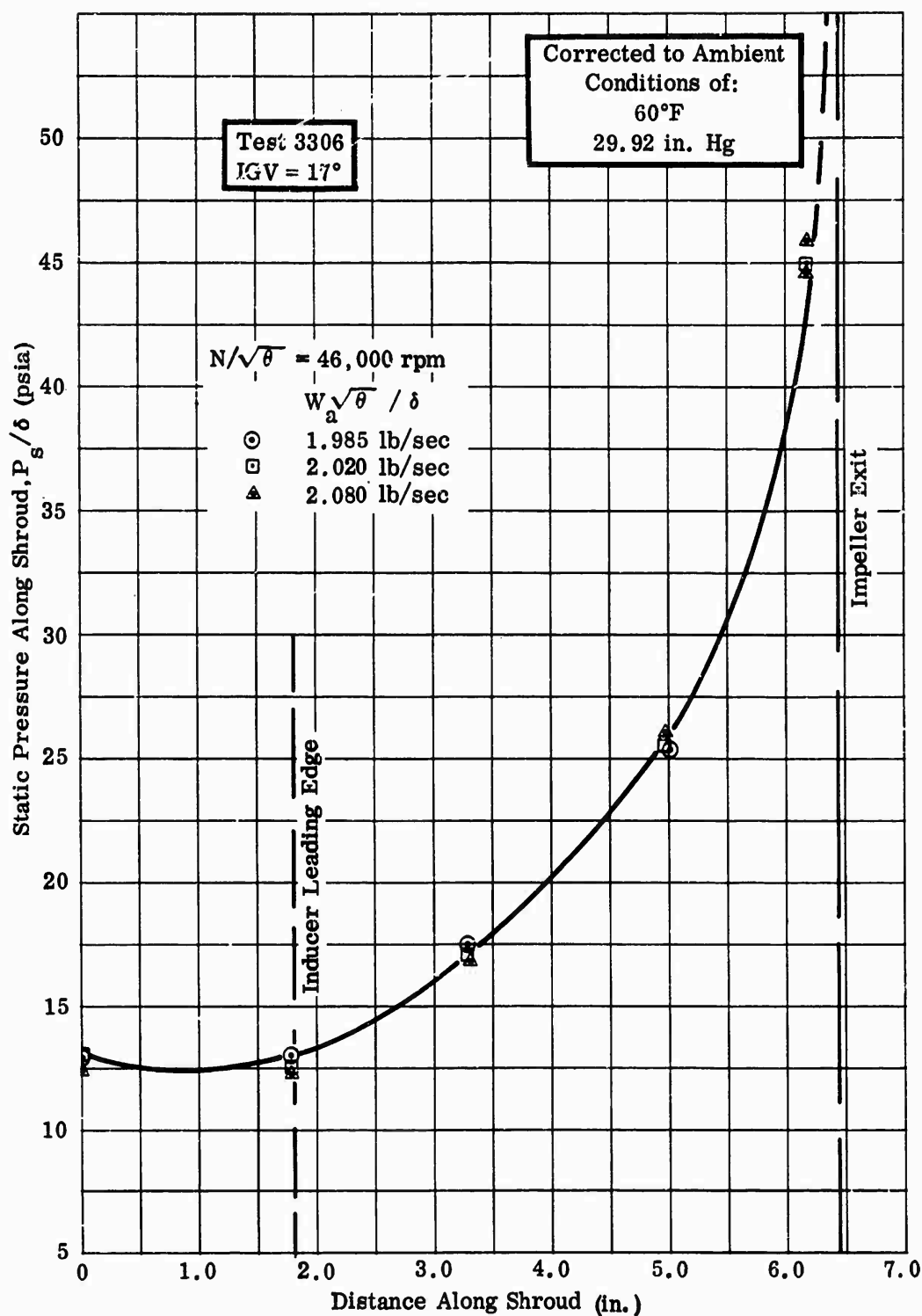


Figure 284. Static-Pressure Rise Along Shroud, Workhorse.

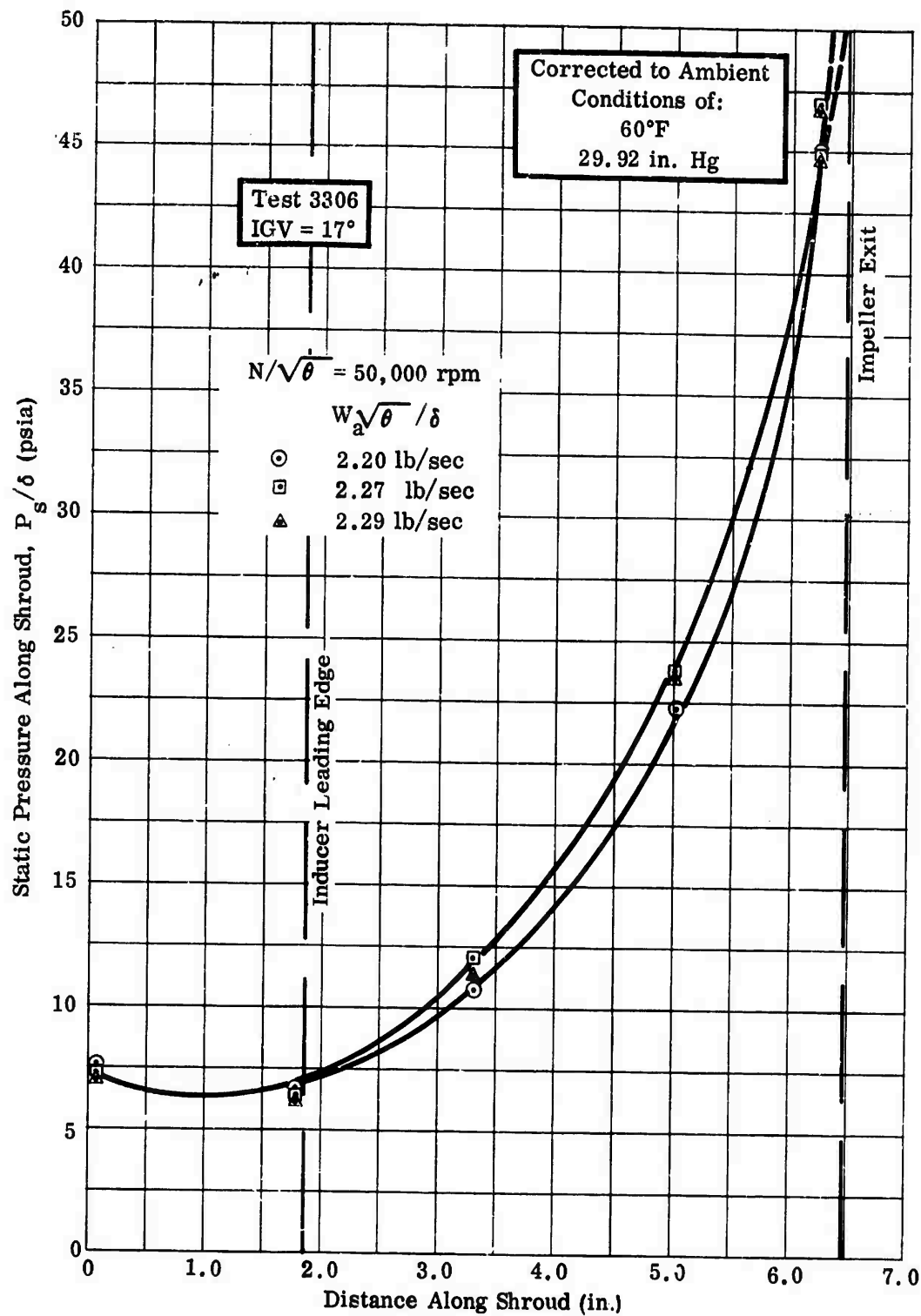


Figure 285. Static-Pressure Rise Along Shroud, Workhorse.

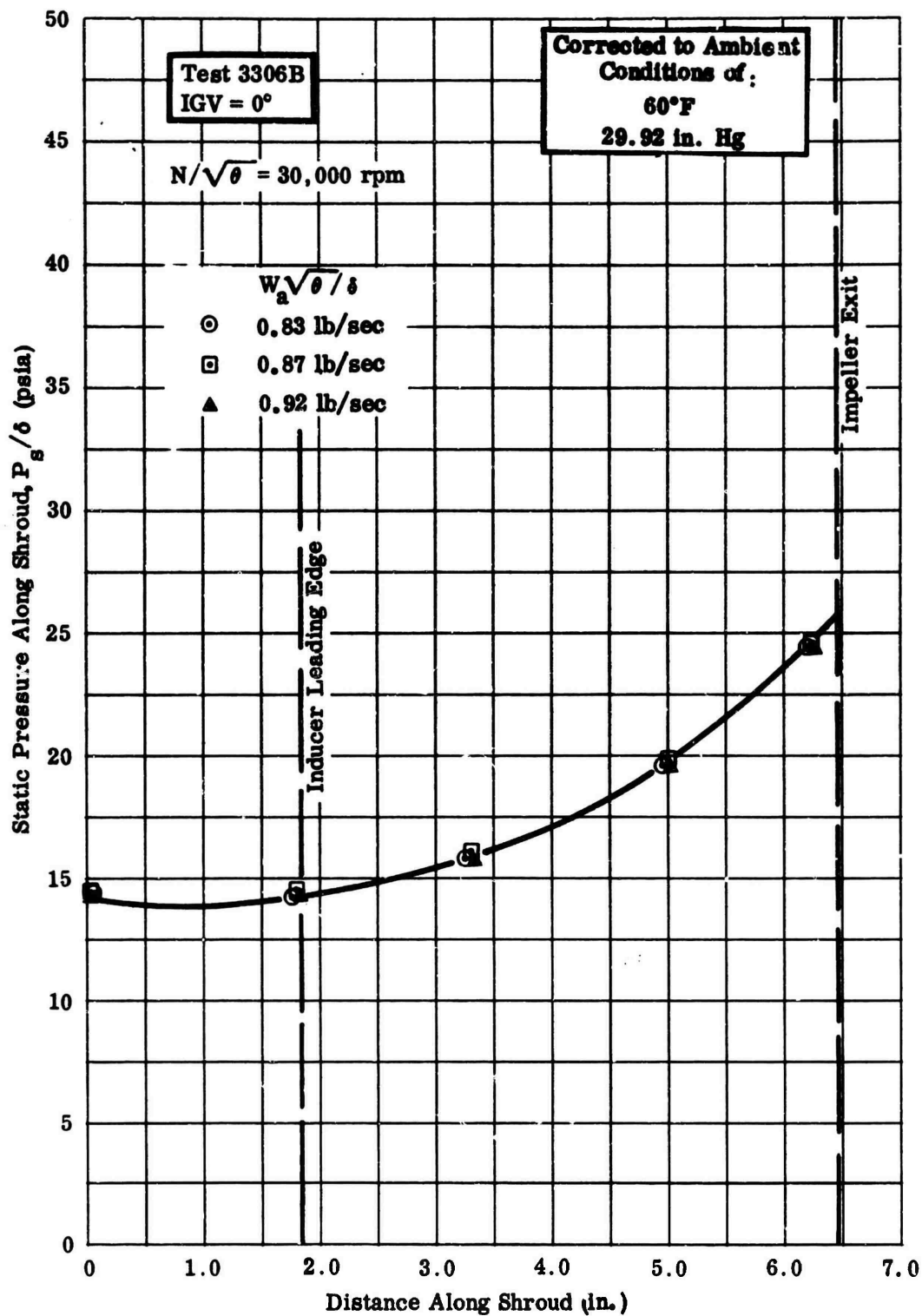


Figure 286. Static-Pressure Rise Along Shroud, Workhorse.

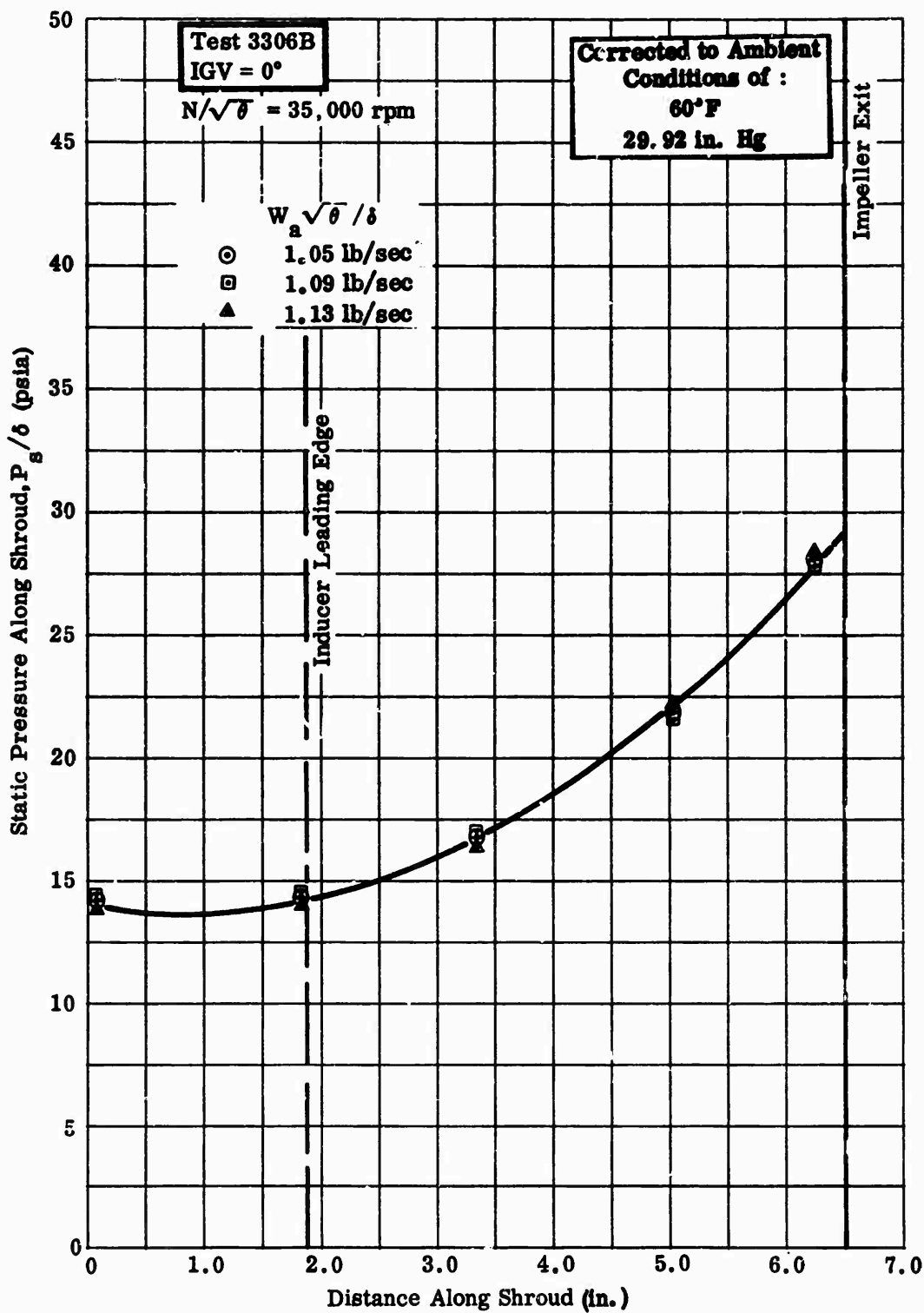


Figure 287. Static-Pressure Rise Along Shroud, Workhorse.

CONFIDENTIAL

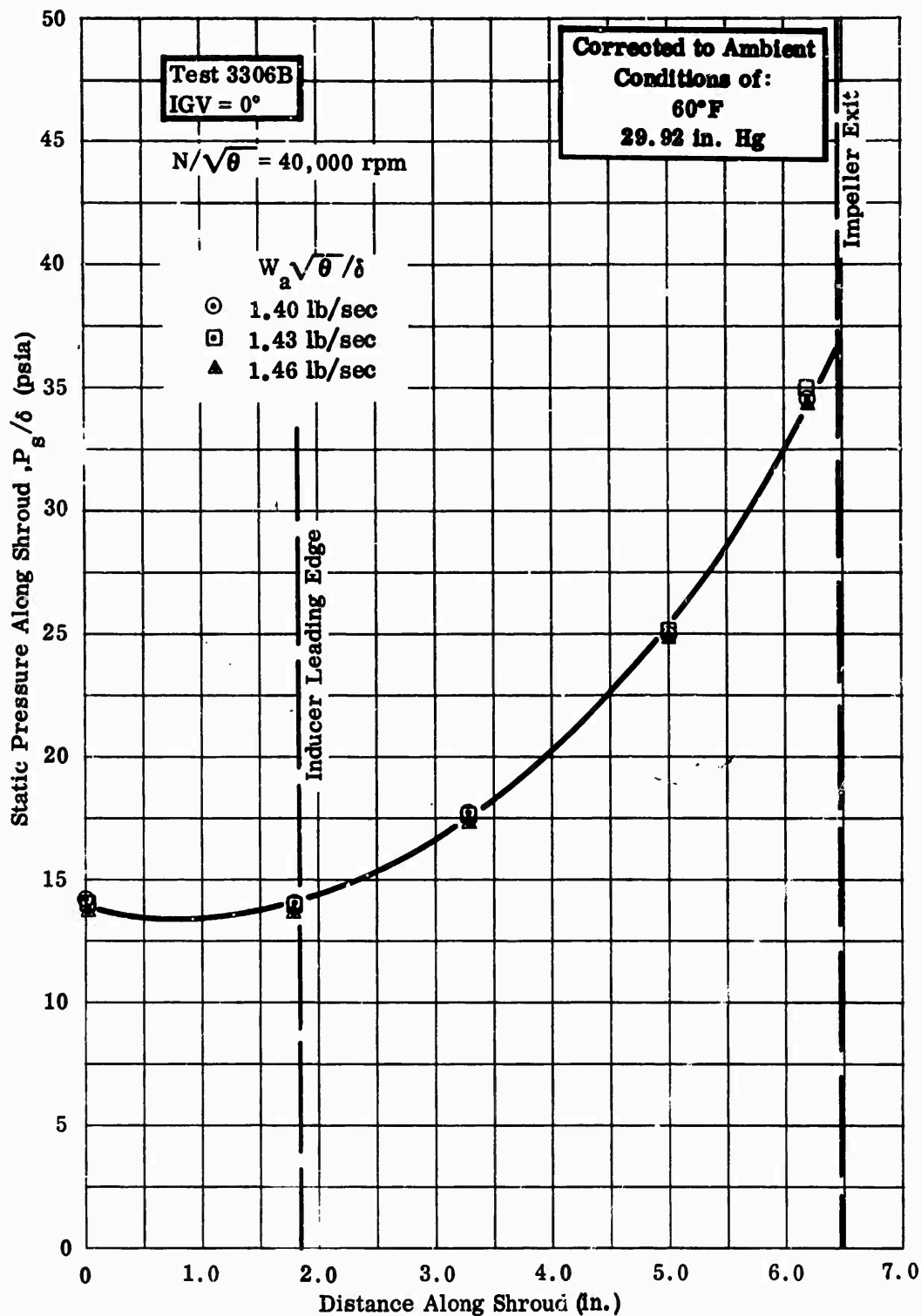


Figure 288. Static-Pressure Rise Along Shroud, Workhorse.

CONFIDENTIAL

CONFIDENTIAL

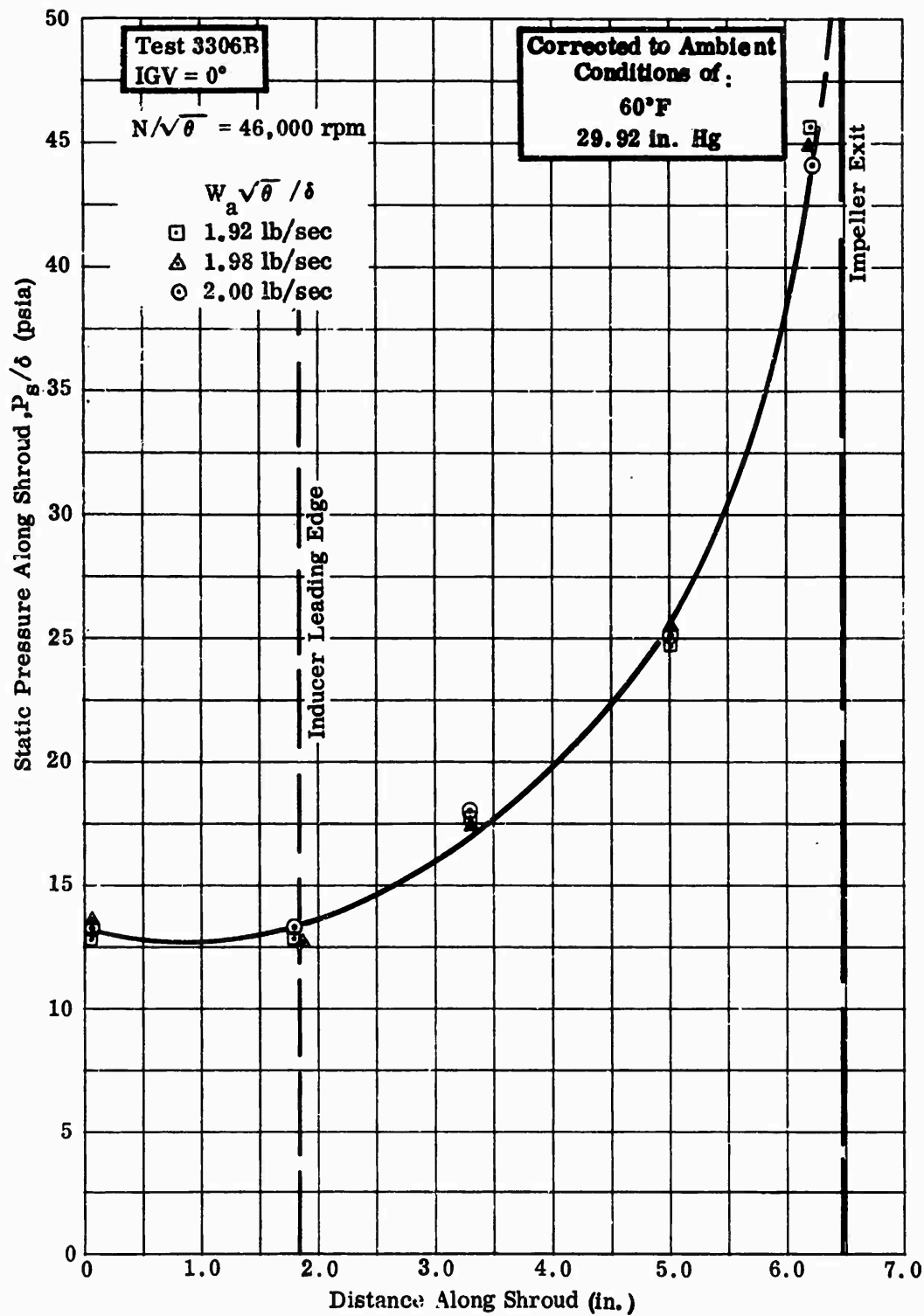


Figure 289. Static-Pressure Rise Along Shroud, Workhorse.

CONFIDENTIAL

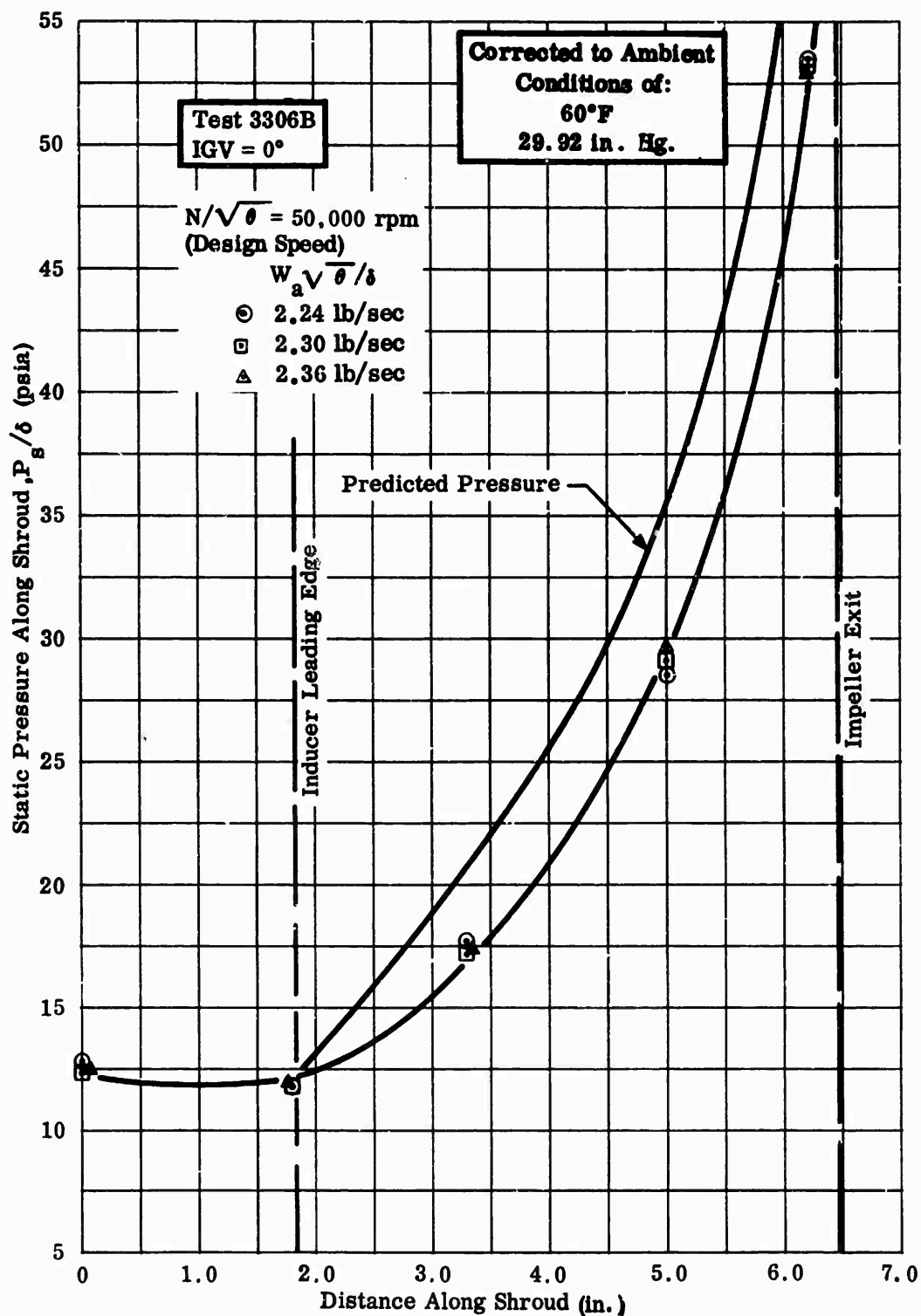


Figure 290. Static-Pressure Rise Along Shroud, Workhorse.

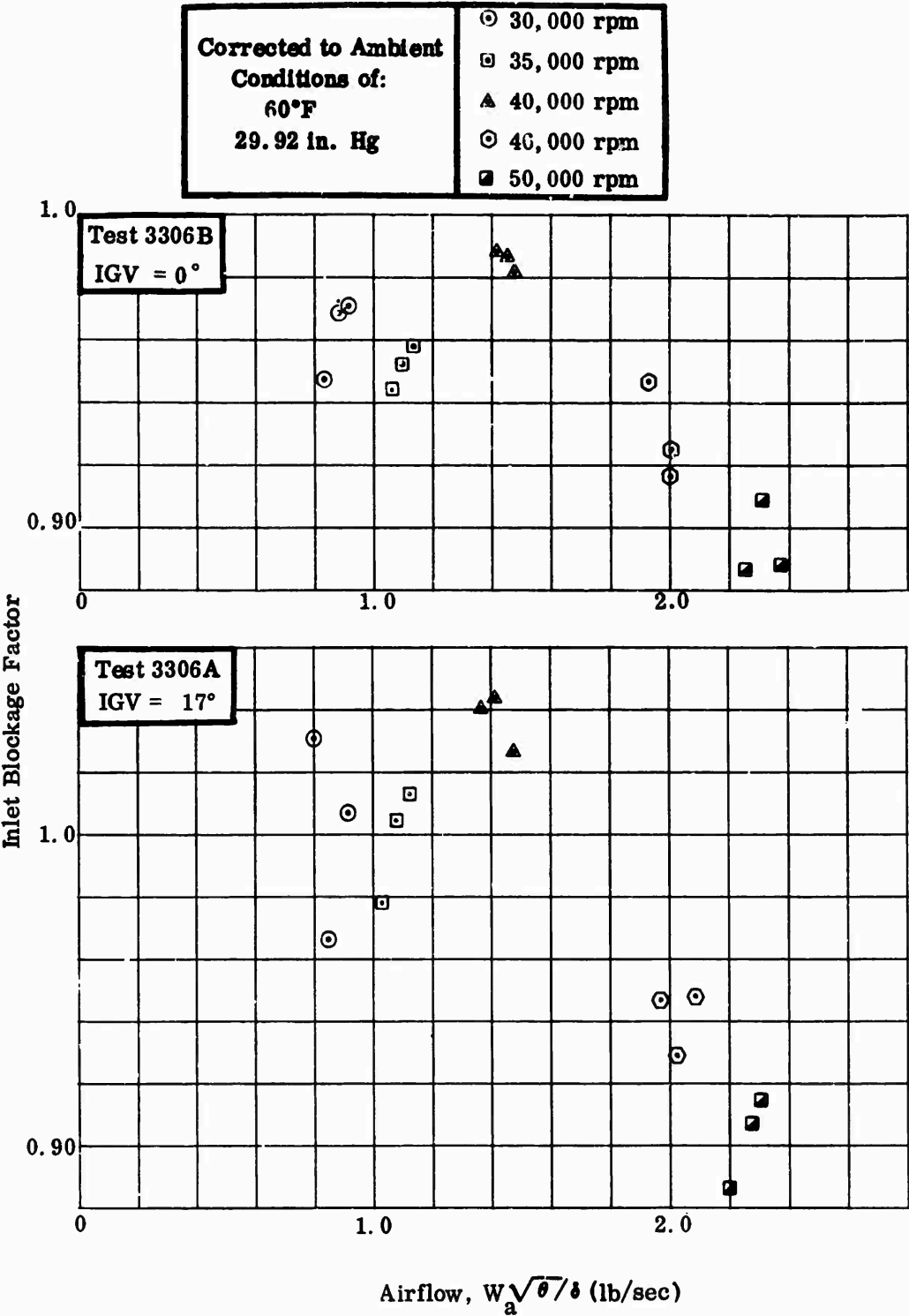


Figure 291. Inlet Blockage Factor, Workhorse.

CONFIDENTIAL

Corrected to Ambient
Conditions of :
60°F
29.92 in. Hg

Test 3306A
IGV = 17°

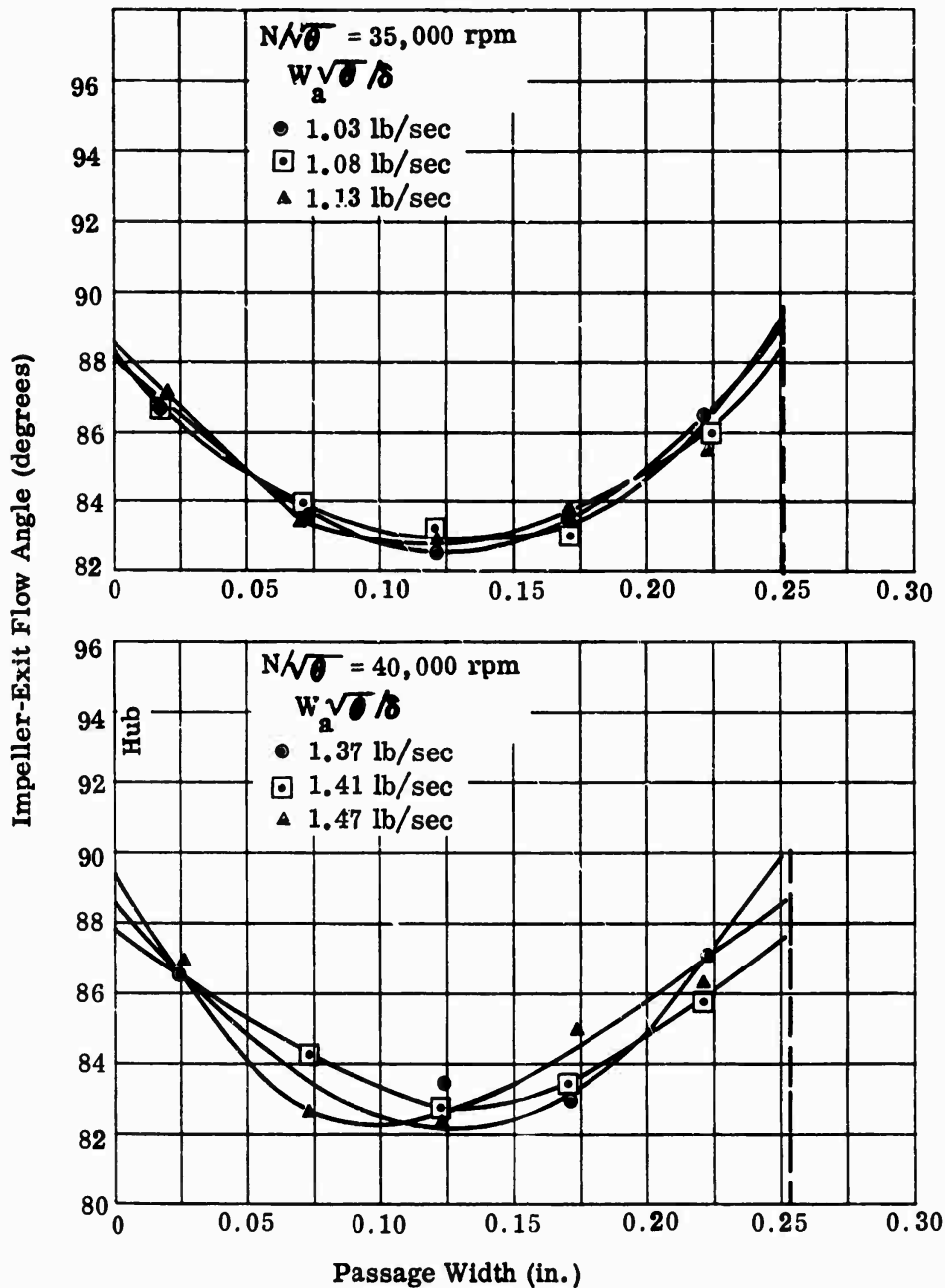


Figure 292. Impeller-Exit Flow Angles, Workhorse.

CONFIDENTIAL

Corrected to Ambient
Conditions of:
60°F
29.92 in. Hg

Test 3306A
IGV = 17°

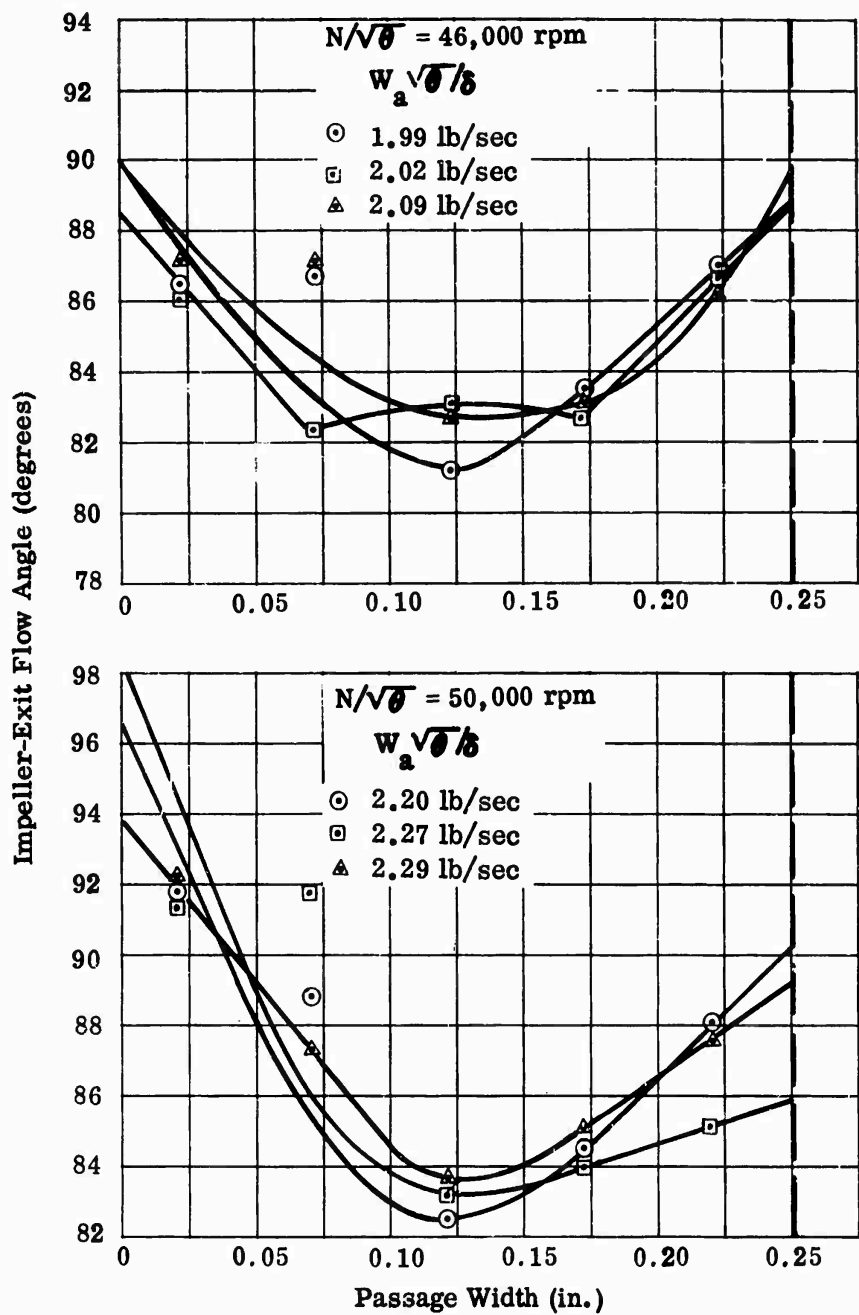


Figure 293. Impeller-Exit Flow Angles, Workhorse.

CONFIDENTIAL

Corrected to Ambient
Conditions of:
60°F
29.92 in. Hg

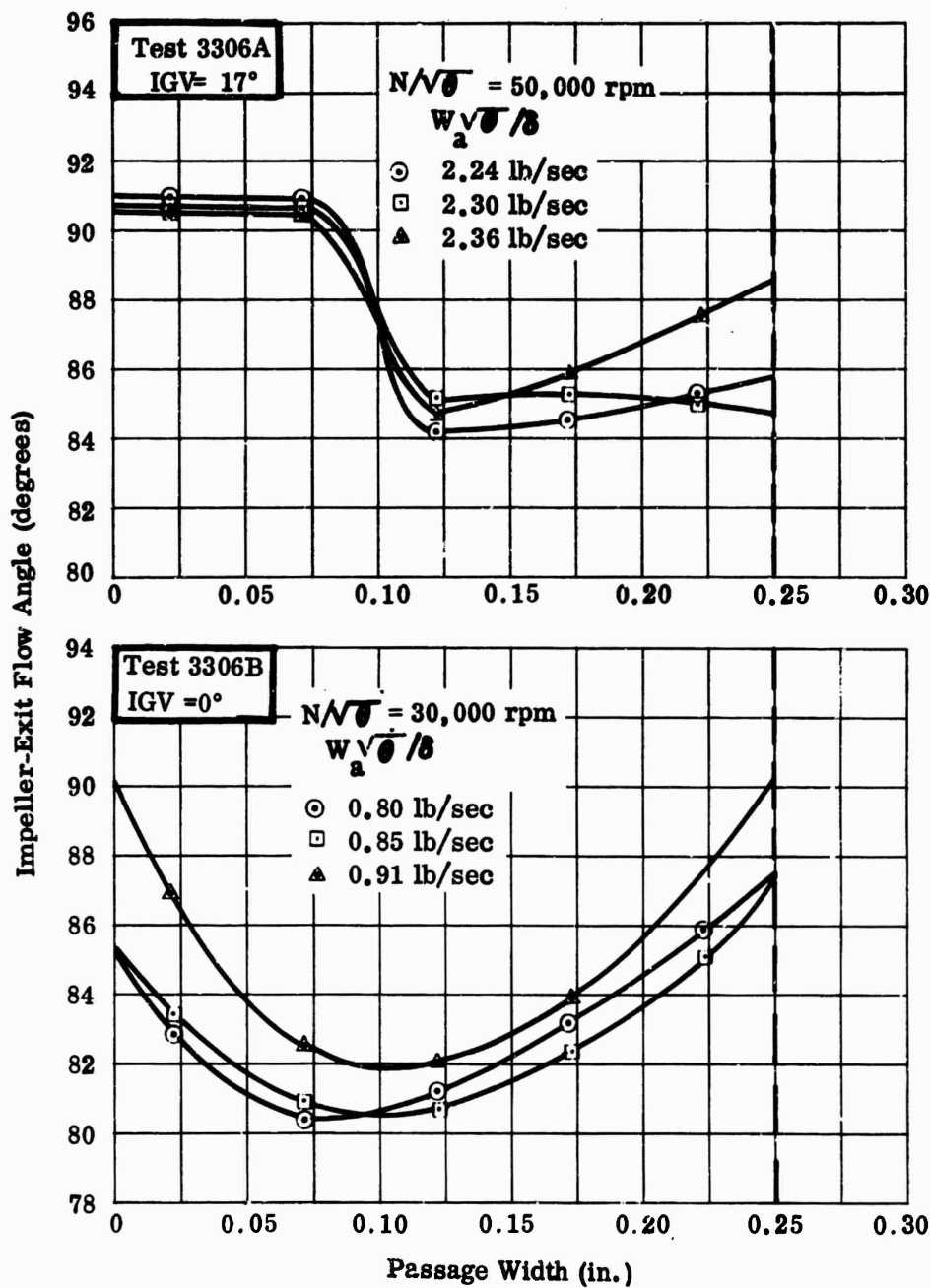


Figure 294. Impeller-Exit Flow Angles, Workhorse.

CONFIDENTIAL

CONFIDENTIAL

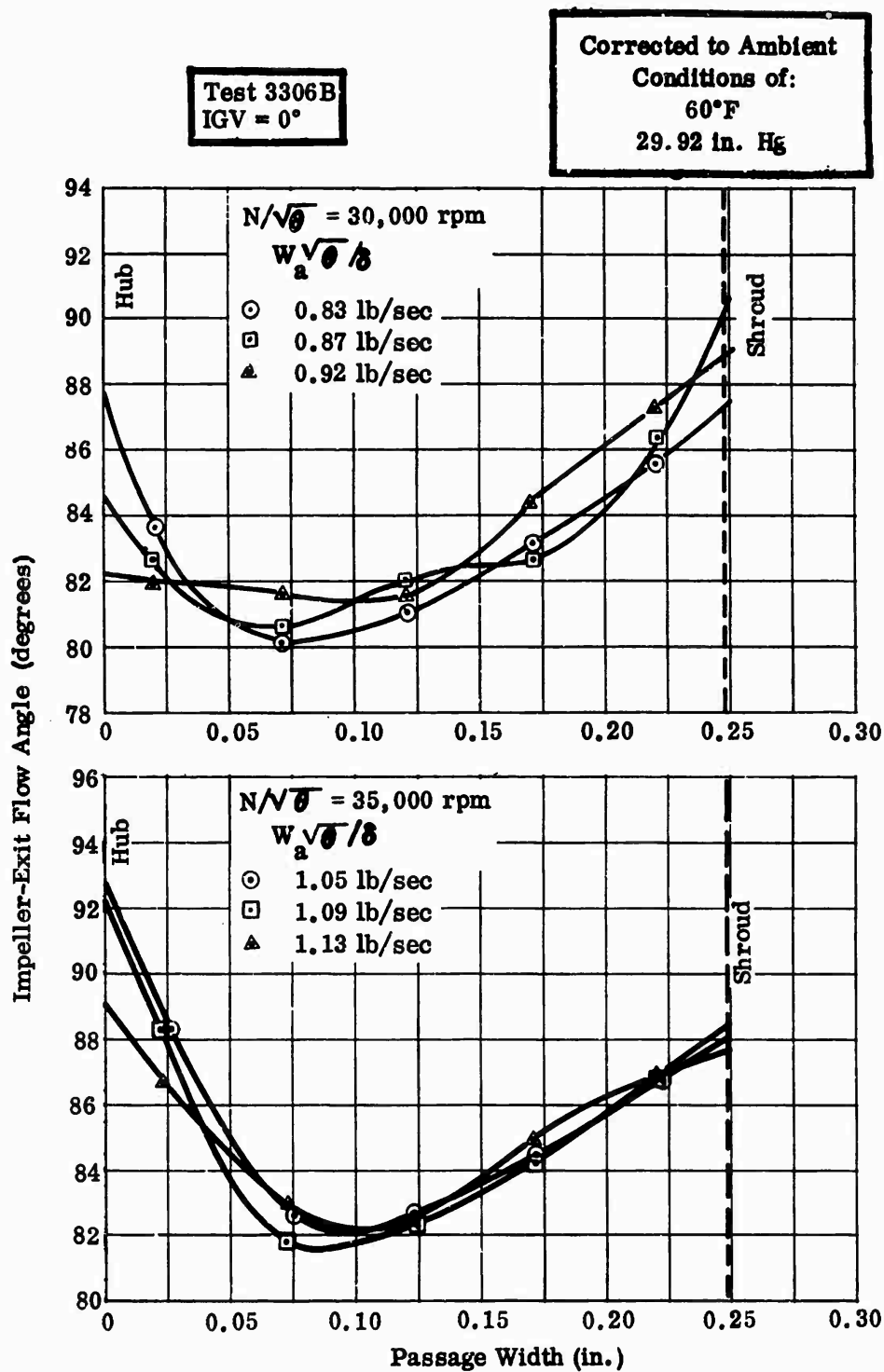


Figure 295. Impeller-Exit Flow Angles, Workhorse.

CONFIDENTIAL

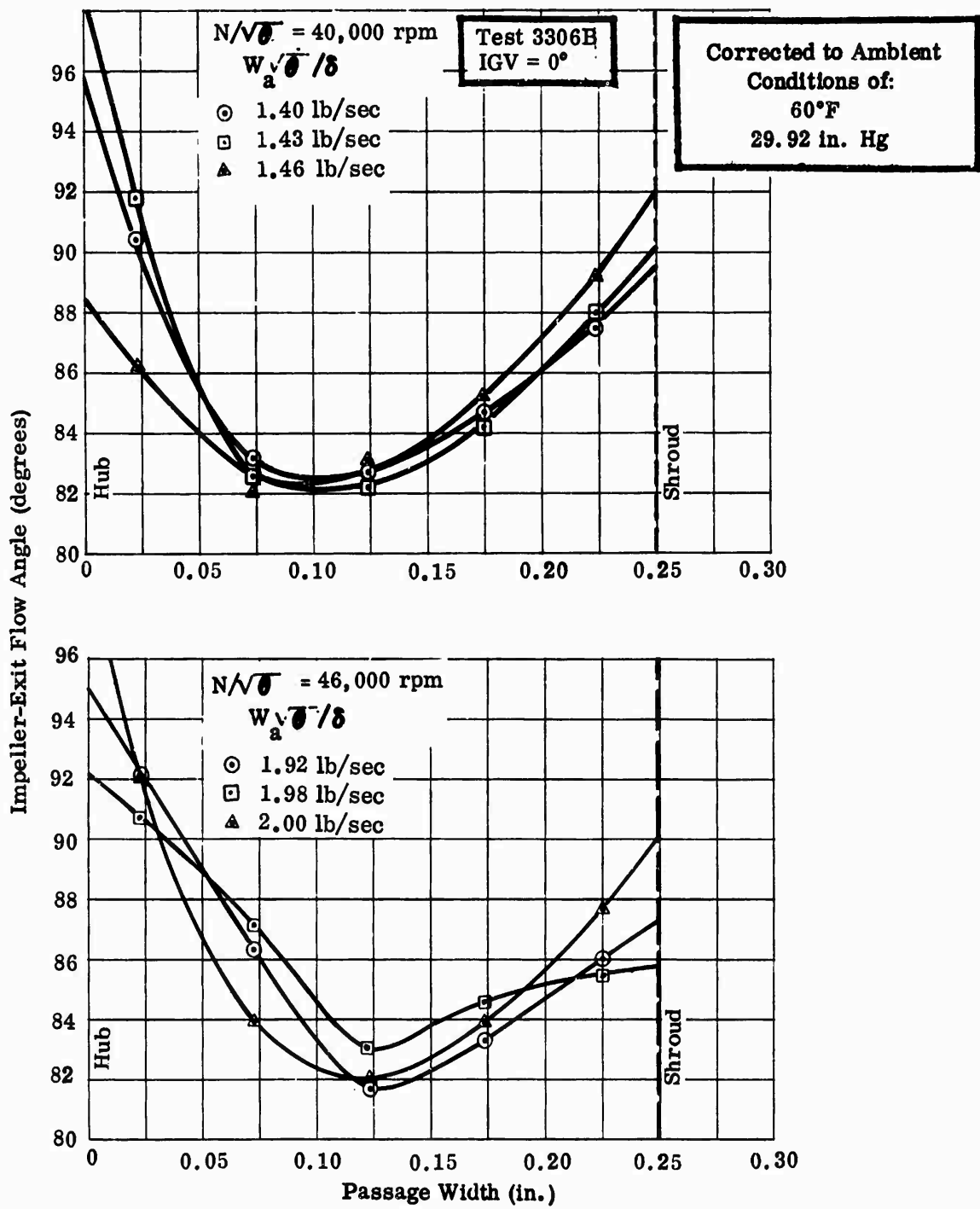


Figure 296. Impeller-Exit Flow Angles, Workhorse.

CONFIDENTIAL

$$N/\sqrt{\theta} = 30,000 \text{ rpm}$$

Corrected to Ambient
Conditions of:
60°F
29.92 in. Hg
Velocities in fps

Test 3306A
IGV = 17°

$$N/\sqrt{\theta} = 35,000$$

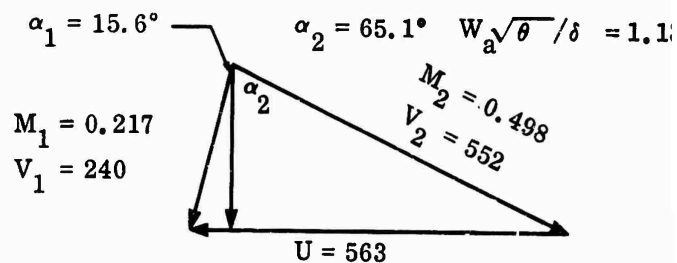
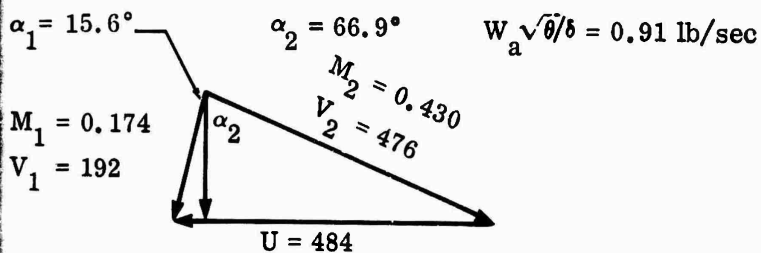
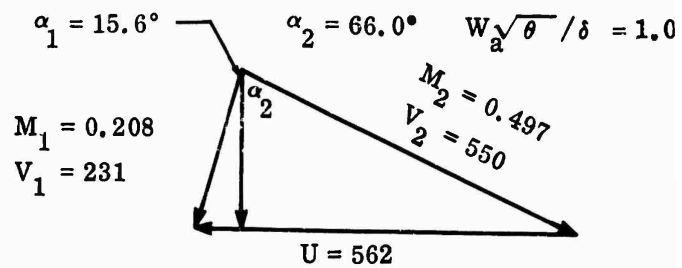
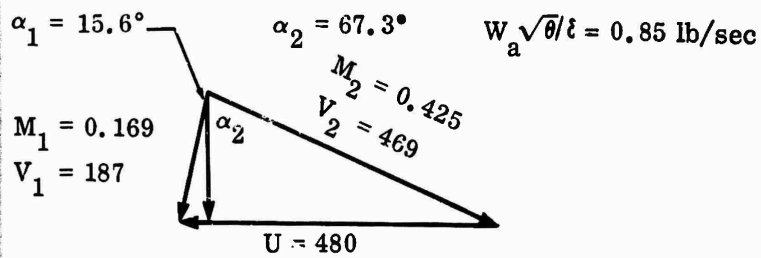
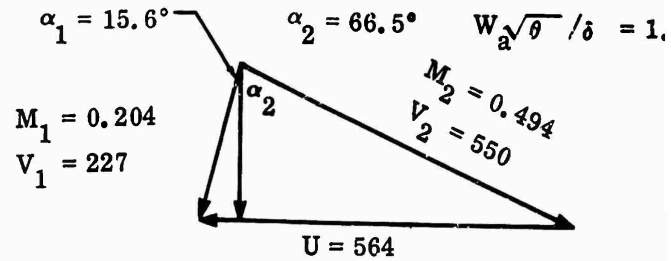
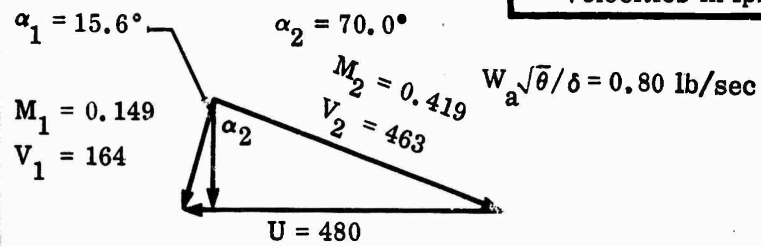


Figure 297. RMS Inlet Vector Diagrams, Workhorse.

467

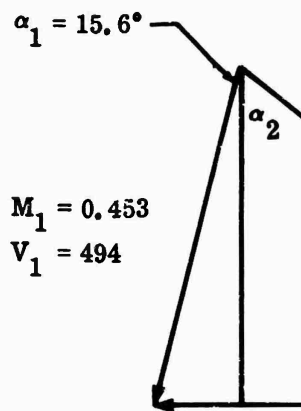
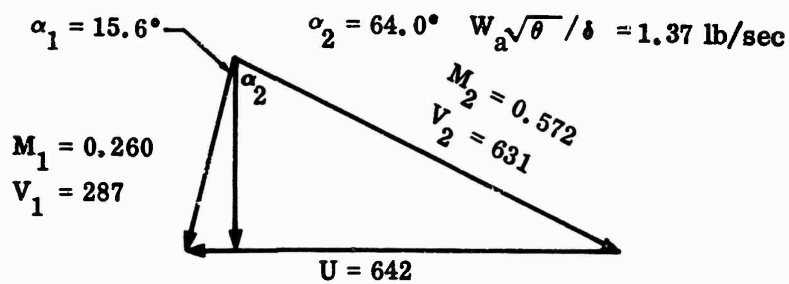
CONFIDENTIAL

1

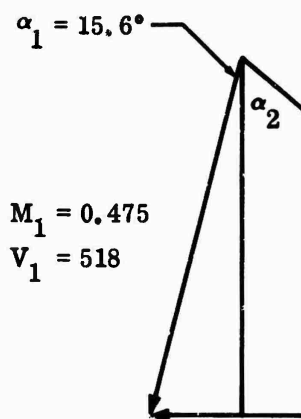
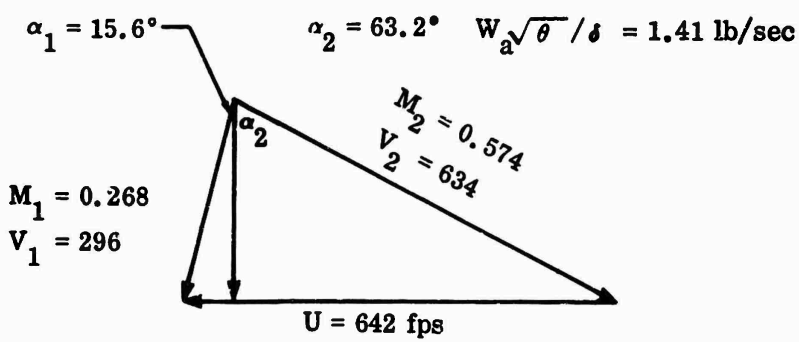
000 rpm

$N/\sqrt{\theta} = 40,000 \text{ rpm}$

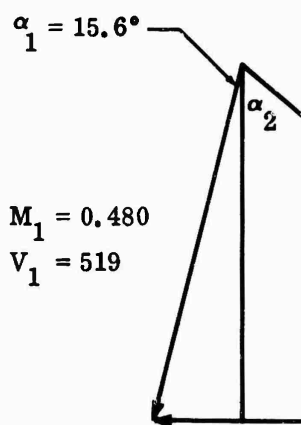
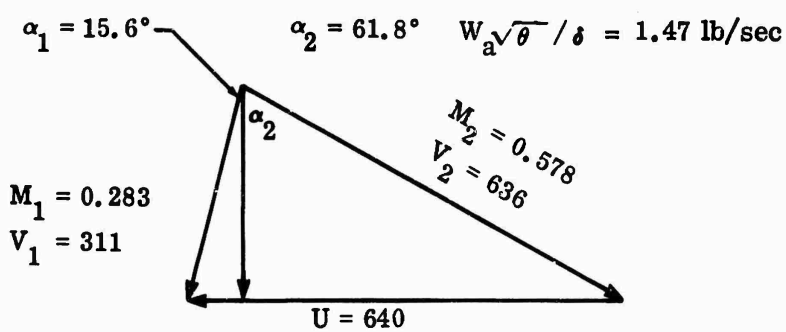
1.03 lb/sec



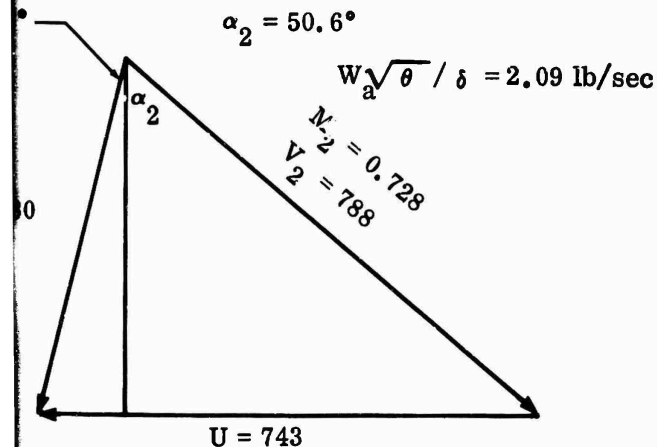
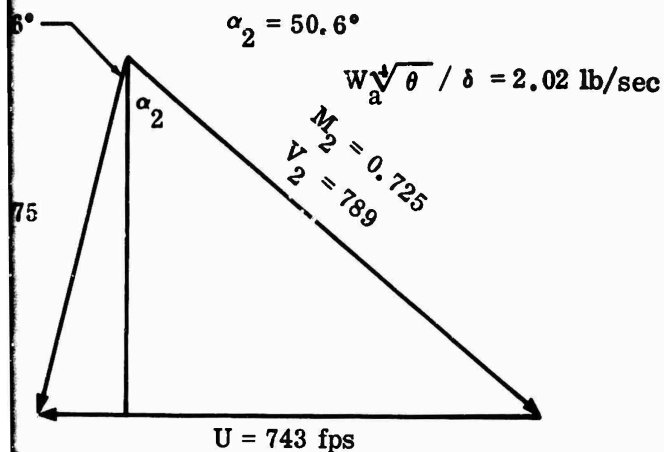
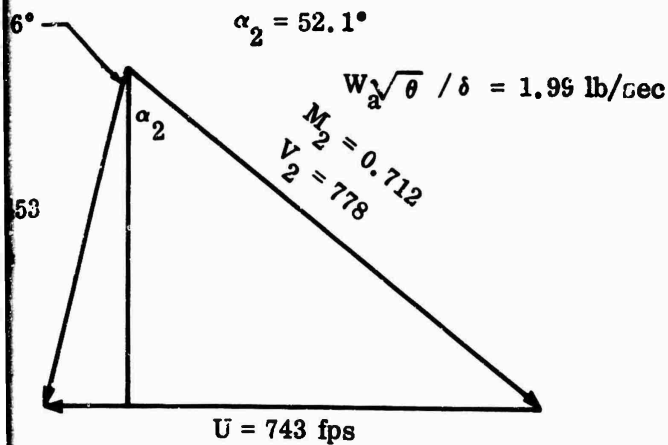
1.08 lb/sec



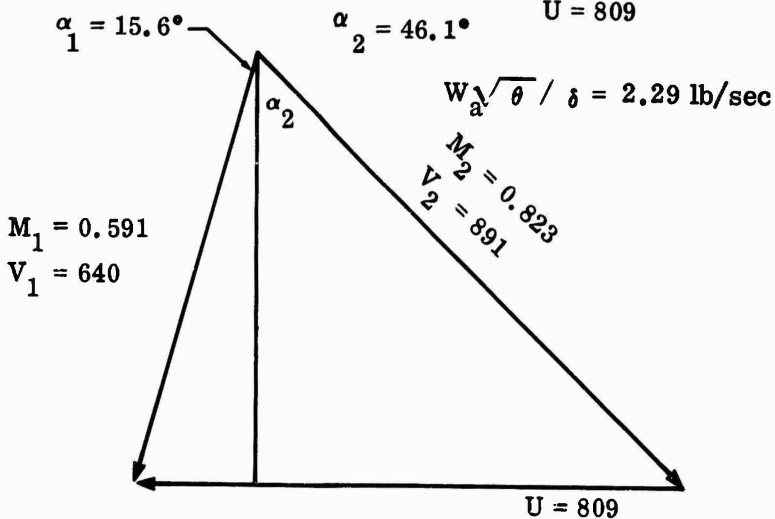
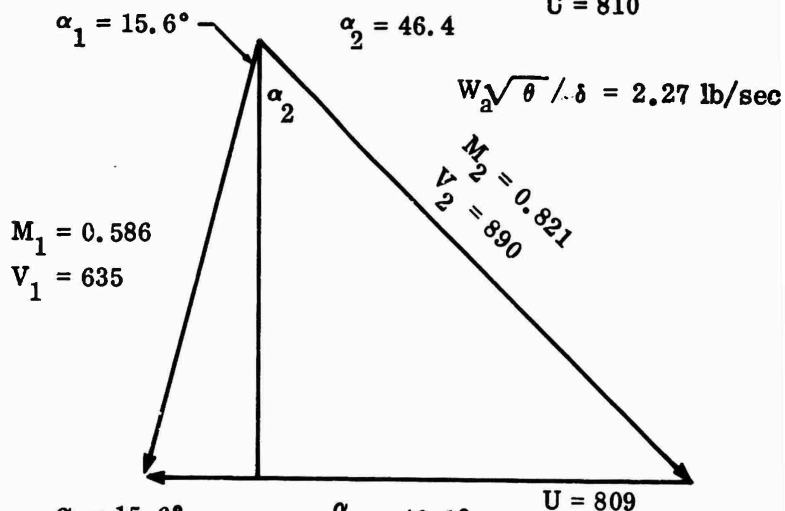
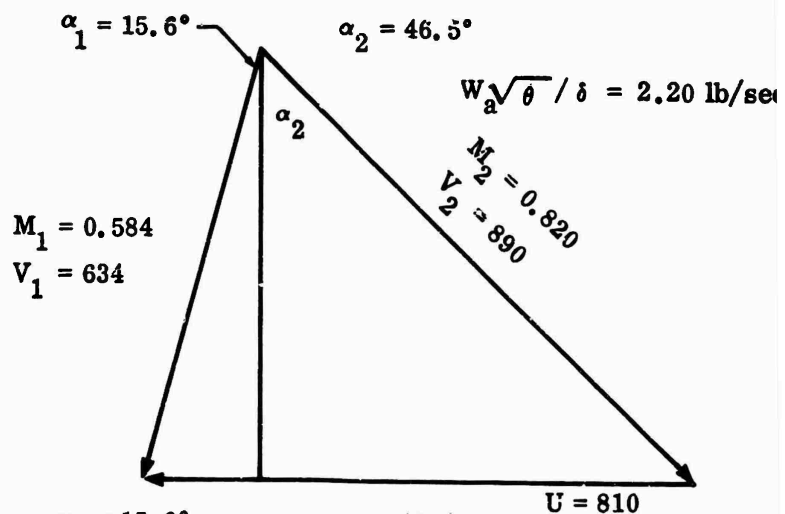
1.13 lb/sec



$$N/\sqrt{\theta} = 46,000 \text{ rpm}$$



$$N/\sqrt{\theta} = 50,000 \text{ rpm}$$



CONFIDENTIAL

Corrected to Ambient
Conditions of:
60°F
29.92 in. Hg
Velocities in fps

Test 3306B
IGV = 0°

$N/\sqrt{\theta} = 30,000$ rpm

$N/\sqrt{\theta} = 35$

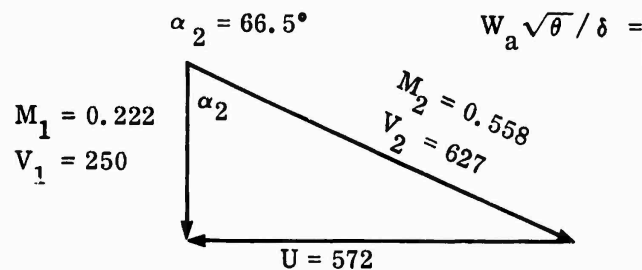
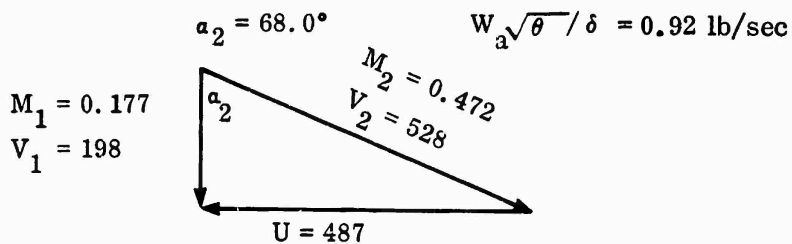
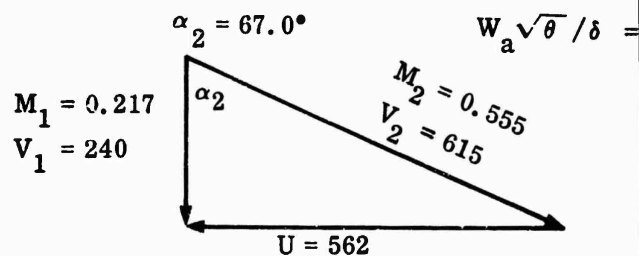
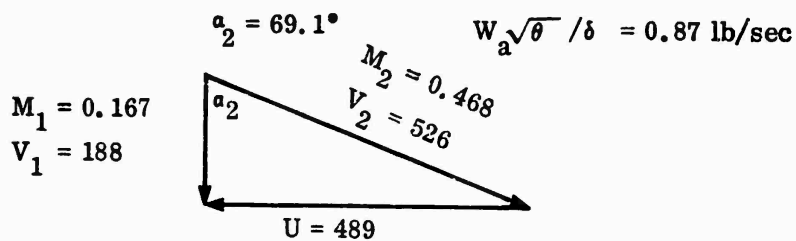
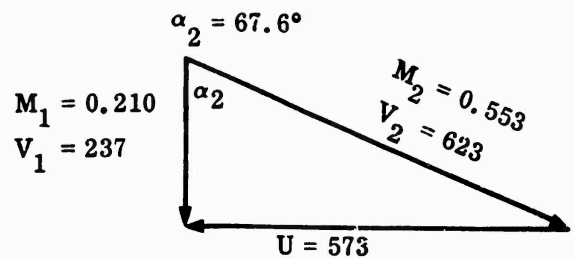
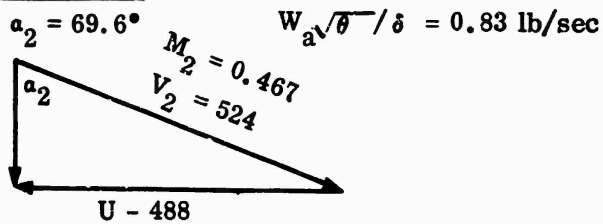


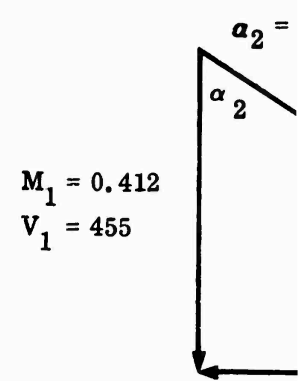
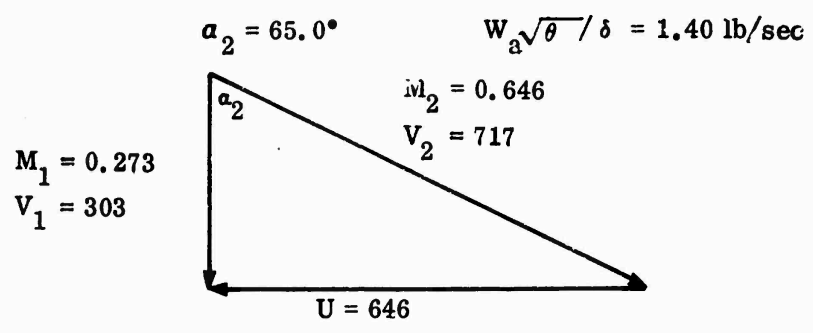
Figure 298. RMS Inlet Vector Diagrams, Workhorse.

CONFIDENTIAL

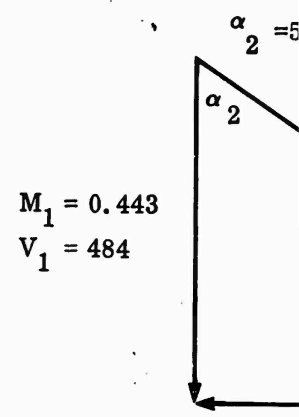
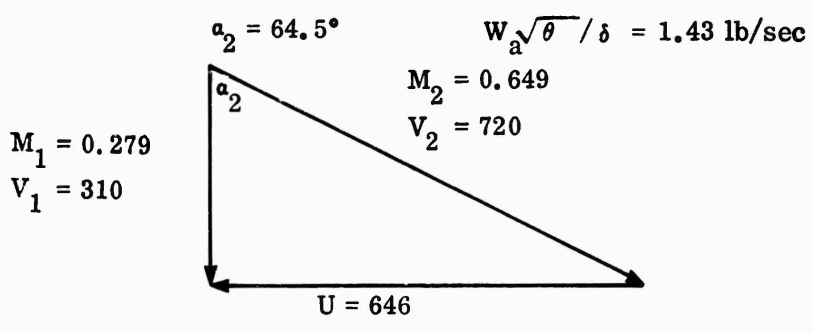
00 rpm

$N/\sqrt{\theta} = 40,000 \text{ rpm}$

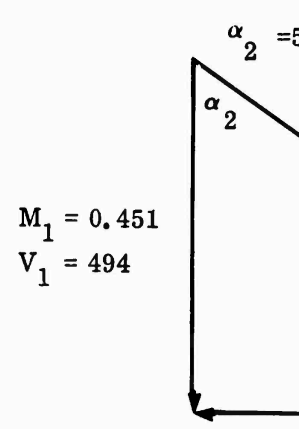
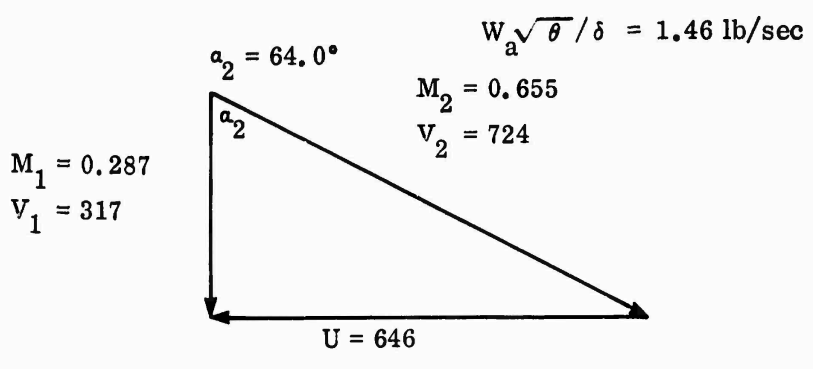
1.05 lb/sec



1.09 lb/sec



1.13 lb/sec



$$N \sqrt{\theta} = 46,000 \text{ rpm}$$

$$\alpha_2 = 58.7^\circ$$

$$W_a \sqrt{\theta} / \delta = 1.92 \text{ lb/sec}$$

$$M_2 = 0.792$$

$$V_2 = 875$$

$$U = 743$$

$$\alpha_2 = 57.1^\circ$$

$$W_a \sqrt{\theta} / \delta = 1.98 \text{ lb/sec}$$

$$M_2 = 0.815$$

$$V_2 = 890$$

$$U = 743$$

$$\alpha_2 = 56.5^\circ$$

$$W_a \sqrt{\theta} / \delta = 2.00 \text{ lb/sec}$$

$$M_2 = 0.918$$

$$V_2 = 896$$

$$U = 743$$

$$N/\sqrt{\theta} = 50,000 \text{ rpm}$$

$$\alpha_2 = 53.5^\circ$$

$$W_a \sqrt{\theta} / \delta = 2.24 \text{ lb/sec}$$

$$M_2 = 0.932$$

$$V_2 = 1009$$

$$U = 806$$

$$\alpha_2 = 53.4^\circ$$

$$W_a \sqrt{\theta} / \delta = 2.30 \text{ lb/sec}$$

$$M_2 = 0.933$$

$$V_2 = 1012$$

$$U = 807$$

$$\alpha_2 = 51.3^\circ$$

$$W_a \sqrt{\theta} / \delta = 2.36 \text{ lb/sec}$$

$$M_2 = 0.964$$

$$V_2 = 1039$$

$$U = 806$$

$$M_1 = 0.555$$

$$V_1 = 600$$

$$M_1 = 0.557$$

$$V_1 = 604$$

$$M_1 = 0.603$$

$$V_1 = 650$$

CONFIDENTIAL

Corrected to Ambient
Conditions of:
60°F
29.92 in. Hg
Velocities in fps

Test 3306A
IGV = +17°

$N/\sqrt{\theta} = 30,000$ rpm

$N/\sqrt{\theta} = 35,$

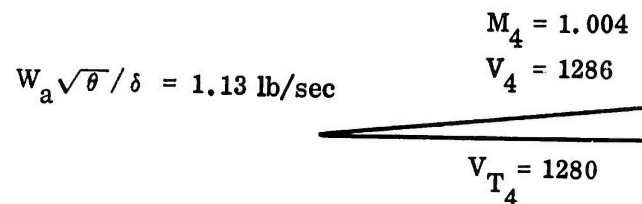
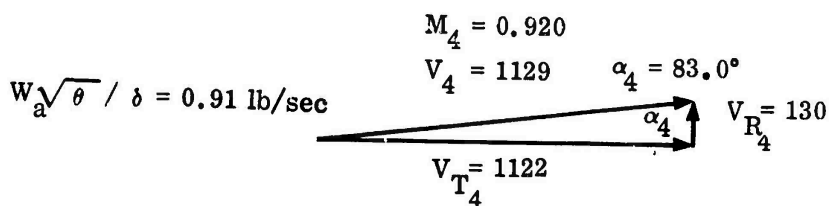
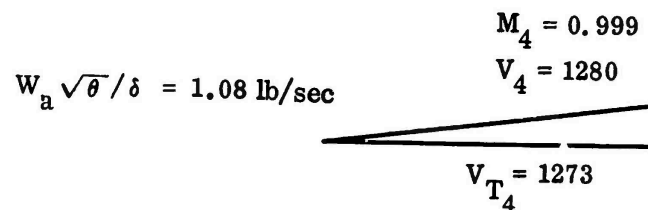
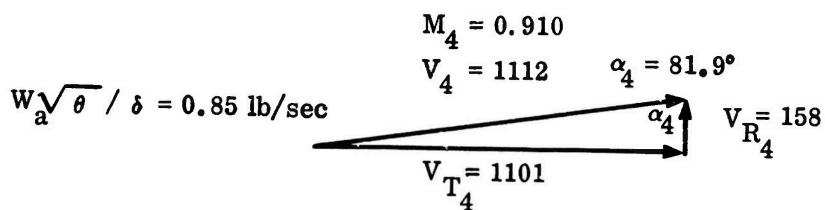
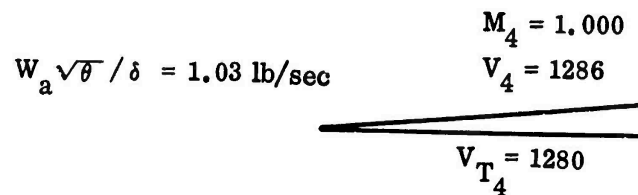
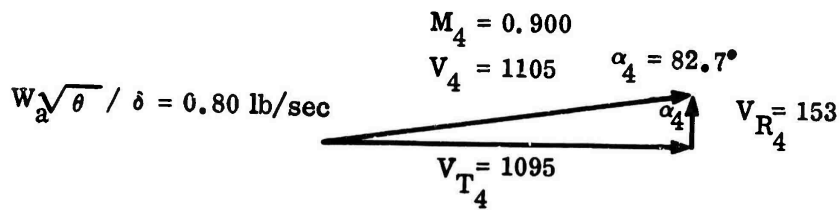


Figure 299. Mean Vector Diagrams at 1.02 Diameter Ratio, Workhorse.

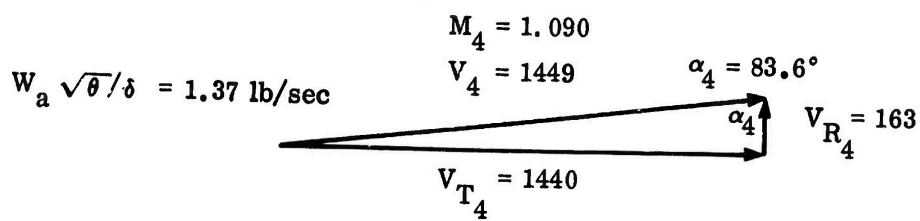
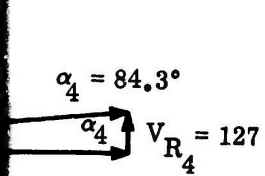
471

CONFIDENTIAL

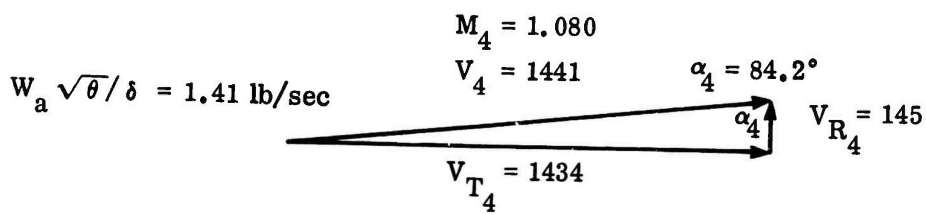
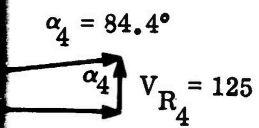
1

5,000 rpm

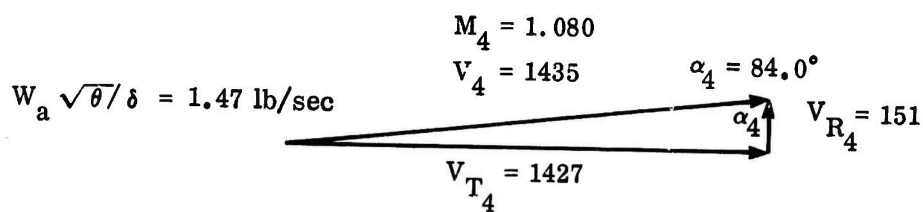
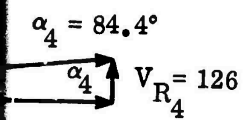
$N/\sqrt{\rho} = 40,000 \text{ rpm}$



$W_a \sqrt{\theta}/\delta = 1.99 \text{ lb/sec}$

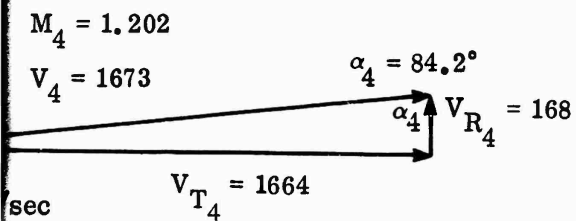
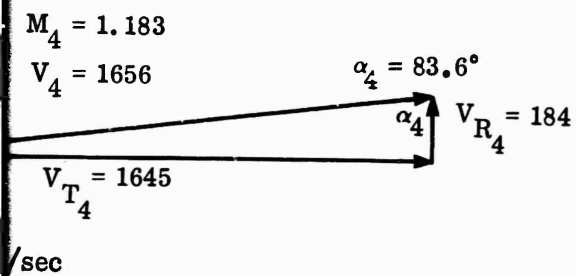
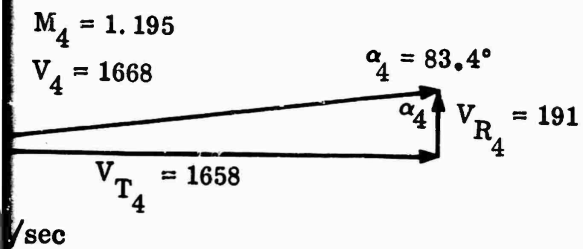


$W_a \sqrt{\theta}/\delta = 2.02 \text{ lb/sec}$

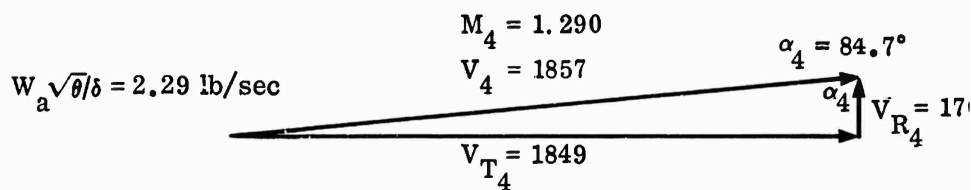
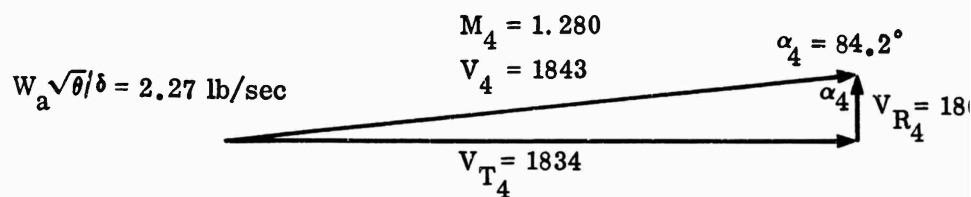
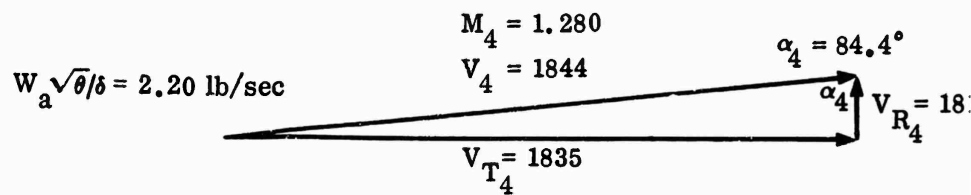


$W_a \sqrt{\theta}/\delta = 2.09 \text{ lb/sec}$

$$N/\sqrt{\theta} = 46,000 \text{ rpm}$$



$$N/\sqrt{\theta} = 50,000 \text{ rpm}$$



CONFIDENTIAL

Corrected to Ambient
Conditions of:
60°F
29.92 in. Hg
Velocities in ft/s

Test 3306B
IGV = 0°

$N/\sqrt{\theta} = 30,000$ rpm

$N/\sqrt{\theta} = 35$

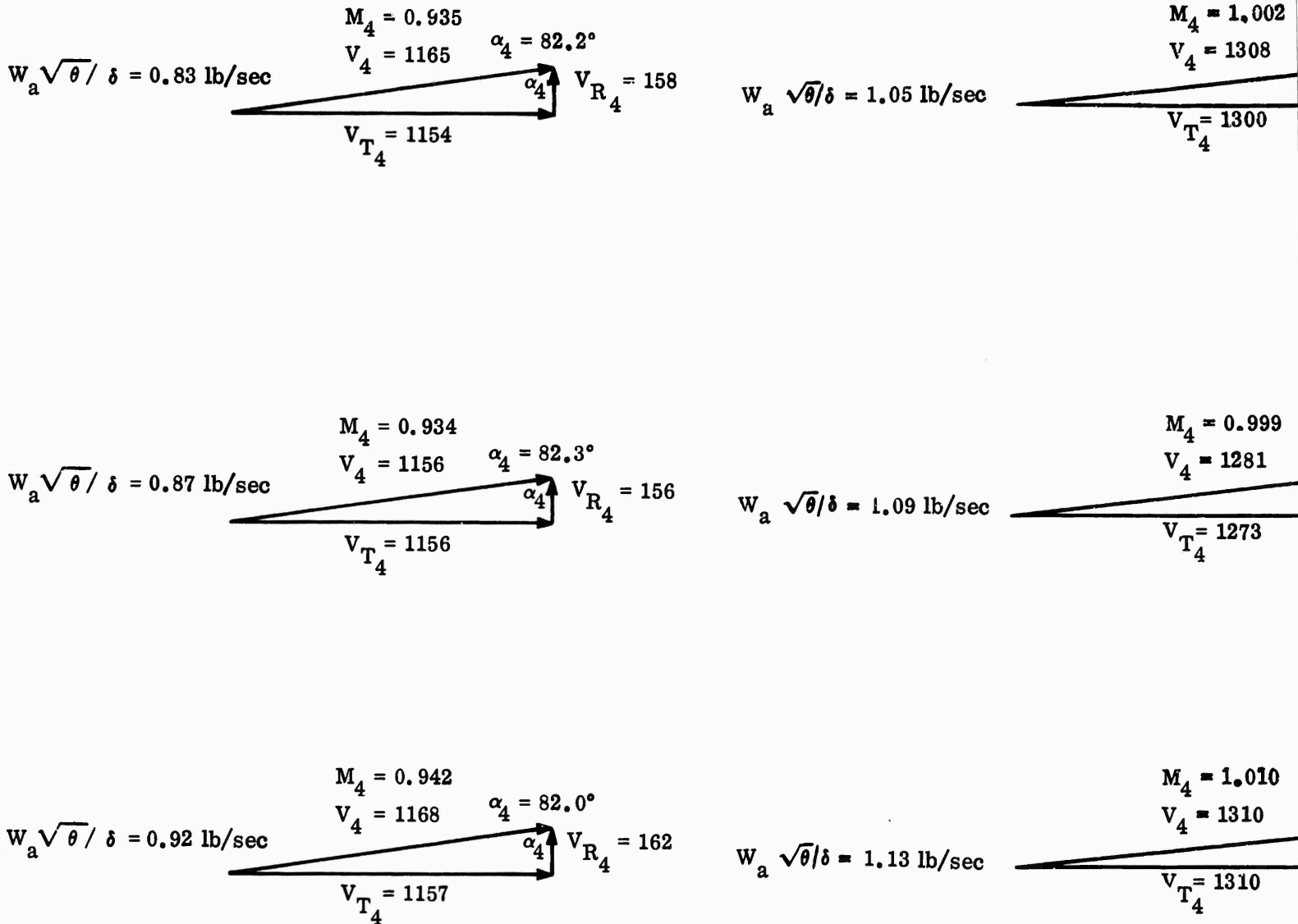
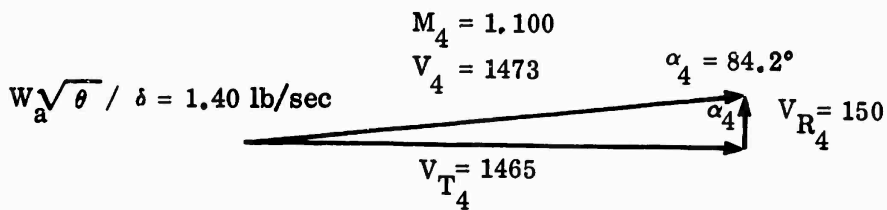
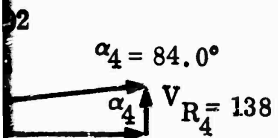


Figure 300. Mean Vector Diagrams at 1.02 Diameter Ratio, Workhorse.

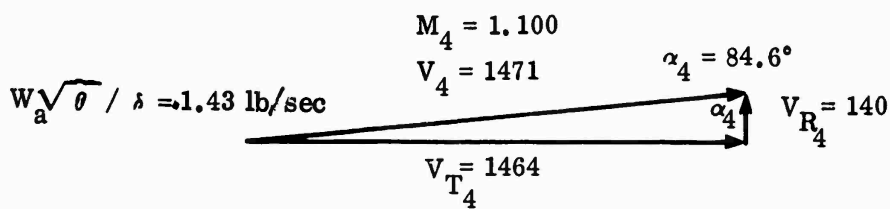
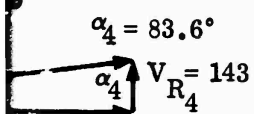
CONFIDENTIAL

35,000 rpm

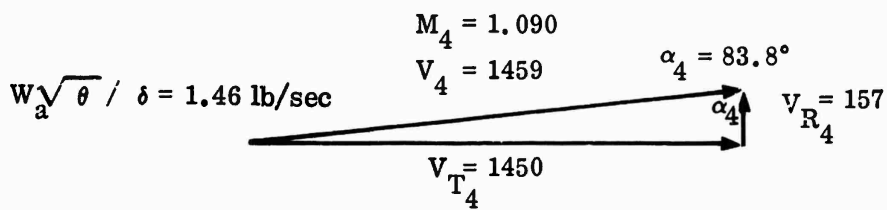
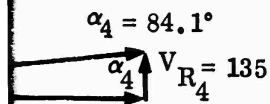
$N/\sqrt{\theta} = 40,000$ rpm



$W_a \sqrt{\theta} / \delta = 1.92$ lb/sec



$W_a \sqrt{\theta} / \delta = 1.98$ lb/sec



$W_a \sqrt{\theta} / \delta = 2.00$ lb/sec

$$N/\sqrt{\theta} = 46,000 \text{ rpm}$$

$$\begin{aligned} M_4 &= 1.190 \\ V_4 &= 1678 \\ \alpha_4 &= 83.7^\circ \\ V_{T_4} &= 1668 \\ V_{R_4} &= 185 \end{aligned}$$

$$\begin{aligned} M_4 &= 1.200 \\ V_4 &= 1682 \\ \alpha_4 &= 84.7^\circ \\ V_{T_4} &= 1674 \\ V_{R_4} &= 156 \end{aligned}$$

$$\begin{aligned} M_4 &= 1.200 \\ V_4 &= 1686 \\ \alpha_4 &= 84.0^\circ \\ V_{T_4} &= 1677 \\ V_{R_4} &= 175 \end{aligned}$$

$$N/\sqrt{\theta} = 50,000 \text{ rpm}$$

$$\begin{aligned} W_a \sqrt{\theta}/\delta &= 2.24 \text{ lb/sec} \\ M_4 &= 1.260 \\ V_4 &= 1829 \\ \alpha_4 &= 84.6^\circ \\ V_{T_4} &= 1821 \\ V_{R_4} &= 172 \end{aligned}$$

$$\begin{aligned} W_a \sqrt{\theta}/\delta &= 2.30 \text{ lb/sec} \\ M_4 &= 1.270 \\ V_4 &= 1837 \\ \alpha_4 &= 84.9^\circ \\ V_{T_4} &= 1829 \\ V_{R_4} &= 165 \end{aligned}$$

$$\begin{aligned} W_a \sqrt{\theta}/\delta &= 2.36 \text{ lb/sec} \\ M_4 &= 1.270 \\ V_4 &= 1838 \\ \alpha_4 &= 85.9^\circ \\ V_{T_4} &= 1834 \\ V_{R_4} &= 131 \end{aligned}$$

CONFIDENTIAL

Corrected to Ambient
Conditions of:
60°F
29.92 in. Hg

Test 3306A
IGV = +17°

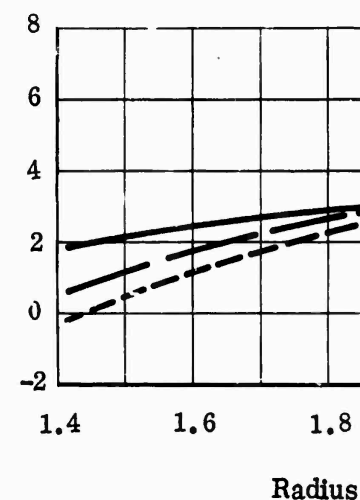
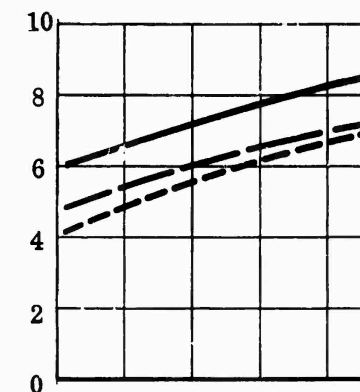
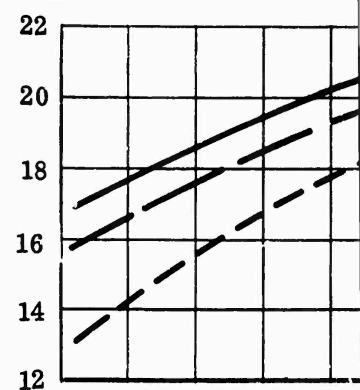
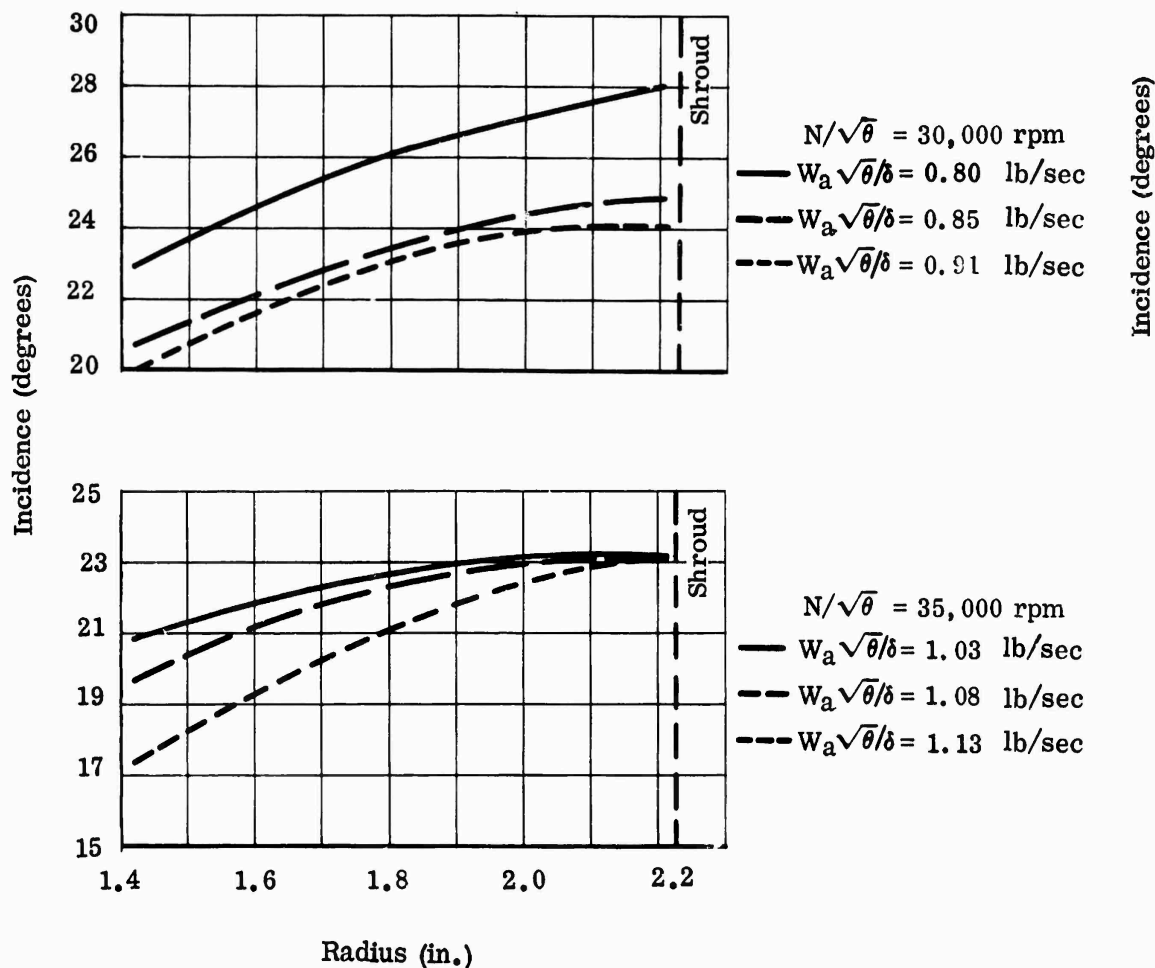
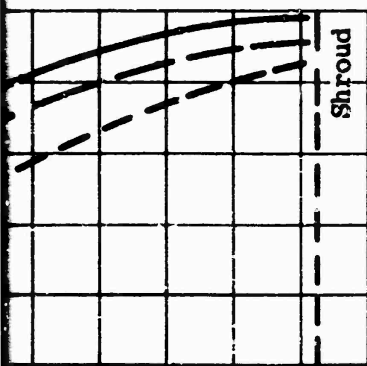
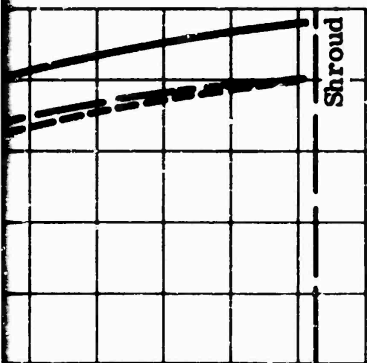


Figure 301. Inducer Incidence, Workhorse.

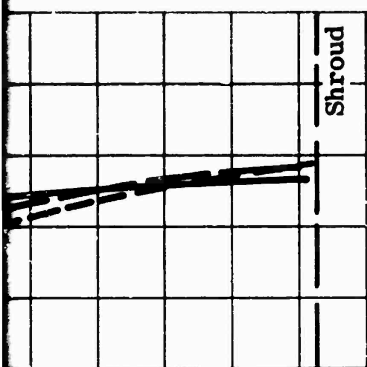
CONFIDENTIAL



$N/\sqrt{\theta} = 40,000 \text{ rpm}$
 — $W_a \sqrt{\theta}/\delta = 1.37 \text{ lb/sec}$
 - - $W_a \sqrt{\theta}/\delta = 1.41 \text{ lb/sec}$
 - · - $W_a \sqrt{\theta}/\delta = 1.47 \text{ lb/sec}$



$N/\sqrt{\theta} = 46,000 \text{ rpm}$
 — $W_a \sqrt{\theta}/\delta = 1.99 \text{ lb/sec}$
 - - $W_a \sqrt{\theta}/\delta = 2.02 \text{ lb/sec}$
 - · - $W_a \sqrt{\theta}/\delta = 2.09 \text{ lb/sec}$

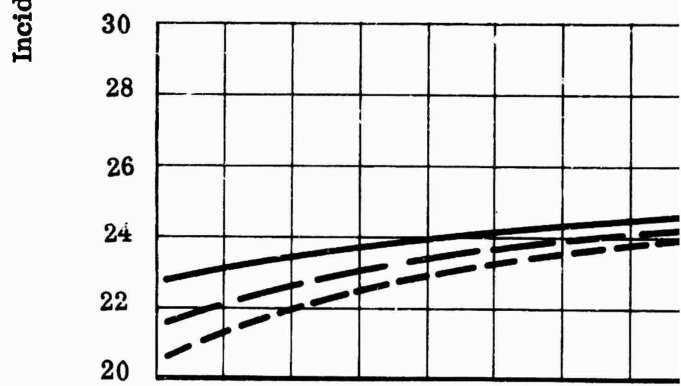
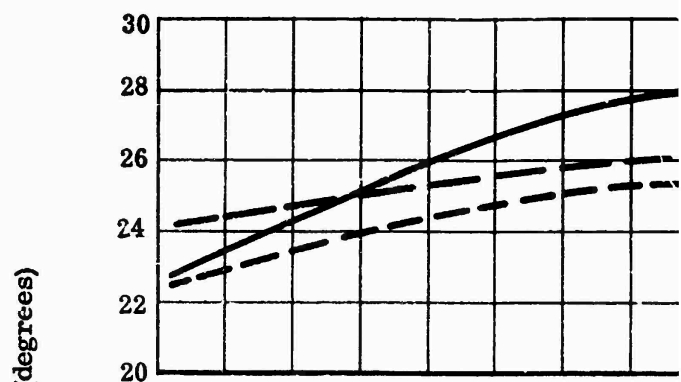


$N/\sqrt{\theta} = 50,000 \text{ rpm}$
 — $W_a \sqrt{\theta}/\delta = 2.20 \text{ lb/sec}$
 - - $W_a \sqrt{\theta}/\delta = 2.27 \text{ lb/sec}$
 - · - $W_a \sqrt{\theta}/\delta = 2.29 \text{ lb/sec}$

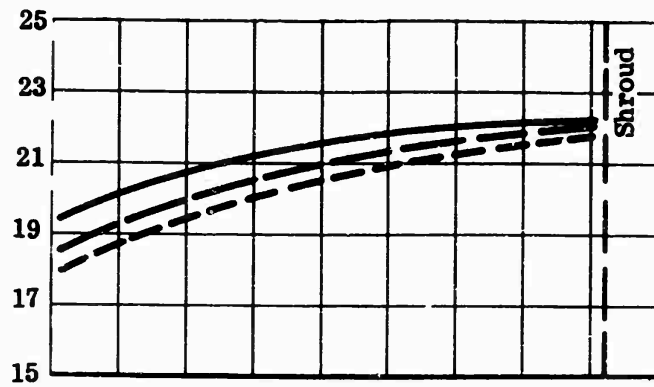
Radius (in.)

Corrected to Ambient
 Conditions of:
 60°F
 29.92 in. Hg

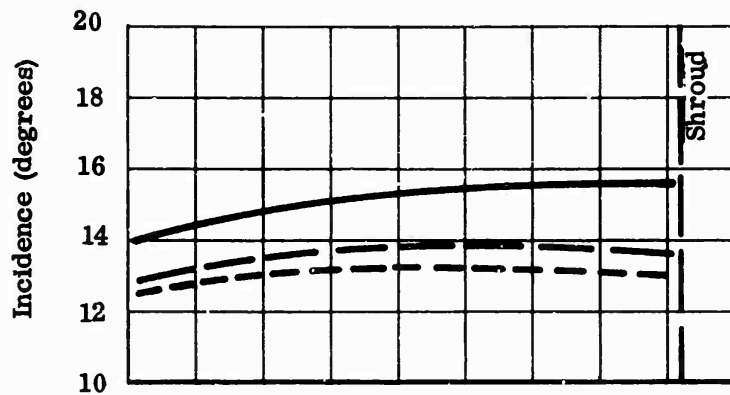
Test 3306B
 IGV = 0°



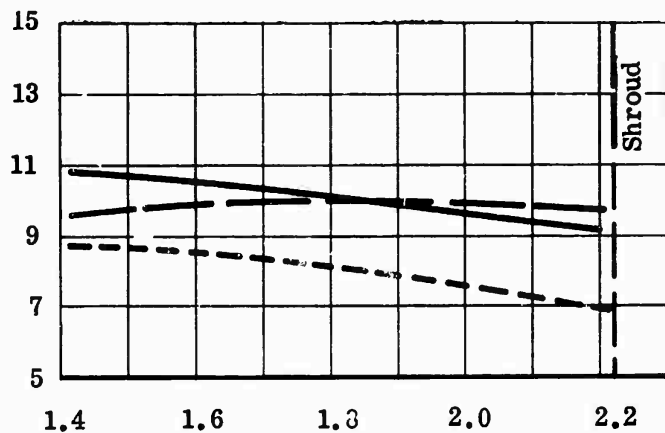
Radius (in.)



$N/\sqrt{\theta} = 40,000 \text{ rpm}$
 $W_a \sqrt{\theta}/\delta = 1.40 \text{ lb/sec}$
 $W_a \sqrt{\theta}/\delta = 1.43 \text{ lb/sec}$
 $W_a \sqrt{\theta}/\delta = 1.46 \text{ lb/sec}$



$N/\sqrt{\theta} = 46,000 \text{ rpm}$
 $W_a \sqrt{\theta}/\delta = 1.92 \text{ lb/sec}$
 $W_a \sqrt{\theta}/\delta = 1.98 \text{ lb/sec}$
 $W_a \sqrt{\theta}/\delta = 2.00 \text{ lb/sec}$



$N/\sqrt{\theta} = 50,000 \text{ rpm}$
 $W_a \sqrt{\theta}/\delta = 2.24 \text{ lb/sec}$
 $W_a \sqrt{\theta}/\delta = 2.30 \text{ lb/sec}$
 $W_a \sqrt{\theta}/\delta = 2.36 \text{ lb/sec}$

Radius (in.)

CONFIDENTIAL

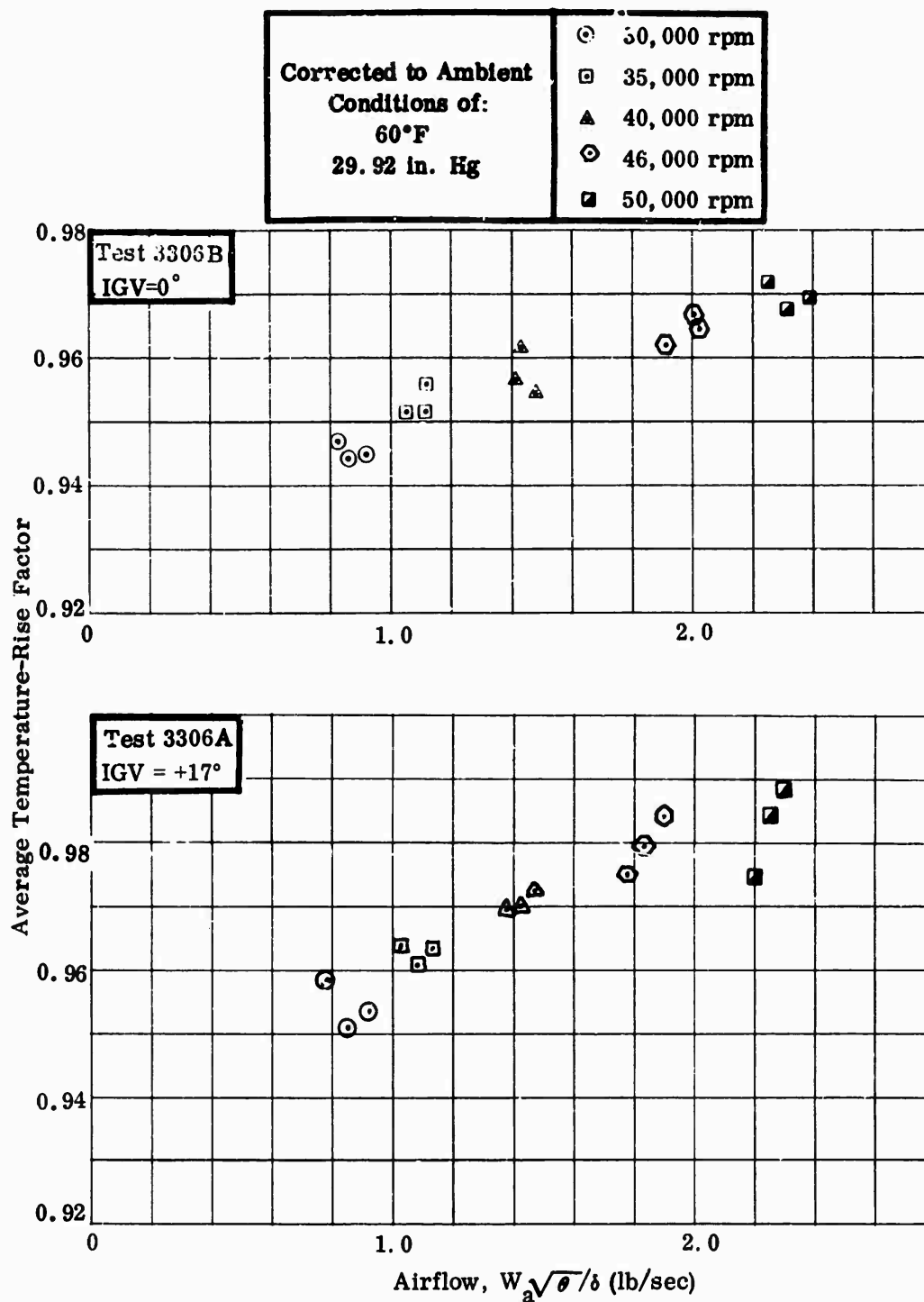


Figure 302. Average Temperature-Rise Factor, Workhorse.

CONFIDENTIAL

Corrected to Ambient
Conditions of:
60°F
29.92 in. Hg

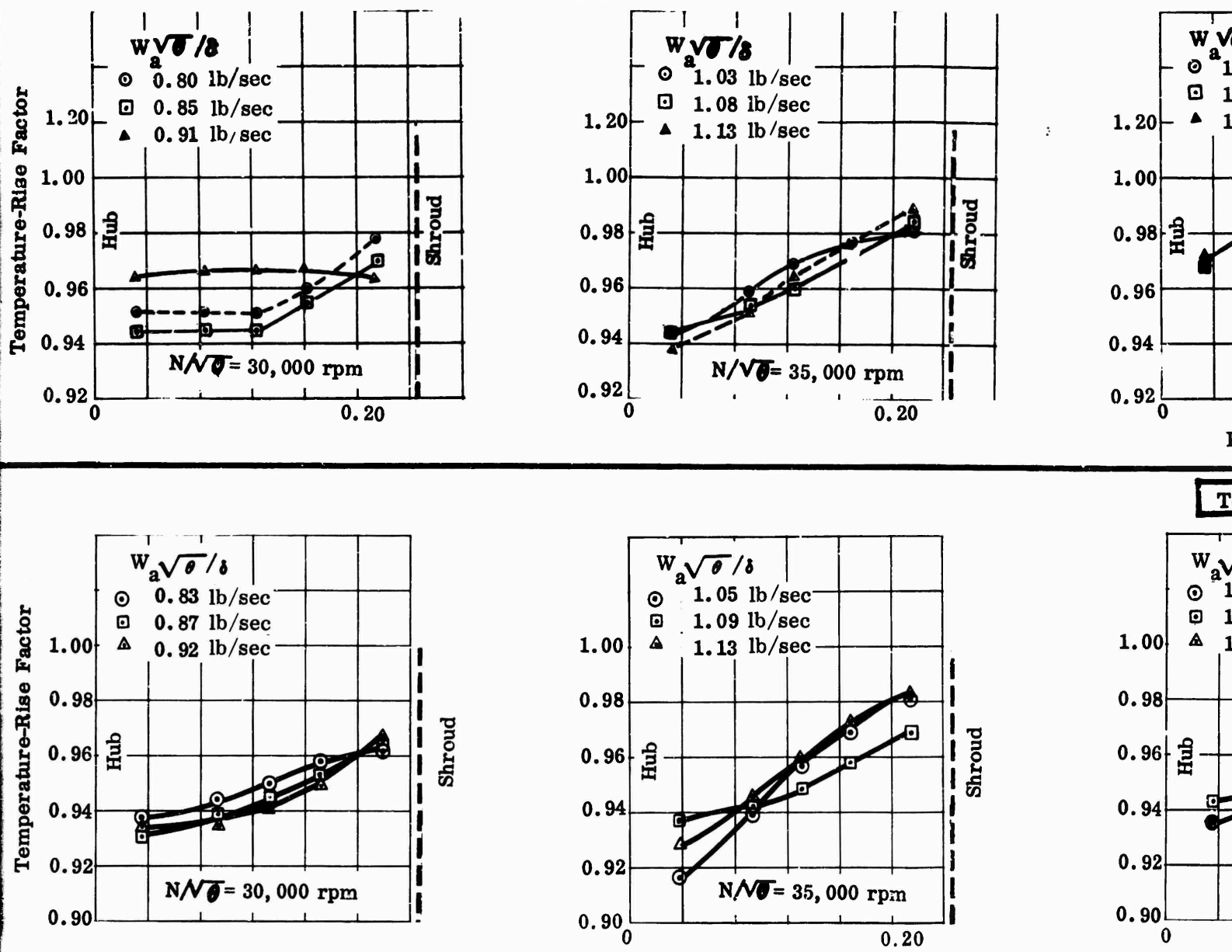
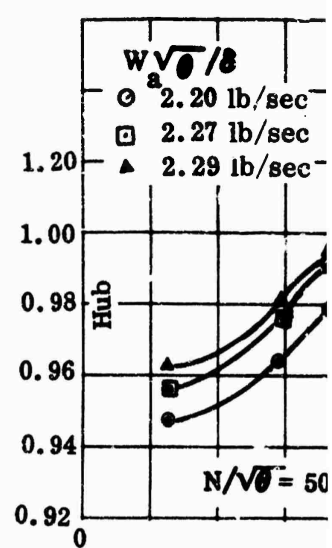
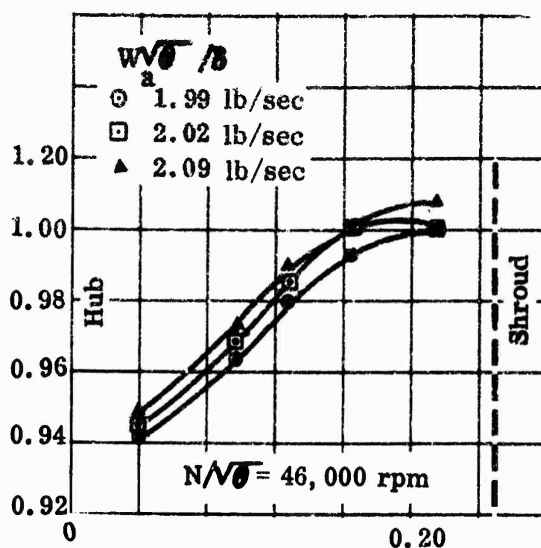
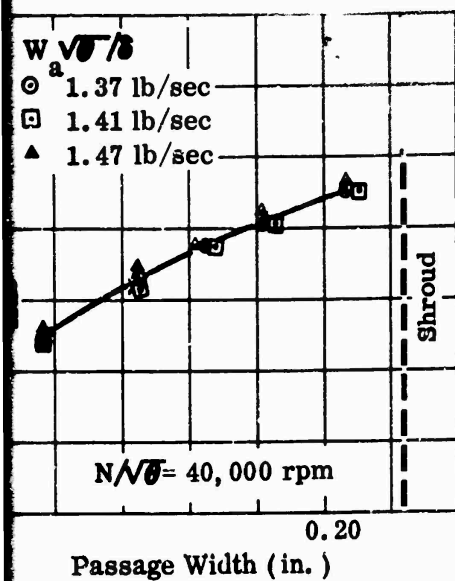
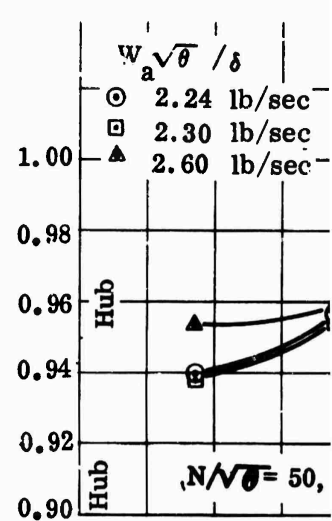
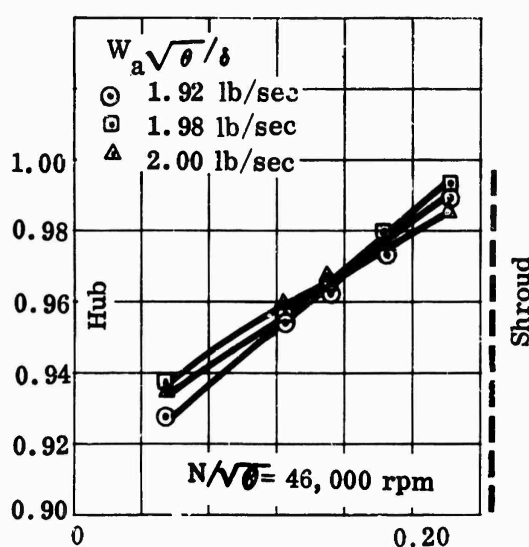
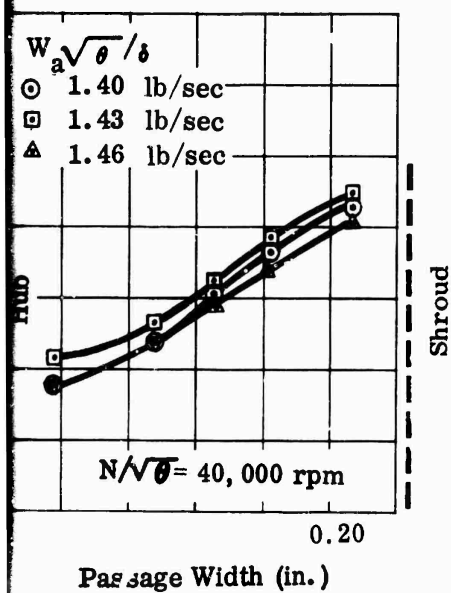


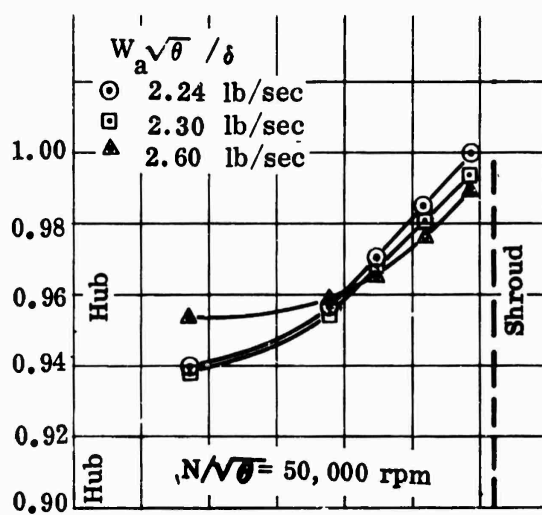
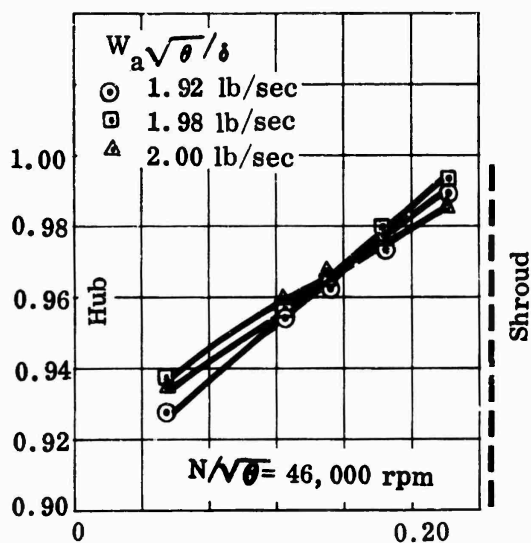
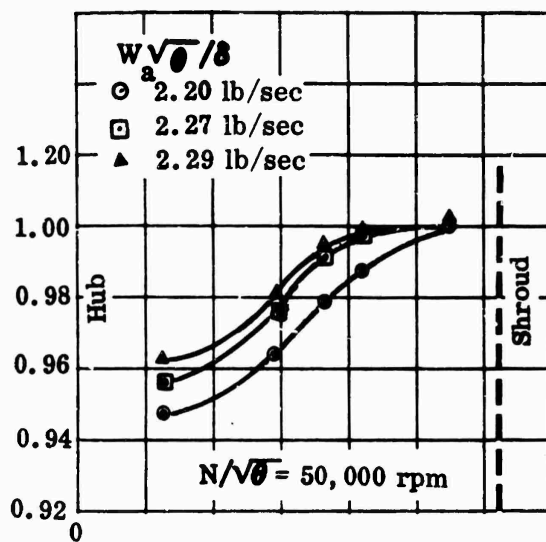
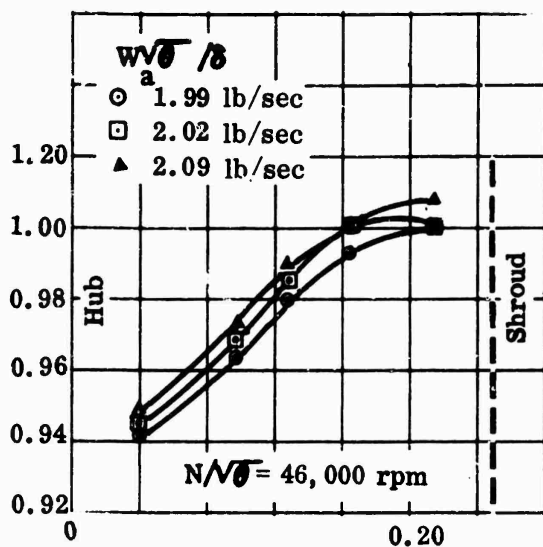
Figure 303. Temperature-Rise Factor Across Impeller Tip, Workhorse.

Test 3306A IGV = +17°



Test 3306B IGV = 0°





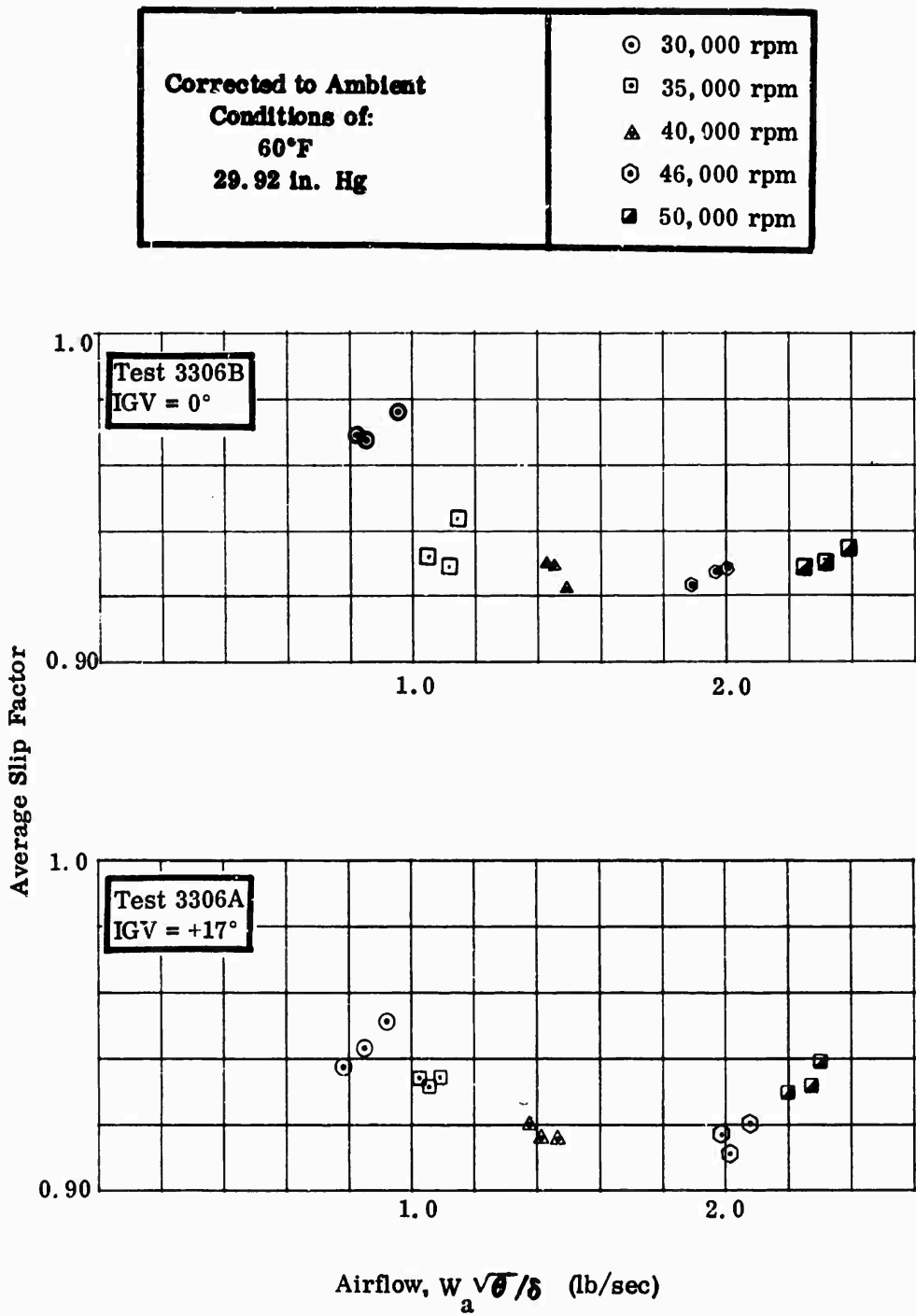
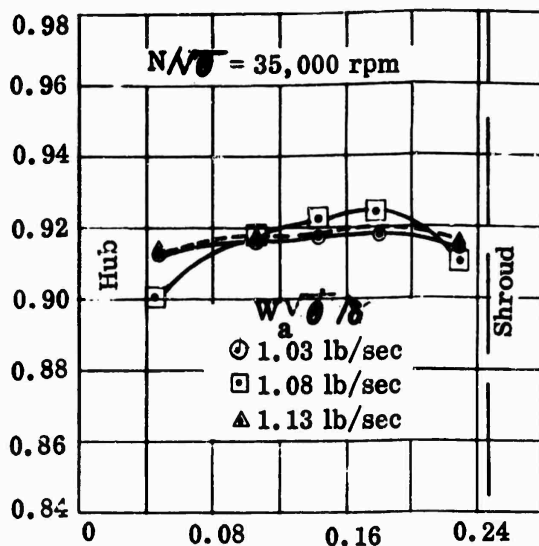
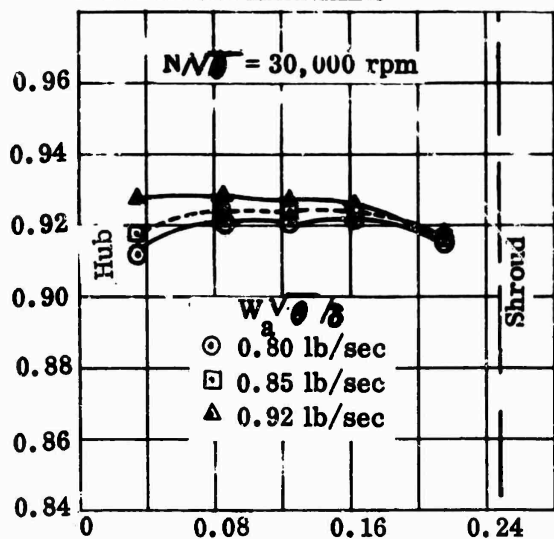


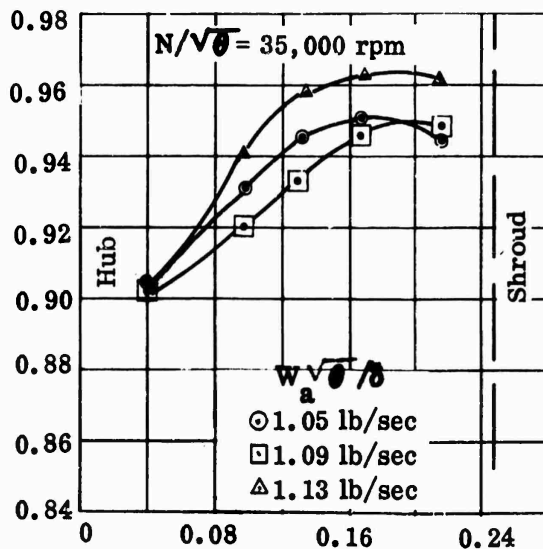
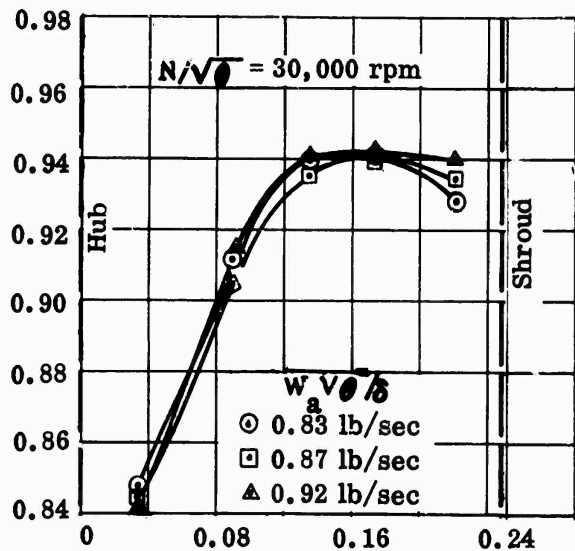
Figure 304. Average Slip Factor, Workhorse.

Corrected to Ambient
Conditions of:
60°F
29.92 in. Hg

Test 3306A
IGV = +17°

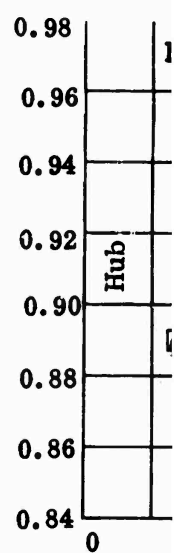
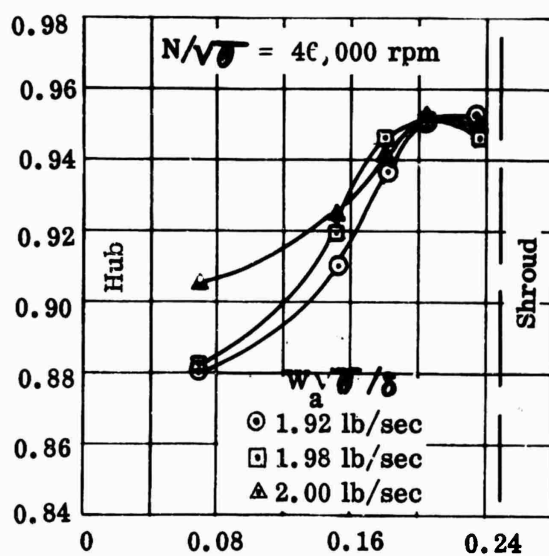
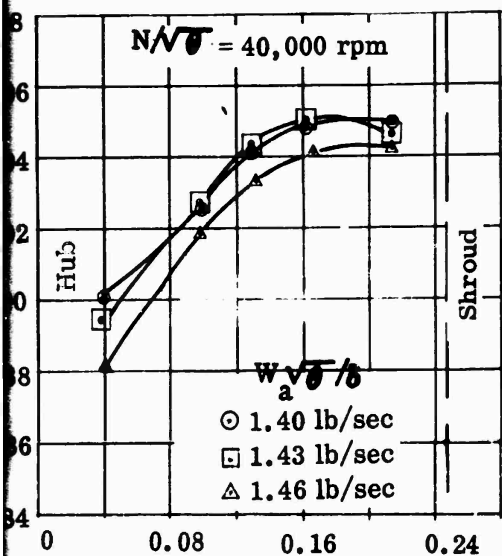
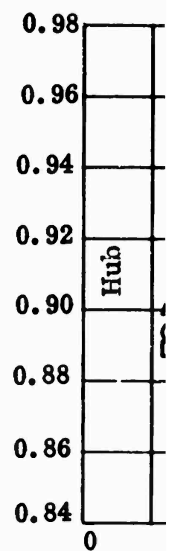
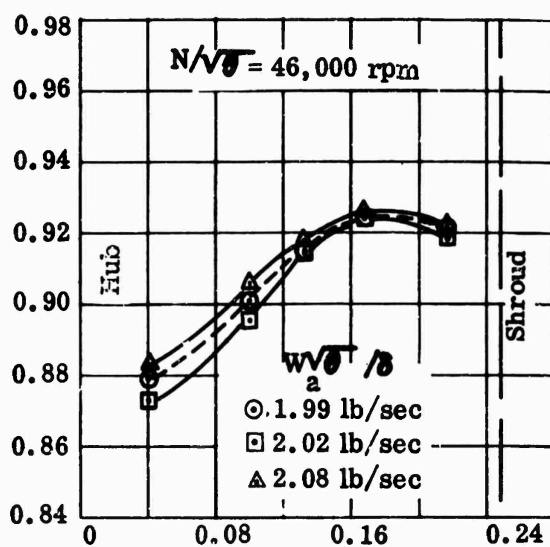
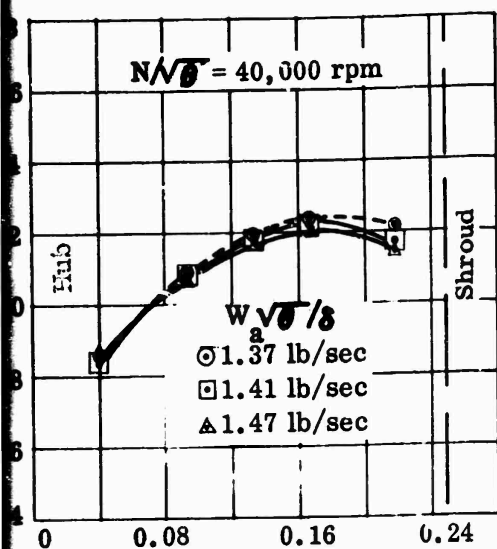


Test 3306B
IGV = 0°

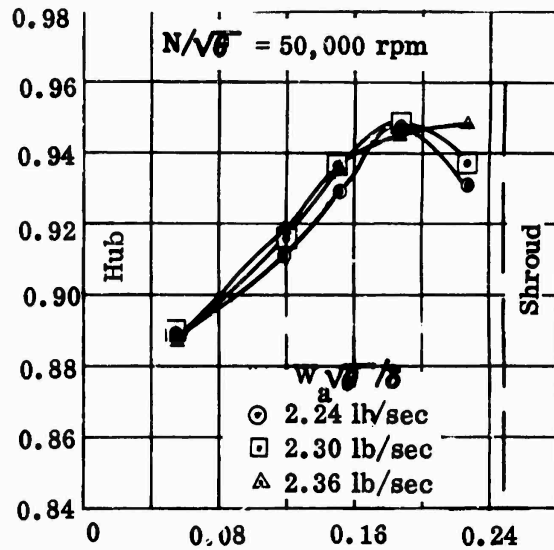
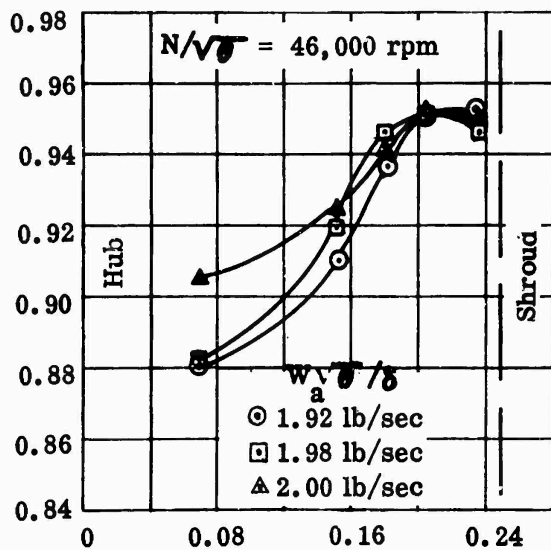
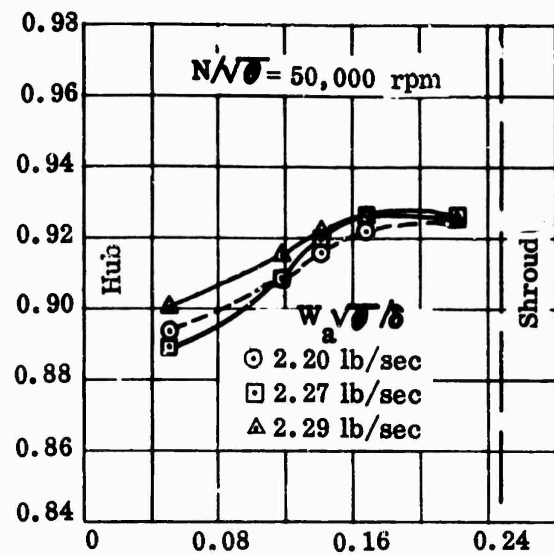
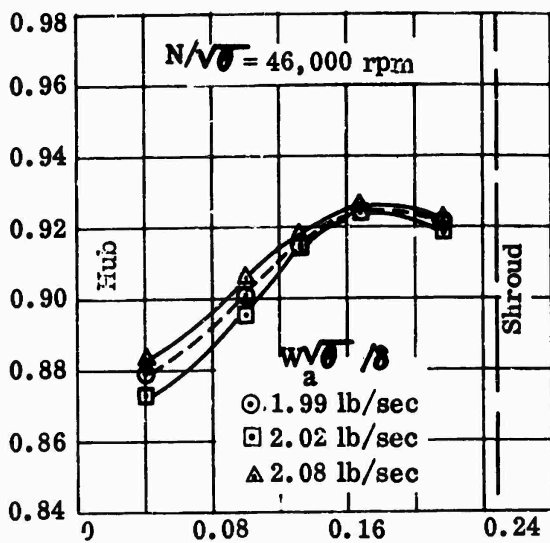


Passage Width (in.)

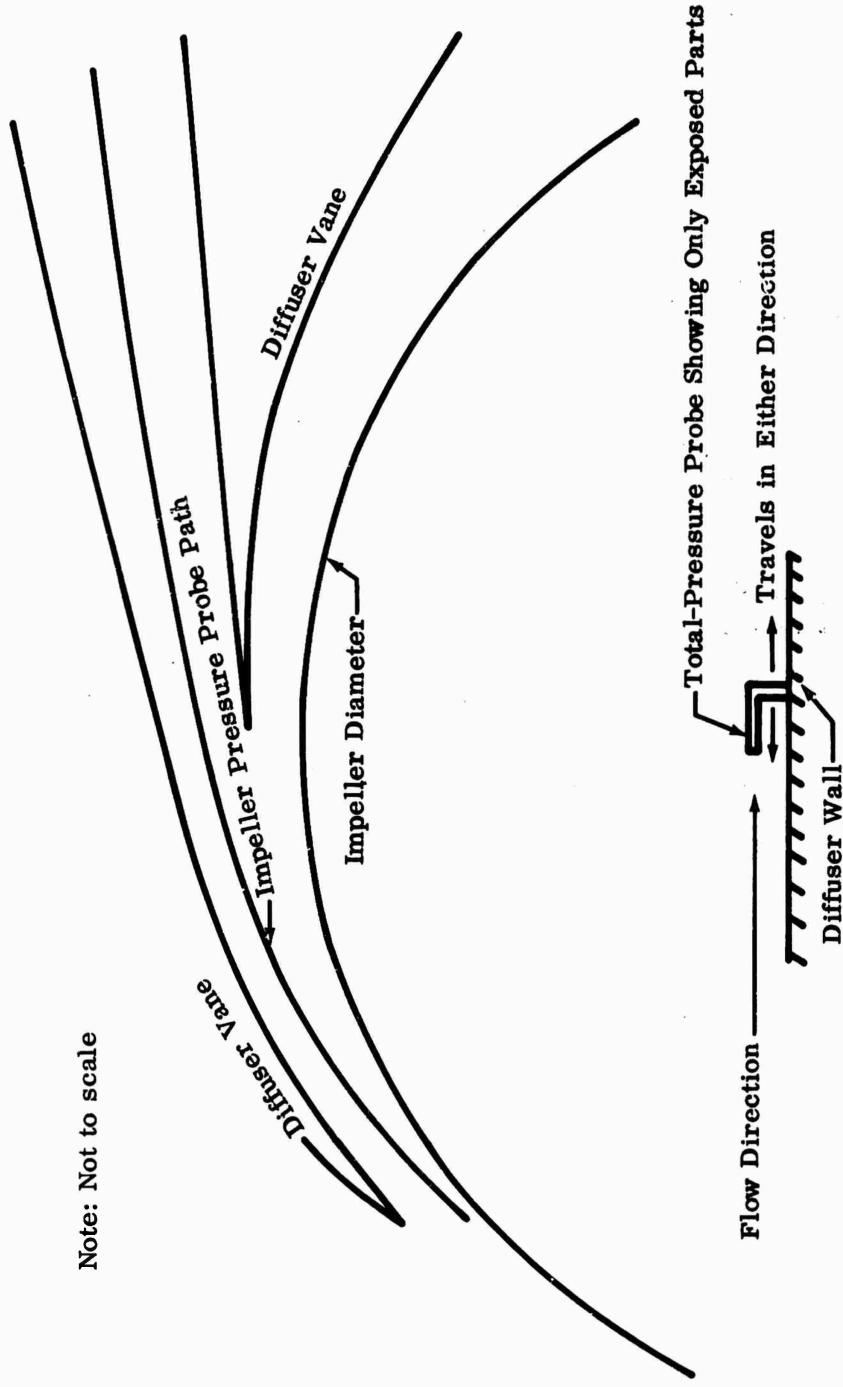
Figure 305. Variation of Slip Factor Across Impeller Tip, Workhorse.



Passage Width (in.)



Passage Width (in.)



Note: Not to scale

Figure 306. Diffuser-Rig Traversing Total-Pressure Probe.

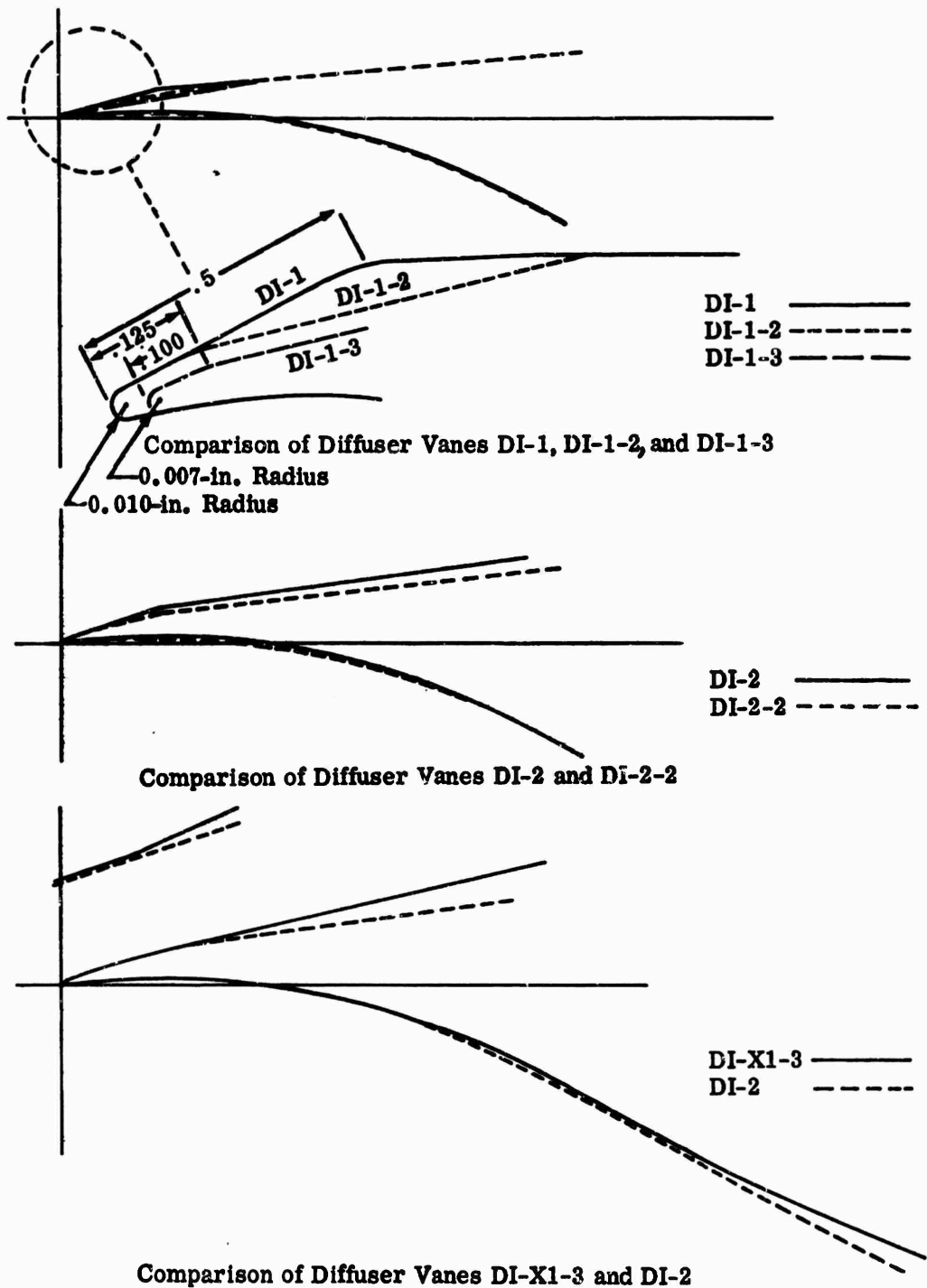


Figure 307. Diffuser-Vane Modifications.

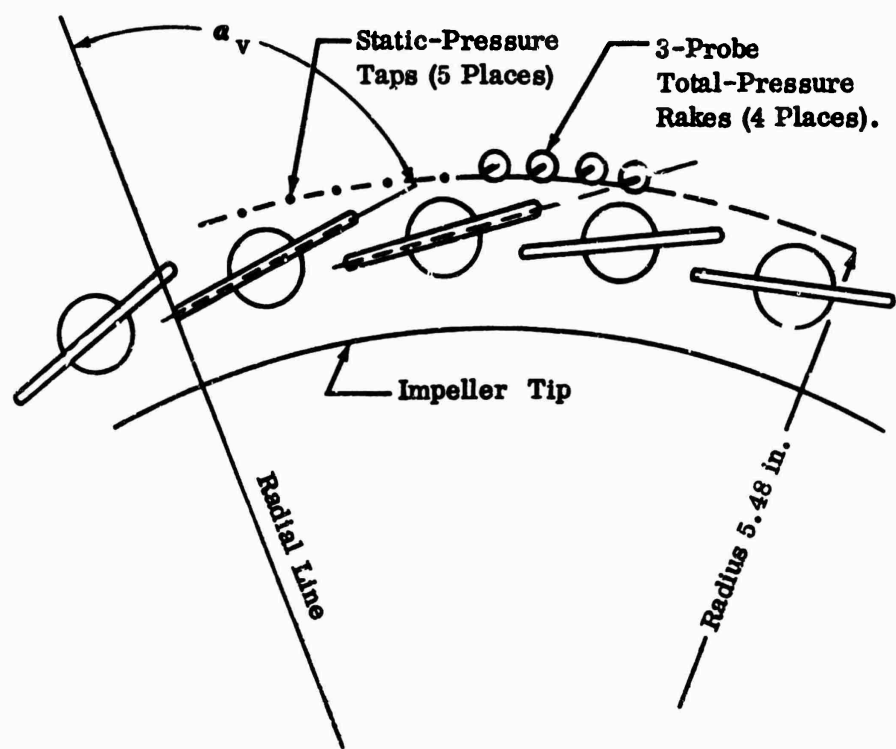


Figure 308. Cascade Configuration.

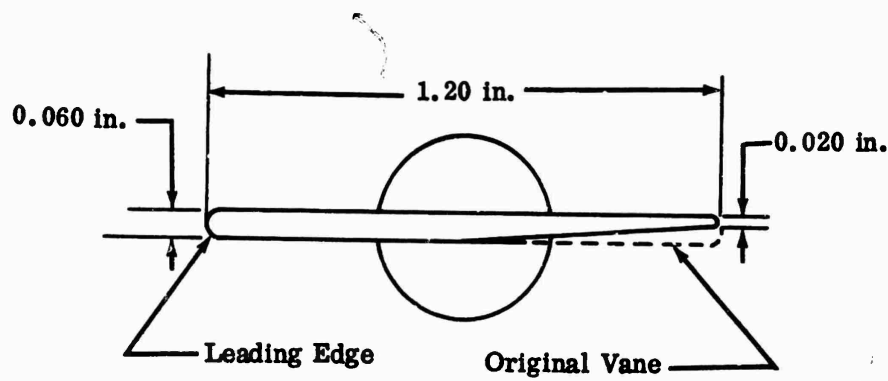


Figure 309. Modified Cascade Vane.

CONFIDENTIAL

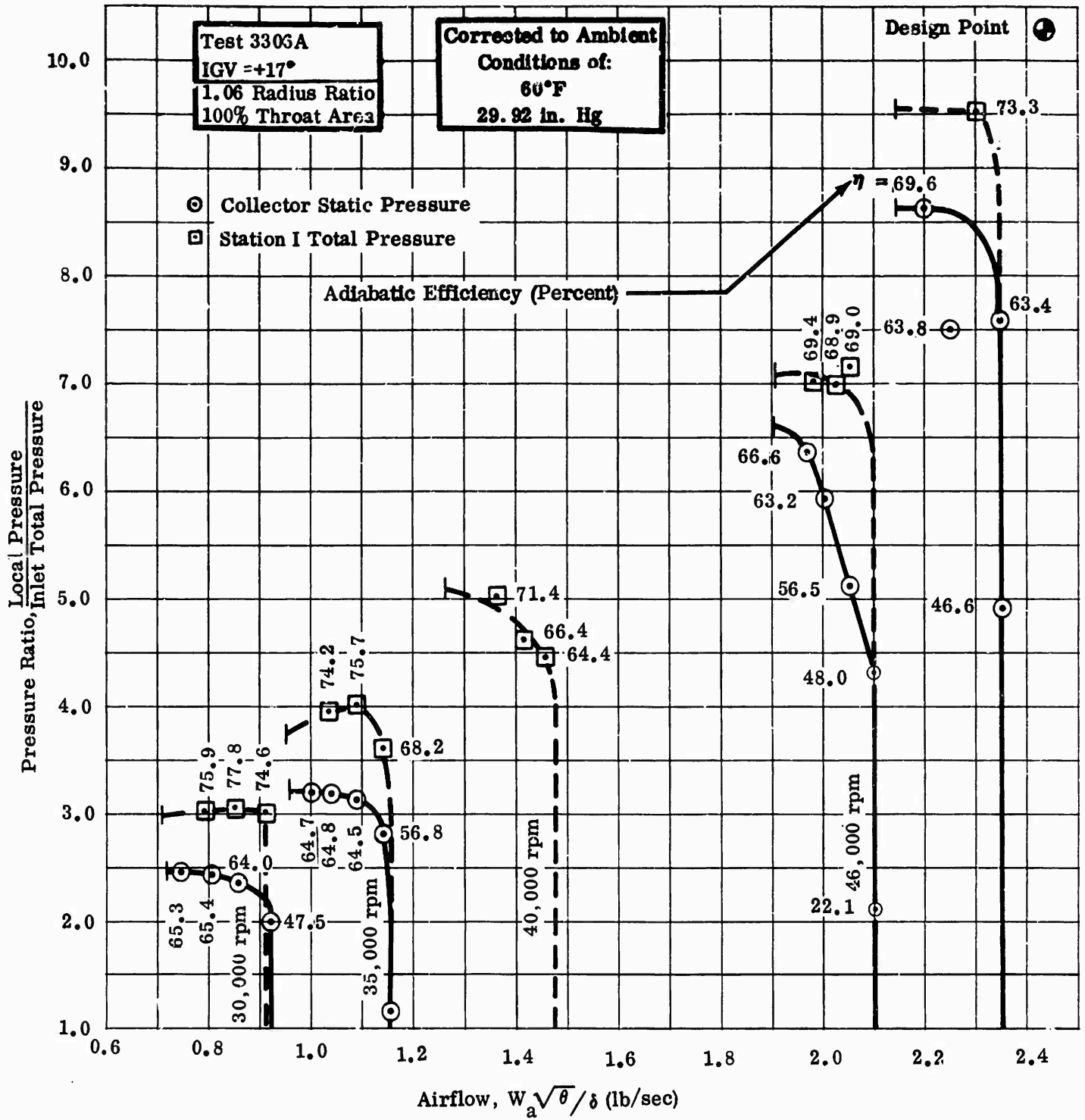


Figure 310. Pressure Ratio Versus Airflow, DI-1.

CONFIDENTIAL

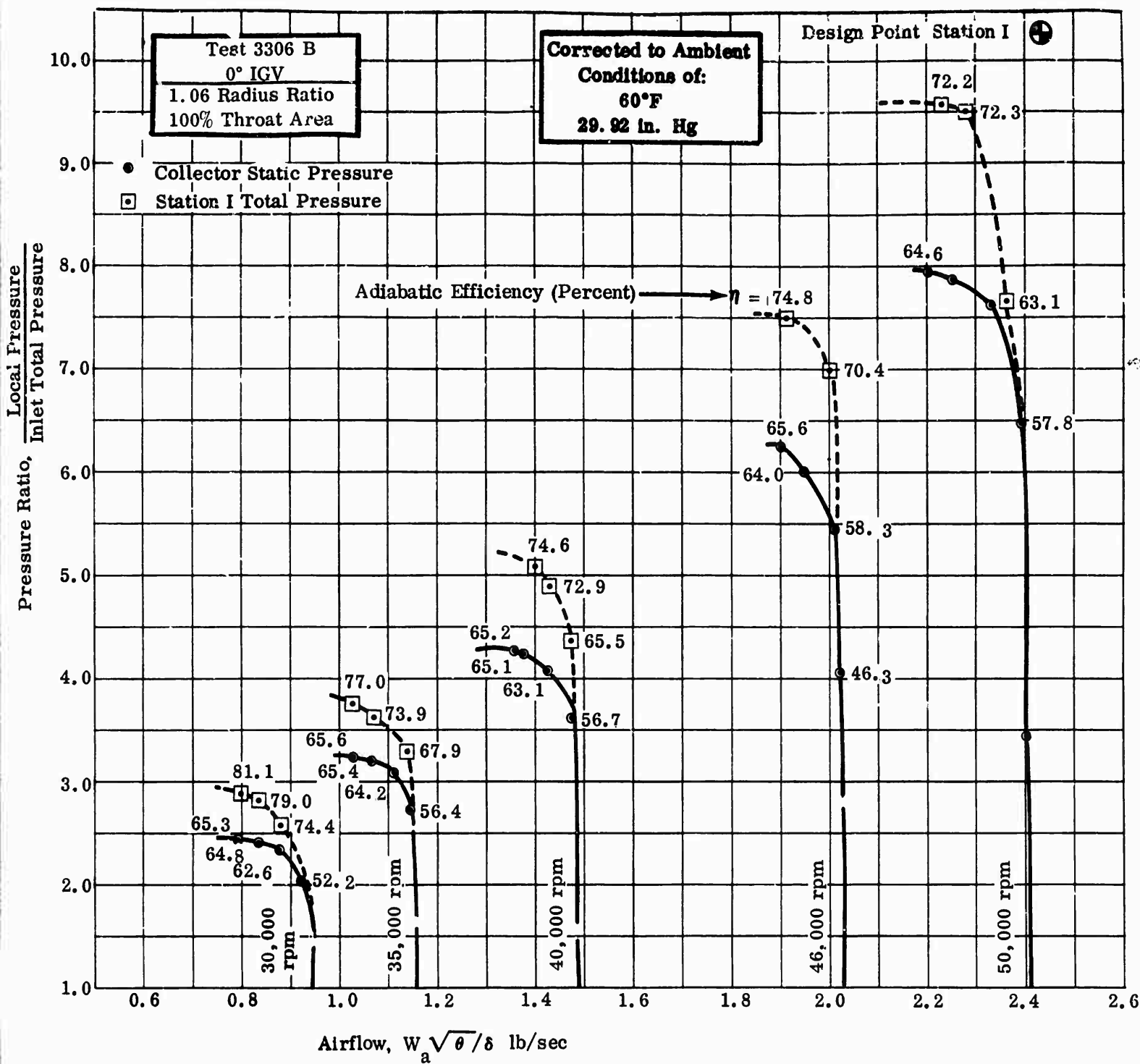


Figure 311. Pressure Ratio Versus Airflow, DI-1.

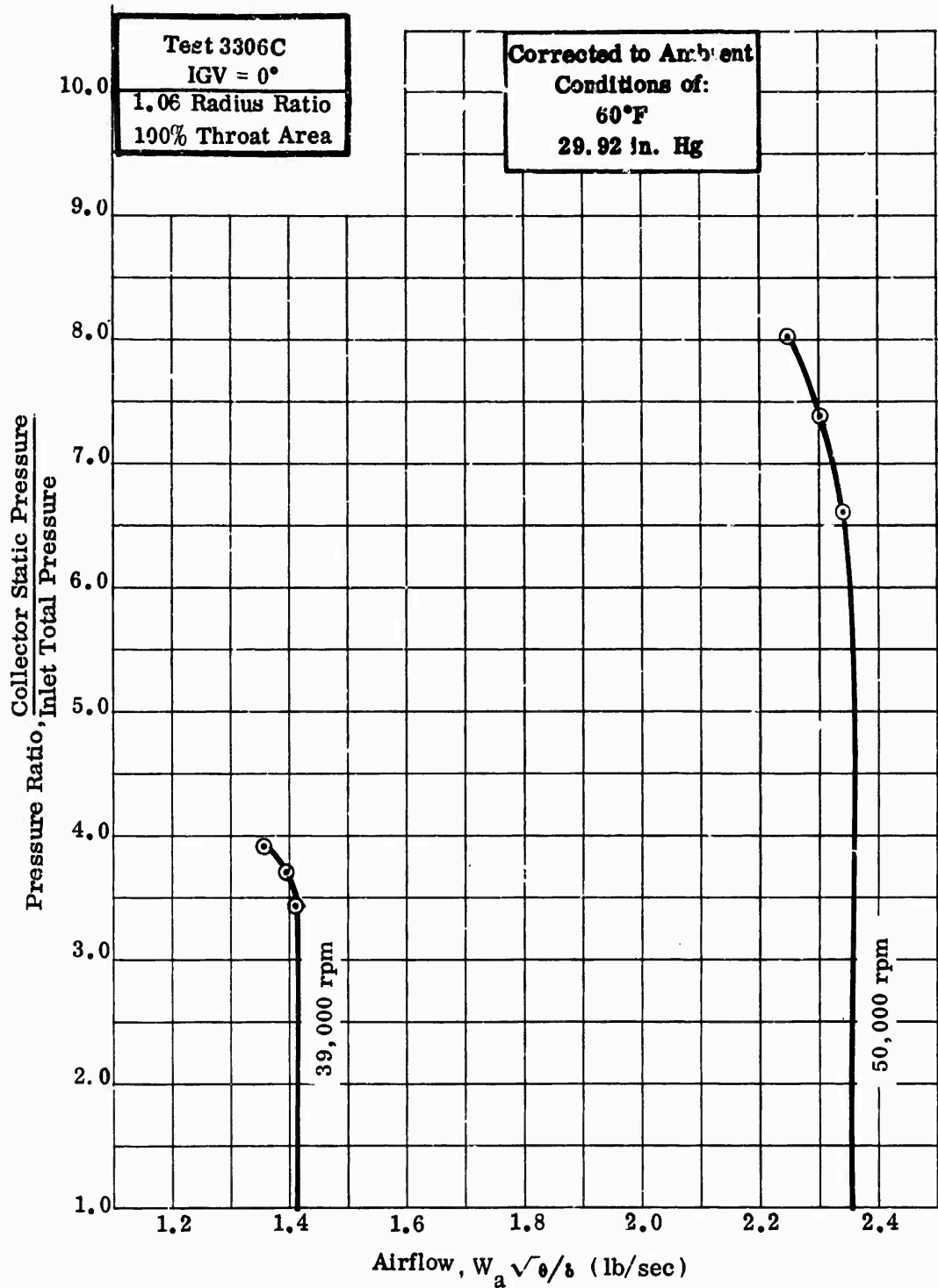


Figure 312. Pressure Ratio Versus Airflow, DI-1.

CONFIDENTIAL

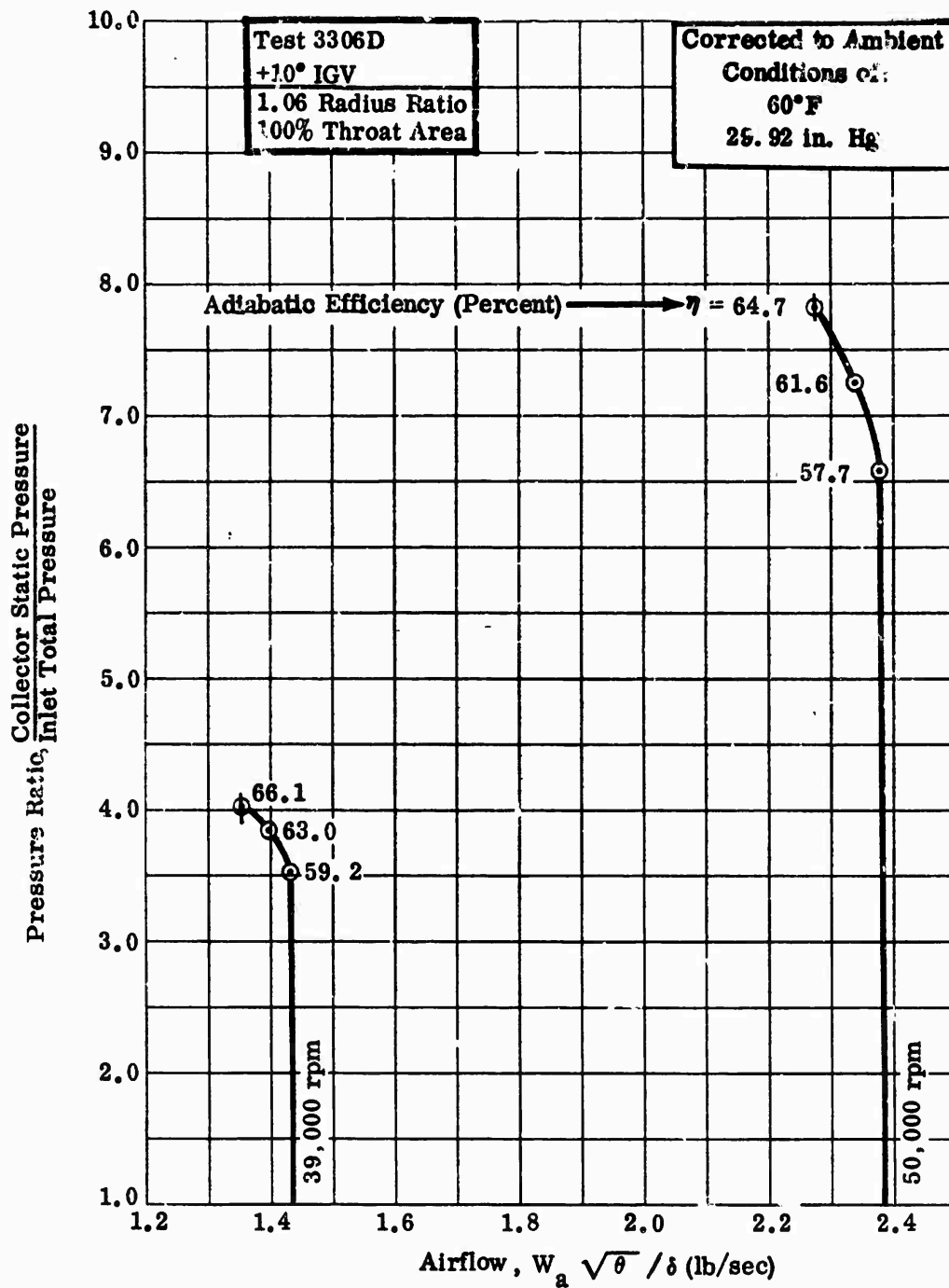


Figure 313. Pressure Ratio Versus Airflow, DI-1.

CONFIDENTIAL

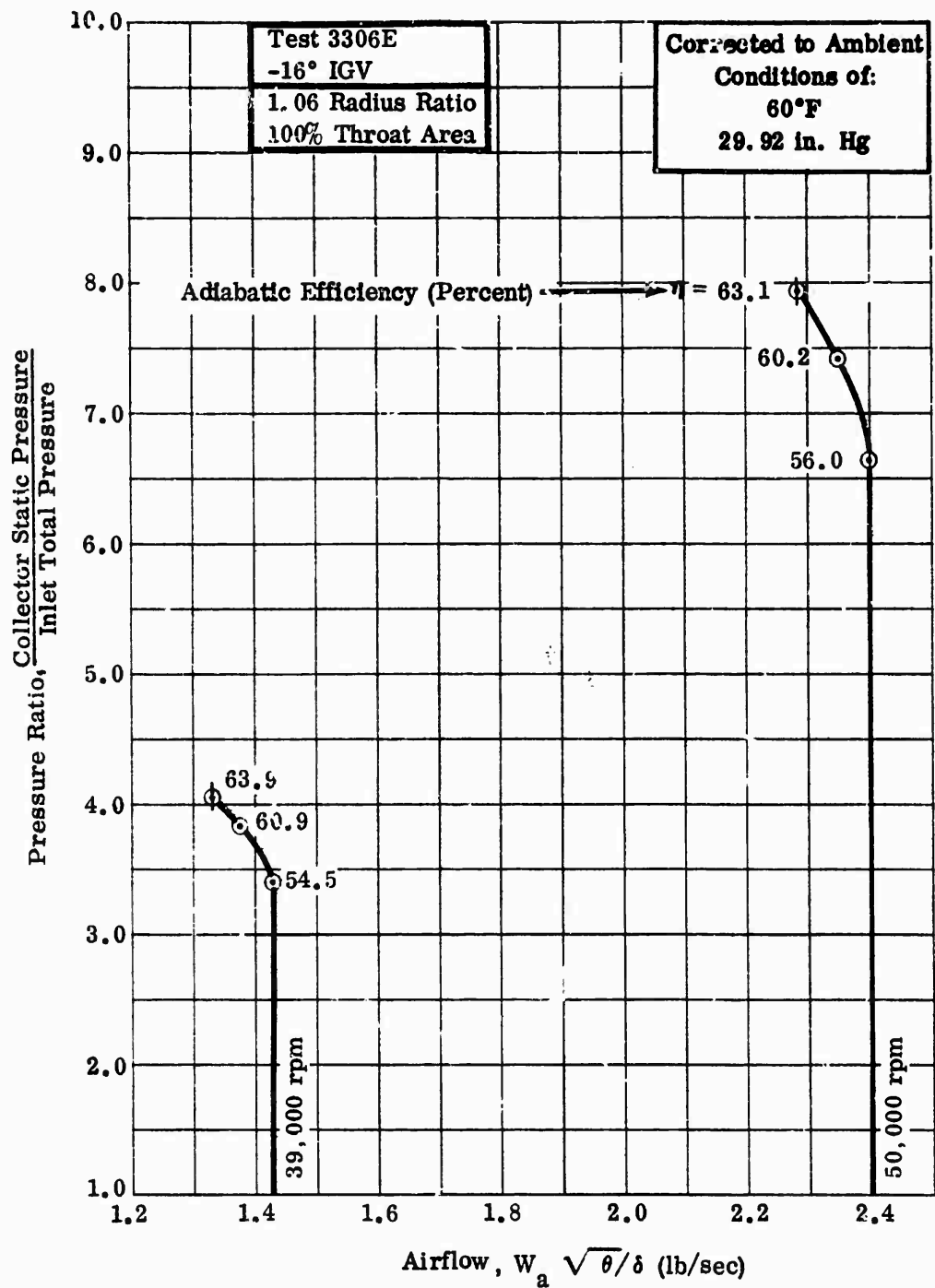


Figure 314. Pressure Ratio Versus Airflow, DI-1.

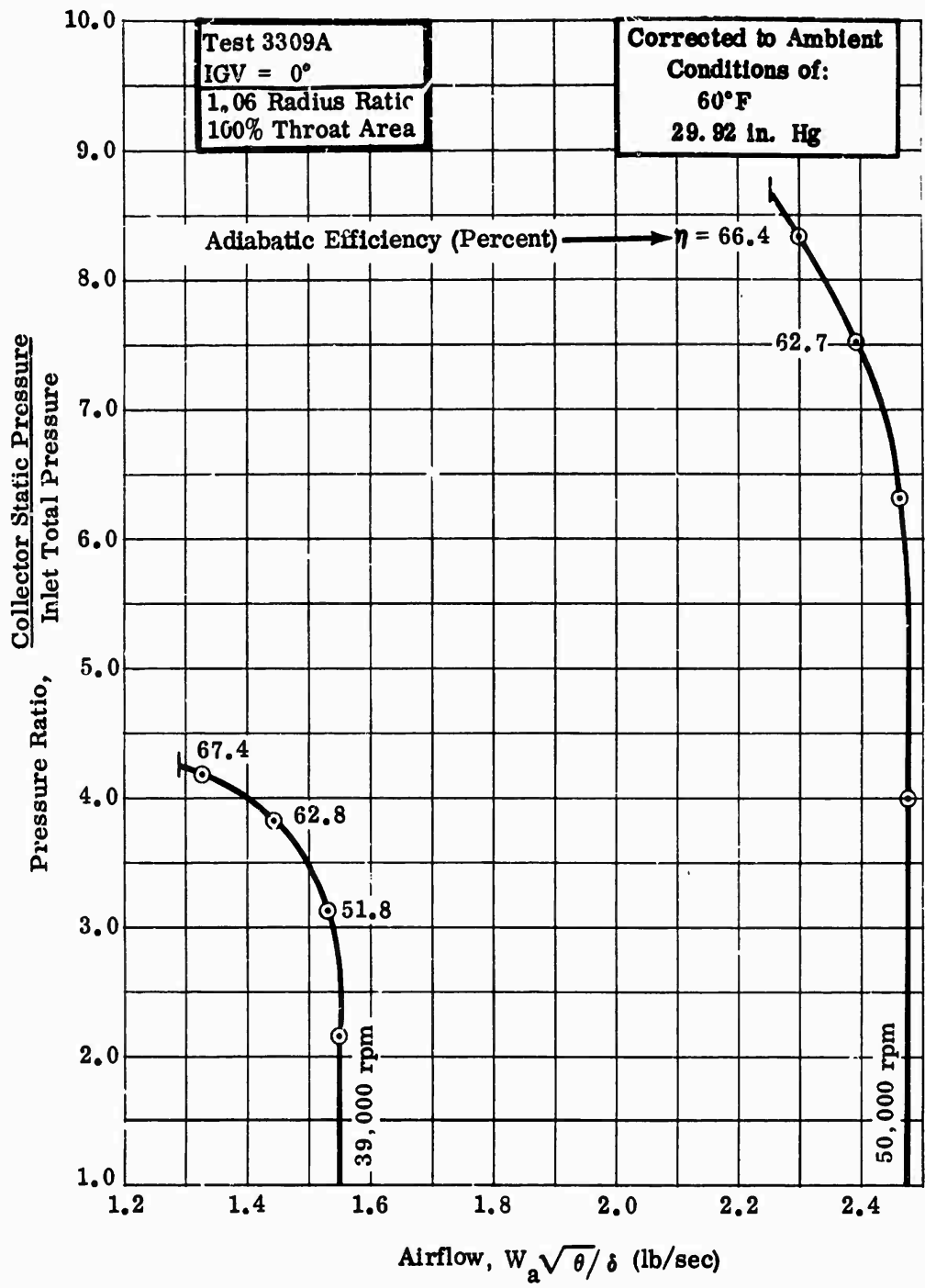


Figure 315. Pressure Ratio Versus Airflow, DI-1.

CONFIDENTIAL

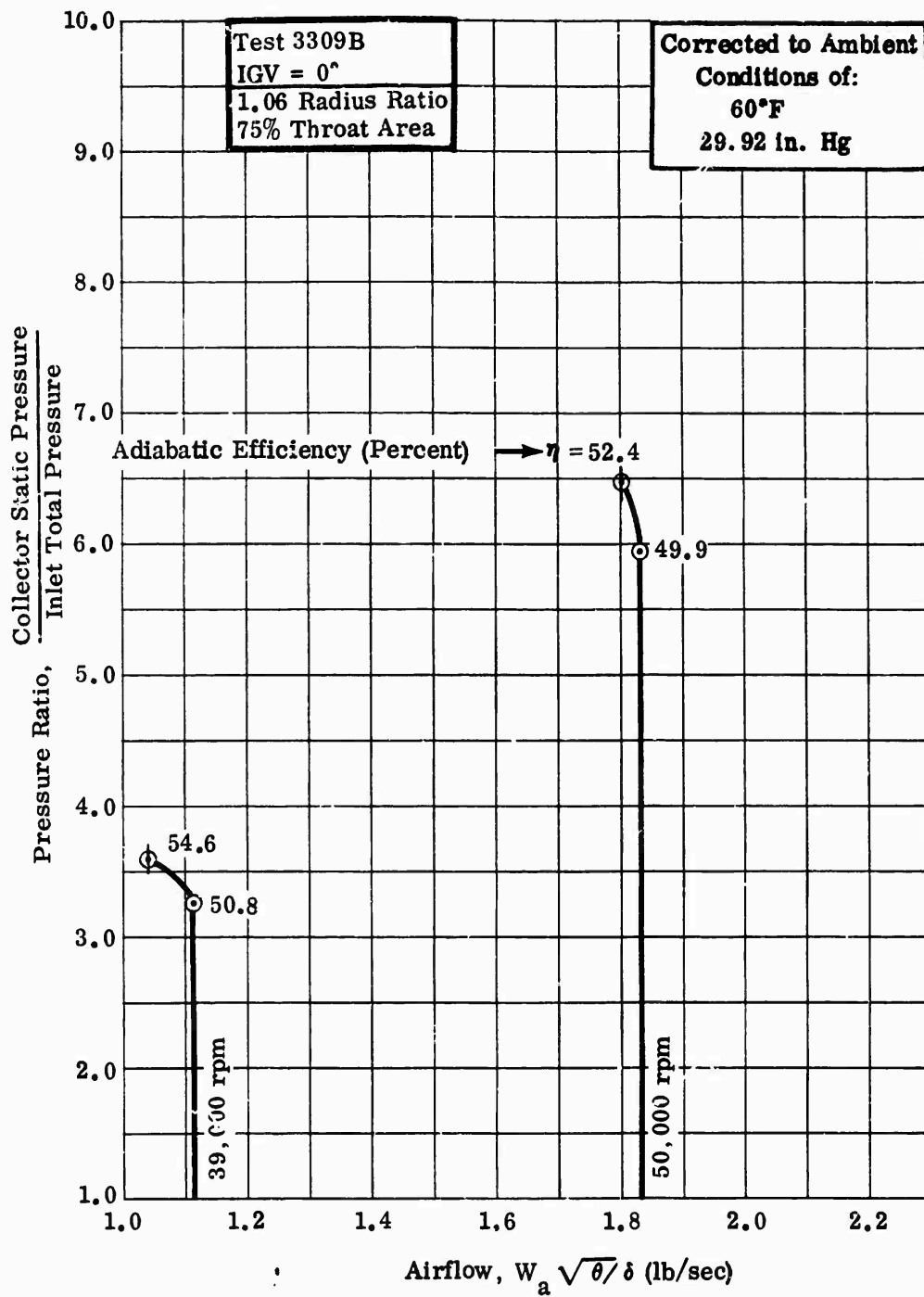


Figure 316. Pressure Ratio Versus Airflow, DI-1.

CONFIDENTIAL

CONFIDENTIAL

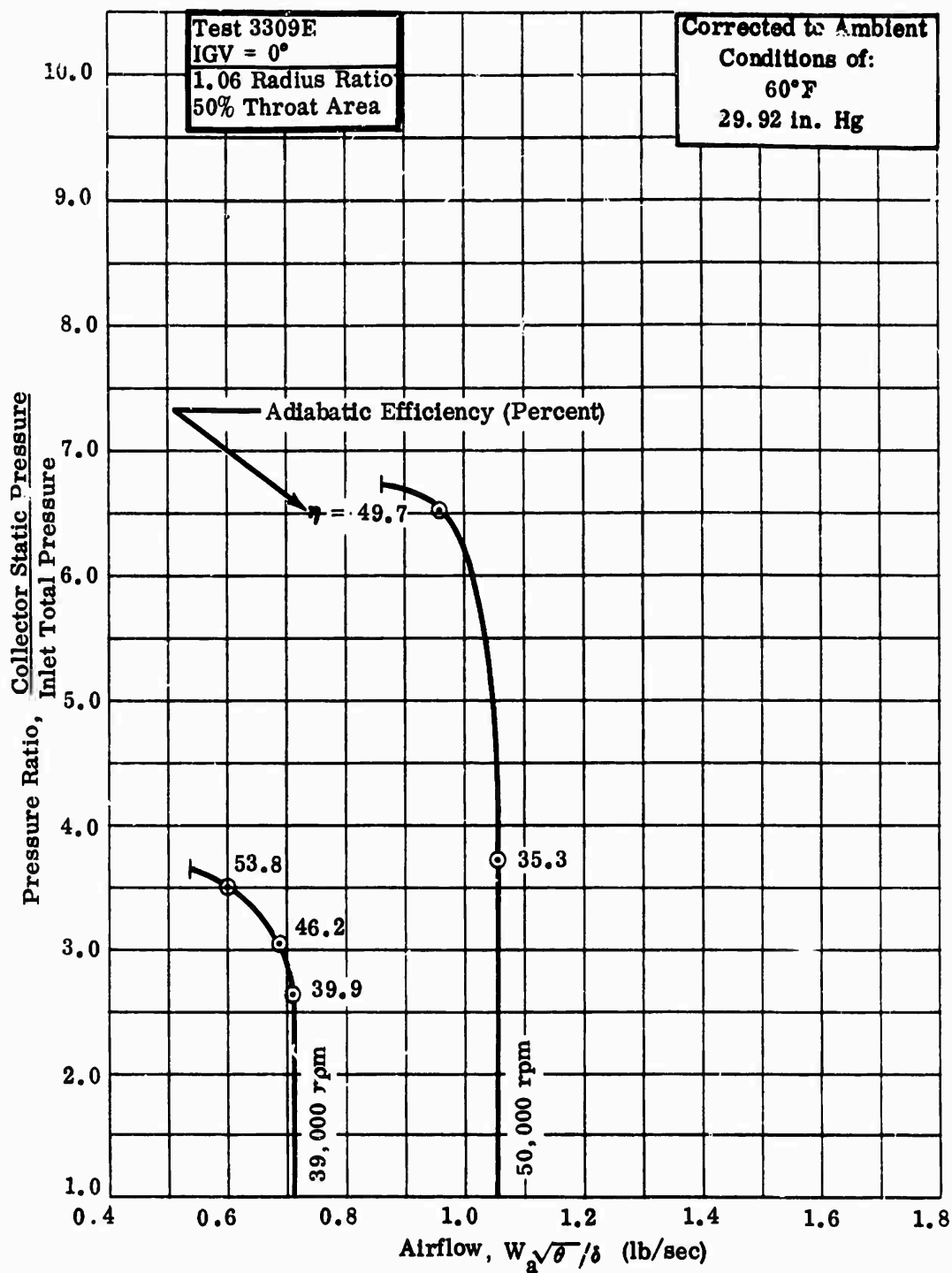


Figure 317. Pressure Ratio Versus Airflow, DI-1.

CONFIDENTIAL

CONFIDENTIAL

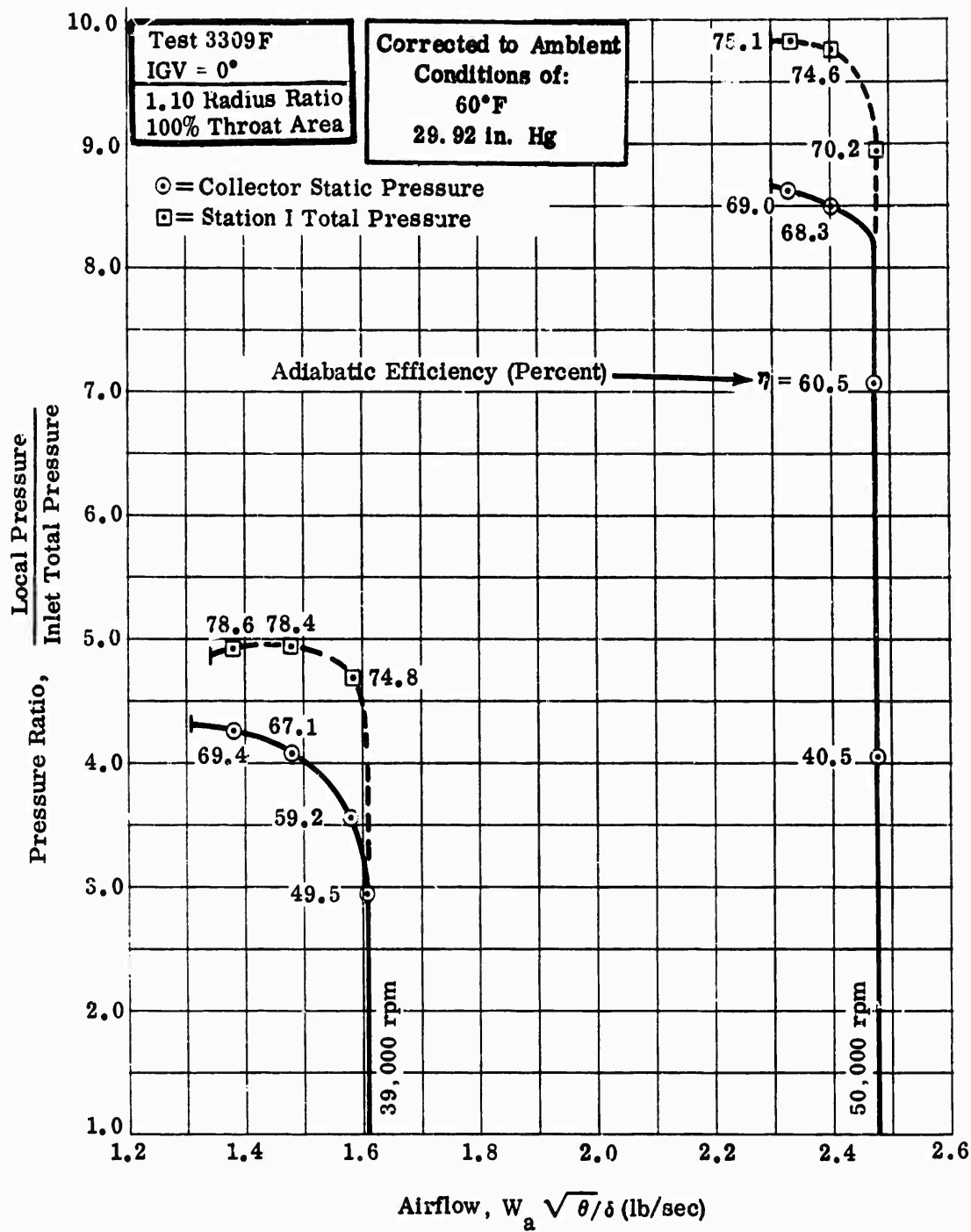


Figure 318. Pressure Ratio Versus Airflow, DI-1.

CONFIDENTIAL

CONFIDENTIAL

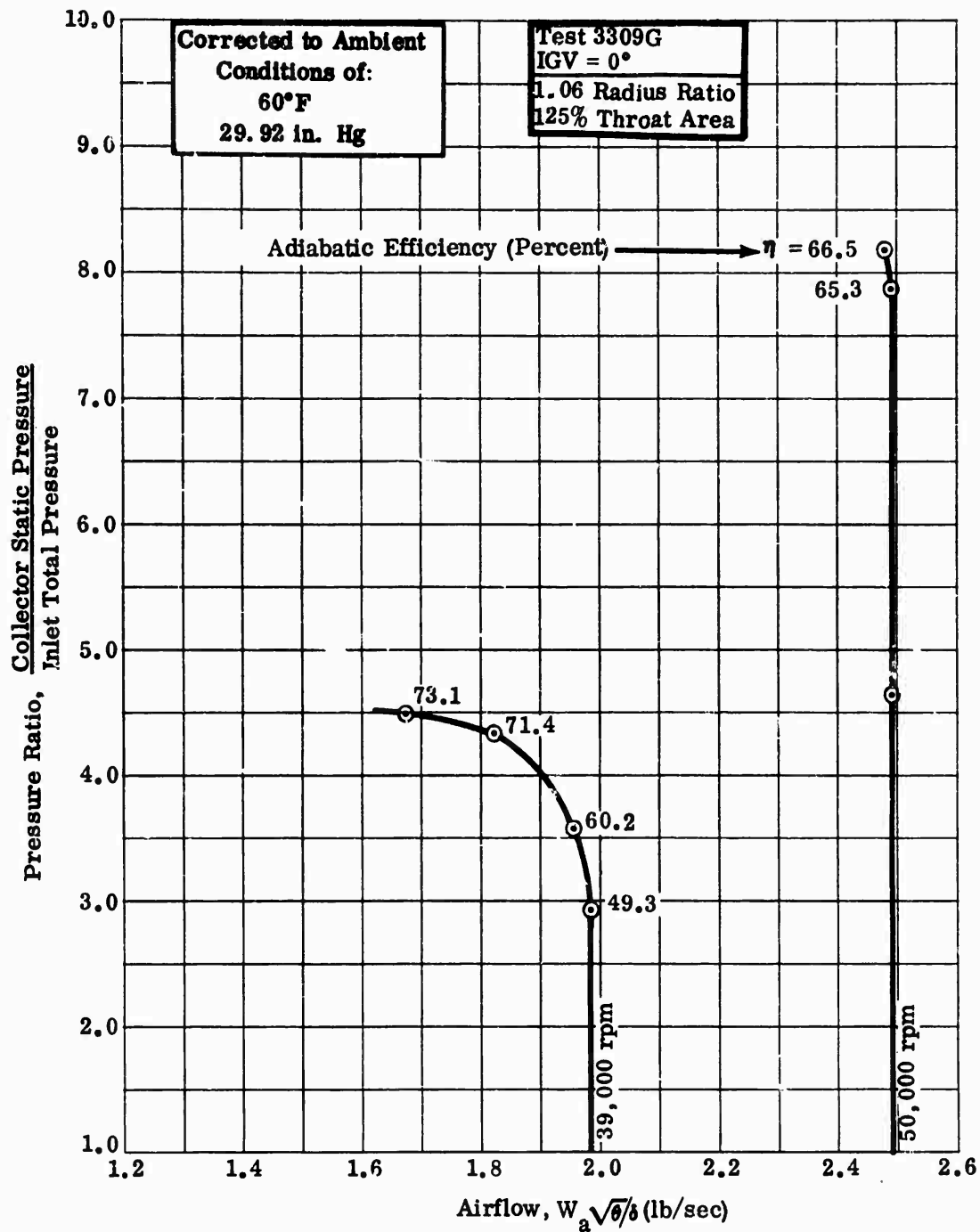


Figure 319. Pressure Ratio Versus Airflow, DI-1.

500

CONFIDENTIAL

CONFIDENTIAL

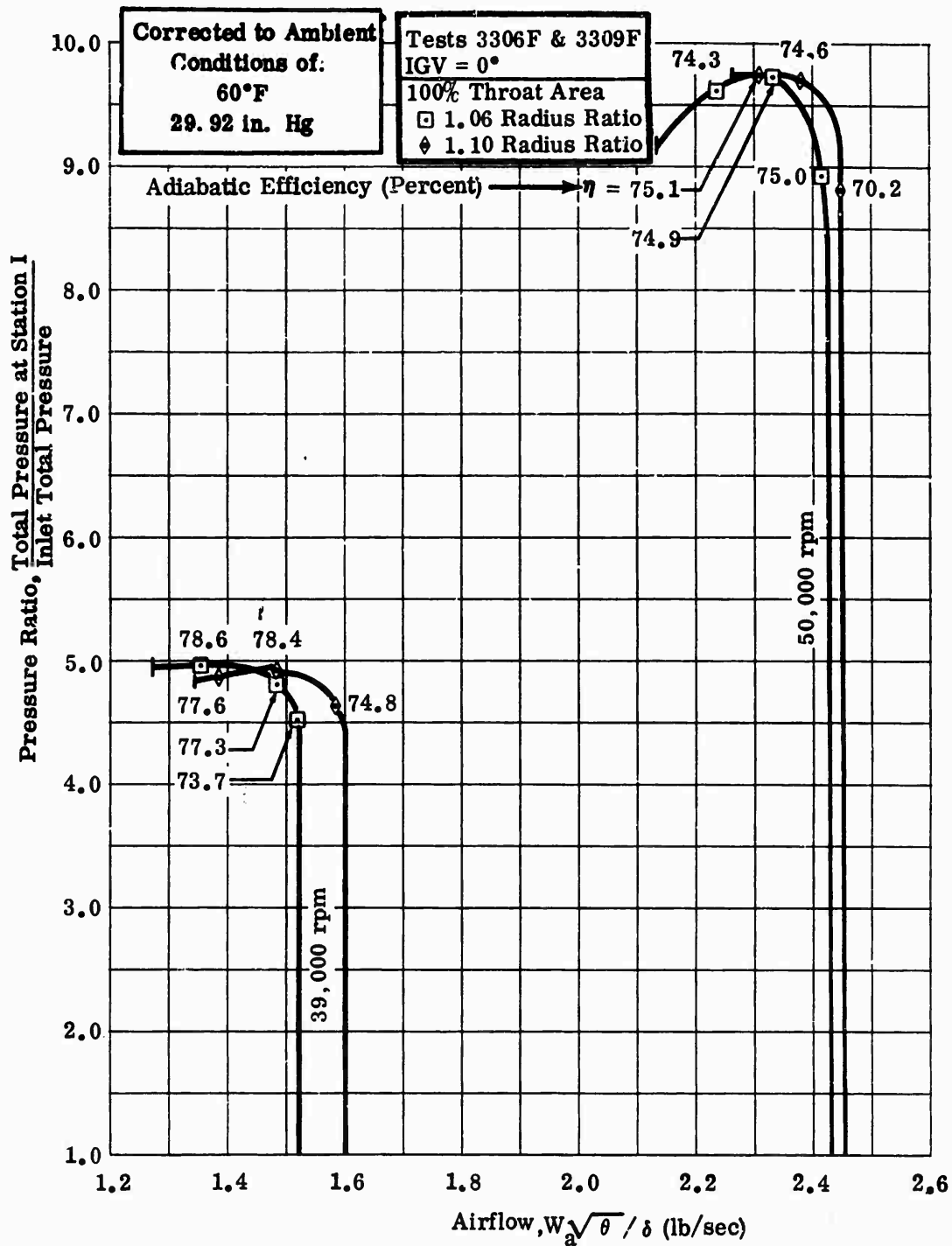


Figure 320. Pressure Ratio Versus Airflow, DI-1
(Comparison at 1.06 and 1.10 Radius Ratio).

CONFIDENTIAL

CONFIDENTIAL

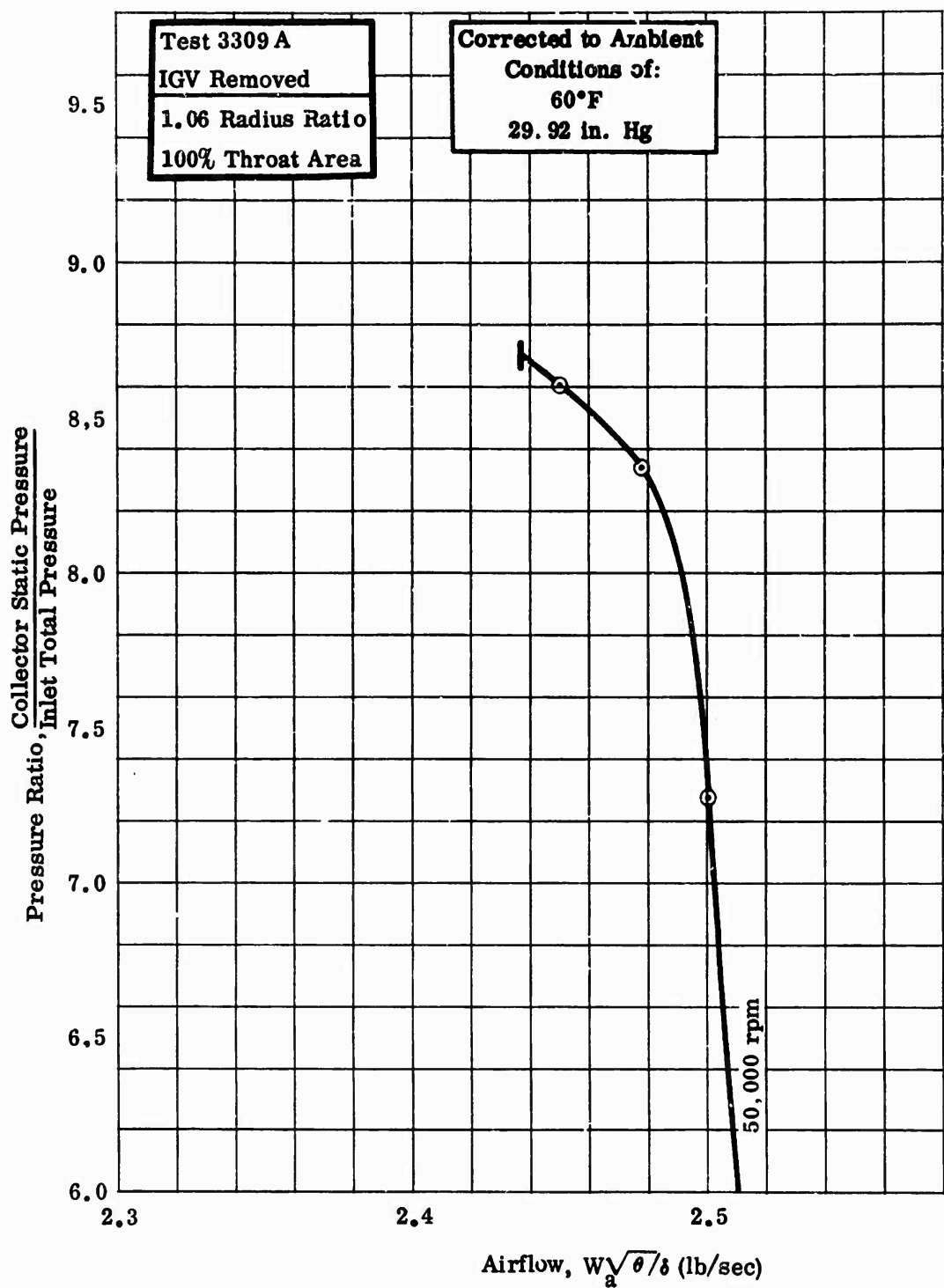


Figure 321. Pressure Ratio Versus Airflow, DI-1.

CONFIDENTIAL

CONFIDENTIAL

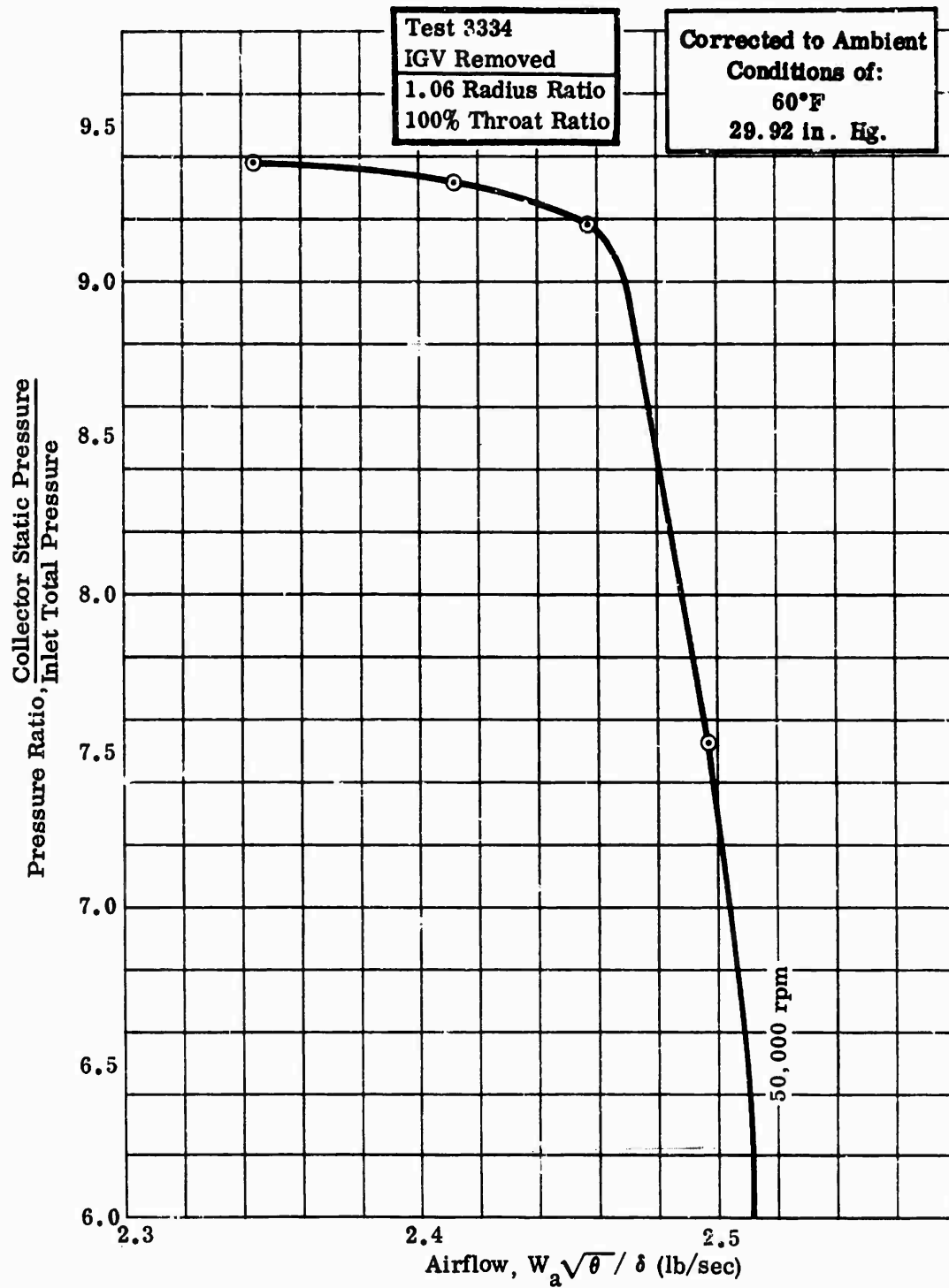


Figure 322. Pressure Ratio Versus Airflow, DI-1-2.

CONFIDENTIAL

CONFIDENTIAL

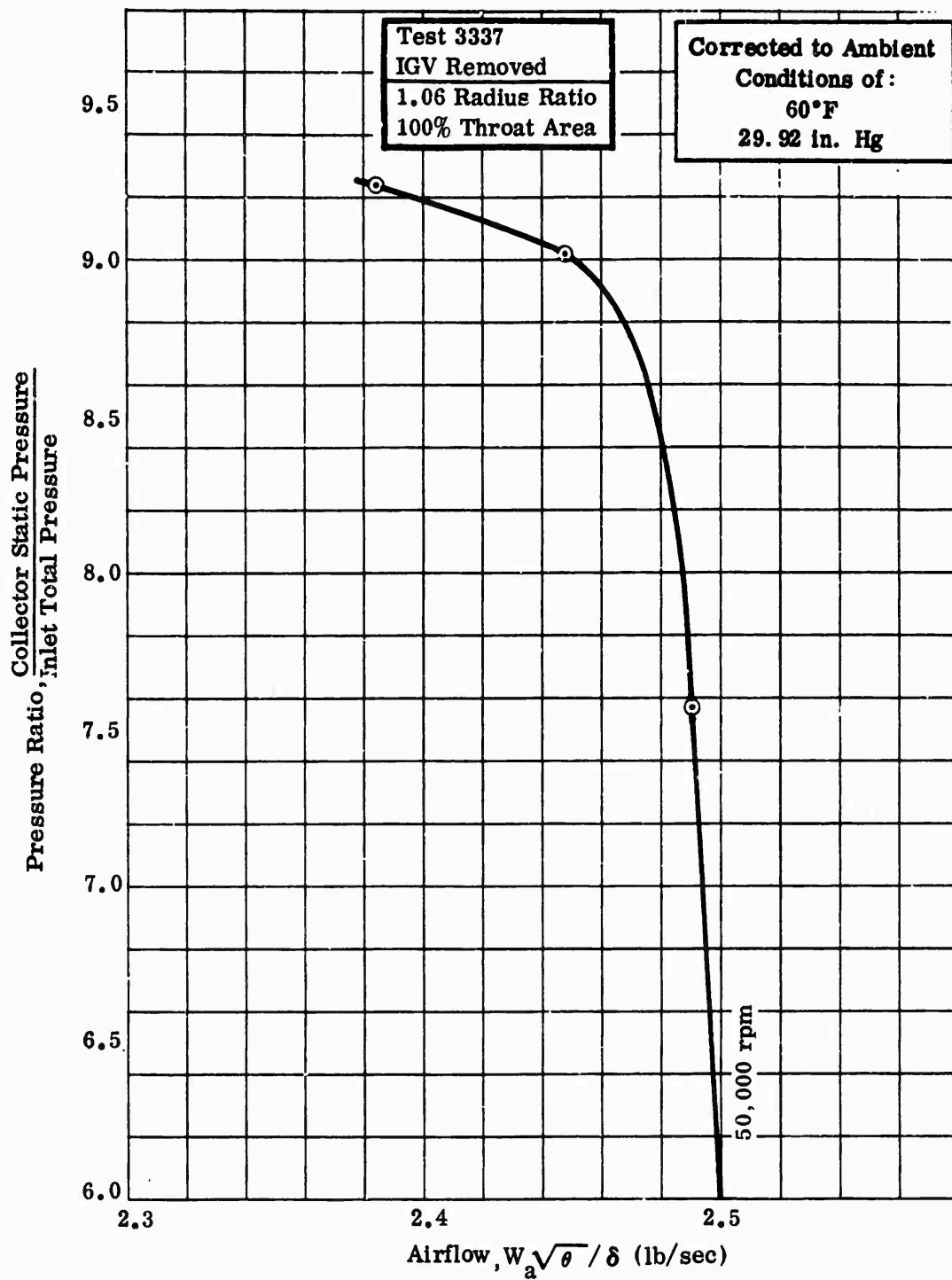


Figure 323. Pressure Ratio Versus Airflow, DI-1-2.

CONFIDENTIAL

CONFIDENTIAL

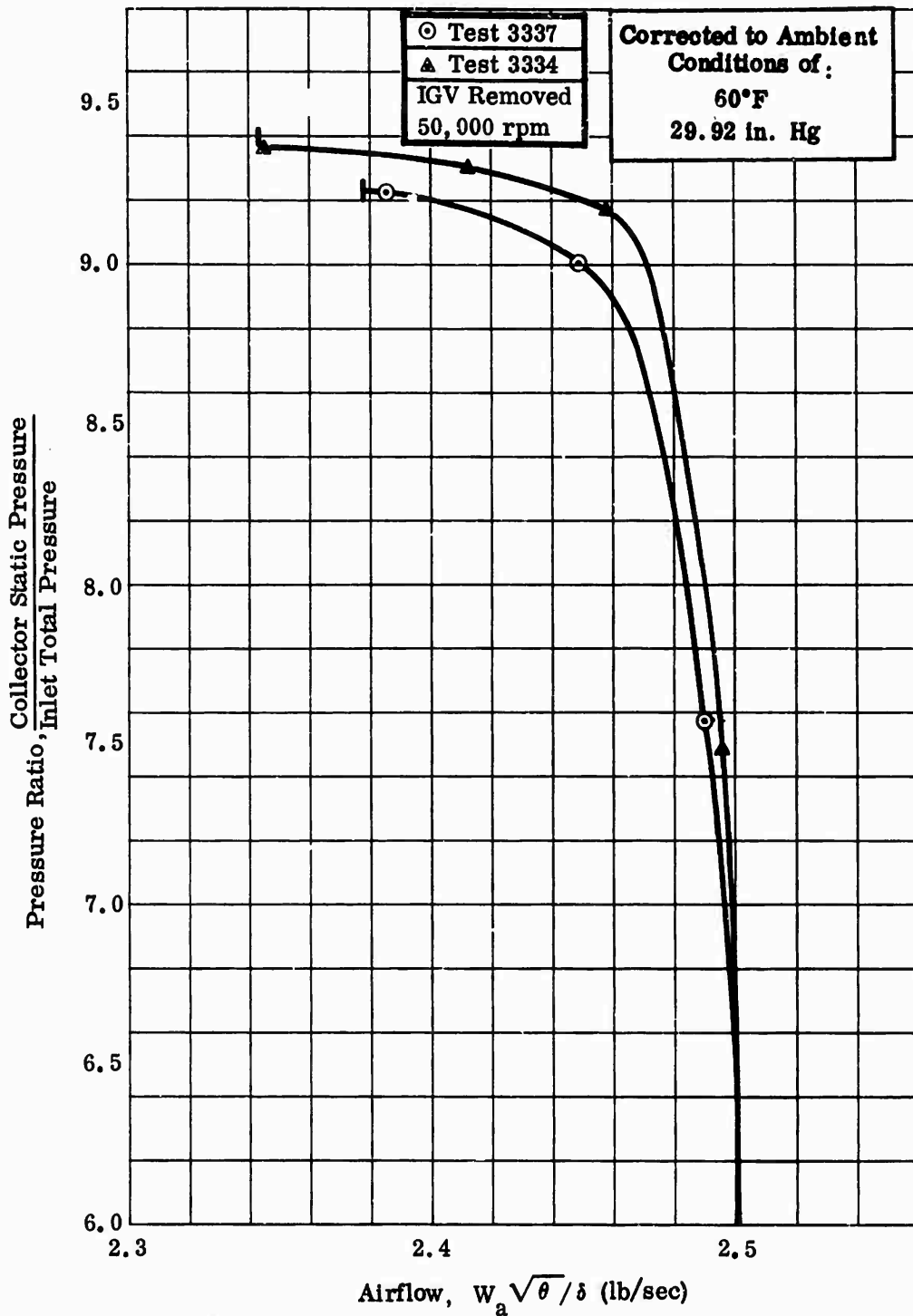


Figure 324. Pressure Ratio Versus Airflow, DI-1-2, (With and Without Schlieren Windows).

CONFIDENTIAL

CONFIDENTIAL

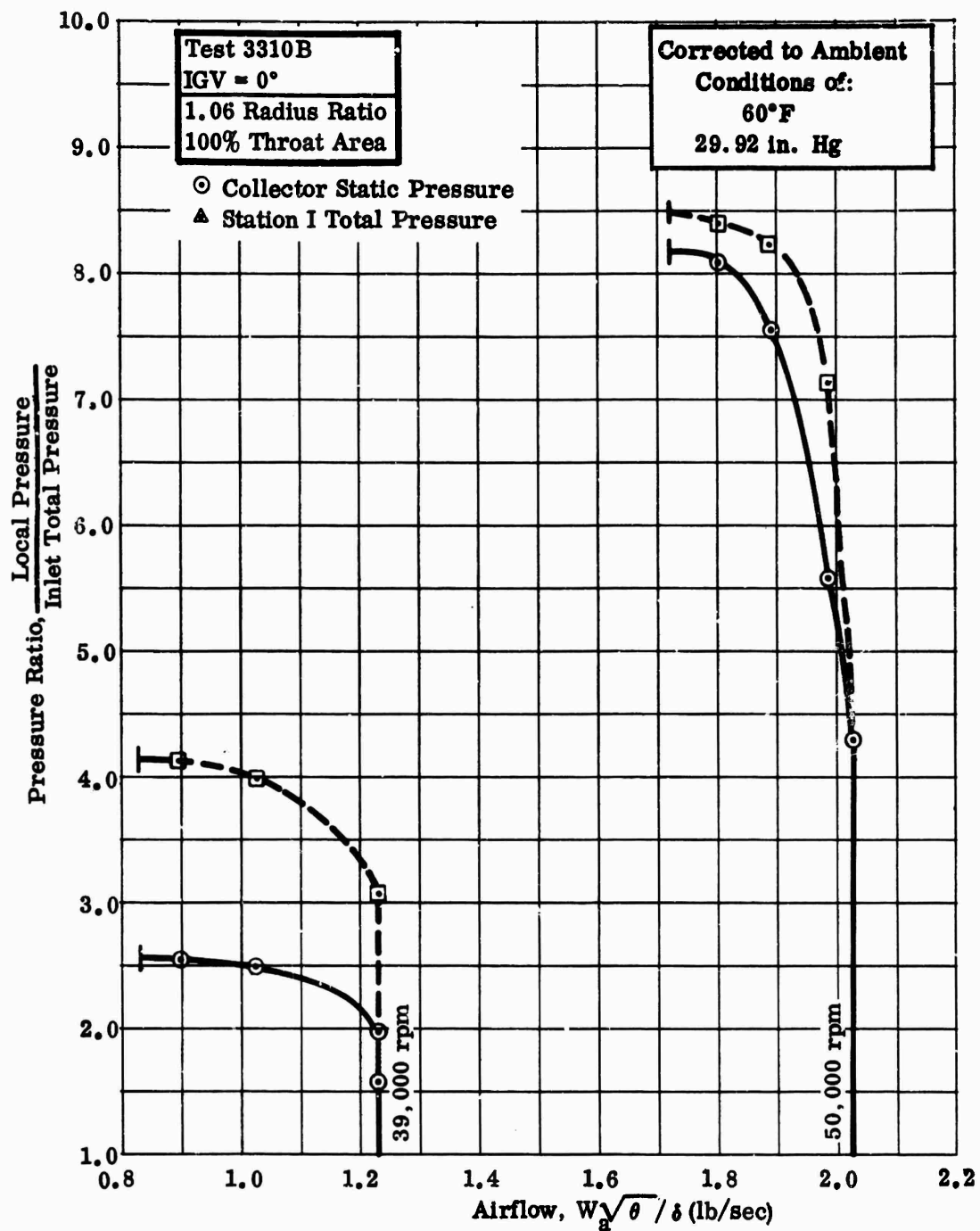


Figure 325. Pressure Ratio Versus Airflow, DI-2.

CONFIDENTIAL

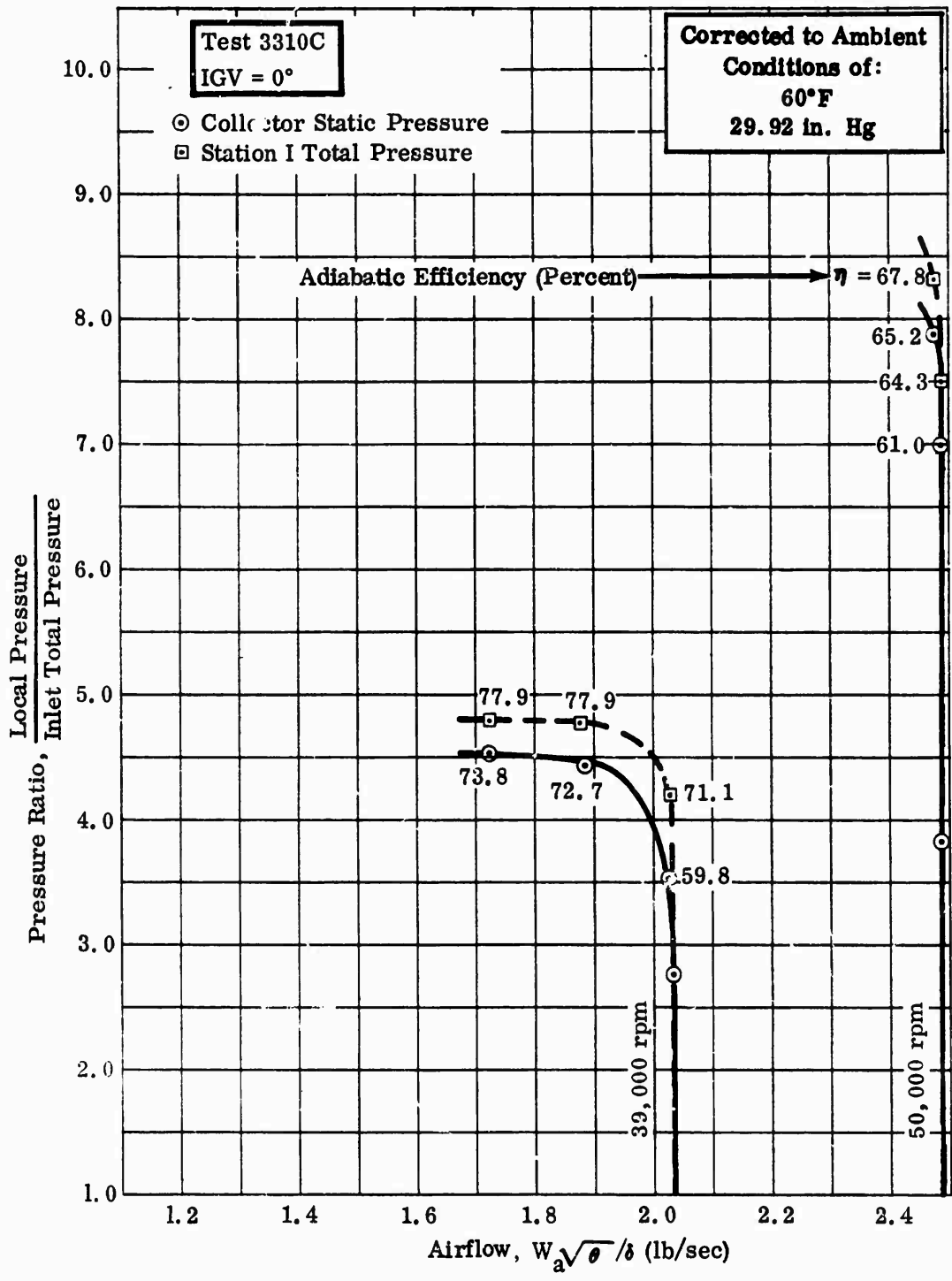


Figure 326. Pressure Ratio Versus Airflow, DI-2.

CONFIDENTIAL

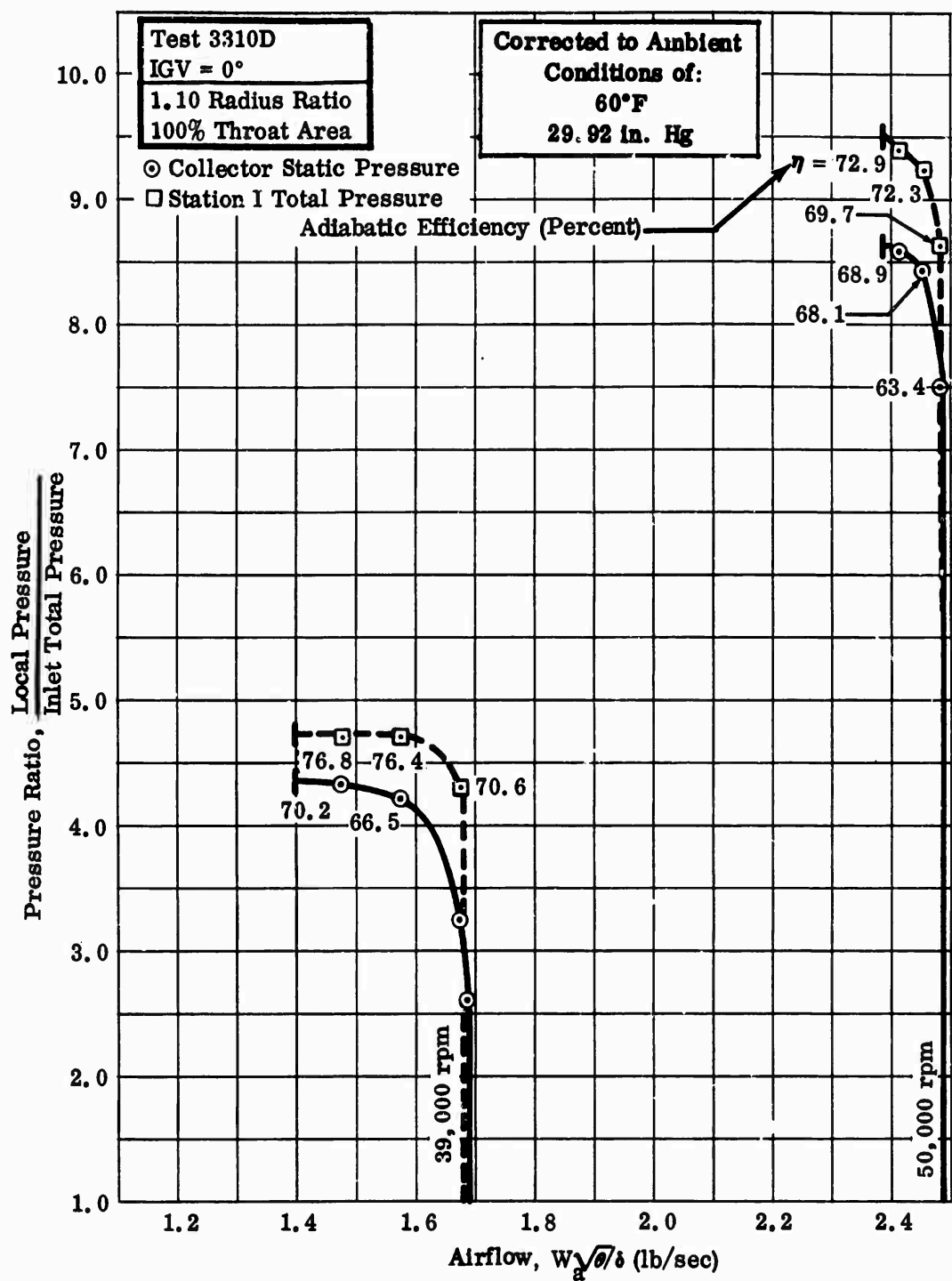


Figure 327. Pressure Ratio Versus Airflow, DI-2.

CONFIDENTIAL

CONFIDENTIAL

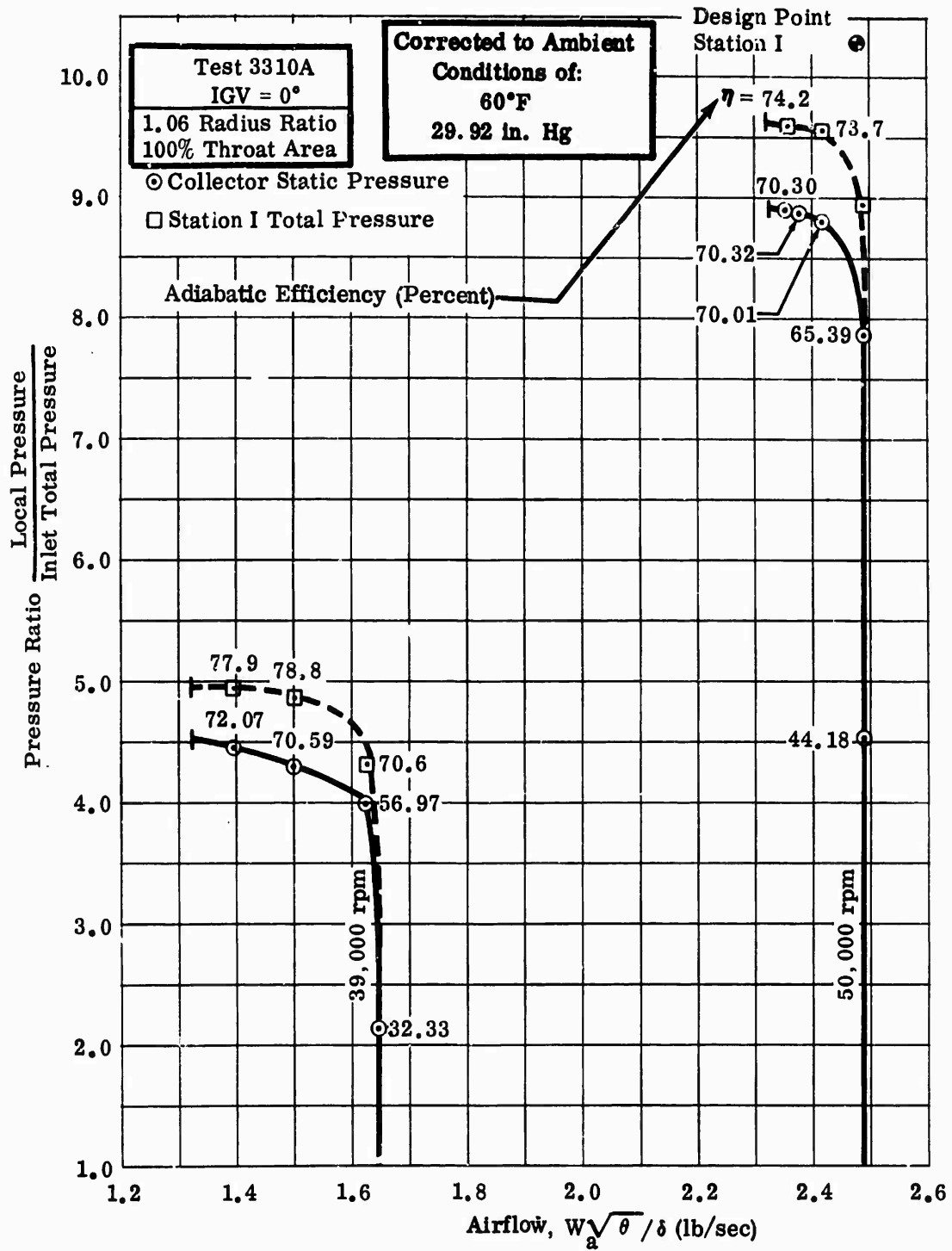


Figure 328. Pressure Ratio Versus Airflow, DI-2.

CONFIDENTIAL

CONFIDENTIAL

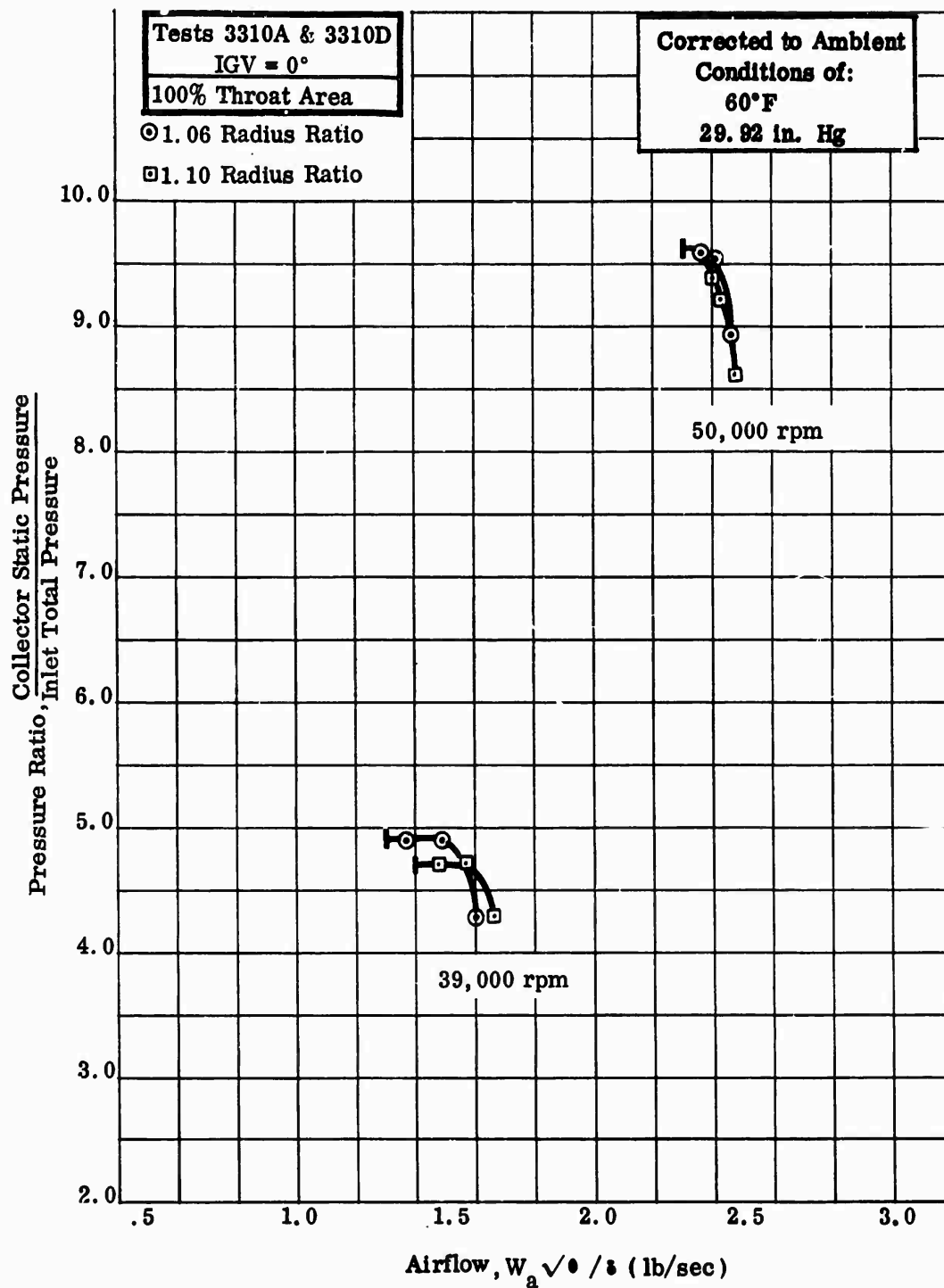


Figure 329. Pressure Ratio Versus Airflow, DI-2
(Comparison at 1.06 and 1.10 Radius Ratio).

CONFIDENTIAL

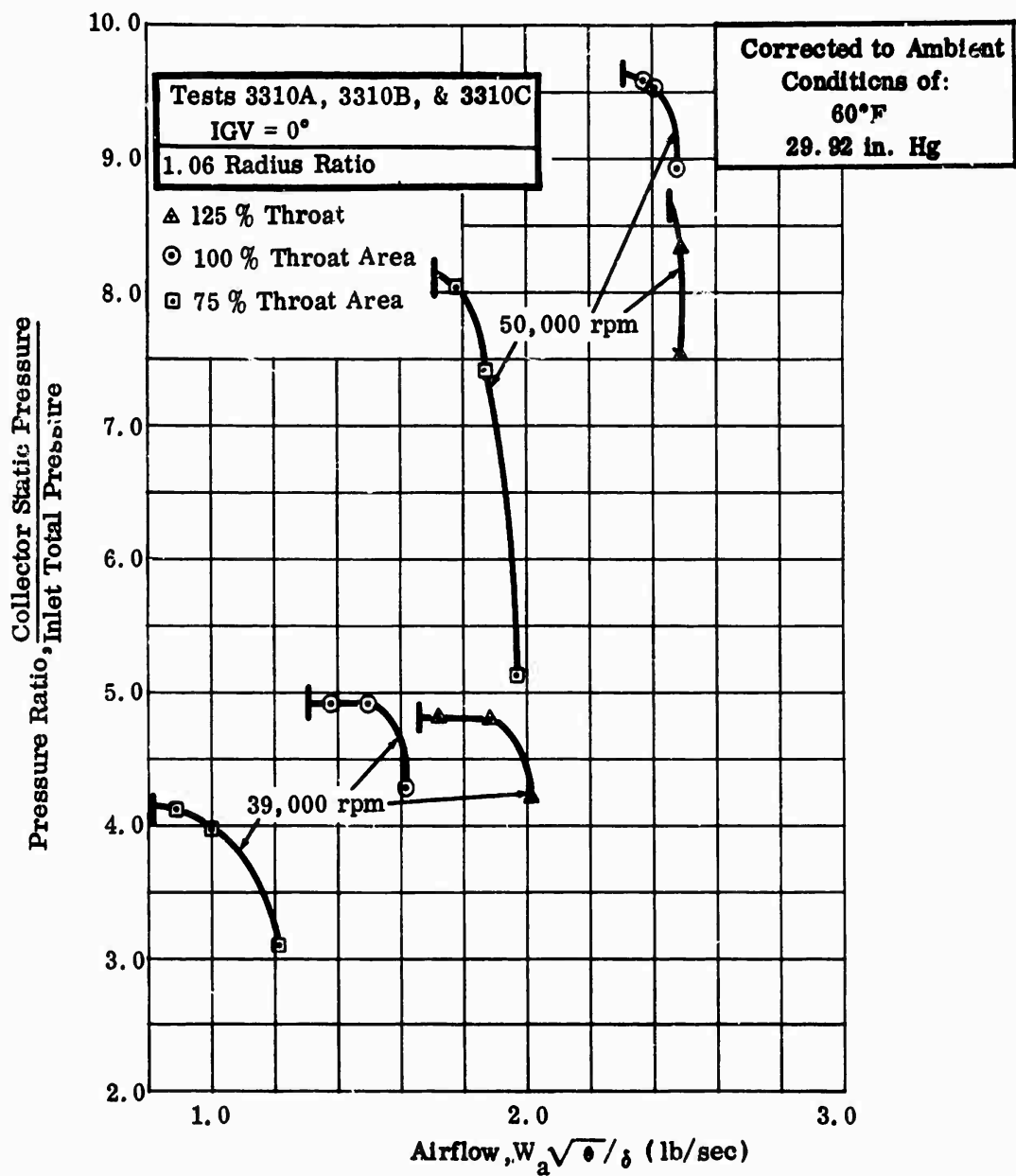


Figure 330. Pressure Ratio Versus Airflow, DI-2 (Comparison at 125-, 100-, and 75-Percent Throat Areas).

CONFIDENTIAL

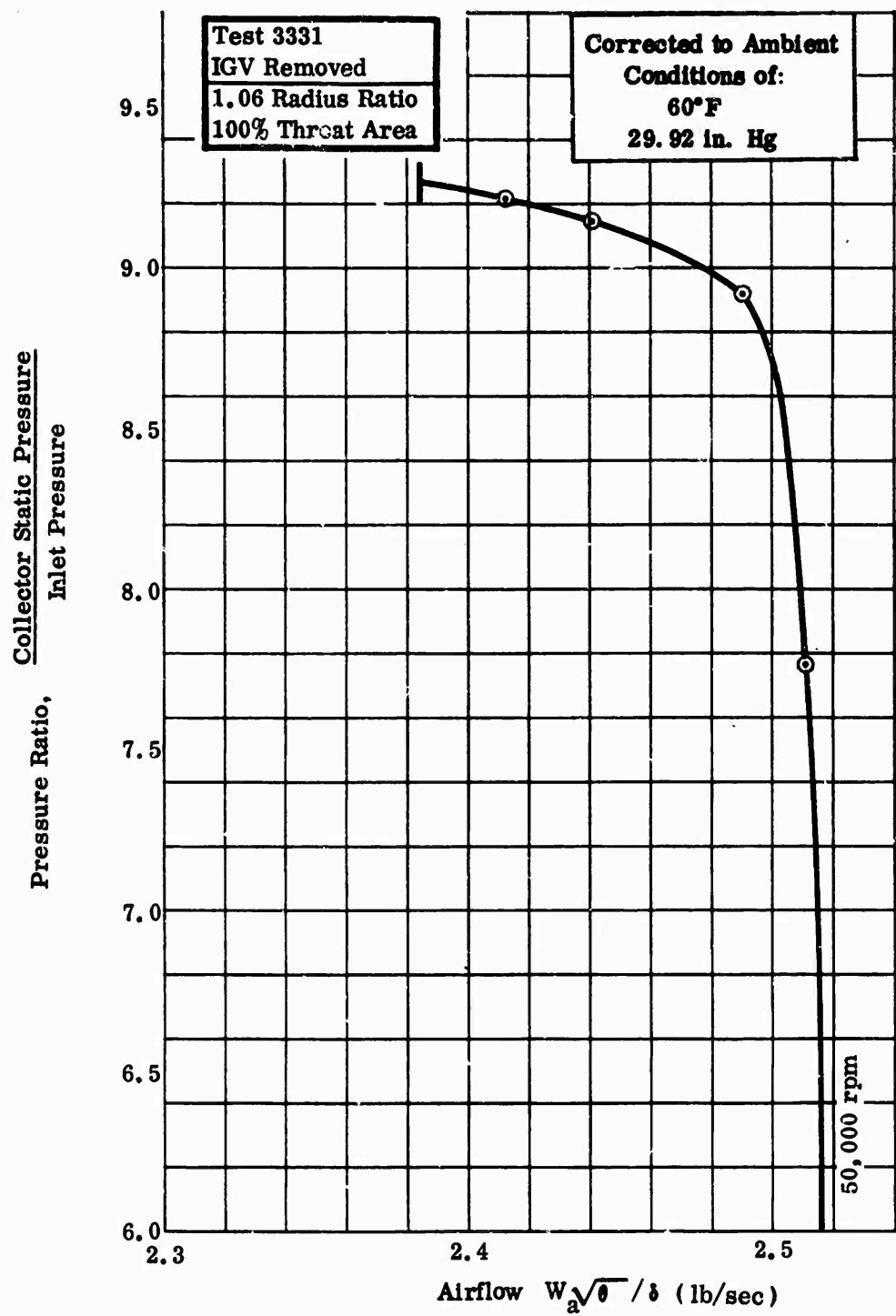


Figure 331. Pressure Ratio Versus Airflow, DI-2.

CONFIDENTIAL

CONFIDENTIAL

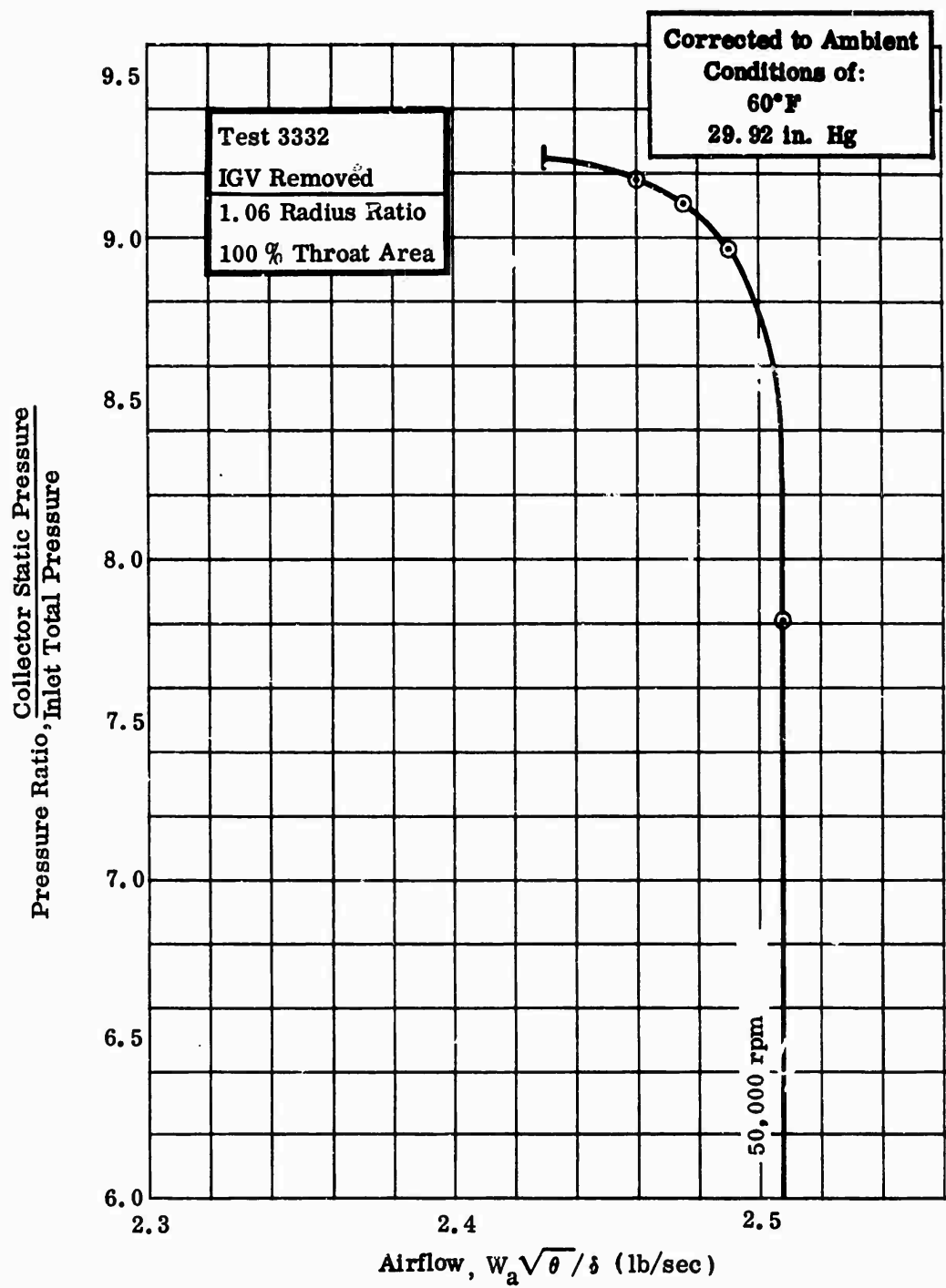


Figure 332. Pressure Ratio Versus Airflow, DI-2-2.

CONFIDENTIAL

CONFIDENTIAL

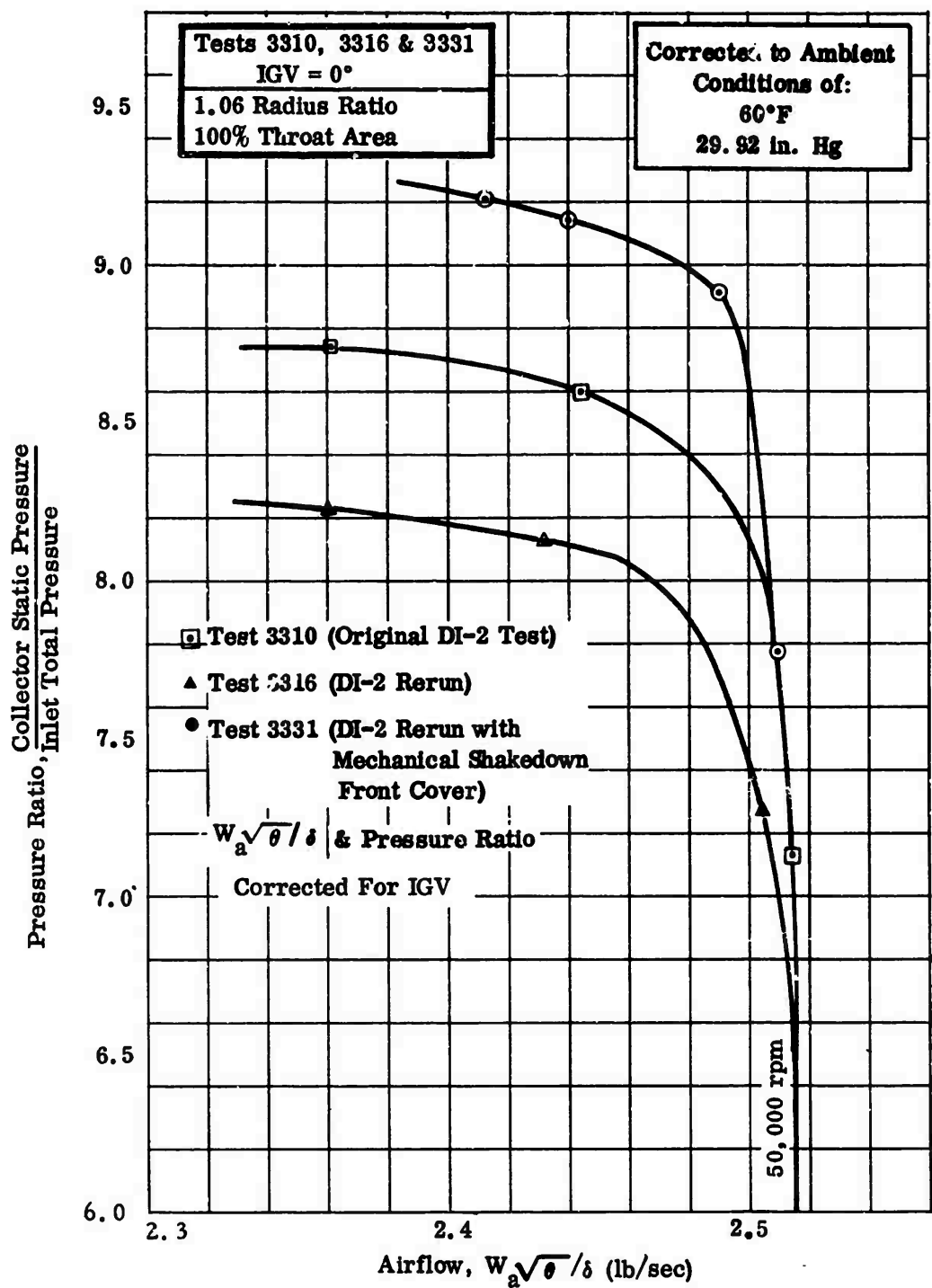


Figure 333. Pressure Ratio Versus Airflow, DI-2 (Comparison of Reruns).

CONFIDENTIAL

CONFIDENTIAL

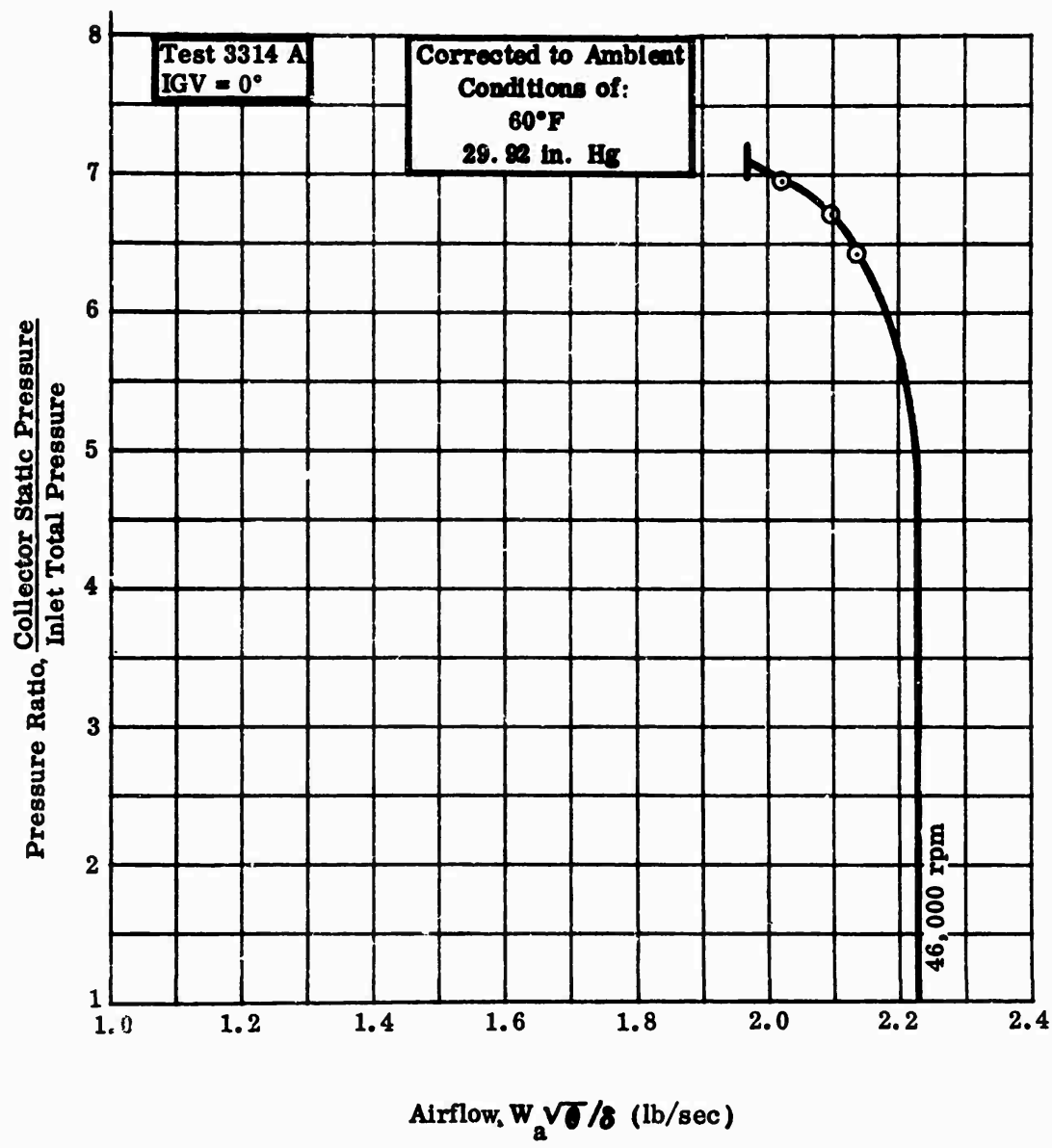


Figure 334. Pressure Ratio Versus Airflow, DI-3.

CONFIDENTIAL

CONFIDENTIAL

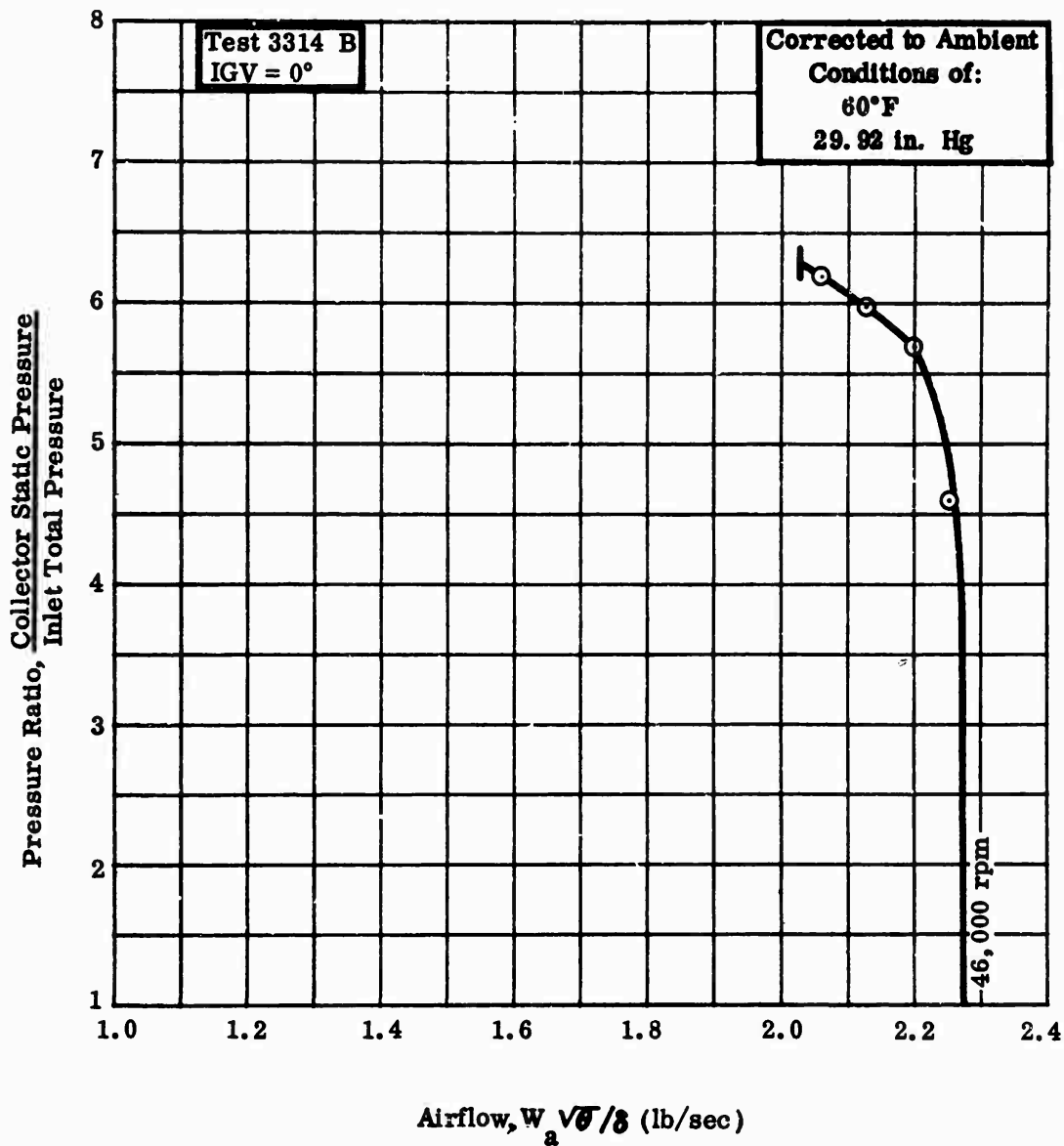


Figure 335. Pressure Ratio Versus Airflow, DI-3.

CONFIDENTIAL

CONFIDENTIAL

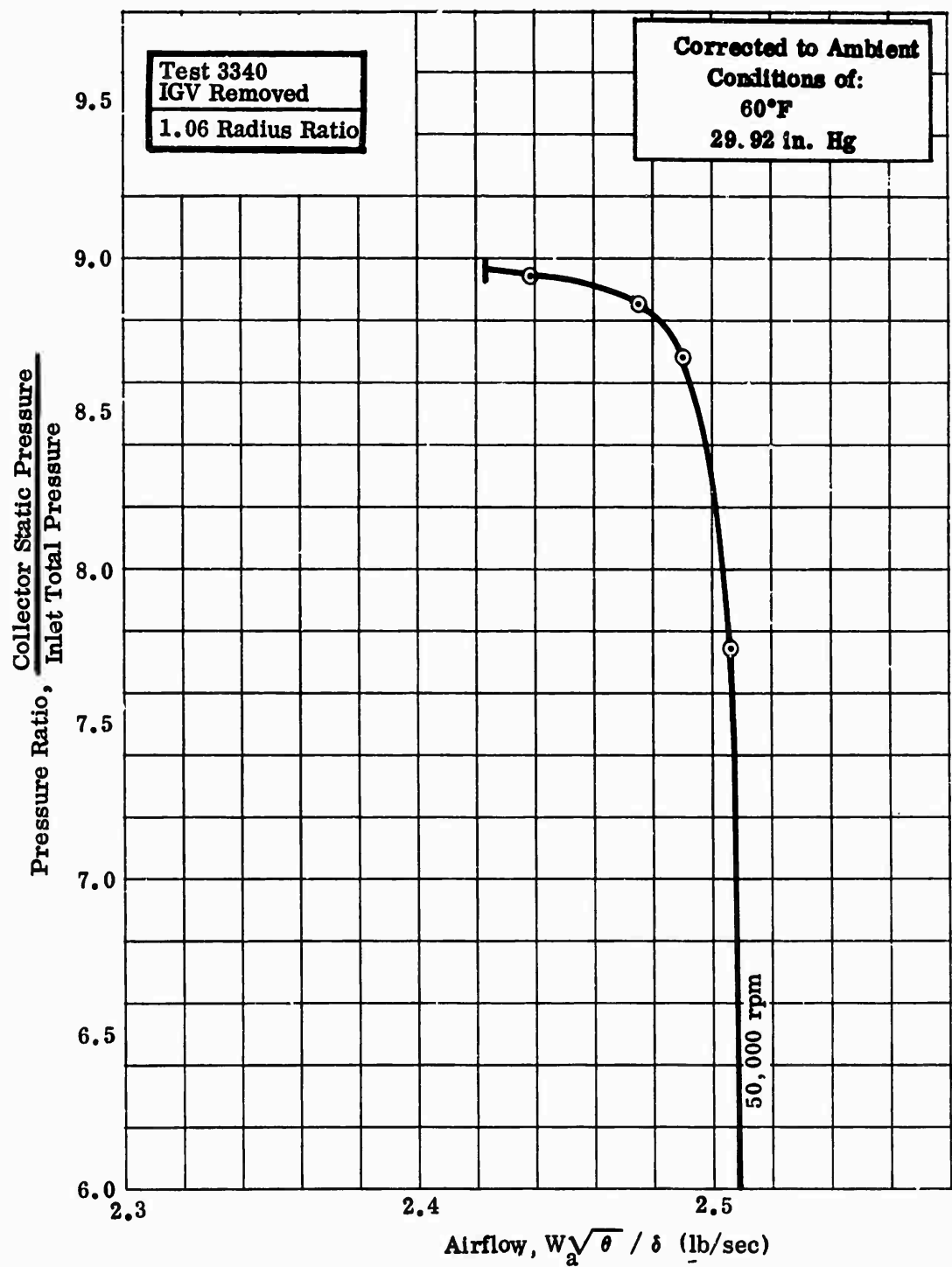


Figure 336. Pressure Ratio Versus Airflow, DI-1-3.

CONFIDENTIAL

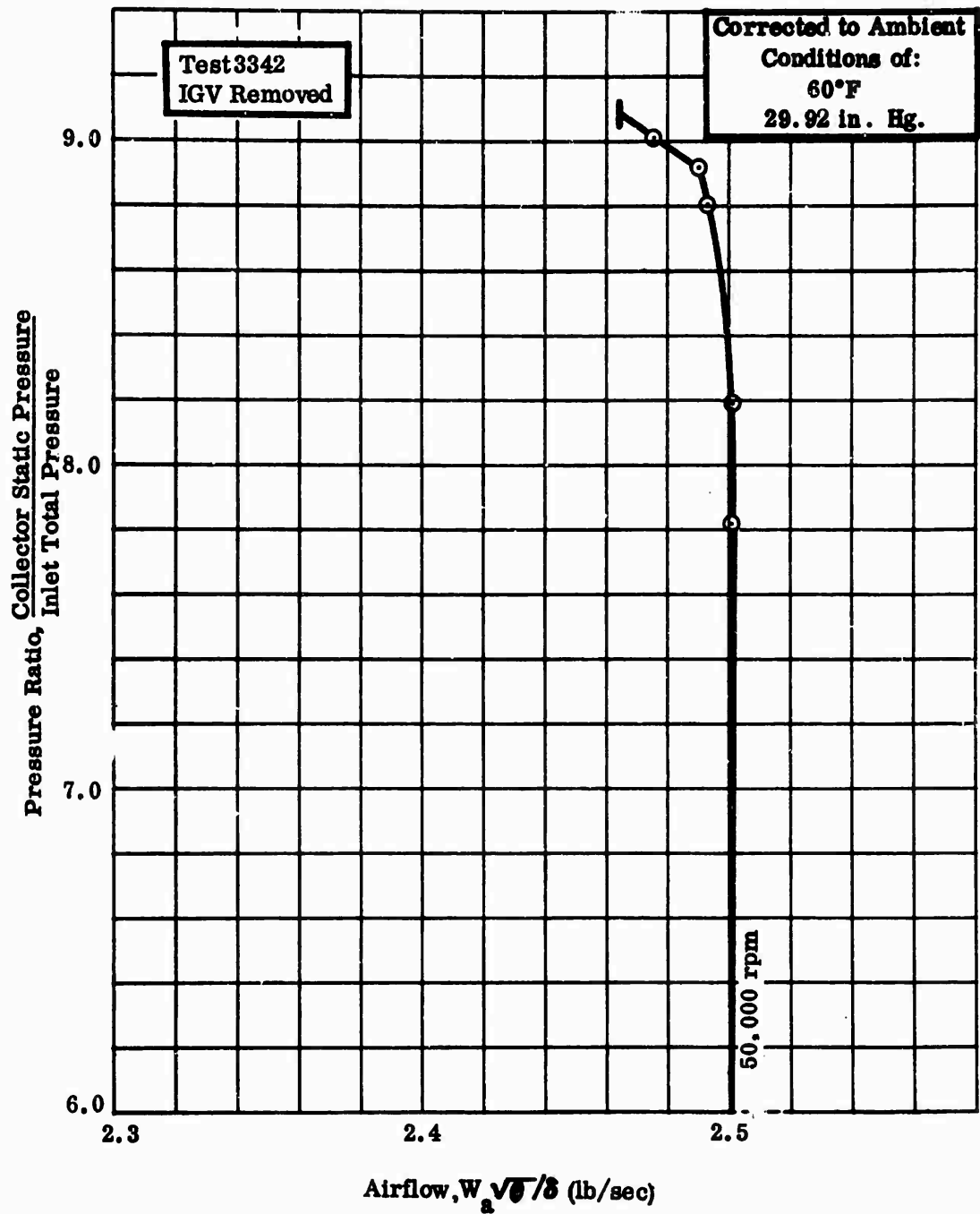


Figure 337. Pressure Ratio Versus Airflow, DI-3.

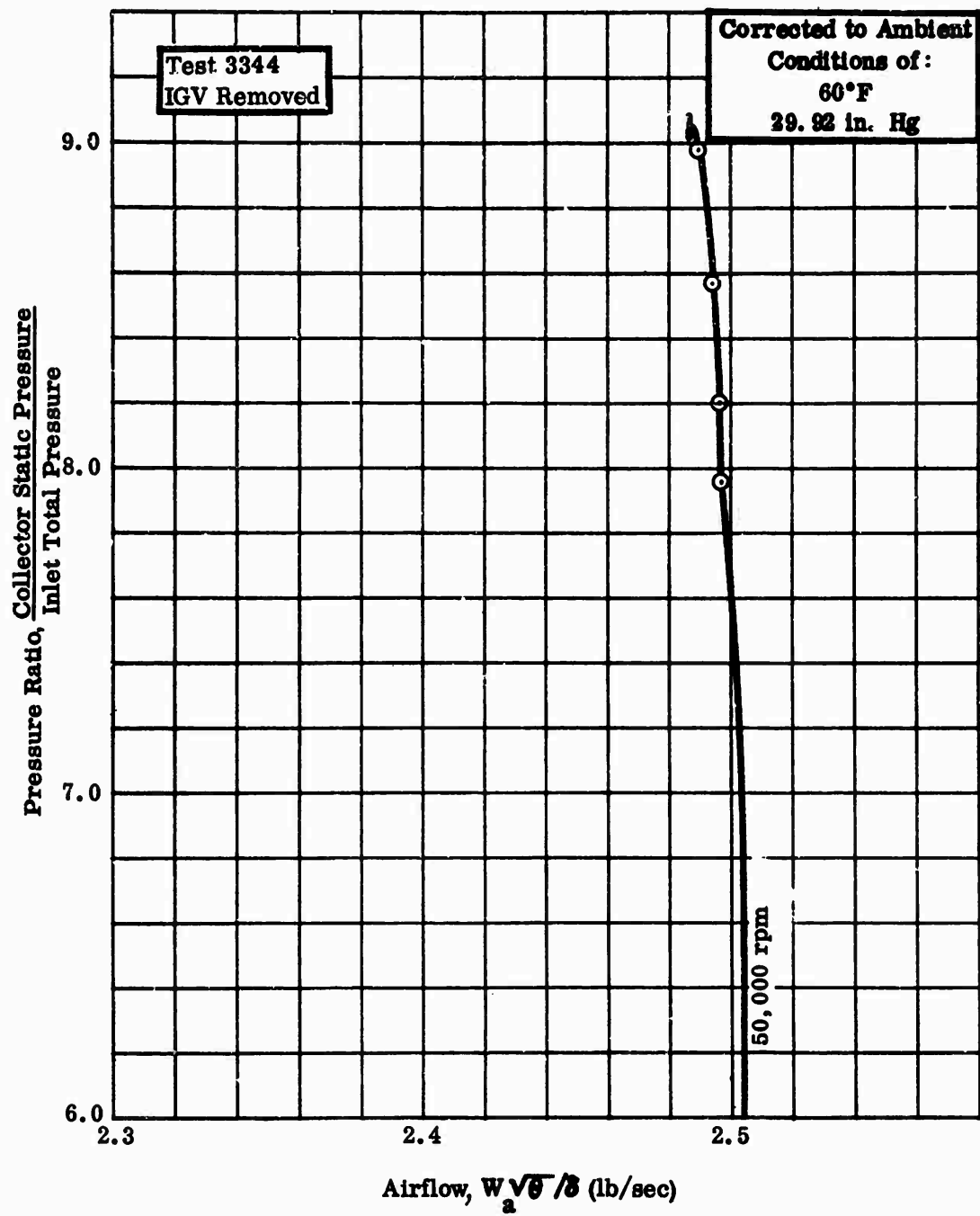


Figure 338. Pressure Ratio Versus Airflow, DI-3.

CONFIDENTIAL

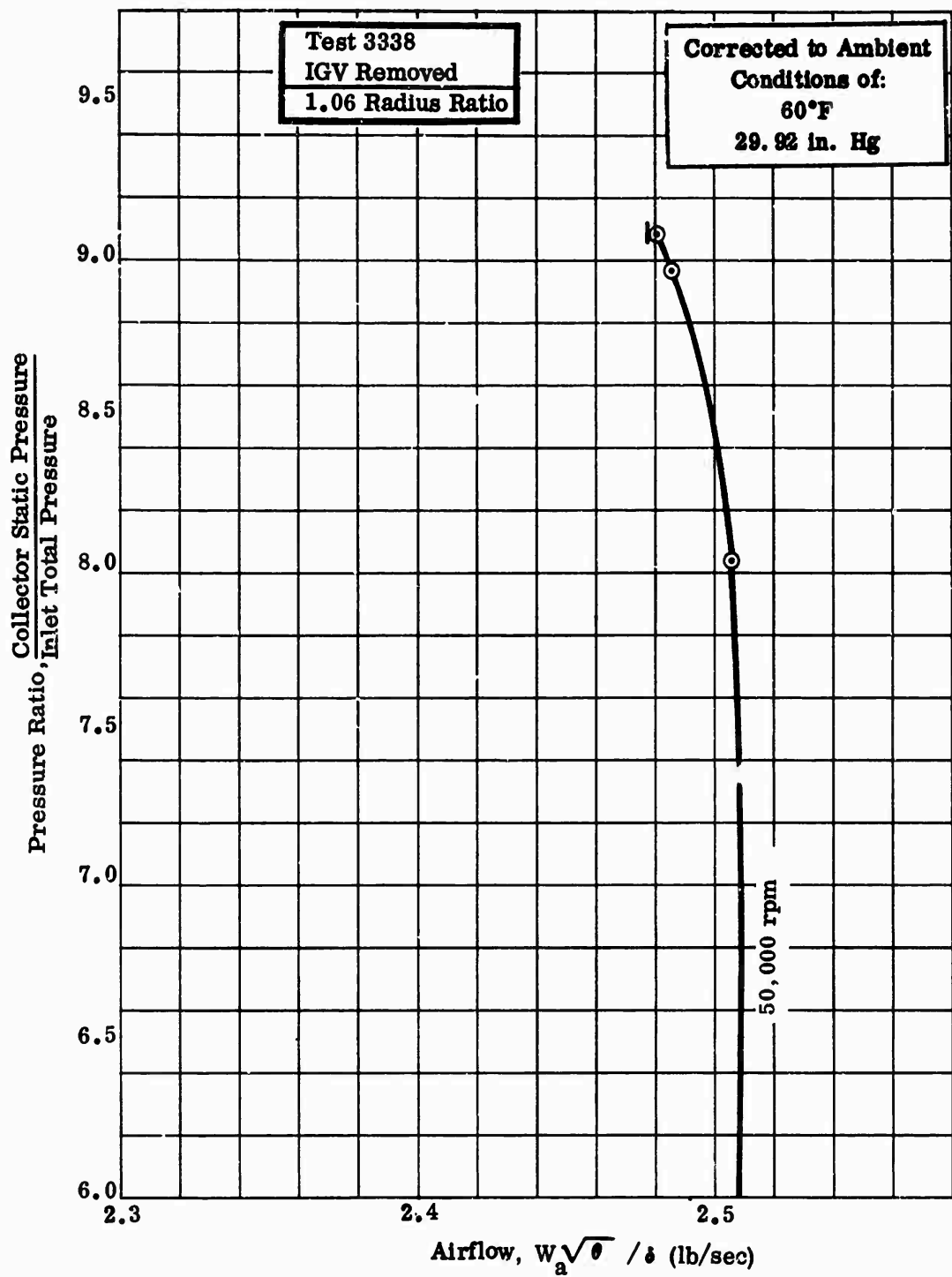


Figure 339. Pressure Ratio Versus Airflow, DI-X1.

CONFIDENTIAL

CONFIDENTIAL

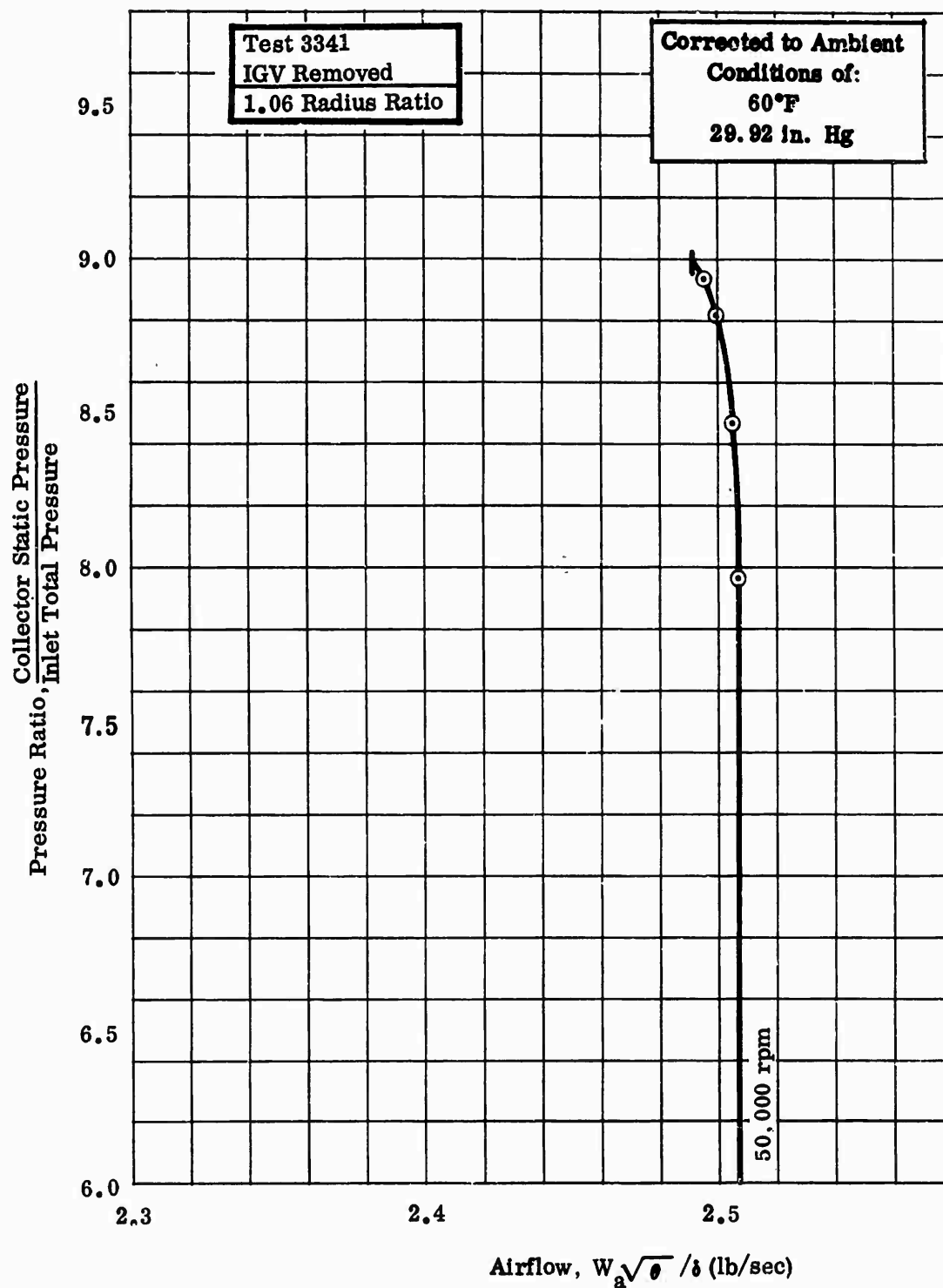


Figure 340. Pressure Ratio Versus Airflow, DI-X1-2.

CONFIDENTIAL

CONFIDENTIAL

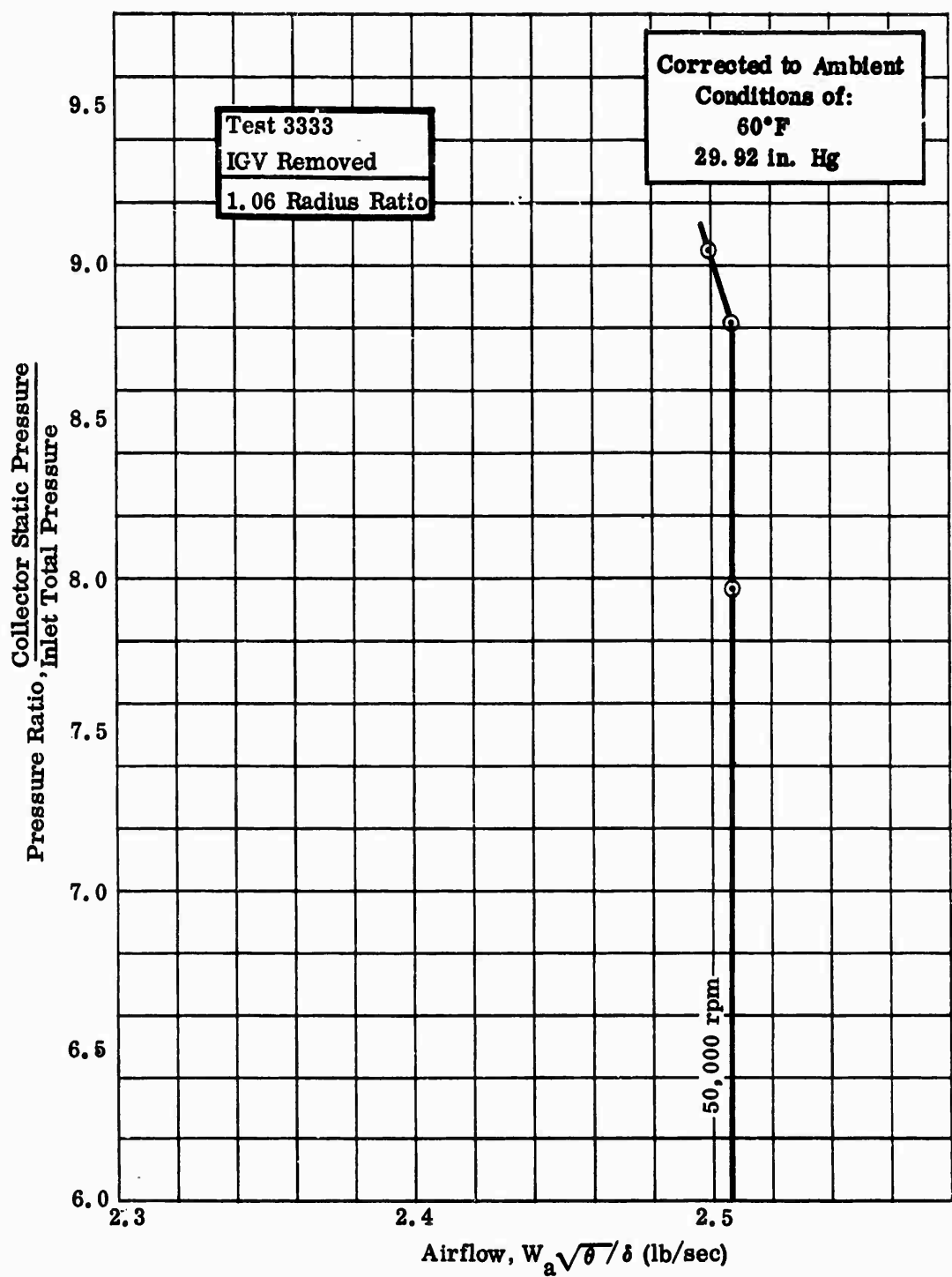


Figure 341. Pressure Ratio Versus Airflow, DI-X1-2.

CONFIDENTIAL

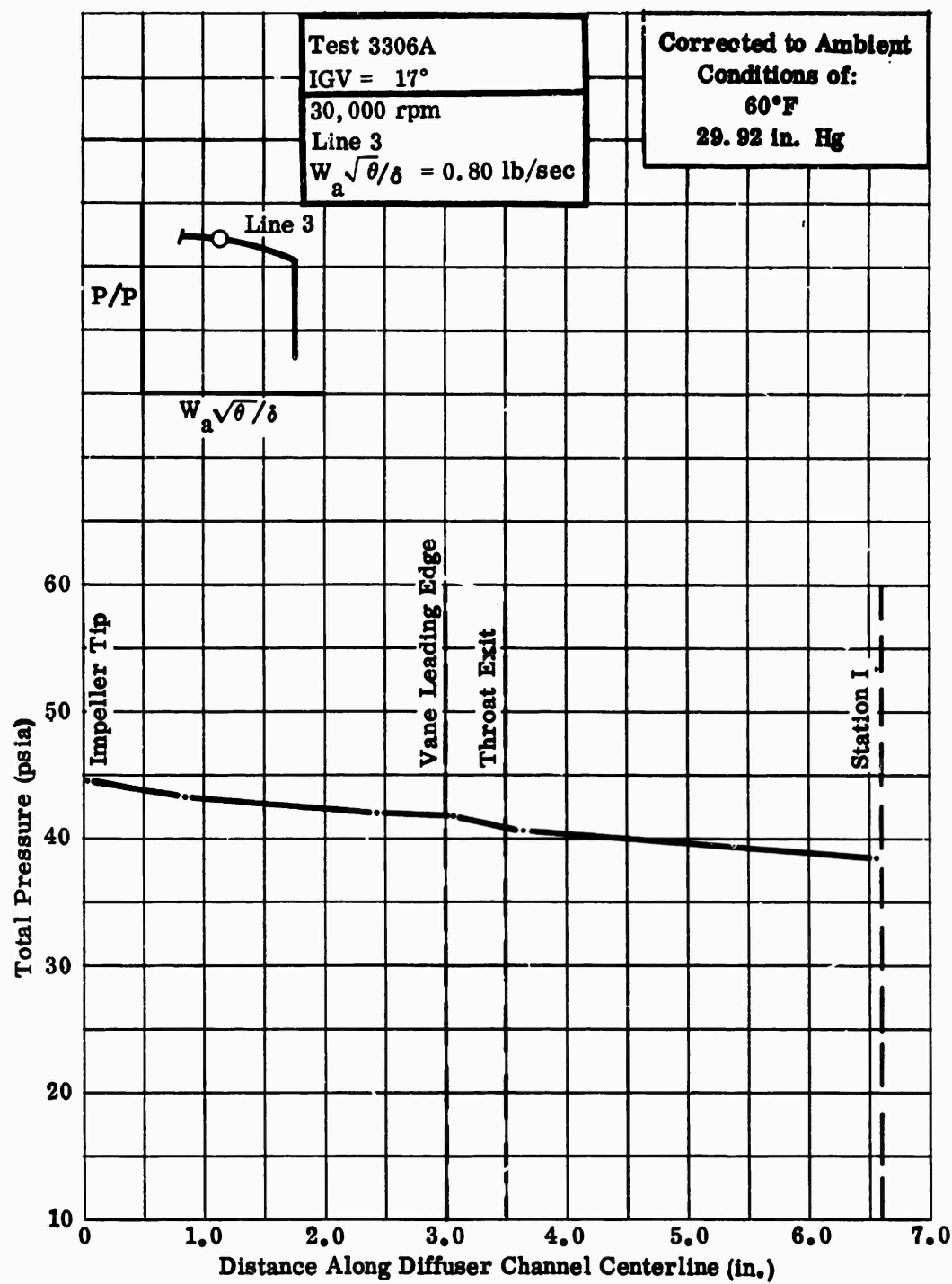


Figure 342. Midchannel Total Pressure Versus Flow-Path Length, DI-1.

CONFIDENTIAL

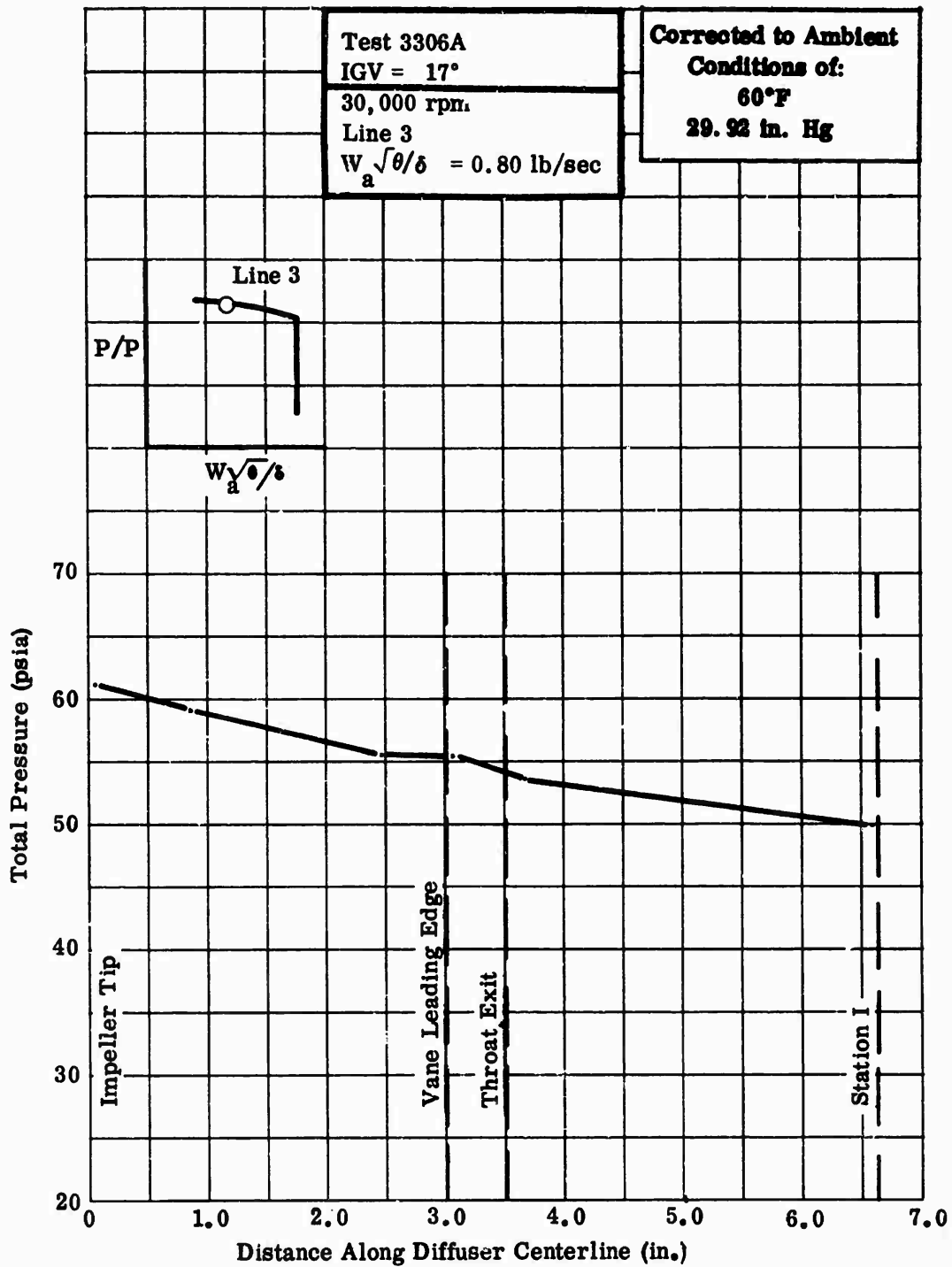


Figure 343. Midchannel Total Pressure Versus Flow-Path Length, DI-1.

CONFIDENTIAL

CONFIDENTIAL

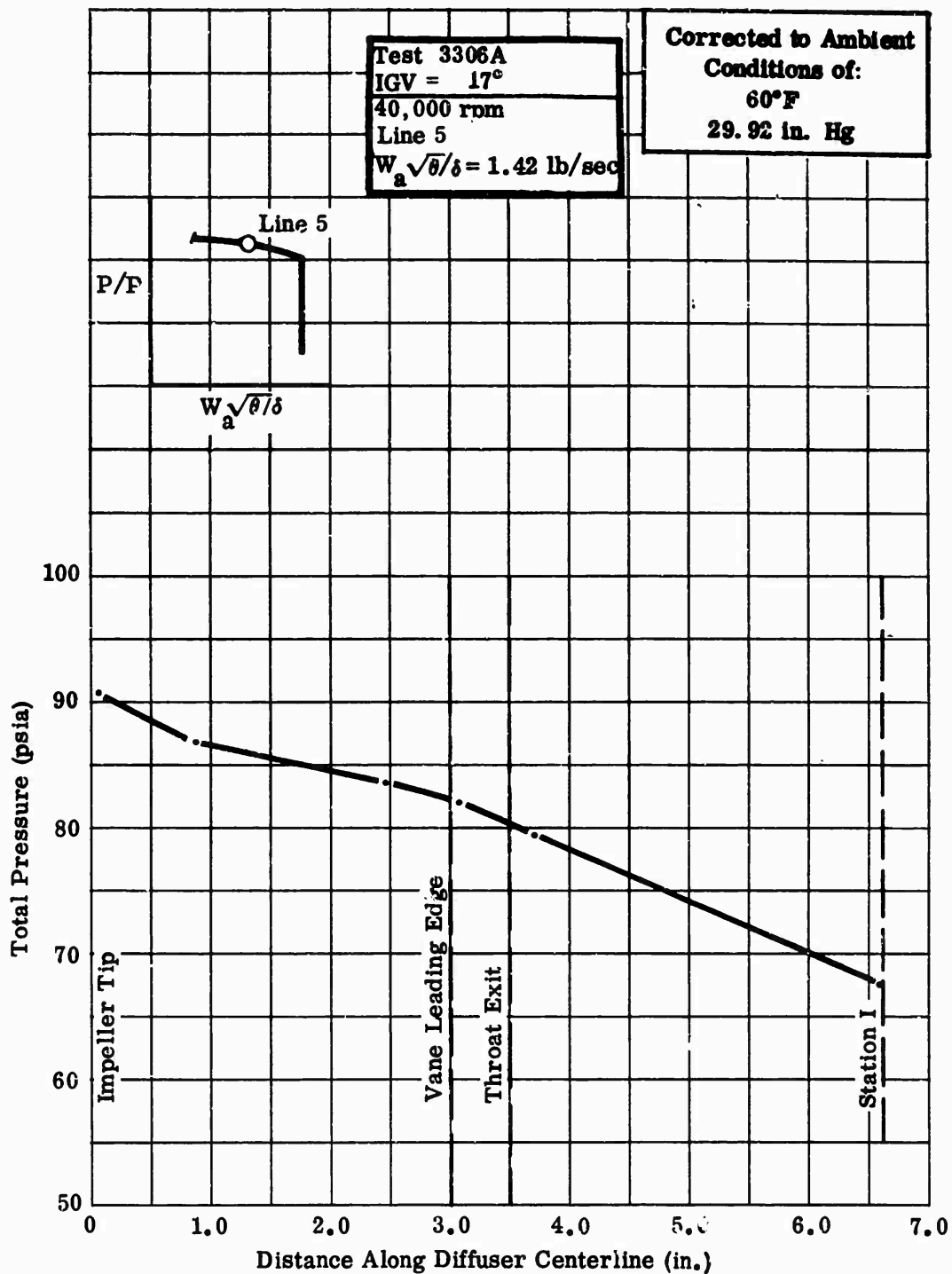


Figure 344. Midchannel Total Pressure Versus Flow-Path Length, DI-1.

CONFIDENTIAL

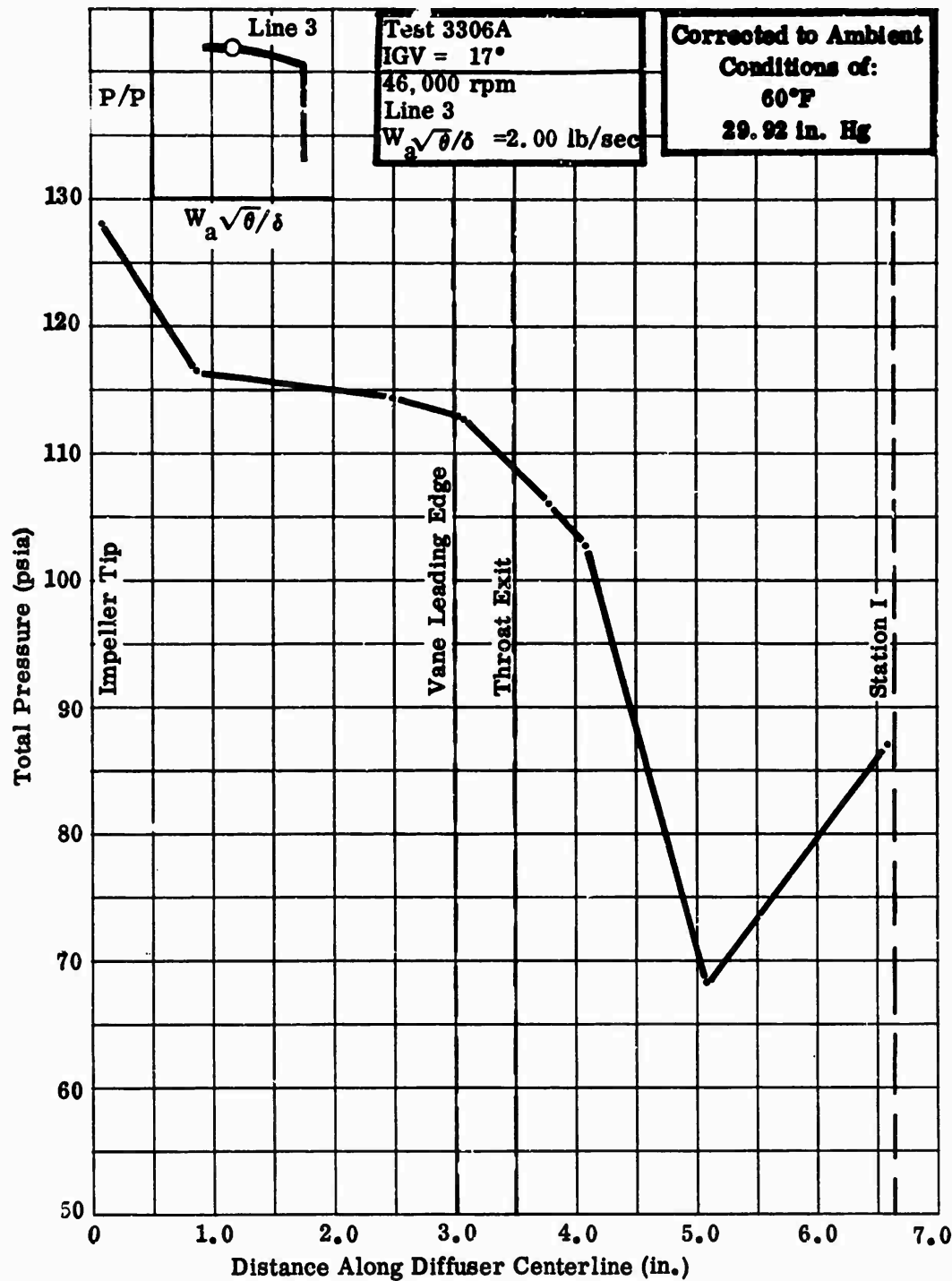


Figure 345. Midchannel Total Pressure Versus Flow-Path Length, DI-1.

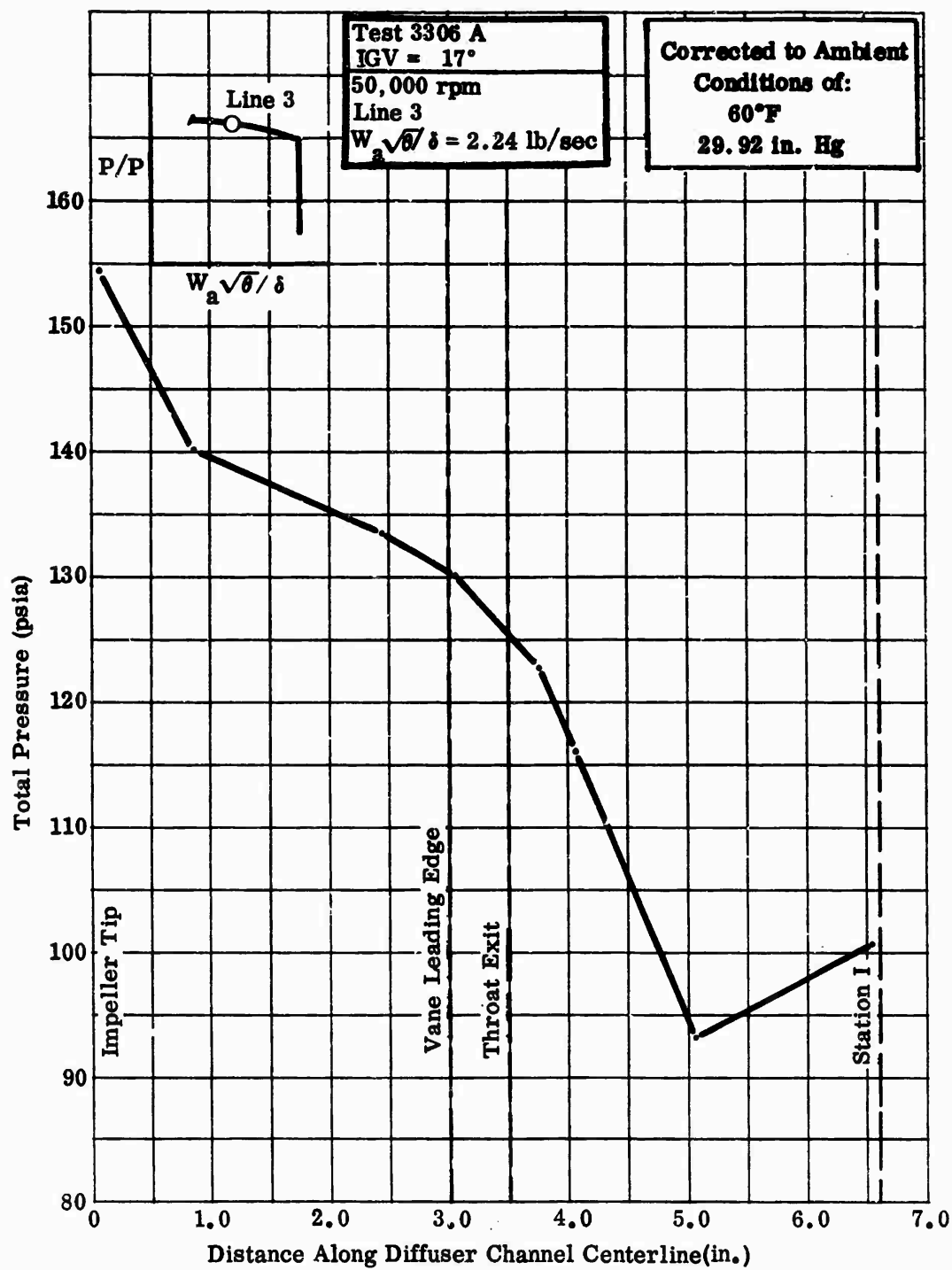


Figure 346. Midchannel Total Pressure Versus Flow-Path Length, DI-1.

CONFIDENTIAL

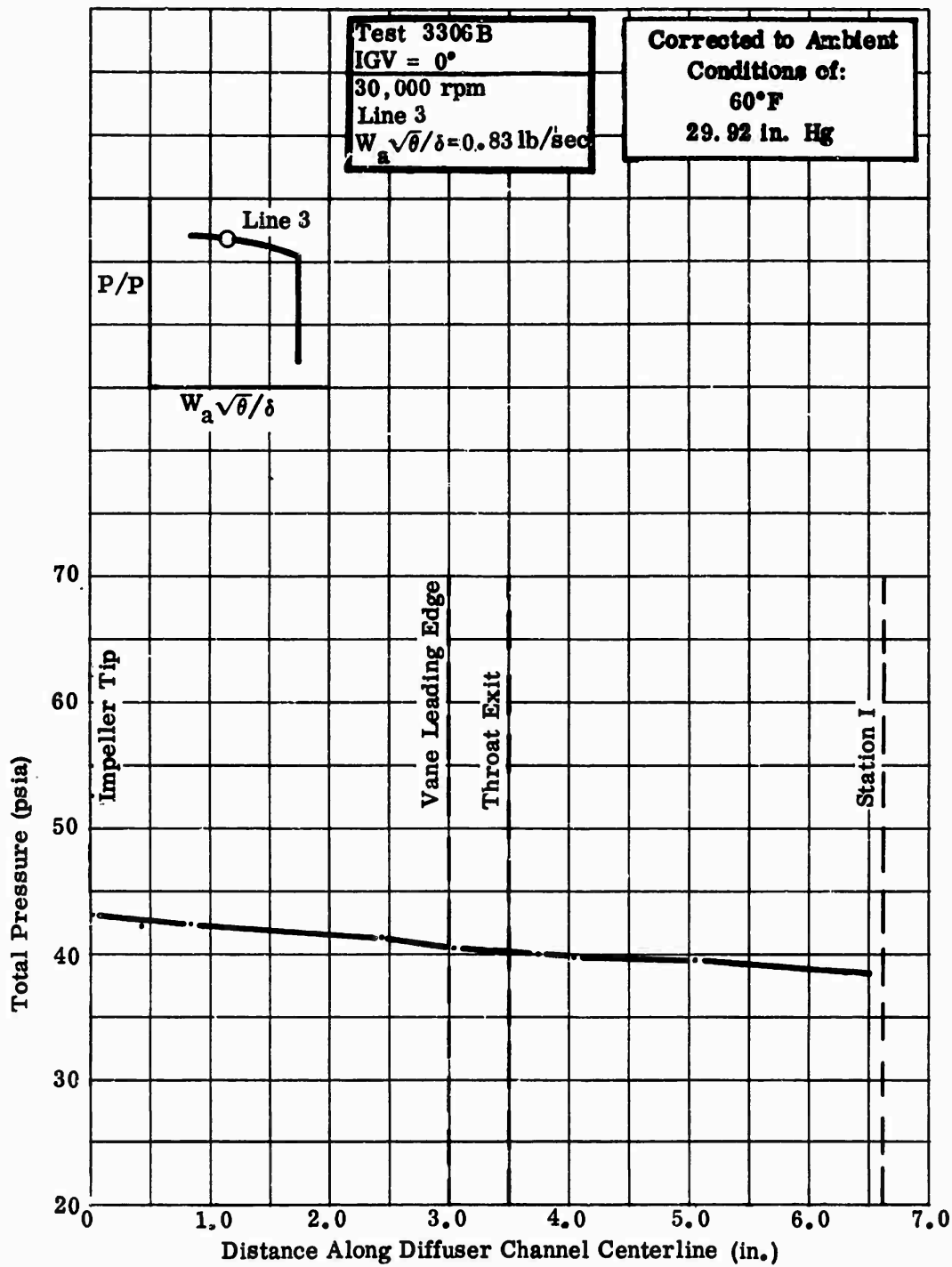


Figure 347. Midchannel Total Pressure Versus Flow-Path Length, DI-1.

CONFIDENTIAL

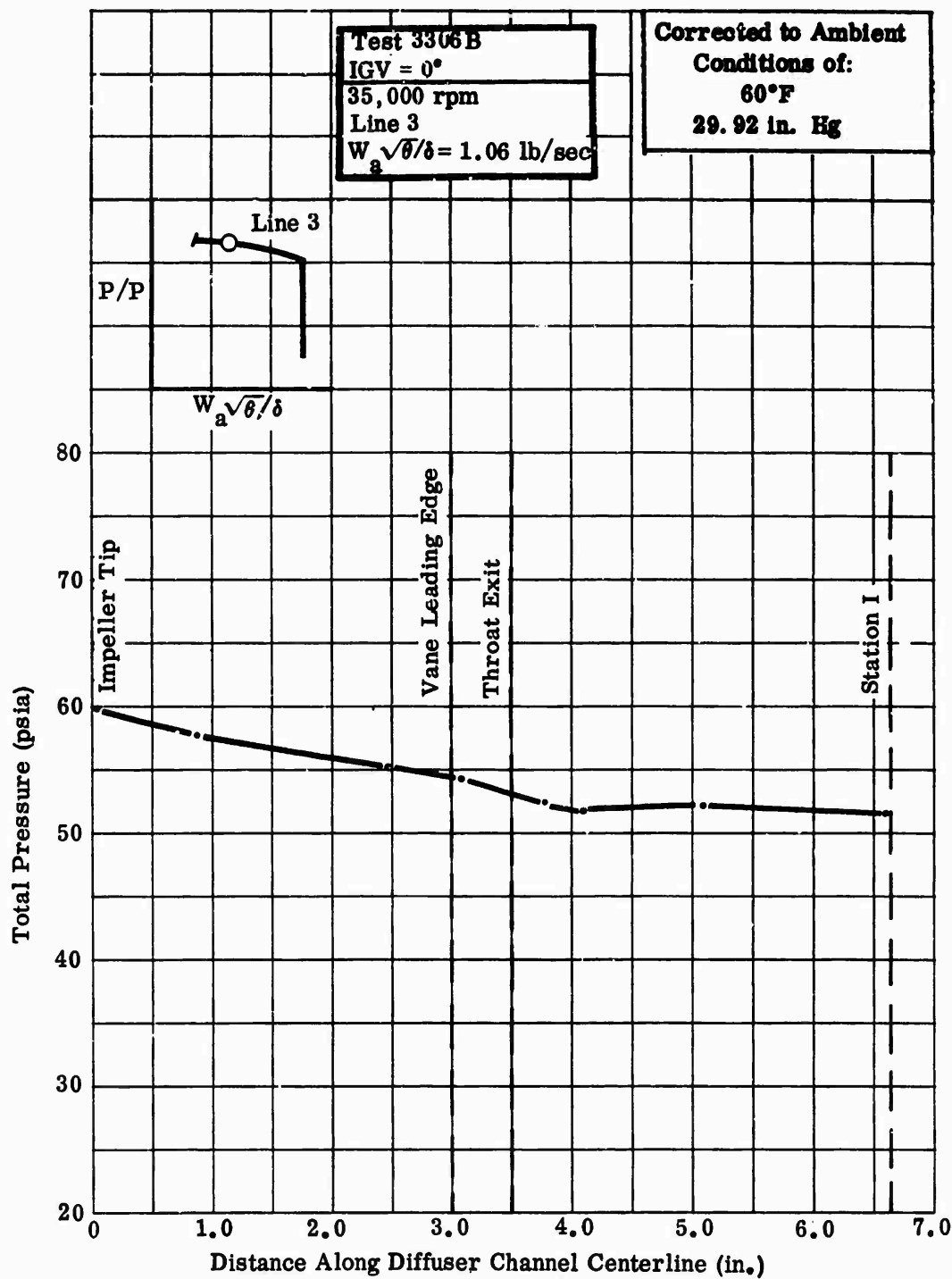


Figure 348. Midchannel Total Pressure Versus Flow-Path Length, DI-1.

CONFIDENTIAL

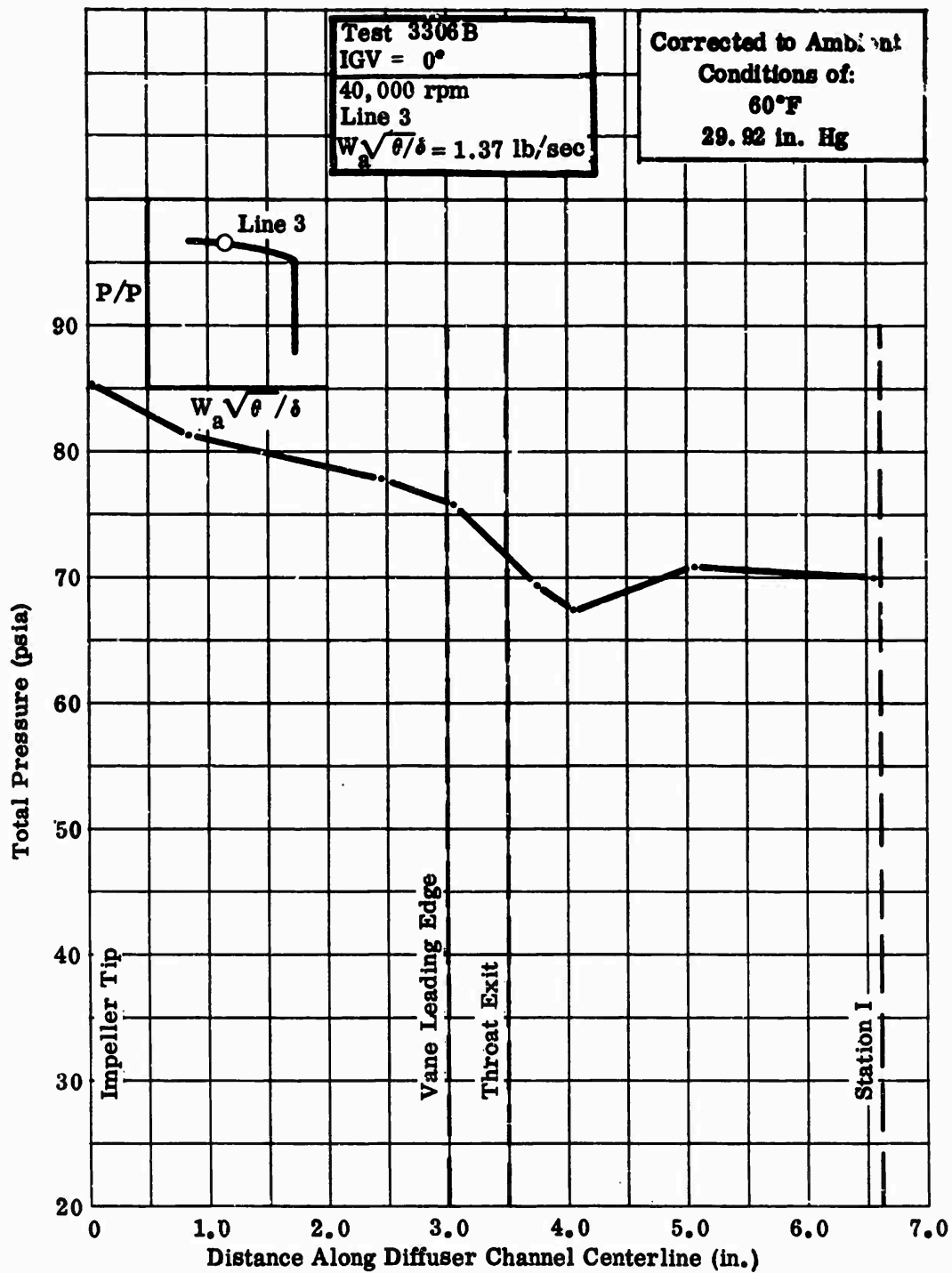


Figure 349. Midchannel Total Pressure Versus Flow-Path Length, DI-1.

CONFIDENTIAL

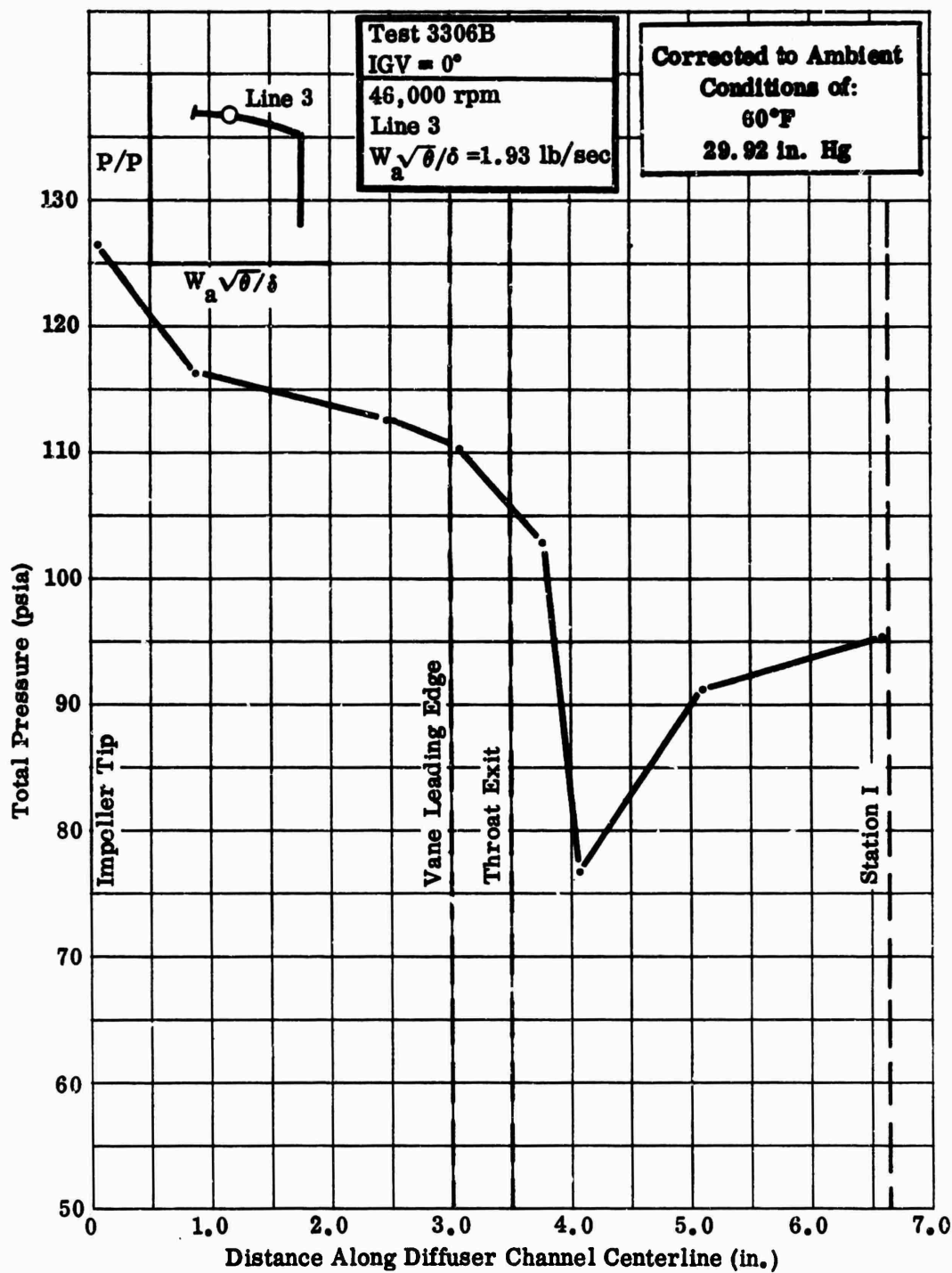


Figure 350. Midchannel Total Pressure Versus Flow-Path Length, DI-1.

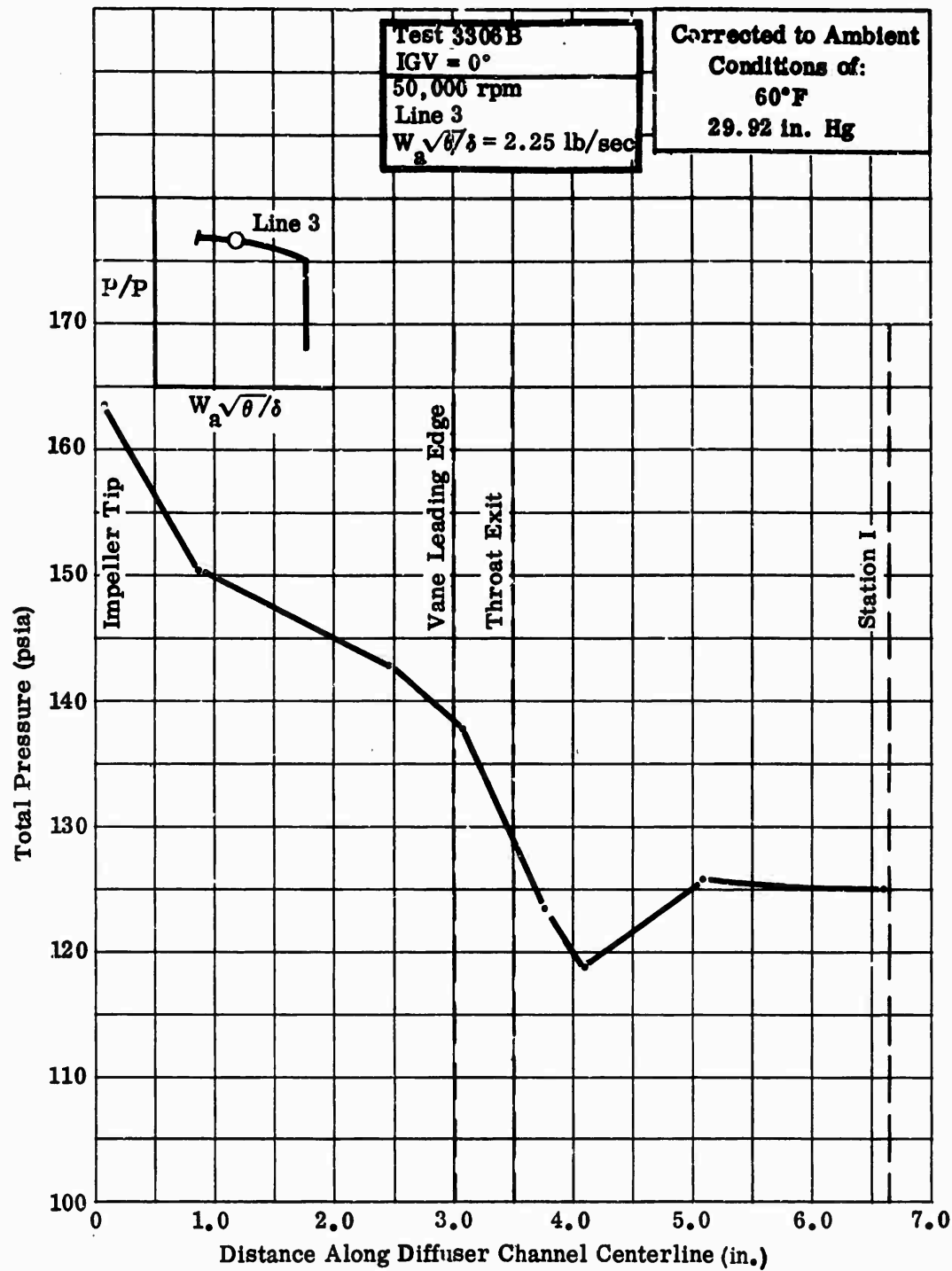


Figure 351. Midchannel Total Pressure Versus Flow-Path Length, DI-1.

CONFIDENTIAL

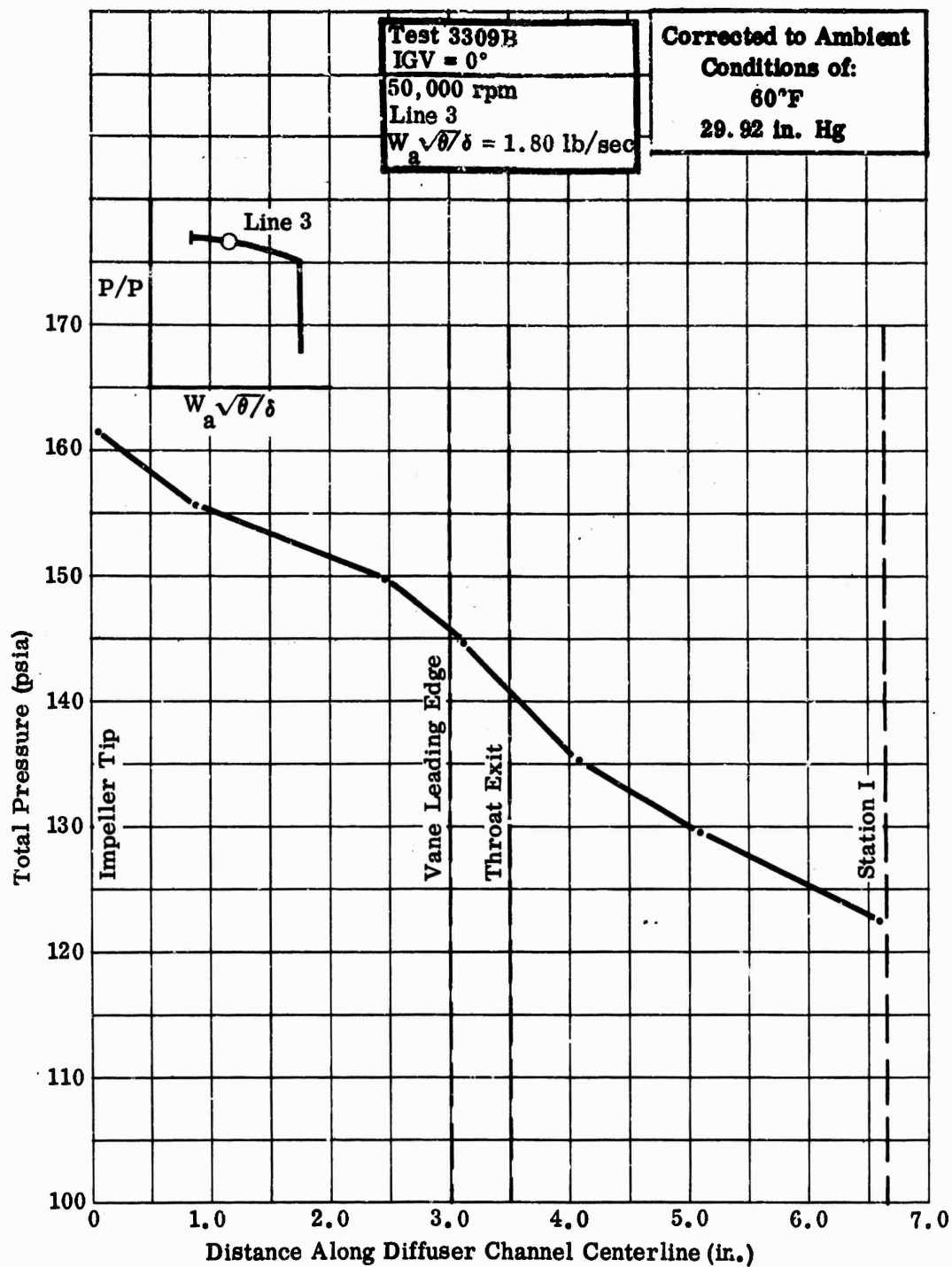


Figure 352. Midchannel Total Pressure Versus Flow-Path Length, DI-1.

CONFIDENTIAL

CONFIDENTIAL

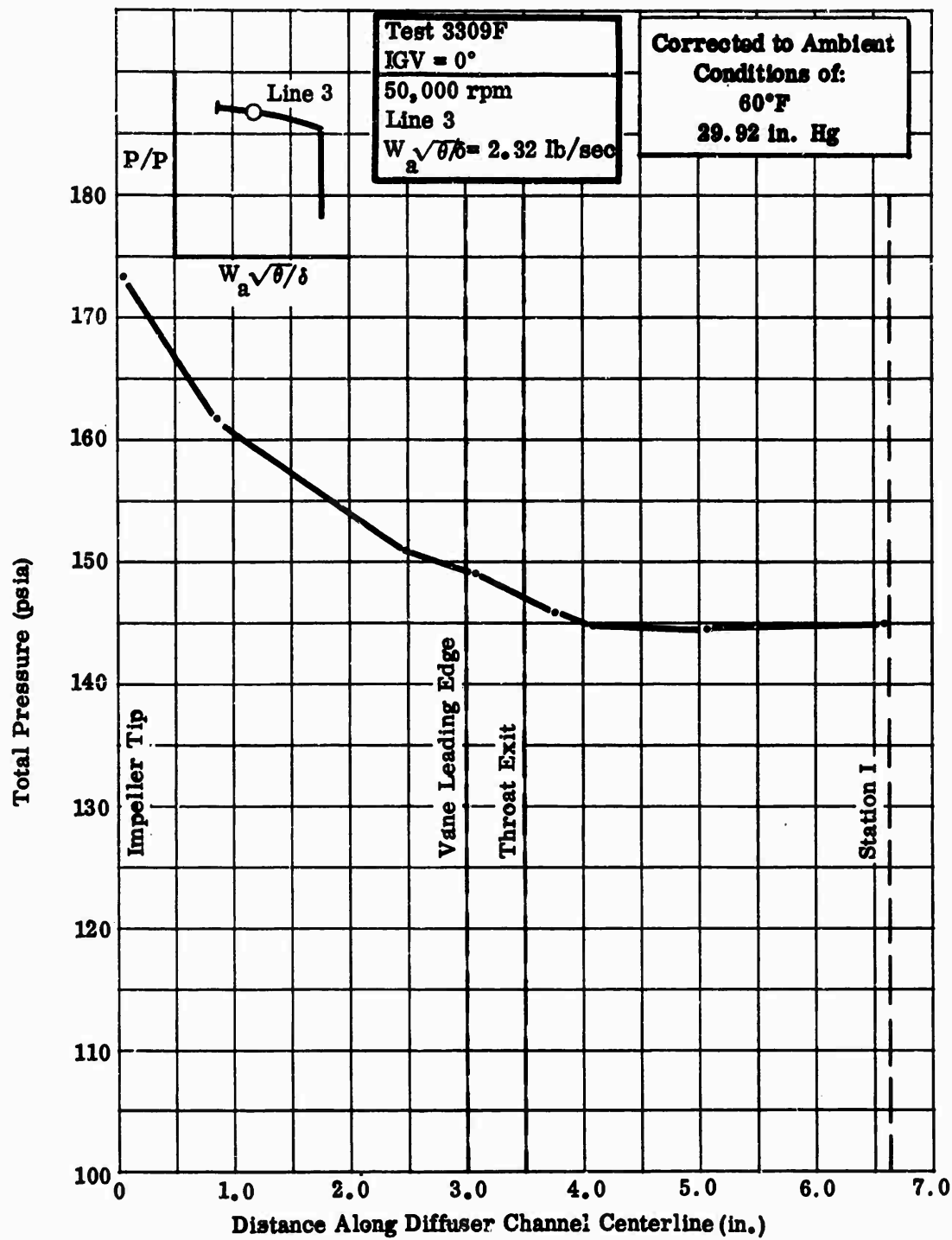


Figure 353. Midchannel Total Pressure Versus Flow-Path Length, DI-1.

CONFIDENTIAL

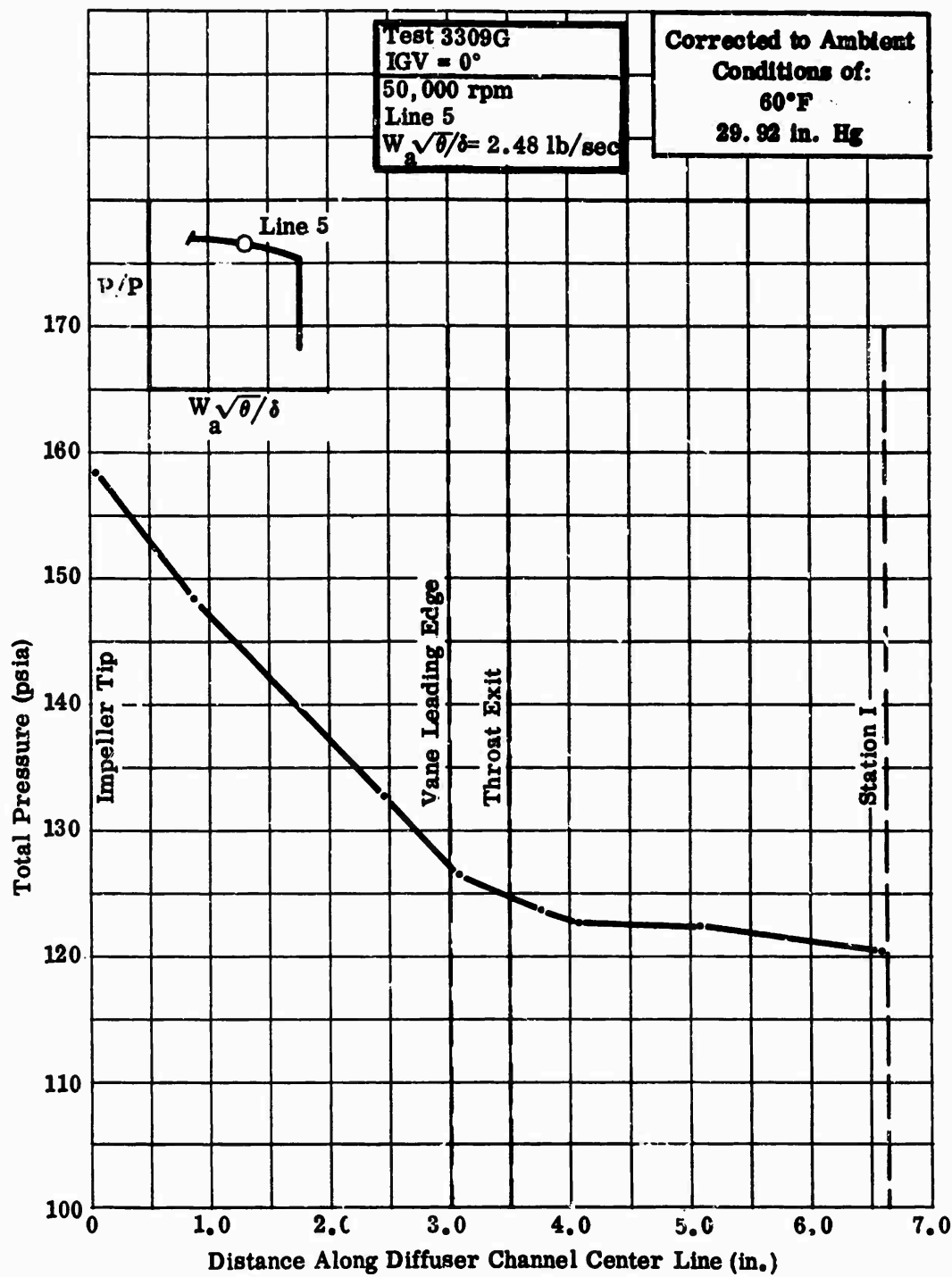


Figure 354. Midchannel Total Pressure Versus Flow-Path Length, DI-1.

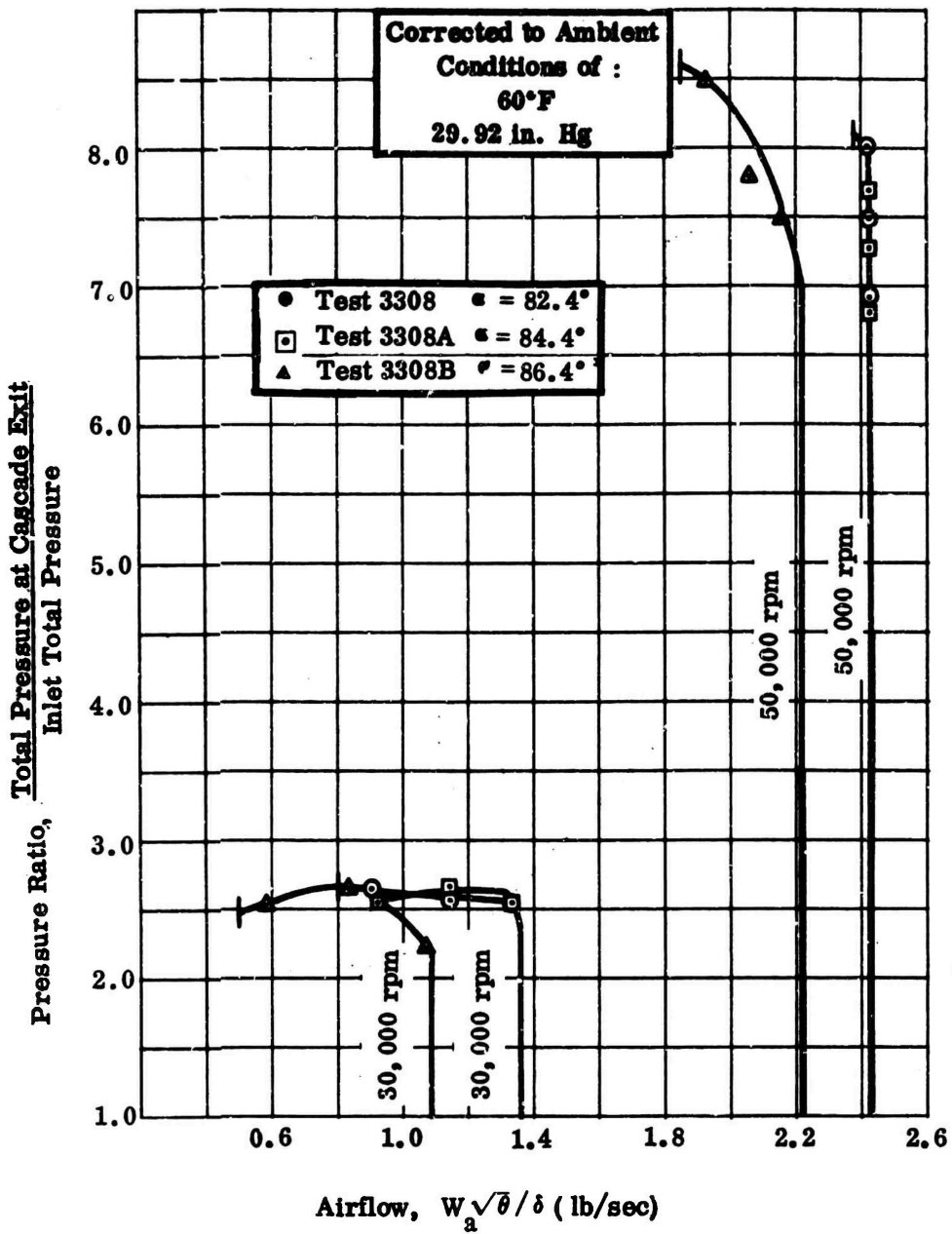


Figure 355. Pressure Ratio Versus Airflow, DC-1 Cascade.

CONFIDENTIAL

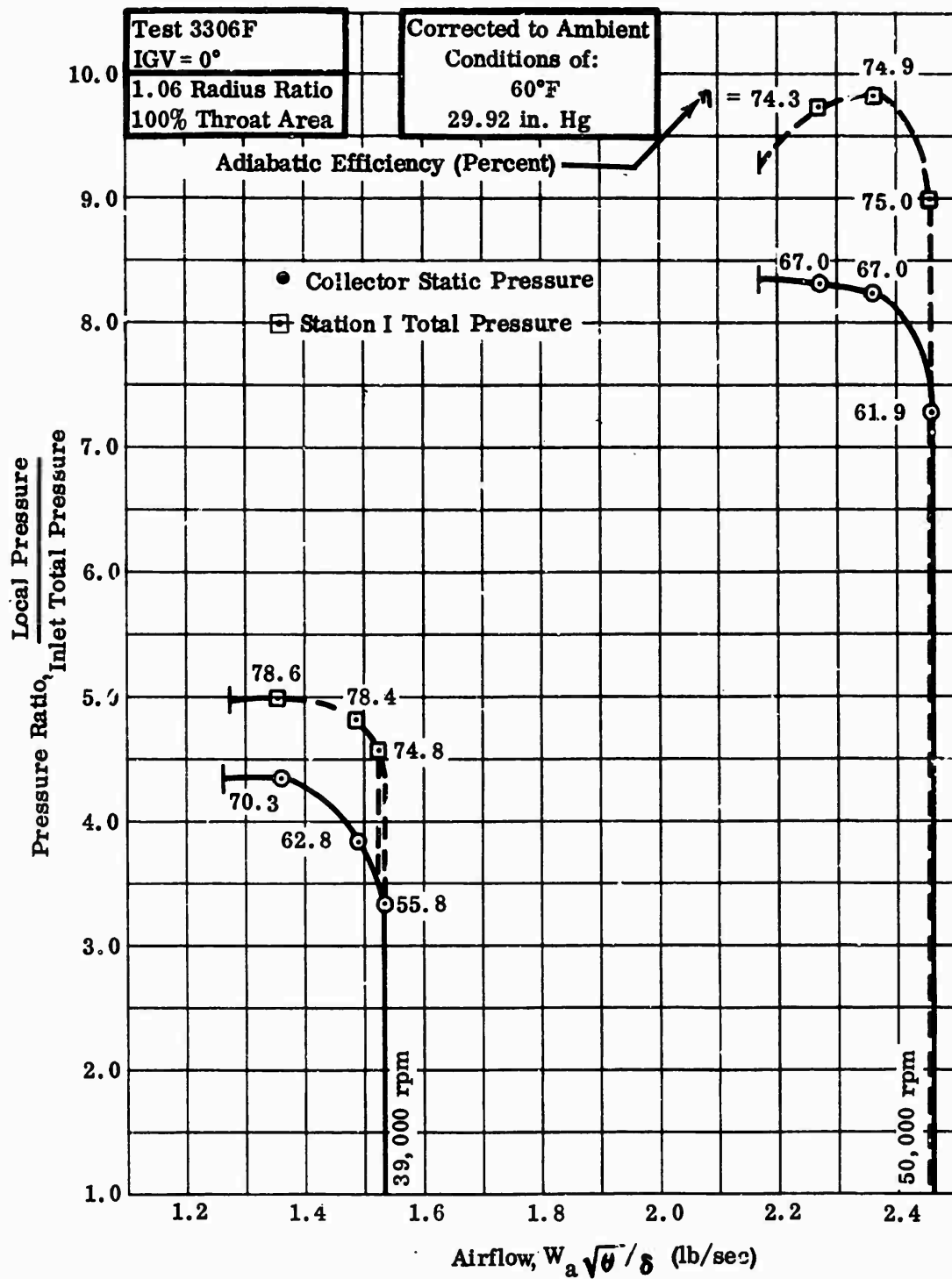


Figure 356. Pressure Ratio Versus Airflow, DI-1.

CONFIDENTIAL

CONFIDENTIAL

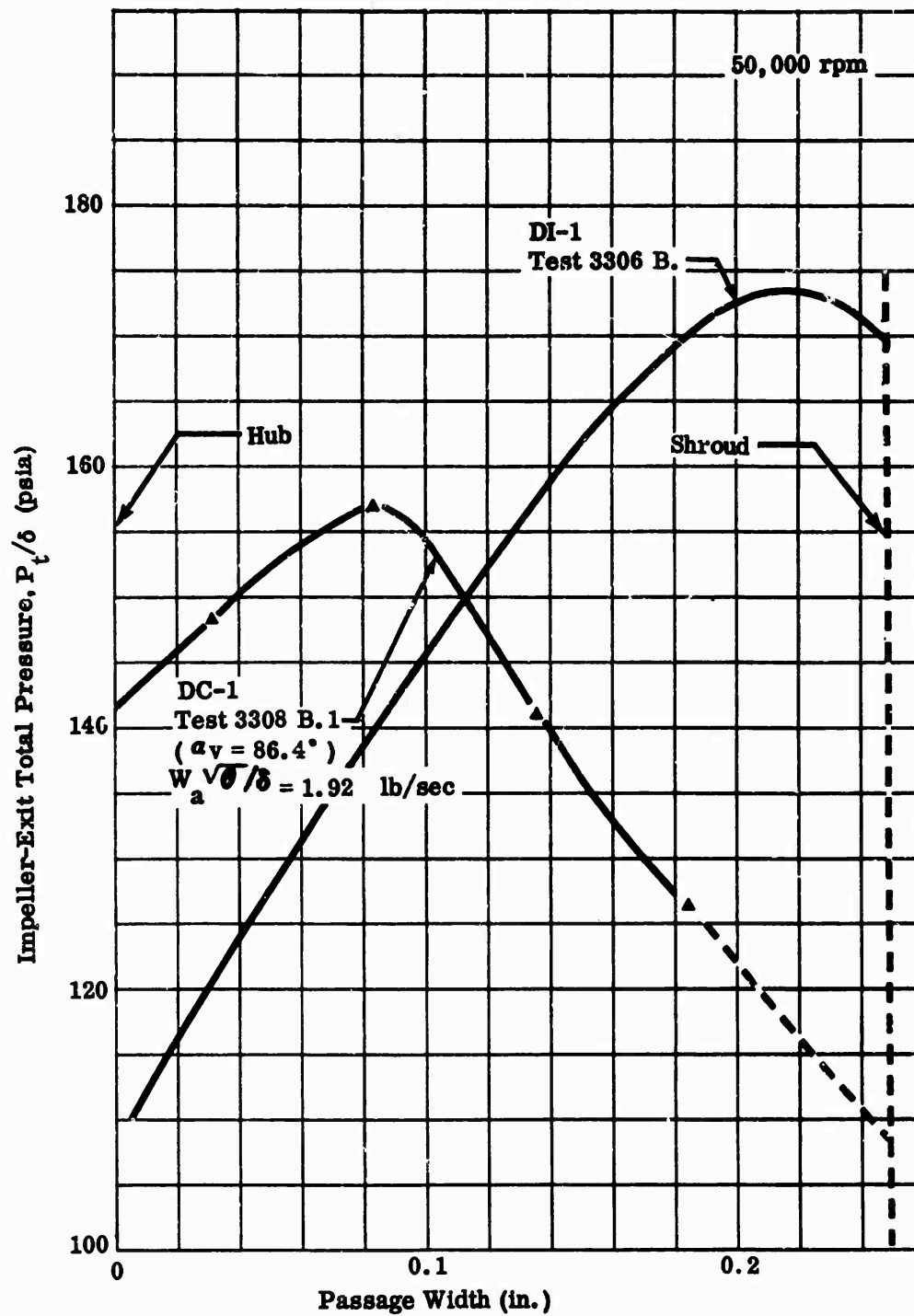


Figure 357. Impeller-Exit Total Pressure, DI-1 and DC-1.

CONFIDENTIAL

CONFIDENTIAL

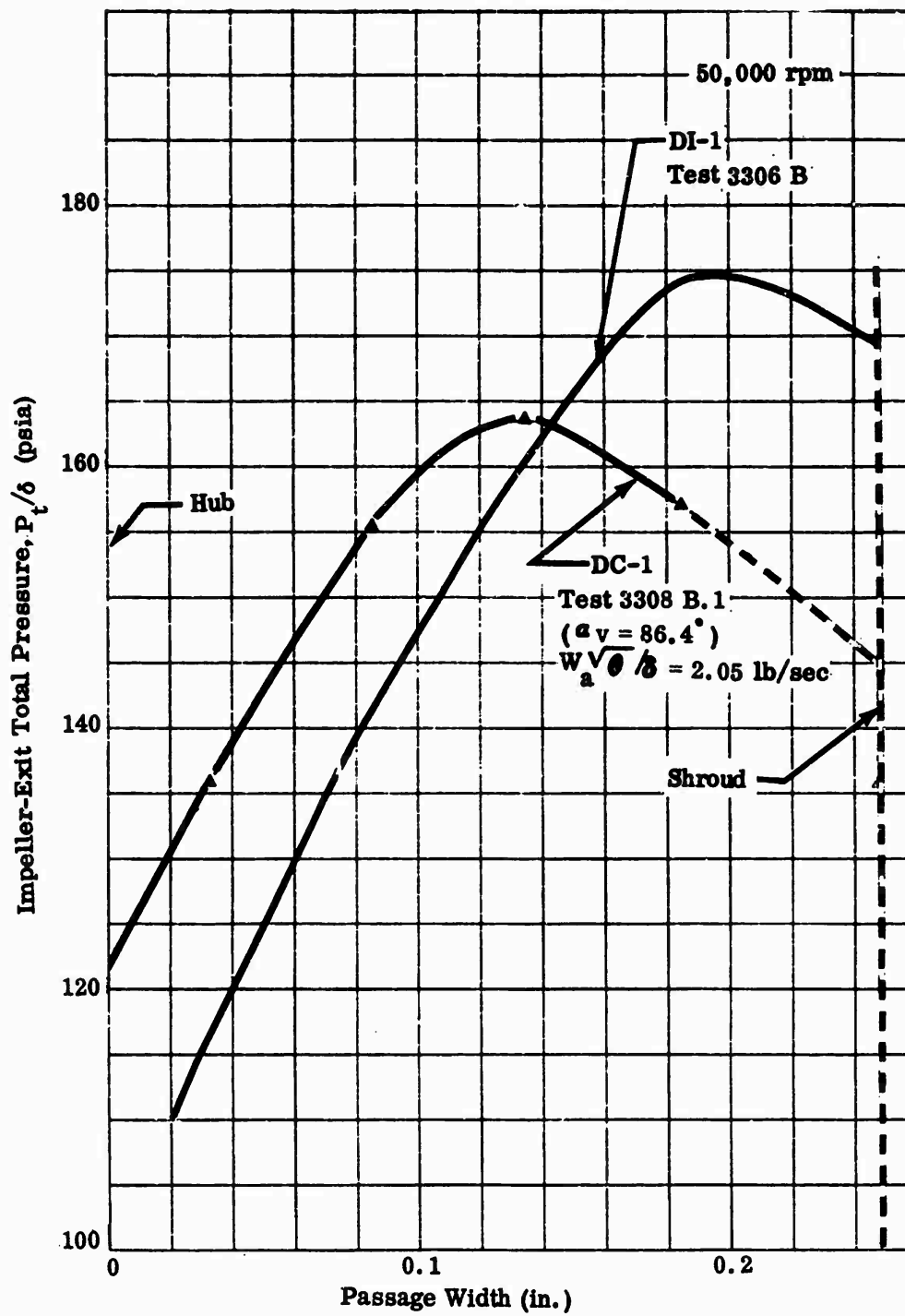


Figure 358. Impeller-Exit Total Pressure, DI-1 and DC-1.

CONFIDENTIAL

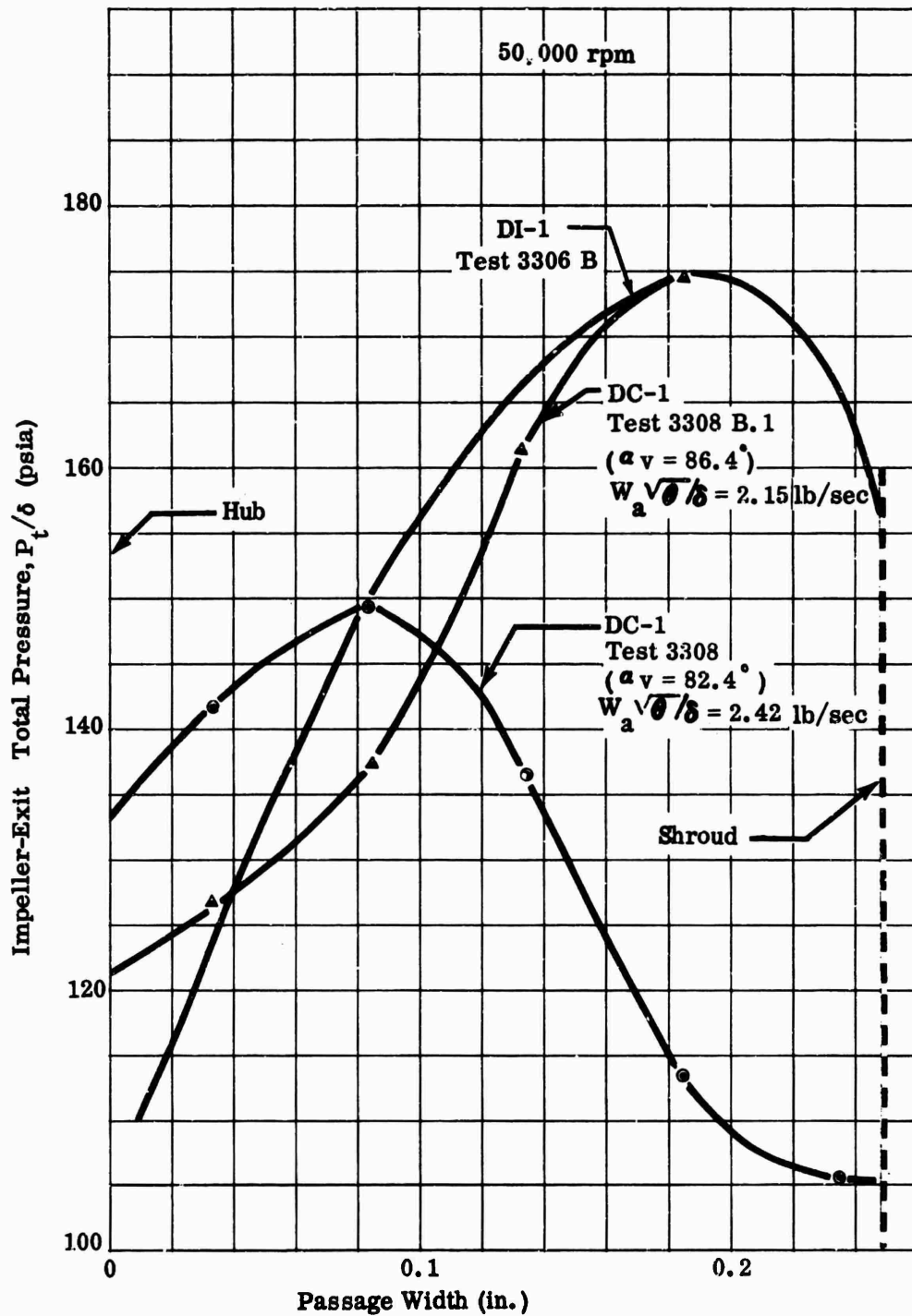


Figure 359. Impeller-Exit Total Pressure, DI-1 and DC-1.

CONFIDENTIAL

(C) 7.0 EVALUATION OF TEST RESULTS (U)

The goal of 10:1 pressure ratio in a single-stage centrifugal compressor requires an impeller pressure ratio from 12.0:1 to 13.0:1. To obtain this performance level, it was recognized that conventional design parameters required refinement in order to extrapolate their influence on high-pressure-ratio designs. The impellers tested in this program were designed with this in mind. A design method was used that had been successful for lower pressure ratio; however, it was planned to evaluate the impellers with respect to the design method and to modify the method and/or the impeller designs as necessary to accomplish the goal. In addition, several diffuser elements with modifications were tested with a workhorse impeller. These studies led to new theories on flow through the compressor, each of which is related to the tests in the following discussions.

7.1 IMPELLER TESTS

Three impellers were tested in the program. Two of the impellers were radial-flow types and 1 was a mixed-flow type. All 3 impellers had lower performance than the design point. The best of the 3 was the workhorse impeller, used in the diffuser test rig. This impeller was 9 percent below the impeller pressure-ratio goal of 12.3:1. During the test program, it was determined that rotating stall was present in both MF-1 and RF-1, as evidenced by the static-pressure transducer instrumentation installed in the MF-1 vaneless diffuser. Diffuser vanes were added to the RF-1 test section, eliminating the stall, and a performance improvement resulted. However, performance was still below the design goal. Analysis of the test data showed that the relative diffusion through the impellers was less than expected. The results led to a reevaluation of the losses used in the design method. Subsequently, an analysis was derived to account for these losses and was compared against the performance of the USAAVLABS impellers as well as other research impellers built by the contractor. Reasonable correlation between measured and calculated pressure ratio was obtained.

The data analysis showed that the flow separated near the leading edge of the inducer in each USAAVLABS impeller, resulting in large wakes at the impeller tip and large mixing losses in the vaneless space; both were chargeable directly to the impeller. The early separation in the inducer was believed to be independent of the design pressure ratio; therefore, a study was conducted to determine the influence of diffusion rates and blade shapes on boundary-layer and flow conditions at the inducer entrance. In addition, methods of predicting points of separation were evaluated. It was believed that these analyses would lead to an improved design technique that could be correlated with available test data. The revised method (see Section 7.1.7) was subsequently used in the design of a new impeller to be tested for verification later in the program.

CONFIDENTIAL

CONFIDENTIAL

The performance of each impeller will be discussed individually and will be compared with the predicted performance emanating from the original design method. Then, where applicable, the performance of the various test impellers will be compared. Finally, alterations to the original design procedure will be presented, along with the parameters which strongly affect the losses.

7.1.1 WORKHORSE IMPELLER

The target performance of the workhorse impeller, as noted in Section 2.3.3, was as follows:

Pressure Ratio	12.3:1
Adiabatic Efficiency	87.8 percent
Airflow Rate	2.43 lb/sec

For comparison, measured performance was as follows.

Pressure Ratio (IGV at 0 degrees)	11.25:1*
Adiabatic Efficiency (IGV at 0 degrees)	79.5*
Pressure Ratio (IGV at +17 degrees)	11.3:1*
Adiabatic Efficiency (IGV at +17 degrees)	81.5 percent*

*These performance figures include losses through the inlet guide vanes.

In comparing the design and measured performance, it was found that the static-pressure rise along the shroud of this impeller fell short of the design expectations. A comparison of test and predicted static-pressure distribution along the shroud at the design speed (Figure 290) shows that little diffusion of the relative flow is accomplished within the impeller. For the design conditions, the impeller-exit static pressure was expected to be 65.8 psia; in the extreme case of no diffusion, where the average inlet and exit relative velocities were assumed to be the same, the exit static pressure would be approximately 59 psia. By comparison, the measured static pressure at the impeller exit was 60.7 psia, close enough to the no diffusion case to indicate early separation.

Further evidence of a performance deficiency was shown by the measured total-pressure and flow-angle profiles at the impeller exit. For the design speed, these data were presented in Section 6.1 (Figures 278 and 279 and Figures 293 and 294). These data showed that most of the air leaves the impeller at the shroud side of the exit annulus. It was also indicated that reverse flow may have occurred along

CONFIDENTIAL

the hub side, as evidenced by the large flow angles measured in that region. These figures also show a large region of separated flow (30 percent of the exit-passage width) close to the hub region at the impeller discharge. Within the first half inch of meridional distance, the design diffusion schedule ($V_{\text{local}}/V_{\text{inlet}}$) was 0.63.

This high deceleration, with its large adverse gradients, may have forced a flow reversal and separation from the impeller-hub surface. An additional cause of the separation within the impeller may have been high incidence at the inducer. The radial variation of incidence at the design speed is shown in Figure 301; average incidence was +8 to +10 degrees. The presence of the positive slope at the lower airflow end of the speed lines on the performance map (Figure 274) was a further indication of losses caused by high incidence at the inducer.

Subsequent tests with an inlet guide vane setting of +17 degrees (positive prewhirl is in the direction of rotation) showed an improvement in impeller efficiency of 1.5 to 2 percent at design speed. The prewhirl was used to reduce the inlet relative Mach number and the flow incidence. Calculations showed that the average Mach number was reduced from 0.93 to 0.81, while the incidence was reduced from 9 to 2 degrees. It should be noted that flow deviation from the inlet guide vanes was determined analytically from Carter's rule, and losses through the vanes were assumed to be zero. It was recognized that a finite loss would reduce the incidence angles by producing a larger inlet absolute velocity for a given airflow rate. A more detailed discussion of the effects of high-incidence is presented in Section 7.1.8.

Two parameters which are important in the evaluation of high-pressure-ratio, small-diameter centrifugal compressors are the temperature-rise factor and the slip factor. The slip factor is indicative of the work imparted to the fluid through the change in its angular momentum (Euler work) and governs the pressure ratio which the impeller will produce. The temperature-rise factor, on the other hand, gives the total work done. The difference between the total work and the Euler work is a measure of the temperature rise resulting from disk friction and recirculation. The disk friction loss is caused by shearing of the fluid in spaces between the rotating impeller and stationary boundaries. The recirculation loss results when the fluid does not have sufficient energy to conform to the diffuser static-pressure gradient and is forced back into the impeller, where it is heated further.

CONFIDENTIAL

CONFIDENTIAL

The design value of slip factor for the workhorse impeller was 0.90 as calculated by a modified form of Eckert's equation (Reference 20). The expression is:

$$SF = \frac{1}{1 + \frac{\pi \cos \beta_e}{2Z \left(1 - \frac{d_{RMS}}{D_{tip}}\right)}} \quad (33)$$

where:

β_e = angle between blade mean line and the meridional plane at the exit (for straight, radial blades, $\beta_e = 0$)

Z = number of impeller blades

d_{RMS} = root mean square diameter at impeller inlet

D_{tip} = impeller tip diameter

A 3-percent allowance was used in the design for disk friction and recirculation temperature rise, resulting in a design temperature-rise factor of approximately 0.93. As shown in Figure 360, a and b, the test value of slip factor at design speed is approximately 0.93 while the test temperature-rise factor is 0.97.

The slip factor of 0.93 was higher than recorded for previous impellers designed by the contractor by approximately 3 percent. The earlier designs, however, were at lower pressure ratios (3:1 to 7:1). Indications were that the previously used conventional methods (such as Reference 5) for predicting slip factors would require modification for use at pressure ratios above 7:1. It was believed that a more complicated internal flow pattern resulted at high tip speeds, causing slip to lie outside the range of predictions. Additional discussion of this subject is contained in Section 7.1.9.

Profiles of the slip factor and the temperature-rise factor are presented in Figures 305 and 303 for both the zero-prewhirl and the +17-degree-prewhirl cases. Nearly all test points showed a low slip factor on the hub side, denoting a lack of

CONFIDENTIAL

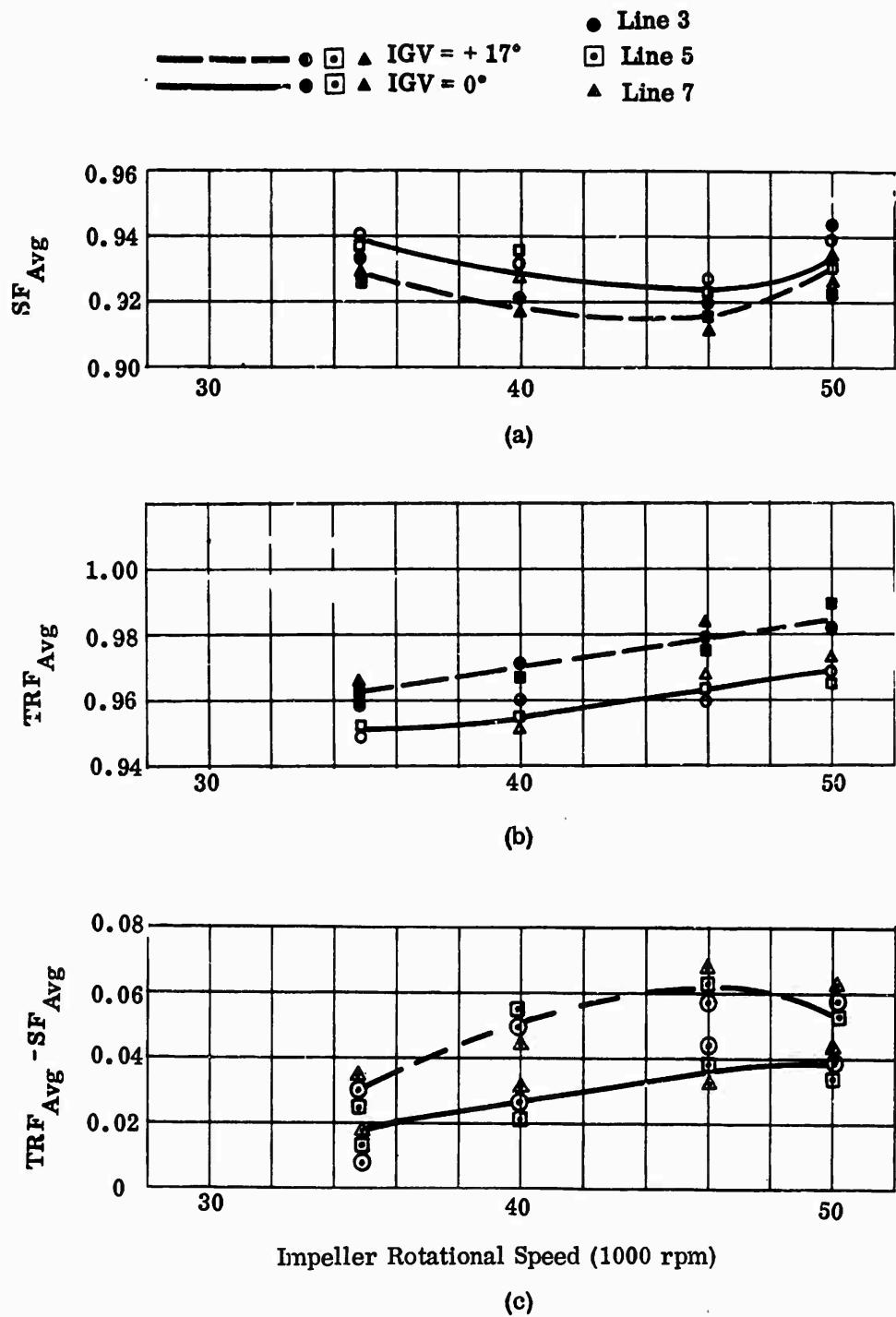


Figure 360. Temperature-Rise Factor and Slip Factor, Workhorse.

flow guidance by the impeller blades in this region. The condition is understandable in light of the previously discussed separation of the flow from the hub surface. The gradient of slip factor from hub-to-shroud increased slightly with speed for the different test points at zero prewhirl, as shown in Figure 361. For the 17-degree prewhirl cases, an anomaly occurred in the hub region. As the speed increased from 35,000 to 40,000 rpm, the slip factor near the hub decreased by 4 to 5 percent. It remained at this lower level until 46,000 rpm when it began to rise again. At 50,000 rpm, the slip factor in the hub region was nearly the same as for the zero-prewhirl case (see Figure 361). Because there was no reasonable explanation for the 17-degree case, subsequent discussions of the slip factor and the temperature-rise factor will be based solely on the zero-prewhirl results.

It was shown that the difference between slip factor and temperature-rise factor remained nearly constant from 46,000 to 50,000 rpm, as shown in Figure 360. Nearly all test points showed that the largest difference between the 2 factors occurred in the vicinity of the diffuser walls.

7.1.2 MF-1 IMPELLER (VANELESS DIFFUSER)

The target performance of the MF-1 impeller at the design point was as follows:

Pressure Ratio	13:1
Adiabatic Efficiency	93 percent
Airflow Rate	2.00 lb/sec

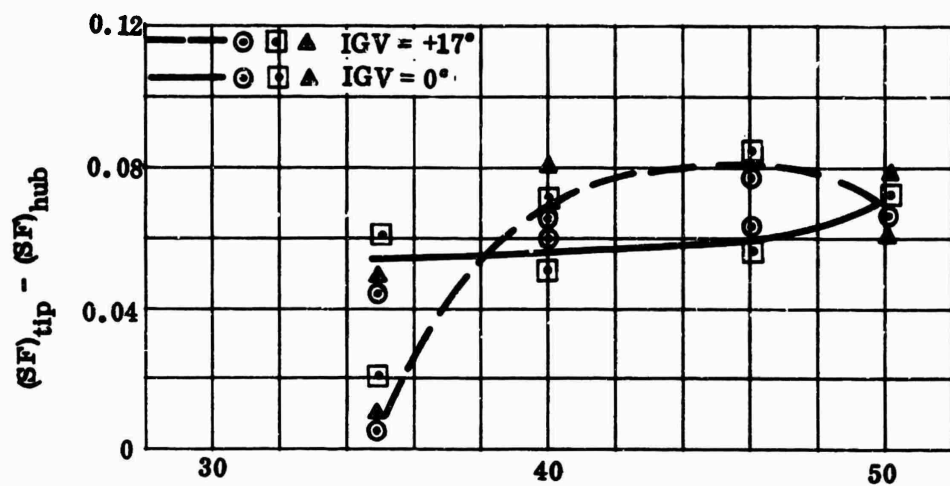
For comparison, measured performance was as follows:

Pressure Ratio	9.3:1
Adiabatic Efficiency	73.9 percent

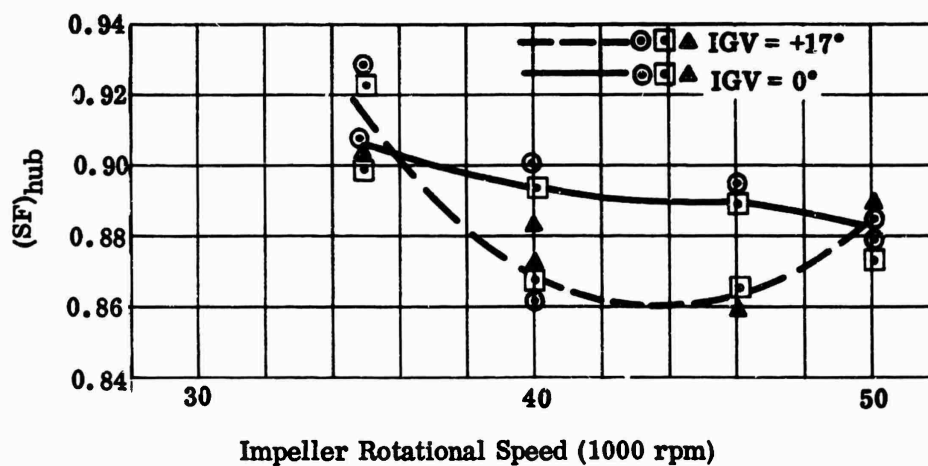
The test results of the MF-1 impeller with the vaneless diffuser showed a condition of rotating stall, which had adverse effects on impeller performance. Correction of the stall phenomenon was accomplished by adding vanes to the radial impeller (RF-1) test section (which also exhibited the condition during initial vaneless runs). Therefore, tests of MF-1 discussed in this section include the results of studies that led to detection of the stall; however, no attempt was made to correct the stall condition in MF-1.

First indications of a deficiency in the impeller were shown by static-pressure measurements along the shroud. The pressure rise was below the design predictions as shown in Figure 232. Figure 232 also shows the extreme case of no

CONFIDENTIAL



(a)



(b)

Figure 361. Temperature-Rise Factor and Slip Factor, Workhorse.

CONFIDENTIAL

CONFIDENTIAL

diffusion of the relative flow at the design speed (57,000 rpm) and the design airflow (2.00 pounds per second). The measured static pressure at the impeller tip was approximately 4 psi below the no-diffusion case, pointing toward higher internal losses in the MF-1 impeller than were assumed in the design predictions. In addition, indications were that the average exit relative velocity was higher than the average at the inlet. Figure 236 shows the outer-radius angle measurements of MF-1, which indicate a velocity profile at the exit similar to that found for the workhorse impeller, i.e., low through-flow velocities in the hub region. However, the average values of flow angle for the 3 test points did not agree. The scatter was also evident in the total-pressure measurements at the impeller exit shown in Figure 230. The data discrepancies were attributed to the rotating-stall condition in the vaneless diffuser.

Because of differences in the measured angles, the slip factor was also scattered, as depicted in Figure 243. The temperature-rise factor showed more consistency, since only the temperature and rotational-speed measurements were used in its determination. By referring to Figure 247, it can be seen that the average value at the design speed is 0.95. In addition, Figure 246 shows that the temperature-rise factor was higher in the hub region than at the shroud.

For the MF-1 impeller and the other impellers which were a part of this program, only the slip factors were considered in the design predictions. The design value of slip factor for MF-1 was 0.90. The predicted pressure ratio and efficiency of MF-1 were based on this slip factor. Although the additional temperature rise caused by friction and backflow was not incorporated in the design analysis, its effect was accounted for by assuming that the efficiency would be 3 to 4 percent lower. The predicted temperature-rise factor would have been about 0.93, or 2 percent lower than the test value. No comparison was made between the test and design values of slip factor because of the data scatter.

Referring to the performance map for the MF-1 impeller in Figure 225, it was noted that the impeller choked at about 98 percent of the design airflow. At this airflow of 1.97 pounds per second, the inducer operated at about +4-degree incidence. Discussion of the choking is presented in Section 7.1.8.

7.1.3 RF-1 IMPELLER (VANELESS DIFFUSER)

The discussion presented in Section 7.1.2 concerning the MF-1 impeller-performance data also applies to RF-1 with the vaneless diffuser. Although the vaneless diffuser of the RF-1 test rig was not instrumented with transducers to identify the frequency of the stall cells, all other measurements showed the same characteristics as MF-1. Calculated impeller-exit vector diagrams were very similar to those for MF-1. Data from the vaneless tests are discussed in this section.

CONFIDENTIAL

During the aerodynamic tests of the MF-1 and workhorse impellers, it was apparent that blade-to-shroud clearance and diffuser-passage height changed with speed because of impeller deflection and thermal distortion of the diffuser-passage walls. Therefore, a break-off-type clearance-measuring probe was developed to determine the dimensional changes. These probes were incorporated in the checkout tests of the RF-1 impeller test section to provide information concerning the relative motion between the impeller and the front and rear diffuser walls and to determine the influence on performance over the entire test-speed range.

The data collected during the checkout tests indicated considerable axial movement of the impeller tip and the front and rear covers as shown in Figure 218. At the design speed of 57,000 rpm, the clearance between the impeller and the front cover was reduced by about 0.054 inch from the buildup value. About 0.014 inch of this reduction was due to the movement of the front and rear covers, while the remaining 0.040 inch was due to the axial movement of the impeller tip. Because the relative motion between the impeller and the front and rear covers was related to rotor speed, separate shimming operations were required before running of each test speed to provide the desired 0.020-inch design clearance to maintain a zero step from the impeller hub to the diffuser rear wall at the tip. The testing sequence is shown in Table XXII.

TABLE XXII			
RF-1 CLEARANCE TESTS			
Run	Principal Speed (rpm) (Shimmed for 0.020-inch clearance and zero step)	Test Speeds (rpm)	Comments
1a	57,000	57,000	Standard Test Components
		34,000	
		42,000	
1b	42,000	42,000	
		34,000	
1c	34,000	34,000	

CONFIDENTIAL

Performance measurements were taken at 34,000 rpm for all three runs to determine the combined effects of clearance and rear-wall mismatch. The clearance and step are noted on the appropriate data plots in Section 6.1.

Performance of the RF-1 impeller at the 57,000-rpm design speed was:

Impeller Pressure Ratio	8.6:1
Impeller Adiabatic Efficiency	68.4 percent

By comparison, the design prediction was:

Impeller Pressure Ratio	13.2:1
Impeller Adiabatic Efficiency	93 percent

The influence of the clearance and step changes on the impeller performance is shown in Figure 249. At 34,000 rpm, the efficiency increased by 6 to 7 percent when the clearance was reduced from 0.058 to 0.033 inch and the step reduced from 0.028 to 0.010 inch. With the clearance and step reduced to 0.024 inch and zero, respectively, no significant effect on the performance was noted. At 42,000 rpm, no noticeable gain in performance resulted when reducing the clearance from 0.044 to 0.022 inch and the step from 0.018 inch to zero. Likewise, the removal of the sharp corner at the vaneless diffuser entrance resulted in no performance change.

As with the workhorse, the decrement in performance of the RF-1 impeller was evidenced by a comparison of predicted and test values of the static-pressure rise along the shroud, as shown in Figure 256. It was apparent that little, if any, diffusion of the relative flow occurred within the impeller. Figure 256 also shows the predicted static pressure at the exit station for no diffusion of the relative flow. The large discrepancy between the no-diffusion value and the test value indicates that the internal impeller losses were higher than predicted or that a higher relative velocity occurred at the exit than at the entrance.

The profile of flow angle at the impeller exit for the design speed, as shown in Figure 262, does not indicate the deficiency in the hub or shroud regions noted with the workhorse impeller. The total-pressure profile, on the other hand, shows a shroud-region deficiency (Figure 260). The temperature-rise-factor profile at the impeller exit (Figure 272) shows a higher value in the hub region (0.96) than in the shroud region (0.93). This trend is in agreement with the results of MF-1. The workhorse impeller, however, displayed an opposite characteristic in that the temperature-rise factor was highest in the shroud region.

CONFIDENTIAL

CONFIDENTIAL

The performance map for the RF-1 impeller (Figure 249) shows that the choking airflow rate was about 99 percent of the design airflow of 2.00 pounds per second. At choke, the average incidence at the inducer is +8 to +9 degrees. A discussion of the high-incidence choking problems is presented in Section 7.1.8.

7.1.4 ROTATING STALL IN THE VANELESS DIFFUSER

Of the 3 impellers, the workhorse showed the best performance — about 8- to 10-percent efficiency points higher than RF-1 and MF-1 at the design rotor speeds. Based on the selected design parameters, i.e., inducer-blade loading (diffusion factor), inducer incidence, inducer-inlet Mach number, and impeller velocity distribution, the MF-1 and RF-1 impellers should have performed better than the workhorse. Because these parameters did not lead directly to an explanation for the large performance difference, it was believed that the deficiency might have been caused by differences between the test sections. Primarily, the difference was that the workhorse had been tested with a vaned diffuser while both MF-1 and RF-1 were tested with a vaneless diffuser. In Reference 21, Jansen suggests that a vaneless diffuser of conventional geometry is prone to rotating stall when the entrance velocity is nearly tangential (within 10 to 15 degrees), as is the case with the USAAVLABS impellers. If the vaneless diffusers of the MF-1 and the RF-1 test rigs were operating in a condition of rotating stall, the unstable flow condition would have an adverse effect on the impeller performance. To determine whether this phenomenon was responsible for the lower-than-expected performance, pressure transducers were installed in the walls of the vaneless diffuser of the MF-1 test section. The transducers were located at radius ratios of 1.10, 1.20, and 1.44.

Subsequent tests showed the suspected stall cells and their influence on performance. The amplitude of static pressure fluctuation increased with speed and decreased with increasing radius ratio, as would be expected. The stall cells rotated in the same direction as the impeller at a fraction of the impeller speed. Also, because the cells extended to the collector, static pressure in the cells was higher than outside. The cells were nearly constant-pressure regions and allowed high static pressure (approximately the collector pressure) to be transmitted to inner radii, resulting in nonuniform back pressure at the impeller tip and an adverse effect on impeller performance.

Figure 223 is a presentation of the static-pressure rise through the vaneless diffuser of the MF-1 test section at 57,000 rpm. For comparison, the amplitude of the pressure fluctuation through the diffuser is presented in Figure 362. If, as mentioned previously, the stall cell allows a pressure very nearly equal to the collector pressure to be transmitted to inner radii, the transducers at these

CONFIDENTIAL

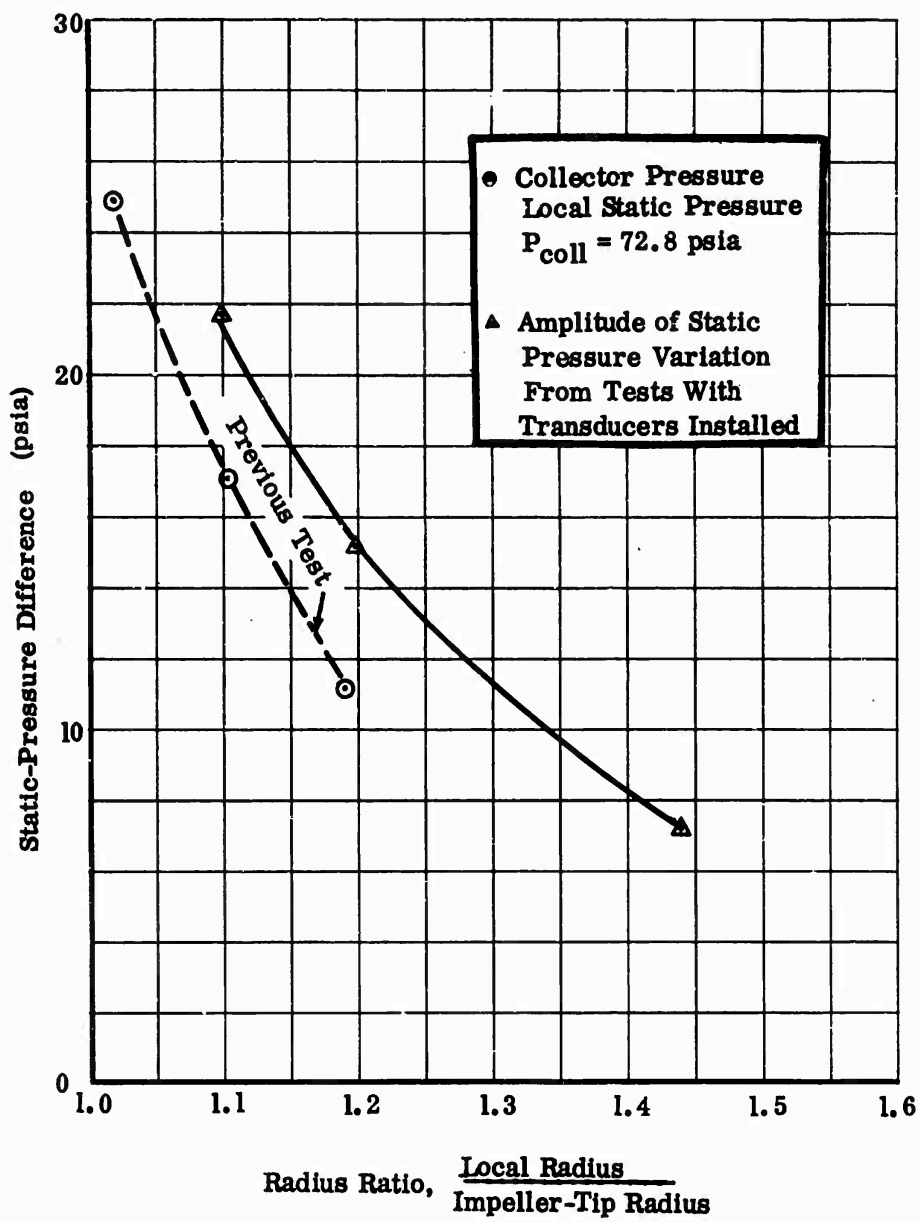


Figure 362. Static-Pressure Amplitude, RF-1.

CONFIDENTIAL

locations would alternately sense a high pressure (collector pressure) and a lower pressure (local static pressure outside the stall cell). Interpretation of the measured static-pressure variation in this light shows good agreement with the earlier static-pressure measurements.

It was not possible to determine the exact rotational speed of the cells because the number, circumferential spacing, and shape of these cells could not be identified with existing instrumentation. Figure 224 shows that the frequency of the pressure fluctuations was approximately a linear function of impeller speed. A sample of the transducer-signal trace taken at 57,000 rpm is shown in Figure 222.

Because of the similarity in RF-1 and MF-1 exit vector diagrams and diffuser geometries, the rotating-stall condition was also believed to exist in the RF-1 diffuser. To eliminate the stall it was necessary to modify the vaneless diffusers by:

- 1) Reducing the vaneless diffuser flow-path length; and/or
- 2) Reducing the diffuser passage height.

The first modification was expected to eliminate the stall by reducing the path length over which the alternating high and low pressures acted. The second was expected to increase the exit radial velocity, and in so doing, increase the radial momentum of the flow while also decreasing the flow-path length.

After careful consideration of both possibilities, it was concluded that the most effective and expedient course of action was to add a set of vanes to the previous vaneless diffuser. This modification was most easily accomplished in the RF-1 section, because the available vaneless diffuser was designed with flat and parallel front and rear walls. Studies of a possible vaned diffuser for the MF-1 test section showed that considerable expense and program delay would result from the fabrication of a set of vanes. It was concluded that further testing of MF-1 would not be advantageous, and that the most value would be derived from thorough testing of RF-1. The modification to the RF-1 test section is presented in Table XXIII.

The vanes were installed at a radius ratio of 1.10 to allow space for the pressure and temperature instrumentation at the impeller exit.

For the modal balance operation and the mechanical-checkout test of RF-1, a pressure transducer was installed at the radius ratio of the vane leading edges (1.10) to determine the effectiveness of the vaned diffuser in eliminating the rotating stall. Throughout the speed range, there was no indication of rotating stall. The results are described in Section 7.1.5.

CONFIDENTIAL

CONFIDENTIAL

TABLE XXIII	
RF-1 DIFFUSER GEOMETRY	
Number of Vanes	12
Throat Depth, d	0.205 inch
Throat Width, W	0.430 inch
Throat Length	0.250 inch
Channel Divergence Angle, 2ϵ	3 degrees (Symmetrical)
Channel Length-to-Width Ratio, L/W	7.65
Vane Leading-Edge Wedge Angle	7 degrees
Angle at Vane Leading Edge (measured from radial direction)	80 degrees

7.1.5 RF-1 IMPELLER EVALUATION (VANED DIFFUSER)

The RF-1 impeller was retested with the vaned diffuser described in Section 7.1.4. The resulting performance (presented in Figures 249 and 250) showed:

Impeller Pressure Ratio	10.0:1
Impeller Adiabatic Efficiency	75.1 percent

The addition of the vanes increased the impeller-exit pressure by 1.4 atmospheres and increased the adiabatic efficiency by 6.7 percent. Although the improvement by eliminating the rotating stall was substantial, the performance still was below the predicted levels shown in Section 7.1.3.

The measured impeller-exit total-pressure profiles for the design speed (Figure 260) showed that the shroud side was deficient, and the flow-angle surveys (Figure 263) indicated that backflow along the shroud occurred. Measured angles were greater than 90 degrees (radially-outward flow is designated by an angle of 0 degrees, while a tangential flow is designated by an angle of 90 degrees).

CONFIDENTIAL

CONFIDENTIAL

Calculations of inducer-inlet conditions showed that the large incidence at which the inducer was forced to operate also contributed to the lower-than-expected performance. As shown on Figure 270, the incidence at design speed (57,000 rpm) was +5 to +8 degrees. At the design conditions, the rms inlet relative Mach number was about 0.9, indicating that the compressibility effects on the suction surface of the inducer blades were substantial.

Despite these indications, the impeller static-pressure rise (Figure 256) improved considerably when the vaned diffuser was added. The measurements suggest that the previously observed large circumferential static-pressure variation at the impeller tip (due to rotating stall) was transmitted into the impeller. It was reasoned that the flow in the impeller was strongly influenced by high static-pressure fluctuations and adverse pressure gradients at the tip. Further, it was believed that this situation led to separation of the flow near the inducer leading edge and was responsible for the inordinate losses in diffusion of the relative flow.

The addition of the vanes in the diffuser also resulted in an increase in exit flow angle (more tangential) of about 5 or 6 degrees. It was evident from a comparison of Figures 262 and 263 that, due to the addition of vanes, little variation of the average exit flow angle occurred with speed, while for the vaneless-diffuser tests, the exit flow angle varied from 64 degrees at 34,000 rpm to 80 degrees at 57,000 rpm.

Average test values of slip factor (0.89) and temperature-rise factor (0.95) were nearly the same as the vaneless case. Temperature-rise factor was rather constant across the middle two-thirds of the passage height as shown in Figure 272. Slip factor, on the other hand, dropped off rapidly near both the hub and shroud (Figure 271), indicating that the temperature rise due to recirculation was highest in these regions.

Because the addition of vanes in the diffuser did not raise the impeller performance to the predicted level, a study was conducted to identify other possible losses.

It was believed that a large loss may have occurred because of jet and wake mixing at the impeller exit. The jet-wake flow was caused by separation of the flow from the suction surface of the blades within the impeller. Basically, this loss was considered to be the result of a sudden expansion of the radial velocity, and the loss coefficient is expressed as $[1 - (A_1/A_2)^2]$, where A_1 is the flow area just inside the impeller tip (jet area) and A_2 is the flow area downstream of the impeller tip (diffuser-entrance annulus area). As noted in Section 7.1.3, one of the earlier RF-1 tests was run with a chamfered corner of the diffuser backplate at the diffuser entrance to minimize the effects of a backplate-to-impeller-hub mismatch. It was later felt that by chamfering the backplate at the diffuser entrance (increasing A_2), the exit mixing losses were inadvertently increased, as

CONFIDENTIAL

CONFIDENTIAL

indicated by total-pressure measurements taken in that region. It was recognized that the chamfer also could have reduced the radius ratio at which mixing was completed. To determine its influence as related to mixing losses, the chamfer was removed and the impeller was retested at the design speed with vanes. However, no change in performance occurred. A comparison of the total-pressure surveys at the impeller exit (with and without the chamfer) are shown in Figure 260. From the calculated incidence at the inducer, it was expected that an improvement could be made by introducing positive prewhirl at inlet. A modification was made to the test section by adding a set of fixed vanes. It was calculated that the prewhirl would reduce the inlet relative Mach number and the incidence on the inducer leading edge such that a shock in the inducer passage, resulting from the expansion of the flow around the leading edge and the curving suction surface, would be weakened and less likely to cause separation of the suction surface boundary layer. If the separation could be delayed until further downstream in the impeller, the relative flow would diffuse and show an increase in static pressure at the exit. The guide vane geometry was as follows:

Number of Vanes	13
Camber Angle	18 degrees
Chord	1.00 inch
Thickness/Chord	0.04
Leading-Edge Radius	0.02 inch
Tip Solidity	1.05
Hub Solidity	1.76

Previous tests of the RF-1 impeller showed that a positive radial gradient of the axial velocity existed at the inlet and caused a greater incidence at the hub than at the tip (see Figure 270). Therefore, the camber angle of the guide vanes was set to be constant from hub to shroud to effect a greater reduction in inlet relative flow angle and, therefore, greater incidence at the hub than at the tip.

Although the inlet guide vane set was not calibrated in a separate flow test to determine the deviation and loss characteristics, the deviation was determined analytically using Carter's rule. At the RMS radius of the inducer inlet, the deviation was calculated to be 2.9 degrees.

The calculated deviation and the assumption of no total-pressure loss across the vane set were used to determine the inlet vector diagrams at the RMS radius.

The resulting vector diagrams are shown in Figure 266. By comparing this figure with Figure 265, it can be seen that the incidence at the choking airflow was

CONFIDENTIAL

CONFIDENTIAL

reduced from +5 to +3.5 degrees, while the inlet relative Mach number was reduced from 0.90 to 0.76.

A comparison of the measured total pressures at the impeller exit is shown in Figure 260. It was evident that no increase in performance resulted from the introduction of the prewhirl. Figure 260 showed that the peak total pressure decreased by about 5-1/2 percent to 151 psia, due to the guide vane losses. This reduction in pressure ratio would result in a decrease in efficiency of about 2-1/2 percent. The calculated inlet vector diagrams showed that the work input was also reduced by about 2-1/2 percent. Therefore, it was concluded that the efficiency of the guide vane-impeller combination was about the same as the impeller without any prewhirl.

7.1.6 AERODYNAMIC EVALUATION

When the diffuser vanes were added to the RF-1 test rig to eliminate the rotating stall, impeller pressure ratio increased from 8.6:1 to 10.0:1, and efficiency increased from 68.4 to 75.1 percent. Subsequent discussions of impeller performance will deal mainly with the workhorse and the RF-1 impellers, each of which was tested with vanes. It was believed that detailed study of the performance difference between these 2 impellers would lead to new understanding of flow mechanics in high-pressure-ratio impellers. An overall comparison of the impellers is given in Table XXIV.

TABLE XXIV		
PERFORMANCE COMPARISON OF RF-1 AND WORKHORSE IMPELLERS		
	Pressure Ratio	Efficiency (percent)
RF-1	10.0:1	75.1
Workhorse (Includes IGV Losses)	11.25:1	79.5

The workhorse impeller was tested with complete aerodynamic instrumentation at the tip only when inlet guide vanes were installed. However, through continued testing with the various diffuser elements, sufficient data were available to establish the ratio of the choking airflow rate of the compressor with the guide vanes installed to the choking airflow rate without the guide vanes. This ratio was 0.967 and was interpreted as the influence of the guide vanes on pressure rise

CONFIDENTIAL

CONFIDENTIAL

through the compressor. When corrected by this factor to eliminate the guide vane effect, the calculated workhorse impeller performance was:

Pressure Ratio	11.63:1
Adiabatic Efficiency	81.0 percent

Parameters used in the design of these impellers were studied, with particular interest placed on diffusion rates and blade shapes, as discussed in the following paragraphs.

Inducer

The inducer parameters were of prime importance, because it was believed that overall impeller performance was strongly dependent on inlet conditions. The principal inducer-performance parameters considered were as follows:

- 1) Blade-loading parameters: Diffusion factor,
 Blade-surface velocity distributions;
- 2) Inlet-tip relative Mach number;
- 3) Incidence at the leading edge.

Loading Parameter — The design diffusion factors for hub, mean, and tip streamtubes are shown in Figure 363 for both the RF-1 and the workhorse impellers. This plot shows that the inducer aerodynamic loading was higher for the workhorse impeller than for the RF-1. In addition, the inducer of RF-1 was designed to have a loading identical to a high-performance inducer developed previously through Boeing research (see Section 2.0, Analytical Studies). Blade-surface velocities for the workhorse and RF-1 impellers are shown in Figures 364 and 365 for hub, mean, and tip streamtubes of the inducer. This comparison shows that more diffusion was required of the workhorse than of the RF-1. With this higher loading, the workhorse impeller was believed to be more prone to separation early in the inducer region. In addition, test data showed that the workhorse impeller operated with a higher inlet relative Mach number and a greater inducer incidence than RF-1. Test values are given in Table XXV.

Therefore, on the basis of the original design criteria, RF-1 was expected to have better performance than the workhorse impeller; this did not occur. Further impeller-design evaluation was necessary to determine causes for the unpredicted difference.

As a first step, the design criteria used for the impellers were reevaluated. Blade-surface-velocity distributions were considered in combination with boundary-layer

CONFIDENTIAL

CONFIDENTIAL

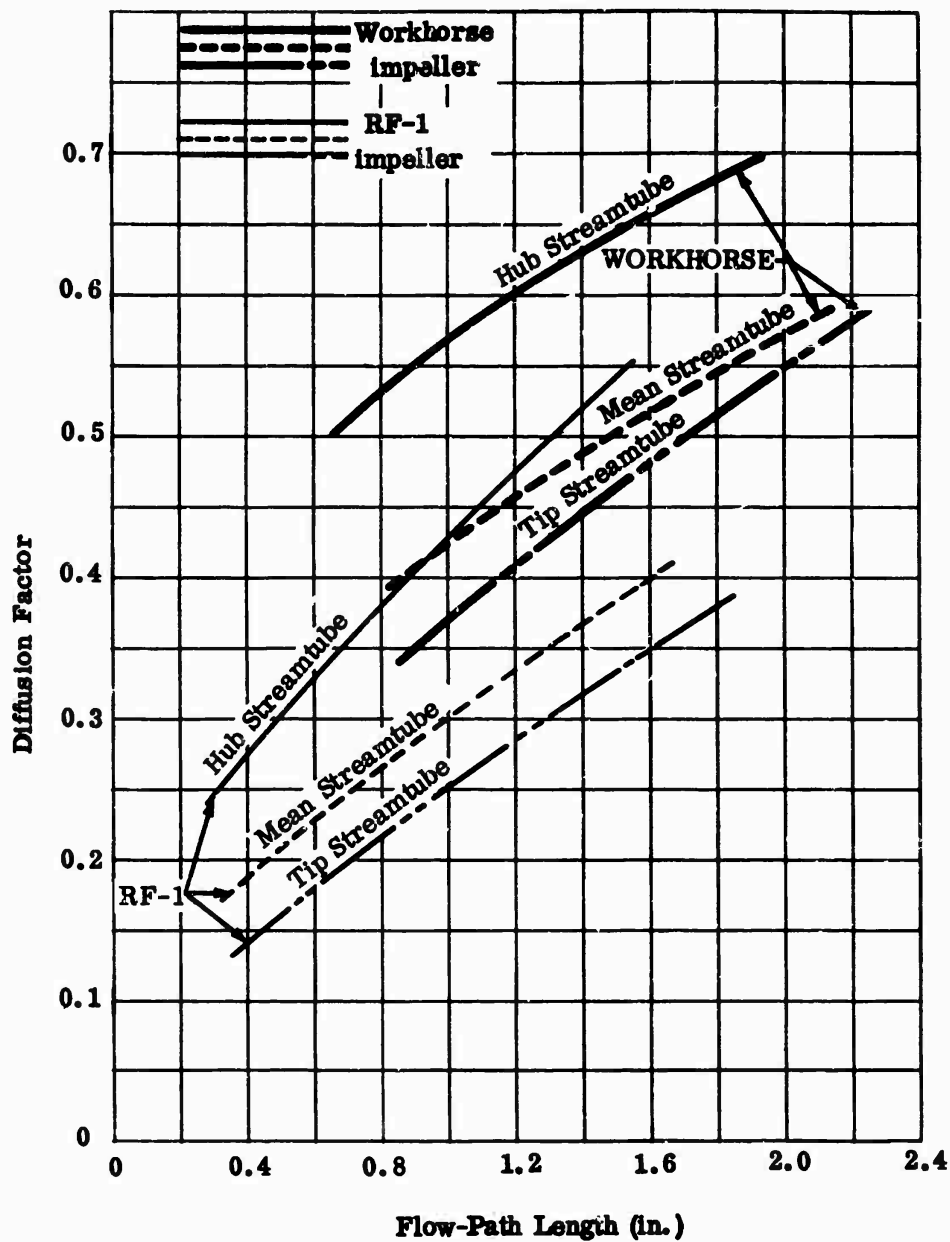


Figure 363. Design Diffusion Factors, Workhorse and RF-1 Inducers.

CONFIDENTIAL

TABLE XXV			
INLET MACH NUMBER AND INCIDENCE, WORKHORSE AND RF-1			
Impeller	Inlet Relative Mach Number (tip)	Inlet Relative Mach Number (RMS)	Incidence (RMS)
Workhorse	1.07	0.93	+6 to +9 degrees
RF-1	1.02	0.90	+5 to +8 degrees

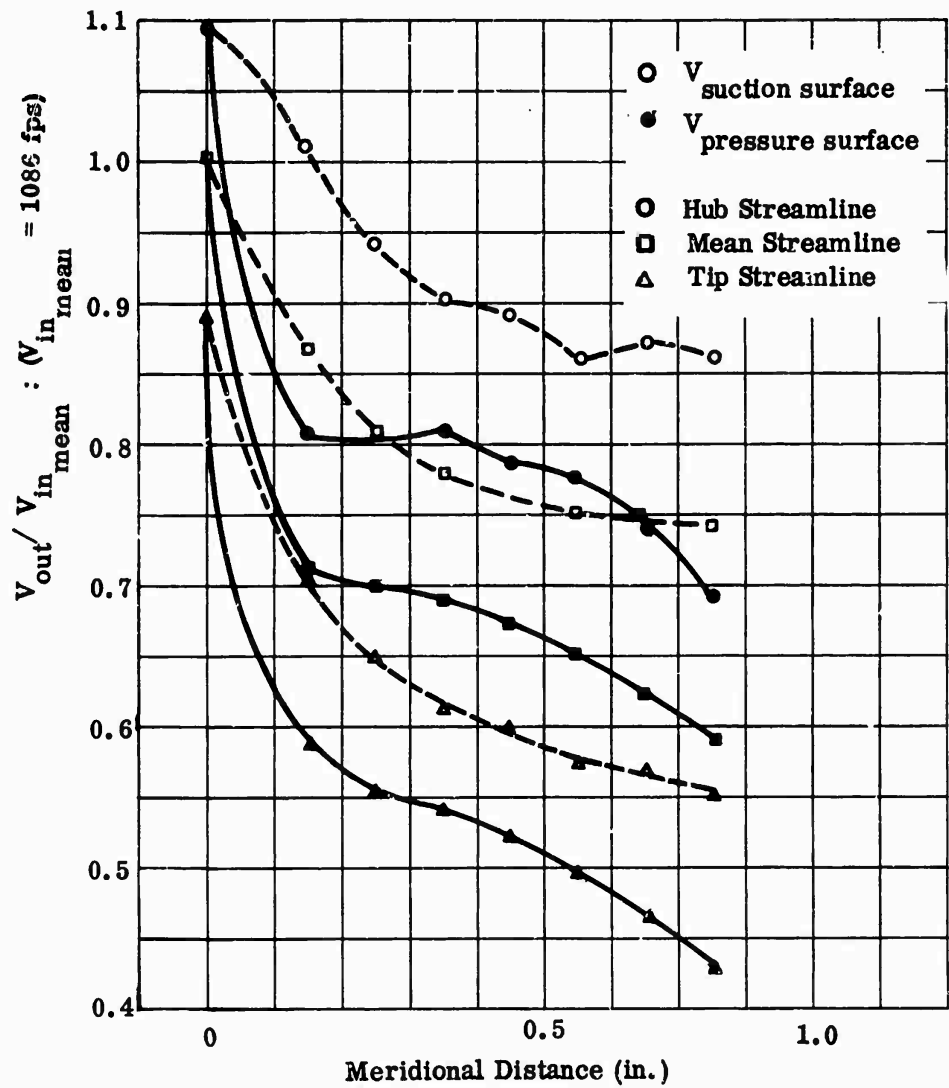


Figure 364. Blade-Surface Velocities, Workhorse.

CONFIDENTIAL

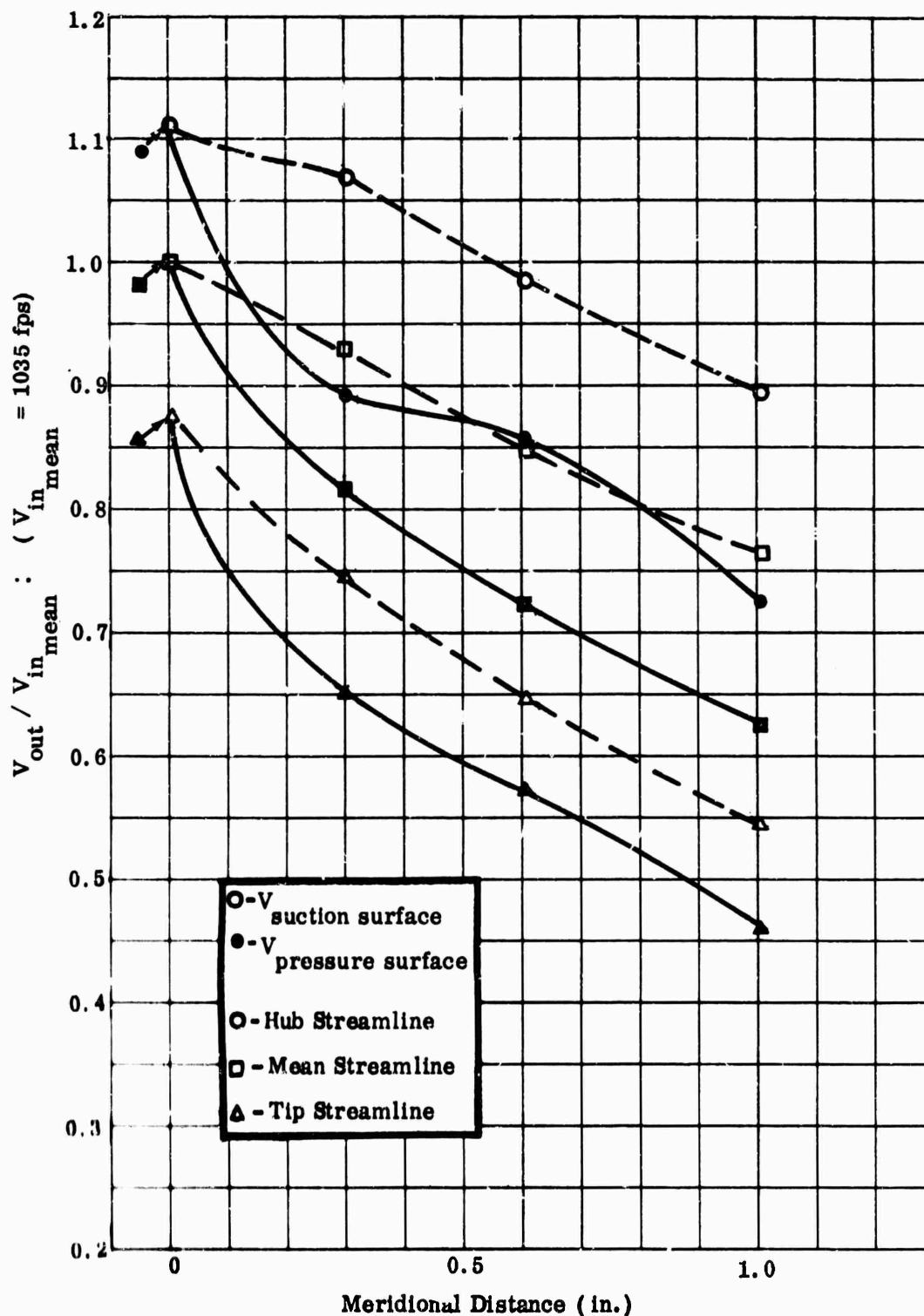


Figure 365. Blade-Surface Velocities, RF-1.

CONFIDENTIAL

calculations (see Reference 22) and revealed that it may be desirable to have a rapid deceleration in the inducer region where the boundary-layer displacement thickness is smallest. The shape factor, which is the ratio of the boundary-layer displacement thickness to the momentum thickness, is a measure of the boundary-layer profile. The larger the shape factor, the nearer the point is for separation; or, for a given momentum thickness, the larger the displacement thickness, the more imminent is separation. When decelerating at a slow rate, the boundary-layer displacement thickness is considerably larger than when the same final velocity is attained by a rapid deceleration. Therefore, rapid deceleration of flow might be considered the most logical way to design an inducer. However, a rapid deceleration of the flow early in the inducer is in contrast to axial-rotor criteria that place limits on diffusion factor, which is primarily a function of the diffusion through the blade row,

$$\text{Diffusion Factor, D.F.} = 1 - \frac{V_{\text{local}}}{V_{\text{inlet}}} + \frac{\Delta V_{\text{tangential}}}{2\sigma V_{\text{inlet}}} \quad (34)$$

If the velocity ratio is low, the diffusion factor can only be reduced through increased solidity. This trend toward high solidity can lead to a large number of inducer blades and high blockage at the inducer-entry region.

Effects of Blockage on Mach Number and Incidence — Section 2.0 has shown that the inducers were designed with high inlet Mach numbers ranging from 0.95 to 1.23. Further, it was apparent from the Analytical Studies that both Mach number and incidence would be strongly dependent on the actual blockage. Therefore, the effects of blockage on the inlet Mach number and the vector diagram were investigated thoroughly.

It can be seen in Table XXV that the RMS incidence of the workhorse and RF-1 impellers was between +5 and +9 degrees. This incidence was determined using the static pressure measured along the inlet hub and shroud, as presented in Section 6.0. Assuming a linear variation between hub and shroud, the absolute velocity was calculated for the given airflow. Knowing the rotor speed, the vector diagram was constructed, and incidence was determined with respect to the mean camber line of the blade. Section 2.0 has shown that the impellers were designed with about 1.0-degree incidence, which is different than that calculated from test data. One reason for this difference has been related to the method of calculating blade blockage at the inducer inlet. Another is the technique used in compensating for the blockage. For example, axial compressor inlet vector diagrams are generally calculated with blockage factors of 1.0, but the design must then incorporate an incidence of +3 to +5 degrees to ensure that the rotor

CONFIDENTIAL

will pass the design airflow. On the other hand, centrifugal impeller designs generally have blockage applied to the vector calculations, and a low incidence is used (1.0 degree).

In the original impeller designs for this program, the blockage was determined based on leading-edge blade thickness (see Figure 366).

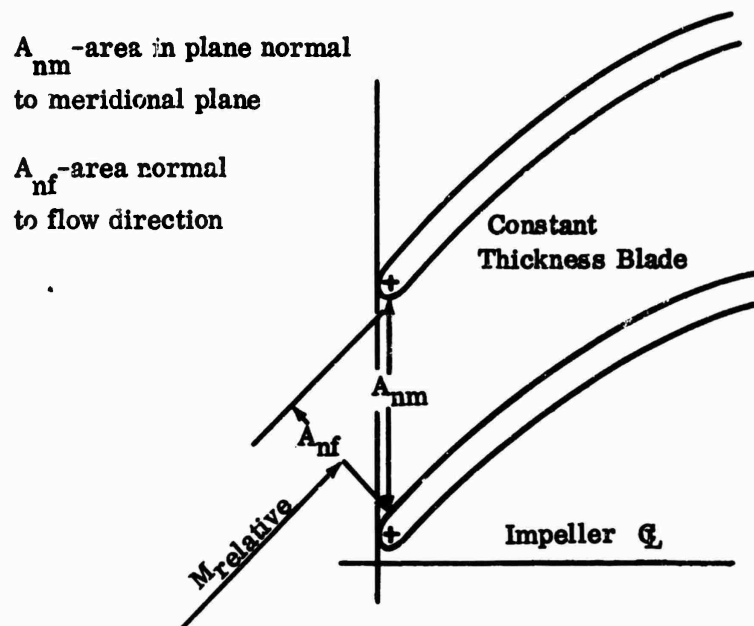


Figure 366. Blockage-Flow and Area Calculation, Constant Blade Thickness.

The available flow area was determined in a plane normal to the impeller centerline and then rotated for the relative flow as shown in Figure 366 for constant-thickness blades. Therefore, the blade blockage was determined as:

$$\text{Blocked Area} = 2 \times (\text{Number of Blades}) \times (\text{Blade Height}) \times (\text{Average Leading-Edge Radius}).$$

The high incidence noted in Table XXV illustrates that the blocked area was greater than that predicted. It was determined that this difference was caused by the double-circular-arc-type blade used in the impeller designs. Figure 367 is a sketch of the inducer leading edge with a double-arc blade.

CONFIDENTIAL

CONFIDENTIAL

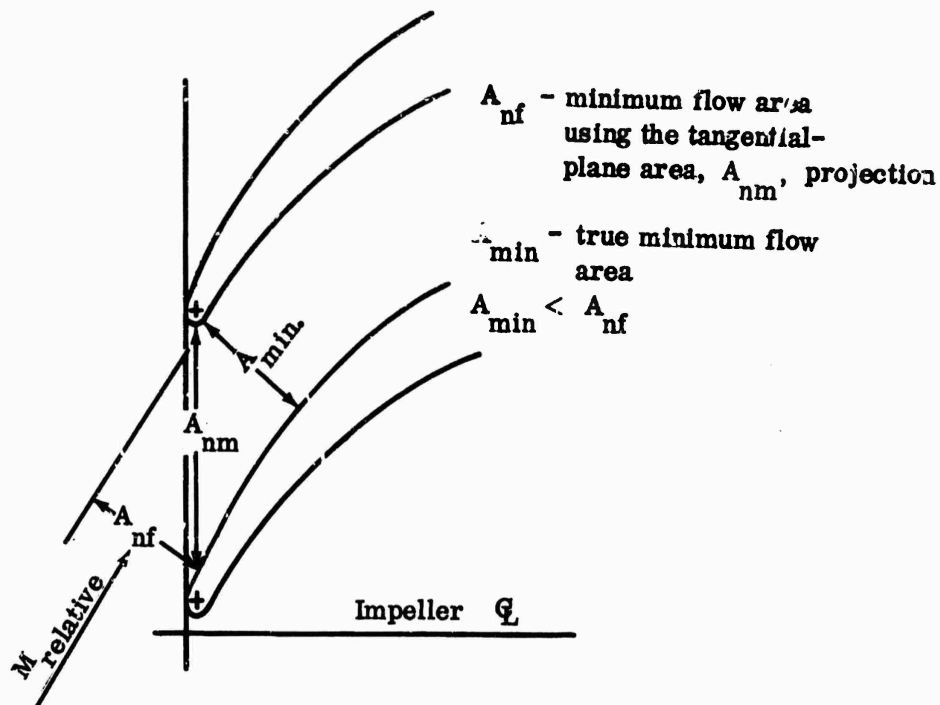


**Figure 367. Blockage-Flow and Area Calculation,
Circular-Arc Blade.**

It can be seen that the thickness increases beyond the leading edge, causing the effective blockage to be further increased. In the case of the previous parallel-type inducer blades, the change in blade angle was sufficient to place the minimum area at the leading edge. With the increased thickness of the double-circular-arc blade, the camber was not enough to compensate; therefore, a minimum area downstream of the leading edge occurred.

Original Impeller Loss Analysis

In designing the impellers, empiric¹ total-pressure-recover data were used. These data were generated from previous tests conducted by the contractor and showed the variation of inducer total-pressure recovery with inlet relative Mach number and incidence. In each design, a loss-accounting analysis was undertaken, and the losses considered were:

- 1) Hub and shroud friction loss;
- 2) Diffusion and blade-loading loss.

The methods described in Reference 20 were used in the calculations. Analytically determined losses were found less than or equal to the empirical data;

CONFIDENTIAL

CONFIDENTIAL

therefore, the designs were considered acceptable. Using either the analytical- or empirical-loss data, the differences between RF-1 and MF-1 could not be explained.

Flow Model

Since the loss analysis failed to point out the large (approximately 15 percent) difference in the total-pressure recovery for the workhorse and RF-1 impellers, it was apparent that the basic impeller flow model and the resulting loss analysis required revision. From technologies available when these impellers were designed (see Section 2.0 and Appendix I), the flow model could be described as follows:

The flow approaches the impeller at some incidence which, as mentioned previously, depends on blade blockage, inlet relative Mach number, and inlet blade angle. Because no reliable method was available for determining the flow field on the blade surfaces near the leading edge, the analysis was concerned mainly with the average flow midway between the blades. Downstream, well into the inducer, the Rapid Approximate Method (Reference 4) was used for predicting the blade-surface velocities. It was believed that the double-circular-arc blade in the leading-edge region would result in best inducer performance. Axial rotors using this type of blade were successful in a similar regime of Mach number and incidence angles.

The analysis recognized that the flow along the suction surface at the leading edge was very important for avoiding separation and achieving best performance. It was expected that by using proved blade sections in this region, the performance objectives would be realized. Downstream of the blade leading edge, diffusion rates provided by 2-dimensional boundary-layer calculations and axial-rotor loss correlations were used to determine the amount of diffusion which could take place before separation occurred. If the local velocities at the leading-edge region were ignored, separation was predicted at velocities low enough so that no large mixing loss (within or downstream of the impeller) was expected. Therefore, no allowance was made for mixing losses other than those associated with diffusion and blade loading.

7.1.7 REVISED LOSS ANALYSIS

In the preceding discussions, it was shown that the original loss analyses for impellers were not adequate for design at rotor pressure ratios near 13:1.

Therefore, an extensive survey of new information relative to fluid mechanics of centrifugal impellers was undertaken. Both empirical and theoretical information were perused. Dean and Senoo (Reference 23) reported that for

CONFIDENTIAL

CONFIDENTIAL

low-specific-speed impellers (such as the workhorse and RF-1), where flow separation may be extensive, the loss caused by mixing of the jet-wake flow in the vaneless diffuser will be significant. Once the flow separates from the suction surface, the main flow acts as a jet along the pressure surface to the exit (see also Section 2.1.1). The separated region (wake) has almost no flow. For compressible flow, Dean's theory of the separated impeller leads to a jet of constant bulk mean relative Mach number. A schematic sketch of flow in the impeller is shown in Figure 368. This theory has been confirmed for the incompressible flow case by water visualization studies which indicate that the cross-sectional area of the jet remains constant from the separation line to the impeller rim.

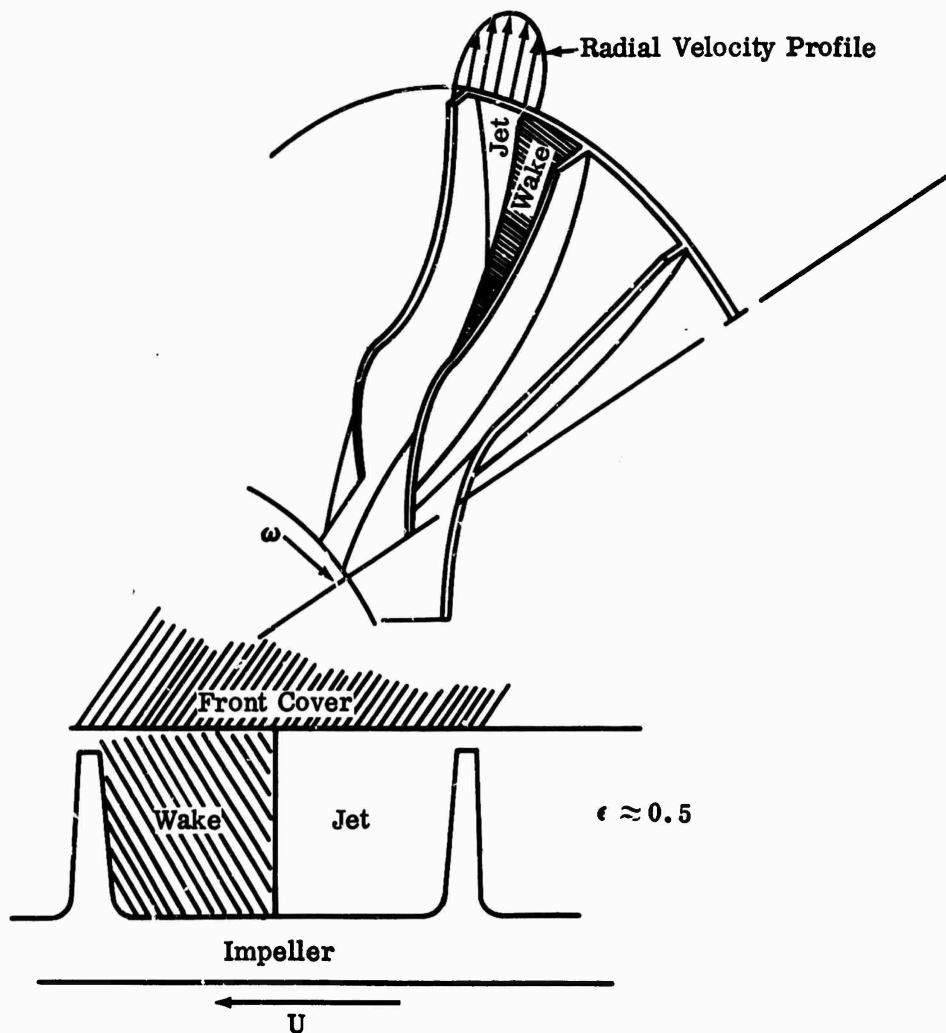


Figure 368. Schematic of Impeller Flow.

CONFIDENTIAL

CONFIDENTIAL

Additional impeller losses are related to friction and clearance. Although friction was included in the design analysis, the exact effects of clearance were not known. However, the need for small blade-to-shroud clearance was well recognized. Another consideration was internal mixing, but it was reasoned that very little mixing of the jet and wake flow took place inside the impeller because of the suppressive nature of the blade-to-blade component of the Coriolis force, which is quite significant for radial-flow machines. Inducer leading-edge shock losses were not included because they were believed to be of secondary magnitude.

Friction Loss

Friction losses within the impeller are dependent on the absolute velocity along the shroud and the relative velocity along the blade and hub. These losses were calculated by using the methods derived for friction-flow analyses from Reference 20.

Shroud Friction Loss — This loss is caused by skin friction as the fluid flows along the stationary-shroud surface. This loss was approximated by using a simple plate-flow analogy as follows:

$$\Delta P = K_1 (4 C_f) \frac{L}{D} \left(\frac{\rho V^2}{2 g_0} \right) \quad (35)$$

where:

ΔP = pressure loss (lb/ft²)

K = empirical constant ≈ 1.4

C_f = friction factor = $0.074/(\text{Re})^{0.2}$

L = flow-path length (ft)

D = local diameter (ft)

ρ = average density (lb/ft³)

V = local velocity (ft/sec)

CONFIDENTIAL

g_0 = proportionality constant in Newton's Law $\left(g_0 = 32.2 \frac{\text{lb}_m \text{ ft}}{\text{lb}_f \text{ sec}^2} \right)$

F = $\frac{ma}{g_0}$ in English units

Re = average Reynolds number = $\frac{\rho (L/2) V}{\mu}$

Hub and Blade Friction Loss — This loss is evaluated using the common expression for pipe loss at equivalent conditions as follows:

$$\Delta P = 3/4 \left[(2C_f \rho) \left(\frac{L}{d_H} \right) \left(\frac{W^2}{2 g_0} \right) \right] \quad (36)$$

where:

ΔP = pressure loss (lb/ft^2)

L = average flow length (ft)

d_H = average hydraulic diameter of passage (ft)

W = average relative velocity (ft/sec)

C_f = friction factor for a pipe with diameter d_H
evaluated for the appropriate surface roughness

at $Re = \frac{\rho d_H W}{\mu}$

The 3/4 factor accounts for the fact that the shroud loss is calculated separately.

Clearance Losses

Clearance losses result from flow leakage from the pressure to the suction side through the finite clearance between the stationary shroud and the rotating blades. The loss was estimated by using the empirical equation presented in Reference 11.

CONFIDENTIAL

For an assumed blade loading, the loss is:

$$\Delta P = K \left(\frac{\Delta n}{b} \right) \left(\frac{V_{T4}}{D} \right) \left[\frac{8 W_a V_{T4}}{U_4 (d_r - d_{si}) b Z (\rho_1 + \rho_4)} \right]^{1/2} \cdot \left(\frac{(\rho_1 + \rho_4) U_4^2}{2 g_c} \right) \quad (37)$$

where:

- ΔP = pressure loss (lb/ft²)
- K = empirical constant ≈ 0.6
- Δn = clearance (ft)
- b = impeller-tip blade width (ft)
- V_{T4} = impeller-tip absolute-tangential velocity (ft/sec)
- U_4 = wheel speed at impeller tip (ft/sec)
- W_a = airflow (lb/sec)
- d_r = impeller-tip diameter (ft)
- d_{si} = inducer-shroud-entrance diameter (ft)
- Z = number of blades
- ρ_1 = density at inducer entrance (lb/ft³)
- ρ_4 = density at impeller tip (lb/ft³)

The friction losses were determined by summing the calculated losses for 8 to 10 small increments of flow-path length, while the clearance loss was calculated in one step for the entire impeller.

CONFIDENTIAL

CONFIDENTIAL

Exit Mixing Loss

Exit mixing loss is related to separation inside the impeller passage. When the flow leaves the impeller tip and enters the vaneless space, a sudden area increase is felt as the jet and wake mix together. The mixing loss is evaluated as a sudden dump of the radial vector. The radial vector is influenced by the exit-jet Mach number, the ratio of wake-width-to-jet-width at the impeller tip, and the angle of the flow leaving the impeller. Because the exit mixing loss can be a large part of the total-pressure loss, it is important in any impeller design to avoid early separation. Therefore, evaluation of the impeller design must include an analysis to determine where separation inside the impeller will occur and a method of selecting inducer-blade shape to delay separations as far along the impeller flow path as possible. It is recognized that overvelocities exist on the suction surface near the blade leading edge and that the magnitude of this velocity is dependent on the inlet relative Mach number as well as incidence. From boundary-layer considerations it can be shown that flow in the passage will separate after a velocity reduction of about 40 percent. In addition, there is an initial overvelocity on the blade which has a major influence on the separation point. If this overvelocity is large enough, separation can occur at the leading edge. Because of the importance of determining the flow conditions at the point of separation, a detailed discussion of the analyses and a literature review on this subject will be presented in Section 7.1.8.

The analytical techniques used are similar to those presented in Reference 23 for the incompressible case. Curves showing the variation of the total-pressure recovery P_0^*/\bar{P}_0 through the mixing process are shown in Figures 369 through 372 as functions of the ratio of the wake-width-to-blade-pitch (ϵ), the tangent of the absolute flow angle (λ) at the impeller tip, and the bulk mean absolute Mach number (M). These mixing loss curves were calculated with the assumption of zero flow out of the wake.

$$\epsilon = \frac{\text{wake width}}{(2\pi) (\text{radius})_{\text{tip}} / \text{number of blades}}$$

$$\lambda = \text{tangent of bulk mean absolute flow angle at the tip}$$

$$\frac{P_0^*}{\bar{P}_0} = \frac{\text{total pressure after mixing}}{\text{mass-averaged total pressure before mixing}}$$

Comparison of Loss Analysis With Test Data — The preceding impeller analysis was used as a tool to determine the magnitudes of losses that occur. Before this analysis can be accepted it must be evaluated with respect to the test data from the program, and finally the loss analysis must be incorporated as part of an

CONFIDENTIAL

CONFIDENTIAL

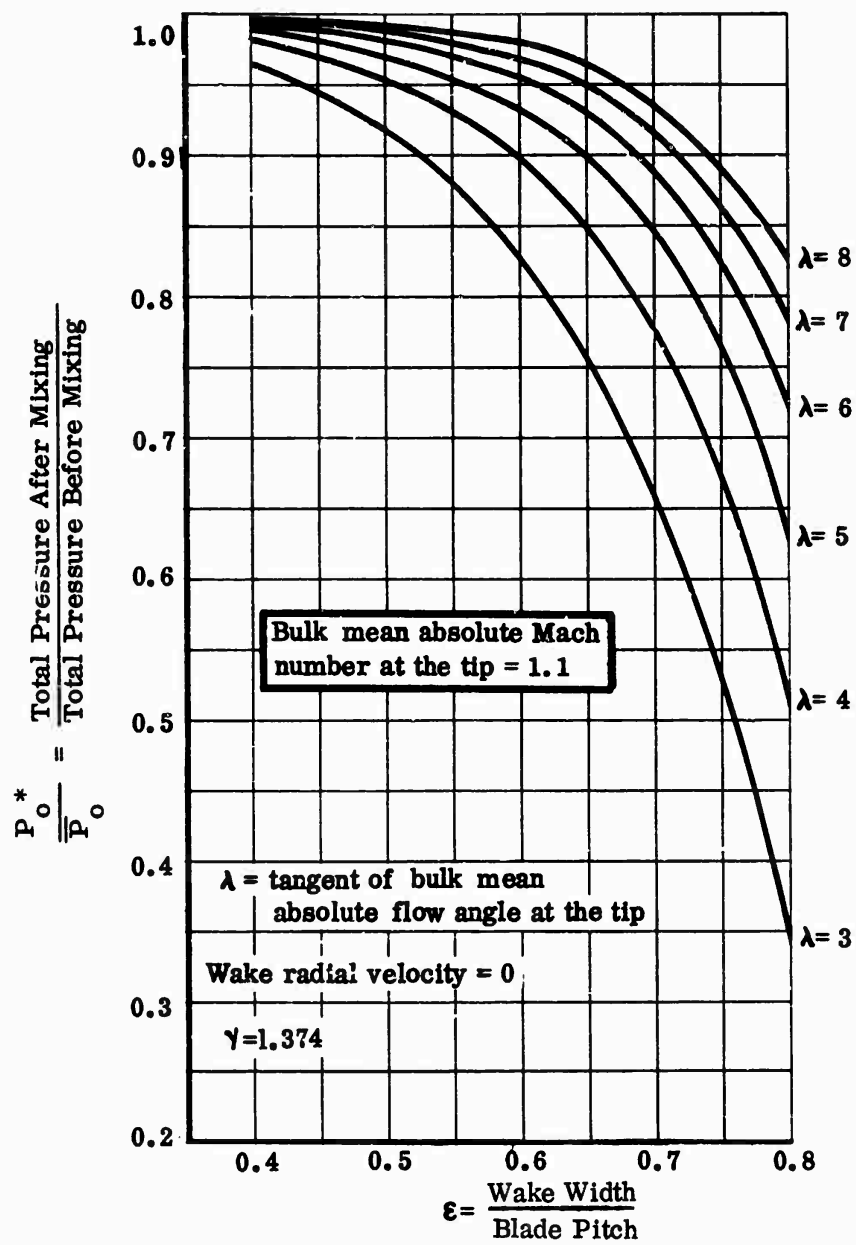


Figure 369. Impeller-Exit Mixing Loss.

CONFIDENTIAL

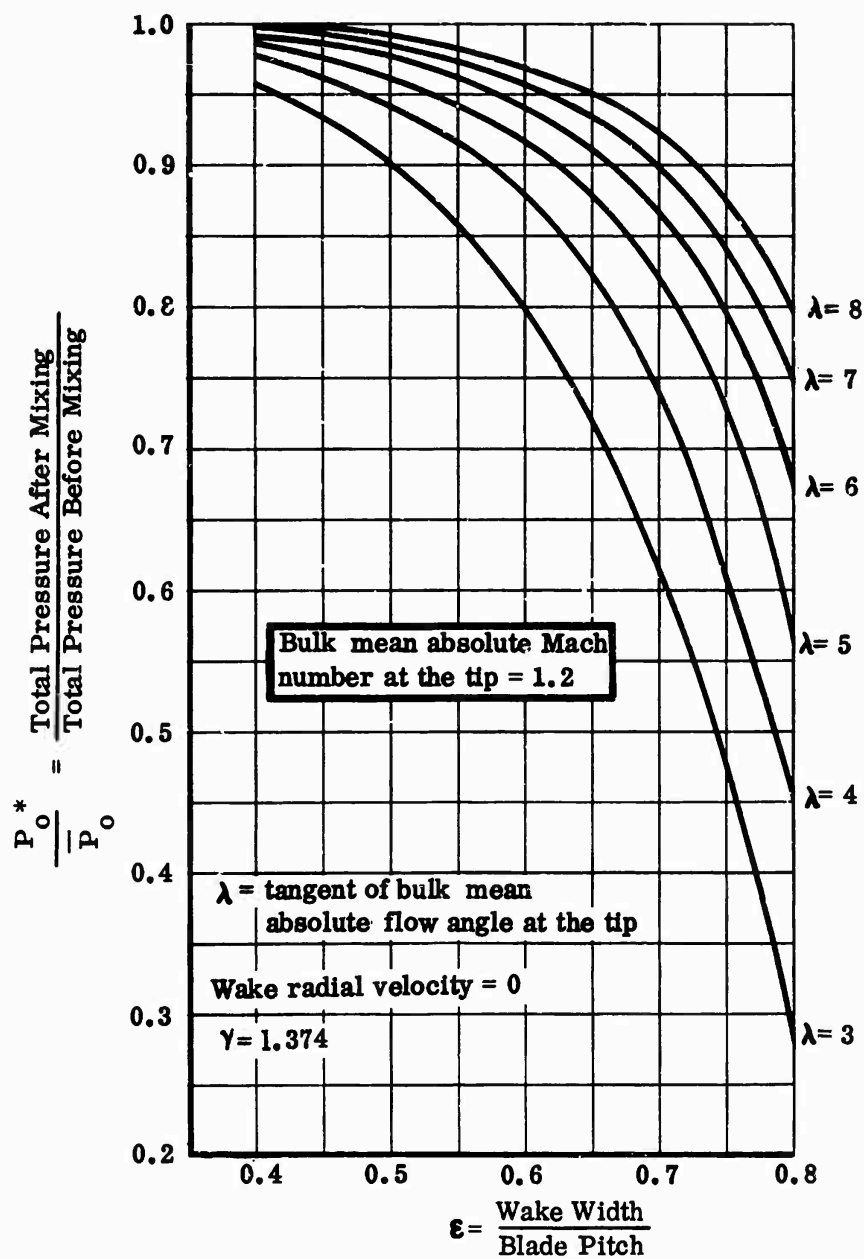


Figure 370. Impeller-Exit Mixing Loss.

CONFIDENTIAL

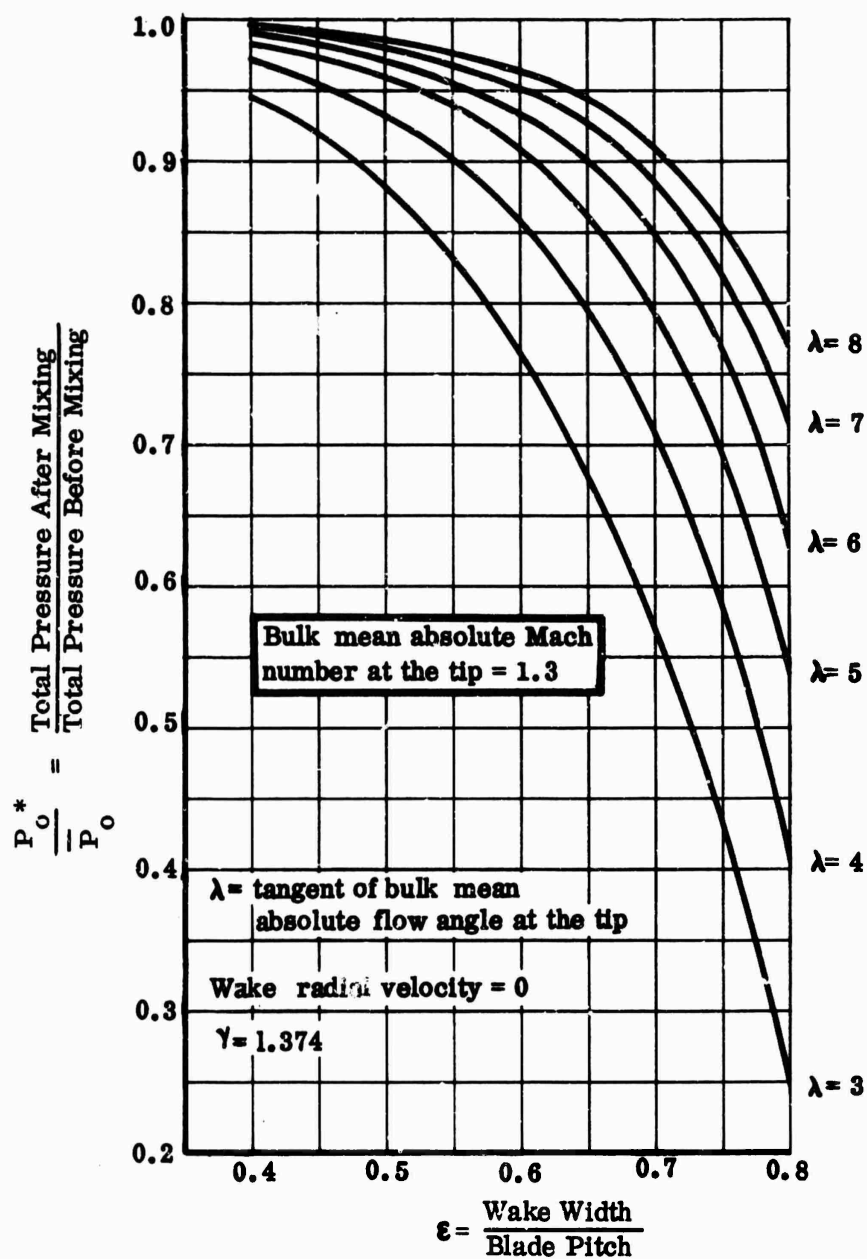


Figure 371. Impeller-Exit Mixing Loss.

CONFIDENTIAL

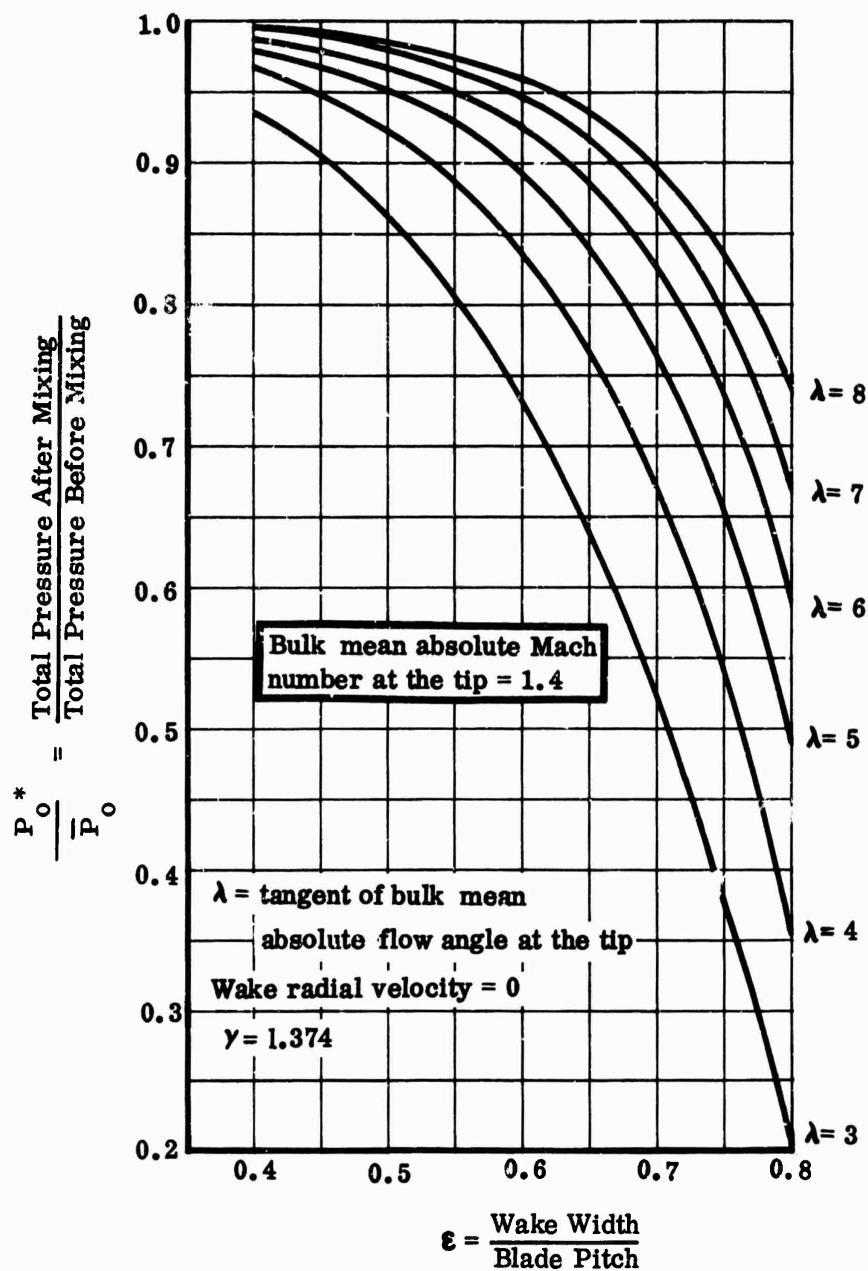


Figure 372. Impeller-Exit Mixing Loss.

CONFIDENTIAL

impeller-design method. Since the flow conditions at the impeller tip were known from test, the loss could be calculated without determining the separation point. For the analysis, the measured static pressure at the exit of the impeller was used with the calculated relative total pressure at the exit to determine the bulk mean jet Mach number in the following manner.

- 1) Static pressure at the exit was obtained from plots of shroud static pressure versus distance along the shroud.
- 2) Relative total temperature at the exit was obtained from the Euler work relationship:

$$h_{T_3} = h_{T_1} + \frac{U_e^2}{2gJ} - \frac{U_i V_{T_1}}{gJ}$$

where:

h_{T_3} = specific relative total enthalpy at impeller exit (Btu/lb)

h_{T_1} = specific absolute total enthalpy at impeller inlet (Btu/lb)

U_e = impeller-exit peripheral speed (ft/sec)

U_i = impeller-inlet peripheral speed (ft/sec)

V_{T_1} = tangential component of the inlet absolute velocity (ft/sec)

g = acceleration due to gravity (32.17 ft/sec²)

J = mechanical equivalent of heat $778 \frac{\text{ft-lb}}{\text{Btu}}$

and $T_{T_3} = f(h_{T_3})$ (38)

CONFIDENTIAL

CONFIDENTIAL

- 3) The isentropic relative total pressure at the exit is obtained from:

$$P_{T_{3i}} = P_{T_2} \left(\frac{T_{T3}}{T_{T2}} \right)^{\frac{\gamma}{\gamma - 1}} \quad (39)$$

where the subscript 2 refers to the inlet-relative conditions.

- 4) The relative total pressure at the exit is calculated by reducing the isentropic value by the internal losses determined from the relationships described above.

$$P_{T_3} = P_{T_{3i}} (e)^{-(J/R) (\Delta S)} \quad (40)$$

where:

P_{T_3} = calculated relative total pressure at the impeller exit (lb/in.²)

e = base of the Napierian system of logarithms (2.7182)

R = gas constant for air ($53.3 \frac{\text{ft-lb}}{\text{lb-}^\circ\text{R}}$)

ΔS = specific entropy change

$$\left[(\Delta S)_{\text{clearance}} + (\Delta S)_{\text{Hub and Blade Friction}} + (\Delta S)_{\text{Shroud Friction}} \right] \left(\frac{\text{Btu}}{\text{lb-}^\circ\text{R}} \right)$$

- 5) The bulk mean jet Mach number is determined from

$$M_{3_{\text{jet}}} = f \left(\frac{(P_s)_{\text{exit}}}{(P_{T3})_{\text{calculated}}} \right)$$

CONFIDENTIAL

For the purposes of analysis, a simple square-wave was assumed for the jet-wake relative-velocity profile at the exit of each blade passage with no axial variation of the relative velocities as shown in Figure 373.

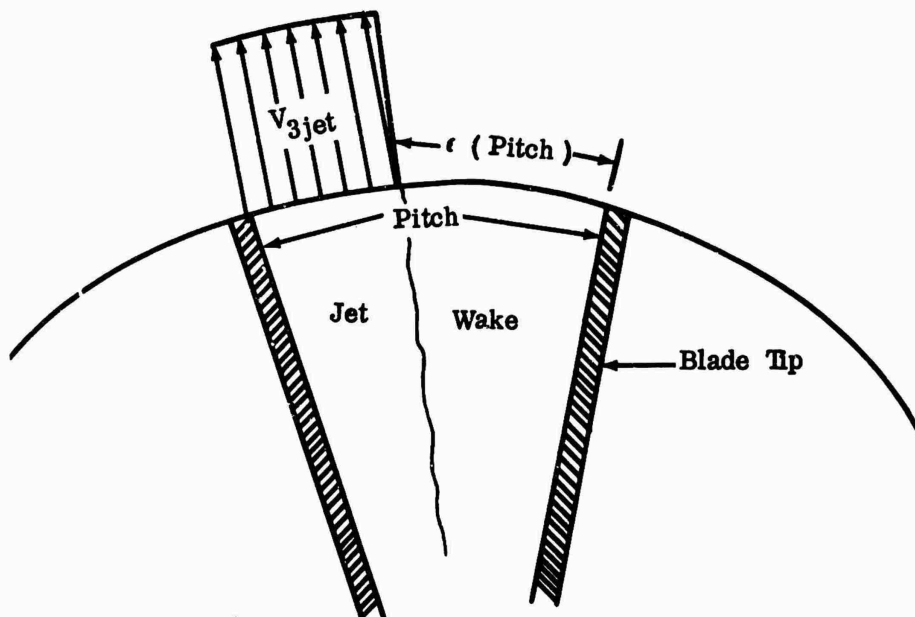


Figure 373. Jet-Wake Relative-Velocity Profile.

These assumptions are consistent with those of the authors of Reference 23. In addition, an initial assumption was made that the wake had a zero through-flow velocity. With the flow model described above, the calculated jet Mach number and total temperature, and the measured value of the slip factor, it was possible to calculate the ratio of the wake width to the blade pitch at the impeller exit from continuity considerations. The bulk mean absolute Mach number and flow angle at the exit were then determined. The appropriate curves (Figures 369 through 372) were used and the exit mixing loss was determined.

Since the exit mixing theory adopted for this analysis (Reference 23) indicates that the mixing is completed at a small radius ratio ($R/R_{tip} \approx 1.02$ to 1.05), it was assumed that the impeller-exit total pressure measured at a radius ratio of 1.02 to 1.03 included the mixing loss. It was recognized that the degree of correlation depended on this assumption. If the predicted impeller pressure ratio agreed with the measured value, it can be assumed that the jet vector diagram and, therefore, the jet relative Mach number (as determined by the test static pressure and the calculated internal losses) were correct. Then, using the free-jet flow model, the

CONFIDENTIAL

CONFIDENTIAL

relative Mach number at the separation line can be determined. The separation Mach number would then help to indicate the amount of diffusion accomplished within the inducer section.

With the zero wake flow assumption, the analysis did not produce the desired agreement between the measured and predicted impeller pressure ratios. The results showed that the predicted pressure ratio was 10 to 15 percent higher than the mass-flow averaged impeller pressure. This difference illustrated that the assumption of zero flow through the wake region, invoked to simplify the analysis, was not valid.

A thorough evaluation was conducted to determine sources of the disagreement, such as increase in the internal losses. For example, an increase in the friction and clearance losses will result in a corresponding decrease in the exit mixing loss, because of the change in jet-wake width, resulting from a decrease in the jet relative total pressure. The evaluation showed that the exit mixing loss must be higher to effect an agreement.

Further analysis showed that agreement could be reached between the calculated and measured pressure ratio when the assumed airflow through the wake was increased from zero to near 20 percent. This causes an increase in the wake width, resulting in the higher exit mixing loss necessary to reach agreement. Therefore, during an impeller design, it would be necessary to add a further complication of predicting the percent of airflow through the wake to determine the losses. Predicting flow in the wake appears to be a complex problem and may require extended empirical study. The empirical study should be conducted to determine the wake velocity distributions from hot-wire traces and/or relative-total-pressure measurements.

7.1.8 OVERVELOCITY AND SEPARATION CONSIDERATIONS

The previous analysis showed that the overall loss was very dependent on the location of suction-surface separation and the static-pressure rise through the impeller. Therefore, refinement of the design method was necessary to permit prediction of the velocity at the point of separation. Accurate prediction of this velocity requires a solution of the flow around the nose of the inducer blades. Three approaches were evaluated, and the overvelocity at the nose of the blade suction surface was calculated and was followed by a determination of the allowable velocity-reduction ratio before separation occurred.

Thin Airfoil

To define the velocity distribution at the blade-nose region, it was necessary to revert to perfect-fluid theory in the form of either the method of conformal mapping or the method of singularities. The former method is more exact, but

CONFIDENTIAL

CONFIDENTIAL

the latter is more easily applied and is suitably accurate in view of the inherent limitations of perfect-fluid theory. In the method of singularities, blade profiles are assumed thin and slightly cambered and the blades are replaced by vortices arranged along the chord. The theory has been developed by Glauert (Reference 24), Riegels (Reference 25), and Schlichting (Reference 26) and is referred to as thin-airfoil theory. The extension of Schlichting's analysis to mixed-flow cascades is presented in Reference 27. Using this method, however, requires a modification to the solution in the nose region in the form of Riegel's factor. This modification eliminates an anomaly at the nose that developed from the method of singularities, where an infinite velocity at the leading edge at any incidence other than ideal would be calculated.

Using Schlichting's method for cascades (as presented in Reference 27) gives a solution which is valid for the assumptions and is consistent with 2-dimensional perfect-fluid theory.

Potential Flow

A more simple overvelocity prediction is obtained by using the results of the potential-flow analysis from Reference 28. This analysis shows overvelocity coefficients of 1.26 for a modified-arc nose and a velocity peak of 1.5 times the free-stream value for a half-cylinder on a plate (see Figure 374).

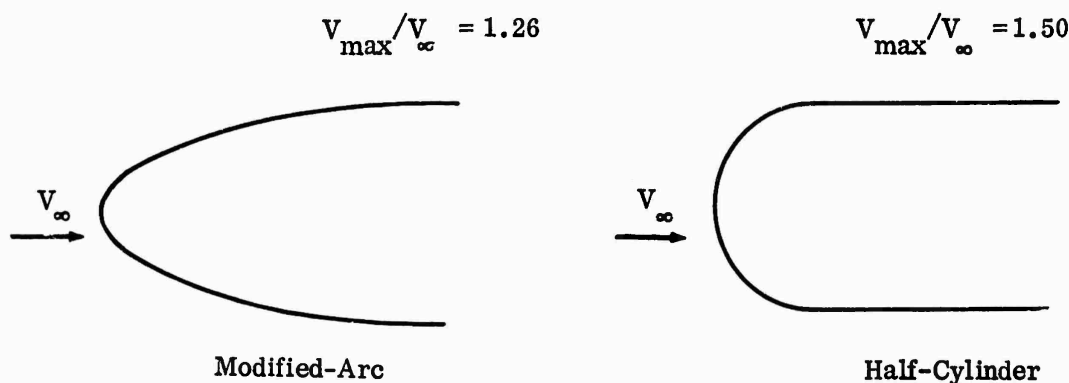


Figure 374. Overvelocity Coefficients.

Compressibility Corrections — In applying the results of Schlichting's method (or the isolated-airfoil potential-flow method) to inducer blading, corrections must be made first for the effects of compressibility, and second, for the spanwise (along the blade height) variation in the blade loading. The compressibility effects, which can be incorporated using Gothert's rule if sonic velocities are not reached on the profile, greatly increase the predicted overvelocity. This is still only

CONFIDENTIAL

two-dimensional, and, therefore, is not representative of the flow conditions on the blading of an inducer. The inclusion of the 3-dimensional effects is much more difficult.

There are some considerable 3-dimensional effects in the inducers of centrifugal impellers. First there is the leakage of flow over the tip of the blade through the clearance space which may approach the thickness of the blade itself. Tip leakage over the usual high-performance centrifugal blade is such that it most likely improves flow conditions on the suction surface of the blade near the tip in the leading-edge region. Leakage attenuates the highest Mach number spikes on the blades (that is the lowest static pressures) by fluid flowing into these regions and relieves the severe acceleration there. Of course, tip leakage causes some loss in efficiency and cannot be ignored, but it has been shown to be relatively small by comparison to separation or mixing. Rains shows the attenuation effect of the leakage in Reference 29.

Another cause of 3-dimensional effects is the variation of loading along the span of the blade, caused by the necessity to design radial-element blades — fluid at the tip of the inducer blade absorbs much more work than that at the hub. The result is that the pressure loading on the blade is greater at the tip than at the hub. Therefore, strong spanwise pressure gradients, which are not balanced by the centrifugal acceleration, can develop. These gradients tend to promote outward flow on the suction side of the blade and inward flow on the pressure side. The spanwise flows further influence pressure distribution around the blading.

Wing Theory

In the preceding sections, the flow field was defined by using an ideal fluid with a compressible modification from Gothert's rule. It has been shown that this solution is not valid for supersonic flow where the blades are susceptible to the influence of shock-boundary-layer interaction (Reference 9). Therefore, application of analyses of cascade and single-transonic-wing theory was pursued.

It was believed that inducers at high subsonic Mach numbers generate fluid-flow conditions similar to transonic-axial-compressor blades and wings. However, no detailed experimental investigations of flow analogies with inducers was available in the literature. The transformation appears to be valid, although flow through transonic-axial-compressor cascades may require a separate detailed confirmation. Most of the prior experimental work was aimed at establishing overall cascade characteristics (and has been useful to the understanding), but such data are difficult to tie explicitly to the flow phenomenon which occurs. As an example, Reference 30 is a study of the fluid-mechanics treatment of transonic cascade in some detail. This work offered some insight of the basic investigations necessary. However, the most important region for the inducer appears to be the leading-edge section of the airfoil, where the axial-cascade investigations in the literature

CONFIDENTIAL

CONFIDENTIAL

do not provide sufficient information. Therefore, data from wing profiles must be used instead. With these data, some particular studies have been made of the leading-edge region (Reference 31). Undoubtedly, there are other studies in the literature which have not been discovered. Although the inducer appeared to operate in a manner similar to a transonic-axial-compressor rotor, the blading was conventionally stacked in a different fashion, as previously noted. The inducer and the axial cascade do have so-called cascade effects which do not occur with the single wing; i.e., the influence of one blade upon another which may alter the fluid dynamics from the wing case. But most inducers, particularly near the tip where the Mach numbers are highest, have relatively large stagger angles (inlet angles between 45 and 60 degrees from axial). The blades usually are also closely spaced so that a considerable portion of the leading-edge region extends as a wing into the entry space. For this reason, it is believed that single-wing theory, methods, and experimental data can be applied.

One of the principal differences between the inducer (and axial cascade) and the aircraft wing is in Reynolds number. For example, at a free-stream Mach number of 0.85, transition occurs on a flat plate about 1/2 inch behind the leading edge. If the flow is sharply accelerated, transition will be delayed; but as soon as diffusion begins, transition should occur. In the actual case, transition to turbulent flow will occur on an aircraft wing near the airfoil nose. By comparison, a considerable fraction of the inducer blade (up to the throat) may be in the laminar regime. Therefore, a significant alteration in the fluid-mechanics analogy was necessary. According to Reference 9, the laminar boundary layer can withstand only about a 6-percent velocity change before it separates. In contrast, the turbulent boundary layer can stand about 35-percent velocity change. Thus, a weak shock will more readily separate a laminar boundary layer than a turbulent one. In general, shocks will not occur on a blade profile until the high-curvature nose portion has been reached. For an aircraft profile, this shoulder will come in the turbulent boundary layer, while for inducers it may well lie in the laminar region.

Even for flat plates with Reynolds numbers about an order of magnitude higher than those typical of small inducers, the authors of Reference 31 observed laminar shock-induced separation below an approach Mach number of about 0.83. If the Reynolds number were reduced an order of magnitude (as in the inducer case), the Mach number at which the boundary layer under the shock changed to turbulent would rise considerably. Very likely, laminar separation could persist up to an approach Mach number of unity. This consideration must be kept in mind, or it might preclude use of much of the airfoil data in the literature.

Shock-Induced Separation — Pearcey (Reference 32) summarizes separation of laminar and turbulent boundary layers caused by the impingement of shock waves and shows that the important physical factor is the pressure rise to the point of separation and not whether the shock is oblique or normal. It is also shown that this pressure rise is not to be taken as that which occurs by reason of the shock

CONFIDENTIAL

CONFIDENTIAL

interaction with the boundary layer — there is often a subsequent pressure rise caused by the recovery of the boundary layer from the effects of the shock, downstream of the shock location. This overall pressure rise across the shock-affected region may not be the only parameter against which to correlate separation tendencies. Pearcey (Reference 32) summarizes the separation criteria for both laminar and turbulent boundary layers.

The separating-pressure coefficient depends upon the skin friction parameter. The relationship between the skin-friction coefficient and the lengthwise Reynolds number can be determined, and methods are available for both the laminar and turbulent boundary layer which should allow a sufficiently accurate prediction of skin friction. This means that one should be able to predict quite well the separating pressure rise.

Shock-wave interaction with a laminar boundary layer near transition to turbulent flow can be fairly complex, because transition may be induced by the shock itself, causing different behavior downstream from the shock than in the purely laminar case. The separation is still predicted on the basis of the laminar model, but whether separation persists or the boundary layer reattaches depends upon the Reynolds number ahead of the shock. Whichever of the conditions occurs depends on the nature of the flow downstream from the shock. Pearcey states that a particularly important consideration is whether the Mach number after the shock is subsonic. He suggests that in subsonic flow, the divergence of the decelerating stream tubes tends to force the flow back toward the wall and enhance the likelihood of reattachment. On the other hand, if the flow downstream of the shock is supersonic, but diffusing, the convergence of the stream tubes tends to pull the main flow away from the wall. Obviously, the curvature of the wall itself is important; if it curves away (convex) too sharply, the flow will not reattach.

Effect of Shock on Downstream Boundary Layer — The literature search did not reveal new information relative to the effect of shocks on downstream boundary layer. Pearcey, however, discusses the severity of separation effects. This discussion is qualitative; apparently, the aircraft designer depends upon wind-tunnel tests and the effect of separation on the measured overall force and moment coefficients as the critical-input data for the design process.

For an inducer, the occurrence of a shock on the leading part of the vanes will affect the ultimate diffusion possible in the impeller. As the shock on the suction surface of the blading becomes stronger due to increasing Mach number (such as with thicker and blunter leading-edge blades or an increase in incidence), the boundary layer will eventually reach the point where it separates early in the subsequent diffusion process. If the leading-edge separation is severe enough so that the boundary layer does not reattach and recover before diffusion commences downstream of the throat between the vanes, there will be no pressure recovery at all in the passages. The severity of the effect of a shock depends upon the

CONFIDENTIAL

CONFIDENTIAL

configuration of the blading after the shock. Of particular concern is the adverse pressure gradient required of an attached flow; it depends upon whether this adverse pressure gradient is imposed upon a laminar or turbulent boundary layer. Therefore, if the shock separates a laminar boundary layer and that boundary layer does not transition to turbulent flow, but reattaches, a subsequent adverse pressure gradient from diffusion may cause a second separation. On the other hand, if the shock caused transition or if the boundary layer were already turbulent ahead of the shock, the effects of a given pressure gradient would be much improved. It is plain that the conditions of the boundary layer after the inevitable shock must be known if conclusions are to be derived from theory and other experimental work in the absence of data on inducer-like units or cascades. Apparently, profile characteristics are not reported in the literature.

Therefore, the need for extensive test data concerning the mechanics of the flow in an inducer-like cascade is apparent. Because such data are lacking for the present, characteristics of airfoils, as affected by shock-induced separation, must be used to provide qualitative criteria for the design of inducers.

Airfoil Characteristics — The characteristics of airfoils, as affected by shock-induced separation, may be presented in a number of ways. These will be discussed below.

The aerodynamicist marks the point where the static pressure at the surface of the airfoil starts to change, i.e., diverge, as the critical state at the beginning of significant effects of shock separation on airfoil performance (see Figure 375). This criterion is successful for airfoils and marks the start of the drag rise and loss of lift. It is argued that this criterion is also applicable to the centrifugal-compressor inducer, although the downstream boundary-layer conditions behind the shock are somewhat different. In the case of the inducer, the boundary layer flows inside a channel, formed between two blades, which can have different separating characteristics than those of an isolated airfoil. This is well illustrated by the case of straight-walled diffusers which can achieve their maximum performance when the boundary layer is in transitory separation. For an isolated airfoil, such unsteady separation could easily be undesirable. Nevertheless, this airfoil criterion is the best available.

For single airfoils (Figure 376), Pearcey correlates the local Mach number ahead of the shock to the onset of pressure divergence at the trailing edge. This Mach number is a function of the shape of the nose of the airfoil and the included angle at the trailing edge. This trailing-edge-angle effect is fairly weak and can be safely ignored for inducers, which makes Figure 376 only a function of nose geometry. It should be remembered that this figure is based on data taken at typical-wing Reynolds numbers. At the lower Reynolds number of inducer blades, the critical Mach numbers could be considerably lower. The parameter includes nose shape and incidence. The Mach number is the Mach number ahead of the

CONFIDENTIAL

Reference 32

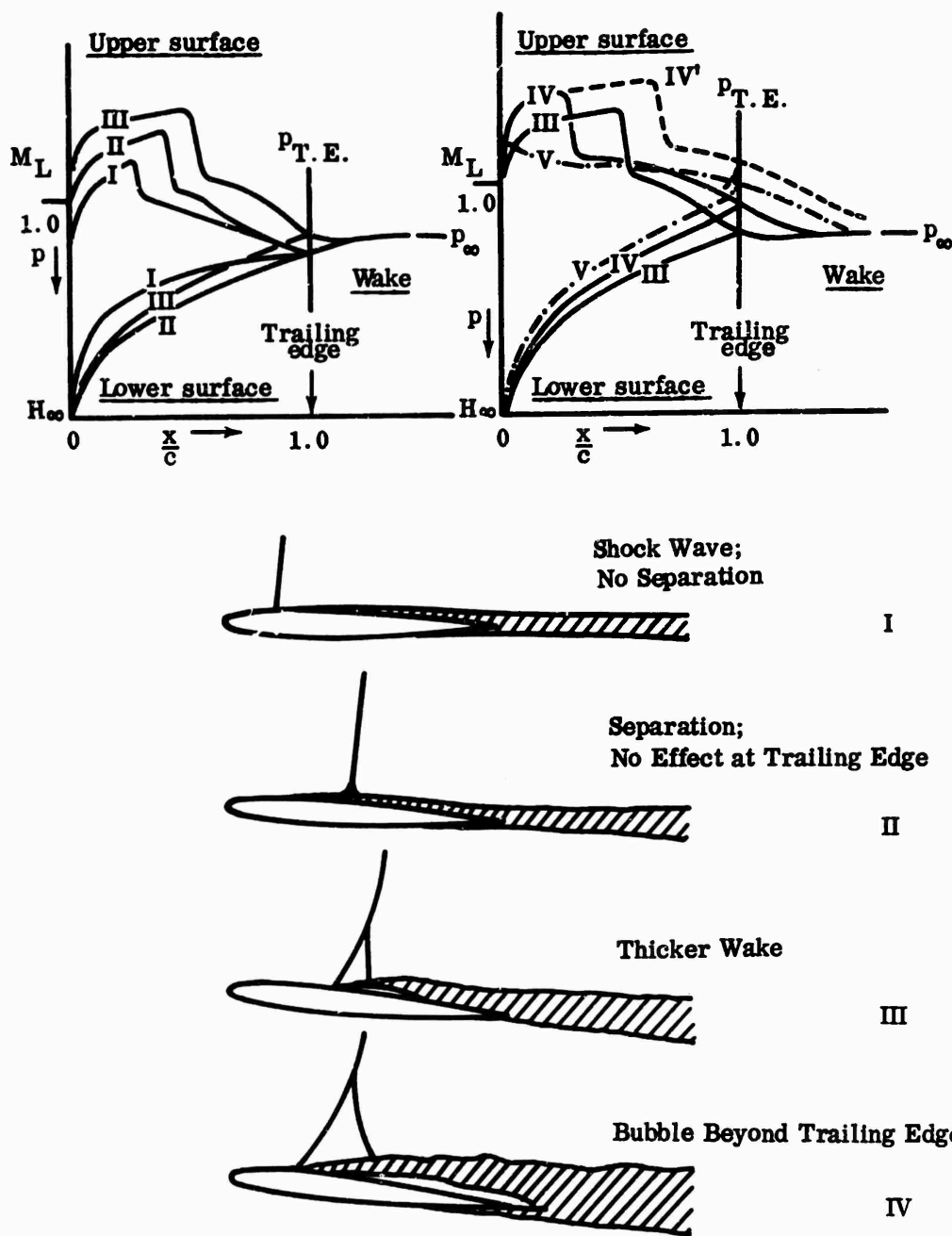


Figure 375. Trailing-Edge Pressure Divergence.

CONFIDENTIAL

shock, not the upstream infinity Mach number. As X increases, the airfoil nose becomes progressively blunter, which raises Mach numbers over the nose for a given upstream value. Therefore, one cannot say that a large value of X is desirable; it depends on whether the local Mach number increases more or less rapidly than the critical value at trailing-edge pressure divergence. In any event, a given airfoil can be rated, according to this correlation, as to whether separation effects are serious.

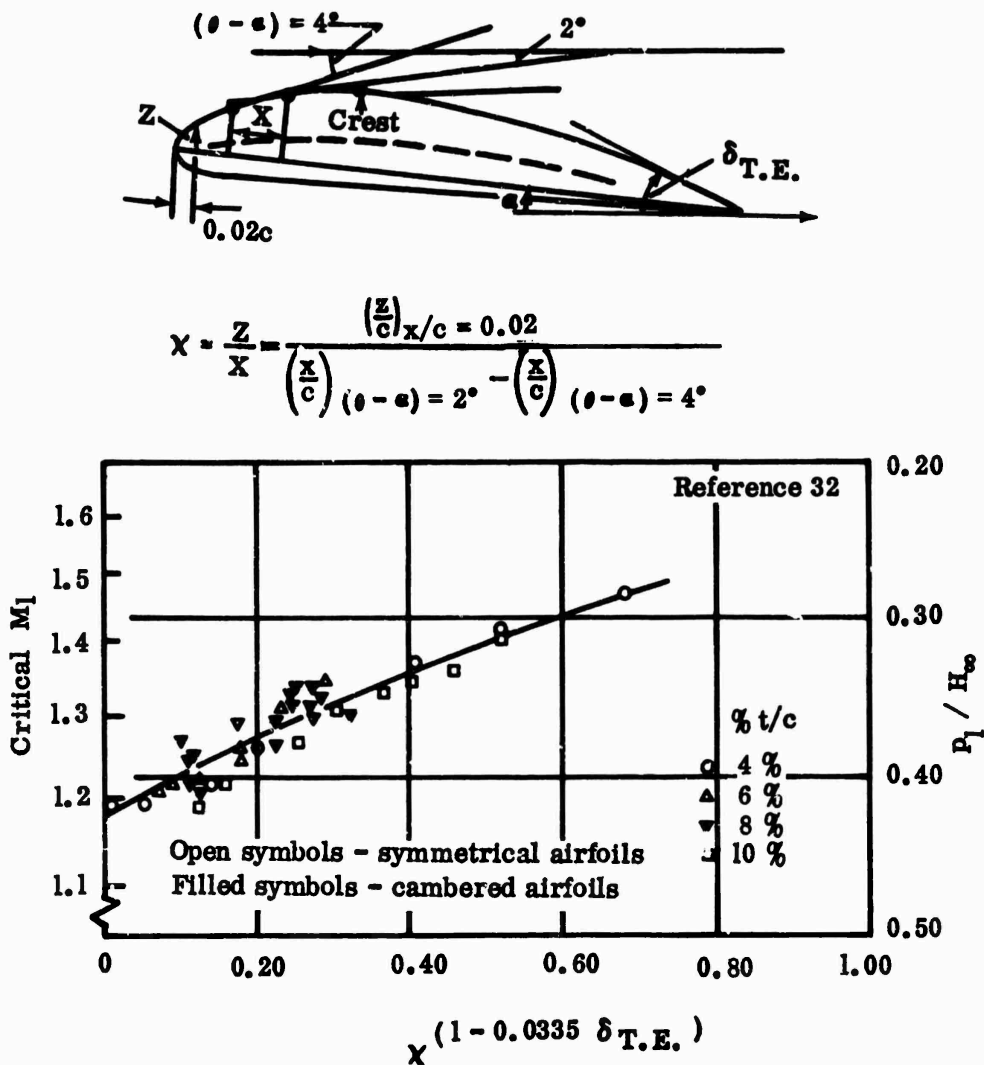


Figure 376. Critical Mach Number Versus Nose Geometry.

CONFIDENTIAL

The method of Sinnot and Osborne (Reference 33) for calculating the relationship between the upstream Mach number and the local Mach numbers on the airfoil surface is recommended by Pearcey. For the shock standing well forward on the airfoil, it is suggested that the method of Randall (Reference 34) be used. Although these references have not been studied in detail, they present methods by which to predict the Mach number distribution of the airfoil, including the shock which is matched to the downstream conditions.

Airfoil Performance Maps — A convenient performance map for an airfoil is shown in Figure 377 from Reference 32, where lift coefficient or incidence is plotted against upstream Mach number. There are 4 regions:

- 1) Lower left, where separation effects are absent;
- 2) Upper left, at low Mach number, where leading-edge (probably laminar) separation occurs. (There is a boundary marked B-B' between the low-speed leading-edge-separation regime and shock-induced separation at higher Mach numbers);
- 3) Lower right, extending on out to infinity, is the supersonic zone where separation again disappears;
- 4) The general range of high subsonic Mach numbers where it is not possible to avoid shock-induced separation.

A considerable control can be exerted over the location of the lower Mach number boundary of the shock-induced separation line. This is illustrated in Figure 378 from Reference 32. It would be very desirable to use a compressor inducer blade which exhibits a sizable region of separation-free operation at high incidence and at the value of the approach Mach number. Because this is important, the factors which affect it will be discussed below.

It can be seen that an impeller might exhibit its worst performance at low as well as high Mach numbers with the same incidence. Therefore, a well-developed compressor for full-speed operation might not perform as well at lower speeds, or it might not have as much range.

An interesting case, documented by interferograms, is contained in Reference 31. The authors observe the effect represented by line B-B' on Figure 378, where the flow went from a leading-edge separation at low Mach number to separation-free flow at a higher Mach number. The reason seems to be quite plain: an airfoil operating at a given incidence can pass from a shock-free flow into leading-edge separation as the Mach number is reduced because the Reynolds number is also reduced. As the free-stream Mach number is decreased, the sonic region on the airfoil shrinks in size, and the shock which terminates it moves forward

CONFIDENTIAL

CONFIDENTIAL

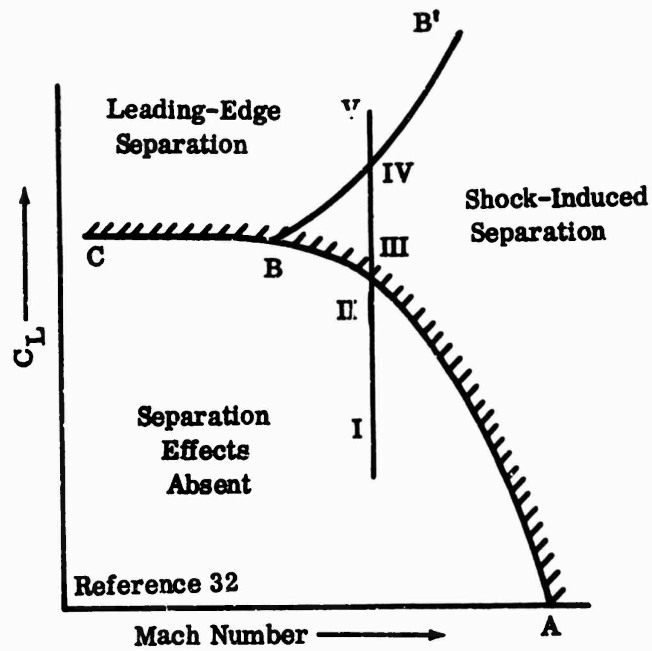


Figure 377. Airfoil Separation Regimes.

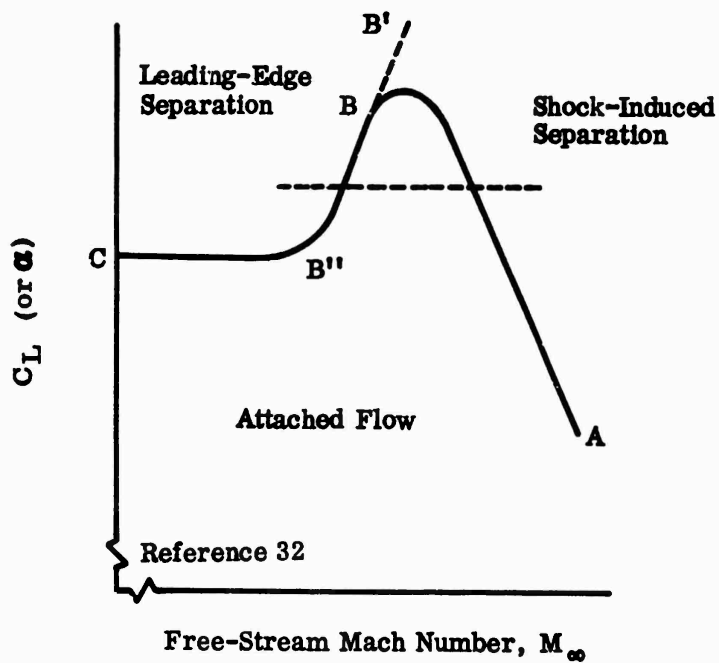


Figure 378. Flow-Attachment Boundary.

CONFIDENTIAL

CONFIDENTIAL

toward the leading edge. However, the extent of the laminar boundary layer on the nose is increasing toward the trailing edge due to the decreasing Reynolds number. If the laminar boundary layer extends beyond the peak-velocity point on the nose of the airfoil and into the succeeding region of adverse pressure gradient, the boundary layer is likely to separate. The result is a change in the boundaries of the free flow, such that a new pattern occurs with the shock standing on the shoulder of the nose and with the laminar boundary separating instead of lying at a position further aft. The change from an aft shock to a nose shock may be quite sudden or may be continuous. The pressure data from Reference 31 indicate that for this profile, a peak Mach number of 1.3 was achieved at the shoulder of the nose without separation. After the shoulder, there was a gradual recompression caused by waves reflected from the sonic line (as will be explained below), reducing the Mach number ahead of the shock substantially.

As has been pointed out above, a small inducer will likely have laminar boundary layers extending a considerable distance aft of the leading edge. It is important that this region not be subjected to shock waves; otherwise, the boundary layer will most certainly be separated from near the leading edge. The degree to which this region can maintain shock-free flow is discussed in the following paragraphs.

Supersonic Recompression — It is possible to recompress isentropically the flow over the airfoil and cause a substantial decrease in local Mach number to the position of a shock. In fact, it is possible to operate with no shock at all standing on the airfoil, except at the trailing edge (page 867 of Reference 9). In the inducer case, the best that can be expected is to reduce the Mach number ahead of the shock, for it is quite likely that the peak Mach number on the airfoil will be too high for compression all the way back to subsonic flow without shocking (page 891 of Reference 9). A further explanation is shown by Pearcey on pages 1223 to 1249 of Reference 32. The basic idea is to utilize compression waves that are reflections from the sonic line of expansion waves generated near the nose of the airfoil. When the compression waves strike the airfoil surface they tend to be reflected with like sign unless the surface is very convex. Modification of the leading-edge shape can considerably affect the incidence-versus- M_{∞} characteristic. As shown in Figure 379, from Reference 32, a modification of nose shape on an otherwise unchanged airfoil can make a significant difference in the boundary between unseparated and shock-separated flow. Pearcey proposes a parameter κ which seems to correlate this effect, although it is not understood in detail. In order to maintain a sizable region of separation-free operation on the incidence-versus- M_{∞} curve, a small value of κ is necessary. Likewise, parameter χ can be modified to affect the separation-free region. It is noted that these airfoil results are for Reynolds numbers typical of wings.

For the low-Reynolds-number inducer, it is necessary that the suction surface be designed (both at the nose and further back) so that a gradual supersonic compression

CONFIDENTIAL

CONFIDENTIAL

occurs without shocks until after the natural transition from laminar to turbulent flow in the boundary layer.

It is believed that flow about the airfoil of an inducer can be analyzed by application of single-airfoil theory, so long as these methods are not used downstream of the throat between the blades further than about 1 throat width. It is also believed that the method of Sinnott and Osborne (Reference 33) or that of Randall (Reference 34) can be applied. Other techniques may be employed as discussed in Chapter 12 of Reference 9. A relaxation solution is the most powerful, but simpler methods like the streamline-curvature solution of Perl (Page 387 of Reference 9) will give sufficiently accurate results. Because the flow has locally supersonic regions, many of the subsonic-similarity laws cannot be employed (i.e., the Prandtl-Glauert rule and Gothert's rule break down when the local Mach number reaches unity). On the other hand, the Prandtl-Glauert method, Kaplan's method, the relaxation techniques, and plural streamline curvature methods are applicable in mixed flow, as shown in Reference 9.

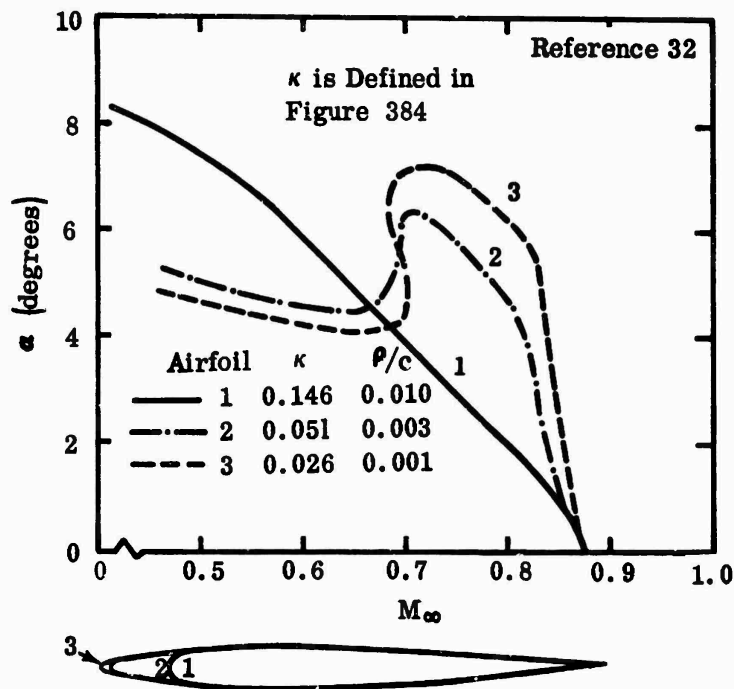


Figure 379. Boundaries for Onset of Separation.

These parameters were found useful in estimating whether the boundary of the separation effects will fall progressively from the low-speed level to the position at the highest Mach number (large κ), or whether it will rise before falling to

CONFIDENTIAL

its highest Mach-number position (small κ). These 2 trends are illustrated in Figure 380.

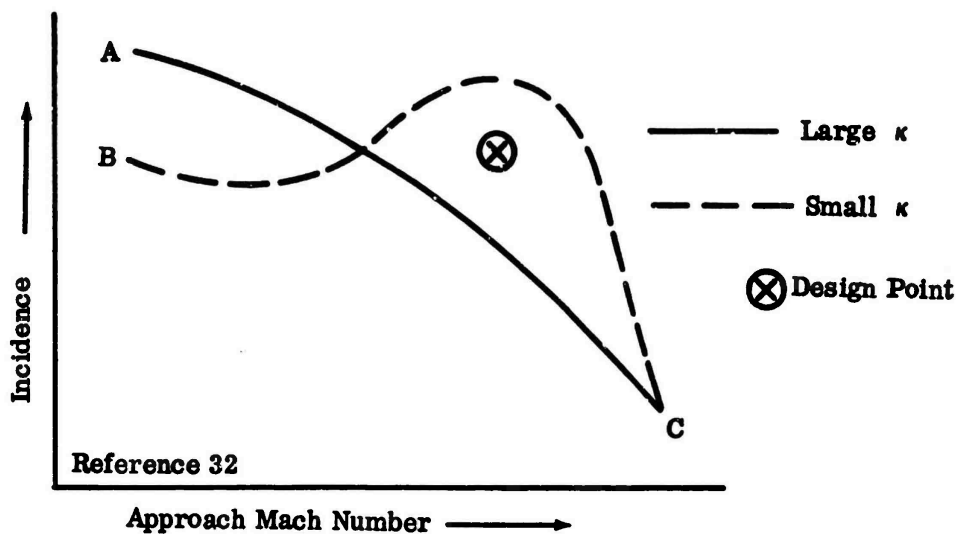


Figure 380. Boundaries of Separation Effects.

For the sake of discussion, a possible design point is also shown. It is evident that a large κ inducer design would yield a poor impeller, since little or no diffusion would occur. The same impeller with a small κ leading edge would most likely have high performance.

The physical significance of the κ parameter is that low values are associated with suction-surface-slope distributions which are known to be favorable in the intermediate range of Mach numbers (0.6 to 0.9). These favorable distributions have a rapid change in curvature near the leading edge from a high value to a near constant low value, as shown in Figure 381.

If the rapid change in curvature and the accompanying degree of turning are too extreme (large κ) the supersonic expansion will be too severe, and there will be insufficient distance between the end of the expansion and the surface-crest positions at the given incidences (about 4 degrees, corresponding to $\theta = 4$ degrees) to allow the reflected compression to return to the surface and cancel the effects of the expansion. This case is shown in Figure 382.

Reference 32

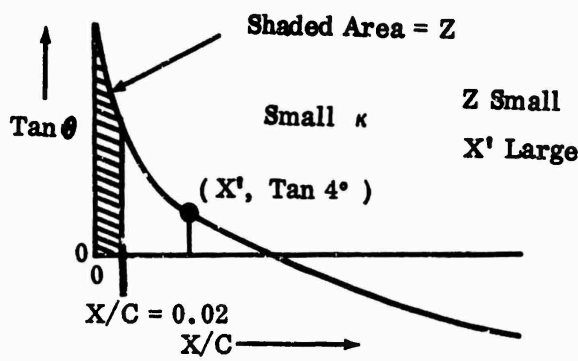


Figure 381. Suction-Surface Slope Distribution.

Reference 32

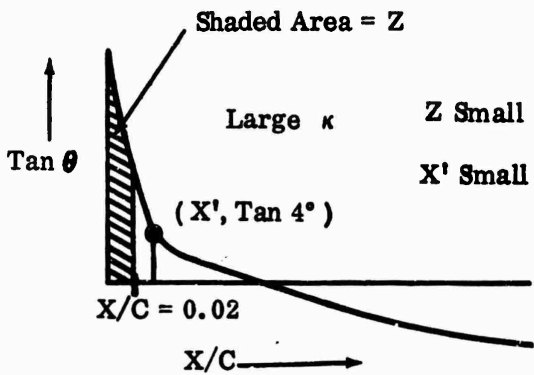


Figure 382. Suction-Surface Slope Distribution.

A large κ could also result from a nose shape on which the rapid expansion is absent, as shown in Figure 383.

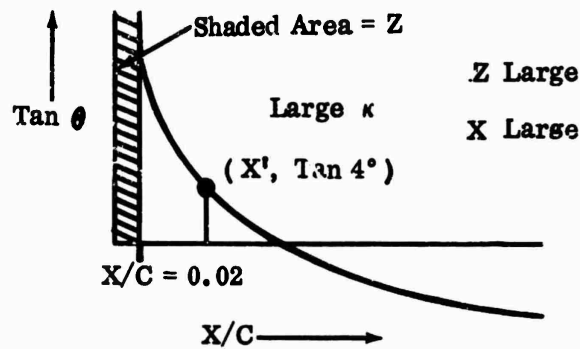
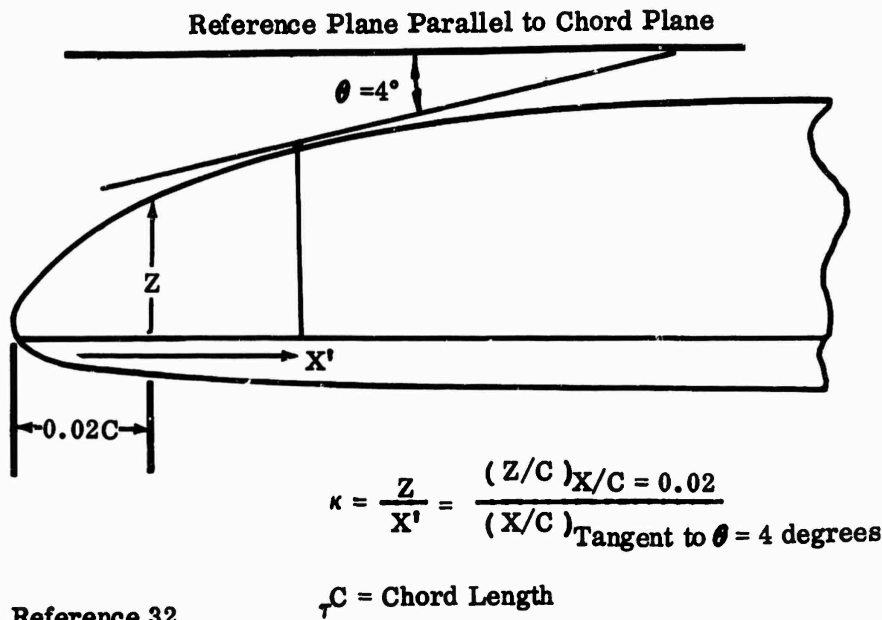


Figure 383. Suction-Surface Slope Distribution.

Analysis of Inducer Using Pearcey Parameter, κ

Not having fully developed the previously mentioned theoretical methods into a quantitative and specific analytical tool for inducer blading, it was desirable to evaluate the impellers by using Pearcey's κ parameter. This parameter is defined in Figure 384.



Reference 32

Figure 384. Pearcey Parameter, κ .

CONFIDENTIAL

For analyzing the RF-1 workhorse and inducer sections, a chord length of 1 inch was assumed. The results obtained from a 20-times-size layout are given in Table XXVI.

TABLE XXVI				
INDUCER κ CALCULATIONS				
Impeller	Blade Section	κ	Approach Mach Number	Incidence*
Workhorse	RMS radius	0.044	0.93	+8°
Workhorse	Tip radius	0.095	1.06	+9°
RF-1	RMS radius	0.2 to 0.8**	0.90	+5°
RF-1	Tip radius	0.424	1.03	+5°
*The quoted incidences are with respect to the blade mean camber line before leading-edge modifications.				
**The exact tangency point of the $\theta = 4$ degrees line was difficult to locate due to the rather constant slope of the surface.				

It was determined that the workhorse impeller has a low κ and most likely has a separation-effects boundary that will rise before falling to its highest Mach number value. The RF-1 impeller, on the other hand, has large values of κ and probably has a separations-effects boundary that drops progressively from the low-speed value to the highest Mach number value. Then, even though the workhorse operates at a higher incidence and a higher approach Mach number than does RF-1, it could be well within the separation-effects boundary while RF-1 is outside the boundary, as shown in Figure 385.

For an inducer of a centrifugal impeller, 3-dimensional effects are introduced through the radial variation of incidence, approach Mach number, and the parameter κ . Even for the case of constant incidence, we have the effects of Mach number and κ . Unfortunately, in the regions of the blade span where Mach numbers are the highest, κ values are the highest. This condition is caused by the spanwise taper built into the blades. It is possible (like the workhorse) that the tip section was operating outside the separation-effects boundary, while sections just inside the tip were in the region of no-separation effects, as shown in Figure 386.

CONFIDENTIAL

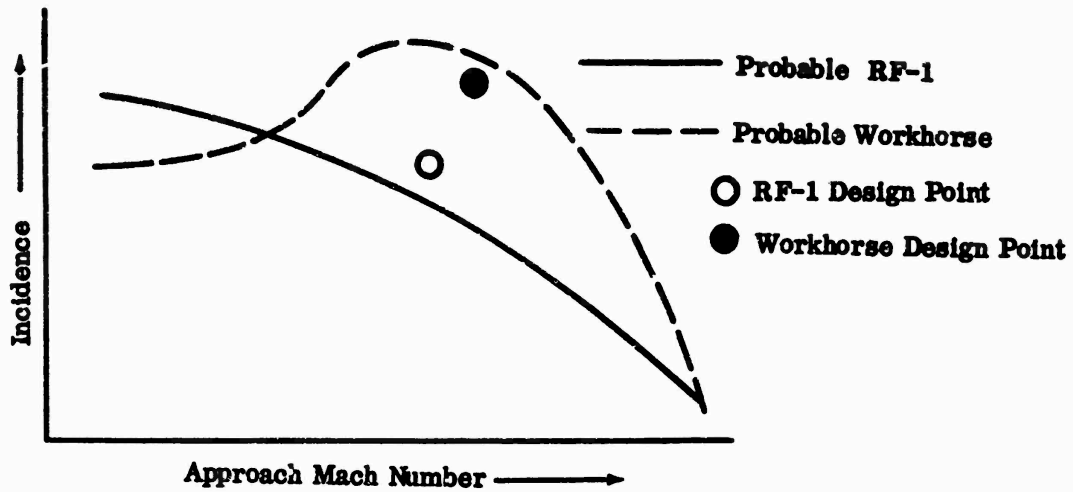


Figure 385. Incidence Versus Mach Number, RF-1 and Workhorse.

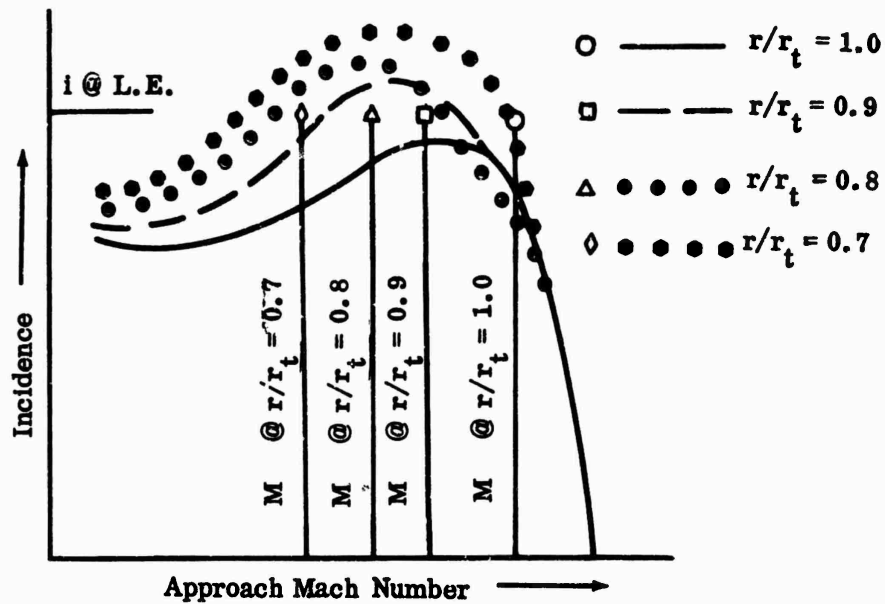


Figure 386. Incidence Versus Approach Mach Number.

CONFIDENTIAL

CONFIDENTIAL

An inducer characterized by the preceding sketch would have a performance map as shown in Figure 387.

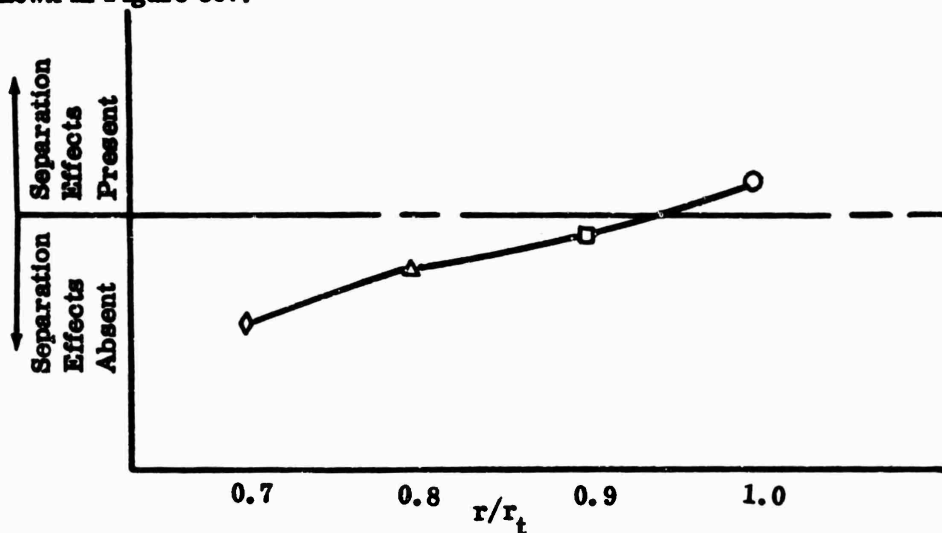


Figure 387. Separation Effects.

The RF-1 impeller has a large κ at the RMS radius as well as at the tip radius. It is quite possible, therefore, for the RF-1 impeller to be operating outside the separation-effects boundary over more than half of its blade height. This leads to separation of a greater percentage of the total flow and higher exit mixing losses.

As mentioned previously, the 4 impellers (MF-1, MF-2, MF-3, and RF-1) were designed with double-circular-arc blading in the inducer sections. The workhorse did not have this type of blading. As reported in Reference 35, the double-circular-arc blades have a high subsonic drag-divergence Mach number for a moderate incidence ($i = +4$ degrees). Considerations of Mach number and incidence represent a point on the separation-effects boundary, and the value of approach Mach number for an incidence of $+4$ degrees is about 0.80. Subsonic-type airfoils, which are more like the workhorse-impeller blading in the leading-edge region, exhibited drag-divergence Mach numbers of from 0.65 to 0.70 in the same incidence range. In Reference 35, the incidence coordinate on the separation-effects boundary for the double-circular-arc blade is approximately $+7$ degrees with an approach Mach number of 0.8.

In answering the questions as to why the RF-1 blading looks so poor, by using Pearcey's parameter κ , it can be seen by referring to Figure 388 that the RF-1 blading is only a true double-circular-arc-type blade in the hub half of the span. The blade at the extreme tip is more like a cambered-flat-plate section. Therefore, the numerator of the κ parameter is small, but the denominator of the κ parameter is even smaller. It follows that in the tip region of the RF-1 inducer

CONFIDENTIAL

CONFIDENTIAL

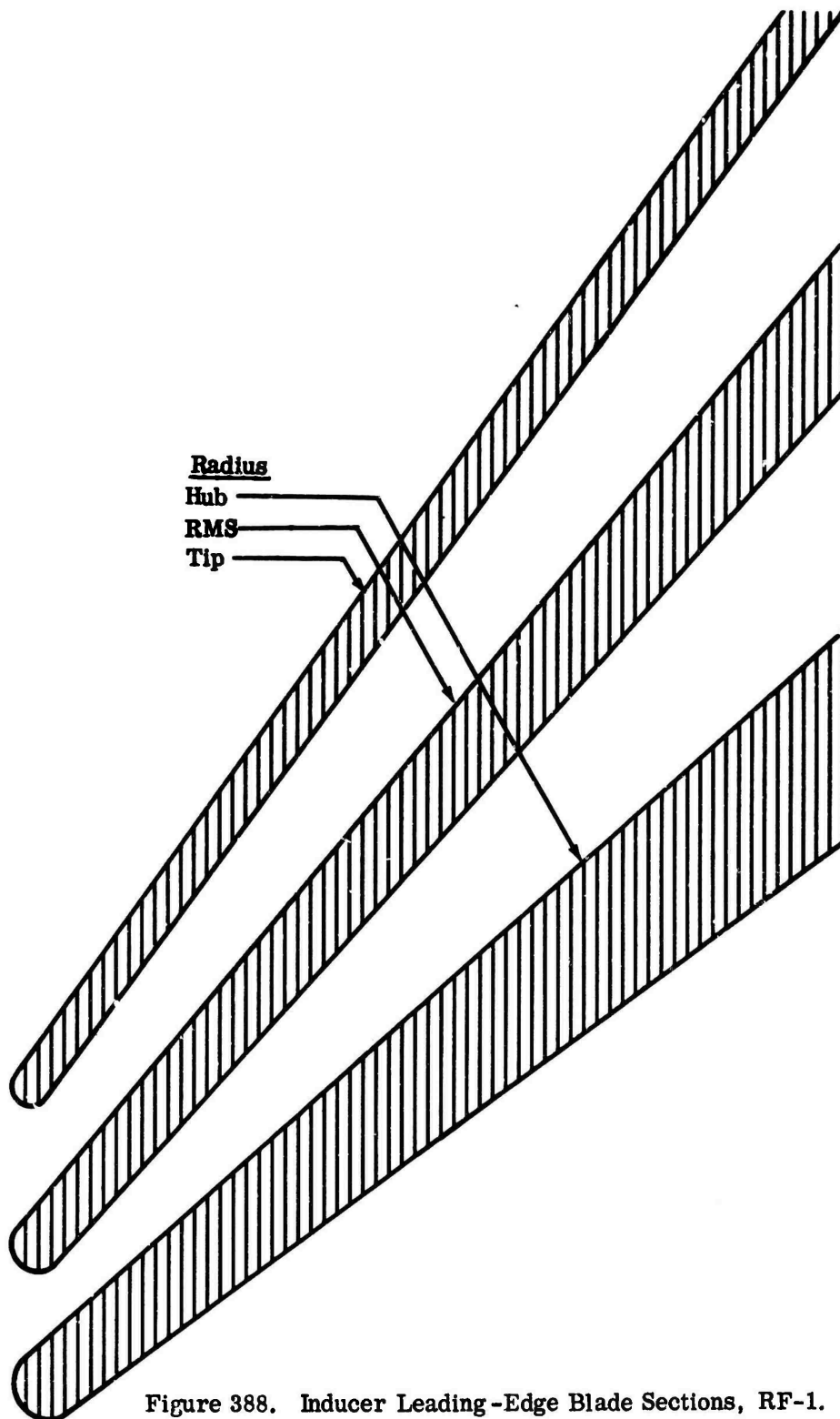


Figure 388. Inducer Leading -Edge Blade Sections, RF-1.

596

CONFIDENTIAL

CONFIDENTIAL

the expansion is too rapid, and there is insufficient distance between the end of the expansion and the crest on the suction surface for the reflected compression to return to the surface.

The workhorse inducer, on the other hand, had blading which was approximately of constant thickness at any given radius, and it was considerably thicker in the tip region than was the RF-1. For example, at the extreme tip, the RF-1 blade thickness was about 0.025 inch while that of the workhorse was 0.056 inch. The leading-edge radius at the tip of RF-1 was 0.0125 inch, while the leading-edge radius of the workhorse was 0.010 inch. To fabricate the 0.010-inch radius on the leading edge of the workhorse inducer, material was removed from the suction surface of the blading. The thin leading-edge section was blended with the downstream blading through a long, gradual radius as shown in Figure 389, placing the crest of the airfoil section further aft and resulting in a smaller κ parameter. Therefore, sufficient distance is available with the workhorse for the reflected compression to return to the surface and cancel some of the over-velocity prior to the shock. In the tip region of the workhorse, the suction-surface shock most likely takes place at a lower Mach number than it does for the RF-1, and it also takes place further downstream where the boundary layer is more likely to be turbulent. The 2 cases are shown in Figure 390.

The RMS blade section of the RF-1 inducer also has a high value of parameter κ . The blade is thicker for this section than it is at the tip, but the blending of the thicker part of the blade downstream with the small-radius leading edge was accomplished with a long, nearly straight taper. The resulting shape closely resembles a wedge of small included angle with a leading-edge radius. This type of configuration also results in the crest being far forward.

In addition, by benching (removing material) the suction surface of the inducer blades of the workhorse, the mean camber line of the airfoil was directed into the flow direction, similar to the effect reported by Pearcey (Pages 1234-1236 of Reference 32).

Therefore, from the preceding analysis it was possible to explain why the workhorse impeller had better performance than the RF-1, even though the former operated in a more severe environment. The conclusion was derived from seemingly small differences in the nose geometry. More diffusion of the relative flow is accomplished prior to separation in the workhorse than in RF-1, resulting in smaller friction losses and, more important, smaller mixing losses at the impeller exit.

CONFIDENTIAL

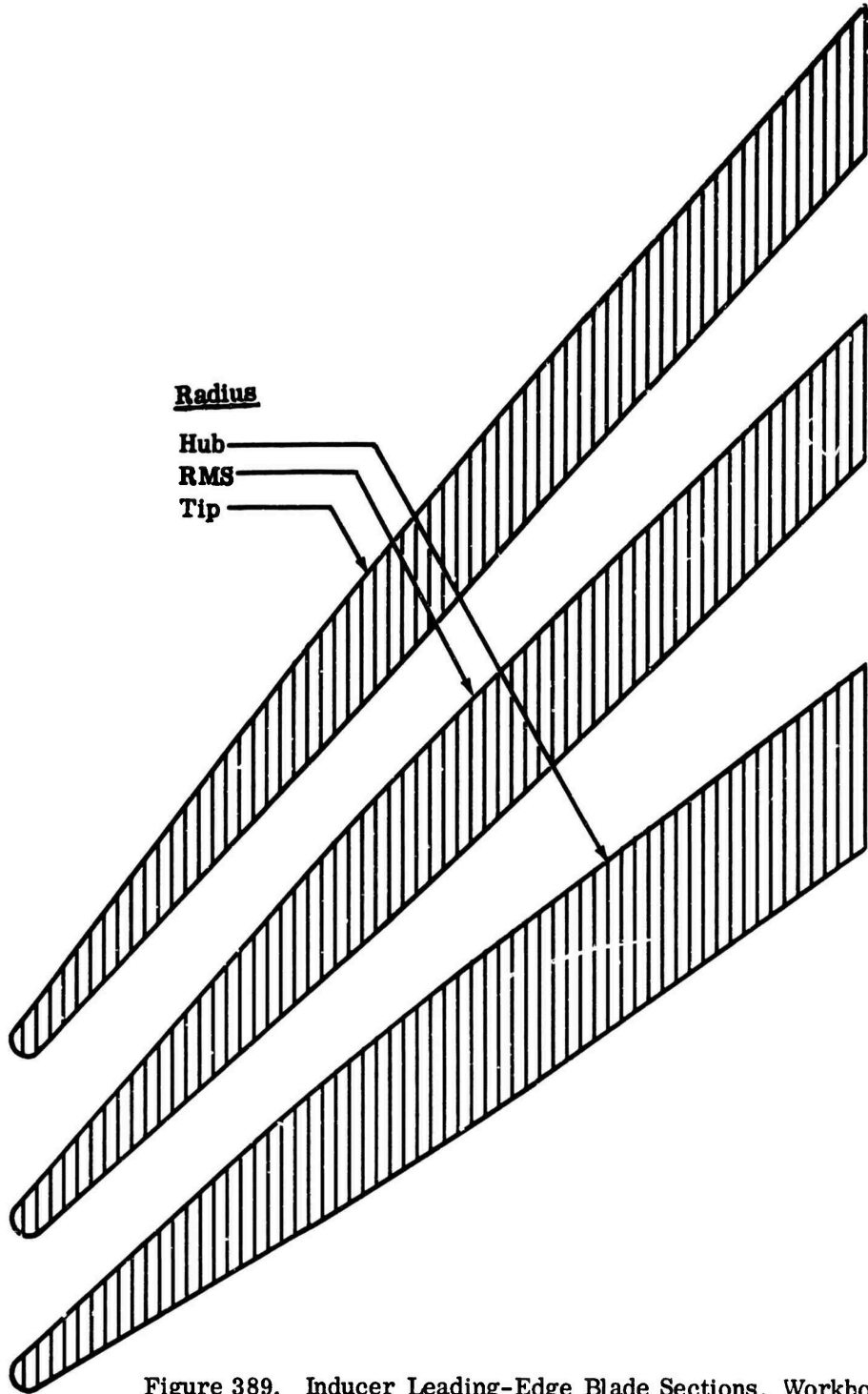


Figure 389. Inducer Leading-Edge Blade Sections, Workhorse.

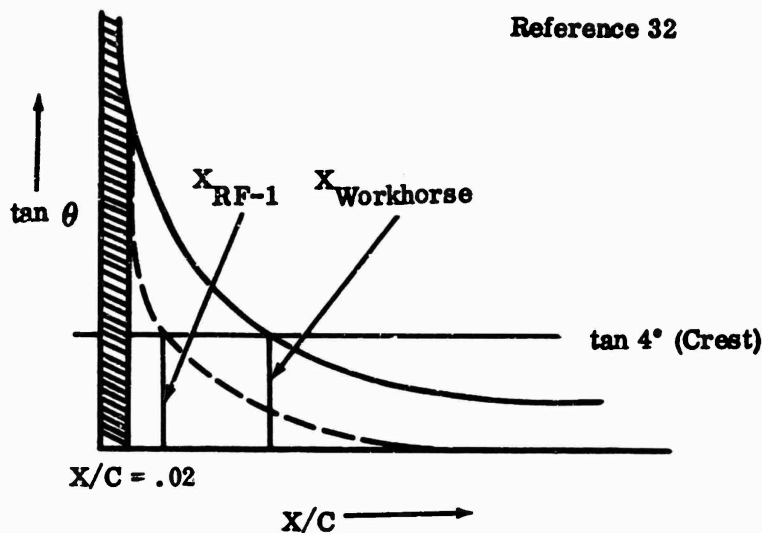


Figure 390. Suction-Surface Slope Distribution, RF-1 and Workhorse.

7.1.9 PROPOSED DESIGN TECHNIQUE

Based on the analyses in Sections 7.1.6 through 7.1.8, the following general guidelines are presented for the design of high-pressure-ratio centrifugal impellers.

- 1) Design for the lowest possible inlet relative Mach number within the geometric limitations imposed by engine-size requirements. For example, the minimum inducer hub-to-tip ratio may be determined by such mechanical design considerations as size of bearings and/or shaft, while the rotational speed may be set by overall engine dimensions and/or the speed requirements of other engine components.
- 2) A proper balance must be established among design incidence, inducer loading, and impeller work requirement. It is of prime importance that the inducer not be forced to operate at a high incidence when the inlet relative Mach number is in the high subsonic range (0.7 - 0.9); a low incidence (+1 degree) will keep the compressibility effects and the strength of the resultant shock at a minimum. The loading in the inducer should be consistent with good axial-rotor design practice. The diffusion factor is recommended as a reliable parameter. For a given tip diameter, the impeller work input requirement is a function of the rotational speed and the slip factor. Existing methods for predicting the slip factor show the dependence of this parameter on the number of blades; i.e., to obtain a high slip factor for a given size

CONFIDENTIAL

impeller requires that a large number of blades be used. For high-pressure-ratio impellers, it is recommended that the modified form of Eckert's equation (see Section 7.1.6) be used along with a correction of +0.02 to +0.03.

where:

$$\text{Predicted Slip Factor} = (\text{Slip Factor})_{\text{Eckert}} + (0.02 \text{ to } 0.03) \quad (41)$$

This increase in the predicted slip factor is empirical and is based on the fact that the workhorse impeller showed a slip factor that was from 0.02 to 0.03 higher than the originally predicted value.

To keep the incidence at a minimum in this high subsonic Mach number regime requires that the blockage be kept at a minimum. Because it has been shown that these impellers have smaller slip than predicted, the designer can relax the number of inducer blades as indicated above. However, to maintain an acceptable diffusion rate, less turning of the flow in the early part of the inducer may be required.

- 3) The airflow rate per unit geometric area at the impeller exit should be maintained at a maximum to minimize the wake width and the exit mixing losses consistent with diffuser requirements. For an impeller of given diameter, it is required that minimum impeller-exit-blade height not jeopardize the aerodynamic design of the diffuser.
- 4) Following good aerodynamic-design practice, the velocities along streamlines should vary in a smooth, continuous manner, avoiding large gradients where possible.
- 5) Considerations must be given to the effects of the Coriolis forces on the performance of the inducers. The component of the Coriolis force in the blade-to-blade direction is proportional to the product of the rotational speed and the radial component of the through-flow velocity. The direction of this force is from the pressure surface to the suction surface. If present, this force can deposit low-energy fluid on the suction surface from the pressure surface, and, in so doing, reduce the amount of flow deceleration which takes place prior to separation. Due to difficulties arising from the influence of this force, it is recommended that it be kept at a minimum, or that it be non-existent in the inducer, where the tangential turning and flow deceleration take place. This can be accomplished by completing the tangential turning prior to turning to the radial direction. It may require an axial inducer of considerable length.

CONFIDENTIAL

CONFIDENTIAL

- 6) For the design of the leading-edge regions of the inducer blading, the method of Schlichting should be used in conjunction with Pearcey's α parameter to determine the configuration which produces the minimum overvelocity while showing the least tendency to be adversely affected by shock-induced separation.
- 7) To estimate the performance of a given impeller, the following losses, which have been described earlier in Section 7.1.7, should be taken into account:
 - a) Friction loss on the shroud, hub, and blades;
 - b) Clearance loss;
 - c) Exit mixing loss.

The loss curves are presented in Figures 369 through 372. Shock loss can be included if the Mach numbers are high enough to make it significant.

- 8) Having defined the velocity distribution on the suction surface of the blade, it becomes necessary to establish criteria to determine the point of separation. To obtain limits for the deceleration of the relative flow along the suction surface, it is necessary to revert to boundary-layer calculations. The complexity of the differential equations for the boundary layer (equation of motion and the continuity equation) prohibit a calculation of the flow field. Therefore, the solution of turbulent boundary-layer flows is accomplished through the use of approximate methods.

In Reference 11, the approximate, momentum-integral method was employed in the boundary-layer calculations to determine the following separation criteria:

- a) For concave upward velocity distributions (Figure 391 (a)), the velocity at which the separation occurs is:

$$V_{\text{Sep}} = V_{\text{Max}} / 1.8 \quad (42)$$

- b) For velocity distributions with constant gradient (Figure 391(b)), the velocity at separation is:

$$V_{\text{Sep}} = V_{\text{Max}} / 1.6 \quad (43)$$

CONFIDENTIAL

- c) For convex upward velocity distributions (Figure 391(c)), the velocity at separation becomes:

$$V_{\text{Sep}} = V_{\text{Max}} / 1.4 \quad (44)$$

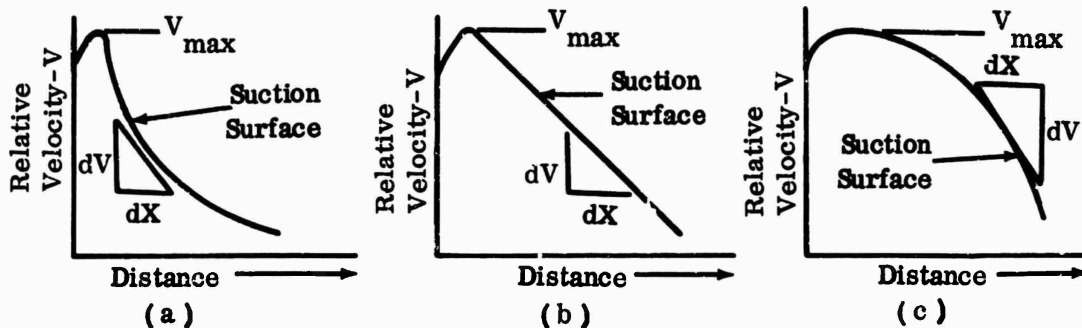


Figure 391. Relative Velocity Distributions.

These criteria are consistent with the qualitative findings from an equilibrium-boundary-layer concept of Clauser (Reference 36). In this case, the assumption is made that the velocity profile remains similar at successive downstream stations. This condition is dependent upon a balance between wall shear and pressure gradient, as shown in Figure 392.

The $\frac{\delta}{V} \frac{dV}{dx}$ term is negative for decelerating flows, and when this parameter is less than a certain value (i.e., greater in absolute magnitude than the critical value), separation may be expected.

This theory adds that, with $\frac{\delta}{V}$ increasing with flow-path length, it is desirable to have an increasing dV/dx term (less negative) with flow-path length, so that the product of the 2 terms is nearly a constant behind the peak. The increasing dV/dx suggests a concave upward velocity distribution.

Lieblein (Page 203 of Reference 37) reports empirical results which show that a ratio of V_{Max} to V_{Sep} of 2.0 can be attained prior to the onset of separation.

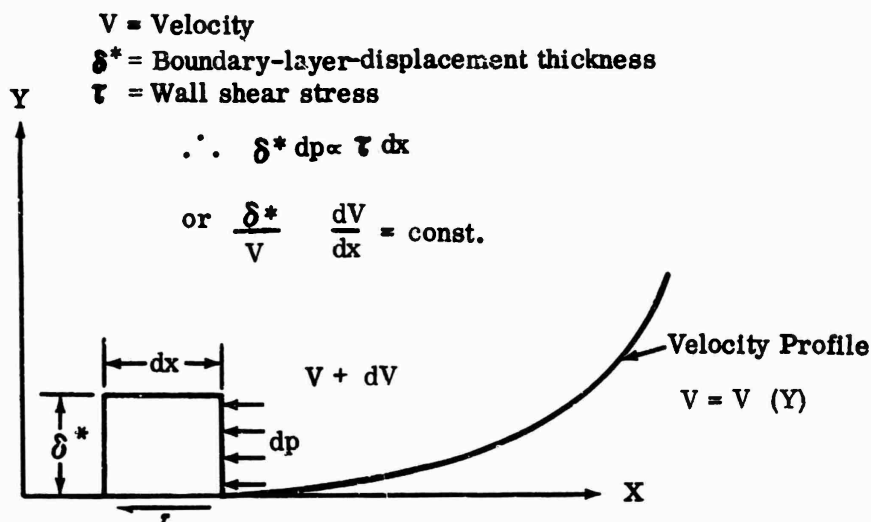


Figure 392. Equilibrium — Boundary-Layer Notation.

On the basis of the above discussion, it is recommended that a velocity ratio ($V_{\text{Max}}/V_{\text{Sep}}$) of 1.6 to 1.8 be used in conjunction with the overvelocity calculation according to Schlichting's method to predict the velocity at separation.

7.2 DIFFUSER TESTS

Basic tests of the vane-island diffuser elements were conducted with static-pressure surveys in 1 channel, total pressure at the impeller tip and in the collector, and schlieren photographs. The test data for all diffuser elements are presented in Section 6.0. Results of the tests showed that DI-2 had the best performance of the 3 elements tested and DI-1 had the best range. The 16-vane-island diffuser (DI-3) had shorter range and lower performance than DI-2. The results of these tests led to analysis of the fluid flow through the diffusers in an attempt to explain the causes for performance and airflow range differences. In particular, the study was centered around DI-1 and DI-2. A discussion of the findings of this study is presented below. Also, new questions arose which were not specifically considered in the original test plan. Therefore, a second test series was conducted to supplement the first tests and to provide essential information relative to the specific questions. This test program included full-scale rig tests with the workhorse impeller and single-channel tests with a separate diffuser-flow rig. Basic diffuser data were derived from these single-channel tests.

CONFIDENTIAL

7.2.1 INFLUENCE OF IMPELLER ON DIFFUSER PERFORMANCE

Before entering into detailed diffuser analysis, it was first necessary to establish the characteristics of the workhorse impeller used in the diffuser test rig. This impeller has been discussed in detail in Section 7.1; however, certain aspects are presented here. A speed line for the workhorse impeller with DI-1 diffuser was obtained using data from Tests 3306B and 3347A. Figure 393 shows a comparison of the results at design speed. The overall compressor performance was higher for the second test, suggesting a difference in the rig between the 2 tests. Because 2 impeller-shroud covers were used in the program, it was believed that the impeller performance was different for each shroud. Inspection of the 2 shroud covers showed little difference in their geometry; however, the one used in Test 3347A was flatter and did not have provisions for schlieren windows. Therefore, the data analysis of the diffuser section was based on the impeller design speed line from Test 3347A. It was also believed that the diffuser had an effect on the impeller performance. Static pressure at the impeller tip showed considerable change in the regions nearest to each diffuser vane. The schlieren photographs (Appendix X) also showed shocks at the vane leading edge and along the suction surface which appeared to project into the impeller. The exact effect of these conditions on the impeller is not known, but the fact that they existed should be kept in mind. In some cases the diffuser models were retested to establish the impeller performance, using a shroud cover without schlieren windows or plugs. Also, on occasion it was found (where a direct comparison could be made) that the schlieren pictures did not agree exactly with static pressures measured during the retests. Considerable care was taken during the tests and analyses to evaluate and eliminate anomalous data. Therefore, the reader is reminded that some of the data presented in Section 6.0 was not used in the following discussions.

7.2.2 CHARACTERISTICS OF COMPRESSOR SPEED LINES

In the diffuser test program, the characteristics of the impeller and the diffuser had to be considered. The impeller characteristic curve, as discussed previously, shows relatively little change in pressure ratio until the maximum airflow is reached, at which point the pressure ratio drops abruptly (Figure 394).

The diffuser has a characteristic shape which drops off gradually from surge to maximum airflow. The point in the following sketch where the pressure ratio starts to drop rapidly is defined as W^* . Combining these 2 curves gives the overall compressor-system characteristic. The resulting shape will be dependent on the matching of the diffuser to the impeller. If the impeller limits the maximum airflow to a value lower than W^* , the compressor characteristic curve will have a sharp drop at maximum airflow. If, on the other hand, the diffuser limits the airflow, the characteristic curve will drop more gradually.

CONFIDENTIAL

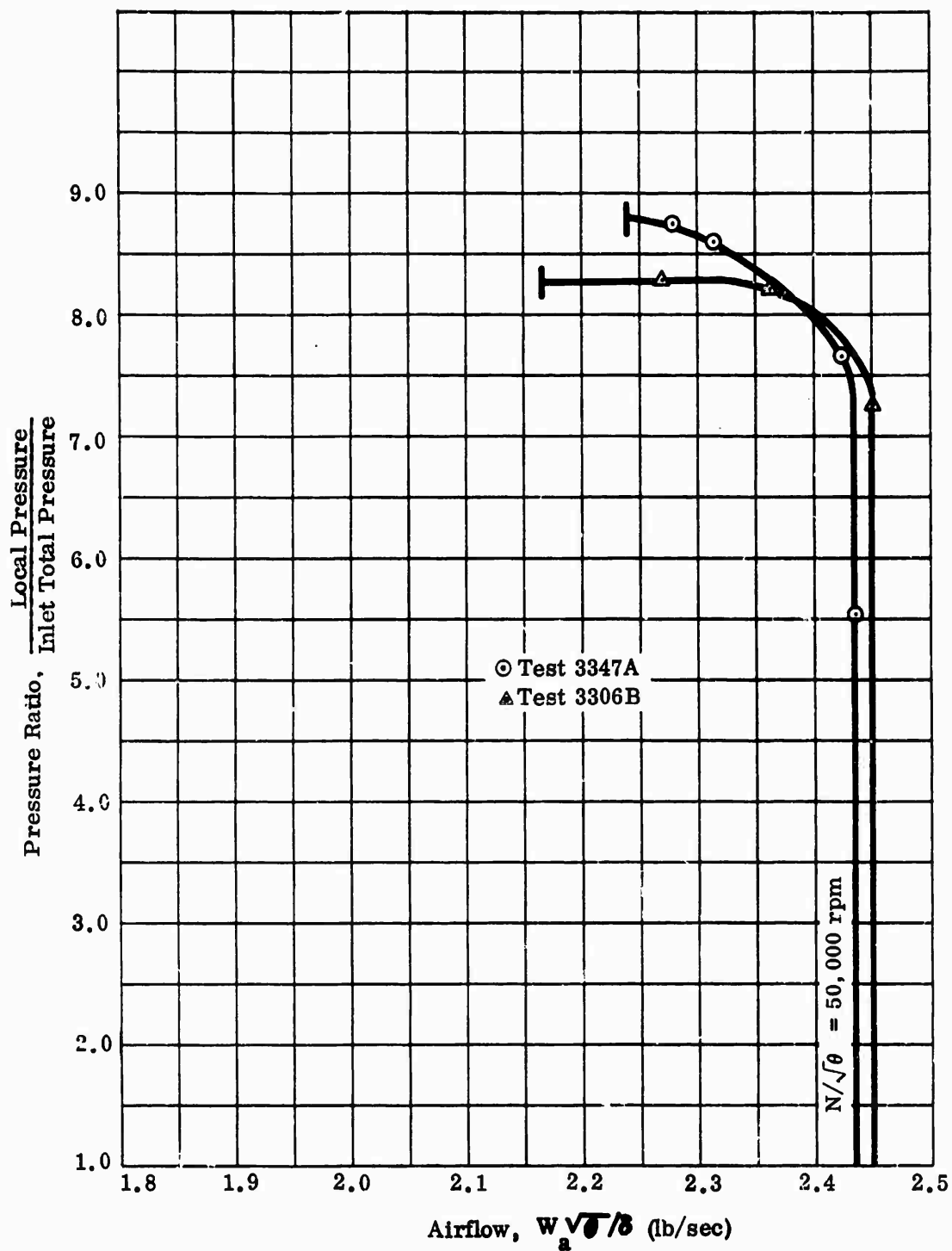


Figure 393. Pressure-Ratio Comparison, DI-1.

605

CONFIDENTIAL

CONFIDENTIAL

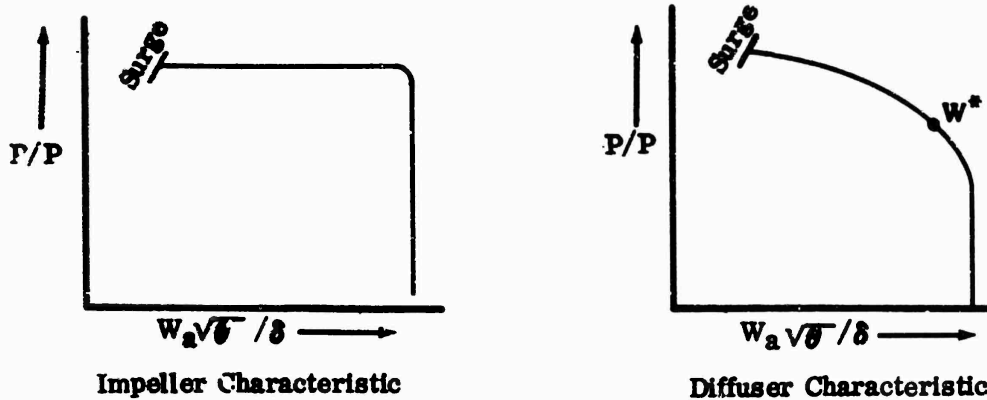


Figure 394. Characteristic Shape of Pressure Ratio Versus Airflow for Impeller and Diffuser.

The sketch below (Figure 395) shows the 2 cases.

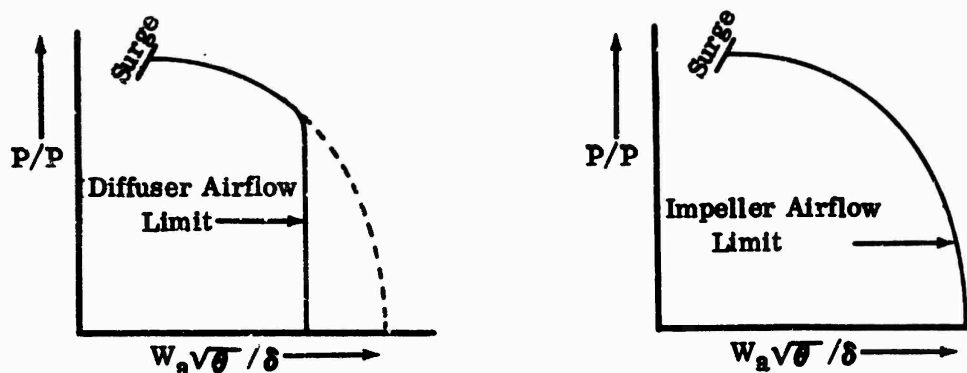


Figure 395. Compressor Characteristic Showing Impeller and Diffuser Airflow Limit.

In this compressor program, the impeller set the maximum airflow in all but a few tests (3310A, 3310B).

During the diffuser investigation, single-channel diffusers were tested separately to determine the pressure recovery, C_p , as a function of channel entrance Mach number and boundary-layer thickness. It was found that recovery remained nearly constant until the Mach number ahead of the shock in the diverging channel reached 1.1 to 1.2. Figure 396 shows channel performance at throat Mach numbers below 1.0. In addition, the figure shows static-pressure recovery for channel Mach numbers greater than Mach 1.0 (just ahead of the shock). In the diffuser channel, the core flow reaches Mach 1.0 at the throat and then

CONFIDENTIAL

CONFIDENTIAL

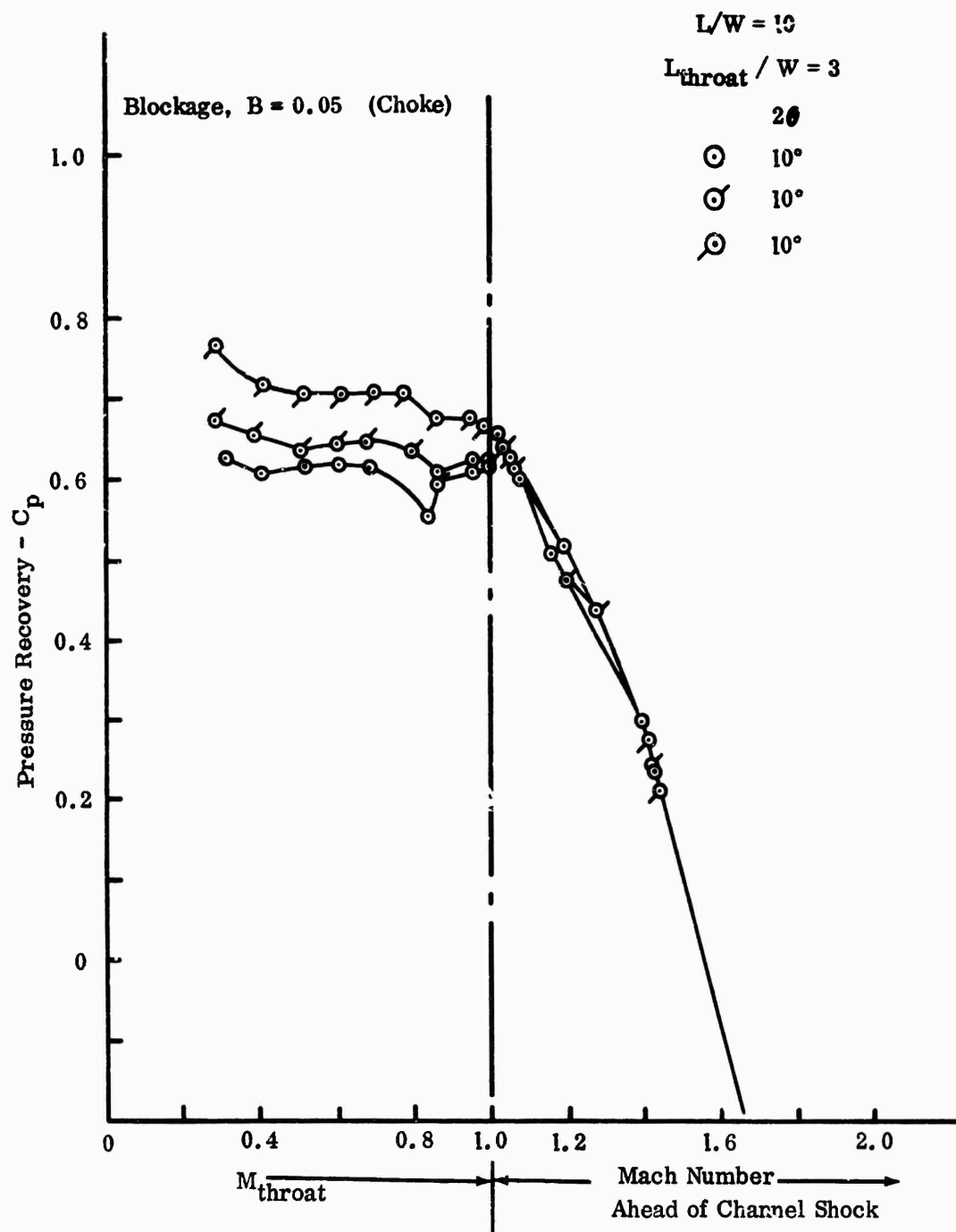


Figure 396. Two-Dimensional Diffuser Channel Performance.

CONFIDENTIAL

accelerates supersonically as the back pressure is reduced. The slope of this static-pressure recovery line is reflected in the characteristic shape shown in Figure 394. Therefore, in evaluating the performance of a channel diffuser, it is advantageous to present the performance based on W/W^* or the corrected airflow divided by the airflow where Mach 1.0 first occurs in the core flow of the diffuser throat (see Figure 397). Note that the mass flow rate is not maximum when the core Mach number reaches 1.0 because a sizable part of the throat (up to 45 percent) area is boundary layer and subsonic. There may be a 2- to 3-percent increase in W beyond W^* . This change is significant for a compressor which may have only 7-percent range.

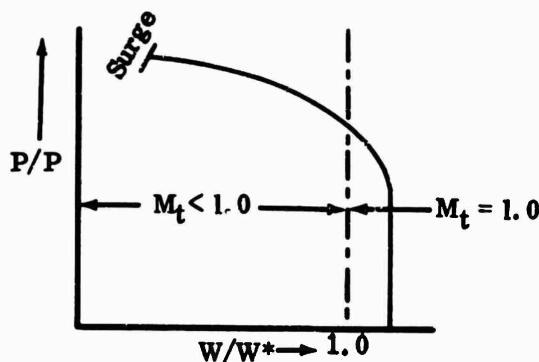


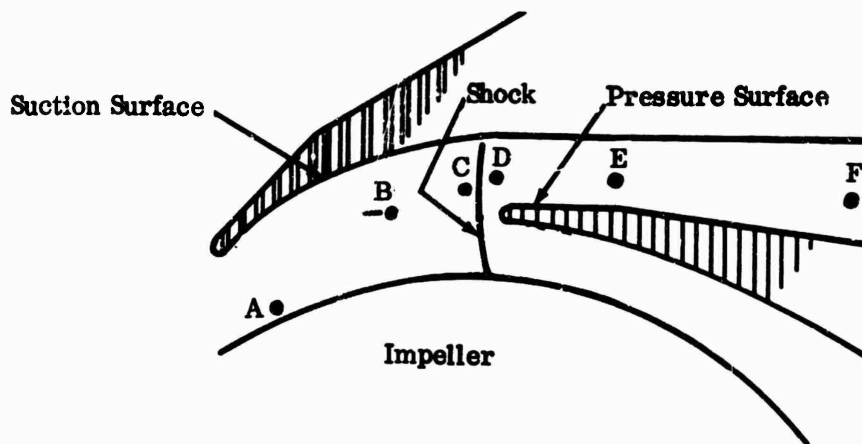
Figure 397. Compressor Characteristic Curve.

The airflow range to the left of $W/W^* = 1.0$ can be predicted with some accuracy as discussed in Section 7.2.4, Channel Performance and Surge.

The region to the right of the $W/W^* = 1.0$ line is influenced by the interaction of channel geometry, back-pressure variation, and throat boundary-layer adjustment; therefore, it is difficult to predict now. Analysis of the mixed Mach number flow in throat and channel with empirical confirmation or reliance on straight channel tests is required to predict W^* and C_p as functions of back pressure.

7.2.3 GENERAL DISCUSSION OF FLOW THROUGH A VANE-ISLAND DIFFUSER

To understand the flow through a diffuser of this type, it was generally advantageous to divide the flow path into several regions. Figure 398 shows these regions for a vane-island diffuser.



- A-B Vaneless space (region of wake mixing);
- B-C Semivaneless space (region of flow transition from the vaneless space to the entry shock);
- C-D Entrance to channel throat (region of rapid flow adjustment);
- D-E Channel throat (region of transition from vortex to channel flow);
- E-F Channel diffuser (region of major static-pressure rise).

Figure 398. Vane - Island Diffuser.

Vaneless Space

The vaneless space is a region of rapid mixing where the wakes and jets from the impeller blades (see Section 7.1) are mixed out. One of the objectives of the schlieren investigation was to determine if the flow at the diffuser throat entrance was steady. Schlieren photographs were taken at 5 blade positions and at constant rig speed (rpm) and airflow. The flow was shown to be steady at the vane leading edge, which indicates that the wakes from the impeller mixed out through the vaneless and semivaneless spaces. Figures 118 through 122 in Appendix X show that the shock system is unchanged for each impeller position and that any unsteady effects are minor by the time the vane region is reached. This was shown despite the large wake regions that existed at the impeller tip (over 50 percent); however, other researchers have also concluded that mixing is nearly complete at a radius ratio of 1.05 (see Reference 15) for flat impeller discharge angles.

In Reference 15, Johnston and Dean showed the relationship of the radius ratio (where impeller mixing is complete) to the diffuser-inlet-swirl parameter, λ , for various work-input coefficients (where λ is defined as the tangential component of the absolute velocity at the impeller exit, divided by the radial vector).

Referring to the workhorse impeller-exit vector diagrams in Section 6.1, it can be seen that this impeller has a λ value between 7 and 8. Figure 399 (from Reference 15) shows the relationship between radius ratio and λ values. As λ varies from 7 to 8 it can be seen that the radius ratio where mixing is complete is between 1.05 and 1.08.

In Section 2.0, loss analyses through the vaneless space showed that 10 percent of the total pressure at the impeller could be lost. Data from the movable total-pressure probe (measurements along a streamline from the impeller tip to the throat) show that a loss of this magnitude exists in the core flow (Figure 400). This loss can be attributed to several causes. First, if mixing occurs to a large radius ratio as shown in Figure 399 (from Reference 15), much of the measured loss in the core flow can be attributed to this parameter. Second, the loss may come from wall friction where the wall $\partial p / \partial x$ mixes into the mainstream by secondary flow. Third, the measured loss is a combination of the above 2 cases, where the vorticity diffusion is aided by the impeller mixing and secondary flow. Further investigation would be necessary to define the exact nature of this loss. Further understanding is vital, for it will direct improvement attempts toward the impeller or diffuser.

Semivaneless Space

This is a transition region from the vaneless space to the zone of rapid adjustment, characterized by low static pressure ahead of the bow shock. The flow is bounded by the suction surface of the vane. Mathematical solution of flow in this region has proved difficult for supersonic flow because a field-type solution is required. However, some useful discussion can be made concerning the semivaneless space.

It is suggested that the boundary layer is essentially 1-dimensional, although some secondary flow exists, as seen from oil or carbon-black traces (see Figure 401). The principal effect of the secondary flow is to bleed the boundary layer off the suction surface of the vane into the sidewalls. These flows are beneficial, since they keep the boundary layer thin along the suction surface and delay separation under adverse pressure gradients. The pressure gradients along the streamlines in the semivaneless space are not severe, however, as shown from the static-pressure measurements (for the supersonic case).

Figure 402 is a static-pressure survey of the DI-1 diffuser. It shows that the pressure gradient is slight, which also suggests that the flow does not undergo a large Mach number change in this region, as might be imagined at first. It is suggested that 1-dimensional turbulent boundary-layer theory can be used to predict the boundary-layer growth from the impeller tip to the channel throat. This has been done and will be discussed in Section 7.2.6 of this report. It is believed that flat-plate (constant pressure) theory is valid because the fluid

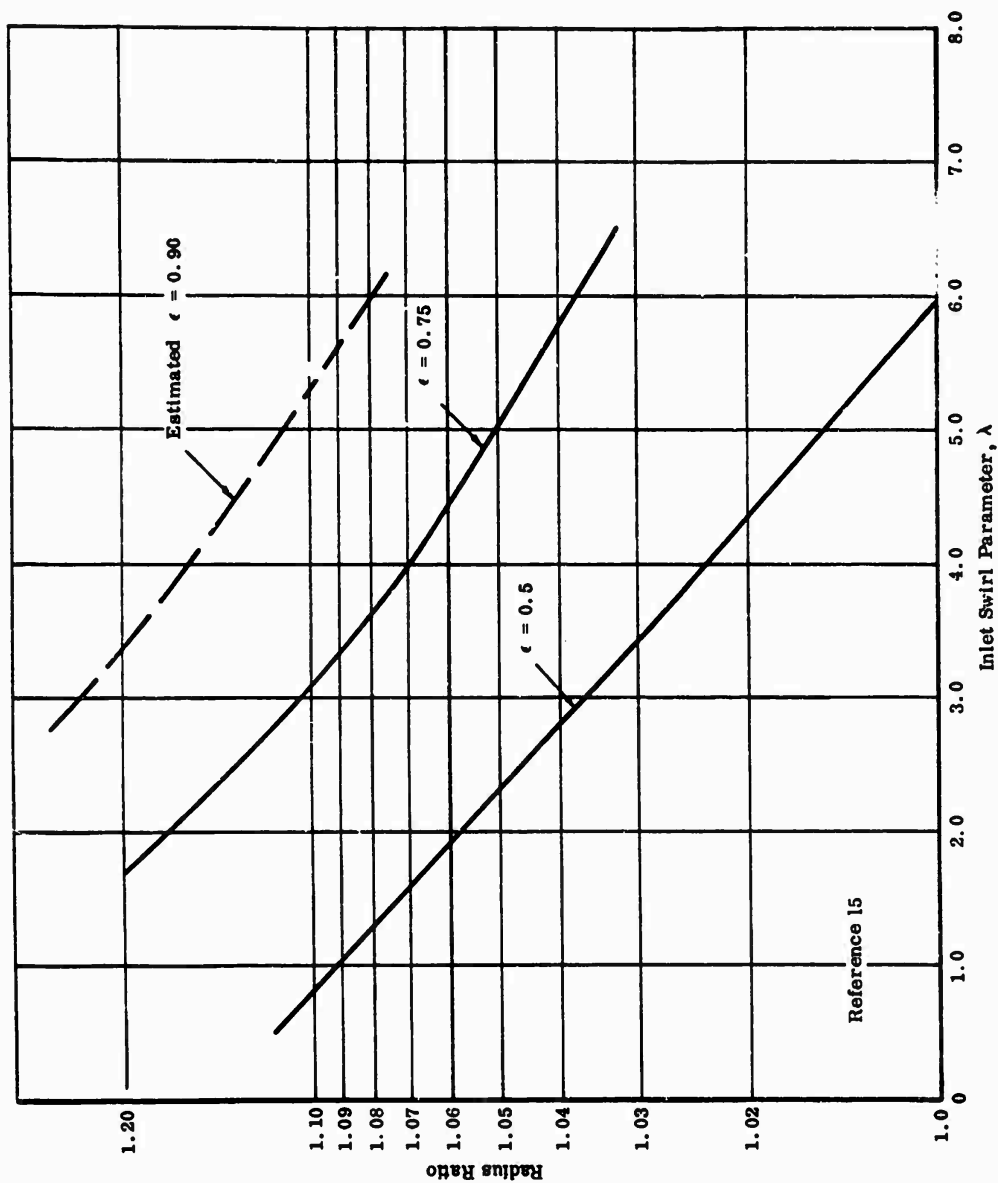


Figure 399. Length of Impeller Mixing in Vaneless Space.

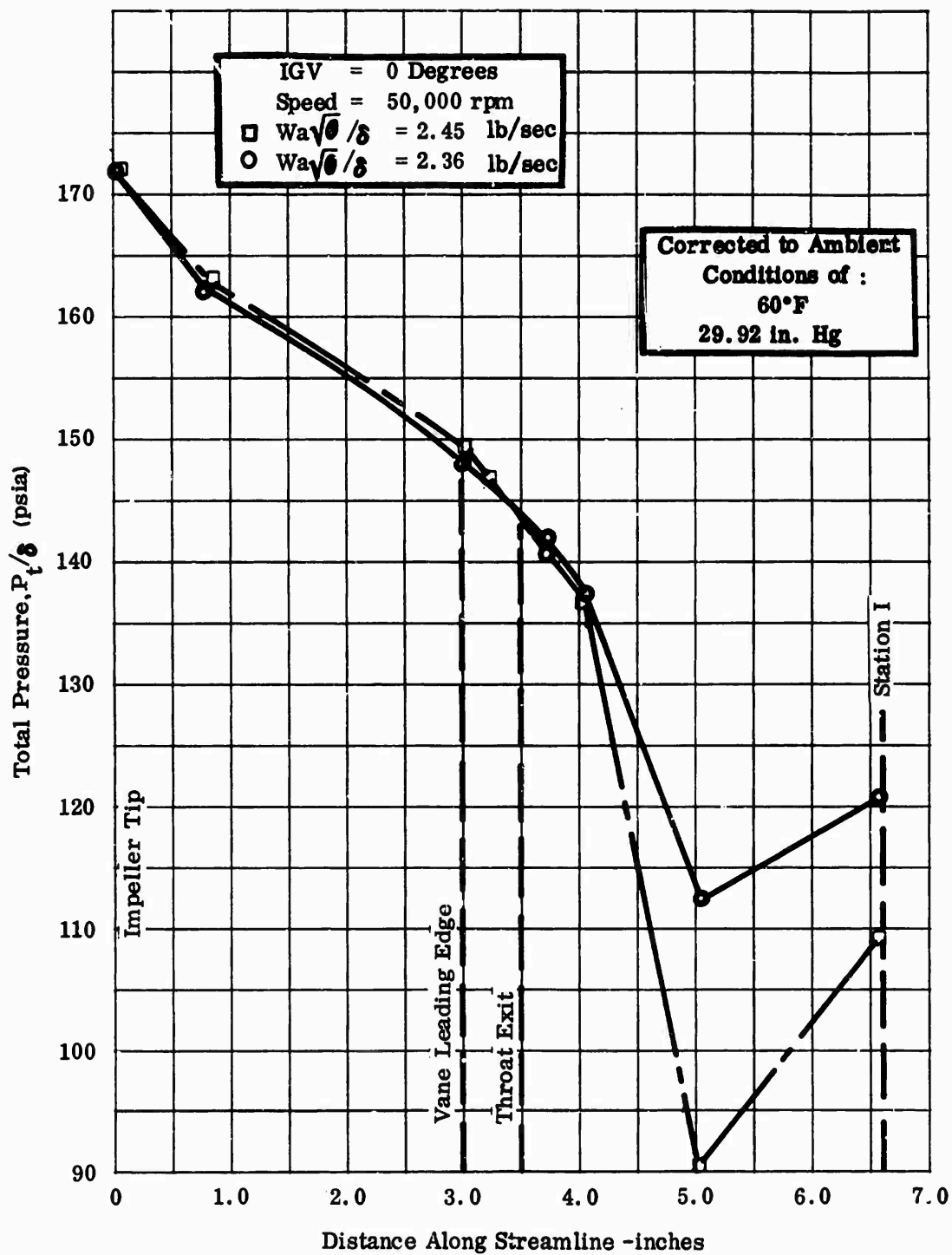


Figure 400. Total Pressure Measured Along Streamline With Channel Movable Probe.



Figure 401. Carbon - Black Traces (Shows Bleeding of Suction Surface).

CONFIDENTIAL

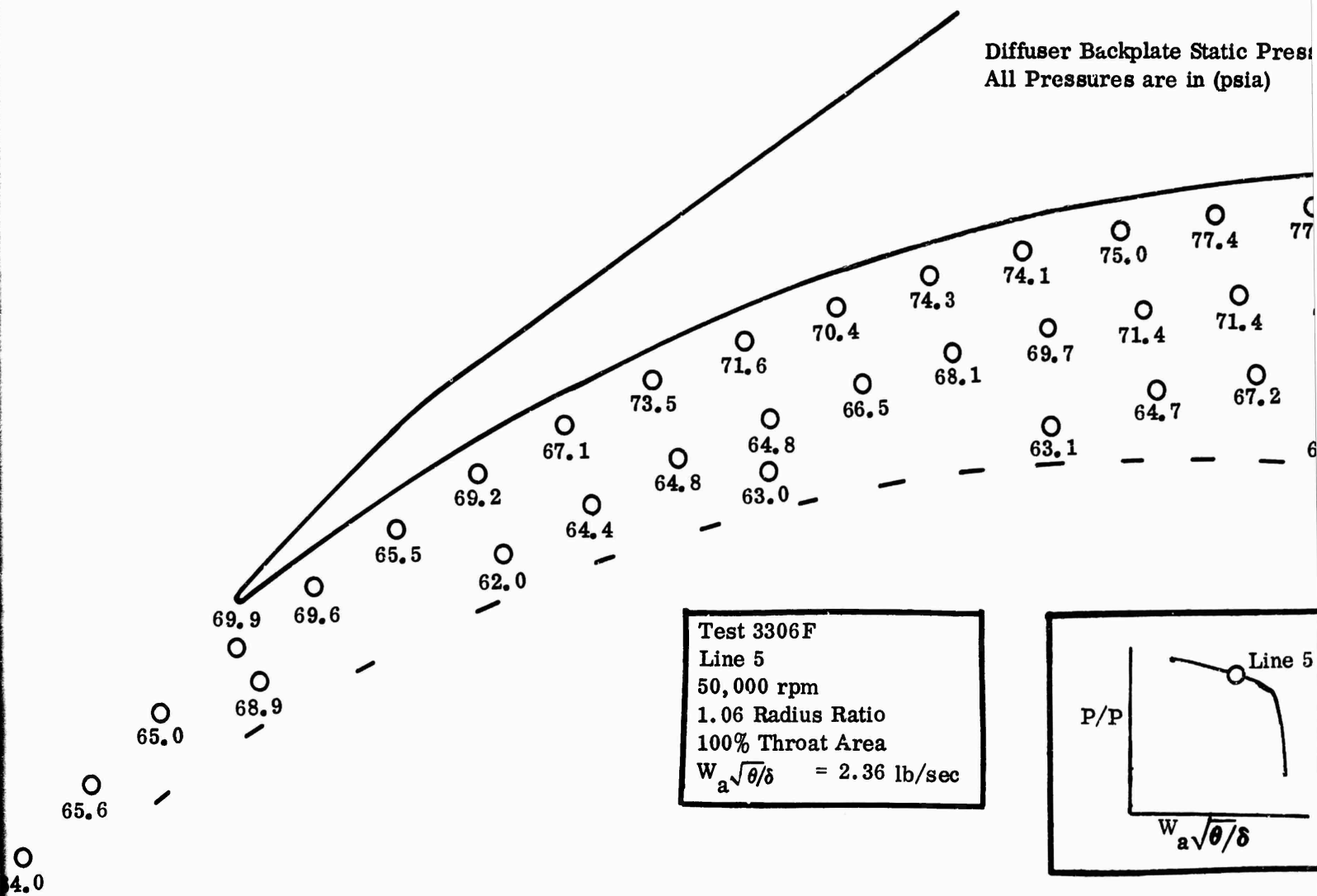
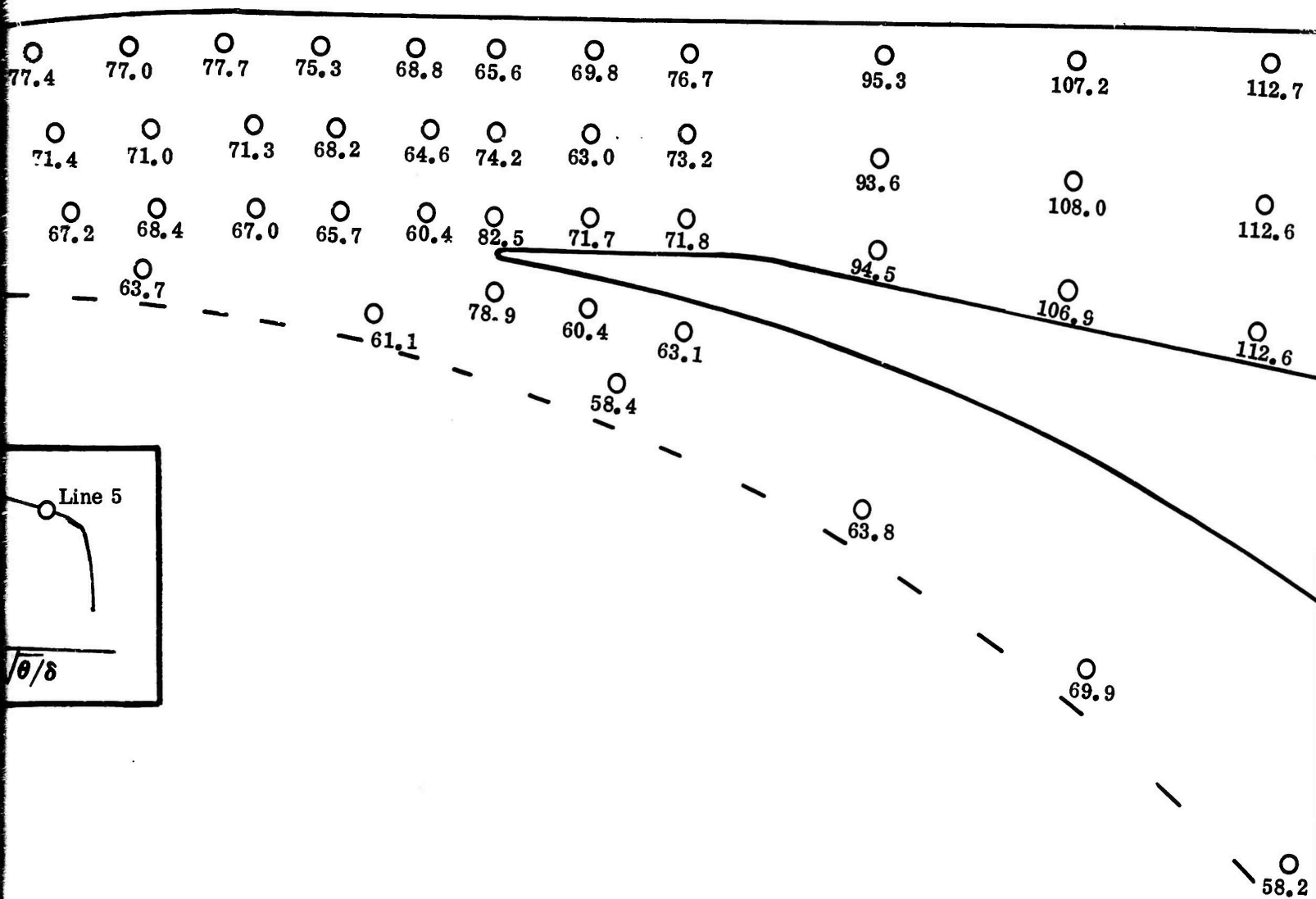


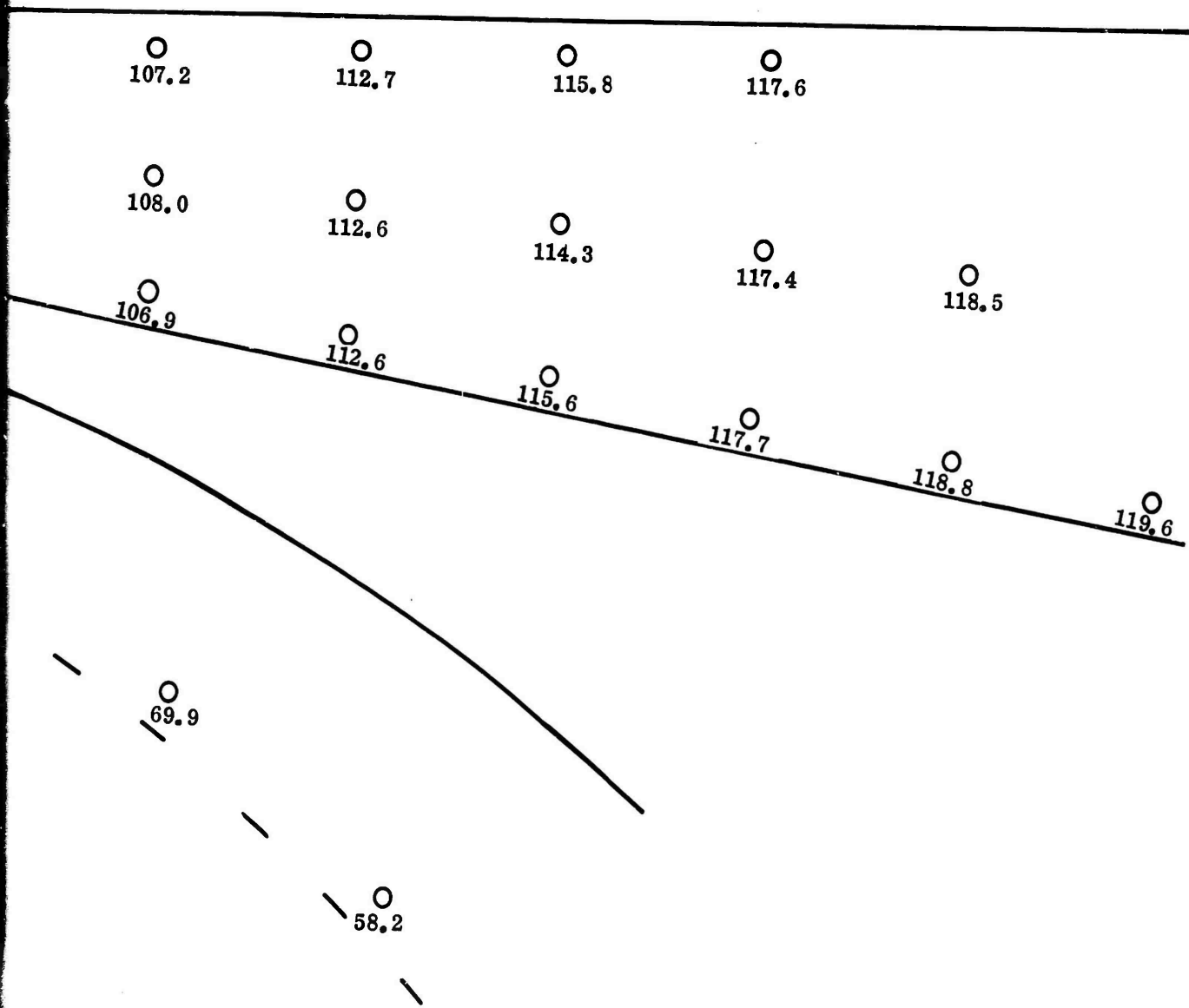
Figure 402. Static-Pressure Field, DI-1.

615

CONFIDENTIAL

Static Pressures
in (psia)





CONFIDENTIAL

pressure gradients were small. A refinement could be made by calculating according to the actual pressure gradient measured, but it is believed that this would have a small effect on the final displacement thickness calculated at the channel throat.

The static-pressure field shown in Figure 402 also gives insight to the nature of the streamlines through the semivaneless space. An expansion region occurs near the leading edge of the suction surface (Region I of Figure 403). In Region II, a radial static-pressure gradient occurs, suggesting a vortex flow; but the gradient is smaller than that of free vortex, indicating that the vanes exert some force on the flow in the semivaneless space. The flow is known to depart from vortex theories used in conventional subsonic-diffuser designs. The measured gradient further shows that the streamlines must curve in Region II to satisfy the Euler-n equation:

$$\frac{\delta p}{\delta n} = \frac{\rho V^2}{g_0 R} \quad (45)$$

where:

V = fluid absolute velocity
 R = streamline radius of curvature
 ρ = local fluid density
 g_0 = Newton's gravitational constant

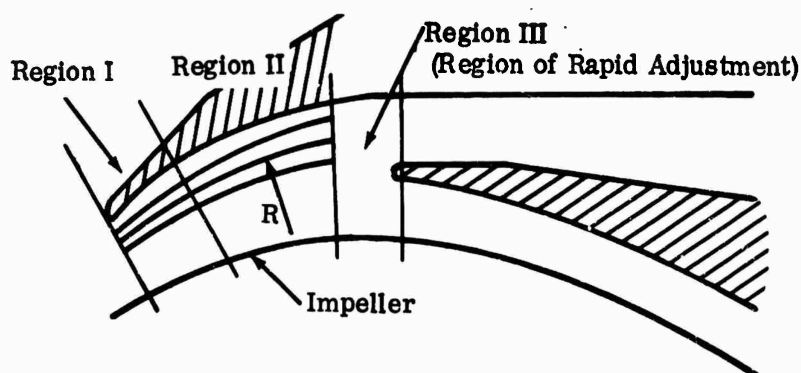


Figure 403. Streamlines Through Vaneless and Semivaneless Space.

CONFIDENTIAL

The radial pressure gradient and the curving flow indicate that no separation takes place. This can be seen from the continuity of the flow process through Regions I and II. The flow leaves the impeller tip and starts to diffuse because of the increasing area. The streamlines in the vaneless diffuser are dependent on area distribution along the flow path. In addition, the semivaneless space is bounded by only 1 vane wall and the sidewalls, so little control can be exerted on the flow by comparison to a fully bounded channel.

Another indication that separation does not occur is that the streamlines are in a direction nearly parallel to the suction surface. For a separation bubble to exist, a force would have to be exerted on the streamlines to alter their directions and divert them from the suction surface. It is not possible to exert this force in the unbounded region. The absence of separation leads to the conclusion that the only loss generated in the semivaneless space results from wall friction, where $\Delta P_{\text{friction}} = f(R/R)$.

Entrance to Channel Throat — Region of Rapid Flow Adjustment

As discussed above and as shown by the data, the Mach number reduction is less than free-vortex rate from the impeller tip through the semivaneless space. In any high Mach number diffuser design, such as the case in this program, it is necessary to have a large Mach number change from the impeller tip to the throat where the Mach number must be 1.0, or less, if the channel is to produce the major pressure rise desired. Conventionally, this change has been assumed to occur in the vaneless and semivaneless spaces. The data show that the change does not occur until the diffuser throat is approached. Figure 404 shows the static-pressure field of the DI-2 diffuser. A small change in static pressure is shown along the streamline until near the throat entrance. As discussed in Section 2.0, the impeller-tip Mach number is near 1.3, and the diffuser throat design Mach number ranges from 0.75 to 0.90. Therefore, a new flow model was adopted to explain the relationship between the small Mach number change through the semivaneless space and the subsonic throat Mach number. An explanation is offered by the above static-pressure data and schlieren data of Appendix X. A rapid adjustment of the flow takes place in a region from just in front of the throat to just inside the throat (from Point C to Point D in Figure 398). There is a shock system in this region which allows the flow to become subsonic in a very short path length. The schlieren photograph of Figure 23 in Appendix X shows a bow shock at the leading edge of the vane and a second shock just inside the throat. In this region of rapid adjustment, the flow changes from vortex to essentially 1-dimensional flow, as can be seen from the static-pressure fields, where the constant-pressure contours just inside the throat entry are nearly perpendicular to the axis of the passage. In Figure 403, the data show a pressure gradient in the radial direction in Region II of the semivaneless space and in the region of rapid adjustment. A complete adjustment to 1-dimensional flow has

CONFIDENTIAL

CONFIDENTIAL

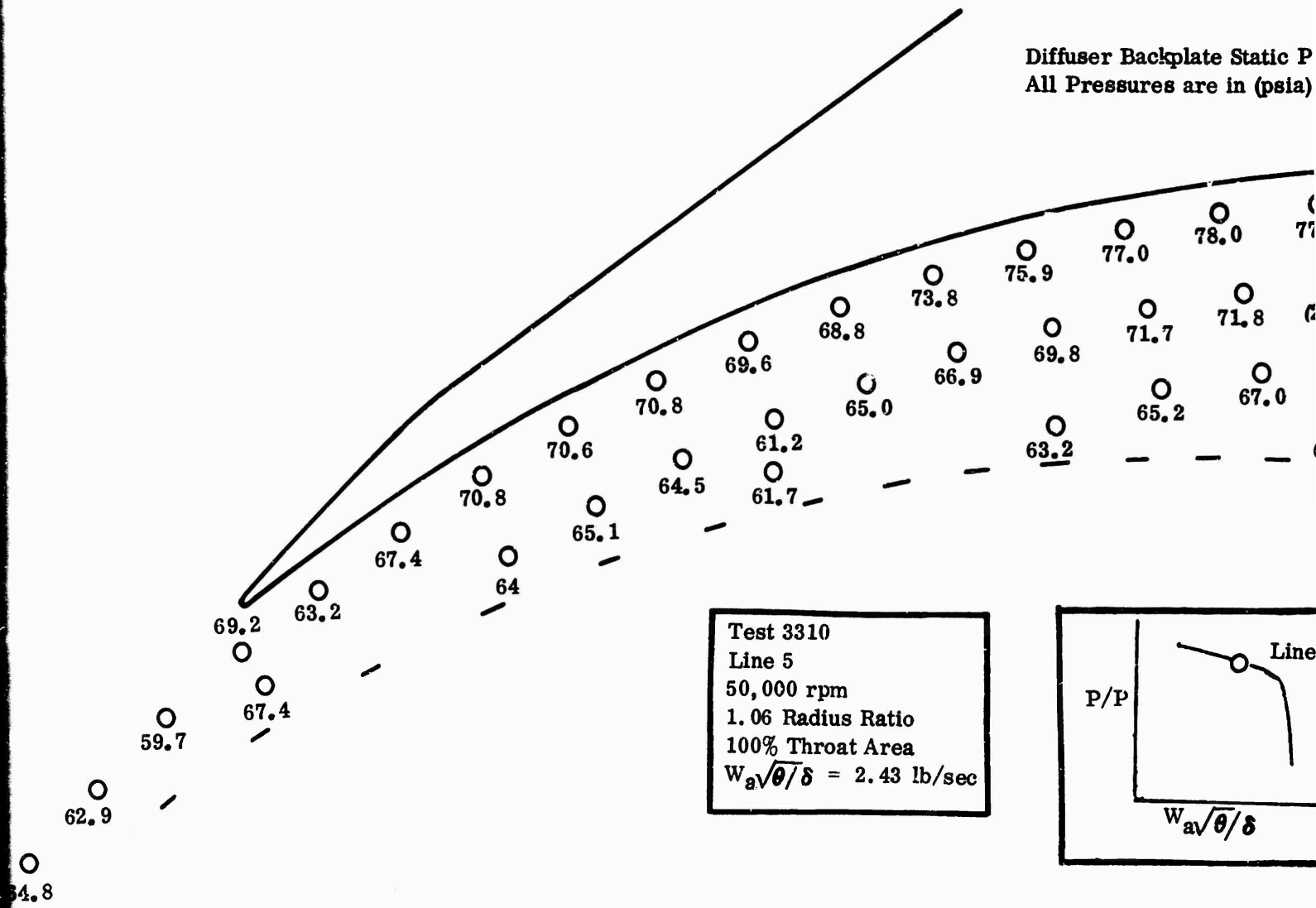
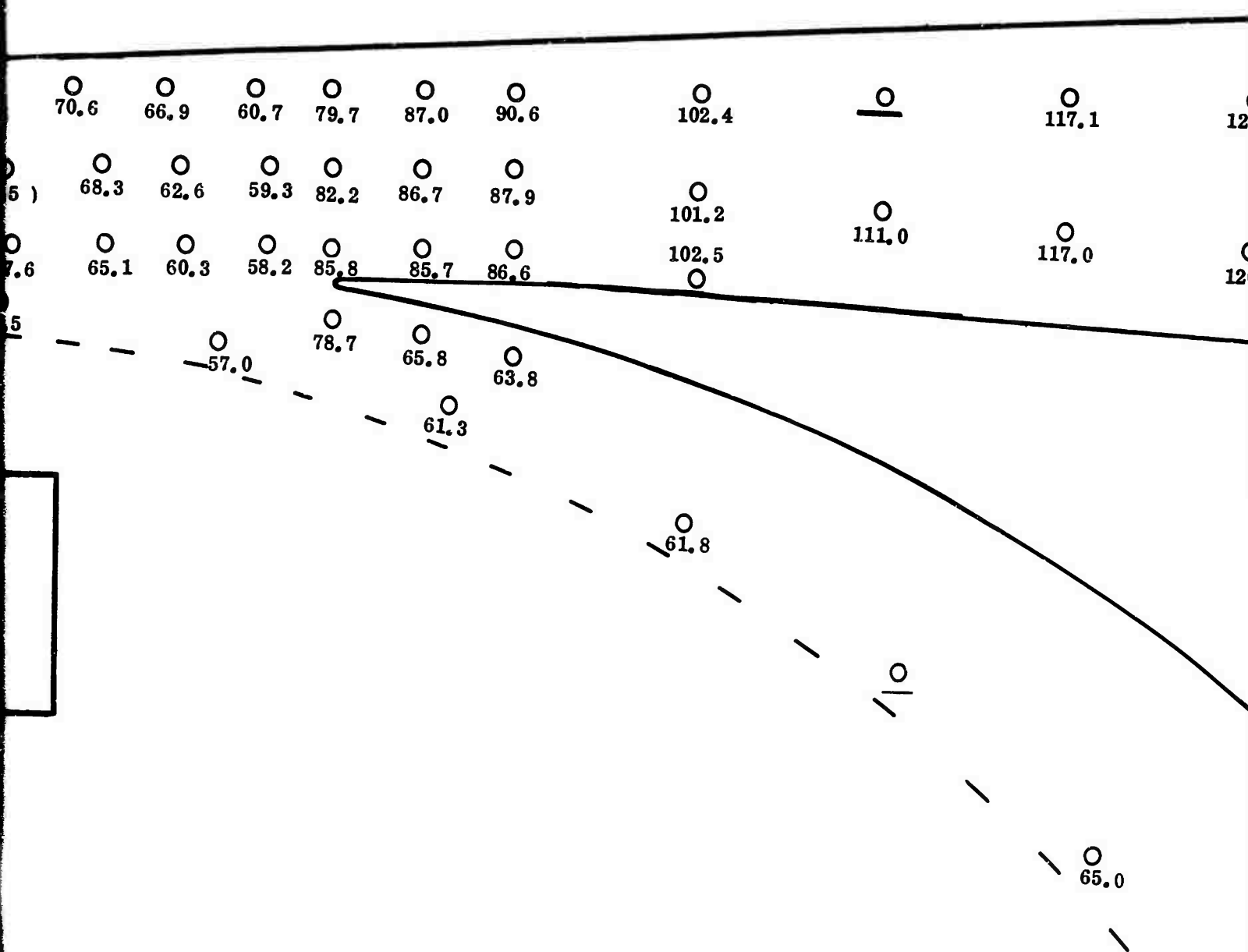


Figure 404. Static-Pressure Field, DI-2.
619

CONFIDENTIAL

asures



10

117.1

120.7

123.2

111.0

117.0

120.7

123.0

124.8

10

65.0

CONFIDENTIAL

taken place at a 1/4-inch distance from the vane leading edge inside the throat. This rapid adjustment caused the heavy loading needed to change the angular momentum of the flow at the leading edge of the vane on the pressure surfaces. Thus a strong shock occurs there and high pressures occur locally on the pressure surface (see Figure 404). As the flow becomes 1-dimensional, the pressure drops rapidly on the pressure surface just behind the leading edge.

Channel Throat

The channel throat (Point D to E, Figure 398) is designed with a straight section. As discussed in Section 2.0, the conventional purpose of the straight section is to give the flow time to adjust from the vortex flow in the semivaneless space to 2-dimensional flow in the diffusing channel. The throat length was selected from past Boeing experience. The length of the throat in relation to the design throat Mach number has a very powerful effect on the overall performance of the diffuser, as will be shown later in the discussion.

Channel Diffuser

The channel part of the diffuser (Point E to F, Figure 398) is the region where a large part of the static-pressure increase occurs. As shown above, the static pressure increases only a small amount from the impeller tip through the semivaneless space. Therefore, most of the static pressure gained in the diffuser comes in the region of rapid adjustment and in the diffuser channel. Table XXVII shows the static-pressure change for each section of the DI-2 diffuser. In the region of rapid adjustment the pressure rise is due to a shock which also thickens the boundary layer. This thickening of the boundary layer has a detrimental effect on the channel pressure recovery, as will be shown later. It must be emphasized at this point that this discussion concerns diffusers with supersonic impeller-discharge Mach numbers. Extensions of these conclusions to lower subsonic cases should be done with caution.

It is obvious that the actual flow processes in the diffuser are quite different from the conventional flow models. The conventional model of the diffuser is one in which the flow leaves the impeller tip at a supersonic Mach number, follows a modified free-vortex streamline pattern (where the flow goes from a supersonic to subsonic condition), enters the throat at a subsonic Mach number, and diffuses subsonically in the channel. This model also generally included an incidence limit at the vane leading edge which was believed to have an effect on the surge margin of the compressor. The angle of flow at the impeller tip and the vane suction-surface angle are conventionally used to determine incidence. In contrast to the conventional model, the proposed model from this investigation shows that the flow leaving the impeller tip at a supersonic Mach number undergoes little Mach number change through the vaneless and semivaneless space, has radial pressure gradients in this region (less pronounced than a free vortex), accelerates

CONFIDENTIAL

TABLE XXVII	
STATIC-PRESSURE RISE THROUGH DIFFUSER	
<u>Diffuser Section</u>	<u>Static-Pressure Rise</u>
Vaneless Space	2.9 (psi)
Semivaneless Space	1.4 (psi)
Region of Rapid Adjustment	8.4 (psi)
Throat	5.7 (psi)
Channel	36.9 (psi)

to shock at the throat entrance, and either diffuses subsonically in the channel or reexpands to a supersonic Mach number. The reexpansion to over Mach 1.0 is followed by a shock prior to the subsonic diffusion in the channel. The supersonic expansion depends on the throat conditions and the channel back pressure.

The channel performance is strongly dependent on the inlet boundary-layer conditions and the Mach number at its entrance. The flow is always subsonic at Point D (see Figure 398), but it may accelerate to Mach 1.0 due to friction in the straight section of the throat if the throat is long enough. For any throat entrance Mach number (the subsonic Mach number after the entry shock), the throat-exit Mach number can be determined if the friction factor is known, using Fanno line calculations where:

$$\frac{4 f L_{\max}}{D} = \frac{1 - M^2}{\gamma M^2} + \frac{\gamma + 1}{2 \gamma} \log_e \frac{(\gamma + 1) M^2}{2 \left(1 + \frac{\gamma - 1}{2} M^2 \right)} \quad (46)$$

f = friction factor

D = hydraulic diameter

M = Mach number

L_{\max} = length required to reach Mach 1.0 at exit

γ = ratio of specific heat at constant pressure to specific heat at constant volume

CONFIDENTIAL

If the throat is shorter than the critical length, L_{\max} , the flow will not reach Mach 1.0 at the throat exit and will diffuse subsonically through the channel.

The schlieren photograph of Figure 137 (Appendix X) shows a series of shocks in the channel of the DI-1 diffuser. These channel shocks appear to be 1-dimensional and need not take the form of a single shock, but rather are repeated quasi-normal shocks. This pattern is typical of the shock structure which occurs in a 1-dimensional channel (Reference 9). The multiple shock is occasioned by shock-wave-boundary-layer interaction. As demonstrated by Neumann and Lustwerk (Reference 38), the pressure rise across a repeated shock in a duct is almost equal to that across a thin normal shock. All the other changes of fluid properties are similarly related. Therefore, the finite length of the normal shock can be ignored (except when straight section is shorter than repeated shock). The second shock system in the channel diffuser must be avoided for best performance. Subsonic diffuser performance after a shock in the channel is directly related to the Mach number upstream of that shock. It has been found that the static-pressure recovery in a 2-dimensional diffuser deteriorates rapidly for channel Mach numbers above 1.1 to 1.2 (see Figure 396).

7.2.4 CHANNEL PERFORMANCE AND SURGE

In analyzing the diffuser it was necessary to establish a flow model that considers changes in flow along a speed line (i.e., from maximum airflow to surge). Figure 405 shows a compressor speed line and various diffuser-flow patterns. For simplicity of the illustration, it was initially assumed that the impeller-discharge total pressure does not vary with flow. Later in this discussion, the flow model will be supplemented to include considerations of variations of impeller-discharge total pressure. Figure 405a shows the diffuser at an operating condition below the knee of the speed line (the knee is the point where the pressure ratio drops abruptly). The flow leaves the impeller tip near Mach 1.3, and has essentially constant Mach number through the vaneless and semivaneless spaces up to the region of rapid adjustment. Shocks occur in this region and a subsonic Mach number results at the throat entrance. The level of this Mach number is dependent on the effective area of the throat, and the shock strength will adjust to meet the continuity requirement at the throat entrance. Effective area is less than the geometrical area by the amount of boundary-layer blockage. The flow accelerates in the throat due to friction and reaches Mach 1.0 at the throat exit. In this case, it expands supersonically and passes through a series of shocks whose location in the channel is dependent on the downstream (collector) static pressure. After the channel shocks, the flow is subsonic and may not diffuse if separation takes place. Therefore, a large part of the total pressure is lost in a dump from a high exit Mach number into the collector, and the resulting pressure ratio is reduced as shown on the compressor map (Figure 405a). As the back pressure increases to the point where W^* is reached, the positioning of

CONFIDENTIAL

CONFIDENTIAL

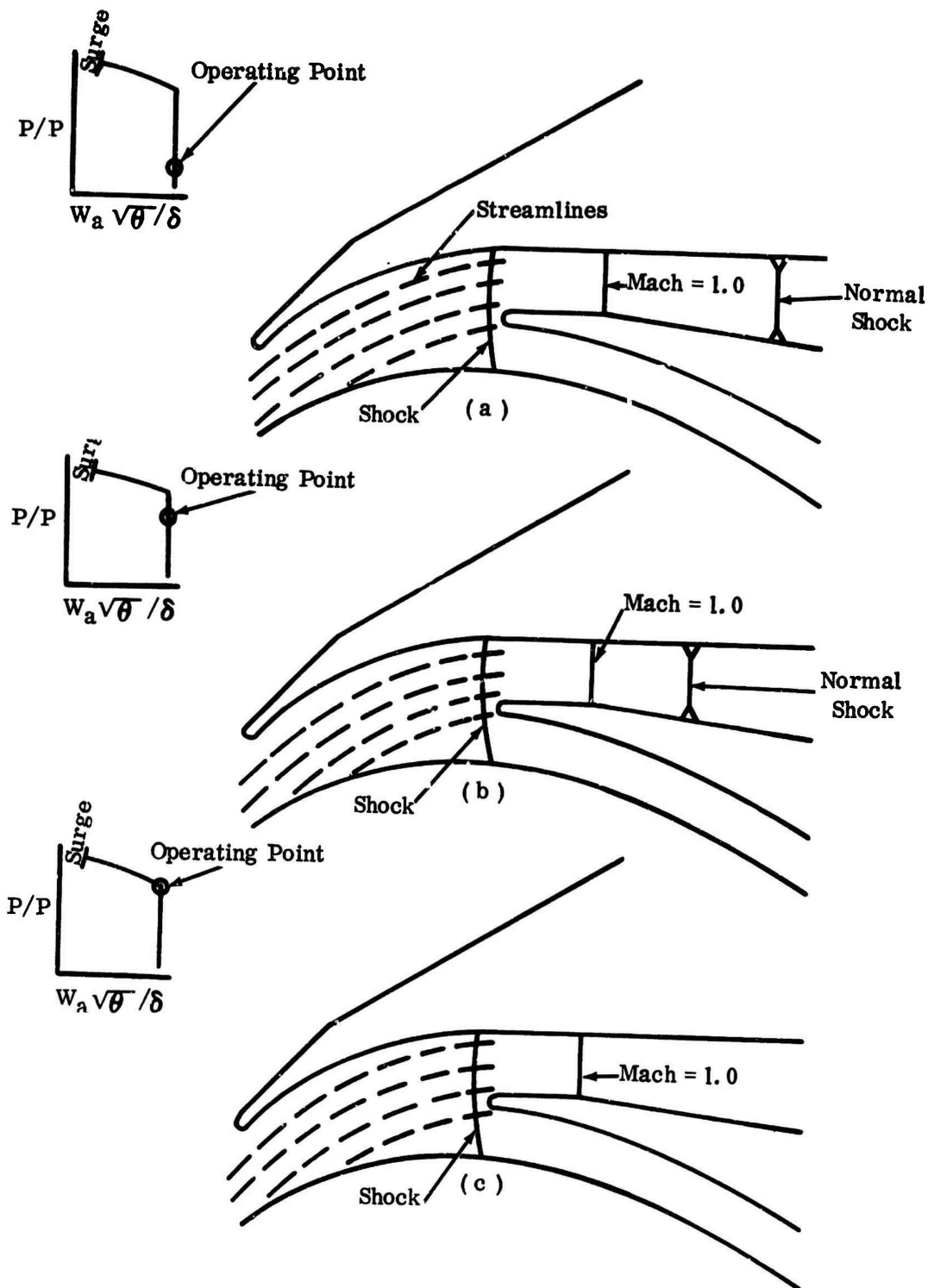
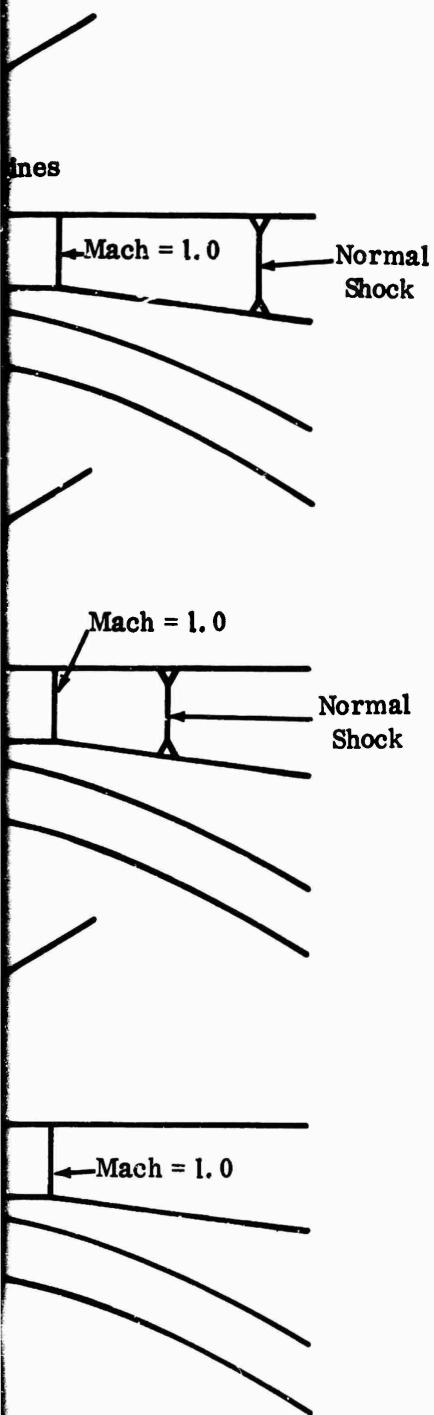


Figure 405. Flow Patterns Through a Vane-Island Diffuser.

625

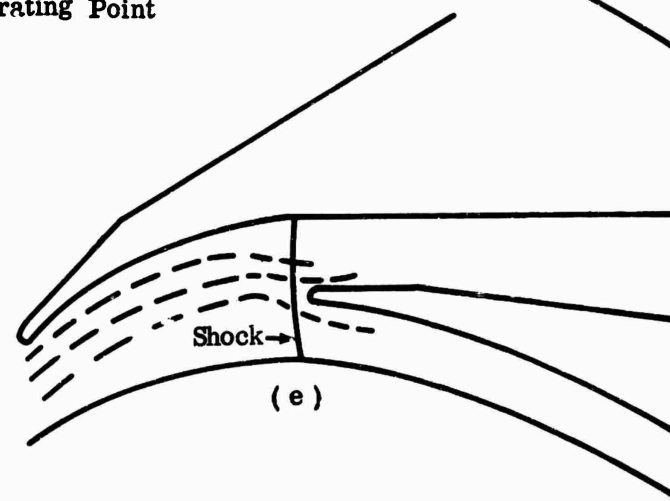
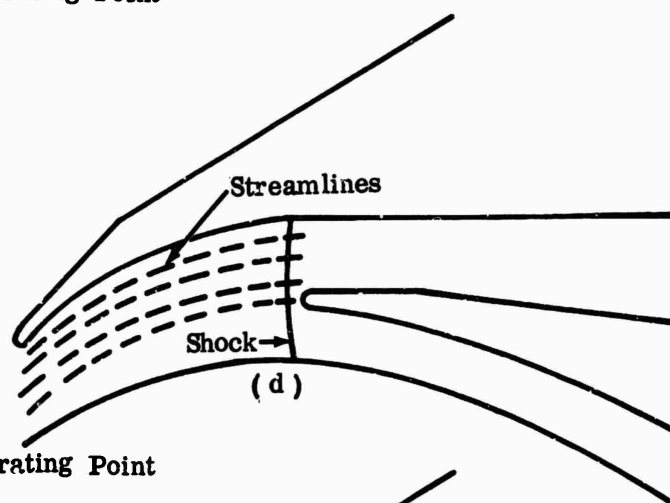
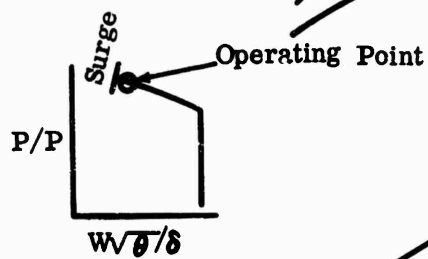
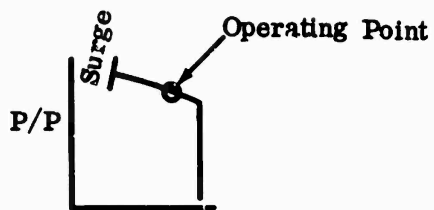
CONFIDENTIAL

TIAL



in a Vane-Island Diffuser.

TIAL



CONFIDENTIAL

the shock in the channel is controlled by the collector static pressure. Similar flow conditions have been reported by Stodola (Figure 406) for supersonic nozzles. The single-channel-diffuser data obtained on a separate flow rig also showed these characteristics for flows above W^* with diverging-channel Mach numbers above 1.1 to 1.2 (see Figure 396).

In Figure 405b the collector back pressure has been increased and the channel shock has moved upstream. Therefore, the Mach number of this shock is reduced, and the static-pressure recovery of the channel has increased. All conditions upstream of the throat exit remain essentially the same as at the knee, except for a small decrease in effective throat area. This decrease alters the flow but does not affect the upstream pressure distribution. A typical schlieren photograph of the same condition is shown in Figure 124 of Appendix X, giving visual evidence of the channel-shock location.

In Figure 405c the compressor back pressure has been increased to a point where the channel shock disappears. The channel entry is now at just the critical condition ($M_{\text{core}} = 1.0$, $W = W^*$); the channel-diffuser static recovery has improved further (Figure 405c), but all conditions upstream still remain essentially the same, as is confirmed by static-pressure data of DI-2 shown in Figure 407. The static pressure at the throat and the entry-shock strength are essentially unchanged by the increase in back pressure. This condition will remain until the core Mach number at the throat exit drops below 1.0 ($W < W^*$). At W^* on the speed line, any further increase in back pressure will cause a large reduction in airflow and the diffuser throat exit will be subsonic. Figure 405d shows such a case — the flow has been reduced and the throat exit is subsonic. Without the sonic condition at the throat exit, the flow upstream becomes affected by changes in back pressure. Figure 404 shows the static-pressure field for this case in the DI-2 diffuser.

In Figures 405a, b, and c, the radial-pressure gradient just ahead of the throat entrance was positive (pressure increasing with radius). This gradient remained essentially unchanged with reductions in back pressure, because the shock strength in front of the throat remained constant. Between Figures 405c and d, the radial-pressure gradient decreased and the shock strength increased. This change resulted from the decrease in airflow below W^* . Therefore, the subsonic throat-entrance Mach number had to decrease from considerations of continuity. To reach this subsonic condition, the entry-shock strength had to increase, causing a local acceleration ahead of the shock. It was assumed that the total-pressure drop across the shock was small (isentropic). The acceleration required that the streamtubes expand so that the streamlines locally shift away from the suction surface and straighten (Figure 405d). The shift appears as a reduction in the radial-pressure gradient, where the static pressure ahead of the shock approached the static pressure at the impeller tip. The streamlines diverged in this region to satisfy continuity. As the flow accelerated locally, its

CONFIDENTIAL

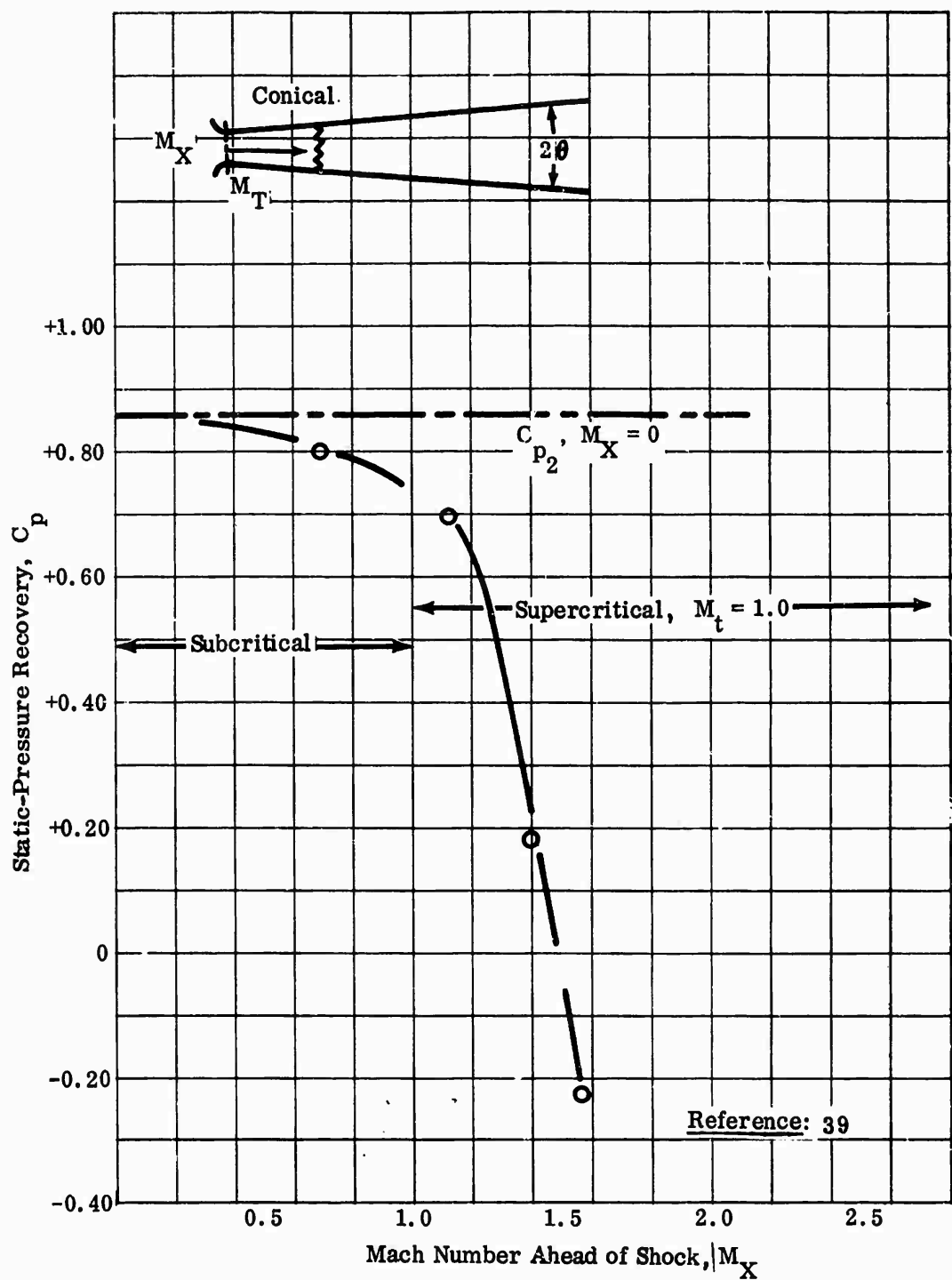


Figure 406. Conical Diffuser Performance.

CONFIDENTIAL

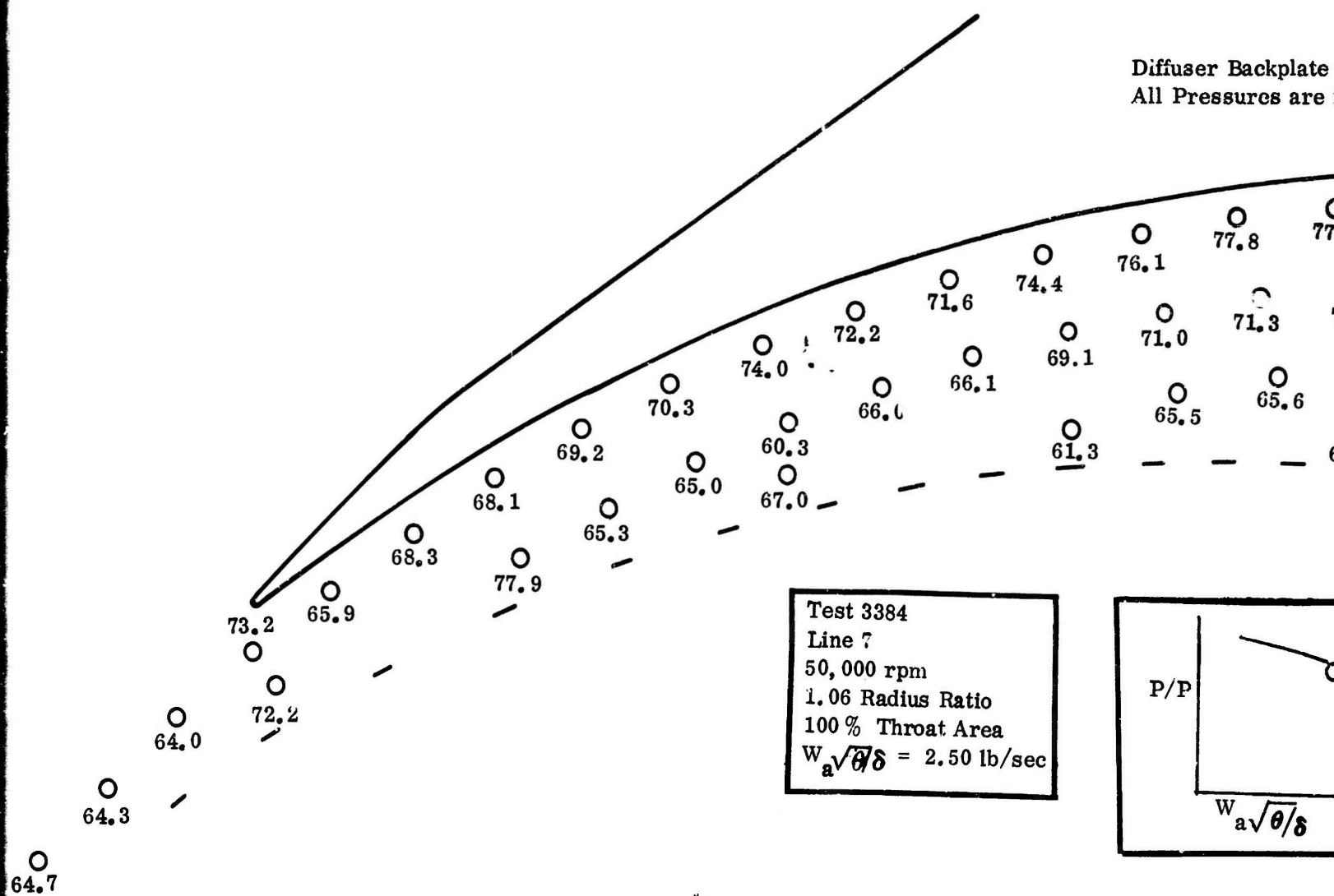
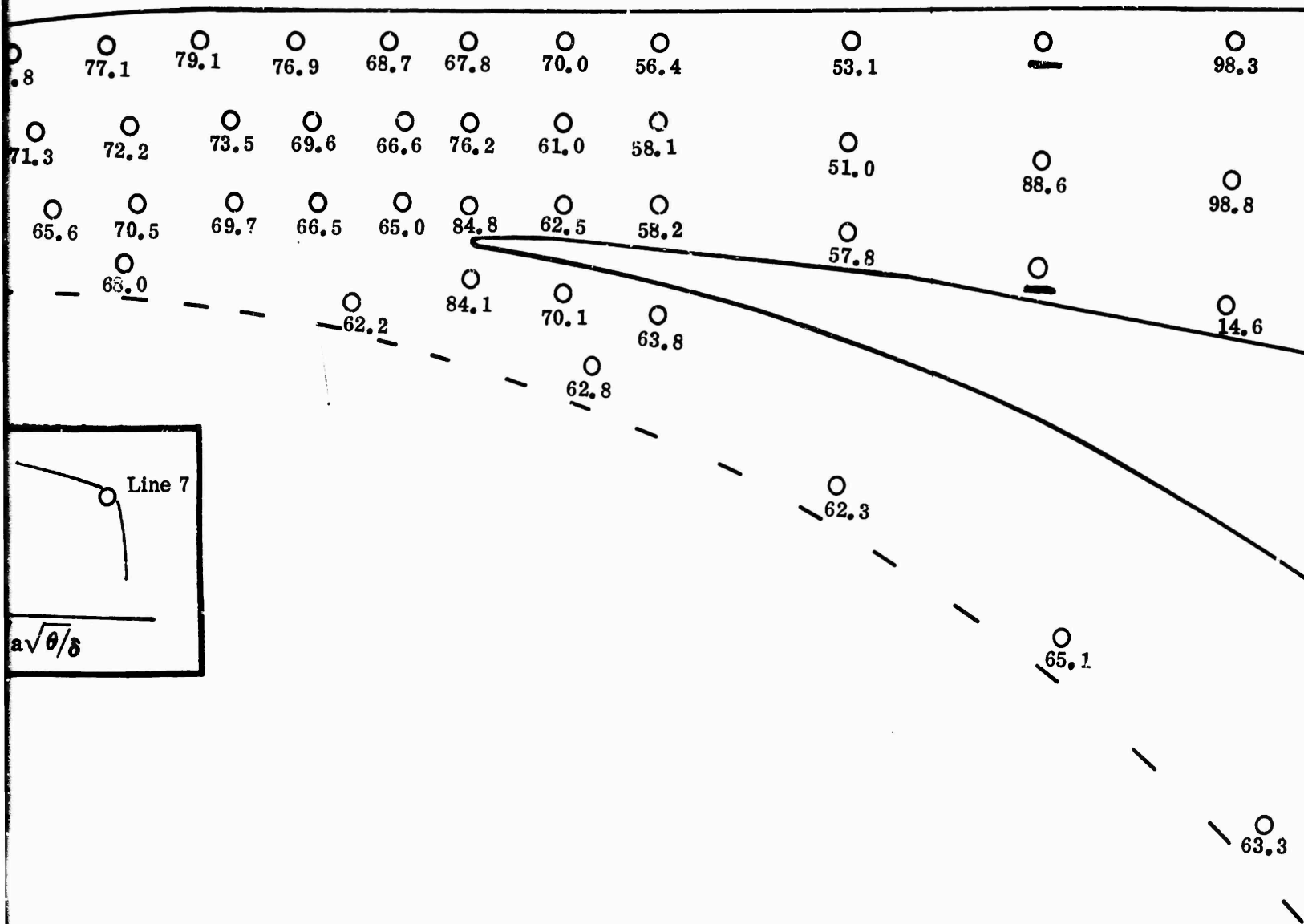
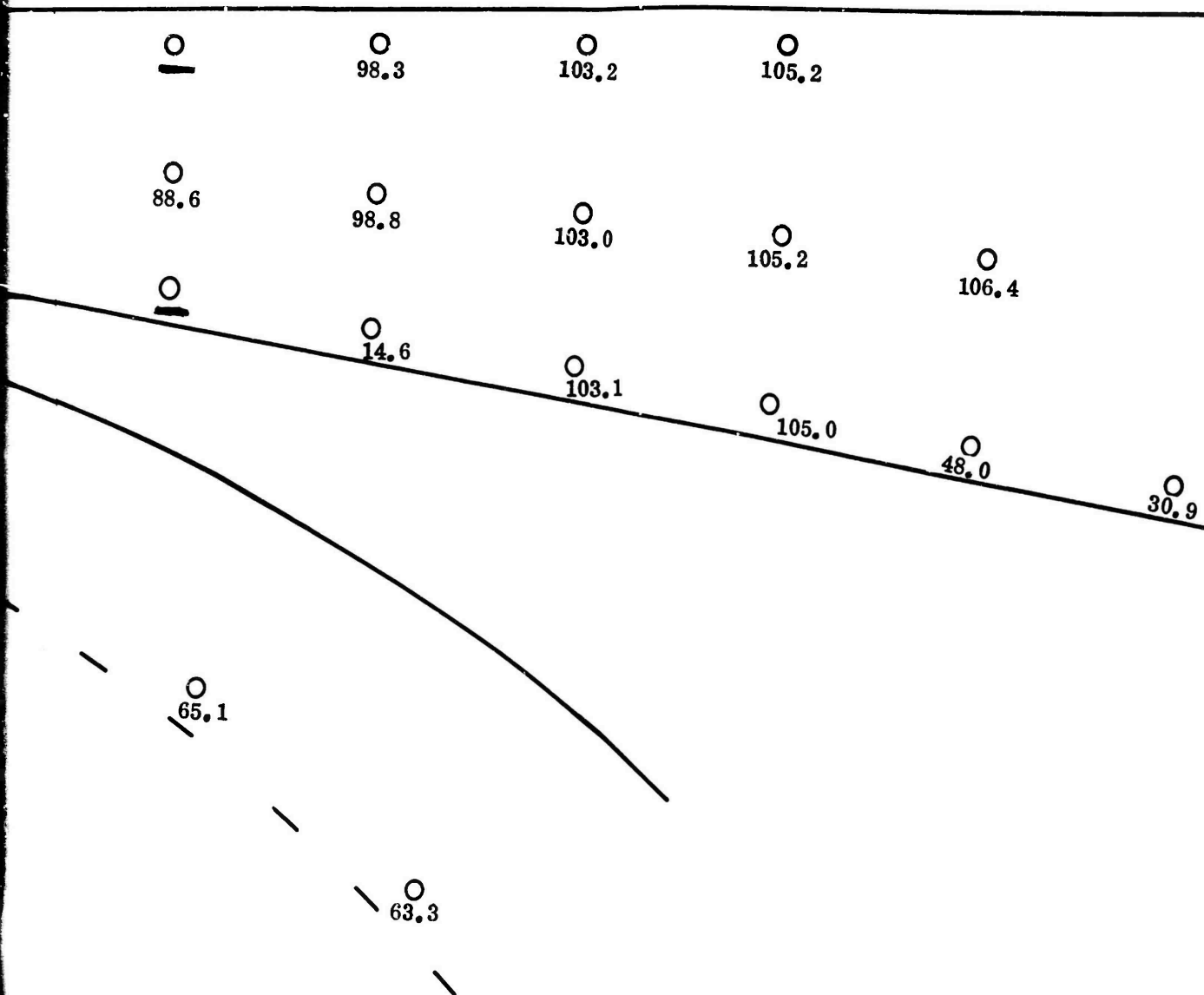


Figure 407. Static-Pressure Field, DI-2.

CONFIDENTIAL

Backplate Static Pressures
 ures are in (psia)





CONFIDENTIAL

direction was dictated by the path of area increase required to maintain supersonic flow. A second effect can also be seen by comparing the static-pressure fields of Figures 404 and 407. The straightening of the streamlines resulted in an incidence change on the vane leading edge from negative toward positive (see Figure 408), which caused a stronger expansion around the vane leading edge onto the suction surface. Note the reduced static-pressure region on the suction surface near the vane leading edge. At lower airflows than those shown in Figure 405d, the throat Mach number was further reduced, amplifying the streamline divergence. Figure 405c shows a sketch of the streamlines at a condition when the compressor was operating near surge. The throat Mach number was reduced from the case of Figure 405d, and the Mach number ahead of the entry shock was so high as to cause a reversal in the static-pressure gradient upstream of the throat entry. The streamlines turned toward the impeller rim, then around the leading edge onto the vane suction surface, causing a change in the direction of streamline curvature and a reversal in static pressure. Figure 409 shows the static-pressure field of DI-2 just prior to surge. The expansion region at the leading-edge suction surface increased in strength, leading to the conclusion that the airflow angle was in the direction of positive incidence with respect to the airfoil (see Figure 408). Note that local incidence at the vane leading edge is more a function of events in the zone of rapid adjustment than it is of impeller-discharge angle. This conclusion for the supersonic case must be extrapolated with great care to lower Mach number cases.

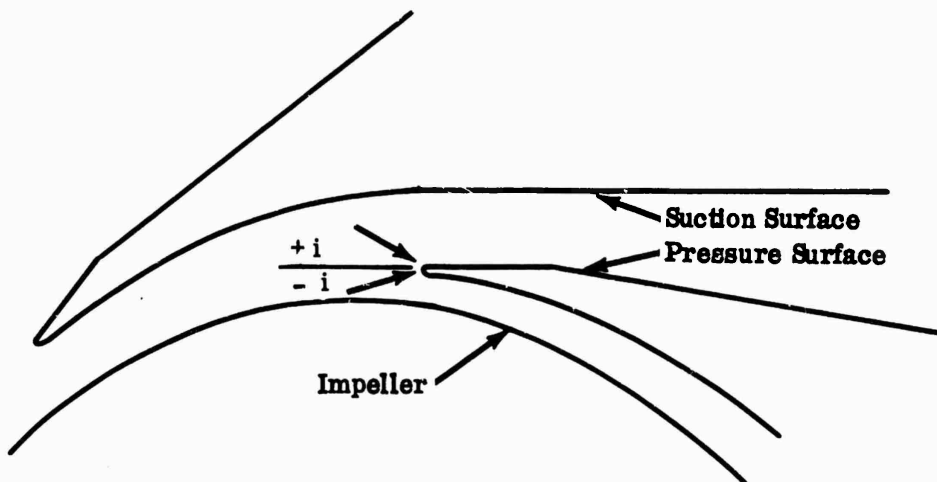


Figure 408. Incidence on Diffuser Vane.

The basic mechanism that causes surge is not clearly apparent. However, 2 possible explanations were derived. The first was based on the streamline shift

CONFIDENTIAL

CONFIDENTIAL

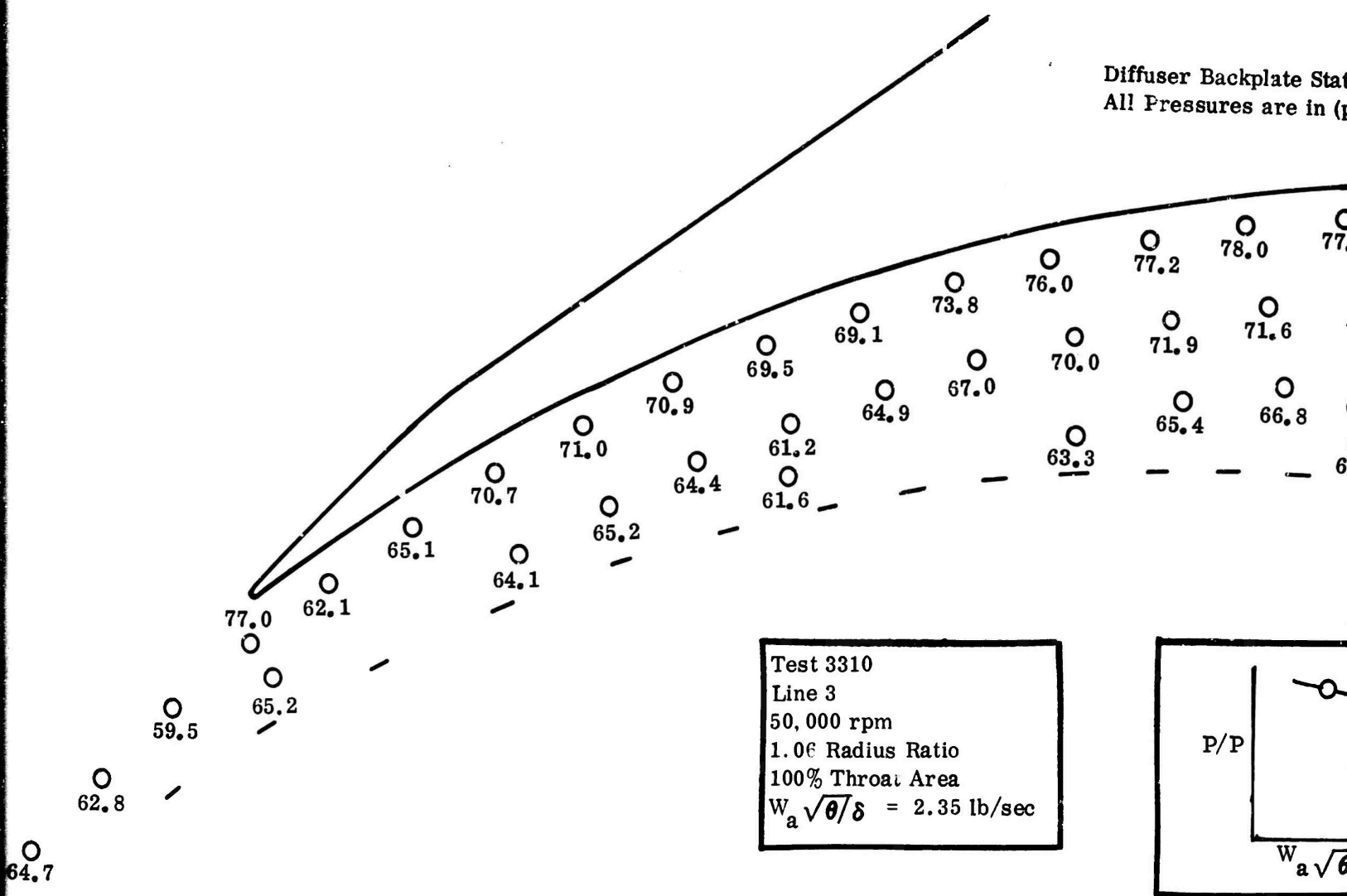
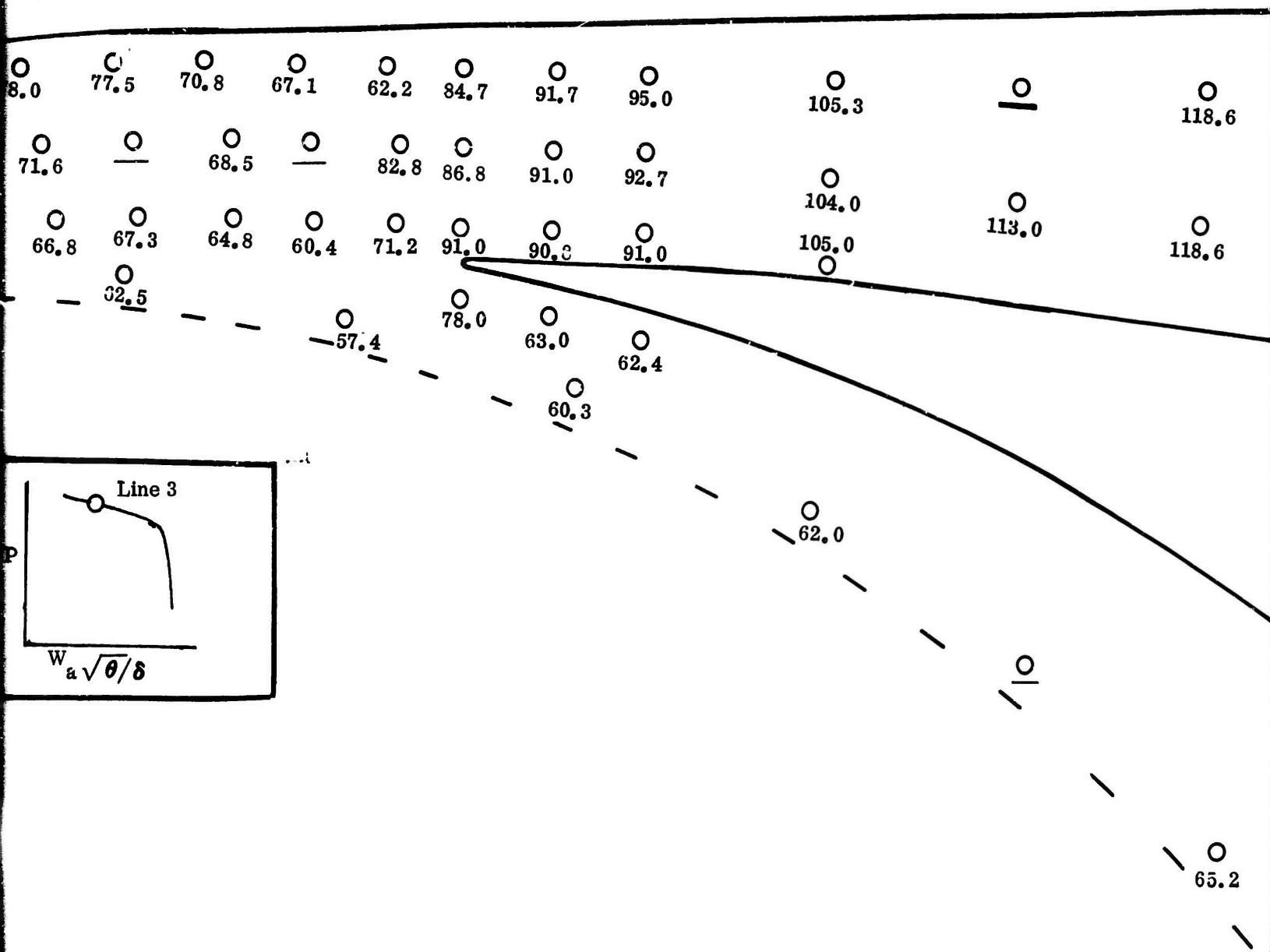


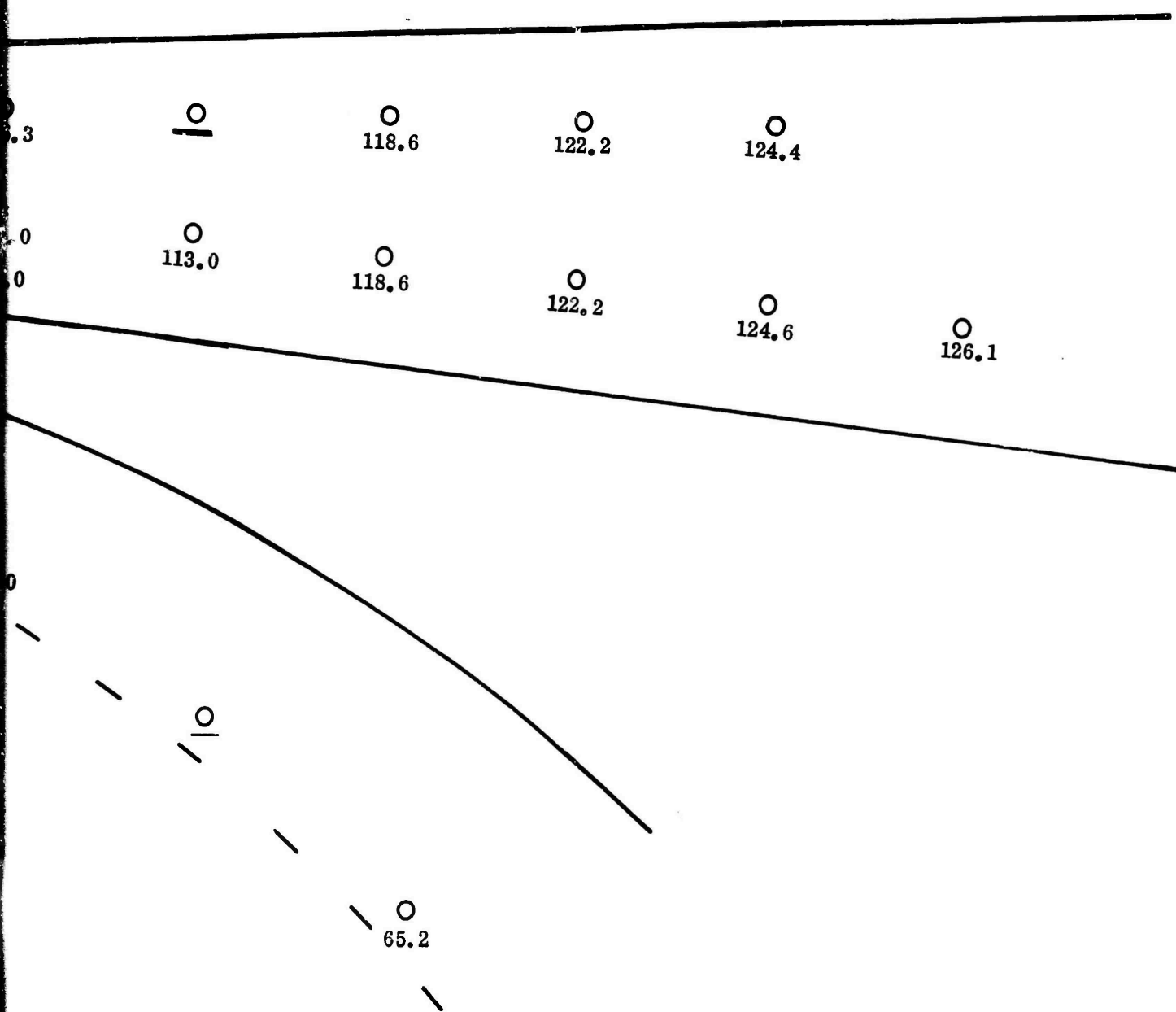
Figure 409. Static-Pressure Field, DI-2.

633

CONFIDENTIAL

Backplate Static Pressures
 are in (psia)





CONFIDENTIAL

and the second was based on the shock-boundary-layer interactions. The static pressure ahead of the shock can drop below the static pressure at the impeller tip, as shown in Figure 409. The accompanying change in streamline curvature seen in Figure 405e was observed earlier on the water table while testing other vane-island-type diffusers, but could not be explained at that time. The flow incidence on the vane resulted in a Prantl-Meyer expansion around the vane leading edge to the suction surface. The circumferential static-pressure profiles in Figures 407 and 409 show the change in the expansion region for DI-2 from the knee of the speed line towards surge. It was believed that the incidence unfavorable to the suction surface caused the flow to separate, resulting in surge of the compressor. Figure 405e suggests that the flow was spilling around the entrance of the channel, analogous to the spilling phenomenon of supersonic aircraft inlets. In applying this analogy, it must be recognized that the spilling carries over to each adjacent channel in swallowing the total flow.

The alternate explanation offered for surge is that the increasing entry-shock strength causes breakdown of the channel flow. It can be argued that with the increase of shock strength, the boundary layer is thickened in the throat and eventually will enter the channel detached. Therefore the blockage at the channel diffuser entrance is increased. Correlation of throat blockage with channel static-pressure recovery has shown a strong dependence of the recovery on blockage. Figure 410 shows this correlation for single-channel diffuser tests. Neumann and Lustwerk (Reference 38) also show that subsonic-diffuser efficiency downstream of a shock is a function of the Mach number preceding the shock, and that in a straight channel, where the flow shocks down from some entrance Mach number through a series of quasi-normal shocks, the boundary-layer growth will be essentially the same as that through a single, strong normal shock. Therefore, these conditions suggest that when the flow is reduced toward surge and the entry shock in the region of rapid adjustment is strengthened, the throat boundary layer will be increased and will eventually enter the channel detached, at which point surge will occur.

7.2.5 THROAT MACH NUMBER

The DI-1 and DI-2 diffusers were designed to evaluate the effects of throat Mach number on diffuser performance. It was recognized that the throat area had a large effect on the behavior of a diffuser, but the exact flow mechanism was not understood. It was believed that a critical Mach number existed for channel diffusers and that when the throat-entrance Mach number reached 0.8 to 0.9, the diffuser channel performance would fall off rapidly. Shadowgraph tests in previous investigations had shown that shocks were present at the diffuser-vane leading edge for impeller-tip Mach numbers near 1.2. For the workhorse impeller, even higher Mach numbers, near 1.3, could be expected at the design speed.

CONFIDENTIAL

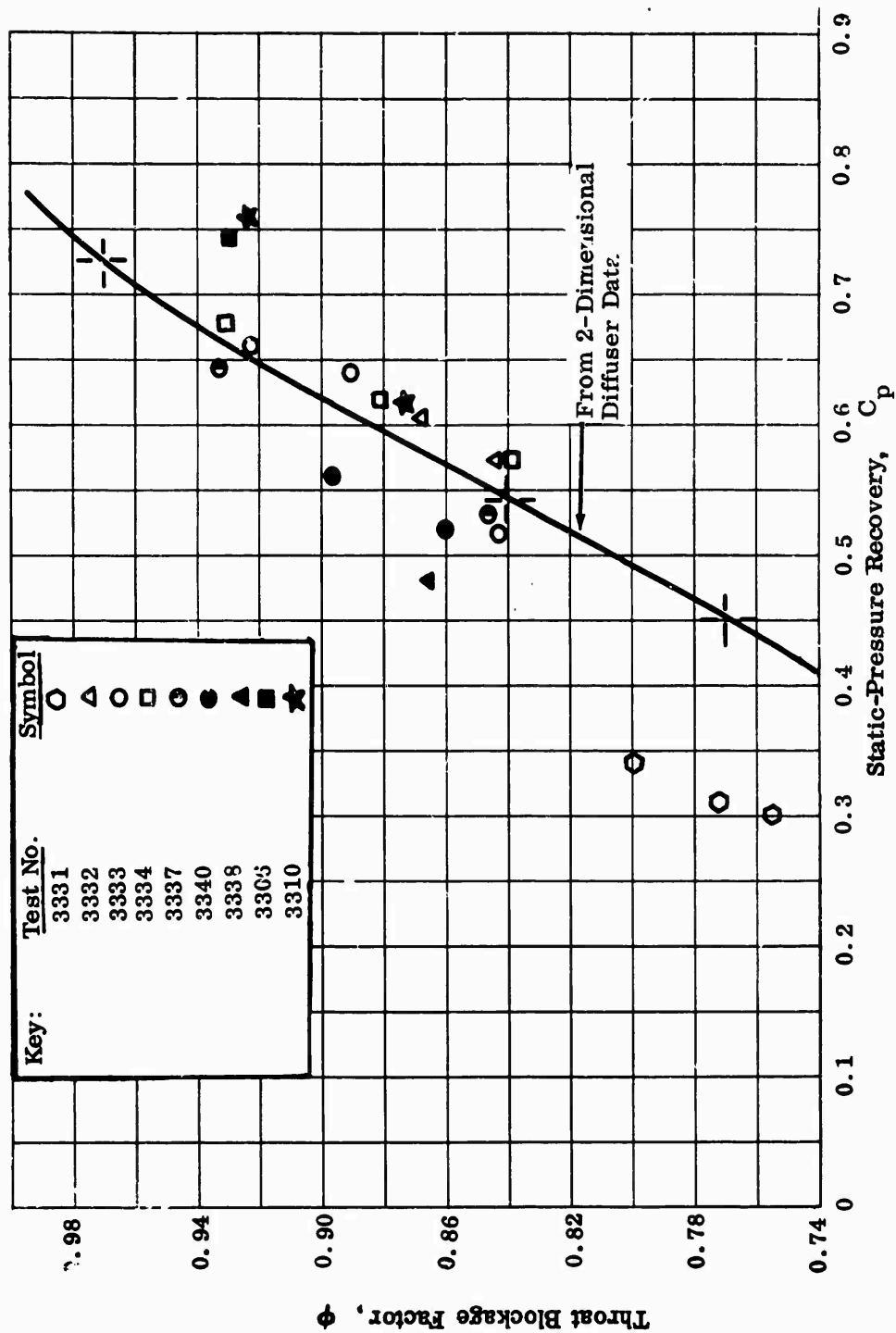


Figure 410. Comparison of Pressure Recovery for Compressor Channel With Two-Dimensional Diffuser Data.

CONFIDENTIAL

For evaluating the effects at the throat, consider an impeller and a diffuser with a certain airflow. The amount of flow the compressor will pass is governed by the diffuser-throat conditions (i.e., total pressure, total temperature, and the effective area) and the collector back pressure. The diffusers in this program have a constant-area straight section at the throat from Station D to E (see Figure 398). At the entrance of the throat (Station D), the Mach number is always subsonic. There is an entry shock upstream of Station D through which adjustment of the flow from the supersonic impeller-tip Mach number to the subsonic diffuser-throat-entrance Mach number occurs. The strength of this shock at any point along the speed line is dictated by the throat entrance Mach number, which is determined by continuity. It is important to note that at airflows lower than W^* , the entry shock M_x increases with decreasing airflow because the throat-entrance subsonic Mach number at Station D is decreasing. If the throat area is designed for an entrance Mach number of 0.90 or 0.75 (DI-1 and DI-2, respectively), the strength of the shock system upstream of the throat will adjust accordingly. The lower this Mach number, the stronger the shock, and the closer the design point is to surge point. Figure 411 shows the basic difference in DI-1 and DI-2.

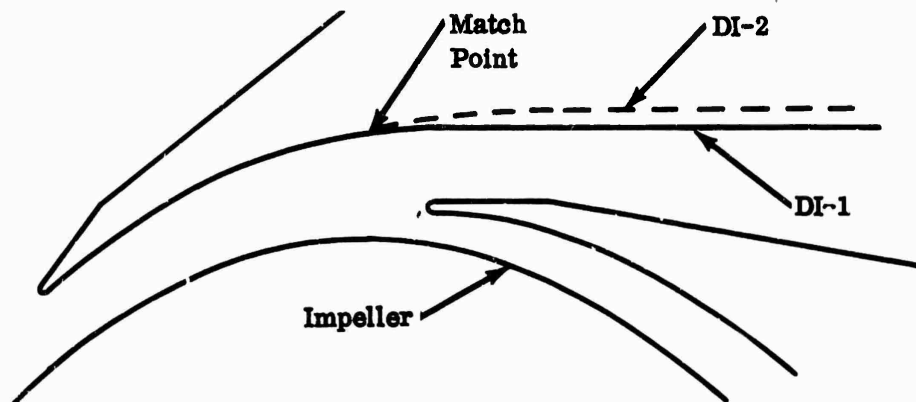


Figure 411. Difference in Vane Geometry Between DI-1 and DI-2.

Figures 409 and 402 show examples of the static-pressure fields of the 2 diffusers. The data show that the static-pressure rise of both diffusers is about the same up to the match point (compared at the same impeller speed and airflow). Beyond this point, the flow accelerates more in DI-2 than in DI-1, causing a lower static pressure at Station C and a stronger shock. The performance maps of DI-1 and DI-2 are presented in Section 6.0. DI-2 had a throat Mach number of 0.80 at 50,000 rpm (Line 7). This Mach number was slightly higher than the design throat Mach number of 0.75. The difference can be attributed primarily to a

CONFIDENTIAL

CONFIDENTIAL

lower than expected total pressure at the throat. The flow accelerated in the throat because of the friction in the straight section. However, the straight section was not long enough to accelerate the flow to Mach 1.0. Therefore, in DI-2, the flow left the impeller tip near Mach 1.3, shocked down at the vane leading edge to Mach 0.8 at the throat, accelerated again in the straight section but did not reach Mach 1.0, and diffused subsonically through the channel. Static-pressure data of DI-2 at 50,000 rpm showed no indication of a shock system in the channel when operating between the knee of the speed line and surge.

DI-1, on the other hand, had a throat Mach number of 0.95 at 50,000 rpm. Because of this high subsonic Mach number, the flow accelerated to Mach 1.0 in the straight section of the throat, accelerated in the channel with downstream shocks, and then diffused at a subsonic Mach number. The performance of DI-1 was below DI-2 because of less efficient channel diffusion caused by the high Mach number ahead of the shock at the start of the diffusion. Later single-channel test data confirmed this conclusion.

However, the lower throat Mach number of DI-2 with the stronger bow shock and the absence of the downstream channel shock (from maximum airflow to surge) appeared to have reduced the airflow range of DI-2 as compared to DI-1. Airflow range is defined as:

$$\text{Percent Airflow Range} = \left(\frac{\text{Maximum Airflow}}{\text{Surge Airflow}} - 1 \right) 100$$

The airflow range of DI-2 was 6-1/2 percent compared to 12-1/2 percent for DI-1. The result was not unusual in view of previously observed characteristics of a vaned diffuser; i.e., high performance is associated with short range, and vice versa. The airflow range difference of the two diffusers can now be explained with some degree of confidence. Referring to Figure 412, speed lines of the 2 diffusers are plotted against W/W^* , the ratio of the local airflow to the airflow when the core flow just reaches Mach 1.0. Both diffusers surged at essentially the same Mach number upstream of the entry shock ($M_x = 1.15$ to 1.20). Therefore, the range from $W/W^* = 1.0$ to surge on Figure 412 was greater for DI-1 than DI-2 because the entry shock at W^* was weaker for DI-1. With the weaker entry shock, a greater airflow reduction was realized before DI-1 reached the surge Mach number.

It is not surprising that both diffusers surge at the same shock-entry Mach number when considering that the throat length of both diffusers is the same. Neumann and Lustwerk, Reference 38, showed that the length of the shock system necessary to reach maximum pressure rise is a function of the upstream Mach number. Figure 413 shows the data from Neumann and Lustwerk with a suggested extrapolation of their data, which indicates that the shock length for maximum

CONFIDENTIAL

CONFIDENTIAL

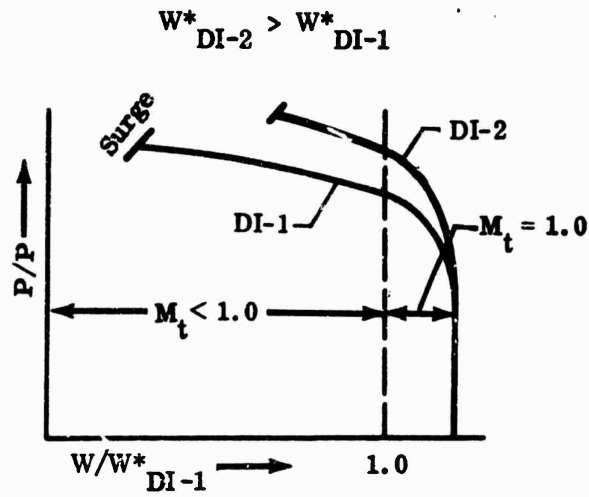


Figure 412. W/W^* on Characteristic Speed Line.

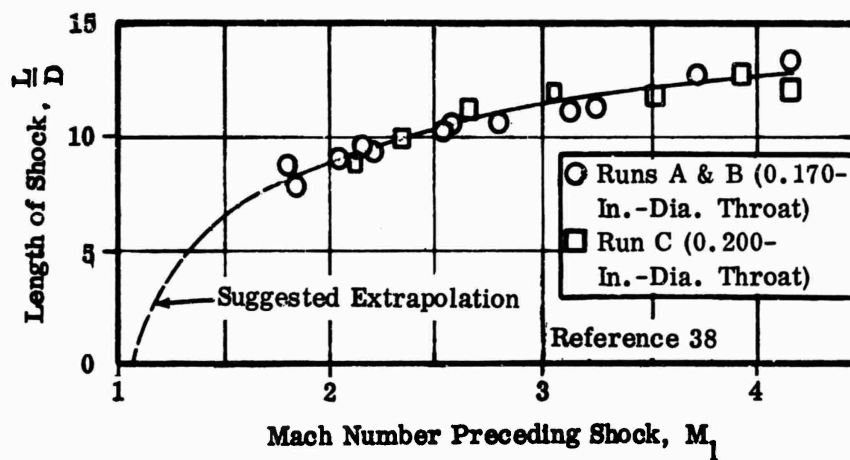


Figure 413. Length of Shock Versus Mach Number Preceding Shock (1.000-In.-Diameter Tube).

CONFIDENTIAL

CONFIDENTIAL

pressure rise becomes zero at about 1.1 entry Mach number. This deduction agrees with the single-channel diffuser data obtained in this program (see Figure 396). Further, if the throat lengths are the same, the entry-shock Mach number at surge should be the same if it is shock separation of the boundary layer in the throat that causes surge. It can also be seen from the comparison of the 2 diffusers in Figure 412 that W^* for DI-2 is not actually reached. The reason is that the impeller limits the maximum airflow, rather than the diffuser throat. This conclusion is reached from the impeller test data, where maximum airflow of the compressor did not increase when the diffuser throat was opened 25 percent during the variable airflow tests. The impeller flow limit also contributes to the overall shorter range of DI-2.

Therefore, the flow process of DI-2 can be explained for the flow range from surge to maximum airflow. As maximum flow is approached, the subsonic throat-entrance Mach number increases and causes the Mach number ahead of the entry shock to decrease. After entering the throat, the flow accelerates because of friction (Fanno process), but the throat is not long enough to cause the core flow to reach sonic conditions. Therefore the flow diffuses subsonically in the channel.

7.2.6 THROAT BOUNDARY LAYER

In the case of DI-1 the flow reaches W^* as maximum airflow is approached. The core-flow Mach number at the throat exit of DI-1 remains sonic; however, the airflow can still increase beyond W^* until the impeller reaches maximum airflow. This difference from DI-2 can be explained by examining the boundary-layer conditions at W^* . The boundary-layer displacement thickness at the throat is estimated to be 0.0069 inch, using the 1/7th-power-law profile suggested by Schlichting for turbulent flow over a smooth, flat plate. A constant pressure along the surface is assumed, but the actual Mach number conditions at various stations along the flow path are used. Displacement thickness at throat entry is given by:

$$\delta^+ = \left(\frac{g_o \mu}{\rho V} \right)^{0.139} \left(0.01738(L) \right)^{0.861} \quad (47)$$

δ^+ = displacement thickness

μ = viscosity

ρ = density

V = fluid velocity

CONFIDENTIAL

L = length along the pressure or suction surface

g_0 = Newton's gravitational constant

The entry shock at $M = 1.05$ has a small effect on the boundary layer and was neglected. The actual boundary-layer thickness or the distance from the walls where core flow reaches sonic conditions is approximately 7 times the displacement thickness. By calculation, about 47 percent of the flow area is actually subsonic at W^* . As the back pressure is reduced from the W^* condition, it can be seen that the supercritical condition of the core flow downstream from the throat can affect the flow upstream through the throat and into the space ahead of the vanes because of the subsonic flow at the surfaces of the throat. At airflows above W^* , the magnitude of the subsonic area decreases.

The difference in characteristics between DI-1 and DI-2 can also be explained in terms of blockage change due to change in geometrical throat area. It has been mentioned that the channel static-pressure recovery is strongly dependent on the throat-inlet-boundary-layer blockage and that the blockage in turn is dependent on the entry-shock Mach number. A comparison of the 2 diffusers at the same Mach number upstream of the entry shock shows that the overall pressure recovery difference is about 5 psi out of 36 psi. Because upstream Mach numbers and flow conditions are essentially the same, it is believed that the boundary-layer thickness will be the same. Therefore, due to the difference in physical throat area, the blockage of DI-1 will be greater than DI-2 by 4.5 percent. Referring to the blockage-static-pressure-recovery curve (Figure 410), the change in recovery due to the difference in blockage can be determined. This comparison shows an absolute channel-pressure-recovery difference of 5.0 psi, suggesting that the difference in performance of DI-1 and DI-2 can indeed be accounted for by throat blockage.

Effect of Increased Number of Vanes

A 16-channel diffuser (DI-3) was designed to evaluate the effects of an increased number of vanes on diffuser performance. This diffuser was of interest because more vanes shorten the flow-path length from the impeller tip to the throat entrance. Therefore, the boundary-layer thickness at the diffuser throat would be lessened, with a possible improvement in diffuser performance. It was also believed that the 16 vanes would exert more control on the flow and would result in delayed separation on the suction surface in the semivaneless space.

The 16-channel diffuser was tested and the results are shown in Figure 334. Schlieren photographs of these tests are presented in Appendix X, Figures 138 through 142. The test results showed that the 16-channel diffuser had shorter range and lower performance than the best 8-channel diffuser. No reason for

CONFIDENTIAL

CONFIDENTIAL

lower performance of the 16-channel diffuser was found; however, the shock waves from the increased number of vanes may have adversely affected the impeller performance, causing a decrease in overall compressor performance.

7.2.7 CRITICAL THROAT MACH NUMBER

In Section 7.2.5, Throat Mach Number, it was established that the DI-1 diffuser (with the 0.90 design throat Mach number) had the better airflow range and that the DI-2 (with the 0.75 design throat Mach number) had the better pressure recovery. It was also found that the overall pressure recovery of DI-1, while lower than DI-2, did not show a large difference in performance. Further, the diffuser tests had demonstrated good performance at a high throat Mach number, consistent with the contractor's past experience. However, available information in the literature clearly showed that a critical throat Mach number, significantly less than 1.0, existed for channel diffusers. The critical Mach number was defined as the value (usually near 0.8) above which diffuser performance deteriorated rapidly. Henry, Wood, and Wilbur (Reference 16) present rectangular diffuser data which illustrate this rapid drop in performance near an inlet Mach number of 0.8 for a range of cone angles from 8 to 31 degrees and an area ratio of 4.0.

Straight Diffuser Studies

Analysis of the contractor's diffuser data indicated good channel-diffuser performance for entry Mach numbers near 1.0 (such as DI-1 performance). Because of this anomaly, the question of diffuser critical Mach number was pursued further. It was believed that a resolution of this question would lead to a better understanding of the whole flow process. Therefore, a thorough literature survey was conducted to evaluate current published information on the subject.

The results of this survey showed:

- 1) Inlet Mach number is not an important performance parameter when the Mach number is below 0.30. Performance can be predicted by using incompressible data and analysis;
- 2) At inlet Mach numbers above 0.30, performance variation as a function of inlet Mach number can be categorized into 3 different groups. The typical variation of the pressure recovery coefficient, C_p , for each group is shown in Figure 414.

When the geometry of the diffusers studied at high subsonic inlet Mach number is plotted on an incompressible-flow-regime map, Figure 415, it is found that the performance variation classifications, Groups A, B and C, correlate directly with the geometric classification of the flow map. The flow-regime map shown

CONFIDENTIAL

CONFIDENTIAL

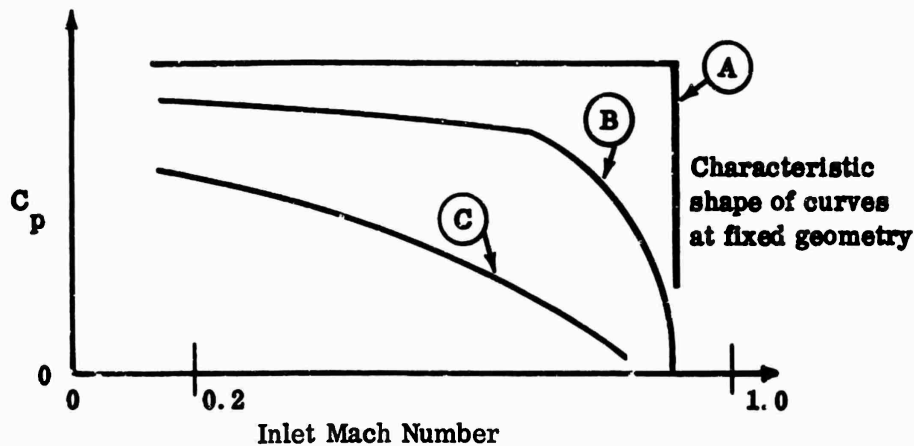


Figure 414. Characteristic C_p Versus M for Fixed-Geometry Diffusers.

in Figure 415 resulted from subsonic investigations (for example Fox and Kline, Reference 40), where it was shown that the included angle of divergence between walls and the length-to-initial-width ratio were the important parameters. The major influence on performance of the diffuser was identified as the presence and location of boundary-layer separation. In Figure 415, no boundary-layer separation was found below the Line a-a. Between Line a-a and the Line of Appreciable Stall - 2-Dimensional, the wall boundary layer separated at the end of the channel. The flow was highly unsteady from the Line of Appreciable Stall - 2-Dimensional to Line b-b. Above Line b-b, the flow was essentially a jet and fully separated with no diffusion. The Line of Appreciable Stall - 2-Dimensional was added to Kline's earlier map, Reference 42. The Line of Appreciable Stall - Conical was obtained from Reference 41.

All diffusers exhibiting the Group A performance characteristic lie to the right of the appropriate Line of Appreciable Stall. Those with the characteristics of Group B lie between the Line of Appreciable Stall and Line b-b, and the diffusers with the characteristics of Group C lie to the left of Line b-b.

The classifications and correlations found were valid for normal inlet-boundary-layer-velocity profiles; preliminary evidence indicated that these results would have to be modified for separating types of profiles.

CONFIDENTIAL

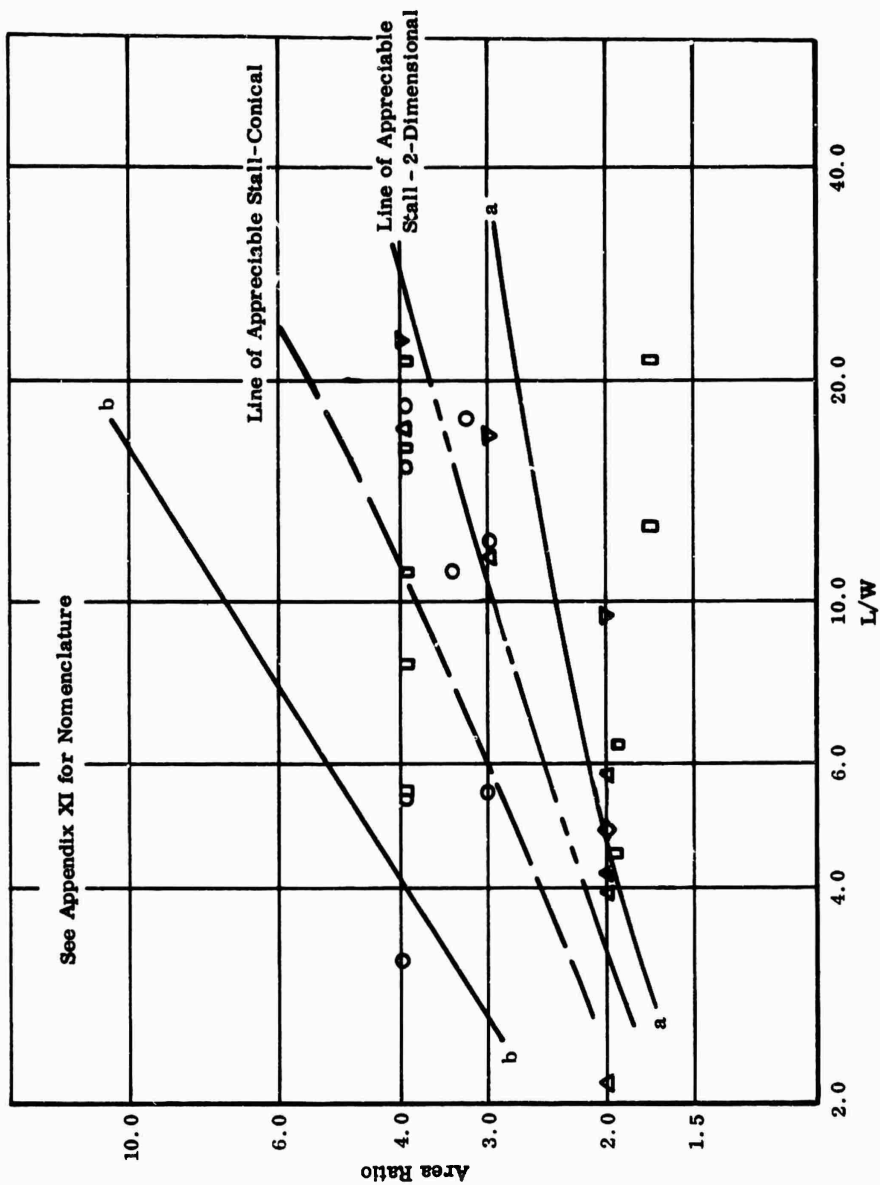


Figure 415. Flow-Regime Map.

CONFIDENTIAL

It was concluded from this literature search that:

- 1) A critical Mach did exist according to all available information. It was indicated that high static-pressure recovery cannot be obtained in channel diffusers with inlet Mach numbers above 0.8;
- 2) Performance variation of each classification correlates directly with diffuser geometry;
- 3) The critical Mach number of Group A diffuser shown in Figure 414 above correlates directly with entrance boundary-layer blockage.

Arguments for the existence of a critical Mach number for Group A diffusers were available, but no analytical procedure existed for predicting the appropriate critical value. A report on this literature survey by Halleen and Johnston is presented in Appendix XI.

The results of the literature survey are in direct contradiction to the diffuser test results of this program, where experimental data from the compressor tests showed that performance did not deteriorate even though throat Mach numbers were higher than the critical values reported by Halleen and Johnston. Since no analytical procedure existed for predicting the critical Mach number, it was necessary to test channel diffusers at high subsonic Mach numbers with sufficient instrumentation to evaluate this anomaly.

Several possible reasons for the anomaly were considered:

- 1) The consensus of the literature surveyed by Halleen and Johnston regarding a critical Mach number at high subsonic inlet conditions is incorrect; or
- 2) The channel-diffuser inlet Mach numbers calculated from the contractor's research data were incorrect; or
- 3) A critical Mach number did exist producing a region of poor diffuser performance, followed by a gain at still higher Mach numbers; i.e., the static-pressure coefficient with respect to inlet Mach number characteristics may show a dip at some high subsonic inlet Mach number.

With these additional questions, it was necessary to enlarge upon the available basic channel-diffuser information to determine the actual channel characteristics. Therefore, supplemental research was initiated to test diffuser channels in the Mach number range of 0.2 to 1.4. The tests were conducted with single channels in a flow rig. It was anticipated that the data from a single-channel rig would correlate directly with the compressor-diffuser channel static pressure test data of DI-1 and DI-2. These earlier compressor tests showed that the flow changed

CONFIDENTIAL

CONFIDENTIAL

from vortex to 1-dimensional channel flow just inside the throat (static pressure was nearly constant across the channel diffuser from the inlet to the exit). Because of the constant static pressure, a straight 2-dimensional test rig was considered acceptable to evaluate the channel of a compressor diffuser if the blockage factor, Mach number, and Reynolds number at the channel entrance were simulated properly and if the geometry corresponded.

For these diffuser tests, pressure recovery was correlated on 5 independent parameters (Figure 416):

- 1) Divergence angle, 2θ ;
- 2) Diffuser length-to-throat width ratio, L/W ;
- 3) Throat aspect ratio, AR or b/W ;
- 4) Flow boundary-layer blockage at the diffuser throat, where,
$$1 - B = \frac{\text{flow area (equivalent 1-dimensional)}}{b W}; \quad (48)$$
- 5) Throat inlet-core flow Mach number, M_T .

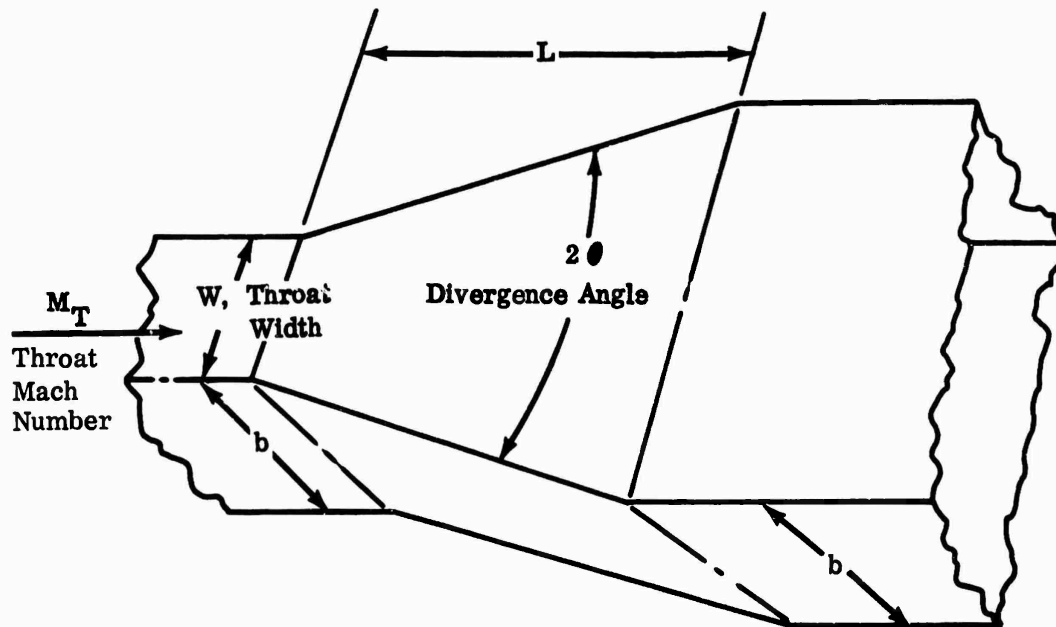


Figure 416. Diffuser Geometric Parameters.

CONFIDENTIAL

A range of these parameters was chosen for test to cover the region of interest for centrifugal vane-island-type diffusers. The variables built into the diffuser models are listed in Table XXVIII.

TABLE XXVIII			
VARIABLES FOR 2-DIMENSIONAL DIFFUSER TESTS			
Aspect Ratio	2θ (degrees)	Throat Length W	Diffuser $\frac{L}{W}$
5.7	4	3	10
	6	11	
	8		15
	10	19	
	12	35	17
0.25	4	0.25	15
	6	1.25	
	8	2.25	
	10	4.25	
	12	7.25	

Different throat-approach lengths were used at both aspect ratios to give different inlet blockage factors at the diffuser-channel entry. Because of the rig setup, all entry velocity profiles were of the accelerating type; therefore, the conclusions reached here apply only to this profile. Further work (beyond the scope of this investigation) should be done to determine the effect of velocity profiles on the diffuser recovery. Aspect ratios much greater and less than 1.0 were tested to ensure that both diffusers which diverge in the meridional and in the radial plane were evaluated. The low aspect ratios demanded by high-pressure-ratio machines were emphasized.

The results of the tests showed that no critical subsonic Mach number existed below $M_{core} = 1.0$. This result contradicted the consensus of the literature.

CONFIDENTIAL

Figure 396 shows performance of a diffuser channel at an aspect ratio of 5.7 for a range of inlet Mach numbers from near 0.2 to 1.0 and beyond (by lowering the back pressure). The pressure recovery was essentially constant up to an internal-shock Mach number of 1.1, after which performance fell off. It should be noted that for flows larger than W^* , $M_{core} = 1.0$, the Mach number ahead of the shock in the channel is plotted rather than M_{core} at entrance which remains 1.0. After the throat-entry core Mach number reached 1.0, further reduction in back pressure caused a shock in the channel, as was also found in the compressor-diffuser channels (see schlieren photographs, Appendix X).

From the experimental program, the following conclusions were reached.

- 1) Performance in terms of static-pressure recovery versus inlet Mach number does not show a critical subsonic inlet Mach number above which performance suffers a drastic drop.
- 2) Performance for supercritical flow (back pressures lower than for $M_{core, inlet} = 1.0$) is approximately the same as for diffusers on the verge of choking, if the diffuser-channel shock Mach number is less than about 1.1 to 1.2.
- 3) The range of new data includes diffusers in Groups A and B, speculated by Halleen and Johnston to have different behavior. No well defined groupings are apparent from these tests.
- 4) There is a strong dependence of the optimum diffuser geometry (for maximum pressure recovery) on aspect ratio. For example, at a given blockage and L/W , maximum pressure recovery occurs at $2\theta = 6$ degrees for an aspect ratio of 5.7 and at 10 degrees for an aspect ratio of 0.25. For given values of blockage, somewhat higher recovery occurs for the larger aspect ratios. This conclusion may not be valid for all values of blockage and aspect ratios. However, the effect of aspect ratio is not as large as might be expected.
- 5) In all cases, pressure recovery declines with increasing blockage for fixed values of 2θ , L/W , and inlet Mach number.
- 6) Pressure recovery variation with inlet Mach number appears to be correlated with divergence angle (2θ) and blockage ratio (B). At low values of blockage ($B = 0.04$), pressure recovery increases slightly with increasing subsonic Mach number at small divergence angles ($2\theta = 4$ degrees). Static-pressure recovery decreases slightly with increasing Mach number at the larger divergence angles ($2\theta = 12$ degrees). At large values of blockage ($B = 0.15$), pressure recovery is relatively constant with inlet subsonic Mach number for divergence angles (2θ) from 4 to 12 degrees.

CONFIDENTIAL

CONFIDENTIAL

- 7) The appearance of a critical Mach number in the published literature for a Group A classification of diffusers is perhaps a miscalculation of true inlet Mach numbers by previous investigators. The reason may be that many pressure taps are needed near the throat to determine inlet Mach number because of the large gradient of static pressure in a straight throat at high subsonic Mach numbers due to friction effects.

7.2.8 DIFFUSER MODIFICATION AND RETEST

The evaluations thus far have been related to the basic tests of the 3 vane-island diffuser elements DI-1, DI-2, and DI-3, and the straight-wall, 2-dimensional diffuser channels. The results led to considerations of modifying the vanes for possible performance improvements. Therefore, questionable areas which merited further investigation were identified, and additional tests were conducted in this modification and retest portion of the program.

Effect of Entry Shock Strength on Diffuser Performance

The flow model previously proposed in Section 7.2.2 described the effects of throat conditions on flow range and performance. It was shown that the entry-shock strength (ahead of the throat) was a function of the downstream subsonic throat Mach number. This Mach number was established by the throat area and continuity in the throat. Also, as the throat Mach number was reduced across the speed line, the shock strength increased. It was determined that the streamlines adjusted upstream of the shock, and the flow accelerated because of the increased shock strength. The strongest shock and lowest throat Mach number occurred with DI-2. This vane set also showed promise of producing the best performance, but its range from full-flow to surge was below expectations. It was believed either that the expansion process on the vane suction surface or the entry-shock strength caused separation and surge.

To investigate these effects further, a new diffuser was designed, similar to DI-2, except with a 3 percent larger throat area. It was expected that a new diffuser would show a lower throat Mach number (0.7) at the same design airflow as DI-2. Further, it was expected that a stronger entry shock (1.5) would occur ahead of the throat. It was recognized that if the flow responded to these design inputs, the upstream acceleration would cause the Mach number ahead of the entry shock to be greater than at the impeller tip, which was a nominal 1.3. If the diffuser could sustain the 1.5 Mach number without surging, it was expected that the increased static-pressure rise through the shock would result in an overall diffuser performance increase. But another important consideration was that the increased shock strength might further reduce the airflow range.

The new diffuser element, designated as DI-X1-3, was tested on the diffuser rig at design speed. The results are compared with DI-2 in Figure 417. DI-X1-3

CONFIDENTIAL

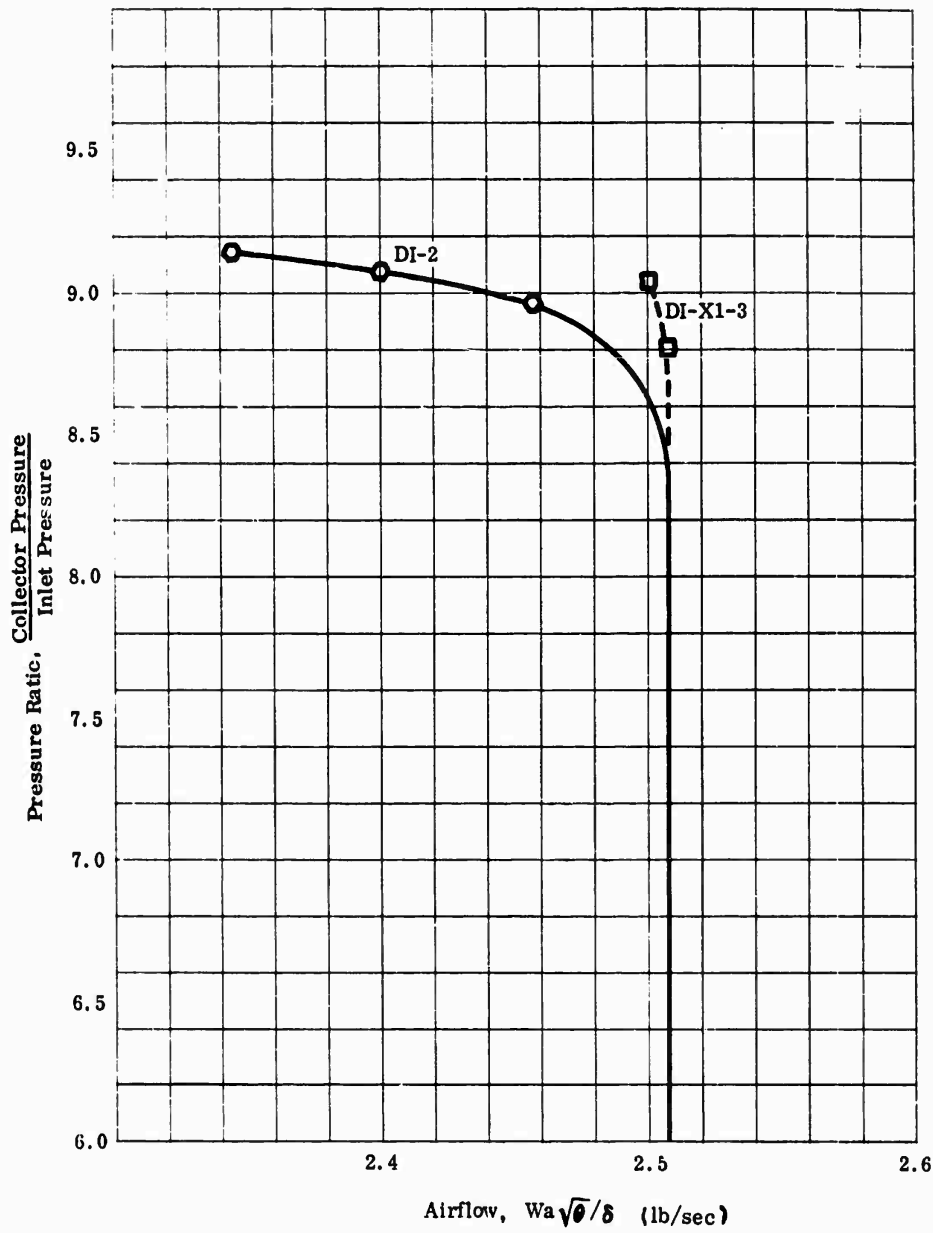


Figure 417. Pressure-Ratio Comparison, DI-2 and DI-X1-3.

CONFIDENTIAL

showed a trend toward higher performance; however, the range was reduced significantly (diffuser surge and impeller choke occurred at nearly the same airflow). The Mach number upstream of the entry shock was about the same as that of DI-2 near surge ($M_x \approx 1.2$). The radial static-pressure gradient found with DI-2 at the vane leading edges occurred also for DI-X1-3 tests. The radial static-pressure gradient ahead of the vane leading edge was positive when the compressor was at maximum airflow, but this gradient was reduced and again reversed near surge. Figure 418 shows the static-pressure field of DI-X1-3 near surge. DI-X1-3 had a static-pressure difference of -8.5 psi across the throat entrance (from the vane leading edge to the pressure tap nearest the suction surface). At the same airflow (2.5 pounds per second), DI-2 had a pressure difference of +3.7 psi. It was believed that this difference in gradient was caused by the change in shock strength. Combining this test with the data of DI-1 and DI-2, it can be concluded that:

- 1) The airflow range of the diffuser is directly related to the entry-shock strength at the vane leading edge;
- 2) When the entry-shock Mach number reaches 1.15 to 1.20, the diffuser will surge for impeller-tip Mach numbers near 1.3;
- 3) The overall diffuser recovery is increased with the higher entry-shock Mach number and lower throat Mach number.

Because surge occurred at a given Mach number ahead of the shock, matching of the diffuser to the impeller required further examination. Maximum airflow of the impeller was determined from the 125-percent area test discussed in Section 6.2 (Figure 319). By examining the impeller speed lines of DI-1, DI-2, and DI-X1-3, the best match can be determined. Figure 419 is a sketch of the operating line of each diffuser, showing the effect of varying the diffuser throat area for a given impeller.

Because maximum flow was limited by the impeller, the largest throat area (DI-X1-3) produced the Mach number ahead of the entry shock necessary for surge at almost the maximum airflow.

Effect of Throat Length

From the results of the above test, it was apparent that to achieve best compressor performance (both pressure recovery and airflow range) the diffuser must have a low Mach number ahead of the entry shock and still avoid the channel shock. The lower Mach number ahead of the shock of DI-1 (near 1.05) produced the best airflow range; however, this Mach number also resulted in a high throat-entrance Mach number, a downstream channel shock, and a low W^* . Because the shock in the channel was related to the sonic condition at the throat exit,

CONFIDENTIAL

CONFIDENTIAL

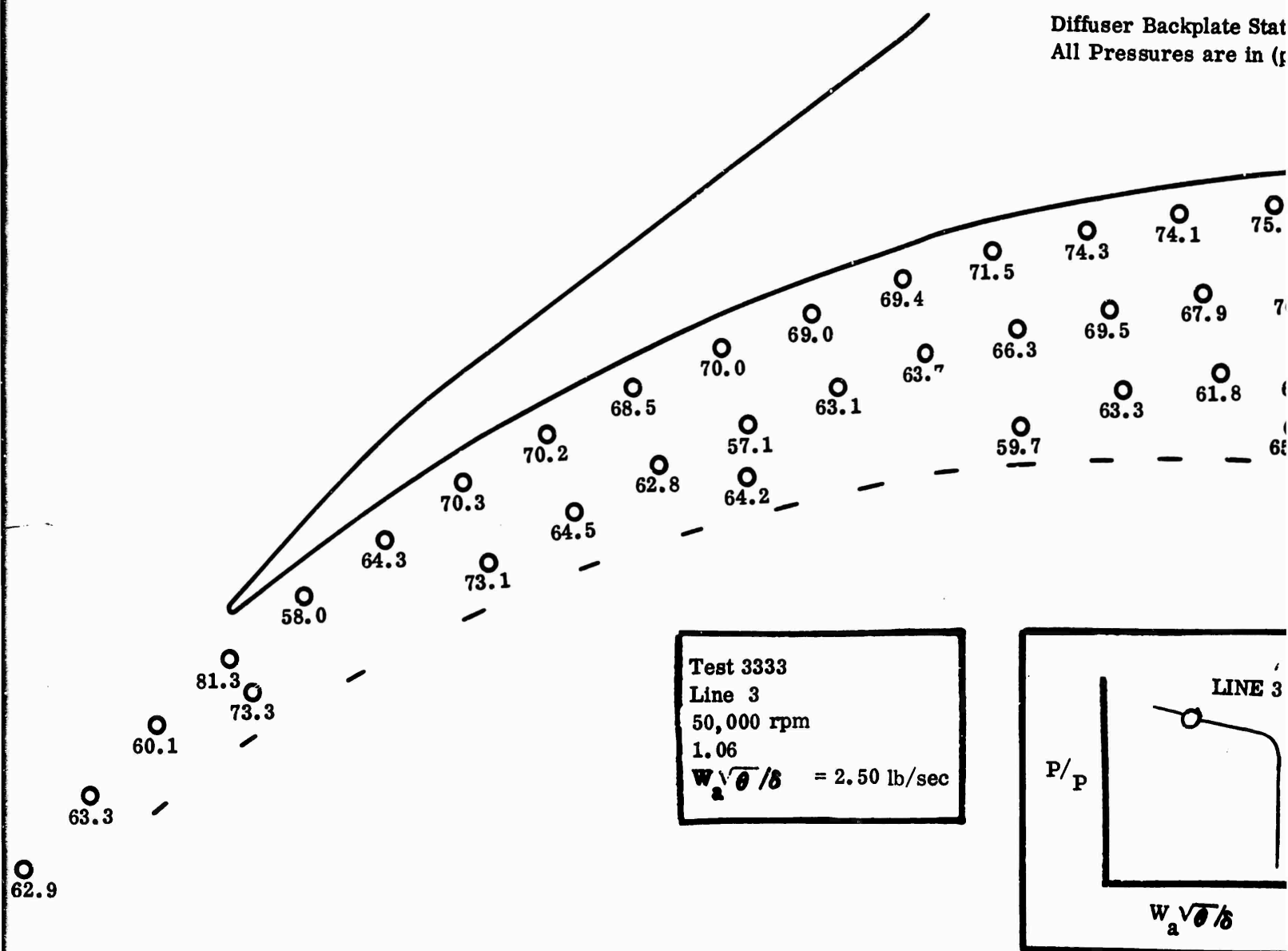
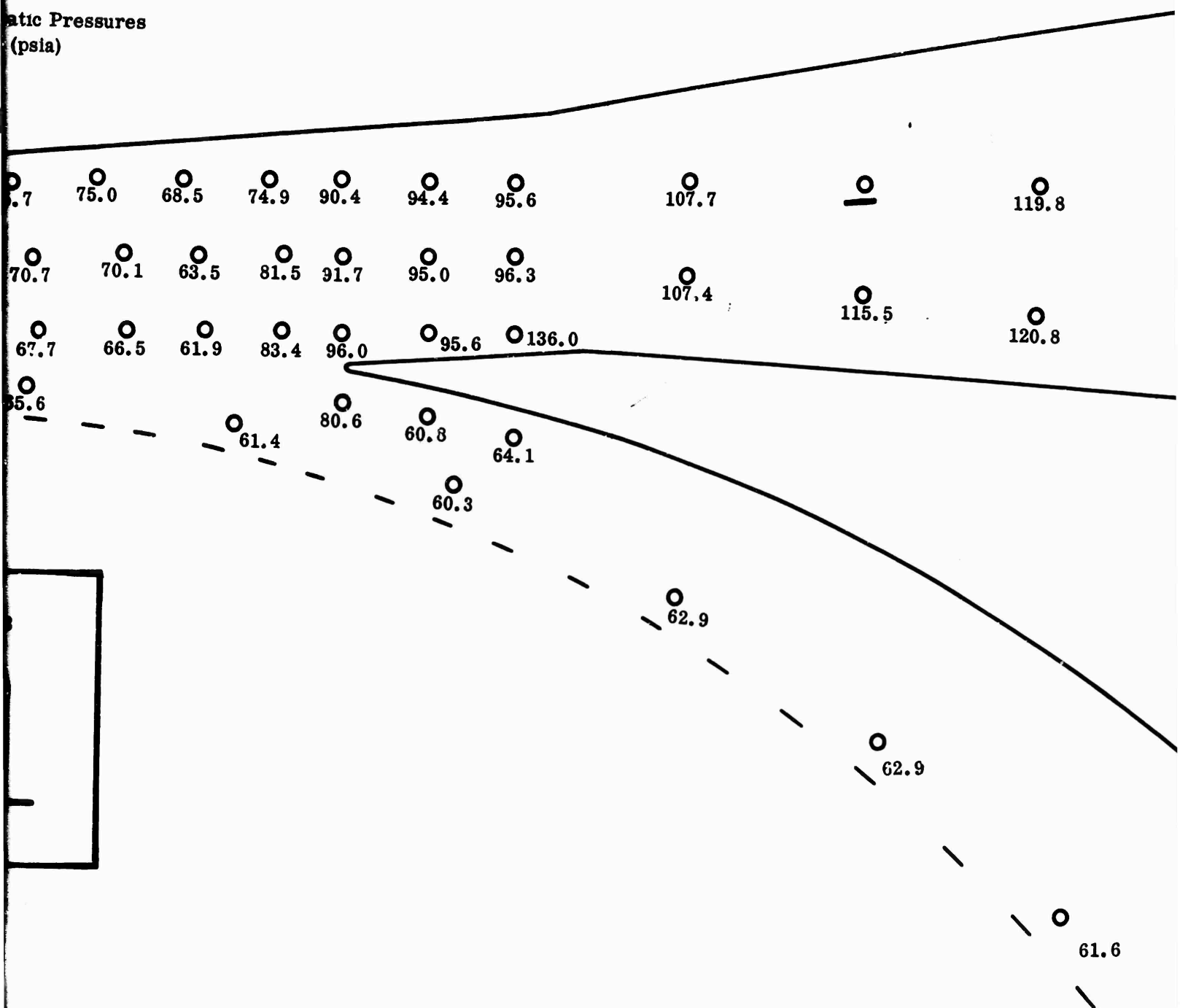


Figure 418. Static-Pressure Field, DI-X1-3.
653

CONFIDENTIAL

atic Pressures
(psia)



10

119.8

124.2

126.4

115.5

120.8

124.3

126.8

128.4

62.9

61.6

CONFIDENTIAL

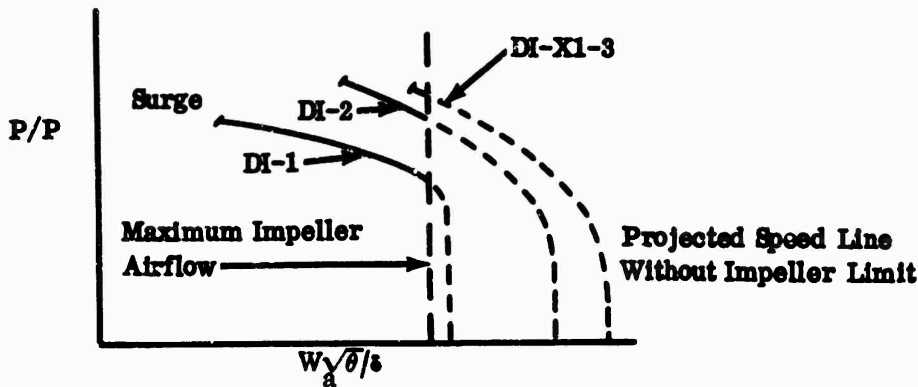


Figure 419. Comparison of Three Diffusers Showing Match to Impeller.

consideration was given to methods of eliminating this shock. It was expected that the lower throat-exit Mach number would be achieved with DI-1, using a shortened throat. Fanno line calculations showed that if the throat length were reduced from the original 1/2 inch to 1/8 inch, the flow would not accelerate to Mach 1.0 at the throat exit. Therefore, it was reasoned that pressure recovery would improve at the same airflow range.

It was also recognized that the shorter throat might not allow enough path length for the flow to adjust from the vortex flow of the vaneless space to channel flow; the channel entry might not accommodate the early aerodynamic loading and flow turning without separation. However, it was anticipated that the previously observed multiple-shock system in the throat section would not extend into the diverging channel.

Neumann and Lustwerk (Reference 38) showed that the length of the flow path required to complete the multiple throat shock was a function of the entry Mach number. If the Mach number level at entry remained the same, the shock might extend downstream into the channel and separate the diffuser boundary layer. To avoid this situation when the throat was shortened, a double taper was cut into the pressure surface as shown in Figure 420.

With this small area increase after the short throat, it was believed that the flow would not accelerate to Mach 1.0 in the core or separate the boundary layer because the area increase was slightly greater than the expected blockage.

The modified DI-1 diffuser, designated DI-1-2, was tested in the diffuser rig at impeller design speed. The results of the test are shown in Figure 421. The overall pressure ratio of the compressor was increased from near 8.5:1 to 9.3:1. This performance was the highest obtained in the program to this point. The

CONFIDENTIAL

CONFIDENTIAL

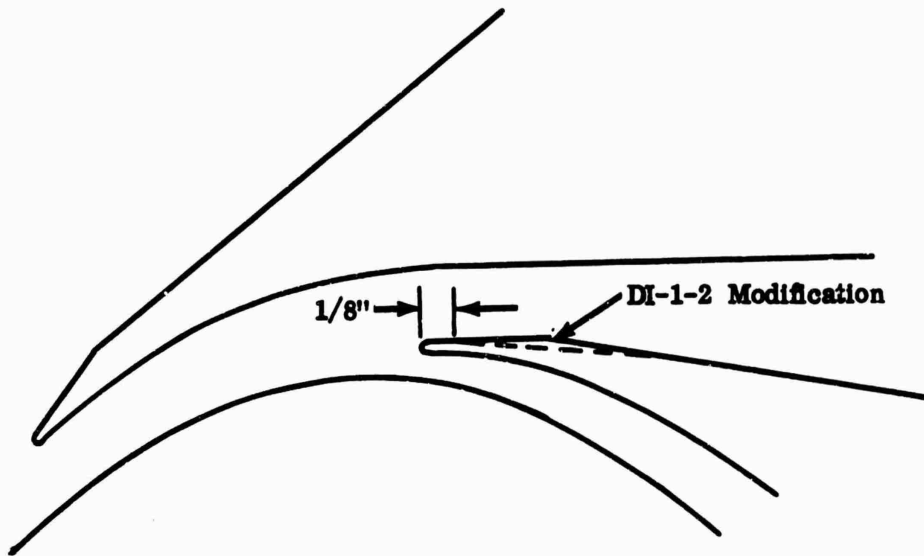


Figure 420. Modification of DI-1 to DI-1-2.

surge point moved to a slightly lower airflow than shown for the original DI-1; however, the test demonstrated that high pressure ratio can be obtained with substantial airflow range. A possible explanation is that the blockage was lower in the throat of the DI-1-2 diffuser because of the shorter throat. With the larger effective diffuser throat, a higher-than-expected entry-shock strength occurred.

The test data also showed that the flow did adjust from vortex to nearly 1-dimensional in the shortened throat straight section. The static-pressure field of DI-1-2 in Figure 422 shows only a 4.3-psi pressure difference across the throat at 1/4 inch from the entrance while a 13.3-psi pressure difference occurred just upstream of the throat. The shock system was also more concentrated in the throat, as shown in the schlieren photographs, Appendix X, Figures 131 and 143.

From this test, it can be concluded that:

- 1) Friction in the straight section of the throat has a major influence on the overall performance of the diffuser;
- 2) It is important in a diffuser design to ensure that the flow does not reach Mach 1.0 at the throat exit and expand supersonically (i.e., that $W^* > W$ design);
- 3) Throat Mach numbers near 1.0 will result in best overall diffuser performance if the channel shock can be avoided;

CONFIDENTIAL

CONFIDENTIAL

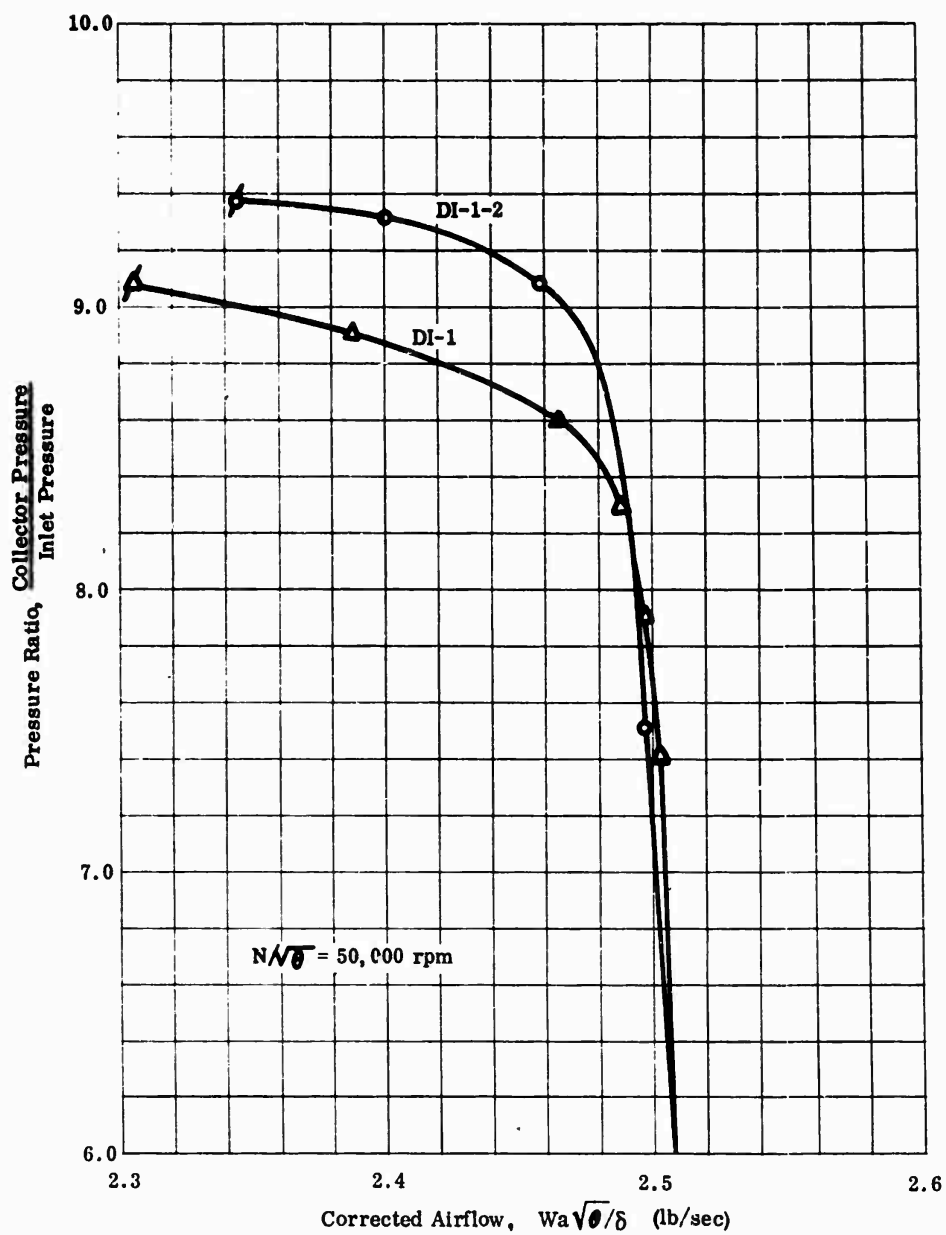


Figure 421. Pressure-Ratio Comparison, DI-1 and DI-1-2.

CONFIDENTIAL

Diffuse
All Pre

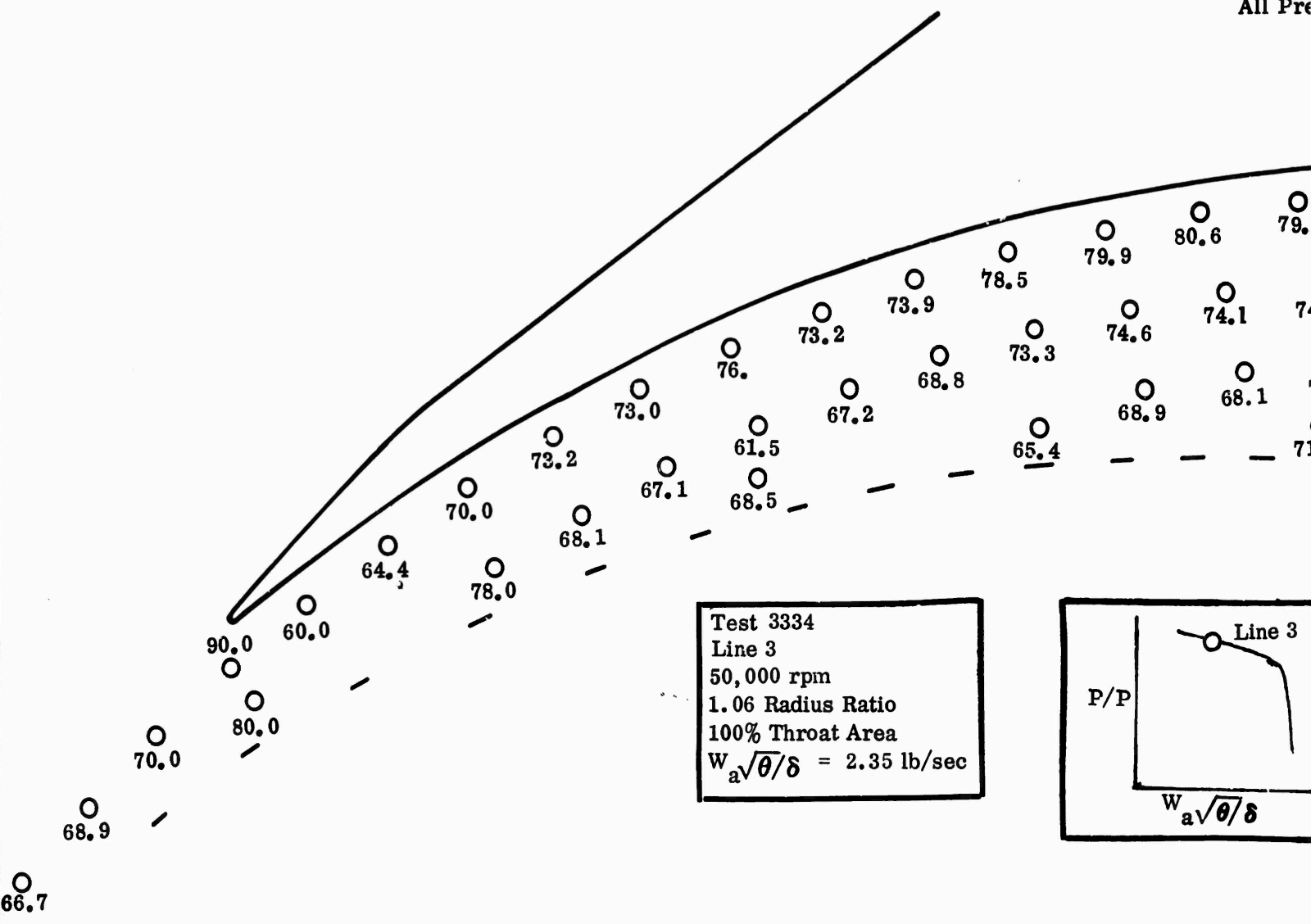
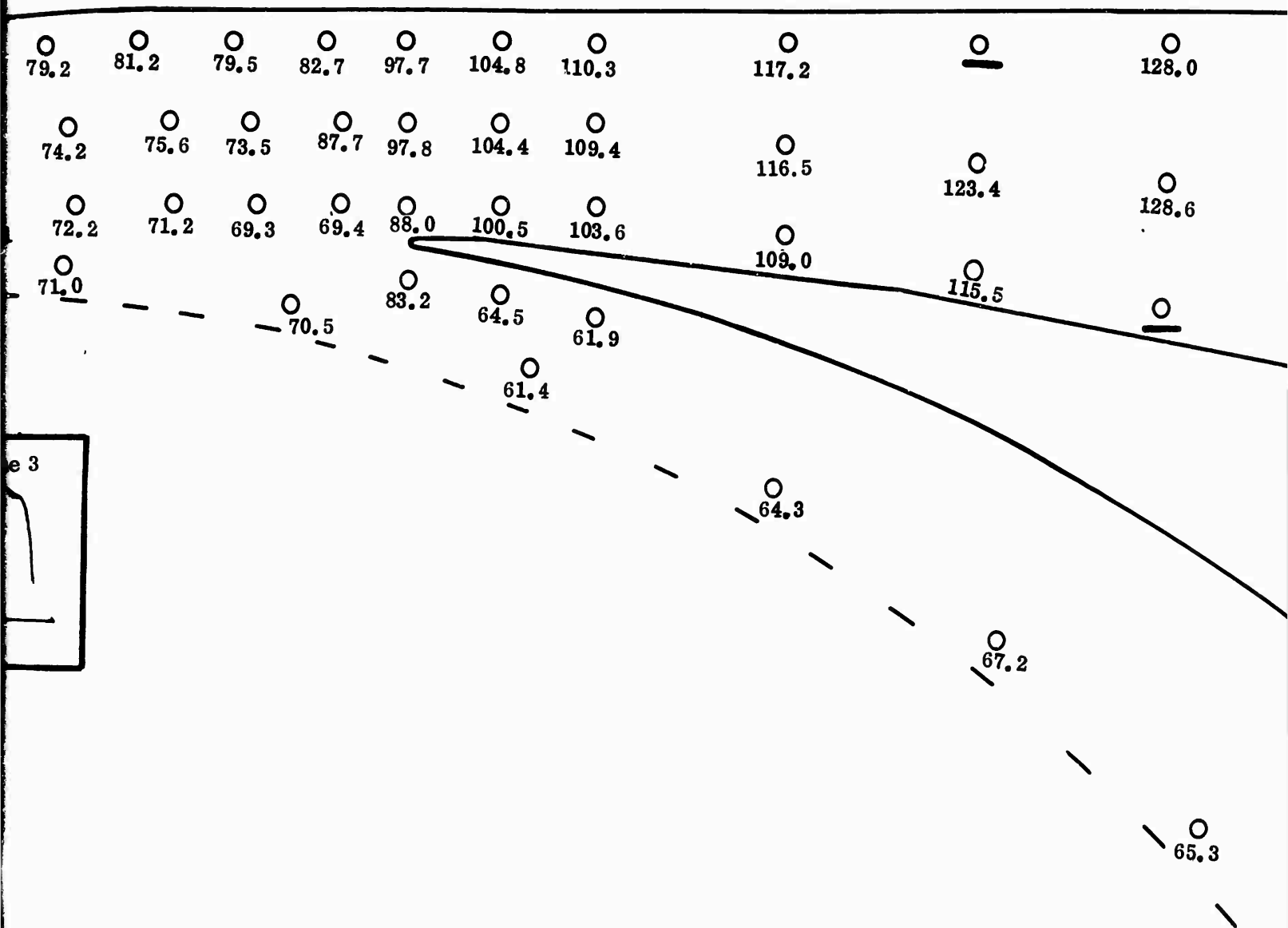
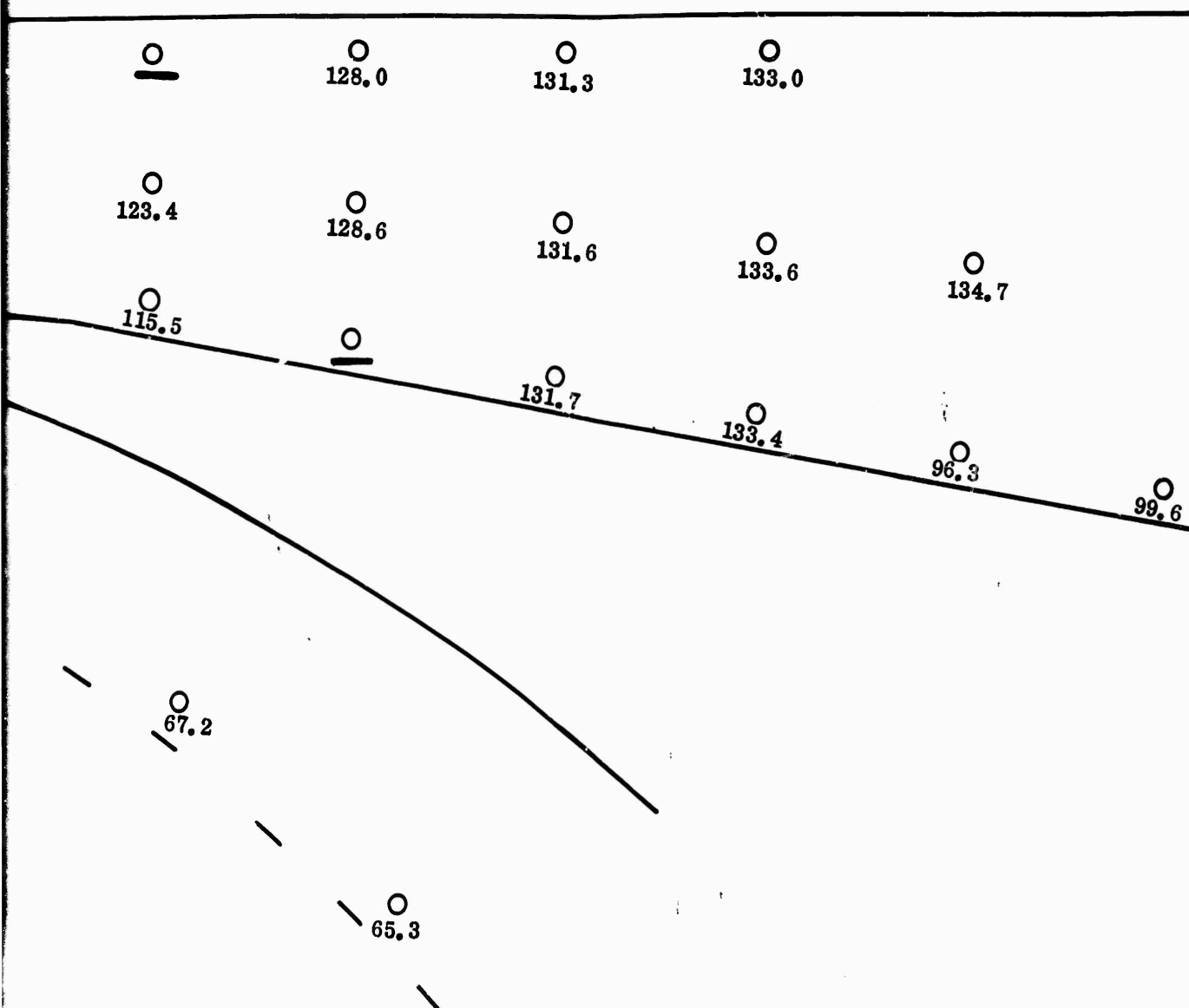


Figure 422. Static-Pressure Field, DI-1-2.
659

Diffuser Backplate Static Pressures
 All Pressures are in (psia)





CONFIDENTIAL

- 4) The Mach number upstream of the entry shock depends in part on the diffuser throat length;
- 5) The short throat length was sufficient to allow the flow to adjust from vortex to nearly 1-dimensional flow;
- 6) The Fanno line calculation which suggested the throat length reduction was in the right direction.

Symmetrical Channel and Reduced Divergence Angle

In all of the tests discussed thus far, the diffuser models were designed with 10-degree asymmetrical divergence angles. All of the divergence was on the pressure surface; the suction surface was straight (see design discussion and sketches in Section 2.3, Diffuser Design).

As discussed earlier in Section 7.2, oil traces showed that the secondary flow was bleeding the boundary layer from the suction surface and perhaps was causing it to migrate to the pressure surface (Figure 401).

Because all of the divergence was taken on the pressure surface, it was believed that the boundary-layer buildup was sufficient to cause separation just after the throat. By reducing the divergence in this region, it was expected that this separation would be reduced. Therefore, it was planned that a new diffuser similar to DI-2 be investigated with similar upstream geometry but with a symmetrical channel divergence.

In the work of Reneau, et al (Reference 42), diffuser static-pressure recovery was shown on maps with respect to geometric variables for various entrance boundary-layer conditions. This work was for the incompressible case; its applicability to the compressible case was not known. The concurrent straight-wall 2-dimensional compressible-diffuser tests had not progressed far enough at this point in the program to be used. The geometry of DI-1 and DI-2 is shown plotted on a channel diffuser pressure-recovery map from Reference 42 (see Figure 423). According to this incompressible case, both diffusers lie outside the region of maximum recovery, while maximum pressure recovery would be predicted with an 8-degree divergence angle. Therefore, the new diffuser, designated as DI-X1, was designed similar to DI-2 except for an 8-degree symmetrical-divergence angle.

DI-X1 was tested on the diffuser rig at impeller design speed. The results are compared with DI-2 in Figure 424. The trend of the speed line was towards a higher pressure ratio than DI-2; however, the airflow range was shorter with an earlier surge.

CONFIDENTIAL

CONFIDENTIAL

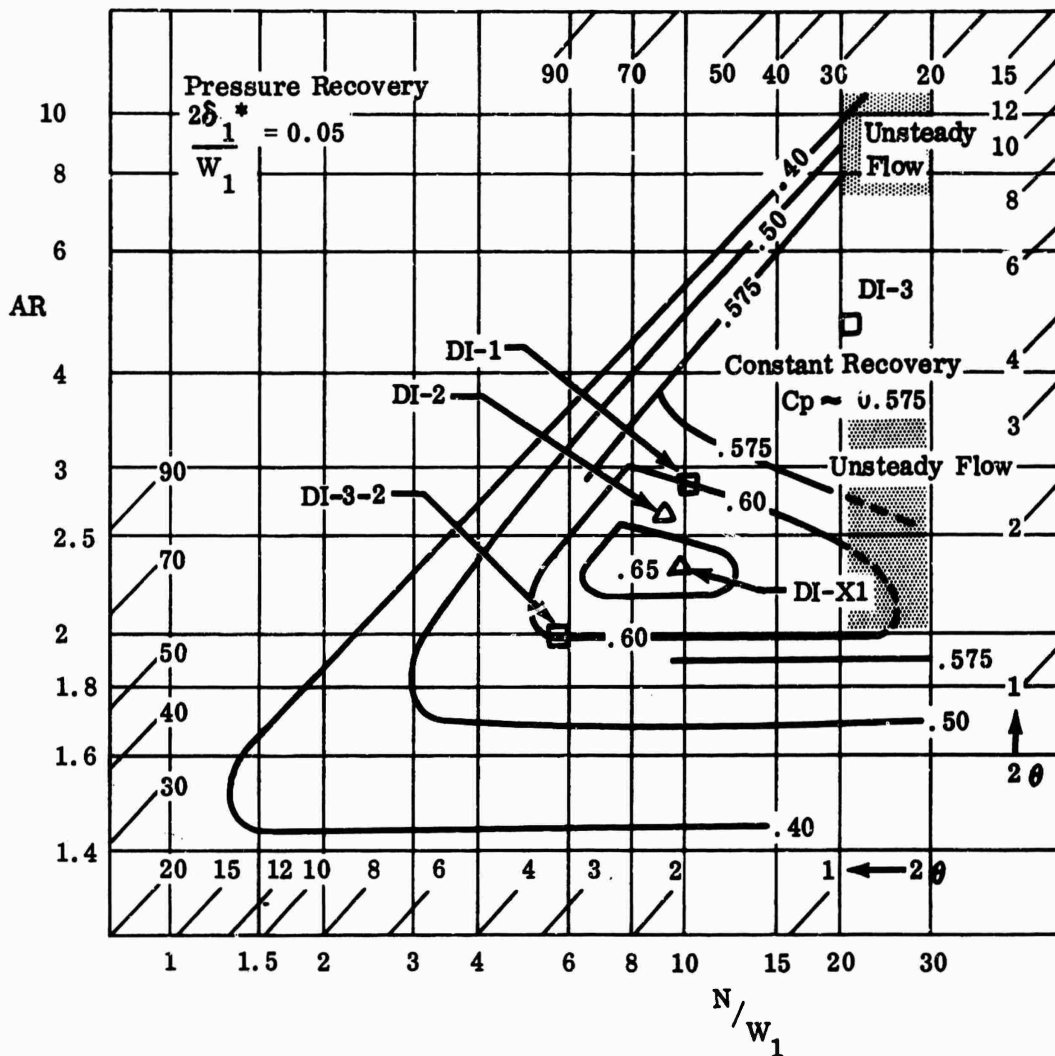


Figure 423. Pressure Recovery of Two-Dimensional Diffusers With Turbulent Inlet Boundary Layers.

The test results suggest that the suction-surface divergence caused the channel to be less stable.

Change in Incidence Angle

The effects of the entry shock on the streamlines at the throat entrance have been discussed in Section 7.2.2. The flow acceleration caused the streamlines to turn locally into the pressure surface, creating a positive incidence on the vane (Figure 408). The expansion region on the suction surface resulted from this incidence, which might separate the flow and lead to surge.

CONFIDENTIAL

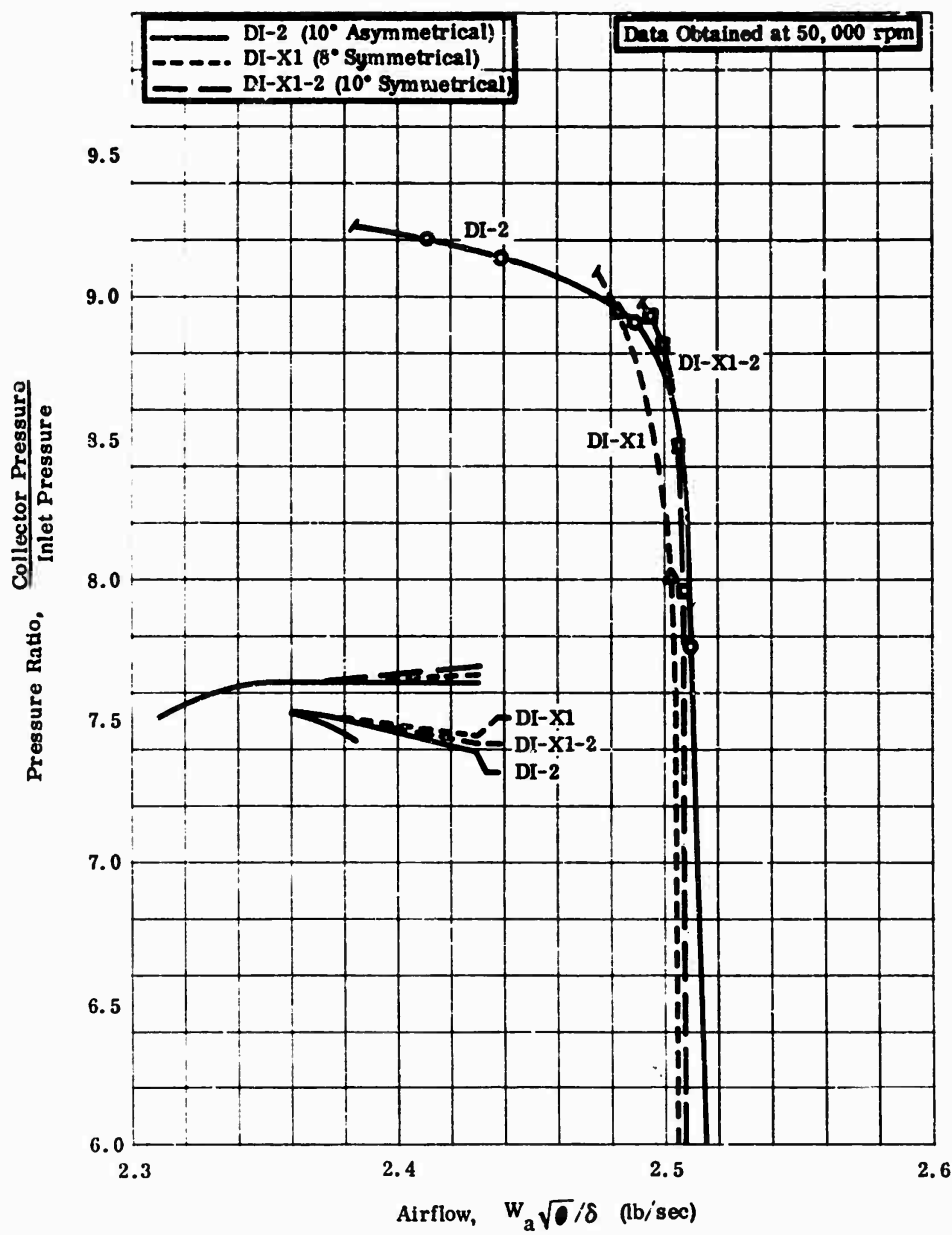


Figure 424. Pressure-Ratio Comparisons, DI-2, DI-X1, and DI-X1-2.

CONFIDENTIAL

If this flow model was correct, an adjustment could be made to the vane angle which would extend the airflow range of the diffuser. To correct the incidence, a new diffuser was designed with an angle 2 degrees flatter on the suction surface than the DI-2 diffuser; i.e., the suction-surface metal angle was 2 degrees closer to the tangential direction (Figure 425).

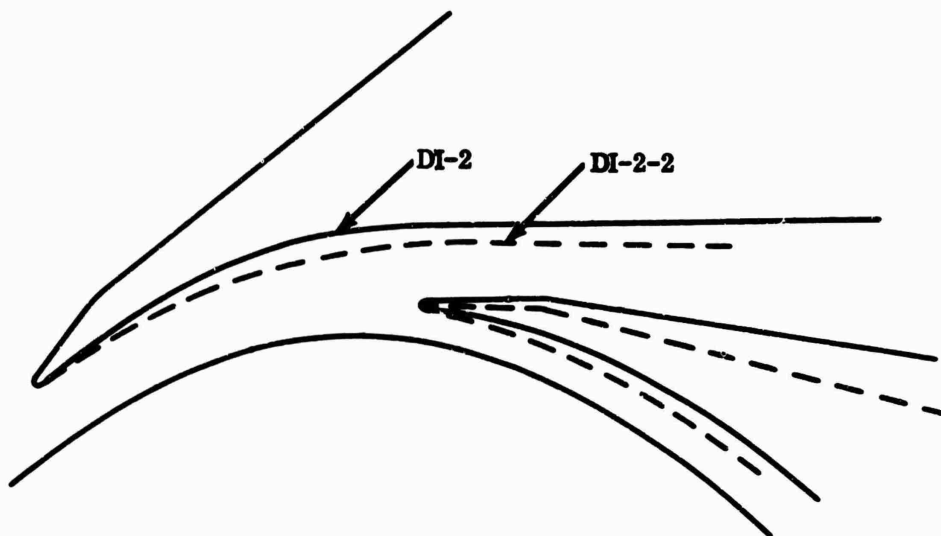


Figure 425. Increase in DI-2 Vane Angle.

The new diffuser (DI-2-2) was tested at design speed. The test results are compared with DI-2 in Figure 426. The range of the new diffuser was less than that of DI-2, and the static-pressure data indicated that the expansion region actually increased when compared to the same airflows as DI-2. The pressure ratio was better for this diffuser, which suggests that the shock structure at the throat was altered, resulting in improved boundary-layer conditions in the channel. If the boundary layer were thinner, the airflow range would have been reduced in a manner similar to that of DI-1-2. Conversely, with an increased entry-shock strength, the result would be higher pressure recovery and shorter range. However, the conclusion can be reached that the flatter vane angle resulted in less airflow range, which was opposite to what was anticipated.

Changes in DI-3

The original 16-channel-diffuser design was evaluated using Reneau's incompressible data, Reference 42. Figure 423 shows the 16-channel diffuser plotted on a static-pressure recovery map from Reference 42. The performance prediction

CONFIDENTIAL

CONFIDENTIAL

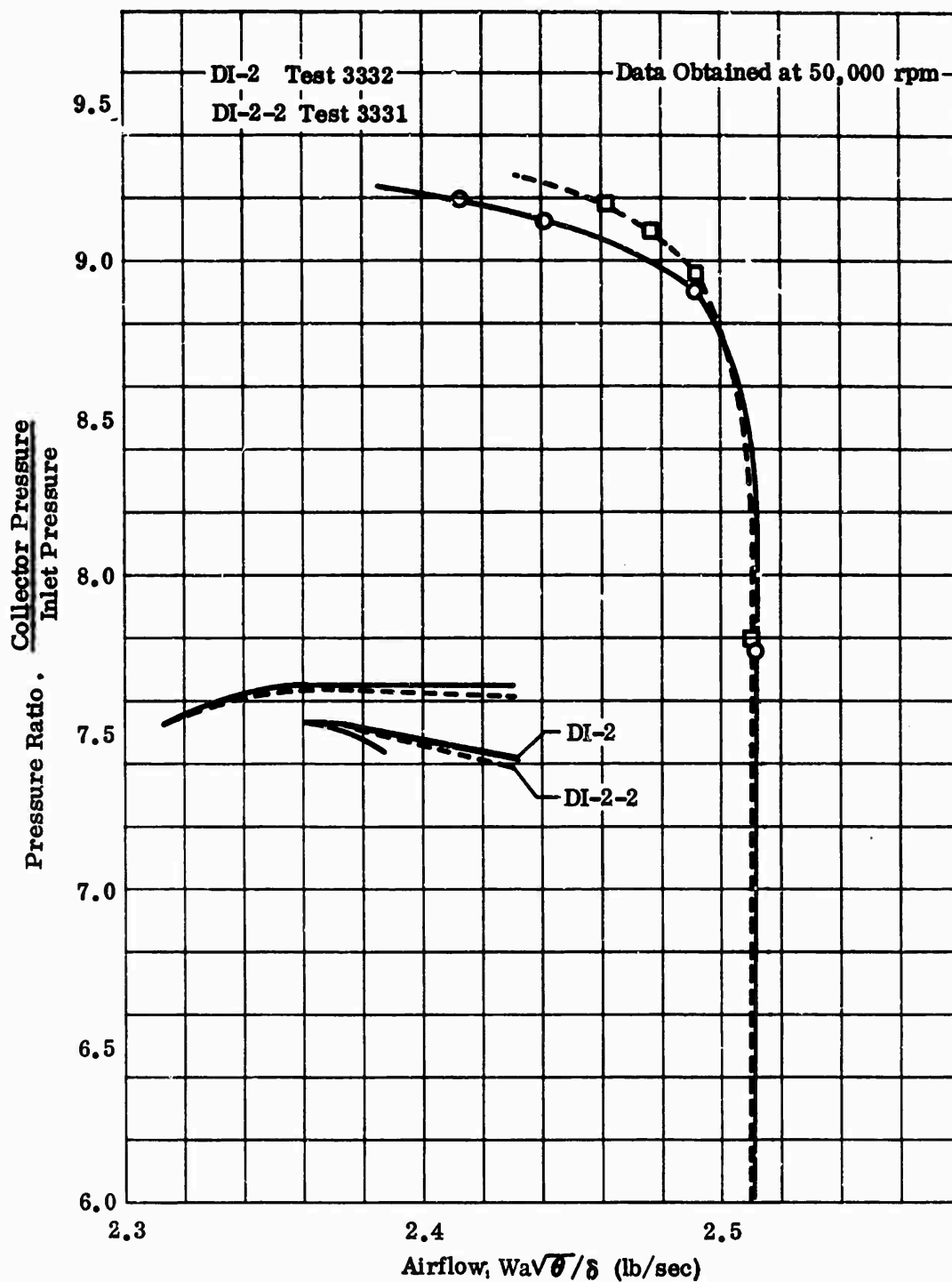


Figure 426. Pressure-Ratio Comparison, DI-1 and DI-2-2.

CONFIDENTIAL

CONFIDENTIAL

was based on the large 2θ and L/W selected in the design. Therefore, to improve the expected recovery, the diffuser was notched in the channel to reduce the effective L/W and bring DI-3 into a favorable region on Figure 423. Test data from this configuration are shown in Figure 335.

A second 16-channel diffuser was designed and tested with a 6-degree symmetrical-divergence angle. The test results of this diffuser are also presented in Figure 336. Again the airflow range was very short. The range of the modified DI-3 was about the same as that of the DI-X1-3 diffuser. Results of the single-channel diffuser tests were not available when this test was conducted, but they later showed that the channel geometry selected was not optimum for best performance in the compressible case.

7.2.9 CORRELATION OF DIFFUSER CHANNEL DATA

The single-channel diffuser tests have shown the relationship between static-pressure recovery (C_p), entrance Mach number (M_x), and blockage (B). The data from the compressor-diffuser tests were analyzed in a similar manner and the results were compared to the single-channel data. Calculations of C_p , M_x , and B were made from compressor test data to permit basic comparisons. Shock strength was obtained using the static-pressure rise across the shock, from the vane entrance to the throat exit. It was assumed that the pressure rise across a series of shocks will be equal to that across a single normal shock as shown by Neumann and Lustwerk. From the shock static-pressure rise, the Mach number ahead of and behind the shock was determined. With this Mach number, the total pressure ahead of and behind the shock was determined. Knowing M_y , the blockage factor can be calculated from continuity, where:

$$(1-B) = \frac{W_a \sqrt{T_T} A/A^*}{K P_T A_{\text{geom}}} \quad (49)$$

B = blockage, $1-A_{\text{effective}}/A_{\text{geometry}}$

W_a = airflow (pounds per second), (per channel)

T_T = total temperature ($^{\circ}R$), (core)

A/A^* = area ratio of actual area to area required for flow at $M = 1.0$ (based on M_y).

† When no uniform core exists in the flow, centerline values are employed.

CONFIDENTIAL

CONFIDENTIAL

P_T = total pressure (psia), (core)

K = constant, 0.532

A_{geom} = geometric area of throat per channel (in.²)

M_y = Mach number behind entry shock (core)

The static-pressure recovery was determined from the total and static pressures at the end of the throat and the collector static pressure. The total pressure at the throat exit was also affected by the Fanno process, which required consideration of the wall-friction factor. Although friction factor was not known, high values (as suggested by Reference 38) produce little change in total pressure through the throat. Uncertainty of this factor had little effect on the reduced data. For pressure recovery calculations:

$$C_p = \frac{P_{sf} - P_{se}}{P_{tc} - P_{se}} \quad (50)$$

C_p = static-pressure recovery coefficient

P_s = static pressure

P_{tc} = core total pressure

e = throat exit station

f = diffuser collector station

Comparison Between Straight Channel and Compressor-Diffuser Tests

Good agreement was found between the compressor and straight channel diffuser tests; therefore, it was determined that single-channel test data could be used directly for compressor-channel-diffuser design.

The change in static-pressure recovery and entrance Mach number with respect to throat blockage is shown in Figures 410 and 427. The single-channel data are also shown for comparison. It can be seen that the static-pressure recovery has a strong dependence on blockage, illustrating the importance of the entry shock on channel performance. Figure 427 shows the relationship between entry shock Mach number and blockage; small changes in M_x will have a large effect on blockage and therefore on the channel C_p . Note that the blockage at any shock

CONFIDENTIAL

strength greater than 1.0 is substantially larger than the blockage predicted from friction effects in the vaneless and semivaneless space. No information could be found in the literature relating the effect of a normal shock on the characteristics of a boundary layer passing through it. If the effect of M_x on the blockage is to be predicted analytically in the future, such an analysis must be coupled with an experimental investigation.

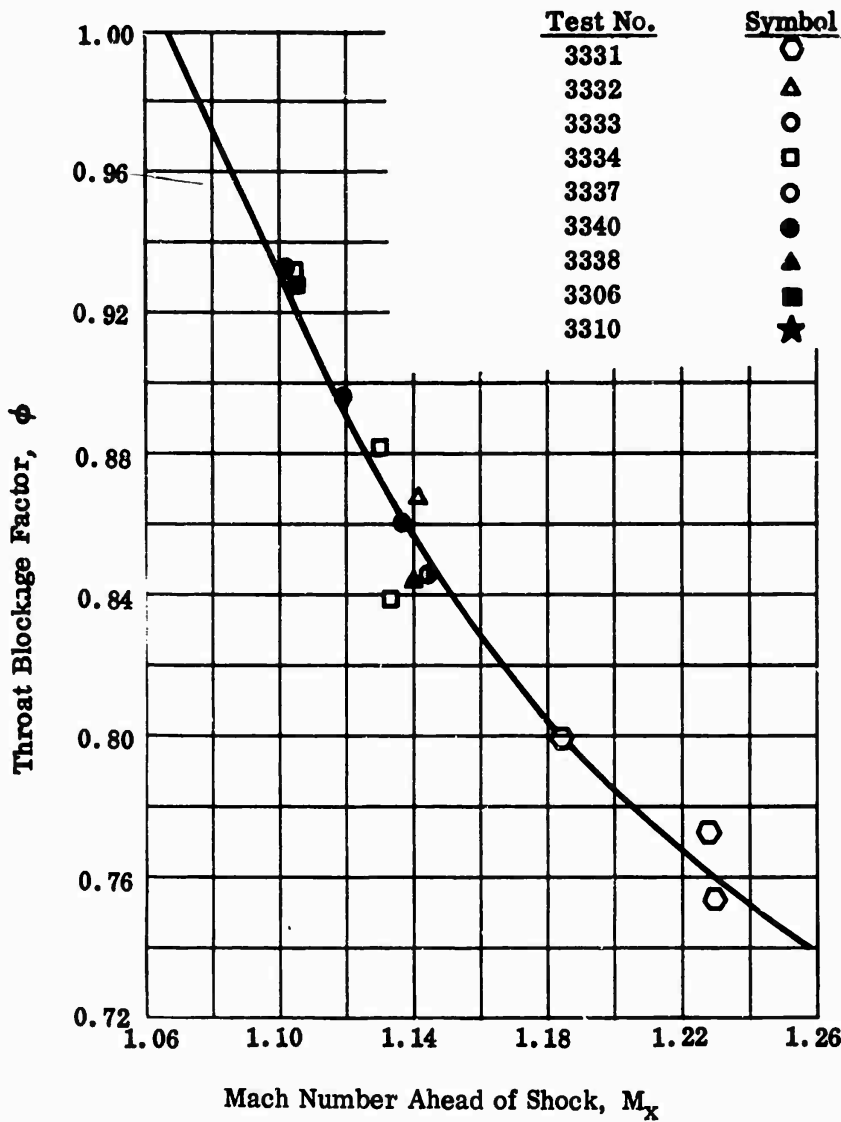


Figure 427. Throat Blockage Factor Versus Mach Number Ahead of Shock.

UNCLASSIFIED

It should also be noted that the performance of the compressor channels is slightly better than that of the single channel, which might be expected from the high-turbulence level of the actual entry flow in the compressor compared to the single-channel rig. The high turbulence would tend to keep the blockage lower for a given Mach number condition and energize the boundary layer in the diffuser.

7.2.10 VARIABLE AIRFLOW

Tests on variable airflow capacity were conducted to determine if the airflow of a high-pressure-ratio single-stage compressor can be significantly reduced by rotating the vanes to change the throat area while holding the incidence to the surface constant. A previous contractor-sponsored research program successfully demonstrated significant airflow changes for lower-pressure-ratio compressors. The diffuser throat area was reduced with a blade-height change rather than by rotating the vanes (see Section 2.0, Analytical Studies). The overall compressor performance to measuring Station I with the DI-1 diffuser is presented in Figure 315 for 50,000 rpm and Figure 317 for 39,000 rpm (see Section 6.0). Figure 317 shows that the airflow of DI-1 was reduced an amount corresponding to the throat area changes at 50,000 rpm. However, when the throat area was increased above 100 percent, the airflow did not respond and the flow range was reduced, and flow choking in the impeller was indicated (the diffuser was not yet choked). The compressor efficiency dropped off for each vane position tested, which was as expected. During the contractor-sponsored program, the extreme incidence at the inducer was corrected with adjustable inlet guide vanes.

These tests conducted in the Army program showed that the flow at surge could be varied as necessary by adjusting the diffuser. Considerable loss was introduced at 50-percent airflow; however, this loss could be corrected with an inlet guide vane. Since the adjustable airflow concept was demonstrated, no further tests of this type were conducted in order to concentrate the efforts at design airflow.

7.2.11 RADIUS RATIO

Tests were also conducted to determine the effects of diffuser-vane leading-edge radius ratio on performance. A comparison of the compressor performance with the diffuser vanes set at 1.06 and 1.10 radius ratio (Figure 320, Section 6.0) shows essentially no performance difference.

In light of the proposed model of the diffuser flow, it is apparent that a radius ratio change from 1.06 to 1.10 should not have a large effect on performance. These early tests were planned using a conventional approach, based on the theory that the flow at the vane leading edge would be subsonic, having undergone a transition in the vaneless space. However, the new flow model shows that the Mach number must be essentially constant to satisfy the Euler-n equation in the

UNCLASSIFIED

vaneless and semi-vaneless spaces. Therefore, the small change in radius ratio should produce little effect on the overall performance or airflow range.

7.2.12 LOW-SPEED SCHLIEREN DATA

The previous discussion related to the test and analysis at design speed (50,000 rpm), where the impeller-tip Mach number was near 1.3. Also of concern were the flow characteristics and diffuser performance at lower wheel speeds. The Mach number at the impeller tip reaches 1.0 at 33,500 rpm. Referring to Appendix X, schlieren photographs are presented for DI-1 from 15,000 to 50,000 rpm. At 15,000 rpm the impeller-tip Mach number is just over 0.6 and no shock system is visible. However, at 20,000 rpm, where the impeller-tip Mach number is only 0.75, shocks can be seen on the vane pressure surface near the leading edge and in the channel. The shocks show that the flow accelerated around the nose of the vane, went through a two-dimensional shock, reaccelerated to Mach 1.0 at the throat exit, expanded supersonically in the channel, and finally went through a normal shock. It was concluded that this flow process introduced extra loss in the overall diffuser from many sources, because the flow accelerated and required diffusion at high Mach numbers, similar to the cases at higher speed.

One of the series of schlieren photographs in Appendix X shows DI-2 at varying speeds. The throat shock system does not occur at 20,000 rpm, but does show up at 25,000 rpm, where the impeller-tip Mach number is near 0.85. Since the throat area of DI-2 is larger than DI-1, it suggests that a different design philosophy may be necessary to obtain maximum performance at lower tip-speed compressor designs. The larger area and lower throat Mach number may be necessary to avoid the shock complication. It is presumed that at the lower wheel speed and impeller-tip Mach number, the airflow range would not be shortened by a larger throat, as was the case at design speed. Other schlieren photographs in Appendix X are given for the 16-channel vane-island diffuser (DI-3). The throat design Mach number of DI-3 was the same as DI-2 ($M_t = 0.75$). The schlieren photographs again show that the shock system did not occur in DI-3 until near 25,000 rpm, which is similar to the DI-2 case.

7.2.13 CASCADE TESTS

The first test of the cascade diffuser (3308) showed that pressure recovery and flow range were below expectations. Furthermore, investigation of the total-pressure profile at the tip of the impeller revealed that the total pressure had been adversely affected by the cascade diffuser. Data analysis and the earlier investigation on the water table showed that excessive flow incidence caused a strong supersonic expansion on the underside (suction surface) of the vanes. This expansion was believed to extend into the impeller, causing the deterioration of impeller performance.

UNCLASSIFIED

CONFIDENTIAL

To correct this situation the vanes were restaggered 2 degrees to 84.4 degrees. However, the throat area of the cascade was kept constant to pass the design air-flow. Achieving the required area was accomplished by the modification shown in Section 6.2.4. The retest (3308A) with the modified and restaggered vanes produced approximately the same results as the first test.

A third test was run with the same vanes restaggered to 86.4 degrees (3308B). Figure 355 shows that this configuration produced an increase in range and pressure recovery, but the values were still far below expectations. The total-pressure profile at the tip of the impeller showed that the pressure at full flow was up to almost the level of DI-1 (Test 3306B). However, at reduced airflow the pressure was still below predictions.

Analysis of the data showed that the aerodynamic loading of the cascade was too high for good performance to be achieved. In the radial-flow field at the impeller tip, the flow without vane interference tends to follow the path of a log spiral. Calculations showed that effective air turning with straight vanes was 14 degrees, resulting in a diffusion factor of 0.86 through the vanes.

These results were not predictable from the earlier water-table tests, which had shown that the straight vanes could be used successfully. The effects of high diffusion with the expansion on the suction surface were believed to have resulted in conditions that caused large separations and wakes through the vanes. In addition, the shock patterns produced by the 31 vanes and their closely spaced reflections into the impeller were presumed to have influenced the flow field to a far greater extent than expected. These conditions were found to be significantly different from the vane-islands, and changes in vane shape to add camber were studied. However, if this change were incorporated, it was apparent that the shock pattern would persist. Furthermore, a large number of tests would be required to develop the cascade diffuser to obtain a performance level comparable to the vane-island-type diffuser.

It was concluded that the expenditure of effort required to refine the cascade was beyond the time phasing of the program and would dilute the research necessary to develop the flow model of the vane-island-type diffusers. In addition, the better potential shown by the vane-island tests led to the decision that further work on the cascade be deleted from the program.

7.2.14 DIFFUSER DESIGN METHOD

It has been shown that the major static-pressure rise through the diffuser occurs in the diverging channel and that the channel static-pressure recovery is dependent on throat-entrance blockage and the entrance Mach number.

CONFIDENTIAL

REF ID: A66012

The channel diffusers tested in this program were designed with a straight section at the diffuser throat, and it was determined that channel performance was dependent on the relation of this throat length to the diffuser-entrance Mach number. In addition, the entrance subsonic Mach number accelerated through the throat straight section in accordance with Fanno line calculations. If the throat has a critical length with respect to the entrance Mach number, the flow at the throat exit will be sonic. Therefore, the flow at this condition may undergo supersonic acceleration into the diffuser channel and will be accompanied by a normal shock. At shock entrance Mach numbers above 1.1 to 1.2, the channel performance deteriorates rapidly as shown by the two-dimensional channel-diffuser data in Appendix XII. The best channel performance with respect to inlet conditions and geometry is also shown in Appendix XII.

Based on the flow model, and the analyses in Sections 7.2.1 through 7.2.12, the following general guidelines are presented for the diffuser design to be used in a high-pressure-ratio centrifugal compressor.

- 1) Determine the total pressure, total temperature, and flow angle after mixing in the vaneless space. Based on these impeller parameters the radius ratio where mixing is complete should be determined. Locate the leading edge of the diffuser vane at the radius where impeller mixing is complete. Because little diffusion takes place in the vaneless space, there is no advantage in designing for a larger radius ratio.
- 2) Design the vane suction surface with an angle equal to the flow angle after mixing.
- 3) Establish the suction-surface contour using the log spiral equation as a first-try guideline.
- 4) A proper balance must be established among the throat area, blockage, diffuser-throat thermodynamic state and Mach number upstream of the entry shock. The boundary-layer growth through the vaneless and semivaneless spaces can be estimated by using flat-plate boundary-layer theories; however, because no reliable analysis is available to predict the sudden growth of boundary layer through the entry shock, the data correlation between entrance Mach number, blockage factor, and channel static-pressure recovery can be used to determine the throat-design conditions and the final channel static-pressure recovery. The throat entrance Mach number should be 0.8 to 0.9 and the throat straight section must be short enough to avoid reacceleration of the flow to Mach 1.0 at throat exit.

REF ID: A66012

UNCLASSIFIED

- 5) Optimum diffuser-channel performance can be predicted on the basis of throat blockage and throat aspect ratio. The compressible 2-dimensional-diffuser data presented in Appendix XII can be used directly for the diffuser-channel design.

UNCLASSIFIED

(U) REFERENCES

1. Johnsen, Irving A. and Bullock, Robert O., Aerodynamic Design of Axial-Flow Compressor, NASA SP36, 1965.
2. Hamrick, J. T., Ginsburg, A., and Osborn, W.M., Method of Analysis for Compressible Flow Through Mixed Flow Centrifugal Impellers of Arbitrary Design, NACA 1082, 1952.
3. Keenan, J. H. and Kaye, J., Gas Tables-Thermodynamic Properties of Air, Products of Combustion and Component Gases, Compressible Flow Functions, John Wiley and Sons, Inc., New York, N. Y., 1948.
4. Stanitz, J. D. and Prian, V. D., A Rapid Approximate Method for Determining Velocity Distribution in Impeller Blades of Centrifugal Compressors, NACA TN 2421, July 1951.
5. Stahler, Alfred F., The Slip Factor, ASME 64 GTP-1, 1963.
6. Stahler, Alfred F., Transonic Flow Problems in Centrifugal Compressors, SAE 268C, January 1961.
7. Patterson, G. N., "Modern Diffuser Design," Aircraft Engineering, Vol. 10, No. 115, pp 267-273, September 1938.
8. Henry, J. R., Design of Power Plant Installations Pressure-Loss Characteristics, NACA, No. L4F26, 1945.
9. Shapiro, Ascher H., The Dynamics and Thermodynamics of Compressible Fluid Flow, Volumes I and II, The Rolland Press Company, New York, New York, 1953.
10. Laitone, E. V., "A Study of Transonic Gas Dynamics by the Hydraulic Analogy," Journal of the Aeronautical Sciences, p 265, April 1952.
11. Northern Research and Engineering Corporation, The Design and Performance Analysis of Radial-Inflow Turbines, Volumes I and II; Cambridge, Mass., 1963.
12. Stanitz, J. D., One-Dimensional Compressible Flow in Vaneless Diffusers of Radial and Mixed Flow Centrifugal Compressors, NACA TN 2610, January 1952.
13. Brown, W. B., Friction Coefficients in a Vaneless Diffuser, NACA TN 1311, 1947.

REFERENCES (Continued)

14. Faulders, C. R., Experimental and Theoretical Study of Vaneless Diffuser Flow with Supersonic Entry, M.I.T. Gas Turbine Laboratory, Massachusetts Institute of Technology, Cambridge, Mass., June 1952.
15. Johnston, J. P. and Dean, R. C., "Losses in Vaneless Diffusers of Centrifugal Compressors and Pumps," Journal of Basic Engineering, Vol. 87, Series D, 1965.
16. Henry, J. R. and Wood, C. C. and Wilbur, S. W., Summary of Subsonic Diffuser Data, NACA RML56F05, October 12, 1956.
17. Friedlich, Sylvain, Performance Characteristics of Plane Wall Diffuser and Some New Concepts of Diffuser Flow Mechanisms, Volume W, University of Washington, Seattle, Washington, 1959.
18. Schlichting, Hermann, Boundary Layer Theory, McGraw, New York, N. Y., 1955.
19. Volluz, R. J., Handbook of Supersonic Aerodynamics, Naval Ordnance Report 1488, Volume 6, Bureau of Naval Weapons, January 1961.
20. Coppage, J. E., et al, Study of Supersonic Radial Compressors for Refrigeration and Pressurization Systems, WADC Technical Report 55-257, ASTIA Document Number AD 110467, Wright Air Development Center, Dayton, Ohio, December 1956.
21. Jansen, W., Quasi-Steady Flow in a Vaneless Diffuser, M.I.T. Gas Turbine Laboratory, Massachusetts Institute of Technology, Cambridge, Mass., Report No. 60, 1960.
22. vonDoenhoff, A. C. and Tetervin, N., Determination of General Relations for the Behavior of Turbulent Boundary Layers, NACA Report 772, 1943.
23. Dean, R. C. and Senoo, Y., "Rotating Wakes in Vaneless Diffusers," Journal of Basic Engineering, Volume 82, Series D, September 1960.
24. Glauert, H., The Elements of Aerofoil and Airscrew Theory, Cambridge University Press, New York, N. Y., 1948.
25. Riegels, F., "Das Umstromungsproblem Bei Inkompressiblen Potentialströmungen," Ingenieur-Archiv Vol. 16, pp. 373-376, 1948, and Vol. 17, 94-106, 1949.

REFERENCES (Continued)

25. Schlichting, H., "Berechnung der Reibungslosen Inkompressiblen Stromung fur Ein Vorgegebenes Ebenes Schaufelgitter," Verein Deutscher Ingenieure-Forschungsheft, Number 464, 1957.
27. Schlichting, H., "Problems and Results of Investigations on Cascade Flow," Journal of Aeronautical Sciences, Vol. 21, p 163, March 1954.
28. Miline-Thompson, L. M., Theoretical Hydrodynamics, MacMillan, New York, N. Y., 2nd Edition, 1950.
29. Rains, Dean A., Tip Clearance Flows in Axial Flow Compressors and Pumps, CIT Report No. 5, California Institute of Technology, Pasadena, Calif., June 1954.
30. Emery, J. C., Dunavant, J. C., and Westphal, W. R., Experimental Investigation of a Transonic Compressor Cascade and Test Results for Four Blade Sections, NASA TMX-197, January 1960.
31. Wood, G. P. and Gooderum, P. P., A Factor Affecting Transonic Leading-Edge Flow Separation, NACA TN 3804, 1956.
32. Pearcey, H. H., "Shock-Induced Separation and Its Prevention by Design and Boundary Layer Control." Boundary Layer and Flow Control. Edited by Lachman, G. V., Vol. 2, Pergamon Press, New York, N. Y., 1961.
33. Sinnott, C. S. and Osborn, J., Review and Extension of Transonic Aerofoil Theory, Aeronautical Research Council Reports and Memoranda, No. 3156, October 1958.
34. Randall, D. G., Transonic Flow Over Two-Dimensional Round-Nosed Aerofoils, Royal Aircraft Establishment, Technical Note Number Aero. 2579, September 1958.
35. Lindsey, W. F., Daley, Bernard N. and Humpherys, Milton D., The Flow and Force Characteristics of Supersonic Airfoils at High Subsonic Speeds, NACA TN 1211, March 1947.
36. Clauser, F. H., "The Turbulent Boundary Layer," Advanced Applied Mechanics, Vol. IV, Academic Press, Inc., New York, N. Y., 1956.
37. Lieblein, Seymour, Experimental Low-Speed Loss and Stall Characteristics of Two-Dimensional Compressor Blade Cascades, NACA RM E5 7A28, 1957.

REFERENCES (Continued)

38. Neumann, E. P. and Lustwerk, F., "Supersonic Diffusers for Wind Tunnels," Journal of Applied Mechanics, June 1949.
39. Stodola and Loewenstein, Steam and Gas Turbines, Vol. I, pp 82-105, 1945.
40. Fox, R.W. and Kline, S.J., "Flow Regime Data and Design Methods for Curved Subsonic Diffusers," ASME, Journal of Basic Engineering, Vol. 84, Series D, pp 303-312, September 1962.
41. McDonald, A. T. and Fox, R.W., Incompressible Flow in Conical Diffusers, Purdue Research Foundation, Project No. 3684, Technical Report No. 1, September 1964.
42. Reneau, L.R., Johnston, J.P. and Kline, S.J., Performance and Design of Straight, Two-Dimensional Diffusers, Thermosciences Division Report No. PD-8, Stanford, Calif., September 1964.
43. Welliver, A.D. and Acurio, J., Design and Development of Small, Single-Stage Centrifugal Compressor: (U) (Classified Confidential), USAAVLABS Technical Report 67-47 (to be published).

DOCUMENT CONTROL DATA - R&D		
(Security classification of title, body of abstract and indexing annotation must be entered when the overall report is classified)		
1. ORIGINATING ACTIVITY (Corporate author)		2a. REPORT CLASSIFICATION
The Boeing Company Seattle, Washington		2b. GROUP
3. REPORT TITLE		
Element Design and Development of Small Centrifugal Compressor (U) - Volume I		
4. DESCRIPTIVE NOTES (Type of report and inclusive dates)		
5. AUTHOR(S) (Last name, first name, initial)		
Welliver, A. D. Acurio, J.		
6. REPORT DATE	7a. TOTAL NO. OF PAGES	7b. NO. OF REFS
August 1967	723	43
8a. CONTRACT OR GRANT NO.	8a. ORIGINATOR'S REPORT NUMBER(S)	
DA 44-177-AMC-173(T)	USAAVLABS Technical Report 67-30	
b. PROJECT NO.	9b. OTHER REPORT NO(S) (Any other numbers that may be assigned this report)	
Task 1M121401D14413	D4-3434	
c.		
d.		
10. AVAILABILITY/LIMITATION NOTICES		
In addition to security requirements which apply to this document and must be met, each transmittal outside the agencies of the US Government must have prior approval of US Army Aviation Materiel Laboratories, Fort Eustis, Virginia 23604.		
11. SUPPLEMENTARY NOTES		12. SPONSORING MILITARY ACTIVITY
		US Army Aviation Materiel Laboratories Fort Eustis, Virginia
13. ABSTRACT		
<p>This research program involved the advancement of single-stage centrifugal compressor technology to attain high pressure ratio (10:1) at a usable efficiency. The main elements, namely, the impeller and the diffuser, were designed, tested, and developed as elements; the results are analyzed and described.</p> <p>An analysis of the loss of flow through the impeller passage and conditions contributing to early flow separation are discussed as well as suggestions for their prevention. The flow behavior in the vaneless and semivaneless areas and in the channel passage was evaluated from pressure data and schlieric photographs.</p>		

14. KEY WORDS	LINK A		LINK B		LINK C	
	ROLE	WT	ROLE	WT	ROLE	WT
Compressor: Single-Stage Centrifugal High-Pressure-Ratio						

INSTRUCTIONS

1. **ORIGINATING ACTIVITY:** Enter the name and address of the contractor, subcontractor, grantee, Department of Defense activity or other organization (*corporate author*) issuing the report.

2a. **REPORT SECURITY CLASSIFICATION:** Enter the overall security classification of the report. Indicate whether "Restricted Data" is included. Marking is to be in accordance with appropriate security regulations.

2b. **GROUP:** Automatic downgrading is specified in DoD Directive 5200.10 and Armed Forces Industrial Manual. Enter the group number. Also, when applicable, show the optional markings have been used for Group 3 and Group 4 as authorized.

3. **REPORT TITLE:** Enter the complete report title in all capital letters. Titles in all cases should be unclassified. If a meaningful title cannot be selected without classification, show title classification in all capitals in parenthesis immediately following the title.

4. **DESCRIPTIVE NOTES:** If appropriate, enter the type of report, e.g., interim, progress, summary, annual, or final. Give the inclusive dates when a specific reporting period is covered.

5. **AUTHOR(S):** Enter the name(s) of author(s) as shown on or in the report. Enter last name, first name, middle initial. If military, show rank and branch of service. The name of the principal author is an absolute minimum requirement.

6. **REPORT DATE:** Enter the date of the report as day, month, year; or month, year. If more than one date appears on the report, use date of publication.

7a. **TOTAL NUMBER OF PAGES:** The total page count should follow normal pagination procedures, i.e., enter the number of pages containing information.

7b. **NUMBER OF REFERENCES:** Enter the total number of references cited in the report.

8a. **CONTRACT OR GRANT NUMBER:** If appropriate, enter the applicable number of the contract or grant under which the report was written.

8b, 8c, & 8d. **PROJECT NUMBER:** Enter the appropriate military department identification, such as project number, subproject number, system numbers, task number, etc.

9a. **ORIGINATOR'S REPORT NUMBER(S):** Enter the official report number by which the document will be identified and controlled by the originating activity. This number must be unique to this report.

9b. **OTHER REPORT NUMBER(S):** If the report has been assigned any other report numbers (*either by the originator or by the sponsor*), also enter this number(s).

10. **AVAILABILITY/LIMITATION NOTICES:** Enter any limitations on further dissemination of the report, other than those imposed by security classification, using standard statements such as:

- (1) "Qualified requesters may obtain copies of this report from DDC."
- (2) "Foreign announcement and dissemination of this report by DDC is not authorized."
- (3) "U. S. Government agencies may obtain copies of this report directly from DDC. Other qualified DDC users shall request through _____."
- (4) "U. S. military agencies may obtain copies of this report directly from DDC. Other qualified users shall request through _____."
- (5) "All distribution of this report is controlled. Qualified DDC users shall request through _____."

If the report has been furnished to the Office of Technical Services, Department of Commerce, for sale to the public, indicate this fact and enter the price, if known.

11. **SUPPLEMENTARY NOTES:** Use for additional explanatory notes.

12. **SPONSORING MILITARY ACTIVITY:** Enter the name of the departmental project office or laboratory sponsoring (*paying for*) the research and development. Include address.

13. **ABSTRACT:** Enter an abstract giving a brief and factual summary of the document indicative of the report, even though it may also appear elsewhere in the body of the technical report. If additional space is required, a continuation sheet shall be attached.

It is highly desirable that the abstract of classified reports be unclassified. Each paragraph of the abstract shall end with an indication of the military security classification of the information in the paragraph, represented as (TS), (S), (C), or (U).

There is no limitation on the length of the abstract. However, the suggested length is from 150 to 225 words.

14. **KEY WORDS:** Key words are technically meaningful terms or short phrases that characterize a report and may be used as index entries for cataloging the report. Key words must be selected so that no security classification is required. Identifiers, such as equipment model designation, trade name, military project code name, geographic location, may be used as key words but will be followed by an indication of technical context. The assignment of links, rules, and weights is optional.